Greg McFarquhar

13th International Conference on Clouds and Precipitation

Proceedings – Volume 2

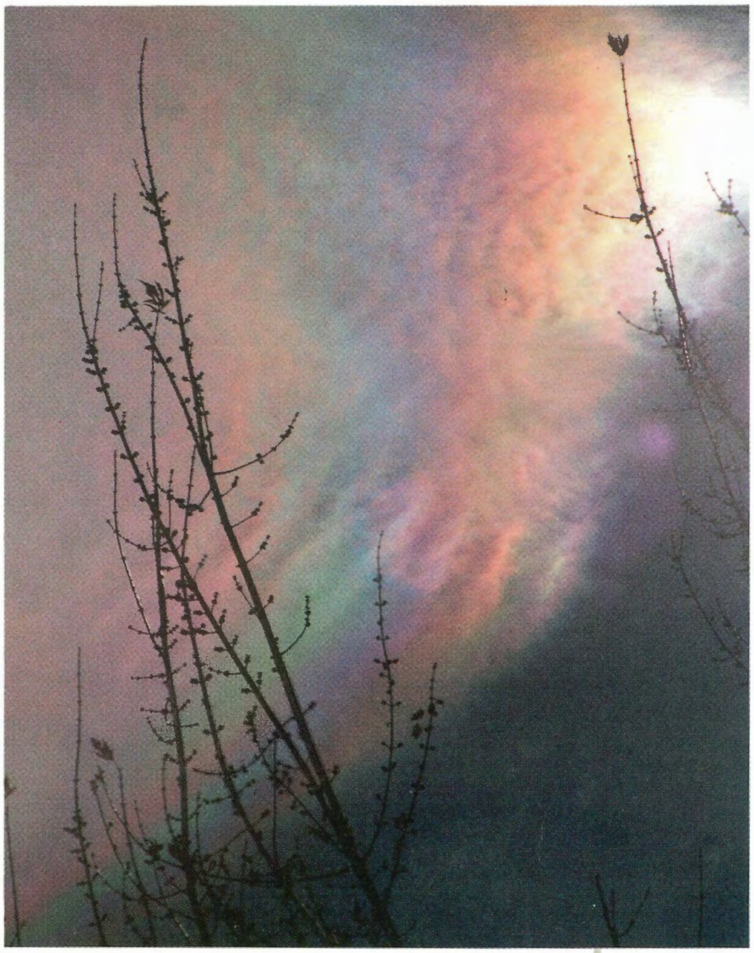

Reno, Nevada USA
14–18 August 2000

International Cloud Physics Meetings

1954	I	4–6 October	Zurich, ETH
1956	II	January	London, Imperial College
1960		9–13 August	ATTI
1961	III	September	Canberra, Sydney
1965	IV	24 May–June 1	Tokyo, Sapporro
1968	V	26–30 August	Toronto
1972	VI	August	London, Royal Society
1976	VII	26–30 June	Boulder, Bur. St.
1980	VIII	15–19 July	Clermont Ferrand
1984	IX	21–28 August	Tallinn
1988	X	15–20 August	Bad Homburg
1992	XI		Montreal, McGill
1996	XII	19–23 August	Zurich, ETH
2000	XIII	14–18 August	Reno, DRI

Proceedings
Volume 2
(Pages 661-1318)

13th International Conference on Clouds and Precipitation

Sponsored by
International Commission on Clouds and Precipitation (ICCP) of the International Association of Meteorology and Atmospheric Sciences

Supported by
World Meteorological Organization
American Meteorological Society
Desert Research Institute
Meteorological Service of Canada

Hosted by
Desert Research Institute
Reno, Nevada

Front Cover – Diffraction colors in a wave cloud suggests droplet growth and evaporation with a narrow size spectrum

Back Cover – Extreme shear above rapidly evolving rotor clouds downwind of the Sierra mountains (21 November, 1998), demonstrating the presence of narrow sheets and filaments of cloud. Time between sequences: 15 seconds

Welcome to Reno – the Biggest Little City in the World!

As we welcome participants to the 13th International Conference on Clouds and Precipitation, we do so from a perspective that our subject is putting on our shoulders a responsibility to the scientific community which was not there before. More than ever, the enjoyment and interpretation of cloudscapes are taking second place to application of our knowledge in important political and technological decisions. Such decisions are based on an assessment of complex atmospheric processes including, for example, the influence of cloud particles on the global radiation budget or atmospheric chemical reactions.

Fundamental to this responsibility is assessing the reality—or otherwise—of how our technological society is influencing global climate through the generation and use of energy. This involves use of satellite remote sensors to attempt to retrieve cloud properties on a global scale, leading to insights into energy budgets related to radiation absorption and scatter, and latent heat transfer through different phase changes.

Meanwhile, more immediate problems include predicting likely precipitation rates, providing accurate warnings of severe storms, and assessing the impact of clouds on air quality. Solutions to these challenges require improved interpretations of radar signatures and more reasonable parameterizations within numerical weather and air quality forecast models. With all of these endeavors, from the use of remote sensing to improved modeling, there is a great danger that our drive for simplicity will lead to divergence from the reality we seek, and thus result in misleading information. Herein lies our responsibility.

We must advance the concept that algorithms for computing things work better if they are based on physical or chemical insight. This has been considered heretical in some circles and may have slowed advance in both understanding and representing certain problems. And there are areas where our understanding is still thin—the nature and role of mixing processes on a variety of scales, ice nucleation, the role of the surface layer on ice, and cloud electrification, to name a few.

Our perspective must encompass all approaches—observational, experimental, theoretical, and numerical. We seek to further our basic understanding as well as promote application to topics possibly well outside our immediate interests. Our goal for this meeting must be to further these objectives by successfully following the long tradition of scientific leadership set by the preceding International Conferences on Clouds and Precipitation.

John Hallett – Chair, Local Arrangements
George Isaac – Chair, Program Committee

June 2000

Paper	Table of Contents for Papers	Page

Paper | Table of Contents for Papers | Page

Paper	Table of Contents for Papers	Page

Paper | # Table of Contents for Papers | Page

Session 3: WARM CLOUD MICROPHYSICS

Paper	Table of Contents for Papers	Page

Sessions 1 - 9.1, pages 1-660, are in Volume 1
Sessions 9.2 - 19, pages 661-1318 are in Volume 2

13th International Conference on Clouds and Precipitation
Reno Area, Nevada, USA
14-18 August 2000

Conference Organization

International Commission on Clouds and Precipitation

G.A. Isaac*, President	Canada	G. Vali*, Vice President	USA
B. Albrecht	USA	S. Bakan*	Germany
J.-L. Brenguier*	France	A. Blyth	USA
R. Bruintjes	USA	A. Chernikov	Russia
A. Flossman*	France	P.C.S. Devara*	India
D. Hegg*	USA	S. Fuzzi*	Italy
J. Joss	Switzerland	J. Jensen*	Australia
M. Murakami*	Japan	A. Korolev	Canada
C.M. Platt	Australia	Z. Levin*	Israel
R. Rosset	France	M. Nicolini*	Argentina
A.S. Stepanov	Russia	D. Starr*	USA
H. Sundqvist	Sweden	J. Stith*	USA
B. Wielicki	USA	G. Zhang*	P.R. China
M.K. Yau	Canada		

Honorary Members: Sir John Mason, UK and H. Pruppacher, Germany
Past Presidents: P. Jonas*, UK and P. Hobbs, USA

* Program Committee Members along with John Hallett of DRI. The Program Committee also wishes to express its appreciation to Elena Korolev and Natty Urquizo for their assistance.

Local Arrangements Committee

John Hallett, Chair, Desert Research Institute (DRI)
Peter Barber, DRI
James Hudson, DRI
Marcin Szumowski, DRI
Marilyn Allen, DRI
Margie Stuart, DRI
Morien Roberts, DRI
Roger Kreidberg, DRI
Olga Garro, DRI

Paper	Table of Contents for Papers	Page

Paper	Table of Contents for Papers	Page

Paper	Table of Contents for Papers	Page

Session 10: BOUNDARY LAYER CLOUDS

Paper	Table of Contents for Papers	Page

SESSION 12: **CLOUD CHEMISTRY**

Paper	Table of Contents for Papers	Page

Session 13: CLOUD ELECTRICITY

Session 14: HAIL

SESSION 19: CONVECTIVE CLOUDS

Paper	Table of Contents for Papers	Page

List of Authors

List of Authors

List of Authors

CONVECTIVE CLOUDS WITH SUSTAINED HIGHLY SUPERCOOLED LIQUID WATER UNTIL –38°C

Daniel Rosenfeld[1] and William L. Woodley[2]

[1]Inst. of Earth Sciences, the Hebrew University of Jerusalem, Jerusalem 91904, Israel
[2]Woodley Weather Consultants, 11 White Fir Court, Littleton, CO 80127, USA

1. INTRODUCTION

Highly supercooled water at temperatures < -35°C were previously observed in small quantities < 0.15 gm^{-3} in cirrus (Sassen, 1985) and orographic wave clouds (Heymsfield and Miloshevich, 1993). The high supercooling was attributed to the very small droplet size and to the lack of ice nuclei at these heights. No similar measurements were reported for deep convective clouds, which have much larger droplets near their tops (>10 mm) and ingest aerosols from near the ground. However, remote sensing from satellites (Rosenfeld and Lensky, 1998) suggested that highly supercooled water up to nearly –40°C is a common occurrence in vigorous continental convective storms. To validate that, in situ measurements with a Lear Jet have shown that most of the condensed water remained liquid droplets up to –37.5°C, where they reached median volume diameter of 17-mm and amounted to 1.8 gm^{-3}, which is 13 times the previous maximum report (Heymsfield and Miloshevich, 1993). Only ice was found at slightly colder temperature, suggesting homogeneous freezing. Because of the poor knowledge of mixed phase cloud processes (Pruppacher and Klett, 1997), cloud models cannot properly simulate them. Therefore, the insights from these unique observations have major implications for rainfall, hail, cloud-electrification and climate.

2. PREVIOUS OBSEVATIONS

Cloud droplets do not readily freeze at 0°C, but often remain liquid at colder temperatures in a "supercooled" state. The cloud droplets can freeze by either ice nuclei or by homogeneous freezing. The lowest temperatures to which pure water droplets can exist in a supercooled state for times longer than a fraction of a second before homogeneously freezing depends on the drop size. According to both theory (Jeffery and Austin, 1997) and laboratory experiments (Pruppacher, 1995), a 10-mm cloud droplet freezes homogeneously near –39°C. The coldest previously reported *in situ measurements* of supercooled liquid water content (SLWC) colder than –32°C, in excess of the sensitivity of the measuring instruments (0.02 gm^{-3} for hot wire probes, Heymsfield and Miloshevich, 1989), was 0.14 gm^{-3} at –36°C, measured in 1989 by Heymsfield and Miloshevich in orographic lenticular wave clouds.

Corresponding author's address: Daniel Rosenfeld, Inst. of Earth Sciences, The Hebrew University of Jerusalem, Jerusalem 91904, Israel;
E-Mail: Daniel@vms.huji.ac.il.

Sassen, in 1985, reported SLWC of 0.06 gm^{-3} at the base of cirrus clouds, between –35° and –36°C. He stated that "*in comparison with earlier reported aircraft measurements, the detection of such highly supercooled water is unique*".

Both reports (Sassen, 1985; Heymsfield and Miloshevich, 1993) suggested that the dearth of ice nuclei derived from the earth's surface at the upper troposphere prevented heterogeneous nucleation, allowing for the observed homogeneous nucleation at such cold temperatures in altocumulus and cirrus clouds (Sassen, 1992). No previous reports are available for observations of similar highly supercooled water and homogeneous freezing in convective clouds with roots near the surface. In view of the reported findings to the contrary here, one can only speculate about the reasons they have not been reported previously:

- Low priority was given to such measurements, because it was felt that clouds ingesting air rich in ice nuclei from the boundary layer would glaciate long before reaching the point of homogeneous freezing (Houghton, 1985).
- The safety problems involved in penetrating vigorous cumulonimbus towers at the –30° to –40°C isotherm levels in storms that typically contain hail and frequent lightning.

The first indications available to the authors that highly supercooled water might exist in convective clouds were obtained by remote sensing from satellites over Thailand, using the technique developed by the first author (Rosenfeld and Lensky, 1998). The inference of supercooled water at temperatures below –30°C prompted the authors to fly with the Thai King Air cloud physics aircraft to measure the cloud microstructure in Thailand clouds. Penetrating feeders of cumulonimbus clouds, a SLWC of 2.4 gm^{-3} was measured at the operational ceiling of the aircraft (9300 m above sea level) at a temperature of –31.6°C (Sukarnjanaset et al., 1998). The cloud base temperature was +13°C at 2800 m above sea level. The SLWC was measured by the King hot wire instrument.

3. THE NEW OBSERVATIONS

The satellite inferences with the methodology of Rosenfeld and Lensky (1998) suggested that supercooled water occasionally occurred at temperatures approaching –40°C in cumulonimbus clouds over the western USA. An opportunity to validate these satellite inferences came when Weather Modification, Inc. gave the authors access to its Lear jet cloud physics aircraft in the period 9-14 August 1999 for measurements in Texas clouds. The aircraft cloud physics instrumentation included:

- Hot wire cloud liquid water probe, model LWC-100, manufactured by Droplet Measurement Technologies (DMT). The measurement efficiency of the sensor depends on the drop sizes. For the observed distribution it underestimated the SLWC by not more than 10%.
- Air temperature probe, model 102AU1AP, manufactured by Rosemount.
- Forward Scattering Spectrometer Probe (FSSP) for the range 0.5-47 mm, model FSSP-100, manufactured by Particle Measuring Systems Inc.
- Optical array particle imaging probe, for the range 25-800 mm, model OAP-2D2-C, manufactured by Particle Measuring Systems Inc.

High level measurements in the tops of vigorous growing convective elements of cumulonimbus clouds were done with the Lear Jet on 11 and 13 August 1999. The authors, also the flight scientists onboard the Lear Jet, selected for penetration the visibly most-vigorous new convective elements as they grew through the measurement flight level. In addition, extensive measurements were made at all levels down to cloud base for documenting the vertical microphysical evolution of the cloud. Cloud base on both days was near 3500 m at a temperature of 10°C.

On the flight of 11 August (20:28-23:42 GMT) just to the west of Lubbock, Texas (34N 102W), a supercooled liquid water content (SLWC) of 0.6 gm^{-3} was observed at –35.9°C, 0.9 gm^{-3} at –35.6°C, and 1.5 gm^{-3} at –34.4°C. Larger SLWC, up to 2.4 gm^{-3}, were recorded at warmer cloud temperatures. Direct measurements of the updraft velocity were not available. However, a rate of climb of 6 m/sec was sufficient to keep up with the rate of growth of the tops of some of the clouds containing highly supercooled water. The residence time of the water was measured by repeated penetrations in the same cloud, which was narrow and clearly isolated. In 3 passes spaced at 3.5-min intervals the temperatures and maximum cloud water contents were 1.2 gm^{-3} at –32.9°C, 1.5 gm^{-3} at –32.7°C, and 0.4 gm^{-3} at –35.2°C. That means that the large amounts of highly supercooled cloud water were not a transient feature, but rather long lasting, with freezing time of about 7 minutes.

On the flight of 13 August (20:26-23:09 GMT), to the north of Midland, Texas (33N 102W), the effort was focused on documentation of the transition from water to ice clouds in vigorous convective elements. Extensive documentation of the clouds from their bases was done as on the 11 August. The vertical evolution of cloud microstructure was found to be similar for both days. Therefore, only figures from the 13 August are provided here. As illustrated in Figure 1A, maximum SLWC values of nearly ½ adiabatic water content was measured throughout the cloud depth, up to the –37.5°C isotherm. The aircraft windshield was instantly covered with rime ice during the readings of high SLWC despite the windshield heater, demonstrating that there was really ample supercooled water at these very low temperatures. An abrupt vanishing of the SLWC was recorded at colder temperatures in the same clouds. The remaining reading of up to 0.2 gm^{-3} in obviously fully glaciated clouds (i.e., at temperatures < -40°C, where theory dictates that droplets >1-mm must freeze homogeneously, Jeffery and Austin, 1997) is attributed to the cooling effect of the frozen cloud drops on the hot wire (Personal communications, D. Baumgardner).

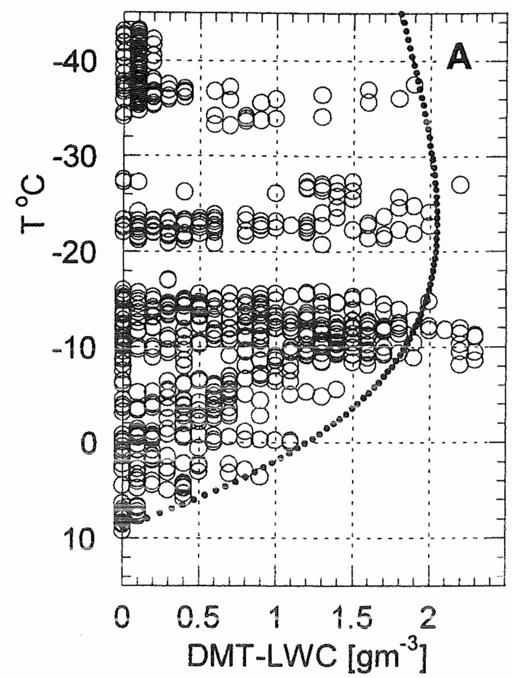

Figure 1: The supercooled cloud liquid water content as a function of temperature, in all the clouds on the 13 August 1999. Each point represents one second of measurements, or 150 - 200 m of cloud path. Note the abrupt decrease of the water at –38°C, indicating the point of homogeneous freezing. The dotted curve marks the ½ adiabatic water content, as reference for the rate of consumption of cloud water to freezing and other processes.

The accuracy of the instrument reading is critical in the context of these findings. A calibration check was made to the instruments before and after the reported flights, and they were found to have been properly calibrated. The temperature readings were validated against the rawinsonde-sounding balloon, which was launched from Midland at 00 GMT, on 14 August. The sounding was quite representative, because it was within 100 km and 1 hour of the time of the aircraft measurements. The intercomparison of the aircraft temperature (T_a) with the sounding temperature (T_s) at the point where 1.8 gm^{-3} of SLWC was measured shows in cloud: Static pressure 265 mb; T_a=-37.5°C; T_s at the same pressure was -38.1°C. Out of cloud in level flight: T_a=-37.5°C at a static pressure of 260 mb whereas T_s was -39.3°C at the same pressure. Direct checks of the temperature probe on the ground provided T_a=+0.4°C at 0°C and T_a=-9.7°C at –10°C. These comparisons suggest that

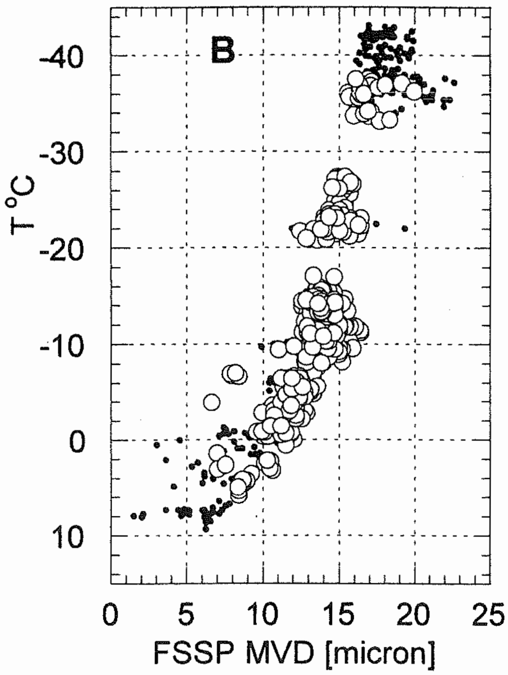

Figure 2: The FSSP measured median volume diameter of the cloud particles as a function of temperature, in all the clouds on the 13 August 1999. Each point represents one second of data, or 150 - 200 m of cloud path, containing more than 100 cm^{-3} FSSP-measured cloud particles. The red symbols denote cloud segments with hot-wire measured liquid water contents $\geq$0.3 gm^{-3}.

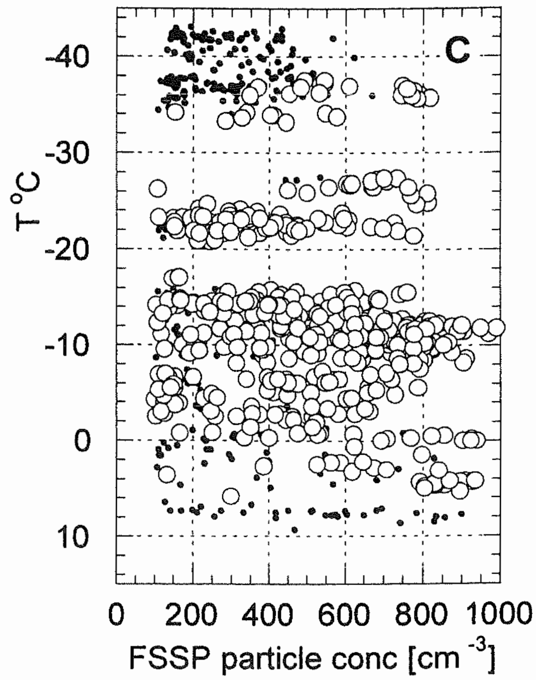

Figure 3: The same as Fig. 2, but for the FSSP-100 measured concentration of cloud particles.

our measurements provide a conservative estimate of the temperature at which homogeneous freezing took place. It might actually have taken place at a slightly lower temperature.

4. THE SIGNIFICANCE OF THE FINDINGS

The lack of significant freezing at higher temperatures, and the sudden freezing at –38°C are indicative of homogeneous freezing as the major glaciating mechanism in the measured convective clouds. This is a remarkable observation with far reaching implications:

- Heterogeneous nucleation by ice nuclei was incapable of freezing much of the cloud water. However, it not likely that it was because of a dearth in ice nuclei. The air ingested into the cloud base had substantial amounts of aerosols of unknown composition. The FSSP measured average concentrations of 0.5 cm^{-3} particles >0.5-mm. Most insoluble aerosols of that size become ice nuclei below –25°C. A possible explanation might be the very small collision efficiencies between the ice crystals that were nucleated heterogeneously and the cloud droplets <~40-mm, for ice crystals <~200-mm[4].
- Most of the water remained in the form of large concentrations of small cloud droplets (Figure 1B), with FSSP measured median volume diameter (MVD) increasing with height, reaching 17 mm at –37.5°C isotherm, just below the height of homogeneous freezing (see Figure 1C).
- The FSSP cannot resolve ice from water. However, the fact that the SLWC was ½ of the adiabatic water content implies the existence of liquid water droplets of at least the MVD size of 17-mm. Such droplets freeze homogeneously near –38°C.
- The nearly constant half adiabatic water content (see Figure 1B) and the small MVD of the cloud droplets suggest that only a small fraction of the cloud water was converted into precipitation. That is confirmed by the 2DC measurements, showing ice particles > ~50 mm exceeding the concentrations > 10 l^{-1} in the high SLWC clouds only at temperatures <-30°C.
- The maintenance of the MVD through the glaciation at –38°C indicates that the cloud droplets freeze into small ice particles, presumably in the form of frozen droplets. That ice is exhausted through the cumulonimbus anvil and is not likely to contribute to the precipitation. Therefore, the observation of the apparent homogeneous freezing in cumulonimbus clouds is indicative of very poor precipitation efficiency.
- The deep layer of high SLWC provides large growth potential for the small concentration of ice precipitation particles that are initiated in the lower parts of the updraft. This means that such highly supercooled and persistent SLWC represents favorable conditions for the growth of large hail.
- Given the empirical necessity for liquid water for appreciable electrification in laboratory experiments (Williams et al., 1991), the extension of supercooled droplets to greater heights above the 0°C isotherm

might explain the observations that deep continental clouds have the strongest electrification of all cumulonimbus types.

It should be noted that the Lear Jet was available for only 6 days, and on only 2 days were attempts made to document the highly supercooled portions of the clouds, although potentially suitable clouds occurred also on other days of that week. The fact that the highly supercooled water was found in two of the two attempts strengthens the evidence from the satellite indications that the reported observations are not rare occurrences. Furthermore, similar observations conducted in the last week of January and first week of February 2000 at Mendoza, Argentina, documented additional five such cases, with up to 4 gm^{-3} of supercooled cloud water at $-38^{o}C$.

5. CONCLUSIONS

The discovery that in some clouds most of the condensed cloud water remains liquid until the point of homogeneous freezing requires a major revision in cloud models simulating rain, hail and cloud electrification. Incorporation of these changes in global circulation models will likely incur substantial differences in our understanding of the way aerosols, clouds and precipitation are affecting the global climate. For example, aerosols that serve as small cloud condensation nuclei, which make the clouds more continental (i.e., with smaller droplets), are likely to reduce their precipitation efficiency and thus inhibit rainfall in polluted areas. The reduced precipitation means more water vapor flux to the upper troposphere and lower stratosphere, and reduced net latent heat release, which in fact change both the radiative and heating forcing of the climate system.

6. ACKNOWLEDGEMENTS

We are most grateful to Mr. Patrick Sweeney, President of Weather Modification, Inc. for providing the WMI Lear jet at no charge for the cloud physics measurements in Texas clouds. We thank also Mr. Roger Tilbury and Mr. Steve Gordon for skillfully piloting the aircraft through the vigorous Texas clouds and Mr. Kelly Bosch for his technical support.

7. REFERENCES

Heymsfield J. A, and L. M. Miloshevich, 1993: Homogeneous ice nucleation and supercooled liquid water in orographic wave clouds. *Jou. Atmos. Scie.*, **50**: 2335-2353.

Heymsfield J. A, and L. M. Miloshevich, 1989: Evaluation of liquid water measuring instruments in cold clouds, sampled during FIRE. *Journal of Atmospheric and Oceanic Technology*, **6**: 378-388.

Houghton H. G., 1985: Physical Meteorology. MIT Press, Cambridge, Mass., 442pp.

Jeffery, C. A., and P. H. Austin, 1997: Homogeneous nucleation of supercooled water: results from a new equation of state. *J. Geophys. Res.*, **102**: 25269-25279.
Pruppacher H. R., 1995: A new look at homogeneous ice nucleation in supercooled water drops. *Jou. Atmos. Scie.*, **52**, 1924-1933.

Pruppacher, H. R., and J. D. Klett, 1997: Microphysics of Clouds and Precipitation. Kluwer Academic Publishers, 954p.

Rosenfeld D. and I. M. Lensky, 1998: Spaceborne sensed insights into precipitation formation processes in continental and maritime clouds. The *Bulletin of American Meteorological Society,* **79**, 2457-2476.

Sassen, K, 1985: Highly supercooled cirrus cloud water: confirmation and climatic implications. *Science*, **227(4685)**: 411-413.

Sassen, K., 1992: Ice nuclei availability in the higher troposphere: implications of a remote sensing cloud phase climatology. In: Fukuta, Norihiko and Wagner, Paul E. (eds.), Nucleation and atmospheric aerosols., Hampton, VA, A. Deepak Publishing. p. 287-290.

Sukarnjanaset, W., P. Sudhikoses, N. Tantipubthong, W.L. Woodley and D. Rosenfeld, 1998: Cloud water, rainwater, temperature and draft relationships in Thai supercooled convective clouds. Preprints, *AMS Conf. On Cloud Physics* 17-21 August 1998, Seattle, Washington.

Williams, E. R., R. Zhang, and J. Rydock, 1991: Mixed-phase microphysics and cloud electrification. *J. Atmos. Sci.*, **48**: 2195-2203.

A STUDY OF AGGREGATION CHARACTISTICS IN A WINTERTIME OROGRAPHIC STORM

W. D. Hall, R. M. Rasmussen, E. Brandes, H. Hsu, and J. E. Dye [1]

[1]National Center for Atmospheric Research, Boulder, Colorado, USA

1. INTRODUCTION

The development of ice particle spectra in clouds has long been a major research topic in cloud physics for many years. To quantitatively understand the aggregational process of ice crystals forming snow requires knowledge of many ice particle physical factors under varying thermodynamic and dynamical conditions of rising and mixing currents within clouds. The physical factors governing aggregation of ice crystals into snow involve ice particle shape, bulk density, sedimentation characteristics, ice particle collection rates by sweep out and wake capture, adhesion rates after collision which involve details of surface mechanical, electrical properties, and particle fragmentation.

To model the complex aggregation process one must include considerable empirical observational data to sort out the dominate physical characteristics. Due to many uncertainties and variations of ice particle type and behavior observational evidence needs to be critically examined.

The qualitative aggregation characteristics have been established over 40 years ago in the literature by Austin and Bemis (1950), Magono (1953), Langleben (1954), Imai et al (1956) and Fujiwara (1957). These characteristics can be generally summarized for temperatures warmer than -22°C where the aggregate size increases with warmer temperatures with a secondary peak between -10°C and -15°C (Kajikawa and Heymsfield, 1989). These early works also noted bright bands with thicknesses less that 300 meters appear near the 0°C isotherm, and that snowflake melting generally occurs between the temperatures of 0°C and +3°C. Exponential size spectra were often cited for particle sizes larger than 2mm. Fujiwara (1957) further showed by simply comparing the fall speeds and shapes of ice particles to water drops that the collision frequency for a given fall distance of interacting ice particles could be 100 to 1000 times larger than for water droplets of the same mass. He also noted the difficulty in determining the coalescence rates.

In more recent times the works of Passarelli (1978), and Mitchell (1991) have used spectral functions and have approximated analytical solutions of the spectra equations governing vapor growth and aggregation to arrive at steady state and time dependent solutions. Mitchell (1988) states that that the treatment of updraft velocities is perhaps the most serious theoretical deficiency in both models. Modern day three dimensional cloud scale models can yield improved descriptions of the dynamical and thermo-dynamical conditions for such studies.

The purpose of the current paper is to perform numerical experiments with three dimensional cloud model simulations to better estimate the updraft spatial and temporal characteristics of the clouds and to use simple Lagrangian ice particle growth models to predict the location where aggregation is expected within an orographic winter storm. The results of these calculations will be compared with in situ aircraft ice particle measurements and radar bright band observations taken during the Winter Icing Storm Project of 1994 (WISP 94) to improve our understanding of the physical conditions that control ice particle aggregation. This case study will use observational data collected during the WISP 94 field study. Numerical simulations applying a non-hydrostatic 3-dimensional model with mesoscale forcing and parameterized warm rain and ice microphysical processes will be used. Simpler Lagrangian parcel microphysical models that contain more cloud physical details of the particle spectrum than that of the three dimensional cloud model will be also used to identify the microphysical charactistics of aggregational snow formation. Additional goals of this study are to improve the microphysical parameterization of the aggregation process within cloud dynamical models and to enhance the physical interpretations of modern radar data.

2. PRELIMINARY RESULTS

The modeling procedure is to first run the Penn. State/NCAR mesoscale model, MM5, to provide information on the large scale forcing for a WISP observational period. The last 12 hours of the MM5 36 hour forecast is then used to drive the smaller scale cloud model by using the data to initialize the cloud model and update the cloud models outer boundary conditions with time.

Some preliminary low resolution (3 km horizontal and 200 m vertical gird) cloud model results are shown in figures 1, 2 ,3 and 4. The results are for the cloud model 6 hours into the 12 hour run. Figures 1, 2, 3, and 4 show various model fields over

---

Corresponding author address: William D. Hall, NCAR, P.O. Box 3000, Boulder, CO 80307-3000. Email: hallb@ucar.edu

the 432 km by 432 km domain centered at 39.75°N and 105.0°W. The domain covers most of the State of Colorado and parts of Wyoming, Utah and New Mexico. On each of the figures the topography is shown with the white areas indicating regions above 3 km MSL. Figure 1 shows the low level vector for a constant elevation of 1.87 km MSL and figure 2 shows the same vector field at 2.7 km MSL. These figures indicate a low level circulating system that dominates the location and intensity of the snowfall. Figure 3 shows a three dimensional depiction of the .1 g m^{-3} iso-surface of simulated cloud ice mass field. Figure 4 shows a vertical southwest to northeast cross-section along approximate ice particle growth path illustrating a typical winter time upslope snowstorm structure with low level flow coming from the north east and the upper level return flow from the west. These early results indicate that the simulated mesoscale currents compare well with observations. Continued calculations using high resolution nested grids will focus on the fine scales and details within the orographic precipitating cloud. Finally, a Lagrangian growth model will be used to examine details of the aggregation process. These results will be presented at the conference along with comparisons of available mesonet, in-situ aircraft and radar data.

3. REFERENCES

Austin, P.M. and Bemis, A.C. 1950: A Quantitative study of the bright band in radar precipitation echos. *J. Meteor.* , **7**, 145-151.

Fujiwara, M. 1957: Preliminary investigation of snowflake size-distribution. *Papers in Meteor. and Geophys.* , **8** , 171-213.

Imai, I, M. Fujiwara, I. Ichimura and Y Toyama, 1955: Radar reflectivity of falling snow. *Papers in Meteor. and Geophys.* , **6** , 130-139.

Kajikawa, M., and A.J. Heymsfield 1989: Aggregation of ice crystals in cirrus. *J. Atmos. Sci.*, **46** , 3108-3121.

Langleben, M.P. 1954: The terminal velocity of snowflakes. *Quart. J. Roy. Meteor. Soc.*, , **80** , 174-181.

Magono, C. 1953: On the growth of snowflakes and graupel. *Sci. Rep. Yokohama Nat. Univ.* , Ser. I, no.2. 18-40.

Mitchell, D. L. 1988: Evolution of snow-size spectra in cyclonic storms. Part 1: Snow growth by vapor deposition and aggregation. *J. Atmos. Sci.***45** , 3431-3451.

Mitchell, D. L. 1991: Evolution of snow-size spectra in cyclonic storms. Part 2: Deviations from the exponential form. *J. Atmos. Sci.***48** , 1885-1899.

Passarelli, R.E. 1978: An approximate analytical model of the vapor deposition and aggregation growth of snowflakes. *J. Atmos. Sci.***35** , 118-124.

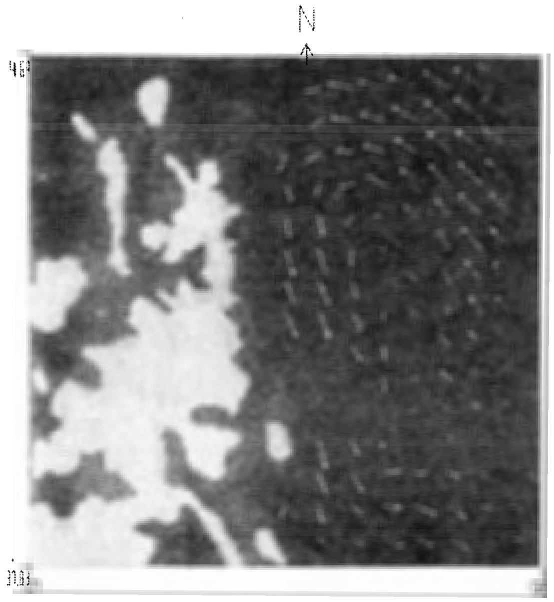

Figure 1. Low level wind vectors at 1.87 km MSL at 18 UTC

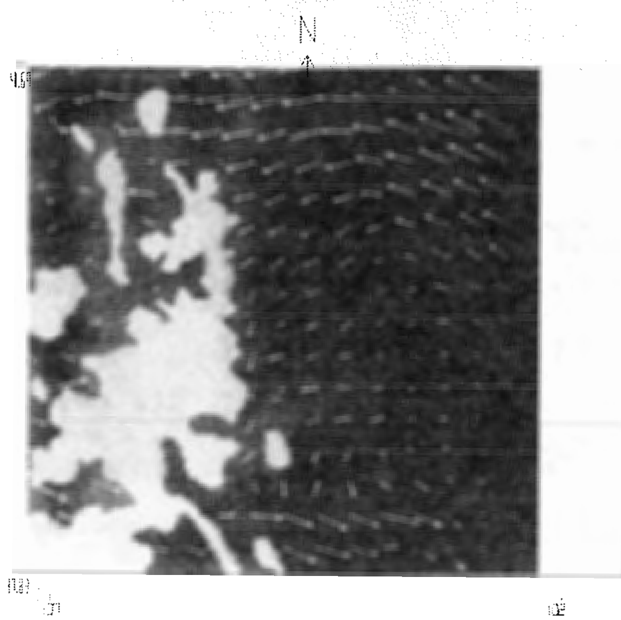

Figure 2. Low level wind vectors at 2.7km MSL at 18 UTC

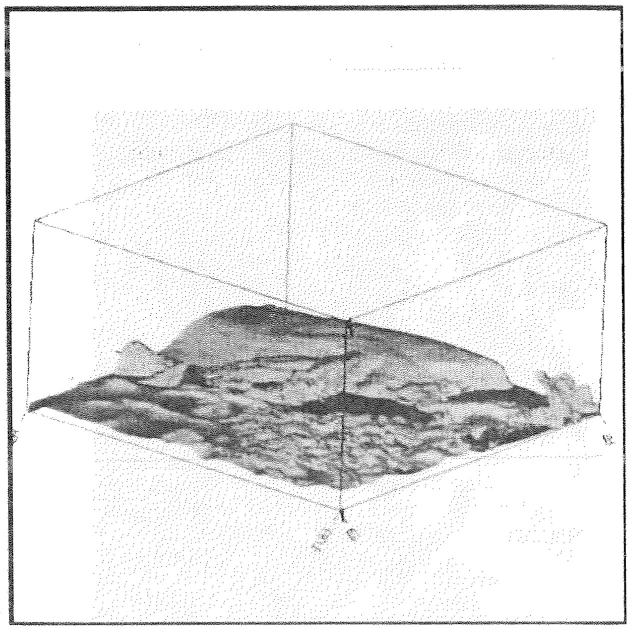

Figure 3. View from the southwest of the 0.1 g m^{-3} ice mass

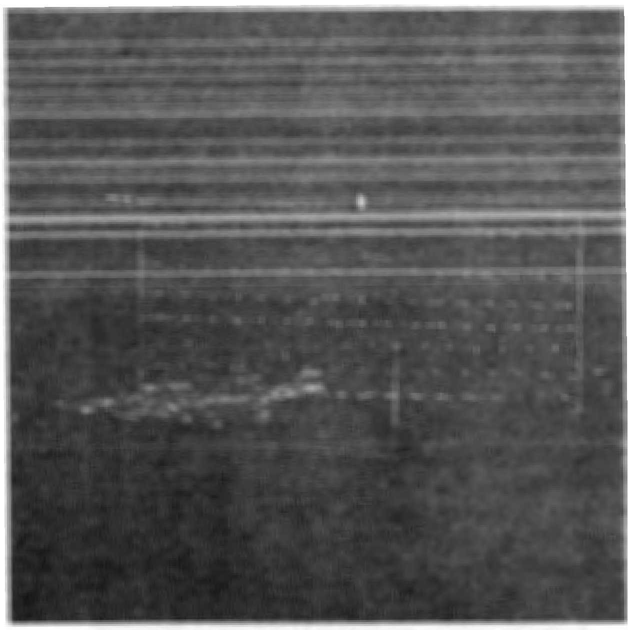

Figure 4. Cross-section of wind vector along a particle trajectory

ICE PARTICLE EVOLUTION IN TROPICAL STRATIFORM ICE CLOUDS: RESULTS FROM TRMM FIELD PROGRAMS

Andrew J. Heymsfield
National Center for Atmospheric Research
Boulder, Colorado

Paul R. Field
Met. Res. Flt., UK Met Office
Farnborough, UK

Jeffrey Stith and James E. Dye
National Center for Atmospheric Research
Boulder, Colorado

Tony Grainger
University of North Dakota
Grand Forks, ND

1. INTRODUCTION

During 1998 and 1999, the Tropical Rain Measuring Mission (TRMM) program conducted four focused field campaigns to evaluate the performance of the TRMM radar and radiometer retrieval algorithms and to provide validation data for TRMM mesoscale and regional scale models. The experiments were conducted in subtropical and tropical regions: Texas and Florida (TEFLUN-A and -B), Brazil (LBA), and Kwajalein, Marshall Islands (KWAJEX). Measurements were acquired with multi-polarization ground-based Doppler radars, raingauges, *in-situ* aircraft, and overflying aircraft with a host of active (Doppler radar) and passive (microwave radiometers) instruments.

As part of the validation effort, *in-situ* measurements were acquired by the University of North Dakota Citation in the latter three field campaigns. The microphysical data set from the Citation probably constitutes the most complete set of *in-situ* data in subtropical and tropical regions to date, as it includes particle size distributions and habit information over a broad range of particle sizes and temperatures, using recently developed instruments. This study reports on some of the Citation microphysical data in deep anvils and stratiform ice clouds.

There have been few opportunities to collect and analyze anvil and stratiform ice cloud microphysical data from the tropics. Knollenberg et al. (1993) documented cirrus anvils over northern Australia in the -60 to -90°C temperature range, while Heymsfield and McFarquhar (1996) and McFarquhar and Heymsfield (1996) described the microphysical characteristics of cirrus clouds over a wide temperature range (-20 to -70°C) from observations near Kwajalein, M. I., and during CEPEX. These observations were limited by the lack of high-quality particle habit information, especially in the smaller particle sizes, and the absence of probes with large sampling volumes to ascertain the sizes of the largest particles.

In this article, the particle size distributions (PSD) and habit information from a number of slow, "Lagrangian-type" spiral descents through cloud by the Citation in Brazil and Kwajalein are examined. The Lagrangian spiral descents were conducted to provide information on the vertical structure of the particle size distributions (PSD) through the depths of anvils and deep stratiform clouds; the descents often began at or close to cloud top, and ended at or close to cloud base. The profiles also provide information on the evolution of the ice particle population, as the aircraft usually descended at approximately the mean mass-weighted terminal velocity of the ice particles, about 1–2 m s^{-1}.

This article is organized as follows. Section 2 identifies the instrumentation and the cases selected for analysis in this study. Section 3 presents the observations and Section 4 summarizes the results of this study.

2. OBSERVATIONS

The data herein are primarily in anvils and dissipating deep stratiform ice clouds in Brazil and Kwajalein (see Table 1). Of the seven cases examined, cloud top temperatures at the sampling location were < -35°C in four instance and > -20°C in two instances. The lowest temperature, -50°C, is relatively warm for tropical anvils, hence the observations apply primarily to relatively warm, dissipating tropical anvils and stratiform ice clouds.

The Citation usually descended at 1–2 m s^{-1} as it spiralled downwards from the coldest temperature

* *Corresponding author address:* Andrew Heymsfield, NCAR/MMM, 3450 Mitchell Lane, Boulder, CO 80303; e-mail: heymsl@ncar.ucar.edu

Table 1

TRMM Lagrangian Spiral Descents

Date	Location	Times (UTC)	Alt (m)	Temp(C)	No. of Loops
990217	Puerto Velho, Bra.	194224 195601	10042 4602	-38 0	4
990818	Kwajalein, M.I.	035139 040701	8508 5695	-27 -5	7
990819	Kwajalein, M.I.	220448 225000	6950 3346	-15 7	23
990822	Kwajalein, M.I.	211958 220451	11268 6993	-50 -16	14
990823	Kwajalein, M.I.	031423 034550	10408 6176	-42 -9	10
990830	Kwajalein, M.I.	201056 203730	7376 3694	-18 6	13
990911	Kwajalein, M.I.	194955 203121	10055 4514	-39 7	11

to base, usually representing a vertical depth of 3 to 4.5 km (Table 1). Most spirals consisted of ten or more loops, thus an average spectrum was obtained over vertical distances of 300 m. The loop diameter was approximately 5 km (Fig. 1).

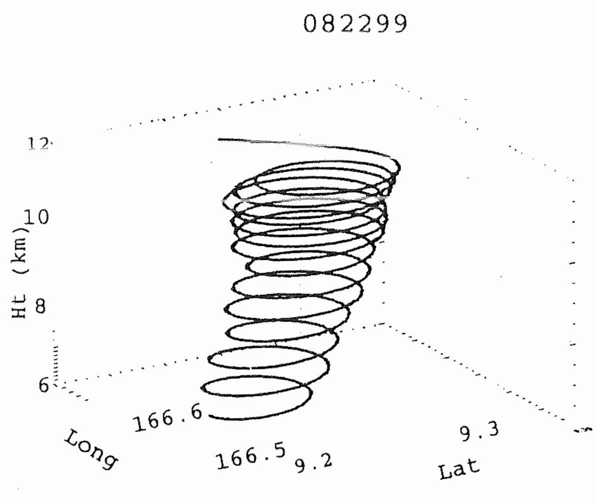

Figure 1. Flight track of the UND Citation during a Lagrangian spiral descent on 082299.

Particle shapes and size distributions were measured over a broad range of particle sizes. The SPEC, Inc. Cloud Particle Imager (CPI) provided detailed information on the shapes and sizes of particles from about 20 to above 500 μm. Because the probe's sampling volume is relatively small and still the subject of study, the size distributions obtained from the CPI are not used in this study. The PSD's are obtained primarily from the PMS 2D-C imaging probe, 100 μm and above, and the SPEC, Inc., High Volume Particle Sampler (HVPS), sizing from about 1 mm to the instrument's limit of 6.1 cm. All particles imaged by the 2DC above 100 μm were included in the calculation of the concentration; partially imaged particles were "reconstructed" (Heymsfield and Parrish, 1978) to yield their maximum dimension. State parameters were obtained from the aircraft' standard suite of instruments.

The PSD often varied over the course of a loop. With horizontal wind shear, variations in the PSD could complicate comparisons of the size distributions between successive loops. To reduce errors in interpretation produced by size sorting, each loop was divided into an upwind and a downwind half-loop. Average size distributions were obtained over each half-lop.

From the particle size distributions, bulk microphysical properties including the ice water content, the radar reflectivity factor, and the precipitation rate were calculated. A variety of mass-dimensional relationships were used, and for the discussion here the relationships of Mitchell (1996) for side planes ($\leq$ 400 μm) and aggregates of side planes (> 400) are used as the observed particle shapes are best-represented by these types.

3. RESULTS

Size distributions and habit information for the 22 August 1999 case (Figs. 2 and 3) is typical of the broader data set in that it exemplifies the development of the size distribution by aggregation from the upper to lower levels of the cloud. Between 11.2 and 10.0 km, the maximum particle size increases from 3 to 8 mm (fig 2, left panels). Note that there is excellent overlap between the 2D and HVPS size distributions, giving confidence to the size distribution measurements. As the aircraft progressed downward to 6.9 km, the size

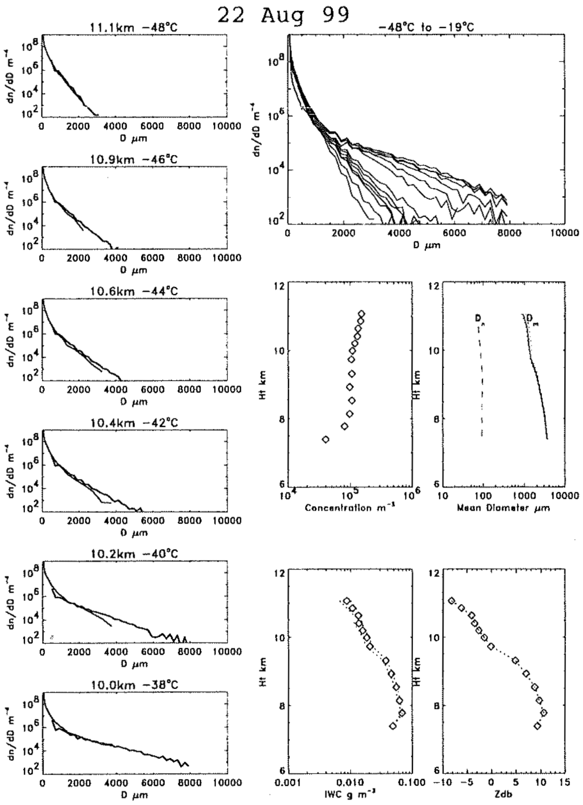

Figure 2. Summary of microphyiscal data collected during the spiral descent on 22 August 1999. Left panels: PSD from 2D probe (from 25 to about 1500 μm) and HVPS (above 1000 μm) for selected heights between 10 and 11.1 km. Right, top panel. Size distributions from upwind part of each loop. middle panels: Concentration and number and mass-weighted diameters. bottom panels. Calculated ice water content and radar reflectivity (see text).

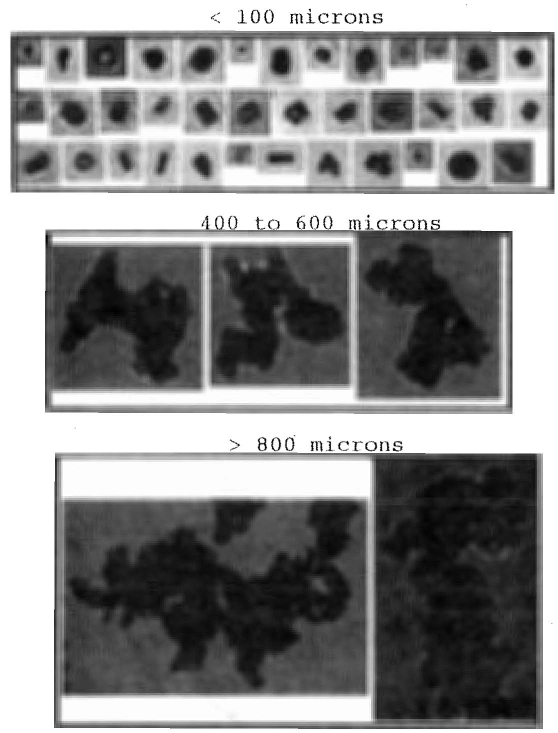

Figure 3. CPI images of particles in three different size ranges

distribution continued to broaden (Fig. 2, upper right panel).

An examination of the CPI imagery revealed that virtually all particles above 200 μm were aggregates, and those below 100 μm were single crystals. This tendency is illustrated in Fig. 3, where habits in three size ranges are presented: $<$ 100 μm, between 400 and 600 μm, and $>$ 800 μm. It is apparent from these particle images, and from the data set in general, that the particle shapes are complex. The very small particles are almost always circular, suggesting that they are either frozen drops or sublimated ice crystals, although near cloud top the latter are not likely. The aggregates are often composed of a variety of crystal types and often indicate riming. Aggregates often contain capped columns.

A minima in concentration, not apparent in Fig. 2, is found between 100 and 200 μm, conforming to the observations of Field (1999) which attributes the minima to aggregation. The collection efficiency of crystals below 100 μm by aggregates is apparently near zero, whereas the collection efficiency for crystals above 100 μm is quite high, thus the crystals in the 100–200 μm range are depleted. An examination of the CPI imagery for aggregates supports the idea that particles below 100 μm were not involved in the aggregation process.

The tendency for aggregation is further exemplified in Fig. 2, right panels, second row. Concentration decreases systematically with height as a result of aggregation. While the mean diameter changes only slightly with height because the number concentration is dominated by sub-100 μm crystals, the mass-weighted diameter increases progressively with distance below cloud top.

The ice water content (IWC) and radar reflectivity factor (dbZ$_e$, in db) increased progressively with distance below cloud top. It is unclear why the IWC (or the derived precipitation rate, which is not shown) increases downwards, if the cloud is essentially a region of fallout, with no growth and some sublimation. One must question whether the mass-dimensional relationships used to derive the IWC is applicable to this situation. Other relationships were used to derive the IWC, but these produced unrealistically-low dBZ's for the situation. Improved estimates of the IWC involve comparing

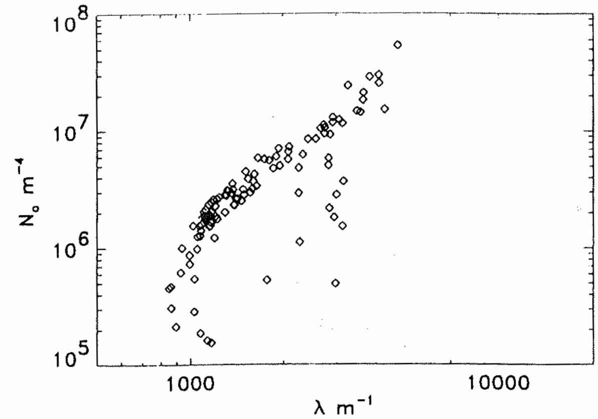

Figure 4. Coefficients N_0 and slope λ in the exponential curves fit to the average size distributions for all Lagrangian spirals.

the calculated to measured reflectivity at the aircraft location, a topic of investigation.

The size distributions above 1 mm in Fig. 2 conform to an exponential form, therefore, curves of the form $N = N_0 e^{-\lambda D}$ were fit to the PSD's above diameters $D = 1$ mm to examine whether there were systematic trends in the PSD's with height. Fig. 4 indicates that there may be a systematic relationship between N_0 and λ. Near cloud top, the N_0 and λ are each relatively large, because the slope of the PSD is relatively large. In the middle and ice portion of the clouds, the N_0 values decrease to about 10^6 m^{-4} and the λ decrease to about 1000 m^{-1}. These changes are clearly the result of aggregation.

Three of the Lagrangian spiral descents concluded in regions below the melting layer (Table 1). In these situations, a systematic relationship between N_0 and λ was also observed. In Fig. 4, N_0 in the melting layer decreases from the value at higher levels to approximately 10^5 m^{-4}, whereas λ remains constant at about 1000 m^{-1}. Continued aggregation in the melting layer must lead to larger particles but fewer particles overall to produce this trend. Once significant melting begins, the slope begins to increase. Since it is likely that the larger particles are less dense than the smaller ones, the former melt to relatively smaller diameter, leading to an increase in λ and N_0. Below the melting level, the λ and N_0 increase, presumably due to breakup, and must tend to a Marshall-Palmer type PSD.

4. SUMMARY AND CONCLUSIONS

This study has examined the evolution of the particle size distribution in layers of anvil and stratiform ice cloud during TRMM field campaigns in Brazil and Kwajalein, Marshall Islands. Lagrangian spiral descents through the cloud layers showed that the size distributions broaden substantially by aggregation, even though most of the cloud layers were dissipating. Above 1 mm, the PSD could be represented accurately by an exponential size distribution of the form $N = N_0 e^{-\lambda D}$. In the ice region, a systematic relationship between N_0 and λ was found with distance below cloud top. The aggregation process was found to be responsible for the changes in the form of the PSD with distance below cloud top. In and below the melting layer, a systematic relationship between N_0 and λ was also found for particles < 1 mm.

The relationship between N_0 and λ in dissipating layers of stratiform ice cloud can therefore be parameterized in terms of normalized height or distance below cloud top. Examination of the constant-altitude legs from the TRMM data set can be used to examine whether the findings are general.

5. ACKNOWLEDGMENTS

This research was supported by the NASA TRMM Project Office through Grant Number NAG5-7743. The authors are grateful to Martin Brown and the University of North Dakota Citation crew for their help over the course of this study.

REFERENCES

Field, P. R. , 1999: Aircraft observations of ice crystal evolution in an altostratus cloud. *J. Atmos. Sci.*, **56**, 1925-1941.

Heymsfield, A. J. and G. M. McFarquhar, 1996: On the high albedos of anvil cirrus in the tropical Pacific warm pool: Microphysical interpretations from CEPEX and from Kwajalein, Marshall Islands, *J. Atmos. Sci.*, *53*, 2401–2423.

______, and J. L. Parrish, 1978: A computational technique for increasing the effective sampling volume of the PMS 2–D particle size spectrometer. *J. Appl. Meteor.*, **17**, 1566–1572.

Knollenberg, R. G., K. Kelly, and J. C. Wilson, 1993: Measurements of high number densities of ice crystals in the tops of tropical cumulonimbus, *J. Geophys. Res.*, *98*, 8639–8664.

McFarquhar, G. M., and A. J. Heymsfield, 1996: Microphysical characteristics of three cirrus anvils sampled during the Central Equatorial Pacific Experiment, *J. Atmos. Sci.*, *53*, 2401–2423.

Mitchell, D. L., 1996: Use of mass- and area-dimensional power laws for determining precipitation particle terminal velocities. *J. Atmos. Sci.*, **53**, 1710–1723.

LOW-TEMPERATURE ELECTRODYNAMIC BALANCE STUDY OF THE EVOLUTION AND GROWTH RATES OF SUPERCOOLED WATER DROPLETS AND ICE PARTICLES

Neil J. Bacon, Brian D. Swanson, Marcia B. Baker, and E. James Davis
University of Washington, Seattle, Washington

1. INTRODUCTION

We describe here preliminary hydrometeor growth rate measurements made using a new instrument built for studying ice and water droplet evolution. While numerous experiments on ice growth have been performed on substrates (e.g., Lamb and Scott 1971) and in cloud chambers (Fukuta and Takahashi 1999), the evolution and light-scattering properties of single isolated ice particles have not been studied in detail in the laboratory. Using the principle of electrodynamic trapping, we are able to hold single ice particles or aqueous droplets for periods of up to several hours under controlled conditions, and we have developed techniques to measure their sizes both optically and via the levitating voltages. With calibrations using aqueous droplets and by close control of chamber temperatures, we can characterize the temperature and humidity in the vicinity of the levitated particle.

2. APPARATUS AND EXPERIMENTAL METHOD

We have shown the electrodynamic balance (EDB) to be a useful tool for studying single ice particles at lower-tropospheric temperatures (Bacon et al. 1998, Swanson et al. 1998, 1999, Bacon and Swanson 2000). We have built a new EDB for studies of ice particle formation, light scattering, and growth/sublimation (g/s) rates under cirrus temperature, pressure, and humidity conditions. The main features of the new instrument are illustrated in Fig. 1. The central cylindrical thermal diffusion chamber (TDC), bounded by a cylindrical quartz window for optical access, is mounted within an octagonal vacuum jacket with 8 optical windows for illumination, video-telemicroscopy, and angular light-scattering measurements. To isolate the TDC thermally, we pump the outer vacuum jacket to 10^{-5} Torr with a diffusion pump. The TDC is cooled by cryogenic fluid flowing though its walls from a temperature-controlled refrigerated bath (Neslab ULT-80). The current flowing through Peltier devices (set by a digital/analog temperature-control feedback circuit capable of milliKelvin control) heats or cools the top and bottom vapor sources of the TDC relative to the chamber temperature. In practice, we find that the temperatures of the ice surfaces, walls, and cylindrical window, monitored with calibrated thermistors, can be controlled to within 0.1 $^{\circ}$C over several hours.

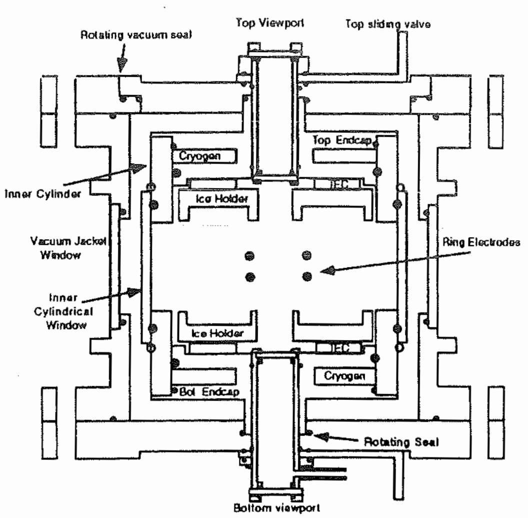

Fig. 1. Schematic of the apparatus

Corresponding author address: Neil J. Bacon, Geophysics Program, Box 351650 University of Washington, Seattle, WA 98195-1650; e-mail: neilb@geophys.washington.edu

Superimposed dc and ac potentials, applied to two coaxial ring electrodes at the center of the chamber, can be adjusted to trap single particles. Sliding ports on the chamber top and bottom allow for particle insertion and chamber access, with optional windows for illumination and video-telemicroscopy. A vacuum-sealed rotation stage at the chamber top allows re-orientation of the particle for measurement of the particle shape. Video-telemicroscopic cameras with 1 um/pixel resolution provide two views of the particle. The two views are electronically combined side-by-side and recorded on VCR.

Water droplets can be charged and introduced into the balance using either a pulsed high-voltage charging system or a droplet-on-demand system constructed using an inkjet printer cartridge. The former method results in variable droplet radius and charge, while the latter gives more closely matching parameters – though the charge is generally smaller. By adjusting the temperature difference between the upper and lower vapor sources we can create either growth or sublimation conditions at the EDB center. If needed, we can accelerate sublimation by illuminating the particle with a broadband light source modulated with infrared filter-mirror combinations. For normal operation, we illuminate the particle with pulsed monochromatic (590 nm) light-emitting diodes that have a negligible heating effect. The g/s rate of a water droplet or frozen ice particle can be measured by continuously monitoring both the dc levitation voltage necessary to balance particle weight and the frequency of the ac field necessary for stable trapping. The general experimental method is discussed in more detail in Swanson et al. 1999.

3. ICE PARTICLE GROWTH HABITS

We have observed the evolution of ice particles grown from 40 μm diameter frozen HPLC water droplets and of ice particles grown from small frost seeds (Swanson et al. 1998, 1999). While particles grown from a frost seed a few microns in diameter often adopt hexagonal habits (see Fig. 2), all of the frozen droplets to date have evolved as polycrystals.

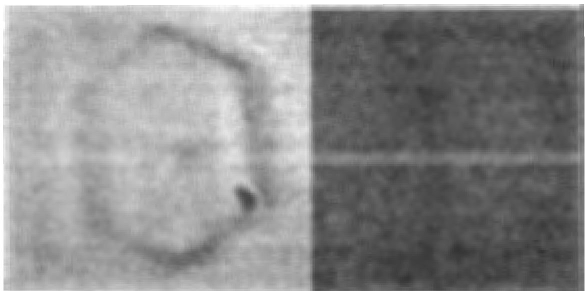

Fig. 2. Two side views of a thin platelike crystal grown from a frost seed at about – 25 °C

Figure 3 shows the shape evolution of one such ice particle grown from a frozen water droplet at about –30 °C. The typical evolution of frozen droplets has been from sphere to a partially faceted (but not pristine) polyhedron, which then sprouts several faceted platelike crystallites. Given their size and freezing temperature (below –35 °C), such polycrystallinity is consistent with earlier findings (Pruppacher and Klett, 1997). It is notable that particles grown between about –20 °C and –40 °C are almost always platelike, contrary to received wisdom.

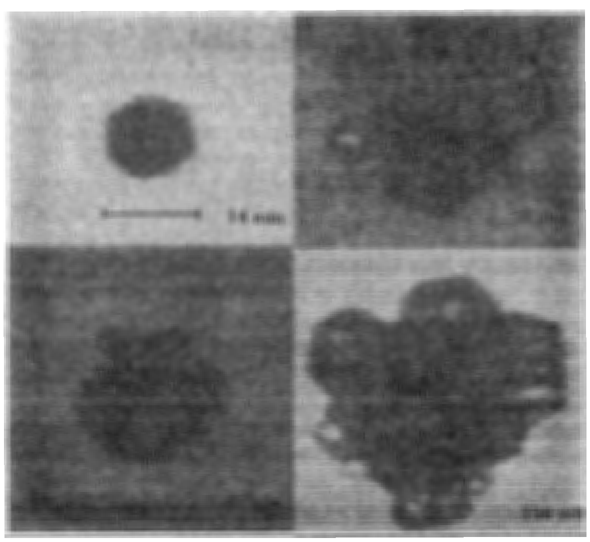

Fig. 3. Evolution of a frozen droplet over 2 ½ hours at –30 °C. The line in the first frame gives the 100 μm scale.

4. GROWTH RATES OF AQUEOUS DROPLETS AND ICE PARTICLES

At lower-tropospheric temperatures, we have found (Swanson et al. 1998, 1999) frost particle g/s to be consistent with diffusion-limited growth

$$m^y = m_0^y + ct \qquad (1)$$

where m is the mass, and m_0, y, and c are constants ($y=2/3$ when thermal and vapor diffusion control the mass growth rate). In those studies we were unable to measure the humidity directly, but we have subsequently developed a technique to introduce aqueous droplets under identical conditions to those experienced by our ice particles. By comparing the g/s of pure (HPLC) water and lithium chloride (LiCl) solution droplets, we are able to strongly constrain the humidity and temperature at the center of the chamber. To this end, we have selected conditions close to water saturation at temperatures down to about –40 °C.

We have measured the size evolution of HPLC water droplets, 1 molar LiCl solution droplets and ice particles held at about –30 °C under identical humidity conditions. The endcap (vapor source) temperatures were controlled to ± 0.05 °C and the cylindrical window temperature to ± 0.1 °C, while the mean temperatures between different data sets have standard deviations of 0.1 °C and 0.4 °C for the endcaps and window, respectively. From the dynamic stability characteristics of the trapped particle, we measure (Swanson et al. 1999) the equivalent spherical radius (radius of an equal-volume sphere). By choosing the conditions to be at or near water

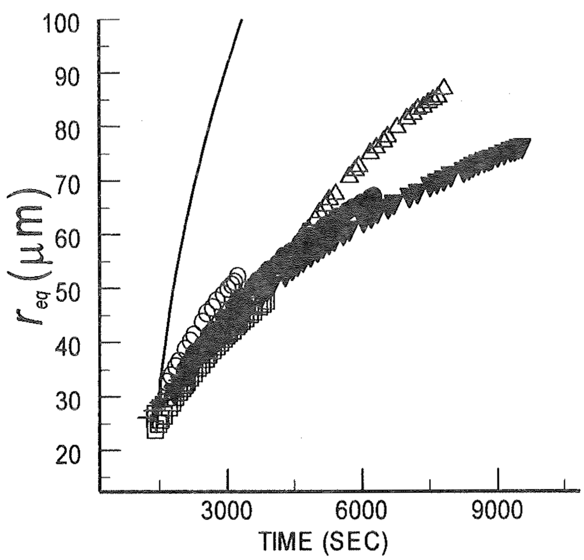

Fig. 4. Growth of ice particles under controlled conditions, with model result for diffusion-limited growth.

saturation, we are able to derive the humidity from our water-droplet data with little dependence on the droplet-growth model. The LiCl solution droplets provide an additional check of the temperature and humidity (see Sec. 5).

Figure 4 shows 6 data sets of HPLC ice particle growth. From the size evolution of HPLC water droplets in the chamber, we infer a partial pressure of water vapor e_w of 50.65 ± 0.95 Pa at around -30 ° C, based on a polynomial parameterization of water saturation given by Pruppacher and Klett (1997). The line in Fig. 4 is the model result for spherical ice particle growth (at partial pressure e_w =49.7 Pa) with both condensation coefficient and thermal accommodation coefficients (Fukuta and Walter 1970, Choularton and Latham 1977) set to unity. We find the exponent y in Eq. (1) derived from this set of ice particle growths to be 0.83 ± 0.18. This, by itself, is consistent with diffusion-limited growth (y=2/3). However, the rate of growth of the ice particles (both frozen water droplets and frost seeds) appears to be too small to be consistent with simple diffusion-limited growth (solid line in Fig. 4), given the humidity implied by the water droplets held under matching conditions.

We have explored the possibility of water contamination, and have measured the impurity concentration in the droplet generator at a few parts per billion (Song Gao, private communication). In addition, we have not observed any difference between droplets from different sources and methods of injection, and the humidity implied by growth rates of solution droplets is consistent with the HPLC droplet data, within experimental error.

5. LICL SOLUTION DROPLET GROWTH

We have studied the growth of 1 molar lithium chloride solution droplets to calibrate the temperature and humidity at the center of the TDC. The solution droplets are useful since they evolve in LiCl concentration as they grow and become more dilute.

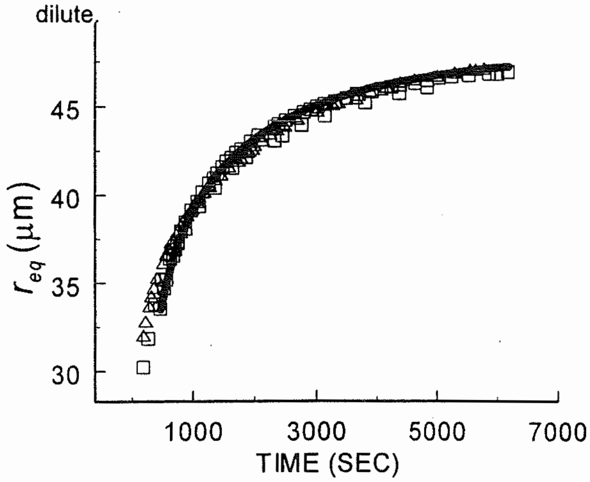

Fig. 5. Lithium chloride solution droplet growth, with model

We have used melting-point data to parameterize the water activity as a function of molarity. From this, we can model the growth of solution droplets and compare with data. To make model and data agree, both temperature and humidity must be adjusted independently (due to the dilution effect). Currently we are testing the accuracy of this method, using tabulated data to deduce the water activity in supercooled solutions. Figure 5 shows the growth of LiCl solution droplets under the same conditions as the ice particles in Fig. 4, with the droplet growth model indicated by the solid line.

6. DISCUSSION

We are currently collecting more data to better understand the low growth rates of the ice particles. One possible explanation could be that the condensation (or thermal accommodation) coefficient is much smaller than presumed (to the extent that it can be represented as a constant). An advantage of our method is that any model must not only give the correct growth rate, but must also match the measured time dependence of the evolution. For example, growth limited by surface processes leads to a linear r(t) in the case of a spherical particle growth. This translates as y=1/3 in Eq. (1). However, nonspherical particle growth can lead to a different exponent. Comparisons with a more sophisticated growth model (Wood et al. 2000) are under way.

We plan to take more data at higher temperatures in order to compare with published data of other workers (e.g., Fukuta and Takahashi, 1999), and also to grow ice particles at reduced pressure under true cirrus conditions.

7. ACKNOWLEDGMENTS

This work was supported by National Science Foundation grants NSF-ATM-9528049 and NSF-ATM-9906538.

8. REFERENCES

Bacon, N. J., B. D. Swanson, M. B. Baker, and E. J. Davis, 1998: Breakup of levitated frost particles. J. Geophys. Res., Vol. **103**, 13,763-13,775.

Bacon, N. J., and B. D. Swanson, 2000: Laboratory Measurements of Light Scattering by Single Levitated Ice Crystals, J. Atmos. Sci. , in press.

Choularton, T.W., and J. Latham, 1977: Measurements of the deposition coefficient for ice, and its application to cirrus seeding. Quart. J. R. Met. Soc. **103**, 307-318.

Fukuta, N., and T. Takahashi, 1999: The growth of atmospheric ice crystals: a summary of findings in vertical supercooled cloud tunnel studies. J. Atmos. Sci. **56**, 1963-1979.

Fukuta, N., and L.A. Walter, 1970: Kinetics of hydrometeor growth from a vapor-spherical model. J. Atmos. Sci. **27**, 1160-1172.

Lamb, D., and W.D. Scott, 1972: Linear growth rates of ice crystals grown from the vapor phase. J. Cryst. Growth **12**, 21-31.

Swanson, B. D., N. J. Bacon, E. J. Davis, and M. B. Baker, 1998: Levitated ice crystals: laboratory measurements of ice particle breakup and growth/sublimation rates. Proceedings of the AMS conference on cloud physics, Everett, WA, Aug. 1998.

Swanson, B. D., N. J. Bacon, E. J. Davis, and M. B. Baker, 1999: Electrodynamic manipulation of ice crystals. Quart. J. R. Met. Soc. **125**, 1039-58.

Wood, S.E., M.B. Baker, and D. Calhoun, 2000: New Model for the vapor growth of hexagonal ice crystals. Preprint, 13th International conference on clouds and precipitation, Reno, NV (this volume).

EXPERIMENTAL STUDIES ON THE DENDRITIC GROWTH OF A SNOW CRYSTAL IN A WATER CLOUD

Tsuneya Takahashi[1] and Tatsuo Endoh[2]

[1]Hokkaido University of Education, Sapporo, 002-8501, Japan
[2]Hokkaido University, Sapporo, 060-0819, Japan

1. INTRODUCTION

Snow crystal growth by vapor diffusion plays a dominant role in the development of both natural and seeded precipitation.

Laboratory studies of the snow crystal habits have been carried out in a convection or diffusion cloud chamber, in which ice crystals have been grown on a hair or a fiber (e.g. Nakaya 1954; Hallett and Mason 1958; Kobayashi 1961). Dendritic crystals have been shown to grow at temperatures between -12 and -16 ℃, while sectors grow at temperatures greater or less than this range. Also, several percent of supersaturation relative to water is needed for dendritic growth, although snow crystal growth in the atmosphere usually occurs at, or somewhat below, the water saturation level.

Using a supercooled cloud tunnel in which the growth of an isolated snow crystal was successfully simulated for a period of more than 30 min, Takahashi and Fukuta (1988), Takahashi et al. (1991) and Fukuta and Takahashi (1999) showed that dendrites grow under the conditions of water saturation at temperatures between -14 and -16℃ and the dimensional and mass growth rates are pronouncedly highest. Dendritic growth is helped by the increased vapor density gradient at the edges due to the ventilation effect. This finding agrees with that of Keller and Hallett (1982), who conducted experiments using forced ventilation.

Since natural snow crystals grow in a water cloud, the effect on snow crystal growth of the cloud droplets surrounding a snow crystal, which also serve to enhance the vapor and sensible heat transfers, should be considered. In this paper, we address the effect of coexisting cloud droplets on the dendritic growth of a snow crystal.

Corresponding author address: Tsuneya Takahashi, Hokkaido Univ. of Education, Integrated Center for Educ. Res. & Training, Sapporo 002-8501, JAPAN; e-mail: takahasi@sap.hokkyodai.ac.jp

2. EXPERIMENTS

The present study was carried out using a supercooled cloud tunnel, in which a snow crystal can be suspended freely and grown by applying aerodynamical mechanisms for horizontal stability, described in detail by Fukuta et al. (1982) and Takahashi and Fukuta (1988).

Fog droplets were continuously generated by an ultrasonic atomizer and were supplied into a fog chamber. The concentration of fog droplets was controlled by impressed voltage to the atomizer. In the fog chamber, the dense fog was immediately mixed and supercooled by

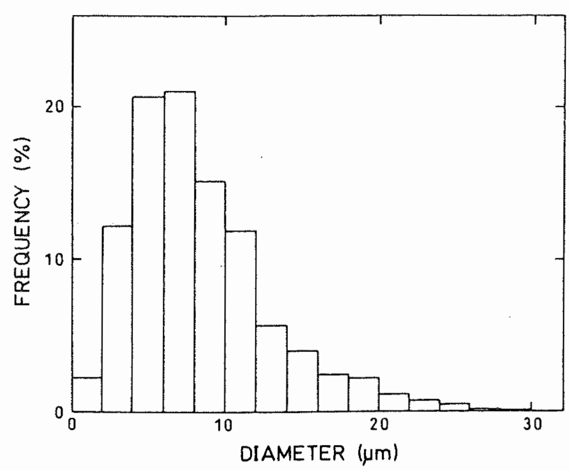

Fig. 1. Averaged size distribution of fog droplets in the working/observation section of a supercooled cloud tunnel.

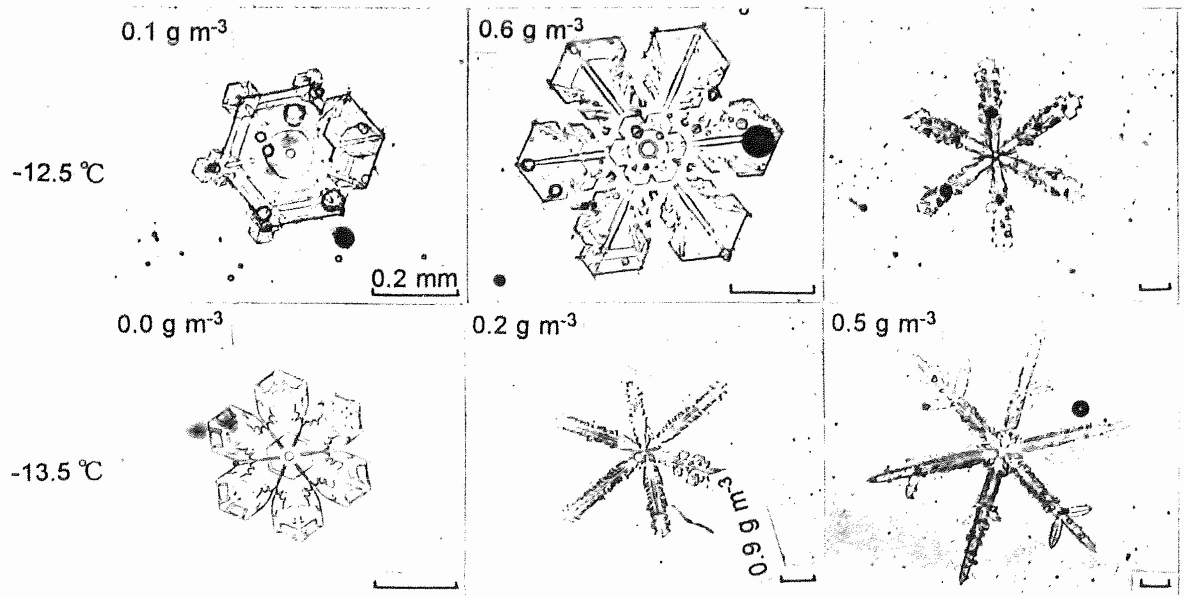

Fig. 2. Snow crystals grown for 10 min at -12.5℃ and -13.5℃ with the different liquid water contents, which are shown in respective photographs.

cold air that was introduced by an air suction device using a vacuum cleaner. Three vertical partitions were used to divide the fog chamber (which is 92 cm long, 165 cm high and 46 cm wide) into four sections. While the air containing the supercooled droplets moved through these sections, turbulence was damping, the air was saturated with water, and the fog became uniform in terms of both temperature and droplet concentration. The fog was then introduced into the working/observation section, where a snow crystal was to be freely suspended.

The liquid water content of the fog was calculated from the air temperature and the dew point of air obtained by evaporating the fog. The air temperature and the dew point of air were continuously monitored by a thermister thermometer and a quartz dew point hygrometer, respectively. The maximum fluctuation in air temperature in each experiment was ±0.3℃. Experiments were carried out at growth time of 10 min under isothermal conditions from -11℃ to -17℃ with liquid water contents between 0 and 1.5 g m^{-3}. Figure 1 shows the averaged cloud droplet size distribution measured by an impaction method. The average diameter was 8.3 μm.

3. RESULTS AND DISCUSSION

3.1 Experimental Results

Figure 2 shows examples of snow crystals grown under various liquid water contents at -12.5℃ and -13.5℃, where a plate and a sector were grown under the conditions of a liquid water content of about 0.1 g m^{-3}, respectively (Takahashi et al. 1991). The crystal shape changed with increases in the liquid water content. At -12.5℃, a plate, a sector and a dendrite grew when the liquid water contents were 0.1, 0.6 and 0.9 g m^{-3}, respectively. At -13.5 ℃, the crystal shape changed from a sector when the liquid water content was 0.0 g m^{-3} to a dendrite when the liquid water content was 0.2 g m^{-3}. Six branch tips of a dendrite grown with a liquid water content of 0.5 g m^{-3} had rounded figures, while the tips of a dendrite grown at -12.5℃and at -13.5℃ with a liquid water content of 0.2 g m^{-3} had angular figures.

The variation of crystal shapes formed with different temperatures between -11 and -17℃ and liquid water contents between 0 to 1.4 g m^{-3} are summarized in Fig. 3. The crystal shape depended on the liquid water content in the temperature range of -12℃ and -13℃; i.e., fog droplets enhanced the dendritic growth of a

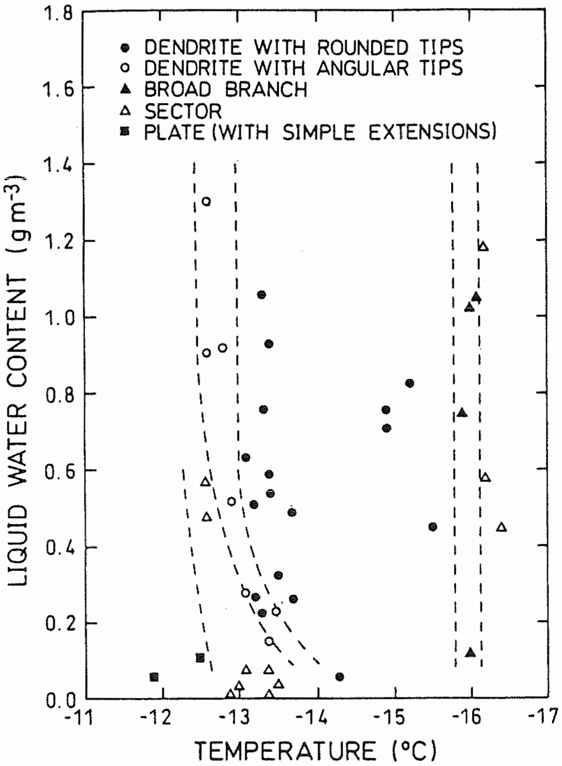

Fig. 3. Snow crystal shape as a function of temperature and liquid water content for a growth time of 10 min.

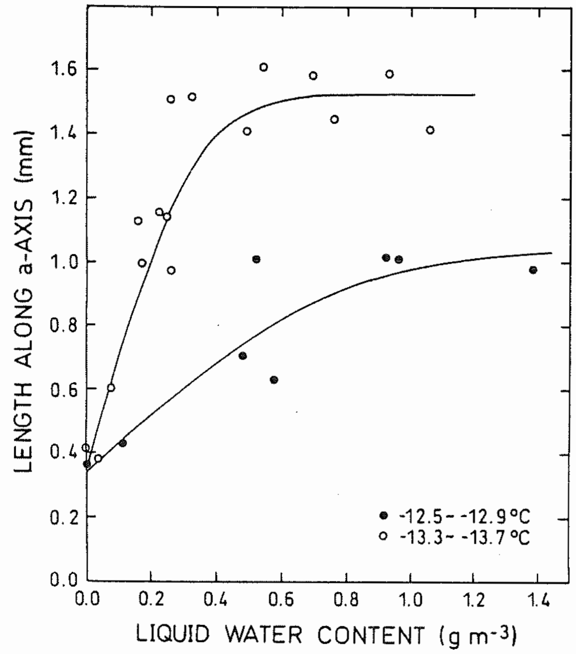

Fig. 4. Variation in crystal dimensions with changes in liquid water content for a growth time of 10 min.

snow crystal. On the other hand, at a temperature below about -16℃, there was no dendritic growth. Because the crystal shape did not change with increases in liquid water content, the fog droplets did not notably affect snow crystal growth. Thus, dendritic growth was observed at temperatures from -12℃ to -16℃, which coincides with the results obtained by Hallett and Mason (1958) using a static chamber.

Figure 4 shows the changes in crystal dimension along a-axis with changes in liquid water content at temperatures between -12.5℃ to -12.9℃ and between -13.3℃ and -13.7℃. The sizes of the snow crystals increased as the fog became denser up to a liquid water content of about 0.9 g m^{-3} in the former case and about 0.5 g m^{-3} in the latter case. The sizes became almost constant over these liquid water contents, where dendrites with angular tips and dendrites with rounded tips were grown, respectively. Also, the dendrites were about 3 to 5-times heavier than crystals in case of a liquid water content of 0.1 g m^{-3}. This indicates that dendritic growth was induced by a high vapor supply.

3.2 Theoretical Considerations

The mass growth rate of a snow crystal can be obtained by using the diffusion equations for water vapor and heat together with the Clausius-Clapeyron equation at the surface. In cloud, corrections due to the coexistence of cloud droplets and crystal fall are needed.

$$dm/dt = f_f \, f_v \, (dm/dt)_0, \qquad (1)$$

where dm/dt is the mass growth rate of a crystal, $(dm/dt)_0$ is the mass growth rate for a stationary crystal grown under conditions of water saturation and the absence of supercooled droplets, f_f is the fog factor, and f_v is the ventilation factor. Takahashi et al. (1991) showed that the ventilation effect is recognizable after the Reynolds numbers exceeded 2 at -12.2℃ (a sector) and 5 at -14.4℃ (a dendritic crystal).

The droplets act as local sources of water vapor. Marshall and Langleben (1954) presented the following derivation of f_f:

$$f_f = 1 + (4\pi \, \Sigma r_d)^{1/2} \, r, \qquad (2)$$

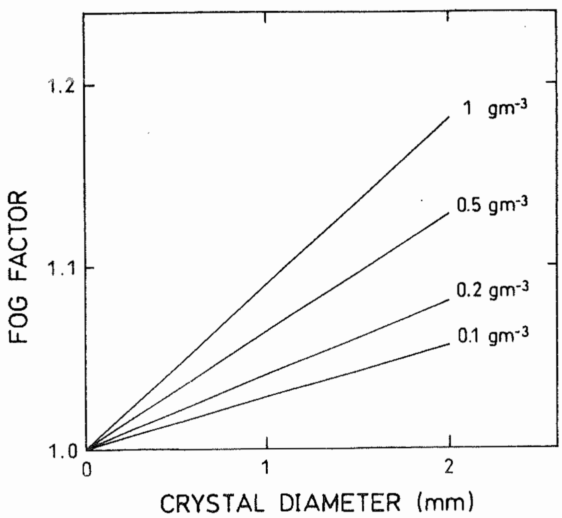

Fig. 5. Relationship between the fog factor and crystal diameter at liquid water contents of 0.1, 0.2, 0.5 and 1.0 g m^{-3} based on the assumption of a relative size distribution as shown in Fig. 1.

where Σr_d and r are the sum of the radii of droplets per unit volume and the radius of a spherical ice crystal, respectively. For nonspherical crystals, the shape factor C should be used in place of r. For a very thin plate whose radius of a circle circumscribed to the basal plane is a,

$$C = 2a / \pi . \quad (3)$$

The fog factor linearly increases with crystal dimensions and the square root of the sum of the radii of droplets. Smaller cloud droplets work more effectively as local sources of water vapor.

Figure 5 shows the fog factor as a function of crystal diameter (2a) at liquid water contents of 0.1, 0.2, 0.5 and 1.0 g m^{-3}, where Σr_d was estimated from Fig. 1. For a crystal whose diameter is 0.5 mm, the effect of fog on the snow crystal growth is several percent.

4. CONCLUSIONS

By simulation experiments on snow crystal growth under a free-fall condition in a supercooled cloud, it was found that a dendrite grows at temperatures between -12℃ and -16 ℃. It coincides with the results in the static chamber by Hallett and Mason (1958), although several percent of supersaturation with respect to water was needed for dendritic growth in the chamber. At temperatures between -14℃ and -16℃, a dendrite can grow only with the ventilation effect, as described by Takahashi et al. (1991). At temperatures between -12℃ to -14℃, growth enhancement by cloud droplets that coexist with a snow crystal is essential for dendritic growth in a water cloud in addition to the ventilation effect: the droplets can steepen the thermal and vapor fields, thereby increasing the growth rate and inducing dendritic growth.

ACKNOWLEDGEMENT. This work was carried out with the approval of the Advisory Committee of the Institute of Low Temperature Science, Hokkaido University (proposal No. 98-037 and 99-37).

REFERENCES

Fukuta, N., M. H. Kowa and N. H. Gong, 1982: Determination of ice crystal growth parameters in a new supercooled cloud tunnel. *Preprints Conf. on Cloud Phys.*, Chicago 15-17 Nov. 19 82, 325-328.

Fukuta, N. and T. Takahashi, 1999: The growth of atmospheric ice crystals -a summary of findings in vertical supercooled cloud tunnel studies. *J. Atmos. Sci.*, **56**, 1963-1979.

Hallett, J. and B. J. Mason, 1958: The influence of temperature and supersaturation on the habit of ice crystals grown from the vapour. *Proc. Roy. Soc. London*, **A247**, 440-453.

Keller, V. W. and J. Hallett, 1982: Influence of air velocity on the habit of ice crystal growth from the vapor. *J. Cryst. Growth*, **60**, 91-106.

Kobayashi, T., 1961: The growth of snow crystals at low supersaturation. *Phil. Mag.*, **6**, 746-755.

Marshall, J. S. and M. P. Langleben, 1954: A theory of snow-crystal habit and growth. *J. Meteor.*, **11**, 104-120.

Nakaya, U., 1954: *Snow crystals*. Harvard Univ. Press, 510 pp.

Takahashi, T., T. Endoh, G. Wakahama and N. Fukuta, 1991: Vapor diffusional growth of free-falling snow crystals. *J. Meteor. Soc Japan*, **69**, 15-30.

Takahashi, T. and N. Fukuta, 1988: Supercooled cloud tunnel studies on the growth of snow crystals between -4℃ and -20℃. *J. Meteor. Soc. Japan*, **66**, 841-855.

THE RELATIVE IMPORTANCE OF WARM RAIN AND MELTING PROCESSES IN FREEZING PRECIPITATION EVENTS

Robert M. Rauber[1], Larry S. Olthoff[1], Mohan K. Ramamurthy[1] and Kenneth E. Kunkel[2]

[1] Department of Atmospheric Sciences, 105 S. Gregory St., University of Illinois, Urbana, Illinois
[2] Midwestern Climate Center, Illinois State Water Survey, Champaign, Illinois

1. INTRODUCTION

Freezing precipitation (freezing rain or drizzle) forms through one of two microphysical paths. The first occurs when ice particles fall from aloft into an atmospheric layer where the temperature exceeds 0°C. The ice particles melt into raindrops within the layer, then fall into a sub-freezing surface layer, supercool, and freeze on contact with surface objects. This process, which for simplicity we will refer to as the "melting process", has been recognized by meteorologists since the early part of this century. Freezing precipitation can also form by collision and coalescence of droplets, a process commonly referred to as the "warm rain process". The importance of the warm rain process in freezing precipitation events was first recognized when temperature profiles from soundings taken during some events were discovered to be entirely sub-freezing (Bocchieri 1980). Huffman and Norman (1988) coined the phrase "supercooled warm rain process" to emphasize that, under these conditions, droplets are continuously supercooled during their growth.

Huffman and Norman (1988) concluded from a 10-year sounding climatology that about 30% of freezing precipitation events occur during times when the atmosphere was sub-freezing, and must therefore be associated with the warm rain process. However, their analysis did not consider situations where the atmosphere contains a warm (> 0°C) layer, but freezing precipitation still develops through the warm rain process. This situation can occur when a warm layer overrides a subfreezing layer, but the cloud top temperature (CTT) exceeds about -10°C. When the CTT > -10°C, ice can only initially form through a heterogeneous process that involves ice nuclei. In general, measurements of ice nuclei suggest that few nuclei will be active at temperatures warmer than -10°C, and that clouds with CTT > -10°C will, for the most part, consist of supercooled water.

In this paper, we examine the relative importance of the warm rain process and the melting process in freezing precipitation events. This work expands on the work of Huffman and Norman (1988) in five ways. Specifically, we 1) consider the importance of these processes in conditions where the atmosphere contains a warm (> 0°C) layer; 2) examine the geographic distribution of different sounding types associated with warm rain and melting processes; 3) examine the frequency of freezing drizzle vs rain occurrence at the sounding sites; 4) examine the range of cloud depths associated with clouds where warm rain processes occur; and 5) expand the size of the database to 25 years.

Corresponding Author email: r-rauber@uiuc.edu

2. DATA

Soundings from all United States stations east of the Rocky Mountain States during the 25 year period from 1 January 1970 through 31 December 1994 were considered for this analysis. Freezing precipitation (freezing rain or freezing drizzle) events were first identified using the National Climatic Data Center's Storm Data reports (Storm Data, 1970-94). Each state report was carefully screened for any occurrence of the terms "freezing rain" or "freezing drizzle". The three hourly surface charts for the entire storm associated with each freezing precipitation event were then analyzed to determine the regions of freezing precipitation. With this procedure, we identified 1023 12 hour periods when freezing precipitation occurred, an average of 40/winter or about 8/month (Nov.-Mar.). We then examined the 0000 and 1200 UTC charts to identify those sounding sites within the area of freezing precipitation that reported freezing drizzle or freezing rain at the time of launch. In the case where there was not a surface report at the site itself, nearest-neighbor stations surrounding the site had to be reporting freezing drizzle or rain for the sounding to be included in the database. These soundings were retained for analysis. We also recorded whether the precipitation was reported as freezing drizzle or rain.

A total of 972 soundings were identified. The soundings were divided into six categories based on the cloud top temperature (CTT), the presence or absence of a warm layer, and the altitude of cloud top relative to the warm layer. "Cloud top" in this study was defined as the first level above the low-level cloud layer where the dewpoint depression exceeded 3°C, provided that the dewpoint depression remained > 3°C through a layer of at least 1 km depth. This method leaves open the possibility of ice falling from higher cloud layers and melting, provided the ice particles can survive the transit through the dry layer above the cloud top. Higher cloud layers were indeed present in some of the soundings. However, in most soundings where warm rain processes were suspected, a significant deep dry layer capped the clouds. We provide examples of both situations in the following section.

The six categories used were: 1) no warm (> 0°C) layer present; 2) cloud top below the warm layer; 3) cloud top within the warm layer; 4) cloud top above the warm layer and 0°C > CTT ≥ -5°C; 5) cloud top above the warm layer and -5°C > CTT ≥ -10°C; and 6) cloud top above the warm layer and CTT < -10°C. Once the soundings were categorized, they were interpolated logarithmically to 10 mb intervals. The soundings in each category were then composited.

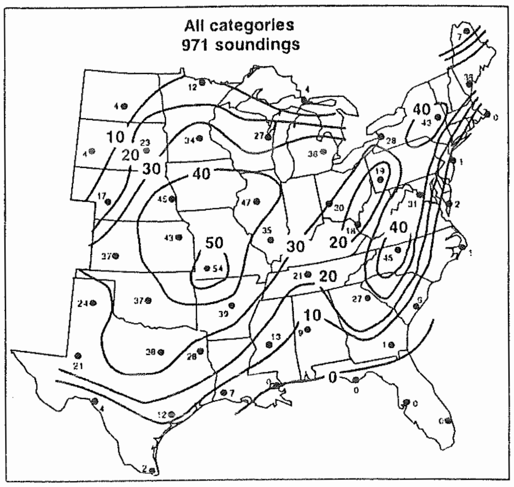

FIG. 1: Geographic frequency distribution of 972 soundings reporting freezing precipitation in the 25 year period from 1 January 1970 through 31 December 1994. The total number of freezing precipitation soundings at each station in the database is also shown.

Figure 1 shows the geographic distribution of the 972 soundings reporting freezing precipitation in the 25 year period. A large region of high reporting frequency appears across the western and central Plains from Oklahoma and Kansas into Indiana. A second region of high reporting frequency appears east of the Appalachian Mountains. The reporting frequency decreases northward toward the Canadian border and southward to zero at the Gulf of Mexico. This distribution conforms very well to distributions of cumulative hours of freezing precipitation derived from surface observations (Robbins and Cortinas 1996, Bernstein and Brown 1997).

3. Sounding climatology

Figure 2a shows the composite sounding, and an example, for the category where the temperature profile on the entire sounding was below freezing. In about 90% of these soundings, the CTT was warmer than -10°C. Figure 2a suggests that a dry airmass typically capped the cloud layer during these events. This was borne out by examination of the individual soundings. The composite hodograph suggests a common synoptic pattern, with low level northeasterly winds and southwesterly winds aloft. Category 1 soundings occurred most frequently in the north-central Plains region of the United States. The frequency decreased southward and eastward, with no stations reporting this profile in the southern half of the U.S. The vast majority of these soundings, 95.4%, were associated with freezing drizzle. Fig. 3 shows a cumulative frequency distribution of the cloud top altitude (above ground level, AGL) for the category 1 soundings. Fifty-three percent were less than 2 km deep, 85% were less than 3 km deep, and 97% were less than 4 km deep. On four soundings, the clouds were surprisingly deep, with cloud tops > 5 km AGL. Despite the depth of the clouds, 3 cases were associated with light freezing drizzle. In the fourth, deepest case (7.1 km), the precipitation was a mix of light snow, ice pellets, and freezing rain. In this case, the -10°C level was at 550 mb.

In category 2 soundings (Fig. 2b), the cloud top was located below the warm layer, so the entire cloud was still supercooled. The cloud layers for all category 2 soundings were shallow, virtually none extending above 2 km AGL (Fig. 3). The majority of surface reports, 83.8%, were freezing drizzle. When freezing rain was reported, neighbor stations often reported freezing drizzle. Except for the presence of the warm layer aloft, the distribution and composite sounding structure for category 2 is essentially the same as category 1, except that there are fewer soundings.

The high frequency of category 1 and 2 soundings in the northern Plains, together with the composite wind, temperature and moisture profile, suggests that these soundings were commonly taken after the passage of arctic fronts over the Plains. Soundings in categories 1 and 2 were not observed in the southeastern part of the U.S during the 25 year period and were seldom observed along the East Coast.

The composite sounding for category 3, the case where the cloud top resided within the warm layer aloft, is illustrated in Fig 2c. The composite hodograph shows that winds were commonly northerly at the surface, veering rapidly to southerly and southwesterly aloft. The cloud top in these cases was virtually always < 3 km AGL (Fig. 3). As in the previous two categories, the cloud layer was typically capped by a very dry layer aloft. In contrast to the previous two categories, this type of sounding most commonly occurred across the southern states, particularly in the southwest Plains and along the southeastern Appalachians. A local maximum also occurred in the New England States. This type of sounding is associated with shallow arctic fronts that approach the Gulf Coast and displace warm air aloft, creating a shallow cloud layer. Freezing precipitation also develops in clouds associated with overrunning as these fronts become stationary or return northward as warm fronts. A maximum in reporting frequency along the east side of the Appalachian mountains suggests that this type of sounding also can occur when cold air becomes dammed on the east side of the mountain chain. The cloud layer was typically capped by a dry layer containing southwesterly winds.

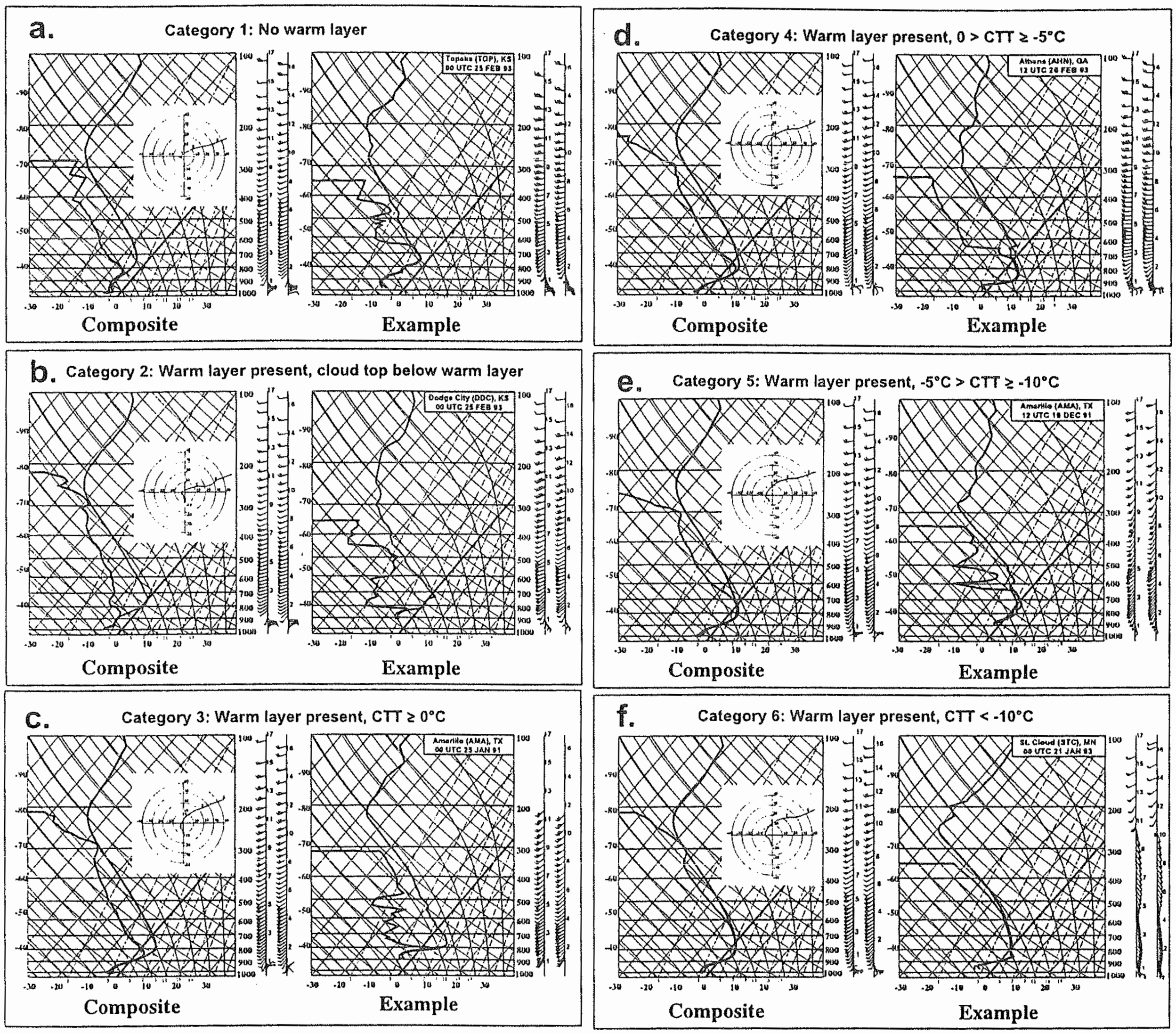

FIG. 2: a) Composite (left) and example (right) sounding using a standard Skew-T Log-P format for Category 1; b-f) same as a, but for categories 2-6 respectively. The winds are plotted in knots. The 0°C isotherm is highlighted for clarity. A standard wind hodograph is shown for the composite.

The warm rain process is the only process possible in the first three categories described above, since the clouds are either entirely sub-freezing (category 1 and 2), or the sub-freezing region of the cloud is topped by a cloud layer that is above freezing (category 3). These clouds characteristically produce freezing drizzle. The three categories respectively account for 15.6%, 4.4%, and 26.8% of the 972 soundings taken during freezing precipitation events. The data demonstrate that the warm rain process was unambiguously responsible for freezing precipitation nearly 47% of the time soundings were taken during freezing precipitation.

It is noteworthy that our value of 15.6% for category 1 differs from Huffman and Norman's earlier estimate of 30%. There appear to be three sources for this difference. First, there is ambiguity in Huffman and Norman's (1988) actual value from their paper. Second, the stations in their database differed significantly from ours. Sixteen of the 48 stations used in their database were in the Western U.S. and were not included in our database. On the other hand, 11 stations in our database, including Monett, MO, Paducah, KY, Omaha, NE, Dayton, OH, and Sterling, VA, were not included in their database. These stations are all in the region of highest reporting frequency on Fig. 1. The third is the size of the database, 10 versus our 25 years. Huffman and Norman did not specify which 10 year period was used in their study, making further comparison with their analysis difficult.

The soundings where the cloud top extended above the warm layer, but the cloud top temperature was ≥ -10°C are shown on Figs 2d and 2e. Those with tops between

-5°C and -10°C (Fig. 2e) may be more likely to contain ice particles. The warm rain process is likely to be important in both categories. These two categories accounted for 15.3% and 13.0% of the freezing precipitation soundings respectively.

The composite soundings appear quite similar, differing from the soundings in the first three categories only in that the cloud tops are colder and the clouds are deeper (Fig. 3). Nearly all the sample in category 4, and 80% of the sample in category 5 had cloud tops under 4 km AGL. Freezing drizzle was still the most common precipitation type (62.4% in category 4 and 53.1% in category 5). Like the other composite soundings, these categories show easterly surface winds veering to southwesterly aloft, and a dry layer aloft above the cloud. Again, this pattern is commonly observed when shallow clouds form over cold, shallow arctic air masses, as illustrated in the example sounding for category 5. Category 4 and 5 soundings were also common along the East Coast, primarily in situations where cold air damming occurred.

Considering the first five categories together, the warm rain process was potentially important in 75.1% of the freezing precipitation soundings. This estimate, based on a 25 year sounding database, is significantly higher than the estimate of ~30% previously determined by Huffman and Norman (1988) in their 10 year climatology, which only considered soundings corresponding to the first category.

The composite and example soundings for the sixth category, where the cloud top temperature was colder than -10°C and melting processes presumably predominate, is shown in Fig. 2f. Freezing rain was reported nearly 80% of the time for these soundings. Soundings in this category frequently had a deep layer of moisture, as one might expect for freezing rain events. The depths of the clouds in this category differed significantly from those in other categories (Fig. 3). Like the other composite soundings, the composite for this category showed the characteristic easterly flow near the surface veering to southwesterly aloft. The geographic distribution of these soundings shows a strong maximum on the east side of the Appalachian mountains. These types of soundings often occur during periods where a cyclone tracks up the East Coast immediately following a cold air damming event. A second maximum occurs just north of the Ohio River valley, a region where freezing rain events commonly occur in association with warm frontal overrunning. Category 6 soundings also were found in the vicinity of low pressure systems crossing the Midwestern U.S.

4. Conclusions

The warm rain process was unambiguously responsible for the freezing precipitation 47% of the time soundings were taken during freezing precipitation. In these cases, the clouds were either entirely below freezing, or had their tops within an above-freezing layer. Freezing precipitation is likely to have developed through the warm rain process as much as 75% of the time, if one considers that clouds that have top temperatures > -10°C often have an active warm rain process. Because of the shallow nature of the clouds, the precipitation produced is typically in the form of freezing drizzle. The distribution of soundings, together with the temperature and moisture profiles, suggests that these events occur most commonly when shallow cloud decks form above arctic fronts.

The more "classic" freezing rain sounding, with a deep moist layer (CTT < -10°C) and a mid-level warm (> 0°C) layer, was observed only 25% of the time. In these cases, the melting process was presumably important to precipitation production. These cases appeared from their geographic distribution and the sounding profile to be associated with cold air damming and overrunning during storms on the U.S. East Coast, and with warm frontal overrunning in the Midwestern U.S.

Acknowledgements

This work was supported by the NSF under grants NSF-ATM-94-06725, and NSF-ATM-97-08170, and by NOAA under grants NA46WP0228 and NA67RJ0146.

References

Bernstein and Brown 1997: A climatology of super-cooled large drop conditions based upon surface observations and pilot reports of icing. *Ppt, 7th Conf. on Aviation, Range and Aerospace Met., AMS.*, 82-87.

Bocchieri, J., 1980: The objective use of upper air soundings to specify precipitation type. *Mon. Wea. Rev.*, **108**, 596-603.

Huffman, G.J., and G.A. Norman Jr., 1988: The supercooled warm rain process and the specification of freezing precipitation. *Mon. Wea. Rev.*, **116**, 2172-2182.

Robbins, C. C., and J. V. Cortinas, 1996: A climatology of freezing rain in the contiguous United States: Preliminary results. 15th Conference on Weather Analysis and Forecasting, Amer. Met. Soc., 124-126.

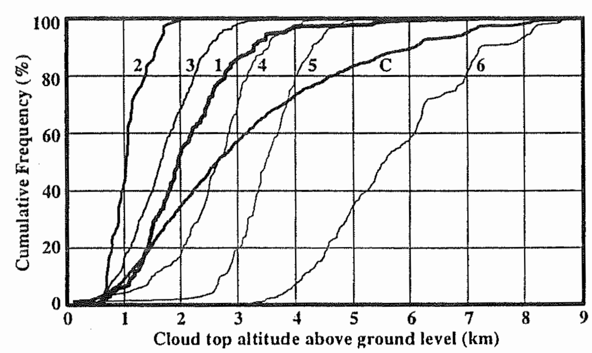

FIG. 3: Cumulative frequency distributions of cloud top altitudes (above ground level) for each of the six categories of soundings. The line labeled "C" is the cumulative frequency distribution for the entire 972 sounding database.

RIMED AND AGGRAGATED ICE CRYSTALS WITH SPECIFIC ORIENTATIONS IN CUMULUS CLOUDS

Steven K. Chai, William G. Finnegan, Arlen W. Huggins, and Richard L. Smith

Desert Research Institute, Reno, NV 89512-1095, USA

1. INTRODUCTION

The understanding of the "chain-of-events" that occurs between the initiation of the ice phase and precipitation falling to the ground has not been well established. A field program was conducted in Texas during August 1999 to gain information on the initiation of natural precipitation. It was hypothesized that the precipitation process in cumulus clouds and orographic clouds, containing liquid supercooled cloud water, is initiated by the aggregation of single ice crystals having charge separations. Electric charge separations between the crystal ice phase or body and the liquid or liquid-like layer at the growing ends or edges of the crystals promote the aggregation process, as shown in laboratory studies. The electric charge separations are the result of preferential ion inclusion in the growing crystals (Finnegan and Pitter, 1988 and 1997). This is an extension of the Walkman and Reynolds (1950) freezing potential to single crystals. The aggregation process is accompanied by a secondary nucleation process (Pitter and Finnegan, 1990) which is hypothesized to influence the duration of the precipitation process. Further confirmation of the ion separation and charge development process is shown by the occurrence of coupled chemical oxidation-reduction reactions in growing ice crystals (Finnegan et al, 1991).

The electric charge separation development occurs when the appropriate ionizable salt concentrations in the liquid layers at the growing ends or edges are less than about 10^{-3} molar, by analogy with the laboratory findings for the linear freezing of dilute salt solutions of mono-valent cations (Murphy, 1970). At higher concentrations, the charge separations vanish and the promoted aggregations and secondary nucleation do not occur. Evidence suggests that solutions of divalent cations, such as Ca^{+2} and Mg^{+2} are active in suppressing charge separation development at even lower concentrations (Finnegan, 1998). Fundamental explanations for these phenomena are found in published Colloid and Interface Science literature (see Finnegan, 1998 for information and relevant literature citations). These findings suggest that cold cumulus clouds and orographic clouds containing relatively low concentrations of atmospherically common salts, such as sodium chloride or ammonium sulfate, in their cloud water droplets, are successful in producing precipitation on the ground. Cumulus clouds that may contain only an order of magnitude higher concentration of these salts in their cloud droplets are hypothesized not to be successful, due to suppression of promoted ice crystal aggregation and secondary nucleation. Clouds traveling over desert regions, which are strong sources of alkali dusts, such as calcium carbonate and soluble neutral salts of divalent cations, such as calcium sulfate, may display consistently reduced rainfall characteristics, because of the relatively low concentrations of divalent cations required for suppression of aggregation and secondary nucleation.

2. BACKGROUND

Electrical charge separations occur between the growing ice phase and supercooled water during linear freezing of solutions of certain salts of 10^{-4} to 10^{-5} molar concentrations, due to the preferential inclusion of specific ions into the ice phase. The oppositely charged counter-ion remains with the liquid phase, leading to the measured electric charge separation. This process is called the Workman-Reynolds effect, after the discoverers (Workman and Reynolds, 1950). This phenomenon has been studied extensively by others (Cobb and Gross, 1969 and Murphy, 1970, for example). The charge separations were attributed to the inclusions in the ice phase of either cations or anions of the salts in solution depending on their composition.

As described in the introduction, Finnegan and Pitter, working with the cloud chamber at the Desert Research Institute, established that charge separations occurred in single ice crystals at temperatures from -4°C to at least -25°C when salts were present in the growing crystals. The charge separations were deduced from the observation of geometrically regular point-to-center two crystal aggregates. Experiments, suggested by Dr. Bernard Vonnegut, demonstrated that two different salts, such as sodium chloride and ammonium sulfate, which give ice phases with opposite sign charges in bulk solution freezing experiments, give single ice crystals with opposite charge separations in cloud chamber experiments (Finnegan and Pitter, 1988). This was shown by point-to-point aggregations, observed when the two types of crystals were generated simultaneously. The authors believe that these laboratory experiments, taken together, gave results that are completely translatable to atmospheric clouds. The ice phase processes in supercooled orographic and cumulus clouds should respond to the presence of soluble inorganic salts that promote charge separations following the Workman-Reynolds Effect. The hypothesis that aggregation of single ice crystals and secondary ice nucleation are involved in the initiation and duration of natural precipitation is then a reasonable and testable one.

While one author (Finnegan) was surveying the colloid and surface science literature in preparing to write the article on the mechanism of heterogeneous nucleation (Finnegan, 1998), it became apparent that the mechanism of the Workman-Reynolds "Effect" was incorrect. In colloid chemistry, the potential determining ions that are responsible for the development of charged and, hence stable, colloidal systems, are constituent ions of the colloid compounds themselves. For example, the potential determining ions for silver iodide colloids are Ag^+ and I^- ions, and the colloid potential can be changed by adding excess Ag^+ or I^- ions as $AgNO_3$ or NaI, respectively, to the colloid-water system. These additions force the additional potential determining ions onto the colloid particles in order to maintain the AgI solubility product that must be kept constant at 10^{-16} gram moles per liter of solution. Similarly, for oxide colloids, the potential determining ions are H^+ and OH^- ions (protons and hydroxyl ions). Since the ionization constant for water is 10^{-7}, and water is neutral, addition of acidic or basic salts in low concentrations (from 10^{-4} to 10^{-6}) will increase or decrease the potential determining ion concentrations and change the charge on ice particles in contact with the water solution. Acidic and basic salts are those that hydrolyze in water solution (react with water) to give acidic or basic solutions. Ammonium chloride, a salt of a strong acid and a weak base, gives acidic solutions and freezing dilute solutions of this salt yields ice with a positive charge and residual supercooled solution with a negative charge during freezing. Similarly, potassium cyanide, KCN, is a salt of a strong base (KOH) and a very weak acid (HCN). It's dilute solution, on freezing, gives ice with a negative charge and residual supercooled solution with a positive charge. It is postulated that protons (H^+ ions) add to the ice phase in the first instance and leave the ice phase in the second instance to establish the charge separations. This study led to the article by Finnegan and Pitter (1997) which corrects the Workman-Reynolds mechanism of charge separation development during the linear freezing of dilute salt solutions. The background knowledge in colloid chemistry and surface science then led to an understanding of the potential effect on cloud precipitation of inorganic salt compositions and concentrations in the cloud water.

3. FUNDAMENTAL ASPECTS

A fundamental aspect of colloidal systems is the development of electrochemical double layers on the surfaces of colloidal particles or, in the case of the ice water system, on the ice surface. These layers develop on addition of soluble salts to the aqueous colloid. At salt concentrations below about 10^{-3} molar, the electro-chemical layers are mainly diffuse. At concentrations above 10^{-3} molar, the double layer develops a compact structure with layers termed the inner and outer Helmholtz layers and a layer adjacent to the solid surface called the Stern layer. The Stern layer, which may extend to the particle solid surface, is the location of counter-ions from the supporting electrolyte (the added salt) with charge opposite to the particle charge. As the supporting electrolyte concentration is increased, ions of both signs are adsorbed in the Stern and inner Helmholtz layers and the induced charge separations are suppressed. Further, in the growing ice system, either in bulk or during growth of single crystals, ions in the Stern layer are apparently incorporated into the ice phase, which limits the charge separation to a steady-state value. It is apparent that the compositions and concentrations of the added salts (the counter ion source) are important in the behavior of colloid systems and to that of the growing ice system.

4. AIRBORNE MEASUREMENTS

An S2 Tracker aircraft was used in the Texas field experiment in August 1999. Cumulus penetrations were made primarily at the –6°C level early in the clouds lifetime. The aircraft was equipped, in addition to the standard air measuring probes, with a formvar replicator, a cloud scope with video output, and a cloud water riming probe to collect data necessary to verify the hypothesis. The cloud scope provides video images of cloud particles that impact it. These images were used for real time identification of the optimum regions of study within a cloud. The replicator produces clear impressions of cloud ice particles on a 16mm film coated with formvar. The replicator data will be used to document the initial ice crystal sizes and types, and provide clear evidence of the existence of two-crystal aggregates that are expected to form if cloud water contains inorganic salts. *In situ* cloud water collections, by means of the riming probe, and subsequent analysis of the water samples by ion chromatography and atomic absorption provided data on the composition and concentration of the inorganic ions. This data will be used to study the correlation between the presence of two-crystal aggregation and the presence of inorganic salts within the effective range of concentrations. A strong correlation will verify the hypothesis concerning precipitation initiation.

5. PRELIMINARY RESULTS

Analysis of the "formvar" replicator tapes has provided evidence for the existence of oriented two crystal aggregates of columnar prisms in the atmosphere. The "formvar" replicator film data also revealed the existence of geometrically rimed columnar prisms. Generally, supercooled cloud droplets collected at the ends of the columnar prisms although occasionally the cloud droplets formed a girdle around the center of the columnar prisms. (Please see the replicator pictures collected at the end of the paper.)

Analysis of collected rime ice (supercooled cloud water) demonstrated that concentrations of sodium chloride, ammonium sulfate, and calcium bicarbonate were within the concentration range tested in the laboratory experiments and the range where the Walkman Reynolds freezing potential appears.

6. ACKNOWLEDGEMENTS

This research was supported by the Texas Natural Resource Conservation Commission, George W. Bomar, program manager.

7. REFERENCES

Cobb, A.W. and G.W. Gross, 1969: Interfacial electrical effects observed during the freezing of dilute electrolytes in water. J. Electrochem. Sci., **116**, 796-804.

Finnegan W.G., 1998: Rates and mechanisms of heterogeneous ice nucleation on silver iodide and silver chloroiodide particulate substrates. J. Colloid and Interface Sci., **202**, 518-526.

Finnegan, W.G. and R.L., Pitter, 1988: A postulate of electric multipoles in growing ice crystals: their role in the formation of ice crystal aggregates. Atmos. Res., **22**, 235-250.

Finnegan, W.G. and R.L. Pitter, 1997: Ion-induced charge separations in growing ice crystals: effects on growth and interaction processes. J. Colloid and Interface Sci., **189**, 322-327.

Finnegan, W.G., R.L. Pitter and L.G. Young, 1991: Preliminary study of coupled oxidation-reduction reactions of included ions in growing ice crystals. Atmos. Environment, **25A**, 2531-2534.

Murphy, E.J., 1970: The generation of electromotive forces during the freezing of water. J. Colloid and Interface Sci., **32**, 1-11.

Pitter, R.L., and W.G. Finnegan, 1990: An experimental study of effects of soluble salt impurities on ice crystal processes during growth. Atmos. Res., **25**, 71-88.

Workman, E.J. and S.E. Reynolds, 1950: Electrical phenomena occurring during the freezing of dilute aqueous solutions and their possible relationship to thunderstorm electricity. Phys. Rev., **78**, 254-259.

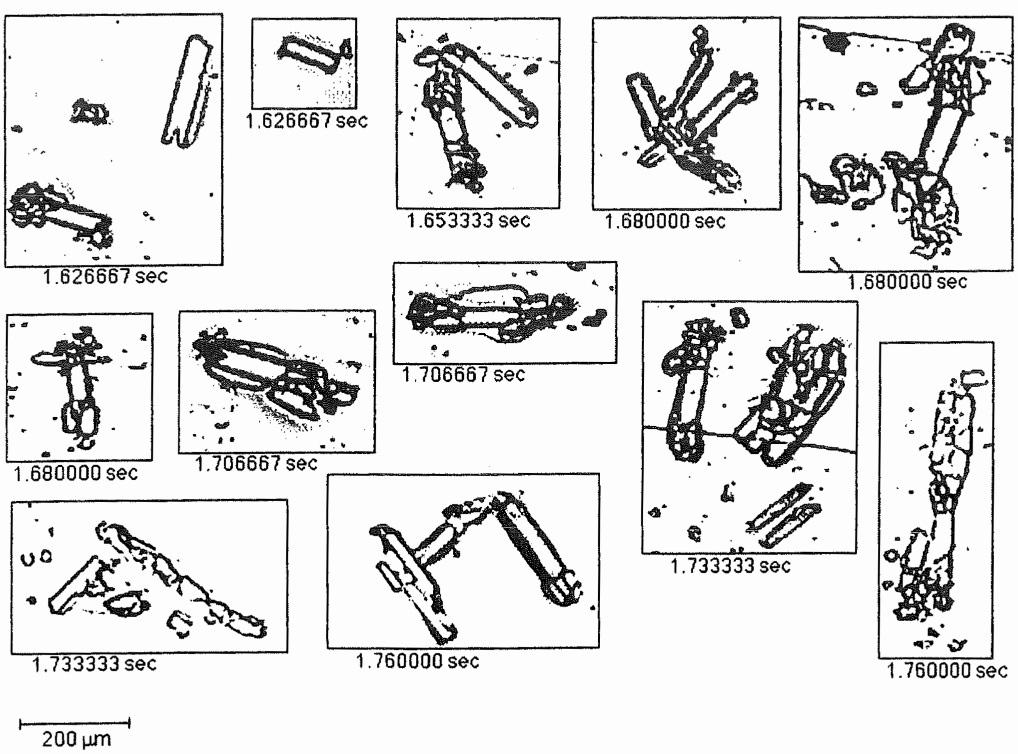

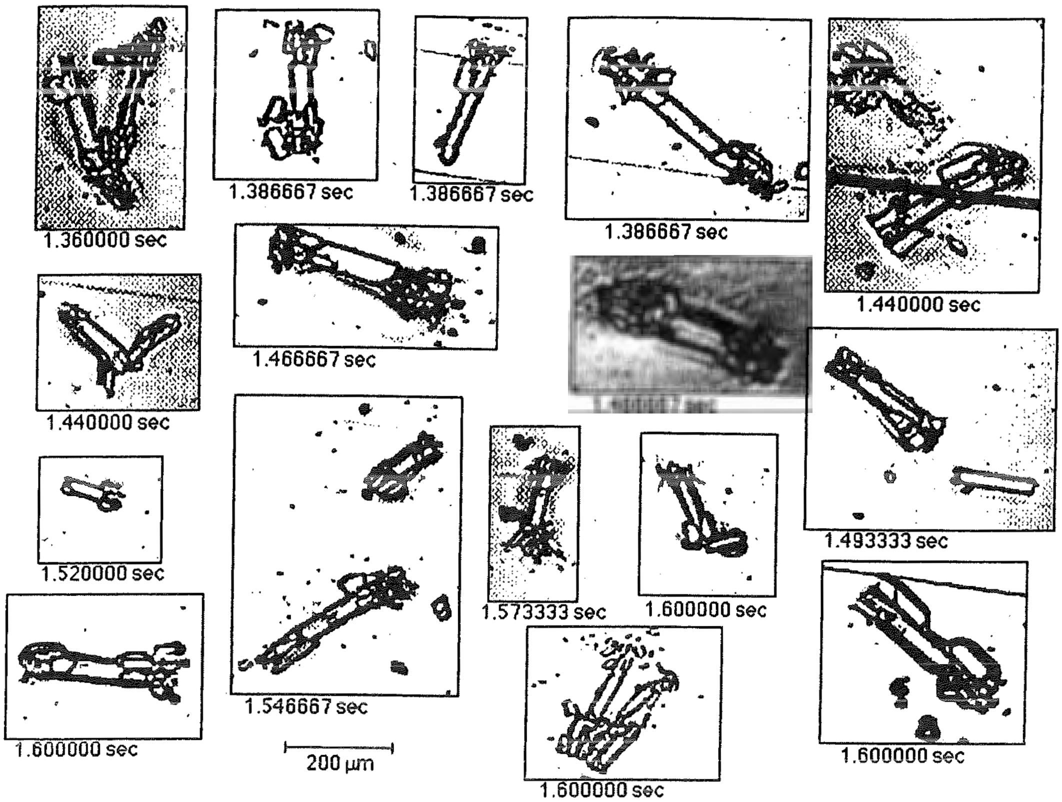
1.360000 sec
1.386667 sec
1.386667 sec
1.386667 sec
1.440000 sec
1.440000 sec
1.466667 sec
1.493333 sec
1.520000 sec
1.546667 sec
1.573333 sec
1.600000 sec
1.600000 sec
200 μm
1.600000 sec
1.600000 sec

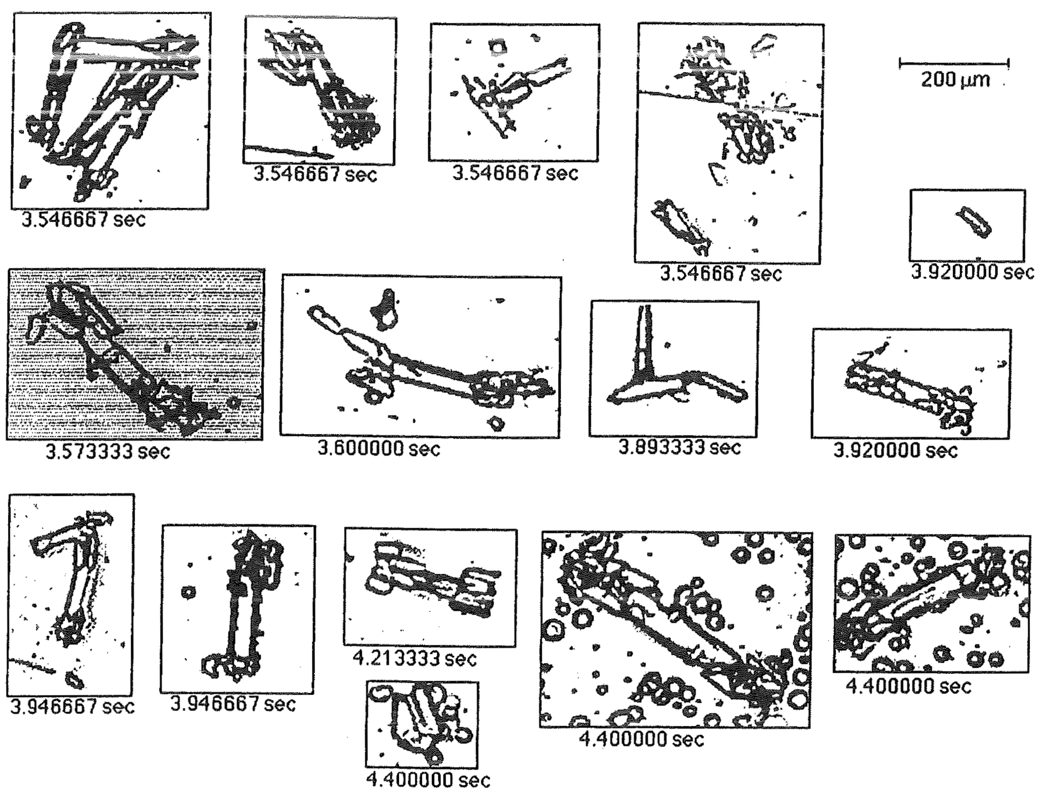
200 μm
3.546667 sec
3.546667 sec
3.546667 sec
3.546667 sec
3.920000 sec
3.573333 sec
3.600000 sec
3.893333 sec
3.920000 sec
3.946667 sec
3.946667 sec
4.213333 sec
4.400000 sec
4.400000 sec
4.400000 sec

ASSESSING THE RELATIVE CONTRIBUTIONS OF LIQUID AND ICE PHASES IN WINTER CLOUDS

Stewart G. Cober, George A. Isaac, Alexei V. Korolev and J. Walter Strapp

Meteorological Service of Canada
Toronto, Ontario, Canada

1. INTRODUCTION

To characterize cloud environments associated with aircraft icing, accurate measurements of cloud liquid water content (LWC) and drop spectra are required. Such measurements are complicated when ice crystals are present because most instruments designed for making in-situ measurements respond to both liquid and ice hydrometeors. Most reports that provide characterizations of icing environments also include observations of mixed phase conditions (Sand et al. 1984, Bain and Gayet 1982, Cober et al. 1995), although the liquid and ice components have usually been determined independently. In each of these studies, mixed phase conditions were commonly observed. Cober et al. (1995) discussed how a PMS King probe measured an artificial LWC as high as 0.1 g m^{-3} in glaciated clouds, while Korolev et al. (1998a) showed that the Nevzorov LWC probe could show an artificial LWC of 10% of the total water content (TWC) in glaciated clouds. Strapp et al. (1999) have shown that the Nevzorov and King probes respond to as much as 40% of the ice water content (IWC) in certain situations. Gardiner and Hallett (1985) showed that PMS FSSP probes could measure artificial droplet spectra in ice crystal clouds. The misinterpretation of droplets as ice crystals for 2D-C measurements has been discussed by Rauber and Heggli (1988). In this paper, the relative responses to ice and liquid particles for several instruments will be discussed. A methodology for segregating ice and liquid components will be presented, and the results will be compared to other factors such as drop concentration and temperature.

2. FIELD PROJECTS

The data were obtained during the First and Third Canadian Freezing Drizzle Experiments (CFDE I and III), which were conducted during the winters of 1995 and 1997-98 respectively (Isaac et al. 1999). Both projects were designed in part to characterize aircraft icing environments in winter storms through the collection and interpretation of in-situ microphysics data. CFDE I included 12 flights over the North Atlantic Ocean in the area of Newfoundland, while CFDE III included 26 flights over Southern Ontario and Quebec. The majority of flights targeted the warm frontal regions of winter storms. The National Research Council Convair-580 was used as the instrument platform for both projects.

Corresponding Author: S.G. Cober, Environment Canada 4905 Dufferin Street, Toronto, Ontario, Canada, M3H 5T4

3. INSTRUMENTATION

Instrumentation on the Convair-580 has been described in Isaac et al. (1999). Important parameters were normally measured with redundant systems to avoid errors associated with malfunctioning instruments. Temperature was measured within ± 1°C with three sensors including Rosemount and Reverse Flow probes; LWC was measured within ± 15% (or 0.02 g m^{-3} for low LWC values) with two PMS King probes and Nevzorov LWC and TWC probes; and droplet concentrations were measured with two PMS FSSP probes. The FSSP concentrations agreed within ± 34% for 85% of the data points. In addition, the hydrometeor spectra were measured with three PMS 2D probes including 2D-C mono 25-800 μm, 2D-C grey 25-1600 μm, and 2D-P mono 200-6400 μm. The first four channels of each 2D probe were ignored because of the depth of field and sizing uncertainties that exist for these channels (Korolev et al. 1998b). The rate of ice accumulation was measured with a Rosemount Icing Detector (RID).

4. INSTRUMENT RESPONSES TO CRYSTALS

4.1 Rosemount Icing Detector

The RID is a valuable tool for segregating glaciated and non-glaciated conditions, since it does not respond to ice crystals (Baumgardner and Rodi 1989, Cober et al. 2000). The absence of a voltage rise for in-cloud observations normally implies that the cloud contains only ice crystals, or that the LWC is below the threshold detection level for a RID. Mazin et al. (2000) showed that the threshold LWC is approximately 0.003 g m^{-3} for a RID operated at airspeeds characteristic of the Convair-580 (100 m s^{-1}). High LWC values can cause the RID surface temperature to reach 0°C, which can in turn result in the probe showing no response. Therefore glaciated conditions should only be assessed for temperatures that are well below 0°C and LWC values which are below the Ludlam limit (Cober et al. 2000).

4.2 PMS 2D-C Probes

The segregation of liquid and ice hydrometeors (≥ 5 pixels) can be assessed using 2D images obtained from

PMS 2D-C mono or grey probes. Particle images were processed following the centre-in technique of Heymsfield and Parrish (1978). Images were segregated into circles and non-circles using several geometric tests including particle axis ratio, area (A) to diameter (D) ratio, area to perimeter (P) ratio, perimeter to diameter ratio and symmetry in the length and height dimensions. Each geometric ratio was calibrated using data from warm (> 0°C) clouds where there were no ice crystals, and where each image (less spurious artifacts) could be interpreted as a circle. Fig. 1 shows the maximum and minimum observed calibration values for particles with diameters ≥ 5 pixels (125 μm) as a function of size. In order for a particle to be interpreted as a circle, it had to pass every geometric test, while non-circles would normally fail one or more of the tests. It is clear that with increasing diameter, the geometric criteria becomes more restrictive, and the identification of circles and non-circles more accurate. Fig. 2 shows the relative fractions of circles and non-circles in entirely liquid and glaciated clouds respectively. In liquid clouds, the geometric criteria identify approximately 90% of the particles as circular. Conversely, in glaciated clouds the percentage of circular particles is as high as 40% for particles of 5-8 pixels in diameter, dropping to < 10% for particles with diameters > 13 pixels. Therefore, in mixed phase clouds, the errors in interpreting circular particles as liquid drops could average 40% for 6 pixel particles.

4.3 Nevzorov LWC and PMS King LWC Probes

Glaciated cloud conditions at temperatures colder than -5°C were identified using the RID, and confirmed by examining the 2D-C segregation of circles and non-circles. Fig. 3 shows the response of the Nevzorov LWC probe for these conditions (the response for entirely liquid cases and a 1:1 correlation curve are shown for comparison). The results are similar to those shown by Korolev et al (1998a). The lower curve in Fig. 3 can be used as a threshold for inferring glaciated cloud. Fig. 4 shows the relative ratio of LWC/TWC for TWC values ≥ 0.075 g m^{-3} for both the Nevzorov and King LWC probes. The average LWC response is 15-20% of the TWC for the Nevzorov probe and 10-15% for the King probe. There are fewer King probe data points because it was not working on several flights. In general, the response to ice is similar for both instruments. When assessing a mixed phase condition, the response to ice should be subtracted from the LWC signal (Section 6).

4.4 PMS FSSP Probes

Fig. 5 shows the median volume diameter (MVD) for glaciated and liquid phase conditions as measured with the FSSP 5-95 μm instrument. As shown by Gardiner and Hallett (1985), ice crystals can cause counts in higher FSSP channels that cause apparent high MVD values in glaciated clouds. The FSSP 5-95 μm MVD values are higher than the FSSP 3-45 μm values (not shown) for this reason. For the 3-45 μm and 5-95 μm probes, MVD values > 30 μm accounted for 99% of the glaciated cloud cases, and 4% of the liquid cloud cases observed. Similarly, concentrations measured with both probes were < 15 cm^{-3} for 100% and 8% of the glaciated and liquid phase conditions respectively. These thresholds are useful when attempting to infer glaciated and non-glaciated conditions, although they cannot be used in isolation because there is some overlap at these values between liquid and glaciated conditions.

5. PHASE ASSESSMENT

The data were averaged into 30-second periods representing approximately 3 km in horizontal extent. In-cloud regions were identified using a TWC > 0.01 g m^{-3}, droplet concentration > 0.1 cm^{-3}, and temperature < 0°C. In total there were 2301 in-cloud cases from CFDE I and 5040 cases from CFDE III. Liquid phase conditions were identified when the LWC and TWC measurements agreed within 15%, when the 2D images indicated circular images within the error limitations shown in Fig. 2, and when there were no obvious ice crystal images. In cases with no hydrometeors ≥ 125 μm, the 2D instruments were not used. In cases with significant drizzle drops, the LWC measurements tended to be less than the TWC because of the fall off in response discussed by Biter et al. (1987) and Strapp et al. (2000). Some liquid phase cases will contain an IWC that cannot be separated from the TWC signal, since agreement within ± 15% between the LWC and TWC probes can mask a small IWC signal. In addition, some irregular images observed with the 2D probes were likely ice crystals. The IWC for the liquid phase cases was estimated to be less than 5% of the TWC for the majority of cases observed. Glaciated clouds with temperatures < -5°C were identified using the RID and 2D images. Cases with LWC below the RID threshold of 0.003 g m^{-3} (Section 4.1) could not be differentiated from entirely glaciated cases. Glaciated clouds with temperatures between 0 and -5°C were identified using the combination of the Nevzorov threshold (Fig. 3), fraction of non-circular 2D images > 0.6, FSSP MVD > 30 μm and concentrations < 15 cm^{-3}. When these criteria were applied to the RID data at temperatures colder than -5°C, they identified 900 of 973 cases (92%) correctly as glaciated. Therefore, the combination of FSSP, Nevzorov, and 2D criteria were adequate for assessing glaciated cases in the absence of a reliable RID measurement. An identification of mixed phase was given to cases that were not identified as liquid or glaciated.

6. RESULTS AND DISCUSSION

Table 1 shows the percentages of liquid, mixed and glaciated phase conditions for CFDE I and CFDE III. There were substantially more mixed and less glaciated phase conditions in CFDE III than in CFDE I. This may be related to the cloud drop sizes. In CFDE I, the median droplet concentration was significantly smaller than in CFDE III (Table 1), while the median MVD was significantly larger.

Table 1

Project	CFDE I	CFDE III
Liquid Phase (%)	40	39
Mixed Phase (%)	25	47
Glaciated Phase (%)	35	14
Median Temperature (°C)	-4.5	-6.9
Median Concentration (cm^{-3})	65	157
Median MVD (μm)	24	19

In addition, 81% of the CFDE I cases had drops > 40 μm as measured with the FSSP 5-95 μm probe, compared to 57% for CFDE III. These statistics were based on the liquid phase cases only, so that ice crystals did not affect these conclusions. The observations are consistent with differences between maritime and continental clouds. The presence of cloud drops > 25 μm is a necessary condition for ice multiplication as discussed by Hallett and Mossop (1974). The Hallett and Mossop effect is only believed to be active between -4 and -8°C, which accounts for 35-40% of all the in-cloud data for CFDE I and III. These observations are consistent and sufficient to explain the differences in Table 1. Table 1 also shows the average temperature for clouds with LWC > 0 for both projects. Since the frequency of liquid phase cases was the same for both projects, the colder temperatures during CFDE III do not appear to have caused a greater activation of ice nuclei. Hence, temperature effects are not believed to account for the differences between mixed and glaciated phase cases for CFDE I and III. The mean and standard deviation for ice crystal concentrations ($\geq$ 125 μm) for CFDE I and III were 5$\pm$5 and 4$\pm$5 L^{-1} respectively. These data show no distinct differences in crystal concentrations between the two projects. Fig. 6 shows the fraction of liquid water for the mixed phase cases listed in Table 1. The calculations assume that the Nevzorov TWC probe measured both LWC and IWC while the Nevzorov LWC probe measured LWC and 20% of the IWC. Errors associated with the fall off of the LWC probes for drizzle sized drops were neglected for the mixed phase cases. The curve is relatively flat which may imply that clouds undergo a relatively constant rate of transition from liquid to glaciated phase conditions, or that a mixed phase cloud can maintain its relative liquid/ice ratio for a considerable length of time.

7. ACKNOWLEDGEMENTS

This work was supported by the Canadian National Search and Rescue Secretariat, Transport Canada, the Meteorological Service of Canada, and Boeing Commercial Airplane Group.

8. REFERENCES

Bain, M., and J.F. Gayet, 1982: Aircraft measurements of icing in supercooled and water droplet/ice crystal clouds. *J. Appl. Meteor.*, **21**, 631-641.

Baumgardner, D., and A. Rodi, 1989: Laboratory and wind tunnel evaluations of the Rosemount icing detector. *J. Atmos. Oceanic Technol.*, **6**, 971-979.

Biter, C.J., J.E. Dye, D. Huffman, and W.D. King, 1987: The drop-size response of the CSIRO liquid water probe. *J. Atmos. Oceanic Technol.*, **4**, 359-367.

Cober, S.G., G.A. Isaac and A.V. Korolev, 2000: Assessing the Rosemount Icing Detector with in-situ measurements. Submitted to *J. Atmos. Oceanic Technol.*

Cober S.G., G.A. Isaac, and J.W. Strapp, 1995 : Aircraft icing measurements in east coast winter storms. *J. Appl. Meteor.*, **34**, 88-100.

Gardiner, B.A., and J. Hallett, 1985: Degradation of in-cloud forward scattering spectrometer probe measurements in the presence of ice particles. *J. Atmos. Oceanic Technol.*, **2**, 171-180.

Hallett, J., and S.C. Mossop, 1974: Production of secondary ice particles during the riming process. *Nature*, **249**, 26-28.

Heymsfield, A.J., and J.L. Parrish, 1978: A computational technique for increasing the effective sampling volume of the PMS two-dimensional particle size spectrometer. *J. Appl. Meteor.*, **17**, 1566-1572.

Isaac, G.A., S.G. Cober, A.V. Korolev, J.W. Strapp, A. Tremblay, and D.L. Marcotte, 1999: Canadian Freezing Drizzle Experiment. *37th Aerospace Sci. Meeting*, Reno Nevada, 11-14 January 1999.

Korolev, A.V., J.W. Strapp, and G.A. Isaac, 1998a: Evaluation of the accuracy of PMS optical array probes. *J. Atmos. Oceanic Technol.*, **15**, 708-720.

Korolev, A.V., J.W. Strapp, G.A. Isaac, and A.N. Nevzorov, 1998b: The Nevzorov airborne hot wire LWC/TWC probe: Principles of operation and performance characteristics. *J. Atmos. Oceanic Technol.*, **15**, 1496-1511.

Mazin, I.P., A.V. Korolev, A. Heymsfield, G.A. Isaac, and S.G. Cober, 2000: Thermodynamics of icing cylinder measurements of liquid water content in supercooled clouds. Submitted to *J. Atmos. Oceanic Technol.*

Rauber, R.M., and M.F. Heggli, 1988: The influence of cloud droplets on the measurement of ice particle concentrations with a Particle Measuring System's 2DC optical array probe. *J. Atmos. Oceanic Technol.*, **5**, 123-128.

Sand, W.R., W.A. Cooper, M.K. Politovich, and D.L. Veal, 1984: Icing conditions encountered by a research aircraft. *J. Climate Appl. Meteor.*, **23**, 1427-1440.

Strapp, J.W., J. Oldenburg, R. Ide, S. Bacic, and L. Lilie, 2000: Measurements of the response of hot wire LWC and TWC probes to large droplet clouds. *Proceedings 13th Intl. Conf. on Clouds and Precipitation*, Reno Nevada, 14-18 August 2000.

Strapp, J.W., P. Chow, M. Maltby, A.D. Bezer, A.V. Korolev, I. Stromberg, and J. Hallett, 1999: Cloud microphysical measurements in thunderstorm outflow regions during Allied/BAE 1997 flight trials. *37th Aerospace Sci. Meeting*, Reno Nevada, 11-14 January 1999.

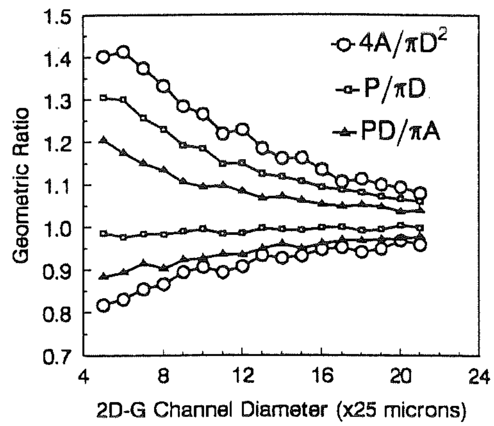

Figure 1. Maximum and minimum limits for three geometric ratios for the 2D-C grey probe with a 50% shadowing threshold.

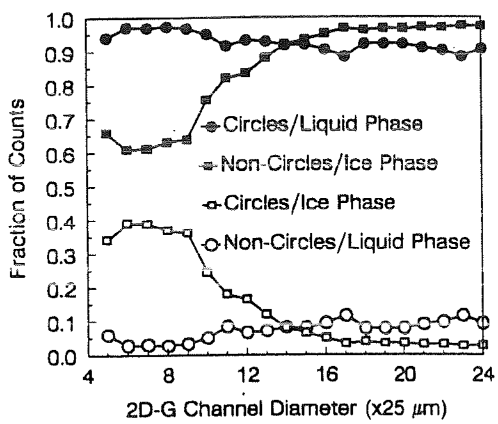

Figure 2. Relative fractions of circles and non-circles for liquid and glaciated cloud conditions, when the six geometric tests were applied.

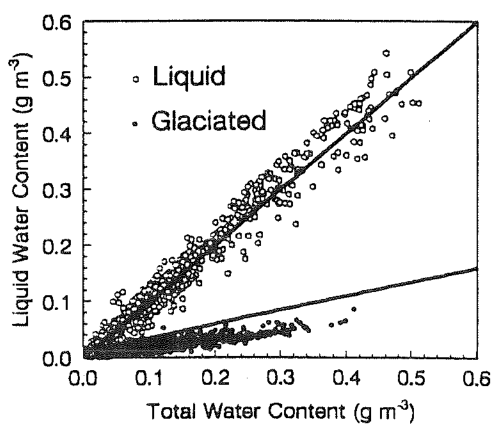

Figure 3. Nevzorov LWC and TWC measurements for glaciated and liquid phase clouds for the complete CFDE I and III data set.

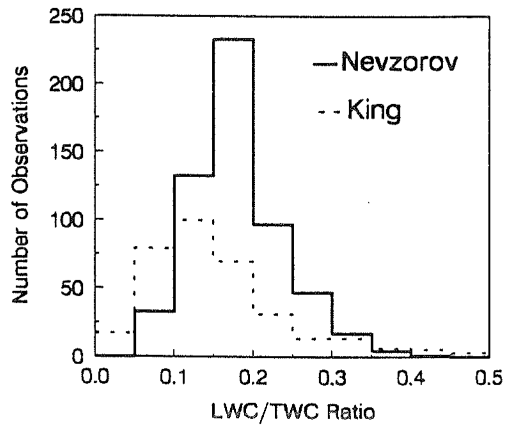

Figure 4. Ratio of LWC/TWC for Nevzorov and PMS King probe measurements in glaciated clouds for the complete CFDE I and III data set.

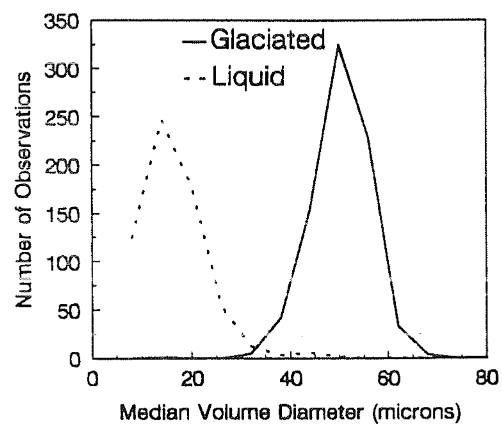

Figure 5. MVD measurements from the FSSP 5-95 μm probe, for liquid and glaciated cloud cases for the complete CFDE I and III data set.

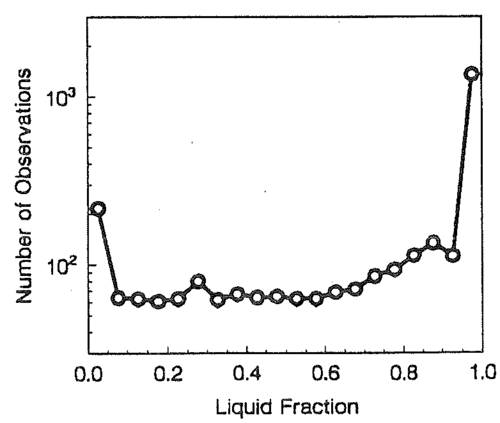

Figure 6. Histogram of liquid water content fraction (LWC/(LWC+IWC) for mixed phase cloud conditions.

EVOLUTION OF MICROPHYSICAL STRUCTURE OF OROGRAPHIC SNOW CLOUDS ASSOCIATED WITH THE PASSAGE OF UPPER TROUGH

Mizuho Hoshimoto[1], Masataka Murakami[1], Narihiro Orikasa[1]
Kennichi Kusunoki[1], Yoshinori Yamada[2] and Masanori Takahashi[3]

[1]Meteorological Research Institute
[2]Japan Meteorological Agency
[3]Tone River Dams Integrated Control Office

1.INTRODUCTION

Snow clouds form while a cold airmass from the Eurasian Continent crosses the Sea of Japan under a winter monsoon pressure pattern of west-high and east-low, and bring about snowfall over the west coast of Japan. Eventually the airmass is forced up the mountains with the crest height of 2000 m, causing further condensation and heavy snowfall. Microphysical structures of the snow clouds over the coastal areas have been studied by some researchers (Magono and Lee, 1973, Murakami et al., 1994b, Murakami et al., 1996, etc.). However, the snow clouds modified by the mountains topography have not been investigated so far. Meteorological Research Institute (MRI), Japan Meteorological Agency and Tone River Dams Integrated Control Office, Ministry of Construction carried out the orographic snow cloud project over the north-western slope of the Mikuni Mountains from 1994 to 1999. An instrumented aircraft has been introduced since 1997. During the field campaign of this project, an upper trough extending from a cold low at the Kamchatka passed through the observation area early in the afternoon of 21st February 1999. In this paper the evolution of microphysical structures associated with the passage of the trough are described.

2.OBSERVATION FACILITIES

Figure 1 shows the topography around the observation area. The main observation area was one of valleys extending southeast to northwest, perpendicularly to the mountain range. The instrumented aircraft was equipped with microphysical, thermodynamical and dynamical sensors. The ground-based observations were concentrated at Shiozawa and Shimizu. The principal observation facilities were hydrometeor videosonde (Murakami and Matsuo, 1990) and rawinsonde system, Doppler radar and a microwave radiometer at Shiozawa and a microwave radiometer at Shimizu. We also used an instrumented automobile. The automobile run along the valley and measured the vertically integrated cloud water, precipitation particle images and so on. The aircraft operated from Niigata Airport made in-site measurements of snow clouds over Shiozawa and the Mikuni Mountains. On 21st February 1999, the aircraft flew three or four legs with different altitudes along the valley in the morning (1110 JST -1148 JST) and in the afternoon (1549 JST - 1626 JST). Rawinsondes were launched at 0601 JST, 1154 JST, 1426 JST and 1726 JST. At 1426 JST, the rawinsonde was launched together with hydrometeor videosonde. The instrumented automobile went up and down the valley four times in the morning and did three times in the afternoon.

3.OBSERVATION RESULTS

3.1 Synoptic Situations

Surface weather map (Fig.2) at 0900 JST shows a pressure pattern of winter monsoon. The upper trough extending from a cold low at the Kamchatka Peninsula passed through the observation area between 1200 JST and 1400 JST.

Two major changes associated with the passage of the trough were found in vertical profiles of winds and microphysical structures of snow clouds. We will examine the relation be-

[0]Corresponding author's address: Mizuho Hoshimoto, Meteorological Research Institute, Dept. of Physical Meteorological Research, 1-1, Nagamine, Tsukuba City, Ibaragi, JAPAN 305-0052; e-mail: mhoshimo@mri-jma.go.jp

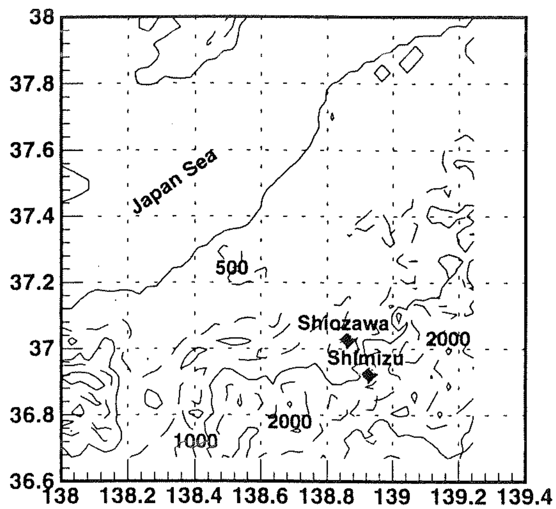

Fig. 1: Topography around the observation area

tween these two changes.

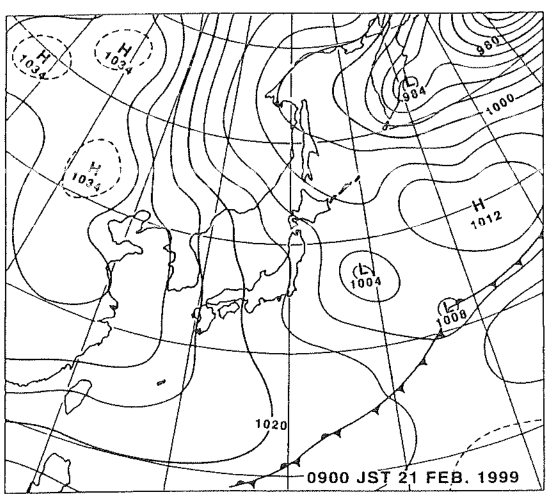

Fig. 2: Surface weather map at 0900 JST 21 Feb. 1999.

3.2 Evolution of wind

Figure 3 shows a time-height cross section of equivalent potential temperatures and horizontal winds. Before the passage of the upper trough (0601 and 1154 JST), the wind was north-westerly with a speed of 5-10 m/s below the 3.5 km level and west-southwesterly with a speed of 20 m/s above the level. After the passage (1426 and 1726 JST), the wind changed to westerly below the 3.5 km level and to west-northwesterly above the level. By 1726 JST, the weak temperature inversion gradually rose from 3.5 km MSL to 4 km MSL and the wind directional shear across the cloud top weakened. The cloud top height was coincident with the base of inversion layer and its temperature was ~ -27 °C during the observation period.

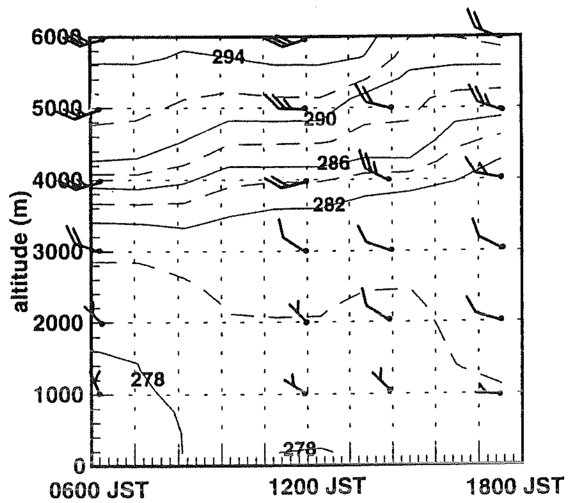

Fig. 3: Time-height cross section of equivalent potential temperatures and horizontal winds at Shiozawa

3.3 Evolution of Microphysical Structure

We compared the observation results before the passage of the trough (1110 - 1148 JST) with those after the passage (1549 - 1626 JST). Figure 4 gives cloud liquid water contents (CLW), measured by FSSP before and after the passage of the trough. The maximum CLW was above 0.1 g/m^3 in the both cases. Before the passage, there were two peaks of CLW, which were over the Uonuma Hills and the Mikuni Mountains. After the passage, only one peak, over the Uonuma Hills, was observed. The hydrometeor videosonde, launched at 1426 JST, did not detect cloud droplets.

Figure 5 gives number concentrations of snow particles, measured with 2DC probe, before and after the passage of the trough. The peaks of snow particle concentrations, that was 5 times larger than mean value, were not at the cloud top but were collocated with the peaks of CLW. As shown in Fig.6, mean diameters of snow particles increased with decreasing altitude over the hills and the mountains before the passage of the trough. After the passage of the trough, however, snow particles over the Mikuni Mountains did not show any significant growth.

RHI of reflectivities measured with Ka-band radar showed that precipitation type changed from stratiform to convective associated with the passage of the trough.

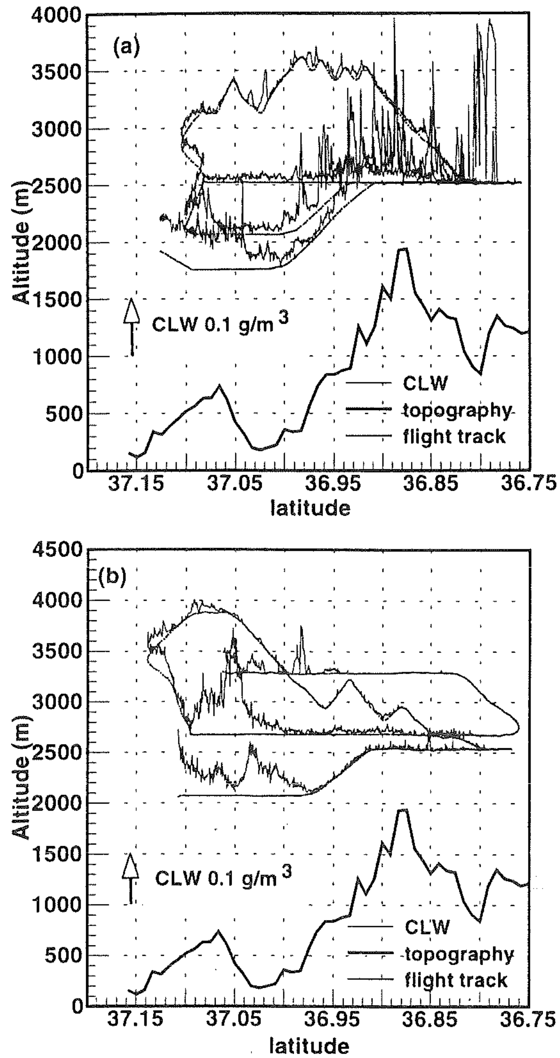

Fig. 4: Distributions of cloud water contents before (a) and after (b) the passage of upper trough.

4.DISCUSSION

Interactions between the low-level wind and

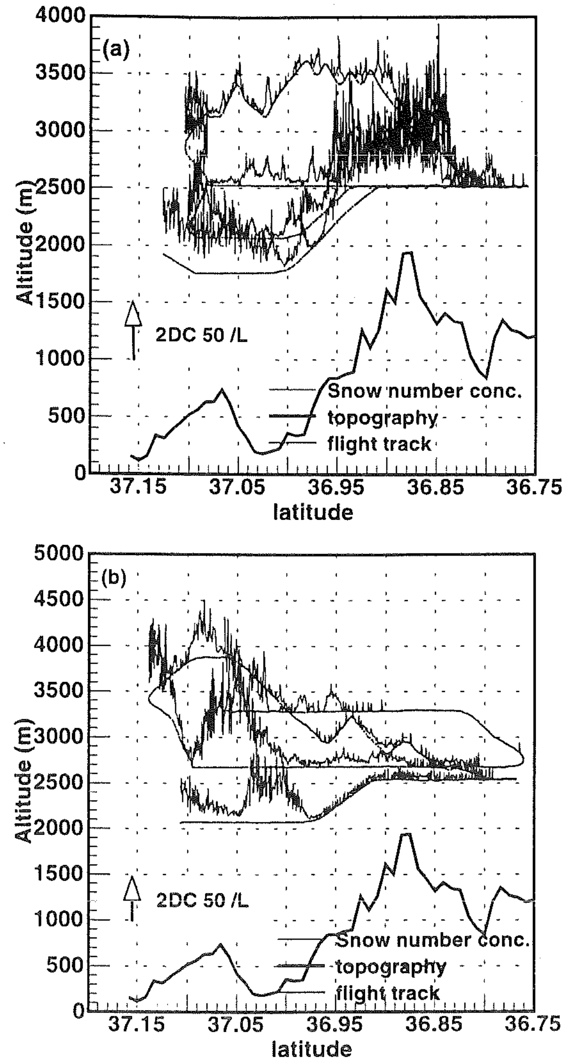

Fig. 5: Distributions of number concentrations of snow particles measured with 2DC before (a) and after (b) the passage of upper trough.

orographic topography seemed to modify the spatial distributions of hydrometeors in the snow clouds. Several mountains with the crest of $\sim$ 2000 m are situated west (upstream) of the Mikuni Mountains. The upstream mountains decelerated the westerly wind, resulting in weakening of the orographic lift. Furthermore, the upstream mountains induced upward motions, causing the precipitation, and drying out the air at lower levels before arriving at the Mikuni Mountains. Thus cloud liquid water disappeared and ice supersaturations decreased in the snow clouds over the Mikuni Moun-

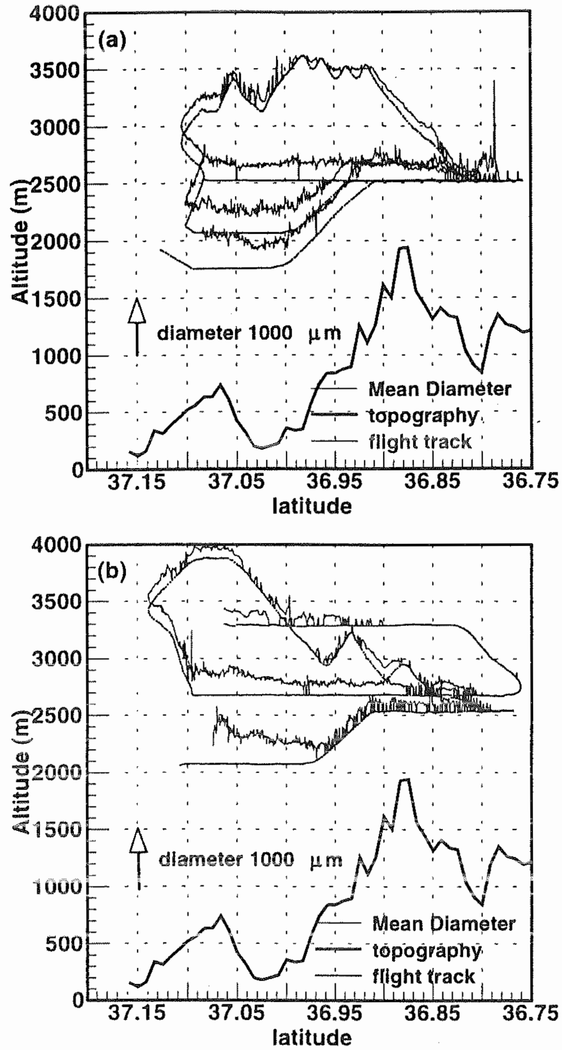

Fig. 6: Mean diameters of snow particles measured with 2DC before (a) and after (b) the passage of upper trough.

tains after the passage of the trough. Such cloud conditions prevented a significant growth of snow particles.

The number concentrations of snow particles increased in places where CLW existed. This suggests that the most likely mechanisms of ice nucleation were the freezing of supercooled cloud droplets and/or the activation of deposition nuclei at high ice supersaturations.

5.CONCLUSION

The evolution of microphysical structures of orographic snow clouds was observed with an instrumented aircraft and ground-based observation facilities. The spatial distribution of hydrometeors changed in association with the passage of the upper trough. A shift of wind directions at lower levels seemed to cause this change in two ways. After the passage of the trough, mountains west (upstream) of the Mikuni Mountains decelerated the westerly wind that would produce the orographic lift. They also consumed the available airflow through precipitaion processes. In consequence, the snow clouds over the Mikuni Mountains dried up and the growth of snow particles in them was suppressed.

The coincidence of the high concentrations of snow particles and cloud liquid water suggests that ice nucleation is closely related to the existence of supercooled cloud droplets.

REFERECNCES

Magono, C. and C. W. Lee, 1973: The vertical structure of snow clouds, as revealed by "snow crystals sonde", Part II. *J. Meteor. Soc. Japan*, **51**,176-190.

Murakami, M. and T. Matsuo,1990: Development of hydrometeor videosonde. *J. Atmos. Oceanic Tech.*, **7**, 613-620.

Murakami, M., T. Matsuo, H. Mizuno and Y. Tamada,1994b: Mesoscale and microscale structures of snow clouds over the Sea of Japan. Part I: Evolution of microphysical structures in short-lived convective snow clouds. *J. Meteor. Soc. Japan*, **72**,671-694.

Murakami, M., Y. Yamada, T. Matsuo, K. Iwanami, T.D. Marwitz and G. Gordon,1996: Mesoscale and microscale structures of shallow snowbads over the Sea of Japan. *Preprints of the 12th Intn. Conf. on Cloud and Presipitation*, 562-565

IN-SITU AND SATELLITE-BASED OBSERVATIONS OF MIXED PHASE NON-PRECIPITATING CLOUDS AND THEIR ENVIRONMENTS

J. Adam Kankiewicz *, Robert P. Fleishauer, Vincent E. Larson, Donald L. Reinke, John M. Davis, Thomas H. Vonder Haar, Stephen K. Cox

Cooperative Institute for Research in the Atmosphere/Center for Geosciences
Colorado State University
Fort Collins, Colorado, 80523-1375, USA

1. INTRODUCTION

The Center for Geosciences recently completed the fifth in an ongoing series of field programs connected with the Complex Layered Cloud Experiment (CLEX). The motivation for CLEX is to further our understanding of the processes inherent to the formation, maintenance and dissipation of mid-level, non-precipitating mixed phased clouds. A better understanding of mid-level clouds has many applications for both military and civilian purposes. For example, during DESERT SHIELD/STORM, mid-level cloud systems often masked target areas and hampered use of electro-optic sensors and weapons systems. For civilian pilots, poorly forecast mid-level clouds often restrict flight visibility and can create icing hazards.

During CLEX-5 (5 Nov - 5 Dec 1999), the University of North Dakota Citation II research aircraft took in-situ microphysical measurements of mid-level clouds over the central and northern Great Plains of the United States. The experiment yielded four mixed-phase cloud cases from 11 Nov and 2, 4, and 5 Dec 99. The 11 Nov 99 case was a Lagrangian measurement over east-central Montana, while the December cases were sampled over the Atmospheric Radiation Measurement (ARM) site in north-central Oklahoma. We now describe the instrumentation, aircraft sampling strategy, and discuss preliminary research results from the 11 Nov case study. A brief look at the subject of cloud glaciation will be performed. Finally, we will compare our measurements to those obtained in previous studies of this cloud type by several authors (Heymsfield, et al., 1991; Hobbs and Rangno, 1985, 1998; Paltridge, et al., 1986; Pinto, 1998; Tulich and Vonder Haar, 1998).

2. INSTRUMENTS

All of the measurements reported in this paper were obtained aboard the University of North Dakota's Citation II research aircraft. The basic instrumentation package measures temperature, dewpoint temperature, pressure, winds and cloud microphysics, along with aircraft position, attitude and performance information.

*Corresponding author's address: J. Adam Kankiewicz, CIRA/CSU, Fort Collins, CO 80523, USA
E-Mail: kankie@cira.colostate.edu

For our study, we focus on the cloud microphysical measurements, which were made with an array of Particle Measuring System (PMS) probes. These probes include the Forward Scattering Spectrometer Probe (FSSP), one-dimensional (1D-C) and two-dimensional (2D-C) optical array imaging probes, and the King Liquid Water Probe. All of these instruments are described in detail in NCAR's Research Aviation Facility Bulletin 24 (Baumgardner, 1981). We also employed the Cloud Particle Imager, a relatively new instrument, which records high- resolution (2.3 micron) digital images of cloud particles and processes them "on the fly" (Lawson and Jensen, 1998).

3. SAMPLING STRATEGIES

We used three basic flight patterns in CLEX-5: a racetrack pattern over a fixed point, Lagrangian racetracks, and a slow, spiral sounding. The racetrack is the basic sampling pattern. It involves a series of racetrack-shaped patterns at different altitudes. For a typical cloud of one kilometer thickness, we made five racetracks at different altitudes: one above cloud, three in-cloud, and another below cloud. Relative rapid descents were made between racetracks. Lagrangian racetracks were horizontally displaced from one another so the aircraft drifted with the horizontal wind at mid-cloud level. We sampled the wind speed and direction during the first mid-cloud racetrack and used this information to determine the horizontal position of subsequent racetracks, so that we stayed in the same relative cloud parcel for the duration of the measurement time.

Airspace restrictions prevented us from making Lagrangian measurements over the Southern Great Plains ARM site on 2, 4 and 5 Dec 99. Hence, we sampled clouds over the ARM site while centered at a fixed latitude and longitude. The racetracks were contained entirely within a reasonably homogeneous cloud region, with the longer dimension of the racetrack approximately 20 km in length. Above and below cloud racetracks were made far enough away from the cloud so they occurred entirely within clear air. The highest racetrack within cloud was made just enough below cloud top so the racetrack was entirely within cloud. Similarly, the lowest racetrack within cloud was just

Flight leg	Height	Temp	LWC	Stdev	W	Stdev	Wind spd	Wind dir	Cloud location
	(m AGL)	(°C)	(gm^{-3})	(gm^{-3})	(ms^{-1})	(ms^{-1})	(ms^{-1})	(deg)	
1	4525	-8.31	0.000	0.0017	0.585	0.2274	23.8	268	Below
2	5279	-13.88	0.018	0.0238	1.174	0.7347	26.3	266	In Bottom
3	5608	-16.40	0.150	0.0635	0.593	0.6396	26.5	269	In Top
4	5794	-16.29	0.000	0.0012	1.020	0.2857	24.5	270	Above
5	5546	-15.76	0.114	0.0579	0.602	0.6799	26.1	270	In Middle
6	5434	-14.90	0.063	0.0306	2.170	0.8421	25.6	271	In Middle
7	5182	-12.71	0.003	0.0038	2.868	0.5020	25.5	271	In Bottom
8	4877	-10.02	0.004	0.0026	1.215	0.6269	25.8	273	Below

Table 1. Mean microphysical and kinematic values for each leg of the 11 Nov 1999 cloud sample.

above cloud base. The racetracks within cloud were vertically separated by 200-500 m, depending on cloud depth. Due to limited upper air data, and the desire to get a vertical sample of the clouds, the aircraft performed slow spiral descents for a thermodynamic sounding. The aircraft sounding extended from about one kilometer above cloud top to a kilometer below cloud base, at a constant 300 meters per minute rate.

5. 11 NOV 1999 CASE STUDY

5.1 Synoptic Overview and Case Summary

A large area of mid and upper level cloudiness was advecting eastward along the Wyoming-Montana border, over the north end of a ridge axis about halfway between Casper, WY and Mile City, MT. An upper level shortwave moving across the area from the Nevada-Utah border enhanced early morning clouds beginning around local noon. Our aircraft sample took place between 1923 and 2040 UTC, as the cloud field crested the ridge axis and eventually dissipated.

As mentioned previously, the 11 Nov 99 case was a Lagrangian sample, so we remained in the same cloud parcel with time and saw the evolution of the various microphysical parameters as we drifted eastward. Table 1 summarizes the mean microphysical and kinematic quantities observed within the Lagrangian sampled cloud. In-cloud temperatures ranged from -12.5 to -16.5°C through a cloud depth of just over 500 m. Liquid water contents were highest in the mid and upper portions of the cloud (0.114 to 0.150 gm^{-3}), and dropped to less than 0.02 gm^{-3} at cloud base, which were just below 5,200 m.

5.1 Mixed Phase Cloud Glaciation

The Lagrangian aircraft measurements obtained from the mixed phase altostratus cloud observed on November 11, 1999 offer a unique opportunity to look at the subject of mixed phase cloud glaciation. How long can mixed phase clouds persist in a mixed phase state?, or alternatively, How fast does glaciation of clouds occur? We find that the rate of glaciation in this cloud was slow, and that by some measures, the cloud in fact de-glaciated.

The answer is not obvious *a priori* because the glaciation rate probably depends strongly on the number of ice-forming nuclei near the cloud, and little is known about the concentration of IFN at mid altitudes over continents. One can imagine two scenarios. First, if the IFN concentration is sufficiently large, a liquid cloud may be entirely converted to ice and only then dissipate either through precipitation or entrainment. Alternatively, if the IFN concentrations are small, a cloud may retain considerable liquid water until the moment it finally dissipates.

Field observations have demonstrated that glaciation can occur rapidly, i.e. within minutes, in the tops of cumulus turrets (Hobbs and Rangno 1985). In contrast, glaciation appears to proceed much more slowly in Arctic stratus clouds. In fact, both field observations (Pinto 1998) and numerical simulations (Harrington et al. 1999) suggest that Arctic stratus may sometimes reach an equilibrium in which the ratio of ice to liquid remains constant. This is possible because as ice particles grow, they tend to fall out of cloud, and then they can no longer deplete cloud liquid water. If the rate of formation of new ice crystals balances the rate of sedimentation of ice crystals, then the cloud can achieve an equilibrium. Both Pinto (1998) and Harrington et al. (1999) state that the rate of glaciation is highly sensitive to the concentration of ice-forming nuclei (IFN).

Hobbs and Rangno (1985) state that glaciation of altostratus and altocumulus clouds can require several hours, in contrast to the rapid glaciation of cumulus turrets. However, the aircraft measurements of Hobbs and Rangno (1985) (and those of Pinto 1998) were not Lagrangian measurements. That is, their aircraft transects did not drift with the horizontal wind so as to subtract out advective effects. With non-Lagrangian measurements, it can be difficult to determine whether an observed change in cloud properties occurs because the aircraft has observed temporal variations of a single patch of cloud or because the aircraft has sampled a horizontally varying cloud.

Aircraft sampling revealed little, if any, ice present in the top of the 11 Nov 99 cloud. However, ice did exist in the base of and beneath the cloud. Therefore we compare the amount of ice measured in two racetracks near cloud base, separated in time by about half an hour. (The earlier and later racetracks are numbered 2 and 7 respectively in Table 1.) The altitude of the later racetrack was about 100 m lower than that of the earlier racetrack. Since the aircraft used a Lagrangian sampling strategy, both racetracks intercepted the same column of air. Therefore the observed changes in ice amount reflect temporal and not horizontal spatial changes.

The ice crystal measurements may be summarized as follows. Though not shown here, both the CPI and 2D-C find that the number concentration of ice particles and the ice water content slightly *decrease* between the two racetracks. Therefore, if glaciation rate is defined as either the change in number concentration of ice crystals or the change in ice water content, then the cloud, instead of glaciating, actually de-glaciates. However, the liquid water content also decreases during this time, so that the ratio of liquid to ice water content, for example, stays roughly constant within the (large) uncertainty of the measurements. What we can say with a fair degree of certainty is that for the Nov. 11 case, the process of glaciation (or de-glaciation) has a timescale longer than 40 minutes. The cloud was sampled until minutes before its disappearance, and considerable liquid water remained in cloud even at the end of sampling.

Since thin cirrus was observed above the altostratus cloud that we sampled, one might hypothesize that the seeder-feeder process was responsible for the fact that the altostratus cloud was mixed phase and that it persisted in a mixed phase state. That is, one might suppose that the ice present in the altostratus originated as ice fallout from the cirrus cloud above. However, neither the CPI nor the Forward Scattering Spectrometer Probe (FSSP) observed hydrometeors falling into the top of the altostratus during the two times when the aircraft flew above the altostratus cloud. These two times occurred when the aircraft first approached the cloud from above and performed a spiral descent, and midway through sampling when the aircraft executed an above-cloud racetrack. Despite the failure to observe seeder crystals, one might argue that ice had fallen into the top of the altostratus cloud before the aircraft arrived, and that the possible de-glaciation we observed occurred because the seeder process ceased as soon as the aircraft arrived. However, the cirrus clouds, as recorded on flight video, appear to be high, thin, and without virga. The possibility that precipitating crystals from the cirrus cloud could have survived the long fall through subsaturated air to the altostratus cloud is remote.

6. COMPARISON OF CLEX-5 RESULTS WITH OTHER STUDIES

Heymsfield, et al. (1991) took aircraft measurements of two clouds near Green Bay, WI in October of 1986. The first was a thin cloud about 200 m thick with a base at 7.3 km altitude, while the second was on the order of 500 m thick with a base at 7.5 km. Liquid water contents in the first case were only .01 to .02 gm^{-3}, while the second was in the range from 0.04 to 0.12 gm^{-3}. These values fall within the range of those measured in CLEX-5, but are closer to the low end of our measurements. The temperatures were –29 to –31°C, which is similar to our coldest day on 2 Dec 99. Vertical velocities in this study varied from .25 to .75 ms^{-1}, which also compares quite favorably to those we measured during CLEX-5.

Hobbs and Rangno (1985) reported the findings on measurements and observations of 90 cumuliform and 72 stratiform clouds. One of their illustrative examples is an altocumulus (AC) cloud over Washington State with bases at 5 km (AGL), temperatures ranging from –8 to –13°C, and approximately 800 m deep. The measured maximum liquid water content was 3 gm^{-3} near cloud top, which more than twice that found in CLEX-5 and over an order of magnitude higher than the October 1986 clouds previously discussed. However, this may be attributed to the difference in maritime and continental climates. Their study also cites ice particle concentrations of 0.1 to 2 liter^{-1}.

Airborne measurements of mid-level clouds over the Beaufort Sea in Alaska were also reported by Hobbs and Rangno (1998). In this study, they found AC 30 to 800 m thick, with temperatures in the 1 to –31°C range. Observed Mean liquid water contents varied from 0.02 to 0.14 gm^{-3}, which are in good agreement with our measurements. Droplet concentrations were 105-450 cm^{-3}, with average effective cloud droplet radius of 10 μm.

Paltridge, et al., (1986) completed a case study of ice particle growth in a mixed-phase altostratus (AS) cloud. The system was divided into two layers, with the first from 2600 to 3300 m and the second from 3300 to 3600 m. Liquid water contents varied from 0.0 to 1.2 gm^{-3}, depending on location within the cloud, which compares favorably with our four cases. Temperatures in cloud ranged from –6 to –11°C, which is comparable to our 5 Dec 99 case. Upward vertical motion was calculated in this study to be approximately .09 ms^{-1}, which is an about an order of magnitude lower than those we measured or those reported by Heymsfield, et al. (1991).

Pinto (1998) analyzed two Arctic mixed-phase cloudy boundary layers in the temperature range –13 to –20°C. He found that liquid water content generally increased with height through the cloud layer with a maximum just below cloud top. Values were on the order of 0.005 to just over 0.1 gm^{-3}, which is in good agreement with our measurements and previously described studies. Total cloud ice generally decreased with height through the layer with a maximum near cloud base. Although we don't show any of these values here, that trend is apparent in our data. Typical vertical velocities in this study were +0.002 ms^{-1} in one cloud and -0.005 ms^{-1} in the other. Due to these low values, Pinto concluded that the sign of vertical velocity is relatively unimportant for cloud existence. These values are much lower than those seen in other cases examined thus far, and are well below the noise level of the Citation instruments.

Finally, Tulich and Vonder Haar (1998) examined measured structures of a multi-layer cloud in great detail. The system started out as an AS layer from 5800 to 6000 m, with an AC layer rising into it from a base of approximately 5125 m. Mean liquid water contents varied from a minimum of 0.03 gm^{-3} to a maximum of 0.31 gm^{-3} through the center of the cloud system. The mean value for most flight legs was 0.08 to 0.16 gm^{-3}. The reason for the higher mid layer value my be due to the fact that this was a summer time system, and appeared to have formed from detrained convective moisture. Mean in-cloud vertical motion ranged from +0.6 to –0.5 ms^{-1}, with maximum values of +2.2 and –1.8 ms^{-1}. All values compare reasonably well to the CLEX-5 measurements.

7. CONCLUSIONS AND FUTURE WORK

We have sampled a mixed phase altostratus cloud and have found the in-situ observations to be similar to those observed in previous studies. We have also found that the rate of glaciation was slow, and that by some measures, the cloud was in fact de-glaciating. We speculate that the cause of the slow or non-existent glaciation was low concentration of ice-forming nuclei (IFN), coupled with the fact that ice particles tend to sediment rapidly after they have grown sufficiently large by vapor diffusion. This hypothesis must remain speculative, since we did not measure IFN concentration.

Future work will center on refinement of the measurements taken thus far, such as retrieving liquid and ice particle sizes and concentrations. We will also be deriving products from the measurements, such as turbulent kinetic energy, potential temperature, lapse rates, radiative heating and cooling rates, etc. Some radiative transfer modeling, as well as cloud microphysical modeling, is also planned. Once the processing of the in-situ data is completed, the next step will to tie the in-situ measurements to satellite imagery, with the emphasis on developing improved forecasting techniques and remote sensing algorithms for mixed phase systems.

ACKNOWLEDGEMENTS

This work was supported by the Department of Defense Center for Geosciences/Atmospheric Research Agreement #DAAL01-98-2-0078.

REFERENCES

Baumgardner, D., 1981: Airborne measurements for cloud microphysics. Research aviation facility bulletin 24, National Center for Atmospheric Research, 1-22.

Harrington, J. Y., T. Reisin, W. R. Cotton, and S. M. Kreidenweis, 1999: Cloud resolving simulations of Arctic stratus Part II: Transition-season clouds. *Atmos. Res.*, **51**, 45-75.

Heymsfield, A.J., L.M. Milosevich, A. Slingo, K. Sassen and D O'C. Starr, 1991: An observational and theoretical study of highly supercooled altocumulus. *J. Atmos. Sci.*, **48**, 923-945.

Hobbs, P. V., and A. Rangno. 1985: Ice particle concentrations in clouds. *J. Atmos. Sci.*, **42**, 2523-2549.

----------, 1998: Microstructures of low and middle-level clouds over the Beaufort Sea. *Quart. J. Roy. Meteor. Soc.*, **124**, 2035-2071

Lawson, R. P., and T. L. Jensen, 1998: Improved microphysical observations in mixed phase clouds. Preprints, *Conference on Cloud Physics*, Everett, WA, Amer. Meteor. Soc., 451-454.

Paltridge, G.W., W.J. King and C.M.R. Platt, 1986: A case study of ice particle growth in a mixed-phase altostratus cloud. *Aust. Meteor. Magazine*, **34**, 149-154.

Pinto, J. O., 1998: Autumnal mixed-phase cloudy boundary layers in the Arctic. *J. Atmos. Sci.*, **55**, 2016—2038.

Pruppacher, H. R., and J. D. Klett, 1997: Microphysics of clouds and precipitation, 2nd Ed. Kluwer Academic Publishers, 954 pp.

Tulich, S.N. and T.H. Vonder Haar, 1998: Measured and Calculated Structures of a Multi-Layer Altocumulus Cloud. M.S. Thesis, CSU Atmospheric Science Paper No. 647, 190 pp.

PRECIPITATION MECHANISMS IN EAST ASIAN MONSOON RAIN

Tsutomu Takahashi
(Obirin University)

1. INTRODUCTION

In addition to their importance to the inhabitants of the region, the East Asian monsoon rains also contribute to the large scale circulation through the heat released during rain formation. There have been only a few attempts to investigate the mechanisms through which rain is formed in such systems (Churchill and Houze 1984, Houze and Churchill 1987). The primary difficulty in such studies is the hazardous nature of aircraft flights in intense echo regions of storms where there is abundant liquid water. A videosonde system has been developed to overcome these difficulties (Takahashi 1990) and more than 200 sondes have been released in various areas of East Asia.

2. VIDEOSONDE SYSTEM

As is illustrated in Fig. 1, the videosonde consists of two parts, one to obtain images of precipitation particles and the other to measure the electric charge on the particles. When a particle larger than 0.5 mm in diameter interrupts a beam of infrared light, a flash is triggered and a videocamera obtains an image of the particle. The electric charge on the particle is measured by an induction ring. In the most recent version of the videosonde ice crystals are collected on a transparent film and magnified. The camera images, the electric charges, and the magnified crystal images are all transmitted to a ground station over 1680 MHz. In addition, the videosonde may also transmit temperature, humidity, and pressure. During the past ten years 227 such videosondes have been released into monsoon rain clouds from various parts of East Asia (Fig. 2).

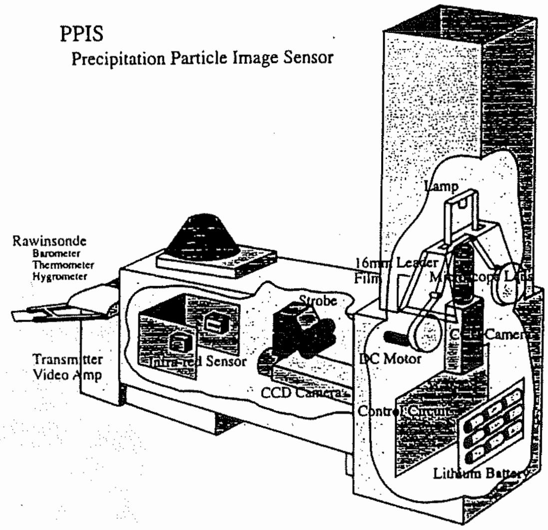

Fig. 1. Videosonde

3. PRECIPITATION MECHANISMS IN PRIMARY CLOUD SYSTEMS

Cloud systems and precipitation mechanisms differ in different monsoonal areas (Fig. 3). In Manus Island., rainbands develop along strong, low-level

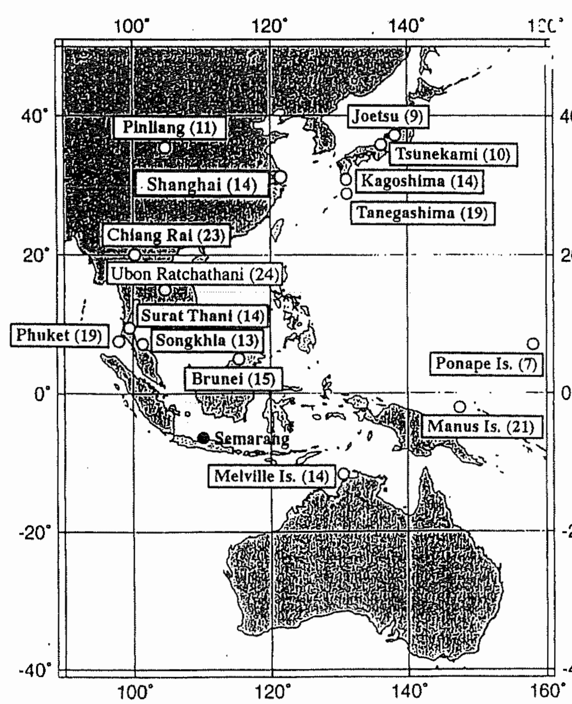

Fig. 2. Videosonde ascent number and location.

Corresponding author's address: Tsutomu Takahashi, Obirin University, 3758 Tokiwa-cho, Machida-shi, Tokyo 194-0294, Japan;
E-Mail: t2@obirin.ac.jp

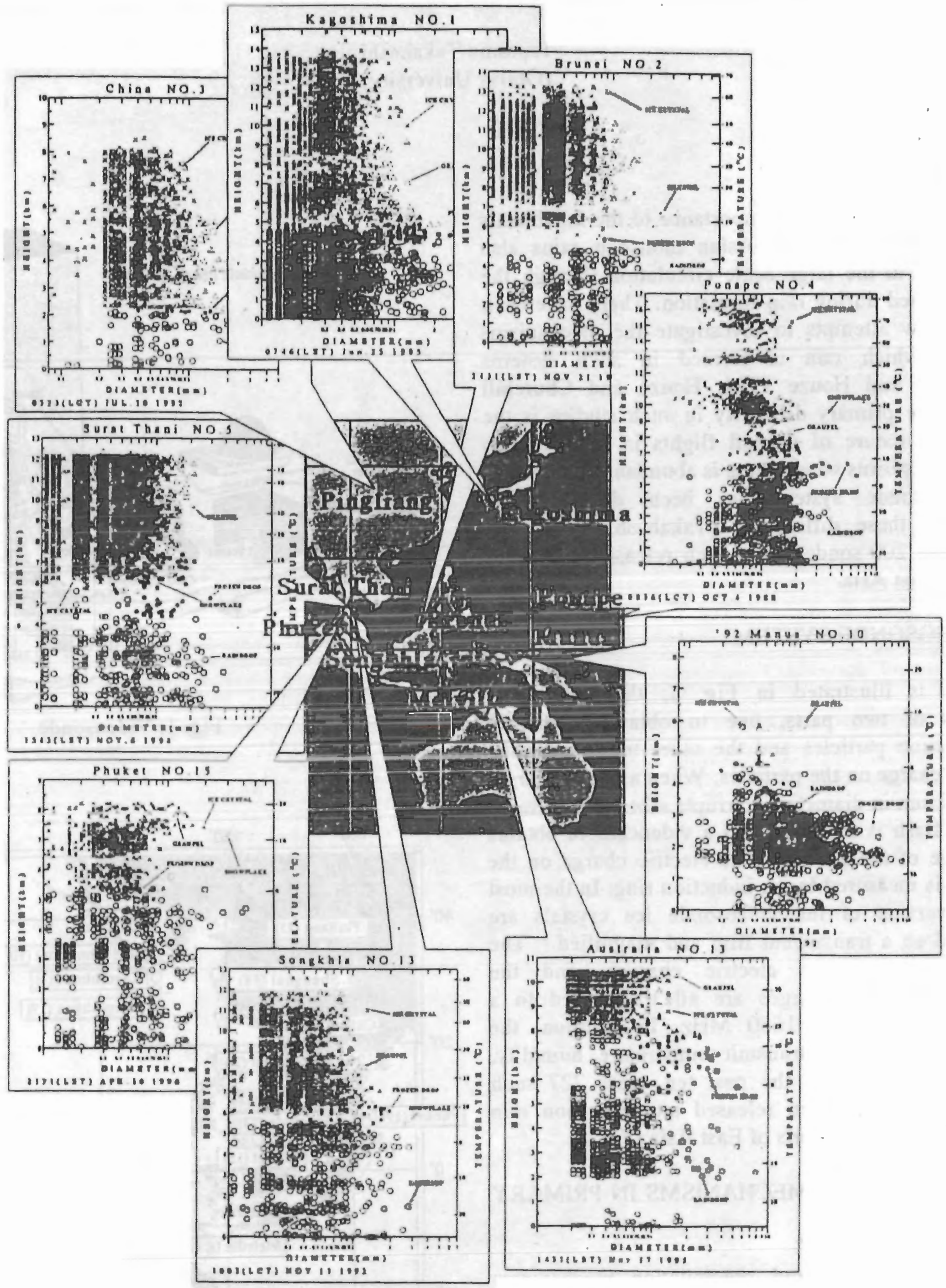

Fig. 3. Typical particle distribution in each location.

convergence formed by interaction between tropical cyclones and easterlies while in Ponape, cloud clusters develop within the intertropical convergence zone. They are very few ice crystals and large raindrops are formed by rapidly growing frozen drops near the freezing level. In Brunei, vortex over the ocean off Brunei build cloud cluster over the land. In Songkhala and Surat Thani, longitudinal rainbands developed by the interaction of easterlies and a cyclone over the South China Sea. Graupel are now active. In Phuket, rainbands developed over the ocean along the coast as southwesterlies were accelerated by the Australian High, the Somalia High and the Indian heat low. Here the rain was formed primarily through the warm rain process with many ice crystals in the upper levels.

In Melville Island, cloud first developed along a sea-breeze front. As the cloud produced heavy rain, it exhibited squall line characteristics. Large frozen drops and enormous numbers of graupel and ice crystals were observed in the cloud. The number concentration of ice crystals increased to as many as 10 cm^{-3} and there was frequent lightning. In Ubon, as cumulonimbus merge and produce intense rain, a series of cloud bands appeared in front. As one of the bands increased in intensity, original cloud clusters showed vortex. In Chiangrai, strong convergence zone developed through interaction with the monsoon southwesterlies and a vortex formed originally over the ocean off Vietnam. When low-level stratocumulus reached the higher, layered cloud, graupel were formed. Ice crystals were widely spread and formed snowflakes. In Shanghai, Tanegashima and Kagoshima, mesoscale cloud clusters lined up the front.

In the convected area, frozen drops and graupel grew. In the upper cloud level, there were wide-spread ice crystals and it rains as snowflakes. In Pingliang, the warm rain process no longer contributes to rain formation and rain is formed through very efficient graupel formation.

4. SUMMARY

a. Results obtained from videosondes show that different cloud systems and different precipitation processes occur in different areas of East Asia during the monsoon period. Near the equator the process is either

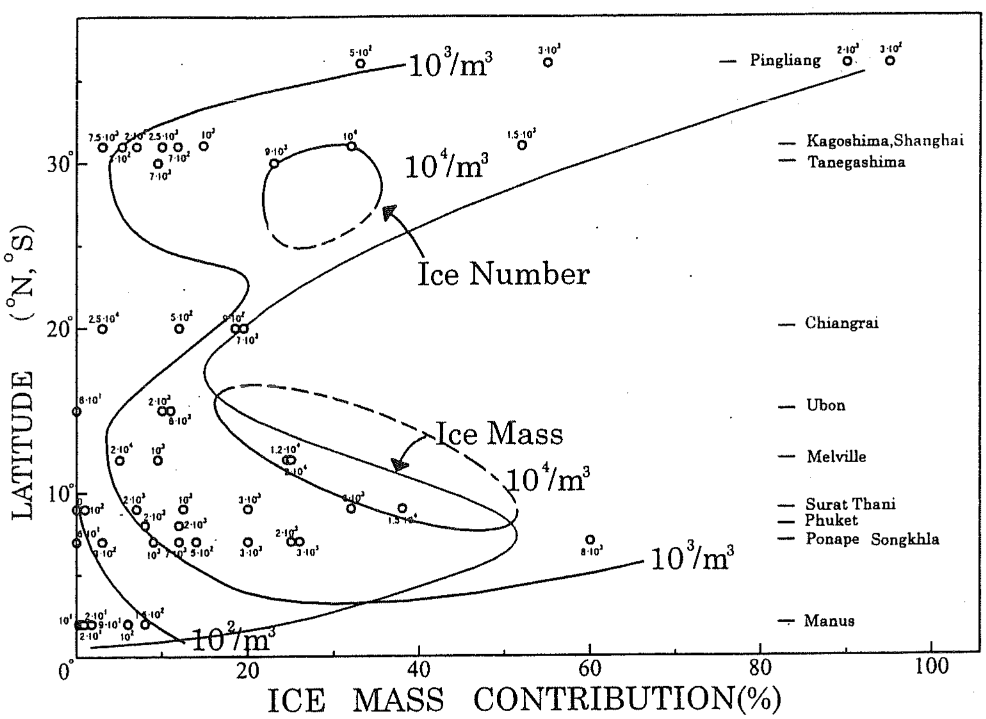

Fig. 4. Contribution of ice-phase particles to total water content and ice crystal number density for different latitudes.

b. warm rain as in Phuket or graupel formation as in Brunei. Over the open ocean as in Ponape and Manus, large raindrops are produced through the growth of frozen drops. At higher latitudes, graupel interact with lower level precipitation processes and, where frontal passages occur, snowflakes are also involved (Fig. 4).

c. Over the ocean in equatorial regions, where there are low number concentrations of graupel and/or ice crystals, lightning activity is also weak (Fig. 5).

ACKNOWLEDGEMENTS. This research was supported by the National Space Development Agency of Japan. Part of this work was also supported by the Climate Center of Tokyo University.

References

Churchill, D.D. and R.A. Houze, Jr., 1984: Development and structure of winter monsoon cloud clusters on 10 December 1978. *J. Atmos. Sci.*, **41**, 933-960.

Houze, R.A. Jr. and D.D. Churchill, 1987: Mesoscale organization and cloud microphysics in a bay of Bengal Depression. *J. Atmos. Sci.*, **44**, 1845-1867.

Takahashi, T., 1990: Near absence of lightning in torrential rainfall producing Micronesian thunderstorms. *Geophys. Res. Lett.*, **17**, 2381-2384.

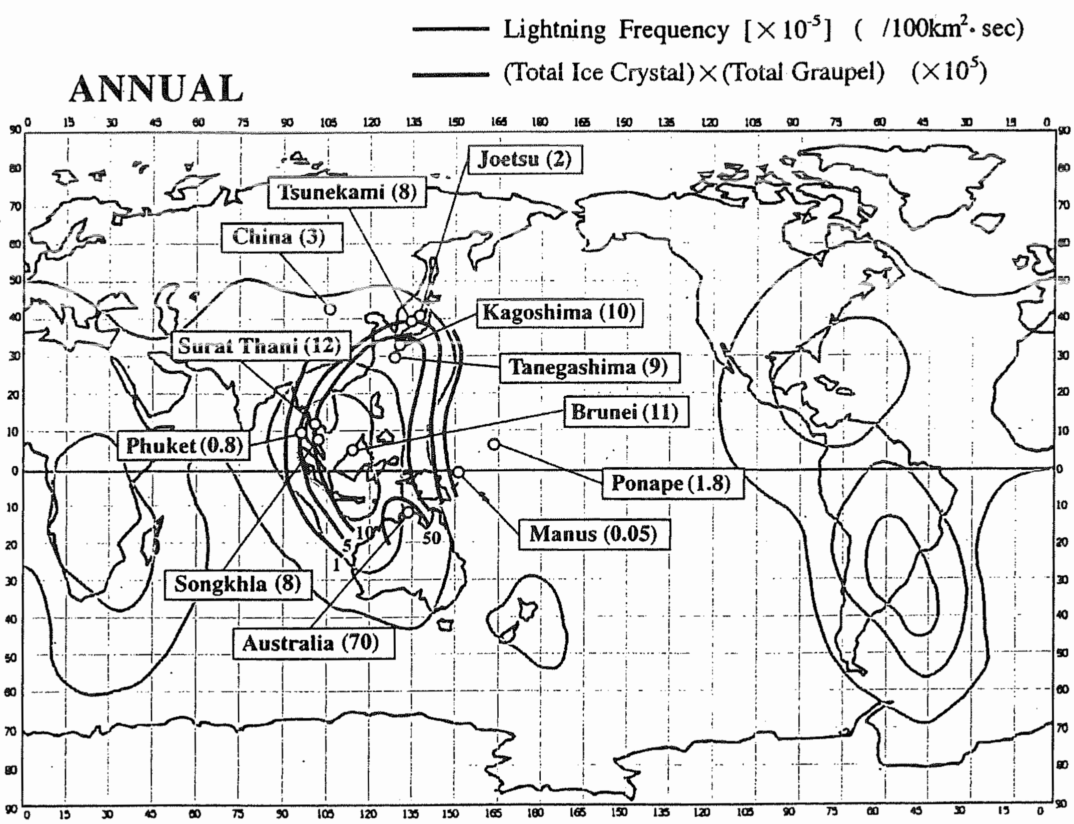

Fig. 5. Lightning activity related to graupel and ice crystal number densities.

CHARACTERISTICS OF MIXED-PHASE CLOUDS FROM RADAR AND LIDAR OBSERVATIONS

Robin J. Hogan[1]*, Anthony J. Illingworth[1] and Paul R. Field[2]

[1]Department of Meteorology, University of Reading, Reading, Berkshire, RG6 6BB, UK
[2]Meteorological Research Flight, The Met Office, Building Y46, DERA, Farnborough, GU14 0LX, UK

1 INTRODUCTION

Of primary importance in determining the radiative properties and evolution of a cloud is its phase. Mixed-phase clouds could potentially play an important role in the climate system, but due to a lack of good observational datasets there is much uncertainty regarding the extent to which ice and liquid water coexist, and hence most models crudely assume that the ice/liquid water ratio varies as a function of temperature alone. In this paper we present radar, lidar and aircraft measurements taken at Chilbolton, England, from which it is shown that supercooled liquid water tends to occur in the form of distinct layers that are strongly reflective at the lidar wavelength, while the radar echo tends to be dominated by the much-larger ice crystals. Analysis of three years of lidar data shows that these layers occur surprisingly frequently. We also demonstrate that the differential reflectivity (Z_{DR}) measured by a scanning radar can attain very high values in the vicinity of supercooled water, indicating the growth of pristine columns and plates in the highly supersaturated environment. These two techniques could prove very valuable in determining the distribution and characteristics of mixed-phase clouds.

2 'CLARE'98' CASE STUDY

Figure 1 shows simultaneous measurements through a mixed-phase cloud over Chilbolton by a 1064-nm nadir-pointing polarization lidar mounted on the DLR Falcon aircraft (top two panels), a scanning 3 GHz polarization radar (third and fourth panels), and the microphysical probes of the UK Met Office C-130 aircraft (last panel). The data were taken on 20 October 1998 during the Cloud Lidar And Radar Experiment (CLARE'98). A number of strongly-reflective layers are clearly present in the lidar backscatter coefficient (β) field, and their low depolarization indicates that they are composed predominantly of spherical water droplets. The radar shows no such features in reflectivity (Z), since the ice crystals are much larger than the liquid water droplets and therefore dominate the signal. However, unusually high values of differential reflectivity (Z_{DR}) are observed beneath the supercooled water layers, indicating the growth of horizontally-aligned, highly non-spherical crystals. This feature is discussed further in section 3. In situ measurements by the C-130 at an altitude of around 4 km (-7°C) reveal the lowest elevated lidar echo to be associated with a liquid water content (LWC) of up to 0.2 g m^{-3}. The vertical velocity exhibits periodicity characteristic of a gravity wave, and simple calculations confirm that it is of sufficient amplitude to be the likely cause of the liquid water. The crystals sampled in the high Z_{DR} region were sector plates, which are known to grow only under high supersaturation conditions.

3 'CWVC' CASE STUDY

A second flight through warm frontal cloud took place on 30 March 1999 and involved only the C-130 aircraft and the Chilbolton radar. Figure 3 shows a radar scan through a high-Z_{DR} 'plume' (values up to 3 dB) which is shown by the simultaneous in situ aircraft measurements at -6°C to be associated with an ascending region of supercooled water with a maximum LWC of 0.19 g m^{-3} and vertical velocities of the order of 1 m s^{-1}. This time the crystal imaging probes on board the C-130 showed that needles were responsible for the high Z_{DR}. Similar high-Z_{DR} features have been observed before (e.g. Bader et al. 1987), although this is the first time that it has been suggested that liquid water is responsible.

To better interpret the radar measurements, Fig. 2 shows Z_{DR} as a function of ice-air ratio for homogeneous oblate spheroids with a variety of different aspect ratios, calculated using Rayleigh-Gans theory (Seliga and Bringi 1976). Usually the Z_{DR} of cirrus and mid-level cloud at Rayleigh-scattering frequencies is less than 0.5 dB, indicating that typically crystals are of fairly low density and do not have extreme aspect ratios. This has been confirmed by aircraft measurements. For example, Korolev et al. (1999) found that only 3% of crystals in a large aircraft dataset spanning the temperature range -45°C to 0°C could be classified as 'pristine' columns, plates or dendrites; the vast majority were irregular aggregates or polycrystals. This would suggest that pristine crystals occur in mid-level clouds only when liquid water is present, and under normal low-supersaturation conditions most particles are aggregates.

4 STATISTICS ON SUPERCOOLED CLOUDS FROM LONG-TERM LIDAR OBSERVATIONS

Supercooled water layers similar to those observed in Fig. 1 are clearly detectable in observations by ground-based lidar, and we have used over three years of data

*Corresponding author address: Robin Hogan, Department of Meteorology, University of Reading, Earley Gate, PO Box 243, Reading RG6 6BB, UK; e-mail: R.J.Hogan@reading.ac.uk.

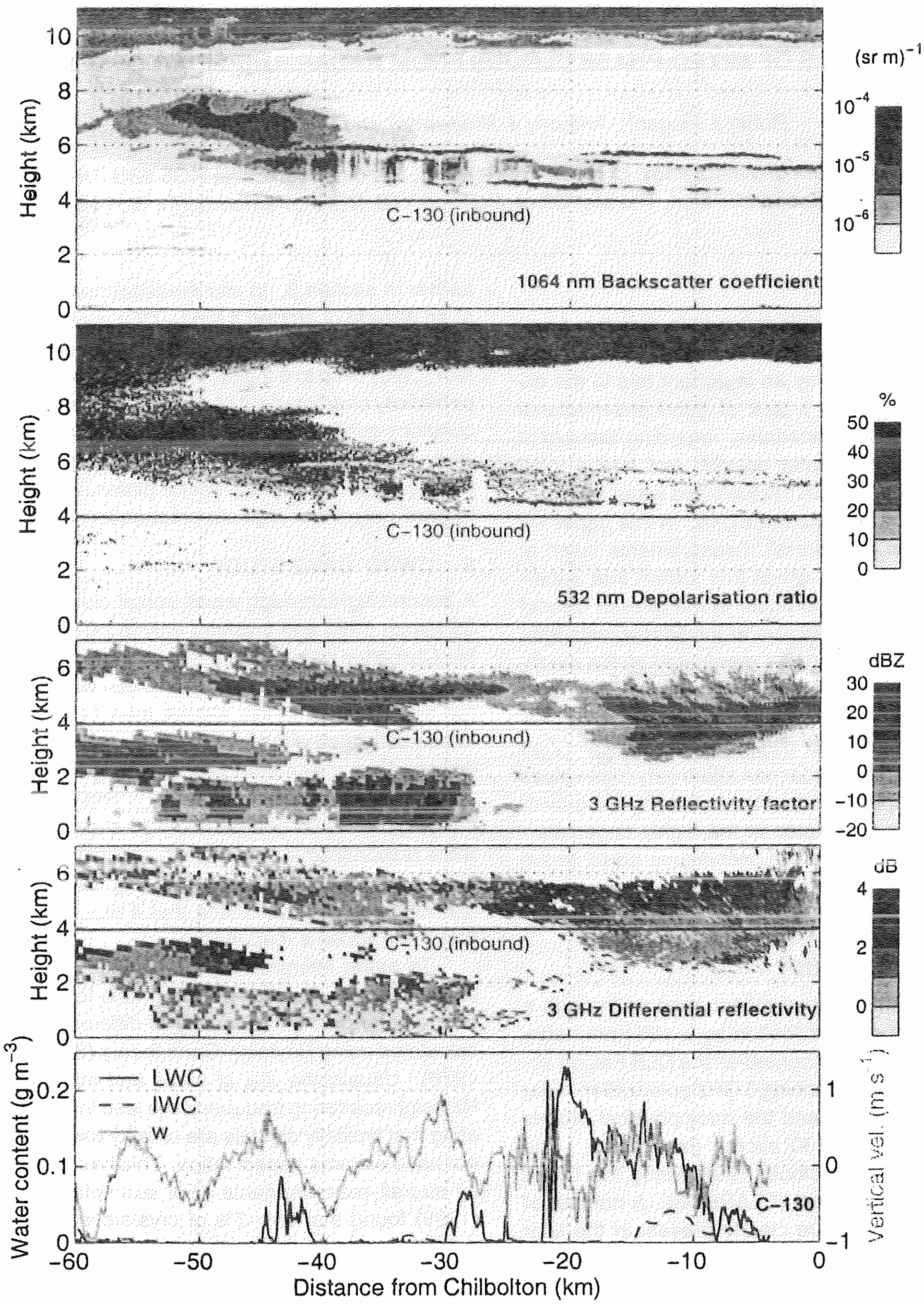

Figure 1: Composite of observations from the 14:20 UTC over-flight of Chilbolton on 20 October 1998 during CLARE'98. The first two panels show measurements by the nadir-pointing lidar on board the DLR Falcon aircraft flying at an altitude of 13 km. Simultaneous measurements of Z and Z_{DR} by the ground based 3 GHz radar are shown in the next two panels, and the last panel shows liquid water content, ice water content and vertical velocity measured by the C-130 aircraft at an altitude of 4 km (−7°C).

from a vertically-pointing 905 nm Vaisala lidar ceilometer (30-s/30-m resolution) at Chilbolton to determine the frequency of such layers as a function of temperature. Since their lidar characteristics are so distinctly different from clouds that consist purely of ice, it is straightforward to devise an objective algorithm for identifying them. We diagnose the presence of a layer wherever β exceeds 2.5×10^{-5} sr^{-1} m^{-1}, provided that this maximum value of β is at

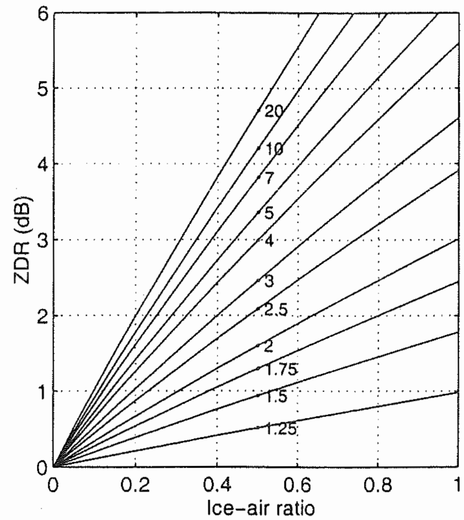

Figure 2: Z_{DR} as a function of ice-air ratio for single horizontally-aligned oblate spheroidal crystals with various aspect ratios. Z_{DR} is not directly related to crystal size.

least 20 times greater than the value 300 m above. Only one layer is diagnosed in any given profile.

An example of the scheme is shown in Fig. 4. A number of layers are present at temperatures down to −30°C, and their location as determined by the lidar has been superimposed on the simultaneous Z field measured by the vertically-pointing 94 GHz Galileo radar. As in Fig. 1, the radar echos are dominated by the larger ice crystals and the layers are not apparent. The radiative significance of the layers is obvious by their rapid extinction of the lidar signal, but it is somewhat surprising that they are able to persist for so long (up to 9 hours on some occasions) when ice crystals are present and presumably growing rapidly by virtue of the difference in saturation vapor pressure.

The algorithm has been applied to all the lidar data taken at Chilbolton, from the summer of 1996 until April 1999. In total 2.47 million 30-s rays have been processed. The 6-hourly radiosonde ascents from Herstmonceux (125 km from Chilbolton) were used to estimate the temperature at the altitude of the layers.

The results are summarized in Fig. 5. Panel a shows the fraction of the dataset for which the instrument observed any cloud in each 5° temperature interval between −50°C and −5°C. Pixels were defined to be cloudy if the lidar backscatter coefficient was at least 2×10^{-7} sr^{-1} m^{-1}. At temperatures warmer than −5°C the data were often contaminated by aerosol so are not shown. Because of frequent obscuration by low stratocumulus, clouds colder than −10°C were observed only 10% of the time. Panel b shows the fraction of observed clouds that contained a supercooled layer satisfying the definition given earlier, in each 5° interval. As one might expect, the fraction of clouds containing a supercooled layer decreases with temperature: 18.5% of clouds between −10°C and

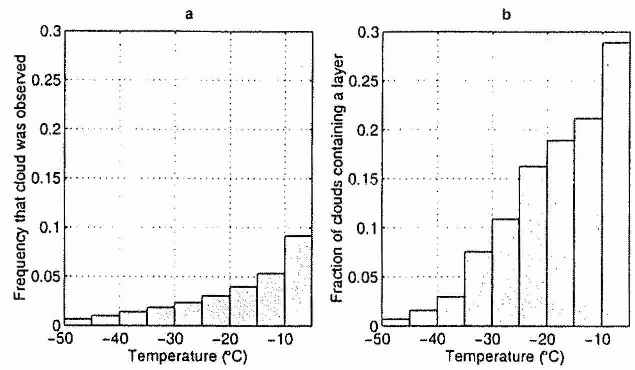

Figure 5: Statistics from the 31-month zenith-pointing lidar ceilometer dataset taken at Chilbolton: **(a)** Fraction of observations in which cloud was seen in each 5° temperature range; **(b)** Fraction of clouds that contain a layer in each 5° temperature range.

−15°C contained a layer, whereas between −30°C and −35°C the value was only 5.5%. The small fraction of clouds colder than −40°C that appear to contain layers are typically very short lived and probably correspond to aircraft contrails.

5 CONCLUSIONS

Two new observational techniques for the study of mixed-phase cloud have been described. Simultaneous lidar, radar and aircraft observations have shown that supercooled liquid water tends to occur in the form of thin layers, and analysis of a large lidar dataset suggests that they occur surprisingly often: around 30% of the time that cloud colder than −10°C was observed, a layer was observed within it. It was also found that pristine needles or plates tend to grow in the vicinity of the liquid water. While this is of considerable microphysical interest, it also means that future radar-aircraft studies could be much more fruitful since the radar would be able to use Z_{DR} to rapidly locate the most promising areas for the aircraft to fly through.

ACKNOWLEDGEMENTS

We are grateful to the Rutherford Appleton Laboratory for the use of the Chilbolton radars and lidar. CLARE'98 was funded by ESTEC and the CWVC experiment by NERC. The DLR lidar data were provided by Harald Flentje and the ECMWF data by Christian Jakob.

REFERENCES

Bader, M. J., S. A. Clough and G. P. Cox, 1987: Aircraft and dual polarization radar observations of hydrometeors in light stratiform precipitation. *Quart. J. Roy. Meteor. Soc.*, **113**, 491–515.

Korolev, A. V., G. A. Isaac and J. Hallet, 1999: Ice particle habits in Arctic clouds. *Geophys. Res. Let.*, **26**(9), 1299–1302.

Seliga, T. A., and V. N. Bringi, 1976: Potential use of radar differential reflectivity measurements at orthogonal polarizations for measuring precipitation. *J. Appl. Meteor.*, **15**, 69–76.

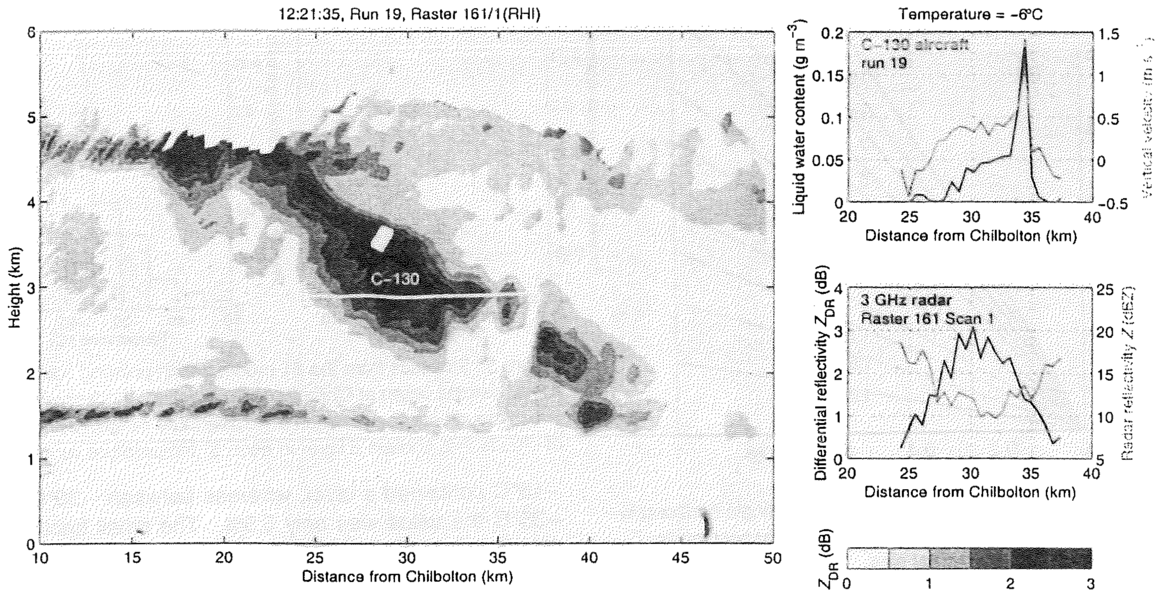

Figure 3: Simultaneous aircraft and radar measurements through a high-Z_{DR} plume associated with ascending supercooled liquid water, on 30 March 1999 at Chilbolton.

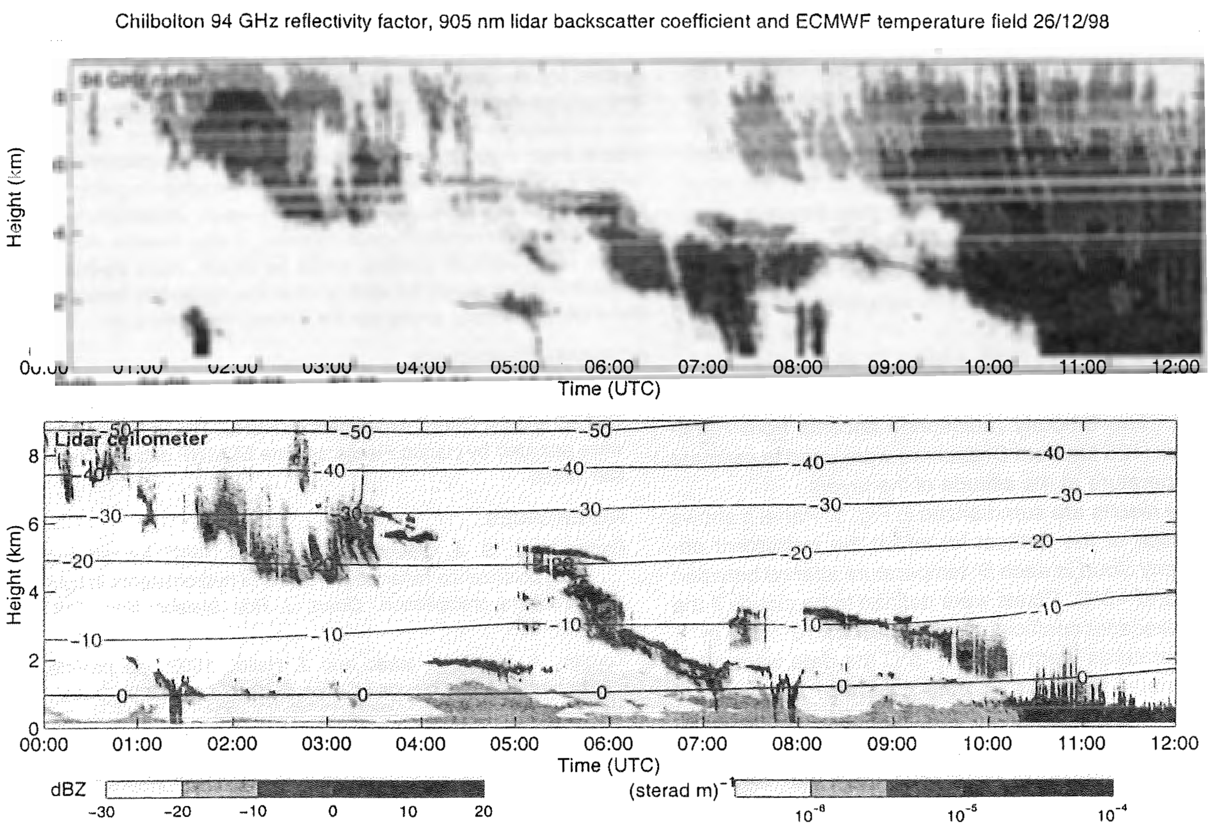

Figure 4: Example of the objective layer identification scheme from Chilbolton on 26 December 1998. The top panel depicts a time-height section of Z at 94 GHz, superimposed on which are black lines indicating the presence of a layer as diagnosed from the lidar ceilometer data shown in the bottom panel. The temperature according to the ECMWF model is also shown (in °C).

Ice particle habits in stratiform clouds

A. KOROLEV[1], G. A. ISAAC[1] and J. HALLETT[2]
[1]Meteorological Service of Canada, Toronto, ON, Canada
[2]Desert Research Institute, Reno, NV, USA

1. INTRODUCTION.

Ice crystals in clouds in the atmosphere have shapes, which relate to their density, terminal fall velocity, growth rate and radiative properties. In calculations for climate change predictions, forecasting of precipitation and remote sensing retrievals, idealized crystal shapes such as spheres, columns, plates and dendrites are often assumed.

The objective of this work is to study the frequency of occurrence of different habits of cloud particles in natural clouds from aircraft observations. Images of the particles were measured by a PMS OAP-2DC at 25 µm resolution installed on National Research Council (NRC) Convair-580.

2. ALGORITHM AND DATA PROCESSING

2.1 Basics of the algorithm

The present recognition technique is based on the originally developed algorithm for particle habit classification (Korolev and Sussman 2000). The particle habit is classified by analyzing dimensionless ratios R of simple geometrical measures such as the X- and Y-dimensions, perimeter and image area. The key to this method lies in considering these ratios for an ensemble of images. It is assumed that each habit category has a unique distribution of ratios. For an ensemble of images presented by a mixture of different habits, the distribution of a particular ratio will be a superposition of distributions of ratios of individual habits. If these distributions are known, than the fraction of each habit for an ensemble of 2D-images can be found as the solution of an inverse problem

$$\vec{f} = \mathbf{B}^{-1}\vec{M} \tag{1}$$

where $\vec{M}$ is a vector describing the measured distribution of the parameter R for an ensemble of 2D-images; $\vec{f}$ is a vector of fractions of images belonging to the different habit categories; **B** is a matrix composed of basis vectors of B_i describing the distribution of the ratio R in each habit category. Images, which did not touch edge elements (or "complete" images) and those that were partially viewed by the probe (or "partial" images) were processed separately.

For "complete" images the ratio

$$R_1 = \frac{\pi\left(N_x^2 + N_y^2\right)}{8N_{total}} = \frac{\pi\left(D_x^2 + D_y^2\right)}{8S} \tag{2}$$

was found to have the most unique features to characterize each category of habits. Here N_x is the number of pixels in the X-direction (perpendicular to the photodiode array, i.e. along the flight direction), N_y the number of pixels in the Y-direction (parallel to the photodiode array), N_{total} the total number of shadowed pixels, D_x=δN_x the X-size; D_y=δN_y the Y-size; S=$\delta^2 N_{total}$ the particle shadow image area; δ=25µm is the probe pixel resolution. "Complete" images with N_{total}<25 were rejected because of limited habit recognition capability.

Partial images were classified using the ratio

$$R_2 = P_{meas} / P_{circ} \tag{3}$$

Here P_{meas} is measured image perimeter; P_{circ} is the perimeter calculated in assumption that the image is perfect sphere. Knowing the number of triggered edge pixels in the image N_{edge1} and N_{edge2}, the perimeter of the sphere can be found as

$$P_{circ} = 2(\theta_2 - \theta_1)r \tag{4}$$

Here $\theta_1 = \arctan\left(\frac{x_1}{2z}\right)$; $\theta_2 = \arctan\left(\frac{x_2}{2(z+y_0)}\right)$;

$$r = \sqrt{\frac{x_1^2}{4} + \left(\frac{y_0}{2} + \frac{x_2^2 - x_1^2}{8y_0}\right)^2}\ ; \quad z = \frac{x_1^2 - x_2^2}{8y_0} - \frac{y_0}{2} + r\ ;$$

x_1=δN_{edge1}; x_2=δN_{edge2}; y_0=32δ. "Partial" images with N_{total}<180 were rejected because of poor habit resolution.

2.2 Habit categories

The present algorithm classifies 2D-images into four habit categories: "spheres", "irregulars", "needles" and "dendrites" (Fig. 1).

The class "spheres" (Fig. 1a) includes particles with circular images. Such particles could be liquid drops or quasi-spherical ice particles like graupel or frozen drops.

The category "needles" (Fig. 1c) includes images having elongated quasi-rectangular projection with aspect ratio C/A>3, here C is the length along the c-axis, and A is the diameter in the a-axis direction. Such projections in the majority of cases are produced by needles or columns. Rosettes with 3 to 5 bullets also fall in the category "needles".

The class "dendrites" (Fig. 1d) includes dendrites, stellar crystals, or aggregates of dendrites.

Polycrystalline ice particles such as combination of plates or columns, heavily rimed particles, graupel, and other forms that do not display features "needles", "dendrites" or "spheres" would fall into the category "irregulars" (Fig. 1b).

The current four categories cover the major habits of ice particles in the troposphere. Plates were not included since the occurrence of this habit in clouds is estimated as 0.5-2% (Zamorsky, 1955, Korolev et. al 1999)

2.3 Accuracy of the method

Figure 2 shows the results of the image recognition analysis. The panels Fig. 2 b, c, d, and e show the fraction of spheres, irregulars, dendrites and needles, respectively,

Corresponding author: Alexei Korolev, Meteorological Service of Canada, 4905 Dufferin St., Downsview, Ontario, M3H 5T4, Canada. e-mail: Alexei.Korolev@ec.gc.ca

derived from the OAP-2DC data. Figure 3 shows the OAP-2DC images measured in zones with a high percentage of circulars (a), irregulars (b), dendrites (c), and needles (d). A comparison of the results of habit recognition using the present algorithm, with those performed by eye, shows that for randomly chosen sets of images contained in five 2D-buffers, the error in misclassifying particle habits does not exceed 10%-15% on average.

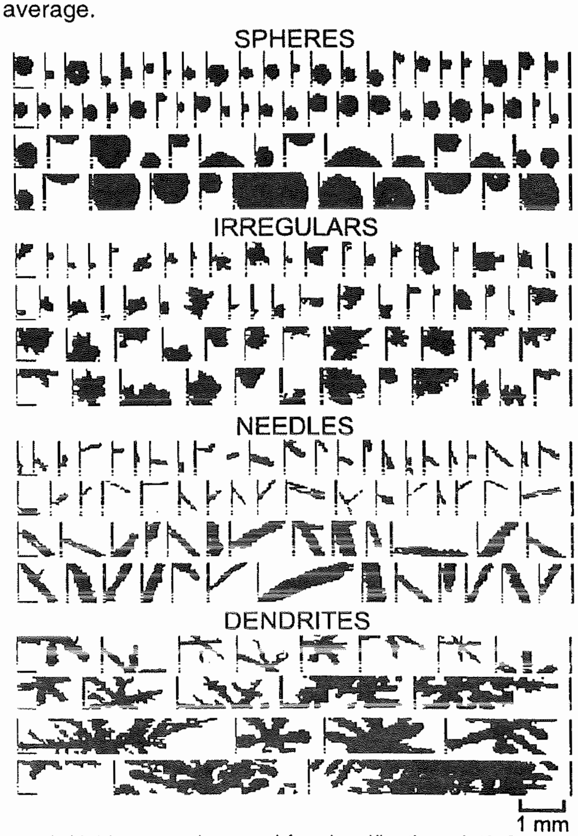

Figure 1. Habit categories used for classification of PMS OAP-2DC cloud particle images.

3 Frequency of occurrence of particle habits

The data on ice particle habits were collected during four field campaigns: the Beaufort Arctic Storm Experiment (BASE) in September-October 1994, the Canadian Freezing Drizzle Experiment I (CFDE I) in March 1995, the Canadian Freezing Drizzle Experiment III (CFDE III) December 1997-February 1998, and FIRE.ACE in April 1998. The main bulk of data were collected in stratiform clouds (*St, Sc, Ns, As, Ac, Cs*), usually associated with frontal systems. The total flight length in cloud was 35,840 km. The temperature and altitude of measurements ranged from 0 to -45°C and from 0 to 7.5 km, respectively.

Within this study, about 3 $\times 10^7$ particle images were analyzed. The frequency of occurrence of ice particle habits was calculated for three size intervals D>125μm, D>250μm and D>500μm in 5-degree temperature intervals in the range 0°C to -45°C. The results of the processing are presented in Fig. 4.

3.1 Irregular particles

The most important finding of this study is that the fraction of irregular particles is dominant over other forms *in all temperature intervals* (Fig. 4a). On average, the fraction of irregulars in the analyzed data set is 84% for D>125μm, and 76% for D>500μm. These results are consistent with observations of ice particle habits with the help of a SPEC Cloud Particle Imager (CPI) in Arctic clouds by Korolev et. al (1999).

The Magono-Lee diagram does not show irregular shaped particles in the temperature interval -20°C<T<-15°C and -35°C<T<-30°C. However, the OAP-2DC imagery of cloud particles indicated that the fractions of irregular particles in these temperature intervals are 84% and 93%, respectively.

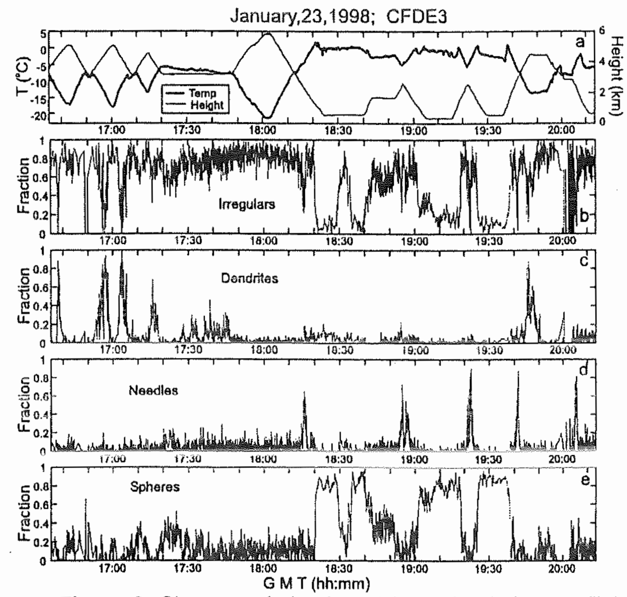

Figure 2. Changes of cloud particle habits during the flight on January 23, 1998 (CFDE III). (a) changes of temperature and altitude. Spatial changes of the fraction of (b) spheres, (c)irregulars, (d) dendrites, (e) needles.

3.2 Dendrites

On average the fraction of dendrites at temperatures -45°C<T<0°C is 3% and 10% for particles with D>125μm and D>500μm, respectively. The fraction of dendrites increases with an increase of particle size at -15°C<T<0°C (Fig. 4b). For example during FIRE.ACE the fraction of dendrites increased from 17% to 55% when the threshold size increased from 125μm to 500μm at -15°C<T<-10°C.

The maximum frequency of occurrence of dendrites was observed at temperatures -15°C<T<-10°C (Fig. 6b). This is consistent with the dendritic growth of ice particles observed in laboratory and in natural conditions (e.g. Hallett and Mason 1958; Magono and Lee 1966). However, in the majority of cases at -15°C<T<-10°C, there are no dendrites at all, and the dominant ice particle habit is irregular. This fact is not reflected in the Magono-Lee diagram. Though the Magono-Lee diagram has categories "graupel" (R3a, R3b, R3c in Magono-Lee classification) and "graupellike" (R4a, R4b, R4c), which would be interpreted as irregulars, there are a large variety of irregular ice particle shapes observed at -15°C<T<-10°C, which do not fit into these two categories.

A significant number of dendrites were observed within the temperature interval -10°C<T<0°C. During FIRE.ACE the fraction of dendrites with D>500μm was 55% in the temperature interval -10°C<T<-5°C. These dendrites were likely formed in the upper layers at colder temperatures and then fell down to the lower warmer layers still keeping their dendritic shape. It is worth noting that the Magono-Lee diagram does not show dendrites at temperatures -10°C<T<0°C.

3.3 Needles and columns

On average the fraction of needles and columns is about 6% and 8% for D>125μm and D>500μm, respectively (Table 4). The fraction of needles/columns increases with an increase of particle size at -5°C<T<0°C and -45°C<T<-40°C. For all four projects the maximum of the fraction of needles was observed in the -5°C <T<0°C temperature interval. There is only a small fraction of columns at temperatures -35°C <T<-10°C.

The observation of the maximum frequency of occurrence of needles at -5°C <T<0°C is in agreement with observations of needle growth in laboratory studies (e.g. Hallett and Mason 1958; Magono and Lee 1966).

The Magono-Lee diagram shows that in the temperature interval -35°C<T<-30°C ice particles in natural clouds should consist of columns or rosettes of bullets. The algorithm used in this study would classify these particles as "columns". However, the OAP-2DC data showed that the fraction of columns is only 2% in this temperature interval. This indicates a big divergence between observation of ice particles in the interval -35°C <T<-30°C obtained in the frame of this study and the Magono-Lee diagram.

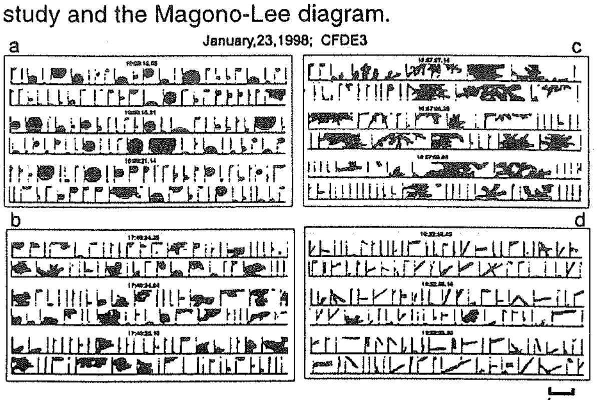

Figure 3. Samples of OAP-2DC images measured in zones of (a) spheres; (b) irregulars; (c) dendrites; (d) needles during the flight shown in Fig. 2.

3.4 Spherical particles

On average, spherical particles represent 7% and 6% of the classified images for the size intervals 125μm and 500μm, respectively. The fraction of spherical particles gradually decreases towards low temperatures. A large number of spherical particles (from 6 to 20%) were observed in the temperature interval -10°C<T<0°C during CFDE I and CFDE III. These particles were mainly associated with freezing drizzle events and were either liquid or frozen droplets. In contrast, in Arctic clouds, the spherical particles were more or less evenly distributed within the -40°C<T<0°C temperature interval. This is consistent with our numerous observations of CPI images of quasi-spherical particles in cirrus and mid-level clouds in the Arctic during FIRE.ACE. It is possible that, due to a poor resolution and digitizing problems of the OAP-2DC (Korolev et. al 1998) some irregulars were categorized as spherical particles. However, these types of errors do not exceed several percent on average and do not affect significantly the statistical results.

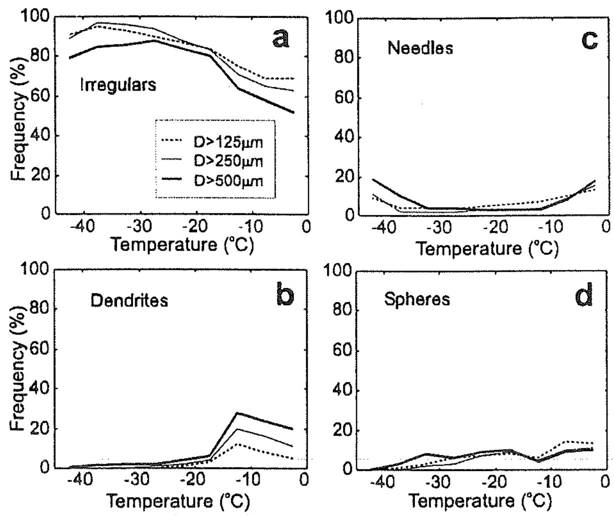

Figure 4. Dependence of the frequency of occurrence of particle habits versus temperature.

4. Cellular structure of needles and dendrites zones

The dendritic ice particles occur in isolated cells embedded in zones of irregular shape ice particles (Fig. 2c). In such cells the fraction of dendrites may reach 100%. Similar to dendrites, the needles at warm temperatures (-5°C<T<0°C) and columns at cold temperatures (-45°C<T<-40°C) occurred in cells (Fig. 2d). The dendrites and needles in such cells are frequently mixed with irregulars. The characteristic size of these cells is several kilometers, though it may range from hundreds of meters to tens of kilometers (Fig. 2c,d).

The observation of needles and dendrites in mainly isolated cells leads to the conclusion that columnar and dendritic growth in clouds at temperatures -5°C<T<0°C and -15°C<T<-10°C, respectively, occurs only in limited conditions.

5. CONCENTRATION OF ICE PARTICLES

The number concentration of ice particles was estimated as

$$N = n/SL_{cloud} \qquad (5)$$

where n is total number of analyzed particles larger than 125μm, 250μm, or 500μm measured over a cloud path length L_{cloud}, S is the sample area of the OAP-2DC.

In order to avoid misinterpretation, it is worth noting that the particle concentration estimated from Eq. 5 is a result of averaging over the distance L_{cloud}, the value of which is of the order of magnitude 10^1 to 10^3km. These results may be most useful for interpretation of meso- and macro- scales associated with satellite images and climate modeling. The estimated concentrations N_{125}, N_{250}, and N_{500} should be interpreted as the concentration of *ice* particles. The effect of supercooled drops is estimated as a few percent.

The constant concentration of ice crystals (N_{125} and N_{250}) with temperature (T>-35°C) in the troposphere shown in Fig. 5 is very important result. Past works have suggested an increase in concentration with colder temperatures (e.g. Meyers et al., 1992). Gultepe et al., (2000) suggest that this lack of relationship also holds for smaller ice particles (< 125 μm). No simple explanation for this observation is possible at this time. However, particle breakup, aggregation, ice multiplication (e.g. Hallett and Mossop, 1974) are temperature dependent processes and do not provide a solution. Ice multiplication due to particle breakup caused by evaporation or sublimation can occur at any temperature under non-steady conditions as ice particles fall from aloft into sub ice saturated regions, or by turbulent mixing with sub-saturated air. However, the exact mechanism for why such a process would lead to the concentration of ice particles being independent of temperature remains unclear and requires further study.

Another surprising result is rather sharp decrease of N_{125} below -35°C (Fig. 5). Small crystals below the 125 μm resolution limit are a key to interpretation of the variations in concentration with temperature.

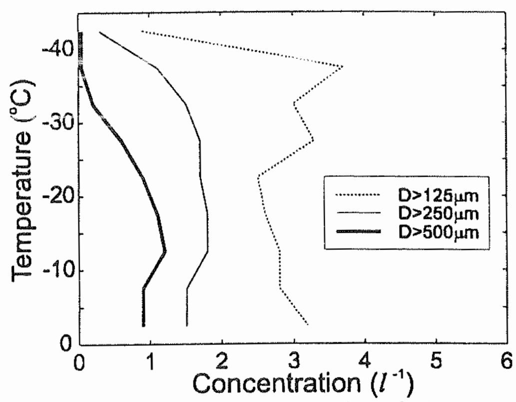

Figure 5. Averaged number concentration of cloud particles larger 125 μm 250 μm and 500 μm measured by the OAP-2DC during BASE, CFDE I, CFDE III, and FIRE.ACE.

6. Conclusion

The following results were obtained:

(a). A new algorithm for particle recognition was developed. One of the advantages of this algorithm is that it processes both "complete" and "partial" images.

(b). The frequency of occurrence of four habit categories (irregulars, dendrites, needles and spheres) was found. The majority of ice particles (D>125μm) were found to have an irregular shape (84%).

(c). The frequency of occurrence of ice particle habit was found to depend on particle size. The fraction of irregulars decreases with increasing particle size in the temperature intervals 0°C<T<-15°C and -35°C<T<-45°C. In the temperature interval -35°C<T<-15°C, the fraction of irregulars stays approximately constant with size.

(d). Ice particles observed in natural clouds frequently did not fit into the Magono-Lee diagram.

(e). The concentration of ice particles larger 125 μm averaged over 10^2-10^3 km scale is approximately 2.5-3.7l^{-1} and it does not depend on temperature in the range -35°C<T<0°C. The concentration of ice particles larger than 500 μm decreases below -15°C.

(g). Needles and dendrites were found to form in cells with a horizontal scale of hundreds of meters to tens of kilometers embedded in zones of irregularly shaped particles.

Since the data were collected in different climatic zones within many cloud types, and covered a significant cloud path length (3.6x10^4 km), the conclusions are applicable to most stratiform clouds containing ice. The details of this study are presented in Korolev et al. (2000).

Acknowledgements

The Panel on Energy Research and Development provided financial support for BASE and FIRE.ACE. Additional support for the collection of the FIRE.ACE data was given by NASA. The National Search and Rescue Secretariat of Canada, Boeing Commercial Airplane Group, Transport Canada, and the Canadian Department of National Defense provided funding for the CFDE project. The aircraft data were obtained using the National Research Council of Canada Convair-580 and the scientific and technical efforts of many NRC and MSC staff. J. Hallett was supported by grant ATM-9413437 and ATM-9900560 from Division of Physical Meteorology, National Science Foundation, Arlington VA and a grant from NASA NAG-1-20466.

References

Gultepe, I., Isaac, G. A., Cober, S. G., and Strapp, J. W. 2000: Ice crystal concentration versus temperature. *Submitted to J. Appl. Meteor.*

Hallett, J. and Mason, B. J. 1958: The influence of temperature and supersaturation on the habit of ice crystals grown from the vapor, *Proc. Roy. Soc.*, **A247**, 440 -453

Hallett, J. and Mossop, S. C. 1974: Production of secondary particles during the riming process, *Nature*, **249**, 26 -28

Korolev, A., G. A. Isaac and J. Hallett, 2000: Ice particle habits in stratiform clouds. *Q. J. Roy. Meteor. Soc.*, Accepted for publication.

Korolev, A. V., Isaac, G. A. and Hallett, J. 1999: Ice particle habits in Arctic clouds. *Geoph. Res. Lett.*, **26**, 1299-1302

Korolev, A. V. and Sussman, B. 2000: A technique for habit classification of cloud particles. *J. Atmos. Ocean. Tech.* in press

Magono, C. and Lee, C. 1966: Meteorological classification of natural snow crystals, *J. Fac. Sci.*, Hokkaido Univ. Ser. VII, **2**, 321-335

Meyers, M. P., P. J. DeMott, and W. R. Cotton, 1992: New primary ice-nucleation parameterizations in an explicit cloud model. *J. App. Meteor.*, **31**, 708-721

Zamorsky, A. D. 1955 *Ice in the atmosphere.* Akademia Nauk SSSR, Moscow

SHORTWAVE, SINGLE-SCATTERING PROPERTIES OF ARCTIC ICE CLOUDS

Timothy J. Garrett[1], Peter V. Hobbs[1], and H. Gerber[2]

[1]Department of Atmospheric Sciences, University of Washington, Seattle, Washington, 98195-1640, USA
[2]Gerber Scientific Inc., Reston, Virginia, 20190, USA

1. INTRODUCTION

Clouds play important roles in the energy balance of the Earth by trapping longwave terrestrial radiation and by absorbing and scattering shortwave solar radiation. When light impinges on a particle it is either scattered or absorbed. Three optical parameters can be used to describe how a beam of light interacts with a cloud of particles: the extinction coefficient, β_{ext}, the single-scattering albedo, ω_0, and the asymmetry parameter, g. At visible wavelengths, light absorption by cloud particles is small, therefore, β_{ext} and g depend only on scattering.

The asymmetry factor is given by [*van de Hulst*, 1981]:

$$g = \frac{1}{2}\int_{-1}^{1} P(\mu)\mu\, d\mu \qquad (1)$$

where, $P(\mu)$ is the phase function which is the probability that a photon is scattered into $d\mu$ ($\mu = \cos\theta$). Low values of g imply greater back-scattering and therefore greater reflectance. Exact scattering solutions are known only for relatively simple and mostly rotationally-symmetric particle shapes such as spheres, infinite and finite circular cylinders and spheroids [*Mishchenko et al.*, 1999]. Measurements of angular light scattering by ice crystals exist for only parts of the scattering phase function [e.g. *Sassen and Liou*, 1979]

Some attempts have been made to derive the asymmetry parameter of ice crystals by measuring radiative fluxes in cirrus clouds, and then deducing values of g that when input into radiative transfer models best reproduce the observations [e.g. *Stephens et al.*, 1990]. Theoretical approaches for deriving g have involved calculating how a beam of radiation interacts with idealized model ice crystals [e.g. *Takano and Liou*, 1989]. The observational and theoretical approaches have led to very different estimates of the asymmetry parameter for cirrus clouds. The values of g derived from various observational studies lie between 0.6 and 0.84; the theoretical approaches suggest values of g between 0.74 and 0.94 for various ice crystals types. Differences of this magnitude can lead to large differences in computed cloud albedo, and large differences in the derived values of solar heating of the Earth's surface and the upper troposphere [*Stephens et al.*, 1990]. It is still unclear which of these approaches best describes scattering by the wide variety of ice crystals that occur in clouds.

The first direct measurements of the single-scattering properties of ice crystal clouds were obtained using a prototype Cloud Integrating Nephelometer (CIN) built by Gerber Scientific, Inc. [*Gerber, 1996, Gerber et al., this issue*] when it was flown aboard the University of Washington's (UW) Convair-580 research aircraft during the 1998 FIRE-ACE/SHEBA field study in the Arctic. Also aboard the UW's Convair-580 aircraft was another new instrument: the Cloud Particle Imager (CPI), built by SPEC Inc. [*Lawson and Jensen,* 1998]. The CPI provides high frequency digital photographs of particles, with diameters down to 10 μm with a resolution of 2.3 μm, in the free airstream.

2. SINGLE-SCATTERING PROPERTIES OF CIRRUS CLOUDS

To derive the extinction coefficient and asymmetry parameter from measurements by the CIN a value must be used for the fraction of light *(f)* scattered in the forward 10°. This can be estimated from the fractional-scattering coefficient based on phase function calculations for ice crystals. Such computations have been performed by *Gerber et al.* [2000], based on the phase functions described by *Takano and Liou* [1995] for a variety of crystal habits and sizes. The value of *f* is moderately sensitive to crystal habit and size. For cirrus clouds, which are cold and frequently composed of bullet rosettes, the values of *f* range from 0.546 to 0.572. We use a value 0.56 for cirrus clouds composed solely of ice particles.

The UW Convair-580 research aircraft flew in a cirrus spissatus band ~300 km long, located between 70° and 72°N and 157° and 166°W, between 2230 UTC on June 1 and 0010 UTC on June 2, 1998. Cloud top was at ~8.2 km. A profile of this cirrus cloud was flown between 2220 and 2250 UTC on June 1 (Fig. 1). The maximum value of β_{ext} measured in the cirrus cloud was 13 km^{-1}. Precipitation extended below the base of the cloud down to 5.8 km. The total optical depth was 5.3; the ground was not visible when the aircraft was flying near the top of the cirrus.

Corresponding author's address: Peter V. Hobbs, Department of Atmospheric Sciences, University of Washington, Seattle, Washington, 98195-1640; E-mail: phobbs@atmos.washington.edu

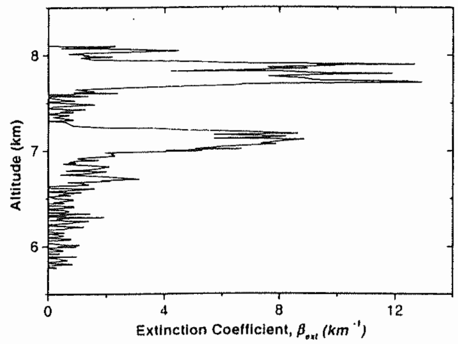

Figure 1: *Values of β_{ext} for the vertical profile through the cirrus cloud on June 1, 1998.*

Between 2357 UTC on June 1 and 0009 UTC on June 2 the UW CV-580 flew a horizontal segment ~80 km long in the cirrus cloud at an altitude of 7.65 km. Seven segments of the cloud were chosen where the cloud particle habits were fairly uniform. Within each of these segments, we analyzed 100 frames, evenly dispersed. Crystal habits were classified into the eight types shown in Figure 2. The predominant crystal habits were bullet rosettes, droxtals, and germs.

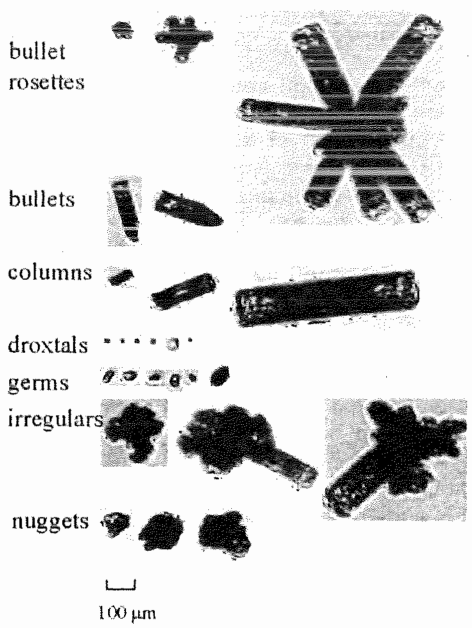

Figure 2: *SPEC CPI images of ice crystals in the cirrus cloud at ~-40 °C measured on June 1, 1998.*

The maximum dimension, L, and the projected area, P, of each classified crystal was measured. From these data we estimated particle volume using characteristic relations between volume and maximum dimension [*Mitchell and Arnott*, 1994; *Arnott et al.* 1994]. The ratio of the average volume to the projected area of a distribution of crystals gives the crystal generalized effective radius [*Fu*, 1996]:

$$r_{ge} = \frac{\sqrt{3}}{3}\frac{\overline{V}}{\overline{P}} \qquad (2)$$

Figure 3 shows g versus r_{ge} for the cirrus cloud sampled on June 1. The measured asymmetry parameter ranged from 0.73 to 0.76 in segments of the cirrus cloud that were saturated with respect to ice. Modeling studies have indicated the potential sensitivity of the asymmetry parameter to the degree of forward scattering is closely tied to the size of the particle [*Takano and Liou*, 1989]. However, our data do not show a clear relation between either the size or the habit of ice crystals and their asymmetry parameter. If δ-function transmission is included in the derivation of g from the CIN measurements, the asymmetry parameter is somewhat higher (g = 0.76 ± 0.03). However, there remains a large difference between parameterizations of g designed for representations of cirrus clouds in climate models [*Fu*, 1996] and the values of g for cirrus clouds measured by the CIN (Fig. 3). This difference is important, since it can lead to a significant change in the inferred value of the cloud albedo [*Mishchenko et al.*, 1996]. For example, the albedo of the cirrus cloud for which values of β_{ext} were measured, calculated for a solar zenith angle of 50° using the DISORT radiative transfer code [*Stamnes et al.*, 1988], is 42% for g = 0.837 and 53% for g = 0.74.

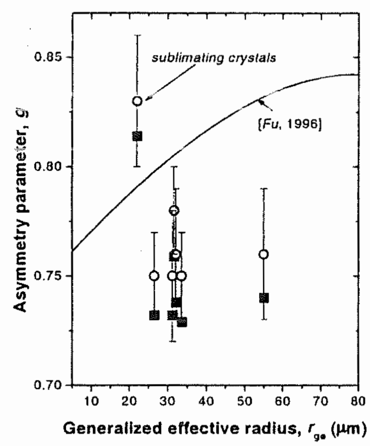

Figure 3: *Values of g derived from CIN measurements versus r_{ge} of the ice crystals shown in Fig. 2.*

3. SINGLE-SCATTERING PROPERTIES OF MIXED-PHASED CLOUDS

Between 2020 and 2300 UTC on June 2, 1998, the UW Convair-580 aircraft flew in, above, and below boundary-layer stratocumulus perlucidus clouds. Beginning at 2247 UTC the Convair-580 made a spiral descent through the stratocumulus. Cloud top temperature was -4.8 °C. Both ice and water were observed in the cloud. Images of cloud particles from the CPI showed the majority of the ice crystals to be small columns and frozen droplets (e.g., spheres with spicules). The images from the CPI were used to obtain the relative fractions of ice and water at each level in the cloud. Combining these ice/water fractions with total particle concentrations measured by the PMS FSSP-100, we derived profiles of the concentrations of ice and water. The average ice particle concentration in the supercooled portion of the cloud was 8.3 ± 7.6 cm^{-3} and the maximum concentration 31.5 cm^{-3}. The average droplet concentration in the supercooled portion of the cloud was 29 ± 30 cm^{-3}. Significant increases in ice particle concentrations occurred over a depth of 800 m, between -0.7 and -4.8°C.

The optical properties of the cloud layer were measured with the CIN. The entire optical depth of the cloud (obtained by integrating the extinction coefficient over the vertical extent of the cloud) was 21.3.

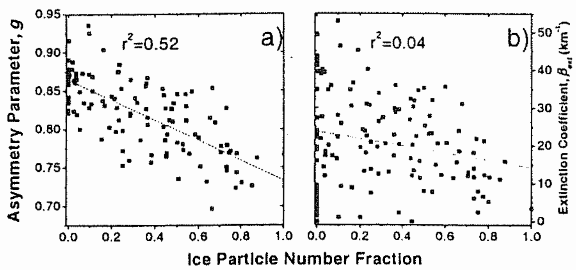

Figure 4: Measurements of g and β_{ext} versus ice particle number fraction in a profile of a stratocumulus cloud measured on June 2, 1998.

In Figure 4a the asymmetry parameter is plotted against the fractional number of particles in the cloud that were ice. Although there is significant scatter in the data, due in part to a low signal-to-noise ratio, a least-squares best fit shows that as the ice particle fraction increases the value of g decreases significantly. The value of g varies linearly from 0.87 for clouds containing no ice to 0.73 for completely glaciated cloud. Our field results show that the asymmetry parameter of mixed-phase arctic clouds is intermediate between that of ice and water clouds, the exact value depending on the relative number fraction of ice particles in the cloud. The albedo of a plane parallel cloud can be approximated by [*Meador and Weaver*, 1980]

$$A = \frac{(1-g)\beta_{\text{ext}}\Delta z}{1+(1-g)\beta_{\text{ext}}\Delta z} \tag{3}$$

where, Δz is the cloud thickness. The best-fit line to the measurements shown in Figure 4a yields the expression

$$1-g = 0.13(1+\varphi) \tag{4}$$

where, φ is the fractional number concentration of ice particles in the cloud (i.e., φ = number of ice particles/(number of ice particles + number of water drops)). For the case illustrated in Figure 4b, the contribution of φ to the observed variance in β_{ext} is very small (r^2 = 0.04). Therefore, we derived an expression for the sensitivity of cloud albedo to ice particle fraction by substituting (4) into (3) and taking the first derivative with respect to φ, which yields

$$\frac{\partial A}{\partial \varphi} = \frac{A(1-A)}{1+\varphi} \tag{5}$$

A plot of this relation (Fig. 5) shows that the sensitivity of cloud albedo A to ice particle number fraction φ is largest when A = 0.5 and the cloud contains little or no ice. In this case, a 1% increase in ice particle fraction produces about 0.25% increase in cloud albedo. Thus, the radiative properties of supercooled clouds are particularly sensitive to the onset of ice formation.

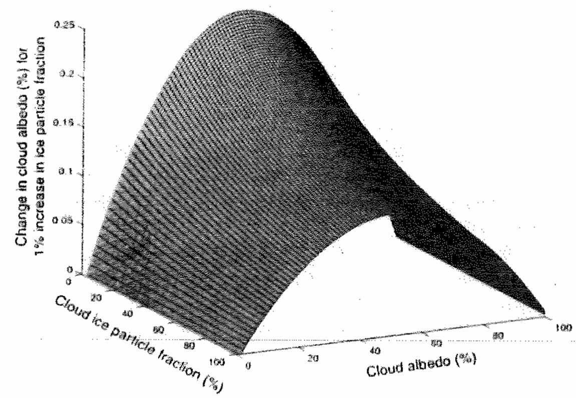

Figure 5: Three-dimensional plot of the relation given by (5) showing the sensitivity of cloud albedo to ice particle number fraction and cloud albedo. For example an increase in the ice particle number fraction from 0 to 1%, in a cloud with an albedo of 50%, produces an increase in cloud albedo of 0.25%.

4. SUMMARY

In this paper we have analyzed and interpreted the first direct measurements of the asymmetry parameter (g) and extinction coefficient (β_{ext}) in a glaciated and a mixed phase cloud. Measurements of g in a cirrus cloud were ~0.75. This value is considerably lower than those used in numerical models that assume ice clouds to be composed of spheres (g ~0.87) or regular hexagonal crystals (g ~0.82). The mixed phase cloud had values of g intermediate between those of all-ice and all-water clouds. We have shown that the albedo of clouds is most sensitive to changes in ice number concentrations at the onset of ice formation.

5. ACKNOWLEDGMENTS

We thank Arthur L. Rangno, Jack D. Russell (deceased), Donald A. Spurgeon, and Olivia Allen for their help in collecting and/or analyzing data. This research was supported by grants from the NASA Science Radiation Program (NAG-1-2079), and the NSF Arctic Sciences Section (OPP-9808163). Partial support for the University of Washington's Convair-580 research facility is provided by NASA Cooperative Agreement NCC5-326.

6. REFERENCES

Arnott, W. P., Y. Dong, J. Hallett, and M. R. Poellot, Role of small ice crystals in radiative properties of cirrus: A case study, FIRE II, November 22, 1991, *J. Geophys. Res., 99,* 1371-1381, 1994.

Fu, Q., An accurate parameterization of the solar radiative properties of cirrus clouds for climate models, *J. Climate, 9,* 2058-2082, 1996.

Gerber, H., *Measurement of the Asymmetry Parameter and Optical Extinction Coefficient of Ice Crystals and Water Droplets. Final Report. NAS1-20506,* 23 pp., NASA Langley Research Center, 1996.

Gerber, H., Y. Takano, T. Garrett, and P. V. Hobbs, Nephelometer measurements of the asymmetry parameter, volume extinction coefficient, and backscatter ratio in arctic clouds. *J. Atmos. Sci.*, 2000 (in press).

Lawson, R. P., and T. L. Jenson, Improved microphysical observations in mixed phase clouds, *Preprints of American Meteorological Society Conference on Cloud Physics*, Everett, Washington, 451-484, 1998.

Meador, W. E., and W. R. Weaver, Two-stream approximations to radiative transfer in planetary atmospheres: A unified description of existing methods and new improvement, *J. Atmos. Sci., 37,* 630-643, 1980.

Mishchenko, M. I., J. W. Hovenier, and L. D. Travis (eds.), *Light Scattering by Nonspherical Particles: Theory, Measurements, and Applications,* 690 pp., Academic Press, 1999.

Mishchenko, M. I., W. B. Rossow, A. Macke, and A. A. Lacis, Sensitivity of cirrus cloud albedo, bidirectional reflectance and optical thickness retrieval accuracy to ice particle shape, *J. Geophys. Res., 101,* 16,793-16,985, 1996.

Mitchell, D. L., and W. P. Arnott, A model predicting the evolution of ice particle size spectra and radiative properties of cirrus clouds, Part II: Dependence of absorption and extinction on ice crystal morphology, *J. Atmos. Sci., 51,* 817-832, 1994.

Sassen, K., and K. N. Liou, Scattering of polarized laser light by water droplet, mixed-phased and ice crystal clouds, Part I: Angular scattering patterns, *J. Atmos. Sci., 36,* 838-851, 1979.

Stamnes, K., S.-C. Tsay, W. Wiscombe, and K. Jayaweera, A numerically stable algorithm for discrete-ordinate-method radiative transfer in multiple scattering and emitting layered media, *Appl. Opt., 27,* 2502-2509, 1988.

Stephens, G. L., S.-C. Tsay, P. W. Stackhouse, and P. J. Flatau, The relevance of microphysical and radiative properties of cirrus clouds to climate and climate feedback, *J. Atmos. Sci., 47,* 1742-1753, 1990.

Takano, Y., and K.-N. Liou, Solar radiative transfer in cirrus clouds, Part I: Single-scattering and optical properties of hexagonal ice crystals, *J. Atmos. Sci., 46,* 3-18, 1989.

Takano, Y., and K.-N. Liou, Radiative transfer in cirrus clouds, Part III: Light scattering by irregular ice crystals, *J. Atmos. Sci., 52,* 818-837, 1995.

van de Hulst, H. C., *Light Scattering by Small Particles,* 470 pp., Dover Publications, 1981.

BIDIRECTIONAL REFLECTION AND ANGULAR SCATTERING PROPERTIES OF LABORATORY ICE CLOUDS

B. Barkey, K. N. Liou and Y. Takano

Department of Atmospheric Sciences, University of California, Los Angeles, California

1. INTRODUCTION

This report describes an ongoing experimental program to measure the bulk optical properties of ice clouds generated in a cloud chamber along with a characterization of the cloud's microphysical properties. The purpose is to cross check the theoretical spectral radiative transfer and light scattering programs developed for ice crystal clouds with experimental results and to explore the information content of ice clouds which may not be available from theory.

The cloud chamber and the spectral experimental measuring setup are described, then the reflective properties of the ice cloud are compared to theoretical results based on the measured microphysical properties. Finally, a polar nephelometer designed for eventual balloon born measurements is described and some scattering results derived from this instrument are presented.

2. EXPERIMENTAL SETUP

The light from a 250 watt tungsten-halogen lamp is sent through a diffraction grating spectrometer and directed into the cloud chamber with spherical and flat mirrors as shown in Fig. 1. With this lamp the monochromator outputs light between 0.2 to about 3 μm with a spectral resolution of 0.01 μm. To ensure the spectral accuracy of the experiment, the transmission properties of water vapor are measured as shown in Fig. 2. This result is derived by comparing the transmitted spectral intensities through the chamber with a water vapor pressure of 34 Mb ± 3 Mb to that of the chamber dried (to < 5 Mb) with compressed nitrogen gas. A mirror placed at the bottom of the chamber completes the 1 m optical path. The theoretical results shown in Fig. 2 are derived from a radiative transfer model based on the correlated k-distribution method (Liou et al. 1998) which compare well with the experimental measurement.

3. MICROPHYSICS AND ICE CLOUD GENERATION

The cloud chamber is a stainless steel box, 0.76 m by 0.76 m by 50 cm high placed inside a larger insulated plywood box. There is a 25 cm by 30 cm square hole at the top of the box and the chamber is cooled by placing dry ice around the steel box. Electronic temperature sensors (± 2°C) are placed near the top, middle and bottom of the chamber. Due to stratification, the temperature at the top of the cloud is less than that near the bottom by 5 to 6°C and because the ice cloud is much colder than the ambient surroundings, the ice cloud has a flat and relatively stable boundary at the chamber opening. Temperatures reported are those nearest the top. Ice crystals are produced by injecting water droplets generated by ultrasonic humidifiers into the chamber and because our focus is on the optical measurements, no attempt has been made to control the ice microphysics. A diode laser and silicon photo diode are placed near the chamber hole to monitor the extinction properties of the ice cloud.

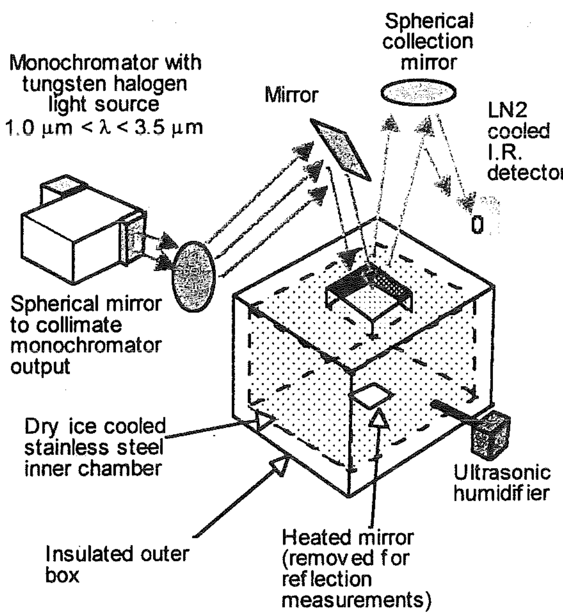

Fig. 1 The ice cloud chamber and optical setup.

Fig. 3 shows a photomicrograph of a typical replica and the size distribution taken just after spectral reflection measurements of the ice cloud at -37°C are made. Details on the ice microphysical measurements are given in Barkey et al. (2000). Extinction properties based on these concentrations and the particle projected area agree, within experimental uncertainties

Corresponding author's address: Brian Barkey, 1437 29th St., Ogden Utah, 84403 E-Mail: barkey@bibbs.com.

and assumptions, with the extinction of the laser beam through the ice cloud. Because this method does not characterize the ice cloud when reflectance measurements are taken, a continuous optical video method is being developed.

4. ICE CLOUD REFLECTANCE

The optical arrangement for reflection measurements, shown in Fig. 1, is exactly the same as that of the transmission measurements except that the heated mirror at the bottom of the chamber is removed. Because the reflected light intensity is considerably less than the direct beam used for transmission measurements, the intensity output of the monochromator is increased with a corresponding reduction in spectral resolution to about 0.1 μm. There is no detectable reflection signal without a cloud because the chamber walls are coated with a non-reflective paint. Fig. 4 shows the result of comparing the light reflected from the top of an ice cloud measured at an angle of 22°, with the incident light at nadir to that of the same measurement from a diffuse reflectance standard (IRT-94-100 from Labsphere Inc.). Details on the experimental error are given in Barkey et al. (2000) and are about 3-4% from 1 to 2 μm, 5% from 2 to 2.6 μm and between 10-20% above 2.6 μm as shown by the error bars. The maxima located at 1.3, 1.7, 2.2 and 3.1 μm are shown in the spectrum, along with minima at about 1.5 and 2.0 μm, which correspond to the absorption properties of bulk ice. The strong minima at about 2.8 μm is associated with the Christiansen effect, which is caused by the real part of the refractive index going towards unity accompanied by an increase of absorption at this wavelength.

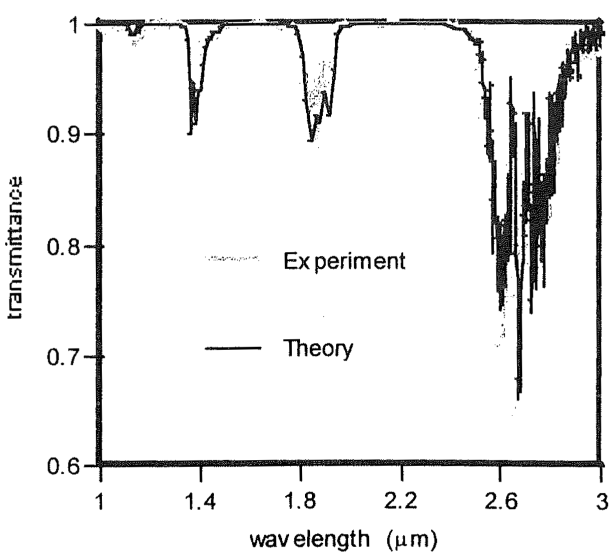

Fig. 2 Theoretical and experimentally measured water vapor absorption.

Using the line-by-line equivalent radiative transfer model (Liou et al. 1998) with an ice crystal mean effective size of 10 μm, a number of calculations have been carried out. The model employs a combination of plate and other irregular crystals in the light scattering and radiative transfer calculations. The model assumptions are close to the ice crystal shapes that were seen in the replicas and to the mean crystal size (~7 μm) that was obtained in the experiment. The amount of water vapor in the cloud chamber was taken to be the saturation water vapor over ice at the chamber temperature. Due to uncertainties in the ice cloud microphysical determination, three optical depths of 0.4, 0.5 and 0.6 were used in the calculations. The spectral resolutions of the theoretical expectations, which are calculated in the wavenumber domain, were about 0.3 μm for wavelengths less than 2.6 μm, and 0.05 μm for wavelengths above 2.6 μm. The theoretical points, which are not shown on Fig. 4, are connected using a spline fit. The optical depth of 0.5 appears to give the best match over the entire spectral

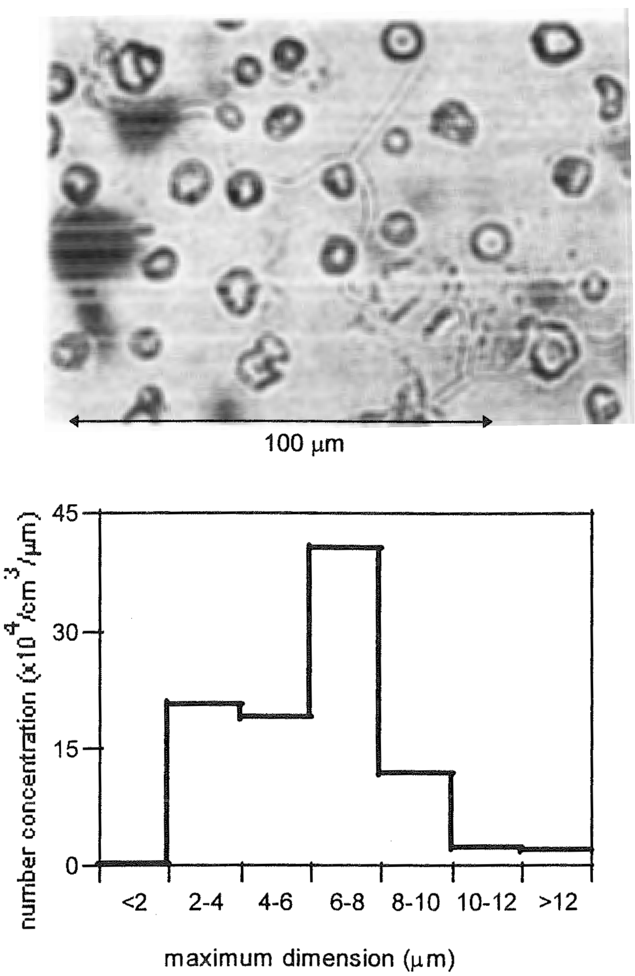

Fig. 3 Representative ice crystals and size distribution.

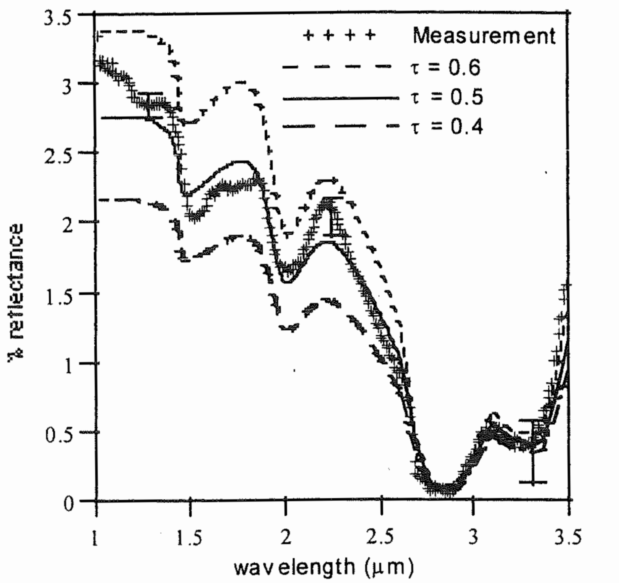

Fig. 4 Experimental and theoretical ice cloud reflectance.

interval, except in the vicinity of the 1.0 and 2.2 μm wavelengths.

5. POLAR NEPHELOMETER

As shown in Fig 5 there are 33 fiber optic light guides positioned to measure the light scattered from ice particles in a two dimensional plane between 5° and 175° in a lightweight instrument designed for *in situ* measurements. The 3 mm diameter unpolarized spherical beam from a small diode laser (λ = 670 nm, 0.95 mw) illuminates the scattering sample which is allowed to freely fall into the center of the detector array by a small, (3 mm inside diameter) tube. A larger tube (5 mm inside diameter) directs the falling crystals out of the bottom of the instrument. The amount of unwanted scattered light in the instrument is minimal because there is a beam dump to collect the laser beam in the forward direction and 2 three dimensional light absorbers positioned to absorb light scattered anywhere besides the detector array. The fiber light guides direct the scattered light to 33 amplified linear, large area photo diode detectors which convert the intensities to voltage signals. A data acquisition card mounted on a 486 PC motherboard are used to collect, analyze and store the resulting voltage signals. Another light guide measures the laser beam extinction through the sample by measuring the intensity of the laser beam inside the forward beam dump. The system is capable of measuring the signals voltages over 5 decades of light intensity at 70000 samples/sec.

The photo diode detector array is calibrated with a small Teflon Lambertian source in a manner similar to that by Barkey et al. (1999) and the system response is verified by measuring the scattering properties of water droplets as shown in Fig. 6, generated by an ultrasonic humidifier. The theoretical results in this figure are generated via Mie calculations and the lognormal size distribution with a mean effective radius of 4.5 μm and a variance of 0.1. The error bar, of 10% represents the system error at the low intensity limit of the instrument's response, while the 1% error at the upper end of the instruments response is not shown. These errors are due to electronic noise and the inherent response differences between the detector/amplifier units which are not corrected for by the calibration. The experimental results compare quite well to the theoretical expectation. The differences are attributed to errors not corrected for by the calibration at the low intensity range of the instrument response.

The nephelometer was placed inside the cloud chamber and an ice cloud was generated in the manner described above to produce the scattering measurement shown in Fig. 7. The ice crystal habit and concentration are similar to that seen in Fig. 3. The theoretical curve is for irregular crystals calculated with the unified geometric-ray-tracing and finite-difference

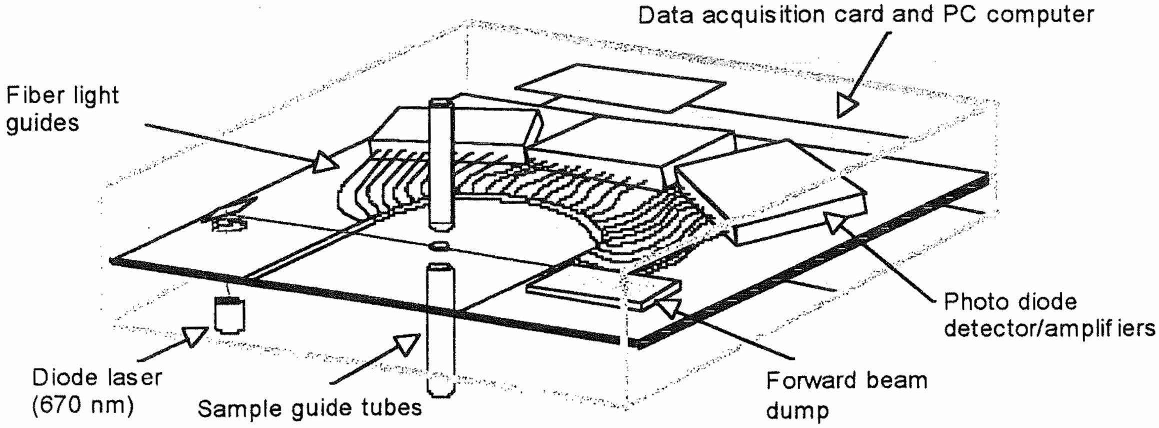

Fig. 5 View of the polar nephelometer showing the scattering geometry. Not shown are the three dimensional light absorbers placed above and below the scattering plane. The instrument is approximately 50 cm x 50 cm by 18 cm.

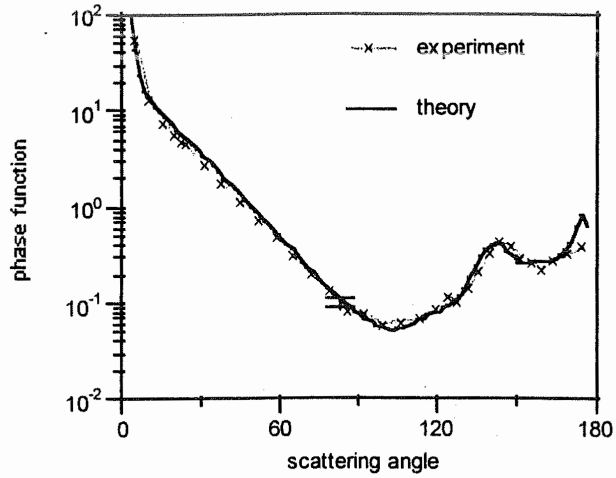

Fig. 6 Theoretical and experimental phase function of water drops generated by an ultrasonic humidifier.

time domain method using the same crystal size (Liou et al. 1998) . The error bar (10%) is determined as above. The absence of halo peaks is indicative of the irregular crystal type and because the theoretical result is based on a bullet rosette habit with rough surfaces and not the irregular crystal type seen in the photo micrograph of Fig. 3 there are small differences between the two results.

6. SUMMARY

The optical characteristics of a preliminary experimental setup to measure the reflectance properties of an ice cloud. of the system have been verified via measurements of water vapor transmission properties. The experimentally measured bidirectional reflectance from an ice cloud compares reasonably well with theoretical results based on the measured ice crystal habits, concentrations and sizes of the ice particles. Due to the preliminary nature of this study, there are uncertainties in the optical measurement associated with the assessment of the microphysical properties of the cloud. Considerable difficulties remain in matching the experimental and theoretical results in a precise manner. Future improvements will include temperature controlled refrigeration of the cloud chamber and a continuous and concurrent method to determine the cloud microphysical properties and optical depth. Measurements of the reflectance properties at other wavelengths and using a variety of incident and reflection geometry's will be conducted in future experiments.

The experimentally measured two dimensional scattering phase function of very small water drops made with a new polar nephelometer design, compare closely with theoretical expectations based on Mie theory. Measurements of the scattering properties of ice particles generated in the laboratory cold chamber have been measured by the nephelometer and as seen in comparable theoretical expectations, there are no

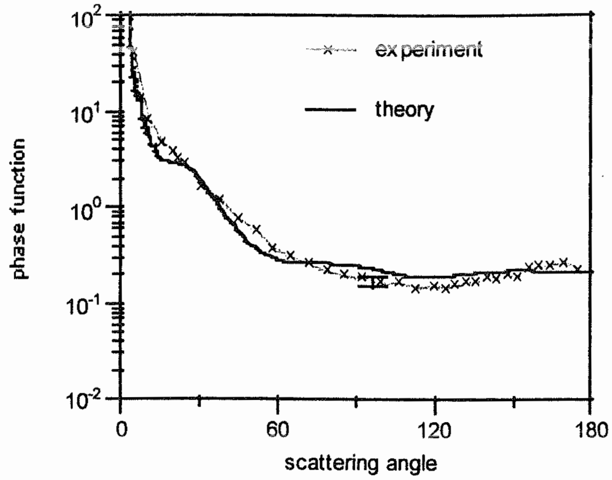

Fig. 7 Theoretically derived phase function of irregular ice crystals and the experimentally measured scattering properties of ice crystals generated in the cold chamber.

indications of halo phenomena. The production of larger, more regular ice crystals for experiments with the polar nephelometer are underway. We expect to place the polar nephelometer on a balloon borne platform to measure the scattering properties of actual cirrus cloud particles in the near future.

ACKNOWLEDGMENTS

The authors wish to thank W. G. Gellerman and Dr. N. Fukuta of the University of Utah for help with the optical and ice microphysical aspects of this program, This program was supported by NSF Grant ATM-9907924.

REFERENCES

Barkey, B., K. N. Liou, W. Gellerman, and P. Sokolsky, 1999: An analog light scattering experiment of hexagonal icelike particles. Part I: Experimental and apparatus and test measurements. J. Atmos. Sci., **56**, 605-612.

Barkey, B., K. N. Liou, Y. Takano, and W. Gellerman, 2000: Experimental and theoretical spectral reflection properties of ice clouds generated in a laboratory, chamber. Appl. Opt., in press.

Liou, K. N., P. Yang, Y. Takano, K. Sassen, T. Charlock, and W. Arnott, 1998: On the radiative properties of contrail cirrus. Geo. Res. Let., **8**, 1161-1164.

REPRESENTATION OF A HEXAGONAL ICE CRYSTAL BY A COLLECTION OF INDEPENDENT SPHERES FOR SCATTERING AND ABSORPTION OF RADIATION

Timothy F. Rahmes, Thomas C. Grenfell, Stephen G. Warren
University of Washington, Seattle, Washington

1. INTRODUCTION

The use of "equivalent" spheres to represent the scattering and absorption properties of nonspherical particles has been unsatisfactory in the past because the sphere of equal volume has too little surface area and thus too little scattering, whereas the sphere of equal area has too much volume giving too much absorption. Their asymmetry factors are also too large. These problems can largely be avoided if the real cloud of nonspherical particles is represented by a model cloud of spheres such that the model cloud contains the same total surface area as well as the same total volume. Each nonspherical particle is then represented not just by one sphere but rather by a collection of independent spheres, each of which has the same volume-to-surface area ratio (V/A) as the nonspherical particle. To demonstrate the broad utility of this approach, we show results for ice, whose absorption coefficient varies with wavelength by 8 orders of magnitude. The method is thus useful for a variety of geophysical modeling problems requiring an efficient computation scheme for radiative fluxes.

This work is a continuation of our comparison of equivalent spheres with nonspherical particles. The previous publication (Grenfell and Warren, 1999) showed that the equal-V/A formulation adequately represents the irradiances for clouds of infinite circular cylinders of ice for sizes 1-500µm, wavelengths 0.2-50µm, and ice water paths of 0.4-200,000gm^{-2}. The comparison is now extended to hexagonal crystals by comparing equivalent spheres with scattering by randomly oriented hexagonal ice prisms using the geometric optics method (GOM) (e.g., Takano and Liou, 1989, Yang and Liou, 1996, and Fu, 1996).

2. THE EQUAL-SURFACE-TO-VOLUME-RATIO PRINCIPLE

As discussed by Grenfell and Warren (1999), a particle of volume V and surface area A is represented by a collection of spheres. The ratio V/A for a sphere is set equal to r/3 yielding a radius of an equal-V/A sphere of

$$r_{VA} = 3\frac{V}{A}. \qquad (1)$$

The number of equivalent spheres n_s relative to the number of nonspherical particles n is given by

$$\frac{n_s}{n} = \frac{3V}{4\pi\, r_{VA}^{\;3}}. \qquad (2)$$

* Corresponding author address: Stephen G. Warren, Atmospheric Sciences, Box 351640, Univ. Washington, Seattle, WA 98195; email: sgw@atmos.washington.edu

For hexagonal columns, with dimensions *a* and *c*, as shown in Figure 1, the volume and radius for the equal-V/A sphere are given by

$$V = \frac{3\sqrt{3}a^2c}{2} \qquad (3)$$

$$r_{VA} = \frac{3\sqrt{3}ac}{4c + 2\sqrt{3}a}. \qquad (4)$$

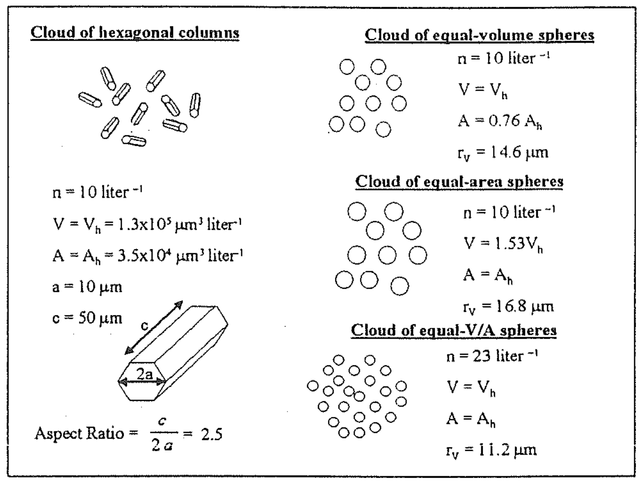

Figure 1. Hexagonal columns represented as spheres of equal volume, equal surface area, and equal-V/A.

3. THE GEOMETRIC OPTICS METHOD (GOM)

The principles of the geometric optics method are asymptotic approximations of electromagnetic theory, valid for light-scattering computations involving particles with dimensions much larger than the incident wavelength (Takano and Liou, 1989). The geometric optics method has been used to evaluate single-scattering properties of cirrus clouds (Fu, 1996) and is useful for terrestrial snow packs. The method becomes more accurate as the size parameter increases. It is known to be accurate for typical sizes of cirrus crystals at solar wavelengths, but is often inappropriate for thermal infrared wavelengths where the ice crystals are no longer large compared to the wavelength (Fu *et al.*, 1998).

Using the GOM2 of Yang and Liou (1996), we perform computations for crystals as large as a few millimeters, to cover sizes found in surface snow as well as those found in clouds. "Shimizu" crystals, shown in Fig 1b of Grenfell and Warren (1999), commonly have aspect ratios (c/2a) near 50. Hexagonal plates have aspect ratios less than 0.5.

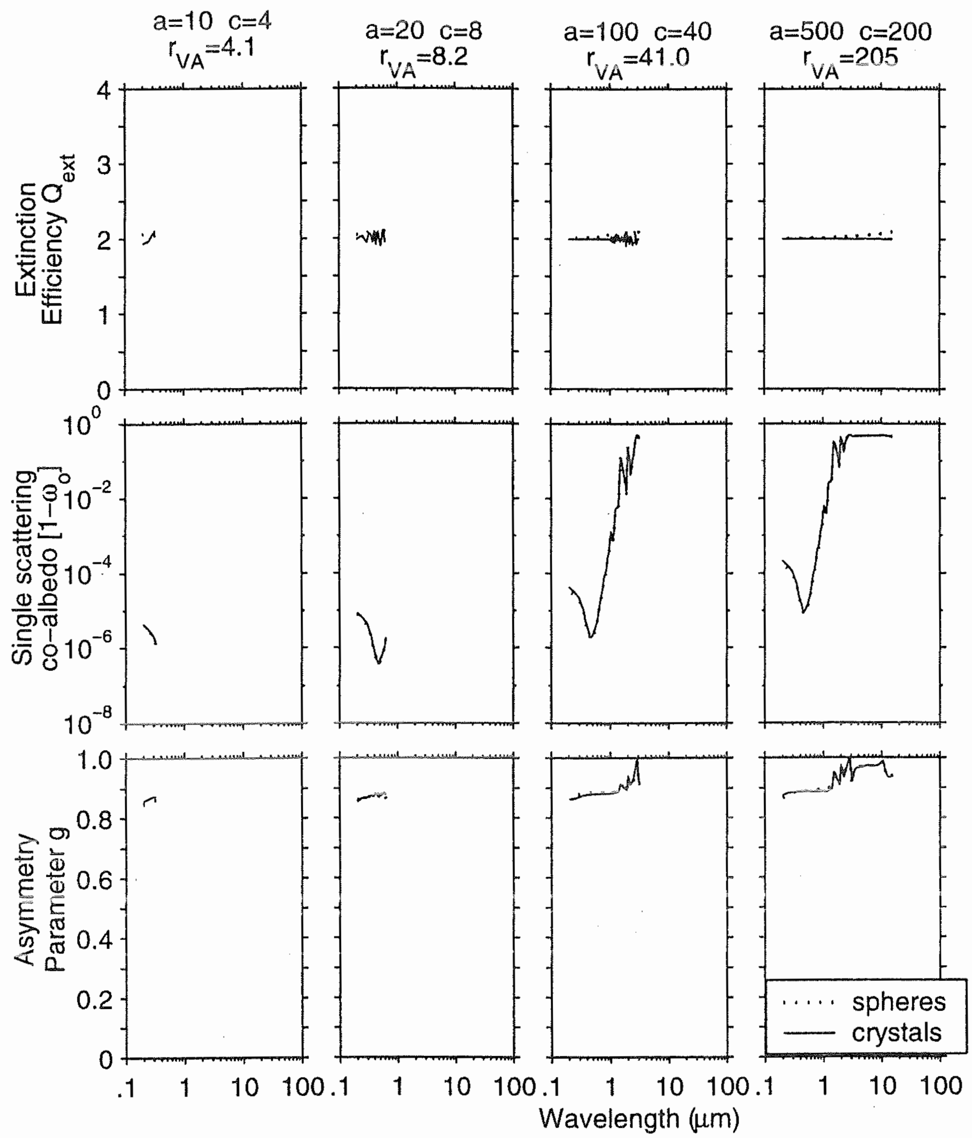

Figure 2. Extinction efficiency (Q_{ext}), single-scattering coalbedo ($1-\omega_o$), and asymmetry parameter (g) versus wavelength from 0.2 to 100 μm (for sizes where GOM is applicable) for randomly oriented hexagonal crystals (solid lines) and equal-V/A spheres (dashed lines). The geometric dimensions of each are indicated at the top of each column. [aspect ratio = 0.2]

The size parameter for GOM is defined as

$$x = \frac{2\pi}{\lambda}\sqrt{\frac{ac}{2}}. \qquad (4)$$

To ensure validity of the GOM, we require

$$x \geq 40 \; ; \; \frac{2\pi \; a}{\lambda} \geq 40 \; ; \; \frac{\pi \; c}{\lambda} \geq 40 \cdot \qquad (5)$$

These criteria account for the situations in which very high and low aspect ratios give large size parameters but a small dimension "a" or "c" compared to the wavelength of light.

4. SINGLE-SCATTERING PROPERTIES

Figures 2, 3, and 4 show the single-scattering properties for three crystal morphologies; plates, stubby columns, and elongated columns. These correspond to aspect ratios of 0.2, 1.0, and 5.0, respectively. The dimensions "a" and "c" are as shown in the figures. Wavelengths, as discussed above, are chosen so that equation 5 is satisfied. The equal-V/A spheres give excellent agreement for extinction efficiency and single-scattering albedo. The major difference between the two models occurs in the asymmetry parameter for the aspect ratio of 1

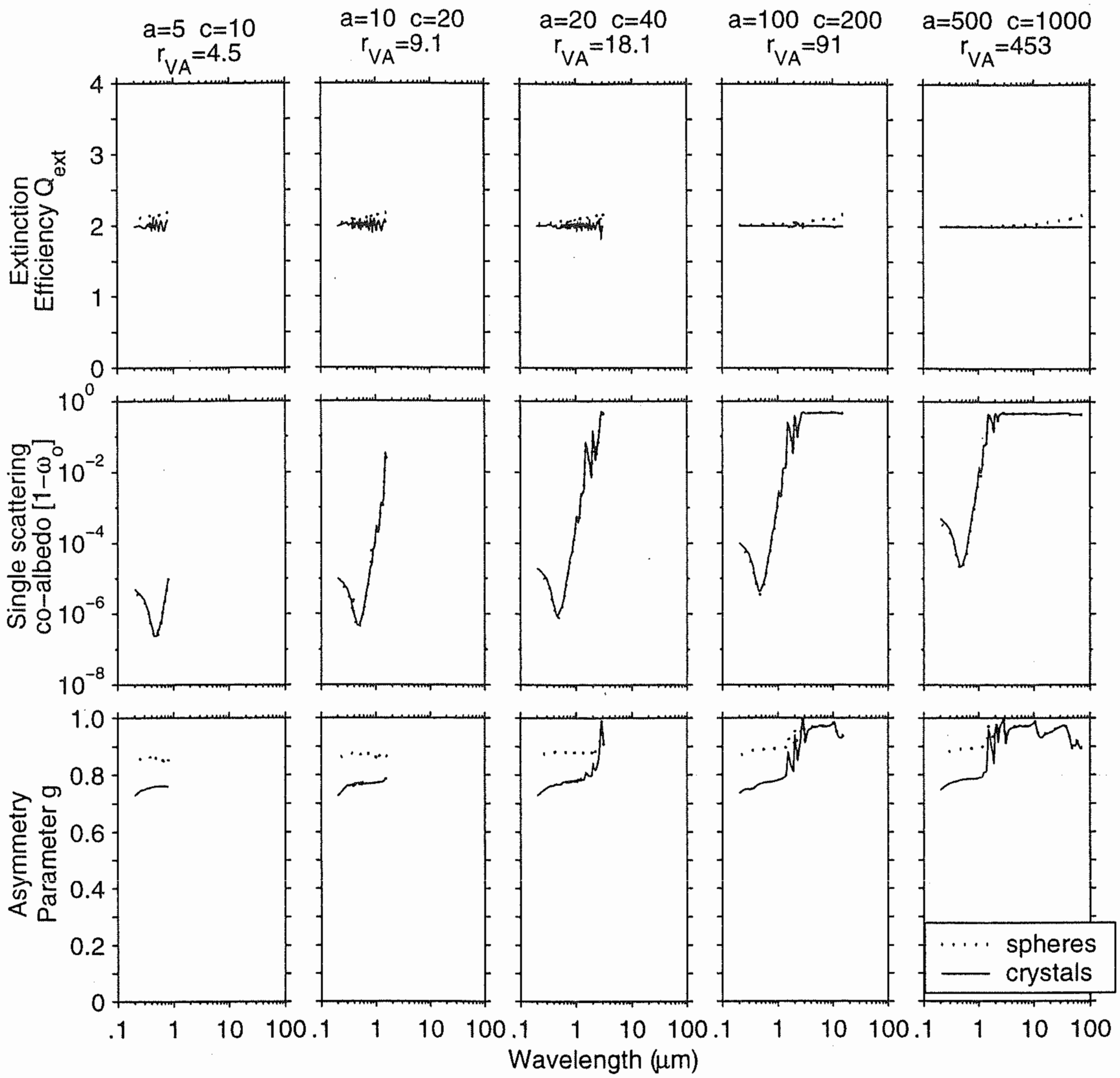

Figure 3. Same as Figure 2, but for aspect ratio = 1.

(stubby column). Surprisingly, the asymmetry parameter for plates and elongated columns is well-matched by that of the equal-V/A spheres.

5. FUTURE WORK

The work will be extended to other aspect ratios, and a radiative transfer model will be used to compute multiple-scattering errors for a variety of ice-water paths.

Acknowledgements. We thank Drs. K. N. Liou, Y. Takano, and P. Yang for providing GOM2 code, as well as Q. Fu for helpful discussions of the model results. This research was supported by the National Science Foundation under grant ATM-98-13671.

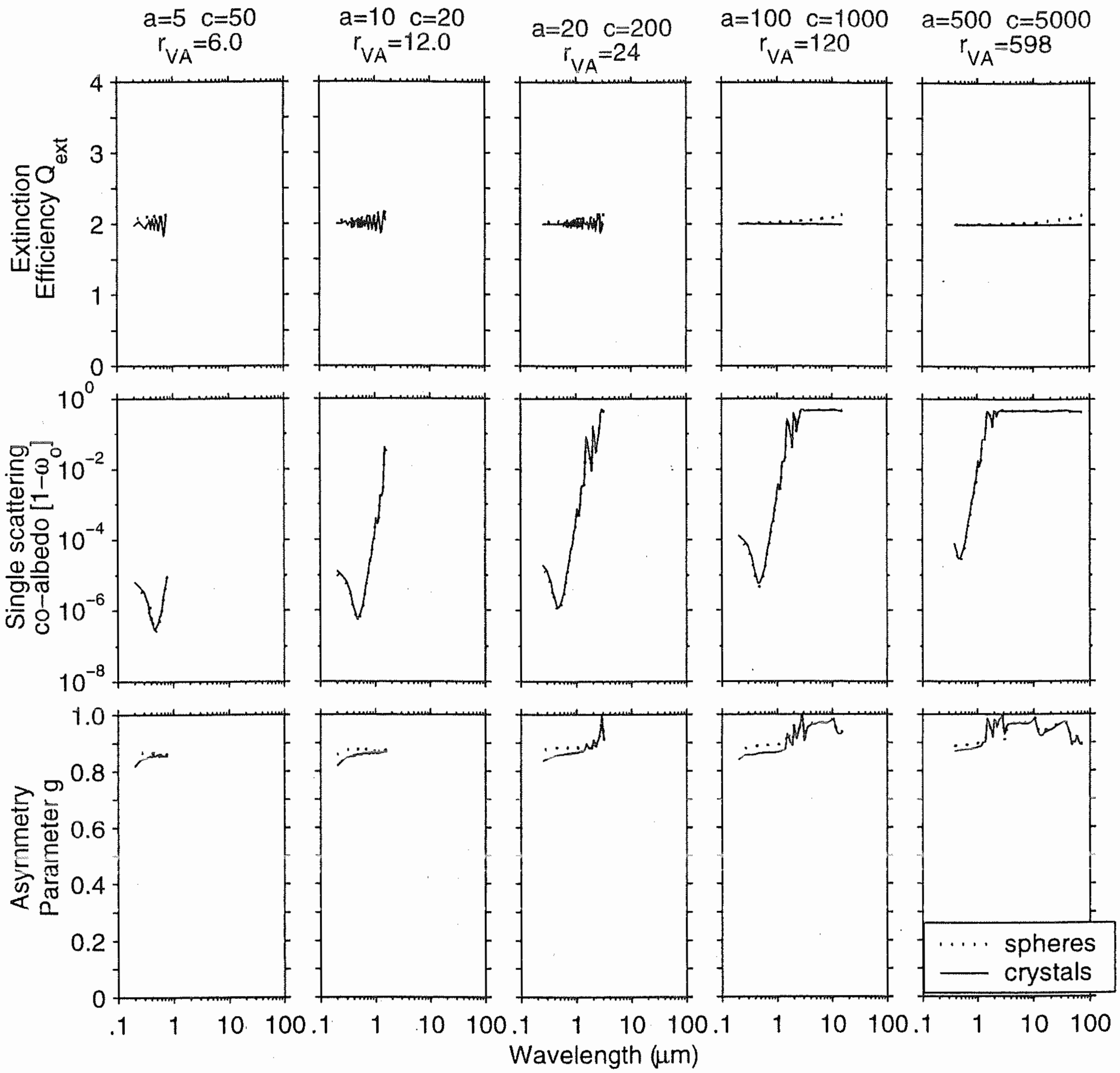

Figure 4. Same as Figure 2 but for aspect ratio = 5.

6. REFERENCES

Fu, Q., 1996: An accurate parameterization of the solar radiative properties of cirrus clouds for climate models. *J. Climate*, 9, 2048-2082.

Fu, Q., P. Yang, and W.B. Sun, 1998: An accurate parameterization of the infrared radiative properties of cirrus clouds for climate models. *J. Climate,* 11, 2223-2237.

Fu, Q., W.B. Sun, and P. Yang, 1999: Modeling of scattering and absorption by nonspherical cirrus ice particles at thermal infrared wavelengths. *J. Atmos. Sci.*, 56, 2937-2947.

Grenfell, T.C., and S.G. Warren, 1999: Representation of a nonspherical ice particle by a collection of independent spheres for scattering and absorption of radiation. *J. Geophys. Res.*, 104, D24, 31,697-31,709.

Takano, Y., and K.N. Liou, 1989: Solar radiative transfer in cirrus clouds, part I: Single scattering and optical properties of hexagonal ice crystals. *J. Atmos. Sci.*, 46, 3-18.

Yang, P., and K.N. Liou, 1996: Geometric-optics-integral-equation method for light scattering by nonspherical ice crystals. *Applied Optics*, 35, 6568-658.

Phase composition of stratiform clouds

Alexei Korolev* and George Isaac
Meteorological Service of Canada, Toronto, Canada

1. Introduction

Cloud droplets may stay in metastable liquid condition down to about –40°C. In natural clouds this results in a population of cloud particles below 0°C which may consist of mixture of ice particles and liquid droplets. Due to the difference of saturation over ice and liquid the mixture of ice particles and liquid droplets is condensationaly unstable and may exist only during a limited time. The phenomenon of mixed phase clouds is important for both theoretical and applied cloud physics. The proportion between ice and liquid phase or phase composition of clouds is an important parameter. The phase composition affects the rate of precipitation formation, lifetime of cloud, radiation properties of clouds. Up to date the studies of phase composition of clouds were significantly limited by a lack of aircraft instruments capable of discriminating the ice and liquid phase in a wide range of particle sizes. The objective of this study is to get statistics of the ice and liquid phase in cold clouds. For this study, the phase composition of clouds was measured using a Nevzorov LWC/TWC probe (Korolev et al. 1998).

2. Instrumentation

The Nevzorov LWC/TWC probe is a constant temperature hot wire instrument consisting of two sensors: (1) for measurement of liquid water content (LWC) and (2) for total (ice+liquid) water content (TWC). The phase discriminating capability of the TWC and LWC sensors are a result of the difference in the behaviour of liquid and solid particles impacting with their surfaces. Small liquid droplets after collision with the LWC or TWC collector sensors are flattened into a thin surface film and completely evaporate. At the same time, ice particles tend to remain inside the conical hollow of the TWC collector until they melt and evaporate. In contrast, ice particles are expected to instantly break away from the convex surface of the LWC collector with negligible heat expended relative to that for complete ice evaporation. The questions related to the accuracy of measurements were discussed in detail in Korolev et. al (1998).

The phase discriminating capability was tested in the National Research Council (NRC) wind tunnel. The residual response of LWC sensor to ice in natural clouds was estimated on average as about 10% of the ice water content (IWC) (Korolev et al. 1998). The phase discriminating capability of the Nevzorov probe is demonstrated in Fig. 1. Figure 1 shows synchronous measurements of the Nevzorov probe and the Rosemount Icing Detector (RICE) in a supercooled cloud. The zones where the RICE signal is oscillating or gradually increasing are associated with the presence of liquid water. In zones where the RICE signal is constant or gradually decreasing, the LWC is less than about 0.01gm^{-3} (Mazin et. al 2000). Figure 1a shows that the zones with the Nevzorov LWC>0.01gm^{-3} are well correlated with those where the RICE probe is triggering (Fig 1b), which indicates the presence of liquid water. At the same time, for most of the cloud measured Nevzorov TWC>LWC (Fig. 1a), which indicates the presence of ice.

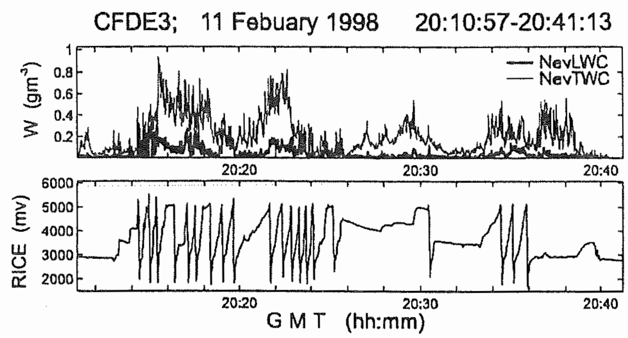

Figure 1. Measurements of LWC and TWC by the Nevzorov probe (a) and RICE response to liquid water (b) in supercooled cloud. The temperature changed from –1°C to –10°C.

The Nevzorov probe was installed on the National Research Council (NRC) Convair-580. Measurements of LWC and TWC in clouds were collected during two field campaigns: the Canadian Freezing Drizzle Experiment 1 (CFDE1) in March 1995 in Newfoundland (Isaac et al. 1998), and CFDE3 in December 1997-February 1998 in the Great Lakes region (Isaac et al. 1999). The data were measured mainly in stratiform clouds *St, Sc, As, Ac, Ns* associated with frontal systems in the altitude range 0.5 to 6 km. The statistics presented here were calculated for clouds with TWC>0.01g/m^3. The remaining cloud zones were rejected from the analysis. The scale of spatial averaging is about 100m (1s). The total length of the analysed cloud legs with TWC>0.01g/m^3 is 7986 km for CFDE1 and 16157 km for CFDE3. The statistics of water content were calculated for three temperature intervals -10°C<T<0°C, -20°C<T<-10°C, -30°C<T<-20°C. At temperatures below -30°C there are only 22 km of measurements and these numbers are statistically insignificant. For this reason these cases were not included in the general statistics.

*Corresponding author: Alexei Korolev, Meteorological Service of Canada, 4905 Dufferin St., Downsview, Ontario, M3H 5T4, Canada. e-mail: Alexei.Korolev@ec.gc.ca

3. Ice, Liquid and Total Water Content

Ice water content (IWC) was derived from the Nevzorov probe measurements as

$$W_{IWC}=k(W_{TWC}-W_{LWC}), \quad (1)$$

here W_{TWC}, W_{LWC} are measured TWC and LWC, k≈0.89 is a correction for the difference between the latent heat of evaporation and sublimation.

Figure 2 shows the cumulative probability of IWC, LWC and TWC for different temperature intervals for CFDE1 and CFDE3. The cumulative probability for TWC is in general agreement with that obtained by Mazin (1995) for midlatitude continental clouds. The surprising result is that the cumulative probability for IWC for the three temperature intervals does not change much and stays approximately the same. Table 2 shows median values of IWC, LWC and TWC for clouds with TWC>0.01gm^{-3}. It is seen that the LWC and TWC decreases with the decrease of temperature, whereas IWC stays approximately constant. The decrease of TWC occurs mainly due to the decrease of LWC.

Table 1. Average IWC, LWC, TWC during CFDE1 and CFDE3

Temperature	IWC gm^{-3}	LWC gm^{-3}	TWC gm^{-3}
-10°C<T<0°C	0.05	0.10	0.14
-20°C<T<-10°C	0.04	0.07	0.10
-30°C<T<-20°C	0.04	0.03	0.06

Table 2 shows median values of IWC, LWC and TWC. The LWC and TWC decrease with a decrease of temperature.

Table 2. Median IWC, LWC, TWC and μ during CFDE1 and CFDE3

Temperature	IWC gm^{-3}	LWC gm^{-3}	TWC gm^{-3}	μ
-10°C<T<0°C	<0.02	0.06	0.11	0.1
-20°C<T<-10°C	<0.02	0.03	0.06	0.35
-30°C<T<-20°C	<0.02	<0.02	0.03	0.4

4. Phase composition of clouds

To characterize the phase composition the following parameter was used (Korolev and Isaac, 1998)

$$\mu=\frac{TWC-LWC}{TWC}=\frac{IWC}{TWC} \quad (2)$$

The advantage of this parameter is that it changes in a limited interval, i.e. from μ=0, when the cloud is liquid, to μ=1, when the cloud is completely glaciated. In further consideration we imply the clouds with μ<0.2 as "liquid"; clouds with 0.2≤μ≤0.8 as "mixed"; and clouds having μ>0.8 as "glaciated". The definition of "liquid", "mixed" and "ice" is not that simple and needs special consideration. So far, there is no consensus regarding this question in the cloud physics community. It may require a more rigorous definition than that suggested above. The definitions of "liquid", "mixed" and "ice" clouds used in this work were mainly limited by the coarse phase resolution of the instruments.

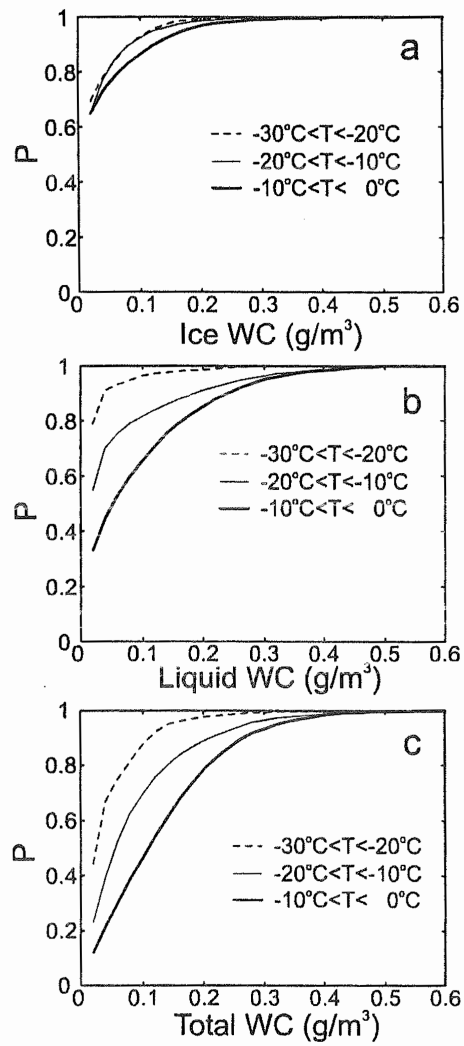

Figure 2. Cumulative probabilities of IWC (a), LWC (b) and TWC (c) for different temperature intervals

Figure 3 shows the density distributions of μ in different temperature intervals. The diagrams in Fig. 3 show explicit maximums around μ<0.2 in the all temperature intervals at -30°C<T<0°C. The amplitude of these maximums decrease with decreasing temperature. It indicates that the frequency of occurrence of "liquid" clouds is decreasing with decreasing temperature. This result is consistent with the laboratory studies of droplet freezing, which showed that the probability of freezing increases with a decrease of the temperature (e.g. Vali, 1971).

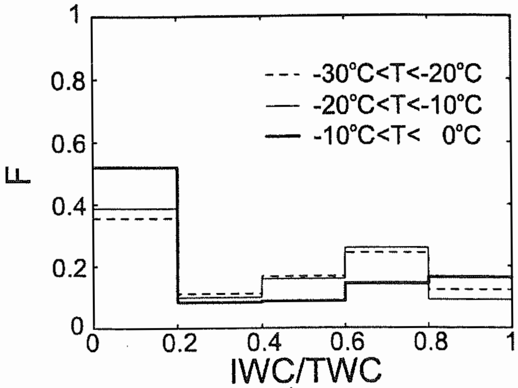

Figure 3. Differential probability the parameter μ=IWC/TWC derived from the Nevzorov probe measurements for different temperature intervals

In the temperature interval -10°C<T<0°C approximately 50 to 60% can be considered as liquid. Approximately 10% to 20% of all clouds at -30°C<T<0°C are glaciated and 40% to 60% have mixed phase. The minimum of μ is observed in the interval 0.2<μ<0.4. In general the frequency of occurrence of clouds with μ>0.2 stays approximately constant and changes somewhat from 15% to 25%. The median values of μ are shown in Table 2. It is worth mentioning that 90% of the clouds at 35°C<T<-30°C are glaciated.

5. Conclusions

In this study the following results were obtained:

(a) Statistics of the parameter μ=IWC/TWC characterizing the phase composition of clouds were obtained for different temperature intervals. It was found that the frequency of occurrence of mixed clouds is approximately constant for μ>0.2 at -30°C<T<0°C. The frequency of occurrence of μ has an explicit maximum for μ<0.2.

(b) It was found that the LWC decreases with a decrease of temperature. This result is consistent with the results of Gultepe and Isaac (1997).

(c) The statistics of IWC for different temperature intervals is a unique results. It was found that the IWC stays approximately constant in the temperature interval -30°C<T<0°C.

The observation of phase composition μ looks quite unusual and unexpected, and it needs further explanation.

No simple explanation at this time is possible for the observation that the IWC is independent of temperature for the temperature interval -30°C<T<0°C. In this regard it is worth mentioning that on average the ice particle concentration with D>125μm stays approximately constant for the temperature range -35°C<T<0°C as well (Korolev et al. 2000 a, b). Both results obviously complement each other. These two observations of ice concentration and IWC in natural clouds were conducted by quite different set of instruments. That increases the confidence of these results.

ACKNOWLEDGEMENTS

The National Search and Rescue Secretariat of Canada, Boeing Commercial Airplane Group, Transport Canada, and the Canadian Department of National Defense provided funding for the CFDE project. The aircraft data were obtained using the National Research Council of Canada Convair-580 and the scientific and technical efforts of many NRC and MSC staff.

References

Gultepe, I., and G.A. Isaac, 1997: Relationship between liquid water content and temperature based on aircraft observations and its applicability to GCMs. J. Climate, 10, 446-452

Isaac, G. A. Cober, S. G. Korolev, A. V. Strapp, J. W. Tremblay, A. and Marcotte, D. L. 1998: Overview of the Canadian Freezing Drizzle Experiment I, II and III. *Conference on Cloud Physics*, Everett, August 17-21. American Meteorological Society, Boston, USA, 447-450.

Isaac, G. A. Cober, S. G. Korolev, A. V. Strapp, J. W. Tremblay, A. and Marcotte, D. L. 1999: Canadian Freezing Drizzle Experiment. *37th Aerospace Sci. Meeting,* Reno NV, 11-14 January 1999.

Korolev, A. V., J. W. Strapp, G. A. Isaac, and A. N. Nevzorov, 1998: The Nevzorov airborne hot-wire LWC-TWC probe: principle of operation and performance characteristics. *J. Atmos. Oceanic Technol.* **15**, 1495-1510.

Korolev, A.V., and G.A. Isaac, 1998: Phase composition of stratiform clouds. *Proc. Of FAA Workshop on Mixed-Phase and Glaciated Icing Conditions,* Dec.2-3 1998, FAA, Atlantic City, NJ, 129-146.

Korolev, A., G. A. Isaac and J. Hallett, 2000a: Ice particle habits in stratiform clouds. *(ibid)*

Korolev, A., G. A. Isaac and J. Hallett, 2000b: Ice particle habits in stratiform clouds. *Q. J. Roy. Meteor. Soc.*, in press.

Mazin, I.P., 1995: Cloud water content in continental clouds. *Atmos. Res.*, **35**, 283-297

Mazin, I. P., A. V. Korolev, A. Heymsfield, G. A. Isaac, and S. G. Cober, 2000: Thermodynamics of icing cylinder for measurements of liquid water content in supercooled clouds. Submitted to

Vali, G., 1971: Quantitative evaluation of experimentalresults on the heterogeneous freezing nucleation of supercooled liquids. *J. Atmos. Sci.*, **28**, 402-408

CLOUD PHASE COMPOSITION AND PHASE EVOLUTION AS DEDUCED FROM EXPERIMENTAL EVIDENCE AND PHYSICO-CHEMICAL CONCEPTS

Anatoly N. Nevzorov

Central Aerological Observatory, Dolgoprudny, Moscow Reg., 141700 Russia. E-mail: rain@caravan.ru

1. INTRODUCTION

The current knowledge of the phase composition and phase evolution of atmospheric clouds with temperatures below 0°C (cold clouds) is much deficient suffering a variety of uncertainties and manifest paradoxes. This statement may be briefly illustrated by the following examples.

Despite the fact that ice-forming nuclei (IFN) are permanently present in both dry and cloudy atmospheric air, being relatively instantly developed while sampling, purely water clouds typically retain with no detectable glaciation as long as during many hours. Next, a typical mixed cloud is believed from various studies to be transformed with the Bergeron–Findeisen process into an ice cloud in a matter of minutes. However, even routine observations reveal that natural stratiform clouds conserve their phase-mixed state many orders longer than thus predicted. Moreover, in defiance of water evaporation, ice-containing clouds as a rule contain much bigger droplets than purely water ones usually do, which is exhibited by the crystal riming phenomenon, in impactor samples, and on.

The concentrations of cloud ice particles are commonly found to exceed by several orders those of the known IFN and little or not vary with cloud temperature, which is hardly explicable in the context of the temperature-dependent activity of both IFN and hypothetical mechanisms of ice multiplication. Besides, at temperatures below −40°C ice particle concentrations keep the same order in magnitude as at higher temperatures, even though the physical prohibition as taken of liquid water existence itself at so low temperatures makes one suggest that an ice generation mechanism is here other than the result of water freezing.

Yet unsolved remain such problems related to so-called "quasiliquid" transient layer on ice particle surface (Jellinek, 1967) as its physico-chemical nature, its association with ice saturation humidity, and its role in ice – vapor exchange.

Up to now, only speculative hypotheses have been at best offered to explain this kind of gaps and contradictions with no success achieved in their experimental and/or theoretical examination. Unfortunately, the available measurements on cloud microphysics leave aside those properties of cold clouds which might best contribute to adequate explanations of their "abnormal" features.

An effort to solve this problem has been made by CAO in the late 80s, using original aircraft instrumentation (Nevzorov, 1996a, 1997). The assembly of cloud microphysical probes was designed to measure directly or to estimate by calculation from the combined measurements a series of properties of phase mixed clouds: (i) both liquid and solid phase components of water content with the sensitivity of ~0.003 $g{\cdot}m^{-3}$, (ii) cloud optical extinction, (iii) number concentration of separately spherical and non-spherical particles greater than 12–30 μm depending on their nature, (iv) various approximations of the size spectra of these particles up to 6 mm, (v) the lower estimation of the effective diameter of water droplets, and some others. The size spectra of non-spherical (ice) particles are determined in terms of area-equivalent diameters of their orientation-averaged optical sections.

The representative enough measurements made in layer-type clouds (over 20,000 km of total path of penetration of over 300 clouds at temperatures between 0°C and −55°C) have stated that the above "anomalies" are indeed totally inherent in natural cold clouds. The use of different high-sensitive techniques enabled us to obtain more complete, than ever before, general notion of the phase composition and two-phase microstructure of these clouds. Also among the data obtained there are such that give certain clues to an adequate understanding of the phase kinetic of cold atmospheric clouds.

The measurement results with some physical conclusions made have been previously described in more or less detail (Nevzorov, 1992, 1993, 1996b; Nevzorov and Shugaev, 1992a, 1992b). Briefly summarized here are the most notable and important results obtained, the physico-chemical aspects of their interpretation, and new inference regarding the nature, formation, and evolution of cloud dispersion phases.

2. KEY EVIDENCE

The measurements above have revealed that a vast majority of cold clouds contain simultaneously both liquid and solid disperse phases and thus are phase mixed even at temperatures down to −55°C, the lowest of met with.

In about 75% of clouds, referred by common evidence to purely water ones, detected was the presence of ice particles smaller than 20–25 μm, contributing 10 to 30 percent to total condensed water content (TWC). The concentrations of these particles were estimated to be well exceeding 3 cm^{-3} to 20 cm^{-3} for different clouds, thus being comparable with those of cloud droplets. Such "latent-ice-containing" clouds (LICC) were classed as having the mixed structure of the 1-st type (M1). Taking into account that the lower limit of ice detection was 10–15% of LWC, the assurance arises that at least a part of the rest conventionally water clouds can actually contain smaller relative amounts of the fine-dispersed ice.

On the contrary, clouds commonly considered as purely ice ones were found to contain free liquid phase in the form of droplets with diameters from several tens to 1–2 hundred micrometers. Only at temperatures below −45°C and, correspondingly, at TWCs lying close to the instrumental sensitivity limit, the LWC component failed to be detected in about 10% of events, which by no means excludes its presence in these clouds as well.

All clouds corresponding to the common notion of ice-containing (ice and mixed) ones include as expected as large ice particles as >200 μm in size. If particles smaller than 20 – 30 μm made a detectable contribution to the cloud extinction (optical density), such clouds were referred to the mixed structure of M2 type. Otherwise mixed clouds were placed in the M3 type that constitutes the vast majority of clouds at temperatures below −20°C. Let us term clouds of M2 and M3 types together as "developed mixed clouds" (DMC) from the following reasoning.

The relative occurrences of the selected types of cloud phase-disperse structure against local cloud temperature are illustrated in Figure 1. Not shown here is the intermediate structure between M1 and M2, M12, where the largest crystals are between 20 μm and 200 μm, because this occupied less than 0.7% of the total cloud space at given temperature. All the listed structure types often alternate with each other within the same cloud.

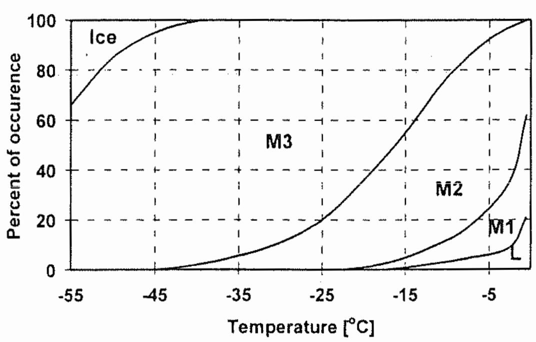

Fig. 1. Temperature diagram of relative occurrence (between the curves) of the types of cloud phase-disperse structure. Here "Ice" and "L" signify the situations where no liquid and ice, respectively, were detected.

The positive space correlation between ice and liquid contents was traced in DMC almost without exceptions.

All the above contain ample evidence that in clouds of M2 and M3 types, or DMC, the condensation equilibrium takes place between ice and liquid particles. At the same time, the relative humidity in these clouds corresponds closely to ice saturation as measured by Mezrin at al. (1991) in parallel with our measurements. Also accounting for the stable existence of liquid droplets at T < −40°C, this in turn offers that the liquid droplet substance in DMC differs from the ordinary supercooled water in fundamental physical properties though remaining chemically as pure H_2O as possible under the effect of actual atmospheric pollution. That this liquid substance constitutes an alternative phase state of H_2O, will be demonstrated just below.

3. PROPERTIES AND NATURE OF LIQUID PHASE IN DEVELOPED MIXED CLOUDS

A special, as described in detail by Nevzorov (1992, 1993), analysis of comparative microphysical measurements, made in M3 type clouds using the physically different techniques, have revealed that the substance of liquid droplets has the density 2.17±0.12 $g{\cdot}cm^{-3}$, the refractive index 1.8 – 1.9, and the evaporation heat 550 $J{\cdot}g^{-1}$ ±40% at −30°C (around 4.7 times less than that of the familiar ordinary water). To support these results, such yet poorly explained phenomenon as the colored glory around the airplane shadow against sunlight on cold cloud tops alone (!), with its red outer ring viewed under the invariant radial angle of 3.6°, is readily calculated to be the first order bow on spheres with the refractive index of ~1.83. As for the density, a similar value 2.32±0.17 $g{\cdot}cm^{-3}$ has been earlier found by Delsemme and Wenger (1970) for the low-temperature (around 100 K) water condensate known as "amorphous ice", representing a specific phase state of H_2O.

Numerous laboratory studies reviewed in depth by Skripov and Koverda (1984) have shown that this water condensate: (i) unlike the crystalline ice and ordinary liquid water, is fully disordered in internal structure as examined by structure-sensitive techniques, thus is devoid of at least regular intermolecular hydrogen bonds, (ii) with temperature rising, experiences smooth fall in viscosity taking the softened state at temperature 137±1 K (vitrification point) and then flowable (liquid) state as temperature becomes above ~150 K (or −120°C), (iii) can originate from vapor directly into any of the listed states, (iv) is metastable relative to crystallization into ice I , like supercooled ordinary water, in the softened and liquid states only. Note that the superhigh density of the amorphous phase of water is expected as the end effect of the decrease in concentration of hydrogen bonds, starting from the transition from crystalline ice I to liquid water acquiring higher density with a part of initial bonds broken.

The conclusion to be drawn from the above reasoning is that droplets in DMC consist of the same amorphous phase of water in liquid state, previously referred to as amorphous, or A-water (Nevzorov, 1992, 1993). The field experiments interpreted in the context of the structural physical chemistry have served to extend our knowledge of the properties of this thus far poorly investigated state of water.

One of the most important features of A-water for the cloud physics, the condensation equilibrium with ice at ice saturation, suggests that the so-called "quasiliquid" film covering ice particles has the surface structure identical to that of free A-water and therefore consists of A-water (similar idea has been earlier proposed by Fletcher (1970)). This in turn implies that it is rather A-water than supercooled water as per Pruppacher and Klett (1978) that contributes a step transient phase in ice deposition from vapor in accordance with the universal Ostwald's rule. Hence the initiation of a cloud ice particle is always preceded by the nucleation of an embryonic droplet of A-water with its subsequent crystallization if a crystallization center is embedded in its condensation nucleus

Table 1: Averaged microphysical parameters of mixed clouds of M2 and M3 types at given temperatures

Temperature interval (°C)		−5...−15	−15...−25	−25...−35	−35...−45	−45...−55
A-water content (AWC) ($g \cdot m^{-3}$)	M2	0.42	0.29	0.060	-	-
	M3	0.19	0.18	0.088	0.050	0.028
Ice water content (TWC) ($g \cdot m^{-3}$)	M2	0.031	0.024	0.006	-	-
	M3	0.17	0.12	0.022	0.012	0.007
Ratio AWC/TWC × 100%	M2	93	92	91	-	-
	M3	53	61	80	81	80
Concentration of droplets >12 μm (l^{-1})	M2	203	162	193	-	-
	M3	435	248	231	299	582
Concentration of ice crystals >20 μm	M2	45	63	127	-	-
	M3	192	196	202	259	380

or captured externally. Otherwise the A-water droplet even while growing is capable of preserving its metastable state, as supercooled ordinary water does.

4. ON THE TWO-PHASE MICROSTRUCTURE OF DEVELOPED MIXED CLOUDS

The summarized results of microphysical measurements in stratiform DMC, corrected for the affecting physical properties of A-water, were presented by Nevzorov (1997) in the form of data averaged over sampled clouds of separate types and temperatures, as displayed in Table 1. All the parameters concerned exhibit a very wide scatter from cloud to cloud and as a rule inside the same cloud, whence the statistical uncertainty of the averages is rather great.

Nevertheless, as seen from the Table 1, the distinction between the selected cloud structure types M2 and M3 is pronounced enough in almost all averaged data, and most of all most in ice particle concentration and TWC. The average concentrations of A-water droplets exceeding 12 μm in diameter exhibit markedly less difference between both cloud types than those of ice particles. The concentrations of both kinds of particles with similar threshold sizes are of the same order in magnitude and little, if at all, depend on temperature. The share of A-water in the total condensed water content (TWC) is surprisingly high and essentially independent of temperature. In addition to the presented data, the though roughly estimated average droplet size spectra differ distinctly between the both cloud types in that that in M3 type they possess modes lying between 30 μm and 45 μm equally at all temperatures, whereas those in M2 type always lie to the left of 12 μm.

5. PROCESSES OF PHASE EVOLUTION OF COLD CLOUDS

Being of the highest internal energy among all water condensed phases, A-water can originate only directly from vapor. Therefore, the permanent coexistence of free A-water with cloud ice implies that the processes of condensation and partial crystallization of A-water necessarily play the significant role in the formation of cloud phase composition. Moreover, the high and temperature-independent concentrations of ice crystals, close to those of A-water droplets (see Table 1) and well far from those of the known ice-forming (water freezing) nuclei, give evidence that these processes are dominant in formation of DMC, and that the primary nucleation of A-water occurs on alternative, specific nuclei.

The question arises about the nature of these A-water condensation nuclei (AWCN) as well as about their origination, because the abundance of atmospheric layers, free of cloud though at ice supersaturation, signifies that no such active nuclei are as a rule present in dry air. One of the mechanisms of their natural initiation is indirectly pointed to by Rosinski et al. (1991) who have found that a supercooled water droplet being just evaporated can be immediately replaced by a newly formed ice crystal. In fact, as follows from the foregoing, the dehydrated residuals of ordinary water droplets acquire the properties of catalytic centers of condensation, and only some part of them of crystallization of A-water. Such secondary AWCN are enable to be collectively generated within a supercooled water cloud, when relative humidity lowers to a degree sufficient for the smallest droplets to evaporate. This occurs near cloud edges, or due to dry air entrainment, or as the final of the cycle of wetting of non-hygroscopic nuclei, etc. In any case, a supercooled water cloud is bound to acquire the "latent-ice-containing" structure M1, containing A-water droplets as well, most probable from the very beginning of its lifetime. The above-mentioned superhigh concentrations of fine ice particles in M1 type clouds evidence that the ice forming mechanism of droplet evaporation is many orders more productive than that of droplet freezing. This thereby removes the need for the ice multiplication version.

In spite of the high vapor supersaturation, just nucleated particles of A-water and ice are initially growing extremely slowly because of the molecular-diffusion growth mode. As they increase and their gravitational sedimentation accordingly accelerates, the resulting microscale disturbance of air makes the Bergeron transcondensation to become progressively faster. When the particles achieve critical sizes of order of 20 μm, this process proceeds to its avalanche-like stage that culminates in complete evaporation of droplets of ordinary water. A minute duration of this stage is expressed in the negligible occurrence of the transient structure M12.

A developed mixed cloud (DMC) thus formed consists of ice and liquid A-water alone and may be considered, depending on the physical application involved, as either a condensation-stable biphase cloud or a "quasi-ice" cloud wherein a part of potential ice remains in the form of a metastable transient substance.

The two-phase microstructure of DMC is formed under the combined effect of a variety of factors such as: (i) a disbalance in vapor saturation with respect to ice, caused by air motions, trends of air temperature, etc., (ii) a direct relationship between vapor supersaturation and concentration of active AWCN, (iii) an inverse dependence of saturated vapor pressure on particle size, (iv) low condensation enthalpy of A-water, responsible for its small thermal resistance to both condensation and evaporation processes, and so on.

The last factor suggests that the liquid fraction serves as the most fast-acting regulator of relative humidity in clouds, being the most sensitive in microstructure to its variations. All these together provide a certain explanation for the distinction between M2 and M3 cloud structure types. The M2 structure is formed under as high ice supersaturation of vapor as being sufficient for the activation a supplementary portion of condensation nuclei to produce the distinctive fraction of fine-sized particles. Subsequent condensation of vapor occurs preferably on the biggest particles and resulting fall in its supersaturation causes evaporation of the smallest particles if progressively increasing sizes. The cloud thus transforms into the conceptually stable structure of M3 type wherein all droplets are large enough to provide, under given thermodynamical conditions, the best approach to equilibrium between all three phases.

6. CONCLUSION

The great diversity of evidence related to cold clouds are paradoxical to an extent that they need to be interpreted from physical concepts to be radically improved. The conclusions made in this paper include, as a basic finding, the established existence and specific properties of the little- known amorphous phase of water, A-water, constituting a certain part of liquid droplets in mixed clouds. A series of missing physical properties of A-water have been gained in our field studies of cloud properties.

The concepts suggested are most strongly supported by the fact that unlike those leading in today's cloud physics, they furnish the simplest and quite obvious explanation for every conceivable poorly understood phenomenon associated with cold clouds. Apart from the mentioned above, these are for example such phenomena as the formation of graupel and freezing drizzle in ice-containing clouds, the burst-like and bald-formed glaciation of the tops of cumulus congestus clouds (occurring due to collective evaporation of supercooled water droplets near the cloud boundary), the occurrence of precipitating ice in a initially water cloud while merely penetrated by an aircraft (producing heavy air disturbance that strongly encourages the growth of "latent" fine ice), and others to be encountered.

It is of great importance that the high relative content of free A-water imparts to ice-containing clouds different, than considered up to now, properties in formation and phase composition of winter precipitation, in accumulation, transformation and global transfer of atmospheric aerosol, in propagation and scattering of light and other electromagnetic as well as corpuscular radiation, in aircraft icing, and possible in other problems involved.

There are all reasons to believe that free A-water is an essential constituent of noctilucent and nacreous clouds as well as of clouds encountered in cold atmospheric layers on other planets, all being known to contain spherical particles as found with optical methods.

REFERENCES

Delsemme, A. H., and A. Wenger, 1970: Superdense water ice. *Science*, 167, 44-45

Fletcher N.H., 1970: *The chemical physics of ice*. Cambridge Univ. Press

Jellinek H.H.G., 1967: Liquid-like (transition) layer on ice. *J. Colloid and Interface Sci.*, 25, 192-197.

Mezrin, M. Yu., and G. V. Mironova, 1991: Some results of research of air humidity in stratiform clouds. *Proc. of CAO*, issue 178, 125–132 (in Russian)

Nevzorov, A. N., 1992: Permanence, properties and nature of liquid phase in ice-containing clouds. *11th Int. Conf. on Clouds and Prec., Montreal, Canada*, 270-273

Nevzorov, A. N., 1993: Studies into the physics of liquid phase in ice-containing clouds. *Russian Meteorology and Hydrology*, No 1, 47-59

Nevzorov, A. N., 1996a: CAO aircraft instrumentation for cloud physics. *12th Int. Conf. on Clouds and Precipitation, Zurich, Switzerland*, 371-374

Nevzorov, A. N., 1996b: Observations of initial stage of ice development in supercooled clouds. *Ibid.*, 124-127

Nevzorov, A. N., 1997: An experience and promising results of advanced measurements into microphysics of cold clouds. *WMO Workshop on Measurements of Cloud Properties for Forecasts of Weather and Climate. Mexico City*, 173-182.

Nevzorov, A. N., and V. F. Shugaev, 1992à: Observations of the initial stage of evolution of ice phase in supercooled clouds. *Soviet Meteorology and Hydrology*, No 1, 69-76.

Nevzorov, A. N., and V. F. Shugaev, 1992b: Experimental studies of phase-dispersion structure of stratiform clouds at negative temperatures. *Ibid.*, No 8, 41-51.

Pruppacher H.R., Klett J.D., 1978: *Microphysics of clouds and precipitation*. D. Reidel.

Rosinski, J., and G. Morgan, 1991: Cloud condensation nuclei as a source of ice-formation nuclei in clouds. *J. Aerosol Sci.*, 22, No. 2, 123–133.

Skripov, V. P., and Koverda, V. P., 1984: *Spontaneous crystallization of supercooled liquids*. Nauka, Moscow, 232 pp. (in Russian).

MICROPHYSICAL CHARACTERIZATION OF THE ISRAELI CLOUDS FROM AIRCRAFT AND SATELLITES

Ronen Lahav and Daniel Rosenfeld

Institute of Earth Sciences, The Hebrew University of Jerusalem, Jerusalem, Israel

1. INTRODUCTION

Preliminary results of extensive cloud physics measurements in Israel are reported. These measurements were done during the 1998-1999 winter as part of the research program of the Israeli rain enhancement project.

In this study we tried to document the cloud evolution in a way that would be easy for comparison with NOAA/AVHRR data. The AVHRR microphysical inferences were validated by the in-situ measurements. Based on 10 flights, we were able to identify four major factors determining the cloud microstructure in Israel, which are used for a microphysical classification of the clouds.

2. THE AIRCRAFT MEASUREMENTS

Data was obtained from the Israeli King air C90 cloud physics aircraft, in which the authors were the flight scientists.

The main instruments used in this study were SPP-20, 2DC, King hot wire cloud liquid water contents, temperature, dew point, pressure, GPS and ball variometer. The data system was the SEA-200.

2.1 Data Processing

All the research flights were conducted in the same way so we could compare them to each other.

a. The takeoff was from Sde-Dov, which is located just 200 meters from the Tel Aviv coast line, in a parallel orientation. Therefore sea spray was readily detectable by the SPP-20, starting from the takeoff run.

b. We flew to the target area passing and penetrating the cloud bases.

c. After reaching the target area we penetrated young growing convective elements in vertical steps of 1000 feet from cloud base to the altitude were the SLWC (supercooled liquid water content) completely depleted or up to the cloud top if water persisted there. The parameters that were analyzed are cloud liquid water content (CLW); maximum up and down drafts; 2DC particle types and their maximum sizes; drop size distribution and their number concentrations; temperature and dew point.

d. Monitoring clouds separately over sea and inland, for documenting potential differences between the two areas.

The AVHRR and TRMM overpasses within 2 hours of the flight were analyzed. The analyses were done using the methods of Rosenfeld and Lensky (1998), and Rosenfeld (1999; 2000)

3. RESULTS

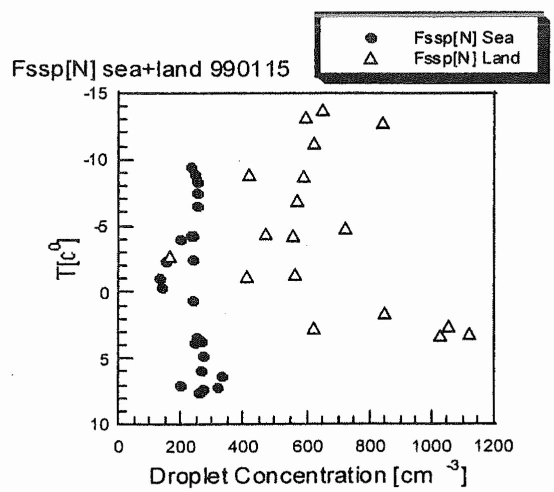

FIGURE 1. Cloud droplet concentration [cm-^{3}] as function of depth above cloud base, as determined by the temperature. Cloud base is at 7^0 C over the sea and 4^0 C over land.

Corresponding author's address: Ronen Lahav, Inst. of Earth Sciences, The Hebrew University of Jerusalem, Jerusalem 91904, Israel;
E-Mail: ronenl@vms.huji.ac.il.

Figures 1 and 2 show the large difference between the land and the sea as measured at 15.1.99. The air in this day was hazy, probably from local air pollution. No sea spray was seen or detectable. Fig 1 shows that inland the drop concentration is higher than over the sea, with local concentration above 1000 drops cm^{-3} near cloud base decreasing with height. Over the sea the concentration varies between 200-350 drops cm^{-3}. Fig 2 shows the difference in the effective radius of the same case. Over the land the effective radius is smaller by about 2-3 µm for the same depth, as obtained from the temperature relative to cloud base temperature.

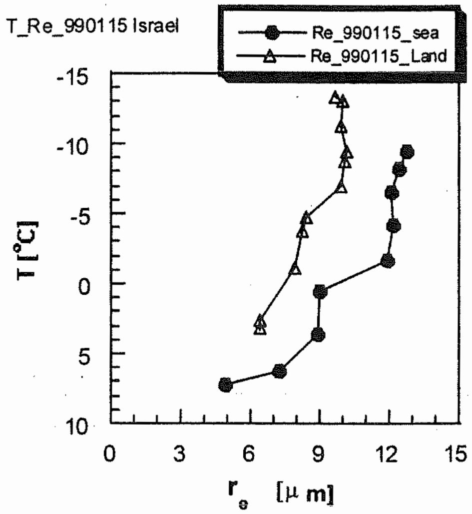

FIGURE 2. Same as Fig 1, but for the SPP-20 measured cloud droplets effective radius [µm].

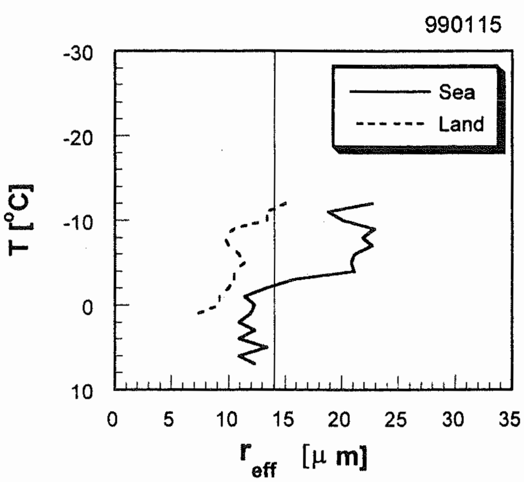

FIGURE 3. *The 30th percentile effective radius [µm] of cloud droplets as measured by the NOAA-14 Satellite over Sea and Galilee (inland) on the 15.1.99. The vertical line is the 14-µm precipitation threshold.*

Fig 3 shows that the satellite retrieved r_e (effective radius) decreases when moving from sea inland, following the aircraft measurements. The clouds over the sea exceeded the 14-µm precipitation threshold at -2°C isotherm while inland it barely reached it at -11°C isotherm. The differences between the land and the sea are probably due to the local air pollution above the land.

Figures 4-8 show a case of clouds forming in air mass containing desert dust limiting the visibility to 5 km. The flow was from the sea inland. The dust was originated over North Africa, and moved through the east Mediterranean to Israel. The strong surface wind (SW, 20 knot) caused a stormy sea with much sea spray.

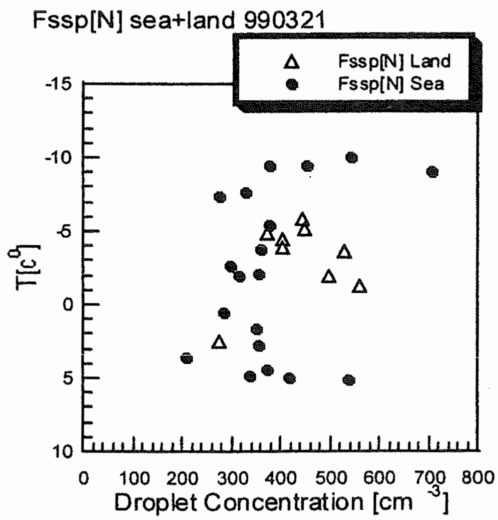

FIGURE 4. *Cloud Droplet concentration [cm-3] as measured by the SPP-20 over the Sea and Land on 21.3.99.*

Fig 4 shows that the concentration is changing in the range 300-600 droplets cm^{-3} and there is almost no differences between sea and land. However according to Fig 5 the r_e over land is smaller by 2 µm than over the sea.

Figures 6 and 7 show the drop size distribution at different depths above cloud base, as indicated by the temperature relative to cloud base temperature. The distribution over the sea is wider. We suggest that the sea spray is responsible for that. Because the desert dust prevailed equally over sea and land, it is unlikely that the desert dust was responsible for widening the distribution over sea. When the clouds are moving from sea inland they lose their large CCN (sea spray), but remain with the desert dust, and so become more continental.

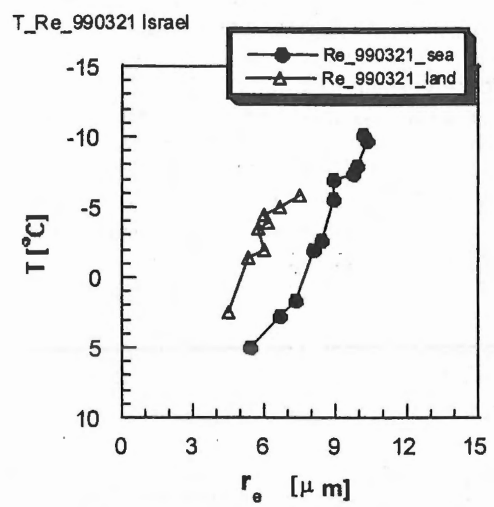

FIGURE 5. The effective radius [μm] of cloud droplets as measured by the SPP-20 over the Sea and Land on 21.3.99.

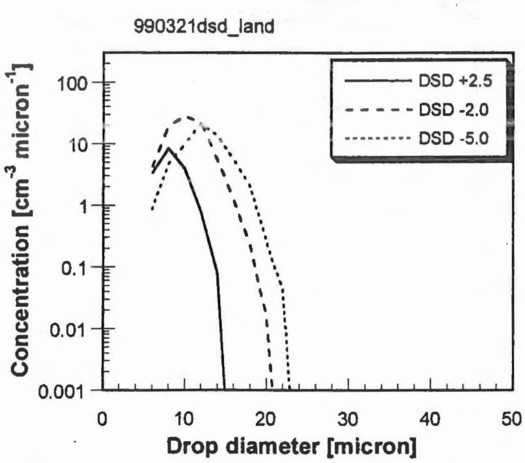

FIGURE 6. The Drop Size Distribution as measured by the SPP-20 at a distance of about 40-km inland on the 21.3.99

According to the satellite analysis presented in Fig 8, the r_e decreased moving from sea inland and farther east over Jordan. The clouds at the -10°C isotherm exceeded the 14-μm precipitation threshold (Rosenfeld and Gutman, 1994) over sea, barely reached it over Israel, and were mostly below it over Jordan.

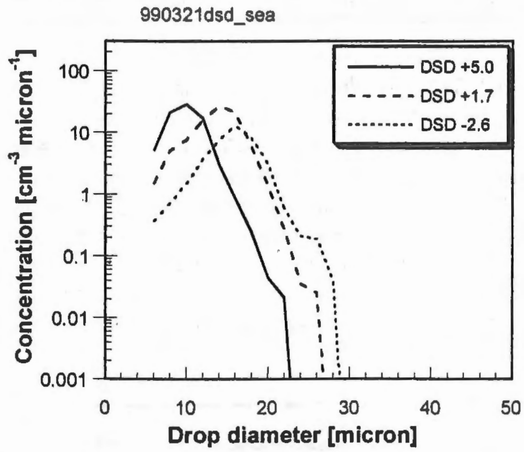

FIGURE 7. The Drop Size Distribution as measured by the SPP-20 over the sea on the 21.3.99.

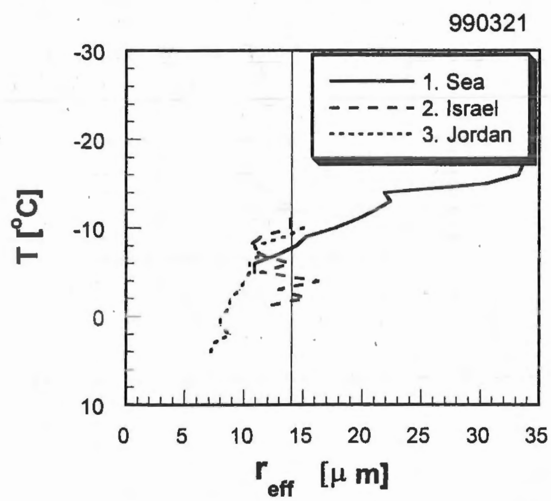

FIGURE 8. The 30th percentile effective radius [μm] of cloud droplets as measured by the NOAA-14 Satellite over Sea, land (west of the Jordan River) and Trance Jordan on 21.3.99. The vertical line is the 14-μm precipitation threshold.

4. DISCUSSION AND SUMMARY

Based on analyses of all 10 flights, we were able to identify four major factors determining the cloud microstructure in Israel:

A. Desert dust.
B. Continental aerosols that are not desert dust (air pollution).
C. Sea spray.
D. CCN-lean Clean Maritime air.

Based on those factors we classified the Israeli clouds into the following types:

1. Maritime clouds in clean marine air.
2. Continental clouds in locally polluted air without desert dust.
3. Continental clouds in CCN rich Mediterranean air.
4. Clouds with warm rain in air with non-desert-dust-haze.
5. Clouds in air with desert dust, without warm rain.
6. Clouds in air with desert dust, with warm rain.

We characterized the microphysical properties of the clouds in each flight. According to that we found that Maritime clouds in clean marine air with low concentration of CCN (cloud type 1) changes to Continental clouds in the center of Israel (cloud type 2) 10-20 km after crossing the coast line. Because instability over sea is at least as strong as over land, the likely explanation of the differences is the effects from the locally polluted air. Occasionally the air arrives from the sea already rich with CCN, forming cloud type 3.

In days with warm rain and poor visibility due to non-desert-dust-haze (cloud type 4), the cloud base drop size distribution (DSD) was wide, yet containing large concentrations of droplets. The DSD narrowed gradually as the clouds moved farther inland until most of the warm rain processes ceased at the eastern border of Israel. The reason for that may be the wash out of the large and giant CCN originated as sea spray, and the added continental aerosols from local sources.

Convective clouds in heavy dust storm, limiting the visibility to less than 2 km, had no warm rain, and up to 3 g m^{-3} of liquid water were observed up to -20^{0}C. At colder temperatures that water froze quickly. These clouds are defined as cloud type 5.

In days where desert dust was observed with warm rain (cloud type 6), the warm rain decreased gradually inland, transforming the clouds into cloud type 5. The warm rain was not likely caused by desert dust, but rather from the sea spray that was depleted inland. We suggest that clouds in hazy (cloud type 4) and dusty air (cloud type 6) became continental inland slower than clouds in maritime clean air (cloud type 1) because the slow deposition of the large CCN as compared to the fast inclusion of the continental small CCN.

Those observations help us to understand better the causes for the large variability of Israeli clouds. This understanding will lead eventually to the possibility to assess the suitability of the clouds to the various possible treatments for rain enhancement: hygroscopic seeding, glaciogenic seeding, or no seeding at all.

5. ACKNOWLEDGEMENTS

This study is supported by the Israeli Water Commission, and by Electrical Mechanical Services, a subsidiary of MEKOROTH, the Israeli National Water Company.

6. REFERENCES

1. Rosenfeld, D, and I. M. Lensky, 1998: Satellite based insights into precipitation formation processes in continental and maritime convective clouds. *Bull. Amer. Meteor. Soc.,* ***79****, 2457-2476.*

2. Rosenfeld, D., and G. Gutman, 1994: Retrieving microphysical properties near the tops of potential rain clouds by multispectral analysis of AVHRR data. *J. Atmos. Res.,* ***34****,259-283.*

3. Rosenfeld, D., 1999: TRMM observed first direct evidence of smoke from forest fires inhibiting rainfall. *Geophys. Res. Lett.* ***26****, 3105-3108.*

4. Rosenfeld, D., 2000: Suppression of rain and snow by urban and industrial air pollution. *Science.* ***287****, 1793-1796.*

FREEZING PRECIPITATION CLIMATOLOGY IN THE FORMER EUROPEAN USSR

N.A. Bezrukova[1], L.S. Minina[2], A.Ya. Naumov[1]

[1]Central Aerological Observatory, Dolgoprudny, Moscow Region, 141700, Russia
[2]Hydrometeorological Centre of Russia, Moscow, 123242, Russia

1. INTRODUCTION

Ice accretion, i.e. freezing precipitation deposition on objects in the air or on the ground, is one of the most hazardous phenomena for aviation. Most often in-flight aircraft icing occurs at temperatures between 0° and -20^{0}C, while for supersonic aircraft this temperature may be still lower. At low heights and low speeds aircraft icing generally occurs at temperatures from 0° to -10^{0}C. Glaze-ice or grains of frost may deposit on an airplane body on the land causing the deterioration of the airplane's aerodynamics, increasing its weight, and leading to its intense icing, if after take-off it penetrates supercooled clouds.

The knowledge of the spatial distribution of glazed frost occurrence frequency, based on ground-based observations, is very important for aircraft servicing at take-off and landing. Runway covered with glaze-ice is particularly dangerous for aircraft of today with their high take-of and landing speeds. Braking on ice may result in a ground-loop, loss of control at take-off running, and getting beyond the runway. Icing of wires may cause their rupture and thus damage ground-based communication.

Our aim is to clarify some aspects of freezing precipitation climatology of the European Territory (ET) of the former USSR for the last two decades of regular observations when the conditions of the observational network were still satisfactory.

2. BACKGROUND DATA

The data analyzed were borrowed from four-time and continuous daily observations reported in issues of "USSR Weather Monthly" for the period of 1971-1990. These data refer to the overall network of weather stations (over 50 stations) involved in the international data exchange. The available data included the type of weather phenomenon based on four-time daily observations (at 03:00, 09:00, 15:00, and 21:00 Moscow time) and duration of phenomena from continuous daily observations.

Routine surface observations include (1) visual determination of supercooled liquid precipitation and (2) combined visual and instrumental determination of the characteristics of ice accretion on wires resulting from freezing precipitation deposition. Data on icing are considered to be high importance for practical purposes, when mapping with regard to wire icing these data were also involved.

Corresponding author's address: Natalia A. Bezrukova, Central Aerological Observatory, Dolgoprudny, Moscow Region, 141700, Russia;
E-Mail: natalia_bezrukova@ mtu-net.ru.

Therefore, we have treated the fields of both the icing of wires (caused by freezing precipitation) and liquid precipitation at negative temperatures. Duration (in hours) was taken as the basic feature to describe the occurrence frequency of icing or freezing precipitation at a given station.

3. WEATHER CONDITIONS FAVORABLE FOR FREEZING PRECIPITATION

For many years, some research teams in Russia were involved with studying atmospheric ice, freezing rain and such phenomena as glaze-ice and frost or rime, as well as their detrimental effect on flight vehicles, power transmission lines, transport and communication (Zamorsky, 1955; Mazin, 1957; Buchinsky, 1960; Rudneva, 1967; Jakovlev, 1971; Abramovich, 1979; Baranov, 1983). Based on measurements from a specialized observational network, weather conditions under which ice accretion caused by freezing precipitation occurs have been summarized. The extreme values of freezing precipitation temperature range are 0° and -16^{0}C. The maximum frequency is between 0° and - 5^{0}C (Fig.1).

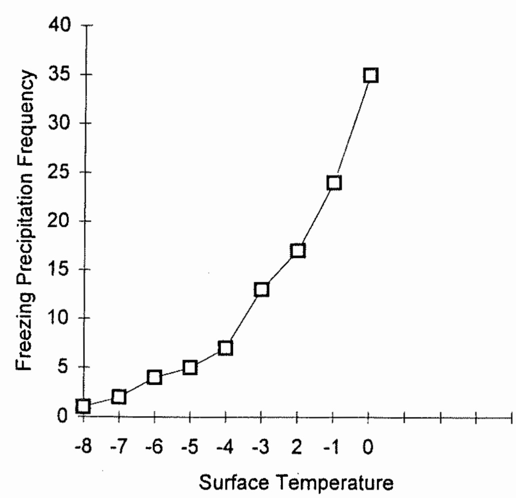

Fig.1 Frequency of occurrence of freezing rain (%) as a function of surface air temperature (°C), Buchinsky (1960).

Temperatures between 0° and -1^{0}C account for 35-40% of all freezing precipitation occurrences. As temperature goes down freezing precipitation frequency decreases abruptly. This temperature range, though quite narrow accounting for the highest frequency offering precipitation occurrence is in agreement with the temperature lapse-rate in winter, which is generally 0.2 - 0.3^{0}C/100 m.

According to Buchinsky (1960), Abramovich (1979) and others, the mean monthly icing temperature varies as shown in Table 1 for freezing precipitation and, for comparison, grained rime.

Table 1

Mean monthly icing air temperature, Abramovich (1979).

Precipitation type	X	XI	XII	I	II	III	IV
Freezing Precip.	-	-1.6	-2.3	-2.9	-2.2	-1.4	-
Grained Rime	0.0	-3.3	-5.1	-8.7	-11.8	-3.8	2.3

On the average, ice sheet density varies between 0.6 and 0.9 g/cm^{3}.

Freezing precipitation frequency and its intensity depend on relative humidity. Humidity range of 96-100% accounts for 96-100% of icing occurrences, while a 91-100% humidity gives rise to 90% of all cases of icing. Observational sites elevated relative to the surrounding areas generally register 94% of icing occurrences at 96-100% humidity.

4. SYNOPTIC AND CLIMATIC ICING CONDITIONS

The most intense and durable ground icing is observed in zones of supercooled rain falling from As-Ns cloud system that are at an intensive development stage, have the highest moisture content, and are associated with active fronts.

According to Dubrovina (1982), based on airplane sounding data, the highest drizzle frequency is connected with St clouds; in other words, almost 2% of the total amount of precipitation in winter (Table.2).

Table 2

Frequency (%) of occurrence of drizzle for the various type of clouds in winter, Dubrovina (1982).

Precipitation type	Sc	St	Ns-(As-Ns)
Drizzle	0.1	1.7	0.1
Rain	0.9	0.5	1.6

Many authors believe that 3/4 of all cases of ground icing are connected with fronts, while only 1/4 are accounted for by uniform air masses. More over, cases of the most severe icing are associated with warm fronts between maritime tropical air (0 - ÷ + 5^{0}C) and the air of middle latitudes (-5 ÷ -10^{0}C). This has been confirmed by the spatial icing distribution, with the highest values in the southern belt of the USSR ET, obtained by the authors (Fig.2). Far less intense freezing precipitation are observed in conditions of maritime air advection caused by westerly cyclones, which usually have not layers with positive temperatures in winter.

Over the major part of the ET, supercooled rain and icing occur in winter, without layers with positive temperatures aloft being observed, as in Isaac (1996).

The mechanism of freezing rain formation due to melting of hydrometeors in a warm layer was discussed as early as at the beginning of the last century. This and some other mechanisms have been discussed by Zamorsky (1955) and by other experimentators, Knight (1979). At present, there is experimental evidence of the presence of supercooled water drops and rain-size drops at essentially all atmospheric levels.

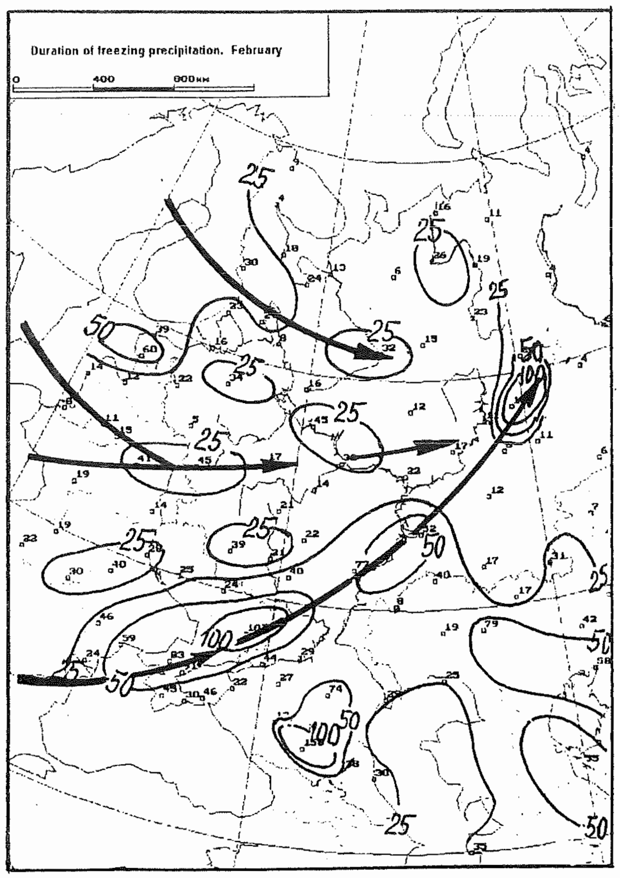

Fig.2 Mean monthly duration depositions of ice caused by freezing rain (in hours) on the USSR ET in February.

The fall of supercooled water in the form of freezing precipitation and its intensity is governed by frontal mechanisms and depends on front intensity.

This paper analyzes the spatial distribution of icing duration (in hours) and basic cyclone paths during the cold season for the USSR ET, discussed by Krizhanovskaya (1977). This analysis has been made for each autumn, winter, and spring month. Fig. 2 exemplifies such a map of icing occurrences (in hours)in February. The frequency distribution of icing occurrences on the USSR ET is not at all uniform. However, despite this nonuniformity of its field, its general features correspond to the climatic and synoptic conditions of the area concerned.

In general, the southern part of the USSR ET, where the Mediterranean cyclones carrying warm and moist air are most frequent, is exposed to icing most of all. In the south, icing is known to ruin communication and power transmission lines very often and sometimes even break electric cable poles.

In the northern part of the ET, icing occurs far less frequently, with frost rather being encountered.

In the central part of the ET, mainly on a high ground, there are zones of maximums associated with the passage of westerly fronts.

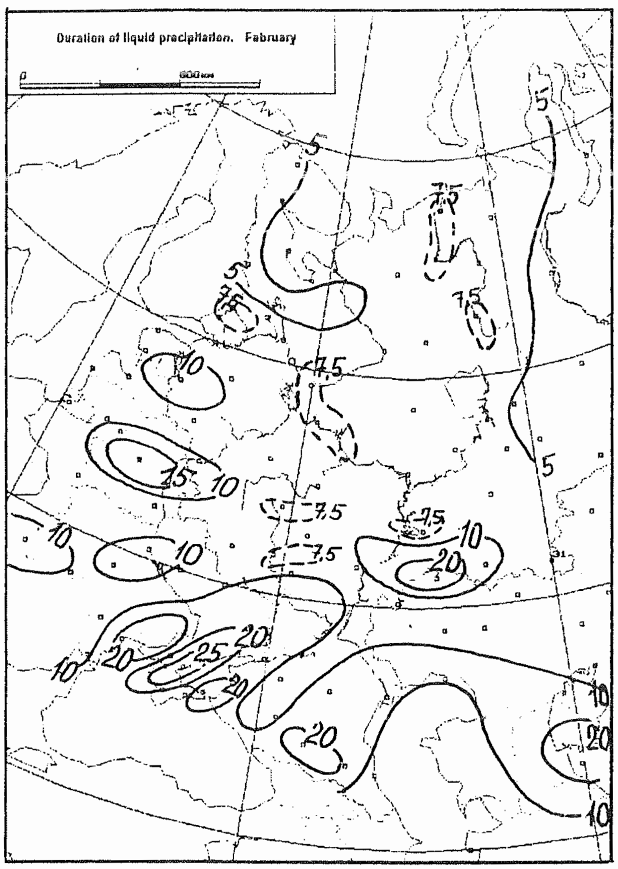

Fig.3 Monthly mean duration of liquid precipitation (in hours) at negative temperatures on the USSR ET. February.

Based on the climatic data, essentially no freezing precipitation is caused by the Siberian anticyclone, which creates a steady background of negative temperatures, in the eastern part of ET.

Figure 3 shows a map of the distribution of liquid precipitation at negative temperatures on the ET in February.

It can be seen that this pattern is in full agreement with ice accretion (caused by freezing precipitation) field for the same period (Fig. 2). The largest duration values are also observed in the southern part of the USSR ET most often influenced by the Mediterranean cyclones. At the fronts of these cyclones moist air actively interacts with the cold air of middle latitudes.

We believe that the distribution of icing field maximums fairly well agrees with that for liquid precipitation and with the cyclone paths in the corresponding months of the cold season.

5. FREEZING PRECIPITATION DEPENDENCE ON ALTITUDE

Apart from the above conditions, the spatial distribution of freezing precipitation depends on altitude and relief. Most exposed to icing are areas at larger heights and on upwind slopes.

We have ventured to estimate the relation between altitude and freezing precipitation duration for various ET areas. This relation has proved to be rather pronounced for the central part of the ET between 45^0 - 60^0 N and $30^0 - 60^0$ E. The correlation coefficient has been found to be 0.2 - 0.3 in October, 0.6 – 0.7 in November and December (Fig.4 and Fig.5, P is significance level) and 0.5 – 0.6 in January,

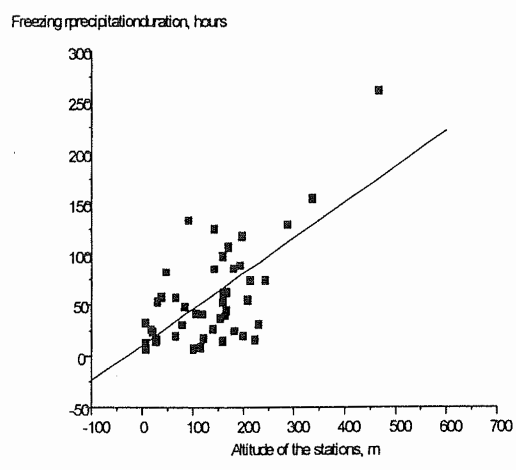

Fig.4 Dependence of freezing rain duration on altitude in the central part of the USSR ET, December, P< 0.01.

The relation between ice duration and height in November – January is due to climatic reasons. A steady winter circulation with low ground air temperatures settles, i.e. the likeliness of significant contrasts and deep inversions is preserved at fronts with relatively warm air advection.

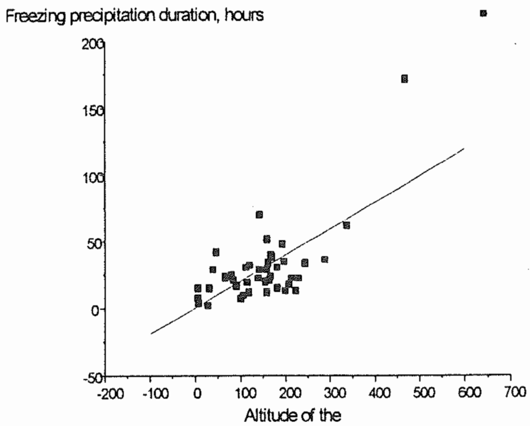

Fig.5 Dependence of freezing rain duration on altitude in the central part of the USSR ET, November, $P < 0.01$

The correlation coefficient has been found to be 0.2 – 0.3 in February and March (Fig. 6, P is significance level).

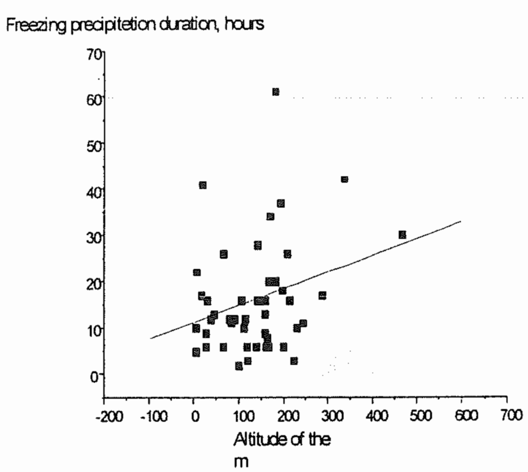

Fig.6 Dependence of freezing rain duration on altitude in the central part of the USSR ET, March, $P = 0.06$.

The loosening of this dependence in February and March is due to circulation change, warming, and lower probability of big temperature contrasts at fronts, i.e. the fronts' activity.

6. RESUME

The output of this work is an atlas of maps of the monthly occurrence of ice accretion, caused by freezing precipitation and liquid precipitation at negative temperatures in the USSR European Territory. This atlas is supplemented with statistical assessment and basic routes of civil aviation. Unfortunately, this abstract does not permit presenting the work done in sufficient detail. The authors have set an objective of compiling such an atlas for the whole territory of the USSR.

6.1 Acknowledgments

The authors wish to express their sincere appreciation of the assistance rendered through his comments and advice by Prof. A.D. Zamorsky, the author of the fundamental monograph «Atmosphere Ice» and one of the early makers of maps on icing caused by freezing precipitation for the territory of the USSR.

6.2 References

Abramovich, K. G., 1979: Forecasting of Aircraft Icing. Gidrometeoizdat, 27p (in Russian).

Baranov, A. M., 1983: Clouds and Flight Safety. Gidrometeoizdat, 231p (in Russian).

Buchinsky, V. E., 1960: Freezing Rain and Ice Control. Gidrometeoizdat, 192p (in Russian).

Dubrovina, L.S., 1982: Cloudiness and Precipitation According to the data of Airplane Soundings. Gidrometeoizdat, 216p (in Russian).

Isaac G.A., A. Korolev, J.W. Strapp, S.G. Cober, A. Tremblay, and R.A.Stuart, 1996: Freezing drizzle formation mechanisms. Proceedings of 12th Intl. Conf. Clouds and Precipitation, 11-14 .

Knight, C.A., 1979: Observations of the Morphology of Melting Snow. J. Atmos. Sci., **36**, 1123-1130.

Krizhanovskaya, A. P., 1977: Atlas of the Annual mean cyclone tracks over the Northern Hemisphere. Gidrometeoizdat. 58p (in Russian).

Mazin, I. P., 1957: Physics Basic of Aircraft Icing. Gidrometeoizdat, 120p (in Russian).

Narovliansky, G. Ja., 1968: Aeronautical Climatology. Gidrometeoizdat, 267p (in Russian).

Rudneva, A. V., 1961: Freezing Rain and Wire Freezing on the Territory of the USSR (in Russian).

Jakovlev, A. M., 1971: Aviation Meteorology. Transport, 246p (in Russian).

Zamorsky, A. D., 1955: Atmosphere Ice. Academy of Sciences of the USSR, 377p (in Russian).

LARGE CLOUD DROPS RIMED ON SNOW CRYSTALS OBSERVED AT NY-ÅLESUND, SVALBARD, ARCTIC

Hiroyuki Konishi[1] and Makoto Wada[2]

[1]Osaka Kyoiku University, Kashiwara, Osaka, 582-8582, Japan
[2]National Institute of Polar Research, Itabashi, Tokyo, 173-8515, Japan

1. INTRODUCTION

Non-ordinary large cloud drops were found on snow crystals in a wintertime snowfall during an observation period on January 1999 at Ny-Ålesund(79°N,12°E), Svalbard, Norwagian high Arctic. The maximum size of drops were larger than 200 μm. It is interesting that the cloud drops could grow to large size under supercooled condition below the freezing point. The large supercooled cloud drops are considered to be one of the typical precipitation particles only grown in polar region.

This type of rimed snow crystals with large cloud droplets and/or small raindrops were already observed in the polar region: e.g. at Syowa Station, Antarctica (Kikuchi 1972; Iwai 1981), at Inuvik, Arctic Canada (Kikuchi and Uyeda 1979; Magono and Kikuchi 1980) and at Fairbanks, Alaska (Sakurai and Ohtake 1981). Localities of these observation sites suggest that the rimed snow crystals with large cloud droplets and/or small raindrops are a characteristic type of snow crystals in polar regions.

The present paper first describes the condition for formation of growing large cloud drops by using the data of the vertical pointing meteorological radar, microwave radiometer and an aerosol particle counter. Next we discuss the formation process of the large supercooled cloud drops with comparing to the data obtained when the normal size frozen drops were found.

2. INSTRUMENTS AND OBSERVATION

Precipitating snow clouds at Ny-Ålesund have been observed continuously from 1992 by means of a vertical pointing radar. The radar measures echo intensities every 10 seconds from the ground level to 6.4 km in altitude with 50 m vertical resolution, which specifications were reported in Wada and konishi (1992). A microwave radiometer and an aerosol particle counter were also operated in 1998 and 1999 for continuous measuring of vertically integrated liquid water contents in the atmosphere and the number of aerosols at the ground surface respectively.

Precipitation particles were also recorded by photographs under a stereoscopic polarization microscope at the radar site.

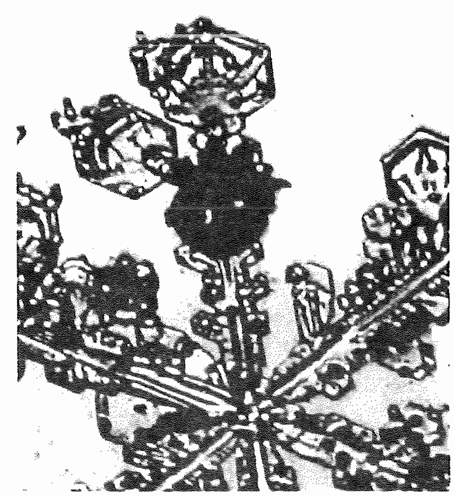

Fig.1. An example of large size rimed drops. In the center of this figure, the large drop (240 μm in diameter) is rimed on a blanch of a dendrite crystal. This particle was observed at 0725UT on 28 January 1999 when the ground surface temperature was -8℃ and echo top height was 2.5km.

Corresponding author's address: Hiroyuki Konishi, Osaka Kyoiku University, Kashiwara, Osaka, 582-8582, Japan;
E-Mail: konishi@cc.osaka-kyoiku.ac.jp.

3. Result

Rimed crystals with frozen drops larger than 200 μm in diameter were found in a snowfall on 28 January 1999. The examples of this type of crystals are shown in Fig. 1. The rimed crystals with large cloud drops were observed for several hours. The shape of the snow crystal collecting the large size frozen drops was almost all dendrite type.

Vertical profiles of temperature, humidity and the radar echo intensity when the large cloud drops were observed are shown in Fig. 2 and Fig. 3.

The features of vertical profiles are as follows.

1) Cloud top height was comparatively low: about 2 km, assuming that the cloud layer was defined as the relative humidity was larger than 70 %.
2) The humidity decreases sharply to less than 50 % above the cloud top.
3) The temperature between cloud top and ground was under freezing point throughtout. The temperature was −23 ºC and −10 ºC respectively.
4) The cloud top height was several hundred meter higher than the echo top height where the echo intensity decrease with height under 1 dBZ.
5) The convective activity was not so strong because the pattern of radar echo intensity change moderately with time.
6) The height of maximum radar echo intensity was scarcely change for several hours and the height was nearly equal the level of temperature at -15 °C.

Figure 4 shows the time series of vertically integrated liquid water contents derived from the data of a microwave radiometer for 3 days. The contents ran up to 0.4 cm during the time when the large cloud drops were found. At Ny-Ålesund in winter the contents rarely went over the value of 0.5 cm and the frequency of high water content larger than 0.4 cm was a few days in a month.It is thought that there would be plenty of liquid water content in the clouds consisting of the large cloud drops on 28 January 1999.

On the other hand the number of aerosol at ground surface was very small during the time when the large cloud drops were found. Figure 5 shows the time series of the number of aerosol at ground surface for the same duration in Fig. 4. The number of aerosol begins to decrease at the time when the large cloud drops were first observed. Especially the number of small size aerosol (<0.3μm) change to the minumum value during the snowfall. The number decreases from several thousands to one thousand by a litter. At Ny-Ålesund in winter the number usually went over several thousand and the frequency of the aerosol number smaller than 1000/l was a few times in a month. The time series of the number indicate that the air brought the large cloud drops is cleaner than usual.

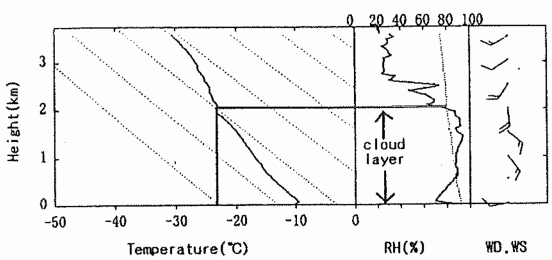

Fig.2. Vertical profiles of temperature and humidity derived from the radio sonde launched at 1118UT on 28 January 1999. The temperature profile is drawn by solid line and iso-potential temperature is also drawn by dotted line. The relative humidity is drawn by solid line and ice saturated line is also drawn by dotted line.

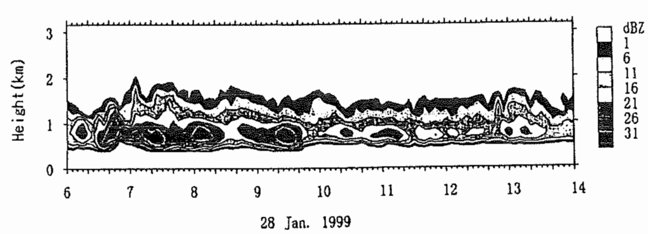

Fig.3. Time height cross section of echo intensity measured by a vertical pointing radar. Contour lines depicted every 5dBZ from 1dBZ.

4. Discussion

4.1. Condition of formation

The observation results indicate that the large size cloud drops would be grown in the supercooled condition with much smaller number of aerosol particles. Since part of aerosols play a role as condensation nuclei and /or freezing nuclei, the cloud drops grew larger in the clouds without sharing the water among the many nuclei and without freezing. The humid and clean air would be needed to form the large cloud drops.

The snowfall in Svarvard were mainly brought by clouds which were accompanied by a depression moving from midlatitude to high latitude, however, that brought the large cloud drops stayed for several days in polar region near Greenland. The back trajectory of the air also indicates that the cloud drops have been formed with staying for several days in polar region.

4.2. Formation process

The vertical profile of echo intensity and humidity suggests that the cloud was divided into two layers by echo top height. Upper part of cloud is the layer between the echo top and the cloud top, and lower part of cloud is the layer below the echo top. In the upper cloud, cloud particles were expected to be small size because the radar echo indicates low reflectivity and aerological sounding data shows high relative humidity. If snow particles grow in the upper cloud, the snow crystals observed on the ground would show the shape grown at lower temperature such as column and bullet. However the shape of snow crystal with large frozen drops was mostly dendrite type. Thus it is expected that the cloud particles were mostly consist of cloud drops in the upper cloud. On the other hand, in the lower cloud, radar echo profile suggests that the size and the number of particles were larger than those in the upper cloud. The vertical sharp increase of radar reflectivity in the lower cloud would indicate that the crystal grew rapidly at this height. Since the temperature was near -15 °C in the lower cloud, which is preferable temperature to grow dendritic crystal, the snow particles would grow fast and become large by coalescence each other.

Usually rimed snow crystals are considered

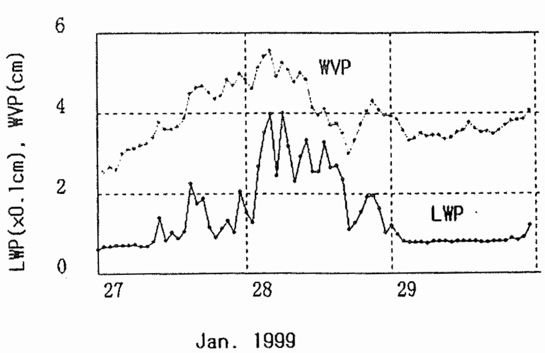

Fig.4. Time series of vertical integrated liquid water contents (thick line), and ice water contents (thin line) for 3 days. Solid lines at bottom of the figure indicate the duration of particle observation at radar site.

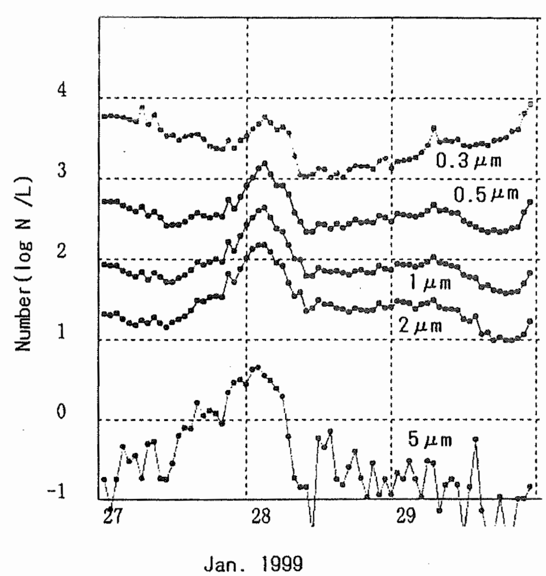

Fig.5. Time series of aerosol number measured at ground surface for 3 days. The 5 sizes of aerosol in diameter are shown. The aerosol number by a litter is expressed as logarithms in a vertical axis

to be formed by collection of the cloud droplets when the crystals are falling among the cloud droplets, because crystal usually falls faster than cloud droplet. But fall velocity of cloud drops larger than 200 μm was larger than 0.8 m/sec, which was faster than that of snow crystal. Therefore it is expected that the large cloud drops grew in the upper cloud and fell into the lower snow crystal cloud and accreted the snow crystal. Sakurai and Ohtake (1981) also guessed without radar data that the large supercooled cloud drops were produced in upper part of a cloud and snow crystals were formed in the lower part of a cloud from their observation at Fairbanks, Alaska.

The size distribution of cloud drops on snow crystal may also suggest that the large cloud drops were made in upper part of a cloud. If the cloud drop were made in lower cloud, not only large cloud drop but small size cloud droplets should be observed on snow crystals. However, small size droplets were not observed in this case.

5. Summary

Large cloud drops larger than 200 μm in diameter were found on the snow crystals in winter 1999 at Ny-Ålesund, Svalbard, Arctic.

The formation condition and process are investigated by using the data of a vertical pointing radar, a microwave radiometer and an aerosol counter. The data indicate that the large cloud drops were made in the humid and clean air in polar region..

The formation process was considered as follows. There are two layers in the clouds. These snow crystals are inferred to be formed by the following way: Small supercooled rain drops grown in upper cloud of temperature about -20 to -25 ºC formed in Arctic air with dendrites grown in a lower cloud of temperatures about -15 ºC formed in polar maritime air.

Acknowledgement

We wish to thanks the Alfred Wegener Institute (AWI) for offering their radio sonde data. We also wish to thanks the staff members of Kings Bay Kull Compani (KBKC) and National Institute of Polar Research for set up and keep the instruments for observation.

References

Iwai, K., 1981: On the frozen small raindrops observed at Syowa Station, Antarctica. Memor. NIPR Special Issue, 19, 160-168.

Kikuchi, K., 1972: On Snow Crystals with Small Raindrops. J.Meteor.Soc.Jpn., 50, 142-144.

Kikuchi, K. and Uyeda, H., 1979: Clouds droplets and rain drops collected and frozen on natural snow crystals. J. Meteor. Soc. Jpn., 57, 273-281.

Magono, C. and Kikuchi, K, 1980: Some observations of snowfall and meteorological conditions in Arctic Canada. Mon.Wea.Rev., 108, 1656-1664.

Sakurai, K. and Ohtake, T., 1981: Frozen drops observed at Fairbanks, Alaska. Seppyo, 43, 73-76.

Wada, M. and Konishi, H., 1992: A study of precipitation in the coastal area of Antarctica as observed at Syowa station using a vertical pointing radar. Nankyoku Shiryo (Antarc. Rec.), 36, 341-349.

IN SITU OBSERVATIONS OF CIRRUS CLOUD SCATTERING PHASE FUNCTION WITH 22° and 46° HALOS

Guy Febvre[(1)], Jean – François Gayet [(1)], O. Jourdan [(1)], Laurent Labonnote[(2)] and Gérard Brogniez[(2)]

(1) Laboratoire de Météorologie Physique, UPRESA/CNRS n°6016, Université Blaise Pascal, Clermont-Fd, France.
(2) Laboratoire d'Optique Atmosphérique, UMR n° 8518, Université des Sciences & Techniques de Lille, France

1. INTRODUCTION

Theoretical studies of various optical phenomena caused by light-scattering properties of ice crystals have been subjected to considerable works these last ten years within the critical global climate issue involving cirrus clouds. Different techniques have been used to model the scattering phase functions for crystals of different regular shapes (see among others : Macke et al., 1998). Most of the theoretical results addressed to simple geometric ice crystals show rather sharp peaks related to the well known 22° and 46° halos. Nevertheless, the rare ground-observed occurrence of these optical phenomena indicate serious deficiencies in the theoretical approaches mainly due to the fact that highly regular ice crystals are rarely observed in cirrus clouds (Korolev et al., 1999). In support to this finding, first direct measurements of scattering phase function from ensemble of ice crystals made by Gayet et al. (1998) showed that the 22° halo was absent in cirrostratus clouds. Direct measurements of the scattering phase function in laboratories confirm this finding whereas Crépel et al. (1997) did detect very smoothed 22° peak. On the contrary, ground-based aureolemeter measurements by Brogniez et al. (1995) showed a pronounced 22° halo. However, the authors also showed that the radiance field around the halo is smoother than the modeling results relative to hexagonal ice crystals can predict.

In this paper we show that in some cirrus uncinus cloud parts, measured scattering phase function do exhibit 22° and 46° halo features. These optical properties are compared to subsequent ice particles characteristics .

2. INSTRUMENTATION & SITUATION

An instrumented TBM700 aircraft was operated during the CIRRUS'98 experiment. This aircraft is a single turbo-propeller developed and manufactured by SOCATA in Tarbes (South-West of France). For this experiment, the operational ceiling of the aircraft was extended from 30 000 to 35 000 ft and the standard avionics has been supplemented with an inertial plateform, an airdata unit and a GPS (Durand et al., 1998). Two in situ microphysical probes were mounted on the TBM700 : a PMS 2D-C for recording the cloud particle images ranged from 25 to 800 μm diameter and the Polar Nephelometer. We recall that the Polar Nephelometer is an unique airborne *in situ* instrument which is compatible with PMS canister (Gayet et al., 1997). This instrument measures the scattering phase function of an ensemble of cloud particles (i. e., water droplets or ice crystals or a mixture of these particles from a few micrometers to about 500 microns diameter) which intersect a collimated laser beam near the focal point of a paraboloidal mirror.

The observations presented in this study were obtained on 19 February 1998 and the TBM700 flight lasted from 13 :40 to 17 :00 UTC. The meteorological situation was characterized by a persistent high pressure system centered over France with humid air at higher troposphere levels coming over the experimental area from the South-west. The vertical sounding revealed a wet layer which roughly corresponds to the cirrus cloud detected from the aircraft, namely between 7200 m MSL/ -30°C to 10800 m MSL/ -60°C. Much dryer air characterizes the lower layers. From satellite NOAA14/AVHRR image the cirrus cloud field appeared rather scattered and put together with visual observations from the aircraft, the studied cirrus may be classified as cirrus uncinus.

3. EVIDENCE OF 22° & 46° HALOS

In order to determine a quantitative criteria for the occurrence of the 22° and 46° halos respectively, we define the ratio of the values measured by the Polar Nephelometer at the scattering angles of 22° and 18.5° (ratio of channel 7 on channel 51 : P7/P51) and the ratio of the values measured at 46° and 44.5° (ratio of channel 47 on channel 10 : P47/P10).

A representative example of 22° & 46° halos displayed on Figure 1.a concerns a 6 sec. cirrus sampling at 7600 mMSL/-35°C level. This figure represents the mean scattering phase function measured by the Polar Nephelometer (solid circles) with an arbitrary example of theoretical scattering phase function (solid line) relative to ramdomly oriented hexagonal crystal plates with an aspect ratio (*Q*) of 0.2. The Fig. 1.b displays the corresponding 2D-C size histogram with the subsequent mean values of the relevant parameters and examples of ice particle images sampled by the 2D-C. The results show that the measured scattering phase function clearly exhibits the 22° and 46° halos feature. As a matter of fact the measured value at 22° (channel 7) is significantly larger than the 18.5° one (channel 51) leading to a

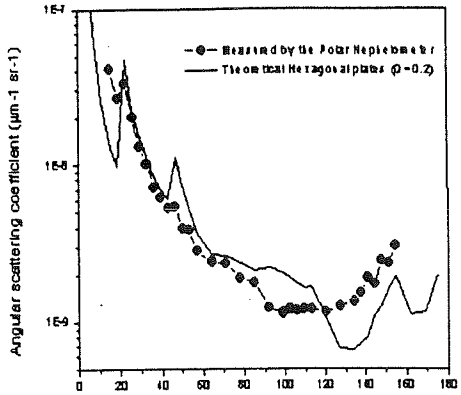

Figure 1.a : Measured scattering phase function & theoretical results (hexagonal crystal).

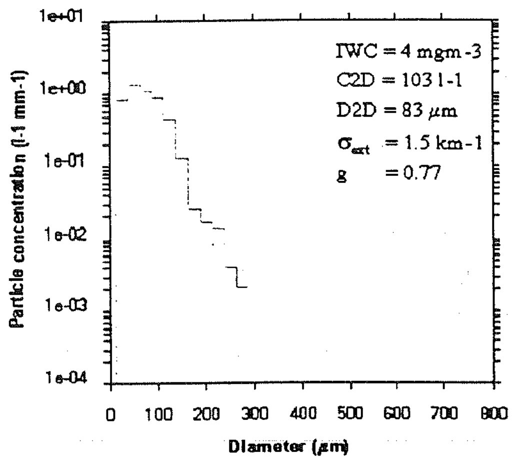

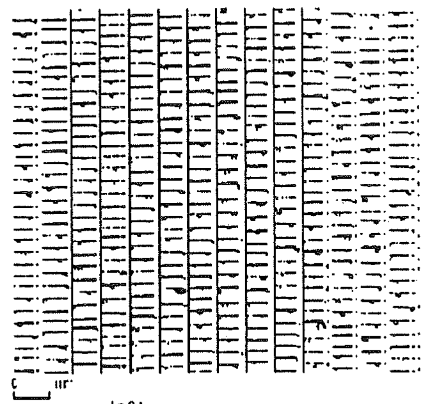

Figure 1.b : 2D-C size histogram with the subsequent mean values of the relevant parameters and examples of ice particle images sampled by the 2D-C.

P7/P51 ratio of about 1.5. As for the 46° halo, the ratio P47/P10 is only 1.1 leading to a smoothed peak at 46°. In order to show that the 22° and 46° peaks evidenced from the measured scattering phase functions represent actual optical characteristics we have reported on Figures 2.a & b the scattering plots of P7 (22°) versus P51 (18.5°) and P47 (46.5°) versus P10 (43°) respectively. In the both cases, the results show that most of the data points are distributed with a low dispersion and the exceptions of P7/P51 and P47/P10 ratios larger than 1 characterize halo occurrences. Such a feature observed wathever the signal to noise ratio leads to claim that the observed 22° and 46° peaks are not artefacts (due to optical or electronical noise problems for instance) but can be regarded as physical phenomena. Nevertheless, the examination of the measured scattering phase function on Fig. 1 reveals that the 22° and 46° peaks are rather smoothed when compared with the theoretical approach. This characteristic is systematically evidenced for all the observations reported here.

Coming back on the microphysical and optical properties of cirrus cloud segment exemplified on Figures 1, we report that the subsequent mean values of *IWC, C2D, D2D,* σ_{ext} and *g* are respectively 4 mgm^{-3}, 103 l^{-1}, 83 μm, 1.5 km^{-1} and 0.77. The examination of the corresponding 2D-C probe information shows that

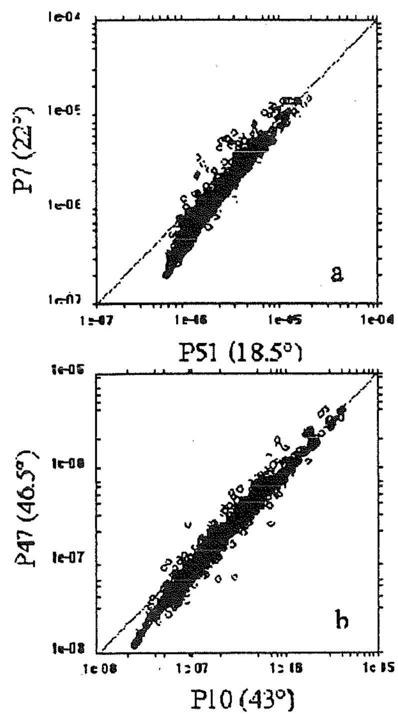

Figure 2 : Ratios P7/P51 & P47/P10

the particle size does not exceed 300 µm with rather irregular shape at least for the largest ice crystals from which the shape recognition is less problematic. A careful examination may suggest that only a few of the largest ice crystals may be shaped by 3-D assemblage like bullet-rosette type. Furthermore, some of the other recognizable ice crystals appear to be transparent because only the shape perimeter pixels are turned-on but this feature could also be due to particles passing out of the depth-of-field. Despite the qualitative information issued from the 2D-C probe measurement, one may conclude that ice crystals with simple geometric shape, at least larger than 100 µm, are not prevailing within this sample of ice particles.

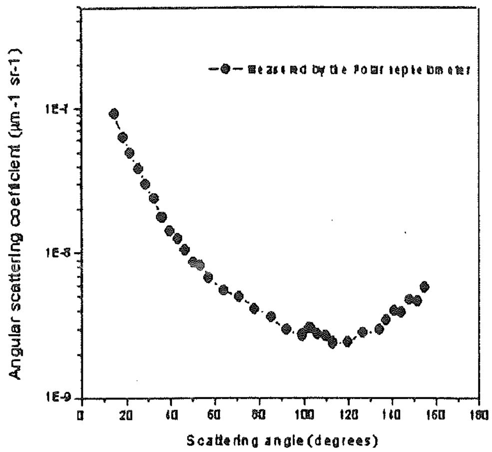

Figure 3.a : Measured scattering phase function

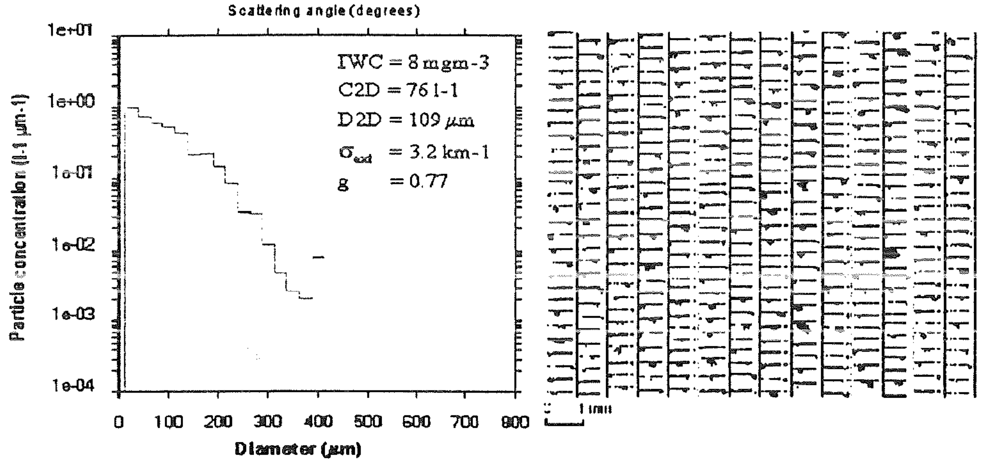

Figure 3.b : 2D-C size histogram with the subsequent mean values of the relevant parameters and examples of ice particle images sampled by the 2D-C.

Contrasting with the last example, the cirrus cloud sampled 7 mn later, still at the same level (-35°C) does not exhibit 22° and 46° halos, as clearly highlighted on Figures 3, despite microphysical and optical properties which are similar to those reported on Fig. 1. As already pointed out, the 2D-C particle images can only be considered as a qualitative information. Nevertheless, a careful comparison between the 2D-C images on Figs. 1 and 3 suggests that no significant difference can objectively be found about the observed shapes of ice crystals.

4. DISCUSSION

These above observations strongly suggest that the dominant ice particles with regards to scattering properties are the small ice crystals (typically < 50 µm) which cannot be accurately documented by the 2D-C probe. Evidence of these small particles in cirrus clouds is now well recognized (see among others, Heymsfield et al., 1990) and the lack of accurate measurements of such ice crystals crucially limit the interpretation of our results. The above assumption is supported by the fact that in cirrus clouds which have a low optical depth, the extinction coefficient is usually dominated by small ice particles (i.e. < 50 µm). As a matter of fact, Auriol (1998) showed that in such clouds the extinction coefficient derived from the Polar Nephelometer measurement is dominated (≈ 70%) by the contribution of particles smaller than 50 µm. Consequently we may reasonably argue that the observed halo feature is due to the presence of small ice crystals typically smaller than 50 µm. This may explain why former works (see for instance, Glass and Varley, 1978) did not observe pristine crystal forms (in cirrus clouds) required by theory to explain optical phenomena simply because they did not use appropriate and reliable in situ instrumentation to measure the smallest ice particles.

For the highly regular crystals responsible for halo phenomena there must be a subsequent main phase of extremely regular crystal growth. Low ice supersaturation are known to favor regular and slow crystal growth (that may be found in low updraft velocities. Accordingly only a few cloud portions which are characterized by small horizontal scales (100 to 400 m) present relevant thermodynamical and dynamical conditions, that may characterize formation areas of fresh ice particles. Following our observations, these areas would represent a proportion of only 2% of the sampled cirrus.

As for smoothed peak features it may be hypothetized that the presence of irregular-shaped crystals with rough surfaces or multiple inclusions inside regular crystals could smooth the peaks in the phase functions predicted by hexagonals crystals (Liou et al., 1997 ; Labonnote et al., 2000).

5. CONCLUSIONS

Using the Polar Nephelometer, a new instrument for in situ measuring the scattering phase function of ice particles, 22° & 46° halo features have been evidenced for the first time in cirrus uncinus clouds between –30°C and –38°C. In halo-producing cirrus clouds, most of the ice crystals larger than 100 µm were observed irregular-shaped and no significant difference in the shape of ice crystal's has been objectively found between the cirrus parts with and without halo. More generally, the halo occurrences were not related to the ice particle properties derived from the 2D-C probe. Therefore, we obtained proof that the cloud scattering properties and subsequent optical phenomena are dominated by the smallest ice particles (smaller than 50 µm) which are poorly documented with conventional PMS probes. Hypothesizing that highly-regular small-crystals are responsible for halo phenomena there must be a subsequent main phase of extremely regular crystal slow growth which requires low ice supersaturation. Only a few cirrus cloud portions which are characterized by small horizontal scales (100 to 400 m) did present such relevant thermodynamical and dynamical conditions, that may characterize formation areas of fresh ice particles. Following our observations, these areas would represent a proportion of only 2% of the sampled cirrus. Moreover, the observed 22° & 46° peak features are smoothed out with regards to modeling results relative to usual geometric crystal shape.

A more convincing interpretation of optical phenomena occurrences in cirrus clouds would need additional pertinent measurements, namely : the shape and size of the small ice crystals, the accurate and fine scale structure of the low water vapour content and of the dynamical parameters (wind vector and turbulence) and vertical profiles of cirrus properties which can be obtained from Lidar measurements.

Acknowledgements. This work was supported by the French DSP/STTC (Direction des systèmes de forces et de la Prospective / Service Technique des Technologies Communes) within the ONERA contract n° 23.140/DA.B1/BC. We are very grateful to J-F Fournol and O. Crépel for their active participation in the experiment. The authors would like to give recognition to G. Durand (ONERA) for his king help in aircraft data processing. Thanks are extended to A-M. Lanquette (LaMP) for her cooperation in the weather analysis. We also thank the members of SOCATA in Tarbes who operated the TBM700 aircraft during the experiment.

References :

Auriol F., 1998 : Mesure in situ de la fonction de phase de diffusion des particules nuageuses au moyen du Néphélomètre Polaire aéroporté : Validation et application aux nuages glacés. *Thèse de l'Université Blaise Pascal*, 17 Décembre 1998.

Brogniez, G., J.C. Buriez, V. Giraud, F. Parol and C. Vanbauce, 1995 : Determination of effective emittance and a radiatively equivalent microphysical model of cirrus from ground-based and satellite observations during the International Cirrus Experiment. The 18 October 1989 case study. *Mon. Wea. Rev.*, 123, 1025-1036.

Crépel, O., J-F Gayet, J-F Fournol and S.Oshchepkov, 1997 : A new airborne Polar Nephelometer for the measurements of optical and microphysical cloud properties. Part II: Preliminary tests. *Annales Geophysicae*, 15, 460-470.

Durand G., J-F Gayet, L. Kaës and P. Matharan, 1998 : Airborne Infra Red and Microphysical measurements in cirrus clouds. *European Symposium on Remote Sensing*. Barcelona (Spain), September 21-25, 1998.

Gayet, J-F, O. Crépel, J-F Fournol and S.Oshchepkov, 1997 : A new airborne Polar Nephelometer for the measurements of optical and microphysical cloud properties. Part I: Theoretical design. *Annales Geophysicae*, 15, 451-459.

Gayet J-F, F. Auriol, S. Oshchepkov, F. Schröder , C. Duroure , G. Febvre , J-F Fournol, O. Crépel, P. Personne and D. Daugeron,1998: In situ measurements of the scattering phase function of stratocumulus, contrails and cirrus. *Geophysical Research Letters*, 25, 971-974.

Glass, M. and D.J. Varley, 1978 : Observations of cirrus particle characteristics occuring with halos. *Preprint Am. Meteorol. Soc. Conference*, Issaquah, Washington, July 31 – August 8, 1978. 126-128.

Heymsfield, A. J., K. Miller and J. D. Spinhirne : 1990 : The 27-28 October 1986 FIRE IFO Cirrus case study : cloud microstructure. *Mon. Weather. Rev.*, 118, 2313-2328.

Labonnote L.C., G. Brogniez, J-F Gayet, M. Doutriaux-Boucher and J. Buriez 2000 : Modeling of light scattering in cirrus clouds with inhomogeneous hexagonal monocrystals. Comparison with in situ and ADEOS-POLDER measurements. *Geophys. Res. Let.*, 27, 113-116.

Liou K. N., P. Yang, Y. Takano, K. Sassen, T. Charlock and W. P. Arnott, 1997 : On the radiative properties of contrail cirrus, *Geophys. Res. Lett.*

Macke A. and M.I. Mishchenko, 1998 : Monte Carlo calculations of light scattering by large particles with multiple internal inclusions. *Preprints Conf. On Light scattering by Nonspherical Particles : Theory, Measurements and Applications*. New York, Am. Meteor. Soc., 143-146.

THE ICE INITIATION BY THE ACOUSTIC-ELECTROSTATIC COALESCENCE

Z.R. Vuković[1] and M. Ćurić[2]

[1]Toronto, Ontario, Canada
[2]Institute of Meteorology, University of Belgrade, Yugoslavia

1. INTRODUCTION

The droplet motion and electrical effects produced by lightning may cause a rapid and effective droplet coalescence process (Goyer 1965; Moore and Vonnegut 1964; Ćurić and Vuković 1988, 1991, 1992; Vuković and Ćurić 1996, 1998; Ling et al. 1999). The model simulations suggest that in the area near where a lightning event happened, after a few seconds, the initial unimodal spectra of supercooled water drops can be changed to the bimodal spectra of unfrozen and frozen water drops. The number of frozen drops is a few orders less than unfrozen water drops, but can be still very important for further transformations due to gravitational coagulation and other known microphisical processes.

2. MODEL DESCRIPTION

2.1 General description

The paper does not deal with mechanism of electrical discharge in a cloud. We only observe the moment when it happened. The lightning channel will be considered vertical and the cloud characteristics are axial-symmetrical around the lightning channel. It is also assumed that before the electrical discharge a cloud is composed of negatively charged supercooled water drops which belong to the horizontal layer of unit thickness with constant temperature T. The size distribution spectra is equal everywhere until the first electrical discharge, while after it there are only positive ions around the lightning channel (Moore et al., 1964). Those ions, carried by shock wave front, will be moved away from the channel and collected by negative droplets. The ions may first neutralise the negative cloud droplets and because of the high space density of the ions, then give them a very large positive charge. According to this picture we will have mostly positive charged droplets near the channel and more negative ions with increased distance from it. Although before electrical discharge we had only supercooled droplets after it some of them will be frozen and the final result is that air motion caused by the acoustic wave suddenly increases the velocity of differently charged frozen and unfrozen droplets. Faster drops move past the slower ones, and create conditions for coalescence growth. Since the droplets are charged, the electric forces cause changing stability in a newly created droplet. Also very fast water drop will be unstable and they will be broken in smaller stabile one. In case that collision between frozen and unfrozen drops is happened, depend of stability of new-formed drop, we can have new bigger frozen drop. This growth of frozen and unfrozen drops, as well as a mass transfer from liquid to ice phase spectra is called acoustic-electric coalescence with temperature influence (*AECT*)

2.2. Freezing

Two main mechanisms of ice generations by drops' freezing are usually considered: immersion freezing and contact freezing nucleation. Observational results suggest that formation of ice in clouds is determined mainly by the transformation of supercooled liquid water. Varieties of studies have suggested that subjecting water drops to mechanical shock could result in freezing the drops. Czys (1989) summarizes several of these studies and presents additional evidence that mechanical shock can induce freezing drops. He relates the shock-induced freezing to the occurrence of cavitation within the drops. The cavitation results as the external pressure drops suddenly and the resulting forces are great enough to exceed the tensile strength of the liquid. The mechanism by which cavitation produces freezing is unclear same as the importance of such processes in the cloud.

In the *AECT* model, we are introducing drops' freezing due acoustic shock wave of electrical discharge in the cloud. The glaciation process of supercooled drops due electrical discharge is assumed to occur in two different ways.

The first process is initiation of ice (frozen drop) as a result of dynamic stress of sonic waves generated from lightning discharge (Goyer et al. 1965; Czys 1989).

The second mechanism of the glaciation is contact freezing, freezing by collisions between ice particles and water drops. The simulation of hydrometeor size spectra evolution by water-water, ice-water and ice-ice interaction was object of investigation by numerous of authors. In *AECT* model we assumed that in case of

[1] Corresponding author's address: Zlatko Vukovic, 1286 Gryphon Mews, Mississauga, Ontario, L4W 3E5, Canada; E-Mail: zlatko.vukovic@ec.gc.ca.

collision of water drops always we have water drops while in case of collision of water-ice drops it is assumed that the result is frozen drop (or drops).

3. RESULTS

Several numerical simulations have been carried out for the temperatures 0, -5, -10, -15, and –20C. They have been classified in Table 1 according to the liquid water content L_{wc} , the average droplet radius R_{av} , the initial energy density of the lightning channel E_0, the values of droplet charge Q and the radius of positively charged droplets area λ. In the case studies we used a radial domain of 25m.

Table 1. Summary of experimental parameters. Liquid water content, L_{wc}; average spectra radius R_{av} ; initially energy density of lightning channel E_0; values of droplet charge: 0 means no charge, $<Q_{mx}$ empirical relation between droplet size and charge, $=Q_{mx}$ *Rayleigh* limit charge; radius of positively charged droplets area λ.

Case	L_{wc} [gm^{-3}]	R_{av} [μm]	E_0 [$Jm^{-2}m^{-1}$]	Q	λ [m]
1	1	100	10^5	$<Q_{mx}$	15
2	3	100	10^5	$<Q_{mx}$	15
3	2	100	10^5	$<Q_{mx}$	15
4	2	100	10^5	$=Q_{mx}$	15
5	2	100	10^5	0	15
6	2	100	10^4	$<Q_{mx}$	15
7	2	100	10^6	$<Q_{mx}$	15
8	2	50	10^5	$<Q_{mx}$	15
9	2	50	10^5	$=Q_{mx}$	15
10	2	150	10^5	$<Q_{mx}$	15
11	3	150	10^6	0	15
12	3	150	10^6	$<Q_{mx}$	15
13	3	150	10^6	$=Q_{mx}$	15
14	2	100	10^5	$<Q_{mx}$	5
15	2	100	10^5	$<Q_{mx}$	25

3.1 Evolution of the initial concentrations

The typical transfer of mass spectra due *AECT* (T = –10°C) for five different distance from lightning channel (x=5,10,15,20 and 25m) are shown on the Figure 1. On the left half of the graph are concentration of water spectra and on the right side are frozen drops spectra. The dashed lines represent initial distributions of unfrozen or frozen water concentration drops. Initial frozen drops are result of the dynamic stress of sonic waves. The full lines are transformed water or ice spectra. The greatest change of the spectra are in the second position (x=10m) and after that the effects decrease with distance. The water mass drop spectra have been shifted to the bimodal distributions (except in the first position).

From the presented graph we can notice concentration decreases below drop radius of 200 microns and as a result of collisions it increase for drops larger than 200 microns. The spectra concentration of frozen drops has deep minimum for the smallest drops although in the initial distribution it didn't exist. The initial glacation is starting for droplet bigger of certain size (depend of temperature and other initial conditions) while later due unsuccessful ice-water collisions we have break up of water drop in the smaller frozen drops.

3.2 Spectra changes for different initial conditions

The model sensibility on the different initial conditions can be tested throw analysing of radar reflectivity factor which includes effects of mass and radius spectra transfers.

In general, for all temperatures we can say that the influence of *AECT* is more significant as the liquid water content, mean radius or drop charge is higher. The energy of lightning discharge also increase effects of *AECT*, except when we have to much energy and all drops are liquid ($E = 10^6 Jm^{-2}m^{-1}$, T=0C) and many of them are unstable. Radius of positive charge area ($S \equiv \lambda$) has bigger influence on *AECT* for $Q = Qmx$ then for $Q < Qmx$. The influence of temperature on *AECT* and variation of total radar reflectivity is smaller as the temperature is lower. In the Table 2 are shown the summary results of *AECT* for five chosen temperatures for 15 cases with different combination of initial parameters (Table 1).

4. DISCUSSION

The model results have given us a two possible explanation regarding to electrical discharge and drop spectra transformations. First, explanation about drastic changes in drop spectra distribution (from unimodular to bimodular spectra and mass transfer toward bigger drops), Second explanation, very fast - almost immediately, freezing of one portion of supercooled water drops. For correct understanding and validation of the model result, we have to be conciseness about the model limitations. In this stage model mainly can give us just estimations in which direction we can expect influence of electrical discharge toward supercooled drops. Quantitative results can be more valid if the model is used inside the bigger, more complex, model where post ice growth and thermodynamic interactions are treat more realistic. However, the actual model results can help us in some explanations of characteristic inferred from Lopez and Aubagnac's polarimetric radar observations (1997).

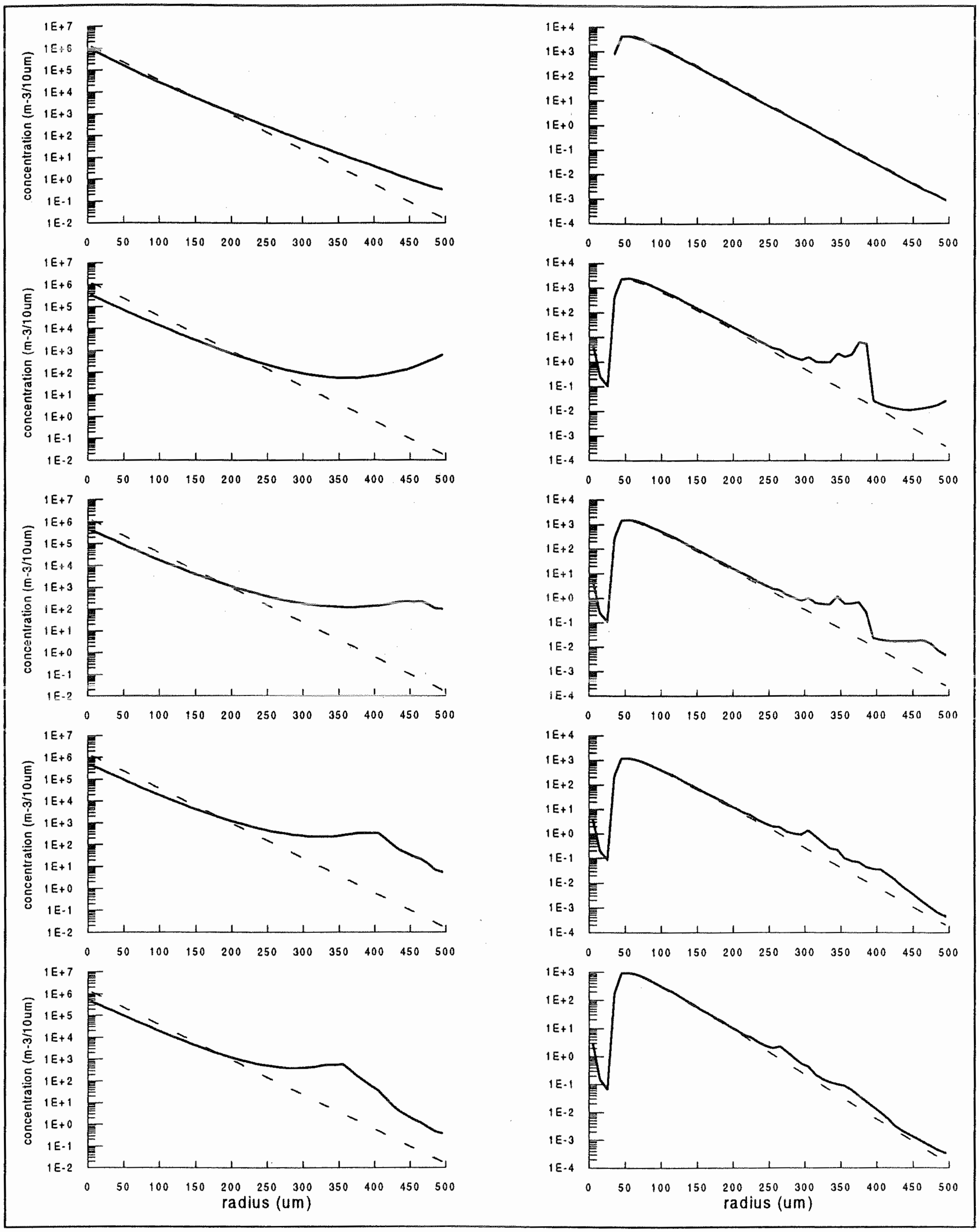

Figure 1. Evolution of the initial concentration spectrums (dashed lines) of unfrozen (left) and frozen water (right) due to acoustic-electrostatic coagulation for T=-10C for initial conditions shown in case 4 for five different distances from lightning channel (x=5,10,15,20 and 25m).

Table 2. Summary of space averaged output model values for relative rates of the mean volume radius dR_{mv} and radar reflectivity factor dZ for total cloud content (frozen and unfrozen drops) for five temperatures.

	dZ (dBZ)					dR_{mv} (%)				
case	0 C	-5 C	-10 C	-15 C	-20 C	0 C	-5 C	-10 C	-15 C	-20 C
1	3.0	2.9	2.8	1.5	1.7	9.0	8.7	8.6	5.6	5.6
2	10.3	10.1	10.2	6.2	6.5	45.6	44.2	44.3	23.9	24.1
3	7.2	7.0	2.6	3.7	4.0	24.9	24.1	23.9	14.0	14.3
4	11.2	10.5	10.7	10.8	10.8	39.1	34.9	35.9	37.7	36.7
5	7.2	6.9	6.8	3.0	3.9	24.4	23.5	23.1	12.1	14.0
6	3.4	3.3	3.2	1.9	1.9	12.6	12.1	11.9	7.9	8.3
7	6.2	7.2	6.9	3.5	3.1	10.5	13.2	14.6	9.1	8.4
8	13.1	12.8	13.0	12.0	12.9	28.2	28.2	27.3	24.2	28.0
9	13.1	12.8	13.0	12.0	12.9	28.2	28.2	27.3	24.2	28.0
10	3.0	2.9	2.8	1.6	1.7	13.5	13.1	12.8	7.4	7.5
11	6.3	6.3	5.8	1.6	1.5	17.0	19.7	21.6	6.1	6.0
12	6.3	6.3	5.8	2.0	1.5	17.1	20.0	22.1	7.3	5.8
13	5.6	5.4	5.9	3.0	2.7	18.2	21.2	31.0	12.8	11.8
14	7.2	7.0	6.9	3.8	4.0	24.7	23.8	23.6	14.3	14.2
15	7.3	7.0	7.0	3.6	4.0	25.0	24.0	23.8	13.9	14.3

5 <u>REFERENCES</u>

Goyer, G.G. 1965: Mechanical effects of a simulated lightning discharge on the water droplets of 'OldFaithful' Geyser. Nature. **206**:1302-04.

Moore, C.B., Vonnegut, B., 1964 Gushes of Rain and Hail After Lightning. J.Atmos. Sci. V21:

Ćurić, M. and Vuković R.Z. 1988: Influence of Thunderstorm Generated Acoustic Wave on Coagulation. Proc. **10**. ICCP, Bad Homburg, Germany.

Ćurić, M. and Vuković R.Z. 1991: The influence of thunderstorm generated acoustic waves on coagulation. Part I: Mathematical formulation. Z. Meteorol., **41**: 164-169.

Ćurić, M. and Vuković R.Z. 1992: Numerical Experiments on the Influence of Thunderstorm - Generated Acoustic Waves on Coagulation Proc. **11**. ICCP, Montreal, Canada.

Vuković, R.Z. and Ćurić M. 1996: A possible relationhip between lightning discharge in cloud and gushes of rain. Pro **12**. ICCP, Zirich, Sviceland.

Vuković, R.Z. and Ćurić M. 1998: The acoustic-electric coalescence and the intesification of precipitation radar echoes in clouds. Atm.Res. **47-48**, 113-125.

Ling Zhou, Xu Huaying, Huang 1999 Experimental and numerical simulation for the effect of

Czys R. Robert 1989: Ice Initiation by Collision-Freezing in Warm-Based Cumuli J. App. Sci., **28**: 1098-1104.

Lopez,E.R. and J-P.Aubagnac 1997: The lightning activity of a hailstorm as a function of charges in its microphysical characteristic inferred from polarimetric radar observations. J. Geophys. Res., **102**, D14, 16799-813.

CRYSTAL GROWTH: 2-D or Not 2-D?

Dennis Lamb

Meteorology Department, The Pennsylvania State University
University Park, Pennsylvania 16802, USA

1. INTRODUCTION

The evolution of the ice phase in atmospheric clouds starts with the nucleation of primary ice particles and their subsequent growth by the deposition of water vapor under supersaturated conditions. Vapor deposition is an important process to understand because it establishes the initial shapes, masses and fallspeeds of the ice particles that subsequently interact collisionally with other cloud particles and contribute to precipitation via the so-called "cold-rain" mechanism (Young 1993, p. 7). Precisely how vapor molecules contribute to the growth of these ice particles is still unknown, posing a limitation to the development of realistic cloud models.

Ice crystal growth is complicated because of the wide variety of shapes found in nature (Bentley 1901; Weickmann 1945). Non spherical forms arise from variations across the surface in the probability with which water molecules are able to build into the crystal. A commonly used descriptor of growth efficiency is the deposition coefficient α, the fraction of molecules striking the surface that successfully incorporate into the ice lattice and contribute to growth of the particle. By virtue of the crystallographic nature of ice Ih (Petrenko and Whitworth 1999, Chapt. 2), vapor-grown ice crystals are typically bounded by two basal faces and six prism faces, the growths of which are kinetically limited. The primary habit of a crystal (whether it is a plate or a column) is thus determined by the relative magnitudes of the deposition coefficients characterizing the basal and prism faces. Plates evolve, for instance, when $\alpha_{prism} > \alpha_{basal}$, whereas columns develop when $\alpha_{basal} > \alpha_{prism}$. At high supersaturations, gradients of vapor density across the faces lead to "hollowing" (Nelson and Baker 1996) and to more complicated forms (Yokoyama 1993).

Author's address: Dennis Lamb, 503 Walker Bldg., Penn State University, University Park, PA 16802, USA; email: lno@ems.psu.edu.

The mechanism of molecular incorporation, although still highly uncertain in detail, is generally thought to involve steps or ledges on otherwise flat surfaces (Hudson 1992, p. 4; Nelson and Baker 1996). The steps are likely to contain numerous "kink" sites, where adsorbed molecules of water find facile incorporation into the lattice (Frenkel 1945; Gilmer *et al.* 1971). Controversy exists mainly over the origins of the steps, whether they result from two-dimensional (2-D) nucleation or from the emergence of screw dislocations onto the growing surfaces (see Frank 1949, 1982; McKnight and Hallett 1978; Nelson and Knight 1998). Each mechanism of step origin yields a different dependence of the deposition coefficient on supersaturation, which should be reflected in the linear growth rates of the various crystal faces.

This paper explores the inter-relationships between these alternative mechanisms and how the presence of a non condensable medium (air) influences the overall dependence of growth on ambient supersaturation. The traditional concern about whether 2-D nucleation is the relevant mechanism or not may be mute if the effects of volume diffusion dominate the surface kinetics.

2. THEORETICAL RELATIONSHIPS

The effect of each mechanism of step origin on the growth of a particular crystal face can be expressed in quantitative terms through the use of appropriate theory. For instance, Burton *et al.* (1951) developed an elaborate theory of growth based on the emergence of one or more screw dislocations on a crystal face exposed to a supersaturation of specified magnitude. The spiral-step mechanism helped resolve the conceptual difficulty of reconciling observed growth rates at low supersaturations with predictions from theory based on the need for steps to be generated by nucleation of new layers on defect-free surfaces (Becker and Döring 1935; Frank 1949). The linear growth rate of a given crystallographic face (i.e., a basal or prism face) can be calculated once certain parameters

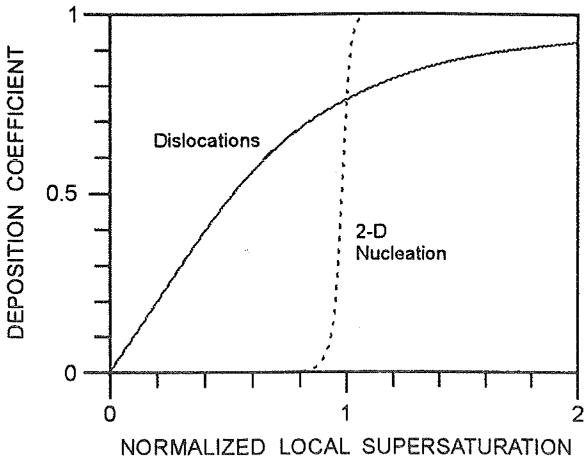

Figure 1. Dependence of the deposition coefficient on local supersaturation and the mechanism of step origin. The supersaturation s has been normalized to the transition value s_1 described in the text. The forms of the curves are based on the parameterization of Nelson and Baker (1996).

characteristic of the crystalline material are known. The appropriate theory predicts the growth in terms of the deposition coefficient, in effect the growth rate normalized to the maximum rate predictable from kinetic theory (Lamb and Scott 1974). The characteristic dependence of α on the ice supersaturation s immediately over the surface is shown in Fig. 1 for each mechanism. Note that the 2-D nucleation of new layers on perfect faces requires that this "local" supersaturation exceed a "transition" value s_1 before significant growth can be expected, whereas growth on defective faces is achievable even when s/s_1 is well below unity. These two mechanisms of step origin yield seemingly large differences in the crystal growth rates. The relationship of s_1 to the growth of ice by either step mechanism is described later.

Lewis (1974) examined the theories for each mechanism of step origin in some detail and pointed out that the edge energy ε, viewed here as the surface free energy integrated over the height of a step, is a material parameter that is common to both theories. The edge energy is best thought of as an empirical parameter characteristic of a given crystalline surface (Frank 1972), as possibly affected by interfacial structure (Fukuta and Lu 1994). Bernal (1958) suggested that the variations with temperature in the surface free energies of the basal and prism faces cause the ice crystal habits to alternate between plates and columns with temperature.

The relationship between the edge energy of a face and the transition supersaturation (s_1) that characterizes the efficiency of growth on that face can be established through consideration of the thermodynamics of "island" formation. If the island is circular and of monomolecular height a, then the critical radius is given by

$$r^* = \frac{a^2 \varepsilon}{\Delta\mu} , \qquad (1)$$

where $\Delta\mu = kT\ln(s+1)$ is the chemical potential difference of molecules in the vapor and condensed phases (Hudson 1992, p. 301). Islands of this size are in unstable equilibrium with the adsorbed molecules in the surface layer. The important point to note is that such critical islands play central roles in both theories of step origin (Hudson 1992, p. 307). On faces with emergent screw dislocations, the spiral steps exhibit local radii of curvature that depend on the distance away from the dislocation. The minimum radius of curvature is equal to the critical value given by Eq. (1). The transition supersaturation for spiral growth is shown through classical theory to be

$$s_1 = \frac{2\pi r^*}{x_s} s \simeq \frac{2\pi}{kT} \cdot \frac{a^2 \varepsilon}{x_s} , \qquad (2)$$

where x_s is the mean distance of molecular diffusion on the surface (Burton *et al.* 1951). Note that s_1 depends directly on r^* (and hence ε) and on x_s. Such a simple relationship between s_1 and r^* has yet to be demonstrated for 2-D nucleation. Nevertheless, once a critical-size island forms on a defect-free surface, a new layer is able to form and propagate rapidly across the surface, causing the face to advance.

Nelson and Baker (1996) have suggested that the deposition coefficient may be related to the transition supersaturation in a general way for all mechanisms of step generation:

$$\alpha = \left(\frac{s}{s_1}\right)^m \tanh\left[\left(\frac{s_1}{s}\right)^m\right] , \qquad (3)$$

where m is a parameter used to distinguish the different mechanisms. The dependencies of α on s shown in Fig. 1, for instance, are based on Eq. (3) with m = 1 for screw dislocations and with m = 30 to represent the effect of 2-D nucleation. Variations in the edge energy with temperature or with crystallographic orientation would manifest themselves as variations in s_1 (Eqs. 1 and 2), thus affecting each mechanism of step origin in qualitatively similar ways.

3. PRACTICAL APPLICATIONS

Given the fact that the two main mechanisms of crystal growth are each influenced by a common property of a crystal face, one should be able to apply theory toward some practical ends. Extrapolations of laboratory data of crystal growth to an atmospheric context, for instance, may be facilitated by appropriate reasoning. Nelson and Knight (1996, 1998) have recently measured the critical supersaturations needed to initiate growth on the basal and prism faces of laboratory ice crystals thought to be free of defects. However, ice grown on substrates (e.g., Lamb and Scott 1972) is likely to be defective because of the artificial contact, whereas ice crystals of atmospheric origin may or may not contain dislocations (McKnight and Hallett 1978; Keller *et al.* 1980; Frank 1982). It is tempting to think that growth rates derived from defective crystals, even if atmospheric crystals prove to be defect free, could be interpreted in terms of a transition or critical supersaturation that would find general application to atmospheric ice.

The presence of a non condensable gas like air imposes practical limitations that need to be understood. Active growth of a crystal in air necessarily lowers the excess vapor density in the immediate vicinities of the growing faces, leading to gradients of vapor and temperature that impact the overall (measurable) growth of the crystal (Nelson and Baker 1996). The dependence of growth rate on supersaturation derived from classical theory (as depicted in Fig. 1) is appropriate only if the supersaturation is that immediately over the surface. This "local" supersaturation cannot, however, be measured during active growth in air. Crystals grown in a pure-vapor environment could be used, but one still faces the challenge of "taking" those findings to the atmosphere.

Lamb and Chen (1995) considered the impact of air on growth controlled by screw dislocations and showed that the mathematical form of the function $\alpha(s/s_1)$ changes markedly when using the ambient, rather than the local supersaturation. Instead of an initially linear dependence of α on s/s_1 (as shown in Fig. 1), the function becomes parabolic, as can be seen in Fig. 2 (solid curve).

A similar analysis has now been performed for the case of growth dominated by 2-D nucleation using the parameterization of the surface physics given by Eq. (3), with m = 30. Simultaneous consideration of the inherent growth efficiency

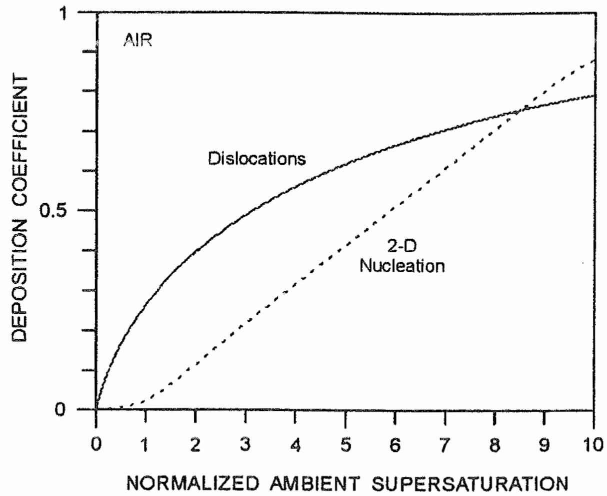

Figure 2. Dependence of the deposition coefficient on ambient supersaturation and the mechanism of step origin when growth occurs in air. Each curve is derived from Eq. (4) with K = 10. The solid curve results from using m = 1, whereas the dashed curve arises when m = 30.

(dashed curve in Fig. 1) and mass continuity of vapor leads to a general relationship of the form

$$\alpha = \left(\frac{x}{1+K\alpha}\right)^m \tanh\left[\left(\frac{1+K\alpha}{x}\right)^m\right] , \quad (4)$$

where $x \equiv s_{ambient}/s_1$ and $K\alpha$ is the ratio of the transport resistances due to volume diffusion and surface kinetics. Equation (4) is an implicit transcendental equation that is typically solved by iteration. The dashed curve in Fig. 2 shows the result for K = 10, a value characteristic of growth under atmospheric conditions (Lamb and Chen 1995). Note in particular how growth in air (Fig. 2, dashed curve) causes the apparent dependence of α on s to be much gentler than in its absence (Fig. 1). In effect, air not only restricts the overall flux of water vapor to the crystal, but it also greatly broadens the range of ambient supersaturations over which moderate growth occurs, even when layers form by 2-D nucleation.

4. CONCLUSIONS

Whereas controversy over the origin of steps responsible for the growth of ice crystals has emphasized the differences arising from 2-D nucleation and screw dislocations, these two mechanisms exhibit a number of similarities that are often overlooked. Both types of steps depend in concept on the existence of islands of water molecules clustered together on the surface in unstable equilibrium with the population of adsorbed water molecules. The size of these critical islands is the same in both cases, being dependent on the surface free energy, as manifested along the periphery of the critical islands. This edge energy, a material property of each crystal surface, is common to both mechanisms of step origin, so any changes in its magnitude, such as arise from changes in temperature, will affect the growth of the face in the same way, regardless which mechanism is operative.

The presence of air further diminishes the distinction between the effects of 2-D nucleation and spiral steps on the growth of ice. Diffusion of water vapor through the air surrounding a growing crystal clearly restricts the vapor flux, but more importantly, the implied gradients of vapor density cause the local supersaturation immediately over each face to respond simultaneously to the environmental conditions and to the inherent growth efficiency of that face. The nonlinear interactions that arise from this coupling of mass transport in the vapor phase and surface physics cause the deposition coefficients of each mechanism to depend on the ambient supersaturation in fundamentally similar ways. More detailed analyses of this problem in the future may well demonstrate that the evolution of ice by vapor deposition in atmospheric clouds is only weakly dependent upon which model of growth is actually used.

5. ACKNOWLEDGMENTS

This research was sponsored in part by NSF Grant ATM-9981511. Discussions with Nathan Magee are greatly appreciated.

6. REFERENCES

Becker, R., and W. Döring, 1935: Kinetische Behandlung der Keimbildung in ubersättigten Dämpfen. *Ann. der Phys.*, [5], **24**, 719-752.

Bentley, W.A., 1901: Twenty years' study of snow crystals. *Mon. Wea. Rev.*, **29**, 212-214.

Bernal, J.D., 1958: Comments on the paper of Hallett and Mason. *Proc. Roy. Soc. London*, **A247**, 534-538.

Burton, W.K., N. Cabrera, and F.C. Frank, 1951: The growth of crystals and the equilibrium structure of their surfaces. *Phil. Trans. Roy. Soc. London*, **A243**, 299-358.

Frank, F.C., 1949: The influence of dislocations on crystal growth. *Disc. Faraday Soc.*, **5**, 48-54.

Frank, F.C., 1972: An outline of nucleation theory. *J. Cryst. Gr.*, **13/14**, 154-156.

Frank, F.C., 1982: Snow crystals. *Contemp. Phys.*, **23**, 3-22.

Frenkel, J., 1945: On the surface motion of particles in crystals and the natural roughness of crystalline faces. *J. Phys. U.S.S.R.*, **9**, 392-398.

Fukuta, N., and Q.J. Lu, 1994: Surface microphysical mechanism for ice crystal growth habit development. *Atmos. Res.*, **32**, 31-43.

Gilmer, G.H., R. Ghez, and N. Cabrera, 1971: An analysis of combined surface and volume diffusion processes in crystal growth. *J. Cryst. Gr.*, **8**, 79-93.

Hudson, J.B., 1992: *Surface Science*. Butterworth-Heinemann, Boston, 321 pp.

Keller, V.W., C.V. McKnight and J. Hallett, 1980: Growth of ice discs from the vapor and the mechanism of habit change of ice. *J. Cryst. Gr.*, **49**, 458-464.

Lamb, D, and J.P. Chen, 1995: An expanded parameterization of the growth of ice crystals by vapor deposition. In Preprints, Conference on Cloud Physics, Dallas, TX, 15-20 January 1995, AMS, Boston, 389-392.

Lamb, D. and W.D. Scott, 1972: Linear growth rates of ice crystals grown from the vapor phase. *J. Cryst. Gr.*, **12**, 21-31.

Lamb, D. and W.D. Scott, 1974: The mechanisms of ice crystal growth and habit formation. *J. Atmos. Sci.*, **31**, 570-580.

Lewis, B., 1974: The growth of crystals at low supersaturation. I. Theory. *J. Cryst. Gr.*, **21**, 29-39.

McKnight, C.V., and J. Hallett, 1978: X-ray topographic studies of dislocations in vapor-grown ice crystals. *J. Glaciol.*, **21**, 397-407.

Nelson, J., and M.B. Baker, 1996: New theoretical framework for studies of vapor growth and sublimation of small ice crystals in the atmosphere. *J. Geophys. Res.*, **101**, 7033-7047.

Nelson, J., and C. Knight, 1996: A new method for growing crystals from the vapor. *J. Cryst. Gr.*, **169**, 795-797.

Nelson, J., and C. Knight, 1998: Snow crystal habit changes explained by layer nucleation. *J. Atmos. Sci.*, **55**, 1452-1465.

Petrenko, V.F., and R.W. Whitworth, 1999: *Physics of Ice*. Oxford University Press, Oxford, 373 pp.

Weickmann, H.K., 1945: Formen und Bildung atmosphärische Eiskristalle. *Beitr. Phys. d. Freien Atmosphäre*, **28**, 12-52.

Yokoyama, E., 1993: Formation of patterns during growth of snow crystals. *J. Cryst. Gr.*, **128**, 251-257.

Young, K.C., 1993: *Microphysical Processes in Clouds*. Oxford University Press, New York, 427 pp.

REGIONAL CHARACTERISTICS OF SNOWFLAKE SIZE DISTRIBUTION

T. Harimaya[1], H. Kodama[1] and K. Muramoto[2]

1 Graduate School of Science, Hokkaido University, Sapporo 060-0810, Japan
2 Faculty of Engineering, Kanazawa University, Kanazawa 920-0942, Japan

1. INTRODUCTION

The snowflake formation process is one of the most important growth processes for the growth of snow particles in snow clouds. As the snowflake size distributions are thought to be affected by the snowflake formation process and growth stages of snow clouds, the mechanism by which snow particles are formed in each area could be clarified by investigations of the characteristics of size distributions and their formation mechanisms.

The first report on the characteristics of snowflake size distributions was that by Gunn and Marshall (1958). They reported that size distributions tended to follow an exponential relationship, and they also reported that size distributions became broad, showing a decrease in both the intercept (No) and slope (λ) with an increase in snowfall intensity. Harimaya et al. (2000) studied the characteristics of snowflake size distributions and their formation mechanisms using a large amount of data. The regional characteristics of snowflake size distributions and their formation mechanisms are discussed in this paper.

Corresponding author's address: Toshio Harimaya, Graduate School of Science, Hokkaido University, Sapporo, 060-0810, Japan; E-Mail: harimaya@taiki.ep.sci.hokudai.ac.jp

2. OBSERVATIONS

Observations were carried out at four stations in coastal and inland areas of northern Japan and in inland and orographic areas of central Japan, as shown in Fig. 1, in the months of January and February from 1991 to 1999. Snowflake size distributions were measured by the use of a snow particle measuring system (INTEC inc., PROSPER-10), and snowfall intensity was measured at one-minute intervals using a system constituting of an electro-balance and personal computer.

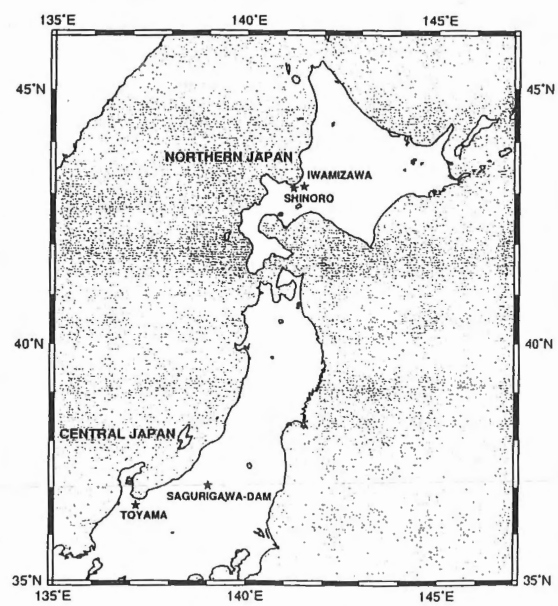

Fig. 1. Location of the observational stations.

The snow particle measuring system includes a CCD camera for photographing snowflakes falling in the measuring tower. The data stored on the computer are the size distributions of snowflakes per 0.5 mm in 1 m^3 volume of air over one-minute intervals. The falling velocity of each individual snowflake can also be simultaneously measured and recorded by this system.

3. RESULTS

3.1 Variation of Snowflake Size Distribution

We used principal component analysis to objectively determine the variation in snowflake size distributions. As the accumulated proportion until the second principal component was over 90%, we can express the major parts of the main variation if we adopt the first and second principal components.

Figure 2 shows the size distributions averaged over each score of the first principal component, which has the largest

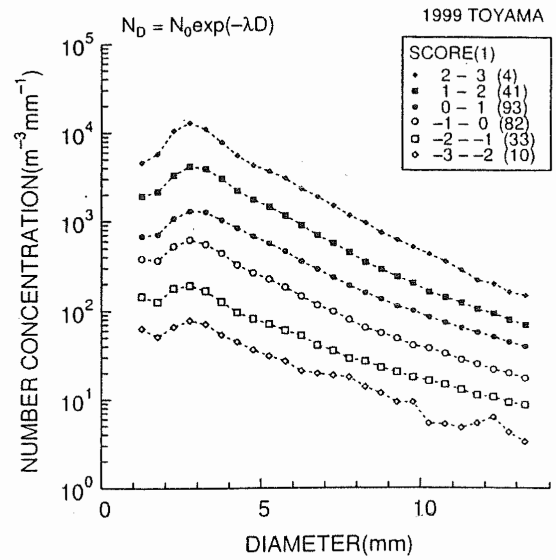

Fig. 2. Size distributions averaged over each score of the first principal component.

variable component. As can be seen in the figure, each averaged size distribution is an exponential distribution and moves parallel to a higher number concentration with an increase in the score value. As the score of first principle component was thought to be related to the snowfall intensity, the relationship of both values was plotted in the figure. It was found that the score values increased with an increase in snowfall intensity. In other words, it was clarified that an averaged size distribution with an equal snowfall intensity moves parallel to a higher number concentration, maintaining an exponential form, with an increase in snowfall intensity.

Next, the second principal component was analyzed in the same manner as that for the first principal component. Figure 3 shows the size distributions averaged over each score of the second principal component. Each averaged size distribution is an exponential distribution, like those in Fig. 2. The characteristic in the second principal component is that the slopes of the size distributions become steeper when the

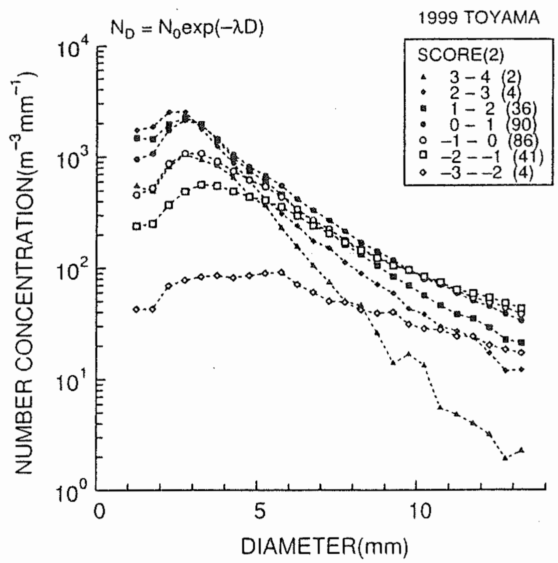

Fig. 3. As in Fig. 2, except for the second principal component.

score values increase.

The difference in density of snowflakes is considered to be the cause of the difference in size distributions even under the condition of equal snowfall intensity. When we plotted the relationship between the score of the second principal component and the ratio of averaged falling velocity to the averaged diameter of snowflakes (*V/D*) of a size distribution, we found that the score values increased when the ratio *V/D* increased. The increase in the ratio *V/D* is thought to correspond to the change from low density to high density. In other words, the score values increase when the properties of snowflakes change from low density to high density. We can therefore say that the slope of the size distribution becomes steeper under this condition.

The trends in variations when principal component analysis was applied to data obtained from the other three stations were almost the same as the results reported in Toyama.

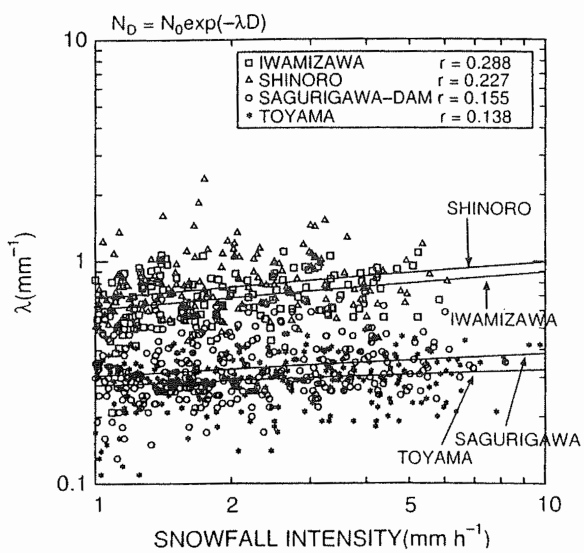

Fig. 4. Relationship between snowfall intensity and slope λ.

3.2 Shape of Snowflake Size Distribution

The shape of the snowflake size distribution was also studied. In order to compare with snowflake size distributions in four station, the intercept (*No*) and slope (λ) were used as the indicator of the shape when a snowflake size distribution was approximately expressed by an exponential function. Figure 4 shows the relation between snowfall intensity and slope (λ). When we made an approximation using a linear equation, we obtained four lines, although λ values varied widely under the condition of equal snowfall intensity. This result shows generally the difference of λ between two stations in central Japan and two stations in northern Japan. Therefore, we conclude that the shapes of snowflake size distributions under the condition of equal snowfall intensity show clear regional characteristics.

4. DISCUSSION

Next, we investigated the possible reason for the difference mentioned in the previous section. As stated in the previous section, variation in slopes in the size distributions is related to the parameter *V/D* which expresses the mean density of snowflakes. Therefore, the parameter *V/D* can explain why the slope λ in central Japan is smaller than that in northern Japan, if the parameter *V/D* in central Japan is smaller than that in northern Japan. When the compact ratio of snowflakes becomes smaller, the density of snowflakes is thought to become smaller. We therefore tried to measure the compact ratio of snowflakes. Maximum diameters (d_i cm) are measured for each snow crystal composing a snowflake. The total areas (A_c cm^2) of each

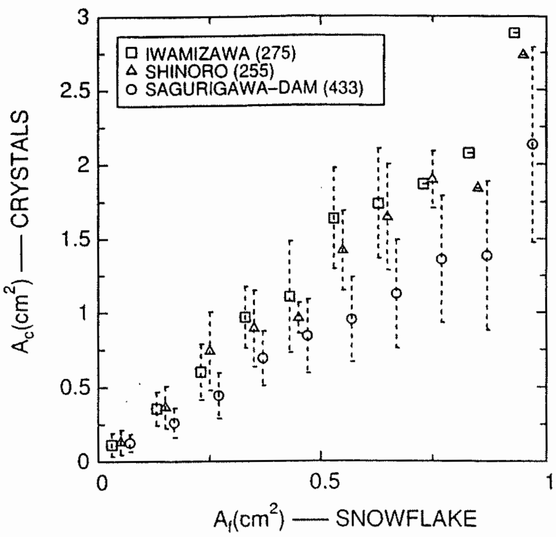

Fig. 5. Relationship between area of a snowflake and total areas of each snow crystal composing a snowflake.

snow crystal composing a snowflake are obtained from the d_i. It can be estimated that snowflakes have more compact structures with an increase in A_c under the condition of equal area of a snowflake (A_f).

Figure 5 shows the relation between A_f and A_c. Each symbol shows the mean values obtained at each station, and vertical broken lines show standard deviations. It can be seen from this figure that the compact ratio of snowflakes in central Japan is smaller than that in northern Japan. Therefore, we could explain the reason why the parameter V/D in central Japan is smaller than that in northern Japan.

As the air temperature in central Japan is higher than that in northern Japan, two snow crystals in central Japan are expected to be able to convert into a snowflake by the touth with both ends, because the force of adhesion increases with an increase in temperature. Therefore, the compact ratio of snowflakes in central Japan becomes smaller than that in northern Japan. Thus, it was shown that the regional characteristics of snowflake size distribution depend strongly on air temperature.

5. CONCLUSIONS

The main variation shows that averaged size distribution with an equal snowfall intensity moves parallel to a higher number concentration, maintaining an exponential form, with an increase in snowfall intensity. The second variation shows that the slope of the size distribution becomes steeper under the change from low density to high density in the property of snowflakes. These variation characteristics of snowflake size distributions were similar at the four stations.

The mean slope of snowflake size distributions in central Japan was more gentle than that in northern Japan. The fact could be explained by the lower density of snowflakes. As the air temperature in central Japan is higher than that in northern Japan, the compact ratio of snowflakes in central Japan becomes smaller than that in northern Japan. Therefore, the density also becomes smaller. Thus, it was shown from the observations that the regional characteristics of snowflake size distributions depend strongly on air temperature.

References

Gunn, K.L.S. and J.S. Marshall, 1958: The distribution with size of aggregate snowflakes. J. Meteor., 15, 452-461.

Harimaya, T., H. Ishida and K. Muramoto, 2000: Characteristics of snowflake size distributions connected with the difference of formation mechanism. J. Meteor. Soc. Japan, (accepted).

RELATIONSHIP BETWEEN RIME SURFACE TEMPERATURE AND CLOUD DROPLET SPECTRA

E. E. Avila[1], R. Pereyra[1], N.E. Castellano[1] and C.P.R. Saunders[2]

[1] Fa.M.A.F, Universidad Nacional de Córdoba, Ciudad Universitaria, 5000 Córdoba, Argentina
[2] Physics Department, UMIST, Manchester, M60 1QD, UK

1. INTRODUCTION

The surface temperature of riming graupel is a variable involved in many physical processes occurring inside clouds. For example, it controls the density of the graupel pellets (Macklin, 1962); the ice crystal multiplication (Hallet and Mossop, 1974); the process of melting and shedding from the surface of riming graupel and hailstones (Rasmussen and Heymsfield, 1987); and charge separation during collisions between ice particles (Avila et al., 1995). The heat and mass transfer process plays an essential role in the surface temperature.

The heat balance equation given by Macklin and Payne (1967) for a cylindrical collector of diameter D, growing by riming, exposed to an air flux of velocity V containing a cloud of supercooled water droplets of liquid water content W, is:

$$\frac{EWV\,\{L_f + c_w(T_a - T_o) + c_i(T_o - T_s)\}}{\pi} = \frac{N_u K(T_s - T_a) + S_h L_s D_f(\rho_s - \rho_a)}{D} \qquad \text{Eq. (1)}$$

where E is the graupel/droplet collection efficiency, c_w the specific heat of water, c_i the specific heat of ice, D_f the coefficient of molecular diffusion of water vapour in air, K the thermal conductivity of air, L_f the latent heat of fusion of water, L_s the latent heat of sublimation of ice, N_u the Nusselt number, S_h the Sherwood number, ρ_s the density of water vapour at the surface of ice deposit, ρ_a the density of water vapour in the environment, T_a ambient temperature, T_o melting temperature of ice, T_s mean temperature of ice deposit.

The term on the left concerns the rate at which heat is being released per unit area by freezing droplets, the first term on the right concerns the rate per unit area at which heat is being dissipated to the surroundings by conduction/convection, and the second term on the right concerns the rate per unit area at which heat is being exchanged with the environment by sublimation or deposition. N_u and S_h are the heat and mass transfer coefficient respectively; in principle they depend on the particular conditions on the surface (Eckert and Drake 1974, Pruppacher and Klett, 1978), however, we are concerned with the average surface temperature. For the range of atmospheric pressures and temperatures N_u and S_h numbers are related by S_h=0.95 N_u.

Corresponding author's address: Eldo E. Avila, Fa.M.A.F, Universidad Nacional de Córdoba, Ciudad Universitaria, 5000 Córdoba, Argentina.
E-Mail: avila@roble.fis.uncor.edu

Incropera and DeWitt (1996) determined that the average Nusselt number for the entire surface is only a function of the Prandtl and Reynolds numbers (R_e) and can be parameterized as:

$$N_u = \chi\ R_e^{m}\ P_r^{\,n} \qquad \text{Eq. (2)}$$

where χ is a coefficient; χ and m take different values depending on the range of Reynolds number, in particular for a circular cylinder and for 40 $\leq R_e \leq$ 1000 χ = 0.51 and m = 0.5 and for 1000 $\leq R_e \leq 2\times10^5$ χ = 0.28 and m = 0.6. Under atmospheric conditions P_r is a constant and P_r=0.71 and n = 0.37, then N_u is only a function of R_e.

An experimental study is presented here, where results obtained by Avila et al. (1999) are re-examined together with new experimental results and it is shown that the coefficient of heat transfer to the environment (N_u) depends on the cloud droplet size spectrum used for the accretion and characterized by the mean volume diameter (d_V). The influences and effects of the cloud droplet size spectrum on the surface temperature and heat transfer coefficient for different velocities and collector sizes are discussed as a function of the Stokes number. This study was carried out for a cylindrical collector.

2. EXPERIMENTS AND RESULTS

The convective heat transfer of a fixed cylindrical rod growing by riming was determined by measuring the rime temperature elevation above ambient of the collector in steady state. The measurements were carried out inside a cold room with controllable air temperature, velocity and liquid water content, which can simulate natural cloud conditions. All the variables and parameters involved in the current work (T_a, V, EW, d_v, and D) were varied taking values within the range of interest in cloud physics.

The water droplets, used to rime the target, were generated by water vapor condensation from a boiler located inside the cold room. The cloud droplet concentration was controlled by the power input to an electrical heater immersed in the boiler. The effective liquid water content (EW) was determined by weighing the deposit of rime collected (Δm) on the rod during a given time (Δt) and was calculated from the rime accretion equation:

$$EW = \frac{\Delta m}{\Delta t V A_e}$$

where A_e is the cross sectional area of the collector.

Different cloud droplet spectra were produced by using boiler nozzles of different diameter following the technique developed by Mossop [1984]. The characteristics of the cloud droplet spectrum were obtained by taking cloud samples on a microscope slide coated with formvar solution, followed by microscopic analysis.

The air temperature was varied from –5 to –27 °C, and the experiments were performed at three different velocities: 4.0, 7.0 and 8.5 m/s and rod cylinders of 2.8 and 4.0 mm in diameter were used as collectors; in consequence, the Reynolds number was varied from 800 $\leq R_e \leq$3000; for this range of R_e it was possible to use Eq. (2) with values of χ = 0.28 and m = 0.6 with a good degree of approximation.

The experiments were started by riming the collector with supercooled water droplets during 60 s approximately. Figure 1 shows the time evolution of the rime temperature for two different cloud droplet spectra under the same conditions of ambient temperature, effective liquid water content and velocity indicated in the figure. Rime temperature increases quickly during the first 20 s to reach a steady state after which it remains fairly constant. The behaviour shown in Figure 1 is representative of most of the measurements and on the basis of this behaviour, the steady state temperature of the collector was determined. In this figure it is possible to observe that the warming produced by large droplets is greater than the warming produced by small droplets.

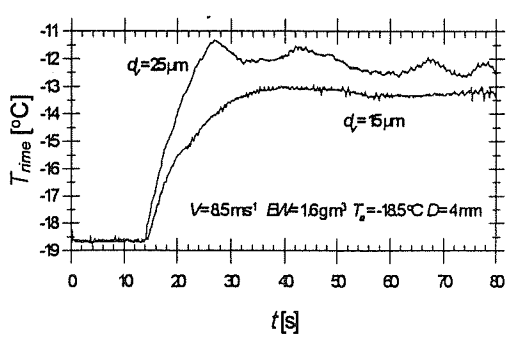

Figure 1. Elevated rime temperatures for two different cloud droplet spectra under the same conditions of velocity, effective liquid water content and size of the rod.

The Nusselt number was determined by using Eq. (1) and is presented as a function of the mean volume diameter of the cloud droplet spectrum in Figure 2. The results obtained with V=4 m/s and D=2.8 mm (R_e=835) are shown in Figure 2a), the horizontal line (N_u=13) belongs to the theoretical value of Nusselt number calculated by using Eq. (2). The results obtained with V=7 m/s and D=2.8 mm (R_e=1462) are shown in Figure 2b), here the theoretical value of Nusselt number is N_u=20; and the results obtained with V=8.5 m/s and D=4 mm (R_e =2536) are shown in Figure 2c), the theoretical value of Nusselt number is N_u=27.

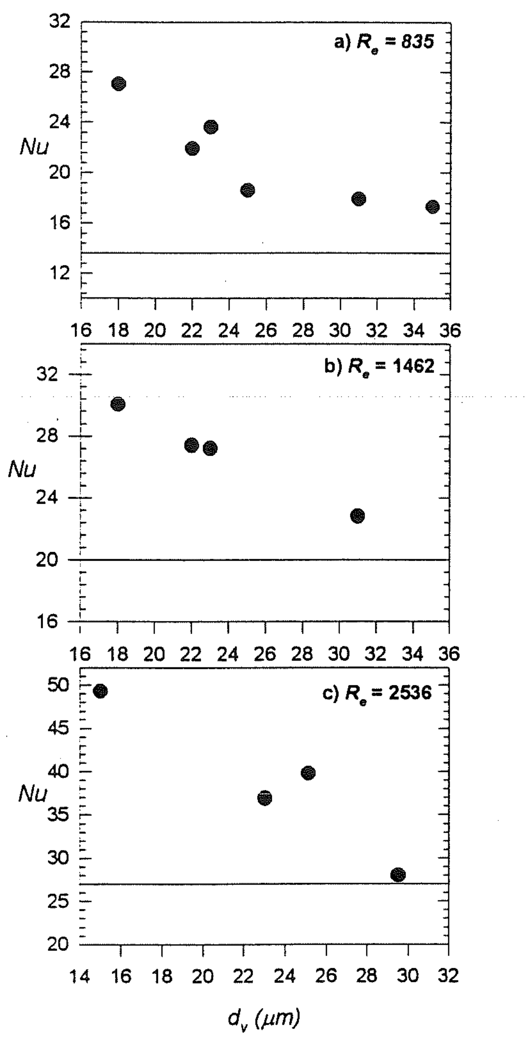

Figure 2. Experimental values of N_u obtained as a function of mean volume diameter of the droplets for different R_e. The horizontal line indicates the theoretical value of N_u obtained with the corresponding R_e.

Clearly, Figure 2 shows that the Nusselt number increases when the size of the cloud droplets is decreased.

4. DISCUSSION

The dependence of the heat transfer coefficient with Reynolds number has been well determined for the present symmetry (Incropera and DeWitt, 1996) and is not the subject of the present work, but here we are interested in how the cloud droplet distribution can modify the heat and mass transfer process. The present results show that the mean surface temperature of an accreting rime deposit, for a given ambient temperature, velocity and effective liquid water content, may be influenced by the size of the supercooled droplets present. Figure 1 shows that the difference in surface temperature between accretions made with different cloud droplet spectra for the same rime accretion rate (same *EW* and *V*) reach more than 1 K. In general, it was found that for the same rate of accretion, large droplets raise the rime temperature more than do smaller droplets. Figure 2 illustrates that the heat transfer coefficient N_u also depends on the size of the cloud droplets used for riming. In all cases Nusselt numbers are higher than those predicted by Eq. (2). Furthermore, it is possible to observe that the theoretical value of N_u is better approached for the largest cloud droplets ($d_V > 30$ μm), while for smaller droplets ($d_V \approx 18$ μm) the experimental values of N_u are 60% or even higher than the theoretical ones.

Heat and mass transfer between the accreted ice and the surroundings, takes place through the boundary layer settled around the surface of the rime. The presence of surface roughness has some important influences in many properties, for instance: it increases the surface area of the collector, changes the drag coefficient, and more important for the present results, it causes the airflow around the particle to be more turbulent because each rough element can create its own wake, which increases the heat and mass exchange process (Achenbach, 1977). Bailey and Macklin (1968) observed that smaller droplets build rime accretions with higher surface roughness than do larger droplets, suggesting that the roughness could be an effect of droplet trajectories and the collector/droplet collection efficiency.

The collision efficiency is related to the dimensionless quantity N_S called the inertia parameter or Stokes number (Langmuir and Blodgett, 1946; Finstad et al. 1988), it provides a measure of the ability of a cloud droplet to persist in its state of motion in a viscous fluid, and is defined as: $N_S = \rho_w V d_V^2 (9\eta D)^{-1}$ where ρ_w is the droplet density, and η is the dynamic viscosity of the air. Figure 3 shows the dependence of the ratio between the experimental value of N_u and its corresponding theoretical value on the Stokes number. In this Figure it is possible to observe that the ratio of the experimental N_u to its theoretical value is related to the Stokes number, indicating that the difference between them increases for lower N_S. For example, for N_S around 2 the ventilation coefficient obtained experimentally is twice the theoretical value predicted; and for N_S around 12, $N_u^{exper} \cong N_u^{theor}$.

These results indicate that Stokes number is also associated with the heat and mass transfer in the process involving accretion of supercooled cloud droplets. The best fit line for the experimental points of Figure 3 is given by the expression:

$$N_u^{exper} / N_u^{theor} = 1 + 1.41 \times exp(-0.173\, N_S)$$

In order to check the consistency of the results, the parameters: velocity (*V*), droplet sizes (d_V) and size of the collector (*D*), all of them involved with the Stokes number, have been varied in this work, and the results summarized in Figure 3.

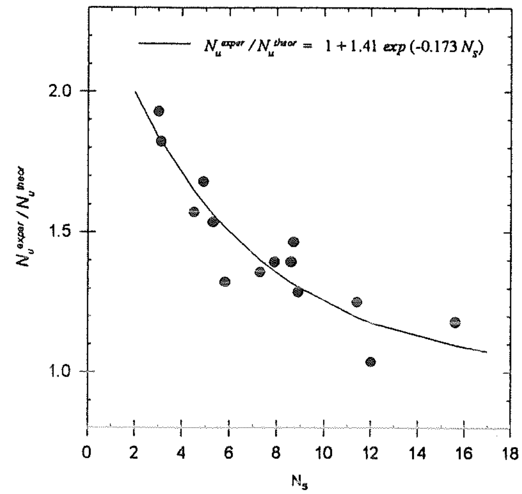

Figure 3. Dependence of the ratio $N_u^{exper} / N_u^{theor}$ on Stokes number.

Some authors have already studied the dependence of the heat transfer coefficient as a function of surface roughness, for example, Achenbach (1977) studied this effect for circular cylinders in the range of $2.2\times10^4 \le R_e \le 4\times10^6$, the surface roughness elements were produced by regular arrangements of pyramids, each having a rhomboidal base. He found that the surface roughness started to influence the Nusselt number when Reynolds number was greater than a critical value, associating the critical value to the point where the transition from a laminar to a turbulent boundary layer occurs. Also, Zheng and List (1996) observed that the heat transfer coefficient is significantly affected by the presence of surface roughness for spheroidal symmetry. They found the following expression for N_u as a function of R_e and the degree of surface roughness (β):

$$N_u = (0.316 + 0.103\beta) R_e^{(0.587 - 0.0095\beta)}$$

for β between 0 and 11% and Reynolds number in the range $1.1\times10^4 \le R_e \le 4.4\times10^4$. Both studies have been carried out for R_e numbers higher than in the present case.

Surface roughness, however, is not a suitable parameter to describe or simulate heat and mass transfer processes in clouds. In general, it is not a measurable parameter and its real values and forms are ignored. Instead, Stokes number could be an appropriate parameter because all its involved variables can be well determined by measurements in situ in the clouds or in laboratory experiments.

Similar results to the present ones have been reported for different symmetry of the collector by Castellano et al. (1999), who worked with spherical symmetry. Therefore, it is possible to suggest that the effect of the droplet size distribution on the heat transfer coefficient could also be present in natural graupel pellets and hailstones in thunderstorms.

5. CONCLUSION

As was mentioned in the Introduction the surface temperature of an accreting ice particle is a very important variable in cloud physics processes and its parameterization depends on a precise determination of the ventilation coefficient. Experimental results presented here show that the heat and mass transfer coefficient of a graupel pellet during the riming process can be substantially modified by using different cloud droplet size distributions. Furthermore, it is suggested that in general the ventilation coefficient depends on the Stokes number as well as the Reynolds number. The following expression can be used for calculating the Nusselt number of a circular cylinder when the correction for the size of cloud droplets is taken into account:

$$N_u = 0.28\, R_e^{0.6}\ P_r^{\,0.37}\,[1 + 1.41 \times exp\,(-0.173\ \mathrm{N_S})]$$

The present results point out the importance of an accurate knowledge of cloud droplet spectra, which are essential for the understanding of several phenomena in clouds.

Acknowledgements

This work was sponsored by CONICET, CONICOR and SECYT-UNC, Argentina. We are grateful to Jose Barcelona for his technical assistance and Dr. G. Caranti for his collaboration in this work.

References

Achenbach, E., 1977: The effect of surface roughness on the heat transfer from a circular cylinder to the cross flow of air. *Int. J. Heat Mass Transfer,* 20, 359-369.

Avila, E.E., N.E. Castellano, and C.P.R. Saunders, 1999: Effect of cloud droplet spectra on the average surface temperature of ice accreted on fixed cylindrical collectors, *Q. J. R. Meteorol. Soc.*, 125, 1059-1074.

Avila, E. E., G. G. Aguirre Varela, and G. M. Caranti, 1995: Temperature dependence of static charging in ice growing by riming, *J. Atmos. Sci.*, *52*, 4515-4522.

Bailey, I. H., and W. C. Macklin, 1968: The surface configuration and internal structure of artificial hailstones, *Q. J. R. Meteorol. Soc.*, *94*, 1-11.

Castellano, N.E, Avila, E.E., and C. P. R. Saunders, 1999: Dependence of the average surface temperature on cloud droplet spectra for rime ice accreted on fixed spherical collectors, *J. Geophys Res., 104*, 23399-27406, 1999.

Eckert, W. C., and R. M. Drake, 1974. Heat and mass transfer, *TATA Mc Graw Hill.*

Finstad K. J., E. P. Lozowski and E.M. Gates, 1988: A computational investigation of water droplet trajectories. *J. Atmos. and Oceanic Technology*, 5, 160-170.

Hallett, J., and S. C. Mossop, 1974: The production of secondary ice particles during riming process. *Nature*, 249, 26-28.

Incropera, F. P., and D. P. Dewitt, 1996: Introduction to heat transfer, 3rd edition John Wiley and Sons.

Langmuir, I., and K. B. Blodgett, 1946. Mathematical investigation of water droplet trajectories. Pg 335-393 in The Collected Works of Irving Langmuir, Pergamon Press, N. Y., 1960.

Macklin, W. C., 1962: The density and structure of ice formed by accretion. *Q. J. R. Meteorol. Soc.*, 88, 30-50.

Macklin, W.C., and G.S. Payne, 1967: A theoretical investigations of the ice accretion process. *Q. J. R. Meteorol. Soc.*, 93, 195-214.

Mossop, S. C., Production of laboratory clouds, *Q. J. R. Meteorol. Soc.*, *110*, 275-279, 1984.

Pruppacher, H. R., and J. D. Klett, 1978. Microphysics of clouds and precipitation, *Reidel Publishing Corp.*

Rasmussen, R. M., and A. J. Heymsfield, 1987: Melting and shedding of graupel and hail. Part 1: Model physics. *J. Atmos. Sci.*, 44, 2754-2763.

Zheng, G. and R. List, 1996: Latitudinal and overall convective heat transfer from smooth and rough spheroidal hailstone models. *Proc. of 12th International Conf. on Cloud and Precipitation. Zurich, Amer. Meteor. Soc., Vol 1,* 224-227.

THE EFFECT OF STOCHASTIC CLOUD STRUCTURE ON THE ICING PROCESS

A. R. Jameson[1] and A.B. Kostinski[2]

[1]RJH Scientific, Inc., Alexandria, Virginia 22306
[2]Department of Physics, Michigan Technological University, Houghton Michigan 49931

1. INTRODUCTION

While it may sometimes be possible to identify dry growth conditions simply by knowing the mean cloud water content, and temperature if the clouds are 'Poissonian', that is, if the droplets are distributed spatially as uniformly as randomness allows, ambiguities are likely in most real clouds because of droplet clustering, i.e., because natural clouds are not 'uniform' but 'patchy' (e.g., Jameson et al. 1998; Kostinski and Jameson 2000).

It is shown that such patchiness leads to a significant increase in frequency of $W > w_c$ than would be expected for Poissonian clouds in which the water content fluctuates very narrowly about the mean value. That is, simply knowing the mean W is not sufficient. One must also know the ratio of the variance to the mean water content for a more complete description of the icing process. The patchiness of clouds not only likely explains much of the fine structure observed in cross-sections of hailstones, but, on a more practical note, likely contributes to unsafe aircraft icing conditions even when, for the same mean water content, a 'Poissonian' cloud would preclude any danger.

A discussion of 'clustering' is presented in a series of articles with regard to rain in Kostinski and Jameson (1997); Jameson and Kostinski (1998); Kostinski and Jameson (1999); Jameson et al.(1999); Jameson and Kostinski (1999); Jameson and Kostinski (2000a) and with regard to clouds in Jameson et al (1998) and Kostinski and Jameson (2000). Simply put, clustering of cloud droplets has been observed in a number of clouds (Paluch and Baumgardner 1989; Baker 1992; Jameson et al. 1998; Kostinski and Jameson 2000) in no small part because of the ubiquity of convective turbulence in clouds.

What is new in the present work is that we apply a simulation procedure developed for our work on rain to generate Monte Carlo realizations of patchy clouds in order to explore the probability distribution functions of cloud water content with an eye toward its interpretation with respect to the icing process. As a result we show (1) that it is not just the mean W, but the ratio of the variance to the mean W that is important, (2) that this ratio depends upon the length scale associated with the measurement volume and (3) that the rate of ice deposition depends on these first two factors through the Schumann-Ludlam limit.

[1]*Corresponding author address:* A.R. Jameson, RJH Scientific, Inc., 8101Hinson Farm Rd., Ste. 112, Alexandria, VA 223 06

2. CLUSTERING PARAMETERS

There are two important quantities required for describing and simulating clustering. These are the clustering intensity parameter, $\aleph$, and the auto-covariance or 'coherence' length, χ_ℓ, as explained in greater detail in Jameson and Kostinski (2000b).

First we define $\aleph$ to be

$$\aleph \equiv \frac{\sigma^2}{\mu^2}\left(1-\frac{\mu}{\sigma^2}\right) = \eta(0)\left(1-\frac{\mu}{\sigma^2}\right) \qquad (1)$$

where μ and σ^2 are the mean and variance of the number of droplets (per unit volume) over the entire observation domain. Note that for Poisson distributions, when there is no clustering, $\aleph \to 0$, because $\sigma^2=\mu$. The second variable is the coherence length, χ_ℓ, of the pair-correlation function (e.g., Kostinski and Jameson 1997). In this work we choose χ_ℓ as that characteristic dimension of the sampling domain, V, such that most droplet clustering ($\aleph>0$) will be observed on scales of order χ_ℓ and smaller. A more detailed discussion may be found in Jameson and Kostinski (2000b).

While there are several techniques in the literature for generating correlated samples, the one used in this study is based upon that given by Johnson (1994) as discussed in detail in Jameson and Kostinski (1999); (2000b).In these simulations, statistical homogeneity (stationarity) is assumed (For some justification, see Appendix A in Kostinski and Jameson 2000). The droplet counts are assumed to obey the geometric distribution (when $\aleph=1$), the binomial distribution with m=2 (when $\aleph=0.5$) and a stretched-exponential type distribution when $\aleph=2$. Nevertheless, because the simulation of clustering requires correlated samples, apparent 'structures' can appear at times solely as a result of these correlations.

3. THE RELATION BETWEEN $\aleph$ AND THE DISTRIBUTIONS OF *W*

As an example, Fig.1 is a plot of a spatial series of 'measurements' in Monte Carlo simulated clouds for χ_ℓ fixed at 300 m for three different $\aleph$ including $\aleph=0$ corresponding to a Poissonian cloud. First we note that any 'structures' in Fig.1 are simply a consequence of

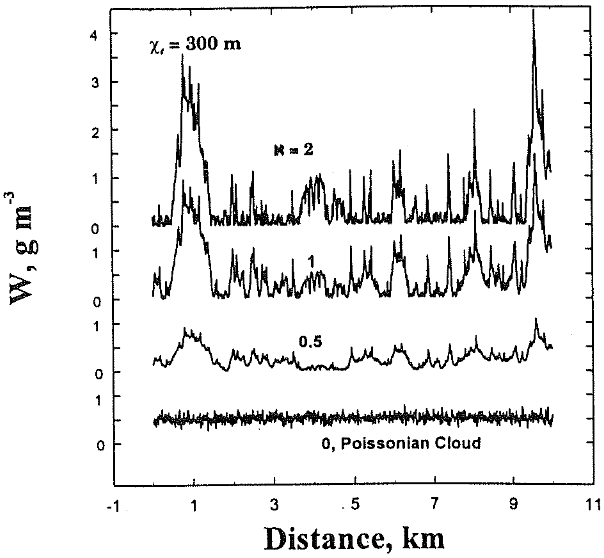

FIG.1: *Spatial series of cloud water content, W, for a simulated, statistically homogeneous cloud of correlated droplet counts having a fixed χ_ℓ and mean water content of 0.5 gm^{-3} for different $\aleph$ in clustered clouds as well as for a 'uniform, Poissonian' cloud. Correlated fluctuations in droplet counts produce the 'structure' in W while increasing $\aleph$ of the droplet counts produces increasing magnitudes of the fluctuations in W.*

FIG.2: *The frequency distribution for cloud water content for a mean of 0.5 g m^{-3} as a function of drop count clustering, $\aleph$ for a fixed χ_ℓ of 300 m. Note that F(W) depends on $\aleph$. Also note the narrow distribution associated with a Poissonian cloud.*

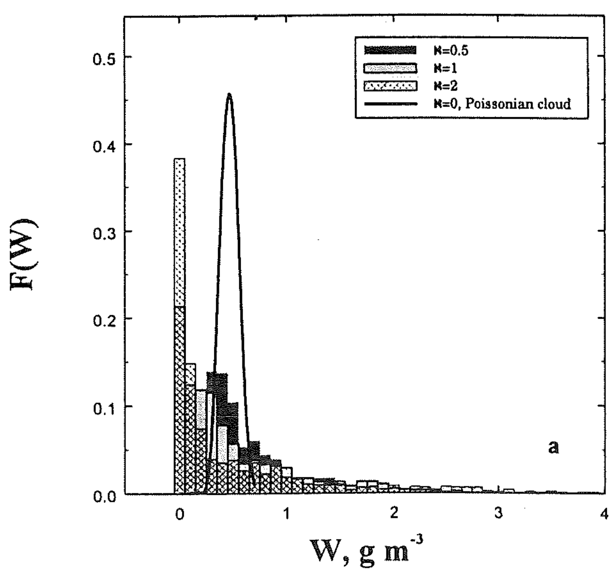

correlated fluctuations associated with a constant mean value and should not be construed to be statistical inhomogeneities in which the mean and other properties are changing. Moreover, as $\aleph$ increases, the effect on the cloud water appears to be a 'squeezing' or confinement of the cloud into narrower regions of increasingly larger *W*. Even modest clustering ($\aleph$=0.5) produces a spatial distribution of *W* considerably different from that for a Poissonian cloud having the same mean water content. Obviously such changes due to clustering must be reflected in the probability distribution *F(W)* as illustrated in Fig.2.

The effect of different degrees of clustering ($\aleph$) of drop counts per unit volume is readily apparent. First, consider the distribution of *W* associated with a Poissonian cloud (Poisson drop concentrations, $\aleph$=0) having the same mean of 0.5 g m^{-3} as for the clustered clouds. This distribution is narrowly confined around the mean value. Note that while the droplet counts per unit volume are Poisson, the distribution of *W* in Fig.6a is actually much narrower having a variance (σ^2) of only 0.0059 g^{2}m^{-6}. By contrast, on the other hand, even for $\aleph$=0.5, there is a significant broadening of the distributions of *W* (σ^2=0.14 g^{2}m^{-6}), a broadening that increases with increasing $\aleph$. That is, as $\aleph$ becomes larger, not only are there ever increasingly larger values of *W*, but there is an increasing frequency of lower values of *W* as well.

4. THE EFFECT OF $\aleph$ ON ICING

For a constant Schumann-Ludlam threshold (w_c), the total length over which dense icing is possible increases as the clustering intensity, $\aleph$, increases because of increasing frequencies of W>w_c as illustrated in Fig.3.

There is a second significant effect of increasing $\aleph$, namely that as $\aleph$ becomes larger, any spongy ice that does form is then more likely to freeze rather than to slough off because of the greater frequency of relative voids deficient in cloud water. These regions will tend to promote heat loss with minimal compensating heat gains derived from the acquisition of significant amounts of new cloud water.

5. CONCLUDING COMMENTS

While Fig.3 likely exaggerates the icing effects due to clustering since the collection efficiency is set to unity, even a value of *E* as small as 0.1 in this example would yield a significant ice thickness of about 0.2-0.4 cm. However, what is important here is not the detail of this particular simulation. Rather, based upon this study we conclude (1) that droplet clustering leads to significant broadening of the probability distribution of liquid water content, (2) that significant dense ice formation may occur even when the mean super-cooled liquid water content

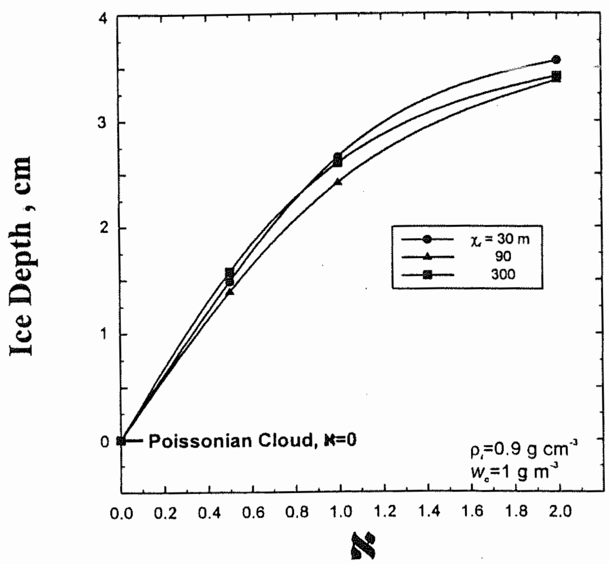

FIG.3: *The total depth of ice accumulated as a function of cloud droplet clustering along a ten kilometer path through a simulated cloud having a mean water content of 0.5 g m^{-3} assuming (1) all water is captured (a collection efficiency E=1) and (2) a Schumann-Ludlam threshold, w_c of 1 g m^{-3}. Note that W for a 'Poissonian' cloud never exceeds w_c.*

would suggest only low density, dry rime for a Poissonian cloud (3) that forecasting of conditions suitable for the formation of dense ice will depend not only on the prognosis of large scale average super-cooled cloud water contents, but also on the forecasting of the variance of *W* at small scales associated with locations of significant convection and turbulence likely to enhance cloud clustering and (4) that these spatial variabilities introduce a 'memory' into the icing process that is lacking in Poissonian clouds.

Acknowledgments: Thanks to Dr. Ron. Taylor (retired) this work was supported by the National Science Foundation under grants ATM95-12685 (AK), ATM94-19523 (AJ) and ATM97-12075 (AJ).

6. REFERENCES

Baker, B.A., 1992: Turbulent entrainment and mixing in clouds: A new observational approach. *J. Atmos. Sci.*, **49**, 387-404.

Jameson, A.R. and A.B. Kostinski, 1998: Fluctuation properties of precipitation. Part II: Reconsideration of the meaning and measurement of raindrop size distributions. *J. Atmos. Sci.*, **55**, 283-294.

_____ and _____, 1999: Fluctuation properties of precipitation. Part V: On the distribution of rain rates - theory and observations in clustered rain. *J. Atmos. Sci.*, **56**, 3920-3932.

_____ and _____, 2000a: Fluctuation properties of precipitation. Part VI: Observations of hyper-fine clustering and drop size distribution structures in three-dimensional rain. *J. Atmos. Sci.*, **57**, 373-388.

_____ and _____, 2000b: The effect of stochastic cloud structure on the icing process. *J. Atmos. Sci.*, **57**, in press.

_____, _____, and R.A. Black 1998: The texture of clouds. *J. Geophys. Res.*, **103**, 6211-6220.

_____, _____, and A. Kruger, 1999: Fluctuation properties of precipitation. Part IV: Fine scale clustering of drops in variable rain. *J. Atmos. Sci.*, **56**, 82-91.

Johnson, G.E., 1994: Constructions of particular random processes. *Proc. IEEE*, **82**, 270-285.

Kostinski, A.B., and A.R. Jameson, 1997: Fluctuation properties of precipitation. Part I: On deviations of single-size counts from the Poisson distribution. *J. Atmos. Sci.*, 2174-2186.

_____, and _____, 1999: Fluctuation properties of precipitation. Part III: On the ubiquity and emergence of the exponential drop size spectra. *J. Atmos. Sci.*, **56**, 111-121.

_____, and _____, 2000: On the spatial distribution of cloud particles. *J. Atmos. Sci.*, **57**, 901-915.

Paluch, I.R., and D. Baumgardner, 1989: Entrainment and fine-scale mixing in a continental convective cloud. *J. Atmos. Sci.*, **46**, 261-278.

CHARACTERIZING THE INFLUENCE OF THE GENERAL CIRCULATION ON MARINE BOUNDARY LAYER CLOUD

M. A. Rozendaal[1] and W. B. Rossow[2]

[1]Program in Earth and Environmental Sciences, Columbia University, New York, NY 10025, U.S.A.
[2]NASA Goddard Institute for Space Studies, New York, NY 10025, U.S.A.

1. INTRODUCTION

According to surface and satellite observations, (Warren et al. 1988, Rossow and Lacis 1990), the eastern subtropical oceans are primarily covered by low-level clouds confined to the boundary layer. The geographical concentration of low clouds and an associated near-total absence of higher clouds imply that large-scale conditions exist which make these areas unusually favorable for low clouds.

Global data and GCM studies of low cloud time variability have focused mainly on seasonal mean properties (e.g. Tselioudis et al. 1992, Klein and Hartmann 1993 (hereafter KH93), Ma et al. 1996, Del Genio et al. 1996). Based on seasonal information alone, it is impossible to tell whether deficiencies in seasonal and annual mean quantities are due to differences in frequency of occurrence or amount of coverage.

Studies of time variability of marine low-level cloud on smaller spatial scales have focused on the Northern Hemisphere (NH) regions during local summer; these cases are summarized by Klein (1997). In addition, such studies are often limited to the variability of low cloud fraction only. The detail offered by these surface datasets is valuable for testing local correlations between clouds and their environment. However, these point measurement data cannot be used to examine the interactions of large-scale meteorology and clouds or to compare multiple regions during the same time period.

These issues are addressed here by combining satellite cloud data and model analysis products (meteorological observations interpolated by model output). Since this combination of information provides global coverage for all seasons, it is possible to compare the seasonal and intraseasonal variability of subtropical low clouds and their environment on a truly synoptic scale in all locations at once. The seasonal and intraseasonal variability of boundary layer cloud in the subtropical eastern oceans are studied using combined data from the International Satellite Cloud Climatology Project (ISCCP) and the European Centre for Medium-Range Weather Forecasts (ECMWF) reanalyses. This study is limited to the Pacific and Atlantic subtropical regions defined by KH93.

Corresponding author address: Margaret A. Rozendaal, NASA GISS, 2880 Broadway, New York NY, 10025, U.S.A.; E-Mail: margaret@giss.nasa.gov.

2. TIME VARIABILITY OF SUBTROPICAL LOW CLOUDS

The temporal power spectrum of daily average cloud liquid water path (LWP) for the Californian and Peruvian regions is shown in Figure 1. (The spectra for cloud fraction and cloud top pressure (CTP) are similar and therefore not shown). Most of the power occurs on seasonal to annual time scales. The power decreases one to two orders of magnitude for each decade of time scale decrease, but there is a plateau at weekly to monthly time scales.

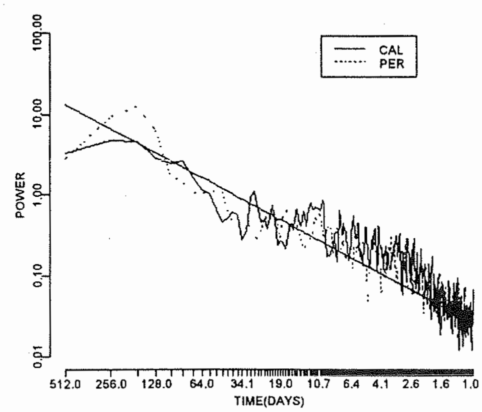

Figure 1. Temporal spectrum of daily average ISCCP cloud liquid water path for eight years (1984-92) in the 10x10° Californian and Peruvian regions. A line representing a power law with exponent −1 is shown for reference.

The length of the dominant time scales indicates that the majority of the variability is under control of the general circulation and its interaction with boundary layer turbulence, rather than the product of boundary layer turbulence alone. Hovmoller time-longitude plots (not shown) indicate that the NH regions experience changes in the frequency of occurrence of large low cloud fraction and LWP events during different seasons. In contrast, the Southern Hemisphere (SH) events show little change in frequency.

We quantify these observations by counting the number of times the cloud fraction reaches a chosen threshold value, and once it does, how many days it remains at this value. For a threshold value of 70%, Table 1 shows that there are more large events in all regions except the Canarian during the May-September (MJJAS) season compared to the November-March (NDJFM) season. Cloud fraction in the Canarian region seldom reaches 70%, but the result is the same if the threshold is reduced to 30%.

Region	MJJAS	NDJFM
Californian	95	56
Peruvian	75	36
Canarian	13	16
Namibian	78	67

Table I. Total number of low cloud fraction > 70% events lasting more than two days in each season for ISCCP 1984-92.

Figure 2 shows that in the NH regions, not only is the frequency of occurrence of these large events greater during the MJJAS season, but so is the persistence. In contrast, the persistence of these events in the SH regions is approximately the same in either season.

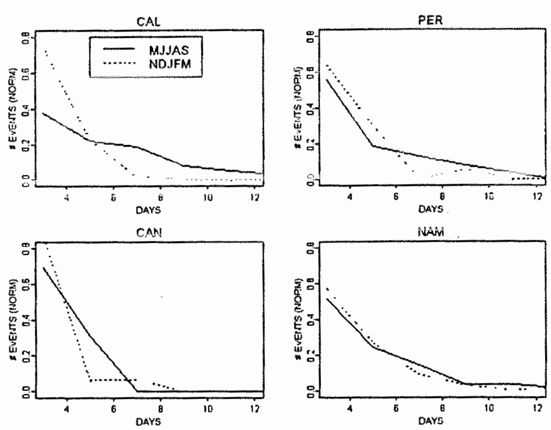

Figure 2. The persistence (in days) of low cloud fraction events larger than 70% during the MJJAS and NDJFM seasons. The number of events is normalized for each season.

Intraseasonal information can be used to interpret changes in seasonal averages. For instance, in the subtropics, seasonally averaged low cloud fraction and LWP decrease from MJJAS to NDJFM. Our analysis shows that this occurs due to decreases in frequency and persistence in the NH and due to decreases in mean values in the SH.

Conclusions about seasonal variability can also be affected by the choice of variable. For instance, cloud fraction estimates can be biased by the size of the spatial averaging domain. Similar to Rossow et al. (1993) and Rossow and Cairns (1995), clear and overcast scenes dominate frequency distributions for subtropical low clouds at domain sizes of 2.5x2.5°. As the domain size is increased to 20x20°, the distribution is increasingly dominated by partly cloud scenes.

Since LWP and CTP are undefined in clear-sky scenes, their frequency distributions are relatively invariant with respect to averaging domain size, indicating that when the clouds are present, their properties are similar over a broad range of spatial scales. Therefore, time variations of low cloud in these regions can be more accurately characterized by changes in CTP-LWP frequency distributions.

Figure 3 shows CTP-LWP frequency distributions for the subtropical regions in different seasons. In general, the distributions are similar during MJJAS for all regions except the Canarian, which tends to have lower values of CTP and LWP. During NDJFM, there is an increase in low CTP (high-altitude), low LWP clouds in the Californian region so than its distribution more closely resembles the Canarian. The SH regions tend to have similar cloud types in both seasons.

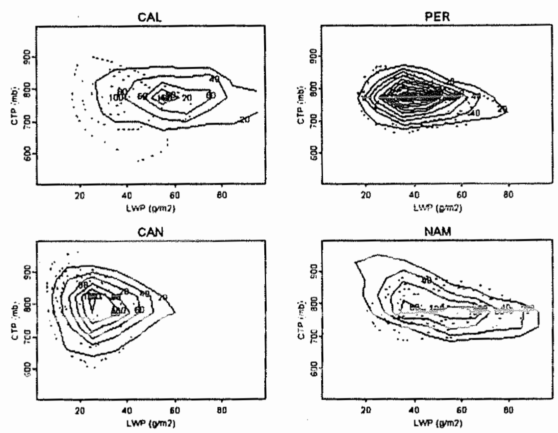

Figure 3. Daily average LWP-CTP distributions for the subtropical regions in different seasons. Solid lines are MJJAS, dashed lines are NDJFM.

Differences in persistence, propagation and cloud type between the seasons indicate a shift in dynamic regime in NH subtropics. During NDJFM, midlatitude storms intrude into the NH subtropical regions, which are located more poleward than their SH counterparts. This is consistent with Trenberth (1991), who observes that while the NH storm-track activity is weaker in summer and shifts poleward, the SH activity is as strong as in winter and remains around 50°S.

3. LOW CLOUDS AND THEIR ENVIRONMENT

3.1 Seasonal

These analyses and many previous studies have suggested that significant correlations exist between the variability of large-scale meteorology and cloud on seasonal and intraseasonal time scales. The largest such relationship is found by KH93, where seasonal variations in surface observed low cloud fraction are correlated with atmospheric static stability with a coefficient (r-squared) of 0.88. Since the coefficient is so large, this relationship is sometimes used to simulate the seasonal cycle of stratiform cloud (e.g. Philander et al. 1996, Miller 1997, Larson et al. 1999, Clement and Seager 1999).

However, as discussed in KH93, this relationship is calculated using seasonally averaged data at many locations (Figure 13 of KH93). Geographic variations in stability between locations during one year are approximately the same magnitude as seasonal variations taken at one location for many years. Therefore, it is not clear how much of this large correlation is due to time variability and how much of it is due to space variability.

Plots of seasonal cycle of low cloud and stability in KH93 indicate that the seasonal correlation alone is probably still large. We test this hypothesis using the ISCCP low cloud cover and static stability, defined as the difference between the potential temperature at 740mb from the Tiros Operational Vertical Sounder (TOVS) and the ISCCP clear-sky skin temperature. We average the data for each season and then remove the annual mean to create seasonal anomalies.

When seasonal anomalies of low cloud fraction and stability are correlated for each region separately, the r-squared coefficients range from 0.43 in the Peruvian to 0.74 in the Californian. If the correlation is calculated similar to KH93, the coefficient is 0.71. As stated in KH93, this suggests that part of the large positive correlation is due to correlations in space, but that the seasonal correlation is high even by itself.

3.2 Intraseasonal

Thus far, synoptic studies of low cloud fraction have found no single good predictor of daily cloud fraction variability (Klein, 1997). Repeating the previous analysis between low cloud fraction and stability on daily anomalies finds that correlation coefficients decrease in magnitude compared to the seasonal, ranging from 0.19 to 0.33 during MJJAS and 0.06 to 0.31 during NDJFM.

Correlation makes the assumption that the frequency distribution is close to normal. Compositing data is an alternative way to look at cloud variations without making assumptions about the frequency distribution. Similar to earlier studies which examine relationships between composite meteorology and cloud (Klein et al. 1995, Lau and Crane, 1995, 1997, Tselioudis et al. 2000, Norris and Klein 2000), we composite ISCCP cloud properties in categories based on daily anomalies of meteorological data from ECMWF. Tselioudis et al. (2000) use 12-hourly sea level pressure (SLP) anomalies to identify the passage of low-pressure systems and to group clouds by dynamic regimes. We apply their method to subtropical clouds using four years of daily ISCCP and ECMWF data during the MJJAS and NDJFM seasons. In addition to SLP, we also examine relationships between cloud properties and daily anomalies of vertical velocity at 700mb (O700), static stability, meridional wind speed and temperature advection. For simplicity, we discuss only the SLP and O700 results.

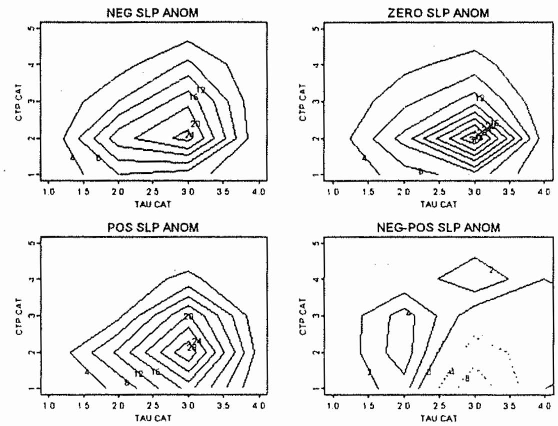

Figure 4. Daily anomalies of ISCCP total cloud TAU and CTP sorted by SLP from ECMWF for the 10x10° Californian region during NDJFM. Contours represent the fractional population, where 100 is the total normalized population (roughly 600 days).

The categories of total cloud CTP and optical thickness (TAU) are the same as those of Tselioudis et al. (2000). Unlike Tselioudis et al. (2000), the data in this analysis is spatially averaged so the dispersion seen in Figure 4 is due entirely to temporal variability in cloud properties and SLP. The fourth panel of Figure 4 shows that days of negative SLP anomaly are more often associated with low TAU cloud. The Canarian picture is similar except that the positive SLP anomaly is also associated with the thinnest, lowest altitude clouds.

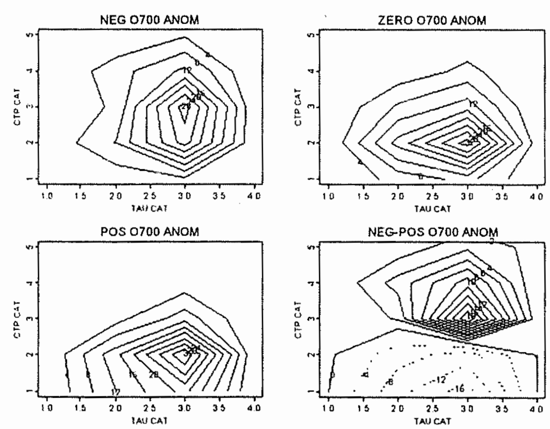

Figure 5. Daily anomalies of ISCCP total cloud TAU and CTP sorted by O700 from ECMWF for the 10x10° Californian region during NDJFM.

In Figure 5, the difference between negative and positive O700 anomalies separates the clouds fairly cleanly into high and low cloud top regimes. Since O700 is positive for descent and monthly mean O700 is always positive, positive O700 anomalies represent times of increased descent. In this figure, positive anomalies are associated with higher clouds top pressures (or lower altitude cloud tops). In this case, O700 has no apparent relationship to TAU.

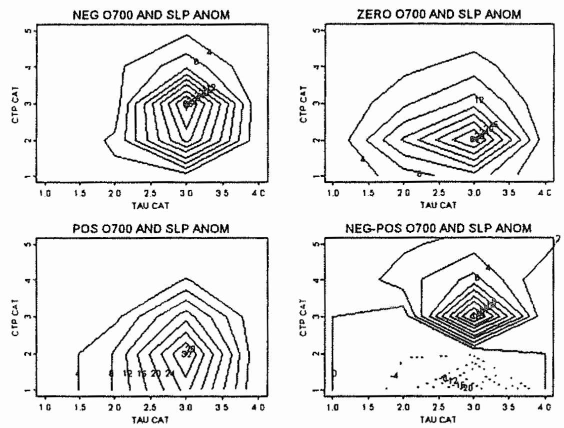

Figure 6. Daily anomalies of ISCCP total cloud TAU and CTP sorted by both SLP and O700 from ECMWF for the 10x10° Californian region during NDJFM.

Since correlations between daily anomalies of SLP and O700 are weak to fair in the subtropics (r values of .15 to .42), we can sort the data using both criteria without redundancy. In Figure 6 days that have the thickest, highest top clouds most often have negative anomalies in both SLP and O700. These are days when the SLP is lower than usual, and O700 is either less strong in the downward direction or upward in direction.

We repeated these analyses for the SH regions during NDJFM and all regions during MJJAS. Thus far, none of the variables mentioned above separate the clouds into particular types. This may be because these intraseasonal variations in cloud and meteorology are smaller, requiring a more careful analysis.

4. REFERENCES

Clement, A., and R. Seager, 1999: Climate and the tropical oceans. *J. Climate,* **12**, 3383-3401.

Del Genio, A. D., M.-S. Yao, W. Kovari and K. K. W. Lo, 1996: A prognostic cloud water parameterization for global climate models. *J. Climate*, **9**, 270-304.

Klein, S. A., and D. L. Hartmann, 1993: The seasonal cycle of low stratiform clouds. *J. Climate*, **6**, 1587-1606.

Klein, S. A., D. L. Hartmann and J. R. Norris, 1995: On the relationships among low-cloud structure, sea surface temperature, and atmospheric circulation in the summertime northeast Pacific. *J. Climate*, **8**, 1140-1155.

Klein, S. A., 1997: Synoptic variability of low-cloud properties and meteorological parameters in the subtropical trade wind boundary layer. *J. Climate*, **10**, 2018-2039.

Larson, K., D. L. Hartmann and S. A. Klein, 1999: The role of clouds, water vapor, circulation, and boundary layer structure in the sensitivity of the tropical climate. *J. Climate,* **12**, 2359-2374.

Lau, N.-C., and M. W. Crane, 1995: A satellite view of the synoptic-scale organization of cloud properties in midlatitude and tropical circulation systems. *Mon. Wea. Rev.*, **123**, 1984-2006.

Lau, N.-C., and M. W. Crane, 1997: Comparing satellite and surface observations of cloud patterns in synoptic-scale circulation systems. *Mon. Wea. Rev.*, **125**, 3172-3189.

Ma, C.-C., C. R. Mechoso, A. W. Robertson and A. Arakawa, 1996: Peruvian stratus clouds and the tropical Pacific circulation: A coupled ocean-atmosphere GCM study. *J. Climate*, **9**, 1635-1645.

Miller, R., 1997: Tropical thermostats and low cloud cover. *J. Climate*, **10**, 409-440.

Norris, J. R., and S. A. Klein, 2000: Low cloud type over the ocean from surface observations. Part III: Relationship to vertical motion and the regional surface synoptic environment. *J. Climate,* **13**, 245-256.

Philander, S. G. H., D. Gu, D. Halpern, G. Lambert, N.-C. Lau, T. Li and R. C. Pacanowski, 1996: Why the ITCZ is mostly north of the equator. *J. Climate*, **9**, 2958-2972.

Rossow, W. B., and A. A. Lacis, 1990: Global, seasonal cloud variations from satellite radiance measurements. Part II: Cloud properties and radiative effects. *J. Climate*, **3**, 1205-1253.

Rossow, W. B., A. Walker and L. C. Garder, 1993: Comparison of ISCCP and other cloud amounts. *J. Climate*, **6**, 2394-2418.

Rossow, W. B. and B. Cairns, 1995: Monitoring changes of clouds. *Climatic Change*, **31**, 305-347.

Trenberth, K. E., 1991: Storm tracks in the Southern Hemisphere. *J. Atmos. Sci.*, **48**, 2159-2178.

Tselioudis, G., W. B. Rossow and D. Rind, 1992: Global patterns of cloud optical thickness variation with temperature. *J. Climate*, **5**,1484-1495.

Tselioudis, G., Y.-C. Zhang and W. B. Rossow, 2000: Cloud and radiation variations associated with northern midlatitude low and high sea level pressure regimes. *J. Climate*, **13**, 312-327.

Warren, S. G., C. J. Hahn, J. London, R. M. Chevin and R. L. Jenne, 1988: Global distribution of total cloud cover and cloud type amounts over the ocean. NCAR Tech. Note, NCAR/TN-317+STR, 42 pp. and 170 maps.

REPRESENTATION OF BOUNDARY LAYER CLOUDS IN THE MET. OFFICE'S UNIFIED MODEL

G.M. Martin, A.L.M. Grant and A.P. Lock

The Met. Office, Bracknell, UK

1. INTRODUCTION

Clouds, through their impact both on latent heat release and the earth's radiation budget, are very important when estimating the earth's sensitivity to climate change. However, prediction of cloud cover and cloud type, particularly in the boundary layer, remains a problem in both the forecast and climate prediction configurations of The Met. Office's Unified Model (UM), in common with many other general circulation models (GCMs). Low-level clouds are very sensitive to the vertical temperature and moisture structure in the boundary layer. Thus, accurate modelling of turbulent mixing in the atmospheric boundary layer is essential for good forecasts of fog, cloud and precipitation. In addition, the model must be able to represent both stratiform and convective clouds, and the heat, moisture and momentum transports associated with them. Finally, the vertical atmospheric structure in a GCM can be dependent upon the vertical resolution. Lower troposphere vertical resolution in in many GCMs is poor, with boundary layer clouds in practice restricted to the lowest 3 or 4 model levels.

A new boundary layer turbulent mixing scheme (hereafter referred to as the PBL-N scheme; Lock et al. 2000) has recently been implemented in the mesoscale configuration of the UM. The PBL-N scheme includes a representation of non-local mixing (driven by surface fluxes and cloud-top processes) in unstable layers which are either coupled to or decoupled from the surface, and an explicit entrainment parametrization. An intrinsic part of this scheme is the diagnosis of different mixing regimes, including stable, well-mixed, decoupled and cumulus. The scheme is implemented in conjunction with increased vertical resolution in the lower troposphere, in order that the different boundary layer types and processes can be identified and treated properly.

However, since other model schemes have been built and tuned in the model at low vertical resolution, problems inevitably arise when the resolution is increased. One of the major contributors to such problems is the UM's convection scheme. Unresolved convection in the UM is represented by a mass-flux scheme with stability dependent closure (Gregory and Rowntree, 1990). Several parts of the convection scheme, including the triggering and the treatment of detrainment, rely on constants which were derived with low vertical resolution and which may not be appropriate at higher resolution.

Another major problem with the current configuration of the UM is that vertical mixing of heat, moisture and momentum can be carried out essentially independently by the boundary layer and convection schemes, and there is no explicit treatment of the interaction between them. Although the PBL-N scheme may diagnose a convective boundary layer type, the convection scheme is not forced to trigger convection (although it is prevented from doing so within the boundary layer when the PBL-N scheme does not diagnose convection), and this can result in unrealistic boundary layer thermodynamic profiles which have undesirable feedback effects on the overall simulation. Thus, it has become clear that improvements to the convection scheme will be required if the PBL-N scheme is to be used in either operational forecasting or long-term climate predictions.

Another aspect of the convection parameterization which requires improvement is the diagnosis and treatment of shallow convection. Currently, shallow convection is diagnosed (by the convection scheme) if an entraining perturbed parcel becomes negatively buoyant below a specified model level (corresponding to about 750 hPa for surface pressure of 1020 hPa). However, the entrainment rates applied during this test are inappropriate (compared with those derived from cloud resolving model (CRM) simulations) for shallow convection, so that this diagnosis is unreliable. In addition, CRM simulations indicate that entrainment rates in shallow cumulus clouds are larger than those in deep convective clouds, whilst the same entrainment factors are used for both cloud types in the model.

2. REVISIONS TO THE MIXING SCHEMES

The first stage on the way to addressing the problems described above is to provide a direct link between the boundary layer and convection schemes. The PBL-N scheme determines the mixing regime and the vertical extent of any mixed layers by the use of an undi-

Corresponding author's address: Gill Martin, Hadley Centre, The Met. Office, Bracknell, RG12 2SY, England. E-mail: gmmartin@meto.gov.uk

lute parcel ascent and examination of the gradients of the thermodynamic profiles (see Lock et al., 2000). In the revised version of the model (hereafter referred to as NEWCONV), we additionally distinguish between deep and shallow convection at this stage, and this information is passed into the convection scheme. The diagnosis of shallow convection relies on finding a suitable minimum (or zero) in buoyancy of the undilute parcel above the maximum which denotes the presence of an inversion, provided that the inversion is located below either 2.5km or the freezing level, whichever is the greater. Once cumulus convection has been diagnosed, the PBL-N scheme is restricted to mixing the model atmosphere below the lifting condensation level (LCL) and the convection scheme is forced to trigger from the LCL using information about the subcloud layer (see below), thus avoiding problems with the two schemes interacting in an uncontrolled manner.

Shallow convection is triggered by creating, at the LCL, a saturated parcel perturbed by an amount which is related to the surface buoyancy flux. Continuity of the thermodynamic fluxes at the LCL is achieved through the use of a jump model (Grant 2000). From CRM results, the convective cloud base mass flux for shallow convection can be parameterized in terms of the subcloud layer velocity scale: $m_b = 0.03 w_* \rho$. Recent work by Grant and Brown (1999) has shown that scaling arguments can be applied to mass-flux schemes to determine the fractional entrainment rate in shallow convection. This can be parameterized in terms of the cloud base mass flux, the characteristic velocity scale of the convective circulation and the fractional height above cloud base. Following CRM results, the detrainment rates in shallow convection are set to a constant factor (currently 1.3) times the entrainment rates.

3. RESULTS OF SINGLE COLUMN MODEL (SCM) TESTS

Here, we examine SCM simulations of (a) a stratocumulus to trade cumulus transition, and (b) trade cumulus, looking at the impact of (i) using the PBL-N scheme and increased vertical resolution, and (ii) using the NEWCONV version. The control runs for (i) are using the model as described by Pope et al. (2000), but with increased vertical resolution in the mid- and upper-troposphere such that there are 30 (irregularly spaced) vertical levels. The L30 model has only four layers at most between the surface and 900 hPa (for a surface pressure of around 1020 hPa). Therefore, when using the PBL-N scheme, the vertical resolution is increased to 38 levels by adding extra levels mainly below about 600 hPa, such that the lower tropospheric resolution is almost tripled.

The SCM simulations presented here are driven by prescribed large-scale divergence, geostrophic winds and sea-surface temperatures (SSTs).

3.1 Stratocumulus to trade cumulus transition

This simulation illustrates the transition from well-mixed stratocumulus to trade cumulus that occurs in the sub-tropics as air moves over a progressively warmer sea-surface and subsidence weakens. The simulation is based on that described in Bretherton et al. (1999) which was driven by the changes in SST and large-scale divergence observed in the first ASTEX Lagrangian experiment.

(i) Impact of using the PBL-N scheme and increasing vertical resolution

Figure 1 shows the time-evolution of the updraught mass flux in convection and the layer cloud liquid water content, from a L30 run with standard physics. Despite the increasing SST and decreasing subsidence during this run, there is little change in the diagnosed boundary layer depth (not shown) because of the poor vertical resolution. The convection does become deeper, which is quite realistic. However, the layer cloud is restricted to a single model level, and is unable to move into the next level when the SST is greater and the subsidence weaker at the end of the run, so it dissipates.

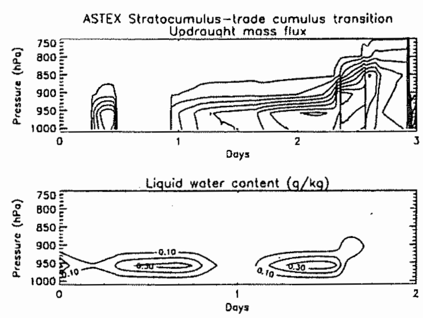

Figure 1

Figure 2 shows results of this case with the PBL-N scheme in the L38 model. The PBL-N scheme diagnoses both the depth of the surface-based mixed layer (solid line) and the top of any decoupled mixed layer (dashed line). Initially the surface layer is stable and the overlying stratocumulus is decoupled from it (type 2). As the SST increases, the layer becomes well-mixed to the surface (type 3). Towards the end of day 1, decoupled cloud with underlying cumuli is diagnosed (type 5). At the end of day 2, the decoupled stratocumulus layer evaporates and trade cumulus alone remains (type 6). This simulation is an improvement on the standard L30 model, although additional tests (not shown) indicate that much of the improvement comes from increasing the vertical resolution. The additional benefit from the PBL-N scheme is in improving the diagnosis of the surface-based and decoupled mixed layer depths, the application of cloud top-driven mixing and entrainment which improve the boundary layer structure, and in preventing the convection scheme from triggering too early, during the period in day 1 when only stratocumulus was observed. However, in both runs with L38 the convection becomes intermittent and dry convection, triggered from the first model level and extending to the LCL, is apparent below the deeper moist convection.

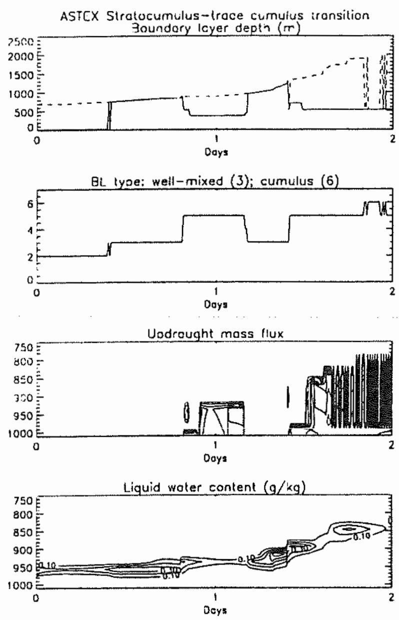

Figure 2

(ii) Using NEWCONV

Figure 3 shows similar timeseries from the L38 run with NEWCONV. The evolution of the boundary layer is similar to that in Figure 2 (since it is largely driven by the large-scale forcing). However, the boundary layer remains well-mixed for longer, allowing more stratocumulus to form, and the convection is triggered consistently from the LCL and is much steadier.

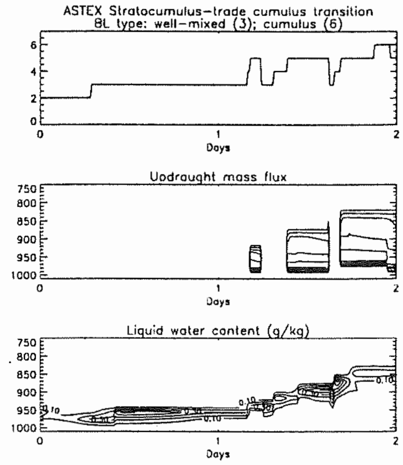

Figure 3

3.2 Trade cumulus

This simulation uses observations from BOMEX (Siebesma and Holtslag, 1996), and represents trade cumulus clouds in equilibrium with a fixed radiative cooling rate of 2 K/day and large scale subsidence such that the mean downward velocity at the inversion is around $5.5 \times 10^{-3} ms^{-1}$.

(i) Impact of using the PBL-N scheme and increasing vertical resolution

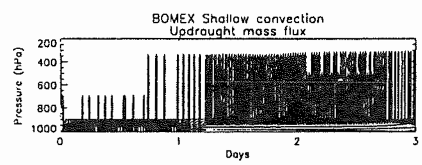

Figure 4

Figure 4 shows a contoured timeseries of the convective updraught mass flux from a L30 BOMEX simulation with standard physics. The convection is very intermittent, and despite the fact that the simulation is meant to be of shallow cumuli, the convection often reaches 350 hPa as a result of incorrect triggering from model level 1, and entrainment rates which are more suited to deep convection. The boundary layer scheme diagnoses a mixed layer depth of 400m throughout the run, but very little mixing is done by the local mixing scheme above about 150m.

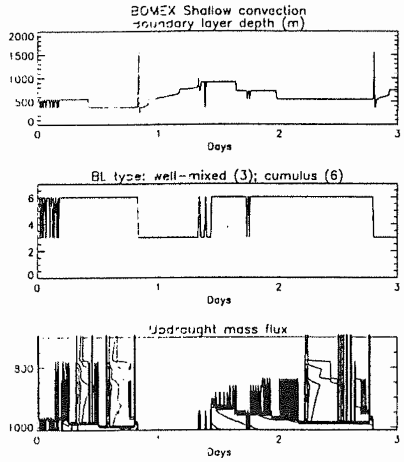

Figure 5

Figure 5 shows results from the L38 run with the PBL-N scheme. This scheme diagnoses convection for much of the time, with occasional periods of a well-mixed boundary layer (in which convection is prevented). However, although the PBL-N scheme diagnoses cumulus, the convection scheme fails to trigger moist convection consistently. In addition, there are several instances of deeper convection, and these are eventually followed by a return to a well-mixed diagnosis, indicating that the profiles are no longer indicative of cumulus convection. These problems are caused by the failure of the convection scheme to trigger consistently or to differentiate properly between shallow and deep convection. During the periods of deeper convection, dry convection is occurring over the first 6 model levels. This is undesirable, partly because this convection scheme is intended for moist convection, and also because the convection and boundary layer schemes are both attempting to mix this subcloud region. Examination of consecutive timesteps reveals that this contributes to the rather random triggering of moist convection from the LCL.

(ii) Using NEWCONV

Figure 6 shows results from the L38 BOMEX simulation with NEWCONV. A shallow cumulus boundary layer is diagnosed throughout this simulation, and the boundary layer depth in Figure 6 marks the LCL, from which the convection scheme is triggered. The contoured mass flux timeseries shows consistent triggering of shallow convection, whose depth is limited by the height of the trade inversion. The profiles and increments from this run show a realistic trade wind boundary layer structure and convection which is in equilibrium with the radiative cooling. Dry convection is prevented in the subcloud layer, although the convective increment from the LCL is mixed uniformly through the subcloud layer to balance the supply of heat and moisture to the convection.

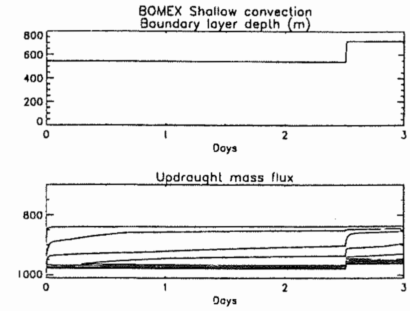

Figure 6

4. FUTURE WORK

The changes described above will require extensive testing in the Unified Model in its different configurations, from operational mesoscale modelling to long climate simulations. However, preliminary tests carried out in the climate model indicate that the diagnosis of deep and shallow convection is reasonable and that there are no major undesirable consequences of forcing the triggering of convection in this way. More extensive testing, in operational forecast models, will follow.

Bretherton, C.S., S.K.Krueger, M.C.Wyant, P.Bechtold, E.van Meijgaard, B.Stevens, and J.Teixeira, 1999. A GCSS boundary-layer cloud model intercomparison study of the first ASTEX Lagrangian experiment. *Boundary-layer Met.*, **93**, 341-380

Grant, A.L.M. 2000. Cloud-base fluxes in the cumulus-capped boundary layer. *Q.J.R. Meteorol. Soc.*, submitted.

Grant, A.L.M. and A.R. Brown 1999. A similarity hypothesis for shallow cumulus transports. *Q.J.R. Meteorol. Soc.*, **125**, 1913-1936

Gregory, D., and P.R. Rowntree, 1990: A mass flux convection scheme with representation of cloud ensemble characteristics and stability dependent closure. *Mon. Weather Rev.*, **118**, 1483-1506

Lock, A.P., A.R. Brown, M.R. Bush, G.M. Martin, and R.N.B. Smith, 2000. A new boundary layer mixing scheme. Part I: Scheme description and single column model tests. *Mon. Weather Rev.*, in press.

Pope, V.D., M. Gallani, P.R. Rowntree, and R.A. Stratton, 2000: The impact of new physical parametrizations in the Hadley Centre climate model - HadAM3. *Clim. Dyn.*, **16**, 123-146.

Siebesma, A.P. and A.A.M. Holtslag 1996. Model impacts of entrainment and detrainment rates in shallow convection. *J. Atmos. Sci.*, **53**, 2354-2364

STRUCTURAL AND PARAMETRIC UNCERTAINTIES IN LARGE-EDDY SIMULATIONS OF THE STRATOCUMULUS-TOPPED MARINE ATMOSPHERIC BOUNDARY LAYER

Andreas Chlond* and Andreas Wolkau
Max-Planck-Institut für Meteorologie, Hamburg, Germany

1. INTRODUCTION

Low-level marine stratus clouds are important modulators of the earth's radiation budget (Klein and Hartmann, 1993). Consequently, comprehensive field experiments and detailed modeling studies of the stratocumulus-topped marine boundary layer are of considerable importance to our understanding of the physics of the atmosphere, including possible effects of this boundary layer regime on climate.

Models of the stratocumulus-topped boundary layer range in complexity from simple mixed layer schemes (Lilly, 1968) to 3D large-eddy simulation (LES) codes (Deardorff, 1980; Moeng 1986). LES is now widely used in small-scale meteorology and is still one of the best techniques we have today for studying turbulence. The strength of LES lies in its explicit calculation of three-dimensional time-evolving turbulent flow fields, which can be used to examine the time evolution of coherent structures and their contribution to turbulent transport. The major deficiency of LES models is that they are computationally demanding. They also generate large volumes of data which require considerable analysis. Moreover, like most modeling techniques LES-modeling is influenced by different uncertainties caused by modeling per se or by assumptions or uncertain values used in the model runs. Two main types of uncertainty affect our confidence in the results from numerical models: parametric uncertainty and structural uncertainty. Parametric uncertainty arises because of incomplete knowledge of model parameters such as empirical quantities, defined constants, and boundary conditions. Structural uncertainty in models arises because of inaccurate treatment of dynamical and physical processes, inexact numerical schemes, inadequate resolutions, and limited domain sizes. In general, the total uncertainty in modelling depends on these factors in a complicated and often counterintuitive way (Tatang, 1997).

In this paper we study three related aspects of LES in the stratocumulus-topped boundary layer. Our study focuses on some aspects of parametric and structural uncertainty and includes the following items:

(1) We investigate the statistical significance of LES-derived data products. This has been done by performing ensemble runs of the stratocumulus-topped boundary layer to demonstrate the stochastic nature of the turbulent processes within the boundary layer.

(2) We examine the sensitivity of our LES-model with respect to the treatment of subgrid-scale processes and microphysical processes. For this purpose we have started model runs using Deardorff's and Schumann's parameterization scheme, respectively. Likewise, we investigate the sensitivity of model results in response to Kessler's and Lüpkes' drizzle parameterization scheme, respectively, and by deactivation of all precipitation processes.

(3) We examine the sensitivity of our LES results with respect to the assumed values of various external, environmental conditions. Moreover, we apply a methodology for objective determination of the uncertainty in LES-derived quantities. The methodology is based on standard error-propagation procedures and yields expressions for probable errors as a function of the relevant parameters (see section 4.3).

* Corresponding author's address: Andreas Chlond, Max-Planck-Institut für Meteorologie, Bundesstr. 55, D-20146 Hamburg, Germany, E-mail: chlond@dkrz.de

2. APPROACH

The approach undertaken is to use a state of the art LES-model (Chlond, 1992, 1994; Müller and Chlond, 1996) that incorporates a detailed description of all relevant physical processes. The model uses Boussinesq-equations for the components of velocity (u, v, w) liquid water potential temperature θ_l and total water content q. These equations are formulated in a Cartesian coordinate system that is translated with the geostrophic wind to follow a trajectory of air in a Lagrangian manner. In that way, the marine cumulus and stratocumulus cases are treated as a time-dependent, quasi-local development. The model takes into account infrared radiative cooling in cloudy conditions (using a simple effective emissivity like approach) and the influence of large-scale vertical motions. The subgrid-scale (SGS) model is based on a transport equation for the SGS turbulent energy. To represent SGS fluxes two different closure schemes could be used: either the parameterization scheme of Deardorff (Deardorff, 1980) or the parameterization scheme of Schumann (Schumann, 1991). The schemes differ in that Schumann's scheme applies the limiting effect of stable stratification only to the length-scales for SGS effects of vertical eddy-diffusivities of heat and scalars but not to those of momentum. In contrast, Deardorff (1980) proposed to reduce all the length-scales for stable stratification. To take into account the microphysical processes we have implemented two different bulk parameterization schemes into our LES-model: Kessler's parameterization scheme (Kessler, 1969) and Lüpkes' 3-variable-parameterization scheme (Lüpkes, 1991). These schemes distinguish between cloud and rain water content and - depending on the parameterization scheme - on the rain number density. The parameterized microphysical processes include condensation, evaporation, coagulation and sedimentation.

The solution of the basic equations is based on a finite differencing method on an equidistant staggered grid. Cyclic lateral boundary conditions were applied and a Rayleigh damping layer in the upper third of the domain was utilized to absorb vertically propagating gravity waves. At the lower boundary prescribed fluxes of momentum, heat and moisture were imposed. The ensemble runs and the runs which utilize different microphysical and subgrid-scale models use a computational domain of size 3.2x3.2x1.5 km^3. The sensitivity runs have been performed in a larger domain (28.8x3.2x1.5 km^3) in order to enhance the signal to noise ratio. The grid intervals fixed to $\Delta x = \Delta y = 50$ m and $\Delta z = 25$. A time step of 3 s was used for all runs.

3. MODEL INITIALIZATION AND FORCING

In this paper the MPI LES-model is tested against observations of the structure of the marine stratocumulus layer observed during the first Lagrangian (Albrecht et al., 1995) experiment of the Atlantic Stratocumulus Transition Experiment (ASTEX). More specifically, the case is based on flight RF06 of the NCAR Electra in the night and early morning of 13 June 1992 at about 37^0 N, 24^0 W. This dataset is extensively described by de Roode and Duynkerke (1997) and Duynkerke et al. (1999), so only a short summary is given here.

The case study was of stratocumulus cloud cover over the North Atlantic which was in a transition stage, changing from a horizontally homogeneous cloud layer to a decoupled boundary layer with cumulus penetrating the stratocumulus deck from below. Observations are made by 7 research aircraft, from a research ship and from the islands of Santa Maria (Azores) and Porto Santo (Madeira). Aircraft flights were made at different levels above, within and below the stratocumulus deck. The navigation was such that the aircraft remained roughly in the same airmass, and the microphysical, radiative and turbulence measurements were made at heights between 30 m and 2800 m. The data were considered suitable for preparing initial and boundary conditions for a 4-hour model simulation of the evolution of the boundary layer, starting at 0700 UTC on 13 June 1992.

The initial conditions for the model have been chosen such as to be broadly consistent with the conditions met during the observations and were specified in the form of simplified vertical profiles of the two horizontal wind components, the liquid-water potential temperature, and the total water content. These were independent of height below cloud base, and varied linearly with height within and above the cloud, with jumps of $\Delta q = -1.6$ g kg^{-1} and $\Delta\theta_l = 5.5$ K in the liquid-water potential temperature and the total water content across the inversion, respectively. Cloud base was at z = 312.5 m and cloud top at z =712.5 m. A uniform geostrophic wind was assumed, and an initial value for subgrid turbulent kinetic energy of 1 m^2 s^{-2} was specified for z < 687.5 m. The friction velocity and the heat and moisture fluxes at the surface were given fixed values, and the net longwave radiation parameterization was a prescribed function of the liquid-water path (the net shortwave radiation was assumed to be zero). The large-scale divergence was set to $1.5 \cdot 10^{-5}$ s^{-1}, resulting in a profile for the large-scale subsidence according to: $w_{LS} = 1.5 \cdot 10^{-5} \cdot (z/m)$ m s^{-1}. All initial profiles were assumed to be horizontally homogeneous, except for the temperature field. In order to start the convective instability, spatially uncorrelated random perturbations, uniformly distributed between -0.1 K and 0.1 K, were applied to the initial temperature field at all grid points with z < 687.5. This specification of model initialization and forcing has also been used in the European Cloud-Resolving Modelling (EUCREM) model intercomparison project where the main focus has been on the entrainment velocity which is the most important parameter for the cloud development (Duynkerke et al., 1999).

4. RESULTS

4.1 Satistical significance of the simulations

Ensemble runs (using initial data described in section 3, but perturbed with different sets of spatially uncorrelated variations to the temperature field within the range ±0.1 K) have been performed to give 21 realizations of the simulation. Examination of profiles of the predicted mean fluxes at a particular instant of time (150 minutes after the initial time) showed considerable spread among the ensemble members (see Fig. 1). The spread was reduced, but was still not negligible, when the results were displayed as 1-hr averages (see Fig.2). An additional run was done for a domain 9 times larger in the cross-wind direction. The spreading was reduced still further for the 1-hour averages over the larger domain (see Fig. 3). These results indicate the need for care in interpreting results from a single model run, and demonstrate that averaging should be done over sufficiently large temporal and spatial domains.

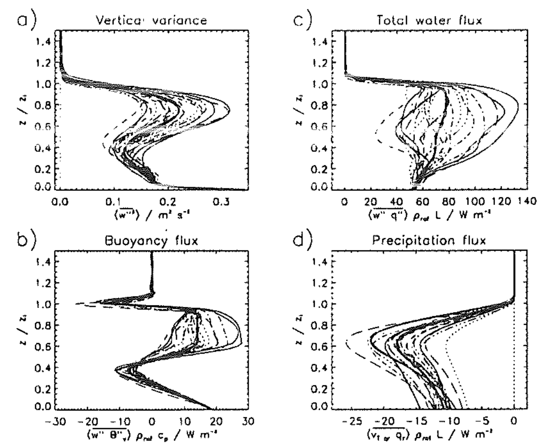

Fig. 1: Vertical profiles of total vertical velocity variance (a), total buoyancy flux (b), total water flux (c), and precipitation flux (d) at t=9000 s generated from 21 LES-model realizations of the stratocumulus case. The thick black line refers to the ensemble average.

4.2 Sensitivity to physical parameterizations

A number of runs was done to test the sensitivity of the results to Deardorff's and Schumann's subgrid-scale scheme, and to Kessler's and Lüpkes's cloud microphysics schemes, as well as a "no-rain" scheme. The Deardorff/no rain run produced the deepest boundary layer and the largest liquid-water path. The impacts of the different subgrid schemes were small, but the primary effects of drizzle in the Kessler or Lüpkes runs were to reduce the buoyant production of turbulent kinetic energy, resulting in shallower boundary layers due to reduced entrainment rates. The removal of water by drizzle lowered the maximum liquid water content at cloud top by 20%. The effects of latent heating within the cloud and evaporative cooling below tended to produce an intermediate stable layer that decoupled the sub-cloud layer from the radiatively-driven turbulence in the cloud layer.

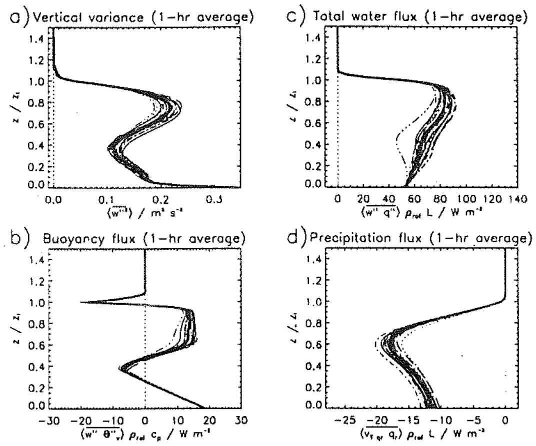

Fig. 2: As in Fig. 1 except profiles of time-averaged quantities from 7200 s to 10800 s.

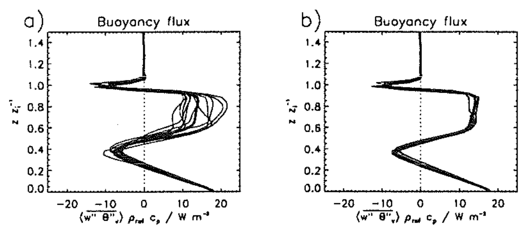

Fig. 3: Vertical profiles of total buoyancy flux at t=2.5 h for (a) the standard domain of size 3.3x3.2x1.5 km^3 (upper panel) and for (b) the extended domain of size 28.8x3.2x1.5 km^3 (lower panel). The thick full lines are used to denote the one-hour averages whereas the thin full lines are used to depict the five-minute averages within the one-hour averaging period.

4.3 Sensitivity to the initial data measurements

A numerical model designed to simulate variables of interest in a given system can be tested by comparing model predictions against observations. Since both observations and predictions may be uncertain, meaningful model verification requires not only the average values but also some measure of the uncertainty of target variables.

Here, we examine the sensitivity of our LES results with respect to the assumed values of various external, environmental conditions. These conditions include all those environmental parameters that are needed to specify all of the mean initial and boundary conditions required to run a model simulation. Our study investigates the sensitivity of the model output with respect to the following parameters: (a) the inversion strength in total water content $(\Delta Q_t)_{inv}$, (b) the inversion strength in liquid water potential temperature $(\Delta \Theta_l)_{inv}$, (c) the large-scale subsidence w_{LS}, (d) the sea surface flux of heat $(\overline{w\theta})_0$, (e) the sea surface flux of moisture $(\overline{wq_t})_0$, and (f) the net longwave radiative cooling ΔF_t. Uncertainties in these external input parameters may arise from instrumental measurement errors, sampling errors, and the instationarity and spatial inhomogeneities of the fields under consideration during the measurements. Central values and uncertainty factors (standard deviations) of the external, environmental input parameters are listed in Table 1.

Table 1: Central values and uncertainty factors (standard deviations) of the external, environmental input parameters

Parameter	Central value	Standard deviation
$(\Delta\Theta_l)_{inv}$	5.5 K	1 K
$(\Delta Q_t)_{inv}$	-1.6 g kg^{-1}	0.5 g kg^{-1}
w_{LS}	-0.0225 m s^{-1}	0.00565 m s^{-1}
$(\overline{w\theta})_0$	14.9 W m^{-2}	3.725 W m^{-2}
$(\overline{wq_t})_0$	51.5 W m^{-2}	12.875 W m^{-2}
ΔF_t	74 W m^{-2}	18.5 W m^{-2}

Simplified linear relationships between the variances of simulated quantities and the variances of measured environmental parameters were used to asses the sensitivity of the model to initial-data uncertainties. The coefficients in these relationships, which depend on the gradients of simulated quantities with respect to the observed parameters, were estimated from a limited number of sensitivity runs. The exercise enabled error bars to be estimated for the simulations.

Figure 4 presents the vertical profiles of (a) liquid water content, (b) total (resolved plus subgrid-scale) buoyancy flux, (c) total (resolved plus subgrid-scale) water flux, (d) precipitation flux, (e) total (resolved plus subgrid-scale) vertical velocity variance, and (f) total (resolved plus subgrid-scale) turbulent kinetic energy (TKE) for the reference run which utilizes the central values for the input parameters. The profiles represent time averages over hour 2 to 3. The vertical axes have been scaled using the inversion height z_i. Data are marked with diamonds and refer to aircraft measurements during the flight ASTEX RF06 (after de Roode and Duynkerke (1997)). In addition, 90% confidence limits (that is, $\pm 1.6\ \sigma$ intervals) have been plotted at selected height levels for the various quantities. Overall, with the exception of the precipitation flux the model predictions of thermodynamic, dynamic and microphysical properties are generally in a reasonable agreement with the measurements during the flight ASTEX RF06 obtained in a stratocumulus topped boundary layer. The differences between the model and measurements are within the modeling uncertainties, but the calculated precipitation rate differs significantly from that derived in the observations. Apart from the confidence limits, the sensitivity analysis also provides a framework for ranking the uncertain parameters according to their contribution to the total model variance. We find that the largest contribution to the variance of the LES-derived data products is due to the uncertainties in the cloud-top jump of total water mixing ratio and the net radiative forcing. However, the calculated precipitation rate was found to differ significantly from that derived in the observations. Therefore, we conclude that the representation of precipitation process within a numerical model of stratocumulus is difficult, and improving the results will prove to be a challenging task.

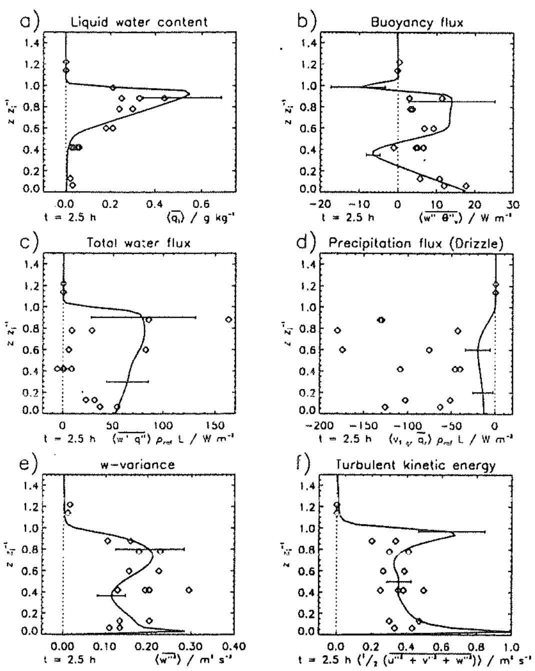

Fig. 4: Calculated and measured vertical profiles of (a) liquid water content, (b) total buoyancy flux, (c) total water flux, (d) precipitation flux, (e) total vertical velocity variance, and (f) total turbulent kinetic energy (TKE). Data are marked with diamonds and refer to aircraft measurements during the flight ASTEX RF06 (after de Roode and Duynkerke (1997)). Error bars correspond to 90% confidence limits.

5. ACKNOWLEDGEMENTS

This work has received financial support by the CEC contract ENV4-CT95-0107 EUCREM (European Cloud Resolving Modelling Program).

6. REFERENCES

Albrecht, B. A., C. S. Bretherton, D. Johnson, W. H. Schubert and A. S. Frisch, 1995: The Atlantic Stratocumulus Transition Experiment - ASTEX. *Bull. Amer. Meteor. Soc.*, **76**, 889-904.

Chlond, A., 1992: Three-dimensional simulation of cloud street development during a cold air outbreak. *Bound.-Layer Meteor.*, **58**, 161-192.

Chlond, A., 1994: Locally modified version of Bott's advection scheme. *Monthly Weather Review,* **122**, 111-125.

Deardorff, J.W., 1980 : Stratocumulus-capped mixed layers derived from a three-dimensional model. Bound.-Layer Meteor., **18**, 495 - 527.

Duynkerke, P. G., P. J. Jonker, A. Chlond, M. C. van Zanten, J. Cuxart, P. Clark, E. Sanchez, G. Martin, G. Lenderink und J. Teixeira, 1999: Intercomparison of three- and one-dimensional model simulations and aircraft observations of stratocumulus. *Bound.-Layer Meteor.,* **92**, *453-487.*

Kessler, E., 1969: On the distribution and continuity of water substances in atmospheric circulations. Meteorological Monographes, **32**, 84 pages.

Klein, S. A., and D. L. Hartmann, 1993: The seasonal cycle of stratiform clouds. J. Climate, **6**, 1587-1606.

Lüpkes, C., 1991: Untersuchungen zur Parametrisierung von Koagulationsprozessen niederschlagsbildender Tropfen, Verlag Dr. Kovavc, Hamburg, 156 pages.

Lilly, D. K., 1968: Models of cloud-topped mixed layers under a strong inversion. *Quart. J. Roy. Meteor. Soc.*, **94**, 292-309.

Moeng, C.-H., 1986: Large-eddy simulation of a stratus-topped boundary layer. Part I: Structure und budgets. *J. Atmos. Sci.*, **43**, 2886-2900.

Müller, G., and A. Chlond, 1996: Three-dimensional numerical study of cell broadening during cold-air outbreaks. Bound.-Layer Meteor., **81**, 289-323.

de Roode, S. R., and P. G. Duynkerke,1997: Observed Lagrangian transition of stratocumulus into cumulus during ASTEX: mean state and turbulence structure. J. Atmos. Sci., **54**, 2157-2173.

Schumann, U., 1991: Subgrid length-scales for large-eddy simulation of stratified turbulence. Theoret. Comput. Fluid Dynamics , **2**, 279 - 290.

Tatang, M. A., W. Pan, R. G. Prinn und G. J. MacRae, 1997: An efficient method for parametric uncertainty analysis of numerical geophysical models. *J. Geophys. Res.*, **102**, 21925-21932.

INVERSION STRUCTURE AND ENTRAINMENT RATE IN STRATOCUMULUS TOPPED BOUNDARY LAYERS

Qing Wang, David W. McDowell, and Michelle K. Whisenhant
Naval Postgraduate School, Monterey, CA

1. INTRODUCTION

We have long recognized that the difficulty in simulating stratocumulus-topped boundary layers (STBL) lies in the parameterization of entrainment rate (e.g., Moeng *et al.* 1996). The difficulty in determining entrainment rate from observations is the uncertainty in turbulent fluxes and particularly in the jump conditions obtained from limited number of soundings. This is seen in the most commonly used entrainment rate equation (Deardorff, 1979):

$$w_e = \frac{\overline{w'c'_{-h}}}{\Delta C} \qquad (1)$$

where w_e is the entrainment velocity, $\overline{w'c'_{-h}}$ is the turbulent flux of variable C at the boundary layer top, and h the boundary layer height. This variable is conserved in an adiabatic process. The changes in the mean quantity across the capping inversion is denoted as ΔC, which indicates the difference between the entrained air parcel and the boundary layer environment. While the entrainment flux shows the amount of C being entrained within a unit time, the entrainment rate is an ensemble measure of the rate at which all quantities are entrained from the free atmosphere to the boundary layer. In order to describe the entrainment rate, one not only needs a statistically significant entrainment flux, but also a jump condition that realistically describes an ensemble average of the differences between the entrained air and the boundary layer air.

The entrainment zone was introduced to describe the interface between the boundary layer and the free troposphere where entrainment occurs. Deardorff (1979) provided an early description of entrainment zone in a clear convective mixed layer (CBL) by experimenting in a laboratory convection chamber. From this, he defined the entrainment zone as the outermost portion of the mixed layer where non-turbulent fluid is being entrained, but is not yet incorporated into the well-mixed layer. The top of the entrainment zone was therefore determined to be the maximum height any mixed parcel could reach. His depiction of the entrainment zone is shown in Fig. 1 where the depth marked Δh is an ensemble-mean of many soundings. The depth of the entrainment zone was typically 25% of the mixed layer depth (Deardorff, 1979), although the local interface between the inversion air and the boundary layer may be shallower. This depth of the entrainment zone depicts the range of updraft penetration into the capping inversion, which can also be regarded as the variation of the boundary layer top.

Figure 1. Depiction of the entrainment zone in a convection tank, from Deardorff (1979). Light areas show the well-mixed fluid. The region indicated by Δh is defined as the entrainment zone.

A few studies on cloudy boundary layers have revealed significant differences between the inversion structure in the cloudy and clear boundary layers (*e.g.*, Nicholls and Turton, 1986). An example of such difference is shown in Fig. 2. This comparison between two soundings taken from the same area on the same day demonstrates the significant changes that can occur at the top of the boundary layer when clouds are present. The strengthening of the inversion in the stratocumulus-topped boundary layer profile suggests the effect of radiative cooling at the cloud top. With these observed differences, more detailed studies regarding the inversion structure and the entrainment process in a stratocumulus-topped boundary layer are needed in order to fully understand the effects of such clouds on boundary layer evolution.

2. THE DATA

Our analysis is based on measurements made during the First International Satellite Cloud and Climate Project (ISCCP) Regional Experiment (FIRE) Marine Stratocumulus Intensive Field Observations (IFO) phase off the coast of southern California in the summer of 1987 (Albrecht *et al.*, 1988). In this study, observations provided by a research aircraft (the NCAR Electra) are used to analyze the turbulence and inversion structure of the cloudy boundary layer. Wang and McDowell (2000) discussed the measurements and the instrumentation used in this study. The aircraft had an

* *Corresponding author address:* Dr. Qing Wang, Naval Postgraduate School, Dept. of Meteorology, Monterey, CA 93940. e-mail: qwang@nps.navy.mil

on-station horizontal speed of about 100 ms^{-1}; the ascending/descending speed was 2.54 m s^{-1} (or 500 feet per minute). The data was sampled at 50 Hz, filtered and recorded at 20 Hz. Thus, the horizontal

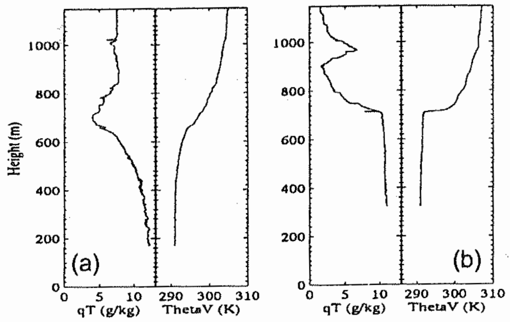

Figure 2. Comparison between a cloud-topped and clear boundary layer from July 7 (flight 5) of FIRE. Total water and virtual potential temperature profiles for the clear case are shown in (a) and for the stratocumulus-topped case in (b).

resolution of the measurements was 5 m, the vertical resolution was 0.13 m. The aircraft soundings hence have sufficient vertical resolution to reveal the fine inversion structure.

3. VARIATION OF CLOUD TOP HEIGHT

Figure 1 shows the penetration of the turbulent updrafts into the capping inversion in the clear convective situation. This picture appears to imply a close correlation between the turbulence updrafts/downdrafts and the shape of the interface. It appears that the scale of variation for the boundary layer top is similar to that of the penetrating updraft. With this in mind, we examined the energy density spectra of the lidar-measured cloud top height and the vertical velocity from the highest measurement level about 100 m below the cloud top. The spectra are shown in the bottom panel of Fig. 3. It is seen that the vertical velocity peaks at 700 m –1.5 km, which is the scale of boundary layer internal circulation. Variation of the cloud top height, on the other hand, is mostly greater than 10 km. The high magnitude of power spectra at the small-scale range is likely caused by noise in the LIDAR-retrieved cloud top height.

The fact that the cloud top varies at a much larger scale than the turbulent updraft and downdraft indicates a different entrainment mechanism in cloudy boundary layers than that depicted in Fig. 1. The cloud top does not seem to be shaped by penetrating updrafts in the cloudy conditions. With a weaker turbulence intensity and a stronger capping inversion (to be discussed in the next section) compared to clear boundary layers, this finding appears to be reasonable.

4. INVERSION STRUCTURE

We analyzed a total of 56 soundings from nine FIRE flights to examine the inversion structure at the cloud top. The exact cloud top was identified using signatures from several variables including the cloud droplet concentration, potential temperature, total water, ozone, and the horizontal wind components. We also performed wavelet analysis on the 20 Hz sampled vertical velocity and potential temperature and kept the small-scale perturbations. The boundary layer top can be clearly identified at the level of sharp decrease of

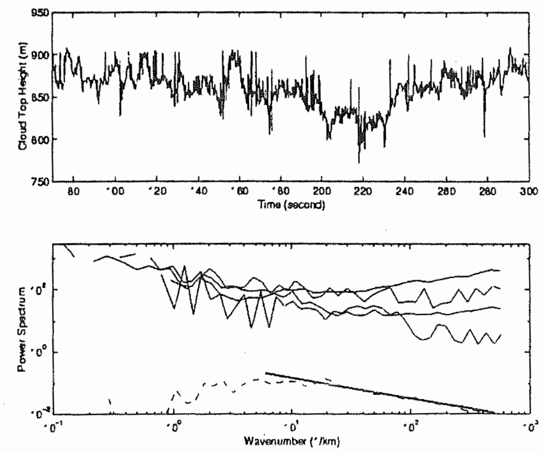

Figure 3. Spatial variation of cloud top height (top) and comparison of power spectra of cloud top height (solid lines) and vertical velocity (dash line) (bottom). The thick solid line shows the –5/3 slope in the turbulence inertial subrange.

turbulence perturbations. An example of the soundings is shown in Fig. 4. From most of the soundings, we found an extremely sharp inversion immediately above the cloud top. This inversion is in general several meters in depth with a potential temperature increase of up to 3 K. We refer to this sharp gradient layer as the initial gradient layer. Yet, this layer is only a portion of the entire inversion layer above the cloud top. The upper inversion layer has a much weaker θ gradient compared to that in the initial gradient layer and generally has a depth of several tens of meters. Table 1 shows the properties of the initial gradient layer from all soundings from July 5, 1987 (flight 4).

There also exists a strong scalar gradient in the initial gradient layer. It seems that the air within the gradient layer is a mixture of the boundary layer and the air from above this layer, as indicated by the mixing line analysis in Fig. 5. Here the total water content (q_T) and ozone concentration (O_3) are both conserved in a adiabatic process. Mixing between the air at the top of the gradient layer with that from the boundary layer should result in mixtures shown by the solid line. Figure 5 shows that most of the (q_T, O_3) pairs from the initial gradient layer are on the mixing line. We therefore consider this initial gradient layer as the

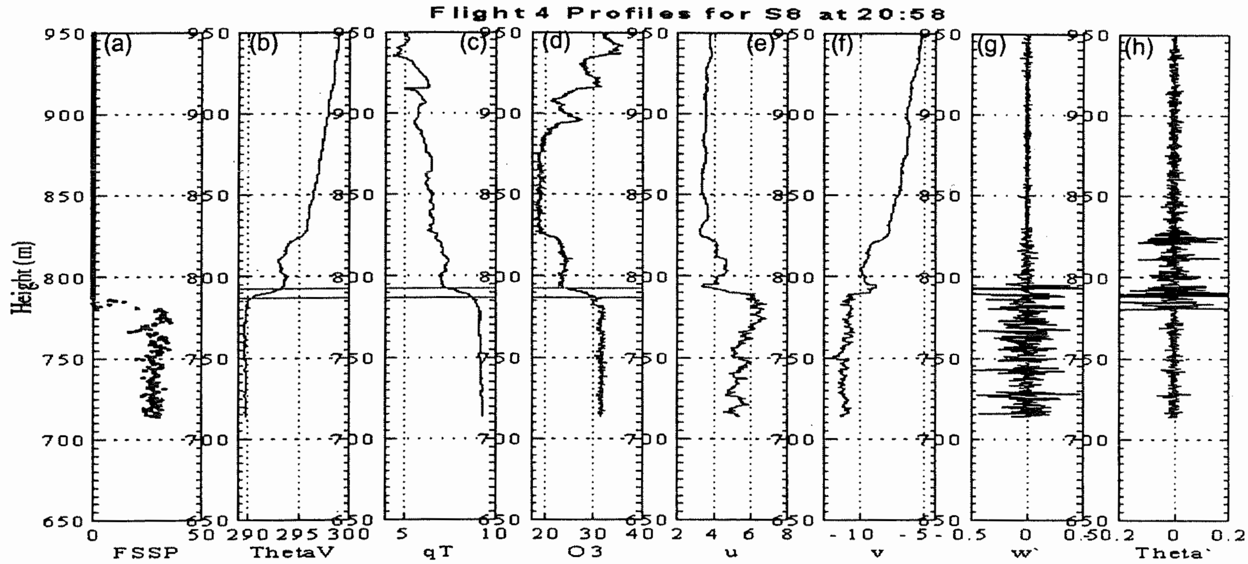

Figure 4. Example of sounding profiles of (a) cloud droplet concentration (N cm^{-3}), (b) virtual potential temperature (K), (c) total water (g kg^{-1}), (d) ozone (ppbv), (e) u wind component (m s^{-1}), (f) v wind component, (g) wavelet decomposition of small-scale vertical velocity perturbations (m s^{-1}), and (h) same as in (g) except for potential temperature (K). Horizontal lines in (b)-(d) indicate the top and bottom of initial gradient layer.

Table 1. Properties of the initial gradient layers from flight 4 soundings. The jump in a variable φ is defined as $\Delta\varphi = \varphi_{top} - \varphi_{base}$. Here, q_T, O_3, θ_v, Δz, $\nabla\theta_v$, and H_{CT} are total water (gkg^{-1}), ozone (ppbv), virtual potential temperature (K), inversion depth, θ_v gradient in the inversion layer (Km^{-1}), and cloud-top height (m), respectively.

Sndg #	Δq_T	ΔO_3	$\Delta\theta_v$	Δz	$\nabla\theta_v$	H_{CT}
S1	-0.5	-2.8	1.1	3.0	0.36	780.0
S2	-0.9	-3.9	2.1	1.8	1.18	805.0
S3	-0.8	-2.4	2.2	2.2	0.98	872.0
S4	-1.2	2.1	2.1	3.6	0.59	842.0
S5	-1.5	4.5	2.3	4.5	0.50	834.0
S6	-1.2	6.0	2.5	2.0	1.24	968.0
S7	-1.4	-2.7	2.6	3.2	0.81	819.0
S8	-1.5	-5.7	2.9	4.7	0.62	788.0
S9	-0.7	-2.7	1.4	2.2	0.64	814.0
S10	-0.5	1.0	0.3	1.6	0.19	734.0
S11	-1.1	4.4	2.0	2.2	0.88	913.0

entrainment zone. The difference of a particular scalar, i.e., total water content, between the top and the bottom of the gradient layer is thus defined as the entrainment jump condition at the location of the sounding. We then use the mean of jump conditions from all soundings as the ensemble jump condition.

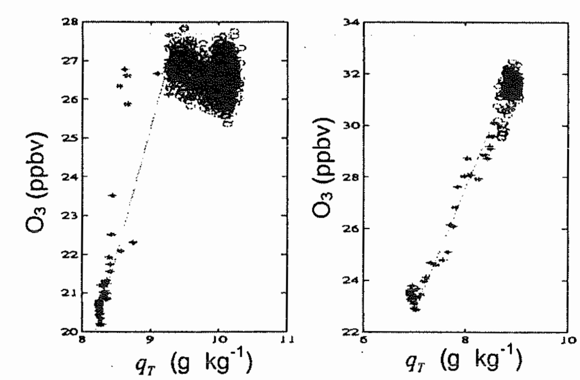

Figure 5. Examples of mixing diagrams from two soundings of flight 4. The boundary layer and inversion air are denoted as (o) and (*), respectively. The solid line denotes the result of adiabatic mixing between the boundary layer and inversion air at different mixing ratios.

5. ENTRAINMENT FLUXES AND RATE

Entrainment flux of total water was determined using the vertical flux profiles linearly extrapolated to the cloud top. In calculating the flux profiles from various measurement levels, a cutoff wavelength of 6 km was used to obtain the flux from the co-spectra between vertical velocity and total water. For a well-mixed layer, the vertical flux profile of a conserved variable is expected to be linear with height through the depth of the layer. This is generally the case for most of the FIRE flights. In this analysis, entrainment fluxes were determined using the best fit linear profile from measurements in the cloud mixed layer. In a well-mixed boundary layer, the cloud mixed layer is the entire boundary layer, while in a decoupled boundary layer the cloud mixed layer is the upper mixed layer associated with the cloud layer (Wang 1993). Cloud top heights were obtained using LIDAR measurements or sounding profiles when LIDAR measurements were not available. Figure 6 shows an example of the vertical flux profiles and the linear fit to the profiles from two flights of FIRE. Table 2 gives the entrainment fluxes, jump conditions, and the corresponding entrainment rate.

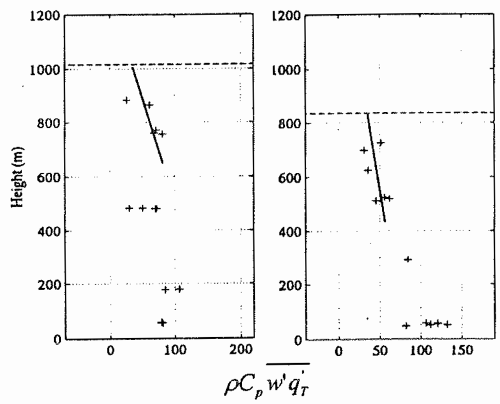

Figure 6. Vertical flux profiles for total water (Wm^{-2}) for flights 3 (left) and 4 (right). The solid line shows the linear fit that was used to obtain entrainment flux.

Table 2. Estimate of entrainment rate (cm s^{-1}) for all flights of FIRE. The jump conditions shown are averages from all soundings of each flight.

Flt	$\rho L \overline{w'q_T'}$	Δq_T	w_e
2	28.7	-0.57	2.0
3	58.9	-0.73	3.2
4	34.1	-1.02	1.3
5	45.8	-1.38	1.3
6	8.0	-0.36	0.9
7	13.6	-0.71	0.8
8	32.0	-0.85	1.5
9	13.0	-0.11	4.7
10	42.2	-0.56	3.0

6. CONCLUSIONS

We analyzed a large number of soundings from 9 flights of FIRE to understand the inversion structure and its implication for entrainment process and entrainment rate estimates. We found that the entrainment zone in the STBL is a thin layer of a few meters in depth. Although this so-called initial gradient layer is only a small part of the inversion layer above the cloud top, it appears to contain a mixture of the air at the top and bottom of the layer. We therefore define this layer as the entrainment zone and define the difference at the top and bottom of the layer as the entrainment jump conditions.

We examined the spectra of the cloud top height measured by airborne lidar and compared the spectra with that of vertical velocity from within the turbulent boundary layer. This comparison reveals that the cloud-top height varied at a scale of more than 10 km, much larger than the scale of the dominate turbulent updraft and downdraft. Updraft penetration into the inversion, as pictured in Fig. 1 for clear convective boundary layers, is thus not likely for stratocumulus-topped boundary layers. It is thus possible that the dominant entrainment process occurs at scales smaller than that of the convective updraft/downdraft. Further studies are needed on this aspect to understand the entrainment process in cloudy boundary layers.

The uncertainty in the estimated entrainment rate (Table 2) has not been discussed and is part of our ongoing work.

7. ACKNOWLEDGEMENTS

This research was supported by National Science Foundation grants ATM-9700845 and ATM-9900496.

8. REFERENCES

Albrecht, B. A., D. A. Randall and S. Nicholls, 1988: Observations of marine stratocumulus during FIRE. *Bull. Amer. Meteor. Soc.*, **69**, 618-626.

Deardorff, J. W., 1979: Prediction of convective mixed-layer entrainment for realistic capping inversion structure. *J. Atmos. Sci.*, **36**, 424-436.

McDowell, D. W., 1999: Determining entrainment rate and the role of entrainment in stratocumulus clouds. Master's Thesis, Naval Postgraduate School, Dept. of Meteorology, Monterey, CA. 67pp.

Nicholls, S., and J. D. Turton, 1986: An observational study of the structure of stratiform cloud sheets: Part II. Entrainment. *Quart. J. R. Met. Soc.*, **112**, 461-480.

Wang, Q., and D. W. Mcdowell, 2000: Entrainment and layered structure above the stratocumulus cloud top. Submitted to *J. Atmos. Sci.*.

LARGE EDDY SIMULATIONS OF CUMULUS CLOUDS OVER LAND AND SENSITIVITY TO SOIL MOISTURE

Jean-Christophe Golaz*, Hongli Jiang, and William Cotton.

Dept. of Atmospheric Science, Colorado State University, Fort Collins, Colorado 80523

1. INTRODUCTION

As participants in the 6th intercomparison of the GCSS boundary layer group, we have conducted large-eddy simulations (LES) of a daytime cumulus cloud-topped boundary layer over land observed at the Southern Great Plains (SGP) ARM site on 21 June 1997 (Brown, 1999).

The first LES was an idealized simulation following the GCSS specifications. In addition, we have tested the sensitivity of the boundary layer clouds to initial soil moisture using a land-surface model and a two-stream radiative transfer code.

2. MODEL SETUP AND IDEALIZED CASE

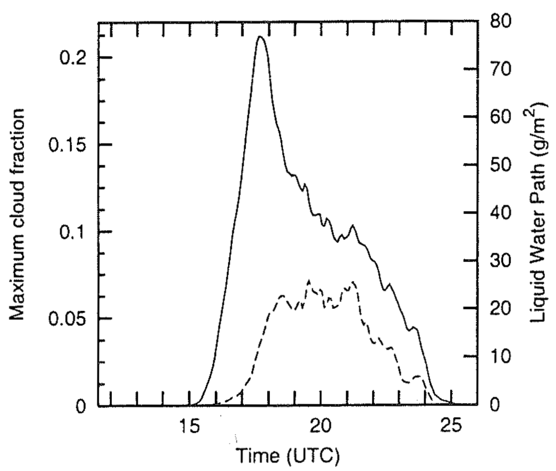

Figure 1: 30-minute running average of maximum cloud fraction (solid line) and liquid water path (dashed line).

All simulations presented here were performed using the LES version of the Regional Atmospheric Modeling System (RAMS) (Pielke et al., 1992). The grid spacing was 100 m in the horizontal and 40 m in the vertical with a domain size of 6700 m in the horizontal and 4400 m in the vertical. Periodic boundary conditions were used in the horizontal and subgrid-scale fluxes were computed with a Deardorff-type turbulence kinetic energy scheme. No microphysics was used, except for the condensation of water vapor into cloud water.

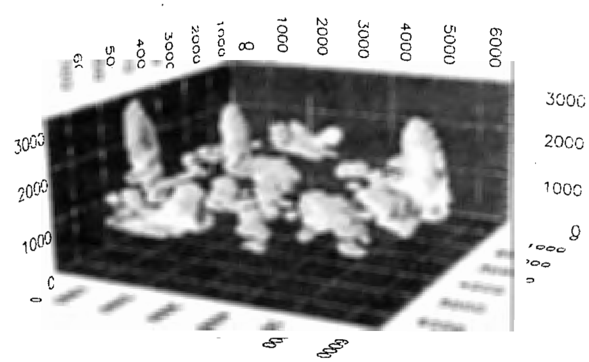

Figure 2: Isosurface representation of cloud water field at 1930 UTC.

The time evolution of maximum cloud fraction and average liquid water path is shown in Figure 1. Cumulus clouds start forming at the top of the convective boundary layer around 1500 UTC and reach a maximum cloud fraction of 20% approximately two hours later. The liquid water path increases to 20 (g/m^2) and remains relatively steady for four hours, whereas the cloud fraction continuously decreases after reaching its early maximum. Clouds completely dissipate towards the end of the simulation. A representation of the cloud field at 1930 UTC is shown in Figure 2. Model output and statistics obtained with RAMS compared favorably with those of other GCSS participants.

3. SENSITIVITY EXPERIMENTS

As a follow-up to this idealized simulation, we performed a series of additional experiments in which the imposed surface fluxes and radiative tendencies were replaced with an interactive land surface model (Walko et al., 1999) and a two-stream radiative transfer code (Harrington 1997).

*Corresponding author address: Jean-Christophe Golaz
Dept. of Atmospheric Science, Colorado State University
Fort Collins, CO 80523, USA.
E-mail: golaz@atmos.colostate.edu

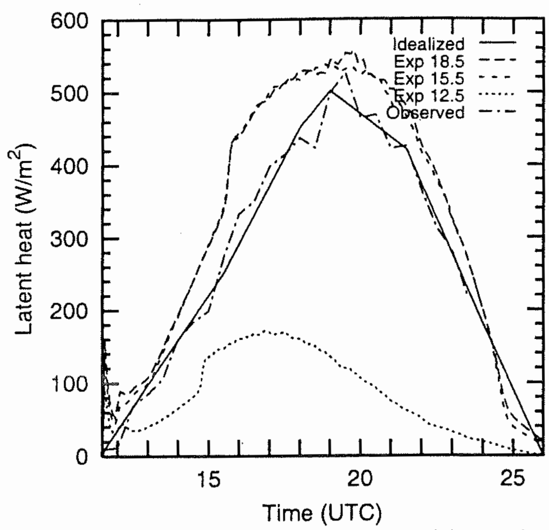

Figure 3: Evolution of domain-averaged latent heat flux for the four experiments and observed values.

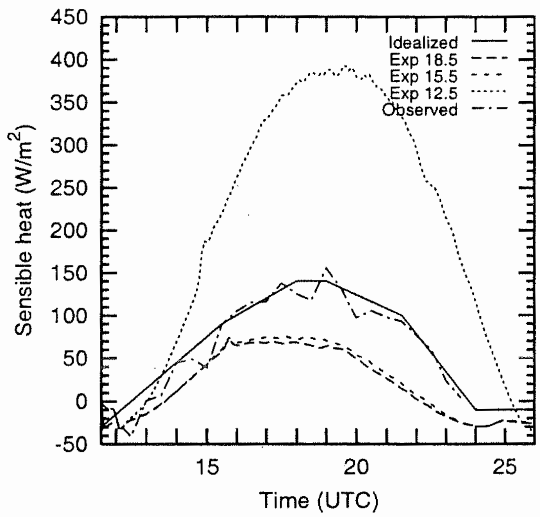

Figure 4: Same as Figure 3 but for sensible heat flux.

The land surface model was initialized with uniform soil moisture. Soil moisture observations from the SGP ARM site on 21 June 1997 ranged from 0.12 to 0.22 mass mixing ratio, where the mass mixing ratio is defined as the mass of water per unit mass of dry soil. In this work, we present results from three different experiments initialized with soil moisture mass mixing ratios of 0.125, 0.155, and 0.185, respectively. Those values correspond to soil moisture ranging from 42 to 62% saturation. The model was otherwise set up and initialized similarly to the idealized case. Table 1 summarizes the various experiments conducted.

Experiment name	*Soil moisture mixing ratio*	*Soil moisture saturation*	*Surface fluxes*	*Radiation*
Idealized	N/A	N/A	Imposed	Imposed
Exp 12.5	0.125	42%	Interactive	Interactive
Exp 15.5	0.155	52%	Interactive	Interactive
Exp 18.5	0.185	62%	Interactive	Interactive

Table 1: Summary of experiments

The differences in initial soil moisture content have a considerable impact on the time evolution of surface heat fluxes as shown in Figures 3 and 4. Experiments 15.5 and 18.5 produce almost identical surface fluxes. Compared to observations, those fluxes have slightly larger values of latent and smaller values of sensible heat. Simulation 12.5 produces very different fluxes. The maximum sensible heat flux reaches almost 400 (W/m^2) compared to approximately 150 (W/m^2) in the reference case. The latent heat flux maximum is of the order of 180 (W/m^2) compared to more than 500 (W/m^2) in the other simulations.

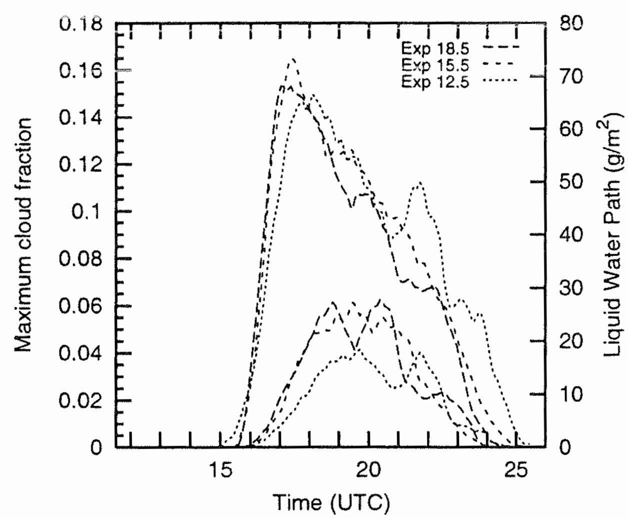

Figure 5: 30-minute running average of maximum cloud fraction (top three curves) and liquid water path (bottom three curves) for the three sensitivity experiments.

The evolution of maximum cloud fraction and liquid water path for the three sensitivity experiments are shown in Figure 5. Timing of the onset of convection is similar for the three runs and comparable with the idealized LES (Fig. 1). Cloud fraction and liquid water path for experiments 18.5 and 15.5 are also close to the idealized simulation except for the initial peak in cloud fraction in the idealized case. Liquid water path is slightly lower for the drier 12.5 simulation. During the decay phase, all three simulations exhibit very similar domain-averaged cloudiness. It is interesting to note that despite the very large differences in surface heat fluxes between the 12.5 experiment and the other two moister simulations, the differences in cloud field appear to be minor with relative differences of the order of 20% or less.

This is further confirmed by looking at profiles of cloud fraction and cloud water mixing ratio. Those fields are depicted in Figures 6 and 7 between 1900 UTC and 2000 UTC.

It is interesting to note that, except for a vertical displacement, the profiles of cloud fraction look strikingly similar among the various experiments. The differences in cloud base are explained in terms of variations in the LCL. Simulation 12.5, with its higher sensible and lower latent heat flux, leads to a significantly warmer and drier subcloud layer compared the the other experiments, and therefore a higher LCL. Also, simulations 15.5 and 18.5 have lower cloud base compared to the idealized case because the larger latent heat fluxes create a colder and moister subcloud layer.

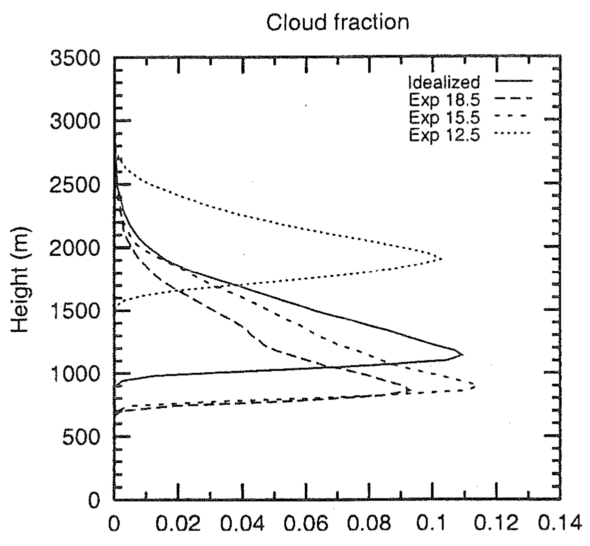

Figure 6: Average profiles of cloud fraction between 1900 and 2000 UTC for the idealized simulation and the three sensitivity experiments.

The profiles of cloud water mixing ratio also show similar features with the main difference being the variation in cloud base, whereas the actual amounts of cloud water remain in a relatively narrow range for all cases. The lower cloud water amount for experiment 18.5 is largely an artifact of the one hour averaging period which is not long enough to always capture a representative ensemble of clouds.

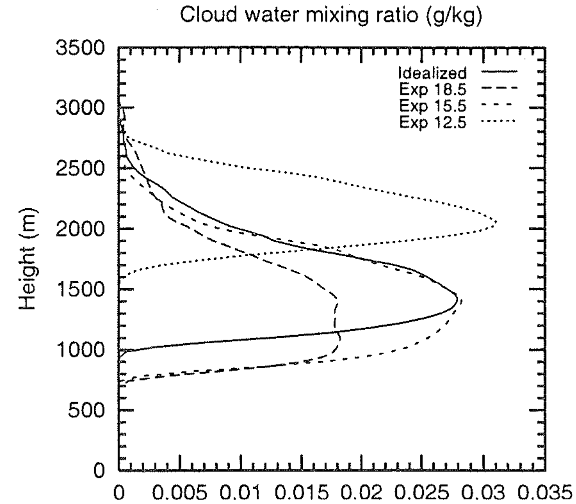

Figure 7: Same as Figure 6 but for cloud water mixing ratio.

4. CONCLUSION

We performed a series of large-eddy simulations of a cumulus cloud-topped boundary layer over land, based on the idealized GCSS intercomparison workshop. This is a case of cloud fraction of less than 20%. Sensitivity in initial soil moisture was investigated by conducting three experiments with initial soil moisture mixing ratios of 0.125, 0.155, and 0.185. The 15.5 and 18.5 experiments produced results that were very similar to each other, both in terms of surface heat fluxes and cloud field properties. The drier 12.5 experiment led to substantially different surface fluxes with a shift from a latent heat dominance to sensible heat flux dominance. Despite this large difference in surface forcing, the impact on the cloud field was moderate. The main difference was a displacement of the cloud base. A slight reduction of domain average liquid water path was also observed, but the maximum cloud fraction remained essentially unchanged.

5. ACKNOWLEDGMENTS

This work was supported by the National Science Foundation under grant ATM-9904128 and the National Oceanic and Atmospheric Administration under contract NA67RJ0152 AMEND 22.

6. REFERENCES

Brown, Andrew R., 1999: *6th GCSS WG-1 Intercomparison: ARM.* See ftp://email.meto.gov.uk/pub/apr/arm.

Harrington, Jerry Y., 1997: *The effects of Radiative and Microphysical Processes on simulated Warm and Transition-Season Arctic Stratus.* Ph.D dissertation, Atmospheric Science Paper No 637, Colorado State University.

Pielke, Roger A., W. R. Cotton, R. L. Walko, C. J. Tremback, W. A. Lyons, L. D. Grasso, M. E. Nicholls, M. D. Moran, D. A. Wesley, T. J. Lee, J. H. Copeland, 1992: *A comprehensive Meteorological modeling System RAMS..* Meteorology and Atmospheric Physics, 49: 69-91.

Walko, Robert L., Larry E. Band, Jill Baron, Timothy G.F. Kittel, Richard Lammers, Tsengdar J. Lee, Roger A. Pielke, Sr., Chris Taylor, Christina Tague, Craig J. Tremback, and Pier Luigi Vidale, 1999: *Coupled Atmosphere-Biophysics-Hydrology Models for Environmental Modeling.* Submitted to Journal. of Atmospheric Sciences.

VERTICAL MOTIONS OF DROPS OF DIFFERENT SIZES IN MARINE STRATUS

Swarndeep S. Gill* and Gabor Vali
Dept. of Atmospheric Science, University of Wyoming, Laramie, WY, 82071

1. Introduction

The mechanism for drizzle formation in warm marine stratus is an important current topic. A key element to understanding the process is the characterization of the spatial and temporal history of drizzle drops. Simple upward moving parcel descriptions are clearly invalid in stratus. While the desired histories are unobtainable, some clues can be derived from the associations of drizzle drops, and of other droplets, of different sizes with air motions. This is the topic addressed in this paper, restricting the analyses at this stage to vertical air motions.

2. Basic features

Vertical motions of cloud (d < 50 μm) and drizzle drops within the cloud are not easily observed. These motions are a combination of turbulence and of regions of updrafts and downdrafts.

Several previous studies have shown positive correlations between upward air velocity (positive *w*) and FSSP measured droplet concentration (N_{FSSP}) in marine stratus or stratocumulus clouds (Curry, 1986; Hudson and Svensson, 1995; Hudson and Li, 1995, Vali et al., 1998, hereafter V98). These correlations apply to *N* and *w*-values averaged over roughly 100-m scales. In contrast, the liquid water content (LWC) contributed by cloud droplets (d < 50 μm) was generally found to be independent of *w*. In concert with these facts, the volume mean diameter of cloud droplets show negative correlations with *w*.

Because the concentrations of drizzle drops (d > 50 μm) are much lower than those of cloud droplets, sampling problems make it difficult to examine correlations with air velocities from in situ data. V98, using an airborne cloud radar showed that higher reflectivities (*Z*), i.e. regions of greater drizzle drop concentrations, coincided with smaller downward Doppler velocities (*V*) in the upper halves of cloud decks. In contrast, the expected coincidences of regions of higher reflectivities and larger downward Doppler velocities were found in the lower half of the cloud decks. These observations were made in unbroken stratus situations.

Dept. of Atmosperic Science, University of Wyoming, P.O. Box 3038, Laramie, WY, 82071. 307-766-4447 (v) 307-766-2635 (fax); sgill@uwyo.edu; vali@uwyo.edu.

For the cases presented in V98 the in situ data from a PMS 1-DC probe (N_{oned}) showed positive correlations with the vertical air velocity. Possible explanations for the *Z*-*V* and N_{oned} - *w* correlations in the upper parts of clouds were seen as either reduced drizzle concentrations in downward moving air originating from entrainment, or increased drizzle concentrations in upward moving air.

3. New analyses.

In order to further refine the analyses, we have now moved from the simple cloud droplet vs. drizzle droplet stratification to an examination of spectral characteristics up to the resolution available from the FSSP and 1-DC probes. We have done this with both the data previously described in V98 and with additional observations made in 1999. Such analyses can only be performed with data of reasonable homogeneity over large sample regions, typically about 50 km in horizontal extent.

Further analyses were also directed toward shedding light on the nature of the correlations between vertical air velocity and drop concentrations. We have tried to identify the local events that lead to the correlations.

The 1999 field studies (Coastal Stratus 1999, or CS99) were again conducted in unbroken marine stratus off the coast of Oregon and utilized the Wyoming King Air and the Wyoming Cloud Radar (95 GHz airborne radar).

4. General cloud characteristics

Data from two days will be discussed in some detail in this paper. On 15 September 1995 a solid cloud cover, without visible breaks, was observed 30-80 km off the Oregon Coast. This day was analyzed in detail in V98. It is recommended that the reader consult this paper for more details about the observations made on this day. Cloud base was at about 380 m and cloud top was at 700 m. The lapse rate from the surface up to cloud top was –5.0 °C/km. The temperature inversion at cloud top was 7 °C over a 100-m height interval. The average LWC near cloud top was about 0.55 g m^{-3}, about 90% of the adiabatic value.

The second day, 17 August 1999 also had a solid cloud cover for most of the region studied. The area studied, again, lies 30-80 km off the Oregon Coast. Cloud base was about 400 m and cloud top ranged from about 730 m to 800 m. The lapse rate from near the surface to 500 m was about –9 °C/km and the lapse rate from this height to the inversion at cloud top was about –4 °C/km. The temperature above cloud top increased 7 °C over a distance of 200 m. The temperature at cloud base was 12 °C. The average LWC value for the cloud was 0.6. An adiabatic value of LWC would be near 0.7.

5. Radar observations

A representative vertical cross-section of the reflectivity field is shown in Fig.1 for 17 August 1999. Maximum reflectivities were about –2 dBZ. The reflectivity field is similar to the reflectivity field for 15 September 1995 in V98. A cellular structure in the echoes can be seen; the high reflectivity cells extend downward from near echo tops. There is a thin layer of relatively uniform structure at the upper echo boundary. Echo top is less uniform in height than was the 15 Sept. 1995 case.

The correlation between reflectivity and Doppler velocity for 17 August 1999 shows the same reverse S shape as was described in V98. This has been also seen in several of the days analyzed so far in the CS99 data. At lower altitudes, higher reflectivity values correspond to downward Doppler velocities as would be expected when drizzle is present. However, the correlation reverses in the upper third of the cloud.

6. Vertical velocity correlations

Correlations between w and in-situ measurements of LWC, N_{FSSP}, N_{oned}, and mean drop size were examined for different level flight segments in the cloud deck. For all the days analyzed in V98 correlations between w and LWC were relatively weak at all heights in the cloud. Most were below 0.1 and the highest correlation of 0.3 was observed only once. The CS99 data yielded different results. For 17 Aug 1999, and for other days from CS99, correlation values are generally above 0.2 at various levels in the cloud deck, both low and high. There are several values above 0.3, and two highest values are 0.41, and 0.46. Correlations between w and N_{FSSP} are also strong. Correlation values for 15 Sept. 1995 were 0.39 in the upper part of the cloud deck and 0.44 in lower part of the cloud deck. For 17 Aug. 1999 correlations are between 0.26 and 0.46 for flight levels ranging from just above cloud base to about two thirds of the cloud depth. Correlations between w and N_{FSSP} are strong for all days studied during CS99.

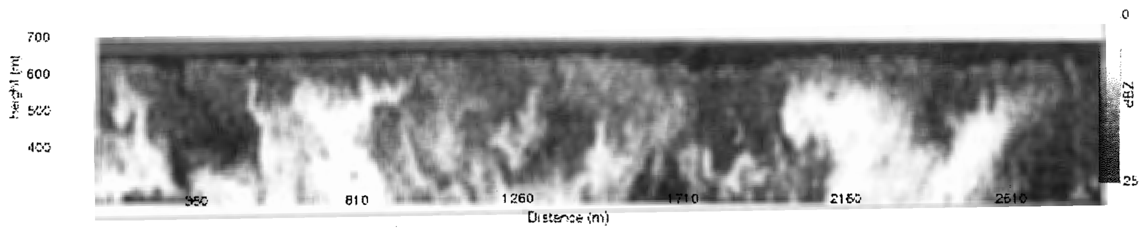

Fig. 1. *Vertical cross-section of the cloud deck for 17 August 1999 as observed by the Wyoming Cloud Radar on board the King Air. The distance traversed in the cross-section is nearly 2.8 km. The y-axis represents height in meters above sea level. Reflectivity ranges from 0 to –25 dBZ.*

A more detailed analysis of the nature of the correlations in the 1999 data was performed by comparing deviations in LWC and in *w from* their surrounding mean values over scales varying from 20-100 m. In general both coincidences of increases in LWC and increases in w, and coincidences of decreases in LWC and decreases in w were found. However, the number of the latter events far outweighed the former. This finding indicates a dominant role of downward moving air with reduced LWC, possibly as a result of entrainment of drier air from cloud top.

It should also be noted that on one occasion during CS99 (21 Aug 1999) we found a fairly strong negative correlation between LWC and w (values between –0.25 and -0.34). This day does not support the claims made above and so the idea of diluted regions of downward moving air does not seem to be a general one. Examination of the specific 'events' showed that on this occasion lower LWC accompanied positive pulses in w, while negative pulses in w had higher LWC. More analysis is needed to determine why this day is different.

Both 15 Sept. 1995 and 17 Aug. 1999 showed strong negative correlations between w and mean drop diameter. Other days studied in both 1995 and 1999 consistently show this correlation at all levels within the cloud deck. Values generally showed magnitudes greater than –0.15, going as high as –0.53. There seems to be no trend between weak correlations and height within the cloud deck. The strong negative correlations between mean drop size and w are also supportive of new drops being created in updrafts. The correlation between w and N_{onedc} (drops with d > 50 μm) is weak for 17 Aug. 1999: a maximum value of 0.26 occurs at lower levels in the cloud. This contrasts with the value of 0.45 for 15 Sept. 1995 in the upper portion of the cloud deck..

7. Vertical velocity correlations with different drop size ranges.

In order to further dissect the correlations described in the preceding, the relationships between w and the concentrations of drops in individual size bins of the 1-DC and the FSSP probes were investigated. A representative result is shown for a data segment (27 km in extent) from 15 Sept. 1995 in Fig. 2. These data are for 480 m altitude, about 1/3rd of the way up in the cloud layer.

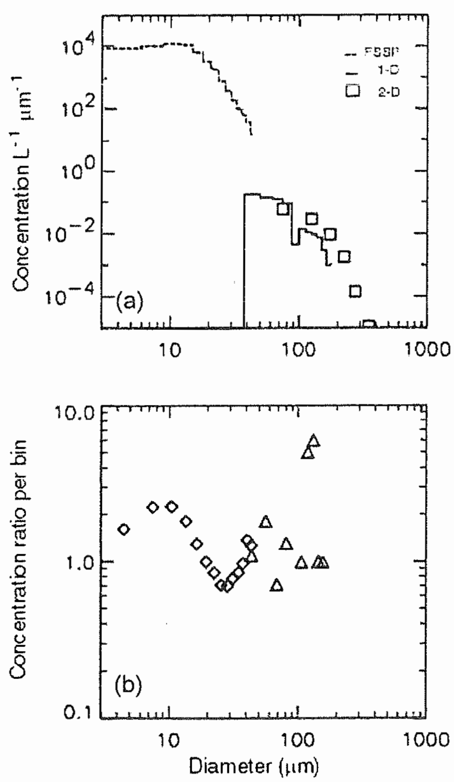

Fig. 2. *(a) Cloud drop distribution from FSSP, 1-D and 2-D data on 15 September 1995. (b) Plot showing the ratio, for each bin of the FSSP and 1-D probe, of drop concentrations in the 80th percentile of vertical velocities to drop concentration in the lower 20th percentile of vertical velocities.*

In order to maintain sufficient sample sizes in spite of the stratification by droplet size, the comparison is restricted to the uppermost and lowest 20% of the vertical air velocity. For the data shown in Fig. 2, the mean value of w for the uppermost 20 % of vertical velocities is +0.38 m s^{-1} . The mean N_{FSSP} value corresponding to these velocities is 196 cm^{-3}, the mean FSSP-calculated LWC is 0.24 g m^{-3}, and the total calculated reflectivity is –20 dBZ. For the lowest 20 percent of vertical velocities, the mean w is –0.48 m s^{-1}, N_{FSSP} = 115 cm^{-3}, FSSP calculated LWC is 0.2 g m^{-3}, and the total calculated reflectivity is –21.5 dBZ.

The ratios of concentrations in the uppermost to the lowest 20 percent of vertical velocities for the different drop sizes is shown in the lower panel of Fig. 2. Values significantly different from unity are evident. A first peak occurs at a diameter of about 10 μm with a ratio of drop concentrations of about 2.5, i.e. there were 2.5 times more droplets of these sizes in areas of the largest upward velocities than they were in areas of largest downward velocities. The second significant region of departures from unity is at a diameter little larger than 20 μm. The ratio at this dip is about 0.6 indicating that there are nearly twice as many drops of this size in downward moving air than in upward moving air. The third size region of interest is that of the drizzle drops (from the 1-DC data) where ratios are generally above unity and have values of about 6 near 120 μm diameter.

The pattern shown in Fig. 2(b) has been observed for about 22 level flight segments from 8 days at various heights within the cloud decks. There seems to be no dependence of the shape of this curve on height within the cloud deck. For almost all the days studied from 1995 and 1999 data, ratios at the first peak ranged from 2-3, for diameters of 9-11 μm. The dip in the curve has also been observed consistently, and found to be similar in amplitude and location, for all days analyzed, at all levels within the cloud deck. For the drizzle sizes, the range of ratios found on other days was from 2 to 7, at diameters from 50-100 μm. In the largest size bins of the 1-DC probe, ratios almost always drop to values of unity or slightly lower.

8. Conclusions

Data from the 1995 and 1999 observations support the findings of previous studies, as well as provide new information about the evolution of the droplet spectrum in unbroken marine stratus.

The positive correlation between cloud droplet concentrations and vertical velocity seems to be a quite general feature of marine stratus and stratocumulus. Our analyses show that this correlation is dominated by droplets of about 10 μm diameter and does not extend over the entire range of cloud droplet sizes. Indeed a negative correlation is the rule for droplets around 20 μm diameter. The pattern reverses again for drizzle drops, which are found in higher concentrations in upward moving air than in downward moving air. This latter finding is also supported by the correlation of radar reflectivity and Doppler velocity. There is a yet unresolved disagreement between the radar data and the in situ data, in that the correlation in the radar is as just described only in the upper 1/3 of the cloud layers while the in situ data show the same pattern at all heights within the cloud. The negative correlation for drops around 20 μm diameter is a puzzling result, which is yet to be explained.

The correlation between vertical air velocity and LWC appears to be variable from case to case. No correlation was reported by V98. Most of the 1999 data so far examined show reasonably strong positive correlations. One case in 1999 exhibited a strong negative correlation.

Examinations of the individual events (coincident local peaks in vertical velocity and in N_{FSSP} or LWC), which lead to the statistical correlations, reveal that in the 1999 data the strongest signals are from downward moving air and reduced N_{FSSP} or LWC. Negative buoyancy due to entrainment of dry air and evaporation may be one of the reasons for this observation, but other possibilities exist and we have not yet pursued the question far enough to know which explanation is the most credible.

Acknowledgements. We would like to thank our sponsor, the Office of Naval Research. As well as all the members of the University of Wyoming King Air Flight Facility. Especially we would like to thank M. Hoshor, L. Irving, L. Oolman, G. Gordon, D. Leon, S. Haimov, and R. Kelly.

9. References

Curry, J. A., 1986: Interactions among turbulence, radiation, and microphysics in Arctic stratus clouds. *J. Atmos. Sci.,* **43,** 90-106.

Hudson, J. G., and H. Li, 1995: Microphysical contrasts in Atlantic stratus. *J. Atmos. Sci.,* **52,** 3031-3040.

Hudson, J. G., and G. Svensson, 1995: Cloud Microphysical Relationships in California Marine Stratus. *J. Appl. Meteor.,* **34,** 2655-2666.

Vali, G., R. D. Kelly, J. French, S. Haimov, D. Leon, R. E. McIntosh, and A. Pazmany, 1998: Finescale Structure and Microphysics of Coastal Stratus. *J. Atmos. Sci.,* **55,** 3540-3564.

Observed Boundary Layer Humidity Distributions and Errors in Parameterised Cloud Fraction

By Jeremy D. Price[1]

The Met. Office, UK

1. Introduction

Cloud fraction parameterisations often use specific probability distributions for humidity, an early example of which was presented by Sommeria and Deardorff (1977). Smith (1990), describes a triangular distribution function which is the scheme currently used by the UK Meteorological Office. The cloud fraction is calculated by estimating the fraction of the distribution which is moister than the saturation value. A variation of the scheme discussed by Smith (1990), is presented in Cusack et al (1999) for use at climate scales. In their work, the width of the triangular function is scaled individually for each grid box in an attempt to simulate the sub-grid scale humidity distribution. The method used to estimate the sub-grid scale humidity variation is a statistical one which interpolates the resolved grid scale features to smaller scales by assuming a spectral power law which follows a –5/3 slope. This approach appears to give improved climatological scale cloud fraction estimates compared to the earlier scheme by Smith. However, spectral power plots often show variation from a slope of –5/3, and therefore it might be expected that a more physically based estimation of sub-gridscale variation of humidity may show further benefits.

The aim of the present paper is to use experimental data to examine boundary layer humidity probability distributions for a selection of different boundary layer types and test the effectiveness of various parameterised distributions. The emphasis is on understanding the small-scale structure on scales of a few kilometres, which are relevant to mesoscale sub-grid parameterisations. Experimental data were examined from nine boundary layer case studies, which were chosen from a much larger number of cases to represent a wide range of atmospheric conditions. From those cases humidity distributions were deduced for forty-two discrete periods/altitudes. Four types of mathematical function are fitted to the data: A normal beta distribution, a symmetric beta distribution, and two triangular functions with different width. The first is scaled to fit the data while the second is scaled to fit the intrinsic distribution (see later). The performance of each of these functions is assessed by comparing their errors in the estimate of cloud fraction. Section two presents the experimental data and discusses various types of humidity distribution and section three presents the analysis of cloud fraction errors.

2. Humidity Distributions

(a) Definitions and initial analysis

Data used for this study were collected with the UK Meteorological Office tethered balloon facility between 1996 and 1999. The experiments were typical boundary layer studies, examples of which can be found in Price (1999) and Price (2000). Data used were from level turbulence runs, where probes are placed at a fixed height for periods of approximately one to three hours. The resulting time series were divided into sectors which represented a range of length scales from ~2-20km. These length scales were simply defined as the distance air was advected during each sector. As such, data in each sector will approximate to the range of values present in a grid box with a size equal to the length scale, and over the time period taken for the air parcel to advect over the observation site. Actual total specific humidity (i.e. liquid plus vapour) probability distributions were calculated using a bin-type method whereby the range of observed values was divided into 100 sub-ranges. It became apparent on plotting a number of distributions that although there was a wide variety of shapes and widths, they could be classified into four basic types. These were defined as: gaussian, skewed, platykurtic and multimodal types, depending on how closely each conforms to a simple unimodal gaussian type distribution. The formal definition is as follows:

> Gaussian, 'G' type: distribution is unimodal, symmetric or nearly symmetric and close to a gaussian or triangular shape.
>
> Skewed, 'S' type: distribution is unimodal, but has significant skewness. Also includes types with small skewness but a flattened non-gaussian/triangular peak.
>
> Platykurtic, 'P' type: distribution is poorly defined with either no clear singular peak in the distribution, or a very wide peak of non-gaussian or triangular shape.

[1] Authors address: Meteorological Research Unit, Cardington Airfield, Shortstown, Bedfordshire, MK42 0SY, UK; E-mail, jdprice@meto.gov.uk

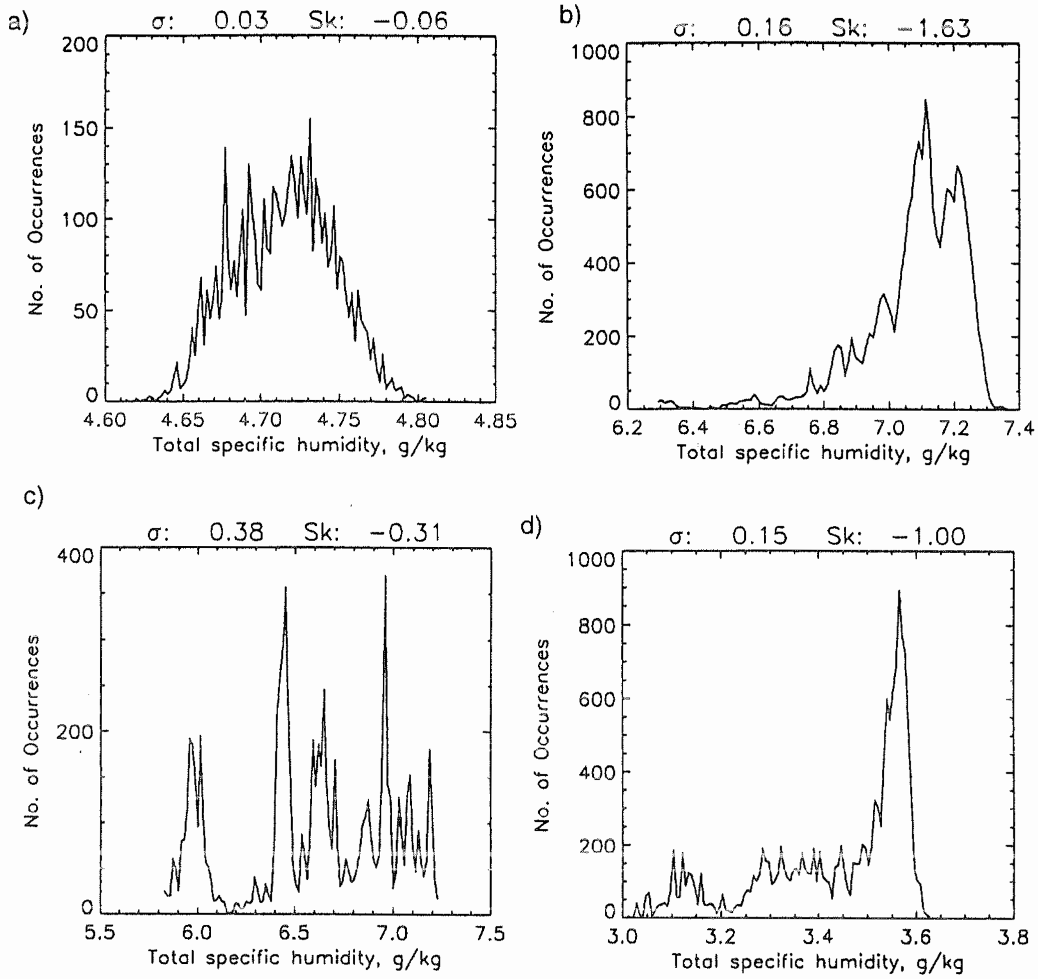

Figures 1a-d. a) Example of an observed total specific humidity distribution, standard deviation and skewness for a G type distribution. b): as a), but for an S type distribution. c): as a), but for a P type distribution. d): as a), but for an M type distribution.

Multi-modal, 'M' type: similar to P type but where there are at least two distinct populations in the distribution.

P and M types are likely to be more difficult to model due to their poorly defined shape. Examples of each type of distribution are given in figures 1a-d. Typically, G type distributions were found to have the narrowest width with maximum and minimum values of specific humidity normally having a difference of $\leq 1 gkg^{-1}$. P type distributions normally have the widest width which can be several gkg^{-1}. The minimum, average and maximum distribution standard deviations of the 42 data series examined were, 0.02, 0.28 and 1.73 gkg^{-1} respectively. The distribution widths therefore showed considerable variation. The relative abundance of each type of distribution in the data sampled is given in table 1.

Table 1

Distribution type	G	S	P	M
Percentage occurrence	12	38	26	24

It can be seen from the table that G type profiles are relatively rare and that S type is the most common. The split between profiles that are relatively well defined (G & S type), and those poorly defined (P & M type) is 50/50. It was found that profiles near the ground were almost always G or S type, whilst those away from the surface layer were rarely G type.

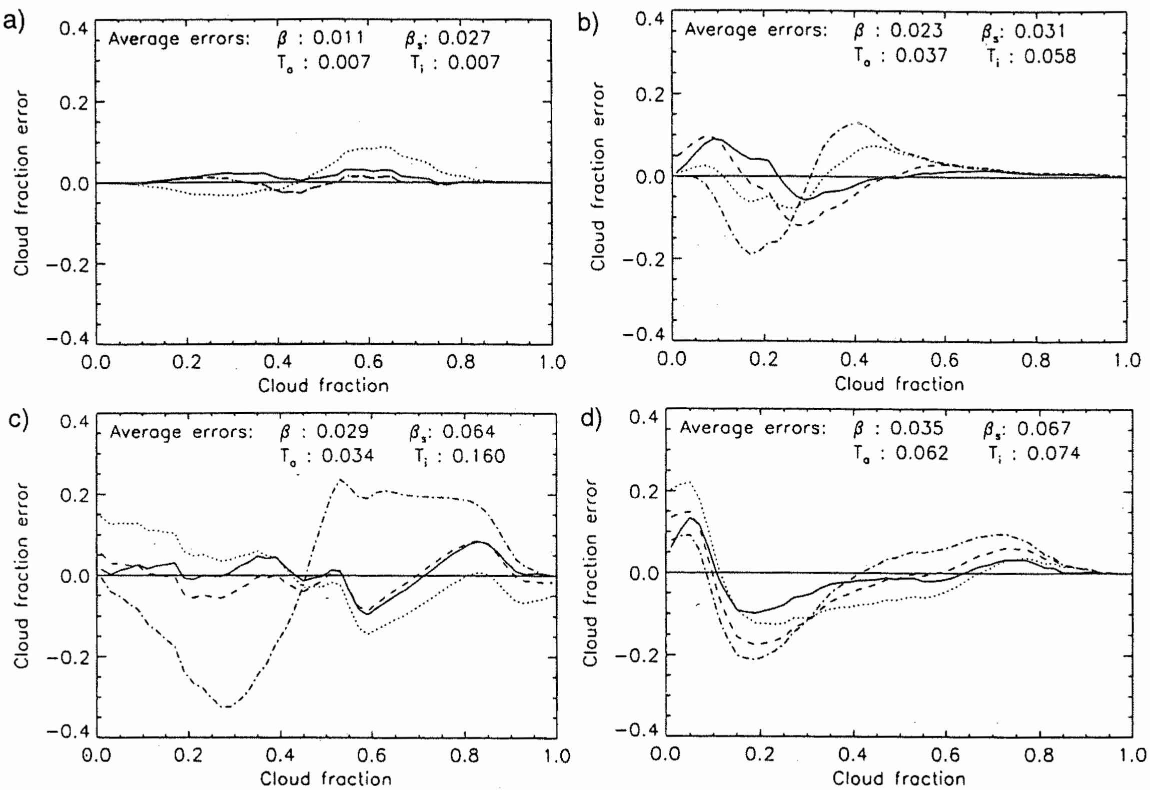

Figures 2a-d Calculated cloud fraction errors as a function of cloud fraction for the four respective distribution types and four fitted functions. Solid line; beta function: dotted line; symmetric beta function: dashed line; advective triangular function: dot-dash line; insitu triangular function. b) as a), but for S type distribution. c) as a), but for P type distribution. d) as a), but for M type distribution.

(b) advective processes

Examination of any time series will normally indicate whether advection modulates the distribution. Advection was seen to have the effect of significantly broadening some distributions. By using a linear or polynomial regression, it is possible to separate the advective from the intrinsic insitu distribution. A quadratic regression was used with the data in this study. It was noted that after removal of advection, the remaining intrinsic distribution usually became more gaussian in nature, indicating that intrinsic distributions are G or S type, and become broadened by advection. The relative importance of advective and insitu effects on the original time series can be deduced from the ratio of their standard deviations. In general the insitu distribution was slightly wider with the average value of the ratio σ_a / σ_i =0.84. Both processes therefore play an important role in forming the distribution.

The data were also used to investigate the relation between σ_a and the length scale of the time series. Results showed a lot of scatter in the data and that for length scales of 5km or less, σ_a may be considered negligible, but becomes larger and increasingly important at longer scales. However, this relation is approximate and estimates of σ_a from length scale will be prone to significant error.

Distributions in relative humidity were also examined and seen to be similar to those in specific humidity

3.Cloud fraction errors

The definition of cloud fraction appropriate to a humidity probability density function, *f(x)* is,

$$C_f = \frac{\int_{q_{sat}}^{\infty} f(x)}{\int_0^{\infty} f(x)}$$

where q_{sat} is the normalised saturation value of specific humidity. At any given value of q_{sat} the cloud fraction error for a given distribution is ,

$$e_c = \frac{\int_{q_{sat}}^{\infty} f(x)}{\int_0^{\infty} f(x)} - \frac{\int_{q_{sat}}^{\infty} f(o)}{\int_0^{\infty} f(o)} \qquad 1$$

where *f(o)* is the observed distribution function. Equation (1) was used to evaluate the cloud fraction error over 50 intervals of humidity for each of the four distribution functions. The results, for the four data series presented in figure 1, are shown in figures 2a-d, which display the error as a function of cloud fraction. The average error over the entire fraction range is also presented. Immediately obvious from these figures is that the cloud fraction error is a strong function of cloud fraction in most cases, and that the location of the maximum errors depends mainly on the observed distribution. Typically the error will oscillate and change sign throughout the cloud fraction range. As expected, figure 2a, which depicts the G type distribution, shows small errors from all of the functions throughout the cloud fraction range. Errors for the S distribution are significantly larger (except β_s) than for the G distribution. Note that since the β function has accounted for the skewness, its error is significantly smaller than the other distributions, and that the T_i function error is significantly larger than average due to its inability to represent the advective term. Figures 2c and 2d shows a similar result to 2b. Note that at certain cloud fractions the errors can be large. Although average errors over a range of climatologies may be small, local errors, which are of significant importance for weather forecasting services, may be very significant. It is therefore important to choose a distribution function which minimises both climatological and local errors. Bearing in mind those criteria, in the study conducted here the β function consistently performed best, followed by (in order) T_a, β_s and T_i. The average of all these data are given in table 2.

Table 2

Distribution function	β	β_s	T_a	T_i
Average cloud fraction error	0.035	0.054	0.039	0.056

The most important conclusion to be made from table 2, by comparison of T_a and T_i is that accounting for advective influences on humidity distributions can significantly reduce the cloud fraction error (by approximately 30%).

References

Cusack, S., J.M. Edwards and R. Kershaw, 1999: Estimating the subgrid variance of saturation and its parametrization for use in a GCM cloud scheme. Q.J.R. Meteorol. Soc., 125, 3057-3076

Price, J.D., 1999: Observations of stratocumulus cloud break-up over land. Q.J. R. Meteorol. Soc., 125, 441-468

Price, J.D., 2000: A Case Study of a Partially Cloudy Boundary Layer. Q.J. R. Meteorol. Soc., 126, No. 563 B,393-413.

Smith, R.N.B., 1990: A scheme for predicting layer clouds and their water content in a general circulation model. Q.J.R. Meteorol. Soc., 116, 435-460

Sommeria, G., and J.W. Deardorff, 1977: Subgrid-scale condensation in models of non-precipitating cloud. J. Atmos. Sci., 34, 344-355

ON THE INFLUENCE OF ICE PRECIPITATION ON STRATUS CLOUD DYNAMICS OVER THE MARGINAL ICE ZONE

Jerry Y. Harrington[1] and Peter Q. Olsson[2]

[1]Geophysical Institute, University of Alaska Fairbanks, Fairbanks, Alaska
[2]Alaska Experimental Forecast Facility, University of Alaska Anchorage, Anchorage, Alaska

1. INTRODUCTION

The marginal ice zone (MIZ), and the overlying atmosphere, make-up a unique coastal environment which is characterized by sharp changes in surface and atmospheric properties as one traverses the ice edge. Of particular importance is the dramatic contrast between the surface sensible and latent heat fluxes of the solid ice sheet and the open ocean.

The atmospheric/oceanic response to this strongly discontinuous region is complicated and reveals sensitivity to ambient stratification, large-scale flow strength and direction, vertical and horizontal shear, and cloud cover. During periods of off-ice flow cold, stable air is subjected to large surface heat and moisture fluxes producing explosive convective development (Lupkes and Schlutzen 1994). This is particularly true when the air originating over the ice pack has been static for a significant period of time (e.g. Curry 1983). The flow of extremely cold air off of the ice pack, which is often referred to as a "cold-air outbreak", is accompanied by intense convection, precipitating mixed-phase clouds, and significant BL modification.

Over the past decade, there has been some effort to model the convective development which occurs during off-ice flow. A large portion of this work to date has focused on either thermal internal boundary layer development (e.g. Lupkes and Schultzen 1996), momentum impacts due to spatial-ice variation induced changes in surface drag (e.g. Kantha and Mellor 1989), and on the development of roll convection (e.g. Chlond 1992). However, few efforts have been directed towards understanding the impacts of cloudy processes on the BL over the MIZ. The work of Rao and Agee (1996) and Olsson and Harrington (2000) showed that both liquid-phase and mixed-phase clouds have a significant impact on TIBL development over the MIZ. An issue left unaddressed by that work, is the influence of ice crystal concentration on BL development. In particular, the impact of ice nuclei (IN) concentrations, which can strongly constrain the cloud dynamics (e.g. Harrington et al. 1999), is not well understood. In this work, we make an initial attempt to examine the potential importance of the ice phase, and IN concentrations, on strongly surface forced BLs.

Corresponding author's address: J. Y. Harrington, Geophysical Institute, University of Alaska Fairbanks, Fairbanks, AK, 99775. E-Mail: jerry.harrington@gi.alaska.edu

2. NUMERICAL MODEL

The numerical model used in this work is a version of the Regional Atmospheric Modeling System (RAMS) developed at Colorado State University. This model has been used in both 2-D eddy resolving model (ERM) and fully 3-D large eddy simulation (LES) mode to study the Arctic BL (e.g. Harrington et al. 1999). Because of the exploratory nature of this study, we use the ERM since it is computationally expedient but still captures the essence of the dynamic-microphysics-radiation interactions (Harrington et al. 1999).

The dynamic framework is coupled to a sophisticated microphysical model (Walko et al. 1995). This model represents the evolution of various liquid and ice hydrometeor species, and the various conversions between different species. While complex and state-of-the-art, the model is limited in that certain components of the hydrometeor size spectra must be prescribed *a priori.*

This microphysical model is coupled to a detailed two-stream radiation scheme (Harrington and Olsson 2000) which computes absorption by gaseous H_2O, CO_2, and O_3, and scattering and absorption by liquid and ice hydrometeors.

3. REFLEX II March 4, 1993 CASE

The case used for these studies is one that was observed during the Radiation and Eddy Flux Experiment (REFLEX II) in 1993 off the northwest coast of Spitsbergen. The off-ice flow on this day brought exceedingly cold and stable air (T_{surace} ~ -35C) over a relatively warm ocean (SST ~ 0C). The surface sensible and latent heat fluxes from the ocean produced intense convection and rapid BL development (Lupkes and Schultzen 1996). Organized roll convection was produced a short distance off the ice edge (~ 50 km) which was transformed to cellular convection further over the open ocean (~ 200 km).

4. NUMERICAL STUDIES

The RAMS model was set up for this study with a (x,z) domain size of 8.4 by 4.6 km. The grid-spacing used was $\Delta X =$

60m and $\Delta Z = 30$ m. To simulate the effect of moving this grid over a warm ocean, the lower SST boundary of the model was warmed using the SST-gradient given in Lupkes and Schultzen (1996).

Studies were conducted in which the hydrometeor phase is varied systematically. Table 1 lists acronyms for the various simulations. We begin with simulations using the non-precipitating, liquid-phase bulk microphysics (LP). We then include the effect of the ice-phase on the MIZ BL evolution by using the standard ice nucleation formulations (IN_S) in the bulk microphysics (MP_INS). This is important because ice nucleation at these temperatures (T > -35C) is predominately heterogeneous (i.e. due to IN), and ice concentration strongly influences precipitation fluxes out of mixed-phase stratus (Harrington et al. 1999). Unfortunately IN are only marginally understood in general, and this is especially true at high latitudes (Bigg 1996).

TABLE 1. MIZ Sensitivity Simulations

Simulation	Acronym
Liquid-phase	LP
Mixed-phase, IN_s	MP_INS
Mixed-phase, $IN_s/10$	MP_INT
Mixed-phase, $IN_s/100$	MP_INH

Because of this, we undertake a set of exploratory sensitivity simulations in which IN concentrations are reduced by a factor of 10 and 100 (MP_INT and MP_INH, respectively). This is done to emulate relatively clean arctic conditions, since the IN formulations used in most models are from lower latitudes (Walko et al. 1995).

4.1 Comparison of microphysical schemes

In this section, we intercompare LP and MP_INS. Figure 1 shows contours of the liquid water content (LWC) and ice water content (IWC) superimposed on contours of turbulent kinetic energy (TKE) as a function of time. In the case of LP, the water content increases in time as strong surface latent ($F_{l,sfc}$ ~ 180 W m^{-2}) and sensible ($F_{s,sfc}$ ~ 300 - 500 W m^{-2}) heat fluxes moisten and deepen the BL (reaching nearly 2400 m by 8 hrs). Significant cloud top radiative cooling, in conjunction with strong surface heating, produces TKE as large as 30 m^2 s^{-2}. The addition of the ice phase produces a drastically different cloud evolution. In MP_INS, the liquid phase is essentially depleted by ~ 1 hr by glaciation. Water contents are lower than LP and they undergo strong undulations with time. The BL is less deep (reaching ~ 1800 m by 8 hrs) and much less turbulent (TKE < 8 m^2 s^{-2}). Comparison with observations show that the inclusion of the ice phase drastically improves the prediction of BL depth and structure.

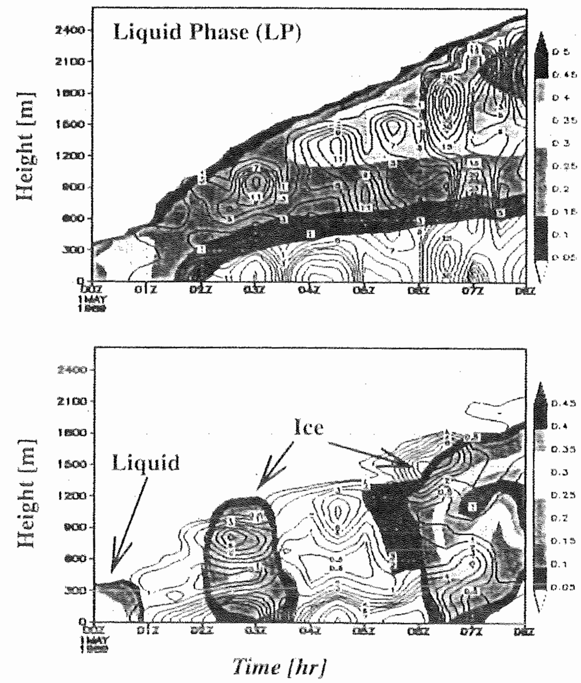

FIGURE 1. Shaded contours are water content (g m^{-3}) while solid contours are TKE (m^2 s^{-2}).

So, what is the reason for the significantly reduced TKE and BL depth in the case of mixed-phase clouds? Figure 2 shows an x,z cross-section of clouds and eddies at ~ 230 km from the ice edge. Note that the water contents (mostly ice) are high in the updraft regions and that the downdraft regions are essentially clear. In comparison to the liquid-phase case MP_INS has significantly less water content at the top of the cloud due to ice precipitation. Thus, weaker cloud-top radia-

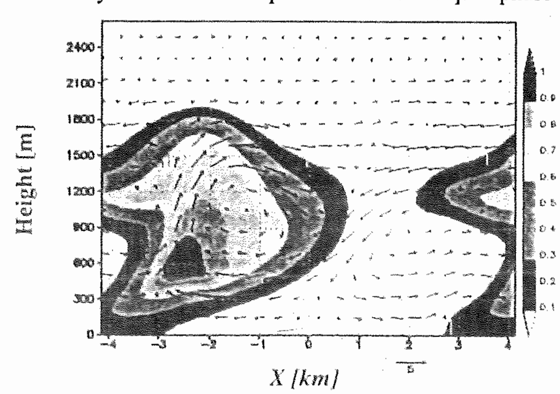

FIGURE 2. Shaded contours are ice water content (g m^{-3}) while solid vectors are w and perturbation u (m s^{-1}) for case MP_INS.

tive cooling occurs in MP_INS and this reduces the strength of the circulations. However, there are two more important reasons for the reduction in TKE and BL depth in MP_INS.

Figure 3 shows profiles of the updraft and downdraft buoyancy flux for both LP and MP_INS corresponding to the location in Fig. 2. Note that in the case of LP both updrafts and downdrafts are producing TKE, except for the negative entrainment flux at the top of the downdrafts. This, however, is not the case for MP_INS. Updrafts are still positively buoyant and producing significant TKE. However, downdrafts are warm leading to TKE consumption, and reduced eddy strength. This occurs because, during significant glaciation, ice is precipitating rapidly out of updrafts (Fig. 2). However, the

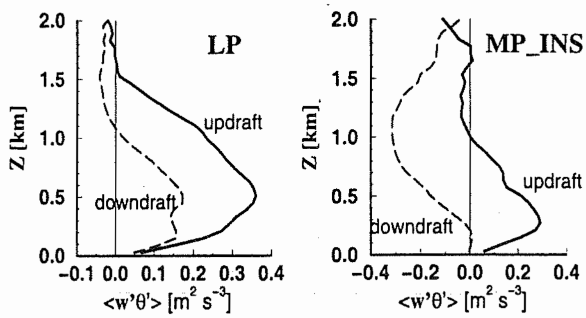

FIGURE 3. Updraft and downdraft buoyancy flux for the time-period shown in Fig. 2. Labels on figure.

latent heat released during vapor deposition remains in the updraft and this warmed air must now be forced down in downdrafts, consuming TKE. This mechanism is similar to that posed by Stevens et al. (1998). Because circulation strengths are reduced during glaciation, so are downward momentum fluxes, and this reduces surface wind speeds and, hence, surface heat fluxes. This process also drives down the TKE, as we shall see in the next section.

4.2 Sensitivity Studies

The above simulations of mixed-phase clouds have ice concentrations that vary between 1 and 25 L^{-1}. This is somewhat higher than ice nuclei measurements in the Arctic (e.g. Bigg 1996). Because of this, we reduce the modeled IN concentrations by a factor of 10 and 100 (MP_INT and MP_INH) for better agreement with observations. Additionally, this allows us to illustrate how strongly BL dynamics are modulated by ice precipitation.

Figure 4 shows the evolution of the liquid and ice water paths (LWP, IWP) for the sensitivities in Table 1. With respect to MP_INS, fewer IN produces larger ice crystals with shorter in-cloud residence times. Thus, the impact of the Bergeron-Findeisen process is weakened, allowing for liquid to persist further into the model run before complete glaciation occurs

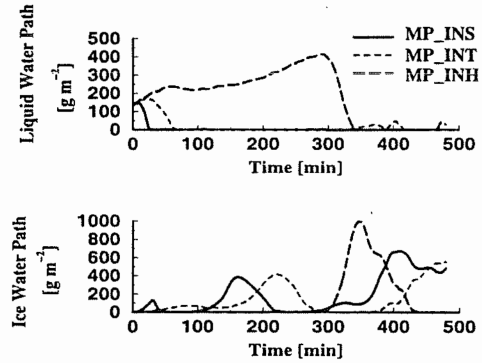

FIGURE 4. LWP and IWP for sensitivities in Table 1.

(MP_INH). This delayed glaciation occurs because it takes a significant amount of time for crystal concentrations to build to critical levels.

The number of IN has a significant impact on the strength of the convection (Fig. 5), even in this strongly surface forced case. The case with few ice crystals (near 0.1 L^{-1} in MP_INH) has BL convection similar to LP (not shown) until glaciation occurs. At that point, heavy ice precipitation reduces TKE and w_* from ~ 7 m s^{-1} to ~ 2 m s^{-1}. Periods of heavy precipitation

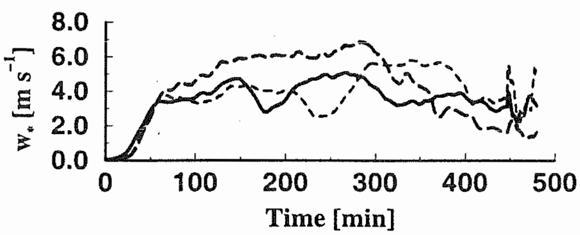

FIGURE 5. Convective velocity for cases labeled in Fig. 4.

from mixed-phase stratus tend to be more prevalent than from pure liquid clouds and this enhances the stabilizing influence discussed above.

As TKE is reduced through ice precipitation, downward momentum fluxes in the BL also decrease. This has the effect of decreasing the surface wind speeds by up to 3.5 m s^{-1}. Since surface sensible and latent heat fluxes ($F_{s,sfc}$ and $F_{l,sfc}$ respectively) depend strongly on surface winds, ice precipitation has a significant impact on these quantities. As one can ascertain from Fig. 6, $F_{s,sfc}$ and $F_{l,sfc}$ can vary by as much as 60 - 120 W m^{-2} depending on the IN concentration. Of course, this feeds back into the BL convection. For example, in MP_INH, the insignificant precipitation at time < 300 min has a weaker stabilizing influence on the BL and $F_{s,sfc}$ is similar to the other sensitivities. Once glaciation occurs, strong precipitation reduces convective mixing which reduces the wind-speeds at the surface and, therefore, reduces both $F_{s,sfc}$ and $F_{l,sfc}$. This

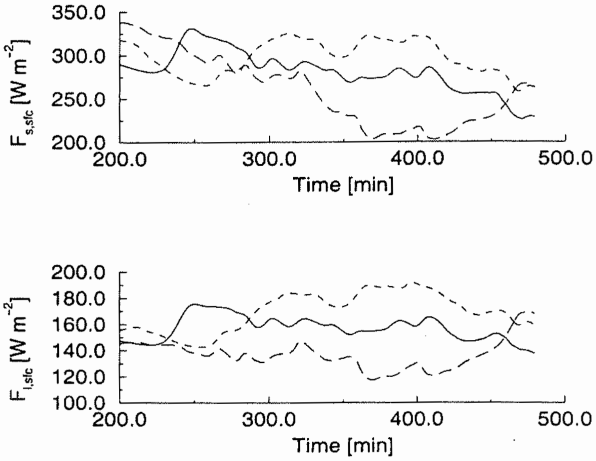

FIGURE 6. Surface sensible and latent heat fluxes. Lines are labeled as in Fig. 4.

causes further reductions in TKE, which further reduces the surface winds. Hence, this constitutes a positive feedback process whereby ice precipitation stabilization of downdrafts works in conjunction with reduced $F_{s,sfc}$ and $F_{l,sfc}$ to further drive down convection.

Whether or not processes such as these would have an effect on phenomena such as ice rafting and the MIZ ice distribution would depend on whether or not significant glaciation occurs closer to the ice edge.

5. CONCLUDING REMARKS

In this work, we have undertaken a set of exploratory studies to examine the potential impact of ice-phase microphysics on the BL and surface processes. Earlier works have, for the most part, ignored detailed cloud processes over the MIZ. The work of Harrington et al. (1999) illustrate that ice-phase processes have a strong impact on cloud-scale dynamics. However, ice nucleation (T < -35C) is predominately due to IN which then controls ice concentration and, hence, ice precipitation. This motivated the current exploratory studies.

The exploratory work of the preceding sections shows the following:

- Mixed-phase clouds have a significant impact on BL dynamics in strongly surface force situations.
- Periods of glaciation, and significant ice precipitation, produces BL stabilization in three ways. The first is through direct stabilization of downdrafts, the second is through reduced surface heat fluxes, and the third is through reduction in cloud-top radiative cooling.
- Glaciation, and the attendant reduction in BL circulation strength, is dependent upon IN concentrations which control precipitation. For cases with lower IN concentrations, LWPs can persist and increase. This delays glaciation, but when glaciation does occur the effects of precipitation are stronger.
- Reduced surface sensible and latent heat fluxes are caused by reductions in surface wind-speed. In turn, this is produced by weakened convection due to precipitation, which reduces momentum fluxes to the surface.

While the above issues are intriguing, they must, at this point, be considered hypothetical. Further studies are needed with more complete data-sets.

ACKNOWLEDGEMENTS

The authors appreciate the funding provided to them by the International Arctic Research Center and NSF Grant OPP-9732733. We are indebted to C. Lupkes for making data from REFLEX-II available.

REFERENCES

Bigg, E. K., 1996: Ice forming nuclei in the high arctic. *Tellus*, **48B**, 223-233.

Chlond, A., Three-dimensional simulation of cloud street development during a cold air outbreak. *Boundary Layer Meteorol.*, **58**, 161-200.

Curry, J. A., 1983: On the formation of continental polar air. *J. Atmos. Sci.*, **40**, 2279-2292.

Harrington, J. Y., T. Reisin, W. R. Cotton, and S. M. Kreidenweis, 1999: Cloud resolving simulations of arctic straus. Part II: Transition-season clouds. *Atmos. Res.*, **51**, 45-75.

Harrington, J. Y., and P. Q. Olsson, 2000: A method for the parameterization of optical properties in bulk and bin microphysical models. Implications for Arctic cloudy boundary layers. Submitted to *Atmos. Res.*

Lupkes, C., and K. H. Schultzen, 1996: Modelling the arctic convective boundary layer with different turbulence parameterizations. *Boundary Layer Meteorol.*, **79**, 107-130.

Olsson, P. Q., and J. Y. Harrington, 1999: Dynamics and energetics of the cloudy boundary layer in simulations of off-ice flow in the marginal ice zone. *J. Geophys. Res.*, In Press.

Rao, G.-S., and E. M. Agee, 1996: Large eddy simulation of turbulent flow in a convective boundary layer filled with snow. *J. Atmos. Sci.*, **53**, 86-100.

Stevens, B. S., W. R. Cotton, G. Feingold, and C.-H. Moeng, 1998: Large-eddy simulations of strongly precipitating, shallow stratocumulus-topped boundary layers. *J. Atmos. Sci.*, **55**, 3616-3638.

Walko, R. L., W. R. Cotton, M. P. Meyers, and J. Y. Harrington, 1995: New RAMS cloud microphysics parameterization. Part I: The single-moment scheme. *Atmos. Res.*, **38**, 29-62.

MULTI-SCALE ANALYSIS OF IN-CLOUD VERTICAL VELOCITY DERIVED FROM 94-GHz DOPPLER RADAR

Natasha L. Miles*, David M. Babb, and Johannes Verlinde

Dept. of Meteorology, The Pennsylvania State University, University Park, PA, 16802, USA

1. INTRODUCTION

When present during cold-air outbreaks over warm water, mesoscale structures, such as cloud bands and hexagonal cells, represent the organization of the vertical transport of heat and moisture from the surface to the cloud layer (Etling and Brown 1993). The continued development of more accurate boundary-layer models examining lake-induced convection therefore requires a better understanding of the vertical velocity structure of clouds and the interaction between different scales of motion. As part of the Lake-Induced Convection Experiment (Lake-ICE, Kristovich et al 2000), The Pennsylvania State University 94-GHz vertically-pointing cloud radar was deployed on the downwind shore of Lake Michigan. The dataset collected during Lake-ICE, with its high resolution and longevity, lends itself to the study of the different scales of motion and their interaction.

The purpose of this project is to better understand the vertical velocity structure of lake-effect snow clouds, thus contributing to more accurate models of lake-induced convection and improved forecasts. Various time series analysis techniques are used to examine the vertical velocity structure of a lake-effect storm.

2. LAKE-ICE

The vertically-pointing PSU cloud radar, deployed in December 97 - January 98 as part of Lake-ICE, was positioned on the downwind shore of Lake Michigan, in Muskegon, MI. The current work focuses on results from 13 January 1998, when the radar operated continuously for over 18 hours. The sounding data on 13 January indicate in-cloud temperatures ranging from -18°C to -14°C, wind speeds of 8-16 m s^{-1}, and wind directions of 240 to 300°. With the lake temperature during the experiment of about 4°C, the synoptic conditions were favorable for intense boundary layer convection.

One set of Doppler power spectra was recorded every 7.5 seconds, with a data collection cycle of about 5 seconds and a processing cycle of about 2.5 sseconds. With typical wind speeds of 8-16 m s^{-1}, the along-wind dimension of the radar resolution volume was thus 40-80 m. The vertical resolution was 30 m.

The data were processed using a technique (Babb and Verlinde 1999) that removes the effects of turbulent broadening from a Doppler power spectrum to give the quiet-air fall velocity spectrum of the population of cloud particles without any assumptions about the shape of the particle size distribution. We assume that the smallest detectable particles have essentially zero fall velocity. Therefore, the mean motion of the air within the radar resolution volume is determined.

3. RESULTS AND DISCUSSION

3.1 Wavelet Analysis

Preliminary analysis of the vertical velocity data indicates that there are several scales of coherent motion. Although the measured data includes vertical profiles from cloud base to near cloud top, the focus of the section is on a time series at one mid-cloud height (900 m, $\sim$0.82 z_i). Throughout this continuous 18-hour time series, beginning at 12:17 UTC on 13 January 1998, the vertical velocity changed in both frequency and amplitude. This non-stationarity in time suggests the use of wavelet analysis. Shown in Fig. 1a is the wavelet power spectrum as a function of both period and time for the time series of vertical velocities, where we have used a Morlet wavelet (Torrence and Compo 1998). In Fig. 1a, white shading corresponds to high power regions and black to low power regions. Zero padding has reduced the power in the area below the black curve. In Fig. 1b, the global power is plotted as a function of period, with the periods of the peaks are indicated to the right of each peak. These peaks correspond to long-scale (184 min), mid-scale (46 min) and short-scale (11.5 min) structures. Since there are only about 6 full oscillations of the 184-minute period, information about the time variation of the long-scale structure is smeared and the power in that period range appears approximately constant throughout the entire analysis

*Corresponding author address: Natasha L. Miles, Department of Meteorology, The Pennsylvania State University, University Park, PA 16802; e-mail: nmiles@essc.psu.edu

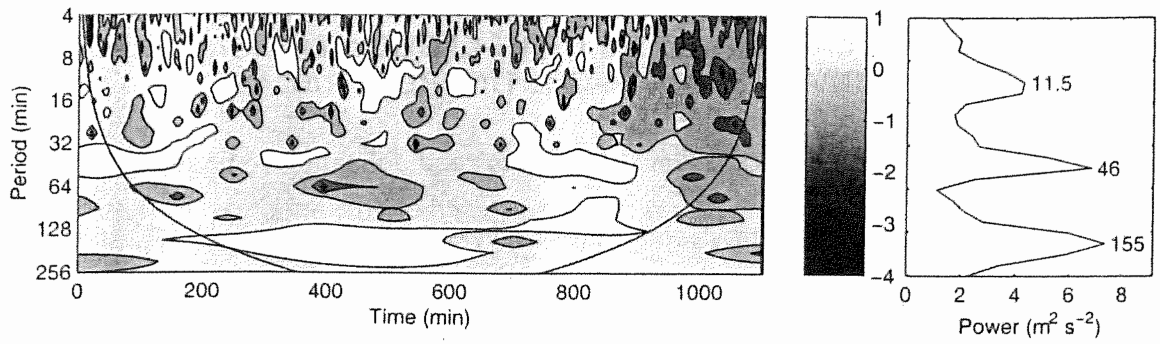

Figure 1: a) Wavelet power spectrum as a function of period and time for a time series of vertical velocities at a height of 720 m ($\sim$ 0.65 z_i). b) Global power as a function of period. Associated periods (in minutes) are indicated to the right of the peaks.

period. The power in the mid-scale is, however, intermittent, with three periods of stronger activity each lasting about 200 minutes and followed by weaker activity. The short-scale variations are stronger during peaks in the mid-scale organization, suggesting a relationship between mid-scale organization and short-scale activity, although some strong short-scale peaks occur during weaker mid-scale activity.

Possible physical explanations for these peaks are: mesoscale gravity wave activity (184 min), cloud bands or cellular structures (46 min) and thermal-scale structures (11.5 min). Although it is difficult to distinguish between banded structure and cellular structure with a vertically-pointing instrument, prior studies have found cloud bands associated with lake-effect storms (Kristovich 1993, LeMone 1973, Walter and Overland 1984). Cloud rolls were observed via satellite over land on 13 January 1998, with a more cellular structure observed over the lake (Fig. 6 in Kristovich et al 2000). The radar's location on the shore of the lake placed it the transition area between these two regimes.

3.2 Conditional Sampling

To investigate the interaction of the different scales of motion indicated by the wavelet analysis, the data were processed with three different amounts of smoothing, each highlighting a different scale. These results are shown in Fig. 2, where the thin black line represents the short-scale variations, the thick black line is the mid-scale variations, and the gray line is the long-scale variations. Results are quantified according to location in a mid-scale updraft. A mid-scale updraft is defined as a time interval where the mid-scale curve is above the long-scale curve; conversely, a mid-scale downdraft is where the mid-scale curve is below the long-scale curve. Subtracting the mid-scale curve from the small-scale curve yields the local variations in the vertical velocity. The local variations are binned according to whether they occur in a mid-scale updraft or downdraft region. Shown in Fig. 2b and 2c are probability distributions of the local variations in mid-scale updraft and downdraft regions, respectively. Positive values represent short-scale updrafts, whereas negative values represent short-scale downdrafts. Both short-scale updraft and downdrafts are larger in magnitude in mid-scale updrafts than those in mid-scale downdrafts. Quantifying this observation, the variance in the local variations in mid-scale updrafts regions is 0.037 m^2 s^{-2}, compared to 0.015 m^2 s^{-2} in the mid-scale downdraft regions. These results suggest that mid-scale updraft regions are characterized by stronger convective activity. Furthermore, the local variations in mid-scale updraft regions are more skewed towards updrafts than the local variations in mid-scale downdrafts.

3.3 Vertical Coherence

Next, we focus on a 90-minute time period spanning a strong mid-scale updraft. Vertical cloud profiles (cloud base to near cloud top) are included in the analysis. The observed cloud base height is at 650 m ($\pm$ 100 m), and cloud top height varies between 900 and 1100 m. Mean vertical velocities are calculated for each radar resolutions volume (Δz = 30 m) throughout the entire cloud depth, and are shown in the Fig. 3. To emphasize the velocity structure, velocities greater than 1.0 m s^{-1} (up) are shown in white and velocities less than -1.0 m s^{-1} (down) are black. Velocities near zero are shown in gray. The maximum magnitude of the vertical velocities is greater than 4.0 m s^{-1}. A downdraft region was measured from 5 to 15 minutes past the starting point of 00:30 UTC, followed by an updraft region from 15 to 55 minutes. Another downdraft region exists between

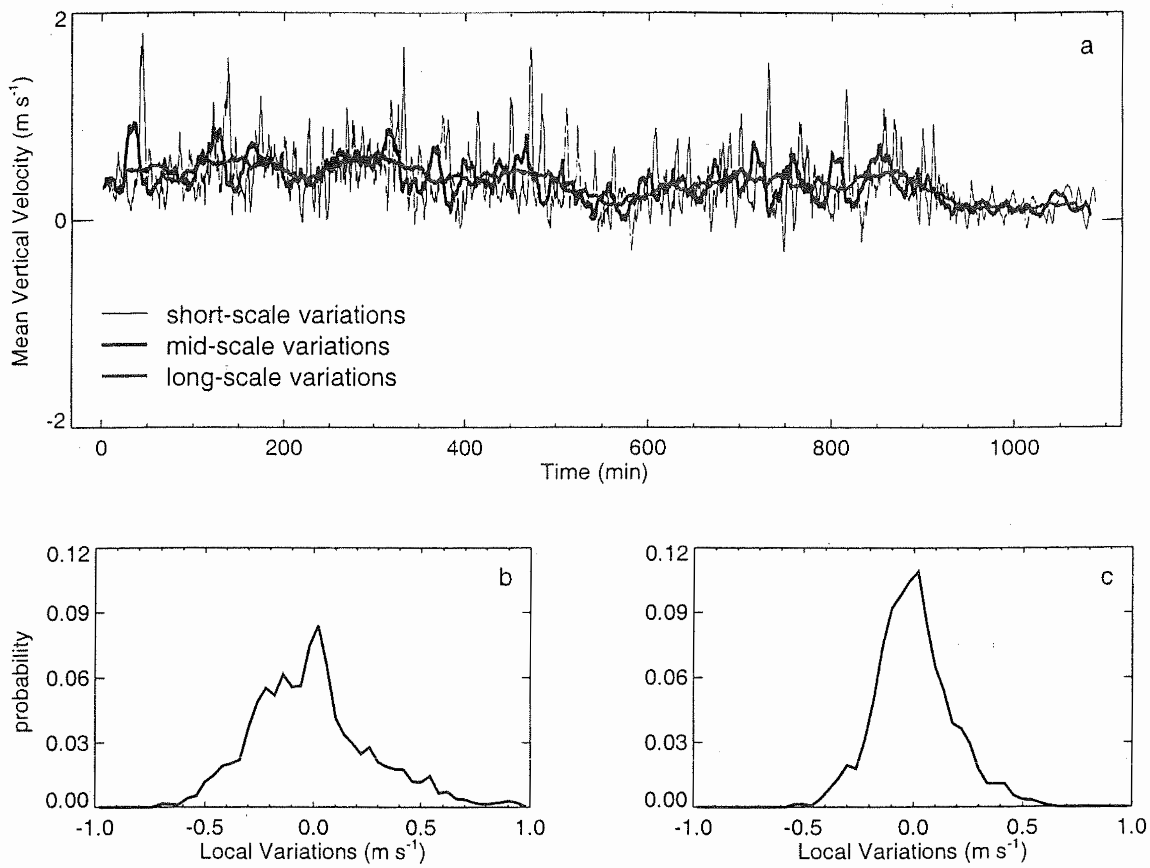

Figure 2: Time series of 18 hours of retrieved vertical velocity processed with varying amounts of smoothing. The thin black line represents short-scale variations, the thick black line mid-scale variations, and the gray line long-scale variations. Vertical velocity probability distributions for local variations on b) mid-scale updraft regions and c) mid-scale downdraft regions.

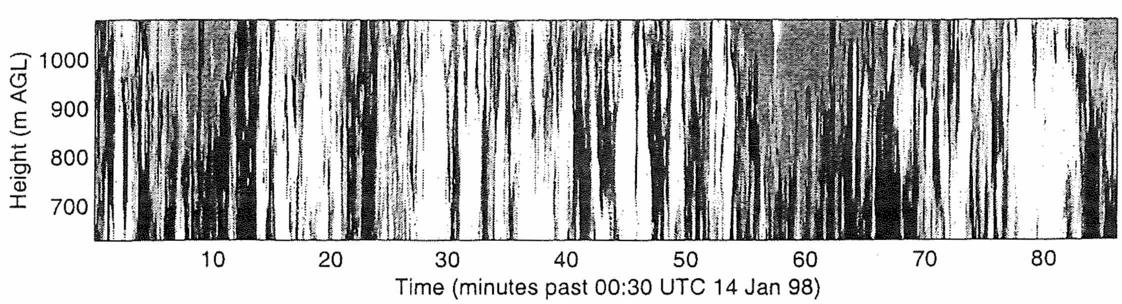

Figure 3: Vertical velocity profile from cloud base to near cloud top. To emphasize the velocity structure, velocities greater than 1.0 m s^{-1} (up) are shown in white and velocities less than -1.0 m s^{-1} (down) are black. The maximum magnitude of the vertical velocities is greater than 4.0 m s^{-1}.

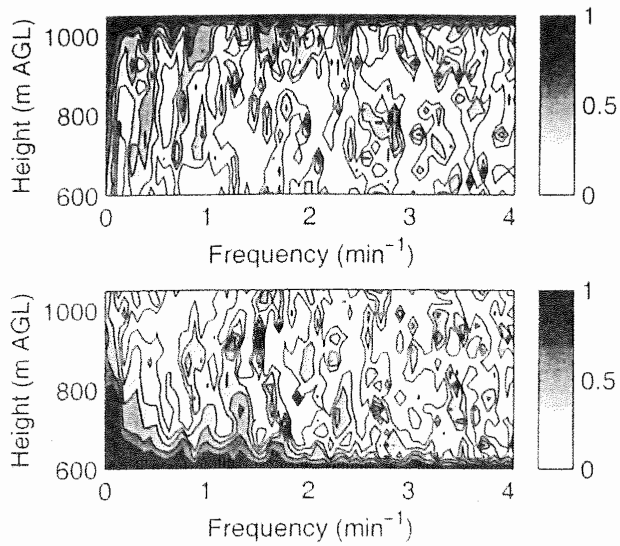

Figure 4: a) Coherence of vertical velocity at each level with cloud top vertical velocity. b) Coherence of vertical velocity at each level with cloud base vertical velocity.

55 and 70 minutes, with an updraft region following. The reflectivity profile indicates lower cloud top heights associated with mid-scale downdrafts and higher cloud tops during mid-scale updrafts (not shown).

In order to study the nature of the convection, coherency analyses were performed. Coherence quantifies the correlation between two signals; the more closely related the signals are, the closer the coherence is to one. The coherence of each level with cloud top and cloud base is shown in Fig. 4 a and 4b, respectively. At low frequencies (periods longer than 25-50 minutes), the coherence with cloud top(base) is high throughout most of the depth of the cloud. Isolated peaks of high coherence are not statistically significant. The coherency of mid-scale and larger structures indicates that they are aligned throughout the depth of the cloud, whereas short-scale structures do not extend throughout the cloud depth.

4. SUMMARY

The Pennsylvania State University 94-GHz vertically-pointing Doppler cloud radar was deployed during December 1997 and January 1998 as a part of Lake-ICE. A lake-effect event, for which a total of over 18 hours of data at a temporal resolution of 7.5 seconds was measured, is analyzed. From the Doppler spectrum, we estimate mean vertical air motion within each radar resolution volume from cloud base to near cloud top, with a vertical resolution of 30 meters. Dominant frequencies are determined using wavelet analysis, showing a spectral gap between the primary scales of motion (short-scale, mid-scale, and long-scale structures). Coherence of the vertical velocity at various heights with cloud-base and cloud-top vertical velocity is also calculated, indicating high coherence throughout the cloud for structures mid-scale and larger. Conditional sampling is used to give insight into the interaction between different scales of motion. For example, it is shown that short-scale variations in mid-scale updraft regions are larger in magnitude than those in mid-scale downdraft regions.

The dataset collected during Lake-ICE, with its high resolution and longevity, lends itself to the study of the different scales of motion and their interaction. The primary applications of this work lie in boundary layer meteorology, and more specifically, in convection in lake-effect storms. By documenting the vertical velocity of cloud bands as they drift past a point on the downwind shore of the lake, we can gain understanding of their structure. This understanding will, eventually, contribute to more accurate models of lake-effect storms, and thus better forecasts of snow in the Great Lakes region.

Acknowledgments. This work was supported by the National Science Foundation (under Grant ATM-9629343).

REFERENCES

Babb, D. M., and J. Verlinde, 1999: Application of a constrained linear inversion algorithm for removing turbulent broadening in Doppler power spectra. *Extended Abstracts, 29th Int. Conf. on Radar Meteor.*, Montreal, Canada.

Etling, D., and R. A. Brown, 1993: Roll vortices in the planetary boundary layer: A review. *Bound. Layer Meteor.*, **65**, 215-258.

Kristovich, D. A. R., 1993: Mean circulations of boundary-layer rolls in lake-effect snow storms. *Bound. Layer Meteor.*, **63**, 293-315.

Kristovich, D. A. R., et al., 2000: The Lake-Induced Convection Experiment (Lake-ICE) and the Snowband dynamics project. *Bull. Amer. Meteor. Soc.*, **81(3)**, 519-542.

Lemone, M. A., 1973: The structure and dynamics of horizontal roll vortices in the planetary boundary layer. *J. Atmos. Sci.*, **30**, 1077-1091.

Torrence, C., and G. P. Compo, 1998: A practical guide to wavelet analysis. *Bull. Amer. Meteor. Soc.*, **79**, 61-78.

Walter, B. A., and J. E. Overland, 1984: Observations of longitudinal rolls in a near neutral atmosphere. *Mon. Weath. Rev.*, **112**, 200-208.

MARINE BOUNDARY-LAYER CLOUD STRUCTURE FROM CM- TO KM-SCALES

Anthony B. Davis,[1] H. Gerber,[2] and Alexander Marshak[3]

[1]Los Alamos National Laboratory, Space & Remote Sensing Sciences Group, MS C-323, Los Alamos, NM 87545, USA
[2]Gerber Scientific Inc., 1643 Bentana Way, Reston, Va 20190, USA
[3]NASA's Goddard Space Flight Center, Climate & Radiation Branch (Code 913), Greenbelt, Md 20771, USA

1. CONTEXT AND OUTLINE

There are many reasons for investigating the internal structure of marine boundary-layer (BL) clouds, not the least being to improve cloud radiation models. Indeed, these typically spatially extensive and temporally persistent systems have a first-order effect in both solar and IR radiation budgets. At the same time, it is widely acknowledged that, due to this internal variability, the standard plane-parallel models used in GCM radiation schemes are inadequate in spite of the external resemblance of these clouds to horizontally infinite slabs. In cloud remote sensing from satellites, sub-pixel (10^1–10^3 m) variability is a concern. Validation of Large-Eddy Simulation (LES) models is another reason for documenting the spatial statistics of BL cloud structure at the scales they resolve, down to $\approx 10^1$ m. Finally, there is a growing interest in the cloud microphysical community about the spatial distribution of cloud droplets (e.g., Korolev and Mazin 1993; Malinovski et al. 1994). Recently, this question of small-scale homogeneity is recast as whether or not the relative droplet positions can represented by a spatial Poisson process (Baker 1992; Brenguier 1993; Kostinski and Jameson 1997; Shaw et al. 1998; Davis et al. 1999; L. Chaumat and J.-L. Brenguier 1998-1999, private communications).

In this report, our considerations sweep five orders of magnitude in scale and thus address both LES-related form tens of kilometers to tens of meters, and microphysically-motivated issues at sub-meter scales. We are able to do this because of the airborne deployment of Gerber et al.'s (1994) Particle Volume Monitor (PVM) which can reliably sample cloud liquid water content (LWC) at 2 kHz, 4 cm at a nominal 80 m/s aircraft speed. The PVM also has a particle-surface area channel (not used here). The data used here were collected on July 26, 1993, during the Southern Ocean Cloud EXperiment (SOCEX – Phase 1) and we refer to Davis et al. (1999) for a detailed description of the extensive dataset and meteorological conditions.

In the following section, we present spectral evidence for a scale-break in cloud structure at 2–5 m. In section 3, we show this is not an instrumental artifact and that it is likely to be a manifestation of locally non-Poissonian droplet distributions. In section 4, we show that the robust low-order scaling exponents of LWC are similar for three major campaigns in vastly different areas while their high-order counterparts are significantly different; this implies that both correlation and intermittence properties of marine BL clouds are universal at first-order but that the details that determine the unstable dynamics of strong LWC inhomogeneities depend on the local climate. We summarize our main findings in section 5.

Corresponding author's address: Anthony B. Davis, LANL/NIS-2, Mail Stop C-323, P.O.B. 1663, Los Alamos, NM 87545, USA; E-Mail: adavis@lanl.gov.

2. SCALE-BREAK AT 2-5 METERS

A convenient way for analyzing spatial variability on a scale-by-scale basis is to invoke the Fourier energy spectrum: $E(k)\mathrm{d}k$ is band-pass variance in $[k,k+\mathrm{d}k)$ where wavenumber k is related to scale r by $k = 1/r$. It is then customary to seek power-law behavior or "scale-invariance":

$$E(k) \sim k^{-\beta_{\rm range}}. \tag{1}$$

For the LWC data from SOCEX–1, we find two distinct regimes (cf. Fig. 1c):

$$\beta_{\rm large} \approx 1.6, \text{ for } 10^{+}\text{ km} < r = 1/k < r^{*} \approx 5\text{ m}; \tag{2a}$$

$$\beta_{\rm small} \approx 0.9, \text{ for } 2\text{ m} \approx r^{*} < r < 1/k_{\rm Nyq} = 8\text{ cm}. \tag{2b}$$

This break in scaling at 2–5 m was not expected on the grounds of atmospheric turbulence phenomenology where one thinks of LWC as a passive admixture, at least at small scales. In this case, one anticipates $1/k^{5/3}$-type behavior down to the Kolmogorov-scale which is centimeters at most; even then the break involve a trend towards smoother behavior since molecular diffusion dominates the stretching-mixing process driven by the passive advection.

Interestingly, scale-invariant processes with $\beta < 1$ and $\beta > 1$ have completely different statistical flavors. A large sample of the large-scale behavior with $\beta \approx 1.6$ can be visualized in Fig. 1a where we have averaged the raw 4-cm resolution data over 5.12 m segments (128 points). One can see both large and small jumps but also a high degree of continuity, hence large variations in local means at all scales up to at least 10 km. In this "nonstationary" situation, one has long-range correlations. The prototype of nonstationarity is Brownian motion (i.e., the running sum of independent increments) with $\beta = 2 > 1$. In contrast, the small scale behavior with $\beta \approx 0.9 < 1$ illustrated in Fig. 1b is "stationary." Again we have large and small jumps, however a jump in one direction is followed most often with one in the opposite direction so there is no continuity and spatial correlations are short. Local averages vary little over the domain (up to a few 5-m segments). The prime example of stationary behavior is δ-correlated or "white" noise with $\beta = 0$.

We discuss the meaning and origin of the large jumps at both small and large scales in the next two sections.

3. SMALL SCALES: EXCESS VARIANCE

The simplest interpretation of the scale-break leading to excess small-scale variability with a stationary (if not completely decorrelated) character is that a turbulence-

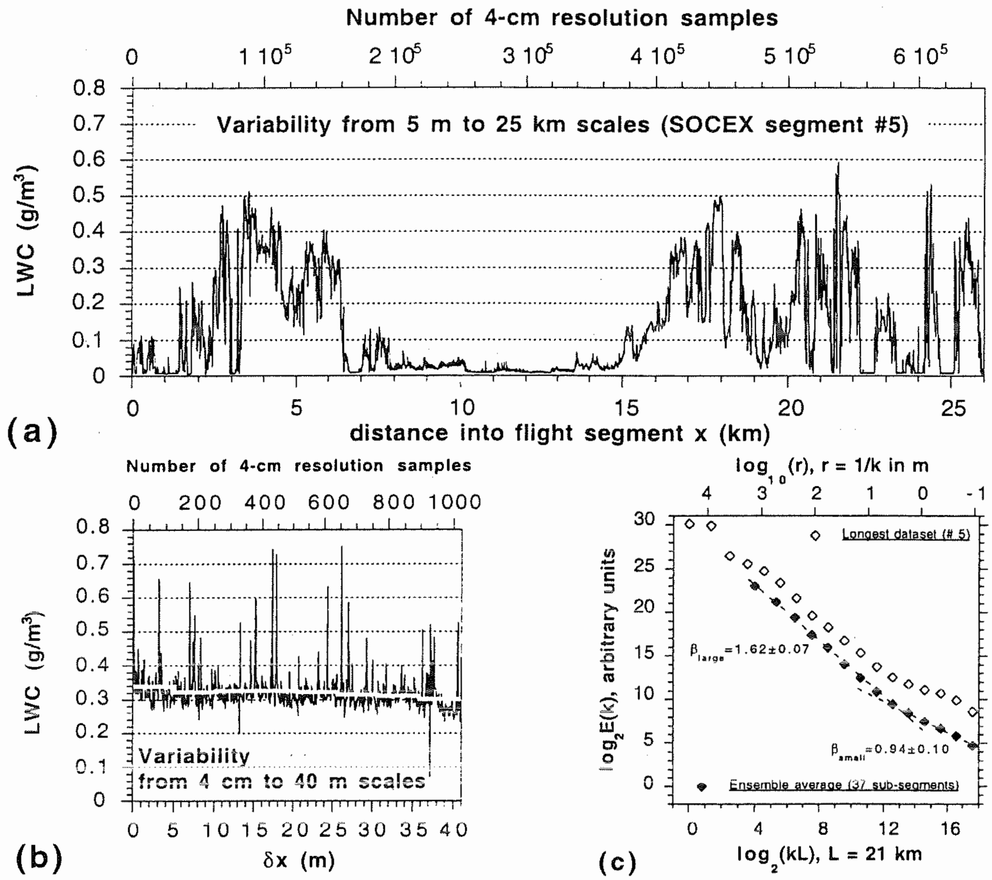

Figure 1: *Fluctuations in PVM-100A's LWC Channel Recorded during SOCEX – Phase 1.* **(a)** Typical large-scale behavior; note the large as well as small jumps. **(b)** Typical small-scale activity; note the spikes, mostly upward here, but that tend to be in both directions when the average LWC is higher (see Davis et al. (1999)); the eight 5.12-m pixels from panel (a) are visible in white. **(c)** Energy spectrum for the data in panel (a) as well as the grand ensemble of 37 different 1.3-km sections; the longest dataset in panel (a) contributes 19 of these, the smallest dataset a single one, and others yield 3, 4, and twice 5 sections (details in Davis et al. (1999)).

based signal with $1/k^{1.6}$ behavior is present but it has become overwhelmed by uninteresting instrumental noise, including the effect of insufficiently fine digitization. To test this hypothesis, we conducted very detailed simulations of PVM-100A operation in a variable LWC environment.

To this effect, we first generated the following coarse-grained version of the field

$$\rho_{\text{large}}(x) = \frac{1}{r^*}\int_x^{x+r^*} \rho_{\text{PVM,obs}}(x')\mathrm{d}x',\ x/r^* = 0, 1, 2, 3, \ldots, \quad (3)$$

which is believed to be free of the alleged instrumental artifacts. We then interpolate the large-scale fractal behavior down to the 0.5 mm ($\approx$20 kHz) scale of instantaneous sampling by the PVM's fine laser beam; we denote this field as

$$\rho_{\text{small,turb}}(x) = \rho_{\text{large}}(x) + \textit{fractal\_interpolation}(x). \quad (4)$$

The parameters of the interpolation scheme were chosen to extend the observed spectral scaling in Eqs. (1) and (2a), with approximately the observed degree of intermittency. This is the droplet environment in which the PVM is presumably operating, mildly non-Poissonian in space.

The LWC obtained in Eq. (4) corresponds to a certain number density $n(x)$ of cloud droplets for given size distribution:

$$n(x) = \left(\frac{6(1+v_e)^3}{\pi\rho_w d_e^{\,3}}\right)\rho_{\text{small,turb}}(x) \quad (5)$$

where we have made a log-normal assumption about the size distribution with effective diameter d_e and effective variance v_e. We will proceed here with d_e = 29.6 μm and v_e = 0.015; however, we varied these parameters within the observed range (typically smaller and more numerous droplets, hence less sampling noise) and this does not change the conclusion we draw below.

For a (laser-beam) sampling volume V_s = 1.25 cm^3, $n(x)V_s$ from Eq. (5) would be only a very rough estimate of the actual discrete number of droplets in the volume at the time of the measurement. So, we equate it to the mean $\langle N\rangle(x)$ of a Poisson variable and generate one value for

$$N(x) = \text{random\_Poisson\_sample}[\langle N\rangle(x) = n(x)V_s]. \quad (6)$$

This random integer is then used to simulate the LWC that the PVM's optical detector would actually measure, conditional to specified vignetting constraints on large and small droplets (see Davis et al. (1999) for details). In other words, we draw $N(x)$ log-normal random deviates for the droplet diameters and compute directly

$$\rho_{\text{small,PVM}}(x) = \left(\frac{\pi\rho_w}{6V_s}\right)\sum_{i=1}^{N(x)} d_i^{\,3}. \qquad (7)$$

This quantity pertains to the instantaneous 1.25 cm^3 volume V_s and the internal 20 kHz sampling of the PVM. [Note that we actually used 16 kHz for the convenience of having a power of 2 in the fractal interpolation in Eq. (4).] We therefore simulated exactly the down-sampling to 2 kHz using the specified frequency response of the A/D converter (see Davis et al. (1999) for details). This filtering/re-sampling of $\rho_{\text{small,PVM}}(x)$ leads to $\rho_{\text{PVM,sim}}(x)$ which can be directly compared to $\rho_{\text{PVM,obs}}(x)$ in Eq. (3). Davis et al. (1999) thus show that the extreme events, the spikes in both directions, are missing and therefore conclude that these features are not instrumental artifacts. In other words, the PVM is operating in a significantly non-Poissonian droplet environment.

Figure 2 summarizes in spectral representation the above attempt to explain the 2–5 m scale break with instrumental noise (sampling strategy and digitization). The unexplained part of the observed variance between 0.1 and 1.0 meter scales is on the order of $2^2 = 4$ or more. We attribute this excess variance to the LWC spikes in Fig. 1b, areas where the droplet distribution is surely not Poissonian in space.

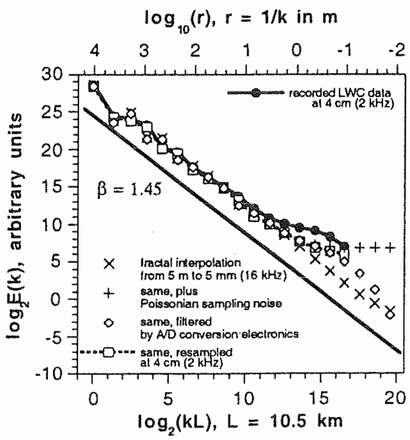

Figure 2: *Evolution of LWC Energy Spectrum in Detailed Simulation of PVM Operation in a Micro-Variable Environment.* See text for an explanation and Davis et al. (1999) for full details.

Using a simplified Gaussian version of Davis et al.'s (1999) model for PVM noise estimation, Gerber et al. (2000) come to the same conclusion as above about the reality of the extreme deviations LWC. These authors also find the same scale-break in data captured in convective clouds and they speculate on the origin of the outliers in terms of entrainment/mixing processes. It has been suggested (Wood and Field 2000) that addition of a drizzle mode can naturally explain the spikes in Fig. 1b without leaving the framework of Poissonian point distributions in space. This is not an impossibility under some circumstances, however Gerber and Davis (2000) recall that the PVM does not respond to drizzle due to a dramatic cut-off in sensitivity between 60 and 100 μm in droplet diameter.

4. LARGE SCALES: MULTIFRACTALITY

Following Davis et al. (1994) and Marshak et al. (1997), large-scale statistical properties of LWC are now characterized, beyond spectral analysis, using higher-order structure functions which is a form of multifractal analysis. Specifically, we compute the l.h. side of

$$\langle|\rho(x+r)-\rho(x)|^p\rangle \sim r^{\zeta(p)},\ r \geq 5\text{ m} \approx r^* \qquad (8)$$

where r is a "lag," and $p \geq 0$ takes real as well as integer values, and $\langle\cdot\rangle$ means averaging over x and flight segments. This is meaningful since the large-scale LWC fluctuations are nonstationary but its increments, that is, the random fields $\rho(x+r)-\rho(x)$ for $r \geq r^*$, are stationary. As suggested by the r.h. side of Eq. (8), we then parameterize the (r,p)-dependent statistics by power laws in scale r, calling for linear regressions in log(*statistic*)-log(*scale*) axes. We clearly have $\zeta(0) = 0$ and $\zeta(p) \geq 0$ for $p > 0$. It can be shown (Frisch and Parisi 1985) that $\zeta(p)$ is necessarily convex, i.e., $\zeta''(p) \leq 0$. Finally, we retrieve at $p = 2$ an equivalent of the power-law spectral analysis that we covered in §2:

$$\beta_{\text{large}} = \zeta(2) + 1; \qquad (9)$$

equivalence follows here from the Wiener-Khinchin theorem generalized to stationary increments, then specialized for power-laws (e.g., Monin and Yaglom 1975). Multifractal analysis can thus be viewed as a natural extension of spectral analysis.

Results for $\zeta(p)$ obtained from our *in situ* LWC data from SOCEX are presented in Fig. 3a and compared with counterparts for two other field programs also focused on marine BL clouds: FIRE'87 (in the Pacific) from the analysis of Marshak et al. (1997), and ASTEX (in the Atlantic) analyzed by Davis et al. (1994). We note the similarity of the exponents from the trivially common point at $p = 0$ up to at least $p \approx 1$, and a significant divergence of results beyond.

Another way of illustrating the similarity of the FIRE, ASTEX and SOCEX results is to use the "bi-fractal" plane with coordinates:

$$H_1 = \zeta(1) \in [0,1], \qquad (10a)$$

$$C_1 = \zeta(1) - \zeta'(1) \in [0,1]; \qquad (10b)$$

the last limit assumes $\zeta(p)$ is non-decreasing, $\zeta'(p) \geq 0$, a property that can be associated with the existence of finite bounds on the absolute moments in Eq. (8) (Marshak et al. 1994). There are other definitions of the C_1 exponent in (10b) but the alternatives lead to the same conclusions as given below; Davis et al. (1994,1999) discuss the details as well as the statistical and geometrical meanings of both quantities in (10a–b). For the present purposes, it suffices to recall that:

- H_1 (the Hurst exponent) is 1st-order an alternative to β that describes the broad fluctuations of the LWC data traceable to the mostly small jumps and their negative or positive correlations;
- C_1 is a 1st-order measure of intermittency in the data which is controlled by the relative frequency of the large versus small jumps in LWC at the scale r^*.

The main advantage of using the lower-order moments in Eq. (8) is the increased robustness with respect to problems of insufficient sampling.

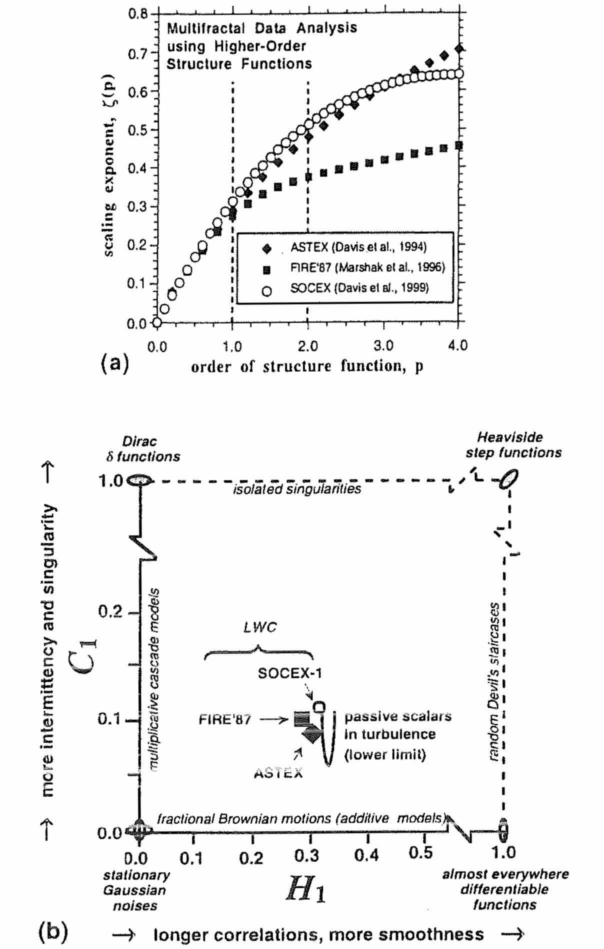

Figure 3: *Multifractal Properties of In-Situ LWC Variability Observed During Three Major Field Programs.* **(a)** Scaling exponents $\zeta(p)$ for the higher-order structure functions in the following 3^+ decade ranges: 20 m – 40 km for FIRE'87; 60 m – 60 km for ASTEX; 5 m – 10 km for SOCEX–1. **(b)** Cloud LWC and other denizens of the "bi-fractal" plane, both models and observations. Details in Davis et al. (1999).

Within all possibilities in Eqs. (10a–b), the LWC data —although collected under vastly different climatic regimes— occupies a very small area: $H_1 \in [0.28,0.31]$, $C_1 \in [0.08,0.12]$. In Fig. 3b, we show the cluster of LWC data in the (H_1,C_1) domain along with passive scalars in turbulence and some of the more popular scale-invariant models (fractional Brownian motion, multiplicative cascades, etc.). As expected, the turbulence data is not far from the LWC cluster but the models are all at the domain boundaries and therefore need refinement (or hybridization) to adequately represent LWC fields. For a survey of lesser-known models that have non-extreme H_1 and C_1 values, see Marshak et al. (1997).

Higher-order moments are the most vulnerable to poor sampling but the results in Fig. 3a have been scrutinized for this, hence the limitation to $p \leq 4$. At the same time, the higher p, the more it is influenced by the large jumps in LWC, their size and/or frequency. So the divergence in $\zeta(p)$ between the three field programs reflects a fundamental difference in the turbulent cloud dynamics as forced by the different climatic regimes.

5. SUMMARY AND DISCUSSION

Our analysis of small-scale LWC fluctuations in PVM data from SOCEX–1 supports the still controversial claim that droplet concentration is not everywhere Poissonian. This does not exclude a slow (spectral exponent $\beta \approx 5/3$) low-amplitude component in the variability of droplet number and size distribution. We believe the cause of the excess small-scale LWC variance causing the scale-break at 2–5 m lies in entrainment-and/or-mixing events; such processes may be related to the intermittency (occasional bursts of variability at the inner-scale) associated with the large-scale multifractality.

Comparing exponents obtained for large-scale behavior with those previously obtained from two other field programs, we uncover remarkable similarities between the basic multifractal (i.e., arbitrary-order structure function) properties of LWC in SOCEX, FIRE'87 and ASTEX clouds and those of passively advected scalars in turbulent flows. However, we also find interesting differences between the three kinds of marine cloud cover and with passive scalars but these are in the details of the various multifractal characterizations (inner and outer scales, high-order scaling). To reproduce these statistical behaviors defines a quantitatively-precise challenge for the cloud-modeling community.

REFERENCES

Baker, B., 1992: Turbulent entrainment and mixing in clouds: A new observational approach. *J. Atmos. Sci.*, **49**, 387–404.

Brenguier, J.–L., 1993: Observations of cloud microsructure at the centimeter scale. *J. Appl. Meteor.*, 32, 783–793.

Davis, A., A. Marshak, W.J. Wiscombe, and R.F. Cahalan, 1994: Multifractal characterizations of non-stationarity and intermittency in geophysical fields, observed, retrieved or simulated. *J. Geophys. Res.*, **99**, 8055–8072.

Davis, A. B., A. Marshak, H. Gerber, and W. J. Wiscombe, 1999: Horizontal structure of marine boundary-layer clouds from cm- to km-scales. *J. Geophys. Res.*, **104**, 6123–6144.

Frisch, U., and G. Parisi, 1985: A multifractal model of intermittency, in *Turbulence and Predictability in Geophysical Fluid Dynamics*, M. Ghil et al. (Ed.), pp. 84–88. North Holland, New York (NY).

Gerber, H., B. G. Arends, and A. S. Ackerman, 1994: New microphysics sensor for aircraft use. *Atmos. Res.*, **31**, 235-252.

Gerber, H., J. Jensen, A. B. Davis, A. Marshak, and W. J. Wiscombe, 2000: Spectral density of cloud liquid water content at high frequencies. *J. Atmos. Sci.*, in press.

Gerber, H., and A. Davis, 2000: Reply to Comment on "Horizontal structure of marine boundary-layer clouds from cm- to km-scales," by R. Wood and P. Field. *J. Geophys. Res.*, in press.

Korolev, A. V., and I. P. Mazin, 1993: Zones of increased droplet concentration in stratiform clouds. *J. Appl. Meteor.*, **32**, 760–773.

Kostinski, A. B., and A. R. Jameson, 1997: Fluctuation properties of precipitation, 1, On deviations of single-size drop counts from the Poisson distribution. *J. Atmos. Sci.*, **54**, 2174–2186.

Malinowski, S. P., M. Y. Leclerc, D. G. Baumgardner, 1994: Fractal analyses of high-resolution cloud droplet measurements. *J. Atmos. Sci.*, **51**, 397–413.

Marshak, A., A. Davis, R. F. Cahalan, and W. J. Wiscombe, 1994: Bounded cascade models as non-stationary multifractals. *Phys. Rev. E*, **49**, 55–69.

Marshak, A., A. Davis, W. J. Wiscombe, and R. F. Cahalan, 1997: Scale-invariance of liquid water distributions in marine stratocumulus, 2, Multifractal properties and intermittency issues. *J. Atmos. Sci.*, **54**, 1423–1444.

Monin, A. S., and A. M. Yaglom, 1975: *Statistical Fluid Mechanics*, Vol. 2. The MIT Press, Boston (Mass).

Shaw, R.A., W.C. Reade, L.R. Collins, and J. Verlinde, 1998: Preferential concentration of cloud droplets by turbulence: Effects on the early evolution of cumulus droplet spectra. *J. Atmos. Sci.*, **55**, 1967–1976.

Wood, R., and P. Field, 2000: Comment on "Horizontal structure of marine boundary-layer clouds from cm- to km-scales." *J. Geophys. Res.*, in press.

Microphysical Properties of Arctic Boundary Layer Clouds Observed during FIRE.ACE

R. Paul Lawson, Bradley A. Baker and Carl G. Schmitt
SPEC Incorporated

1. INTRODUCTION

Cloud-radiative processes in the Arctic have a strong impact on the stability of the Arctic Ocean pack (Curry et al. 1993) and also have ramifications on the global energy budget (e.g., IPCC 1990). Clouds in the boundary layer are persistent during May through September and strongly influence the melting rate of the pack ice (Curry et al. 1996). The optically thin, low-level Arctic boundary layer cloud increases the summertime melt rate of sea ice since the longwave exceeds the shortwave cloud-radiative forcing at the surface. A positive feedback scenario occurs as melt ponds and leads form and the surface albedo decreases.

This paper presents microphysical data collected during May and July 1998 in Arctic clouds by the National Center for Atmospheric Research (NCAR) C-130 research aircraft. The C-130 was one of three research aircraft used for in situ studies of cloud microphysics during the Surface HEat Budget of the Arctic (SHEBA) project (Perovich et al. 1999), and the First ISCCP (International Satellite Cloud Climatology Project) Regional Experiment Arctic Clouds Experiment (FIRE.ACE) (Curry et al. 2000).

2. INSTRUMENTATION

The capabilities of the NCAR C-130 and instrumentation on the research aircraft are described by Curry et al. (2000). Of particular interest to this study are some of the microphysical instruments used to measure cloud particle characteristics and cloud liquid water content (LWC), including a Particle Measuring Systems (PMS) Forward Scattering Spectrometer Probe (FSSP-100), described by Knollenberg (1981),two King hot-wire LWC devices (King et al. 1978) manufactured by PMS with modifications to the electronics by NCAR, a cloud particle imager (CPI) described briefly by Lawson et al. (1998), Korolev et al. (1999) and in more detail by Lawson and Jensen (1998).

3. BOUNDARY LAYER CLOUDS

Sixteen research missions were conducted during FIRE.ACE by the C-130. Half of the 16 missions were flown in May 1998 and the remainder was flown in July 1998. Of the 16 missions, 11 cases were identified when there were boundary layer clouds. However, our definition is not stringent, being based mainly on cases when the lowest cloud layer was < 300 m, and including cases when the lowest cloud was > 300 m only if the subcloud layer was well-mixed to the surface. **Table 1** shows characteristics of the clouds. In May, six out of eight cases had boundary layer clouds and all six boundary layer clouds were mixed from the surface to cloud base. The depths of the mixing layers in May ranged from 150 to 1200 m. In July, five of the eight cases had boundary layer clouds, but none of these were mixed from the surface to cloud base.

Corresponding Author: Dr. R. Paul Lawson, SPEC Inc.
5401 Western Ave., Boulder, CO 80301
plawson@specinc.com

TABLE 1. Some Characteristics of FIRE.ACE Clouds

Flight No.	Date	Temp (° C)	Cloud Depth (m)	B.L. Cld ?	Mixed from Sfc to (m)	Characteristics Observed by CPI
RF01	5/4/98	-22 to -25	640 – 1000	Yes	1200	Mixed phase with Drizzle & Graupel
RF02	5/7/98	-18 to -20	290 – 420	Yes	400	Thin mixed-phase
RF03	5/11/98	-5 to -43	210 – 6600	Yes	350	Thin patchy water with ice above.
RF04	5/15/98	-6 to -9	120 – 650	Yes	550	Mostly water with some ice.
RF05	5/18/98	-7 to -9	180 – 460	Yes	150	Mostly water
RF06	5/20/98			No	-	Clear
RF07	5/24/98	-16 to -21	1500 –3000	No	-	Minimal Cloud
RF08	5/27/98	0 to -2	<50 – 500 1500 – 1700	Yes	250	Water Water
RF09	7/8/98	-19 to -28	5650 – 7150	No	-	Ice
RF10	7/15/98	-2 -20 to -22	<150 4600 – 5200	Yes	None	Fog – Water Water & ice layers
RF11	7/18/98	5 to –25	2000 – 6000	No	-	Layers: ice, water and mixed.
RF12	7/21/98	-2	<240	Yes	None	No CPI data available
RF13	7/23/98	0 to 2 -25	<30 – 280 6150 – 6380	Yes	None	Water Water over ice
RF14	7/26/98	2 to –23	SFC – 6500	Yes	None	Layers: ice, water and mixed.
RF15	7/28/98	2 to –29	2000 – 6700	No	-	Layers: ice, water and mixed.
RF16	7/29/98	0 to –3 -12 to -15	60m – 520 1900 – 2130	Yes	None	All water Glaciated

3.1 Mixing and Drizzle Formation

The C-130 flew a total of 21 vertical profiles through boundary layer clouds on 15, 18, 27 May and 29 July that consisted almost entirely of liquid water. Some of these profiles were flown through clouds that had distinctively adiabatic characteristics, i.e., the temperature followed the adiabatic value and the droplet spectra evolved as expected. An example of vertical profiles of the dispersion in the droplet size distribution, droplet diameter, temperature and LWC measurements during an ascent on 18 May in a boundary layer cloud that is close to adiabatic is shown in **Figure 1**. The droplet spectra were nearly mono-modal with mean size increasing with height, and there was no drizzle detected, hence the cloud LWC is close to adiabatic, as is predicted from theoretical considerations (Lawson and Blyth 1998). Even in these cases, however, there is evidence that isolated entrainment events are occurring. For example, clear air holes are seen that extend to at least 100 m below cloud top. The FSSP and CPI also confirm the lack of cloud in these spots. Presumably, these are entrainment events that bring clear air from above the cloud into the cloud layer. Curry (1986) also observed that cloud top air penetrated downward into boundary layer clouds, however, the maximum entrainment depth she reported was 50 m below cloud top.

In general, the vertical profiles varied from nearly adiabatic (**Figure 1**) to significantly sub-adiabatic, and the droplet spectra varied from strictly mono-modal to significantly bimodal. **Figure 2** shows a profile ascent where the lower one-third of the cloud was well mixed, temperature is nearly adiabatic, LWC is sub-adiabatic and the droplet spectra are mono-modal. In the same cloud, the middle one-third is well mixed, temperature and LWC are sub-adiabatic and the spectra are bimodal. The top one-third of cloud is actively mixing, the drop spectra is bimodal, LWC is highly variable and the temperature fluctuates rapidly, up to 2 ° C warmer than the adiabatic value, due to active mixing from warm air in the inversion layer above cloud top.

In clouds where the LWC and temperature profiles were adiabatic and the drop spectra were mono-modal, drizzle was not observed anywhere along the profile. When the LWC and temperature profiles were significantly sub-adiabatic, the droplet spectra near cloud top were bimodal and drizzle was observed lower in the cloud. These variations occurred in a consistent and physically understandable way. Although the Arctic atmosphere tends to be stable and layered, the boundary layer can be vertically well mixed. On occasion the upper part of the layer is cloudy. The vertical profiles of cloud liquid water and temperature remain adiabatic until, despite the stable flat top appearance, mixing at cloud top occurs, producing bimodal droplet spectra, and the broad bimodal spectra allow drizzle to form. The mixing initially causes a deviation from adiabatic LWC and temperature, while the drizzle precipitation eventually causes significant deviations from adiabatic profiles.

3.2 Microphysical Inhomogeneity

The effects of mixing at cloud top (i.e., **Figure 2**) eventually leads to inhomogeneous distribution of cloud drops, broadening of the drop distribution and the potential for formation of drizzle. In supercooled clouds, broadening of the drop distribution has been associated empirically with enhancement in the production of ice crystals (Hobbs and Rangno 1985). Perhaps the most striking aspect of FIRE.ACE boundary layer clouds, as revealed by initial analysis of CPI data, is the degree to which the characteristics of the hydrometeors can change over short (10 km) spatial distances. Large variations in cloud hydrometeors over scales of a 1 Km are expected in cumulus clouds, and can be explained by the strong vertical motions and levels of turbulence. Turbulence levels in cumulus clouds (MacPherson and Isaac 1977) are typically more than an order of magnitude larger than those observed in Arctic boundary layer clouds by Curry (1986). The clouds studied here also appeared to be fairly quiescent, with very flat cloud tops and minimal turbulence. Even so, as seen in **Figure 1**, in some cases there was significant mixing with apparent penetration of dry air from above cloud top deep into the boundary layer cloud. Curry (1986) reported horizontal variations in cloud microphysics in three of the four missions flown in Arctic boundary layer clouds in 1980. The instrumentation in the 1980 study, however, did not include any particle imaging probes. Therefore, in the 1980 study it was not possible to reliably separate ice particles from water drops, and to identify inhomogeneities in cloud particle characteristics.

One case, 4 May 1998, particularly emphasizes the microphysical inhomogeneity in hydrometeor fields observed in the FIRE.ACE data set. **Figure 3** shows a portion of the flight track when the C-130 was descending and making passes over the SHEBA ship, from cloud top (1025 m) down to cloud base (690 m) and examples of CPI images, water drop and ice particle size distributions during this time period. The data in the figure show that the hydrometeor fields varied considerably over spatial distances of 10 Km horizontally and a few hundred meters in the vertical. When the C-130 skimmed cloud top and then turned and made a pass 30 m below top, it encountered mostly supercooled (-25.5 to –22° C) cloud droplets with a mono-modal size distribution and only a few 100 – 500 μm ice particles. The larger ice particles may have fallen from a higher cloud. The ratio of water drop to ice particle concentration is > 1000:1, so the region near cloud top was predominately composed of supercooled cloud droplets with a monomodal size distribution. On the next pass 75 m below cloud top, **Figure 3** shows that the CPI water drop concentration had decreased by about a factor of six, and the size distribution still had a mode of about 30 μm, but had also broadened slightly. Some ice particles were observed, mostly unrimed with sizes to about 300 μm, and an occasional rimed particle as large as 600 μm. However, just west of this position and 30 m lower (920 mb), while the C-130 was turning to reverse course, a section of drizzle about 10 km in horizontal dimension was observed with supercooled (-25° C) drops with sizes up to 180 μm. After the pocket of drizzle was transected, the C-130 made another pass over the ship while descending to 900 m and encountered supercooled drops with a mode of about 30 μm and ice particles that were mostly < 500 μm, with a few larger rimed particles. But then, when the C-130 reversed course and two minutes later flew only 30 m lower (870 m) over the same flight track, significantly higher concentrations of rimed ice particles from 400 – 800 μm and occasional graupel particles up to 1 mm were observed.

The degree of inhomogeneity in cloud microphysics could possibly be due to mixing downward from cloud top or from the effects of seeding from higher clouds. Even though significant concentrations of ice particles were not observed during the passes over cloud top, the potential for temporal and spatial variability of this type of seeding precludes eliminating this possibility. The presence of the small pocket of drizzle at -25° C, however, cannot be directly explained by either surface or elevated effects. Curry (1986) reported drizzle when there was a relatively large dispersion in the drop spectra. In our case the FSSP drop spectra at cloud top (not shown) were relatively narrow and mono-modal, in contrast to the example shown in **Figure 2**, where the drop spectra were bimodal and drizzle was observed at -1° C. The cloud on 4 May existed for a long time and seeding from above

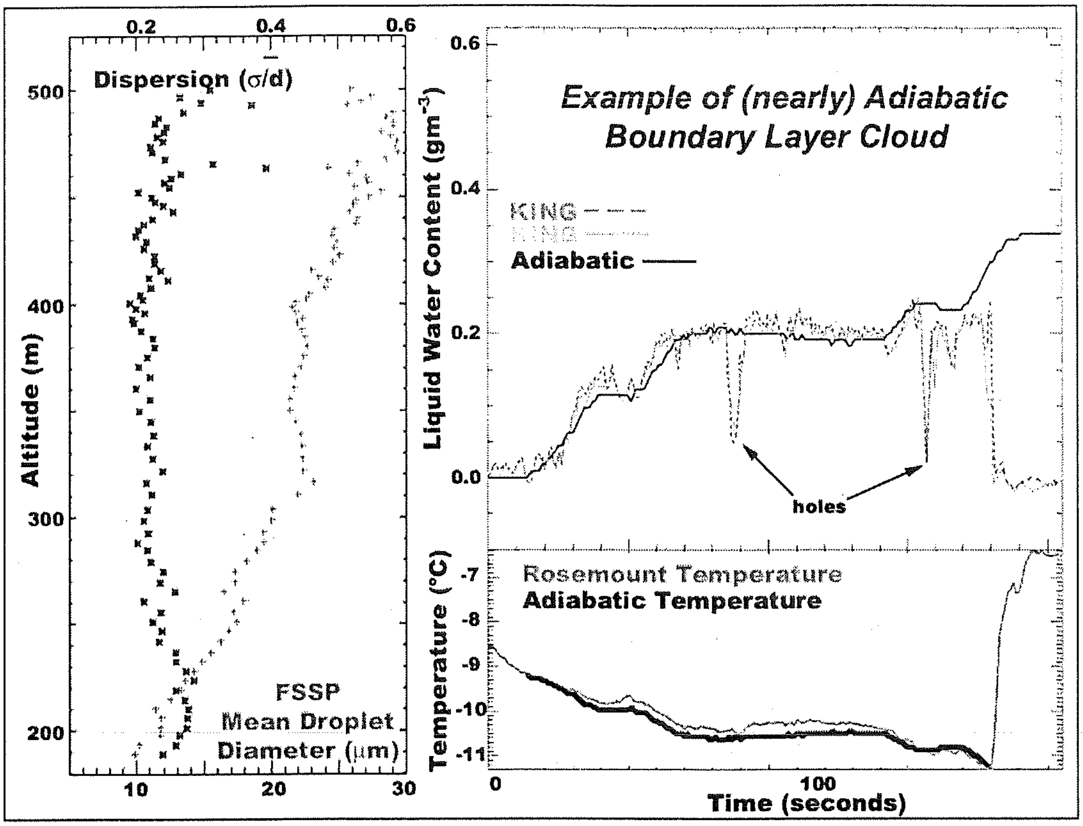

FIGURE 1. NCAR C-130 measurements observed in a boundary layer cloud on 18 May 1998.

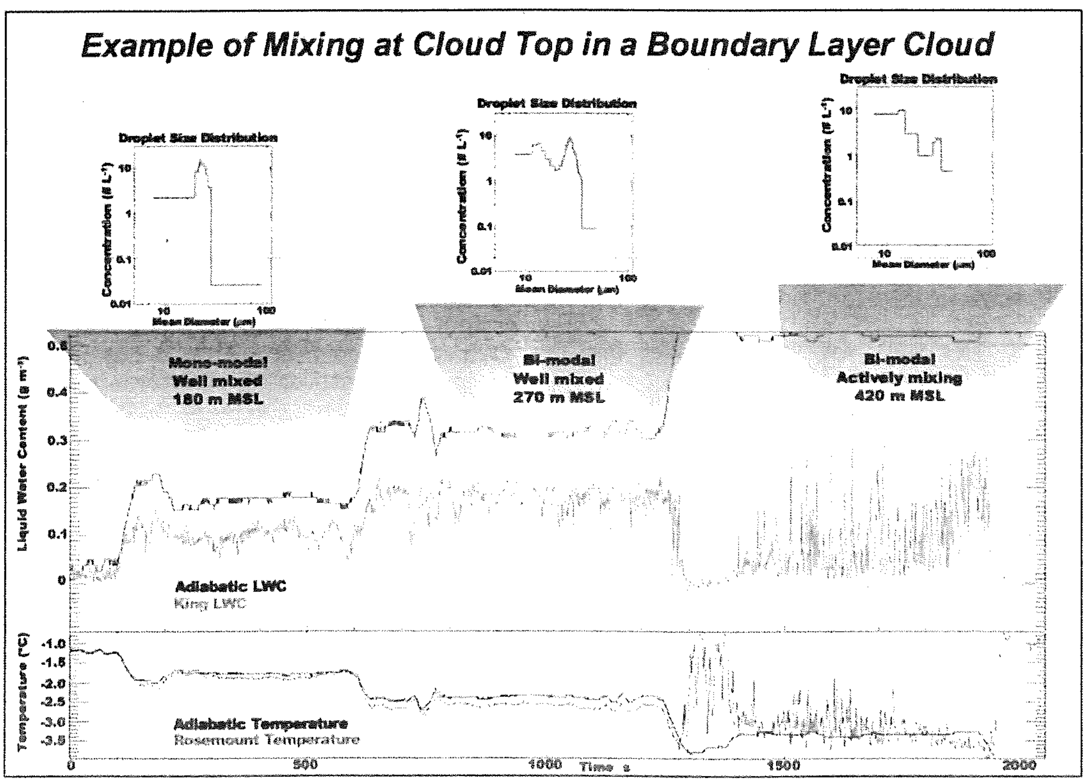

FIGURE 2. NCAR C-130 measurements observed in a boundary layer cloud on 29 July 1998.

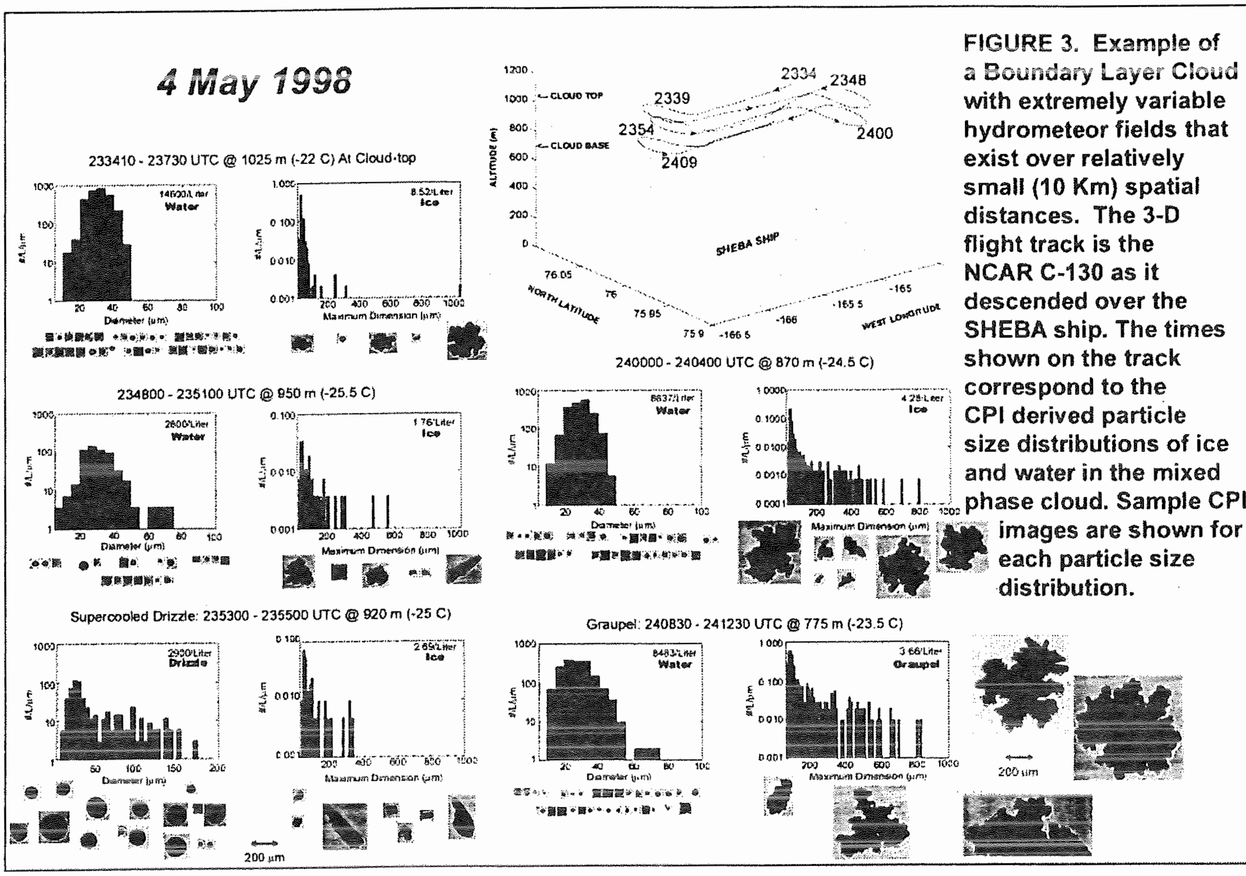

FIGURE 3. Example of a Boundary Layer Cloud with extremely variable hydrometeor fields that exist over relatively small (10 Km) spatial distances. The 3-D flight track is the NCAR C-130 as it descended over the SHEBA ship. The times shown on the track correspond to the CPI derived particle size distributions of ice and water in the mixed phase cloud. Sample CPI images are shown for each particle size distribution.

was sporadic. Perhaps the curious pocket of drizzle was produced by coalescence in a region that was not seeded from above.

3. DISCUSSION

This research focused on data collected by the NCAR C-130 on 11 missions with Arctic boundary layer clouds, derived from the total FIRE.ACE data set of 16 missions flown in May and July, 1998. The boundary layer clouds ranged from adiabatic to well-mixed with drizzle and graupel. In one cloud (4 May 1998) at –25 ° C, the C-130 observed individual 10 Km pockets of supercooled cloud drops, drizzle and graupel while descending through a 400 m thick boundary layer cloud over the SHEBA ship.

Acknowledgments: This work was funded under the NASA FIRE program, Contract No. NAS1-96015.

REFERENCES

Curry, J.A., 1986: Interactions among turbulence, radiation and microphysics in Arctic stratus clouds, *J. Atmos. Sci.*, ***43***, 90-106.

Curry, J.A., E.E. Ebert and J.L. Schramm, 1993: Impact of clouds on the surface radiation balance of the Arctic Ocean, *Meteor. Atmos. Phys.*, ***51***, 197-217.

Curry, J.A., W.B. Rossow, D.A. Randall and J.L. Schramm, 1996: Overview of Arctic Cloud and Radiation Characteristics, *J. of Climate*, ***9***, 1731-1764.

Curry, J.A., P. Hobbs, M. King, D. Randall, P. Minnis, et al., 2000: FIRE Arctic Clouds Experiment, *Bull. Amer. Meteorol. Soc.*, **81**, 5-29.

Hobbs, P. V., and A. L. Rangno, 1985: Ice particle concentrations in clouds. *J. Atmos. Sci.*, **42**, 2523-49.

IPCC, *Climate Change: The IPCC Scientific Assessment*, edited by J.T. Houghton, G.J. Jenkins and J.J. Ephramus, 365 pp., Cambridge University Press, 1990.

King, W. D., D. A. Parkin and R. J. Handsworth, 1978: A hot wire liquid water device having fully calculable response characteristics, *J. Appl. Meteor.*, ***17***, 1809-1813.

Knollenberg, R.G., Techniques for probing cloud microstructure, *Clouds Their Formation, Optical Properties, and Effects,* 1981: Edited by P.V. Hobbs and A. Deepak, Academic Press, New York, NY. 15-91.

Korolev, A.V., G.A. Isaac and J. Hallett, Ice particle habits in Arctic clouds, 1999: *Geophys. Res. Letters*, ***26,*** 1299-1302.

Lawson, R. P. and A. M. Blyth, 1998: A comparison of optical measurements of liquid water content and drop size distribution in adiabatic regions of Florida cumuli, *Atmos. Res.*, ***47-48***, 671-690.

Lawson, R.P. and T.L. Jensen, 1998: Improved microphysical observations in mixed phase clouds, *Presented at the American Meteorological Society Conference on Cloud Physics*, 17-22 August, Everett, Washington, pp. 451-454.

Lawson, R. P, A. V. Korolev, S. G. Cober, T. Huang, J. W. Strapp and G.A. Isaac, 1998: Improved Measurements of the Drop Size Distribution of a Freezing Drizzle Event, *Atmos. Res.*, ***47-48***, 181-191.

MacPherson, J.I. and G.A. Isaac, 1977: Turbulent characteristics of some Canadian cumulus clouds, *J. Appl. Meteorol.*, ***16***, 81-90.

Perovich, D.K., E.L. Andreas, J.A. Curry, H. Eiken, et al., 1999: Year on ice gives climate insights, *EOS*, ***80,*** 484-486.

THE IMPACT OF IMPROVED STRATOCUMULUS CLOUD OPTICAL PROPERTIES ON A GENERAL CIRCULATION MODEL

Jui-Lin F Li[1]. Martin Köhler[2] and C. R. Mechoso[3]
[1, 3] *Department of Atmospheric Sciences, University of California at Los Angeles*
[2]Geophysical Fluid Dynamics Laboratory, Forrestal Campus / US Route 1, Princeton, New Jersey 08542.

1. INTRODUCTION

Persistent stratocumulus clouds are usually observed to be capped by warm, dry subsiding air above and cool ocean surfaces underneath. They cover a significant portion of the Earth's surface and are important with respect to the global radiation budget and coupled atmosphere-ocean system. The major impact of stratocumulus clouds on climate through global radiation budget is that they reflect more solar fluxes (~60%) back to space than the surface does (~ less than 10%).

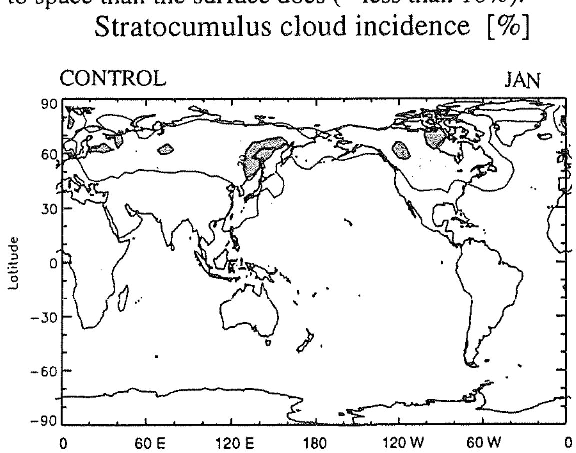

Figure 1

Figure 1. Simulated January mean PBL stratocumulus cloud incidence using the earlier version of the UCLA AGCM. The contour interval 10 %.

In the UCLA atmospheric general circulation model (AGCM), the variable-depth planetary boundary layer (PBL) model with the assumption of well-mixed total water mixing ratio and moist static energy is incorporated as an integral part of the model vertical structure (Suarez et al. 1983). The earlier formulation of the PBL moist processes in the AGCM significantly underpredicted stratocumulus cloud incidence almost everywhere (Fig. 1) when compared to the observations of Warren et al. (1988). This includes the subtropical marine stratocumulus over the eastern subtropical Pacific in both hemispheres, indicating that the simulated PBL was not sufficiently moist (and possibly not sufficiently deep). This relatively dry PBL over the oceans was not a consequence of insufficient surface evaporation. Indeed, the simulated mean surface evaporation was too large compared to observations, while the layer immediately above the PBL was too moist, resulting in an overestimate of mean cloud incidence for that layer (Li and Arakawa 1997). All of these suggest that the redistribution of moisture from the PBL to the layer above was excessive in the model. When this version of the AGCM was coupled with an oceanic GCM initialized with a climatological temperature distribution, the simulated mean sea surface temperatures (SSTs) became too cold over most of subtropical oceans due to overpredicted evaporation, while the SSTs off the coasts of California and Peru became too warm due to underpredicted stratocumulus cloud incidence (Ma et al. 1996; Mechoso et al 1999).

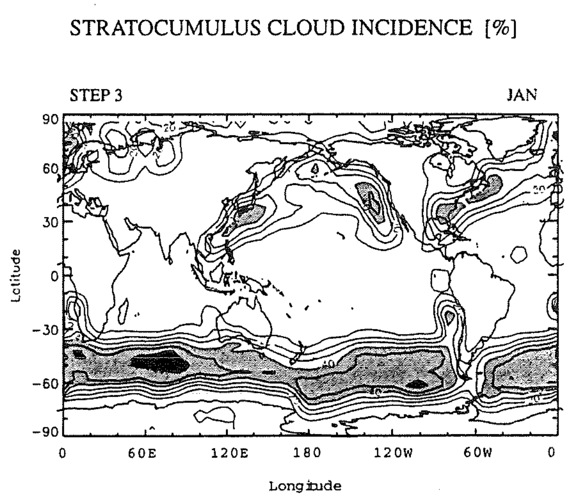

Figure 2

Figure 2. Simulated January mean PBL stratocumulus cloud incidence using the CONTROL version of the UCLA AGCM. The contour interval 10 %.

The formulation of PBL moist processes in the AGCM has recently been revised to address these problems (Li and Arakawa 1997). Three major revisions

Corresponding author address: Jui-Lin, Li, University of California at Los Angeles, Department of Atmospheric Sciences, 405 Hilgard Avenue, Los Angeles, CA 90095-156505; e-mail <li@vortex.atmos.ucla.edu>

have been made: (i) the properties of air entrained into the PBL were reformulated; (ii) entrainment processes associated with cloud top entrainment instability were refined; and (iii) the effect of subgrid-scale orography on the fractional stratocumulus cloudiness was included. With these revisions, the simulation of PBL moist processes is greatly improved. In particular, the surface evaporation and stratocumulus incidence (shown in Fig. 2) are far more realistically simulated than with the original version. Mechoso et al. (1999) presented a coupled GCM simulation in which this version of the UCLA AGCM is used and showed that the cold bias in tropical Pacific SSTs was alleviated.

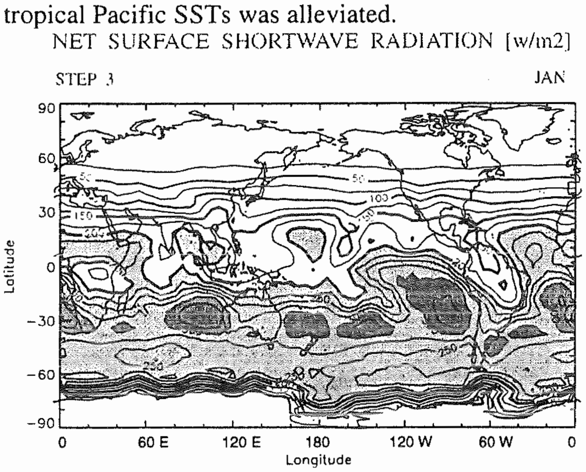

Figure 3a

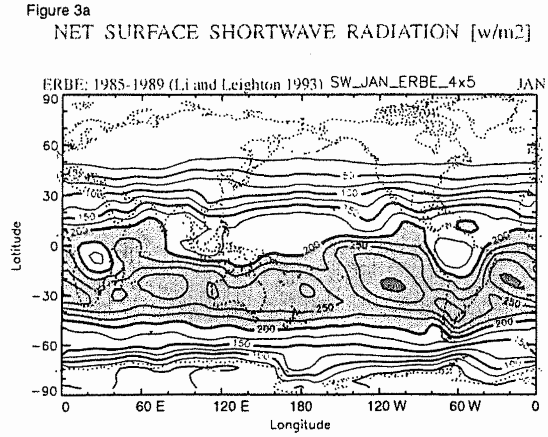

Fihure 3b

Figure 3. (a) Simulated January mean net surface solar flux using the CONTROL version. (b) Same variable for ERBE reanalysis. The contour interval is 25 (Wm^{-2}).

Although this version of the UCLA AGCM is successful in the simulation of PBL stratocumulus cloud incidence, the net surface solar and terrestrial fluxes are generally overpredicted (see Fig. 3a and 3b). This is due to too thin stratocumulus cloud optical thicknesses, when compared to those suggested in ISCCP-C2 data (Rossow and Schiffer 1991). In the current formulation, the stratocumulus cloud optical thickness is proportional to cloud depth, but does not consider cloud liquid water amount (Harshvardhan et al. 1989). With this formulation the AGCM predicts net surface solar fluxes over the low pressure belt around the Antarctic continent in Winter (Fig. 3a) and the Northern Pacific ocean in Summer (not shown) that are too high compared to those of ERBE (Fig. 3b). This results in simulated sea surface temperatures which are too warm when the AGCM is coupled to an ocean general circulation model which includes the North Pacific ocean (J. Farrara; personal communication). We believe that the excessive net solar fluxes reaching the ocean surface are responsible.

This letter describes our attempts to improve the estimate of PBL cloud optical properties by taking into account the liquid water path (LWP) in the calculation of the optical thickness. Results using the UCLA AGCM with the revisions are compared with ISCCP optical thicknesses and ERBE derived surface solar fluxes.

The AGCM is a finite-difference model based on the primitive equations, with horizontal velocity, potential temperature, surface pressure, water vapor mixing ratio, and ground temperature and snow depth over land as its prognostic variables. For this study we use a version of the model that has 15 layers in the vertical, with the top at 1 mb, and a horizontal resolution of 5^{o} in longitude and 4^{o} in latitude. For a detailed description of the model see Mechoso et al. 1999). We note that solar and terrestrial radiation as well as cloud optical properties are parameterized following Harshvardhan et al. (1989).

In section 2 the revision of PBL cloud optical properties is described. In section 3 we present comparisons of simulations with (NEW) and without (CONTROL) the new revisions. Both runs are initialized using October 1 1982 observations and integrated for 5 years. Concluding remarks are contained in section 4.

2. STRATOCUMULUS CLOUD RADIATIVE PROPERTIES

In the UCLA AGCM, the stratocumulus cloud condensation level, p_c, is defined as a level at which $q^* = r_M$. Here $q^*(T, p)$ is the saturation value of water vapor mixing ratio and $r_M = q_v + q_l$, where q_v is the water vapor mixing ratio and q_l represents the liquid water mixing ratio (Suarez et al. 1983). The vertical profile of the saturated water vapor mixing ratio varies approximately linearly with pressure. The vertical profiles of q_v and q_l are then completely defined by the condensation level and the liquid water mixing ratio at cloud top q_{lB}. The liquid water path (LWP, i.e. the vertical integral of q_l) for stratocumulus clouds then becomes (Randall 1994, personal communication):

$$LWP = \frac{1}{2} q_{lB} \frac{\Delta p_{Sc}}{g} \ . \qquad (1)$$

With (1) the optical thickness τ_{Sc} can be calculated as described next.

The calculation of cloud radiative fluxes requires the specification of optical thickness. In Harshvardhan et al. (1989) the stratiform cloud optical thickness is computed as

$$\tau_{Sc} = \frac{\Delta p_{Sc}}{12.5mb} \ , \qquad (2)$$

where Δp_{Sc} ($= p_C - p_B$) represents cloud pressure thickness. Additionally, a cloud fraction of $f_{Sc}=1$ for $\tau_{Sc} > 1$ and $f_{Sc}=\tau_{Sc}$ for $\tau_{Sc} < 1$ is assumed. This formulation produces considerably too thin cloud optical thicknesses τ_{Sc} compared to those indicated by ISCCP-C2 data (on the order of 3 to 30). For example, with a cloud pressure thickness commonly observed on the order of 25 to 50 mb (2) gives τ_{Sc} = 2 to 4.

Here, we propose an alternative to (2) by adopting the formulation of Stephens (1978), which can be written as

$$\tau_{Sc} = \frac{3}{2} \frac{LWP}{\rho_l r_e} , \qquad (3)$$

where r_e ,the effective radius of cloud droplets, is assumed as 10 μm and ρ_l is the density of liquid water. In equation (3) LWP is determined in (1) in a manner consistent with the formulation of the PBL moist processes in the UCLA AGCM (Suarez, et al., 1983). Note that the cloud optical thickness (3) is a function of liquid water mixing ratio at cloud top and cloud pressure thickness.

3. THE IMPACT OF THE REVISION ON NET SURFACE SOLAR RADIATIVE FLUXES

The January stratocumulus cloud incidence (not shown, but similar to Fig. 2) with the NEW version shows that the locations of the maxima off the west coasts of North America, South America, and South Africa, over the northeastern Atlantic ocean, and over the low pressure belt around the Antarctic continents are simulated fairly realistic compared to the observations of Warren et al. (1988). The NEW simulated January mean optical depths shown in Figure 4b have values reaching above 30 and are typically 5 to 10 times larger than the values produced by the CONTROL run (Fig. 4a). These NEW optical depths are comparable to those suggested in the ISCCP-C2 data set (Rossow and Schiffer 1991).

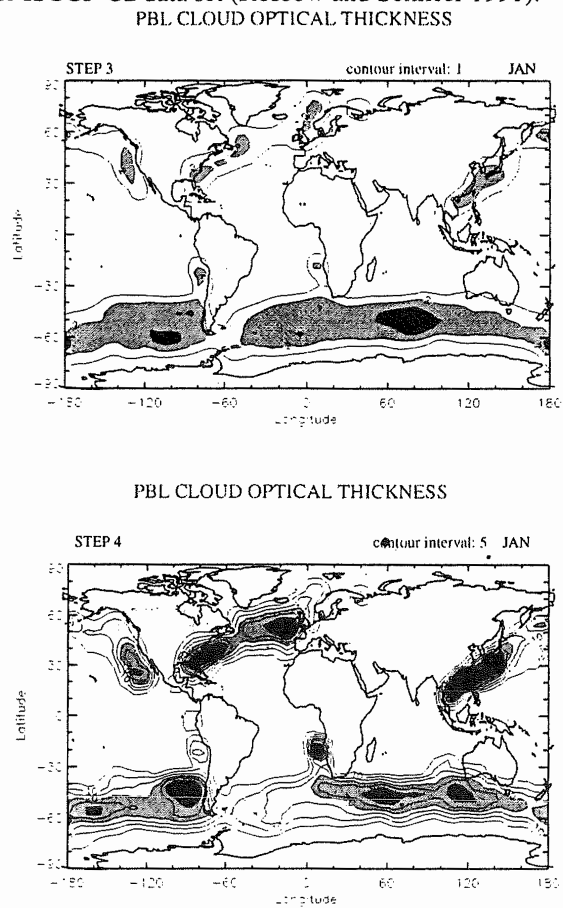

Figure 4. (a) Simulated January mean optical thickness using the CONTROL version. The contour interval is 1. (b) Same variable for the NEW version. The contour interval is 5.

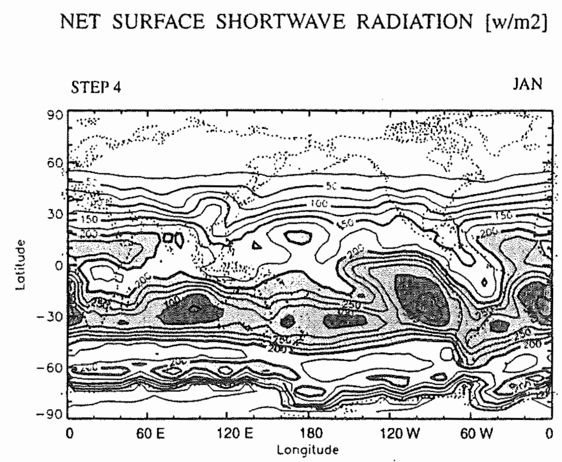

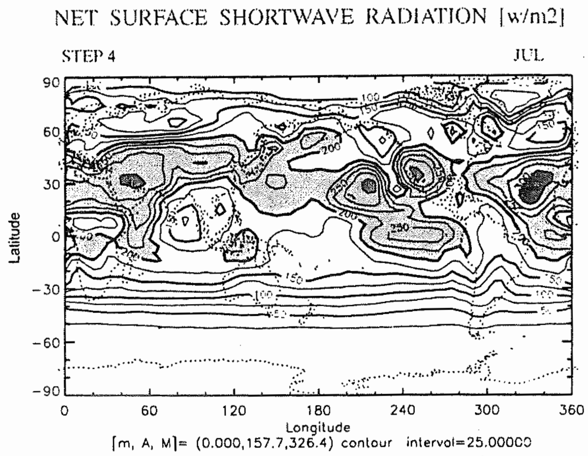

Figure 5. Simulated (a) January mean surface net solar radiative heat fluxes using the NEW version. (b) the same as (a) but for July. The contour interval is 25 (Wm^{-2}).

Consistently, the simulated net surface solar fluxes (Fig. 5a) are more realistic than those in CONTROL (Fig. 3a), in particular over the low pressure belt around the Antarctic continent (Fig. 3b). Similar to those in January, the simulated July mean solar fluxes at the surface are also well simulated, in particular over North Pacific and the northeastern Atlantic ocean (Fig. 5b). For the locations of the maxima off the west coasts of North America, South America, South Africa, the revised model also simulates more realistic surface solar fluxes. Those fluxes reduce by about 75 Wm^{-2} in January over the Southern Hemispheric low pressure belt, by about 100 Wm^{-2} in July over Northern Pacific and Atlantic, and by about 50 Wm^{-2} over off the coast of California (South America) in particular in Fall seasons, to become more realistic as compared to the ERBE derived values (Li and Leighton 1993).

4. CONCLUDING REMARKS

The revised formulation of stratocumulus cloud optical thickness used in the UCLA AGCM is presented. Preliminary results using the UCLA AGCM with this revision are very encouraging and show large impacts on the simulated solar fluxes at the surfaces. We find that the AGCM simulates much more realistic net surface solar fluxes than those of CONTROL throughout all seasons. We conclude that it is important not only to realistically simulate the geographical distribution of stratocumulus clouds but also correctly explicitly specify their optical thickness. This is obviously a crucial requirement for a coupled atmosphere-ocean model.

Acknowledgments. The authors wish to thank Professor Akio Arakawa for his encouragement and Drs. John Farrara and Leslie Hartten for their comprehensive comments. This research was funded under NSF ATM--9613979, NASA NAG5-4420, DOE-CHAMMP-DE-FG03-91ER61214 and NOAA NA66GP0121. Model integrations were performed at the computer facilities at UCLA Department of Atmospheric Sciences and San Diego Supercomputer Center.

6. REFERENCES

Harshvardhan, R D., D. A. Randall, T. G. Corsetti and D. A. Dazlich, 1989: Earth radiation budget and cloudiness simulations with a general circulation model. *J. Atmos. Sci.*, **46**, 1922-1942.

Li, J-L and A. Arakawa, 1997: Improvement of PBL moist processes in the UCLA General Circulation Model. *The Seventh AMS Conference on Climate Variation, Long Beach, Feb.2-7.*

Li, Z. and H. G. Leighton, 1993: Global climatologies of solar radiation budgets at the surface and in the atmosphere from 5 years ERBE data. *J. Geophys. Res.*, **98**, 4919-4930.

Ma, C.-C., C. R. Mechoso, A. W. Robertson, and A. Arakawa, 1996: Peruvian stratus clouds and the tropical Pacific circulation: A coupled ocean-atmosphere GCM study, *J. Climate,* **9**, 1635-1645.

Mechoso, C. R., J.-Y. Yu and A. Arakawa, 1999: A coupled GCM pilgrimage: From climate catastrophe to ENSO simulations. *General Circulation Model Development: Past, present and future*; *Proceedings of a Symposium in Honor of Professor Akio Arakawa*, D. A. Randall, Ed., Academic Press.

Rossow, W. B., and R. A. Schiffer, 1991: ISCCP cloud data products. *Bull. Amer. Meteor.* Soc., **72**, 2-20.

Stephens, G. L., 1978: Radiation profiles in extended water clouds. II Parameterization Schemes. *J. Atmos. Sci.*, **35**, 2123-2132.

Suarez, M. J., A. Arakawa, and D. A. Randall, 1983: The parameterization of the planetary boundary layer in the UCLA general circulation model: Formulation and results. *Mon. Wea. Rev.*, **111**, 2224-2243.

Warren, S. G., C. J. Hahn, J. London, R.M. Chervin, and R.L. Jenne, 1988: Global distribution of total cloud cover and cloud type amounts over ocean. NCAR Tech. Note NCAR/TN-273+STR, National Center for Atmospheric Research, Boulder, CO, 42pp. plus 170 maps.

FOG FORMATION OFF THE U. S. WEST COAST AS INDICATED BY GOES SOUNDINGS, COMPARED TO A SHORE BASED PREDICTION

Dale F. Leipper and Bryan R. Leipper

1. INTRODUCTION

This is an abstact of a technical note prepared by the authors on a similar subject (Leipper and Leipper, 1999). Space does not permit the inclusion here of a number of the important illustrations which may be found in the technical note or seen on the poster.

As far as is known, there is no agreed upon method by which the formation of observed shallow fogs and thin mixed layers off the west coast may be explained or predicted. These events are a critical part of the fog forecasting method called LIBS (Leipper inversion base statistics, see below). This method uses shore based observations and satellite visual imagery in a conceptual model to aid in forecasting offshore fog. It provides indices which allow the process of fog/stratus development to be monitored readily in a way which is very difficult using synoptic maps or other available analyzed products. To date, the paucity of offshore observations has made it difficult to demonstrate the validity of this model offshore but recent availablity of GOES soundings for offshore areas provides indication that the conceptual model does indeed apply.

The LIBS conceptualized development (Leipper 1995), and (Leipper et al. 1999), receives considerable new support from the GOES observations. They show the extension to a distance offshore of the strong surface inversion and a cleared area. They, together with coastal data, give new indication that the OAK RAOB data is applicable over a region along the coast and offshore.

Leipper (1995) concludes, "However, fog creates the mixed layer and not vice versa." Although several extensive field experiments have been conducted in such situations, none has provided hour by hour observations during fog formation at a given location offshore. Direct observations are needed to evaluate the LIBS concept of formation. GOES satellite soundings may provide these.

The physical processes indicated by GOES soundings may be combined with a theoretical and experimental study of fog formation in a stable atmosphere over a moist surface (Fleagle at al. 1952). This combination seems to provide the most satisfactory explanation of fog formation and the creation of a mixed layer offshore in these circumstances.

Although fog formation is a micro-meteorological process, this process is so much controlled by the sequential development or preconditioning of the atmosphere and the existing synoptic situation that a forecaster may base his decisions upon the synoptic and mesoscale factors.

Corresponding author's address:
Dale F Leipper, 716 Terra Court, Reno, NV 89506
(775) 972 6995 dalelr@attglobal.net

2. THE GOES SOUNDINGS

A sequence of GOES soundings made between 22Z August 22, 1999 and 14Z August 23 (locally overnight) is of considerable interest. These follow the Oakland RAOB of 12Z on August 22. This RAOB is an early morning coastal observation which was made at the peak of a strong offshore flow and a coastal hot spell. Except for the surface dew point, the features of the Goes sounding and the OAK RAOB at the same time are almost identical and a strong surface temperature inversion is clearly shown by each.

The similarity of the GOES sounding and the balloon sounding at OAK gives confidence in the use of the offshore GOES soundings when used alone. However, more investigation of the accuracy of the GOES soundings is needed, especially in the surface layers.

The surface synoptic map for 1335Z on August 22 shows the geostrophic wind pattern which included downslope offshore winds. These winds add anomalous heating to the continental air already heated by subsidence over the land. They carry the hot dry air to the coast, where its presence is indicated by the observed temperature structure, see Table 4, and then on offshore. The offshore area showing the presence of the hot dry air is seen as the cleared area on the satellite visual image of Fig. 1.

Fortunately for this event, the normal position for one of the regularly distributed GOES soundings, 35N, 125W, falls within the cleared area on Fig. 1. The sound-

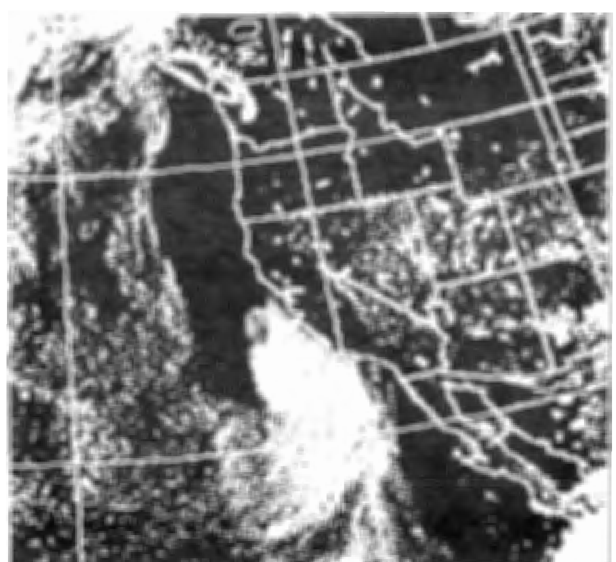

Figure 1. GOES 10 VIS 8/22/99 2100Z (2 p.m. Local) NRL Monterey Code 7541. The visual satellite image of the cleared area offshore is believed to show the extent of the surface inversion.

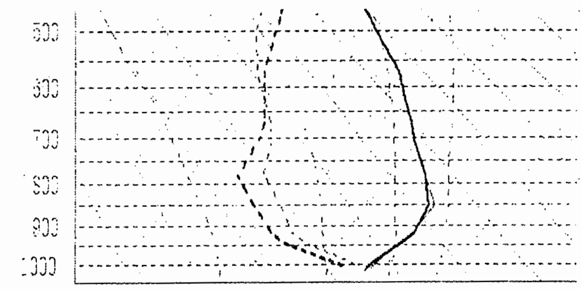

Sounding is 18 nm SW of station.

Figure 2. 3125 8/22/99 20Z. The mid afternoon GOES sounding indicating no change as yet in the surface layer. Strong surface inversions are indicated in both air temperature and moisture. The surface air temperature approaches the sea surface temperature.

ings reported at this site included one made before the surface inversion had been modified by its presence over the sea, Fig. 2. Three features of this observation which was made at 20Z, (1 p.m. local time) are important. One is that the inversion is a surface inversion with no indication of a mixed layer. Secondly, there is no indication of a shallow moist layer and thirdly the humidity is low from low levels to some 500 mb. This is a critical factor in the fog formation and the subsequent increase in depth of the mixed layer. (Leipper 1995).

The features shown in Fig. 2 lead, when the offshore wind eases, to a very shallow layer of high humidity restrained vertically by the strong surface temperature inversion. This humid layer is indicated by the GOES sounding made at 02Z in the late afternoon, see Fig.3. Although this indication is small, it is a definite change from the unmodified surface situation of Fig.2.

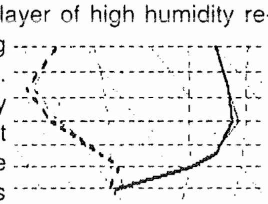

Figure 3
3125 8/23/99 02Z.

3. FOG FORMATION AND CREATION OF A MIXED LAYER

Given the surface moisture source and the vertical restriction of the highly stable atmosphere, Fleagle et al. (1952) describe and test experimentally how fog and a mixed layer are formed during the night by nocturnal radiation and eddy conduction. The GOES sounding made at 10Z, (3 a.m. local time, Fig. 4), now indicates the presence of a mixed layer and that, presumably, fog has formed.

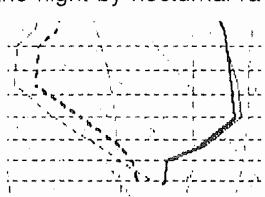

Figure 4
3125 8/23/99 10z.

The visual satellite image of 2100Z on the 23$^{rd.}$ shows that cloudiness (presumably fog) has now developed over the formerly cleared area. Inversion heights of less than 400 m would indicate that it was fog rather than stratus. The OAK RAOB at 14Z on the 23rd, showing an inversion height of 193 m, supports fog rather than stratus.

Sea surface temperature at this time varied from 11 C at the coast to nearly 19 C near 25N, 135W.

4. THE TIME OF FOG FORMATION AT SEA IN THE COASTALLY BASED FOG SEQUENCE OF OBSERVATIONS DURING A HOT SPELL

As mentioned, the formation of new fog at sea and the creation of a mixed layer are important parts of the LIBS forecasting method. Since over-ocean observations were almost never available in the past, this method utilized coastal observations and a conceptual model of what happened offshore. The over-ocean satellite soundings have considerably increased the understanding of the development and therefore in the confidence in this portion of the method.

Table 1 A simplified weather log. The LIBS fog sequence as observed at coastal sites, Aug 99 UTC

Date	*Ta*	*BI*	*MRY*	*SFO*	*SFO-o*
18	17.6	803	10	10	8
19	19.8	513	10	8	4
20	22.4	435	0.5	10	7
21	23.8	335	3	10	9
22	26.4	0	1	8 clr	
23	25.4	193	1.5	9 sct	
24	24.6	320	0.5	4	4

Table 1 shows how the offshore fog formation case presented above fits into the over-all LIBS day-to-day fog sequence, L95 and L99, as observed at two coastal stations which are some 125 km apart. The over-ocean satellite sounding observations occurred on the 22nd and 23rd of August. The night of the 23rd (UTC) was the night when the soundings indicated fog formation in the offshore formerly cleared area. The fog formation occurred the day after the Ta had gradually and regularly reached its maximum of 26.4. It was to decrease after that, indicating that the offshore wind had eased. During the rise of the Ta, the BI gradually decreased from 803 m to zero. When BI had dropped to 435 (near the 400 m guideline for fog), on the 20th, fog occurred at MRY. It then occurred each day at MRY from the 20th through the 24th while the BI remained less than 400 m. The BI had risen gradually from zero to 320 m after the Ta maximum and while the Ta was decreasing.

When the new fog had formed on the 23rd it did not reach SFO that day nor the following two days because the BI was low. Skies at SFO were clear on the 22nd and scattered the following day. On the 24th the BI had grown to 320 m and fog was able to approach SFO. The visibility in the new fog at SFO did drop to 4 miles with an overcast at 400 feet.

5. GOES USEAGE

The GOES calculated soundings are particularly suitable to an analysis of the formation of fog off the coast. Menzel et al (1998) describe the manner by which these soundings are determined and their primary characteristics. When the sky is clear, the GOES products include temperature and moisture profiles that, while containing less detail than radiosondes, do capture the profile in the mean very well. Moisture is more problematic than temperature and the recommendation appears to be to use layer mean and total column values rather than single level values.

The GOES retrievals differ from radiosonde measurements in that they do not use the same measurement characteristics and may not represent the atmosphere at exactly the same location or time. Radiosonde instrumentation errors may also affect comparisons. The GOES retrievals have been found to be more accurate than NCEP short term regional forecasts.

6. WEATHER LOGS

A number of weather logs showing selected and summary data were used in this analysis. Data from the University of Wyoming web site and the National Buoy Data center were converted to a convenient form and then summarized in a daily log. Examples of these logs are shown in tables one through four. Heights are usually in meters (m) and temperatures in degrees Celsius scaled by ten (10C). Column definitions are as follows.

6.1Simple weather log elements (Table 1)

Date - in August 1999
Ta - highest temperature in lowest km (10C).
BI - height of the inversion base (m), OAK 12z
MRY - MRY minimum visibility (miles)
SFO - SFO minimum visibility (miles)
SFO-o - SFO minimum height of overcast (100s feet)

6.2 Surface log elements (Tables 2 and 3)

P12z - surface pressure at 12Z (HPa)
C12z - ceiling at 12z (m)
D21z - surface dewpoint at 21z (10C)
MinV - minimum visibility (m)
CIG - minimum ceiling (m)
mDD - max dewpoint depression during day (10C)

6.3 CdxMap (Condition Map)

A condition map is a map showing the existence of a selected weather condition hour by hour during the weather log day. A single character or symbol is placed in the map for each hour of the day. This representation provides a simple means to illustrate patterns of the selected condition. A question mark ("?") is used to indicate no observations in a particular hour.

6.4low stratus map

The low stratus map symbols represent the number of observations in a particular hour that contain observations of greater than 60% sky cover with a ceiling lower than 1000 m. Normally there is just one observation per hour unless some change in

Table 2 MRY Surface Log

ID	*date*	*P12z*	*C12z*	*D21z*	*MinV*	*CIG*	*mDD*	*Visibility Map*
MRY	8-16-99	1019	91	111	8047	91	67	........___..__._...?...
MRY	8-17-99	1020	213	113	16093	152	61	....??.?.........?......
MRY	8-18-99	1018	335	55	16093	274	67	.............??.?.?.....
MRY	8-19-99	1017	213	118	11265	122	50	........?.........._....
MRY	8-20-99	1016	91	122	805	30	55	.............#=__.......
MRY	8-21-99	1017	152	122	4828	30	61	.............=..........
MRY	8-22-99	1011	91	115	1609	30	89	.........=___==.........
MRY	8-23-99	1012	61	113	2414	61	95	..._...._==__..._.......
MRY	8-24-99	1013	91	111	6437	30	67	.............._.___.....
MRY	8-25-99	1013	61	109	805	61	73	.__=_==_=_.==#=..=_.....
MRY	8-26-99	1010	30	122	322	30	111	__=._=#==_#___..........
MRY	8-27-99	1012	122	131	1609	61	67	............_=.__.......
MRY	8-28-99	1016	30	128	6437	30	34	..........______.__.....

Table 3 SFO Surface Map

ID	*date*	*P12z*	*C12z*	*D21z*	*MinV*	*CIG*	*mDD*	*Stratus Map*
SFO	8-16-99	1017	305	122	16093	305	94	111111111111..1.........
SFO	8-17-99	1019	213	120	8047	152	67	........111211111.......
SFO	8-18-99	1017	427	120	8047	152	67	....?.??11112111?.......
SFO	8-19-99	1015	183	81	16093	183	56	1....11111112?11?1111111
SFO	8-20-99	1015	213	122	12875	122	94	1111111111112111........
SFO	8-21-99	1015	335	122	16093	213	72	..........111111111.....
SFO	8-22-99	1009		122	14484	274	111	11111111................
SFO	8-23-99	1010	6096	127	12875	6096	183	....
SFO	8-24-99	1012	183	124	14484	183	83	............1...........
SFO	8-25-99	1011	152	122	4828	61	100	.......11..111111.......
SFO	8-26-99	1008		122	4023	91	133	..............11........
SFO	8-27-99	1008	6096	122	14484	305	122	.....??.................
SFO	8-28-99	1014	305	135	16093	305	100	............1...........

atmospheric conditions triggered more frequent observation recording.

6.5visibility map - v

The visibility map indicates the lowest visibility observed during the hour with a period for clear; pound sign (#) for visibilities < 1000m; equal sign for 1 to 5 kilometers; or underscore for 5 to 12 kilometers visibility..

6.6Sounding log elements

Table 4 OAK 12z sounding log

ID	*date*	*BI*	*BItop*	*ta*	*dt*	*dc*	*t850*	*h850*	*lyrs*	*grad*	*strength*	*score*
OAK	8-16-99	236	721	208	90	2571	162	1529	2	18	90	65
OAK	8-18-99	803	903	176	92	2413	174	1512	2	100	92	111
OAK	8-19-99	513	1083	198	92	1506	190	1506	2	26	92	69
OAK	8-20-99	435	788	224	110	1750	188	1516	2	47	110	94
OAK	8-21-99	562	848	238	116	1524	200	1524	3	88	116	104
OAK	8-22-99	6	407	264	88	1820	210	1500	3	21	86	37
OAK	8-23-99	193	952	254	126	2003	226	1490	2	36	126	75
OAK	8-24-99	320	944	246	130	1630	212	1497	2	42	130	88
OAK	8-25-99	164	1048	266	142	2759	224	1508	2	33	142	52
OAK	8-26-99	3	559	306	142	1508	256	1508	2	36	156	56
OAK	8-27-99	79	256	264	72	1895	206	1501	4	65	72	71
OAK	8-28-99	516	1008	236	118	2611	208	1513	3	56	118	102

BI - base inversion above MSL (m)
Bitop - primary bi top height (m)
ta - highest temperature in lowest kilometer (10C)
dt - inversion strength (10C)
dc - depth of sounding with <= 5kt winds (m)
t850 -850 mb temperature (10C)
h859 - 850 mb height (m)
lyrs - layers found in sounding
grad - primary bi temp gradient (10C/km)
strength - primary bi strength (10C)
score - primary xLayer calculated BI quality score

7. SUMMARY

The combination of over-ocean GOES sounding data with other readily available observations and the application of the Fleagle et al. theory and experimental results lead to a satisfactory description of how shallow fog forms at sea on the west coast. This has been a topic of considerable concern in the past. These direct observations at sea support the conceptual model of fog formation based upon land Observations.

8. REFERENCES

Fleagle, R. G. , W.H. Parrott and M. L. Barad 1952. Theory and effects of vertical temperature distribution in turbid air. *Jour. of Meteorology*, Vol. **9**, No. 1.

Leipper, D. F. 1995: Fog forecasting objectively in the California coastal area using LIBS. *Weather and Forecasting*, Vol. **10**, No. 4

-- and D. Weygand, J. Millard, and B. R. Leipper 1999: West coast fog and stratus events at air terminals and related weather summaries. Eighth Conference on Aviation, Range and Aerospace Meteorology, 10-15 January, Dallas, Texas, by the AMS, Boston, MA.

-- and B. R. Leipper, 1999: Over-ocean satellite soundings, Technical Note 99NV01, TechComm Labs.

Menzel, W. Paul, et al, 1998. Application of GOES 8/9 Soundings to Weather Forecasting and Nowcasting. *BAMS* **79** # 10

GOES soundings were obtained from
http://orbit-net.nesdis.noaa.gov/goes/soundings/
surface and sounding data was obtained from
http://www-das.uwyo.edu/weather.htm

CLOUD MICROPHYSICAL PROPERTIES ASSOCIATED WITH CONVECTIVE ACTIVITIES WITHIN THE STRATOCUMULUS-TOPPED BOUNDARY LAYERS

Michelle K. Whisenhant and Qing Wang
Naval Postgraduate School, Monterey, CA

1. INTRODUCTION

Although the convective activities within the stratocumulus-topped boundary layers (STBL) are in general weaker compared to the cumulus boundary layers, the turbulent updraft and downdraft in STBL can be clearly defined and were found to possess distinctive thermodynamic properties (e.g., Khalsa, 1993, Whisenhant, 1999). For this reason, attempts have been made to apply the mass flux concept to STBLs in both one-dimensional boundary layer models (Wang and Albrecht, 1986) or climate models (Randall *et al.*, 1992). Large eddy simulations (LES) also revealed significant differences in microphysics properties between the turbulent updrafts and downdrafts. For example, Feingold *et al.* (1986), from a two-dimensional large eddy simulation model with size resolved cloud microphysics, showed larger number concentration and smaller droplet size in the updraft region compared to the downdrafts. The work by Kogan *et al.* (1995) using a three-dimensional LES with explicit cloud microphysics also revealed similar differences in the microphysics properties, which can be explained in the context of the condensation/evaporation in response to supersaturation in updrafts and entrainment in downdrafts. In contrast to the variability in cloud microphysics in response to different aerosol loading (Pawlowska and Brenguier, 1999), we refer to the variability seen between the convective events as the 'natural variability' of cloud microphysical properties.

However, the natural variability of cloud microphysics properties seen in LES has not been studied using in situ observations. Due to the weak nature of the convective elements in the stratocumulus-topped boundary layers, the resulted differences in microphysics properties are likely small and are thus difficult to evaluate. The work presented here attempts to fill this void by examining a large number of aircraft observations. Confidence in the results is gained through consistency in the results from many cases. In addition to the variability associated with turbulent updrafts and downdrafts, we will also analyze the variability on scales greater than the boundary layer internal circulation. These analyses contribute to further in-depth understanding of the interaction between the boundary layer dynamics and the microphysical processes.

* *Corresponding author address:* Michelle K. Whisenhant, Naval Postgraduate School, Dept. of Meteorology, Monterey, CA 93940. e-mail: mkwhisen@nps.navy.mil

2. DATA

The measurements used in this study were obtained during the First International Satellite Cloud and Climate Project (ISCCP) Regional Experiment (FIRE) Marine Stratocumulus Intensive Field Observations (IFO) conducted off the coast of southern California in June and July 1987. In particular, we used the aircraft measurements made by the Electra operated by the National Center for Atmospheric Research (NCAR). The general instrumentation of the NCAR Electra during FIRE experiment has been discussed in several FIRE related publications (e.g., Paluch and Lenschow, 1991, Wang and Albrecht, 1994). The main measurements used in this study are the cloud droplet spectra sampled by the Forward Scattering Spectrometer Probe (FSSP), which measures droplet number concentration between 3 and 45 μm. We utilize data obtained by the NCAR Electra aircraft in seven of the ten flights flown during FIRE to analyze various aspects of the spatial variability in the cloudy BL. The seven flights chosen to study contain level leg measurements at levels both in and out of the cloud. The in-cloud level legs are used to analyze the variations of cloud microphysics properties.

3. ANALYSIS METHOD

A conditional sampling method is used to identify the turbulent updrafts and downdrafts based on vertical velocity. The criteria used to define the convective events is similar to that used in Nicholls (1989), where a minimum event width and a minimum mean vertical velocity are required. The non-zero vertical velocity criterion results in a third group named the 'environment', defined as the regions that are neither occupied by an updraft or a downdraft. Once the events are defined, the geometric, thermodynamic, and microphysical parameters within the updrafts and downdrafts are calculated and analyzed.

An example of the various event properties from July 5, 1987 (flight 4) is shown in Fig. 1. In general, the mean event sizes (Fig. 1, left panel) are between 10 and 30 percent of the BL height (z_i), or about 200-300 m in the cases of FIRE. In all cases (except for one flight near the coast of California), the convective event size in the upper BL is about 0.2 to 0.3 of z_i, while the near-surface event size is between $0.10z_i$ and $0.20z_i$. We observed increased event size below the cloud layer, as shown in the example in Fig. 1, although the updraft and downdraft appear to have similar sizes. The total fractional length coverage, defined as the ratio between the total length covered by the updraft (or downdraft) and the total length of measurements, varied

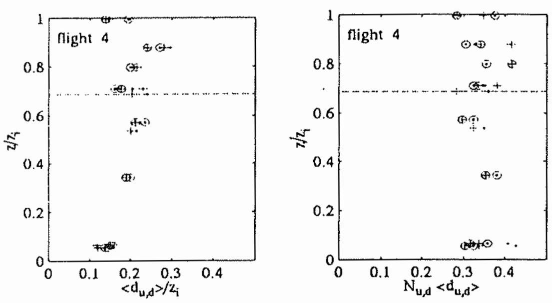

Figure 1. Mean event sizes (*d*) scaled by the boundary layer depth (left panel) and fractional length coverage (right panel) for updrafts (+) and downdrafts (·) for the horizontal measurement legs. Here, N is the total number of events per unit horizontal measurement length. Results from additional legs are denoted with a circle on the updraft or downdraft symbols. The dotted line shows the average height of the cloud base.

between the different flights and between different levels in the BL within each flight. The fractional coverage ranges between 0.3 and 0.5, the magnitude of which seemed to be associated with the strength of the turbulence in each case. Figure 1 also shows that the updrafts occupy a larger fraction than the downdrafts, A phenomenon that was also observed in nearly all the cases. This indicates the presence of some strong downdrafts that may contribute to a negative skewness of vertical velocity perturbations. The results for other flights and detailed discussions can be found in Whisenhant (1999).

4. CLOUD MICROPHYSICS PROPERTIES IN CONVECTIVE EVENTS

1) Mean Droplet Size and Number Concentration

Once the updrafts and downdrafts were identified, the properties of the cloud droplets are calculated for updrafts, downdrafts, and the environment, respectively. We first compared the droplet sizes in the updrafts and downdrafts. The results are shown (Fig. 2) as a fractional difference, defined as the ratio between the difference in volume diameter between the two types of events ($d_u - d_d$) and the average volume diameter of both events ($(d_u + d_d)/2$). The magnitude of difference is small, less than 10%, but is consistently negative in all cases. This trend indicates that the downdrafts, which originated from higher levels, contain larger droplets. Larger differences are observed near the base and top of cloud, with a minimum difference in the mid cloud range, which is consistent with droplet formation in the updrafts near the cloud base and evaporation due to entrainment in the downdrafts near the cloud top.

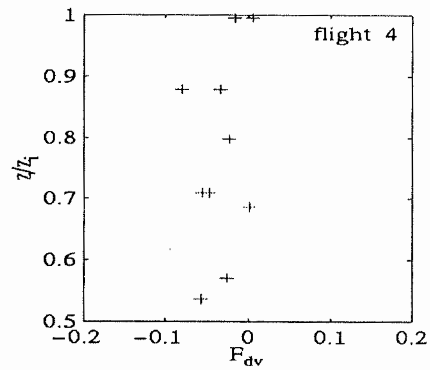

Figure 2. Fractional difference for volume diameter of cloud droplets (F_{dv}). F_{dv} is calculated as: $(d_{v_u} - d_{v_d}) / \frac{1}{2}(d_{v_u} + d_{v_d})$.

The number concentration of droplets in the updrafts is consistently higher than in the downdrafts at all levels within the cloud (Fig. 3). Since activation of cloud

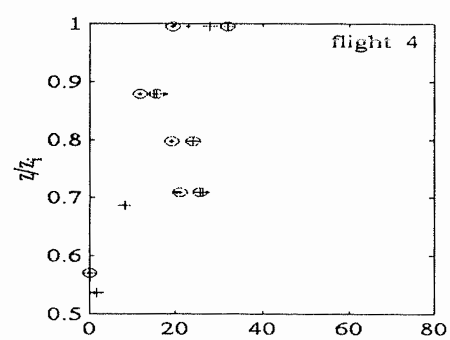

Figure 3. Same as Fig. 1, except for number concentration of cloud droplets (in cm^{-3}).

droplets is occurring in the updrafts and evaporation of droplets is occurring in the downdrafts, these observations are reasonable and are consistent with results from LES models (Feingold *et al.*, 1986, Kogan *et al.* 1995).

2) Cloud Droplet Spectra

The droplet size variation in turbulent updrafts and downdrafts are seen more clearly in the cloud droplet spectra from the FIRE flights. Figure 4 shows an example of the mean droplet spectra in the convective updrafts and downdrafts at three representative levels in the cloud layer. The results are from measurements of

July 10, 1987 (flight 6), but are typical of those observed during FIRE. The droplet spectra in panels a, b, and c

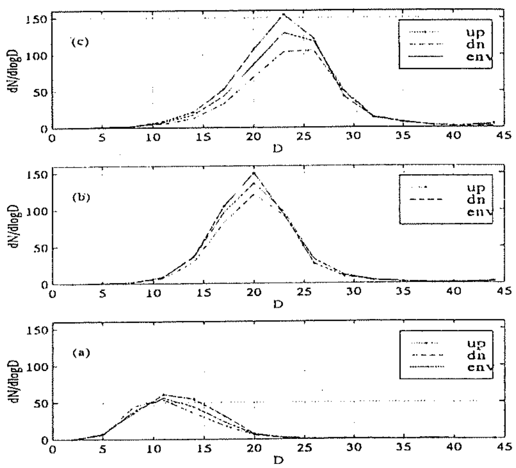

Figure 4. Cloud droplet spectra from three in-cloud measurement legs on flight 6. The vertical axis is dN/dlogD, where N is the droplet number concentration (in cm^{-3}) and D is the droplet diameter (in μm). a) near the cloud base, b) near the middle of the cloud, c) near the cloud top. The symbols for updrafts, downdrafts, and the defined environment are given in the legend.

of Fig. 4 were obtained from measurement legs near the cloud base, in the middle of the cloud layer, and near the cloud top, respectively. As already noted, the updrafts typically contain a larger concentration of droplets at all droplet size bins than the downdrafts for a given in-cloud leg. Additionally, the droplet spectra of the defined environment falls in between the updraft and downdraft droplet spectra, and there is typically no shift in the peak droplet size between the updrafts, downdrafts, and environment at a given height. There is a shift to larger droplet sizes with increasing height in the cloud, independent of the convective events. The difference in peak droplet concentration between updrafts, downdrafts, and environment appears to increase near the cloud top. Additionally, the number of small droplets occurring in the downdrafts appears to decrease near the cloud top, resulting in the observed larger mean droplet diameters in the downdrafts here.

5. OTHER VARIABILITIES IN CLOUD MICROPHYSICS

In most of the flights analyzed, we observed significant differences in the droplet spectra between two legs at the same vertical level in a particular flight, indicating the horizontal variability of the cloud microstructure on a scale larger than the boundary layer internal circulation (50 to 100 km). Figure 5 shows the droplet size distribution from two different turbulence legs from July 3, 1987 (flight 3) that were flown in-cloud near the cloud base. Figure 5a has a spectral shape similar to the typical case in Fig. 4, yet the plot indicates that the droplet concentration is largest in the defined environment, slightly higher than the updraft concentration. This implies that the turbulence is not as active in this region of the cloud base. As a result, the turbulence updraft and downdraft may not be well correlated with the activation and growth of the cloud droplets. Figure 5b shows a bimodal size distribution, with a larger concentration and smaller droplets in the updrafts in both modes. This spectral structure indicates that, in this well-mixed turbulent BL, there are downdraft droplets being recaptured and recycled in the updrafts at this particular horizontal location near the cloud base. This phenomenon was reproduced in a LES model by Kogan *et al.* (1995).

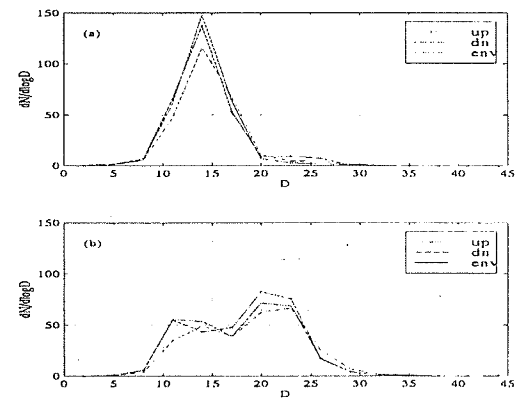

Figure 5. Same as in Fig. 3, except for two horizontal turbulence legs near the cloud base in flight 3. Legs are between 60 and 85 km apart.

We also observed horizontal variability in the cloud droplet spectra in the cases where cumulus clouds penetrate the stratocumulus deck from below. Figure 6 illustrates one example of this occurrence in the FIRE flights using measurements from July 11, 1987 (flight 7). Figure 6 shows two cloud droplet spectra from the same horizontal measurement leg near the cloud top. During this in-cloud flight leg, the observer's notes indicate the presence of thick stratocumulus, with some regions of penetrating cumulus observed. The droplet spectra from the first segment (Fig. 6a) appear similar to those shown earlier for flight 6 for the updrafts, downdrafts, and defined environment, and thus it is consistent with the droplet spectra of stratocumulus with no penetrating cumulus (Fig. 4). In Fig. 6b, however, the total number concentration is much higher, and the updraft and downdraft concentration is much higher than that of the defined environment. Also, the droplet sizes are smaller than those in Fig. 5a. This is consistent with the findings of Martin et al. (1994), who observed that the intrusion of cumulus clouds resulted in a localized increase in droplet concentration and liquid water content in the stratocumulus layer, with a localized decrease in droplet size as more droplets compete for available water vapor.

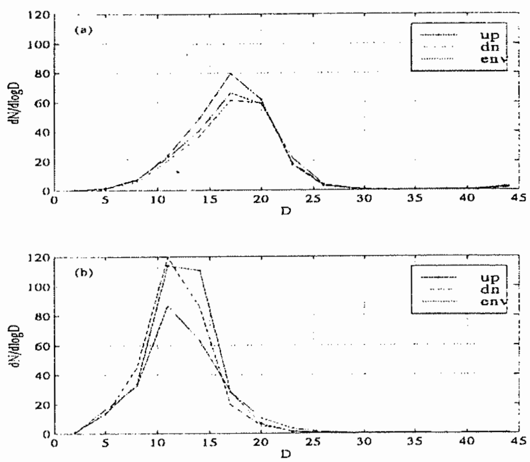

Figure 6. Same as Fig. 4, except for flight 7 where penetration of the stratocumulus by cumulus was observed. Cumulus penetration was recorded by the in-flight observer in (b).

6. SUMMARY

Analysis of updraft/downdraft microphysical parameters revealed consistent differences between updraft and downdraft. In general, the updrafts occupied larger areas and contain smaller droplets. These results were obtained from LES studies utilizing explicit cloud microphysics, but have not been evaluated using observational data. This study fills the void using a large number of cases.

We also studied the variability in cloud microphysical properties on a scale larger than the boundary layer internal circulation. These variability can be identified from the differences in different legs at the same level of the same flight. The differences seen are likely the result of localized changes in the extent of turbulent mixing occurring near the cloud top and base and also the interaction with cumulus forming beneath the stratocumulus deck in a localized area.

We do not present error statistics for the calculations made in this study. In one aspect, there is no accepted method of error representation for these types of calculations. Nevertheless, confidence in the results is obtained through consistency between results from different flights.

The current research provides, for the first time, the microphysical properties in the convective events. These observational results are consistent with those from LES with explicit cloud microphysics, such as in Kogan *et al.* (1995). The differences in the microphysical properties between the turbulent updrafts and downdrafts clearly revealed the physical processes occurring in each type of event. More well-designed in-cloud measurements are desirable to further quantify the findings here.

7. ACKNOWLEDGEMENTS

The authors greatly acknowledge the support by National science Foundation (NSF) Grant ATM-9900496. Part of Qing Wang's work was also supported by NSF Grant ATM-9700845.

8. REFERENCES

Feingold, G., B. Stevens, W. R. Cotton, and R. L. Walko, 1986: An explicit cloud microphysics/LES model designed to simulate the Twomey effect. *Atmos. Res.,* **33**, 207-233.

Khalsa, S.J.S., 1993: Direct sampling of entrainment events in a marine stratocumulus layer. *J. Atmos. Sci.*, **50**, 1734-1750.

Kogan, Y.L., M.P. Khairoutdinov, D.K. Lilly, Z.N. Kogan, and Qinfu Liu, 1995: Modeling of stratocumulus cloud layers in a large eddy simulation model with explicit microphysics. *Amer. Meteor. Soc.*, **52**, 2923-2940.

Martin, G.M., D.W. Johnson, D.P. Rogers, P.R. Jonas, P. Minnis, and D.A. Hegg, 1995: Observations of the interaction between cumulus clouds and warm stratocumulus clouds in the marine boundary layer during ASTEX. *J. Atmos. Sci.*, **52**, 2902-2922.

Nicholls, S., 1989: The structure of radiatively driven convection in stratocumulus. *Quart. J. Roy. Meteor. Soc.*, **115**, 487-511.

Paluch, I. R., and D. H. Lenschow, 1991: Stratiform cloud formation in the marine boundary layer. *J. Atmos. Sci.*, **48**, 2141-2158.

Pawlowska, H., and Brenguier, J.-L., 1999: Microphysical properties of stratocumulus clouds during ACE2, Submitted to *Tellus*.

Randall, D. A., Q. Shao, and C.-H. Moeng, 1992: A second-order bulk boundary layer model, *J. Atmos. Sci.*, **49**, 1903-1923.

Wang, Q., and B. A. Albrecht, 1994: Observations of cloud-top entrainment in marine stratocumulus clouds. *J. Atmos. Sci.*, **51**, 1530-1547.

Wang, S. and B. A. Albrecht, 1986: A stratocumulus model with an internal circulation. *J. Atmos. Sci.*, **43**, 2374-2391.

Whisenhant, M.K., 1999: Convective activities within the stratocumulus-topped boundary layer. Master's Thesis, Naval Postgraduate School, Dept. of Meteorology, Monterey, CA. 85 pp.

CHARACTERISTICS OF DRIZZLE IN COASTAL STRATOCUMULUS CLOUDS

Silke Fritz, B. A. Albrecht and P. Kollias

MPO Division, RSMAS/University of Miami, Miami, FL.

1. INTRODUCTION

Drizzle processes often influence the dynamics and structure of marine stratocumulus clouds. Numerous studies have considered the significance and contribution of drizzle processes to the cloud-topped boundary layer (e.g., Vali et al., (1998), Wang et al., (1994), Bretherton et al., (1995)). However, several issues concerning the formation of drizzle in shallow boundary layer clouds remain unresolved. These include the effects of the depth of the cloud layer, CCN concentration, and turbulence structure on drizzle formation. In this paper, the characteristics of drizzle in coastal stratocumulus clouds and its relation to cloud thickness and turbulence are examined.

The specific goals of this study are to:

1) characterize the vertical distribution of drizzle and its relation to large-eddy cloud circulations, and

2) examine the relative roles of cloud thickness and cloud turbulence levels on drizzle production.

Preliminary analysis of observations from a mm-wavelength radar is presented here to illustrate the techniques being developed to address these goals. Using a case study, characteristics of drizzle observed in marine stratocumulus are discussed and simplified methods are applied to illustrate the horizontal variability and the mean vertical structure of the stratocumulus layer. A comparison of a drizzle and a non-drizzle period is presented to highlight differences in cloud structures for these conditions.

*Corresponding author address: Silke Fritz, Rosenstiel School of Marine and Atmospheric Science, Division of Meteorology and Physical Oceanography 4600 Rickenbacker Causeway of Miami, Florida 33149-1098.

2. EXPERIMENT - INSTRUMENTATION

Various parameters characterizing drizzle and its related formation processes were observed during the Drizzle and Entrainment Cloud Studies experiment (DECS) conducted on the shore of Monterey Bay, California from 14 June to 9 July 1999 using a suite of surface-based remote sensing systems. The principal observing system for this study was a surface-based upward looking 94 GHz Doppler radar. A description of this system can be found in Lhermitte (1987) and Albrecht et al. (1999). Doppler spectra from this radar were collected to provide cloud microphysical and turbulence retrievals. The vertical resolution of the cloud radar for this study is 30 m. The temporal resolution is 3.5 sec. A ceilometer collocated with the cloud radar was used to define the cloud-base height. Continuous observations of boundary layer height and winds were obtained from the Naval Postgraduate School (NPS) 915 MHz wind profiler. Radiosondes were released to obtain the boundary layer structure at the site. In addition to remote sensing, in-situ observations from the Center for Interdisciplinary Remotely-Piloted Aircraft Studies (CIRPAS) Twin Otter were made to assist in the evaluation of the remote sensing retrievals.

3. OBSERVATIONS

The cloud radar data collected during the 4 weeks of the experiment where made as the stratus layer advected on-shore. Here a very small sample of the observations made on 24 June 1999 are used to examine the variability of the marine stratocumulus layer with an emphasis on drizzle variability. A weak surface cold front was located northwest of the experiment area resulting in a NNW flow. During the night the front moved over the site and continued southeast. Early in the night there was a short intensive period of heavy drizzle. The drizzle progressively weakened and eventually dissipated. The cloud/drizzle base temperature was 11 ° C throughout the night.

In the following sections, a subset of the drizzle period lasting 40 minutes between 05:10 and 05:50 UTC and a subset of the non-drizzle period between 07:30 and 08:10 UTC on 24 June 1999 were used for the main characteristics of the cases and to apply simplified retrieval techniques.

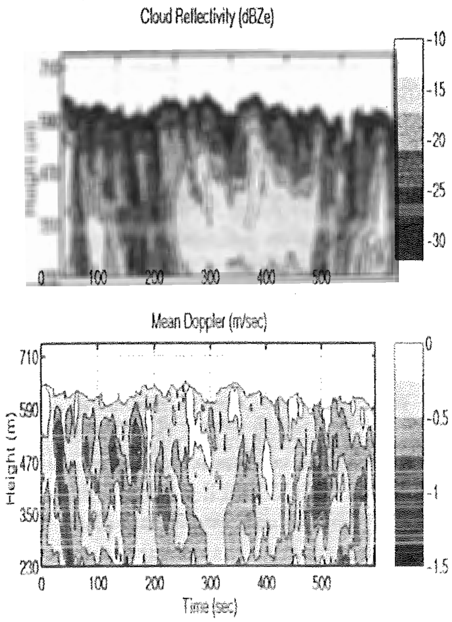

Fig.1 A 10-minute time height mapping of cloud reflectivity and Doppler velocity starting at 05:20 UTC. The height resolution is 30 m and the temporal resolution 3.5 sec. The accuracy of the Doppler velocity measurements is 1.65 cms^{-1}.

The observed reflectivity and Doppler velocity for a 10-minute period during the drizzle period are shown in Figure 1. These provide a typical picture of the horizontal variability of stratus clouds with drizzle. At 05:20 UTC (22:20 PST) the drizzle events occur in wavelike structures with time scales of the order of 3-4 min. within the stratocumulus cloud. This is indicated by the reflectivity mapping of the stratus layer, which exhibits large inhomogeneities in the horizontal. The cloud base is not defined since the drizzle signal clearly dominates the radar returns. The velocity field is dominated by downward motion associated with downdrafts and the drizzle. The strongest downdrafts are located in regions of low reflectivity. Some of the downdraft structures appear to originate from the cloud top as indicated by the penetration of low reflectivity values from the cloud top in association with strong downward motion.

The reflectivity mapping (not shown) for a non-drizzle period observed 2 hours later, has the same variability but with significantly lower reflectivity values and weak updraft structures. The cloud tops for both areas are at approximately the same height with a cloud thickness of about 500 m. The cloud top is detected by the 2 dimensional reflectivity field using a reflectivity gradient method.

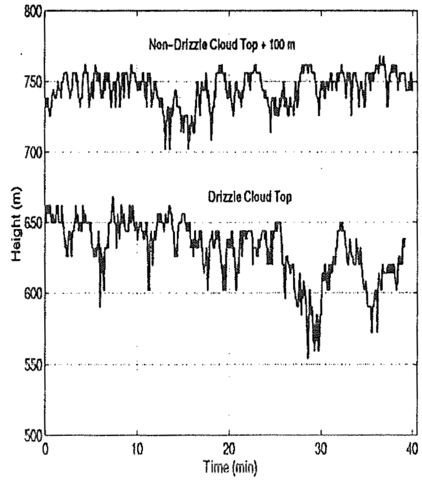

Fig. 2 Cloud top height time series (40 min) for drizzle the and non-drizzle cases.

Figure 2 shows the retrieved cloud top for 40 minutes of observations in a stratus layer with high reflectivities (drizzle case) and 40 minutes with low reflectivities (non-drizzle case). Time series of cloud top boundaries indicate the depth of the entrainment zone. During the drizzle period the cloud top variability is greater than that observed during the non-drizzle case. Further investigation of the cloud-top variability will be made using the entire DECS data set.

Observations of cloud base are difficult since surface-based cloud radars cannot resolve structures below about 200 m. Therefore, the cloud base boundaries are not resolvable by the cloud radar especially in the drizzle case. During the drizzle period, the cloud base detected by the ceilometer was near the ground (30 m). Interpretation of the ceilometer data may make it difficult to discriminate between the real cloud base and the level of the drizzle. In the non-drizzle case the cloud base height for the ceilometer was between 100 – 150 m.

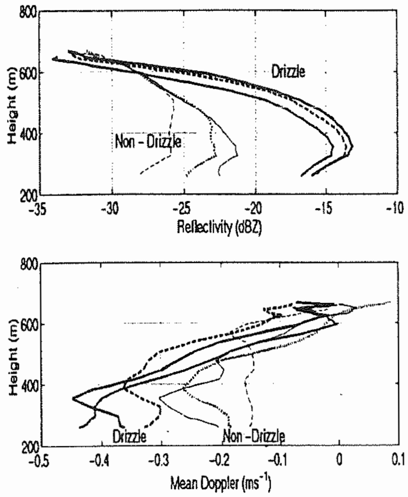

Fig. 3 Average of 10-minute profiles of reflectivity and Doppler velocity for both the drizzle and non-drizzle case.

The mean reflectivity and the mean Doppler velocity computed from the Doppler spectra for the two cases are shown in Figure 3. The reflectivity profiles indicate distinct differences between the drizzle case and the non-drizzle case. Although the reflectivity is substantially lower for the non-drizzle case than for the drizzle case, there is more variability in the profiles for this period. The Doppler velocity profiles for the drizzle case indicate that below 400 m an increase in reflectivity is associated with an increased fall velocity.

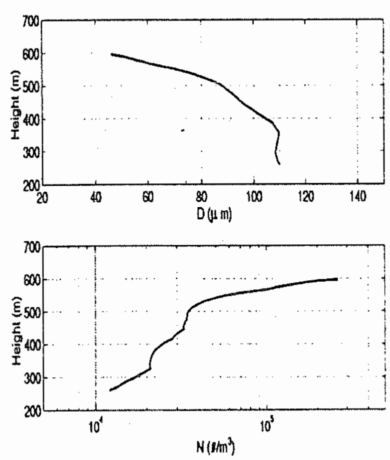

Fig. 4 Retrieved profiles of the droplet diameter and concentration number for the drizzle case.

The Doppler spectra will be used to develop more sophisticated techniques for distinguishing drizzle/non drizzle modes of the stratus layer and retrieving cloud microphysics. Currently, simple parameterization of the cloud microphysical structure is made using the mean profiles of reflectivity and vertical velocity in the drizzle case. Using a mono-dispersed cloud droplet model we estimate the mean equivalent diameter corresponding to the observed mean Doppler profile. The equivalent diameter retrieved by this simplified technique can be used to deduce the number of droplets needed to provide the observed reflectivities.

Figure 4 shows the retrieved profiles of the droplet diameter and number concentration for the drizzle case. The profiles exhibit increasing droplet sizes towards the cloud base and a corresponding decrease in the number of droplets towards the ground. Despite the simplicity of our model, the results are consistent with previous observations in marine stratocumulus clouds (Frisch et al., 1994).

4. CONCLUSIONS

The DECS radar data of marine stratocumulus clouds provides detailed descriptions of drizzle and non-drizzle conditions. The data presented here demonstrate the highly variable character of marine stratocumulus clouds. Furthermore, the results show a clear picture of drizzle structure in the lower cloud part, which has a lower droplet concentration and bigger drops than in the upper part of the cloud. The treatment of the dynamics of the cloud in our study is very simplified. In addition, to the drizzle / non-drizzle modes, each case considered is characterized by substantial internal variability. Nevertheless, the high-resolution data collected during the DECS experiment can be proved extremely valuable in our effort to quantify the variability and highlight the physical processes contributing to the drizzle.

In the future, retrieval techniques using the full recorded Doppler spectrum and data collected by other instruments will be developed to facilitate the study of drizzle characteristics and processes for the entire DECS data set.

5. ACKNOWLEDGEMENTS

This research was funded by ONR N 00014-99-1-0036.

6. REFERENCES

Albrecht, B. A. P. Kollias, R. Lhermitte, and R. Peters, 1999: Observations Of Tropical Cloud Systems With A MM-Wavelength Doppler Radar – An Overview *Proceedings 29th International Conference on Radar Meteorology, Am. Meteorol. Soc.*, Montreal, 454 –456.

Bretherton, C. S. P. Austin, and S. T. Siems, 1995: Cloudiness and Marine Boundary Layer Dynamics in the ASTEX Lagrangian Experiments. Part II: Cloudiness, Drizzle, Surface fluxes, and Entrainment. *J. Atmos. Sci.* **52**, 2724 –2736.

Frisch, A. S. C. W. Fairall, and J. B. Snider, 1994: Measurement of Stratus Cloud and Drizzle Parameters in ASTEX with a K_a -Band Doppler Radar and a Microwave Radiometer. *J. Atmos. Sci.* **52**, 2788-2799.

Lhermitte, R., 1987: A 94 GHz Doppler radar for cloud observations. *J. Atmos. Oceanic Tech.*, **4**, 36-48.

Vali, G., R. D. Kelly, J. French, S. Haimov, D. Leon, R. E. McIntosh, and A. Pazmany, 1998: Finescale Structure and Microphysics of Coastal Stratus. *J. Atmos. Sci.* **55,** 3540-3564.

Wang, S., and Q. Wang, 1994: Roles of Drizzle in a One-Dimensional Third Order Turbulence Closure Model of the Nocturnal Stratus – Topped Marine Boundary Layer. *J. Atmos. Sci.*, **51**, 1559-1576.

MICROPHYSICAL & OPTICAL PROPERTIES OF WINTER BOUNDARY LAYER CLOUDS OVER THE SEA : TWO CASE STUDIES OF CONTINENTAL-TYPE WATER & MARITIME MIXED-PHASE STRATOCUMULI

Jean – François Gayet [1], Shoji Asano [2, 4], Akihiro Yamazaki [2], Akihiro Uchiyama [2], Alexander Sinyuk [3], Frédérique Auriol [1] and Olivier Jourdan [1]

(1) Laboratoire de Météorologie Physique, UPRESA/CNRS n°6016, Université Blaise Pascal, Clermont-Fd, France.
(2) Meteorological Research Institute, Tsukuba, Ibaraki 305-0052 Japan.
(3) Stepanov Institute of Physics, National Academy of Science of Belarus, Bielorussia.
(4) Present affiliation : Center for Atmospheric and Oceanic Studies, Tohoku University, Sendai 980-8578 Japan.

1. INTRODUCTION

It is now well-recognized that boundary-layer clouds have a great influence on weather and climate through their effects on the radiative energy budget in the atmosphere (see among others Fouquart et al., 1989 or Heymsfield, 1993). Despite many researches devoted to field experiments and subsequent cloud-radiation modelings (see for instance Foot, 1988), the well-documented simultaneous observations of cloud microphysical and optical properties are still insufficient and essential to improve our understanding of the relationship between radiation and the boundary-layer clouds, including mixed-phase conditions. During January 1999, an intensive aircraft field observations of clouds and radiation was carried out by the Meteorological Research Institute (MRI) within the Japanese Cloud and Climate Study (JACCS) program (Asano et al., 1994). The experimental strategy was designed to simultaneously document the radiative and microphysical properties of winter-time boundary-layer clouds, including mixed-phase situations, by synchronized formation flights with two aircraft. An instrumented Cessna 404 Titan aircraft was used for radiation and remote-sensing measurements with flight patterns conducted above the clouds. A Beechcraft B200 Super King Air aircraft (B200) was used for in situ cloud microphysic and radiation measurements with collocated flight patterns conducted into the cloud and below the cloud base. In this paper we shall address the microphysical and optical properties for two winter boundary-layer clouds : one relies on a continental and rather uniform stratocumulus water cloud and the other relies on a maritime mixed-phase stratiform cloud.

2. AIRCRAFT INSTRUMENTS

The microphysical probes operated by MRI on the B200 aircraft are the following : a PMS PCASP for the measurement of the aerosol size-distribution from 0.1 to 3.0 µm diameter; a PMS FSSP-100 for the sampling of the droplet size-distribution from 3 to 45 µm diameter, a PMS 2D-C for recording the cloud particle images ranged from 25 to 800 µm diameter and a Gerber PVM-100 for measuring liquid water content and effective diameter of cloud droplets < 50 µm diameter. The Polar Nephelometer operated by the LaMP (Crépel et al., 1997) was also mounted on the B200. We recall that the Polar Nephelometer is an unique airborne *in situ* instrument which is compatible with PMS canister (Gayet et al., 1997). This instrument measures the scattering phase function of an ensemble of cloud particles (i. e., water droplets or ice crystals or a mixture of these particles from a few micrometers to about 500 microns diameter). The PMS probe data were processed with standard methods and the derivation of the extinction coefficient and asymmetry parameter from the Polar Nephelometer measurements have been discussed with details in Gayet et al. (2000). It should be noticed that in stratocumulus water droplet cloud, the measured phase function fits very well with the phase function derived from direct PMS probes measurements. This definitively confirms the reliability of the Polar Nephelometer for airborne measurements.

3. WATER-DROPLET STRATOCUM. CASE

The observation presented in this section was carried out on 21 January 1999 (between 11:10 and 13:30 JST) in an area of 70 km x 70 km centered at 32.2°N and 129.5°E, located about 100 km West of Kyûshû island. On that day we had a typical winter-type pressure pattern with a high pressure system widely covering the East China Sea. Over the observational area, the vertical profiles (see below) reveal that the cloud was about 500 m deep with a cloud-layer base near 1000 m, a temperature of -4°C and a cloud-top height at 1500 m with a temperature of -6°C. The cloud was topped by a strong temperature inversion as much as 5°C and visual observations from the aircraft revealed a rather uniform cloud field. Figures 1.a to c display vertical profiles liquid and ice water content, extinction coefficient (σ_{ext}) and asymmetry parameter (g), respectively. *LWC* monotically increases with height up to 0.65g m^{-3}, which is close to the adiabatic profile indicating a well-mixed cloud. The cloud droplet concentration and effective diameter were about 1000 cm^{-3} and 8 µm respectively indicating continental-type properties. Some ice particles (non-rimed ice columns) have been evidenced at any cloud levels with a low concentration (*i.e.,* a few per liter to 20 l^{-1}). The extinction coefficient profile in Fig. 1.b also exhibits a monotically increase up to 160 km^{-1} near the cloud top and conducts to a visible optical depth (τ) of about 40. The asymmetry parameter monotically increases from about 0.83 near the cloud base to 0.846 at the cloud top (Fig. 1.c). These values are typical of water cloud and highlight that the presence of ice particles mentioned above does not significantly affect the cloud optical properties.

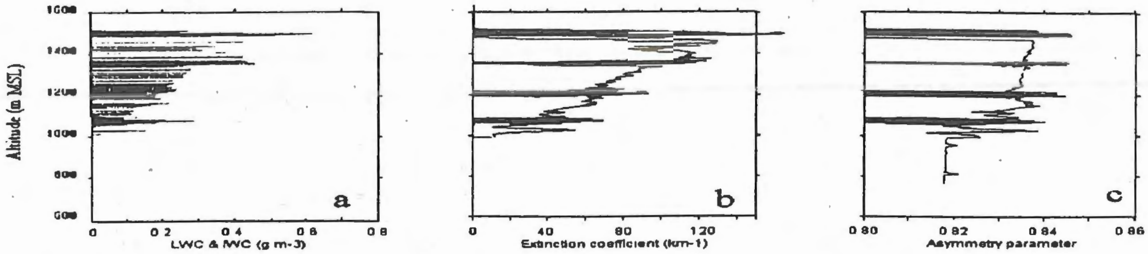

Figure 1 : Vertical profiles of microphysical & optical properties. Water-droplet stratocumulus case.

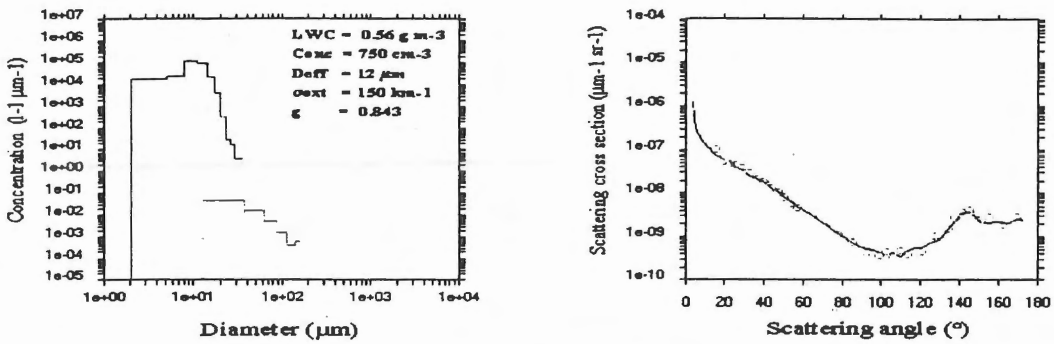

Figure 2 : Example FSSP & 2D-C size spectra with the corresponding scattering phase function measured by the Polar Nephelometer (open circle) and theoretical curve (solid line) calculated by Mie theory for the measured FSSP data. Near cloud-top of the water-droplet stratocumulus case.

For optically thick clouds (τ = 40 in this case), their radiative properties are dominated by the microphysical characteristics in the top 100m depth or so of the clouds. In this way, Figure 2 displays an example of the scattering phase function measured very close to the cloud top and confirms that the cloud layer can be optically regarded as liquid water cloud because the measured scattering phase function agreed very well with those calculated by Mie theory from the corresponding FSSP size distributions.

4. MIXED-PHASE STRATOCUMULUS CASE

The observations relative to this case were obtained on 30 January 1999 (between 10:50 and 13:20 local time) in an area of 50 km x 50 km centered at 35.9°N and 135.4°E, north of the Wakasa bay. From 29 January through the early morning of 30 January, there were intermittently heavy snow falls in the regions facing the Japan Sea of the western parts of Japan Islands. During the observation, the Wakasa bay area was still covered by multi-layered stratocumulus clouds. The cloud layer was about 1300 m deep ; the top was at about 2300 m with a mean temperature of −15°C, and the cloud base was near 1000 m with −7°C. Above the cloud top, the atmosphere was clear and dry. On the other hand, there were still occasional snow falls below the cloud layer.

Figures 3.a to c display vertical profiles of liquid and ice water content, extinction coefficient and asymmetry parameter, respectively. Ice particles were found at any cloud height, whereas supercooled water droplets were observed at specific levels and particularly near the cloud top. The extinction coefficient (σ_{ext}) profile in Fig. 3.b also exhibits strong heterogeneities, which are linked to *LWC* fluctuations, with the maximum up to 80 km^{-1}.

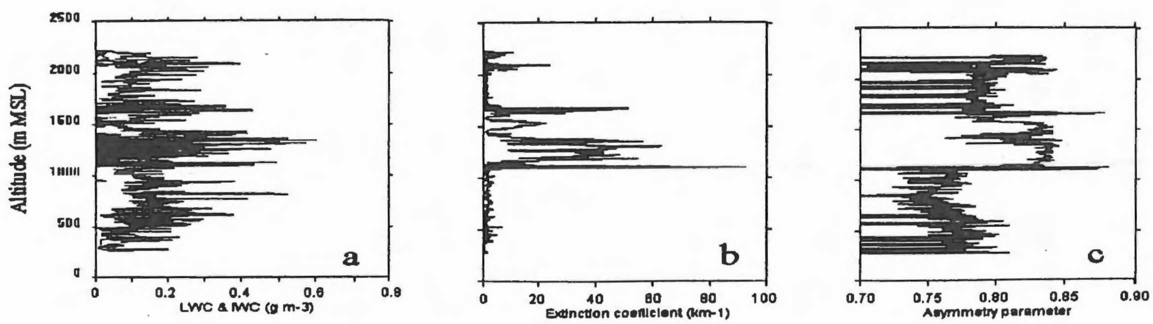

Figure 3 : Same as Fig. 1. Mixed-phase stratocumulus

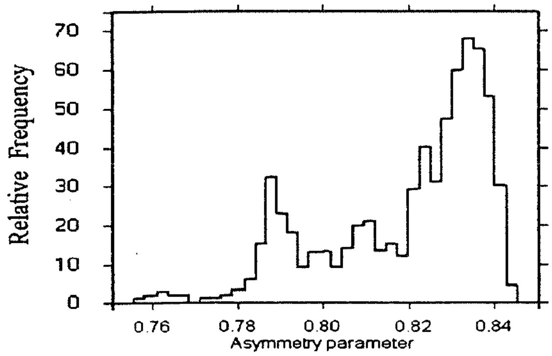

Figure 4 : Relative frequecy of g measured near the top of the mixed-phase stratocumulus cloud

The subsequent optical depth (τ) is difficult to derive but a rough estimate gives a range between 15 and 20. The *g*-values (Fig. 3.c) which range from 0.82 to 0.87 are typical of water droplets and they are linked to the largest values of the extinction coefficient and to the water cloud droplets (*LWC*) occurrences. Significant smaller *g*-values (0.73 to 0.80) are related to small values of σ_{ext} and to noticeable *IWC*. Fig. 4 displays the relative frequency of the *g*-values measured near the cloud top.The results clearly show two modes centered around 0.835 (water droplets with an occurence of 70%) and 0.79 (ice particles with an occurrence of 30%).

In order to put forward interpretation of these near-cloud top properties, we have reported, in Figs. 5 and 6, a few examples of the Polar Nephelometer measurements which address to two typical *g*-values. They both represent measured phase functions with the corresponding particle size-spectra obtained by both the PMS FSSP-100 and 2D-C probes and ice particle images. In the figures are superimposed the scattering phase functions calculated by Mie theory for the measured FSSP mean droplet size-spectra assuming spherical ice particles.

Figure 5 demonstrates a close agreement between the two scattering phase functions. This highlights that a few remaining cloud water droplets (*Conc* $\approx$ 45 cm^{-3}) dominate the optical properties ($g \approx 0.83$) near the cloud top, even the presence of pristine dentric shaped ice crystals which have an ice content twice the liquid content (*IWC/LWC* $\approx$ 2). Compared to the previous example, the results in Fig. 6 show that ice crystals (pristine dentric shaped and some aggregates) with much higher *IWC* (0.28 g m^{-3}) and concentration (*C2D* = 55 l^{-1}) dominate the scattering properties. As a matter of fact, the measured scattering phase function is larger than the theoretical one particularly at the side angles between 80° and 120°, leading to a smaller *g*-value of 0.79. Interestingly, the measured phase function shows a small bump near 145° which suggests that the remaining water droplets, even in a few concentration (15 cm^{-3}) and small size (Deff = 5 µm), may also contribute to the scattering properties. Subsequently, the contribution of such remnant water droplets should bring a slight increase of the *g*-value by comparison with pure ice crystal clouds. The above results clearly show that the present mixed-phased cloud exhibits a cloud topped liquid water layer that yields ice precipitation. This feature may play an important role in cloud radiative properties and remote sensing. Since the scattering properties near the cloud top are mostly dominated by water droplets, the interpretation of satellite remote sensing of mixed-phase clouds (under the assumption of water clouds) may seriously restrict inference of the cloud compositions (Buriez et al., 1997).

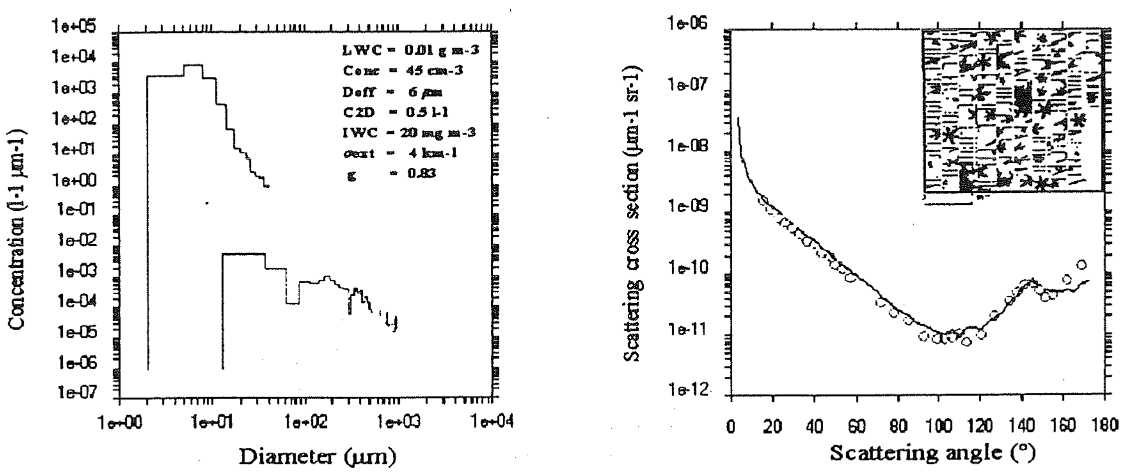

***Figure 5** : Example of measurements obtained by the Polar Nephelometer and PMS FSSP & 2D-C probes near the cloud top at 2300 m MSL / -15°C. Right panel : Mean scattering phase function measured by the Polar Nephelometer (open circle symbols) and scattering phase function obtained by Mie theory (line) calculated with the average droplet size distribution measured by the FSSP. An example of ice particle images sampled by the 2D-C probe is reported in the above right corner. Left panel : Direct FSSP and 2D-C size-distributions with values of the pertinent microphysical & optical parameters.*

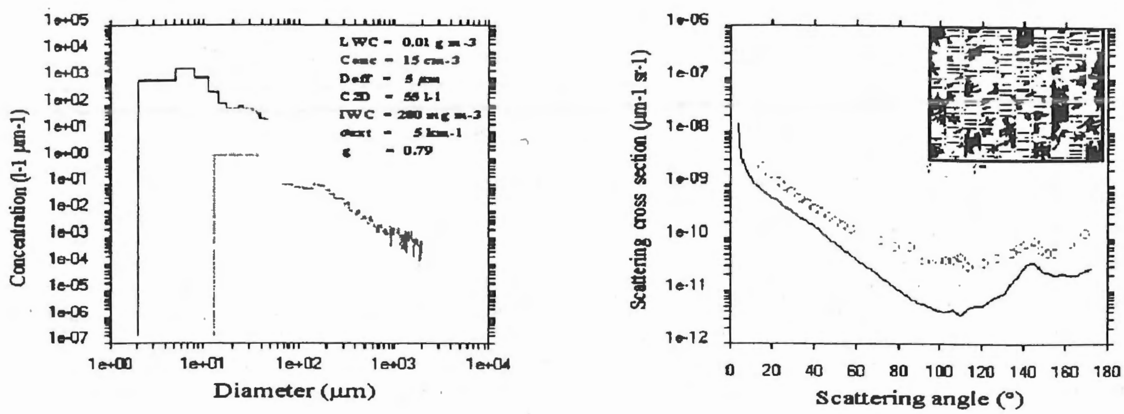

Figure 6 : Same as Fig. 5

5. CONCLUSIONS

The present case studies for the two winter boundary-layer clouds over the sea exhibit essential differences in both microphysical and optical properties. Those of the super-cooled water stratocumulus were strongly affected by aerosols which were estimated to be largely dust particles transported long range from the desert area of the north-east Asian continent. The cloud is characterized by the very high aerosol concentrations in the sub-cloud layer and fairly high cloud droplet concentrations. This feature leads the cloud to a continental-type and non-precipitating structure. The direct measurement of the scattering phase functions by the Polar Nephelometer confirms that the stratiform cloud layer can be optically regarded as liquid water cloud because the measured scattering phase function fits very well with those calculated by Mie theory for the direct FSSP size distributions. Subsequent radiation budget measurements obtained from the collocated B200 and C404 aircraft showed that the cloud layer was characterized by a noticeable amount of solar absorption in the visible region as well as a reasonable amount of absorption in the near infra-red region. The above observations strongly contrast with the microphysical and optical properties of the mixed-phase layer cloud. As a matter of fact, due to a lower cloud top temperature (-15°C) and a maritime-type structure evidenced by rather low aerosol and droplet concentrations, ice crystals efficiently originated at the cloud top. A quasi stable liquid-topped cloud layer that precipitates ice particles has been observed ; the feature may play an important role in cloud radiative properties. Furthermore, because the scattering properties near the cloud top are mostly dominated by water droplets, the interpretation of satellite retrievals of mixed-phase clouds may suffer serious limitations in the inference of cloud compositions. The radiation budget measurements obtained from the collocated B200 and C404 aircraft show that, contrarily to the previous case, no visible absorption has been found in the present mixed-phased cloud.

Aknowledgements : We are very grateful to Y. Mano, J. F. Fournol and the crew of B200 and C404 aircraft (Nakanihon Air Service Co. Ltd) for their helpful collaboration in the JACCS field experiment in January 1999. We also thank S. Oshchepkov and G. Febvre for their kind help in the data analysis. Thanks are extended to M. Chiba for his cooperation in the back trajectory analysis. We are very grateful to Professor H. Isaka, Director of the LaMP, for his helpful suggestions and discussions about this project. The JACCS program is supported by the Science and Technology Agency of Japanese Government.

References :

Asano, S., 1994 : JACCS/MRI Research Group, Japanese Cloud Climate Study (JACCS): Research plan and preliminary results, *Preprint of the 8th Conf. Atmos. Radiation (23-28 Jan. 1994, Nashville, TN)*, Am. Meteor. Soc., 282-284.

Buriez J.C., C. Vanbauce, F. Parol, P. Goloub, M. Herman, B. Bonnel, and Y. Fouquart, 1997 : Cloud detection and derivation of cloud properties from POLDER. *Int. J. Remote Sensing.*, 18, 2785-2813.

Crépel, O., J-F Gayet, J-F Fournol and S. Oshchepkov, 1997 : A new airborne Polar Nephelometer for the measurements of optical and microphysical cloud properties. Part II: Preliminary tests. *Annales Geophysicae*, 15, 460-470.

Foot J., S., 1988 : Some observations of the optical properties of clouds. I : Stratocumulus. *Q.J.R. Meteorol. Soc.*, 114, 129-144.

Fouquart Y., J.C. Buriez and M. Herman, 1989 : The influence of boundary layer clouds on radiation : A review. *Atmos. Res.*, 23, 203-228.

Gayet, J-F, O. Crépel, J-F Fournol and S. Oshchepkov, 1997 : A new airborne Polar Nephelometer for the measurements of optical and microphysical cloud properties. Part I: Theoretical design. *Annales Geophysicae*, 15, 451-459.

Gayet J-F, S. Asano, A. Yamazaki, A. Uchiyama, A. Sinyuk and O. Jourdan, 2000 : Microphysical and optical properties of winter boundary layer clouds over the sea: Two case studies of continental-type water and maritime mixed-phased stratocumuli. Submitted to *J. Atmos. Sci.*

Heymsfield, A., 1993 : Microphysical structures of stratiform and cirrus clouds. *Aerosol- Cloud-Climate Interactions*, P.V. Hobbs Ed., Academic Press, Inc., 97-121.

EFFECTS OF URBANIZATION ON RADIATION FOG IN XISHUANGBANNA AREA

Shen Ying Huang Yuren Huang Yusheng Tan Yingzhong

Meteorological Bureau of Yunnan Province, Kunming 650034, P. R. China

1. INTRODUCTION

Xishuangbanna area is situated in the southwest of Yunnan Province, P. R. China. Radiation fog appears almost every day in winter half year. The period of fog last about 6~7 hours. But the fog has decreased clearly in last teens years along with the change of natural climate and the action of humanity. In order to understand the reason of the variation of fog, we analyzed the data of Jinghong and Damonglong weather station from 1960 to 1996. Jinghong station is situated at 101°04'E, 21°52'N, 552.7m above sea level. Damonglong station is situated 100°40'E, 21°35'N, 621.8m above sea level. The straight distance between Jinghong and Damonglong is nearly 50km. The climatic characters and natural conditions of Jinghong are the same as that in Damonglong. The statistical results are listed in Table 1 and Table 2.

Table 1. Changes of elements

Meteorological elements	Period	Jinghong		Damonglong	
		Average value	Sample variance	Average value	Sample variance
Annual foggy days (day)	1960~1984	116.06	21.19	129.40	18.53
	1985~1996	61.58	11.79	109.42	8.82
Mean annual temperature (℃)	1960~1984	21.90	0.40	21.31	0.32
	1985~1996	22.62	0.23	21.65	0.24
Mean annual relative humidity (%)	1960~1984	81.88	2.05	84.24	1.13
	1985~1996	78.42	1.08	84.08	0.79
Mean annual maximum temperature (℃)	1960~1984	29.35	0.48	28.39	0.39
	1985~1996	29.78	0.27	28.62	0.18
Mean annual minimum temperature (℃)	1960~1984	17.42	0.54	16.77	0.49
	1985~1996	18.18	0.35	17.32	0.27

Table 2. Relationship between Jinghong and Damonglong

Meteorological elements	Period	Correlation analysis	
		Correlation coefficient	Regression equation*
Annual foggy days (day)	1960~1984	0.727	Y=55.6+0.636x
	1985~1996	-0.0926	Y=113.68-0.0693x
Mean annual temperature (℃)	1960~1984	0.540	Y=11.78+0.435x
	1985~1996	0.880	Y=1.26+0.902x
Mean annual relative humidity (%)	1960~1984	0.788	Y=48.67+0.434x
	1985~1996	0.379	Y=62.33+0.277x
Mean annual maximum temperature (℃)	1960~1984	0.778	Y=9.66+0.638x
	1985~1996	0.832	Y=12.11+0.555x
Mean annual minimum temperature (℃)	1960~1984	0.785	Y=4.34+0.713x
	1985~1996	0.839	Y=5.48+0.651x

* Y: Jinghong's elements, X: Damonglong's elements.

2. VARIATIONS OF FOG

The annual foggy days have decreased since 1960, but Jinghong's decrease range is bigger than Damonglong's. Jinghong's annual foggy days decrease from 162 days in 1960 to 45 days in 1996, while Damonglong's annual foggy days decrease from 150 days in 1960 to 102 days in 1996. Table 1 shows: Jinghong's annual foggy days are about the same as Damonglong's before 1984, they are 116.1 days and 129.4 days respectively in the period from 1960 to 1984. After 1985, Jinghong's annual foggy days decrease clearly but Damonglong's decrease slowly.

Corresponding author's address: Shen Ying, Meteorological Bureau of Yunnan Province, 73 Xichang Road, Kunming, Yunnan 650034, P. R. China; E-Mail: yingshen@ynmail.com

They are 61.6 days and 109.4 days respectively from 1985 to 1996.

Besides the decreasing of foggy days, the lasting period of fog is becoming shorter and shorter. Gong (1996) analyzed the Jinghong's and Mengla's (another weather station in Xishuangbanna area) mean lasting period of fog. They found that: Jinghong's mean lasting period of fog decrease from 634 hours in the winter half year of 1960s to 213 hours in the winter half year of 1990s. Mengla's mean lasting period of fog decrease somewhat slowly from 873 hours in the winter half year of 1960s to 554 hours in the winter half year of 1990s.

The microstructure of fog also changes clearly. Huang et al. (1986) detected the microstructure of radiation fog in Xishuangbanna area in the winters of 1986 and 1997. Results are showed in Table 3.

Table 3. Variations of microphysical characteristics of fog in Jinghong

Sounding period	Mean minimum diameter (μ m)	Mean maximum diameter (μ m)	Mean diameter (μ m)	Number density (cm^{-3})	Water content (g/m^3)
86.12~87.2	4.3	58.8	13.6	94.8	0.25
97.11	4.2	37.5	8.0	236.6	0.124

The above results show that the microphysical characteristics of Jinghong's fog have changed clearly in last ten years. The mean diameter decreases from 13.6 μ m to 8.0 μ m. The mean maximum diameter decreases from 58.8 μ m to 37.5 μ m. The change of mean minimum diameter is insignificant. The number density of fog increases from 94.8/cm^3 to 236.6/cm^3. The water content of fog decreases from 0.25g/m^3 to 0.124g/cm^3. The result is about the same as Gong's (1996) result, which showed the decrease of the water content of Xishuangbanna's fog.

3. MEAN ANNUAL TEMPERATURE

The mean annual temperature has increased slowly since 1960. The change range of mean annual temperature is very similar between Jinghong and Damonglong before 1984. From 1960 to 1984, Jinghong's and Damonglong's mean temperature is 21.90℃ and 21.31℃ respectively. From 1985 to 1996, they are 22.62 ℃ and 21.65 ℃ respectively. Jinghong's and Damonglong's mean temperature from 1985 to 1996 is higher 0.72℃ and 0.34℃ respectively than from 1960 to 1984.

4. MEAN ANNUAL RELATIVE HUMIDITY

Jinghong's mean annual relative humidity has decreased since 1960. But Damonglong's has only fluctuant change since 1960. Jinghong's mean annual relative humidity decreases from 84% in 1960 to 79% in 1996. Damonglong's is 85% in 1960 and 85% in 1996. From 1960 to 1984, Jinghong's mean relative humidity is 81.88% and Damonglong's is 84.24%. From 1985 to 1996, the former is 78.42% and the latter is 84.08%.

5. MEAN ANNUAL MAXIMUM TEMPERATURE

Jinghong's and Damonglong's mean annual maximum temperature have not significant change since 1960. The former is 29.3℃ in 1960 and 29.5℃ in 1996. The latter is 29.0℃ in 1960 and 28.6℃ in 1996. From 1960 to 1984, Jinghong's and Damonglong's mean maximum temperature are 29.35℃ and 28.39℃ respectively. From 1985 to 1996, they are 29.78℃ and 28.62℃ respectively.

6. MEAN ANNUAL MINIMUM TEMPERATURE

Jinghong's and Damonglong's mean annual minimum temperature have not significant change since 1960. The former is 17.8℃ in 1960 and 18.4℃ in 1996. The latter is 16.7℃ in 1960 and 17.5℃ in 1996. From 1960 to 1984, Jinghong's and Damonglong's mean minimum temperature are 17.42℃ and 16.77℃ respectively. From 1985 to 1996, they are 18.18℃ and 17.32℃ respectively.

Situated in the same climatic region, effected by the same weather system and having the same relief conditions, the two stations should have the same climatic variations. But the analysis above shows that: Jinghong's and Damonglong's change of annual foggy days, mean annual relative humidity and mean annual temperature are different in last tens years. We think that these differences may be caused by other reasons. Jinghong's data (Table 4) shows: forest covering fraction decreases clearly from 1950s to 1970s, while the annual foggy days, mean annual relative humidity and mean annual temperature have not significant variations. After 1980s, forest covering fraction increases due to afforestation project. Nevertheless, these meteorological elements change clearly. So, we think that Jinghong's urbanization plays important role for the variations of Jinghong's fog. These results about temperature raise, relative humidity decrease, foggy days and lasting period of fog decrease are about the same as Zhou's (1994) results about urbanization effects.

Table 4. Data of Jinghong city

Program	1950s	1970s	1980s	1990s
Urban area (km^2)		16	59	
Urban population		30000	50000	120000
Forest covering fraction(%)	70	30	34	59

7. REFERENCE

Gong, S., Ling, S., 1996: Fog decreasing in Xishuangbanna region. Meteorological Monthly (China), 11, 10–14.

Huang, Y. et al., 1992: An observation and analysis on the radiation fog in Xishuangbanna. ACTA Meteorologica Sinica (China), 1, 112–117.

Zhou, S., Shu, J., 1994: Urban climatology. Meteorological Press (China), 244–262, 418–455.

SENSITIVITY OF THE RADIATIVE PROPERTIES OF STRATIFORM CLOUDS TO ENVIRONMENTAL CONDITIONS

Carynelisa Erlick[1], Alexander Khain[1], Yefim Kogan[2], and Mark Pinsky[1]

[1]Department of Atmospheric Sciences, The Hebrew University of Jerusalem, Jerusalem, Israel
[2]Cooperative Institute for Mesoscale Meteorological Studies, University of Oklahoma, Norman, OK

1. INTRODUCTION

The drop size distribution of stratiform clouds is particularly important for calculating stratiform cloud radiative properties. The formation of a drop size distribution is a complicated process affected by the concentration and size distribution of aerosol particles (AP) as well as by the thermodynamic properties of the atmosphere. A large variation in droplet spectra over a distance of only a few meters is regularly observed in stratiform clouds (Korolev 1995). These spectra differ in width and shape, and some of the spectra are monomodal while others are bimodal. The cause of such variability is not well understood.

The radiative properties of a cloud are influenced by both the size and number concentration of droplets. An increase in number concentration or a decrease in drop size will increase the solar albedo of a cloud (see, e.g., Hansen and Travis 1974). Hence, the widening of a size distribution towards smaller droplets or an overall increase in number concentration caused by an increase in AP will tend to increase a cloud's albedo. Conversely, a shift in the size distribution towards larger droplets will tend to decrease a cloud's total solar albedo and increase the cloud's absorption of near infrared radiation. Therefore, the large variation in width, shape, and number of modes observed in stratiform clouds is likely to cause a correspondingly strong variation in their solar albedo and absorption.

2. CONCEPT

It is well known that drop concentration in the vicinity of a cloud base is determined by the local maximum of supersaturation, which is in turn determined by the vertical velocity at the cloud base (Rogers and Yau 1989). Khain and Pinsky (2000) found that for cumulus clouds, a variable updraft velocity can, under certain conditions, increase supersaturation in the upper levels of a cloud in excess of the supersaturation maximum at cloud base. This leads to in-cloud nucleation of droplets accompanied by a) an increase in droplet concentration, b) droplet spectrum broadening towards smaller droplets, and c) the formation of bimodal spectra. We expect that processes of such kind take place in stratiform clouds as well. Moreover, because vertical velocities at the base of stratiform clouds can be rather small, we expect that turbulent fluctuations in vertical velocity can lead to fluctuations in the supersaturation with amplitude exceeding the maximum at cloud base. Therefore, we expect turbulent velocity fluctuations to play a substantial role in the broadening of droplet spectra in stratiform clouds. Fluctuations of velocity at cloud base (due to large eddies or turbulent fluctuations of a smaller scale) could be responsible for the formation of the wide variety of size spectra observed in these clouds.

To simulate these fine features of the droplet size spectra in stratiform clouds (different width, spatial inhomogeneity, etc.), it is necessary to have the proper relationship between vertical velocity and supersaturation for parcels that circulate within stratiform clouds in updraft and downdraft loops of various scales. One way of accurately modeling such profiles is through three-dimensional large eddy simulations (LES) (e.g., Kogan et al. 1995; Stevens et al. 1998b). These contain advanced advective schemes and microphysics, and can produce stratiform size distributions with reasonable widths. However, LES models tend to be very time expensive and are associated with other computational problems, and are therefore not well suited for sensitivity studies.

Another approach is through a one-dimensional model of the planetary boundary layer (PBL), in which the transport of water vapor, potential temperature, and wind stress in the vertical are averaged horizontally

---

Corresponding author address: Carynelisa Erlick, Department of Atmospheric Sciences, The Hebrew University of Jerusalem, Jerusalem 91904, Israel; E-mail: caryn@sharav.es.huji.ac.il.

(e.g., Bott et al. 2000). This method allows for complicated microphysics, even two-dimensional microphysics schemes in the case of Bott et al. (2000). However, processes such as turbulence and turbulent velocity fluctuations are by necessity parameterized, and there are many assumptions associated with using horizontal mean values of quantities such as supersaturation (Stevens et al. 1998a).

We suggest a third method, using a Lagrangian approach to investigate the droplet spectrum formation in stratiform clouds. According to this approach, a stratiform cloud can be represented as a population of a great number of cloud parcels moving along air streamlines. In this approach, droplet spectra are calculated in each parcel, and the spectrum over the whole cloud can be obtained by proper averaging of the spectra of individual cloud parcels.

Our aim of the Monte Carlo simulations is to restore the microphysical and geometrical structure of a stratocumulus cloud simulated by the LES model of Kogan et al. (1995) (see Khairoutdinov and Kogan 1999), and to compare the spectra we obtain with their results. We will then use the same Lagrangian approach to investigate the effect of atmospheric aerosols on droplet spectrum formation in stratiform clouds, and to reveal the sensitivity of cloud radiative properties to aerosol concentration and size distribution.

3. MODEL DESCRIPTION

3.1 Cloud Microphysics

To simulate stratiform cloud droplet size spectra, we employ a cloud parcel model developed by Khain and Pinsky (2000). In this model, the growth rate of atmospheric particles is described by the equation of diffusional growth (Pruppacher and Klett 1997):

$$r\frac{dr}{dt}=\frac{1}{F}\left(S-\frac{A}{r}+\frac{Br_N^3}{r^3-r_N^3}\right)$$

where r is the radius of the wet particle, r_N is the radius of the dry soluble fraction, S is the supersaturation with respect to water, and F is a thermodynamic coefficient. The second and third terms are related to the drop curvature and soluble aerosol fraction, respectively.

The rate of change of supersaturation is expressed by the saturation development equation (Pruppacher and Klett 1997):

$$\frac{dS}{dt}=A_1 w - A_2\frac{dq_L}{dt}$$

where w is the updraft velocity, q_L is the molar mixing ratio of liquid water in the air, and A_1 and A_2 are thermodynamic coefficients. The two terms in the equation describe adiabatic cooling and the condensation of water vapor on growing particles, respectively. The temperature of the air parcel is described by (Pruppacher and Klett 1997):

$$-\frac{dT}{dt}=\frac{g}{c_p}w-\frac{L}{c_p}\frac{dq_L}{dt}$$

where L is the latent heat of condensation, and c_p is the specific heat of water.

In the calculations of diffusional growth, there is no differentiation between aerosol particles and cloud droplets. The size distribution consists of 2000 mass bins, with the mass increment increasing exponentially up to that corresponding to a drop of radius 20 μm. To eliminate any artificial broadening, we do not use a regular mass grid; particles (aerosols and droplets) grow according to the equation of diffusional growth, so that a new set of drop masses is formed at each subsequent time step. The utilization of a large number of bins allows us to simulate droplet activation smoothly, avoiding sharp jumps in drop concentration.

The velocity field in stratocumulus clouds results from several complicated thermodynamical processes: thermal instability in the boundary layer, entrainment in the vicinity of the cloud top, radiative cooling at the cloud top, and turbulent velocity fluctuations. In contrast to cumulus clouds, latent heat release and droplet weight do not significantly affect the velocity field. Therefore, in stratiform clouds we have as a first approximation a unidirectional influence of the velocity field on cloud microphysics.

We use the velocity field generated by the 3-D LES microphysical model developed by Kogan et al. (1995) for the simulation of air parcel tracks. The model resolution is 75 m in the horizontal and 25 m in the vertical. The initial position of air parcels is chosen to be below cloud base, and the aerosol size distribution at cloud base is taken as suggested by Respondek et al. (1995).

3.2 Radiative Transfer

The cloud single scattering properties are computed from the mean droplet spectra using the Mie scattering subroutine for spheres found in Bohren and Huffman (1983). Since the mean droplet spectra vary with position in the cloud, the cloud single scattering properties are calculated as a function of height (or cloud layer), where a layer is on the order of 50 m deep.

The single scattering properties are then entered into the radiation algorithm, a 26-band solar parameterization for inhomogeneous scattering and absorbing atmospheres, spanning wavenumbers 0 to 57,600 and wavelengths 0.174 μm to greater than 4.0 μm (Freidenreich and Ramaswamy 1999). In the radiation algorithm, the delta-Eddington method (Joseph et al. 1976) is used to calculate the reflection and transmission of scattering layers, and the layers are combined using the adding method (Ramaswamy and Bowen 1994). The exponential sum-fit technique (Wiscombe and Evans 1977) is used for the parameterization of water vapor transmission in the main absorbing bands, while absorption by other gases is computed using a regular absorptivity approach. The solar radiation algorithm provides the albedo, absorption, and transmission of the cloud layer as a function of wavelength and solar zenith angle.

4. PRELIMINARY SIMULATIONS

In our preliminary simulations, the shape of the vertical velocity profile was prescribed to conform to updraft and downdraft loops of either elliptical or sinusoidal shape, with a maximum vertical velocity at cloud center of 0.5 m s^{-1} and zero vertical velocity at cloud top. The elliptical profile (Figure 1a), with a rapid increase in vertical velocity with height, produced a supersaturation profile with maximum supersaturation near the cloud base. As a result, there was no new nucleation above the cloud base, and the size distribution narrows with cloud height (Rogers and Yau 1989; Khain and Pinsky 2000).

The sinusoidal profile (Figure 1b), with a relatively slow increase in vertical velocity with height, produced a supersaturation profile with maximum supersaturation near the cloud center. As a result, new nucleation and spectral broadening occurred from the cloud base up to the cloud center, and the drop distribution at the cloud top (*z* = 200 m) is relatively broad. The spectral broadening in Figure 1b leads to a slightly higher mean radius than in Figure 1a, a slightly lower visible optical depth, and a 2% decrease in visible albedo from ~0.51 to ~0.50.

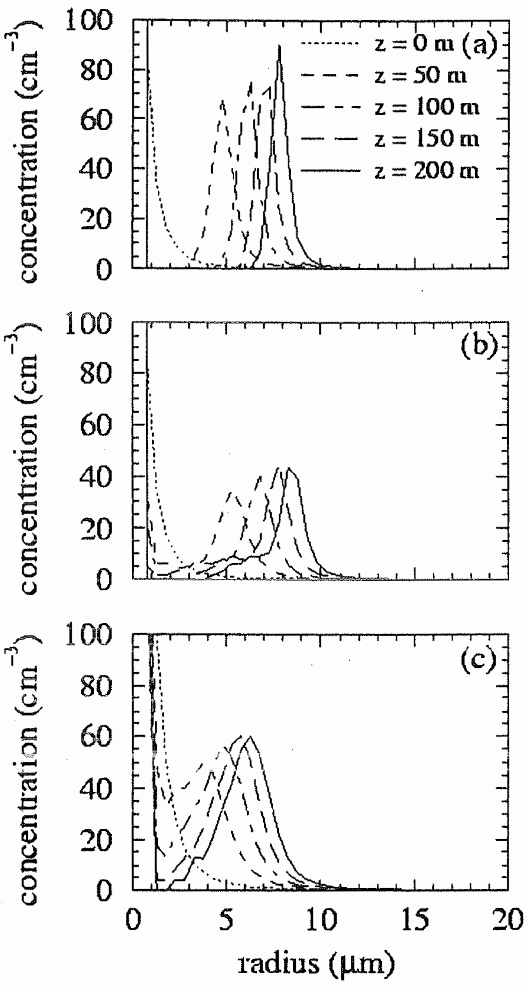

Figure 1. (a) Size distribution resulting from an elliptical updraft vertical velocity profile, as a function of height within cloud (*z*), (b) Size distribution resulting from a sinusoidal updraft vertical velocity profile, as a function of height within cloud, (c) Size distribution resulting from a sinusoidal updraft velocity profile, with 3 times the initial AP concentration, as a function of height within cloud. In all simulations, the vertical velocity at cloud base was 0.05 m s^{-1} and maximum vertical velocity at cloud center was 0.5 m s^{-1}.

In Figure 1c, the updraft velocity profile remained sinusoidal, but the initial AP concentration was increased from 2151 cm^{-3} to 6454 cm^{-3}. In comparison with Figure 1b, the resulting size distribution has a smaller mode radius, a smaller width, and a higher number concentration. This translates into a 74% increase in visible optical depth from ~19 to ~33, and a 28% increase in visible albedo from ~0.50 to ~0.64. This is a clear signature of the effect of AP concentration on increasing the drop number, decreasing the drop size, and increasing the cloud solar albedo. Note that these results are only preliminary; a more detailed sensitivity study will be presented following the method outlined in Sections 2 and 3.

5. CONCLUSIONS

From Figure 1, it is clear that the supersaturation and size distribution are rather sensitive to the shape of the vertical velocity profile and to the initial aerosol concentration. We expect, therefore, that in our Lagrangian approach, the variations in the vertical velocity profile over the various trajectories and the dependence of supersaturation on these vertical profiles as per the saturation development equation, should provide us with a realistic average drop size spectrum with an appropriate width for stratocumulus clouds. Based on our preliminary results, we also expect that, given our realistic stratiform cloud drop size spectrum, this method will provide us with a correspondingly realistic assessment of the sensitivity of the cloud drop spectrum and cloud radiative properties to initial aerosol concentration and size distribution.

REFERENCES

Bohren, C. F., and D. R. Huffman, 1983: *Absorption and Scattering of Light by Small Particles*, John Wiley, 530 pp.

Bott, A., 1999: A numerical model of the cloud-topped planetary boundary-layer: Cloud processing of aerosols in marine stratus, *Environ. Modell. Softw.*, **14**, 635-643.

Freidenreich, S. M., and V. Ramaswamy, 1999: A new multiple-band solar radiative parameterization for general circulation models, *J. Geophys. Res.*, **104**(D24), 31,389-31,409.

Hansen, J. E., and L. D. Travis, 1974: Light scattering in planetary atmospheres, *Space Sci. Rev.*, **16**, 527-610.

Joseph, J. H., W. J. Wiscombe, and J. A. Weinmann, 1976: The delta-Eddington approximation for radiative flux transfer, *J. Atmos. Sci.*, **33**, 2452-2459.

Khain, A., and M. Pinsky, 2000: Droplet spectrum formation in cumulus clouds, Part 1: In-cloud nucleation, *J. Atmos. Sci.*, submitted.

Khairoutdinov, M. F., and Y. L. Kogan, 1999: A large eddy simulation model with explicit microphysics: Validation against aircraft observations of a stratocumulus-topped boundary layer, *J. Atmos. Sci.*, **56**, 2115-2131.

Kogan, Y. L., M. P. Khairoutdinov, D. K. Lilly, Z. N. Kogan, and Q. Liu, 1995: Modeling of stratocumulus cloud layers in a large eddy simulation model with explicit microphysics, *J. Atmos. Sci.*, **52**, 2923-2940.

Korolev, A. V., 1995: The influence of supersaturation fluctuations on droplet size spectra formation, *J. Atmos. Sci.*, **52**, 3620-3634.

Pruppacher H., and J. D. Klett, 1997: *Microphysics of Clouds and Precipitation*, 2nd ed., Kluwer Academic, 954 pp.

Ramaswamy, V., and M. M. Bohen, 1994: Effects of changes in radiatively active species upon the lower stratospheric temperatures, *J. Geophys. Res.*, **99**, 18,909-19,921.

Respondek, P. S., A. I. Flossman, R. R. Alheit, and H. R. Pruppacher, 1995: A theoretical study of the wet removal of atmospheric pollutants, V: The uptake, redistribution, and deposition of $(NH_4)_2SO_4$ by a convective cloud containing ice, *J. Atmos. Sci.*, **52**, 2121-2132.

Rogers, R. R., and M. K. Yau, 1989: *A Short Course in Cloud Physics*, 3rd ed., Pergamon, 293 pp.

Stevens, B., W. R. Cotton, and G. Feingold, 1998a: A critique of one- and two-dimensional models of boundary layer clouds with binned representations of drop microphysics, *Atmos. Res.*, **48**, 505-528.

Stevens, B., W. R. Cotton, G. Feingold, and C.-H. Moeng, 1998b: Large-eddy simulations of strongly precipitating, shallow, stratocumulus-topped boundary layers, *J. Atmos. Sci.*, **55**, 3616-3638.

Wiscombe, W. J., and J. W. Evans, 1977: Exponential-sum fitting of radiative transmission functions, *J. Comput.. Phys.*, **24**, 416-444.

The effect of surface winds on marine stratus microstructure and drizzle

Yefim L. Kogan and Yuri Y. Shprits

Cooperative Institute for Mesoscale Meteorological Studies, University of Oklahoma, Norman OK

1. Introduction[1]

Through their radiative effects, marine stratocumulus clouds play an important role in climate and weather. This role is frequently illustrated by an example showing that a few percent increase of stratocumulus cloud cover would compensate the greenhouse warming due to CO_2 doubling, while similar decrease would double the warming (Randall et al 1984, Ramanathan et al 1989). Cloud radiative parameters, in turn, are affected by cloud microstructure (e.g., effective radius) which is closely related to the CCN concentration and size distribution (Twomey, 1977). The environments with more abundant CCN concentrations should lead to the increased cloud drop concentrations and, therefore, given the same amount of liquid water content, to the decreased drop sizes. Based on many observations in different regions of the globe, Martin et al (1994), O'Dowd et al (1996), among others suggested various analytical relations between the aerosol and cloud drop concentrations. These relations, however, need to be modified for conditions of strong surface winds, which directly affect the number of sea-salt aerosol particles. As was shown by O'Dowd et al. (1997), Ghan et al. (1998), the number of activated drops depends on the concentration of sea-salt CCN, as well as boundary layer (BL) turbulence.

2. Description of model and cases

In this study we investigate the role of the shape of the background (nss) aerosol spectrum under conditions of moderate surface winds (10-17m/s). We performed a series of experiments using the CIMMS LES model (Kogan et al. 1995; Khairoutdinov and Kogan 1999). Cloud physics processes are treated explicitly based on the prediction equations for cloud particle spectra that include cloud condensation nuclei (19 bins), cloud and drizzle drops (25 bins). The equations for particle size distribution functions include processes of advection, sedimentation, turbulent mixing, and individual microphysical processes of nucleation, condensation/evaporation and stochastic coagulation.

The simulations were based on thermodynamical conditions obtained from measurements during ASTEX field campaign. The CCN spectra were taken from observations by Hoppel et al (1990), the surface wind dependent sea-salt distributions were taken from O'Dowd et al (1997). Fig. 1 shows the background aerosol sulfate spectra used in a series of three of experiments.

[1] *Corresponding author address:*
Dr. Yefim L. Kogan, Cooperative Institute for Mesoscale Meteorological Studies, University of Oklahoma, 100 E. Boyd, Norman, OK 73019. E-mail: ykogan@ou.edu

The first experiment, C_L, represented a very clean air mass with a relatively low total sulfate concentration of 70 cm^{-3}. The second experiment, C_H, represents a more polluted air mass with the total sulfate concentration of 230 cm^{-3}. In the third experiment, C_M, the total concentration was slightly lower than in C_H due to lower concentration of particles in the range 0.04-0.1μ (30 versus 110 cm^{-3}). Aitken nuclei in this range of radii correspond to critical supersaturation range from 0.05% to 0.2% which has the highest frequency of occurrence under simulated conditions. The latter are characterized by mean updraft velocities of about 0.3 – 0.4m/s.

For each of the three experiments, C_L, C_M, C_H, we conducted three simulations varying surface winds. In the first simulation, the surface winds were absent, i.e., the background aerosol spectra consisted only of non sea-salt (nss) sulfate particles. In the second simulation the surface winds were specified at 10 m/s, resulting in the production of additional sea-salt CCN distribution of 30 cm^{-3}. Finally, in the third simulation the surface winds were specified at 17 m/s, resulting in the sea-salt particle concentration of 60 cm^{-3}. The size distribution of the sea-salt particles in the latter case is shown in Fig. 1.

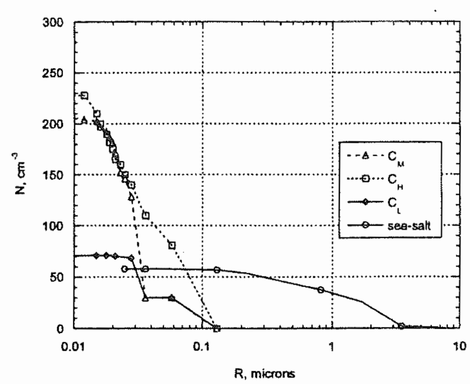

Fig. 1. The non sea-salt (C_L, C_M, C_H,) and sea-salt (at U=17 ms^{-1}) components of CCN spectrum used for model initialization.

3. Results

Fig. 2 shows evolution of the domain averaged drop concentration in experiment C_L after the two-hour spin-up time for three different surface wind conditions.

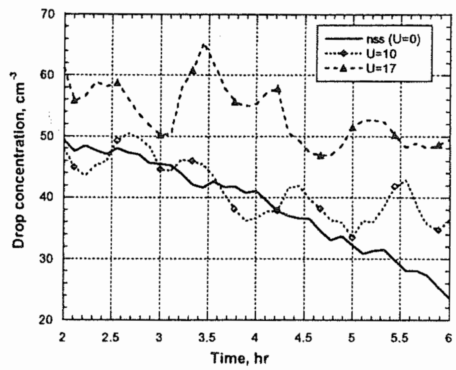

Fig. 2. Case C_L: time evolution of the domain averaged cloud drop concentration as a function of surface wind U (ms^{-1}).

As Fig. 2 shows, the addition of sea-salt particles increases the cloud drop concentration only slightly at moderate winds (U=10m/s), but more significantly, by 20-50%, at higher winds (U=17 m/s). The explanation lies in the fact that the sulfate CCN spectrum in the case C_L has a very narrow left mode at about 0.03-0.04μ (the corresponding critical supersaturation is about 0.2%). As the total number of sulfate and sea-salt particles is rather small (less than 80 cm^{-3} even at the initial stage of activation), it cannot substantially reduce the supersaturation in cloud and all sea-salt, as well as sulfate particles, are activated. Drizzle is easily formed in this rather clean air mass, as a result the drop concentration decreases with time, the decrease is more rapid in the nss case where there is no sea-salt particle source (see Fig. 2).

The effect is different in the case C_H, where sulfate drop concentration is larger and also much broader. Compared to C_L case, the number of sulfate particles in the 0.04-0.1μ range is also substantially larger.

Fig. 3 shows that there is a slight 5-10% decrease in drop concentration. At U=17 m/s the decrease is smaller than at U=10 m/s, most likely due to negative feedbacks caused by the larger drizzle in this case.

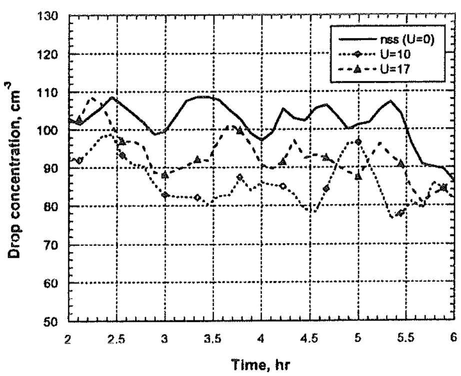

Fig. 3. The same as Fig. 2, but for case C_H.

In the C_M case the effect on cloud drop concentration is the strongest. Fig. 4 shows the decrease in drop concentration from about 100 cm^{-3} to 70 cm^{-3}. The concentration of sulfate particles in the 0.04-0.1μ range is much smaller than in C_H case. The activation of sea-salt particles limits the growth of supersaturation and keeps sulfate particles smaller than 0.04μ from activation.

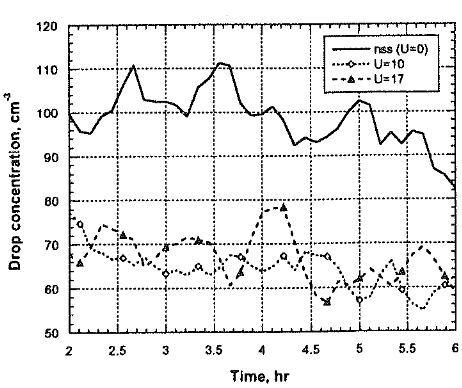

Fig. 4. The same as Fig. 2, but for case C_M.

Interestingly, the effect is almost the same for U=10 and U=17 m/s. Again, a possible explanation is negative feedbacks resulting from interactions between drizzle and supersaturation. Initially, the former is larger at U=17 m/s. As a result, the decrease in drop concentration due to drizzle is more pronounced in this case. The lower drop concentration will lead to larger supersaturations in cloud and increase in CCN nucleation that may counterbalance the drop concentration decrease due to drizzle.

4. Conclusions

The CIMMS explicit microphysics model was used to investigate the effect of surface winds on cloud drop microstructure and drizzle. In particular, we focus on the role of the shape of the background (nss) aerosol spectrum under conditions of moderate surface winds (10-17m/s).

We performed a series of three experiments using the CIMMS LES explicit microphysical model initialized with thermodynamical profiles measured during ASTEX field campaign and the nss marine background spectra observed by Hoppel et al (1990) in the Atlantic. For each of the three background spectra we conducted a set of three simulation for surface winds specified at U=0, 10 and 17 m/s. The sea-salt distributions produced by surface winds up to 17 m/s were taken from observations by O'Dowd et al (1997).

The surface winds affect the stratocumulus drop concentration in a complex way involving many feedbacks between the total concentration of the background CCN sulfate spectra, but also its *shape and amount of drizzle.* Model simulations showed that the total background sulfate concentration does not uniquely define the effect of surface winds.

An accurate formulation of this effect should account for the shape of the background sulfate spectrum. In particular, it is important to account for the number concentration of Aitken nuclei in the radius range from 0.04μ to 0.1μ. The latter are activated at supersaturations of 0 – 0.2% which is the prevailing range in stratocumulus topped marine boundary layers characterized by moderate turbulence.

Acknowledgments. This research was supported by the ONR Grants N00014-96-1-0687 and N00014-96-1-1112 and by the Environmental Sciences Division of U.S. Department of Energy (through Battelle PNR Contract 144880-A-Q1 to the Cooperative Institute for Mesoscale Meteorological Studies) as part of the Atmospheric Radiation Measurement Program.

References

Ghan, S. J., G. Guzman and H. A. Razzak, 1998: Competition between Sea Salt and Sulfate Particles as Cloud Condensation Nuclei. *J. Atmos. Sci.,* **55**, 3340–3347.

Hoppel, W. A., J. W. Fitzegerald, C. M. Frick, and R. E. Larson, 1990: Aerosol size distributions and optical properties found in the marine boundary layer over the Atlantic Ocean. *J.Geophys. Res*., **95**, 3659-3686.

Khairoutdinov, M. F. and Y. L. Kogan, 1999: A Large Eddy Simulation Model with Explicit Microphysics: Validation Against Aircraft Observations of a Stratocumulus-Topped Boundary Layer. *J. Atmos. Sci.*, **56**, 2115-2131.

Kogan, Y. L., M. P. Khairoutdinov, D. K. Lilly, Z. N. Kogan, and Q. Liu, 1995: Modeling of stratocumulus cloud layers in a large eddy simulation model with explicit microphysics. *J. Atmos. Sci*, **52**, 2923-2940.

Martin, G. M., D. W. Johnson, and A. Spice, 1994: The measurment and parameterization of effective radius of droplets in warm stratocumulus clouds. *J. Atmos. Sci.,* **51**,1823-1842.

O'Dowd, C. D., M. H. Smith, A. D. Kaye, and J. Lowe, 1996: The relative importance of NSS-sulfate and sea-salt aerosol to the marine CCN population, *12th International Conference on Clouds and Precipitation,* 19-23 August 1996, Zurich, Switzerland, 334-337.

Ramanathan, V., R. D. Cess, E. F. Harrison, P. Minnis, B. R. Barkstorm, E. Ahmad, D. Hartman, 1989: Cloud-radiative forcing and climate: Results from the earth radiation budget experiment. *Science*, 243, 57-63.

Randall, D. A., J. A. Coakley, Jr., C. W. Fairall, R. A. Kropfli, and D. H. Lenschow, 1984: Outlook for research on subtropical marine stratiform clouds. *Bull. Amer. Meteor. Soc.*, **65**, 1290-1301.

Twomey, S., Pollution and the planetary albedo, 1974: *Atmos. Environ.* **8**, 1251-1256.

REDUCTION OF TROPICAL CLOUDINESS BY SOOT

A. S. Ackerman[1], O. B. Toon[2], D. E. Stevens[3], A. J. Heymsfield[4], V. Ramanathan[5], and E. J. Welton[6]

[1]NASA Ames Research Center, Moffett Field, California, 94035, USA
[2]Laboratory for Space and Atmospheric Physics, Program in Oceanic and Atmospheric Sciences, University of Colorado, Boulder, Colorado, 80309, USA
[3]Lawrence Livermore National Laboratory, Livermore, California, 94551, USA
[4]National Center for Atmospheric Research, Boulder, Colorado, 80301, USA
[5]Center for Clouds, Chemistry, and Climate, Scripps Institution of Oceanography, University of California, San Diego, La Jolla, California, USA

1. INTRODUCTION

A primary objective of the Indian Ocean Experiment (INDOEX) was to quantify the indirect effect of aerosols on climate through their effects on clouds (Ramanathan et al., 1996). Conventionally, increased aerosol concentrations are expected to increase cloud droplet concentrations, and hence, total droplet cross-sectional area, thereby increasing cloud albedo (Twomey, 1974). Furthermore, model simulations of marine stratocumulus (Albrecht, 1989; Ackerman et al., 1993; Pincus and Baker, 1994) and observations of ship tracks (Radke et al., 1989; Hindman et al., 1994; Taylor and Ackerman, 1999) suggest that increased aerosol concentrations can enhance cloud water content, physical thickness, and areal coverage by decreasing precipitation.

Deep layers of dark haze were observed over much of the northern Indian Ocean in the winters (dry monsoons) of 1998 and 1999 (Jayaraman et al., 1998; Satheesh and Ramanathan, 2000) during INDOEX. The clouds were typically embedded in the haze, which filled the marine boundary layer and was often overlain by a residual continental boundary layer advecting pollution over vast areas (Manghani et al., 2000). In apparent contrast to the conventional expectation that aerosols augment cloud depth and coverage, very sparse cloud cover is found in that region during that time of year (Rossow and Schiffer, 1991). These INDOEX observations suggest another mechanism by which aerosols impact clouds, in which a dark haze can significantly reduce aereal coverage of trade cumulus (the predominant cloud type expected at that latitude and season) by amplifying the radiatively-driven diurnal cycle of cloudiness by increasing solar heating of the boundary layer.

2. APPROACH

We use a large-eddy simulation model (Stevens and Bretherton, 1997) with parameterized precipitation (Wyant et al., 1997) and plane-parallel radiative transfer (Toon et al., 1989). For meteorological context, we use measurements from the Atlantic Trade-Wind Experiment (ATEX), characterized as "nearly classic" trade cumulus, n which areal coverage was dominated by stratiform anvils spreading out below a strong trade inversion (Augstein et al., 1973). The simulation setup is derived from a GCSS model intercomparison (Stevens et al., 1999). We compare a sequence of model simulations subject to varying degrees of aerosol-induced solar heating to evaluate the cloud-burning effect of soot, and independently vary droplet concentrations from 50 to 500 cm^{-3}.to incorporate conventional indirect effects. Our approach and results are described at greater length by Ackerman et al. (2000).

Corresponding author's address: Andrew S. Ackerman, NASA Ames Research Center, Moffett Field, California, 94035, USA; E-Mail: ack@sky.arc.nasa.gov.

3. RESULTS

Relative to the baseline fractional cloud coverage of 0.19 (at a droplet concentration of 250 cm^{-3}), the solar absorption in our idealized INDOEX 1998 and 1999 hazes results in 25 and 40% reductions in daytime cloudiness, respectively. The reductions exceed the offsetting increases in cloudiness due to conventional indirect effects.

Diurnally-averaged, the top-of-atmosphere (TOA) radiative forcing due to aerosol-induced solar absorption in our INDOEX 1998 and 1999 hazes is 3.3 and 7.5 W m^{-2}, respectively, amounting to more than 2 and 4 times the globally-averaged forcing due to increases in carbon dioxide since the 1850s (Houghton et al., 1996). The positive radiative forcing due to the cloud-burning effect of soot is opposed by the net direct and the conventional indirect aerosol forcings at the surface and at the top-of-atmosphere (TOA). We find that the net anthropogenic TOA forcing by aerosols can be positive or negative (or zero), depending on assumptions about unpolluted and polluted conditions. We note that this equivocal theoretical finding is analogous to satellite observations showing that absorbing aerosols can decrease (Kaufman and Nakajima, 1993) or increase (Kaufman and Fraser, 1997) horizontally averaged cloud albedo.

4. ACKNOLWEDGEMENTS

We thank the NOAA Pacific Marine Environmental Laboratory (PMEL) and the crews of the R/V Ronald H. Brown and the National Center for Atmospheric Research (NCAR) C-130 aircraft for making the INDOEX measurements possible.

5. REFERENCES

Ackerman, A. S., O. B. Toon, and P. V. Hobbs, 1993: Dissipation of marine stratiform clouds and collapse of the marine boundary layer due to the depletion of cloud condensation nuclei by clouds. Science, 262, 226-229.

Ackerman, A. S., O. B. Toon, D. E. Stevens, A. J. Heymsfield, V. Ramanathan, and E. J. Welton, 2000: Reduction of tropical cloudiness by soot. Science 288, 1042-1047.

Albrecht, B., 1989: Aerosols, cloud microphysics, and fractional cloudiness. Science 245, 1227-1230.

Augstein, E., H. Riehl, F. Ostapoff, and V. Wagner, 1973: The vertical structure of the atmospheric planetary boundary layer in undisturbed Atlantic trade-wind flow. Mon. Wea. Rev. 101, 101-111.

Hindman, E. E., W. M. Porch, J. G. Hudson, and P. A. Durkee, 1994: Ship-produced cloud lines of 13 July 1991. Atmos. Environ. 28, 3393-3403.

Houghton, J. T., et al., 1996: Climate change 1995: The science of climate change (Cambridge University Press, Cambridge), 112-117.

Jayaraman, A., et al., 1999: Direct observations of aerosol radiative forcing over the tropical Indian Ocean during the January-February 1996 pre-INDOEX cruises. J. Geophys. Res. 103, 13827-13836.

Kaufman, Y. J., and R. S. Fraser, 1997: The effect of smoke particles on clouds and climate forcing. Science 277, 1636-1639.

Kaufman, Y. J., and T. Nakajima, 1993: Effects of Amazon smoke on cloud microphysics and albedo. J. App. Meteor. 32, 729-744.

Manghani, V., et al., 2000: Marine boundary layer variability over the Indian Ocean during INDOEX (1998)..Bound.-Lay. Met., in press.

Radke, L. F., J. A. Coakley Jr., and M. D. King, 1989: Direct and remote sensing observations of the effects of ships on clouds. Science 246, 1146-1149.

Ramanathan, V., et al., 1996: Indian Ocean Experiment (INDOEX), A multi-agency proposal for a field experiment in the Indian Ocean (C4, Scripps Institution of Oceanography, UCSD, La Jolla, California, USA, 1996), p 83.

Rossow, W. B., and R. A. Schiffer, 1991:ISCCP cloud data products. Bull. Am. Met. Soc. 72, 2-20..

Satheesh, S. K. and V. Ramanathan, 2000: Large differences in tropical aerosol forcing at the top of the atmosphere and Earth's surface. Nature 405, 60-63.

Stevens, B., et al., 1999: Cloud fraction in the trades: An LES intercomparison study. 13th Symposium on Boundary Layers and Turbulence, 10 to 15 January 1999, Dallas, Texas (AMS, Boston), 269-270.

Stevens, D. E., and C. S. Bretherton, 1997: A forward-in-time advection scheme and adaptive multilevel flow solver for nearly incompressible atmospheric flow. J. Comp. Phys. 129, 284-295.

Taylor, J. P., and A. S. Ackerman, A case study of pronounced perturbations to cloud properties and boundary layer dynamics due to aerosol emissions. Q. J. Roy. Met. Soc. 125, 2643-2662.

Toon, O. B., C. P. McKay, and K. Santhanam, 1989: Rapid calculation of radiative heating rates and photodissociation rates in inhomogeneous multiple scattering atmospheres. J. Geophys. Res. 94, 16287-16301.

Twomey, S.,1974: Pollution and the planetary albedo. Atmos. Environ. 8, 1251-1256.

Wyant, M. C., C. S. Bretherton, H. A. Rand, and D. E. Stevens, 1997: Numerical simulations and a conceptual model of the stratocumulus to trade cumulus transition. J. Atmos. Sci. 54, 168-192.

IS THERE AN INDIRECT AEROSOL EFFECT ASSOCIATED WITH ICE CLOUDS?

Ulrike Lohmann[1]

[1]Department of Physics, Dalhousie University, Halifax, Nova Scotia, Canada

1. INTRODUCTION

Anthropogenic aerosols such as sulfate and carbonaceous aerosols have substantially increased the global mean burden of aerosols from preindustrial times to present-day. While the change in solar radiation at the top of the atmosphere by absorption and scattering of anthropogenic aerosols (direct aerosol effect) remains uncertain (Houghton et al., 1996), the change associated with the indirect effect, where anthropogenic aerosols act as cloud condensation nuclei (CCN) thereby determining the initial cloud droplet number concentration (CDNC), albedo, precipitation formation, and lifetime of warm clouds, is far more uncertain. The indirect aerosol effect is negative and estimated to be between 0 and -2 W m^{-2}. Rotstayn (1999) and Lohmann et al. (2000) included contributions to the indirect sulfate aerosol effect from the change in cloud albedo as well as from an increase in cloud lifetime due to slower precipitation formation (cloud albedo and cloud lifetime effect). They found both effects almost equally important.

The addition of anthropogenic aerosols decreases the mean cloud droplet size and the smaller droplets are less likely to freeze for a given temperature leading to a slower or less frequent glaciation of supercooled clouds. This could potentially change the phase of clouds and the longwave radiative forcing. However, this effect was found to be negligible so far. In the reference experiment described in Lohmann et al. (2000) this effect was included through equation (2). It was found to increase the global mean longwave radiation by only 0.2 W/m^2 which is comparable to the increase of 0.1 W/m^2 in Rotstayn's (1999) experiment.

Anthropogenic aerosols may also change the properties of ice forming nuclei. The presence of salt ions causes a lowering of the effective freezing temperature and foreign gases such as SO_2 or NH_3 occupy the active sites, both effects reduce the nucleability of ice nuclei (see, for instance, Pruppacher and Klett, 1997) and promote the prolonged existence of supercooled clouds which would effect the precipitation efficiency of these clouds as well as their radiative properties. This could effect both the shortwave radiation in a way similar to water clouds and the longwave radiation.

Here we investigate the hypotheses that anthropogenic sulfur compounds reduce the nucleability of ice forming nuclei which are assumed to be dust aerosols. SO_2 on a dust particle will occupy active sites. Additionally, if oxidized to sulfate, the mixed aerosol will be hygroscopic and be incorporated in a cloud drop and, thus, no longer be available as a contact nuclei. It could increase the number of immersion nuclei because the sulfate/dust mixture will have a surface for ice nucleation. However, the parameterization of immersion freezing which we currently use in ECHAM does not depend on the number of immersion freezing nuclei (equation 1). Therefore we only consider the change in the number of contact nuclei due to internally mixed sulfate/dust aerosols. We conduct 2 experiments one in which the number of contact nuclei equals the number of dust aerosols and one where the number of contact nuclei is reduced in proportion to the number of sulfate aerosols.

1. MODEL DESCRIPTION

The ECHAM model used in this study is a modified version based on Lohmann et al. (1999a). Prognostic aerosol variables are mass mixing ratios of sulfate, organic and black carbon, sub- and supermicron dust (0-1 μm and 1-2 μm), and sub- and supermicron sea salt (0-1 μm and 1-10 μm). Sulfate, organic and black carbon are described in Lohmann et al. (1999a). The dust fluxes are provided by Ginoux (personal communication, 1999) and the sea salt fluxes are parameterized as a function of wind speed following Monahan et al. (1986).

Prognostic cloud variables are mass mixing ratios of cloud liquid water and cloud ice, the number concentrations of cloud droplets and ice crystals. Parame-

*Corresponding author's address: Ulrike Lohmann, Atmospheric Science Program, Dept. of Physics, Dalhousie University, Halifax, N.S. B3H 3J5, Canada; (E-mail: Ulrike.Lohmann@Dal.Ca)

terized microphysical processes for the mass mixing ratios are condensational growth of cloud droplets, depositional growth of ice crystals, homogeneous and heterogeneous freezing of cloud droplets, autoconversion of cloud droplets, aggregation of ice crystals, accretion of cloud ice and cloud droplets by snow, of cloud droplets by rain, evaporation of cloud liquid water and rain, sublimation of cloud ice and snow, and melting of cloud ice and snow. The precipitation formation rates for mixed and ice clouds are adopted from the formulation used in the mesoscale model GESIMA (Geesthacht simulation model of the atmosphere) by Levkov et al. (1992).

Cloud droplet number is predicted from nucleation using the modified version of the Ghan et al. (1993) parameterization (Lin and Leaitch, 1993) and parameterized autoconversion, accretion and self collection of cloud droplets.

The ice crystal number assuming equivalent spheres of newly formed ice crystals is estimated from the deposited vapor and a mean ice crystal size, which depends on temperature, as described in Lohmann et al. (1999b). We also consider aggregation, accretion and self collection of ice crystals, the secondary ice production mechanism by Hallett and Mossop and two different ways of freezing of cloud droplets as described below. All of these processes are described in detail in Levkov et al. (1992).

Immersion freezing and condensation freezing are assumed to depend only on the cloud liquid water content in the cloudy part of the grid box q_l and temperature T as follows:

$$Q_{frz,het} = a[exp\{b(273.2 - T)\} - 1]\frac{\rho q_l}{\rho_l} \qquad (1)$$

where ρ is the air density, ρ_l is the water density, a=100 m^{-3} s^{-1} and b=0.66 K^{-1}.

The only parameterization of ice formation which depends on the number of ice nuclei is contact freezing of cloud droplets:

$$Q_{frz,cnt} = m_{io} D_{ap} 4\pi r_l N_{ao}(270.15 - T)\frac{N_l^2}{\rho q_l} \qquad (2)$$

where r_l is the volume mean droplet radius, N_l is the number of cloud droplets, $m_{io} = 10^{-12}$ kg is the original mass of a newly formed ice crystal, $D_{ap} = 1.4 \cdot 10^{-8}$ m^2 s^{-1} is the aerosol diffusivity, $N_{ao} = 2 \cdot 10^5$ m^{-3} is the number of active ice nuclei at 269 K. To connect this equation to our prognosed aerosols, we assume that the number of active ice nuclei at 269K equals the number of dust aerosols. The number of dust aerosols in the reference simulation is obtained from the sub- and supermicron dust mass by assuming log-normal distributions with mode radii of 0.07 μm and 0.39 μm, a density of 2600 kg/m^3 and a geometric standard deviation of 1.95 and 2 μm, respectively (Hess et al. 1998). This is an upper bound for the number of contact nuclei, because an external mixture is assumed. We then conduct a sensitivity study where we assume that the number of dust contact nuclei is reduced according to the abundance of sulfate aerosols. That is, we subtract from the sub- and supermicron dust mass half of the sulfate mass each and convert the remaining dust mass into the number of ice nuclei. As sulfate aerosols are mainly anthropogenic, this difference in contact nuclei could be taken as the anthropogenic impact.

Between -35°C and 0°C mixed clouds can exist. If no cloud ice is present, it is assumed that the cloud consists of supercooled cloud droplets only, and saturation with respect to liquid water is assumed. These cloud droplets can either evaporate again, form rain drops or freeze. Once ice crystals are present the lower vapor pressure over ice causes water vapor to be deposited directly on ice crystals, and if the air is not saturated with respect to liquid water, cloud droplets will evaporate. We considered this process by assuming that, if ice crystals are present, the water vapor is deposited directly on them, i. e. condensation no longer leads to production of liquid water and saturation with respect to ice is assumed. Below -35°C only ice is present and diffusional growth the only source.

2. PRELIMINARY RESULTS

Figure 1a shows the annual mean zonally averaged aerosol number concentration as a function of height from a one-year experiment. Aerosols are most numerous in the midlatitude Northern Hemisphere boundary layer between 25°N and 60°N and rapidly decrease with height and polewards. The number of ice nuclei at 269K is calculated from the number of dust aerosols. Figure 1b shows the product of N_{ao} (270.15 - T). One has to bear in mind that it is not meaningful for temperatures below -35°C where all cloud water is assumed to freeze spontaneously. It allows for the fact that other substances such as industrial metal oxides, volcanic dust and probably soot from forest fires can act as ice forming nuclei as well. The maximum in ice forming nuclei concentration is at the north pole between 300hPa and 400hPa caused by the combination of dust transport to the Arctic and extremely cold temperatures. However, as Figure 1c shows, the number of ice crystals inside the cloudy part of the grid box averaged over cloudy events does not reflect the number of ice forming nuclei. That is, contact nucleation is not the dominant process, but immersion and condensation freezing followed by depositional growth between 0°C and -35°C as well as depositional growth below -35°C seem to be dominant. The ice water content (Figure 1d) has maxima in the tropics associated with convective anvils and midlatitude cirrus.

If sulfate is allowed to reduce the ice forming potential of dust aerosols, than the number of contact nuclei is reduced by up to 3 cm^{-3} at high latitudes of the Northern Hemisphere. Natural variability is quite large between the 2 one-year experiments so that the difference in occurrence of ice clouds is very noisy. The decrease in contact nuclei is not reflected in a decrease in ice crystal number at the North pole, but the ice crystal number has actually slightly increased at the North pole.

3. SUMMARY AND CONCLUSIONS

Preliminary results investigating the importance of contact nuclei for ice cloud formation in the ECHAM model show that contact nucleation is not the dominant process. Accounting for internally mixed aerosols rather than externally mixed aerosols by reducing the number of contact nuclei proportional to the number of sulfate aerosols being present does not change the number of ice crystals nor the ice water content significantly. As sulfate aerosols are mainly anthropogenic, this difference in contact nuclei could be taken as the anthropogenic impact.

However, there are other ways in which anthropogenic aerosols could influence ice clouds such as the reduction in the freezing point of cloud drops or the increased cirrus cloudiness due to aircraft exhaust (see, for instance, Boucher, 1999), which have not been considered here.

4. ACKNOWLEDGMENTS

We thank Glen Lesins for helpful comments and suggestions.

5. REFERENCES

Boucher, O., 1999: Air traffic may increase cirrus cloudiness, Nature, **397**, 30–31.

Ghan, S. J., C. C. Chuang, and J. E. Penner, 1993: A parameterization of cloud droplet nucleation, part I, single aerosol type, Atmos. Res., **30**, 197–221.

Hess, M., P. Koepke, and I. Schult, 1998: Optical properties of aerosols and clouds: The software package OPAC, Bull. Am. Meteorol. Soc., **79**, 831–844.

Houghton, J. T., L. G. M. Filho, B. A. Callander, N. Harris, A. Kattenberg, and K. Maskell (Eds.), 1996: *Climate Change 1995, The Science of Climate Change: Intergovernmental Panel on Climate Change*, Cambridge Univ. Press, New York.

Levkov, L., B. Rockel, H. Kapitza, and E. Raschke, 1992: 3D mesoscale numerical studies of cirrus and stratus clouds by their time and space evolution, Beitr. Phys. Atmos., **65**, 35–58.

Lin, H. and W. .R. Leaitch, 1997: Development of an in-cloud aerosol activation parameterization for climate modelling. In Proceedings of the WMO Workshop on Measurement of Cloud Properties for Forecasts of Weather, Air Quality and Climate, Geneva.

Lohmann, U., J. Feichter, C. C. Chuang, and J. E. Penner, 1999a: Predicting the number of cloud droplets in the ECHAM GCM, J. Geophys. Res., **104**, 9169–9198.

Lohmann, U., N. McFarlane, L. Levkov, K. Abdella, and F. Albers, 1999b: Comparing different cloud schemes of a single column model by using mesoscale forcing and nudging technique, J. Climate, **12**, 438–461.

Lohmann, U., J. Feichter, J. E. Penner, and W. R. Leaitch, 2000: Indirect effect of sulfate and carbonaceous aerosols: A mechanistic treatment, J. Geophys. Res., in press.

Monahan, E. C., D. E. Spiel, and K. L. Davidson, 1986: A model of marine aerosol generation via whitecaps and wave disruption, in Oceanic Whitecaps, edited by E. C. Monahan, and G. MacNiocaill, D. Reidel, Norwell, Mass.

Pruppacher, H. R. and J. D. Klett, 1997: Microphysics of Clouds and Precipitation, Kluwer Academic Publisher.

Rotstayn, L. D., 1999: Indirect forcing by anthropogenic aerosols: A global climate model calculation of the effective radius and cloud lifetime effects, J. Geophys. Res., **104**, 9369–9380.

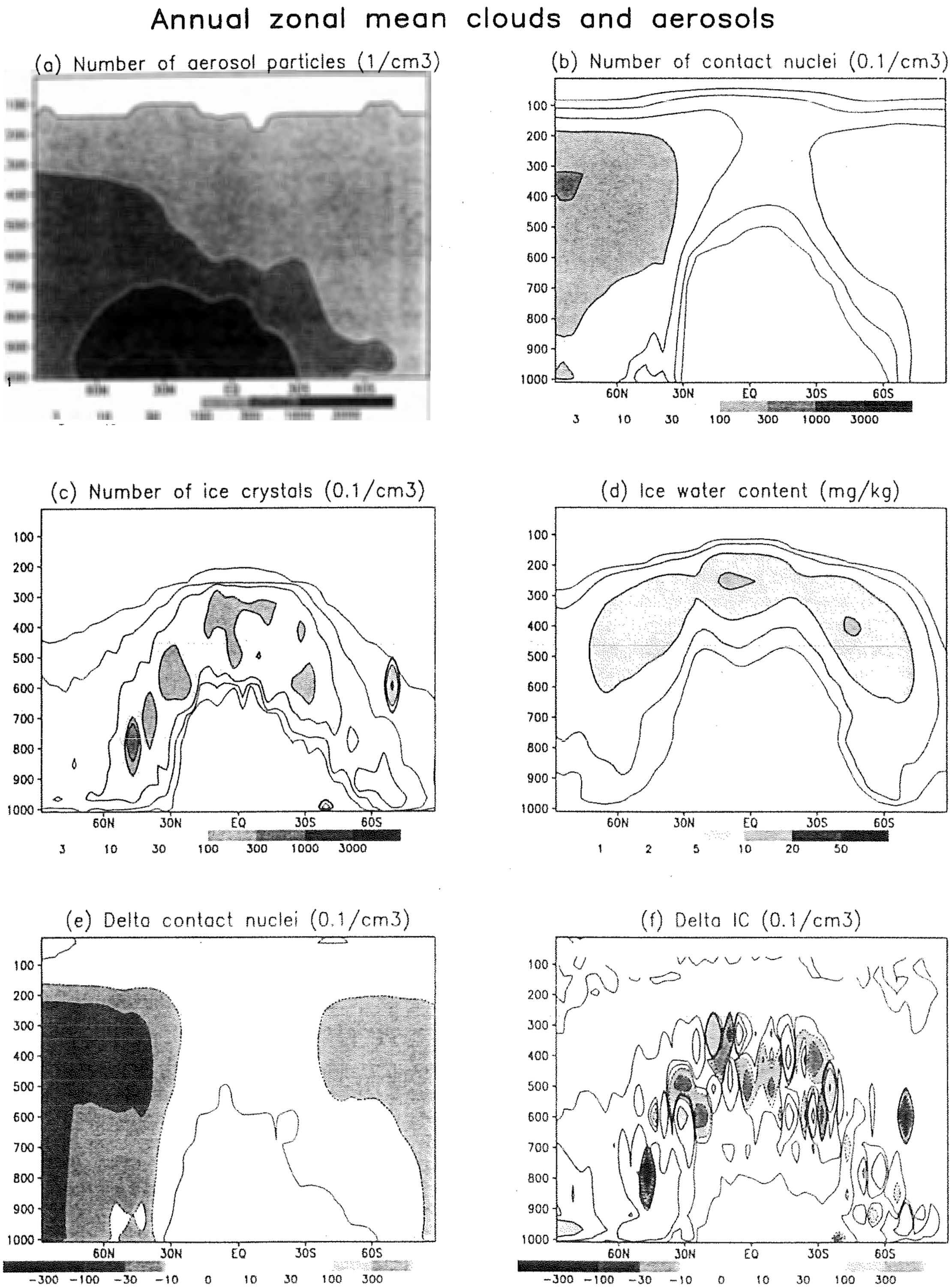

Figure 1: Annual zonal mean cross section of (a) the aerosol number concentration [cm^{-3}], (b) ice forming nuclei number concentration [0.1 cm^{-3}], (c) ice crystal number concentration [0.1 cm^{-3}], (d) ice water content [mg kg^{-1}], (e) difference in ice forming nuclei number concentration between the sensitivity experiment and the reference experiment (see text for details) [0.1 cm^{-3}], and (f) difference in ice crystal number concentration [0.1 cm^{-3}].

THE INDIRECT EFFECT OF AEROSOLS ON CLIMATE: OBSERVATIONS WITH AN AIRBORNE RADIOMETER

L. Schüller[1] , J.-L. Brenguier[2] and H. Pawlowska[3]

[1]Institut für Weltraumwissenschaften, Freie Universität Berlin, Berlin, 14195, Germany, visiting scientist at Météo-France, CNRM/GMEI.
[2]Centre National de Recherches Météorologiques, Météo-France, Toulouse, 31057, France
[3] Institute for Geophysics, University of Warsaw, Warsaw, Poland

1. INTRODUCTION

The indirect effect of aerosols on climate, also referred to as the Twomey Effect, is related to changes in cloud radiative properties due to aerosols acting as cloud condensation nuclei (CCN), via changes in cloud microphysics. This anthropogenic forcing is estimated with global climate simulations supplemented by satellite survey. It is thus crucial to develop techniques for the retrieval of cloud microphysical and optical parameters from space.

The measurement of the reflected solar radiation in the visible (VIS) and near infrared (NIR) spectral regions has been used to retrieve the cloud optical thickness and the effective droplet radius assuming vertically homogeneous clouds (e.g. Twomey and Seton, 1980, Nakajima and King, 1990, King, 1993). The relationship between droplet concentration as derived from CCN properties and the droplet radius is still missing. In actual clouds of stratocumulus type, the droplet effective radius is in fact dependent on both the droplet concentration and the altitude above cloud base: a negative correlation between remotely sensed cloud optical thickness and effective radius thus reflects the Twomey Effect, while a positive correlation illustrates the cloud geometrical thickness dependence.

A conceptual cloud model with an adiabatic profile of the microphysics has been used in radiative transfer calculations instead of the plane-parallel vertically uniform model. The conceptual model is parameterised with cloud geometrical thickness *H* and cloud droplet number concentration (CDNC) *N*, and reflectances in the VIS and NIR are calculated. The inverse procedure is then used to derive *H* and *N* from measurements of the reflectances. The statistical analysis of the results and the comparison with in situ data is presented in this paper.

Corresponding author's address: Lothar Schüller
Institut für Weltraumwissenschaften, Freie Universität Berlin, Fabeckstr. 69, 14195 Berlin, Germany
E-Mail: lothar@amor.met.fu-berlin.de

2. MEASUREMENTS DURING ACE-2

During the ACE-2 Cloudy-Column campaign, the FUB-WeW operated a high spectral resolution downward looking radiometer OVID (Schüller et al. 1997) onboard the DLR-Do228. The OVID instrument consists of two detection units (telescope, fibre cable, spectrometer and CCD detector). The VIS part covers the spectral range between *700 nm* and *1000 nm* with 1024 spectral channels (spectral resolution *0.8 nm*) and the NIR (near infrared) part has 256 channels for measurements between *1000 nm* and *1700 nm*. The spectral resolution is *6 nm*. The sampling frequency during ACE-2 was *10 Hz*, that corresponds to a spatial resolution of approximately *10 m*.

A number of 8 flight missions were flown by the Do-228 in close co-ordination with the Météo-France M-IV instrumented aircraft, equipped with in situ measurements of cloud microphysical properties (Pawlowska and Brenguier, 2000). Observations were made above marine stratocumulus clouds that were affected by different levels of pollution. A more detailed description of the project can be found in Brenguier et al., (2000-a).

3. RADIATIVE TRANSFER SIMULATIONS AND ALGORITHM DEVELOPMENT

Radiative transfer calculation are the basis of retrieval algorithms, that usually compare the measured radiation to simulated ones. The cloud reflectance in a VIS channel is mainly dependent upon cloud optical thickness, while the reflectance in the liquid water absorption bands (NIR) shows more sensitivity to the droplet size. Due to large multi-scattering effects, photons at wavelengths, where absorption occur, carry information from the top-most cloud layer only. A remotely sensed droplet radius refers therefore to the upper cloud layer and it is not necessarily representative of the whole cloud.

Stratocumulus clouds usually show a very pronounced vertical profile of the droplet size, that depends on CDNC. The interpretation of remotely sensed droplet sizes is therefore problematic, since natural variations of cloud geometrical thickness will result in variations of the droplet sizes at cloud top. On the contrary CDNC is more uniform through the cloud layer and it is thus more suited for characterizing the microphysical properties of stratocumulus and their relationship with the aerosol background. Therefore, stratified cloud models are more realistic than vertically uniform models for radiative transfer simulations.

3.1 The adiabatic model

The adiabatic model describes the vertical profile of the microphysics in a closed ascending cloud parcel. The liquid water content increases linearly with height:

$$LWC_{ad}(h)=C_w\, h.$$

In addition, N_{ad} is constant in the adiabatic model. Hence, the droplet mean volume diameter expresses as:

$$r_{v,\,ad}(h) = (A\ h)^{1/3}\ (N_{ad})^{-1/3} \text{ with } A= C_w/(4/3\ \pi\ \rho_w).$$

The effective radius can be derived from $r_{v,\ ad}$ with the factor $k = r_e^3\ /\ r_v^3$. The optical thickness of an adiabatic cloud layer can thus be calculated as a function of H and N (Brenguier et al. 2000-b):

$$\tau = 3/5\ \pi\ Q_{ext}\, A^{2/3}\ (kN)^{1/3}\ H^{5/3}.$$

In the adiabatic model, droplet effective radius and optical thickness are both functions of N and H:

$$r_e = r_e(N,H)$$
$$\tau = \tau\ (N,H).$$

This relation is used to simulate the radiative transfer of vertically stratified clouds.

3.2 Radiative transfer simulations

For the calculation of the radiative transfer a Matrix-Operator Model has been applied (Fischer and Graßl, 1991). The single scattering properties (extinction and scattering coefficient, scattering phase function) are calculated by Mie theory. Upward directed radiances at flight level have been calculated and converted to reflectance values.
Vertical stratification of the simulated clouds were realized by combining homogeneous sub-layers of *25 m* thickness as indicated in Fig. 1. The layer averaged values of τ and r_e are determined by the adiabatic model (previous section). The reflectances at two wavelength (*754 nm* and *1535 nm*) were calculated for different combinations of H (from 0 to *500 m*) and N (from *10* to *800* cm^{-3}). Figures 2 and 3 show the result of the radiative transfer simulations as iso-lines of N and H together with the statistics of the measured reflectances.

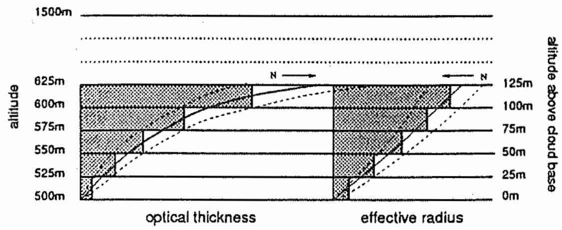

Figure 1: *Optical thickness and effective radius of the homogeneous sub-layers for radiative transfer simulations with the adiabatic stratified cloud model.*

3.1 Inversion technique

The data set of simulated reflectances for different combinations of N and H is inverted by means of artificial neural network training. A number of 1000 learning patterns were used for the training, where each learning pattern consists in the three input values for solar zenith angle, reflectance at *754 nm* and reflectance at *1535 nm*, and the corresponding output values for N and H. The test patterns have the same structure and are used to control and estimate the quality of the inversion.

A back-propagation type of network training was applied to the learning patterns. The resulting neural network is implemented in the OVID processing system.

4. STATISTICAL ANALYSIS

The *754 nm* and *1535 nm* reflectances of the solar radiation were extracted from the OVID spectra and the algorithm for the retrieval of N and H was applied to the OVID measurements performed during ACE-2. Fig. 2 and 3 show the statistics of two flight legs that were flown above clouds in a clean (Fig. 2) and in a polluted (Fig. 3) environment.

There is a remarkable increase of reflection in the polluted case in contrast to the clean case. The comparison of measured data with the radiative transfer simulations (iso-lines) indicates that the largest variation in reflectance is due to variations of cloud thickness while N is rather constant. Generally, the measured data show similar behaviour as predicted by the radiative transfer simulations with the adiabatic stratified cloud model.

The statistics of reflectance can be assigned to typical iso-lines of droplet concentration, such as $N=25\ cm^{-3}$ for the clean case (26 June, 1997, Fig. 2) and $100\ cm^{-3}$ for the polluted case (9 July, 1997, Fig. 3). Since the adiabatic model describes the maximum possible liquid water that can be condensed, it is expected, that the high reflective parts of a flight leg correspond to adiabatic conditions and that the retrieval is more accurate for those samples. For the statistical analysis and comparison with in situ data, we therefore selected samples corresponding to samples with reflectance values in the upper p % of the distribution.

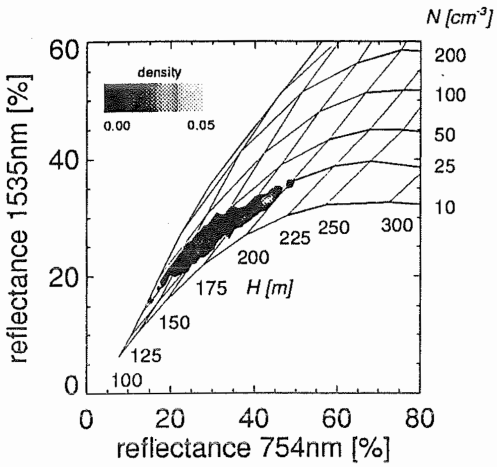

Figure 2: Two-dimensional histogram of measured reflectances at two wavelengths during a flight mission in a marine environment (26 June, 1997). The results of the corresponding radiative transfer simulations are indicated as iso-lines of N and H.

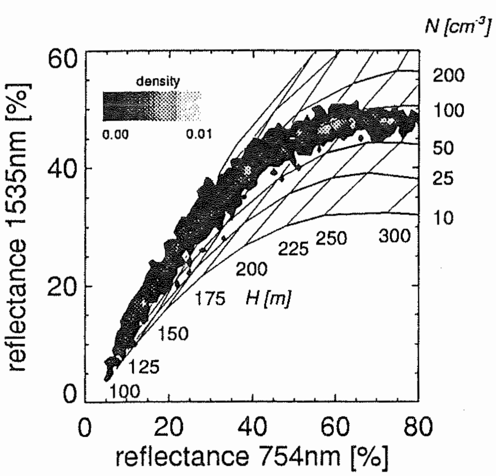

***Figure 3:** Same as Figure 2 in a polluted environment (9 July, 1997).*

An example of the resulting N histograms is displayed in Fig. 4 (polluted case 9 July, 1997, for $p=0$ (all values), 40, 60 and 80 %.

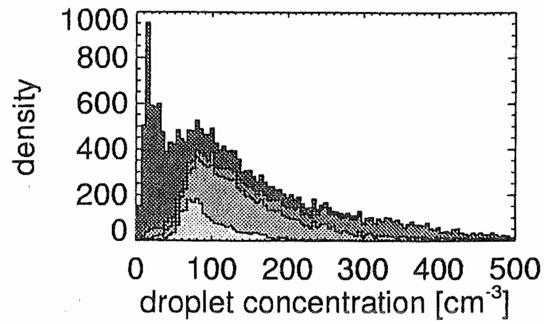

***Figure 4:** Histograms of the retrieved droplet concentration for the Cloudy-Column mission in a polluted environment (9 July, 1997).*

5. COMPARISON WITH IN SITU MEASUREMENTS

The retrieval of N and H has been performed for 8 Cloudy-Column missions. After selection of the most reflective parts ($p=80$ %) of the flight legs, the mean droplet concentration of the histogram (N_{OVID}) is compared (Fig. 5) to the mean droplet concentration, derived from in situ measurements with the Fast-FSSP, after selection of samples that are not affected by mixing with dry air and drizzle scavenging (N_{mean}) (Pawlowska and Brenguier, 2000-a and –b). Fig. 5 demonstrates, that the new remote sensing procedure is able to retrieve correctly the variations of N_{mean}, from the pure marine case to the most polluted one. The figure also shows, that there is a significant bias between in situ derived and remotely retrieved N values. The retrieved values are underestimated by a factor of about 2. The reason for this deviation is not clear. It is probably related to the sub-adiabaticity of microphysics in the cloud layer and to its spatial heterogeneity.

The comparison between remotely sensed and in situ observed cloud geometrical thickness is reported in Fig. 6. N_{max} is first derived as the value at 99 % probability of the cumulated distribution of the measured N values. The typical H value for each case is then derived from the cumulated distribution of the measured values of altitude above cloud base, after selection of samples with $N > 0.2\ N_{max}$. It is calculated as the value at 97 % probability of the distribution and it is referred to as H_{max} (Pawlowska and Brenguier, 2000-a and –b). Fig. 6 shows also a good correlation but with an overestimation by the radiation measurements.

6. CONCLUSION

A new remote sensing technique, based on a realistic cloud model for radiative transfer simulations, has been developed for the retrieval of cloud geometrical thickness and droplet concentration. The anthropogenic Twomey Effect as well as the natural variation of cloud geometrical thickness both affect optical thickness and the effective radius at cloud top. In contrast, using *N* and *H* as co-ordinates, dynamical variations can be separated from the possible modifications of cloud microphysical properties.

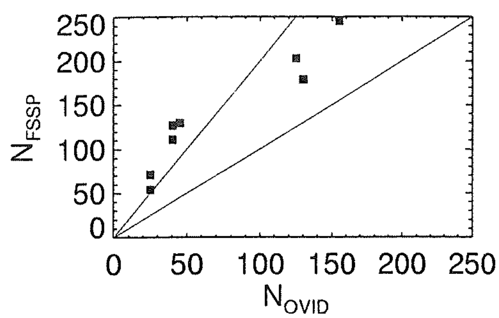

Figure 5: *Comparison of the remotely retrieved (N_{OVID}) and in situ measured (N_{FFSSP}) droplet concentration values, for 8 Cloudy-Column missions.*

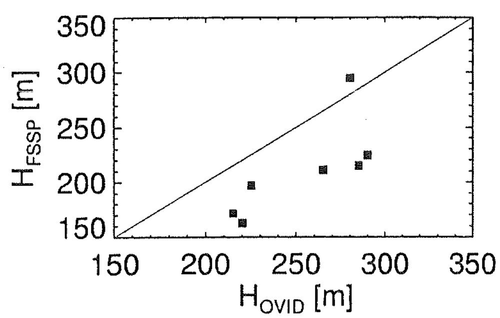

Figure 6: *Comparison of the remotely retrieved (H_{OVID}) and in situ measured (H_{FSSP}) geometrical thickness values for 8 Cloudy-Column missions.*

Simultaneous measurements of the reflected radiation and microphysical properties with two instrumented aircraft have been used to validate the new remote sensing technique. Qualitatively, the validity of the algorithms has been demonstrated by the correlation between the in situ measured and retrieved values of *N* (Fig. 5) and *H* (Fig. 6). The next step will be focused on the analysis of the influence of non-adiabadicity and spatial heterogeneity of the microphysical field on the retrieval method. This might lead to a better parameterization of the aerosol-cloud-radiation interaction processes for the development of remote sensing algorithms as well as for climate models.

7. ACKNOWLEDGEMENTS

The authors acknowledge the contribution of the ACE-2 participants and the support of the European Union under grants ENV4-CT95-0117 (Cloudy-Column) and EVK2-CT-1999-00340 (PACE).

8. REFERENCES

Brenguier, J.-L., H. Pawlowska, L. Schüller, R. Preusker, J. Fischer, and Y. Fouquart, 2000-b: Radiative properties of boundary layer clouds: droplet effective radius versus number concentration. *J. Atmos. Sci.*, **57**, 803-821.

Brenguier, J.-L., P. Y. Chuang, Y. Fouquart, D. W. Johnson, F. Parol, H. Pawlowska, J. Pelon, L. Schüller, F. Schröder and J. R. Snider, 2000-a; An overview of the ACE-2 CLOUDYCOLUMN Closure Experiment. *Tellus,* **52B**, 814-826.

Fischer, J. and H. Graßl, 1991: Detection of cloud-top height from backscattered radiances within the oxygen-A band. Part 1: Theoretical study, *J. Appl. Met.*, **30**, 1245-1259.

King, M. D., L. F. Radke and P. V. Hobbs, 1993: Optical properties of marine stratocumulus clouds modified by ships, *J. Geoph. Res.*, **98**, 2729-2739.

Nakajima, T. and M. D. King, 1990: Determination of optical thickness and effective particle radius of clouds from reflected solar radiation measurements. Part I: Theory, *J. Atmos. Sci.*, **47**, 1878-1893.

Pawlowska, H. , and J. L. Brenguier, 2000-a: Microphysical properties of stratocumulus clouds during ACE-2. *Tellus.* **52B**, 867-886.

Pawlowska, H. , and J.-L. Brenguier, 2000-b: The indirect effect of aerosols on climate: Effect of aerosol properties on precipitation efficiency. *Pre-prints 13th ICCP.*

Schüller, L., J. Fischer, W. Armbruster and B. Bartsch, 1997: Calibration of high resolution remote sensing instruments in the visible and near infrared, *Adv. Space Res.*, **19**, 1325-1334.

Twomey, S., and K. J. Seton, 1980: Gross Properties of Clouds from Spectral Reflectance Measurements, *J. Atmos. Sci.*, **37**, 1065-1069.

PARAMETERIZATION OF THE INDIRECT EFFECT OF AEROSOLS ON CLIMATE : FROM ACE-2 CLOUDY-COLUMN TO PACE

J. L. Brenguier[1], J. Feichter[2], S. Ghan[3], U. Lohmann[4], S. Menon[5], H. Pawlowska[6], D. Roberts[7], L. Schüller[8], J. Snider[9]

[1] Météo-France, CNRM-GMEI (F); [2] Max Planck Institute für Meteorologie (G); [3] Battelle Memorial Institut, PNNL (WA-USA); [4] University of Dalhousie (CAN); [5] Columbia University, GISS (NY-USA); [6] University of Warsaw, IGF (PL); [7] Meteorological Office, Hadley Centre (UK); [8] Freie Universität Berlin, IFW (G); [9] University of Wyoming, DAS (USA)

1. INTRODUCTION

During the second aerosol characterization experiment (ACE-2 1997) , the Cloudy-Column project was dedicated to a column closure experiment on the indirect effect of aerosols on climate, that is to the possible changes of the cloud radiative properties due to anthropogenic changes in the chemical and physical properties of the aerosols. Cloudy-Column was focused on marine boundary layer clouds. The experiment took place in June and July 1997, in the vicinity of the Tenerife Island (Spain), a region of marine aerosol background, with occasional pollution outbreaks originating from Europe.

The strategy in Cloudy-Column was based on simultaneous aircraft measurements of aerosol properties and turbulent fluxes in the boundary layer (UKMO C130 and CIRPAS Pelican), of cloud microphysics and dynamics in the stratocumulus layer (Météo-France M-IV) and of the cloud radiative properties by remote sensing with radiometers and a lidar (DLR Do-228 and ARAT F-27) (Brenguier et al. 2000-a). Besides the aircraft, detailed measurements of the aerosol chemical and physical properties (APP) were performed at the ground site (PDH), on the north-eastern coast of Tenerife (Putaud et al. 2000). Twelve missions were flown between 21 June and 21 July 1997, with various aerosols backgrounds, from pure marine to significantly polluted.

2. CLOUDY-COLUMN SUMMARY

The aerosol indirect effect involves various physical processes which have been examined separately.

2.1 The CCN activation process

The cloud droplet number concentration (CDNC) is dependent upon the activation of a subset of the aerosols, referred to as cloud condensation nuclei (CCN). The activation process is described by a two steps calculation, namely the Köhler theory for characterizing the hygroscopic properties of the aerosols (static), and the convective parcel model which simulates the evolution of the supersaturation and CCN growth in an updraft (kinetic).

Corresponding author's address: J. L. Brenguier, Météo-France, CNRM/GMEI, 42 av. Coriolis, 31057 Toulouse Cedex 01, FRANCE.
Email : jlb@meteo.fr

Closure "A" addresses the activation process as a whole. The APP measured at PDH are used to initialise the complete (static and kinetic) activation model, and calculate CDNC as a function of the updraft vertical velocity of the convective cell *w*. The probability density function (PDF) of *w*, as measured at cloud base, is thus transformed onto a predicted PDF of CDNC. Microphysical measurements inside the cloud layer, after selection of regions that are not affected by mixing and drizzle scavenging (Pawlowska and Brenguier, 2000-a) are then used to derive a measured *PDF(CDNC)*. The level of closure is evaluated by comparing the 10 % percentiles of the predicted and the measured *PDF(CDNC)*.

Sub-closure experiments have also been designed to test both steps of the calculation separately (Snider and Brenguier, 2000; Guibert et al. 2000).

Sub-closure "S" is designed to test the static step of the calculation, that is the Köhler theory. The physical and chemical properties of the sub-micrometric aerosol (APP) measured at the PDH site are used to initialise the Köhler equation and to derive the size distribution of the particles in the range of relative humidity between *87* and *97 %*. The predicted distribution is then compared to the one measured on the M-IV with the FSSP-300 (diameter range between *0.3* and *20* μm) after selection of samples taken below cloud base in the same relative humidity range. The Köhler equation is also used to derive the CCN activation spectrum in the range of supersaturation between *0.2* and *1.6 %*. The predicted spectrum is then compared to the one measured in the sub-cloud layer with a CCN counter (Snider and Brenguier, 2000).

Sub-closure "K" addresses the kinetic step of the calculation. It is similar to closure "A" except that the measured CCN spectra, are used directly in activation calculations.

The same methodology applied to the twelve missions reveals that sub-closure "K" is within the instrumental uncertainty range, thus suggesting that the kinetic step of the calculation is correct, when initialised with the measured *PDF(w)* and the measured CCN spectra. However the overall closure "A" is not satisfactory for the polluted cases, with predicted values of CDNC that are a factor of *2* overestimated with respect to the measured ones. This is confirmed by sub-closure "S" which also suggests that the Köhler theory overestimates the CCN number concentration in the polluted cases. Since the theory has been largely validated in the past, it is likely that the equation is not correctly initialised with the APP measured at PDH. This work needs to be extended with emphasis placed on detailed aspects of the aerosol (water mass fraction at the time of the sampling, hygroscopicity, state of mixing, organic speciation, etc...). The objective in Cloudy-Column is not only to test detailed models of the physical processes but rather their parameterisation for global climate models (GCM). This closure exercise suggests that the kinetic and static models are accurate and also that refinements are needed in understanding of aerosol properties, especially the anthropogenic aerosol. This deficiency shall be addressed before trying pertinent tests of the parameterisations.

2.2 Condensational droplet growth

Most of the radiative transfer calculations have been performed with the implicit assumption that LWC is distributed uniformly through the cloud layer. However, the vertical stratification of the microphysics, characterized by droplet sizes increasing with altitude, significantly influences the calculation. The vertical stratification also regulates the precipitation efficiency which is a key process in the aerosol indirect effect (Albrecht, 1989). It is thus relevant to develop GCM parameterizations based on more realistic models of the boundary layer cloud microphysics. The simplest scheme is referred to as the adiabatic model and it describes droplet growth in an ascending closed cloud parcel.

The Cloudy-Column data set has a unique feature to test such a model: for 8 cases, at least 15, and up to 35, vertical profiles were flown by the M-IV inside the cloud layer. The data set thus provides the most significant available statistics for describing the vertical cloud stratification. Pawlowska and Brenguier (2000-a) have shown (i) that the mean value of CDNC, measured in regions that are void of drizzle drops and not affected by mixing, varies from *55*, for the most marine case, to $244\ cm^{-3}$, for the most polluted one, (ii) that the CDNC values in the selected regions are distributed between *0.5* and *1.5* of the mean value, and (iii) that the frequency distribution of the values of droplet mean volume d_v^3, as a function of altitude above cloud base, is contained within the limits of the adiabatic prediction for a concentration between *0.5* and *1.5* of the mean value. The data set also reveals (iv) that the difference between the effective diameter and the mean volume diameter d_e-d_v, in the upper half of the cloud thickness, is smaller than $2\ \mu m$ (mean value of $1\ \mu m$), independently of the mean CDNC value.

This closure exercise demonstrates that the adiabatic model of droplet growth is more realistic for radiative transfer calculations than the vertically uniform model. However, it also suggests that the droplet concentration varies significantly in a cloud layer, thus reflecting the variability of the vertical velocity at the CCN activation level, the mixing effects and drizzle scavenging. The adiabatic model shall therefore be refined with considerations on the horizontal variability of CDNC and the effects of sub-adiabaticity.

Further analysis has been dedicated to the sensitivity of the precipitation efficiency to CDNC (second indirect effect). The clouds sampled during Cloudy-Column are particularly suited for such an approach because their thickness is such that the maximum droplet sizes reached at the cloud top are close to the threshold value for the onset of precipitation. Among the 8 best documented cases, the two most marine ones in fact develop a significant drizzle concentration, the 3 most polluted cases remain below the precipitation threshold, and three intermediate cases show measurable concentrations of drizzle without precipitation development (Pawlowska and Brenguier, 2000-b). The 8 cases together thus provide a robust estimation of the threshold diameter at $20\ \mu m$, for the onset of precipitation in stratocumulus clouds

2.3 Radiative transfer

Based on the observations reported above, the radiative transfer calculations with a vertically uniform (VU-PPM) and an adiabatic stratified plan parallel (AS-PPM) cloud models were tested (Brenguier et al. 2000-b). The first step was to identify a possible relationship between the effective diameter at the top of the AS-PPM, $d_{eAS}(H)$, and the value of effective diameter to use in the VU-PPM, d_{eVU}, for the two models to produce the same values of reflected radiances in the visible (VIS) and near infra-red (NIR) domains. Simulations were performed over a large range of cloud geometrical thickness *H* and droplet concentration *N*, and it has been demonstrated that there is no simple equivalence between the two models: $0.8 < d_{eVU}/d_{eAS}(H) < 1$, where the value of the ratio depends on both *H* and *N*.

Further calculations of radiative transfer have thus been performed with the AS-PPM to provide *(H,N)* look-up tables of VIS and NIR radiances. A neural network technique has been developed for the retrieval of both *H* and *N* from measured radiances. The comparison with the values measured in situ constitutes the third closure exercise in Cloudy-Column (Schüller and Brenguier, 2000). The test confirms that the differences between a pure marine and a polluted case are clearly revealed by the VIS and NIR reflectances (Fig. 7 in Brenguier et al. 2000-a). However, the retrieved values of CDNC are systematically underestimated by the retrieval technique. This bias has been attributed to the horizontal heterogeneity of the cloud layer and the sub-adiabaticity of the microphysical field. These features are now considered for the development of a more realistic cloud model for radiative transfer calculations.

2.4 Summary

The Cloudy-Column experiment offers presently the most detailed data set for the study of the aerosol indirect effect in boundary layer clouds, with complementary information about the aerosol properties, cloud microphysics and radiation, measured simultaneously by different aircraft. The data set covers a broad range of aerosol and microphysical properties that are reflected in significant variations of the radiative properties: CN and CCN concentrations that range over nearly an order of magnitude, CDNC mean values from *50* to *250* cm^{-3}, effective diameter at cloud top from *12* to *25* μm, peak values of reflectance from *0.5* to *0.8* (VIS), or from *0.3* to *0.5* (NIR). For the study of the second indirect effect (precipitation efficiency), the data set provides 8 well documented cases, where the droplet sizes are close to the threshold for the onset of coalescence, with some cases producing significant precipitation and some void of drizzle drops.

3. THE PACE PROJECT

The second step towards parameterizations of the aerosol indirect effect in general circulation models (GCM) is to extrapolate the Cloudy-Column results to the GCM scale. This will be achieved within PACE (Parameterization of the Aerosol Climatic Effect), a project of the European Commission (2000-2001) with a contribution from US and Canada. Four experimental groups from ACE-2, Météo-France (F), Freie Univ. of Berlin (G), Univ. of Warsaw (PL) and Univ. of Wyoming (US), are involved in the analysis of the ACE-2 data set in order to document the physical processes, to identify the most relevant variables to use in a GCM, and to develop and validate improved parameterizations of the processes in co-ordination with five GCM modelling groups: MPI Hamburg (G), Hadley Centre (UK), Univ. of Dalhousie (CAN), NASA-GISS (US) and PNNL (US).

The methodology in PACE is to test various parameterisations of the aerosol/cloud/radiation interaction in single column versions (SCM) of the GCMs. Reference case studies will be selected from the Cloudy-Column data set, with pure marine, polluted and intermediate aerosol background. The SCMs will be initialised with extracted ECMWF meteorological fields.

Despite the ACE-2 efforts for synthesizing the in situ data, it is difficult to link the data set with SCM simulations. That link will be established with a LES non-hydrostatic model (horizontal resolution between *10* and *100 m*, over a simulation domain between *1x1 km* and *50x50 km*). During the first phase of PACE, the LES simulations will be validated versus the ACE-2 data set, with emphasis placed on vertical velocity statistics at cloud base, on the microphysical field, and on the cloud morphology. The validated 3-D simulations will then be used for a precise evaluation of the radiative bias with Monte-Carlo radiative transfer calculations. Finally, the simulations will be analysed to derive domain averaged values of the prognostic variables used in the SCMs and their relationship with the distribution of the local values for validation of the sub-grid parameterization schemes.

4. CONCLUSION

The aerosol indirect effect remains the most uncertain contribution in the evaluation of global change. In particular, the recent exercise of the IPCC reveals that the estimations of this contribution are doubled when the second indirect effect is accounted for, besides the first Twomey (1977) effect, as shown in GCM experiments by Lohmann and Feichter (1997) and Rotstayn (1999). The Cloudy-Column experiment in ACE-2 directly addressed this subject with a column closure methodology, based on multi-aircraft sampling of the aerosol properties, cloud microphysics and cloud radiative properties. These closure exercises confirm both the first and second indirect effects. They also reveal that pieces of the whole chain between the aerosols and radiation are still inaccurate. The most serious limitations to a precise closure are the aerosol properties, especially those associated with pollution derived from the continent, and the effects of horizontal cloud heterogeneity on radiative transfer. Both will be further examined with the Cloudy-Column data set.

Despite the remaining uncertainties, the Cloudy-Column data set is particularly suited for tests of GCM parameterisations because it covers a broad range of aerosol properties in cloudy fields that are otherwise very similar. This feature prevents biases in the interpretation that could be due to differences in the cloud types. The new PACE project provides an opportunity for experimentalists and modellers to join their efforts and expertises, and thus reduce the uncertainty in the estimation of the indirect effect of the aerosols on climate.

5. ACKNOWLEDGMENTS

The authors acknowledge the contributions of the ACE-2 participants, and the support of Météo-France and the European Union under grants ENV4-CT95-0117 (Cloudy-Column) and EVK2-CT-1999-00340 (PACE).

6. REFERENCES

Albrecht, B. A., 1989: Aerosols, cloud microphysics, and fractional cloudiness. *Science*, **245**, 1227-1230.

Brenguier, J. L., P. Y. Chuang, Y. Fouquart, D. W. Johnson, F. Parol, H. Pawlowska, J. Pelon, L. Schüller, F. Schröder and J. R. Snider, 2000-a; An overview of the ACE-2 CLOUDYCOLUMN Closure Experiment. *Tellus.* **52B,** 814-826.

Brenguier, J. L., H. Pawlowska, L. Schueller, R. Preusker, J. Fischer, and Y. Fouquart, 2000-b: Radiative properties of boundary layer clouds: droplet effective radius versus number concentration. *J. Atmos. Sci.* **57**, 803-821.

Chuang, P. Y., D. R. Collins, H. Pawlowska, J. R. Snider, H. H. Jonsson, J. L. Brenguier, R. C. Flagan, and J. H. Seinfeld, 2000: CCN Measurements during ACE-2 and their relationship to cloud microphysical properties. *Tellus.* **52B,** 842-866.

Guibert, S., J. R. Snider, and J. L. Brenguier, 2000: A closure experiment on the CCN activation process in ACE-2 Cloudy-Column. *Preprints 13th ICCP.*

Lohmann, U., and J. Feichter, 1997: Impact of sulfate aerosols on albedo and lifetime of clouds: A sensitivity study with the ECHAM GCM, *J. Geophys. Res.* **102,** 13,685-13,700.

Pawlowska, H. , and J. L. Brenguier, 2000-a: Microphysical properties of stratocumulus clouds during ACE-2. *Tellus.* **52B,** 867-886.

Pawlowska, H. , and J. L. Brenguier, 2000-b: The indirect effect of aerosols on climate: Effect of aerosol properties on precipitation efficiency. *Preprints 13th ICCP.*

Putaud, J. P., R. Van Dingenen, M. Mangoni, A. Virkkula, H. Maring, J. M. Prospero, E. Swietlicki, O. H. Berg, R. Hillamo, and T. Mäkelä, 2000: Chemical mass closure and assessment of the origin of the submicron aerosol in the marine boundary layer and the free troposphere at Tenerife during ACE-2. *Tellus.* **52B,** 141-168.

Raes, F., T. Bates, F. McGovern, and M. van Liedekerke, 2000: The second aerosol characterization experiment (ACE-2): General overview, and main results. *Tellus.* **52B,** 111-125.

Rotstayn, L. D., 1999: Indirect forcing by anthropogenic aerosols: A global climate model calculation of the effective radius and cloud lifetime effects, *J. Geophys. Res.*, **104**, 9369-9380.

Schüller, L., J. L. Brenguier, and H. Pawlowska, 2000: The indirect effect of aerosols on climate: Observations with an airborne radiometer. *Preprints 13th ICCP.*

Snider, J. R., and J. L. Brenguier, 2000: Cloud condensation nuclei and cloud droplet measurements during ACE-2. *Tellus.* **52B,** 827-841.

Twomey S., 1977: The influence of pollution on the shortwave albedo of clouds. J. Atmos. Sci., **34,** 1149-1152.

THE INDIRECT EFFECT OF AEROSOL ON CLIMATE: EFFECT OF AEROSOL PROPERTIES ON PRECIPITATION EFFICIENCY

H. Pawlowska[1], and J. L. Brenguier[2],

[1]University of Warsaw, Institute of Geophysics (Poland); [2]Météo-France, CNRM-GMEI (France)

1. INTRODUCTION

The basis of the aerosol indirect effect is a relationship between the cloud droplet number concentration (CDNC) and the light extinction in a cloud volume: at a fixed value of liquid water content (LWC), the extinction increases when CDNC increases. Twomey (1977) pointed out that anthropogenic changes of the aerosol physical and chemical properties (APP), and more precisely changes of a subset of the aerosols, referred to as cloud condensation nuclei (CCN), is potentially able to increase CDNC values in clouds, hence increasing light extinction, and modifying the radiative balance. Besides this effect, a CDNC increase results in smaller cloud droplets, that is in a lower efficiency of the droplet to drizzle conversion process (auto-conversion). Therefore, anthropogenic changes of APP are also likely to affect cloud life time and spatial extent (Albrecht, 1989). This process is now referred to as the second aerosol indirect effect, while the Twomey effect is referred to as the first indirect effect.

The aerosol indirect effect is presently the most uncertain process in the estimation of climate change. The recent IPCC exercise reveals that its contribution can be doubled when the second indirect effect is accounted for (Lohmann and Feichter (1997), Rotstayn (1999). It is thus crucial to improve our understanding of the sensitivity of the precipitation efficiency to CDNC. Rosenfeld (1999) showed evidence of rain inhibition by forest fires, but the impact of anthropogenic pollution on natural clouds has not yet been documented. CDNC modifications have little impact on deep clouds, which contribute the most to the global precipitation, because they are producing droplets much larger than the auto-conversion threshold, no matter what their droplet concentration is. The second indirect effect is in fact concerned with boundary layer clouds, because of their large contribution to the global energy balance, because they are directly exposed to anthropogenic pollution in the boundary layer, and because they have a limited vertical extent, so that the largest cloud droplets are close to the auto-conversion threshold, slightly above or below, depending on CDNC.

Corresponding author's address: Hanna Pawlowska, Institute of Geophysics, University of Warsaw, ul. Pasteura 7, 02-093 Warszawa, Poland; e-mail: hanna.pawlowska@meteo.fr

2. THEORETICAL BACKGROUND

The onset of precipitation is a non-linear process. During the initial phase of cloud development, cloud droplets are formed at cloud base from CCN activation and they grow by water vapour diffusion along their ascent. When a few droplets are reaching the auto-conversion threshold, close to cloud top, precipitation embryos are formed. The embryos are then falling into the cloud and collect numerous droplets to form precipitation. Droplet scavenging by drizzle particles results in a rapid depletion of CDNC and the cloud liquid water content is transferred to the drizzle content. This second phase, referred to as the coalescence phase, is no longer sensitive to CDNC. The susceptibility of precipitation efficiency to CDNC shall thus be assessed by investigating the early stage of the precipitation process, namely the formation of the primary precipitation embryos. The first challenge in the experimental study of the indirect effect is thus to identify cloud regions representative of droplet growth by vapour diffusion, that is regions which are not affected by drizzle scavenging or entrainment-mixing processes.

The largest droplet size in a cloud can be approximated by the adiabatic mean volume diameter d_v at cloud top:

$$d_v^3 = \frac{C_w}{(\pi/6)\rho_w} \frac{H}{N}, \qquad (1)$$

where C_w is the moist adiabatic condensation rate, ρ_w is the liquid water density, H is the cloud thickness, and N is the droplet number concentration (Brenguier et al. 2000-b). This formula expresses that a relative increase of N has the same effect as the same relative decrease of H. It is therefore difficult in the interpretation of observations to discriminate between the respective contributions of H and N to the observed changes of precipitation efficiency. The second challenge in the experimental study of the indirect effect is thus to collect a large sample of case studies with a large variability of CDNC and a reduced variability of cloud thickness. The Cloudy-Column experiment in ACE-2 provides such a data set, with 8 cases characterized by N values varying from *55* to *244* cm^{-3}, while the H values are limited to the range from *160* to *290 m*.

2. THE DATA SET

Cloudy-Column, one of the six projects in ACE-2 (Raes et al. 2000), was designed as a column closure experiment on the aerosol indirect effect (Brenguier et al. 2000-a). The sampling strategy was based on a multi-aircraft approach for measurements of aerosol properties in the boundary layer with the UK-C130 and the CIRPAS Pelican, measurements of cloud microphysical properties with the Météo-France Merlin-IV (M-IV), and remote sensing of cloud radiative properties with the DLR-Do228 and the ARAT-F27. Only the M-IV microphysical data are analysed here. They were collected with the Fast-FSSP (Brenguier et al. 1998) for the droplet size distribution in the diameter range *2.6 – 35 μm*, and a PMS-OAP-1DC for the drizzle size distribution in the diameter range *20 – 300 μm*.

The 8 Cloudy-Column cases discussed here are summarized in Table I, with the corresponding date and flight number. A very efficient sampling procedure based on series of ascents and descents through the cloud layer was applied in Cloudy-Column. At least 15 (F28 and F33), and up to 35 (F21), vertical profiles were performed by the M-IV. They are particularly suited for describing the statistical properties of the cloud layer and the vertical stratification of the microphysics.

3. DATA PROCESSING

The first step consists in the characterization of each case in term of a CDNC typical values. The procedure aims at selecting cloud samples that are not affected by mixing with the overlying dry air or drizzle scavenging. Such a value is supposed to reflect the influence of the APP during the CCN activation phase at cloud base.

The cumulated frequency distribution of the *10 Hz* (*10 m*) sampled values of CDNC is used to derive the value at *99 %* probability, which is referred to as N_{max}. The cumulated frequency distribution of the aircraft altitude above cloud base *h*, restricted to samples with $N>0.2\ Nmax$, is then calculated to derive the *h* value at *97 %* probability, which is referred to as H_{max}. Samples are then selected on the basis of the three following criteria (Pawlowska and Brenguier, 2000):

(i) $0.4 < h/H_{max} < 0.6$;
(ii) $LWC > 0.9\ LWC_{ad}$,
(iii) $N_{OAP} < 2\ cm^{-3}$,

where LWC_{ad} is the adiabatic LWC at *h*, and N_{OAP} is the drizzle concentration. The resulting frequency distribution is finally used to derive the mean CDNC value, which is further used as a reference for each case. The largest values of droplet mean volume diameter measured in the cloud layer with the Fast-FSSP are characterized by the value d_{vmax} selected at *97 %* of its cumulated frequency distribution. Finally drizzle concentration is characterized by the value at *95 %* of its cumulated frequency distribution and it is referred to as N_{OAPmax}.

The values of H_{max}, N_{mean}, d_{vmax}, and N_{OAPmax} are reported in Table I. The Cloudy-Column cases can be classified in three categories: F20 and 21 are characterized by a low N_{mean}, large droplets and a significant drizzle concentration. In contrast, F28, 30 and 34 show large values of CDNC, smaller droplet sizes and almost no drizzle. The three other flights, F31, 33, and 35, exhibit intermediate characteristics.

Date	Flight #	H_{max} m	N_{mean} cm^{-3}	d_{vmax} μm	N_{OAPmax} cm^{-3}
25 June	20	287	70	27.0	12.3
26 June	21	207	55	25.8	16.7
17 July	33	267	110	21.1	6.3
19 July	35	272	128	21.7	5.5
16 July	31	227	128	20.9	4.8
18 July	34	187	183	16.8	1.1
8 July	28	182	196	15.3	1.9
9 July	30	162	244	13.6	2.5

Table I: Summary of the 8 Cloudy-Column cases.

4. DRIZZLE SCAVENGING

The second step aims at evaluating the impact of precipitation at the scale of the whole cloud layer. N_{OAPmax} does not provide information about the drizzle particle sizes, which could be indicated by the mean diameter of the OAP distributions, but it is more interesting to look directly at the statistical impact of the drizzle particles on CDNC. Fig. 1 shows scatter plots of the local N_{OAP} values (*1 Hz* or *100 m* average) against the CDNC values measured with the Fast-FSSP (N_{ffssp}), after normalization by N_{mean}. The graphs are presented, from the upper left column to the lower right, in the same order as in Table I.

The two first flights show the same trend, with the largest values of drizzle concentration associated to the lowest normalized CDNC values at about *0.2*. This feature is typical of drizzle scavenging and it makes evident that the precipitation process is efficient in the cloud layer. In contrast, the scatter plots for the last three flights (18, 8 and 9 July) exhibit a rather different trend, with the largest values of drizzle concentration associated to normalized CDNC values close to *1*. This feature suggests that the particles counted by the OAP are large droplets, rather than drizzle particles, and that the precipitation process is not efficient at depleting CDNC. The three intermediate cases (17, 19, and 16 July show the same trend as in the two first graph, though the peak values of N_{OAP} are observed at normalized CDNC values of the order of *0.5* and larger. Drizzle scavenging is thus active but not able to deplete efficiently the droplets that are continuously produced in the cloud layer.

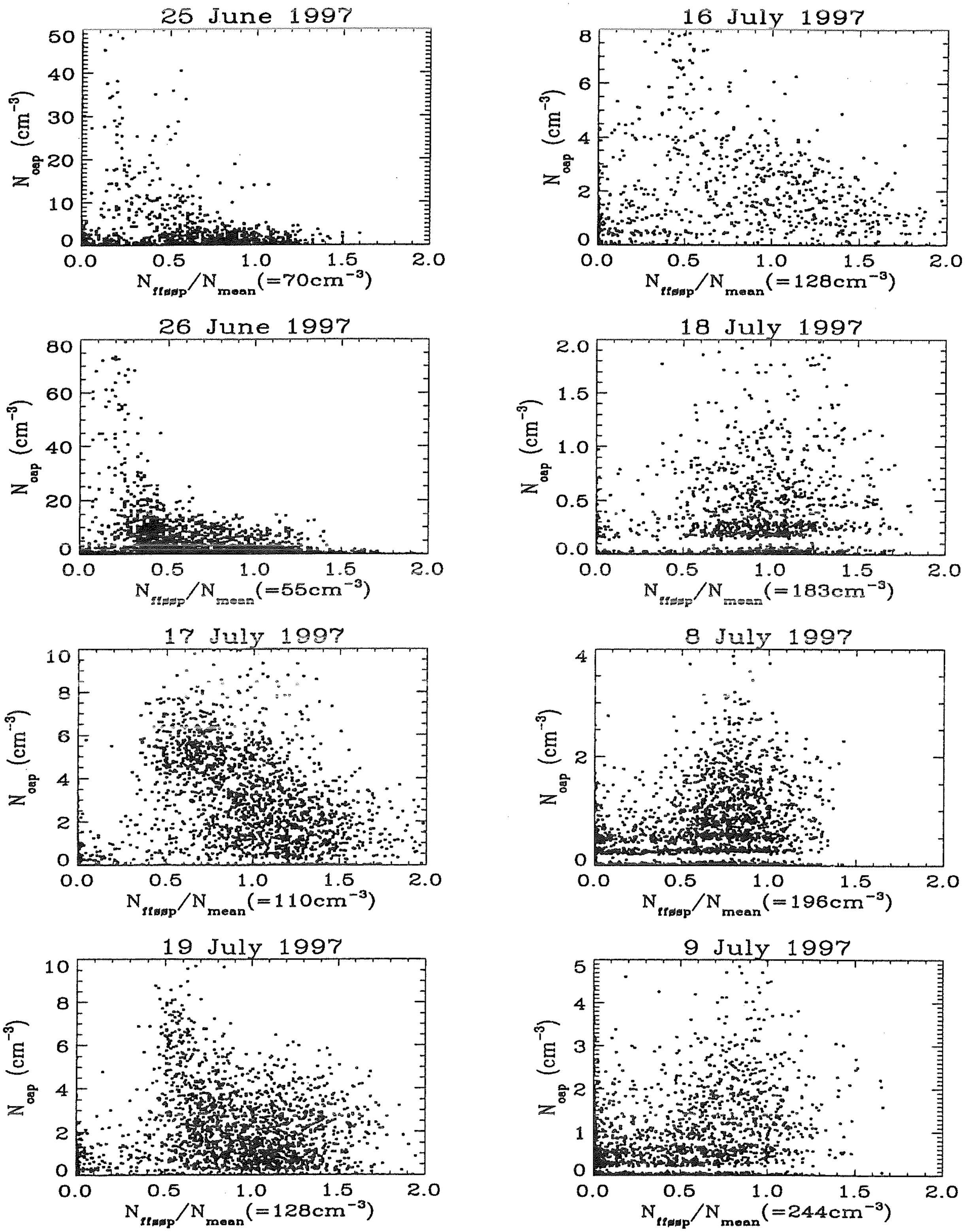

Fig. 1: Scatter plots of drizzle concentration (N_{OAP}) against normalised droplet concentration (N_{ffssp}/N_{mean}) for the 8 cases. Notice the different scales for N_{OAP}.

5. THE AUTOCONVERSION THRESHOLD

The results of the Cloudy-Column closure experiment are now used for the validation of climate model parameterisations within the PACE (Parameterization of the Aerosol Indirect Effect) project. Parameterizations of the precipitation process in boundary layer clouds are dependent upon the value of the auto-conversion threshold. This value is used to compare with a diagnostic of the largest droplets produced in a cloud layer for deriving a rate of drizzle production from the cloud liquid water content. Present values of that threshold are derived from numerical simulations of the auto-conversion process, but data collected in actual clouds are also needed. The 8 Cloudy-Column cases shown here provide a remarkable set for such a validation. Fig. 2 shows the N_{OAPmax} values of Table I, versus the maximum droplet mean volume diameter d_{vmax}. The d_{vmax} value of Table I derived from Fast-FSSP measurements is designated by arrows. A second characterization is obtained with the adiabatic value at cloud top, which is derived from (1) with $N=N_{mean}$ and $H=H_{max}$. It is represented by different symbols for each case.

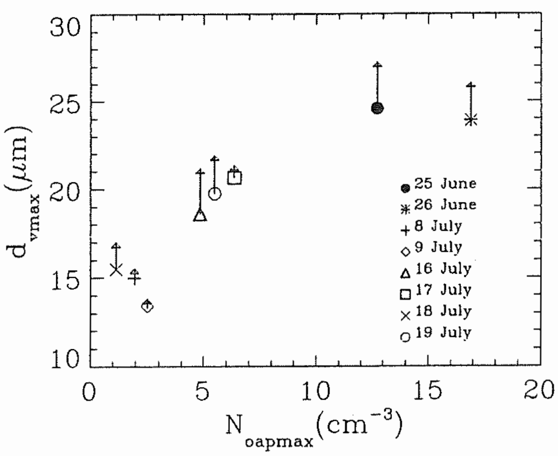

Fig. 2: Maximum value of drizzle concentration N_{OAP}, versus the maximum mean volume diameter d_{vmax}, for each case. (See text for symbols).

It can be noted first that the adiabatic value at cloud top for $N=N_{mean}$ is slightly smaller (by *3 µm* at the most) than the value at *97 %* of the measured d_v frequency distribution. Fig. 5 in Pawlowska and Brenguier, 2000 shows that the largest d_v values correspond in fact to the adiabatic prediction with N smaller than N_{mean}, because of the natural CDNC variability in the cloud layer.

Fig. 2 reveals that droplets with diameters of about *15 µm* (the three polluted cases) are not acting as precipitation embryos, while droplets of the order of *25 µm* (the two marine cases) are efficient. The three intermediate cases are characterized by peak values of the mean volume diameter of about *20 µm*, and it has been shown with Fig. 1 that there is no significant drizzle production on these days. Therefore, this *20 µm* value seems to be a good estimate of the auto-conversion threshold.

These data will be further analysed for the calculation of the cloud water to drizzle water conversion rates that are needed for validation of the general circulation models.

6. ACKNOWLEDGMENTS

The authors acknowledge the contributions of the ACE-2 participants, and the support of Météo-France and the European Union under grants ENV4-CT95-0117 (Cloudy-Column) and EVK2-CT-1999-00340 (PACE).

7. REFERENCES

Albrecht, B. A., 1989: Aerosols, cloud microphysics, and fractional cloudiness. *Science*, **245**, 1227-1230.

Brenguier, J.L., T. Bourrianne, A. Coelho, J. Isbert, R. Peytavi, D. Trevarin, and P. Wechsler, 1998: Improvements of the droplet size distribution measurements with the Fast FSSP, *J. Atmos. Oceanic Technol.*, **15**, 1077-1090.

Brenguier, J. L., P. Y. Chuang, Y. Fouquart, D. W. Johnson, F. Parol, H. Pawlowska, J. Pelon, L. Schüller, F. Schröder and J. R. Snider, 2000-a; An overview of the ACE-2 CLOUDYCOLUMN Closure Experiment. *Tellus.* **52B**, 814-826.

Brenguier, J. L., H. Pawlowska, L. Schueller, R. Preusker, J. Fischer, and Y. Fouquart, 2000-b: Radiative properties of boundary layer clouds: droplet effective radius versus number concentration. *J. Atmos. Sci.* **57**, 803-821.

Lohmann, U., and J. Feichter, 1997: Impact of sulfate aerosols on albedo and lifetime of clouds: A sensitivity study with the ECHAM GCM, *J. Geophys. Res.* **102,** 13,685-13,700.

Pawlowska, H. , and J. L. Brenguier, 2000: Microphysical properties of stratocumulus clouds during ACE-2. *Tellus.* **52B**, 867-886.

Raes, F., T. Bates, F. McGovern, and M. van Liedekerke, 2000: The second aerosol characterization experiment (ACE-2): General overview, and main results. *Tellus.* **52B,** 111-125.

Rosenfeld, D., 1999: TRMM observed first direct evidence of smoke from forest fires inhibiting rainfall. *Geophys. Res. Letter*, **26**, 3105-3108.

Rotstayn, L. D., 1999: Indirect forcing by anthropogenic aerosols: A global climate model calculation of the effective radius and cloud lifetime effects, *J. Geophys. Res.*, **104**, 9369-9380,.

Twomey S., 1977: The influence of pollution on the shortwave albedo of clouds. J. Atmos. Sci., **34**, 1149-1152.

AEROSOLS, CLOUDS, AND CLIMATE OF THE SOUTHEASTERN U.S.

V.K. Saxena[1], B.N. Wenny[1], S. Menon[2], and S.-C. Yu[3]

[1]Department of Marine, Earth and Atmospheric Sciences, North Carolina State University, Raleigh, NC 27695
[2]NASA GISS/Columbia University, New York, NY 10025
[3]Nicholas School of the Environment, Duke University, Durham, NC 27708

1. INTRODUCTION

Anthropogenic aerosols perturb the atmospheric radiation field through direct and indirect interactions with solar radiation, thereby influencing the climate. Through the direct effect, aerosols can scatter and absorb solar radiation in cloud-free air (Charlson et al., 1992). In terms of the indirect effect, aerosols composed of soluble substances such as sulfates can act as cloud condensation nuclei (CCN). Increases in CCN concentrations increase cloud droplet number (N), thereby reducing cloud droplet size, assuming the liquid water content (LWC) stays the same. This enhances cloud albedo and can also act to suppress drizzle production, which then increases fractional cloudiness and cloud lifetime (Twomey, 1977; Albretch, 1989). To investigate the climatic impact of anthropogenic aerosols in the southeastern U.S., the direct and indirect effects of aerosols (primarily sulfates and to a lesser extent black carbon (BC)) were investigated using surface measurements, modeling results and remotely sensed satellite measurements. Since the observational site intercepts relatively clean marine and highly polluted urban industrial air masses, it offers unusual and unique opportunities to observe the impact of the air mass content on the microphysical and optical properties of the ensuing clouds.

2. EXPERIMENTAL SITE AND INSTRUMENTATION

The research site is a mountain top station located on the peak of Mt. Gibbes (35.78^0 N, 82.29^0 W, 2006 m MSL), in the Blue Ridge Mountains of western North Carolina (Bahrmann and Saxena, 1998). Measurements of aerosol and cloud physico-chemical properties have been collected during intensive field campaigns dating back to 1986. The instruments include active and passive cloud water collectors, and a PMS Forward Scattering Spectrometer Probe. The ion concentrations (Na^+, K^+, Ca^{2+}, Mg^{2+}, NH_4^+, Cu^{2+}, Zn^{2+}, Fe^{3+}, Al^{3+}, NO_3^-, Cl^-, SO_4^{2+}) in the cloud water were measured by Ion Chromatography (IC). All measurements of CCN activation spectrum reported in this paper were obtained with the CCN Spectrometer (Fukuta and Saxena, 1979). Real-time, continuous measurements of BC mass concentration were made by a commercial instrument named the Aethalometer (Hansen et al., 1996), manufactured by Magee Scientific. The sources of the cloud forming air masses were analyzed from their back trajectories obtained from the HY-SPLIT model (Draxler, 1987). The continental U.S. is divided into three sectors: (1) the PC sector located between 290° and 65° azimuth relative to Mt. Gibbes that is influenced by highly polluted air from the Ohio valley region, (2) the C sector between 210° and 290° that is influenced by relatively clean continental air from the great plains and (3) the marine (M) sector between 65° and 210° that is influenced by clean maritime air from the ocean. This classification is based on the SO_x and NO_x emission inventory (Ulman and Saxena, 1997) from the U.S. Environmental Protection Agency. However, the marine air masses must traverse over some land before reaching the site, and hence is a modified marine air mass.

Corresponding author's address: V.K. Saxena, Dept. of MEAS, N.C. State University, Raleigh, NC 27695-8208; email: saxena@eos.ncsu.edu

3. RESULTS AND DISCUSSION

3.1. Sector Classification of Aerosol Properties

The chemical characteristics of polluted continental (PC), continental (C), and marine (M) air masses were studied by applying principal component analysis to the cloud water collected during field studies at the field research site. It was found that acids, particularly sulfuric acid, were most abundant in clouds formed in polluted continental air masses. The majority of marine cloud events were characterized by the presence of sea-salt particles. Continental air masses were abundant in Ca^{2+} ions (Deininger and Saxena, 1997).

The role of BC aerosols on cloud microphysical/optical properties was investigated. The average BC mass concentrations for each sector was determined to be 65.6 ± 23.5 ng m^{-3} for M, 169.9 ± 50.6 ng m^{-3} for C, and 216.6 ± 47.8 ng m^{-3} for PC sectors. These results compare well with those obtained by Chylek et al. (1996) in southern Nova Scotia and those found at Mace Head, Ireland by Jennings et al. (1993). Average values of transatlantic BC transport to Mace Head ranged from 7 to 21 ng m^{-3}. The average BC data collected at Mt. Gibbes for M air was 62 ng m^{-3}. The higher value can be expected for Mt. Gibbes because the marine air may have been modified by traversing over land before reaching the site.

Concurrent measurements of CCN and BC mass concentration indicated a positive correlation. This suggests that a percentage of the BC measured may exist in the form of an internal mixture. Incorporation of BC into cloud droplets ranged from 0-70% of the total BC measured in cloud for 11 cloud events that had coincident measurements. On average, the BC incorporated into cloud ranged from 2-30%. The BC mixing ratio (BCMR), a parameter used to model the effect of BC on cloud albedo, was also calculated from the BC incorporated into cloud droplets and the LWC of the cloud. From the 11 cloud events sampled the BCMR ranged from 20-250 μg kg^{-1}, this range of values is too low to significantly affect cloud albedo (Chylek et al., 1984). An estimate of the reduction of direct forcing due to sulfate aerosols is obtained from the BC/SO_4 mass ratio. The BC/SO_4 mass ratios obtained for the 1996 field season ranged from 0.01-0.09 with an average of 0.03. This average will lead to only a slight reduction in the cooling due to sulfates (Haywood and Shine, 1995).

3.2 Evidence of Aerosol Forcing in Surface Temperature Records

The arithmetic average of annual mean daily temperature for 47 stations in the Southeast has decreased by -0.09 C during the past 46 years. There was a slight cooling trend in the Southeast during the past 46 years. The aerosol loading injected by large volcanic eruptions such as due to Mt. Pinatubo on June 15, 1991 was analyzed to provide a validation of aerosol radiative forcing. The three-year mean optical depth at 0.453 μm due to volcanic aerosol mass loading in the Southeast for the periods 1985-87, 1988-90 and 1992-94 was 0.012, 0.006, and 0.037 respectively. We have used the period 1988-90 as representing the background stratospheric aerosol. As expected from the aerosol shortwave forcing, the arithmetic average annual maximum temperature of the period 1992-1994 and the period 1985-1987 for 47 stations in the Southeast US had decreased by -0.57 C and -0.09 C, respectively, when compared to that of the period 1988-1990. However, the three-year annual mean minimum temperature for the periods 1992-94 and 1985-87 increased at 80.9% stations in the Southeast when compared to that of period 1988-90. The arithmetic average annual minimum temperature of the periods 1992-1994 and 1985-1987 for 47 stations in the Southeast US had increased by 0.19 C and 0.32 C, respectively, when compared to that of the period 1988-1990. These results are consistent with the expected shortwave and longwave radiative forcing due to aerosols. According to theoretical analysis, diurnal temperature range (DTR), which is defined as the difference between the maximum and minimum temperature, will decrease as the aerosol radiative forcing increases because of the decrease of maximum temperature and the increase of minimum temperature. It was found that there were dominant decreasing trends of mean DTR for annual and all seasons over the periods 1985-87 and 1992-94 compared to that of the period 1988-90. The aerosol forcing can have effect on the daily temperature and precipitation depending on the season and regional environment.

3.3. Cloud-Climate Interactions

Time series observations of sulfate concentrations in cloud water since 1986 indicate higher sulfate concentrations for 1993-97 as compared to that during 1986-89, as seen in Figure 1. The calculated increase in cloud albedo from changes in CCN and N in cleaner to polluted air masses was higher for the Southeast as compared to the Northeast. Varying levels of sulfate in polluted and marine air masses, lead to changes in R_{eff} that are of sufficient magnitude to counteract warming expected due to doubling of CO_2. Higher sensitivity of N to sulfate content is obtained for the southeastern U.S. as compared to that for eastern North America and Puerto Rico. The indirect forcing effect due to sulfates for the Southeast is of higher magnitude than the –4.0 W m^{-2} estimated by modeling studies. A continual increase in cloud albedo with an increase in cloud water sulfate was not found (both from satellite retrievals and calculations from in situ measurements). Variations in N and R_{eff} with varying sulfate content as well as in dynamical properties such as liquid water content (LWC) and cloud thickness were found to be important in determining variations in cloud reflectivity. Vertical variations in LWC, N and R_{eff} must also be considered. An internal mix of BC and sulfate reduces the sulfate forcing by ~1.12 W m^{-2} for summertime BC and sulfate concentrations. However, despite this reduction, the combination of both direct (average ~ –4.8 W m^{-2}) and indirect (of greater magnitude than –4.0 W m^{-2}) summertime radiative forcing for the sulfate aerosols for the past four years (1993-96) suggest (Saxena and Menon, 1999) that anthropogenic influences could balance any warming expected from the doubling of CO_2 for the southeastern U.S.

Comparison of cloud albedos calculated from in situ measurements was performed with cloud albedos inferred from the AVHRR data for cases that coincided with in situ observations. The AVHRR data retrieved from the NOAA -11, NOAA-12, and NOAA-14 satellites provide visible and near infrared radiances from which cloud albedo is inferred. The raw visible counts are scaled by the solar zenith angle and an anisotropic low (water) cloud reflectance factor is applied to determine the visible albedo. The same procedures and measurement criteria have been used to determine cloud albedo from satellite data as is given in Saxena et al. (1996). All convective type clouds were excluded from the analyses to avoid errors associated with inhomogeneous vertical stratification (Nakajima and King 1990). Only warm orographic stratiform clouds formed in the vicinity of the Mt. Gibbes site were included. Five cases were utilized from the 1993-94 field season and four cases from the 1995 field season. A large number of cases for comparison of cloud albedos are difficult to obtain since a variety of conditions need to be fulfilled, e.g. non–precipitating cloud events, variable sulfate content in the cloud forming air mass, cloud thickness less than 300 m, coincidence of satellite passage with sampling period, etc. The conditions imposed for comparison as well as the five cases from the 1993-94 field season are discussed in detail in Saxena et al. (1996). The relation between satellite inferred cloud albedo and that calculated from in situ measurements is indicated in Fig. 2. The correlation coefficient is about 0.90 for the nine cases and the 95% confidence interval for the correlation coefficient is between 0.58 to 0.98. Some uncertainty in determining cloud albedo from in situ measurements can be expected since vertical variations in R_{eff} and LWC within cloud depth were not determined and satellite inferred albedo is usually dependent on cloud top values. Also, satellite data is obtained for a particular time period whereas in situ measurements are averaged for the whole hour, which might lead to some discrepancy especially for cases where the cloud properties fluctuate during a particular hour. An agreement between the two data sets is however useful since this would lead to confidence in using estimates of cloud albedo calculated from in situ measurements.

The climatic impact of the CCN-cloud albedo interaction has been recently debated although a number of issues concerning this process still remain uncertain. It has been suggested that CCN potentially play an effective role in climate-regulation (i.e. counteracting the greenhouse warming due to CO_2 etc.), and an increase in CCN number concentration, by as much as a factor of four, would cause an global albedo increase of ~1.7%. To look for possible evidence of such a CCN enhancement, we investigated measurements of episodes of enhanced CCN concentrations near cloud boundaries around the world. The analyzed data include (1) airborne measurements made in St. Louis, over the California coast, off the coasts of Nova Scotia and Newfoundland, over Lake Michigan, over Bay of Bengal, and at Boulder of Colorado; (2) polar measurements, both from the Antarctic (off the coast, near the Ross sea and at Palmer Station) and the Arctic (over the Alaska sector (Barrow)); and (3) ground base measurements made at Mt. Gibbes, North Carolina. In light of these observations, the possible mechanisms and atmospheric conditions favorable for CCN enhancements are analyzed. Our results show that the evidence for CCN enhancement near and within clouds is substantial and definitive, however, these processes can only occur under special atmospheric conditions. This implies that such a CCN enhancement could have local and regional impact rather global impact on indirect aerosol forcing.

Although it is believed that organic aerosols play a key role in cloud nucleation and make an important contribution to cloud condensation nuclei (CCN) population, their specific species remain poorly characterized. We find evidence that strongly suggests that organic acids (mainly formic, acetic, pyruvic and oxalic acids) are at least one of the primary sources of CCN in the troposphere due to their ubiquitous presence, physical-chemical properties and sources in the troposphere, especially over the continental forested areas. We have analyzed the extent to which organic acids act as CCN, and compared the physical and chemical properties of organic acids with those of CCN. The results show that aerosol formate and acetate concentrations range from 0.02 to 5.3 nmol/m^3 and from 0.03 to 12.4 nmol/m^3 respectively, and that between 34 to 77% of formate and between 21 to 66% of acetate are present in the fine fraction of aerosols. It is found that although most (98-99%) of these volatile organic acids are present in the gas phase, their concentrations in the aerosol particles are sufficient to make themselves a good candidate for CCN. The results also show that organic acids may make an important contribution to the formation of CCN in some special sources such as vegetation emissions and biomass-burning. Organic acids are expected to contribute significantly to the estimates of indirect (cloud-mediated) forcing due to aerosols.

Sulfate production in clouds is a critical component of the global sulfur cycle. Traditionally, bulk water measurements of cloud water acidity have been used to estimate sulfate production within clouds. While it is easy and convenient to use bulk water measurements to infer in-cloud sulfate production rates, it tends to mask chemical differences between droplets of different sizes, and also between droplets of the same size. Both models, and limited experimental data, suggest that cloud droplet populations are chemically heterogeneous. Investigation of the pH variations between large and small cloud droplets at the Mt. Gibbes site indicated that smaller droplets are often, but not always, more acidic than larger droplets. On an average, smaller drops were more enriched (Menon et al., 2000) in SO_4^{2-}, NO_3^-, NH_4^+ and H^+; whereas larger droplets had higher values of Na^+, Ca^{2+}, Mg^{2+} supporting the findings of Munger et al. (1989). Smaller droplets were usually more acidic than the larger droplets for both marine and polluted air masses, whereas, for continental air masses no such inference could be drawn. Cloud forming air masses from the polluted continental sector had the highest sulfate content for both larger and smaller drops, whereas those from the marine sector had the highest sodium content in the larger drops.

4. CONCLUDING REMARKS

Observations at a remote mountain-top site have been analyzed to investigate aerosol-cloud-climate interactions in the context of the climate change debate. The southeastern U.S. has been identified as a region where the direct and cloud mediated effects of anthropogenic aerosols have been found by modeling studies to counteract the warming due to anthropogenically enhanced greenhouse gases and result in a net regional cooling. The evidence obtained from our field site supports this conclusion of regional cooling in the southeastern U.S.

5. ACKNOWLEDGEMENTS

This research was supported by NASA's Mission to Planet Earth (MTPE) under Contract #NAS1-18944 from Langley Research Center, Hampton, VA and U.S. EPA's STAR grant #R-825248.

6. REFERENCES

Albretch, B.A., Aerosols, cloud microphysics and fractional cloudiness, *Science*, 245, 1227-1230, 1989.

Bahrmann, C.P., and V.K. Saxena, The influence of air mass history on black carbon concentrations in the southeastern U.S., *J. Geophys. Res.,* 103, 23153-23161, 1998.

Charlson, R.J., S.E. Schwartz, J.M. Hales, R.D. Hess, J.A. Coakley, J.E. Hansen, and D.J. Hofmann, Climate forcing by anthropogenic aerosols, *Science,* 255, 423-430, 1992.

Chylek, P., G. Videen, D. Ngo, R.G. Pinnick, and J.D. Klett, Effect of black carbon on the optical properties and climate forcing of sulfate aerosols, *Science,* 255, 423-430, 1995.

Chylek, P., V. Ramaswamy, and R.J. Cheng, Effect of graphitic carbon on the albedo of clouds, *J. Atmos. Sci.,* 41, 3076-3084, 1984.

Deininger, C.K. and V.K. Saxena, A validation of back trajectories of air masses by principal component analysis of ion concentrations in cloud water, *Atmos. Environ.,* 30, 295-300, 1997.

Draxler, R.R., Hybrid single-particle lagrangian integrated trajectories (HY-SPLIT): Version 3.0 - user's guide and model description, *NOAA Technical Memo ERL ARL-195,* Air Resources Laboratory, Silver Spring, MD, 1992.

Fukuta, N., and V.K. Saxena, A horizontal thermal gradient cloud condensation nucleus spectrometer, *J. Appl. Meteorol.,* 18, 1352-1362, 1979.

Hansen, A.D.A., Magee Scientific Aethalometer user's guide, Magee Scientific Company, Berkeley, CA, 56 pp., 1996.

Haywood, J.M., and K.P. Shine, The effect of anthropogenic sulfate and soot aerosol on the clear sky planetary radiation budget, *Geophys. Res. Lett.,* 22, 603-606, 1995.

Jennings, S.G., F.M. McGovern, and W.F. Cooke, Carbon mass concentration measurements at Mace Head, on the west coast of Ireland, *Atmos. Environ.,* 27(A), 1229-1239, 1993.

Menon, S., V.K. Saxena, and B.D. Logie, Chemical heterogeneity across cloud droplet size spectra in continental and marine air masses, *J. Appl. Meteor.,* in press, 2000.

Nakajima, T., and M.D. King, determination of the optical thickness and effective particle radius of clouds from reflected solar radiation measurements. Part I: Theory, *J. Atmos. Sci.,* 47, 1878-1893, 1990.

Saxena, V.K., and S. Menon, Sulfate-induced cooling in the southeastern U.S.: An observational assessment, *Geophys. Res. Lett.,* 26, 2489-2492, 1999.

Saxena, V.K., P.A. Durkee, S. Menon, J.Anderson, K.L. Burns and K.E. Nielsen, Physico-chemical measurements to investigate regional cloud-climate feedback mechanisms, *Atmos. Environ.,* 30, 1573-1579, 1996.

Twomey, S., The influence of pollution on the shortwave albedo of clouds, *J. Atmos. Sci.,* 34, 1149-1152, 1977.

Ulman, J.C., and V.K. Saxena, Impact of air mass histories on the chemical climate of Mount Mitchell North Carolina, *J. Geophys. Res.,* 102, 25451-25465. 1997.

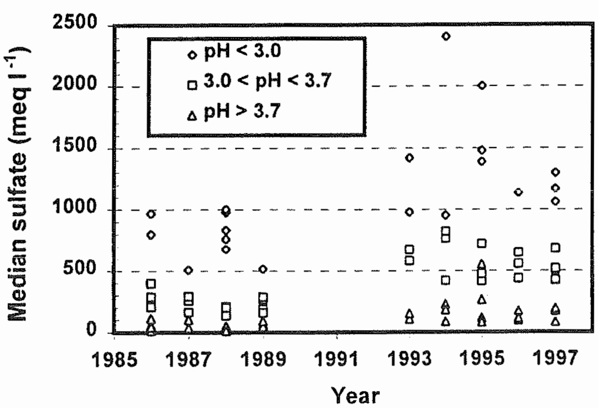

Figure 1. The trend in median values of sulfate for May-August. The data are categorized in terms of cloud water pH. pH < 3.0 represent polluted continental clouds, 3.0 < pH < 3.7 continental clouds and pH > 3.7 marine clouds (Saxena and Menon, 1999).

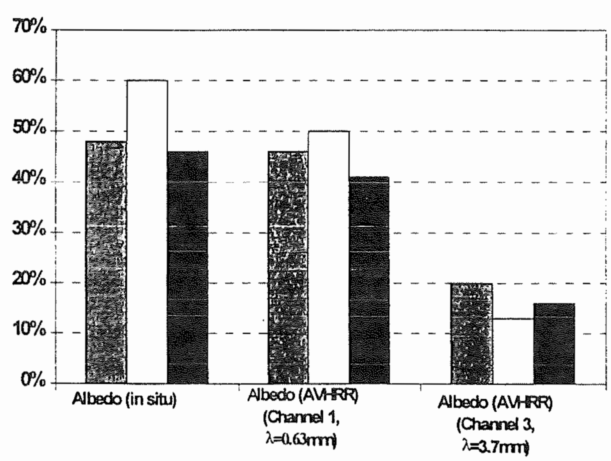

Figure 2. Average values of cloud albedo calculated from in-situ observations and that retrieved from the Advanced Very High Resolution Radiometer (AVHRR) data for two channels for the same three pH categories as Figure 1, left column: pH < 3.0, center column: 3.0 < pH < 3.7, right column: pH > 3.7 (Saxena and Menon, 1999).

LABORATORY STUDIES OF AEROSOL EFFECTS ON ICE FORMATION IN CIRRUS CLOUDS

Paul J. DeMott, Sonia M. Kreidenweis, David C. Rogers, Yalei Chen and D. Eli Sherman

Department of Atmospheric Science, Colorado State University, Ft. Collins, CO

1. INTRODUCTION

The formative conditions, concentrations and sizes of ice particles are important factors determining the radiative properties of highly supercooled clouds in the troposphere (e.g., Baker, 1997). Water uptake and subsequent freezing of aerosols that are wholly or partially composed of sulfate aerosols are thought to be responsible for ice formation in cirrus clouds. The presence of insoluble components in such aerosols may favor heterogeneous nucleation and formation of different ice crystal populations. While evidence exists for the action of both processes in the atmosphere (e.g., DeMott et al., 1998), many uncertainties remain regarding ice nucleation by aerosol particles.

The conditions leading to ice formation by different pure sulfate aerosols and others that have been altered to include an insoluble component are reported in this paper. Continuing specific objectives are to:

1) validate theoretical understanding of ice formation by homogeneous and heterogeneous freezing,
2) determine if sulfate chemical composition and particle size matter in determining the conditions for ice formation at temperatures below -40°C,
3) determine if associating certain insoluble components with mixed sulfate particles causes ice nucleation more readily for cirrus conditions,
4) determine if surrogate aircraft exhaust soot particles serve as nuclei for cirrus cloud formation,
5) determine the effects of various categories of organic aerosol constituents on homogeneous and heterogeneous ice nucleation processes,
6) Examine the implications of aerosol effects and other factors on cirrus cloud properties via numerical modeling studies.

2. EXPERIMENTAL METHODS

Ice nucleation studies are being conducted using a continuous flow ice-thermal diffusion (CFD) chamber. Details are given in Chen et al. (2000) and Rogers et al. (2000). The intent of the method is to expose a stream of aerosol particles to constant temperature and moisture conditions for a known time. Hydration, nucleation and growth processes have to occur within the residence time to detect ice crystals as product. Ice crystals are discriminated from aerosol and liquid particles by size, due to their high growth rates.

Corresponding author address: Paul J. DeMott, Colorado State University, Department of Atmospheric Science, Ft. Collins, CO 80523-1371; Email: pdemott@lamar.colostate.edu

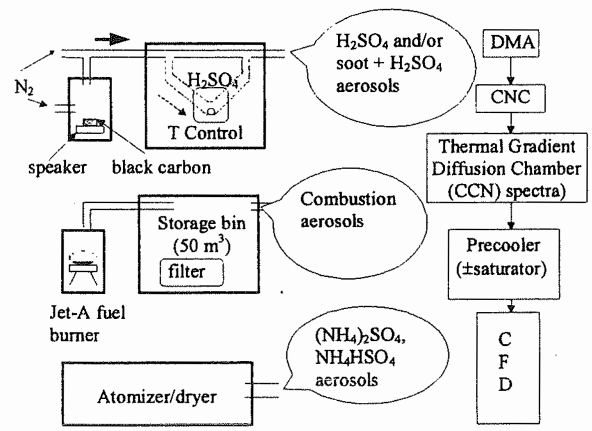

Figure 1. Schematic diagram of aerosol generation and experimental design. See text for description.

In the CFD chamber, aerosols are directed vertically downward between particle free sheath flows and in the annular space between two ice-coated cylinders. The temperatures of the ice walls, which are force-cooled, determine sample temperature and humidity. It is possible to expose aerosol particles to a wide range of constant conditions, from -10 to -65°C and from ice saturation to approximately 10% water supersaturation. Measurement of liquid and ice particle sizes at the outlet of the chamber is done optically.

Aerosol generation systems are shown in Figure 1. Two systems were used to generate soluble aerosol particles. Ammonium sulfate and ammonium bisulfate aerosols were continuously generated by atomization of solutions and drying. Sulfuric acid particles were produced by passing purified nitrogen gas over a small heated sample of H_2SO_4, which led to high supersaturations and particle nucleation upon cooling. Size classification was done with a differential mobility analyzer (DMA). The sizes most often selected were 0.05 μm for H_2SO_4 and 0.2 μm for the sulfates. Particle concentrations in the sample stream were continuously monitored using a condensation particle counter (CNC) and were maintained between 10 and 500 cm^{-3}. The final water relative humidity (RH_w) of the particle stream was controlled to be < 2% at room temperature.

Two types of carbon-containing mixed particles have been generated thus far. The system for generation of black carbon /H_2SO_4 particles has been described by DeMott et al. (1999). It utilizes a speaker to agitate commercial black carbon powders and the H_2SO_4 generator to coat particles with varying amounts of solute. These soot particles could only be generated as polydisperse distributions. High concentrations of soot particles were produced by high-temperature (~1500°C) combustion of jet fuel (jet fuel A with PRIST additive) using a camp stove (MSR Model 31160, Seattle, WA, USA). These particles were generated by short duration "bursts" into an isolated holding bin that had been pre-filtered to remove ambient particles. Particles at a size of 0.05 μm were selected from the holding bin (1 liter min^{-1} flow rate) with a DMA. This size was considered representative of soot particles generated in the upper troposphere by jet aircraft.

Particles were sometimes sampled by a cloud condensation nucleus (CCN) counter (thermal gradient diffusion chamber) operated at room temperature. This device was used to validate soluble particle sizes and estimate the soluble content of mixed particles (DeMott et al., 1999). Before the CFD chamber, particles entered an optional saturator, used to humidify particles above their deliquescence RH_w (at 20°C), and a tube cooled to approximately -25°C. The purpose of the pre-conditioner was to permit studies of initially crystalline versus initially liquid aerosols. The CFD chamber was operated at 840 hPa for reported studies. Typical particle residence times were 10 to 15 s.

3. EXPERIMENTAL RESULTS

Selected experimental results are presented in Figures 2 to 5. Figure 2 shows data on the freezing temperature and calculated composition of small H_2SO_4/H_2O particles. Original data are given as a function of RH_w in Chen et al. (2000). Composition was estimated considering that particles were approximately at their Köhler equilibrium sizes. Nominal uncertainties are ± 1°C and ± 2 weight %. An interesting feature in Fig. 2 is that the degree of supercooling required for freezing increases with H_2SO_4 weight percent. This was also found for liquid sulfate aerosol particles. Furthermore, as discussed by Chen et al. (2000) and DeMott et al. (2000), this increase in supercooling is nearly proportional to the melting point depression (absolute value of the ice/liquid equilibrium line below 0°C in Fig. 2). That is, the "homogeneous freezing temperature" of same sized solution droplets ($T_{hf(solution)}$) and pure water drops ($T_{hf(water)}$) appear related by ,

$$T_{hf(solution)} = T_{hf(water)} - \lambda \Delta T_m, \qquad (1)$$

where ΔT_m is the depression of the melting point and λ is a constant. Since the data points in Fig. 1 represent different sizes of particles as they adjusted to the CFD chamber humidity, Chen et al. (2000) followed Sassen and Dodd (1988) in assuming that an effective freezing temperature (T_{eff}) may also be defined as,

$$T_{eff} = T + \lambda \Delta T_m, \qquad (2)$$

where T is droplet temperature. Then the nucleated fraction (F) is related to droplet volume (V_d), residence time (Δt) and the well characterized homogeneous freezing rate of pure water ($J_{hf}(T)$) by,

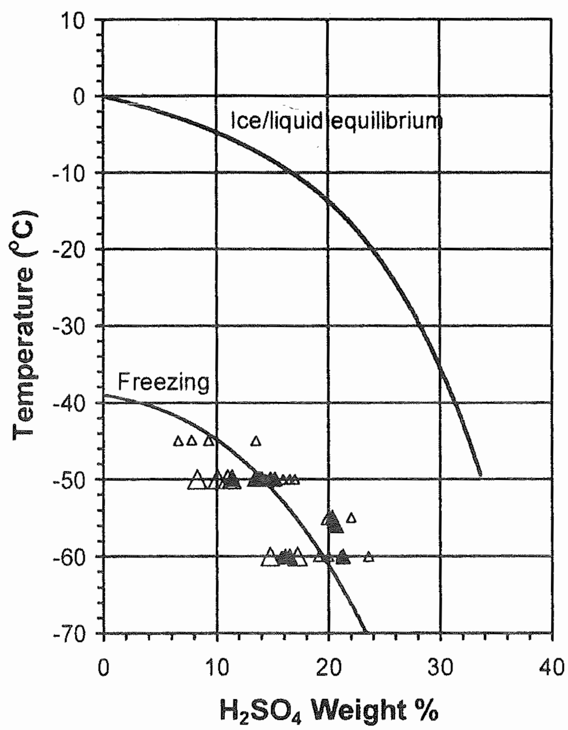

Figure 2. Experimental data on homogeneous freezing superimposed on thermodynamic phase diagram relating sulfuric acid temperature and weight percent composition. Data on the temperature for 0.1 (small triangles), 1 (medium triangles) and 10% (large triangles) particle fractions freezing (in 12±2 s) versus RH_w (Chen et al., 2000) are converted here to H_2SO_4 compositions (see text). The "Freezing" line is not a thermodynamic line in the sense of the ice/liquid equilibrium line, but is fit to the 1% activation data. This line is intended only to indicate the trend toward deeper supercooling at higher weight % composition.

$$F = 1 - \exp[-J_{hf}(T_{eff}) V_d \Delta t] \qquad (3)$$

Expressions (2), (3) and the Köhler equation were used (Chen et al., 2000) to evaluate λ from the experimental data. Average λ (for all fractions nucleating) for H_2SO_4, $(NH_4)_2SO_4$, and NH_4HSO_4 solutions were determined as 1.98±0.27, 1.73±0.35 and 1.38±0.34, respectively. These values in (1), along with specifications of water activities (Clegg et al., 1998), lead to the ice relative humidity (RH_{ice}) versus temperature relations for freezing shown in Fig. 3. In the absence of Kelvin effects, there are only small differences in freezing conditions induced by changes in degree of sulfate ammoniation. RH_{ice} required to freeze small solution drops will always exceed that shown in Fig. 3 because higher volume nucleation rates are necessary and because RH_w exceeds water activity.

Equations (2) to (3) have been used to model homogeneous freezing in numerical simulations of cirrus clouds (e.g., Lin et al., 2000). It is assumed that

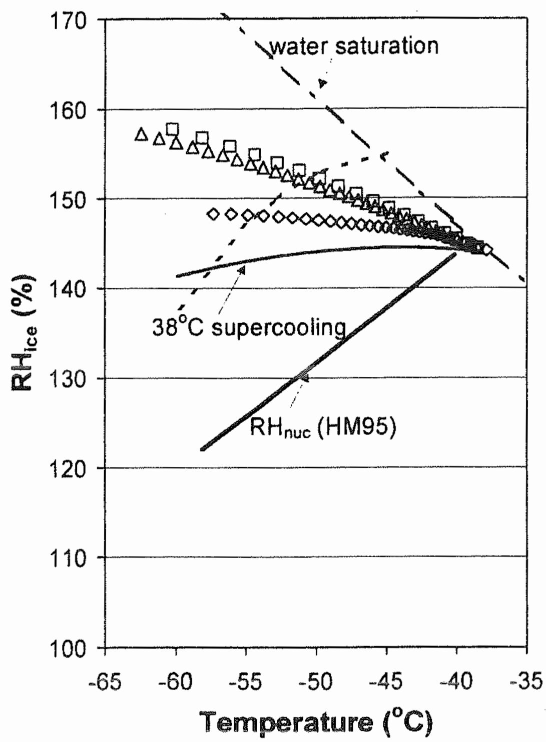

Figure 3. RH_{ice} versus temperature conditions required to freeze H_2SO_4/H_2O (squares), $(NH_4)_2SO_4$(triangles), and NH_4HSO_4 (diamonds) haze droplets. The points represent the median freezing temperature of micron-sized droplets, absent of curvature effects on solution composition which necessitate higher RH_{ice}. Also shown (unlabelled dashed line) are the conditions for ice formation by 0.24 μm (average) diameter black carbon particles coated with multiple layers of H_2SO_4 (DeMott et al., 1999). Other curves show water saturation, cirrus formation conditions (RH_{nuc}(HM95)) from field data (Heymsfield and Miloshevich, 1995), and 38°C supercooling from ice/liquid equilibrium.

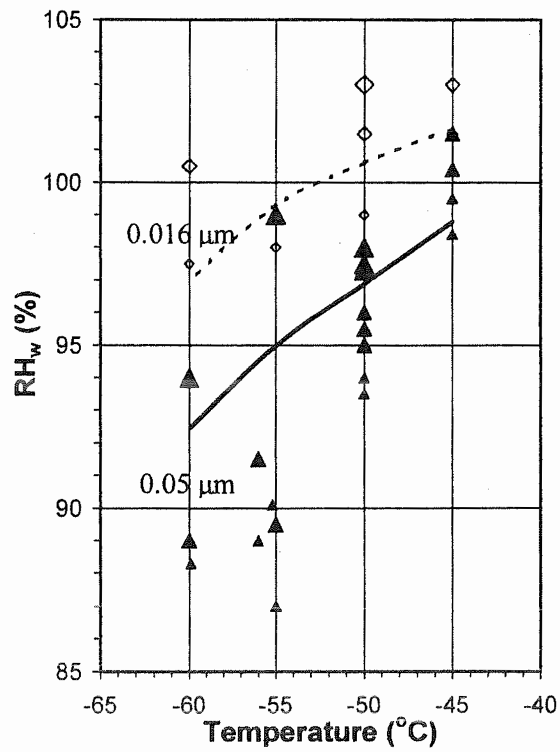

Figure 4. Size dependence of temperature and water relative humidity (RH_w) conditions required to homogeneously freeze H_2SO_4/H_2O aerosol particles in 12±2s. Experiments using 0.016 μm (open symbols) and 0.05 μm (filled symbols) particles (sizes at 1% RH_w at 25°C) are shown. Symbol sizes refer to 0.1 % (smallest), 1% (medium) and 10% (largest) particle fractions activated. Solid and dashed lines are calculated freezing conditions (10% activation) for the larger and smaller particles based on (1), (2), Köhler theory and the average λ derived from all sulfuric acid experiments. Adapted from Chen et al. (2000).

λ is constant for any solution, independent of particle size and nucleation rate. Thus, the slope of the nucleation rate versus temperature for pure water drops is preserved at higher weight % solute conditions. The particle size dependence of freezing conditions predicted by the average experimental λ (lines in Fig. 4) gives satisfactory agreement with observations, suggesting some justification for the constancy of this parameter. Nevertheless, there is much spread in the data in Fig. 4. Additionally, an analysis of nucleation rates in these and other studies (DeMott et al., 2000) suggests a lowered slope of nucleation rate versus temperature for solutions and a systematic increase in λ with per particle nucleation rates. Studies to place results into a classical theory context are underway.

Small soluble particle size (Fig. 4) was not the only factor found to impede cirrus formation. The deliquescence and freezing of crystalline particles was also impeded. Chen et al (2000) describe these results.

Figure 3 also shows that homogeneous freezing nucleation is not a likely explanation for the formation conditions of continental cirrus clouds inferred from field observations. A possibility is that sufficient heterogeneous ice nuclei exist in the upper troposphere. DeMott et al. (1999) describe the results of our experiments on heterogeneous ice nucleation by black carbon particles. It was necessary for H_2SO_4 to be present in the particles in excess of a few weight % in order to stimulate heterogeneous freezing in the rather large (0.24 μm average diameter, σ = 1.8) particles. These results are included in Fig. 3. The trend of decreasing RH_{ice} with decreasing temperature to freeze a given proportion of particles is consistent with that necessary to explain cirrus formation conditions, but it is clear that a much more efficient natural heterogeneous nucleus is required. This conclusion is well supported by studies of the smaller soot particles formed from combustion of certain jet fuels. These small soot particles required high RH_{ice} to initiate ice

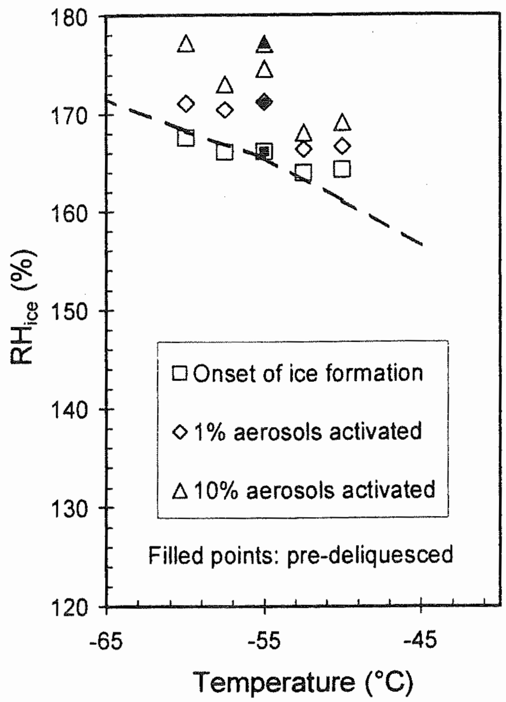

Figure 5. Conditions for various degrees of ice formation, within the CFD chamber residence time (~12s), by 0.05 μm particles produced from combustion of jet fuel A (with PRIST additive). The filled symbols indicate experiments in which particles were exposed RH_w above 90% at room temperature prior to cooling. The dashed curve gives the predicted conditions for ice formation by homogeneous freezing (1% of particles in 12 s), assuming the soluble fraction was H_2SO_4/H_2O.

formation and the slope of the required RH_{ice} versus temperature was opposite that of RH_{nuc} (from Fig. 3). The combusted fuel particles were estimated to be ~10% soluble by mass (H_2SO_4 assumed) based on CCN measurements. Homogeneous freezing calculations provided a sufficient explanation for the observed nucleation conditions (Fig. 5). Singular consideration of these observations lead one to predict little heterogeneous ice nucleation in aircraft exhaust trails until RH_w exceeds 100%.

Studies are underway to investigate heterogeneous ice nucleation by other potential nuclei, guided by field studies of compositions of upper tropospheric aerosols, ice nuclei and cirrus crystal residues.

4. RELATION TO NUMERICAL STUDIES

Previous numerical studies have pointed out that the ice crystal concentrations nucleated in cirrus are limited by vapor supply, which is in turn regulated by upward motion scales. Consequently, the concentrations of ice crystals predicted to nucleate by homogeneous freezing in cirrus are relatively insensitive to changes in aerosol size distribution. In contrast, the existence of heterogeneous freezing nuclei activating at lower RH_{ice} might lead to a reduction in expected ice crystal concentrations (e.g., DeMott et al., 1998). Laboratory data are providing invaluable input to numerical models in order to isolate aerosol effects on ice formation from interactions with other factors affecting water vapor mass transfer rates, such as the ice condensation coefficient (Lin et al., 2000).

ACKNOWLEDGMENTS. This work was supported by funding from NSF-ATM9632917 and the NASA Atmospheric Effects of Aviation Program (Jet Propulsion Laboratory Contract 961353). Yalei Chen was supported by NASA Earth System Science Fellowship (NGT5-30001). Any findings and conclusions are those of the authors

REFERENCES

Baker, M.B., 1997: Cloud microphysics and climate. *Science*, **276**, 1072-1078.

Chen, Y, P.J. DeMott, S.M. Kreidenweis, D.C. Rogers, and D.E. Sherman, 2000: Ice formation by sulfate and sulfuric acid aerosol particles under upper tropospheric conditions. *J. Atmos. Sci.*, (in press).

Clegg, S.L., P. Brimblecombe and A.S. Wexler, 1998: A thermodynamic model of the system H^+-NH_4^+-SO_4^{2-}-NO_3^--H_2O at tropospheric temperatures. *J. Phys. Chem.*, **102**, 2137-2154.

DeMott, P.J., D.C. Rogers, S.M. Kreidenweis, Y. Chen, C.H. Twohy, D. Baumgardner, A.J. Heymsfield, and K.R. Chan, 1998: The role of heterogeneous freezing nucleation in upper tropospheric clouds: Inferences from SUCCESS. *Geophys. Res. Lett.*, **25**, 1387-1390.

DeMott, P.J., Y. Chen, S.M. Kreidenweis, D.C. Rogers, D.C., D.E. Sherman, 1999: Ice formation by black carbon particles. Geophys. Res. Lett. 26, 2429-2432.

DeMott, P.J., S.M. Kreidenweis, D.C. Rogers, Y. Chen, and D.E. Sherman, 2000: Laboratory studies of ice formation by aerosol particles in upper tropospheric conditions. In, *Nucleation and Atmospheric Aerosols 2000*, Amer. Inst. Physics (in press).

Heymsfield, A.J., and L.M. Miloshevich, 1995: Relative humidity and temperature influences on cirrus formation and evolution: Observations from wave clouds and FIRE II. *J. Atmos. Sci.*, **52,** 4302-4326.

Lin, R.-F., D.O.C. Starr, P.J. DeMott, R. Cotton, E. Jensen, and K. Sassen, 2000: Cirrus parcel model comparison project Phase 1 (this conference).

Rogers, D.C., P.J. DeMott, S.M. Kreidenweis, and Y. Chen, 2000: A continuous flow diffusion chamber for airborne measurements of ice nuclei. J. *Atmos. Ocean. Technol.* (in press).

Sassen, K. and G.C. Dodd, 1988: Homogeneous nucleation rate for highly supercooled cirrus cloud droplets. *J. Atmos. Sci.*, **45**, 1357-1369.

INFLUENCE OF THE CLOUD PROCESSING OF AEROSOL PARTICLES ON CLOUD AND AEROSOL RADIATIVE PROPERTIES DURING REPEATED CLOUD CYCLES

N. Hatzianastassiou[1], W. Wobrock[2], and A. I. Flossmann[2]

[1]Environmental Research Laboratory, Foundation for Research and Technology-Hellas, 71110 Heraklion, Greece
[2]Laboratoire de Météorologie Physique (LaMP), Aubière Cédex 63177, France

1. INTRODUCTION

Clouds cover roughly 60% of the Earth's surface (Heymsfield, 1993) and they are very important for climate and climate changes (Liou and Ou, 1989). The aerosol particles (APs), providing cloud condensation nuclei for cloud droplet formation, directly determine the number of cloud drops formed (Flossmann, 1998), and hence the cloud microphysical and radiative properties. This "indirect" radiative effect was observed in-situ (Twoly et al., 1995) or by satellites (King et al., 1995) and is relevant to climatic change scenarios (Twomey, 1977;
Charlson et al., 1987). Besides, the APs directly interact with solar radiation, reducing the solar flux reaching the Earth's surface. This "direct" radiative effect has a negative radiative forcing (cooling). Although its estimation on a global scale is difficult, its anthropogenic component is estimated to be equal to 1-2 W m-2 (Harshvardhan, 1993). Both the direct and indirect effects act in the opposite direction of the effect of greenhouse gases, probably counteracting it (IPCC, 1995). Given the importance of clouds and APs for the Earth's climate, they both have to be taken into account in climatic change scenarios, and their effects have to be quantified. This is routinely being done in general circulation models (GCM). Unfortunately, due to complicate occurring processes linked to APs and clouds, their representation in GCMs is rather crude, mainly based on simplified parameterizations. A better understanding of the cloud and aerosol microphysical processes, and of the effect on their radiative properties is necessary.

We use here a spectral scavenging and microphysics model (DESCAM) (Flossmann et al., 1985; Flossmann, 1994) coupled to the dynamics of a rising and entraining air parcel model. The simulated drop and aerosol particle spectra are introduced in the 2-stream flux radiative transfer model of Zdunkowski et al. (1982). This model has been used to study the role of droplet spectra for cloud radiative properties during a cloud cycle (Hatzianastassiou et al., 1997), while the DESCAM, embedded in either the air parcel model or a two dimension dynamics, was used to study the indirect effect of APs during repeated cloud cycles, and the effect of cloud processing of APs on clouds and and radiation, respectively (Hatzianastassiou, 1997; Hatzianastassiou et al., 1998). Here, we use the model to assess the effect of the cloud processing on both cloud and aerosol particles optical and radiative properties, during a single and a consecutive cloud life time cycle, in a continental and a maritime environment.

Corresponding author's address: Nikos Hatzianastassiou, Foundation for Research and Technology, 71110 Heraklion, Crete, Greece; E-Mail: hatziana@iesl.forth.gr.

2. MODEL DESCRIPTION

The model used contains three different modules. The dynamic module is a parcel model (0-D) which consists in an ascending and entraining air parcel, and is coupled to the microphysical module DESCAM. Both aerosol particles and drops are treated in a spectral form, being discretized in 81 and 69 radius size bins, respectively, and various dynamical and microphysical processes are accounted for. Both modules are interactive and their detailed descriptions can be found in Flossmann et al. (1985), Flossmann (1994), and Hatzianastassiou (1997). Thus, at every 2 s the dynamic, thermodynamic, and microphysical properties are alculated, and are stored every 100 s to yield the input for the radiation module, which calculates "off-line" the radiative properties of cloud and aerosol particles. The radiative transfer model is described by Zdunkowski (1982), and has been modified and coupled to our microphysical-dynamical model (Hatzianastassiou, 1997; Hatzianastassiou et al., 1997). It incorporates the effects of water vapor, carbon dioxide, ozone, pollution gases such as NO_2, dry air, and aerosol particles. The spectral integration is made in six spectral intervals, four covering the shortwave (SW), and the other two the infrared (IR) regions. The model requires optical properties, namely the extinction and absorption coefficients (σ_{ext}, σ_{abs}) as well as the asymmetry factor (g) of the phase function, for the water droplet and aerosol particle spectra, which are derived by Mie calculations for the output spectra of the dynamical-microphysical model (Hatzianastassiou, 1997; Hatzianastassiou et al., 1997).

3. INITIAL CONDITIONS

The model was initialized according to the vertical temperature and humidity profile given by Lee et al. (1980). The initial dry aerosol particle spectrum was assumed to be a superposition of three log-normal distributions as proposed by Jaenicke (1988), with values for the parameters of these distributions pertaining to typical continental and maritime cases (Hatzianastassiou et al., 1998). In a first approximation, all particles were assumed to consist of 100% $(NH_4)_2SO_4$. The absorption and subsequent oxydation of gases was also considered, with concentrations 0.5 ppb(v) for SO_2 and H_2O_2, and 30 ppb(v) for O_3. The air parcel was launched at 1000 mb (about 1000 m) with an initial relative humidy of 99% and a vertical velocity of 1 m/s.

The radiation model was initialized with the same temperature and humidity profiles as the air parcel model. The cloud droplet and aerosol particle spectra were these computed by the air parcel model at the corresponding height, while the aerosol particle spectra outside cloud were taken from the initial conditions. The O_3, CO_2, and NO_2 distributions as well as the surface temperature and albedo, were taken as in Hatzianastassiou et al. (1998). The grid spacing of the radiation code changed in order to meet the heights at which the droplet and aerosol particle spectra from the microphysical model were stored. The radiation model was initialized for 50° latitude, and for the Julian date 212 (30 July) at 12 UTC.

4. MODEL RESULTS

In Figure 1 there are given the cloud droplet number and water mass distribution function for a cloud formed in a continental environment, after 200s and 1900s (beginning and end) of the first cloud life time cycle, as well as at the end (1900s) of its second cloud life time cycle. The second cloud cycle was initiated forming on the evaporated aerosol particle spectrum at the end of the first cloud cycle, which results when all cloud

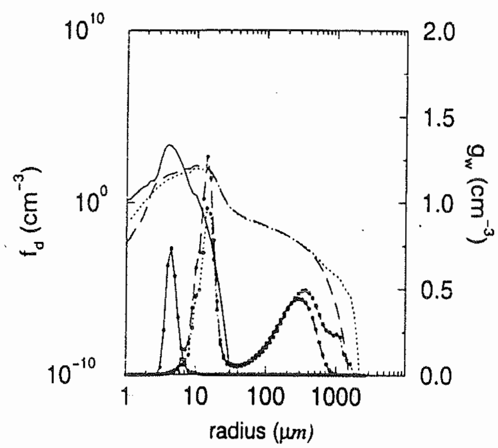

FIG. 1. Number (f_d, lines without circles) and mass (g_w, lines with solid circles) droplet distribution functions at the beginning (200s, solid lines) and the end (1900s) of a first (dashed lines) and a subsequent (dotted lines) life time cycles for a continental cloud.

droplets at the end of the cloud cycle instantaneously evaporate, and their soluble and non-soluble mass automatically converts in one single particle. This, of course, is an approximation, and a time-dependent treatment of the cloud droplet evaporation is the most adequate. Also, note that the immediate introduction of the evaporated aerosol particle spectrum into the second cloud cycle is an approximation too, since the aerosol particles mixe with their environment before they initiate the subsequent cycle. The effect of this mixing has been studied by Hatzianastassiou et al. (1998). The same variables as in Figure 1, but for a maritime cloud are given in Figure 2. Comparing figures 1 and 2 is clear that at the end of the cloud cycle we have more precipitation-sized drops in the maritime than in the

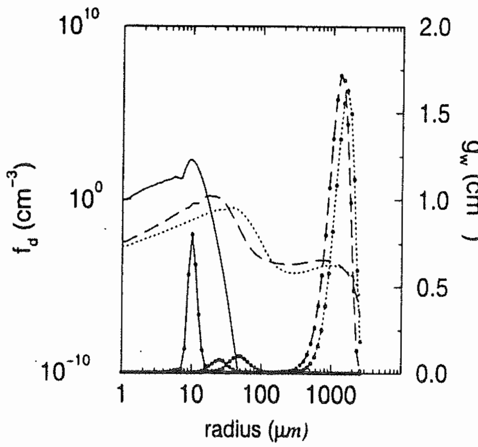

FIG. 2. As in Figure 1, but for a maritime cloud.

continental cloud. This is due to the lower number of initially activated aerosol particles, forming less drops, which enable them to accumulate more water vapor, and thus reach more easily the critical radius, beyond which the processes of collision and coalescence start working. The more efficient growth mechanisms lead to less and bigger in size drops, and hence evaporated aerosol particles, in the maritime than in the continental cloud. These differences reflect in the second cloud cycle, during which one can see an increased precipitation-producing ability for both clouds, decreasing furthermore the cloud droplet number. The computed optical properties of the continental and

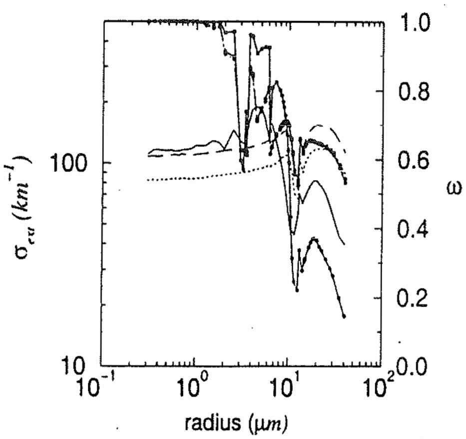

FIG. 3. Extinction coefficient (σ_{ext}, lines without circles) and single scattering albedo (ω, lines with solid circles) for droplet distribution functions at the beginning (200s, solid lines) and the end (1900s) of a first (dashed lines) and a subsequent (dotted lines) life time cycles for a continental cloud.

maritime clouds, at corresponding times, are shown in Figures 3 and 4, respectively. The optical properties are verified in Tables 1 and 2, where the corresponding model computed cloud radiative properties, the cloud-top albedo and cloud visible optical thickness, are given. The albedo of the continental cloud is larger than this of modified at the end of the second cloud cycle, being closely related to the microphysical ones, and warning for modifications of cloud radiative properties. This is

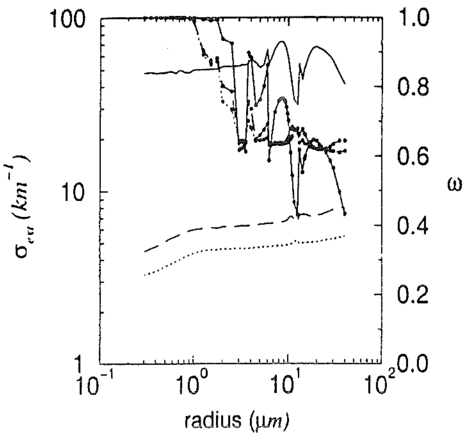

FIG. 4. As in Figure 3, but for a maritime cloud.

the maritime one, due to more in number and less in size drops. However, the cloud radiative properties decrease during a subsequent cloud cycle, this being more pronounced for the maritime cloud, which is important in view of the various climatic change scenarios (Charslon et al., 1987).

TABLE 1. Model computed cloud-top albedo and cloud visible optical thickness at the beginning (200s) and the end (1900s) of a maritime cloud during its first and a subsequent life time cycles.

	1st cycle		2nd cycle	
	200s	1900s	200s	1900s
A	0.56	0.56	0.36	0.49
τ	11.05	16.24	3.93	9.57

TABLE 2. As in Table 1 but for a continental cloud.

	1st cycle		2nd cycle	
	200s	1900s	200s	1900s
A	0.76	0.97	0.75	0.96
τ	27.43	364.92	26.49	277.67

The effect of the cloud processing of aerosol particles on their direct effect was also studied. In Figures 5 and 6 are given the initial and final (evaporated) aerosol particle spectra (before the cloud formation and after its dissipation) for continental and maritime conditions, respectively. The redistribution of the aerosol particles, with less and bigger particles, is stronger for the maritime cloud. The estimated corresponding single scattering albedo and extinction coefficients are given in figures 7 and 8, while in Tables 3 and 4 there are given our model computed downwelling visible radiative fluxes at surface, and the associated radiative forcings, for the cases of a cloud-free atmosphere, with a burden of aerosol particles corresponding at the initial and final

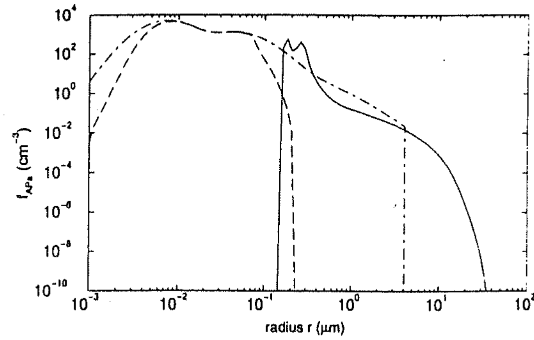

FIG. 5. Initial dry aerosol article spectrum (dash dot line), interstitial dry aerosol particle spectrum at 1900s (dashed line), and drop residual aerosol particle spectrum at 1900s (solid line) as a function of the dry particle radius for a continental cloud.

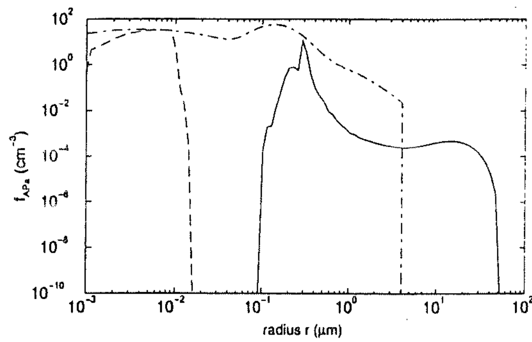

FIG. 6. As in Figure 5, but for a maritime cloud.

TABLE 3. Model computed downwelling visible solar radiative fluxes, and aerosol radiative forcings at surface. The fluxes and forcings are given for clear-sky and current atmospheric conditions, involving vertical initial and final (processed) maritime aerosol particle distributions.

	clear-sky	initial	final
F↓(W m^{-2})	714.15	709.87	713.82
ΔF↓(W m^{-2})		4.28	0.33

TABLE 4. As in Table 3 but for continental aerosol particle spectra.

	clear-sky	initial	final
F↓(W m^{-2})	724.06	716.54	706.72
ΔF↓(W m^{-2})		7.52	17.34

continental and maritime aerosol particle spectra, shown in figures 1 and 2. The clear-sky surface solar fluxes are also given. The radiative forcing ΔF is determined by:

$$\Delta F = F_{clear} - F$$

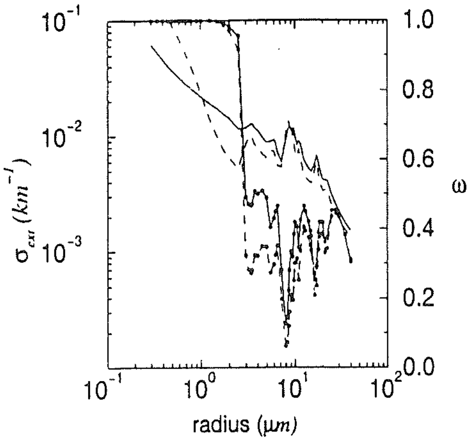

FIG. 7. Extinction coefficient (σ_{ext}, lines without circles) and single scattering albedo (ω, lines with solid circles) for initial (solid lines) and processed (dashed lines) continental aerosol particle spectra..

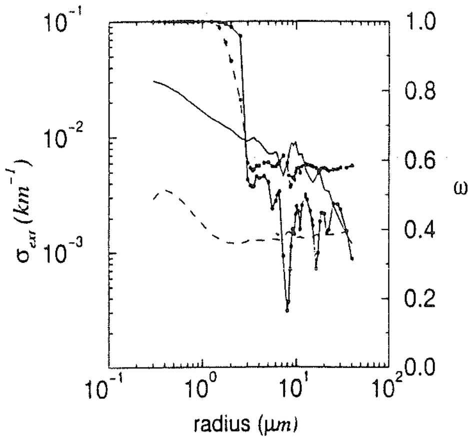

FIG. 8. As in Figure 7, but for maritime spectra.

where F_{clear} and F are the surface fluxes under clear-sky and current atmospheric conditions. Note that the cloud processing has a positive radiative feedback for the continental cloud studied, while for the maritime one its effect is negative, permitting more solar radiation to reach the Earth's surface, due to the dramatic decrease in aerosol particle number. This is interesting in view of the global assessment of the direct effect of aerosol particles.

5. REFERENCES

Charlson, R. J., J. E. Lovelock, M. O. Andreae, and S. G. Warren, 1987: Oceanic phytoplankton, atmospheric sulphur, cloud albedo and climate. *Nature*, **326**, 655-661.

Flossmann, A. I., 1994: A 2-D spectral model simulation of the scavenging of gaseous and particulate sulphate by a warm marine cloud. *J. Atmos. Res.*, **32**, 255-268.

Flossmann, A. I., 1998: Interaction of aerosol particles and clouds. *J. Atmos. Sci.*, **55**, 879-887.

Flossmann, A. I., W. D. Hall, and H. R. Pruppacher, 1985: A theoretical study of the wet removal of atmospheric pollutants. Part I: The redistribution of aerosol particles captured through nucleation and impaction scavenging by growing cloud drops. *J. Atmos. Sci.*, **42**, 583-606.

Harshvardhan, 1993: Aerosol-climate interactions. In: *Aerosol-Cloud-Climate Interactions*. Ed. By P. V. Hobbs. Academic Press, 233 pp.

Hatzianastassiou, N., 1997: *Etude de l'effet indirect des particules d'aerosol sur le bilan radiatif lors de cycles nuageux consecutifs*. PhD Thesis, No. D.U. 935, LaMP (Clermont-Ferrand), France, 155 pp.

Hatzianastassiou, N., W. Wobrock, and A. I. Flossmann, 1997: The role of droplet spectra for cloud radiative properties. *Quart. J. Roy. Meteor. Soc.*, **123**, 2215-2230.

Hatzianastassiou, N., W. Wobrock, and A. I. Flossmann, 1998: The effect of cloud-processing of aerosol particles on clouds and radiation. *Tellus*, **50B**, 478-490.

Heymsfield, A. J., 1993: Microphysical structures of stratiform and Cirrus clouds. In: *Aerosol-Cloud-Climate Interactions*. Ed. By P. V. Hobbs. Academic Press, 233 pp.

IPCC, 1995: *Climate Change 1995. The science of climate change*. Eds. J. T. Houghton et al., Cambridge Univ. Press, 572 pp.

Jaenicke, R., 1988: Aerosol physics and chemistry. In: *Landolt-Boernstein: Zahlenwerte und Funktionen aus Naturwissenschaften und Technick*, Vol. 4b, G. Fischer, Ed., Springer, 391-457.

King, M. D., S.-C. Tsay, and S. Platnick, 1995: In situ observations of the indirect effects of aerosols on clouds, In: *Aerosol Forcing of Climate*. John Wiley & Sons Ltd., 227-248 pp.

Lee, I. Y., G. Hanel, and H. R. Pruppacher, 1980: A numerical determination of the evolution of cloud drop spectra due to condensation of natural aerosol particles. *J. Atmos. Sci.*, **37**, 1839-1853.

Liou, K.-N., and S.-C. Ou, 1989: The role of cloud microphysical processes in climate: an assessment from a one-dimensional perspective. *J. Geophys. Res.*, **94**, 8599-8607.

Twoly, C. H., P. A. Durkee, B. J. Huebert, and R. J. Charlson, 1995: Effects of aerosol particles on the microphysics of coastal stratiform clouds. *J. of Clim.*, **8**, 773-783.

Twomey, S., 1977: The influence of pollution on the shortwave albedo of clouds. *J. Atmos. Sci.*, **34**, 1149-1152.

Zdunkowski, W. G., W. G. Panhans, R. M. Welch, and G. Korb, 1982: A radiation scheme for circulation and climate models, *Beitr. Phys. Atmos.* **55**, 215-238.

EFFECT OF CLOUD CONDENSATION NUCLEI ON THE OPTICAL PROPERTIES OF A LAYER CLOUD: NUMERICAL SIMULATION WITH A CLOUD-MICROPHYSICAL MODEL

N.Kuba[1], H.Iwabuchi[2], K.Maruyama[1], T.Hayasaka[2] and T.Takeda[3]

[1] Frontier Research System for Global Change, Minato-ku, Tokyo, 105-6791, Japan
[2] Center for Atmospheric and Oceanic Studies, Tohoku University, Sendai, Miyagi, 980-8578, Japan
[3] Institute for Hydrospheric-Atmospheric Sciences, Nagoya University, Nagoya, Aichi, 464-8601, Japan

1. INTRODUCTION

The influence of aerosol particles on the atmospheric radiative budget; especially the effect of cloud condensation nuclei (CCN) on the optical properties of clouds is one of the key issues in understanding and predicting global climate change.

Usually the optical properties of a cloud are estimated according to the liquid water path (LWP) in a global model. However the optical properties can be changed due to the difference in CCN or in ascending velocity of air-current even if the LWP of the cloud is fixed, as shown in this paper.

To quantitatively study the effect of CCN on the optical properties of a low-level layer cloud, we have developed a cloud-microphysical model which can estimate the sensitivity of the size distribution of cloud droplets to the size distribution and constituents of CCN and the ascending velocity of air-current. Moreover we studied the effect of the anthropogenic aerosols.

In this paper, the vertical profile of the size distribution of cloud droplets, which form on the CCN and grow through condensation and coalescence processes, is numerically simulated as accurately as possible. It means that we paid special attention to the avoidance of numerical diffusion and the effect of solute of cloud droplets on the growth of cloud droplets.

On the basis of the simulated vertical profile of the droplet size distribution, the optical properties (reflectance, absorptance and transmittance) of clouds for short-wave radiation are computed.

2. CLOUD MODEL

2.1 Assumptions

It is assumed that an air-parcel which contains CCN and water vapor ascends adiabatically in the U.S. Standard Atmosphere without the exchange of heat and substances between the parcel and its environment. The ascending velocity is determined by a given vertical profile. The formation of cloud droplets on CCN and their growth by condensation and coalescence are studied in this model. The sedimentation of droplets is not taken into account.

Corresponding author's address: Naomi KUBA,
Frontier Research System for Global Change, Minato-ku, Tokyo, 105-6791, Japan;
E-Mail: kuba@frontier.esto.or.jp

2.2 Governing equations

The growth rate of a droplet by condensation process is given by:

$$\frac{dM}{dt} = \left\{1 + \frac{W_w^2 D_c L^2}{R^2 T^3 K_c} e_\infty(T)\right\}^{-1} \frac{4\pi r W_w D_c}{RT}(e - e_r'(T))$$

$$e_r'(T) = e_\infty(T)\exp\left(\frac{2\gamma W_w}{\rho_w RTr} - \frac{\nu\phi W_w m}{1000}\right)$$

$$m = \frac{1000 M_s}{(M - M_s)W_s}$$

$$r = \left\{\frac{3M}{4\pi\rho_L}\right\}^{\frac{1}{3}}$$

Notations and the detail of these equations are written in Takeda and Kuba (1982).

The time changes of potential temperature, mixing ratios of cloud water and vapor of air parcel are calculated. The time change of the spectrum of cloud droplets by coalescence process is given by the stochastic formulation. Collision efficiency is computed from Table 1 in Hall (1980).

2.3 Computational scheme

In this model, two types of computational scheme are adopted.

2.3.1 Lagrangian framework in the layer near the cloud base

In the layer near the cloud base (usually up to 50m above cloud base), the activation of CCN and the condensational growth of cloud droplets are computed in the Lagrangian framework to estimate the solution effect of CCN on the condensational growth accurately and to avoid the numerical diffusion of droplet size distribution. Size distribution of CCN is inevitably expressed by discrete radii, so the classification of radius should be decided with caution. The number concentration of the nuclei included in one class should be sufficiently small in comparison with the total number concentration of cloud droplets. In this paper CCN (up to about 14 μm in radius) are classified into 155 classes so that more than 100 classes of CCN will be activated and grow to cloud droplets. The minimum radius of CCN given as initial condition must be smaller than the radius of the smallest CCN which can be activated. If all of given CCN are activated, simulated results would not be valid. The time evolution of representative radius of droplets condensed on CCN in each class is calculated. This is described in Takeda and Kuba (1982) in detail.

The interval of time step is 0.001 to 0.1 seconds according to the minimum radius of CCN prepared in the calculation. Moreover the condensational growth of each droplet during one time step is limited so that the radius of each droplet does not exceed its equilibrium radius at that moment.

2.3.2 Eulerian framework in the middle and upper layers

In the middle and upper parts of a cloud (usually in the layer higher than 50m above cloud base), cloud droplet size distribution is expressed by fixed bin of radius of cloud droplets to estimate the coalescence growth. Size distribution of cloud droplets in the Eulerian framework is represented as follows;

$r_i = r_1 2^{\frac{i-1}{3k}}$, here k indicates fineness of classification. The number concentration of droplets which radius is $(r_i - \Delta r_{i-}) \sim (r_i + \Delta r_{i+})$ is expressed as n_i and the time evolution of n_i is computed.

The growth by coalescence is calculated by the flux method developed in Bott (1998), which is mass conservative and has very little numerical diffusion. In this situation the calculation of condensational growth of cloud droplets needs special attention to avoid the numerical diffusion of the droplet spectrum. We calculated the condensational growth of droplets by using the advection algorithm. We developed it by replacing the polynomial approximation in Bott's (1989) method with dual-linear segments, and it has little numerical diffusion.

In this part, for simplicity the solute effect in condensational growth of cloud droplets is not taken into account. This simplification does not lead to a large error because the solution of almost all cloud droplets is dilute enough except for the very large drops at this stage.

In this paper, we adopted 6 for k, and 140 for the total number of bins (range of droplet radius expressed by these bins is 1.0 – 211.16 μm). The interval of time step is 2.0 seconds in this layer.

2.4 Numerical experiments

We computed 120 cases for five different size distributions of CCN (their cumulative number concentration larger than 0.02 μm in radius are about 200, 500, 1000, 2000, and 4000 cm^{-3}, respectively, but they have the same shape of spectrum), two kinds of constituents (NaCl and $(NH_4)_2SO_4$) of CCN and 12 vertical profiles of ascending velocity of air-parcel (cloud depth is 200m, 300m, 500m or 800m, and maximum value of the velocity is 0.4, 0.2 or 0.1 m/sec).

Moreover, to study the effect of anthropogenic aerosols, we computed the cases of continental CCN, 5 kinds of polluted continental CCN, maritime CCN and five kinds of polluted maritime CCN.

3. RADIATIVE TRANSFER CODE

The reflectance, absorptance and transmittance of the cloud layer are evaluated from the following precise radiative transfer calculation. The radiative transfer code developed by Nakajima and Tanaka (1986, 1988) was used. We assumed the U.S. standard atmosphere, including absorbing gas concentration profile. Gaseous absorption is incorporated by three - term k-distribution method and calculated by using LOWTRAN-7 (Kneizys et al. 1988). Cloud layer is divided into several sub-layers whose thickness is 50 or 100m, and the single scattering in each sub-layer is assumed to be homogeneous. The single scattering properties of water-phase droplets are calculated using Mie-theory from the size distribution of cloud droplets in each sub-layer. The Rayleigh scattering is taken into account, but no aerosol particle is assumed in each sub-layer. The complex refractive indices are referred to Hale and Querry (1973) for 0.2 - 1.8 μm and Downing and Williams (1975) for 2.0 - 4.0 μm. The wavelength region of 0.2 to 4.0 μm is divided into 80 sub-bands, and the spectral solar flux for each sub-band is calculated and integrated for the entire spectral region. The ground surface reflectance is assumed to be zero.

4. RESULTS

Figure 1 shows the relationship between the optical thickness and LWP of a cloud. Our results are plotted as circles. The solid line is the approximate relationship derived by Stephens (1978) with assumption that microphysical properties of a cloud are roughly decided by LWP. This figure shows that the optical properties can be changed due to the difference in CCN or in ascending velocity of air-current even if the LWP of the cloud is fixed.

The relationship between the optical properties and

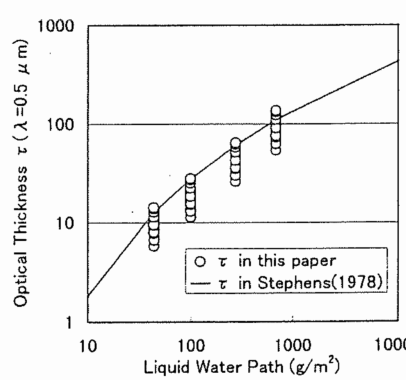

Fig.1 Relationship between optical thickness and LWP of a cloud.

the number concentration of cloud droplets near the cloud base (50 m above the cloud base) in 30 cases of 200m cloud depth (LWP is 44 g / m^2) is shown in Fig.2. This shows that the optical properties of clouds mostly depend on the number concentration of cloud droplets if LWP is fixed.

Figure 3 shows the relationship between the number concentration of cloud droplets near the cloud base and that of CCN (their cumulative numbers are changed without changing their shapes of spectrum) for the same 30 cases as Fig.2. The number concentration of cloud droplets increases with increase in the number of CCN, but it approaches a unique value that depends on the ascending velocity. This tendency can be seen regardless of the altitude in the cloud and cloud depth. Twomey (1959) presented the approximate relationship among droplet number concentration, the ascending velocity and the supersaturation spectrum of CCN. His result was that this relationship is expressed as a straight line in the graph with logarithmic scales. However, as shown in Fig.3, our results do not follow a straight line. This results was discussed in Kuba and Takeda (1985) in detail.

The same relationship in the case in which number concentration of CCN increases due to the addition of only Aitken particles (radius < 0.1 μm) is shown in Fig.4. It shows that the addition of only Aitken particles is more effective to increase in the number concentration of cloud droplets than that of wide range CCN.

Figure 5 shows the relationship between the reflectance of clouds and CCN number concentration for the same 30 cases as Fig.3. The reflectance increases with increase in the number of CCN and approaches unique values that depend on the ascending velocity. This reason is explained from Fig.2 and 3 easily. When cloud depth or LWP is fixed, the reflectance is mostly decided by the number concentration of cloud droplets. The sensitivity of the number concentration of cloud droplets to the CCN number concentration decreases with increase in the number of CCN. When the ascending velocity is fixed, the effect of the constituents of CCN on these optical properties becomes smaller with increase in the number of CCN. It can be said that the effect of CCN on reflectance is larger in the case of lower number concentration of CCN.

Figure 6 shows the same relationship as Fig.5 in the

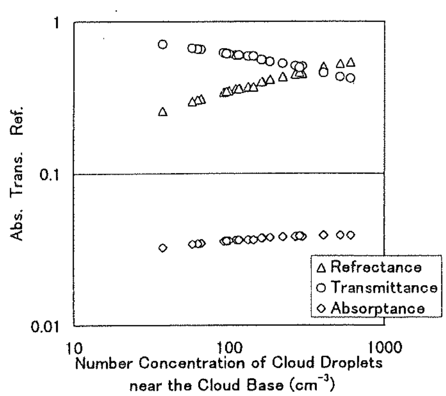

Fig2. Relationship between optical properties (reflectance, transmittance or absoptance) of a cloud and number concentration of cloud droplets near the cloud base for the case of 200m cloud depth (LWP is 44g / m^2).

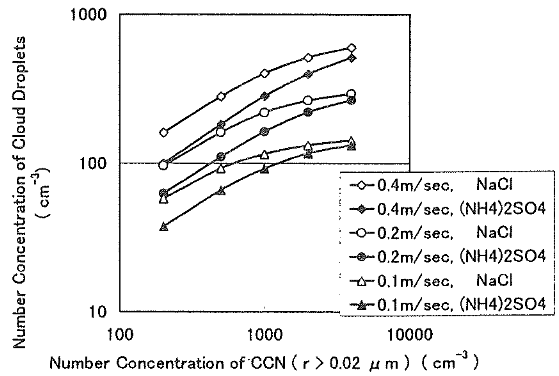

Fig.3 Relationship between number concentration of cloud droplets near the cloud base and that of CCN for the same case as Fig.2. The maximum value of ascending velocity is 0.4, 0.2 or 0.1 m/sec, and the constituent of CCN is NaCl or $(NH_4)_2SO_4$.

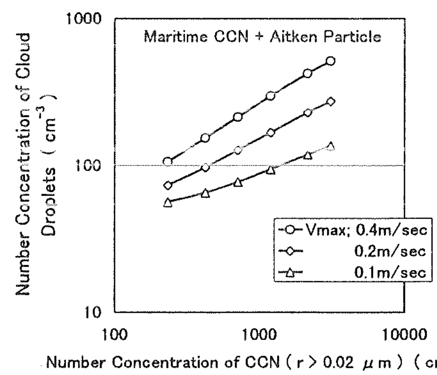

Fig.4 The same relationship as Fig.3, but the number of only Aitken Particle CCN is increased.

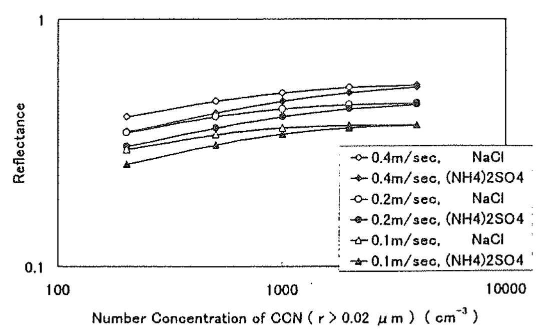

Fig.5 Relationship between reflectance and CCN number concentration for the same cases as Fig.3.

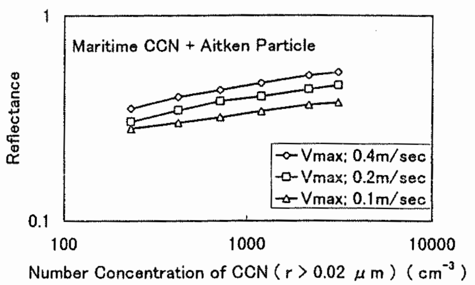

Fig.6 The same relation as Fig.5 but the number of only Aitken Particle CCN are increased.

case in which the number concentration of CCN increases due to the addition of only Aitken particles. It shows that the addition of only Aitken particles is more effective to increase in reflectance than that of wide range CCN.

5. CONCLUDING REMARKS

Generally the optical properties of clouds have been estimated according to LWP, under the assumption that the optical properties of clouds mostly depend on the LWP. However our results show that the optical properties are considerably affected by the size distribution of CCN and the ascending velocity of air current even if the LWP is fixed. Particularly, the addition of only Aitken particle CCN is effective to the optical properties of a cloud. And the optical properties of a cloud are affected more dominantly in the air mass with low number concentration of CCN.

It would be possible to estimate the optical properties of clouds more precisely, if the information about CCN and the updraft velocity near the cloud base is available in addition to LWP.

Twomey's (1974) result that the increase in CCN number concentration leads to the increase in cloud reflectance is supported mostly by our results. However, our results show that the sensitivity of reflectance to CCN number concentration becomes weaker with increase in CCN, especially when large CCN increase together. It can be postulated from our results that the effect of anthropogenic aerosols on the optical properties of layer clouds is more dominant in maritime or clean air mass than in continental or CCN-rich air mass, because the effect is more dominant in the case of lower number concentration of CCN. The sensitivity of optical properties of layer clouds to anthropogenic aerosols becomes weaker with increase in CCN number concentration, especially in the case of smaller updraft velocity near the cloud base, because the sensitivity of cloud droplet number concentration to CCN number concentration becomes weaker. This tendency in the sensitivity of cloud droplet number concentration to CCN number concentration is not derived from Twomey's (1959) approximate equation of cloud droplet number concentration.

Our result showed that reflectance of cloud in clean air mass is largely increased by the addition of anthropogenic aerosols, but absorptance is not sensitive to the number concentration of CCN. This result implies that the indirect radiative forcing of anthropogenic aerosols causes more cooling, when the changes in life time and dirtiness of a cloud and cloud amount can be neglected. However this radiative forcing of anthropogenic aerosols would not be dominant in the air mass rich in CCN.

6. ACKNOWLEDGEMENTS

We are grateful to Dr. Andreas Bott for kindly sending his FORTRAN code concerning the flux method for the stochastic collection, and his allowing us to use it.

7. REFERENCES

Bott,A. 1989: A positive definite advection scheme obtained by nonlinear renormalization of the advective fluxes. Mon.Wea.Rev., 117, 1006-1015.

Bott,A., 1998: A flux method for the numerical solution of the stochastic collection equation. J.Atmos.Sci., 55, 2284-2293.

Downing, H. D., and D. Williams, 1975: Optical constant of water in the infrared. J. Geophys. Res., 80, 1656-1661.

Hale, G. M., and M. R. Querry, 1973: Optical constant of water in the 200-nm to 200 -μm wavelength region. Applied Optics, 12, 555-563.

Hall,W.D., 1980: A detailed microphysical model within a two-dimensional dynamic framework: Model description and preliminary results. J.Atmos.Sci., 37, 2486-2507.

Kuba,N. and T.Takeda, 1985: Note on the effect of number concentration of CCN on the number concentration of cloud droplets. J.Meteor.Soc.Japan, 63, 2, 347-353.

Kniezys,.X. et.al , 1988: Users guide to LOWTRAN-7. AFGL-TR-88-0177. 137pp.

Nakajima,T. and M.Tanaka, 1986: Matrix formulations for the transfer of solar radiation in a plane-parallel scattering atmosphere. J. Quant. Spectrosc. Radiat. Transfer 35, 1, 13-21

Nakajima,T. and M.Tanaka, 1988: Algorithms for radiative intensity calculations in moderately thick atmospheres using a truncation approximation. J.Quant.Spectrosc.Radiat.Transfer, 40, 1, 51-69.

Stephens, G.L., 1978: Radiation profiles in extended water clouds. II: Parameterization schemes J.Atmos.Sci. 35. 2123-2132.

Takeda,T. and N.Kuba, 1982: Numerical Study of the effect of CCN on the size distribution of cloud droplets. Part I. Cloud droplets in the stage of condensation growth. J.Meteor.Soc.Japan, 60, 4, 978-993.

Twomey,S., 1959: The nuclei of natural cloud formation, Part II: The supersaturation in natural clouds and the variation of cloud droplet concentration. Geofis.Pura.Appl., 43, 243-249.

Twomey,S., 1974: Pollution and the planetary albedo. Atmos.Environ., 8, 1251-1256.

INFLUENCE OF CLOUDINESS TRENDS ON THE TOTAL SOLAR RADIATION IN TBILISI

A.G. Amiranashvili[1], V.A. Amiranashvili[1], T.V. Khurodze[2], K.A. Tavartkiladze[3]

[1]Institute of Geophysics of Georgian Academy of Sciences, Tbilisi, 380093, Georgia
[2] Institute of Computational Mathematics of Georgian Academy of Sciences, Tbilisi, 380093, Georgia
[3]Institute of Geography of Georgian Academy of Sciences, Tbilisi, 380093, Georgia

1. INTRODUCTION

Earlier investigations showed that in Tbilisi during the last decades a strong increase of the aerosol pollution of the atmosphere had been taking place Khorguani et al., 1996. Due to this increase a considerable reduction of the direct incident solar radiation occured Amiranashvili et al., 1997. This work presents the results of the investigations of the aerosol pollution and cloudiness effects on the radiation fluxes. The following parameters were considered: annual sums of direct ($\sum S$), diffuse ($\sum D$), total ($\sum Q$) radiation, annual sums of long-wave radiation balance ($\sum B_g$) and radiation balance ($\sum B$), mean anual values of the aerosol optical depth of the atmosphere (τ_a), total (G) and lower (g) cloudiness. The data for 1954-1990 were analysed. Unfortunately after 1990 the data of actinometric observations are unreliable.

2. METHODS

The values of the aerosol optical depth of the atmopshere τ_a were determined using the data of actinometric observations on the direct incident solar radiation irradiance and the method Tavartkiladze, 1989. In this paper the values of τ_a are presented for the wavelength λ = 1 mcm. Cloudiness (G and g) was determined visually at the meteorological station of Tbilisi using the standard methodology Mazin et al., 1989. Actinometric observations of radiation fluxes were also carried out according to the standard methodology Kondratiev, 1965.

Corresponding author's address: Avtandil Amiranashvili, Geophysics Institute of Georgian Academy of Sciences, 1., M. Aleksidze Str., Tbilisi 380093, Georgia;
E-Mail: vazha@excite.com

3. RESULTS

In Table 1 the data on the aerosol optical depth of the atmosphere, radiation fluxes, total and lower cloudiness in Tbilisi are presented for the investigated period. The table also gives an idea on the mean, maximum and minimum values of the mentioned parameters and their variability in time. The biggest variability has the aerosol optical depth of the atmosphere (the variation coefficient C_V is 31.9%), the least – total cloudiness (C_V = 5.5%). Table 2 presents the values of the correlations among all the investigated parameters. As it follows from this table sufficiently high negative correlations of $\sum S$, $\sum Q$, $\sum B$ with τ_a and g are observed. The correlations of radiation fluxes (except of $\sum B_g$) with the total cloudiness are insignificant.

Table 3 presents the values of the coefficients of linear regression equations for the variations of τ_a, radiation fluxes, G and g in Tbilisi from 1954 till 1990. For illustration it may be indicated that according to the data in Table 3 in Tbilisi in 1990 in comparison to 1954 the following changes of the values of the investigated parameters took place. The values of $\sum S$, $\sum Q$ and $\sum B$ decreased respectively by 19%, 14% and 29.5%. The values of $\sum B_g$ increased by 11%. $\sum D$ and G changed insignificantly (by +1.2% and –6.3% respectively).

For the estimation of the effect of the aerosol optical depth of the atmosphere and total and lower cloudiness on radiation fluxes with allowance to the data of Table 1and 2 multiple regression equation were used, which have the following form:

$$\sum S = 5995 - 3885\cdot\tau_a - 314\cdot g$$
$$\sum Q = 5808 - 4111\cdot\tau_a - 117\cdot g$$
$$\sum B = 2855 - 7453\cdot\tau_a + 94.6\cdot g$$

Comparing the calculations using these equations with the corresponding data, given in Table 1, the following conclusions may be drawn:

Table 1

Statistical characteristics of the investigated parameters in Tbilisi in 1954-1990

		MJ/m^2 per year					Amount	
Parameter	τ_a	$\sum S$	$\sum D$	$\sum Q$	$\sum B_g$	$\sum B$	G	g
Min	0.065	3442	1884	4312	-670	2035	5.2	3.3
Max	0.198	5066	2629	5527	-1926	3613	6.9	5.8
Mean	0.116	4166	2135	4815	-1507	2407	6.2	4.4
Std. dev.	0.037	380	170	318	237	355	0.34	0.55
Var.coef.%	31.9	9.1	8.0	6.6	15.7	14.7	5.5	12.5

Table 2

Correlations among the investigated parameters (the minimum significant value of a correlation with the confidence level 95% amounts to ±0.28)

	τ_a	$\sum S$	$\sum D$	$\sum Q$	$\sum B_g$	$\sum B$	G	g
τ_a	1.0	-0.65	0.13	-0.60	-0.21	-0.69	-0.31	-0.60
$\sum S$		1.0	-0.16	0.78	-0.07	0.61	-0.19	-0.68
$\sum D$			1.0	0.44	-0.24	0.08	0.05	0.14
$\sum Q$				1.0	-0.08	0.71	-0.06	-0.49
$\sum B_g$					1.0	0.62	0.30	0.18
$\sum B$						1.0	0.16	-0.32
G							1.0	0.27
g								1.0

Table 3

Coefficients of linear regression equations for the aerosol optical depth of the atmosphere, radiation fluxes, total and lower cloudiness in Tbilisi in 1954-1990 $y = a\cdot(t - 1953) + b$; $1954 \le t \le 1990$.

	τ_a	$\sum S$	$\sum D$	$\sum Q$	$\sum B_g$	$\sum B$	G	g
a	0.00305	-24.4	0.678	-20.1	-4.16	-23.2	-0.01	0.0336
b	0.058	4631	2123	5196	-1411	2851	6.4	3.75

- the share of lower cloudiness in the variations of $\sum S$ is 2.3 – 4 times higher than the share of the aerosol optical depth of the atmosphere;
- in the variations of $\sum Q$ the shares of the atmospheric aerosol optical depth and lower cloudiness are almost similar;
- the variations of $\sum B$ are mainly stipulated by the changes of the aerosol optical depth of the atmosphere.

4. REFERNCES

Amiranashvili, A.G., Amiranashvili V.A., Tavartkiladze K.A., Sajaia E.V., 1997: Some Peculiarities of Atmospheric Aerosol Pollution in Georgia, Bull. of the National Climate Research Centre, Tbilisi, N5(E), 41-47

Amiranashvili, V.A., Tavartkiladze K.A., 1997: The influence of the Atmospheric Pollution on the Solar Radiant Energy Variability in Tbilisi, Bull. of the Georg. Acad. Sci., 155, N3, 360-362

Khorguani, V.G., Gvazava R.A., 1996: Secular Regime of Cloudiness in Georgia, Proc. 12 th Int. Conf. on Clouds and Precipitation, Zurich, Switzerland, vol. 2, 1024-1025.

Kondratiev, K.Ya., 1965: Actinometry, Leningrad, Gidrometeoizdat, p. 647 (in Russian).

Mazin, I.P., Khrgian A.Kh., 1989: Handbook of Clouds and Cloudy Atmosphere, Leningrad, Gidrometeoizdat, p. 647 (in Russian).

Tavartkiladze, K.A., 1989: Modelling of the Aerosol Attenuation of Radiation and Atmospheric Pollution Control Methods, Tbilisi, Metsniereba, p.204 (in Russian).

GCM RADIATIVE FORCING OF SEA SALT AEROSOLS

J. Steven Dobbie
Dept. of Physics, UMIST
Manchester, M60 1QD, England

Jiangnan Li and Richard Harvey
Canadian Centre for Climate Modelling and Analysis
University of Victoria, Victoria, BC, V8W 2Y2, Canada

Petr Chylek
Dept. of Physics and Oceanography
Dalhousie University, Halifax, NS, B3H 3J5, Canada

ABSTRACT

In this work, a general circulation model (GCM) is used to estimate the radiative forcing due to sea salt aerosols. Calculations were performed using a new parameterization of the single scattering optical properties and 3D monthly mean sea salt loadings from tracer simulations. The globally and annually averaged forcing is calculated to be –0.15 W/m^2 (cooling). It is found that the southern hemisphere contributes double that of the northern hemisphere, and that the same monthly trends in forcing are observed for both hemispheres. The forcing is noted to be very sensitive to the amount of cloud cover.

1. INTRODUCTION

The radiative impact of aerosols is key to our undertanding of climate (Hobbs, 1993). Anthropogenic aerosols have received most attention because of their possible offsetting of the radiative changes caused by increases in greenhouse gases. Natural aerosols such as sea salt or mineral dust are also important for understanding climate. Our understanding of the radiative impact of natural aerosols can help in understanding the evolution of past environments and can help in predicting future climate.

The global radiative impact of naturally occurring sea salt aerosols is estimated in this work. To make this estimate, we use a general circulation model (GCM). In the GCM model, we have put a newly developed parameterization of the sea salt single scattering optical properties together with monthly mean sea salt loadings from tracer model output.

2. SEA SALT OPTICAL PROPERTIES

The form of the sea salt optical property parameterization is shown in Li et al. (2000) and Dobbie et al. (2000). Below is summary of the main points.

To perform radiative transfer calculations, commonly used optical property input parameters are the extinction coefficient, Kext, the single scattering albedo, ω, the asymmetry parameter, g, and the upscatter fraction, b.

The optical properties for hygroscopic aerosols such as sea salt are dependent on the ambient relative humidity, H, since this environmental parameter can affect the aerosol size and composition (solid particle or solution droplet). The growth of sea salt particles depends on the history of the particle (hysteresis-type growth curve). If a dry sea salt crystal is in an environment in which H remains below the deliquescence point, DH (75%), then the particle remains dry. If H exceeds DH, then the particle becomes a sea salt particle solution (wet). The solution droplet will remain as a solution for H even below DH but above the crystallization relative humidity CH (46%). Once H decreases below CH then the particle becomes a dry sea salt particle once again. The region between CH and DH is where the hysteresis takes place. In calculations, the Kohler equation is used to describe the growth of the sea salt solution droplet as a function of relative humidity. The refractive indicies of sea salt were taken from Shettle and Fenn (1979) and for water the indicies were taken from Hale and Querry (1973), Kou et al., (1993), and Downing and Williams (1975). The optical properties were combined using the Bruggeman mixing rule.

The sea salt solution droplets are considered to be spheres and Mie calculations were performed to obtain the optical properties for relative humidities above the CH. However, aerosol size distributions are usually given as dry size distributions, as dried on filters for example. To compute the optical properties for the wet solutions droplets, we utilize the following. We define a growth factor, η, as

$$r / rc = \eta(rc,H), \qquad (1)$$

where r is the wet sea salt solution radius and rc is the dry sea salt crystal particle radius. We also constrain the number of particles to be constant before and after drying, which we can write as

$$n(rc)drc = n'(r)dr, \qquad (2)$$

where n and n' are the dry and wet aerosol size distributions, respectively. With equations (1) and (2), we

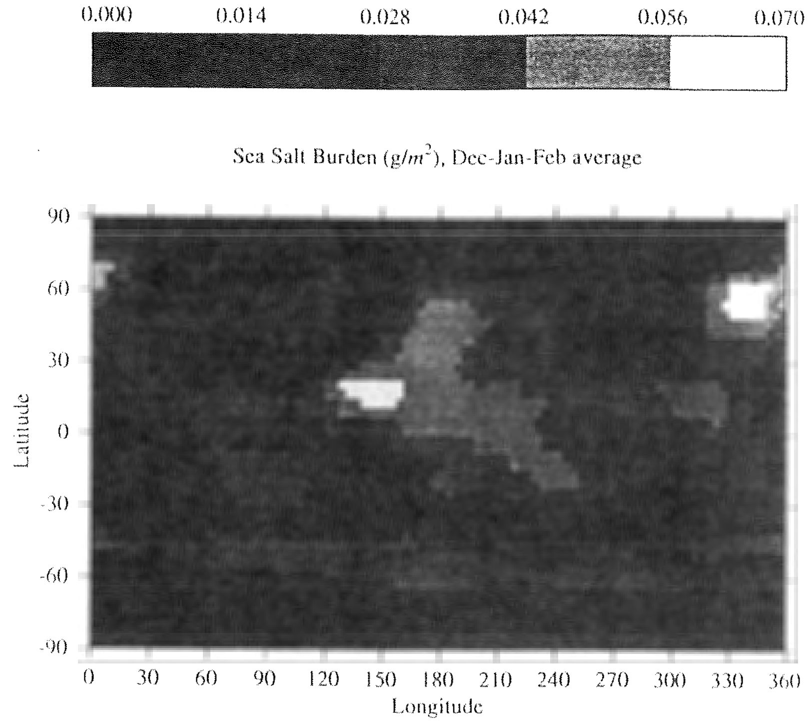
0.000 0.014 0.028 0.042 0.056 0.070
Sea Salt Burden (g/m^2), Dec-Jan-Feb average
90 60 30 0 -30 -60 -90
Latitude
0 30 60 90 120 150 180 210 240 270 300 330 360
Longitude

Figure 1

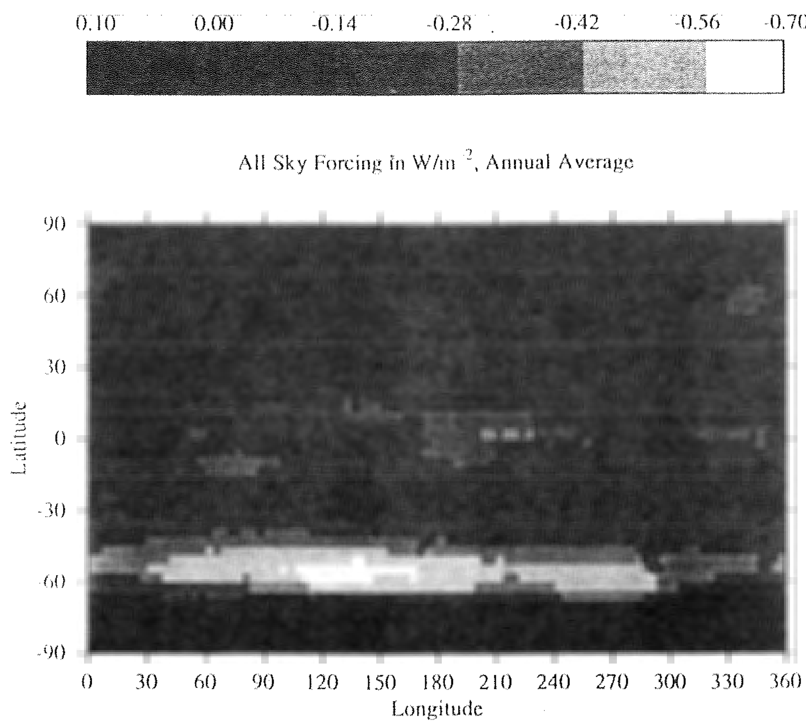
0.10 0.00 -0.14 -0.28 -0.42 -0.56 -0.70
All Sky Forcing in W/m $^{-2}$, Annual Average
90 60 30 0 -30 -60 -90
Latitude
0 30 60 90 120 150 180 210 240 270 300 330 360
Longitude

can write any optical property directly in terms of the measured dry size distribution and the growth factor, η (the growth factor is obtained by iterative solution of the Kohler equation). For example, we illustrate the form of the Mie calculation for Kext (similiarly for the other optical properties). First, in its normal form it is

$$\text{Kext} = \pi \int r^2 Q\text{ext}(r) n'(r) dr. \quad (3)$$

Using equations (1), (2), and (3) the Kext becomes

$$\text{Kext} = \pi \int (\eta rc)^2 Q\text{ext}(\eta r) n(rc\eta) d\eta rc, \quad (4)$$

where Qext is the extinction efficiency. All of the optical properties were computed in this manner and then they were parameterized as simple polynomial (computationally fast) functions of the relative humdity. The optical properties (Kext, 1-ω, g, and b) were parameterized in the following way:

$$\text{Kext} = a + b*H + c*H^8 \quad (5)$$

The accuracy of the parameterization for all of the optical properties is within 10% compared to exact Mie calculations for H between CH and 99%.

3. GCM RADIATIVE PROPERTIES

The optical property parameterization described in the previous section was implemented in the Canadian General Circulation Model GCMIII. Simulations took place using global 3D monthly mean sea salt loadings that were obtained from Tegen (GISS) for the supermicron sizes and Penner (Michigan) for the submicron sizes. Both loadings were obtained from tracer model output. In our calculations, these fixed monthly mean loadings were used in the GCM simulations. Two calculations were performed every time the GCM called the shortwave routine, the first flux calculation with the sea salt present and the second without it present. The difference between the two is the first order forcing due to sea salt aerosols and was accummulated during each month's simulation month (an average for the month was then determined). Note that even though the loadings were fixed for each month the forcing changed during the month because the humidity, cloud cover, etc. were all changing. We treat the hysteresis region in the following way. We computed the forcing for both the wet and dry particles (when H was between CH and DH) and we averaged the resulting forcing.

Shown in Figure 1 is the global distribution of sea salt burden for the boreal winter months. At first, we see some general features: sea salt is generated in all of the oceans and that the highest concentrations are located where the surface winds are greatest. High mass concentrations (bright) are observed in the North Atlantic and West Pacific, caused by the increased baroclinic instability and synoptic disturbances during the boreal winter months. The global sea salt distributions for the boreal summer shows less extreme features, and the concentrations are greatly diminished toward the North in the Northern Hemisphere.

Shown in Figure 2 is the global and annual average distribution of all-sky sea salt direct radiative forcing. We immediately notice that for an annual average the forcing in the Southern Hemisphere is dominant. Forcings up to –0.7 W/m^2 (cooling) are observed. This is greatly reduced from the case of clear sky forcing (not shown here), which had maximums of –3.0 W/m^2 (cooling). Clouds greatly diminish the forcing, and clouds typically exist in all of the regions where there are high sea salt concentrations (high winds). In fact, calculations show that clouds act to essentially negate the sea salt cooling. Clouds, however, which are situated above the sea salt layer, enhance the slight warming in the near infrared bands of sea salt by increasing photon path lengths within the sea salt layers. This is only noticeable when surface albedo is high, a situation in which photon exchange between surface and cloud would be maximized.

Shown in Figure 3 is the monthly mean trends in sea salt forcing for the Southern Hemisphere (SH), Northern Hemisphere (NH), and entire globe. From this, we see that all three forcings have a similar shape. This might be contrary to expectation at first, since the winter months generate the highest concentrations of sea salt in both hemispheres. The NH forcing is as expected; the greatest cooling is during the boreal winter for the NH, when concentrations are peaked (see Figure 1). However, the SH is also, slightly, peaked in concentration during the austral winter, but the maximum forcing appears in the austral summer. The reason for this is that the sea salt concentrations in the SH does not change so drastically with season, so the concentrations are not dictating the maximum. It is the fact that the concentrations are peaked at high latitude that influences the maximum—the solar flux during the austral winter is greatly diminished as compared to the austral summer and so the contribution is greatest during the austral summer months.

The yearly average forcing for the globe and the individual hemispheres was computed from the GCM runs and are reported in Table 1. From this table, we see that the global sea salt forcing is –0.15 W/m^2 (cooling), and that the SH contributes approximately twice that of the NH to the global average. The NH average is –0.11 W/m^2 (cooling) and the SH average is –0.19 W/m^2 (cooling).

Table 1. Yearly-averaged forcing

REGION	FORCING
Global	-0.15 W/m^2
Northern Hemisphere	-0.11
Southern Hemisphere	-0.19

4. CONCLUSIONS

A new parameterization of the single scattering optical properties as functions of the relative humidity was discussed in this paper. This parameterization together with tracer model output for monthly mean global sea salt loadings were used in GCM calculations to estimate the forcing due to sea salt aerosols. It was found that the global, yearly average direct radiative forcing is –0.15 W/m^2 (cooling). The yearly average NH forcing was determined to be –0.11 W/m^2 and the yearly average SH forcing is –0.19 W/m^2. The NH forcing showed much more variability in magnitude throughout the year than the SH. It is also noted that the same trend in the forcing with month for NH and SH is observed.

The forcing spatially averaged over the NH is a maximum in boreal winter, which is when the loadings are increased due to increased baroclinic activity relative to the NH summer. In the SH, the forcing is a maximum in the austral summer. This is because the sea salt loadings in the SH don't change significantly through the year (unlike the NH), so the maximum forcing is in the austral summer when there is a maximum amount of radiative flux reaching the SH,when there is only slightly reduced loadings.

Sea salt forcing is noted to be just under half the estimated direct forcing due to anthropogenic sulfate aerosols (Haywood et al., 1997) and approximately 15% of the forcing, but opposite in sign, due to anthropogenic greenhouse gases since the start of the industrial age (Charlson et al., 1992). The strength of sea salt forcing is non-negligible so it may be important when predicting future climate or when trying to understand past environments in which loadings were at different levels (sometimes much higher) as compared to at present (De Angelis et al., 1997).

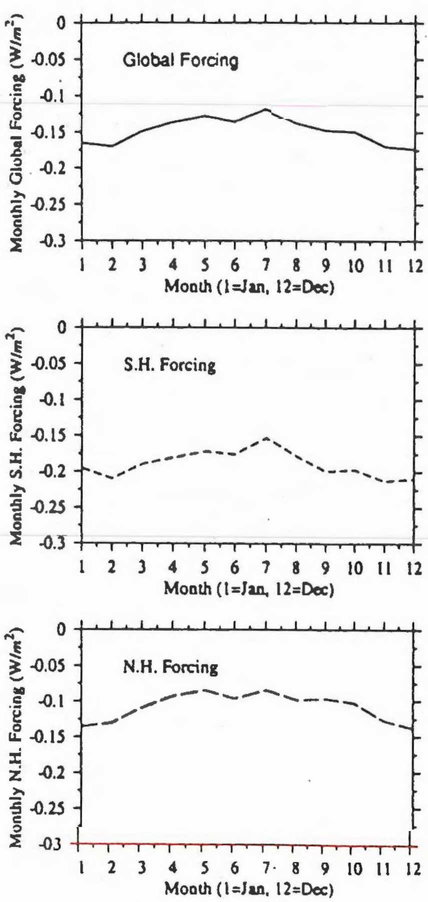

Figure 3

ACKNOWLEDGMENTS

Thanks to Drs. I. Tegen (NASA Goddard Institute for Space Studies) and J. Penner (University of Michigan) for the use of their sea salt tracer model output.

REFERENCES

De Angelis, M., J. P. Steffensen, M. Legrand, H. Clausen, and C. Hammer, 1997: Primary aerosol (sea salt and soil dust) deposited in Greenland ice during the last climatic cycle: Comparison with east Antarctic records. J. Geophys. Res., Vol. 102, No. C12, pp 26,681—26,698.

Charlson, R. J., S. E. Schwartz, J. M. Hales, R. D. Cess, J. A. Coakley Jr., J. E. Hansen, and D. J. Hofmann, 1992: Climate forcing by anthropogenic aerosols. Science, Vol. 255, pp 423—430.

Dobbie, J. S., J. Li, R. Harvey, and P. Chylek, Optical properties and GCM forcing of sea salt aerosols at solar wavelengths. To be submitted to J. Atmos. Sci., 2000.

Downing, H., and D. J. Williams, 1975: Optical constants of water in the infrared. J. Geophys. Res., Vol. 80, pp. 1656—1661.

Hale, G. M., and M. R. Querry, 1973: Optical constants of water in the 200nm to 200um wavelength region. Appl. Opt., Vol. 12, pp. 555—563.

Haywood, J. M., D. L. Roberts, A. Slingo, J. M. Edwards, and K. P. Shine, 1997: General circulation model calculations of the direct radiative forcing by anthropogenic sulfate and fossil-fuel soot aerosols. J. Climate, Vol. 10, pp 1562—1577.

Hobbs, V. P., 1993: Ed., Aerosol-Cloud-Climate Interactions. Academic Press, pp. 235.

Kou, L., D. Labrie, and P. Chylek, 1993: Refractive indicies of water and ice in the 0.65—2.5um spectral range. Appl. Opt., Vol. 32, pp. 3531—3540.

Li, J., J.G.D. Wong, J. S. Dobbie, and P. Chylek, Parameterization of the optical properties of sulfate aerosols. J. Atmos. Sci., accepted, Feb. 2000.

Shettle, A. A., and R. W. Fenn, 1979: Models for aerosols of the lower atmosphere and the effects of relative humidity variations on their optical properties. Environmental Research Paper, No. 675, NTIS ADA 085951, AFGL-TR-79-0214.

THE POSSIBLE EFFECT OF BIOMASS BURNING ON LOCAL PRECIPITATION AND GLOBAL CLIMATE

Hans-F. Graf[1], Daniel Rosenfeld[2] and Frank J. Nober[1]

[1]Max Planck Institute for Meteorology, Bundesstrasse 55, D - 20146 Hamburg, Germany
[2] Institute of Earth Sciences, The Hebrew University of Jerusalem, Israel

1 INTRODUCTION

Considerable efforts have been made in the recent past to estimate the effect of anthropogenically augmented aerosols (mainly sulphate) on the optical properties and also the lifetime of shallow clouds. The overall effect is proposed to counteract the warming due to increased greenhouse gas concentration in the atmosphere and, together with the direct backscatter effect of the aerosol particles, in part to offset the warming [*Lohmann et al.*, 1997]. Increasingly also other aerosol types (like carbon [*Penner et al.*, 1998] or soil dust [*Tegen et al.*, 1996]) are taken into account leading to more complex patterns. However, despite the fact that microphysics and optical properties of shallow (depth up to 1.5 km) clouds today are treated quite well in the sophisticated models [*Lohmann et al.*, 1997, *Penner et al.*, 1998, *Roelofs et al.*, 1998] nearly no attempts were made to do so for the deep convective clouds. This is unsatisfying because it is the energy released by the formation and fallout of precipitation in just these clouds that drives atmospheric circulation. About two thirds of the precipitation in the tropics stems from these clouds in the model, normally clustered in large cloud ensembles that mark the intertropical convergence zone. If the formation of rain is altered in these clouds then also the production of available potential energy is changed and, potentially, global climate can be affected. The tropics are prone to increasing amounts of smoke from biomass burning. This is true especially since the start of rapid deforestation in the tropics in the 1950ies, which culminated in the years 1970 to 1990 when about 20 Million hectares were cut and to a large extent burned per year. The massive population pressure in large parts of Southeast Asia, Africa and South America added to the commercially driven biomass burning activity. There are no reliable estimates for the global tropics, but rather some figures were published for some regions that may indicate a factor of at least five increase in biomass burning since 1950. *Crutzen and Andreae* [1990] estimated the gross production of primary aerosols formed from particulate carbon, elemental carbon and potassium to sum up to 36 to 154 Tg per year from biomass burning alone. In addition globally 2.1 to 5.5 Tg NO_x-N and 1 to 4 Tg sulphur gases form the potential for secondary aerosol production from biomass burning. Sometimes, like in 1997/98 in Indonesia, the smoke is extremely dense and even is a hazard to human health. New satellite observations [*Rosenfeld and Lensky*, 1998, *Rosenfeld*, 1999] clearly demonstrated that under the effect of smoke tropical clouds tend to decrease their effectivity of conversion of cloud droplets into rain. The autoconversion process is suppressed and rain is formed only after the glaciation process started. This effect was found to be highly efficient and reduced the rain from single clouds by up to 100%, depending whether the freezing level was reached or not. If smoke from biomass burning changes cloud microphysics also in deep convective clouds such that many very small droplets are formed which do not grow much by coalescence until freezing, these clouds will also be more effective in producing small ice particles that are suspended in the air and are an important source for cirrus clouds.

Observational data of precipitation changes since the beginning of the century indicate a decrease of rain in the tropics beginning in the 1950ies, very little change in midlatitudes and clear increase in higher latitudes of the Northern Hemisphere [*Hulme*, 1996]. While the increase of precipitation in higher latitudes is consistent with model calculations forced by increased greenhouse gases

Corresponding author's address:
Hans-F.Graf, Max Planck Institute for Meteorology, Bundesstrasse 55, D - 20146 Hamburg, Germany; E-Mail: graf@dkrz.de.

[*Henessy et al.*, 1997], the decreasing precipitation in the tropics is not. All climate models predict higher precipitation in the tropics with higher greenhouse gas concentration. They also predict more cirrus clouds due to intensified convective activity in the tropics. More cirrus is indeed observed, but, as mentioned above, in conjunction with less precipitation. Another important source for these cirrus clouds may be intensified formation of sulphate aerosols from air traffic emissions. The contribution of biomass burning, although potentially significant, is unclear and was not discussed so far. The detection and attribution of smoke impact on precipitation on scales larger than individual clouds requires much improved treatment of convective clouds and of their microphysics in climate models.

2 THE MODEL EXPERIMENT

We used the ECHAM4 atmospheric model in T30 resolution (time step 30 minutes) for our study. The formation of precipitation in convective clouds is treated extremely simple in this model. There exists one globally fixed rate of transformation (C) of diagnostically determined cloud water into precipitation which is assumend to be zero near cloud base and constant at higher levels.

According to observations [*Rosenfeld and Lensky*, 1998, *Rosenfeld*, 1999] we modified this parameterisation by introducing a dependency on the temperatur (T) and the cloud dropled number concentration (CDNC). Where T > 263 K and CDNC > 750 $\#/cm^3$ we reduced the formation of new rain by a factor of 0.25 while we absolutly stoped it where T > 263 K and CDNC > 1000 $\#/cm^3$. The CDNC is calculated using a cloud scheme which was developed for the stratiform clouds in ECHAM4 [*Lohmann et al.*, 1999]. In this scheme the nucleation rate of new cloud droplets, Q_{nucl}, is based on the total number of hygroscopic aerosols N_a, the updraft velocity ω and a factor α, which takes the aerosol composition and size spectrum into account:

$$Q_{nucl} = max(\frac{1}{\Delta t}\frac{N_a\omega}{\omega + \alpha N_a}, 0)$$

The vertical velocity is given as the sum of the grid mean value ($\overline{\omega}$) and a subgrid part.

$$\omega = \overline{\omega} + 0.7 \cdot \sqrt{TKE},$$

where TKE is the turbulent kinetic energy. Instead of the the original version of this cloud scheme where the large scale vertical velocity of the grid point is used (for large scale clouds) we used the mean vertical velocity which is computed from the convective updrafts of the mass flux scheme in ECHAM4. This is of course one of the difficulties we have to deal with, because the spread of ω for convective clouds is much greater than for stratiform clouds.

Other relevant microphysical processes which are parameterised are autoconversion, self collection, accretion, freezing, melting and evaporation. It is known [*Pruppacher and Klett*, 1997] that indeed the growth of ice hydrometeors is reduced in clouds with smaller droplets, and therefore our parameterization of slowing down warm rain formation probably underestimates the real effect.

We performed 5 years of the experiment run to reduce the effect of interannual variability.

3 FORCING

Since the used cloud scheme depends on the full cycles of aerosols including transport by the atmosphere and feedbacks between aerosols and precipitation via rainout and washout, it is not a simple task to find a good description of the forcing of our experiment. Monthly mean fields of the CDNC can only give an uncertain picture of the situation because of the high variability of this field.

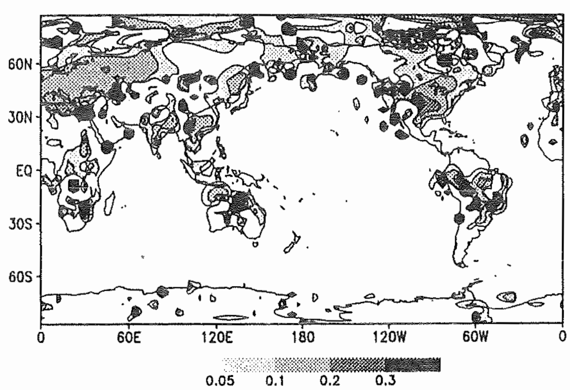

Figure 1: *Statistics of influenced convective rain events for June.*

Figure 1 therefore shows a simple statistics of the convective rain events in the model. Plotted is the (monthly mean for June) sum of events when rain is reduced or stopped, divided by the sum of all convective rain events. (Thus, 0.5 in the picture means that 50% of the time rain were reduced or stopped.)

4 RESULTS

Convective precipitation dominates in the tropics, where also the biomass burning is concentrated. In the zonal mean, convective precipitation shifts with the annual course of the sun and its maximum (the Intertropical Convergence Zone, ITCZ) is always found in the summer hemisphere over the continents while over much of the oceans it is always at the northern hemisphere.

In the global annual average there is nearly no effect in precipitation amount while there are stronger changes in some regions (Table 1). Based on our forcing statistics we defined burning seasons by the months with the most events of modified precipitation and calculated the changes of precipitation in percent for the whole year as well as for the burning season only.

Table 1

Change (in %) of precipitation due to smoke during the whole year and during the burning seasons

Area	Year	Burning Season
Indonesia	-2.7	-7.6
India	-4.3	-1.4
Myanmar ,Thailand, South China	-1.36	-3.1
North Africa	+0.5	-1.2
South Africa	-3.4	+1.2
South America	+2.0	+ 7.4

In Indonesia, North Africa and the region of Myanmar, Thailand and the southern part of China we find a clear reduction of precipitation as expected, while the situation in South Africa and South America is not so straightforward. The contradictory picture for example in South Africa can be explained due to the fact that the regional changes always consist of the direct forcing (i.e. the reduction of rain in the convection scheme) and the feedbacks of the whole dynamical system. This can lead to more precipitation even in regions where we expected less. The situation in South East Asia is caused by the fact that this region is the one with the strongest convective activity and the greatest atmospheric available potential energy production rates of the world. This part of the world therefore is very sensitive against changes in the convective activity.

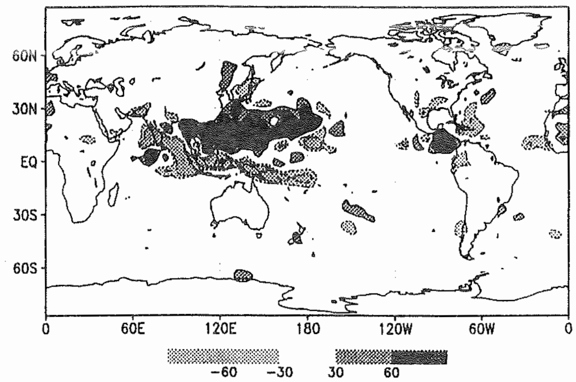

Figure 3: *Precipitation Anomalies in mm/month for August*

Figure 3 shows a typical situation of the global changes of precipitation. In most cases we found that a fraction of the deficit of convective rain (which is the dominant one in the tropics) is balanced by an increase of large scale precipitation. This is no suprise because the detrained cloud water from convective clouds serves as a source for cloud water in the stratiform clouds in ECHAM4.

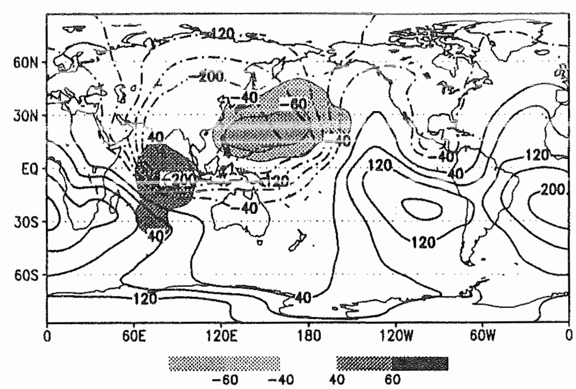

Figure 4: *Velocity Potential for August* ([$10^5 m^2/s$]) *Negativ/Positive values: rising/falling motion*

Nevertheless it is noteworthy that this mechanism leads to significantly more stratiform clouds which are important for radiation. So we find also strong regional anomalies in the radiation budged which are (similar to the ones for precipitation) very small in the global average. As mentioned in the introduction, one interesting point concerns cirrus clouds. In a global annual average we find a slight increase of cirrus from 13.1% cloud cover in the control run to 13.2% in the experiment. This increase is exceeded in some regions by an order of 2 (both decrease and increase). Different processes can be responsible for this fact: First of all, a reduction of convective rain in rising convective towers can lead to more cirrus by transporting more cloud water into such high altitudes. Second the indirect effect of less convective rain and, therefore, less latent heat release in the atmosphere works contrary to the first effect by weakening the velocity potential and thus the large scale rising motion.

The importance of the release of latent heat due to convective rain for the large scale dynamic of the atmosphere and the influence of regional anomalies in the precipitation amount on the large scale behaivor of the model is obvious (in connection with Figure 3) from Figure 4. The increase of precipitation over the northern West Pacific and the decrease over Indonesia and a part of the Indian Ocean leads to prominent changes of the velocity potential. This indicates a shift in the Walker and Hadley circulation.

5 CONCLUSIONS

After running several GCM (general circulation model) studies with different modifications of the convection process related to the CDNC and temperature or some emission data [*Cooke and Wilson*] of biomass burning, we found that even small changes of the generation of convective precipitation can lead to important effects for many atmospheric quantities. This fact, recent observations and analyses concerning the effect of smoke from forest fires on convective clouds in Indonesia show how important the inclusion of mircophysical effects in the convective process is in GCMs. For this purpose different problems are to be solved: Because of the coarse resolution there are no single convective clouds in a GCM. The contributions of convection to the atmospheric processes are calculated within the scope of a mass flux scheme. This makes it very difficult to derive cloud dynamic, and microphysical quantities (like the vertical velocity or liquid water content) from the grid point value. or to handle the entrainment of the environmental air into a single convective cloud. It is therefore necessary to study the evolution of convective clouds with special respect to the microphysics under different conditions (clean air and polluted air) by running model experiments with a high resolution. This will help to find parameterisations for the convective processes which are sophisticated enough to take care of microphysical processes but cheap enough (in the meaning of computer resources) to be applied in a GCM.

6 REFERENCES

Cooke and Wilson, http://blueskies.sprl.umich.edu/geia/

Crutzen, P. J. and M. O. Andreae, 1990: Biomass burning in the tropics: Impact on atmospheric chemistry and biogeochemical cycles, *Science*, *250*, 1669-1678.

Henessy, K. J., J. M. Gregory and J. Mitchell,1997: Changes in daily precipitation under enhanced greenhouse conditions, *Climate Dyn. 13*, 667-680.

Hulme, M., 1995: Estimating global changes in precipitation, *Weather, 50*, No. 2.

Lohmann, U., J. Feichter, 1997: Impact of sulfate aerosols on albedo and lifetime of clouds, *J. Geophys. Res. 102*, 13685-13700.

Lohmann, U., J. Feichter, C. C. Chuang, J. E. Penner, Predicting the number of cloud droplets in the ECHAM GCM, 1999: *J. Geophys. Res.*, *104*, 9169-9198.

Penner, J. E., C. C. Chuang and K. Grant, 1998: Climate forcing by carbonaceous and sulfate aerosols. *Climate Dyn., 14*, 839-851.

Pruppacher, H. R. and J. D. Klett, 1997: Microphysics of clouds and precipitation, Kluwer Academic Publishers,2nd edn.

Roelofs, G. J., J. Lelieveld and L. Ganzeveld, 1998: Simulation of global sulfate distribution and the influence of effective cloud drop radii with a coupled photochemistry-sulfur cycle model, *Tellus* , *50B*, 224-242.

Rosenfeld, D., M. I. Lensky, 1998: Satellite-Based insights into precipitation formation processes in continental and maritime convective clouds, *Bull. of the Am. Meteor. Soc., 79*, 2457-2476.

Rosenfeld, D., 1999: TRMM observed first direct evidence of smoke from forest fires inhibiting rainfall, *Geophys. Res. Let. 20*, 3105-3108.

Tegen, I, A. A. Lacis and I. Fung, 1996: The influence on climate forcing of mineral aerosols from disturbed soils, *Nature, 380*, 419-422.

SCAVENGING OF ORGANIC AEROSOL CONSTITUENTS IN SUPERCOOLED CLOUDS

Hans Puxbaum and Andreas Limbeck

Institute for Analytical Chemistry, Technical University of Vienna, Austria

1. INTRODUCTION

Clouds drive a natural cycling process, which can typically accumulate the soluble material from a large volume of air into a small volume of cloud water. To describe this transfer process, scavenging theories are used. The concentration of a component in cloud water is related to the concentration of the corresponding compound in the air. While sulfate was long considered the major cloud condensation nuclei (CCN) forming species in aerosols, Novakov and Penner (1993) pointed out the importance of organic aerosol constituents in cloud processes. Their measurements in Puerto Rico revealed that organic aerosols may often account for the majority (about 75%) of CCN. This large fraction indicates that organic aerosols may play an important part in cloud processes. A first comparison between the in-cloud scavenging efficiencies of sulfate and non-carbonate carbon (the sum of organic and elemental carbon) by Kasper-Giebl et al. (2000) showed that non-carbonate carbon was scavenged less efficiently than was sulfate. However, no results for the simultaneous measurement of single organic compounds in aerosols and cloud water have yet been reported. Therefore, no field data about the in-cloud scavenging behavior of organic compounds is available from former investigations.

Here we describe in-cloud scavenging efficiencies for individual polar organic compounds. The data have been obtained in a cloud scavenging experiment at a high mountain site in Central Europe.

Corresponding author´s address: Hans Puxbaum, Institute for Analytical Chemistry, Technical University of Vienna, Getreidemarkt 9/1514, A-1060 Vienna, Austria.
E-mail: hpuxbaum@mail.zserv.tuwien.ac.at.

2. EXPERIMENTAL

Aerosol and cloud water samples were taken in April and May 1997 at the Sonnblick Observatory, which is located at 3.106 m elevation on the top of the Mount Sonnblick in the Austrian Alps (12°57´ E; 47°03´ N). The Sonnblick Observatory is a continental background station since no local pollution sources are nearby. The cloud water samples were collected with an impaction based sampler for super-cooled droplets. The interstitial aerosol samples were collected downstream the cloud-water-sampling device via a manifold using Quartz fiber filter (Pallflex TISSUQUARTZ 2500QAT-UP). A more detailed description of the sampling site and the sampling procedure is given by Kasper-Giebl et al. (2000). To exclude any contamination from the sampling procedure itself, field blanks were taken. After sampling the filters were stored in petri-dishes with a parafilm cap in the refrigerator at 4°C. The cloud water samples were kept frozen in polyethylene bags until time of analysis.

Analytical target compounds in the aerosol and cloud water samples were polar organic compounds such as organic acids and related compounds. To allow a simultaneous determination of C2-C9 dicarboxylic acids and C8-C18 monocarboxylic acids we applied the method of Limbeck and Puxbaum (1999). To obtain the oxygenated compounds from the aerosol samples, the filters were extracted with diethylether, methanol and organic free water using ultrasonic agitation. Cloud water samples were melted at room temperature. The aqueous sample solutions were separated into different classes of organic compounds using solid phase extraction. After esterification of the derived sample fractions, the obtained acid esters were extracted with cyclohexane. The GC/MS-analysis of these extracts was performed using a HP® 5890 Series II GC equipped with a capillary column (HP® INNOWax 19091N-133, 30 m, 0.25

mm ID, 0.25 µm film thickness) and a mass selective detector (HP® 5971 A). For the determination of sulfate, ion-chromatography was used (Dionex; analytical column AS4A-SC, suppressor ASRS I recycle mode, conductivity detection, eluent 1.8 mM Na_2CO_3 and 1.7 mM $NaHCO_3$).

3. RESULTS

In both the aerosol and the cloud water samples, a number of phenols, alcohols, aldehydes, monocarboxylic acids and dicarboxylic acids could be identified and quantified. The most abundant compounds in the interstitial aerosol phase (N=4) were octa-decanoic acid (17 ng m^{-3}), phenol-4-methoxy-diisobutyl (15 ng m^{-3}) and hexadecanoic acid (13 ng m^{-3}). Oxalic acid (C2) was the dicarboxylic acid with the highest average concentration (determined amount 9.9 ng m^{-3}).

Cloud water samples showed a difference in composition compared to aerosol samples. The highest average concentrations (N=4) were obtained for dicarboxylic acids. Oxalic acid (C2) was found with an average concentration of 174 ng ml^{-1}, succinic acid (C4) with 85 ng ml^{-1}, pyruvic acid (C3) with 50 ng ml^{-1} and malonic acid (C3) with 39 ng ml^{-1}. Octadecanoic acid was the monocarboxylic acid with the highest average concentration (21 ng ml^{-1}).

The observed presence of polar organic constituents in clouds seems to suggest that clouds are efficient scavengers of polar organic chemicals from the atmosphere. A possible pathway for the incorporation of organic compounds into cloud water is particle scavenging. Supersaturated water vapor can nucleate directly onto aerosol particles containing organic compounds and form a droplet. The mass based scavenging efficiency for an individual compound (IC) is given by equation (1)

$$\varepsilon_{IC} = c_{C,IC} * LWC / (c_{C,IC} * LWC + c_{A,IC}) \quad (1)$$

where $c_{C,IC}$ is the concentration in cloud water, $c_{A,IC}$ is the concentration in the interstitial aerosol and LWC is the liquid water content of the cloud. The use of equation (1) assumes that the individual compounds in cloud water are transferred exclusively from aerosol scavenging and that gas phase scavenging plays a negligible role. This method to calculate scavenging efficiencies via cloud water and interstitial aerosol is modified after an approach described by Daum et al. (1984).

For the calculation of scavenging efficiencies, only paired samples (more than 80% overlapping sampling time) were considered. Therefore, volume weighted mean concentrations of the cloud water samples were calculated to match the sampling times of the corresponding aerosol samples. Together with the measured concentrations of the investigated substances in the aerosol phase, scavenging efficiencies were calculated according to equation (1). From this procedure we derived scavenging efficiencies for individual carboxylic acids and other polar organic aerosol constituents from two different cloud events labeled as sample WW30/F12 (LWC=0.69 g m^{-3}) and WW01/F13 (LWC=0.86 g m^{-3}). From the same aerosol and cloud water samples, the sulfate concentrations were determined via ion-chromatography. Using equation (1), the scavenging efficiencies for sulfate were calculated. The results for sulfate were comparable to data from earlier studies by Kasper-Giebl et al. (2000) at the Sonnblick Observatory. For selected compounds the determined scavenging efficiencies are given in Figure 1. Additionally Figure 1 includes data about the scavenging behavior of sulfate and non-carbonate carbon.

The calculated scavenging efficiencies from the two sample pairs show very good agreement. For the sample-event with the higher LWC for most compounds negligibly higher scavenging efficiencies were obtained. This result fits with scavenging observations for lead and sulfate reported by Kasper et al. (1998). In this study, a dependence of the scavenging efficiency versus the LWC is described - for LWC´s below 0.2 g L^{-1}, a decrease in LWC leads to a decrease in scavenging efficiency for lead and sulfate, yet at higher LWC´s (greater 0.2 g L^{-1}), the scavenging efficiency of sulfate remains virtually constant (ε about 0.9 to 0.95).

By distributing the individual compounds into four classes of organic species, (alcohols, monocarboxylic acids, dicarboxylic acids and polar aromatic compounds), average scavenging

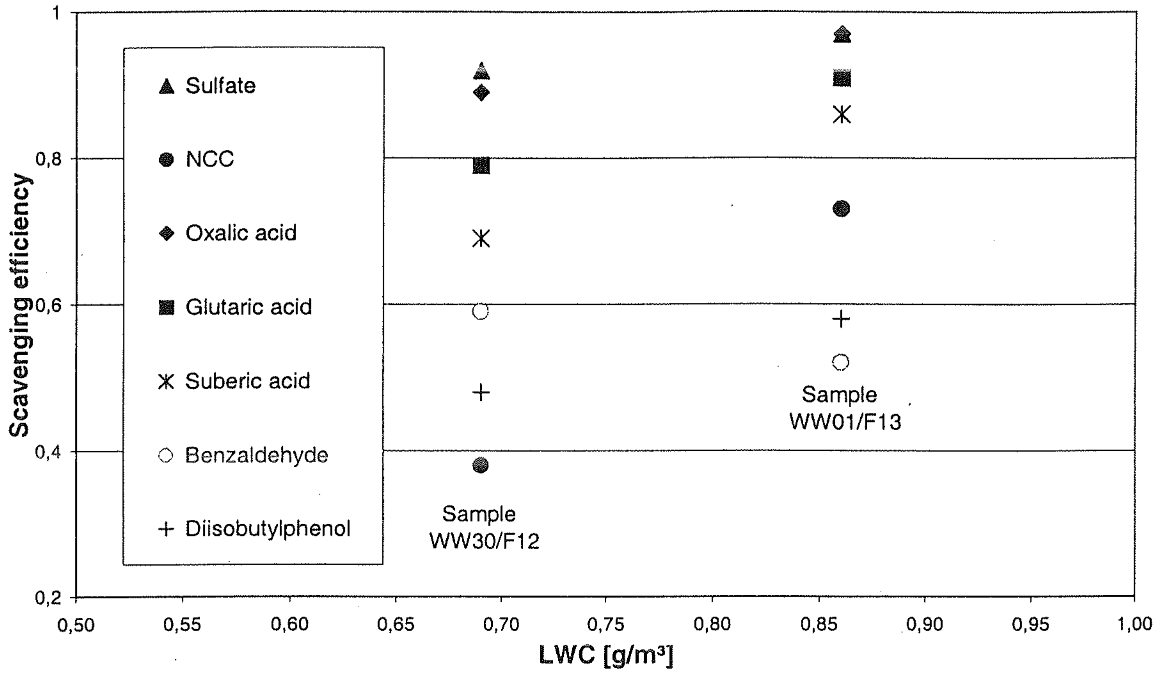

Figure 1: Scavenging efficiencies for selected compounds

efficiencies were calculated to be 0.4, 0.4, 0.8, and 0.6, respectively. The significance of these results is that compounds with less scavenging efficiency exhibit a longer lifetime in the atmosphere. As for fine particles wet scavenging is by far the dominant removal process, a scavenging efficiency of 0.4 compared to 0.8 would imply a longer atmospheric residence time.

The differences in the scavenging efficiency obtained for the different compound classes in our experiment can be explained with the physical and chemical properties of these compounds. For example the polarity changes from strongly polar (e.g. dicarboxylic acids) to weakly polar (e.g. fatty alcoholes). Taking the water solubility as a proxy for the polarity, a dependence between scavenging efficiency and the water solubility was found (Figure 2). The water solubilities used in Figure 2 are the results from a Beilstein-Crossfire search after the physical properties of the investigated compounds. Since there were no water solubilities available for diisobutylphenol, 4-ethoxy-bencoic acid-ethylester, dodecanol and hexadecanol estimated solubility ranges (derived from similar compounds) were used. Furthermore especially for less soluble compounds the different composition between cloud water and pure water must be considered. Therefore, the solubility for hexadecanoic acid and octa-decanoic acid might be higher in the cloud water samples than what is reported in the literature for the system free acid dissolved in pure water. Additionally Figure 2 includes the scavenging efficiency of $(NH_4)_2SO_4$. Comparing the results in Figure 2 for individual polar organic compounds we derive the following result – for different substances a decrease in the water solubility leads to a decrease in the scavenging efficiency reaching a minimum for non-soluble compounds. This result confirms findings by Corrigan and Novakov (1999), they concluded from their laboratory studies that the ability for an organic compound to act as CCN appears to correlate with the compounds solubility.

This behavior of organic aerosol constituents could be explained by the distribution of the investigated compounds between the two major aerosol fractions – the sulfate-mode and the bulk non-carbonate carbon (NCC-mode). Earlier investigations at the Sonnblick Observatory of the main aerosol constituents showed that a smaller mass median diameter occurred for non-carbonate carbon than for sulfate. In fact, it

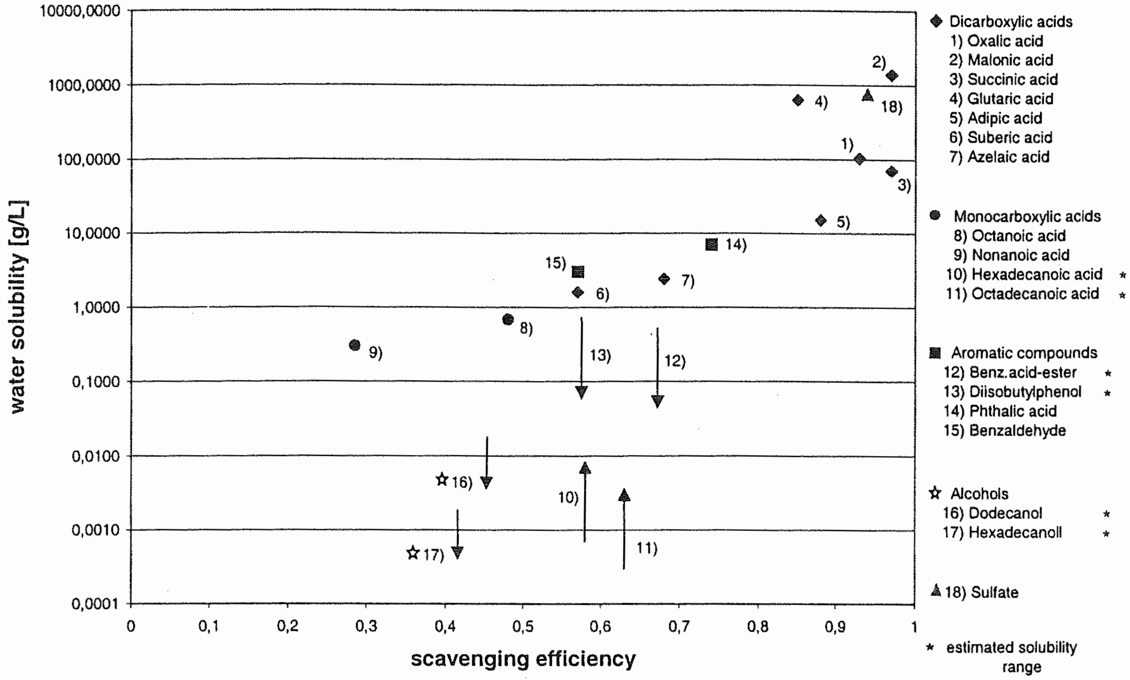

Figure 2: Dependence between scavenging efficiency and the water solubility

appears that a part of the aerosol carbon is associated with the sulfate-mode and another part is present in a smaller sized "carbon-mode". Highly water-soluble acids appear to be more associated with the "sulfate-mode" while the less polar compounds seem to be more associated with the less polar "carbon-mode". Consequently, their scavenging behavior is then dominated by the scavenging of the bulk NCC and will remain constant at the level observed for NCC (ε around 0.6, Kasper-Giebl et al., 2000).

Acknowledgement

We acknowledge founding by the Austrian Science Foundation, P 10328-CHE, technical support from the observatory staff and the Sonnblick-Verein and help from C. Gröllert, W. Tscherwenka and M. F. Kalina during the sampling campaign.

References

Corrigan, C.E., and T. Novakov, 1999: Cloud condensation nucleus activity of organic compounds: a laboratory studie. Atmos. Environ., 33, 2661-2668.

Daum, P.H., T.J. Kelly, S.E. Schwartz, and L. Newman, 1984: Measurement of the chemical composition of stratiform clouds. Atmos. Environ., 18, 2671-2684.

Kasper, A., H. Puxbaum, B. Brantner, and S. Paleczek, 1998: Scavenging efficiency of lead and sulfate in supercooled clouds at Sonnblick, 3106 m a.s.l., Austria. Atmos. Environ., 32, 3967-3974.

Kasper-Giebl, A., A. Koch, R. Hitzenberger, and H. Puxbaum, 2000: Scavenging efficiency of "aerosol carbon" and sulfate in supercooled clouds at Mt. Sonnblick (3106 a.s.l., Austria), J. Atmos. Chem., 35, 33-46.

Limbeck, A., and H. Puxbaum, 1999: A GC/MS-method for the determination of polar organic compounds in atmospheric samples. Int. J. Envir. Analyt. Chem., 73, 329-343.

Novakov, T., and J. Penner, 1993: Large contribution of organic aerosols to cloud condensation nuclei concentrations. Nature, 365, 823-826.

AIRCRAFT OBSERVATIONS OF SEA-SALT AEROSOL, SULPHATE AEROSOL AND CCN EVOLUTION IN THE MARINE BOUNDARY LAYER

S.R. Osborne and R. Wood

Meteorological Research Flight, Farnborough, United Kingdom

1 INTRODUCTION

The main sources of aerosols within the remote marine boundary layer (MBL) are (i) secondary sulphates derived from gas-to-particle conversions of dimethyl-sulphide or DMS, and (ii) primary sea-salt particles produced at the sea surface (O'Dowd et al., 1997). The oxidation pathways of DMS occur both in the MBL and the lower free troposphere (LFT). Subsequent entrainment of particles formed in the LFT into the MBL is thought to act as a 'top-up' mechanism of the MBL aerosol (Raes, 1995). Continental aerosols that have been transported long distances can also be entrained from the LFT into the MBL.

It has been shown that sea-salt particles in the MBL under moderate to high surface wind speeds can act in appreciable concentrations as efficient cloud condensation nuclei (CCN), thereby influencing the cloud droplet concentration (O'Dowd et al., 1997). Global modelling indicates that the presence of sea-salt may influence climatologically important clouds such as stratocumulus enough to play a significant role in the indirect radiative forcing effect of aerosols (Smith et al., 1998).

Bursting bubbles at the sea surface due to wind stress produces film particles of accumulation mode sizes (in concentrations of up to several hundred cm^{-3}) and jet particles of coarse mode sizes (generally less than 10 cm^{-3}). White-capping is caused by entrainment of air into the water surface and starts to take place at wind speeds of 3-4 m s^{-1}. The density of white-caps increases with wind speed, with spume particles (of giant sizes > 10 μm) caused by tearing of wave crests occurring above 10 m s^{-1} (O'Dowd et al., 1997).

This paper uses an observational case study to look at the evolution of a parcel of air within a clean MBL in terms of the aerosol spectra, aerosol chemistry and CCN activation spectra. Particular attention is paid to sea-salt production because of increasing wind strength.

2 DATASET USED

A Lagrangian framework was adopted in order to analyse the processes responsible for evolution. In the field, one method of achieving this is by tagging an air parcel with constant-level smart balloons and following the balloons with an aircraft for as long and as frequently as possible. Such a Lagrangian experiment was carried out on three occasions during the second Aerosol Characterisation Experiment (ACE-2) over the sub-tropical North Atlantic Ocean during June-July 1997. This paper details measurements made during one of these Lagrangians between 4-5 July 1997 (Johnson et al., 2000) consisting of three back-to-back flights of the Meteorological Research Flight C-130 aircraft. One smart balloon was released into the MBL from the ACE-2 ship and followed over a 26 h period.

Previous studies relating sea-salt mass to wind speed have correlated it against the concurrently measured local wind speed. This Eulerian technique does not take into account the previous history of the air being measured. Accumulation and coarse mode particles have atmospheric residence times ranging from a few hours to a few days and so the history of wind speed (which is difficult to determine) can still be evident in the concentration of aerosol particles.

Full details of the C-130 instrumentation during ACE-2 can be found in Johnson et al. (2000).

Corresponding author's address: Simon R. Osborne, Met. Research Flight, Y46 Building, DERA Farnborough, Hampshire, GU14 0LX, UK; email: sosborne@meto.gov.uk.

3 RESULTS

3.1 Wind speed evolution

Fig 1 shows the variation of wind speed with time through the Lagrangian using (i) the C-130 mean wind speed measured below 250 m and adjusted to a 10 m level (U_{10}), (ii) the 10 m mean wind speed from ECMWF model analyses, and (iii) the wind speed derived from the relative motion of the smart balloon which maintained an average altitude of 530 m. The balloon winds are higher than U_{10} which is to be expected within the MBL. The ECMWF winds and U_{10} both show an overall increase over the period from 7-8 m s^{-1} to around 12 m s^{-1}. The balloon and aircraft data show a small increase over the first 12-13 h of the experiment, while the ECMWF data shows a slight decrease. However, during the remaining time there is a large positive gradient with time as shown by all three sources of data.

3.2 Aerosol spectral evolution

Fig 2 shows hydrated aerosol spectra over the accumulation and coarse modes, where each spectrum has been averaged over ~30 mins of sampling within the surface-mixed layer (SML) of the MBL centred at the times given in the key. The distinction between the two modes can be seen at around 0.4 μm. Through the Lagrangian the accumulation mode progressively increases in magnitude but decreases in modal size. The coarse mode does not change significantly during the first 12

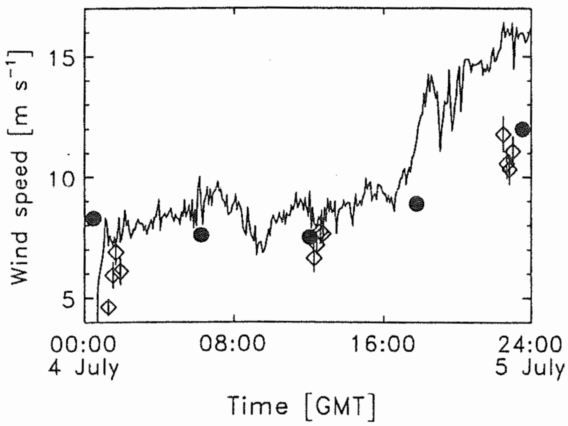

Fig 1. *Wind speed evolution as determined from (a) C-130 measurements (diamonds) adjusted to 10 m with the error bars showing +/- one rms, (b) ECMWF analyses at 10 m (circles), and (c) the change in the GPS position of the balloon (solid line).*

h of the experiment, but increases during the second 12 h. Although small in concentration terms (a few per cm^{-3} at most) there was a large increase in aerosol mass within the coarse mode of at least one order of magnitude.

The possible source of the particles could be one or more of: (1) entrainment from the LFT; (2) fresh particles from the sea surface; (3) growth of Aitken mode particles (i.e. < 0.1 µm). No data on the Aitken mode is available from the aircraft, but the ship data shows that at the start of the Lagrangian, the Aitken mode was positioned at about 27 nanometres dry particle diameter.

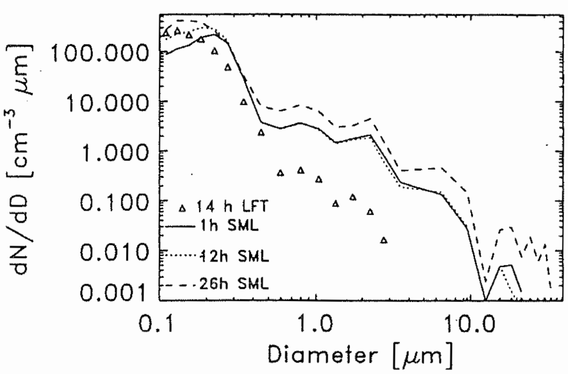

Fig 2. *Hydrated aerosol size distributions from within the SML averaged over 30 mins each and centred on the times shown. One spectrum is also included (diamonds) from the LFT 14 h into the period.*

The aerosol spectra from the LFT in Fig 2 shows the time (about 14 h in to experiment) at which concentrations in the LFT were highest, but still significantly lower than the MBL. In the coarse mode entrainment can be ruled out as a source of particles in this case. Growth from the accumulation to the coarse mode acts on a time scale slower than the residence time of the particles and can also be ruled out. Therefore production of sea-salt particles seems the only possible explanation. For the accumulation mode, entrainment could explain a small fraction of the increase in the range 0.1-0.2 µm. Aerosol entrained into the MBL will also grow by deliquescence due to the 10-15% increase in relative humidity (RH). As predicted by Fitzgerald et al. (1998) entrainment of LFT aerosol tends to fill in the gap (at ~0.1 µm) produced by cloud processing. The overall increase, however, in particle concentration between 0.1-0.4 µm within the SML must be due to processes in addition to entrainment.

3.3 Aerosol chemistry evolution

Table 1 displays the sulphate and 'sea-salt' (Na^+, Cl^- and Mg^{2+}) ionic mass concentrations at three times through the experiment by filter sampling. The aerosol sampling divided the particles into fine (<1.4 µm) and large (>1.4 µm) fractions.

Time	1	12	23
Large sulphate	0.129 (0.009)	0.159 (0.009)	0.227 (0.003)
Fine sulphate	0.257 (0.077)	0.446 (0.030)	0.476 (0.064)
Large sea-salt	1.299 (0.058)	1.485 (0.075)	2.425 (0.108)
Fine sea-salt	0.239 (0.192)	0.413 (0.121)	0.498 (0.194)

Table 1. *Mass concentrations (µg m^{-3}) of SO_4^{2-} and of the sum of Na^+, Cl^- and Mg^{2+} ions (sea-salt) for the large fraction (>1.4 µm) and fine fraction (>1.4 µm) of aerosol particles collected from bulk filter samples within the SML. Times are in hours. Analytical errors shown in brackets.*

Both sea-salt and sulphate increased with time in both size fractions. The fine sea-salt mass more than doubled but the errors are relatively large and they overlap between 1 h and 23 h into the experiment. More sea-salt existed in the large fraction than the fine fraction, although sulphate was higher in the fine than large fractions. It was further determined that the sulphate increase in the large fraction was associated solely with sea-salt particles, although sulphate/sodium mass ratio was only a maximum of 15 % higher than is found in natural sea water. For the fine fraction, the sulphate increase was partitioned approximately equally between sea-salt and non-sea-salt sulphate. Additionally, there was a change from NH_4HSO_4 to $(NH_4)_2SO_4$ which indicates neutralisation through internally-mixed alkaline sea-salt particles.

Therefore it would seem that the increase in mass (and probably also number) in the fine fraction is due to a combination of sea-salt production and non-sea-salt sulphate production, perhaps via cloud processing. But because the fine fraction size range overlaps our definition of coarse mode, then some of this fine fraction sea-salt increase may actually lie within the coarse mode and so not contribute to the modal increase at small sizes shown in Fig 2. This indicates that growth of particles from the Aitken mode into the accumulation mode maybe important in explaining the modal increase.

3.4 Aerosol concentration evolution

The aerosol spectra within the SML has been divided into accumulation (0.1-0.4 µm) and coarse (>0.4 µm) modes with the total particle concentrations denoted as N_A and N_C, respectively. Fig 3 shows the variation of N_A and N_C with U_{10}. N_C is very much lower than N_A and showed an increase between wind speeds of 8-10 m s^{-1}, but no increase at lower speeds. This is consistent with previous observations of a significant increase in the upper end of the aerosol spectrum at wind speeds exceeding 10 m s^{-1} (O'Dowd et al.,1997). N_A increased through the range of measured wind speeds from 50 to around 160 cm^{-3} over the 26 h. However, as this was a Lagrangian

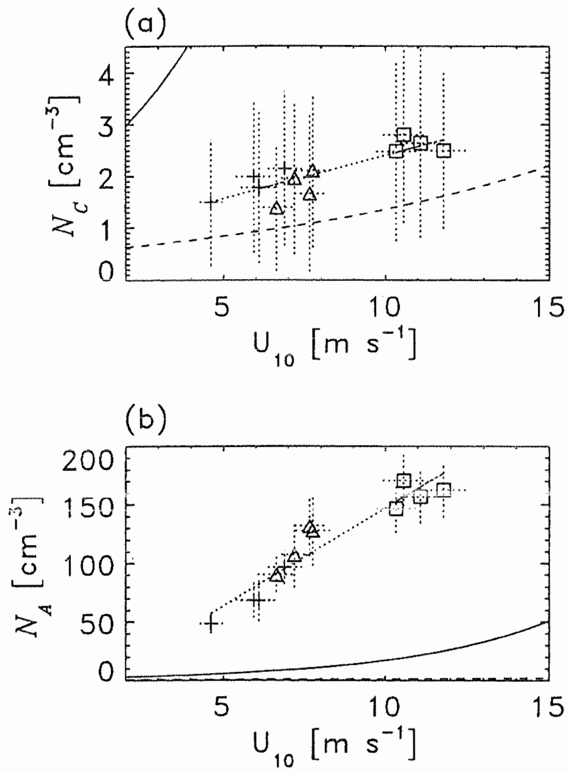

Fig 3. *Variation of (a) coarse mode (N_C >0.4 µm) and (a) accumulation mode (N_A <0.1-0.4 µm) aerosol concentrations with 10 m wind speed (U_{10}). The data has been divided into crosses (in the 0-2 h period), triangles (11-13 h) and squares (22-24 h). Each point is an average over a 40 km run. The error bars are +/- one rms. The solid and dashed lines are the O'Dowd et al. (1999) parametrisations explained in the text.*

experiment where U_{10} increased through the period, Fig 3(b) could actually be showing a correlation between N_A and time and therefore another process may explain the increase.

Also plotted in Fig 3 are the jet and film mode parametrisation of O'Dowd et al. (1999) in the dashed and solid lines respectively. The equations of these lines that represent the film and jet mode number concentrations N_{film} and N_{jet} for log-normal modes positioned at dry particle sizes 0.2 µm and 2 µm are:

$$\log N_{film} = 0.095 U_{10} + 0.283 \quad (1)$$

$$\log N_{jet} = 0.0422 U_{10} - 0.288 \quad (2)$$

respectively. These dry sizes would correspond to sizes of around 0.4 and 4 µm for NaCl at 80 % RH. The gradient of the jet parametrisation curve in Fig 3(a) is similar to that of the observations, although with lower concentrations. This difference in observations could be explained by the difference in position of the observed and parametrised modes, where the observed mode lies at a smaller size where concentrations tend to increase. As for the film mode which is comparable to our accumulation mode, the concentration increase over the observed increase in U_{10} is lower by nearly an order of magnitude than the observations. Even the relative increase in N_A between the start and end of the experiment and the gradient of N_A with U_{10} is much greater than the parametrisation.

3.5 CCN and cloud physics evolution

The changes described above would be expected to cause changes in the cloud microphysics through evolution of the CCN activation spectra. The non-precipitating cloud cover within the MBL was fractional and consisted of cumulus, on occasion reaching the inversion and spreading into stratocumulus. The average cloud droplet concentration increased from 65 cm^{-3} to 120 cm^{-3} over the 26 h period. The increase in aerosol number at sizes between 0.1-0.4 µm (i.e. where at the start of the period there is a Hoppel-type dip) explains this droplet concentration increase. Use of a CCN spectrometer provides with an additional link between aerosol and cloud droplet measurements. Fig 4(a) shows curves produced by the spectrometer for supersaturations (S) between 0.1 and 1% at the times shown in the key. Each spectrum is an average of four curves or samples. The error bars represent the minimum and maximum variability over these four samples at each discrete S.

Through the Lagrangian, the concentration of activated droplets increases for all S, although there is some overlap of error bars between 12 h and 23 h at medium to high S. The gradient of the curve also increases with time indicating more Aitken mode particles can be activated at medium to high S. Even though the total CN within the SML decreased from 1000 cm^{-3} to 750 cm^{-3} through the period, these CCN curves indicate that the Aitken mode grew to larger sizes with time, thereby decreasing the critical S required for activation. The 1 h spectrometer curve is relatively flat and so we would expect a low response to changes in S. At later times with a steeper gradient, this response increases. The LFT spectrum at 14 h shows, like the associated aerosol spectrum in Fig 2, that entrainment of LFT air into the MBL may have played a role in modifying the CCN and hence cloud droplet characteristics.

Fig 4(a) also includes an activation curve derived using Kohler theory from a dehydrated aerosol spectrum taken on the ship at 0 h. This aerosol spectrum covered the accumulation and Aitken modes

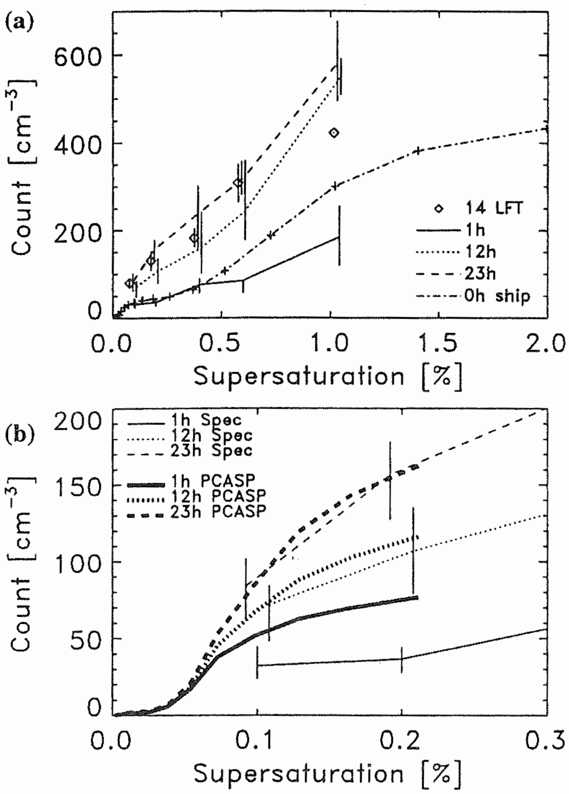

Fig 4. *CCN spectra: (a) measured with a spectrometer at 1h, 12h, and 23h in the SML, at 14h in the LFT, and a derived curve from the ACE-2 ship aerosol spectrum at 0 h; (b) derived from the aerosol spectra in Fig 2 together with the spectrometer curves over a reduced supersaturation range.*

thereby providing information at large *S*. The conversion from an aerosol spectrum to a CCN activation curve assumed all the aerosol was composed of $(NH_4)_2SO_4$. There is good agreement between this curve and the aircraft CCN curve at 1 h for low to medium *S*. At higher *S* the ship curve increases at a greater rate.

In Fig 4(b) are three curves derived from aerosol spectra such as shown in Fig 2, together with the CCN spectrometer curves shown in Fig 4(a) over a reduced range of *S*. The aerosol spectra were 'dehydrated' from their ambient 80 % RH based on a growth factor of 1.4. $(NH_4)_2SO_4$ composition was again assumed. The maximum derived *S* from these spectra is 0.21 %, which represents hydrated particles of 0.1 μm. At 1 h the spectrometer curve is lower than the derived curve, but through the period the curves overlap each other more closely. Discrepancies between the curves could be explained through approximation of the aerosol chemistry and the growth factor. The greater discrepancy at 1 h compared to later on indicates the assumptions used in the Kohler derivation were more accurate later on in the experiment.

4 SUMMARY AND CONCLUSIONS

This unique dataset showing aerosol and CCN modification in a Lagrangian framework where the wind speed markedly increased gave us the opportunity to validate a previous sea-salt production parametrisation. The O'Dowd et al. (1999) jet mode curve (Eq. 2) agreed reasonably well with our observations. The associated film mode (Eq. 1) could not be so well validated due to analytical limitations within the aerosol accumulation mode.

Evolution of accumulation mode aerosol, relative to the coarse mode, is complex even within a clean maritime airmass. There are sources of aerosols from the LFT, sea surface and growth of Aitken mode aerosol by cloud processing, coagulation, trace gas condensation, or a combination of these processes. One missing link in this analysis is a size-resolved chemical composition of the aerosol. Without knowledge of this for the 0.1-0.4 μm size range, then it is difficult to explain the reason for the increase in N_A through the experiment. Detailed aerosol modelling could help resolve this problem.

The three-fold increase in N_A over a 26 h period, contained within the 0.1-0.4 μm size range, controlled the number of CCN and hence cloud droplets. This shows that even in a clean maritime airmass large changes in the cloud physics are possible that will affect the radiative properties of the cloud.

5 ACKNOWLEDGEMENTS

ACE-2 was supported by the European Union under contract ENV4-CT95-0032, and the UK Department of the Environment, Transport and the Regions. Thanks go to the C-130 aircrew of the Royal Air Force.

6 REFERENCES

Fitzgerald et al. (1998), A one-dimensional sectional model to simulate multicomponent aerosol dynamics in the marine boundary layer 2. Model application. *J. Geophys. Res.*, **103**(D13), 16,103-16,117.

Johnson et al. (2000), Observations of the evolution of the aerosol, cloud and boundary layer characteristics during the first ACE-2 Lagrangian experiment. *Tellus*, **52B**(2).

O'Dowd et al. (1997), Marine aerosol, sea-salt and the marine sulphur cycle: a short review. *Atmos. Environ.*, **31**(1), 73-80.

O'Dowd et al. (1999), Coupling sea-salt and sulphate interactions and its impact on cloud droplet concentration predictions. *Geophys. Res. Lett.*, **26**(9), 1311-1314.

Raes, F. (1995), Entrainment of free tropospheric aerosols as a regulating mechanism for cloud condensation nuclei in the remote marine boundary layer. *J Geophys. Res.*, **100**(D2), 2893-2903.

Smith et al. (1998), Role of sea salt aerosol in the indirect radiative forcing of climate. *J. Aerosol Sci.*, **29**(Suppl. 1), S51-S52.

CLOUD PROCESSING OF AEROSOL IN THE MARINE BOUNDARY LAYER

Graham Feingold[1] and Sonia M. Kreidenweis[2]

[1] NOAA Environmental Technology Laboratory, 325 Broadway, Boulder CO 80303

[2] Department of Atmospheric Science, Colorado State University, Fort Collins, Colorado 80523

1. INTRODUCTION

Over the past decade studies have determined that cloud processing of aerosol through heterogeneous chemistry can have a marked effect on the aerosol size distribution. Through this process, hygroscopic particles that have grown into cloud droplets, are modified in size by the addition of nonvolatile mass that remains in the aerosol phase when the water is evaporated. One of the most studied examples is the addition of sulfate mass due to aqueous conversion of S(IV) to S(VI) (e.g., Hoppel et al., 1990; Hegg et al., 1996; Feingold et al, 1998; Zhang et al., 1999). Aerosol size spectra that have undergone cloud processing are characterized by bimodal spectra with one mode of particles resulting from those that did not participate as CCN and a second mode in the region of 0.1 μm radius comprising those that were affected by processing. This process is important because it influences both the aerosol direct effect (Hegg et al., 1996) by generating particles that are efficient scatterers, as well as the indirect effect, by creating particles that are larger in size, and therefore more efficient cloud condensation nuclei (CCN). If this results in a higher drop concentration N, then the clouds will be more reflective (assuming the same liquid water content, LWC), and less apt to form precipitation. Heterogeneous cloud processing is ubiquitous, but particularly effective in SO_2 rich, areas, and therefore there is interest in the climatic implications of this process.

Bower and Choularton (1990) presented results that showed that when aerosol spectra have undergone prior processing there is an enhancement in N in subsequent cloud cycles. Hegg et al. (1996) contrasted a case with significant enhancement in CCN (at a specified supersaturation) with one where enhancement was small. Feingold et al. (1998) showed that heterogeneous processing of aerosol may not necessarily enhance the number of drops in subsequent cloud cycles. For the aerosol size distribution used as input in that study, N was not enhanced by processing. Moreover, the fact that processing had increased the size of some of the particles resulted in a slight enhancement in the growth of larger drops and precipitation formation.

The goal of this paper is therefore to perform a more general evaluation of the effect of this cloud processing on cloud microphysical and optical properties in clouds that form downwind of where processing occurred.

Corresponding author address: Graham Feingold, NOAA ETL, 325 Broadway, Boulder, CO 80303; e-mail: gfeingold@etl.noaa.gov

2. MODEL

2.1 Coupled Microphysical/Chemistry Model

The modeling framework is described in Feingold et al. (1998) and Zhang et al. (1999). Individual parcel models are driven along kinematic trajectories derived from a large eddy simulation of the marine boundary layer. Thus each trajectory has a LWC time history describing its contact time with the cloud. The model simulates aerosol water vapor uptake, condensation growth and sulfate chemistry. Oxidation of S(IV) occurs via O_3 and h2o2. Gas-phase chemistry is not simulated and the parcel is assumed to be closed. The input aerosol is assumed to be a completely soluble ammonium sulfate aerosol, defined by a lognormal function prescribed over the size range (0.011 μm; 1.1 μm) at 50 discrete points. As heterogeneous processing proceeds, the ratio of ammonium to sulfate ions changes accordingly. An example of the effect of cloud processing is shown in Figure 1 for one individual trajectory, and for 1 input aerosol spectrum.

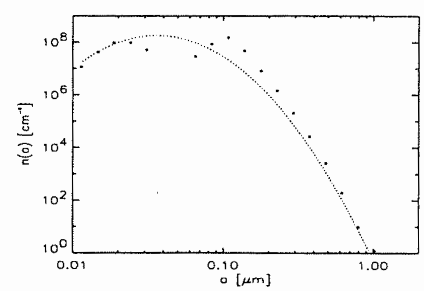

Figure 1: *Example of an unprocessed lognormal input spectrum (dotted line) and the processed spectrum (dots) following cloud contact.*

2.2 Lagrangian Parcel Model

An adiabatic parcel model (APM) (Feingold and Heymsfield, 1992) is now used to assess the impact of processing on a subsequent cloud cycle. The APM represents the hygroscopic growth of the CCN and droplet condensation but does not represent any heterogeneous chemistry. It is used here to determine the number of drops N activated in the adiabatic updraft. It is a convenient way of estimating the sign and magnitude of the impact, although it should be borne in mind that this model is not as realistic a representation of real clouds as, e.g., the LES. The difficulty of using the LES for these exercises is that (a) it does not represent droplet growth and activation as accurately as the APM, and (b) it requires enormous computation time for each simulation, thus limiting the amount of phase space that can be covered.

Both unprocessed (lognormal) and processed CCN spectra (one example of which is shown in Fig. 1), are now used as input to the APM. The input lognormal spectrum is varied such that $0.03 \leq r_g \leq 0.09$ μm, $1.5 \leq \sigma \leq 1.9$, and $100 \leq N_a \leq 5000$ cm^{-3} for a total of 125 CCN spectra. The 125 spectra, together with their processed counterparts, are input to the APM at 7 different updraft velocities, namely, w=20, 50, 75, 100, 150, 200, and 300 cm s^{-1} . This yields a total of 875 APM runs for each of the simulations – i.e., 875 runs for the unprocessed case, and 875 runs for the processed case.

3. RESULTS

Figure 2 shows the % difference between $N$for the processed case and N for the unprocessed case:

$$\delta N = 100 \cdot \frac{N_p - N_{up}}{N_{up}} \qquad (1)$$

where N_p and N_{up} are the drop number concentrations for the processed and unprocessed cases, respectively, calculated when N reaches a maximum in the APM. Note that δN varies over a range of about -30% to 150% and although the positive δN are considerably larger than the negative δN, there are frequent occurrences of negative δN (135 data points for $\delta N <$ -5% and 202 points for $\delta N >$ 5%).

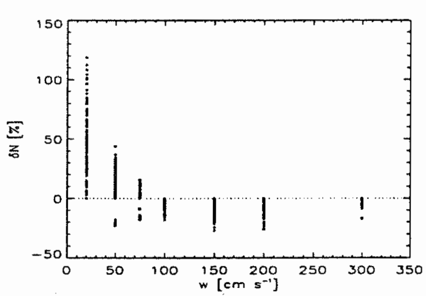

Figure 2: *δN as defined by Eq. (1) as a function of updraft velocity w in the adiabatic parcel model.*

There is no systematic change in δN as a function of either r_g, σ, or N_a.

In order to explore the dependence of δN on w we consider the definition of drop number N :

$$N = \int_{r_{cut}}^{r_{max}} n(a)da \qquad (3)$$

where r_{cut} is the size of the smallest activated CCN, and r_{max} is the maximum particle radius. The cut-off radius r_{cut} can be calculated from simple formulae (e.g. Pruppacher and Klett, 1997), or directly from the model data. Note that w, S_{max}, and r_{cut} are not independent parameters and are intimately related to one another; e.g., larger w are associated with larger S_{max} and smaller r_{cut}. Figure 3 plots S_{max} for the processed cases vs. S_{max} for the unprocessed cases. In all cases, the effect of processing is to diminish the value of S_{max}, regardless of the CCN input or the magnitude of w. The processed particles are larger, their Köhler curves are displaced to larger radii and lower supersaturations, and they are therefore more efficient at taking up vapor and grow more readily. Because processing diminishes S_{max}, r_{cut} for the processed case is always larger than r_{cut} for the unprocessed case. By affecting the solute term in the droplet growth equation, the incorporation of more sulfate material into a droplet through heterogeneous chemistry may differentially enhance the growth of one part of the drop population and can result in drop spectral broadening in weakly forced clouds.

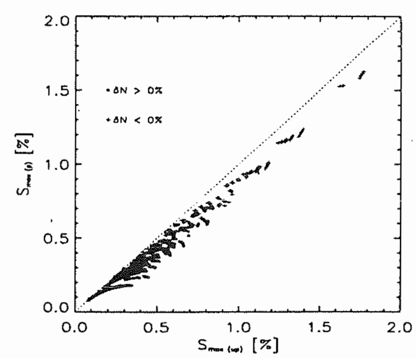

Figure 3: *Maximum supersaturation attained in the APM for the processed cases ($S_{max(p)}$) vs. maximum supersaturation for the unprocessed cases ($S_{max(up)}$).*

We now define three different r_{cut} parameters; the first, $r_{cut(0)}$ pertains to the coupled micro physics/chemistry model responsible for the processing, and is related to the dynamics of the LES-derived trajectory. The second, $r_{cut(up)}$ pertains to the unprocessed lognormal spectra used as input to the APM; the third, $r_{cut(p)}$ pertains to the processed spectra (the output spectra from the microphysics/chemistry model) that are input to the APM. The relative positions of these cut-off radii are illustrated in Figure 4.

At small w, only the larger particles are activated and since this is the region that experiences a large local increase in N_a through the growth of smaller CCN, δN tends to be positive in spite of the fact that $r_{cut(p)} > r_{cut(up)}$. As w increases, increasingly smaller particles can be activated and if w is large enough, r_{cut} is located where there is no difference between the unprocessed and processed spectra ($r < r_{cut(0)}$). Bearing in mind that processing changes only the size of particles but not their total number concentration, the fact that $r_{cut(p)} > r_{cut(up)}$ translates to a decrease in the number of activated drops when $r < r_{cut(0)}$.

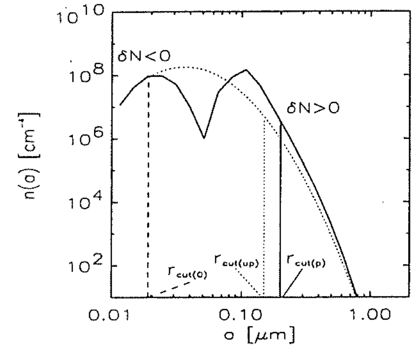

Figure 4: *Schematic of an unprocessed and a processed aerosol size spectrum showing the relative positions of $r_{cut(p)}$ and $r_{cut(up)}$, as well as the -δN and +δN regimes. The -δN regime lies in the region $r_{cut(p)} < r_{cut(0)}$.*

In Figure 5a δN is plotted as a function of $r_{cut(p)}/r_{cut(0)}$. A fairly distinct threshold between +δN and -δN is seen at $r_{cut(p)}/r_{cut(0)} \approx 1$. When the δN data are plotted in $r_{cut(p)}/r_{cut(0)}$; w phase space (Figure 5b) it can be seen that there is a clustering of +δN towards larger $r_{cut(p)}/r_{cut(0)}$ and smaller w while -δN points exist at $r_{cut(p)}/r_{cut(0)}$ <1 and higher w. Further tests show that these results are consistent for different chemical processing scenarios and different cloud trajectories.

4. DISCUSSION

Figure 4 is a schematic representation of a processed and an unprocessed aerosol spectrum showing the -δN and +δN regimes as well as the relative positions of r_{cut} parameters, and serves to summarize the results. In general processed spectra, when input into the APM, generate lower S_{max} than for the unprocessed lognormal regardless of w (Figure 3). This means that $r_{cut(p)}$ is always > $r_{cut(up)}$. Despite this, there is a general enhancement in N at low S_{max} because the difference in r_{cut} does not make up for the fact that the area under the processed spectrum for $r > r_{cut(p)}$ is so much larger due to the local increase in the number of particles that have grown into this range by chemical processing (Figure 4). However, as one gets to the highest S_{max} (or lowest r_{cut}), the fact that S_{max} for the processed case is smaller than that for the unprocessed case, dominates. At these high S, we are entering the regime where the spectra are quite similar. Therefore, lower S translates quite simply to smaller N, and negative δN. Figure 5 is an alternative, but equivalent way of demonstrating this result.

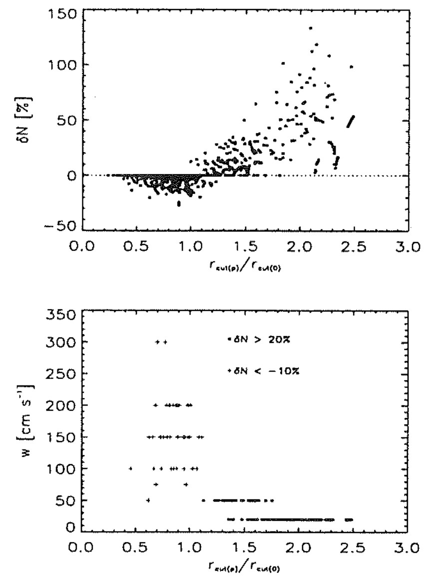

Figure 5: *(a) δN as a function of the ratio of r_{cut} parameters. $r_{cut(p)}$ is the smallest particle radius activated when the processed spectrum is used as input to the APM. $r_{cut(0)}$ is the smallest particle radius activated in the trajectory model. (b) Vertical velocity w in the APM as a function of the ratio of the r_{cut} parameters defined in (a).*

The implications of heterogeneous processing of aerosol for radiative effects are twofold; firstly, the particles on the order of 0.1 μm radius generated by heterogeneous processing are very efficient scatterers in the visible and therefore their direct effect is considerable (Hegg et al., 1996). The implications for the indirect effect are less easily defined. Enhancement in drop number concentration will tend to generate clouds that are more reflective and less apt to precipitate. Their enhanced lifetimes will increase the amount of processing that occurs, provided there are ample sources of SO_2 and oxidants. If all other conditions are equal, this might imply a positive feedback process that produces brighter and more colloidally stable clouds. However, it is intuitive that this process will likely reach saturation. The fact that precipitation does occur intermittently in marine boundary layers suggests that this cycle is broken at some point. We have seen here that δN is negative when w is high, therefore periodic vigorous updrafts may cause a decrease in drop number. These more vigorous clouds will penetrate higher and generate more liquid water, thereby further increasing the chances of a reduction in N as collision-coalescence ensues. Wetter clouds are more likely to precipitate, so all these factors work in unison.

Another mechanism for breaking the cycle of increasing N is the presence of a sufficiently strong background of giant CCN particles emitted by the ocean, or transported from afar. Feingold et al. (1999) showed that concentrations of giant CCN of 10^{-3} cm^{-3} are sufficient to generate collision-coalescence in stratocumulus at background CCN concentrations of up to 250 cm^{-3} and liquid water mixing ratios of about 0.5 g kg^{-1}. Giant CCN may therefore provide another important regulating role in this process.

We have confirmed that under certain conditions, primarily low w in the subsequent cloud, a processed aerosol spectrum does produce an increase in N. However, it has also been shown that processing frequently results in a decrease in N, although these decreases tend to be more modest than the enhancements in N. Because a typical boundary layer probability distribution function of (positive) vertical velocities is such that lower vertical velocities are more frequent, it is hypothesized that the overall result of processing will be an enhancement in N. Bearing in mind that for clouds of similar LWC, the relative decrease in drop effective radius r_e is approximately one-third of the relative increase in N, the fact that negative δN are so frequent, even at w as low as 50 cm s^{-1} , suggests that impacts on cloud radiative properties may be much less than previously suggested.

ACKNOWLEDGMENTS

The authors acknowledge support from NOAA/OGP under grant # NA67RJ0152.

REFERENCES

Bower, K. N., and T. W. Choularton, 1993: Cloud processing of the cloud condensation nucleus spectrum and its climatological consequences. *Quart. J. R. Meteor. Soc.*, **119**, 655–679.

Feingold, G., and A.J. Heymsfield, 1992: Parameterizations of condensational growth of droplets for use in general circulation models. *J. Atmos. Sci.,* **49** , 2325–2342.

Feingold, G., S. M. Kreidenweis, and Y. Zhang, 1998: Stratocumulus processing of gases and cloud condensation nuclei: Part I: trajectory ensemble model. *J. Geophys. Res.,* **103,** 19,527–19,542.

Feingold, G., W. R. Cotton, S. M. Kreidenweis, and J. T. Davis, 1999: Impact of giant cloud condensation nuclei on drizzle formation in marine stratocumulus: Implications for cloud radiative properties. *J. Atmos. Sci.,* **56,** 4100-4117.

Hegg, D. A., R. Majeed, P. F. Yuen, M. B. Baker, and T. V. Larson, 1996: The impacts of SO_2 oxidation in cloud drops and in haze particles on aerosol light scattering and CCN activity. *Geophys. Res. Let.,* **32,** 2613–2616.

Hoppel, W. A., J. W. Fitzgerald, G. M. Frick, and R. E. Larson, 1990: Aerosol size distributions and optical properties found in the marine boundary layer over the Atlantic ocean. *J. Geophys. Res.,* **95,** 3659–3686.

Pruppacher, H. R., and J. D. Klett, 1997: *Microphysics of Clouds and Precipitation.* Kluwer Academic Publishers, 954 pp

Zhang, Y., S. M. Kreidenweis, and G. Feingold, 1999: Stratocumulus processing of gases and cloud condensation nuclei: Part II: chemistry sensitivity analysis. *J. Geophys. Res.,* **104,** 16,601–16,080.

LABORATORY STUDY OF TEMPERATURE CHANGES DURING FREEZING OF SULFURIC ACID/WATER CLOUDS.

Shubhangi Tavker[1] and P. Pradeep Kumar[2]

[1&2]Department of Physics ,University of Pune, Pune, Maharashtra , 411007, India

1. INTRODUCTION

Engine exhaust products of high flying jet aircrafts are assumed to be an important source of new particles in the upper troposphere and lower stratosphere (Hofmann and Rosen,1978; Arnold et al., 1992; Schumann et al., 1996). Even though the absolute emissions by air traffic are small in comparison to surface emissions their residence time is long, their background concentrations are low, and their radiative sensitivity is high in the upper troposphere and lower stratosphere (Goodman et al., 1998). Contrail ice particles are supposed to be formed by the particles generated in combustion process which likely acquire a coating of sulfuric acid in young plume (Jensen et al., 1994). In some regions of heavy air traffic, the frequency of contrails and contrail induced cirrus may reach 10-20% of the natural cirrus amount, suggesting that contrails may cause climatic effects.

Present experiments aim to study in laboratory the varaition in latent heat released on formation of clouds from vapors of H_2SO_4 /H_2O and their subsequent freezing.

2. EXPERIMENTAL DETAILS

Experiments are conducted in a spherical glass chamber with extended cylindrical limbs on top and bottom.The chamber is kept inside a walk in coldroom

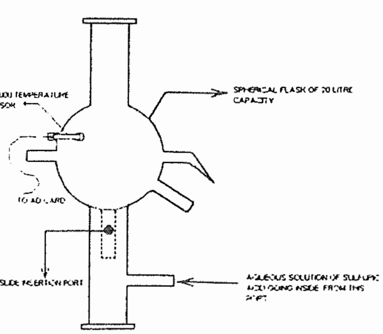

Fig 1 Schematic arrangement of Experimental set up

room having lowest temperature of –30°C. Aqueous solution of sulfuric acid of a particular concentration (either 0%,10%,50% or 70% by weight) is heated at a controlled rate and the vapor is introduced into the precooled chamber to form a cloud of supercooled drops and vapor. A PT-1000 sensor records the temperature at approximately middle of the cloud and the data is recorded in real time on computer. On reaching a steady state temperature, cloud is seeded by introducing a rod dipped in LN_2 momentarily into the cloud. This results in homogenous nucleation and crystal formation due to sudden adiabatic cooling in the region surrounding the rod. The crystal number further increases by other ice multiplication processes.

3. RESULTS AND DISCUSSION

We have observed that during crystallization of a cloud containing supercooled droplets and vapors of H_2SO_4 /H_2O there is a temperature increase just moments after ice crystal formation has started in the cloud. This observed temperature increase is more as the acid concentration increases. It is also observed that the number density and size of ice crystals do not vary significantly with acid strength. It is therefore possible that this increase in temperature with increasing acid concentration is because more latent heat is being released during the freezing of acid drops as compared to pure water. Collins [1933] has determined the latent heat of vaporization for sulfuric acid and has found that it increases with acid concentration and the values at 0 °C for pure water is 587 cal/gm and for 70 % acid it is 674 cal/gm. As latent heat of vaporization is also a function of temperature, Collins (1933) has given an empirical relation for his experimental data set. Pruppacher and Klett (1978) have shown that the latent heat of melting also increases with impurities.

Other possibility also exists that acid does not freeze even in near contact of LN_2 rod, only water part freezes. Even if vapor supply is turned off the ice

[2] Corresponding author's address: P.Pradeep Kumar
Dept. of Physics, University of Pune, Ganeshkhind, Pune, Maharashtra, 411007, India .
Email: ppk@physics.unipune.ernet.in

particle growth tends to produce ice saturation, and it will take a while for evaporation to begin to occur. The end result however, would be the same, an acid coated ice particle.

Fig. 2 shows the microphysical parameters of the cloud one minute after the crystal formation was initiated in the cloud. The values shown are average values for about 25 runs taken at that particular concentration. It is observed that the temperature increase during the first minute after crystals have started forming is 0.2 °C when the cloud is formed from pure water and is 0.4 °C when the cloud is formed from 70 % sulfuric acid. The number density of crystals for pure water is 20 crystals/mm^2/sec and that for 70 % sulfuric acid is 19 crystals/mm^2/sec. The mean size of crystals formed in pure water is 16 and that for 70% sulfuric acid is 18 μm.

Fig. 3 shows the microphysical parameters of the cloud three minutes after the crystals have started forming in the cloud. Fig. 3(a) shows that for pure water the increase in temperature is about 0.4 °C and for 70% sulfuric acid it is 0.7 °C. Fig. 3(b) shows that the number density of ice crystals is about 11 crystals/mm^2/sec for pure water and 9 crystals/mm^2/sec for 70% acid concentration. Fig. 3(c) shows that the mean size of the crystals for pure water is 28 μm and for 70% sulfuric acid concentration it is 32 μm.

To test the significance of the difference between the means of the observed temperature increase, a two-tailed t-test was used. The confidence level was very high (greater than 99%) for cases of water and 50% acid, water and 70% acid and for 50% and 70% sulfuric acid concentration.

The increase in cloud temperature at 50 % and 70% sulfuric acid concentration is almost twice as that seen for pure water runs. The same increasing trend is observed at one minute and three minutes after the crystal formation has started in the cloud. The difference in means for number density and crystal size between water and 50% or 70% sulfuric acid concentration is not significant.

The marginal variation in the mean size of crystals and number densities with increasing acid solution strength in the cloud cannot contribute significantly to the observed large increase in temperature during crystal growth in these clouds. The observed increase in temperature with increasing acid solution strength just after seeding could be because more latent heat is released during the freezing of acid drops

Figs 2 and 3 shows that the mean size of the crystals and the number densities do not vary significantly with acid concentration. Therefore it is unlikely that the observed large increase in temperature with increasing acid solution strength could be because of faster glaciation or crystal growth. It must be pointed out that we have not measured acidity of the cloud droplets directly, we have only measured the acid strength in the solution which was heated to form the cloud. The whole system is a closed system and there is no leakage of air into or out of the system.

In these chamber experiments it is expected that just after seeding the rapid ice growth could cause partial or complete evaporation of the unseeded droplets, producing cooling. Since the heat is higher for acid solutions, the acid droplets should cool the air more as they evaporate; yet the opposite effect is seen here. It is possible that the number of unfrozen droplets is very few in number and the cooling produced by them due to evaporation is not enough to counter the heating produced because of freezing.

In the contrail studies Petzold et al., [1997] have observed temperature excess of upto 11 °K from the ambient inside the plume. In the plume center the contrail particle concentration is of comparable magnitude for both (high and low) fuel sulfur contents while effective diameter and ice water content are lowered in the high sulfur fuel case compared to the low fuel sulfur case. We cannot compare our results to the contrail observations because our experiments were performed at higher temperatures. However, our observation that the increase in temperature with increase in acid solution moments after seeding could have some relevance to the climatic impacts which are likely to occur due to contrails. Condensation trails are formed by aircraft's, that have different engine types, and varying sulfur content and the composition of contrail cirrus differ from the natural cirrus formed at those altitudes.

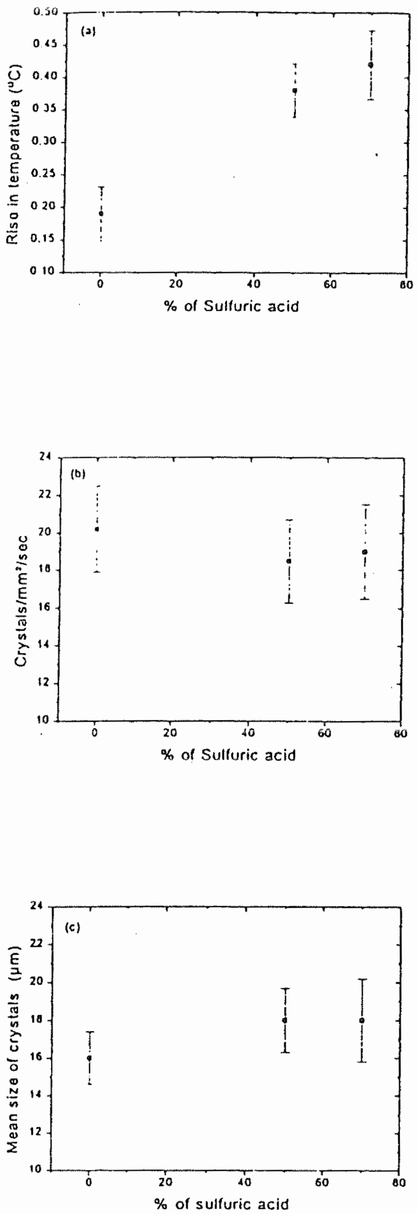

Fig.2 Microphysical parameters of the cloud one minute after seeding for different concentrations of sulfuric acid (a) Temperature rise in cloud (b) Number density of crystals. (c) Mean size of ice crystals

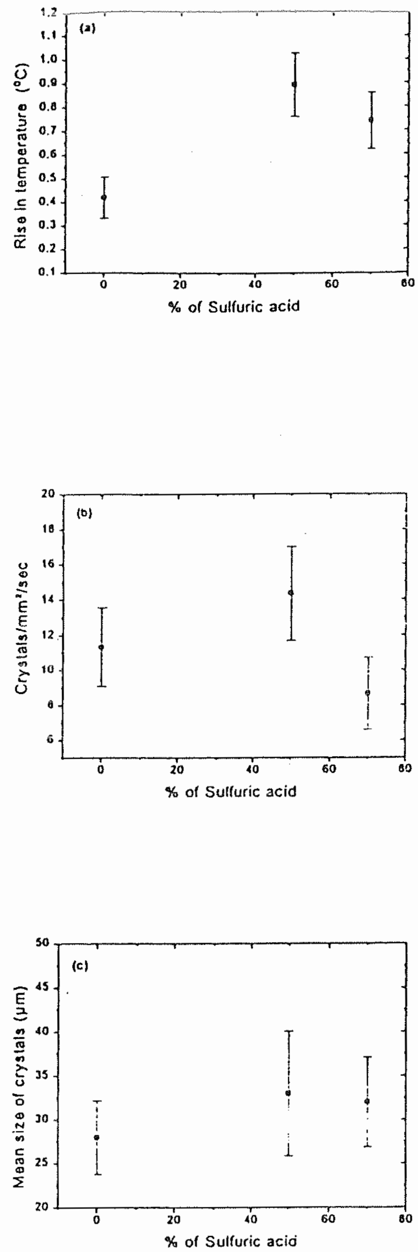

Fig.3 Microphysical parameters of the cloud three minute after seeding for different concentrations of sulfuric acid (a) Temperature rise in cloud (b) Number density of crystals. (c) Mean size of ice crystals

4. ACKNOWLEDGEMENTS

We acknowledge the financial support received from the United States Army for setting up the Cloud Physics Laboratory. We are thankful to Hugh Carlon and Jerry Comati of the United States Army Research for their support. We also thank Ken Sassen, University of Utah and Detlev Moller, Brandenburg Technical University for many helpful discussions. One of the authors S.T. is thankful to CSIR, India for the financial support

5. REFERENCES

Arnold, F., J. Scheid, Th. Stilp, H. Schlager, and M.E. Reinhardt, 1992: Measurements of jet aircraft emissions at cruise altitude I: The odd-nitrogen gases NO, NO_2, HNO_3. Geophys. Res. Lett., 19, 2421-2424.

Collins E.M.,1933: The partial pressures of water in equilibrium with aqueous solutions of sulfuric acid. J. Phys. Chem., 37, 1191-1203.

Goodman, J., R.F. Pueschel, E.J. Jensen, S. Verma, G.V. Ferry, S.D. Howard, S.A. Kinne and D. Baumgardner, 1998: Shape and size of contrail ice particles, Geophys. Res. Lett., 25, 1327-1330

Hofmann, D.J., and J.M. Rosen, 1978: Balloon observations of a particle layer injected by stratospheric aircraft at 23 Km. Geophys. Res. Lett., 5, 511-514.

Jensen, E.J., O.B. Toon, D.L. Westphal, S. Kinne and A.J. Heymsfield, 1994: Microphysical modelling of cirrus, 1., Comparision with 1986 FIRE IFO measurements. J. Geophys. Res., 99, 10,421-10,442.

Petzold, A., R. Busen, F.P. Schroder, R. Baumann, M. Kuhn, J. Strom, D.E. Hagen, P.D. Whitefield, D. Baumgardner, F. Arnold, S. Borrmann and U. Schumann, 1997: Near-field measurements on contrail properties from fuels with different sulfur content,.J. Geophys. Res., 102, 19,867-29,880.

Pruppacher H.R., and J.D. Klett, 1978: Microphysics of clouds and precipitation, 89 pp., D. Ridel publishing, Holland.

Schuman, U., On the effects of emissions from aircraft engines on the state of the atmosphere, 1994: Ann.Geophysicae,12,365-12,384.

NUMERICAL SIMULATION OF PROPAGATION OF AIR POLLUTANTS, RELEASED FROM A COAL POWER PLANT, DURING SNOWSTORM

V. P. Spiridonov1 and B. V. Telenta2

1Hydrometeorological Institute of Macedonia, Skopje 91000, Macedonia
2Foundation for International Studies, University of Malta, Valletta VLT07,Malta

1. Introduction

Some of the most severe exposure to harmful air pollutants occurs near individual industrial plants or industrial areas, usually located outside large centres of population. Metal smelters, oil and coal fired power plants, chemical industry are industrial sectors responsible for some of the major local air pollution problems. Concentration level of air constituents is obviously depends upon type of industry as well as emission conditions, mainly the height of stack, on local topography (e.g. flat terrain or basin or valley) and local meteorology. High air pollution exposure from industrial stacks typically occurs (in the valleys, when residential areas are located downwind from the plant in the prevailing wind direction) under unstable atmospheric dispersion conditions, strong vertical mixing etc. Principal air pollution impact near industrial sources is usually short-term (one to a few hours, although in favourable meteorological conditions, industrial plants may also give extremely high long-term impact).

In present study air pollution from a lignite power fired plant during snowstorm has been analysed. Investigation was done by numerical simulation of propagation of emitted gases such as: C02 , S02, N0x dust and C0. Air pollutants during cloud development are being transported in vicinity, affecting air quality and deposition in adjacent city.

A two dimensional cloud model (1) based on Klemp and Wilhelmson dynamics (2) and Lin, Farley and Orville microphysics and thermodynamics (3), has been used.

2. Model characteristics, numerical techniques and initial conditions

The current version of the model contains 10 prognostic equations: two momentum equations, thermodynamic and pressure equation, 4 continuity equations for the water substance (mixing ratios of the water vapor, cloud water and cloud ice are treated by one continuity equation), concentration equation and a subgrid kinetic energy equation (1). The concentration equation is written in the form

$$\frac{\partial C}{\partial t} = - V \cdot \nabla C + \nabla \cdot K \, \nabla C - W_d - W_w + S \qquad (1)$$

where, C is the concentration of pollutant, V is the wind vector, K is turbulent diffusion coefficient, W_d and W_w are wet and dry deposition, and S is the source term.

Model equations are solved on a semi - staggered grid. All scalar variables are block centered, while the velocity components are node centered. Horizontal and vertical advection terms are calculated by the centered fourth and second-order differences, respectively. Integration domain of the model was 34 km in x-direction and 9 km in vertical. Grid step was 1 km in horizontal and 0.5 in vertical direction. large time step was 10 s smaller one 2 s. Centre of the perturbation domain is located 17 km in

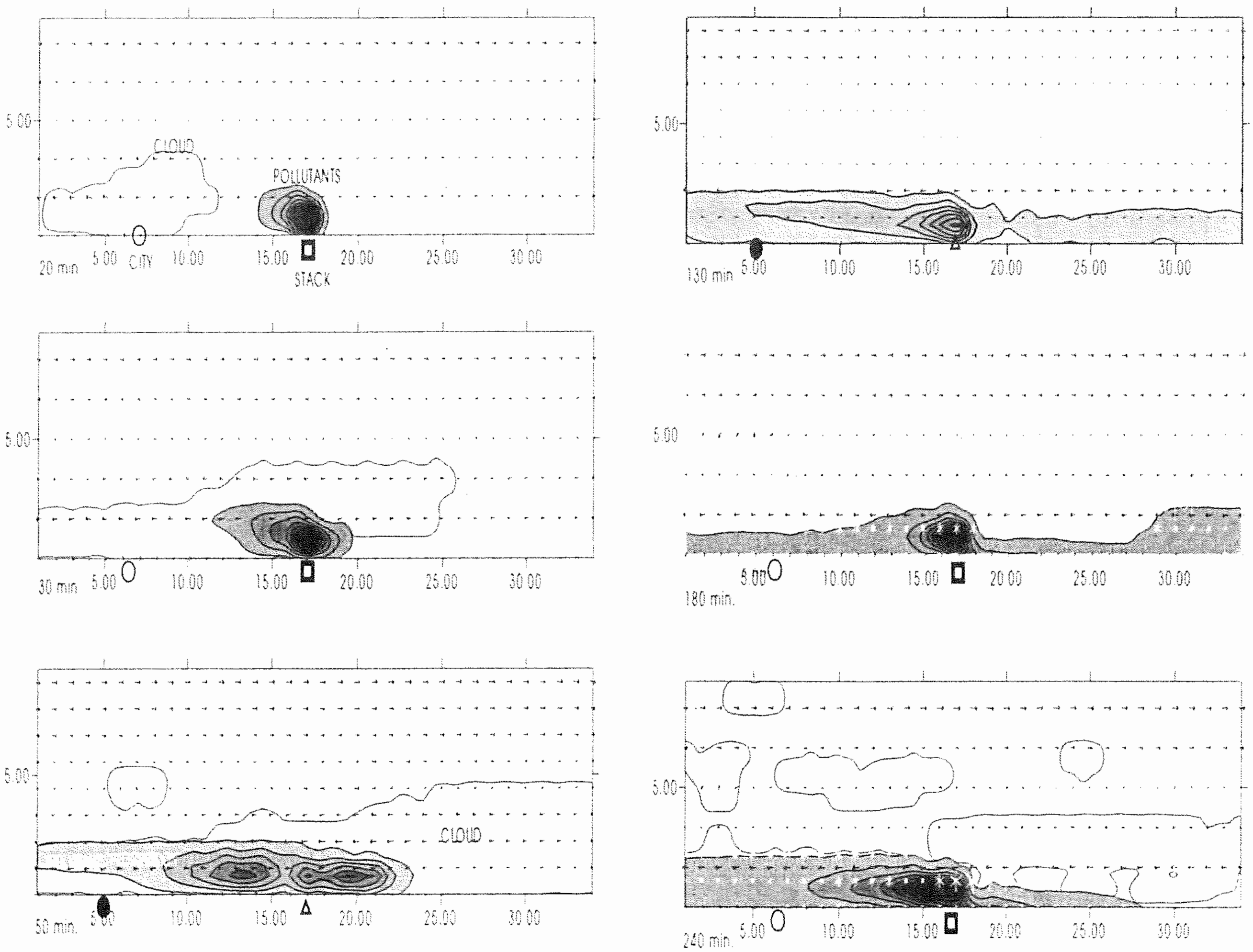

Fig.1 Simulation of cloud and pollutants progression , released from a plant on 2 December 1983

horizontal and 0.8 km in vertical direction. Model is initialised on atmospheric sounding for Skopje, Macedonia, on 2 December, 1983. Initial parameters for the horizontal velocity components, specific humidity , potential temperature and pressure are tnen interpolated in the geodetic co-ordinates of plant. A set of calculated data for emission rates of air pollution from a plant (hstack=252 m , dstack=8.75 m, emission rates for components: dust=61.2 mg/m^3 ; SO_2 =,1861 mg/m^3; CO_2 =11.2 % , NO_x= 188 mg/m^3 and CO=30 mg/m^3.The total volume of gas from two stacks reaches amount of 3,900,987 Nm^3/h .

3. Transport simulation during snowstorm

Cloud and pollutants progression from a plant which is find in centre of domain, in near surface layer (planetary boundary layer) has been simulated. Similar experiments have been done by Telenta and Antic (4) as well as Antic and Telenta (5). Cloud evolution and the spatial distribution of the air pollution at 20, 30, 80 , 130, 180 and 240 min are shown in fig. 1.

Maximum calculated values for parameters during simulation are: vertical velocity wmax = 5.1 m/s, horizontal velocity = 18.3 , the cloud base = 0.75 km, cloud top = 8.75 km , mixing ratios for cloud water =2.5 g / kg, cloud ice 0.16 g/kg, hail = 0.6 g/kg and snow 1.26 g/ kg.

Numerical simulation has shown typical appearance of snowstorm. Cloud development, evolution and stratification was followed by air pollution transport, released from a lignite power fired plant. Meteorological conditions were convenient for pollutants progression during dry case in first phase of simulation. Horizontal distance of spreading from the centre of the domain is 5 to 10 km in initial time of simulation, up to 15 km in both sides in later phase. Vertical diffusion of polluted cloud is around 2 km. Maximum calculated concentration rate of pollutants is 16 gr / m ^{3} in 130 min, when snow in small amounts was observed . Wet removal processes of pollutants during snowfall is started in 180 minute. Influence of the snow is evident , especially on upwind side of integration domain, where large amount of dose are calculated, even in the adjacent city. Total 24h accumulated height of fresh snow cover, observed on meteorological station located near plant, was 36 cm . Model calculated values for total accumulated snow for 240 min. simulation time, was 32.67 gr / cm ^{2} , or in terms of snow height taking into account snow density, is 3.3 cm for 4 hours simulation.. Good agreement is obtained for the calculated concentration of pollutants, especially for SO_2 , although model calculated results are compared with results from another winter cases, since the lack of measurements in the analysed period.

4. Conclusion

This paper presents a summary of simulation transport of air pollutants, released from a coal fired power plant during snowstorm. It was done by numerical simulation of passive pollutants transport in complex meteorological conditions using cloud model. Numerical experiment has shown growth, evolution and stratification of snowstorm. Accompanied air pollution components are transported through the atmosphere in dependence of atmospheric conditions. Wind conditions in the planetary boundary layer, has a dominant role of pollutants progression in first dry phase of simulation. Effects of buoyancy, turbulent diffusion and viscous dissipation are also evident. Vertical progression through diffusional growth is in reasonable limits. Wet removal processes together snowfall, are evident in later phase of simulation. Location of the city on the upwind side of the prevailing wind, is also influenced by the air pollution.

These investigations show that present model can be used for transport simulation od pollutants, and for the assessment of pollution impact of power plants or other sources, in safety and control assessment and comparative studies. Model is valuable in the presence of complex meteorological winter conditions.

REFERENCES:

Telenta, V. B. , 1988: A three-dimensional simulation of the 17 June 1978 HIPLEX case with observed ice multiplication. Second International Cloud Modeling Workshop, Touluse.

Klemp, B. J. and R.B. Wilhelmson, 1978: The simulation of three-dimensional convective storm dynamic. Journal of Atmospheric Science 35, 1070-1096.

Lin, Y.L. , R.D. Farly and W.D.Orville, 1983: Bulk parameterization of the snow field in a cloud model. Journal of Applied Meteorology, 22, 1065-1092.

Telenta, V. B. and D.Antic, 1990: An analysis of radiological impact of radionuclides from a coal fired power plant using cloud model. III. Italian-Yugoslav symposium. Low level radiation: Achievements, Concerns and Future Aspects. Plitvice, Yugoslavia.

Antic, D., and B. V. Telenta, 1991: Transport of radionuclides in the atmosphere during complex meteorological conditions. Transactions of the American nuclear Society. San Francisco, California.

NUMERICAL SIMULATION OF THE INTERACTION OF BIOMASS BURNING AEROSOLS AND CLOUD MICROPHYSICS

Christiane Textor[1] Hans-F. Graf[1] and A.P. Khain[2]

[1]Max-Planck-Institute for Meteorology, Bundestrasse 55, D-20146 Hamburg, Germany
[2]Institute of the Earth Science, The Hebrew University of Jerusalem, Givat Ram, Jerusalem, Israel

1 INTRODUCTION

Observations showed that emissions from vegetation fires influence cloud development (e.g. *Kaufman and Nakajima*, 1993). Not only the radiative properties of the clouds are changed but also their precipitation efficiency. Recent data demonstrated that smoke from vegetation burning could actually suppress warm rain in convective tropical clouds (*Rosenfeld*, 1999). Aerosol particles (APs) from biomass burning can serve as cloud condensation nuclei (CCN). High concentrations of APs result in high concentrations of nucleated droplets. This slows down droplet growth by diffusion of water vapor, and the sizes for the process of drop collisions to become efficient can not be reached. Vegetation burning can induce deep convective clouds, especially when the atmosphere is unstably stratified. Inside these clouds, fire emissions are lifted to higher altitudes where they can be transported over great distances. Differences in the cloud micro structure caused by biomass burning APs might affect the vertical transport of gases and particles: Scavenging by hydrometeors or aerosols removes the emissions from the gas phase, precipitation will finally lead to their deposition at the ground.

In addition, aerosol caused changes of precipitation rates in deep convective clouds over areas influenced by biomass burning, especially in the tropics, lead to differences in the vertical distribution of latent heat, probably affecting the atmospheric circulation (*Graf et al.*, 2000).

The processes inside the convective plume of a vegetation fire are investigated with the cloud-resolving numerical model ATHAM (Active Tracer High Resolution Atmospheric Model) (*Oberhuber et al.*, 1999; *Herzog*, 1998; *Graf et al.*, 1999). This model permits the consideration of both fire parameters (emission strength, fire temperature, etc.) and environmental conditions (atmospheric stability and humidity, etc.) on the mesoscale development of the plume. This study focuses on the investigation of the interaction between biomass burning aerosols and hydrometeors in the convective plume. We examine the effect of smoke particles on cloud microphysics, i.e. on precipitation efficiency.

Corresponding author's address: Christiane Textor, Max-Planck-Institute for Meteorology, Bundestrasse 55, D-20146 Hamburg, Germany; Email: textor@dkrz.de

2 THE PLUME MODEL ATHAM

The non-hydrostatic model ATHAM is especially designed to simulate high energy plumes. ATHAM consists of several modules: The dynamic part efficiently solves the Navier-Stokes equations for the gas-particle-mixture and includes the transport of active tracers (*Oberhuber et al.*, 1999; *Herzog*, 1998). The turbulence closure scheme provides the turbulent exchange coefficients for each dynamic quantity, thereby describing the entrainment of ambient air into the plume. The two moment bulk parameterization is used for the description of the model microphysics (*Textor*, 1999). The aerosol module describes particle growth and coagulation based on microphysical interactions between hydrometeors and particles ((*Textor et al.*, 2000). The soil module determines the amount of settled particles and hydrometeors and provides a consistent lower boundary condition for temperature and humidity.

The simulations have been performed in two dimensional cartesian coordinates, hence cross wind effects could be considered. The model domain was 25 km in the horizontal and 20 km in the vertical direction with a focusing grid ($\Delta x_{min} = 50\,m$). The simulation time was 30 min.

3 MICROPHYSICS

We expanded the two-moment bulk scheme following the approach of *Walko et al.* (1995) and *Meyers et al.* (1997) to include the interaction of hydrometeors with aerosols in ATHAM (*Textor*, 1999). The particles in the plume are described by their specific mass and number concentration as prognostic variables. Apart from water vapour, we consider the specific masses of four classes of hydrometeors, liquid as well and solid categories. We specify two different modes of biomass burning APs. For each AP size class, we define a category above the freezing temperature and one below. All classes of hydrometeors are allowed to contain APs. We assume that APs are always active as condensation nuclei for liquid and ice clouds. The microphysical formulation is based on the concept of pure water with the biomass burning APs acting similar to hydrometeors as soon as they are coated with water.

4 NUMERICAL EXPERIMENTS

The conditions of the fire were chosen according to the FIRESCAN campaign in Central Siberia (*Team*, 1996). The simulations took place at 60.45 °N with tropopause at 12 km. The relative humidity in the lower troposphere was rather low, the wind blew from the right with a velocity of 1 m/sec in the boundary layer and turns around to blow from the opposite side above. The fire emitted $8.6\ 10^{-6}$ kg/(m^{2}sec) aerosol particles with 90 wt % in the fine (radius= 0.1μm) and 10 % in coarse the mode (radius=50μm). The heat flux was about 10^4 W/m^2, and the water vapour flux amounted to $9.3\ 10^{-4}$ kg/(m^{2}sec).

The development of the biomass burning plume has been simulated with ATHAM. To illustrate the effect of interaction of hydrometeors and smoke particles we perform two sensitivity studies: In the Experiment A we consider the biomass burning aerosol particles to be active as CCN, in the experiment B only a background concentration of CCN as observed in rural areas influenced by maritime air is present (~200 CCN per cm^3). The results will be presented at the conference.

To illustrate the effect of interaction of hydrometeors and smoke particles we performed sensitivity studies with the two moment microphysics in a box model. An adiabatically rising air parcel with different numbers of CCN (200, 500 1000, 2000, and 5000 CCN per cm^3) was simulated in order to investigate the CCN effect on the amount of precipitation. The initial temperature was 294 K, the parcel was rising with a vertical velocity of 5 m/sec which corresponds to a cooling rate of ~0.03K/sec.

5 RESULTS

5.1 ATHAM

The plumes of total burning aerosol and condensed water after 30 min of fire as simulated by ATHAM are shown in Fig. (1). The plume tops reach a height of ~ 5 km. This is consistent with the observed plume height.

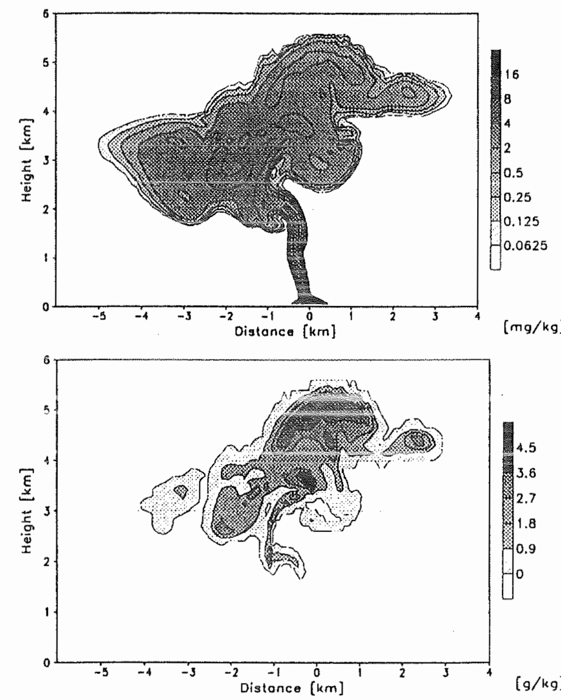

Figure 1: Plumes of total burning aerosols (upper panel) and total condensed water and ice (lower panel) after 30 min of simulated fire in [g/kg].

Caused by the lifting of humid air, a considerable amount of hydrometeors condenses, the highest fraction is in the liquid phase.

5.2 BOX MODEL STUDIES

In all experiments a similar amount of cloud water and cloud ice condenses, however, the more CCN are present, the smaller the droplet radius. The smaller droplet size suppresses the development of rain as shown in the upper panel of Fig. (2). However, the presence of high CCN concentrations does not only result in a decrease of rain water amount, it also suppresses the development of frozen precipitation as indicated in the lower panel of Fig. (2).

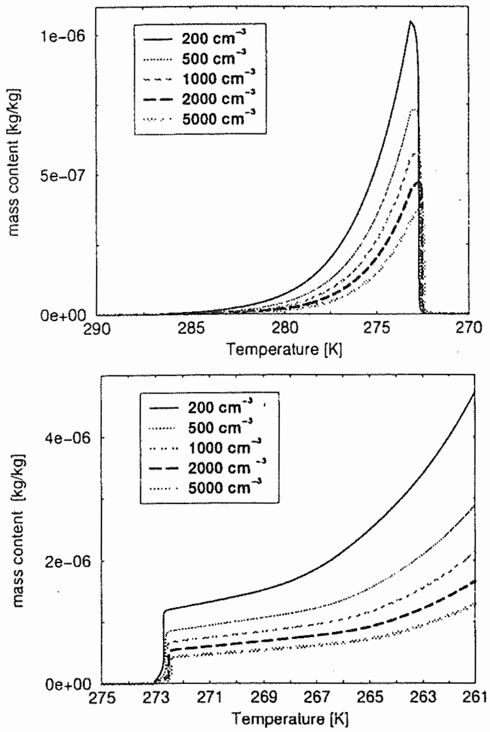

Figure 2: Mass content of rain (upper panel) and graupel (lower panel) in the box model simulation

6 CONCLUSIONS

This study shows the effect of biomass burning aerosol on the development of liquid and frozen precipitation in the convective cloud. Model simulations with the plume model ATHAM could represent the observed cloud shape and showed that a considerable amount of water condenses in the plume. Microphysical studies in a box model showed the number of CCN has a strong effect on the development of precipitation: the same amount of condensing water but a different supply of CCN leads to different drop sizes decreasing the amount of both rain and graupel.

The results are based on the assumption that vegetation burning APs are always active as CCN. This is not always true in reality. However, the knowledge of the size and the chemical properties of smoke particles is rather limited at the moment.

7 REFERENCES

Graf, H.-F., M. Herzog, J. M. Oberhuber, and C. Textor, The effect of environmental conditions on volcanic plume rise, *Journal of Geophysical Research*, *104*, 24309–24320, 1999.

Graf, H.-F., D. Rosenfeld, and F. Nober, The possible effect of biomass burning aerosols on local precipitation and global climate, *submitted to Geophysical Research Letters*, 2000.

Herzog, M., Simulation der Dynamik eines Multikomponentensystems am Beispiel vulkanischer Eruptionswolken, Ph.D. thesis, University of Hamburg, 1998.

Kaufman, Y. J., and T. Nakajima, Effect of amazon smoke on cloud microphysics and albedo analysis form satellite imagery, *Journal of Applied Meteorology*, *32*(4), 729–744, 1993.

Meyers, M. P., R. L. Walko, J. Y. Harrington, and W. R. Cotton, New RAMS cloud microphysics parameterization. Part II: The two moment scheme, *Atmospheric Research*, *45*, 3–39, 1997.

Oberhuber, J. M., M. Herzog, H.-F. Graf, and K. Schwanke, Volcanic plume simulation on large scales, *J. Volcanol. Geotherm. Res.*, *87*, 29–53, 1999.

Rosenfeld, D., TRMM observed first direct evidence of smoke from forest fires inhibiting rainfall, *Geophysical Research Letters*, *26*, 3105, 1999.

Team, F. S., Fire in ecosystems of boreal eurasia: The bor forest island fire experiment, fire research campaign asia-north (FIRESCAN), in *Biomass Burning and Global Change*, edited by J. S. Levine, pp. 848–873, MIT Press, Cambridge, Mass., 1996.

Textor, C., Numerical simulation of scavenging processes in explosive volcanic eruption clouds, Ph.D. thesis, University of Hamburg, 1999.

Textor, C., H.-F. Graf, and M. Herzog, Ash particle growth in explosive volcanic eruption plumes, *submitted to Journal of Volcanology and Geothermal Research*, 2000.

Walko, R. L., W. R. Cotton, M. P. Meyers, and J. Y. Harrington, New RAMS cloud microphysics parameterization. Part I: The single moment scheme, *Atmospheric Research*, *38*, 29–62, 1995.

Effects of cloud-aerosol interaction on precipitation formation and size distribution of atmospheric aerosols: numerical simulations using a spectral microphysics model

A. P. Khain and A. Pokrovsky
Institute of the Earth Science, The Hebrew University of Jerusalem, Givat Ram, Jerusalem, 91904, Israel

1. INTRODUCTION

Cloud-aerosol interaction is increasingly recognized as a one of the key factors controlling precipitation regimes on local-, meso- and even global scales. Recent observations have demonstrated that large concentrations of natural and anthropogenic aerosols in the atmosphere can lead to a significant reduction of precipitation (Rosenfeld, 1999). A high concentration of cloud condensation nuclei (CCN) leads to a high concentration of nucleated droplets, slowing down droplet growth by diffusion and retarding raindrop formation by drop collisions. Growing cumulus clouds forming in a smoky air contain a significant concentration of cloud droplets with contents of 2 –3 g/m^3 at temperatures as low as -35 ^{o}C to -38 ^{o}C (Rosenfeld and Woodley, 1999). Because the processes of ice formation (drop freezing, riming, ice multiplication, etc.) depend on the size of drops, atmospheric aerosol particles (AP) influence ice microphysics as well.

Aerosol in- and below cloud scavenging is the main mechanism of the atmospheric cleaning. Some AP serving as CCN are eliminated from the atmosphere through nucleation and drop formation (nucleation scavenging). Some fraction of AP is scavenged from the atmosphere being collected by raindrops and ice particles. Non-nucleated AP can be transported in convective updrafts to middle and upper troposphere.

Observational studies show that adequate simulation of cloud-aerosol interaction and process of precipitation formation requires an advanced spectral (bin)-microphysics approach that allows one to simulate adequately the spectra for droplet and ice that can be changed freely under different AP concentrations.

We present preliminary results of deep cumulus cloud simulations under conditions typical of Thailand summer time under intermediate (the CCN concentration (562 cm^{-3} at 1% supersaturation) and high concentrations (a smoky air case) of CCN (1410 cm^{-3} at 1% supersaturation).

*Corresponding author address: Prof. Alexander P. Khain, Institute of the Earth Science, The Hebrew University of Jerusalem, Givat Ram, Jerusalem 91904, Israel, Khain@vms.huji.ac.il

2. CLOUD MODEL

To evaluate the effect of atmospheric aerosols on the rain rate and accumulated amount of precipitation in deep convective clouds, a spectral (bin) microphysics Hebrew University Cloud Model (HUCM) was used (Khain et al, 1999a). In the model water drops, ice crystals (plate-, columnar- and branch type), snowflakes, graupel and frozen drops, as well as atmospheric aerosols are described using number density size distribution functions, calculated in the course of the model integration. The model is specially designed to take into account the effect of atmospheric aerosols on the cloud development and precipitation formation. The droplet nucleation is described on the basis of analytical calculations of supersaturation, which is used for calculation of sizes of aerosol particles to be activated and the corresponding sizes of nucleated droplets. Primary nucleation of each type of ice crystals takes place within certain temperature ranges. The rates of ice generation by nucleation and freezing of droplets is calculated using a semi-lagrangian approach allowing us to calculate changes in supersaturation and temperature in moving cloud parcels attaining model grid points. Secondary ice generation is described by Halett and Mossop mechanism, according to which each 250 collisions of graupel with droplets of radii exceeding 20 μm lead to the formation one ice splinter. According to measurements, this process takes place within –3^{o}C- - 8^{o}C temperature range. Diffusion growth of water droplets and ice particles is calculated using analytical solutions for supersaturation with respect water and ice. We take into account the shape of ice crystals to calculate diffusional growth of different ice crystals. The stochastic equation of collisions is used for description of the collision growth of cloud hydrometeors. A recent version of HUCM uses an effective and precise method suggested by Bott (1998) for drop-drop collisions to calculate collisions between hydrometeors of all types. The model uses height dependent drop-drop and drop-graupel collision kernels calculated using a universal hydrodynamic method valid within a wide range of drop and graupel sizes (Pinsky et al, 1999, Khain et al, 1999b). Ice-water and ice-ice collision kernels are calculated taking into account shapes of ice crystals and a dispersion of terminal velocities of crystals of the same mass, but of different shape. Ice-ice collision rates are assumed to be temperature dependent.

The model provides the following parameters: precipitation amount, precipitation rates, mass contents, radar reflectivity from water and ice, mean and effective radii of droplets and ice particles, brightness temperatures within microwave range, optical depths, albedo, etc. Other diagnostics can also provide information on particular physical mechanisms, to better assess the importance of each.

The computational domain size is 64 km x 10 km with increments of 500 m and 250 m in the horizontal and vertical directions, respectively.

3. EXPERIMENT DESCRIPTION

Two pairs of numerical experiments were conducted. In the control set we use the sounding data of 30.04.98-2.05.98 revealing low relative humidity ranged from 60% to 70% in the boundary layer. Air temperature near the surface was 36 ^{o}C, the freezing level is located at 5 km. While thermodynamical conditions were rather similar during these days, concentrations of CCN were substantially different. Using in-situ observed CCN concentration measured below the cloud base (Rosenfeld, personal communication), the CCN concentration was represented as $N=CS^k$, where S is supersaturation in %, C=562 cm^{-3} and 1410 cm^{-3}, and k= 0.462 and 0.308 under intermediate CCN concentration and in a smoky air (high CCN concentration), respectively. The size distributions of aerosol particles serving as CCN was reconstructed using these formulas.

In the first pair of experiments the evolution of deep tropical clouds was simulated under the same thermodynamic conditions, but with different concentrations of CCN mentioned above: an intermediate concentration (EXP.1) and a high concentration (smoky air) (EXP.2).

In the second experiment pair (EXP.3-intermediate CCN concentration) and EXP.4-high CCN concentration) air humidity in the boundary layer was increased by 10 % as compared with the control case.

3. RESULTS

Calculations reveal significant effect of aerosol concentration on the time evolution of cloud microstructure and precipitation formation. In case of high CCN concentration (EXP.2) droplet concentration turned out to be 3-4 times higher than in the case intermediate CCN concentration (EXP.1) (Figure 1). Concentration of droplets in

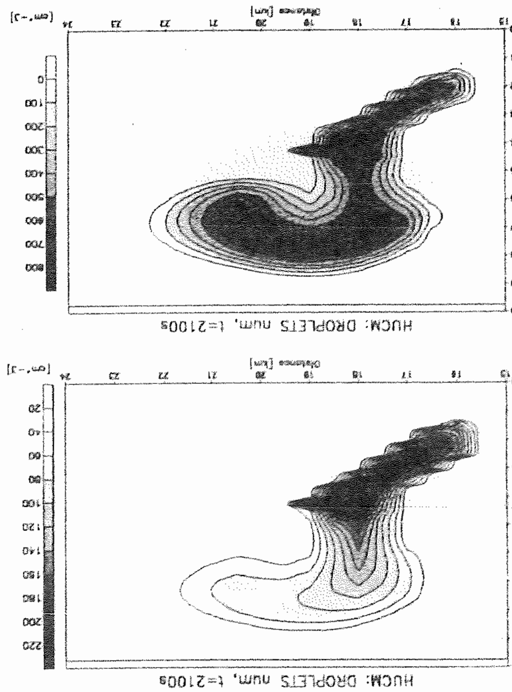

Figure 1. Droplet concentration in clouds formed in cases of intermediate (above) and high CCN (below) concentrations.

EXP.2 exceeds 200 cm^{-3} at the level of 9 km. Maximum cloud water content (CWC) attains 3 gm^{-3} in EXP.2 as compared to 1.6 gm^{-3} in EXP.1 (Figure 2 a,b). The CWC maximum is located 1.5 km higher in EXP.2 as compared to that in EXP.1.

These results agree well with in-situ measurements: in deep clouds arising in smoky air high droplet concentrations and significant CWC exist at high levels up to –30^{o}— - 35 ^{o}C. This is because droplet size is small, droplet-droplet and ice-droplet collisions are not efficient and cannot decrease drop concentration and CWC significantly. In addition, processes of droplet freezing, is inefficient until droplets are small. Thus, there is no mechanism, that would be able to decrease droplet concentration and the CWC in the smoky air.

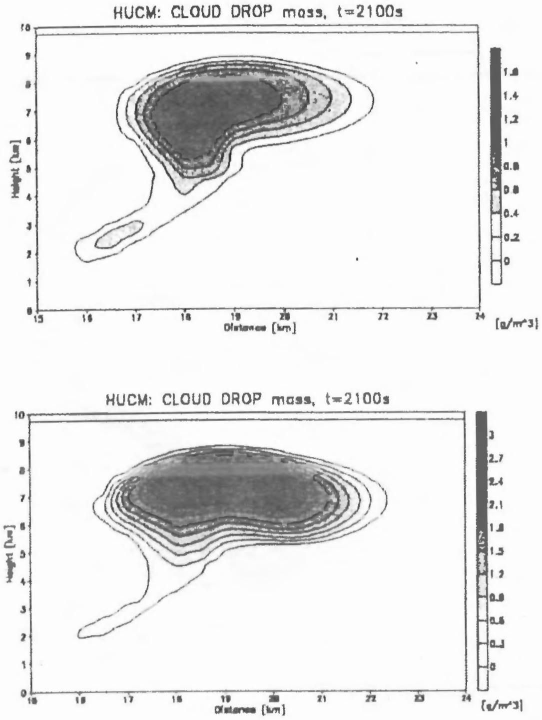

Figure 2. Cloud water content in clouds formed in cases of intermediate (above) and high CCN (below) concentrations.

In contrast, in case of smaller drop concentration droplets are larger and their concentration rapidly decreases by collisions above 4 km. The effect of collisions is illustrated in Figure 3: raindrops form faster and the rain water content (RWC) reaches higher magnitudes in case of the intermediate CCN concentration than in smoky air. These results are in a good agreement with the in-situ measurements.

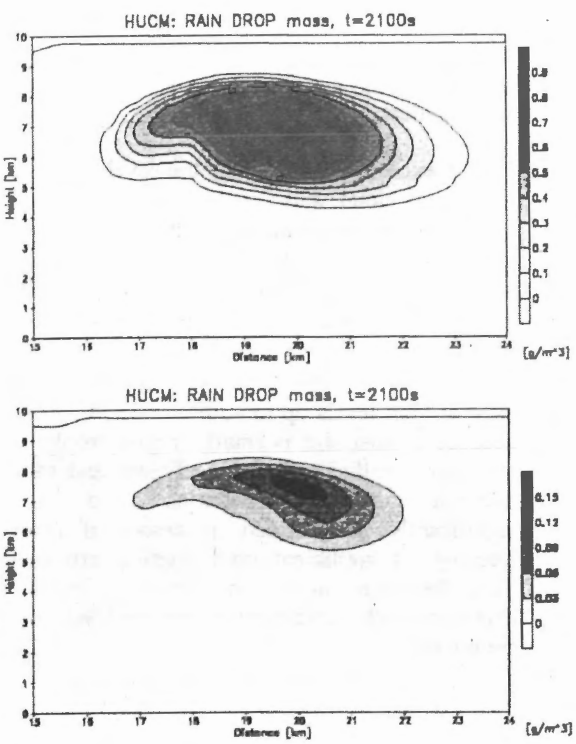

Figure 3. Rain water content in cases of intermediate (above) and high (below) CCN concentration.

The increase in the CCN concentration (resulting in an increase in the droplet concentration and a decrease in the droplet size) leads to a 10-15 minutes delay in the formation of cloud ice. Note that ice content in the smoky air case increases with time and becomes the same and even higher than in the case of the intermediate CCN concentration. Life time of the cloud arising in the smoky air turns out to be longer, and at the dissipation stage the rate of precipitation (formed by melted particles) from this cloud exceeds that from the cloud formed under intermediate CCN concentration. However, amount of precipitation from melted ice (cold rain) was significantly smaller than the amount of warm rain formed by unfrozen drops.

The incerase in the boundary layer humidity (EXP.3 and EXP.4) by 10% leads to about 4 times increase in the rain rate and the accumulated rain.

Rain forms faster by about 6-8 min. as compared to the "dry" experiments. The increase in the humidity of the subcloud layer leads to a significant increase both in CWC and RWC. The increase in the accumulated rain is, therefore, not a result of slower evaporation of falling drops in the dry boundary layer, but the result of changes in the cloud microstructure. The effects of humidity on droplet size spectra evolution is discussed by Khain and Pinsky (2000) and Segal et al. (2000) in more detail. An increase in the humidity in the boundary layer leads to a decrease in the cloud base height. It leads to a) a decrease in the updraft velocity at the cloud base; and b) to an increase in the instability within the cloud layer. As a result, the magnitude of the supersaturation maximum in the vicinity of the cloud base decreases, and the supersaturation in updrafts exceeds this local maximum at the cloud base. This leads to the formation of a wider spectrum as a result of in-cloud nucleation. The latter results in more rapid rain formation.

Hight sensitivity of the accumulated rain amount to CCN concentration remains in the case of higher humidity too. Accumulated rain amount calculated all over the period of 100 min of cloud evolution both in "dry" and "wet" experiments turns out to be 1.5-1.8 higher in the intermediate aerosol concentration case than that in the smoky air case. This results can be attributed to a larger loss of cloud water by droplet and ice particles spreading and evaporation in the upper and middle atmosphere in case of small droplet sizes (high CCN concentrations).

Analisis AP size distributions at the cloud base and in-and around cloud indicates crucial effect of nucleation scavenging in clouds, which decreases the CCN concentration by factor of about 2. As a result, only smallest AP remain in the AP size spectrum. We did not take into account collisional scavenging as well as partial restoring AP distribution by droplet evaporation. This problem requires further investigations.

We calculated radiative properties of clouds in microwave range. It was shown a high correlation between RWC (and rain rate) and the brightness temperature calculated at frequency 10GHz. At the same time, the brigthness temperature at frequency of 250 GHZ turns out to be sensitive to amount of cloud ice. We intend to use the cloud model for aims of remote sensing as a connection link between radiative fluxes (radiative cloud properties) measured from space, radar reflectivity and a microphysical cloud structure including precipitation rates.

4. CONCLUSIONS

Numerical experiments conducted using a spectral microphysics cloud model HUCM indicate strong effects of aerosols on cloud microphysics, rain formation and rain amount. We suggest that adequate simulation of cloud-aerosol interaction and processes of precipitation formation requires the utilization of spectral (bin) microphysics models (SM). Only SM allows one to realistically reproduce formation of the size spectra of water drops and ice particles from aerosols with different size distributions.

Crucial effect of thermodynamical conditions (in particular, humidity in the subcloud layer) on cloud development and rain amount is found. It means that effects of atmospheric aerosol should be detected at the background of significant fluctuations caused by natural variations of stability conditions in the atmosphere.

Note that decay of some clouds leads to formation of secondary ones. Time evolution of clouds in different AP fields is different. That is why, one need to conduct calculations over a larger area and during a longer period of time to evaluate the effects of aerosols on the accumulated rain amount more precisely.

5. ACKNOWLEDGMENTS

The authors are grateful to Prof. D. Rosenfeld for providing with the observed data and valuable discussions. This study was supported by the Israel Science foundation administrated by the Israel Academy of Sciences and Humanities (grant 572/97).

REFERENCES

Bott, A., 1998: A flux method for the numerical solution of the stochastic collection equation *J. Atmos. Sci.,* 55, 2284-2293.

Khain A.P., A. Pokrovsky, and I. Sednev, 1999a: Some effects of cloud-aerosol interaction on cloud microphysics structure and precipitation formation: Numerical experiments with a spectral microphysics cloud ensemble model. *Atmos. Res.,* 52, 195-220.

Khain A.P., Pinsky, M. B., M. Shapiro and A. Pokrovsky, 1999b: Graupel-drop collision efficiencies. *J. Atmos. Sci.* (in press).

Khain A. P., and M. Pinsky, 2000: Droplet spectrum broadening: effects of in-cloud nucleation and droplet collisions (this issue).

Pinsky, M., A. P. Khain, and M. Shapiro and A. Pokrovsky, 1999: Collision efficiency of drops in a wide range of Reynolds numbers: Effects of pressure on spectrum evolution. *J. Atmos. Sci.* (in press).

Rosenfeld, D., 1999: TRMM observed first direct evidence of smoke from forest fires inhibiting rainfall. Geophysical Research Letters, 26, 20, 3105.

Rosenfeld, D., W.L. Woodley, 1999: Convective clouds with sustained highly supercooled liquid water until –38 C. Submitted to "Nature".

Segal, Y., A. Khain and M. Pinsky, 2000: The influence of thermodynamic conditions in the boundary and cloud layers on the droplet spectrum formation in cumulus clouds (this issue).

A MODELLING STUDY OF CIME 98

Andrea Flossmann, Wolfram Wobrock and Marie Monier

Laboratoire de Météorologie Physique, Université Blaise Pascal/CNRS/OPGC
Clermont-Ferrand (France)

1. INTRODUCTION

Due to the lack of in-situ measurements of multiphase processes in mixed clouds, the fate of the scavenged pollutant material during the freezing of a drop is poorly understood. In the few numerical models which treat the ice phase in clouds and the associated chemical processes it is assumed, e.g., that when a drop freezes all uptaken material is retained and incorporated into the crystal structure. However, it is not known whether this is true or whether not part of the material is expelled, redistributed or changed in any way during the freezing process.

This problem was studied during two joint field experiments in clouds at a mountain station (Puy de Dôme, France). These CIME (=cloud ice mountain experiment) field experiments were funded by the European Commission and combined the efforts of the LaMP, the IfT (Germany), the FISBAT (Italy) and the ECN (Netherlands). Results of these campaigns are published in Geremy et al (1999), Schwarzenboeck et al (2000) and CIME(1998).

In order to address the problem a CVI (Counterflow Virtual Impactor) was constructed by IfT which was built into the windtunnel on the summit of the Puy de Dôme which captured and evaporated cloud droplets and ice crystals larger than 5µm diameter. Equally, a RJI (Round Jet Impactor) was used to sample the interstitial gas phase and aerosol particles smaller than 5µm diameter. FISBAT and ECN sampled and analysed the main gases released during evaporation in the CVI and the RJI (NH_3,SO_2 and H_2O_2). LaMP, IfT and FISBAT provided complementary measurements of the drop spectrum, ice crystal spectrum and liquid water content inside and outside of the wind tunnel.

During the experiment the content of important trace gases and aerosol particles *in liquid drops* was evaluated by evaporating these drops in the CVI and by measuring the released gas content and the residual particles in the air.

Corresponding author's address: Andrea Flossmann, LaMP; Univ. Blaise Pascal/CNRS/OPGC ; 24, avenue des Landais ; F-63177 Aubière Cedex ; France; E-Mail: A.Flossmann@opgc.univ-bpclermont.fr.

The same trace species were studied in the RJI for the complementary interstitial aerosol particles. In a second step of the experiments, the *liquid drops were converted to ice particles* prior to entering the CVI by seeding the cloud with propane or CO_2.

The procedure of evaporation and analysis in the CVI and RJI was repeated for *the ice particles*.

A comparison between the chemical characteristics of liquid drops and ice particles and the additional measurements of the trace gas concentrations in the ambient air allows to determine the fate of the trace constituents during the freezing process of a cloud.

In order to evaluated the results on chemistry, in a first attempt we will try to understand the functioning of the seeding.

2. THE SEEDING

In order to study the seeding applied during CIME we consider this process which takes place along the way between gas bottle and windtunnel in 2 parts:

I the nucleation and generation period

II the evolution or growth period

The main difference between both parts is that: during part **I** the thermodynamic environment is mainly determined by the isentropic gas release or expansion, and during part **II** the nucleated crystals evolve under the ambient atmospheric conditions (RH, T, p, LWC, and wind)

3. GENERATION OF ICE CRYSTALS BY THE ISENTROPIC EXPANSION OF CO_2 OR PROPANE FROM COMPRESSED GAS BOTTLES

We consider the release of propane or CO_2 as the flow of compressed air through a narrow valve. This process is treated in classical fluid dynamics as an isentropic gas expansion which is typically associated with the formation of sound waves in the narrowest section of the valve. This concept allows the calculation of the temperature T_{eject} of gas coming out of the bottle by:

$$\frac{T_{eject}}{T_i}=\left(\frac{p_{eject}}{p_i}\right)^{\gamma/(\gamma-1)}$$

T_i and p_i are temperature and pressure in the gas bottle and p_{eject} is supposed to be identical with the ambient atmospheric pressure of 845 hPa, $\gamma = c_p ./c_v$.

For the conditions during CIME the temperature of the gas bottles T_i was about 5-10 °C, the bottle pressure p_i for CO_2 about 50 bar, for propane p_i about 8 bar.

Using this equation for an isentropic release we receive a strong cooling immediately behind the valves (reference): This leads to:

T_{eject} = - 185 °C for the CO_2 release and
T_{eject} = - 124°C for the propane release.

For both temperatures - also if they might be higher - we can assume that an instantaneous formation of solid or liquid ice germs takes place. For CO_2 whose sublimation temperature is -78°C we can expect the spontaneous formation of solid CO_2 germs. For propane, however, where the boiling temperature is -54 °C and the melting temperature -182°C, the formation of liquid propane germs is most likely. Exposing these ice nuclei to the ambient ice-supersaturated air a fast growth to large ice crystals can be expected.

There are two more possible pathways for the formation of ice crystals in the very cold expansion cone of the escaping gas:

For an ambient temperature of -4°C and a relative humidity (RH) of 98-99% a water vapor mixing ratio of 3.2 g/kg results. During the mixing of the cold escaping gas with the ambient air a strong ice supersaturation can locally occur. Presuming a temperature of -80°C an ice supersaturation of 177 %. results under these ambient conditions, and still 120% at -20 °C. Under such high supersaturation a homogenous nucleation of small water drops can take place which will immediately start freezing (see Pruppacher and Klett, 1997). But also interstitial aerosol particles can serve as ice nuclei under these thermodynamic conditions.

However, we will persue here only the first possiblility of forming CO_2 germs and propane droplets, thus residual free crystals, as it seems to be the dominant mechanism.

In order to better understand this generation process in the very cold expansion cone behind the valve we assume, that the gas, leaving the bottle valve at -95°C and at ambient pressure, forms immediately ice nuclei. Supposing these germs have an initial size of 1 nm we follow their diffusional growth in an ice supersaturated atmosphere, under the assumption that their temperature and the temperature in their next environment increase during 1 s to the ambient value of -4°C as displayed in Fig. 1. The resulting growth evolution of the ice particles is given on the right ordinate.

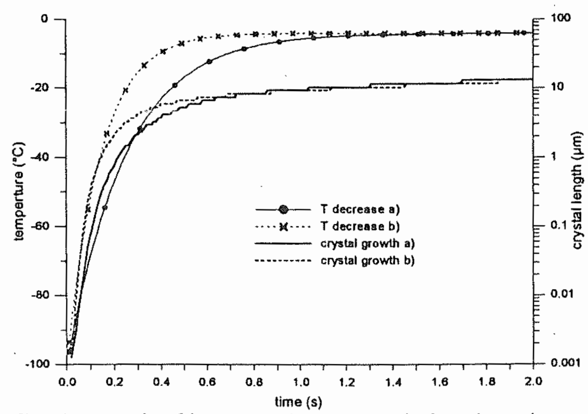

Fig. 1: growth of ice crystal columns during the release of compressed gas from a bottle. The thin solid and dashed lines give two different scenarios for the imposed temperature evolution of the ice germs after leaving the bottle, the fat corresponding lines the evolution of the crystal length.

Thus, we can assume that during the generation part of the seeding experiment instantaneously ice crystals of sizes between 1 and 10 µm were formed. In chapter 5 the growth and evolution of these crystals to larger sizes will be calculated with the EXMIX model and the results will be compared to the measurements.

4. THE MICROPHYSICS MODULE EXMIX

The model EXMIX was developed by Wobrock (1986) in order to study the growth of *ex*ternally *mix*ed condensation nuclei in fog and clouds. It allows at all times to follow the individual activated aerosol particles through the droplet spectrum as it considers only one number density distribution function f_d for all aerosol particles and droplets together. The information on the aerosol nucleus and the attached water mass are followed via two coordinates m for the droplet mass and $m_{AP,N}$ for the mass of the dry aerosol nucleus. In order to take into account the externally mixed aerosol a third coordinate x_i for the chemical composition is considered with

$$x_i = x_i(\varepsilon_s, \rho_n, M_s, \nu_s) \qquad , i=1,...n$$

Herein, n types of condensation nuclei can be distinguished differing in solubility fraction ε_s, density of aerosol particles ρ_n, molecular weight M_s, and number of free ions υ_s. For the present study the model xas extended to a second number density distribution function f_i for the formed ice crystals. Thus, the time rate of change of ψ=f_d *and* f_i is:

$$\frac{\partial\psi(m,m_{AP,N},x_i)}{\partial t} = -\frac{\partial}{\partial m}[\psi(m,m_{AP,N},x_i)\frac{dm}{dt}]$$

for f_d *dm/dt* represents the droplet growth equation as described in Pruppacher and Klett (1997) for the liquid drop case:

$$\frac{dm}{dt} = 4\pi r \frac{\dfrac{e}{e_{sat,w}} - \exp(Y)}{\dfrac{\rho_w R'T}{e_{sat,w} D'_v M_w} + \dfrac{L_e \rho_w}{k'_a T}\left(\dfrac{L_e M_w}{TR'} - 1\right)}$$

$$Y = \frac{2\sigma_s}{\rho_w R_v T a} - \frac{\varepsilon_s M_s \rho_n r^3 \phi \nu_s}{M_s \rho_w (a^3 - r^3)}$$

With e: actual water vapour pressure; $e_{sat,w}$: saturation vapour pressure; M_w: molecular weight of water; ϕ: osmotic coefficient of salt in solution; a: radius of moist aerosol particle or drop; r: radius of the dry aerosol fraction of insoluble material in the aerosol nucleus; ρ_w: density of water; R': universal gas constant; R_v: gas constant of water vapour; σ_s: surface tension; L_e: latent heat of evaporation. D_v' is the modified diffusion coefficient and k_a': the modified thermal conductivity (Pruppacher and Klett, 1997).

For f_i the growth equation for ice particles can be found in Pruppacher and Klett (1997) as

$$\frac{dm}{dt} = \frac{4\pi \, C \, S_{v,i}}{\dfrac{\rho_i R'T}{e_{sat,i} \, D'_v \, M_w} + \dfrac{L_S \rho_i}{k'_a T}\left(\dfrac{L_S \, M_w}{R'T} - 1\right)}$$

where L_S is the specific latent heat of sublimation, $S_{v,i}$ is the ice supersaturation over water, and $e_{sat,i}$ = saturation vapour pressure over ice.

For the application of this equation we assume the ice crystals in the form of columns (as observed during the seeding), with the following characteristics: the mass m is given by $m = \rho_c V_c$, where the crystal density $\rho_c = 0.848 L_c^{-0.014}$, the crystal volume $V_c = 4.06 \; 10^{-2} L_c^{2.841}$, the crystal length L_c.

The capacitance C of the crystal was assumed to follow the relation:

$$C = \frac{A}{\ln[(L_c + A)/d]} \quad \text{with} \quad A = (L_c^{\,2} - d^2)^{1/2} \qquad (3)$$

Herein the following relationship between diameter d and length L_c of the column was used: $d = 0.263 \, L_c^{0.93}$.

5. COMPARISON OF THE OBSERVATIONS WITH THE EXMIX MODEL RESULTS

During the night of 22 Feb. 98 air masses which passed the summit and started descending to the observational site and were slightly subsaturated. 20 m below the summit the simulations with an adiabatic air parcel give values of 99.8 - 99.9 % relative humidity. Thus, the liquid drops in the subsaturated environment start to evaporate. Under the same conditions of temperature (-4°C), however, ice supersaturation is maintained for RH until 97.4 %. Consequently, the ice crystal growth will continue but supercooled droplets will evaporate (effect of Bergeron-Findeisen).

In order to illustrate this counteracting behaviour of cloud droplets and ice crystals we simulate the seeding process in a descending cloud parcel and follow the evolution of ice crystals, droplets and their residual particles during the following 15 s. When the air parcel arrives close to the altitude of the experiment platform we reduce the downdraft to a few cm/s in order to keep the parcel on the same height for its way from the gas bottle to the wind tunnel (see Fig. 2 at 572 s). (This modification of the simulated wind is necessary as the trapped wind conditions which occur in the lee of the observatory and the other summit buildings could not be resolved by the 50 m grid of the dynamical model).

The coupling of the cloud parcel with ice crystals starts immediately after the generation process described in section 3. Due to this mechanism we can assume that ice crystals over a wide size range are present at least 1 s after the start of the gas release. For our first simulation we initialize a number distribution of ice crystals which fills all size categories from 10 nm to 1 µm of crystal length with 4 particles per model bin. This results in a total ice crystal number concentration of 200 /cm^3 and an ice mass of 10 mg/m^3. The ice crystals are considered to be free of residual particles.

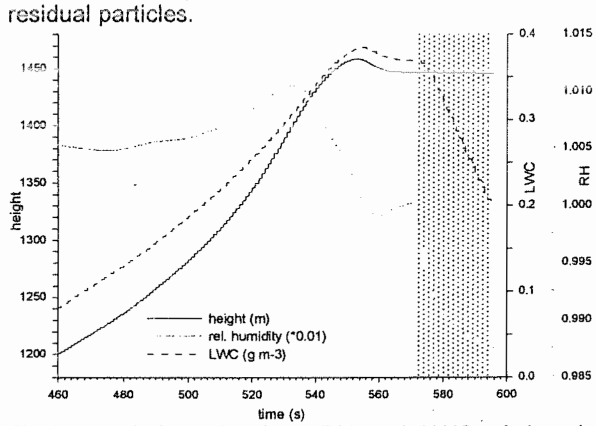

Fig.2: simulation of height, RH and LWC of the air parcel prior and during (shaded time period) seeding

We apply this numerical seeding experiment to the cloud parcel of EXMIX. The seeding was started at 572 s and its consequences for LWC and relative humidity can clearly be detected in Fig. 2. The strong drop of both parameters starts immediately after the adding of ice particle into the cloud parcel. This decrease of the LWC is similar to that of a descending cloud parcel. Fig.2 also displays that the parcel remains in the same altitude of about 1450 m during the seeding period.

At the start of the seeding an ice super-saturation of 2% causes a fast growth of the ice crystals to 0.15g m^{-3} during 10 s only. During this period the LWC looses about 0.1 g m^{-3} and 50 droplets (whose d < 5 μm) disappear. The increase in IWC continues although the ice supersaturation drops very fast simultaneously with the relative humidity (see Fig.2). Despite this decrease the total water content (LWC+IWC) in the cloud parcel increases continuously.

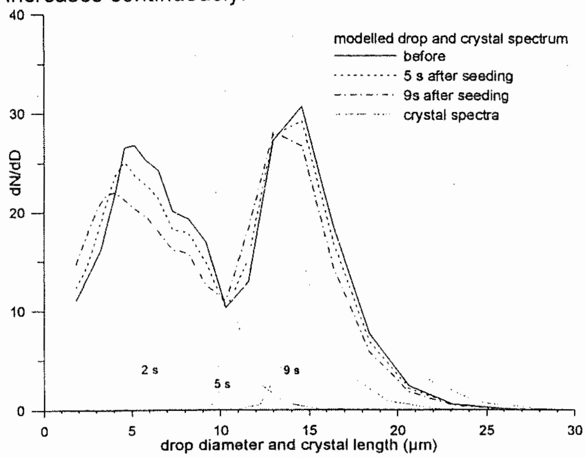

Fig.3: simulation of the drop and the ice crystals spectrum before and during seeding

In Fig. 3 the ice crystal spectra are displayed for 2, 5, and 9 seconds after seeding. This figure illustrates that the IWC increase is due to the growth of crystals generated by seeding. The same figure includes the droplet spectra before, 5 s and 9 s after the seeding. We see that only numbers of droplets smaller 10 μm are affected by the strong drop in relative humidity, which causes them to evaporate. The large droplets keep almost in the same sizes, as they react much more inert on changes in the relative humidity.

In order to compare these results with the measurements performed by FSSP and the CVI, we have to sum up the ice crystal spectrum and the droplet spectrum, as both instruments cannot distinguish solid and liquid hydrometeors. Adding the crystal number to the droplet number for one distinct moment (at t = 5s or 9s) results in a significant number increase of 20-30 cm^{-3} μm^{-1} for a narrow size interval with a width of about 5 μm.

Comparing the model results with the FSSP observations we find that the general concept of seeding is confirmed. We can even detect the growth of the crystals created by seeding as a function of time in the different FSSP channels.

The table below gives the mean CWC (total cloud water content) and the mean number of residual particles measured by the instruments coupled to the CVI.

CWC(g m-^{3}) Outside seeding	0.43 ± 0.06
CWC(g m^{-3}) During seeding	0.49 ± 0.07
Residual particle number (cm^{-3}) Outside seeding	213 ± 54
Residual particle number (cm^{-3}) During seeding	151 ± 31

We see from the table above that the total cloud water content increases during seeding and that the residual particle number decreases.

6. CONCLUSIONS

The measurements of CVI and FSSP confirm the model results obtained with the assumption of particle free ice germs created by the seeding which grow due to a Bergeron Findeisen process. This concept will yield the basis for the ongoing interpretation of the chemical measurements obtained during the seeding. This will allow general conclusions about the redistribution of pollutants during the Bergeron-Findeisen process in mixed phase clouds.

7 ACKNOWLEDGEMENTS

The authors acknowledge with gratitude the support by the European Commission under ENV4-CT95-0012. The calculations for this paper have been done on the CRAY C98 and C94 of the IDRIS (CNRS) under project no. 940180.

8 REFERENCES

CIME, 1998: Cloud Ice Mountain Experiment final report. European Commission; ed: A. Flossmann.

Gérémy, G., W. Wobrock, and A.I. Flossmann, A. Schwarzenboeck, and Stefan Mertes, 1999: A modelling study on the activation of small aitken-mode aerosol particles during CIME 97. In press *Tellus*.

Pruppacher, H.R. and J.D. Klett, 1997: Microphysics of clouds and precipitation. Kluwer Academic Publishers. 2nd revised and enlarged edition. 954pp.

Schwarzenboeck, A., J. Heintzenberg, and S. Mertes, 2000: Incorporation of aerosol particels between 25 and 850nm into cloud elements. Atmos. Res., 52, 241-260.

Wobrock, W., 1986: Numerische Modellsimulationen von Strahlungsnebelepisoden unter Berücksichtigung spektraler Wolkenmikrophysik. PhD Thesis, available from Johann Wolfgang Goethe Universität, Frankfurt, Germany.

ORGANIC AEROSOL: INFLUENCE ON CLOUD MICROPHYSICS

M.C. Facchini, M. Mircea*, S. Decesari and S. Fuzzi

Istituto di Scienze dell'Atmosfera e dell'Oceano – CNR, I-40129, Bologna, Italy

1. INTRODUCTION

The influence of the chemical and physical properties of aerosol on cloud droplet formation and growth is still incompletely understood.

Cloud droplet number concentration and size depend on both macroscale cloud dynamics and cloud microphysics through the air mass supersaturation. Supersaturation within clouds is the result of the balance between the cooling rate and the water condensation rate, which is determined by the physical and chemical properties of the aerosol population.

The lack of information on aerosol properties represents a large source of errors in atmospheric models. For example, Shulman et al. (1996), Li et al. (1998), Facchini et al. (1999) have shown that, taking into account the presence of organic compounds in aerosol particles and the variation of surface tension with the concentration of soluble organic carbon (WSOC), significant variations in cloud droplet number can be obtained.

The WSOC aerosol, for which measurements are still scarce, accounts for a significant fraction of the aerosol mass (Saxena and Hildemann, 1996; Zappoli et al., 1999), but its influence on cloud microphysical parameterizations still needs to be quantified in order to establish reliable relationships between aerosol and cloud droplet populations.

Here, we discuss the influence of realistic models for the chemical composition of different aerosol types on CCN supersaturation spectra and droplet growth time. Organic and inorganic chemical composition of the aerosol and the variation of surface tension due to WSOC are considered.

The supersaturation spectrum of CCN, i.e., the cumulative concentration of CCN as a function of supersaturation and droplet growth time are important variables in cloud models, because they influence cloud formation and development.

2. DEPENDENCE OF THE SUPERSATURATION SPECTRUM OF CCN ON SURFACE TENSION AND AEROSOL SIZE DISTRIBUTION

Three aerosol size distributions for marine, rural and continental aerosol (Jaenicke, 1993) are considered in this study. The distributions are described as a sum of three log-normal functions:

$$n(\log D)=\sum_{i=1}^{n}\frac{N_i}{\sqrt{2\pi}\log\sigma_i}\exp\left(-\frac{\left(\log D-\log \overline{D}\right)^2}{2\log^2\sigma_i}\right) \quad (1)$$

where D is dry aerosol diameter, N_i is the aerosol particle number concentration, $\overline{D}_i$ is the aerosol geometric mean diameter and σ_i is the geometric standard deviation of the i^{th} log-normal mode. Table 1 lists the values for N_i, $\overline{D}_i$ and σ_i for each mode and each aerosol type.

Table 1. Parameterizations of aerosol size distributions (Jaenicke, 1993).

Aerosol	Mode I			Mode II			Mode III		
Type	N(cm^{-3})	D(μm)	log σ	N(cm^{-3})	D(μm)	log σ	N(cm^{-3})	D(μm)	log σ
Marine	133	0.008	0.657	66.6	0.266	0.210	3.1	0.05	0.396
Rural	6650	0.015	0.225	147	0.054	0.557	1990	0.084	0.266
Urban	9.93×10^4	0.013	0.245	1.11×10^4	0.014	0.666	3.64×10^4	0.58	0.337

The chemical composition of the three different aerosol types (marine, rural, urban) have been derived from experimental measurements and are presented in Table 2.

* Permanent affiliation: National Institute of Meteorology and Hydrology, Bucharest, Romania

Corresponding author address: M.C. Facchini, ISAO-CNR, Via Gobetti 101, Bologna, Itlay; E-Mail: mc.facchini@isao.bo.cnr.it.

The WSOC composition is modelled as a mixture of mono- and dicarboxylic acids of low molecular mass (MA) and polyacidic compounds of higher molecular mass (MMC) (Decesari et al., 2000). INS represent the insoluble part of aerosol.

Table 2. Chemical composition of aerosol expressed as a fraction of total mass

Aerosol type	NH_4HSO_4	$(NH_4)_2SO_4$	NH_4NO_3	NaCl	MA	MMC	INS	Reference
Marine	0.17	0.20	0.04	0.21	0.07	0.03	0.28	Putaud et al., 2000
Rural	0.12	0.14	0.20	0.04	0.14	0.06	0.30	Zappoli et al., 1999
Urban	0.10	0.11	0.27	0.03	0.14	0.06	0.29	Putaud, personal communication

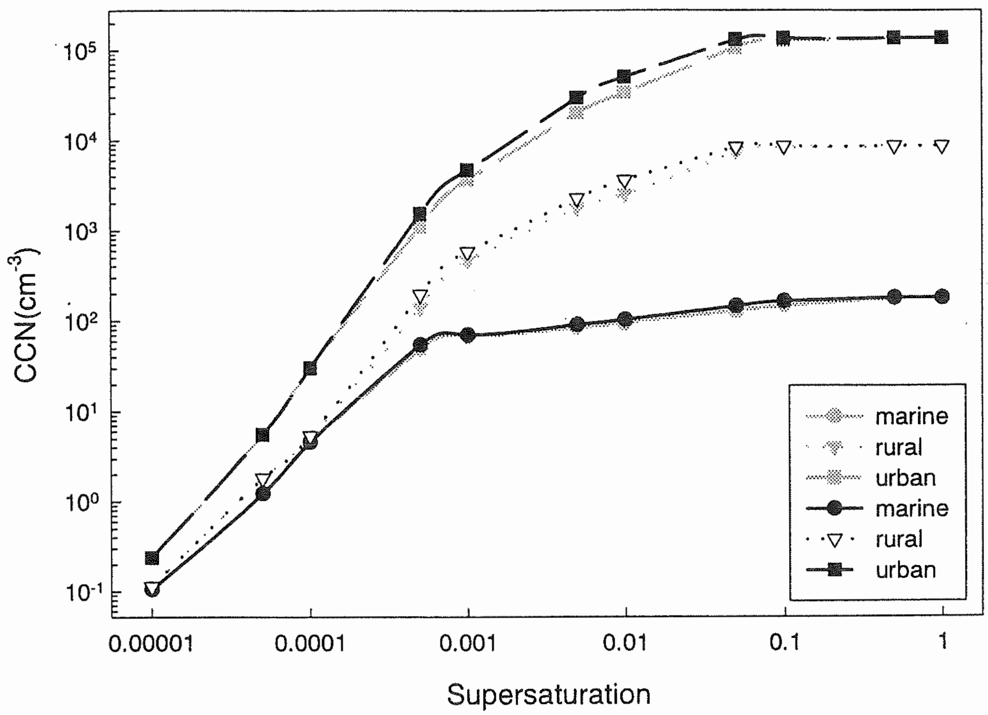

Figure 1. CCN concentration as a function of supersaturation for three aerosol types: marine, rural and urban. Black lines consider variable surface tension with the WSOC concentration, grey lines are computed with constant surface tension (72.8 dyne/cm).

Based on data from Tables 1 and 2 and using a modified Köhler equation (Mircea et al., 2000), the cumulative number concentration of CCN was computed as:

$$CCN(S) = \int_{r_S}^{\infty} n(r)dr \qquad (2)$$

where $n(r)$ is the number distribution of the aerosol population and r_S is the activation radius for the supersaturation S.

Fig. 1 shows variations of supersaturation spectra of CCN for marine, rural and urban aerosol when surface tension decrease due to WSOC is considered (Facchini et al., 1999).

The CCN concentration is higher when the surface tension is considered variable with the

WSOC concentration than in the case of constant surface tension, equal to that of pure water (72.8 dyne/cm). The difference is important for a range of supersaturations between 0.0001 and 0.1. This range includes the supersaturations usually encountered in the atmosphere. It can also be seen that at very low supersaturation the number of activated particles is practically zero while at very high supersaturation all particles are activated.

3. CLOUD DROPLET GROWTH

The equation that describes droplet growth by vapour diffusion (Pruppacher and Klett, 1997) is:

$$r\frac{dr}{dt} \approx \frac{s - s_{eq}}{\dfrac{\rho_w RT}{e_{sat,w}(T) D_v^* M_w} + \dfrac{L_{e,0}\rho_w}{k_a^* T}\left(\dfrac{L_{e,0} M_w}{TR} - 1\right)} \qquad (3)$$

where r is the droplet radius, s the air mass supersaturation, s_{eq} is the equilibrium supersaturation as computed by the modified Köhler equation, T is the temperature, ρ_w is water density, $e_{sat,w}$ is the saturation water vapour pressure, D_v^* is the diffusivity of water vapour in air, k_a^* is the thermal conductivity of the air, M_w molecular weight of water, R is the gas constant and $L_{e,0}$ is the latent heat of evaporation.

The growth history of individual solution droplets nucleated on aerosol particles with dry radius of 0.5 μm and different chemical compositions are shown in Fig. 2. It can be seen that a droplet needs different times to grow to the same size and this depends on chemical composition (rural and marine case). Large overestimation of droplet radius occurs considering the growth time for the "classical" chemical compositions: NaCl for marine aerosol and $(NH_4)_2SO_4$ for rural aerosol.

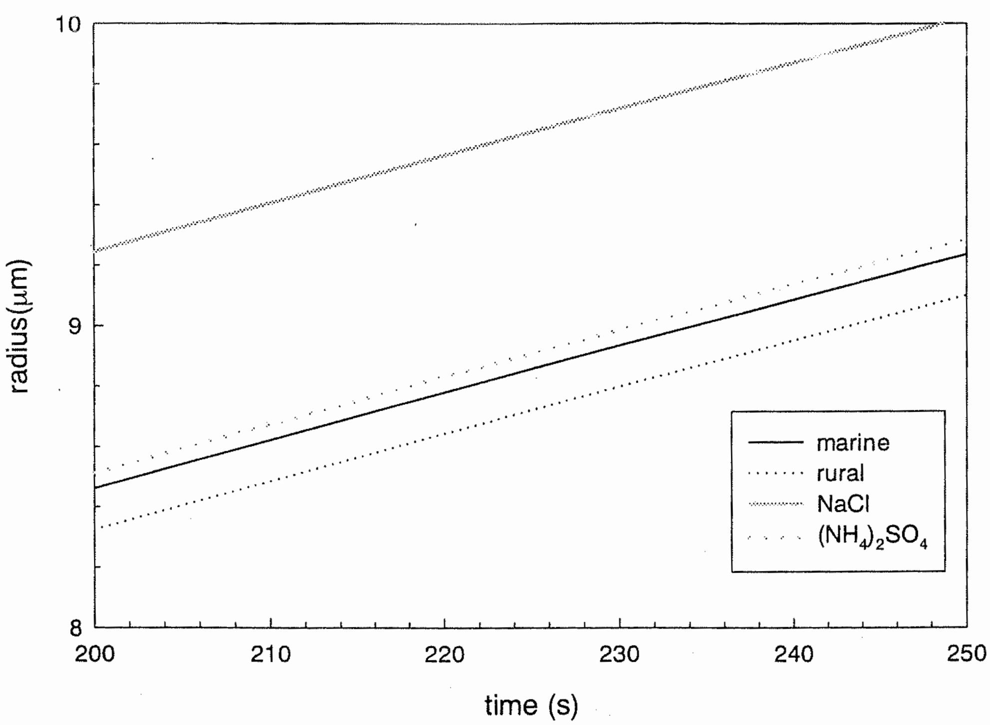

Figure 2. Droplet radius as a function of time for two aerosol types, marine and rural, and for pure ammonium sulphate and sodium chloride. Air mass supersaturation is 0.1%, temperature 20°C, a_T=0.96, a_C=0.045 and the initial drop radius corresponds to relative humidity of 80%.

4. CONCLUSIONS

The results show a large underestimation of the CCN number concentration in the submicron range for the supersaturations usually encountered in the atmosphere (below 1%), if the role of organic aerosol is ignored. An increase of CCN number concentration up to 50 % can be seen in the urban case, up to 40 % in the rural case and up to 12 % in the marine case.

The estimated increase in CCN number concentration can significantly influence the evolution of the drop size spectrum and the rate of rain formation (*Khain et al.* 1999) and can lead to significant errors in cloud albedo calculations and, consequently, in indirect radiative forcing (*Chuang et al.*, 1997; *Facchini et al.*, 1999).

The cloud lifetime and microstucture are also determined by the droplet growth time, especially at low supersaturations, which are characteristic of stratiform clouds.

Improved parameterizations of aerosol-cloud interaction requires more knowledge on aerosol chemical composition and associated physical properties, as well as the mathematical framework for representing the complex processes of droplet nucleation and growth.

5. ACKNOWLEDGEMENTS

The present work was financed by the European Commission (EUROZEP Project ENV4-CT98-0785). J.-P. Putaud (JRC-Environment Institute) is acknowledged for providing unpublished data on aerosol composition and for useful discussions. Mihaela Mircea was supported by the "ICTP Programme for Training and Research in Italian Laboratories", Trieste, Italy.

6. REFERENCES

Chuang, P.Y, R.J. Charlson and J.H. Seinfeld, 1997: Kinetic limitations on droplet formation in clouds. *Nature*, **390**, 594-596.

Decesari, S., M.C. Facchini, S. Fuzzi and E. Tagliavini, 2000: Characterization of water soluble organic compounds in atmospheric aerosol: a new approach. *J. Geophys. Res.*, **105**, 1481-1489.

Facchini, M.C., M. Mircea, S. Fuzzi and R. J. Charlson, 1999: Cloud albedo enhancement by surface-active organic solutes in growing droplets, *Nature*, **401**, 257-259.

Jaenicke, R., 1993: Tropospheric aerosols, in *Aerosol-Cloud-Climate Interactions*, edited by P.V. Hobbs, Academic Press, San Diego, CA; 1-31.

Khain, A., A. Pokrovsky and I Sednev, 1999: Some effects of cloud-aerosol interaction on cloud microphysics structure and precipitation formation: numerical experiments with a spectral microphysics cloud ensemble model, *Atmos. Res.*, **52**, 195-220.

Köhler, H., 1936: The nucleus in the growth of hygroscopic droplets. *Trans. Faraday Soc.* **32**, 1152-1161.

Li, Z. , A. L. Williams and M.J. Rood, 1998: Influence of soluble surfactant properties on the activation of aerosol particles containing inorganic solute, *J. Atmos. Sci.*, **55**, 1859-1866.

Mircea, M., M.C. Facchini, S. Decesari and S. Fuzzi, 2000: Size dependent composition of aerosol particles and CCN spectrum, *Proc. 13th International Conference on Clouds and Precipitation*, Reno, Nevada, (this book).

Pruppacher, H.R. and J.D. Klett, 1997: *Microphysics of clouds and precipitation*, Kluwer Academic Publishers, Dordrecht, 954 pp.

Putaud, J.P., R. Van Dingenen, M. Mangoni, A. Virkkula, F. Raes, H. Maring, J.M. Prospero, E. Swietlicki, O.H. Berg, R. Hillamo and T. Makela, 2000: Chemical mass closure and assessment of the origin of the submicron aerosol in the marine boundary layer and the free troposphere at Tenerife during ACE-2, *Tellus*, in press.

Saxena, P. and L. M. Hildemann, 1996: Water-soluble organics in atmospheric particles: a critical review of the literature and application of thermodynamics to identify candidate compounds. *J. Atmos. Chem.* **24**, 57-109.

Shulman, M.L, M.C. Jacobson, R.J. Charlson, R.E. Synovec and T.E. Young, 1996: Dissolution behaviour and surface tension effects of organic compounds in nucleating cloud droplets, *Geophys. Res. Lett.*, **23**, 277-280.

Zappoli, S., A. Andracchio, S. Fuzzi, M.C. Facchini, A. Gelencser, G. Kiss, Z. Krivacsy, A. Molnar, E. Meszaros, H.C. Hansson, K. Rosman, Y. Zebuhr, 1999: Inorganic, organic and macromolecular components of fine aerosol in different areas of Europe in relation to their water solubility. *Atmos. Environ.*, **33**, 2733-2743

THE EFFECTS OF ANTHROPOGENIC AEROSOL ON THE MICROPHYSICS OF WARM CLOUDS

K.N. Bower, T.W. Choularton, M.J. Flynn and M.W. Gallagher

The Physics Department, UMIST, P.O. Box 88, Manchester M60 1QD. United Kingdom.

1. INTRODUCTION

In recent years a number of experiments have been carried out using a hill-cap cloud in contact with the ground as a natural flow through reactor to investigate the interaction of aerosols with cloud. These experiments have been conducted at an increasing number of different sites around the world in order to compare the effects that aerosols of different origins and history have on the microphysics and chemistry of clouds forming on them and to see how this affects the processing and subsequent changes in the properties of the aerosol emerging downwind of these processing systems.

The broad aims of these investigations have been to derive parameterisations for use in large scale models of the relationships between cloud properties and those of the sub-set of aerosols on which they form (cloud condensation nuclei, CCN), and also of the evolution of the aerosol population in the atmosphere; and thence to lead to parameterisations of the so called indirect and direct radiative effects of aerosols.

In this paper, the results from two such ground based hill cap cloud experiments will be reported and contrasted. In both multi-site experiments there was an opportunity to investigate the interaction of a polluted airmass of anthropogenic origin with a cloud forming over elevated terrain, but in contact with the ground.

2. THE EXPERIMENTS.

2.1 The PROCLOUD experiment at Holme Moss

In Spring 1997 and 1999 experiments were carried out at the UMIST field site at Holme Moss (a hilltop in the Southern Pennines, about 40km to the east of the city of Manchester), to investigate the interaction of the Manchester urban plume with the hill cap cloud which often forms at the site

Measurements carried out at UMIST in central Manchester, show the city to be a major source of aerosol (from motor vehicle exhausts and other sources), with particles from 3nm to 300nm being observed in high concentrations. The aim of the Holme Moss experiments was, therefore, to examine the effects of the properties of the urban aerosol and trace gases in the airmass flowing out from the city, on the microphysics and chemistry of the cloud and to investigate the role of the cloud in modifying the properties of the aerosol and trace gases emerging downwind of the cloud system. The 1997 experiment was a pilot study, but in 1999 a collaborative field project was carried out by four international groups at and around Holme Moss. This experiment was conducted under the auspices of the EUROTRAC II subproject PROCLOUD. Collaborating institutes included the University of Lund, Sweden (LUND), the University of Vienna, Austria (IEP), and the Institute for Tropospheric Research in Leipzig, Germany (IFT).

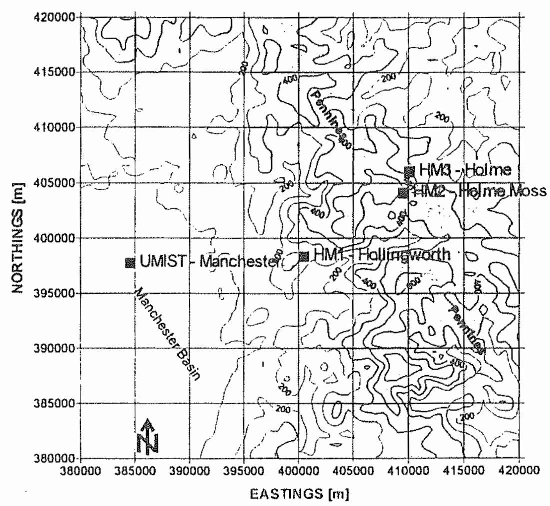

Figure 1: The Ground Based Measurement Sites at Holme Moss in 1999. Site elevations (masl) are : HM1 - 310m; HM2 - 525m; HM3 -368m; and UMIST - at roof top level ~110m

Corresponding author: Dr. Keith N. Bower. The Physics Department, UMIST, PO Box 88, Manchester M60 1QD, United Kingdom.
E-mail: k.bower@umist.ac.uk

In order to achieve the aims, measurements were made at four ground-based sites (Fig.1). Measurements of the aerosol properties (concentration, size distribution in the range 3nm to 3μm diameter, composition, and hygroscopicity) and trace gas concentrations (including organic species) were made at out of cloud sites both upwind and downwind of the cloud (HM1 & HM3). At the in-cloud site (HM2), cloud microphysical measurements (liquid water content, cloud droplet size distribution, and the cloud droplet-aerosol particle relationship) and bulk and size segregated cloud water (and rain water) chemical measurements (including organic species) were made along with measurements of the aerosol and gases interstitial to the cloud droplets. Meteorological measurements were undertaken at all sites throughout the experiment. The evolution of the plume was further investigated by measurements made routinely upwind within the city at UMISTs rooftop laboratory site.

2.2 The ACE-2 HILLCLOUD experiment on Tenerife

In the summer of 1997, a similar experiment called ACE-2 HILLCLOUD was carried out on Tenerife, (one of the Canary Islands which are located in the eastern North Atlantic, to the west of NW Africa, and SW of the Iberian peninsular) as part of ACE-2 (the second Aerosol Characterisation Experiment of IGAC). In this experiment the hill-cap cloud forming over the Anaga ridge to the north east of the island of Tenerife was used to investigate cloud-aerosol interactions in a maritime region influenced at times by pollution outflow from continental Europe and desert dust from the Sahara. A comprehensive overview of the experiment is given in Bower *et al.* (2000).

3. RESULTS

In both PROCLOUD and ACE-2 experiments the number concentration of aerosol in the accumulation mode size range and below varied considerably depending on whether pollution events were reaching the measurement sites. However, the relationship between cloud droplet number and aerosol number was quite different in the two cases. Figure 2 shows this relationship for both the PROCLOUD and ACE-2 data sets. On Tenerife, the number of cloud droplets present in the cap cloud was nearly proportional to the number of accumulation mode aerosol, with droplet concentrations as high as 2500 cm^{-3} observed in the most polluted cases. These very high droplet concentrations were measured by the Droplet Aerosol Analyser, DAA (of LUND) which employs an electrostatic mobility technique to size and count droplets. The normal laser light scattering technique employed by the Forward Scattering Spectrometer Probe (FSSP) was unable to detect concentrations above ~1500 cm^{-3} (even with upgraded fast electronics). In contrast, at Holme Moss, droplet numbers observed in cloud were seen to be much lower, and nearly independent of accumulation mode aerosol number during the polluted episodes. In these cases, most of the particles remained interstitial to the cloud droplets.

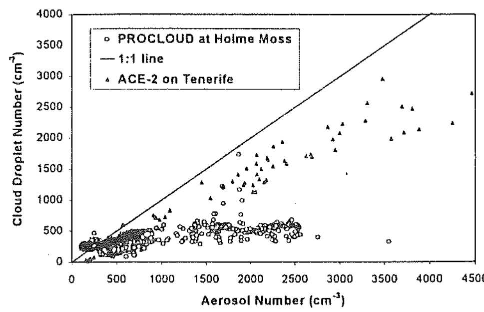

Figure 2: Relationship between Cloud Droplet Number and Aerosol Number for PROCLOUD and ACE-2 data sets. Droplet Numbers for Holme Moss are from the FSSP measurements and for Tenerife from the DAA. Aerosol Numbers N are for particles >0.1μm and >0.042μm for PROCLOUD and ACE-2 datasets respectively.

During the outbreaks of the most polluted air on Tenerife, back trajectory analysis indicated that the air had crossed over northern Iberia some 1.5 to 2 days earlier, and had probably originated over the UK or Northern Europe prior to this. During PROCLOUD, however, the transit time of air advecting from the city and into the clouds forming at Holme Moss was only of the order of a few hours at maximum. It is this difference in the age of the polluted aerosols arriving at the respective cloud sites that is expected to be the key to the different microphysical behaviour in the two studies.

Figures 3 and 4 show the DMPS aerosol size spectra measured at Holme Moss (by IFT) and on Tenerife, respectively (both during pollution episodes). It can be seen that the majority of aerosols are significantly larger in the ACE-2 case the modes peaking at around 15 nm and 100 nm respectively. This observation is consistent with the polluted airmass at Tenerife being more aged and there having been more time for the pollutant aerosol particles to have grown by the addition of soluble inorganic material during transit to the island.

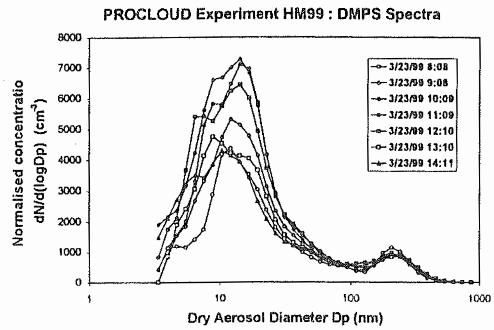

Figure 3: DMPS dry aerosol size distribution measured during a pollution event at the Holme Moss downwind site HM3 during PROCLOUD (Run 6, 23/03/99)

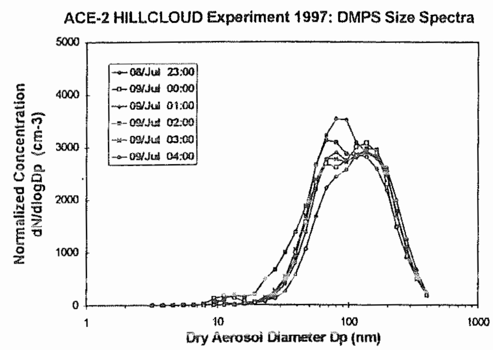

Figure 4: DMPS dry aerosol size distribution measured during a pollution event at upwind Tenerife site TG1 during ACE-2 (Run 3, 8-9/07/97)

Analysis of the hygroscopic properties of the two aerosol populations as measured by Tandem Differential Mobility Analysers (TDMAs, employed at the upwind sites in both PROCLOUD (by LUND) and ACE-2 experiments) reveals that the aerosols arriving at Tenerife are significantly more hygroscopic than those arriving at Holme Moss in the Manchester plume. Figures 5 and 6 show the hygroscopic growth factors for aerosol of 166nm dry size (measured by TDMAs at 90% relative humidity). When observed in this way aerosols usually fit into modes of relatively well defined growth factors. Usually, these comprise a mode of more hygroscopic aerosol with a high growth factor (GF0 in figs. 5 & 6) and a mode of only weakly hygroscopic (or hydrophobic) aerosol with a very low growth factor (GF1). Sometimes a mode of intermediate hygroscopicity (GF2) is also observed. Figures 5 and 6 show values of GF0, GF1 (and when observed GF2) as well as the fraction of the total aerosol at 166nm observed in these modes (GF0 fraction and GF2 fraction etc.). Although the growth factors of the more hygroscopic mode GF0 are similar in both PROCLOUD and ACE-2 plots at this size, in the polluted episode of 8th-9th July in ACE-2, all of the 166nm aerosol are observed in the high growth factor mode. In contrast, at Holme Moss, following the arrival of the Manchester plume (second half of Run 6) less than two thirds of the 166nm aerosol belong to the more hygroscopic mode. At smaller aerosol sizes (e.g. at 50nm) this fraction is even less, and falls to below 40%. In addition, the more hygroscopic mode particles are considerably less hygroscopic at Holme Moss at the smaller but considerably more numerous sizes (<50nm), while GF1 values at this size are close to 1 (i.e. show little or no growth at all).

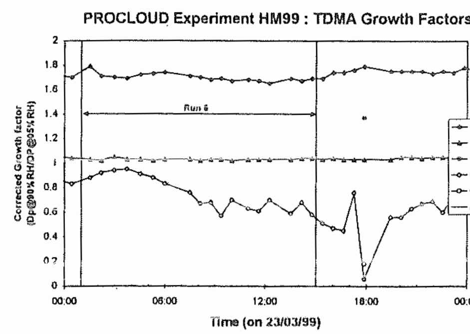

Figure 5: TDMA Hygroscopic Growth Factors (at 166nm) during PROCLOUD Run 6, and fractions of total aerosol in each mode (GF0: more hygroscopic mode; GF1: less hygroscopic mode)

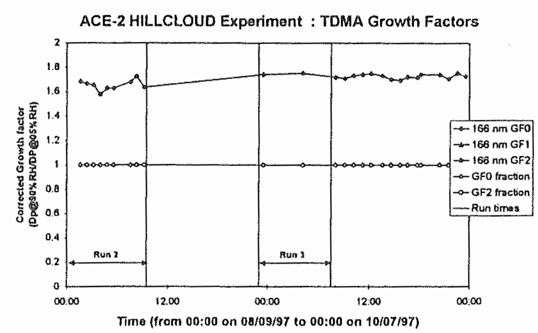

Figure 6: TDMA Hygroscopic Growth Factors (at 166nm) during ACE-2 HILLCLOUD Runs 2 and 3, and fractions of total aerosol in each mode (GF0: more hygroscopic mode; GF1: less hygroscopic mode)

Analysis by ion chromatography (IC) of the size segregated aerosol samples collected by 5 stage

Berner Impactors (of IEP and IFT in PROCLOUD) deployed during both experiments, revealed that at Tenerife (in the polluted episode presented), often a larger fraction of the inorganic soluble material at the smallest size cut (<0.1μm) was comprised of nitrate than at Holme Moss. This is consistent with absence of detectable levels of NOx in the polluted air arriving at Tenerife, most of which will have been converted to nitrates in the aerosol phase in transit from Europe. The remaining soluble fraction of material consisted of sulphate and ammonium salts as well as varying levels of sodium and chloride in both studies.

4. CONCLUSIONS

The city of Manchester acts as a major source of aerosol (from motor vehicle exhausts and other sources), and particles from 3nm to 300nm are observed in high concentrations.

When air from the city is advected into the clouds forming over Holme Moss, however, only a small fraction of these particles are able to act as CCN. The majority of fresh aerosols produced within the city are mostly insufficiently hygroscopic for them to activate to form cloud drops. These particles are externally mixed with respect to their chemical composition.

The more soluble portion of the urban aerosols (probably the more aged background aerosol) are found to consist of the usual sulphates, nitrates, chlorides, and ammonium salts, however, the externally mixed weakly hygroscopic aerosols produced in the city are expected to be composed largely of insoluble organic material. These particles dominate the aerosol number particularly at smaller sizes (<60-70 nm).

The consequence of the properties of aerosol in the fresh urban plume is that the cloud droplet number concentration at Holme Moss is generally seen to be insensitive to the number of accumulation mode aerosol during polluted episodes. On these occasions the majority of the additional particles remain interstitial to the cloud. When aerosol numbers are low, however, the droplet concentration closely tracks the aerosol number. These generally correspond to periods of low NOx and CO, when highly polluted air is not reaching the Holme Moss sites. These periods occur mainly at night when urban emissions are at a minimum.

In contrast to the PROCLOUD results at Holme Moss, during periods of polluted air outbreaks on Tenerife (during ACE-2), the aerosol particles were generally seen to be fully hygroscopic with growth factors similar to those of ammonium sulphate. As a consequence of this, a large fraction of the total aerosol population were able to activate to form cloud drops in the Tenerife cloud. An almost proportional relationship was observed between cloud droplet number and aerosol number across the full range of aerosol numbers. This led to exceptionally high concentrations of cloud drops (>2500 cm^{-3}) being observed in the most polluted events.

Back trajectory analysis suggested that in certain conditions, European aerosol were transported over several thousands of kilometres in the boundary layer and lower free troposphere into the ACE-2 experimental region. During this transit, heterogeneous chemical reactions will have occurred leading to a significant increase in the fraction of soluble material comprising these aerosol. This will have led to growth, and a significant increase in hygroscopicity of the aerosol population. This is in agreement with the observations that the majority of aerosol were larger on Tenerife (forming a mode at around 100nm) and with the results of the TDMA measurements presented.

5. ACKNOWLEDGEMENTS

This work was supported by the UK Natural Environment Research Council (NERC) and by the European Commission. ACE-2 was part of the International Global Atmospheric Chemistry (IGAC) Aerosol Characterization Experiments (ACE) series. IGAC is a Core Project of the International Geosphere-Biosphere Programme (IGBP). The authors would like to thank their colleagues from LUND, IEP and IFT who took part in PROCLOUD and for access to, and use of, their data in this paper. Similarly, thanks go to all participating institutions in the ACE-2 HILLCLOUD experiment.

6. REFERENCES

Bower,, K.N., Choularton, T.W., Gallagher, M.W., Beswick, K.M., Flynn,M.J., *et al.* 2000.
ACE-2 HILLCLOUD: An Overview of the ACE-2 Ground Based Cloud Experiment. Tellus, 52B, No.2, (in press - April 2000).

POLLUTANT AEROSOL EFFECTS ON OROGRAPHIC SNOWFALL RATES

R.D. Borys, D.H. Lowenthal and D.L. Mitchell

Desert Research Institute, Reno, NV, 89512, U.S.A.

1. INTRODUCTION

The effect of anthropogenic aerosol particles on climate forcing is the subject of considerable interest (Charlson et al., 1992; Penner et al., 1994; Chuang et al., 1997). Twomey et al. (1984) suggested that increased loadings of anthropogenic CCN would increase cloud droplet number, leading to enhanced cloud albedo. For adiabatic, non-precipitating clouds, increasing the droplet number necessarily decreases droplet size for a constant liquid water content (LWC). As the droplet size approaches 10 μm diameter or less, riming (the collection of supercooled cloud droplets by falling ice crystals) efficiency rapidly approaches zero for all snow crystal sizes (Pruppacher and Klett, 1980). An anthropogenically-induced decrease in cloud droplet size may affect precipitation in cold clouds through inhibition of the riming process. This aspect of climate-related effects of pollution aerosols has received little attention.

2. METHODS

2.1 Sampling site

Precipitating clouds were sampled between 13 and 28 January, 1995 at the Desert Research Institute's Storm Peak Laboratory, located on the west summit of Mt. Werner in the Park Range near Steamboat Springs in northwestern Colorado at an elevation of 3210 m MSL (Borys and Wetzel, 1997). In the orographic cloud, the updraft near the mountain keeps the growing ice particle in the cloud for a relatively longer period than would be the case in a cloud of the same thickness in the free atmosphere. The ice particle is thus exposed to a longer cloud path and more riming by cloud droplets in this region of the mountain cloud. The region of the cloud in the updraft on the upwind side of the mountain is therefore crucial in determining the final precipitation rate on the mountain. Air from the polluted boundary layer is also most likely to pass through the cloud in the updraft near the mountain. If this air contains high concentrations of anthropogenic CCN, the droplet size distribution is expected to shift to smaller mass mean diameters (MMD), and riming efficiency should decrease as a result.

Corresponding author address: Douglas H. Lowenthal, Desert Research Institute, 2215 Raggio Parkway, Reno, NV 89512-1095; email: dougl@dri.edu.

2.2 In-cloud measurements

Snowing clouds were sampled in discrete periods ranging from 3 to 33 minutes (average 17±7 minutes) on eight days in January, 1995 (13, 14, 16, 17, 18, 26, 27, 28) for a total sampling time of 15 hours. When SPL was enveloped by a snowing cloud, simultaneous measurements were made of the cloud droplet size distribution, ice water content (IWC), and snowfall rate. Cloud water was collected for chemical analysis.

The cloud droplet size distribution was measured with a PMS FSSP-100 (Forward Scattering Spectometer Probe) mounted on a wind vane to orient the deiced (heated), aspirated intake into the wind. The droplet size distributions were recorded every ten seconds and integrated later over the cloud water collection period to produce a single spectrum. The cloud LWC was calculated from the FSSP size distributions as the sum of the volumes of the particles in each of the 15 FSSP channels.

Mean snowfall rate was measured over the sample period with a high-sensitivity electronic gravimetric balance mounted in a truncated, vented pyramid, four feet high and four- and three-feet square at the base and top, respectively, with a collection pan area of 2564 cm^2. Snow samples for determination of IWC were collected in polyethylene bags inserted into two 15 cm diameter aluminum tubes mounted to a vane which oriented the bag openings into the wind. This device functions as a virtual impactor, as described by Borys et al. (1988).

Cloud droplets >2 μm dia. were collected by impaction on monofilament "cloud sieves" (Hindman, et al., 1992). The rime ice was removed from the filaments with a Teflon scraper under clean conditions, weighed, and stored frozen in clean polyethylene bags for chemical analysis. The amount of water collected ranged from 0.5 to 388 g (average, 120 g). An average wind speed was obtained from wind speeds measured with a hand-held anemometer at the beginning and end of the cloud sieve sampling period. The cloud water was analyzed for pH and conductivity, for sulfate, nitrate, and chloride by ion chromatography, and for trace elements by instrumental neutron activation analysis.

3. RESULTS AND DISCUSSION

3.1 Chemistry

Clear-air equivalent (CAE) concentrations (μg/m^3) were obtained by multiplying the chemical concentrations in the cloud water (μg/g) by the corresponding LWC (g/m^3). Average sulfate and nitrate CAE concentrations were 0.51 and 0.26 μg/m^3. Sulfate is a major component of the water-soluble continental aerosol, particularly in areas where fossil fuels, especially coal, are burned for electric power generation (Rahn and Lowenthal, 1985). There are numerous coal-fired utilities in Utah, Colorado, and Wyoming, including two within 60 km west of SPL. A strong indication that sulfate at SPL is related to coal combustion is its high correlation (0.91) with Se, a tracer for coal-combustion emissions (Thurston and Spengler, 1985; Eldred, 1997).

3.2 Microphysical and Meteorological Parameters

Snowfall rate was highly correlated with IWC (0.92), demonstrating that the sheltered gravimetric balance was not subject to wind-inducted (turbulence) artifacts. Droplet MMD ranged from 7.7 to 19.7 μm. Droplet number concentration (N_c) ranged from 9 (extremely clean) to 695 cm^{-3} (polluted). Droplet concentrations less than 20 cm^{-3} were associated with very low LWC (<0.02 g/m^3). Such low N_c and LWC are indicative of ice formation at the expense of cloud droplets.

Temperatures ranged from -1.4 to -17.3 °C. Correlations between temperature and N_c, LWC, IWC, and snowfall rate were not significant. Wind speeds ranged from 2.9 to 10.7 m/s. Wind speed was not significantly correlated with LWC, IWC, MMD, N_c, or snowfall rate, but was inversely correlated with temperature (-0.28). The lack of correlation between wind speed and droplet number is puzzling because higher updraft velocities should have activated more CCN.

There was no apparent relationship between cloud microphysical properties and synoptic conditions. This suggests that the lower reaches of the cloud where the measurements were made were influenced more by orography than by synoptic-scale forcing. Snowing clouds were observed under both high and low pressure conditions. The coldest conditions occurred under flow from both the northwest and the southwest. Wind speeds were not dramatic, averaging 5.5±1.6 m/s. The highest daily snowfall rate, IWC, droplet MMD, and the lowest daily sulfate concentration were observed on January 27, when there was an intense low over Kansas. Neither wind speed (4.6 m/s) nor temperature (-7.0 °C) were remarkable on this day.

3.3 Relationship Between Chemistry and Cloud Microphysics

Figure 1 presents the relationship between CAE sulfate concentration and N_c. The correlation is 0.89 (P=0.0001). This does not imply that sulfate is the only or even the major component of the CCN, only that it is correlated with the cloud droplet, and by inference, the CCN number concentration. Other chemical components such as nitrate and organic carbon, and geological material may also contribute to CCN activity.

The relationship appears to be linear for droplet concentrations between about 100 and 500 cm^{-3}. The intercept of 74±14 is consistent with continental background CCN numbers reported for Yellowstone National Park (15-78 cm^{-3}).

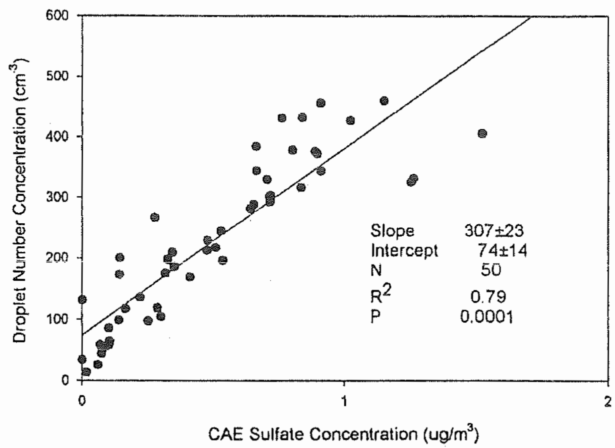

Figure 1. Relationship between CAE sulfate concentration and droplet number concentration (P is the significance level for the regresion).

Figure 2 presents the relationships between droplet concentration (N_c) and MMD, between MMD and snowfall rate, and between CAE sulfate concentration and snowfall rate. The data have been segregated according to LWC: a) all samples; b) samples with LWC > 0.1 g/m^3; and c) samples with LWC > 0.2 g/m^3. At constant LWC, droplet diameter varies as the one-third power of the inverse of N_c. At very small droplet concentrations (<50 cm^{-3}) the droplet MMD should increase rapidly. However, for the range of values presented in Figure 2, the relationship is much less curvilinear. For all data points, the inverse correlation of -0.38 (N=53) between N_c and MMD is statistically significant. For samples with LWC > 0.1 and >0.2 g/m^3, the correlations increase to -0.68 (N=29) and -0.85 (N=15), respectively, and remain significant.

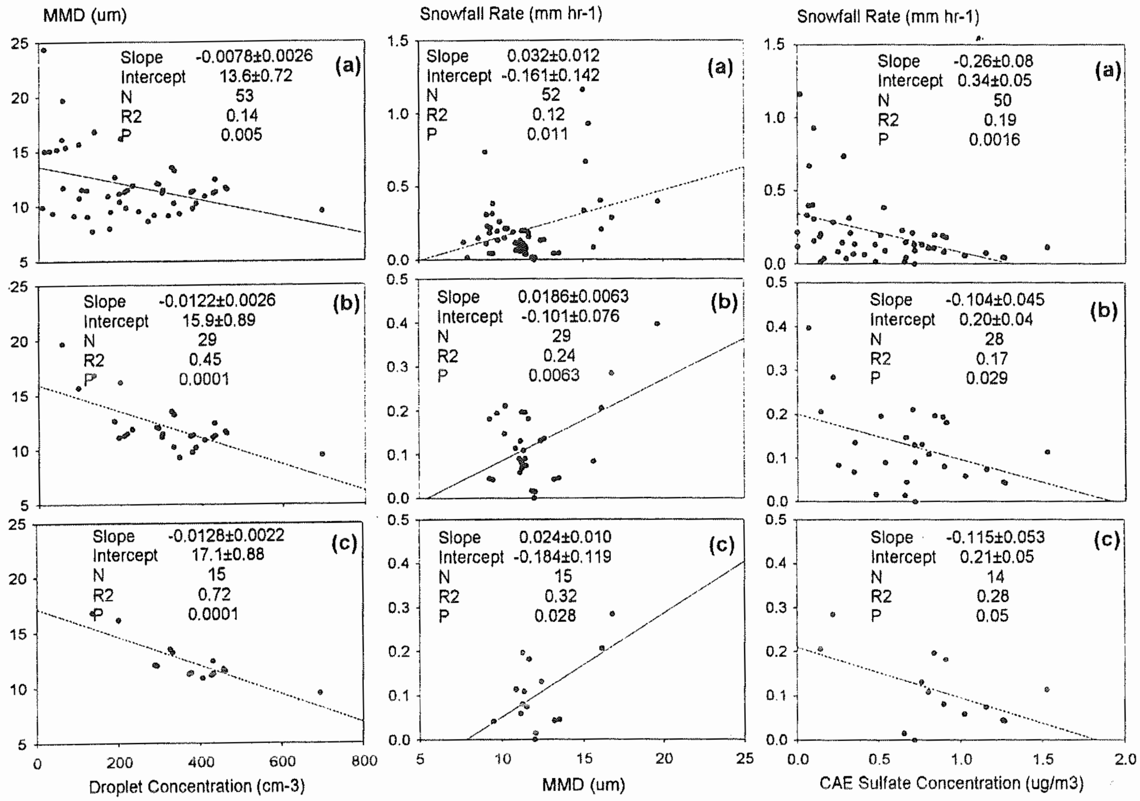

Figure 2. The relationships among N_c, MMD, snowfall rate, and CAE sulfate concentration: a) all data; b) LWC>0.1 g/m^3; c) LWC>0.2 g/m^3 (P is the significance level for the regression).

We believe that the relationship between droplet size and number concentration deteriorates at low LWC because of increased competition for water vapor between crystals and droplets.

For all data points, the correlation between droplet MMD and snowfall rate (Figure 2) is low (0.34) but significant. The highest snowfall rate data point, which raised the correlation to 0.63, was not included. For samples with LWC > 0.1 and >0.2 g/m^3, the correlations between MMD and snowfall rate increase to 0.50 (N=29) and 0.55 (N=15), respectively, and remain significant.

Finally, Figure 2 plots the relationship between CAE sulfate concentration and snowfall rate. The correlation coefficient for all samples is low (-0.44) but significant. For samples with LWC > 0.1 and >0.2 g/m^3, the correlations (-0.41 and -0.53, respectively) are also low, and are marginally significant. The data indicate a direct relationship between CAE sulfate concentration and droplet number concentration, an inverse relationship between droplet number concentration and droplet size, a direct relationship between droplet size and snowfall rate, and an inverse relationship between CAE sulfate concentration and snowfall rate.

4. CONCLUSIONS

Clear-air equivalent concentrations of pollution-derived sulfate in cloud water were directly correlated with cloud droplet number concentrations. Droplet number concentrations were inversely correlated with droplet size, which was directly correlated with snowfall rate. Finally, there was an inverse correlation between sulfate and snowfall rate. These relationships suggest that pollution-derived-CCN-induced changes in the cloud droplet size distribution cause a decrease in snowfall rate by inhibiting the riming process.

The relationships between droplet number and size, droplet size and snowfall rate, and sulfate concentration and snowfall rate improved as a function of cloud liquid water content. We suggest that this represents the effect of competition between ice crystals and cloud droplets for water at low liquid water content. This also implies that the effects of variations in riming on snowfall rate are less important at low liquid water content.

5. ACKNOWLEDGMENTS

This work was supported by the Department of Energy, National Institute for Global Environmental Change, grant W/GEC 93-001. Logistical assistance from the Steamboat Ski and Resort Corporation is greatly appreciated. Storm Peak Laboratory operates under a Special Use Permit under the auspices of the U. S. Forest Service, Hahn's Peak District, Colorado.

6. REFERENCES

Borys, R.D., E.E. Hindman, and P.J. DeMott, 1988: The chemical fractionation of atmospheric aerosols as a result of snow crystal formation and growth. *J. Atmos. Chem.* **7**, 213-239.

Borys, R.D. and M.A. Wetzel, 1997: Storm Peak Laboratory: A research, teaching and service facility for the atmospheric sciences. *Bull. Amer. Meteor. Soc.*, **78**, 2115-2123.

Charlson, R.J., S.E. Schwartz, J.M. Hales, R.D. Cess, J.A. Coakley, Jr., J.E. Hansen, and D.J. Hofmann, 1992: Climate forcing by anthropogenic aerosols. *Science*, **255**, 423-430.

Chuang, C.C., J.E. Penner, K.E. Taylor, A.S. Grossman, and J.J. Walton, 1997: An assessment of the radiative effects of anthropogenic sulfate. *J. Geophys. Res.*, **102**, 3761-3778.

Eldred, R.A., 1997: Comparison of selenium and sulfur at remote sites throughout the United States, *J. Air & Waste Manage. Assoc.*, **47**, 204-211.

Hindman, E.E., E.J. Carter, R.D. Borys, and D.L. Mitchell, 1992: Collecting supercooled droplets as a function of droplet size. *J. Atmos. Ocean. Tech.*, **9**, 337-353.

Pruppacher, H.R. and J.D. Klett, 1980: Microphysics of Clouds and Precipitation. D. Reidel, Dordrecht, 714 pp.

Rahn, K.A. and D.H. Lowenthal, 1985: Pollution aerosol in the northeast: North-eastern-Midwestern contributions, *Science*, **228**, 275-284.

Thurston, G.D. and J.D. Spengler, 1985: A quantitative assessment of source contributions to inhalable particulate matter pollution in metropolitan Boston, *Atmos. Environ.* **19**, 9-25.

Twomey, S., M. Piepgrass, and T.L. Wolfe, 1984: An assessment of the impact of pollution on global cloud albedo. *Tellus* **36B**, 356-366.

A NUMERICAL MODEL OF THE CLOUD-TOPPED PLANETARY BOUNDARY-LAYER: CHEMISTRY IN MARINE STRATUS AND THE EFFECTS ON AEROSOL PARTICLES

Andreas Bott
Meteorologisches Institut, Universität Bonn, Germany

1. Introduction

Aerosol measurements in remote maritime regions (e. g. Hoppel et al. 1994) indicate that very often the size distributions are characterized by a bimodal structure with peaks in the 0.02–0.03 μm (nucleation mode) and 0.08–0.15 μm (accumulation mode) radius range. Hoppel and co-workers found strong evidence for the hypothesis that the accumulation mode particles are formed during several cycling processes through nonprecipitating clouds in which chemical species are transferred from the gas phase to the aerosols via heterogeneous reactions in cloud droplets, henceforth referred to as ACC (Aerosol-Cloud-Cycling) process. In the present paper the ACC hypothesis will be investigated by means of a numerical sensitivity study with the microphysical stratus model MISTRA of Bott et al. (1996) and Bott (1997). In order to describe the modification of the aerosols due to their cloud processing, MISTRA has been extended by a chemical module describing chemical reactions in the gas phase and in cloud droplets yielding the combined model CHEMISTRA (chemical microphysical stratus model).

2. Description of CHEMISTRA

CHEMISTRA is a one-dimensional model for the cloud-topped planetary boundary-layer consisting of a set of prognostic equations for the horizontal wind field, the specific humidity and the potential temperature. Aerosol particles and cloud droplets are treated in a joint two-dimensional particle distribution with 40 aerosol and 50 water classes. The chemical module of CHEMISTRA has been extracted from the chemical microphysical radiation fog model of Bott and Carmichael (1993). The gas phase chemical reaction set is based on the condensed mechanism of Lurmann and co-workers (1986). The aqueous phase chemical reaction mechanism is due to Chameides and Davis (1982). In the chemical module the particle distribution is subdivided into three size categories. The first region mainly consists of unactivated aerosol particles which are assumed to be chemically inert. Aqueous phase chemical reactions are considered only in the second and third particle region consisting of small and large droplets, respectively. The uptake of trace gases by cloud droplets and subsequent aqueous phase chemical reactions yield a mass increase of the aerosol nucleus after evaporation of the droplet. In the present model it is assumed that the only contribution to this mass increase is due to the direct uptake of gas phase HNO_3 and NH_3 and due to concentration changes of aqueous SO_4.

Corresponding author's address: Andreas Bott, Meteorologisches Institut, Universität Bonn, Auf dem Hügel 20, D-53121 Bonn, Germany; E-Mail: a.bott@uni-bonn.de

3. Model Results

In a particular model simulation a tremendous set of chemical data is produced so that here only a small fraction of the results can be shown. Since in CHEMISTRA chemical reactions in the liquid phase are separately calculated for small and large droplets, one obtains in the two droplet regimes different concentrations of all species. The concentrations of most of the liquid phase chemical species are increasing with height. At each time the concentrations of highly water soluble species are larger in small than in big cloud droplets. In contrast to this, the concentrations of species with low water solubility closely follow the liquid water content in the two droplet regimes, i. e. their concentrations are lower in small than in large droplets. This phenomenon which was also found in the fog model of Bott and Carmichael (1993) is explained as follows: If in a particular layer cloud droplets form, the highly water soluble species are quickly transferred from the gas phase into the droplets which at the beginning belong to the small droplet regime. Due to their continuous condensational growth, after a while some droplets leave the small droplet regime and enter the large droplet regime. However, at this time the vapor pressure of the highly water soluble species is already so small that the direct mass transfer from the gas phase into the big droplets is not important. In contrast to this, the vapor pressure of species with low water solubility is always relatively high. Thus, after some time the direct mass transfer from the gas phase is still efficient and is mainly directed towards the big droplets.

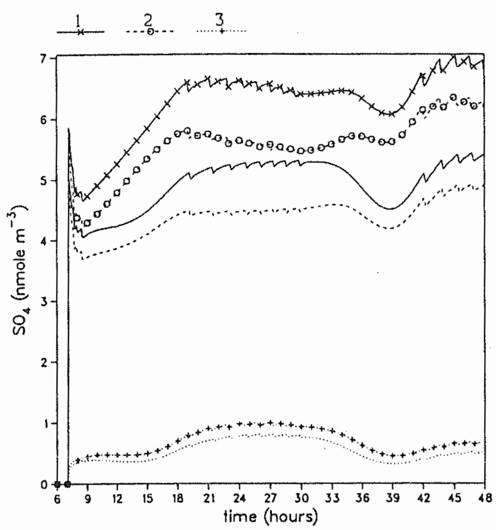

Figure 1: Time evolution of aqueous phase sulfate at 505 m height. Curves with symbols: Nucleation of aerosols and chemical production of sulfate. Curves without symbols: Only nucleation of aerosols. Curve 1: Total value, curve 2: small droplet regime, curve 3: large droplet regime.

Of particular interest is the behavior of sulfur within the cloud because the ACC process is largely affected by the sulfate mass increase of the droplets. The largest values of aqueous phase SO_2 are found at cloud base where the uptake of gas phase SO_2 which has been produced below the cloud is most efficient. With increasing height the SO_2 concentrations decrease due to the oxidation and the corresponding formation of sulfate. Since during the night no SO_2 is produced, the liquid phase concentrations decrease below 10^{-7} nmole m^{-3}. In addition to the oxidation of SO_2 another important sulfate source is the nucleation scavenging of aerosols. In order to distinguish between the two sources, Figure 1 shows the time evolution of sulfate as calculated in 505 m height in the small and the large droplet regime as well as the total concentrations. In this figure the three curves with symbols denote the SO_4 concentrations resulting from the nucleation scavenging and from the oxidation of sulfur dioxide. The curves without symbols are produced by considering only the nucleation process, that is in these curves the contribution by the oxidation of SO_2 is ignored. Comparison of the three corresponding curve pairs clearly demonstrates that the major contribution to the liquid phase sulfate is due to the nucleation process. This is expressed by relatively high values of the curves without symbols.

Nucleation scavenging is also the reason for the peak which is observed in the small droplet regime immediately after cloud formation. The concentration increase between 9.00 h and 15.00 h is mainly due to the SO_2 oxidation since this increase is much weaker in the curves without symbols which neglect the contribution by chemical reactions. It is also seen that most of the sulfur oxidation takes place in the small droplet regime because the difference between the two curves of the large droplet regime is relatively small, (see the dotted curves of Figure 1). The oscillations of the curves during the night are caused by the vertical increase of the cloud in discrete steps of 10 m as given by the numerical grid mesh which is accompanied by the entrainment of free tropospheric air. The decreasing concentrations during the second day are caused by the net evaporation of the cloud which results in a loss of cloud droplets and an increase of the number concentration of unactivated aerosols.

Among the different oxidation pathways of sulfur, in the present model study the reaction of S(IV) with ozone is most important. Even the contribution by the reaction of aqueous SO_2 with hydrogen peroxide is negligibly small. This behavior is explained by the high pH values of the cloud water which are relatively constant in space and time varying only between 4.4–4.6 (small droplets) and 5.2–5.4 (large droplets) during day and night, respectively.

Due to the treatment of aerosols and cloud droplets in a joint two-dimensional size distribution, in CHEMISTRA it is always possible to extract from a given particle distribution the dry aerosol spectrum which results if the entire water mass is removed from the particles. By comparing the particle spectra at different times and heights the following four features are observed:

i) At a fixed time the droplet spectra are strongly varying with height.

ii) At a given relative position within the cloud (e. g. cloud base, cloud top etc.) the shapes of the droplet number distributions are barely changing with time.

iii) Within the entire boundary-layer the dry aerosol spectra are constant with height. There is particularly no difference in the spectral distributions between cloudy and cloud free regions.

iv) After cloud formation the dry aerosol spectra are continuously modified by the ACC process.

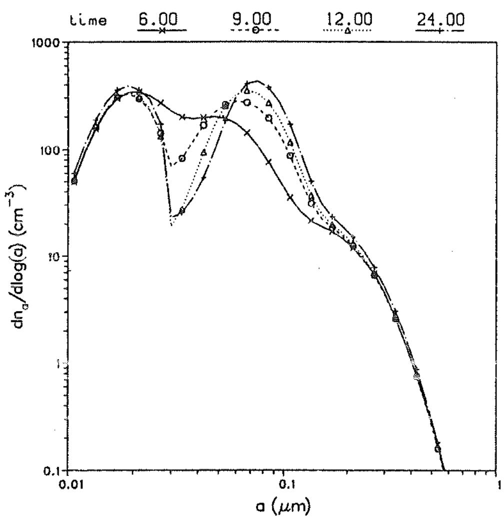

Figure 2: Evolution of aerosol particle spectrum due to the ACC process.

The temporal modification of the aerosol spectrum by the ACC process is impressively demonstrated in Figures 2 and 3 depicting four different spectral number and mass distributions calculated at 505 m height at the times indicated in the figures. The curve obtained at 6.00 h describes the situation immediately before cloud formation. This curve is very similar to the initial aerosol spectrum. The largest modification of the aerosol distributions takes place during the first three hours after cloud formation. During this time the gas phase concentrations of all water soluble chemical species are still relatively high so that their uptake by the cloud droplets yields an efficient mass increase of the aerosol nuclei. After 12.00 h the shapes of the curves remain relatively stationary (compare the 12.00 h with the 24.00 h curve of Figure 2). From Figure 3 it is, however, seen that the aerosol mass of the accumulation mode is still increasing.

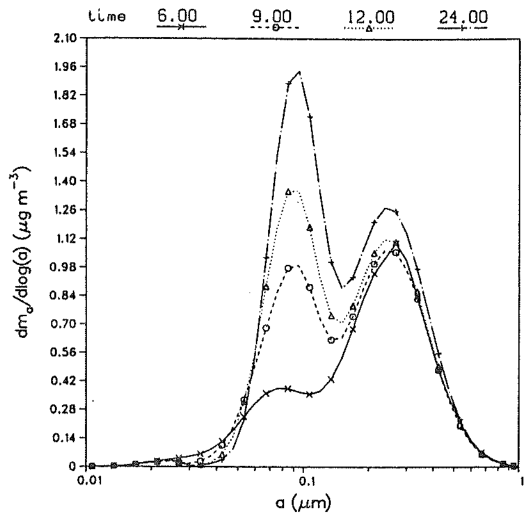

Figure 3: Evolution of aerosol mass spectrum due to the ACC process.

Due to the large scale subsidence and the vertical increase of the cloud, the total aerosol number concentration is continuously increasing in the MBL at an average rate of ≈ 2 particles cm^{-3} $hour^{-1}$. The corresponding aerosol mass increase is, however, small in comparison to the modification by the ACC process. In a separate model run where the cloud processing of aerosols was omitted, the total aerosol mass increased from 0.63 $\mu g\ m^{-3}$ at 6.00 h to 0.73 $\mu g\ m^{-3}$ at 24.00 h. By comparing these findings with corresponding values of the base model run it is seen that at 24.00 h 0.49 $\mu g\ m^{-3}$ of the total aerosol mass results from the ACC process while only 0.1 $\mu g\ m^{-3}$ is due to the large scale subsidence and vertical increase of the cloud top.

4. Conclusions

In a numerical model study with the chemical microphysical stratus model CHEMISTRA the modification of aerosol particles by stratiform clouds has been investigated. CHEMISTRA is based on the one-dimensional microphysical stratus model MISTRA which has been extended by a module describing chemical reactions in the gas phase and in cloud droplets. From the numerical results presented in the paper the following conclusions are drawn:

Within the boundary-layer the concentrations of chemical species are mainly affected by chemical reactions, turbulent mixing, dry deposition, emission from the surface and by the uptake by cloud droplets. Since turbulent mixing is very efficient within the entire cloud-topped planetary boundary-layer, the gas phase concentrations of the highly water soluble species are very small not only in cloudy regions but also below the cloud. Due to the strong temperature inversion at cloud top, the exchange of air between the boundary-layer and the free troposphere is unimportant so that in both regions the time evolution of the trace gases might differ.

The concentrations of aqueous phase chemical species differ between small and large droplets. While highly water soluble species are mainly found in small droplets, the opposite is true for reactands with low water solubility. In the aqueous phase sulfate is produced by the oxidation of S(IV) and by the nucleation of aerosols whereby the latter process is more efficient than the sulfate production by chemical reactions. Due to the high cloud water pH, in the particular model simulation the oxidation of sulfur by H_2O_2 *is* not important. Instead, sulfur is oxidized by ozone whereby the reaction takes place mainly in small droplets.

In the microphysical aerosol/droplet distributions four striking features are observed. (i) At a fixed time the particle spectra are strongly varying with height. (ii) At a given relative position within the cloud the distributions are barely changing with time. (iii) Within the entire MBL the dry aerosol spectra are constant with height. (iv) The ACC process strongly modifies the shape of the dry aerosol spectra. This modification is expressed by the formation of a bimodal structure in the aerosol number distributions with an increase of the number concentrations in the accumulation mode and the evolution of a local minimum at around 0.03 μm. This minimum separates interstitial aerosols from cloud condensation nuclei. The total aerosol mass increase caused by the ACC process alone is $\approx$78 % in 18 hours.

Acknowledgements

The author wishes to thank H. Wagner for her constructive criticism and helpful discussions during the preparation of this manuscript. This research was funded by the Deutsche Forschungsgemeinschaft, Sonderforschungsbereich 233, Chemie und Dynamik der Hydrometeore.

References

Bott, A., 1997: A numerical model of the cloud-topped planetary boundary layer: Impact of aerosol particles on radiative forcing of stratiform clouds. *Quart. J. Roy. Meteor. Soc.*, **123**, 631–656.

Bott, A., and G. R. Carmichael, 1993: Multiphase chemistry in a microphysical radiation fog model — a numerical study. *Atmos. Environ.*, **27A**, 503–522.

Bott, A., T. Trautmann, and W. Zdunkowski, 1996: A numerical model of the cloud-topped planetary boundary-layer: Radiation, turbulence and spectral microphysics in marine stratus. *Quart. J. Roy. Meteor. Soc.*, **122**, 635–667.

Chameides, W. L., and D. D. Davis, 1982: The free radical chemistry of cloud droplets and its impact upon the composition of rain. *J. Geophys. Res.*, **87**, 4863–4877.

Hoppel, W. A., G. M. Frick, J. W. Fitzgerald, and R. E. Larson, 1994: Marine boundary layer measurements of new particle formation and the effects nonprecipitating clouds have on aerosol size distribution. *J. Geophys. Res.*, **99**, 14,443–14,459.

Lurmann, F. W., A. C. Lloyd, and R. Atkinson, 1986: A chemical mechanism for use in long-range transport/acid deposition computer modeling. *J. Geophys. Res.*, **91**, 10,905–10,936.

A THREE-DIMENSIONAL MODELING STUDY OF THE EFFECTS OF SOLID-PHASE HYDROMETEOR-CHEMICAL INTERACTIONS IN CUMULONIMBUS CLOUDS ON TROPOSPHERIC CHEMICAL DISTRIBUTIONS

A.L. Stuart[1], M.C. Barth[2], W.C. Skamarock[2], M.Z. Jacobson[1]
[1]Stanford University, Palo Alto, CA
[2]National Center for Atmospheric Research, Boulder, CO

1. INTRODUCTION

Clouds can significantly impact trace chemical distributions in the troposphere and the chemical composition of precipitation. Clouds affect chemical distributions through convection of air and hydrometeors containing trace chemicals. They also provide a multi-phase environment for chemical phase changes and reaction. Due to the large vertical motions and turbulence of strong convective cloud systems, they can transport and mix trace chemicals between the atmospheric boundary layer and upper troposphere. If strong enough, they can also penetrate into the lower stratosphere. Hydrometeors in these clouds provide surfaces for chemical phase changes. They also act as condensed phase reactors for chemical reactions. Finally, hydrometeors serve as conduits for chemical transport from the atmosphere to the ground through scavenging and precipitation. Hence, storm clouds can impact acidic precipitation, urban pollutant dispersal, and concentrations of ozone and other atmospheric cleansing species (such as odd hydrogen radicals) in the upper troposphere and lower stratosphere.

Due to the variety of effects of convective clouds on surface and atmospheric chemistry, there has been considerable effort to understand the complex processes involved in these systems, including modeling studies. In these studies, interactions of volatile chemicals with ice- and mixed-phase hydrometeors (cloud ice, snow, graupel, and hail) are often excluded or limited due to their complexity as well as lack of theoretical understanding. Modeling studies which have included representations of interactions of ice-phase cloud hydrometeors with volatile chemicals have found that they may significantly impact chemical distribution and deposition (Audiffren et al., 1999; Chen and Lamb, 1990; Cho et al., 1989; Rutledge et al., 1986; Wang and Chang, 1993). However, the available studies use differing representations of these interactions, yield varying results, and give no consistent picture of the effects of these interactions on chemistry. A systematic investigation of the range of potential impacts of these interactions on chemical distributions and deposition is still lacking.

In this paper, we 1) review the state of current knowledge on the interactions between solid-phase cloud hydrometeors and chemicals, 2) describe modeling simulations we use to investigate the effects of these interactions on tropospheric chemistry and chemical deposition for the case of a thunderstorm, and 3) present results of model simulations comparing two representations of solid-phase interactions. For this work, we use a three-dimensional dynamical, microphysical, and chemical model. Interactions considered include sorption of chemicals from the gas phase, entrapment of chemicals in the solid-phase during liquid hydrometeor freezing, and chemical reactions in / on solid-phase hydrometeors.

Corresponding author's address: Amy L. Stuart, Dept. of Civil and Environmental Engineering, Stanford University, CA, 94305-4020; E-Mail: astuart@stanford.edu

2. ICE- AND MIXED-PHASE CHEMISTRY

2.1 Gas-Solid Transfer

Gas-phase chemical species can diffuse to the surface of a solid-phase hydrometeor. They may remain in that hydrometeor through adsorption at the surface, or absorption or incorporation in the bulk phase. In several laboratory studies, researchers have investigated the uptake by ice of several gas phase chemicals, including HCl, HNO_3, H_2O_2, CO_2, and SO_2, and found that uptake is dependent on the type of gas, the temperature, the crystal structure of the ice, and whether the ice phase is growing (e.g. Clapsaddle and Lamb, 1989; Valdez et al., 1989

A few cloud modeling studies have begun to incorporate these processes and determine their potential impacts on cloud chemistry. Rutledge, et al. (1986), incorporated the adsorption of HNO_3 on snow and graupel in their 2-D numerical modeling study. Incorporating a parameterization based on a theoretical development of chemical diffusion and sticking to hydrometeors, they found the process was partially responsible for the differences in the modeled nitrate and sulfate fields. Chen and Lamb (1990) compiled three semi-theoretical parameterizations of SO_2 sorption, based on the experimental data of Valdez et al. (1989) and Clapsaddle and Lamb (1989). By incorporating these parameterizations into a Lagrangian air parcel model, they found that removal due to ice phase sorption, though significantly lower than that due to liquid removal, is potentially important. They found that the locations of removal and the temperature dependencies were different from liquid phase removal.

2.2 Retention During Riming or Freezing

During freezing of aqueous solutions, solutes may be excluded or retained in the solid phase substrate depending on the characteristics of the solute, concentration of the solute in solution, and the rate and temperature of freezing (Pruppacher and Klett, 1997). In cold clouds, riming is known to lead to the efficient retention of nonvolatile species, such as sulfate. Models of cloud chemistry usually assume full retention of these species in the solid phase during hydrometeor freezing (e.g. Rutledge et al., 1986). The degree of retention of more volatile species is less well characterized.

Several laboratory and field observational studies have measured retention efficiencies of gases in freezing substrates for a limited number of chemical species found in clouds, including H_2O_2, SO_2, O_2, HCl, NH_3, HNO_3 (e.g. Lamb and Blumenstein, 1987; Snider et al., 1992). (The retention efficiency represents the concentration of solute in the solid phase versus that in the original liquid hydrometeor). These studies have resulted in varying estimates of retention efficiencies (sometimes for the same gas), ranging from 0.01 to 1. Although these differences may be due to different experimental (freezing) conditions, there is currently little theoretical analysis to explain the variations.

A few cloud chemistry modeling studies, which have incorporated the freezing transport mechanism, have explicitly examined the effects of including these processes on chemical distributions in clouds or precipitation. Chen and Lamb (1990) used a temperature dependent retention coefficient for SO_2, based on Lamb and Blumenstein (1987) data, in a Lagrangian air parcel model. Audiffren et al. (1999) used a similar retention parameterization for SO_2 in their 2–D modeling studies. Wang and Chang (1993), in their 3-D cloud modeling study, assumed all processes that convert liquid hydrometeors to the solid phase also transfer the solutes contained. Both Chen and Lamb (1990) and Wang and Chang (1993), found that the ice phase chemical transfer mechanisms impacted the pollutant distributions and their time evolution. Audiffren et al. (1999) found that the dependence of the chemistry on the ice-phase is strongly non-linear and chemical dependent, among other results. Cho et al. (1989), through a test of the sensitivity of their 1-D cloud model to including full solid retention of SO_2 and H_2O_2, found 37% less deposition of sulfate when solid retention was excluded.

2.3 Chemical Reaction

Solid phase hydrometeors may also impact the chemistry occurring in clouds by providing appropriate conditions for chemical reactions. Many types of chemicals reactions are know to proceed at significant rates in the ice phase or partially frozen ice phase, including hydrolysis, dehydration, oxidation, and peroxide decomposition reactions (Grant and Alburn, 1965). For some reactions, studies have shown an accelerated reaction rate when ice is present over the reaction rate in liquid solution (e.g. Grant and Alburn, 1965; Sato et al., 1996; Takenaka et al., 1996). Experimental studies of reactions in / on ice that are potentially important to cloud chemistry have primarily focused on the oxidation of sulfur dioxide and nitrite (e.g. Iribarne and Barrie, 1995; Sato et al., 1996; Takenaka et al., 1996) . No modeling studies of convective cloud chemistry to date have included ice-phase reactions.

3. DESCRIPTION OF MODEL SIMULATIONS

We use the COllaborative Model for Multiscale Atmospheric Simulation (COMMAS), a 3-D non-hydrostatic convective cloud model (Wicker and Wilhelmson, 1995; Wicker and Skamarock, 1998) for this work. The model contains a bulk parameterization of microphysics, described by Tao and Simpson (1993), which includes three glaciated hydrometeor species (cloud ice, snow, and hail). The model includes gas-liquid inter-phase transfer of chemical species and their advective transport in the gas and hydrometeor phases (Barth et al., 2000; Skamarock et al., 2000). The base chemical mechanism, representing daytime nitrogen and ozone chemistry in the troposphere, includes 15 chemical species undergoing 27 gas-phase and 15 aqueous-phase reactions.

We apply the COMMAS model to the July 10, 1996 STERAO thunderstorm observed in northeastern Colorado for the simulations in this work. The model domain is 120 x 120 x 20 km with 1 km horizontal resolution and variable vertical resolution (stretching from 50 m at the surface to 750 m at the domain top). Detailed discussion of the initialization and modeling of the storm dynamics and insoluble tracer transport can be found in Skamarock et al., 2000). Barth et al. (2000) include discussion of the effects of gas-liquid transfer on tracer fate. For the purposes of the work here, it is important to note that species mixing ratios are initially highest (135 ppbm) in the boundary layer , and decrease to 70 ppbm by 9.5 km above the ground (11 km MSL).

To determine the range of potential effects of solid-phase hydrometeor-chemical interactions on tropospheric chemical distributions and deposition, we follow the fate of chemicals during model simulations in which several distinct parameterization of these solid-phase hydrometeor-chemical interactions are implemented.

4. MODELING RESULTS

As discussed by Skamarock et al. (2000) the simulated storm evolved from a Northeast to Southwest multicellular convective line to supercellular after about two hours. During the simulated storm lifetime, the largest heights reached by the convective cells was approximately 15 km, with the storm anvil above approximately 8 km. The simulated storm anvil consisted primarily of snow and ice, while liquid and frozen hydrometeors coexisted in the storm core (Barth et al., 2000). Rain precipitated below cloud level to reach the ground surface. Analyses of passive tracer fate and parcel trajectories indicate that the storm transported air from the boundary layer, between 0.5 – 2 km above ground, to the anvil, with some entrainment and dilution in the convective updrafts and anvil (Skamarock et al., 2000).

To begin our investigation of the effects of interactions between chemicals and solid hydrometeors on chemical fate, here we will compare and discuss results of two simulations with distinct representations of chemical transfer during riming and freezing. For the first simulation, we assume that all dissolved species evaporate when a hydrometeor freezes (degassing run) For the second, dissolved species are retained in the frozen hydrometeor and are transported throughout the storm with the parent hydrometeor (solute retention run). We investigate the effects on species of varying solubilities by considering pseudo-species with a range of solubilities. Results shown are for simulations in which chemical reactions were not activated.

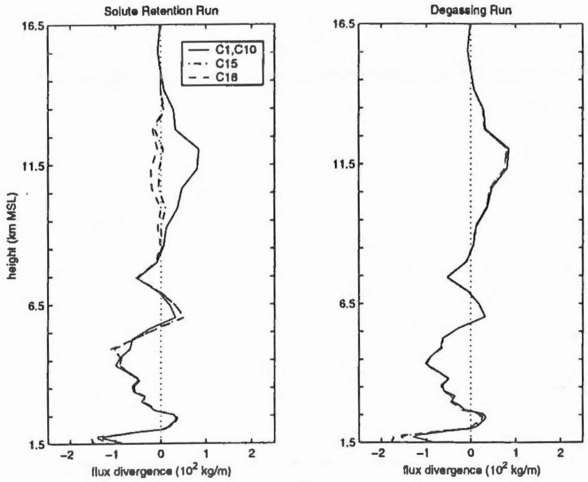

Figure 1. Time and horizontally integrated, vertical flux divergence (a measure of mass accumulation) versus height after 3 hours of storm simulation for four pseudo-species of varying solubility. C1 is a passive tracer (only transported in air). C10, C15, and C18 have increasing solubilities, with Henry's constants (K_h) of 100, 10^5, 10^{12} M atm^{-1}, respectively. Mass is summed over the gas and hydrometeor phases. (a) gives results for the simulation in which solutes are retained during hydrometeor freezing. (b) gives results for the simulation in which solutes are degassed.

The effect of retention of solutes during hydrometeor freezing on species mass transport due to the storm is shown in Figure 1. The figure shows a measure of mass accumulation versus height after 3 hours of storm simulation for pseudo-species of varying solubilities (Henry's constants, K_h, of 0, 100, 10^5, and 10^{12} M atm^{-1} for C1, C10, C15, and C18, respectively). For the simulation in which solutes evaporate during hydrometeor freezing, Figure 1b, shows that, over the storm's lifetime, mass of species of all solubilities is generally lost from lower levels (below 6 km MSL) and gained in the anvil region (above 8 km MSL). In other words, overall mass transport is mainly due to transport of species in air. The simulation allowing species to remain in the frozen hydrometeor, Figure 1a, leads to less accumulation of species in the anvil as species solubility increases. For highly soluble species ($K_h >= 10^5$ M atm^{-1}), leads to mass loss at anvil levels. As species are carried with their parent frozen hydrometeor, mass in the anvil outflow air is instead depleted and more is transported to the ground by precipitation. Table 1 lists the total mass of the most soluble species, C18, deposited to the ground and accumulated in the anvil.

Simulation	Accumulation in Anvil (kg)	Surface Deposition (kg)
Solute retention	-5.59×10^4	2.82×10^5
Degassing	2.13×10^5	5.79×10^4

Table 1. Total mass accumulation in the storm anvil (8 to 15 km MSL) and deposited to the ground, of C18 after 3 hours of storm simulation (kg).

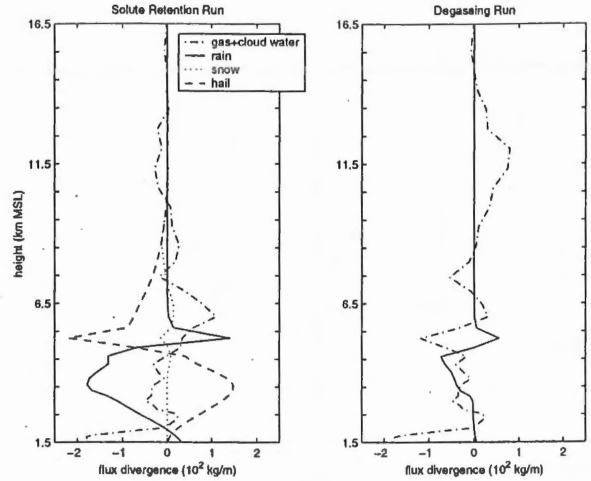

Figure 2. Hydrometeor specific time and horizontally integrated vertical flux divergence versus height after 3 hours of storm simulation for a highly soluble species, C18 ($K_h = 10^{12}$ M atm^{-1}). (a) gives results for the solute retention simulation. (b) gives results for solute degassing simulation.

The impact of specific hydrometeor motion on the fate of a highly soluble species, C18 (Kh = 10^{12} M atm^{-1}), is shown in Figure 2. For the solute retention simulation Figure 2a, we see that chemical transport in ice and snow play a very minor role compared with that in rain and hail. Transport of trace species in rain plays a more significant role when solutes are retained versus evaporated during hydrometeor freezing. Transport of species in gas and cloud water together also play a less significant role in chemical redistribution when solutes are retained. Though not shown, for less soluble species, transport in hydrometeors becomes insignificant compared with that in air.

5. DISCUSSION AND CONCLUSIONS

Despite their potential impact on chemical fate, interactions of chemicals with solid-phase hydrometeors, including gas-solid transfer, liquid-solid transfer, and chemical reaction, are not represented in many cloud models. A thorough understanding of the effects of these interactions on chemical distributions is lacking.

In a first step toward a systematic investigation of the range of potential impacts of these interactions on chemical distributions and deposition, we compared 3-D modeling simulations of chemical tracer transport in the July 10, 1996 STERAO thunderstorm. We compared fates of species for simulations including two representations of liquid-solid chemical transfer during hydrometeor freezing, in order to investigate the effects of these representations on tracers of varying solubilities. We found that allowing species to be retained in solid hydrometeors during freezing, rather than evaporating to the gas phase, may significantly impact the fate of highly soluble species ($K_h >= 10^5$ M atm^{-1}). Relevant natural species falling within that range of solubilities include hydrogen peroxide and nitric acid. For the simulation in which solutes were retained during freezing, increasing solubility of pseudo-species led to less transport of species mass upward into the anvil outflow air and more transport to the ground, as compared with a passive tracer transported in air only, and as compared with the transport of tracers which undergo evaporation during hydrometeor freezing. For highly soluble pseudo-species ($K_h >= 10^5$ M atm^{-1}), overall depletion of species mass at some levels of the anvil outflow area occurred due to the storm. Analysis of the hydrometeor specific transport reveals that precipitation of hail and rain were largely responsible for this trend reversal. With retention of species in frozen hydrometeors at lower levels of the storm, less mass was available for significant upward transport in air. Instead species mass was transported in hail, and in rain formed by melting hail. Ice and snow were insignificant contributors to the chemical fate because less species mass was available at upper levels, where ice and snow hydrometeors resided.

The results discussed here are a first step, using a 3-dimensional model framework, towards understanding the potentially significant impacts of chemical interactions with solid-phase hydrometeors on trace species fate during and after a convective storm. Further work is needed to understand the breadth of effects of these types of interactions. This will be achieved through systematic analysis and comparison of results from simulations including several representations of chemical / solid-phase hydrometeor interactions and including chemical reactions.

6. ACKNOWLEDGEMENTS

This material is based on work supported under a National Science Foundation Graduate Fellowship and a USEPA STAR Graduate Fellowship. Support has also been provided through the National Center for Atmospheric Research which is funded by the National Science Foundation.

7. REFERENCES

Audiffren, N., Cautenet, S. and Chaumerliac, N., 1999: A modeling study of the influence of ice scavenging on the chemical composition of liquid-phase precipitation of a cumulonimbus cloud. Journal of Applied Meteorology, 38: 1148-1160.

Barth, M.C., Stuart, A.L. and Skamarock, W.C., 2000: The fate of soluble tracers in deep convection. in preparation.

Chen, J.-P. and Lamb, D., 1990: The role of precipitation microphysics in the selective filtration of air entering the upper troposphere, 1990 Conference on Cloud Physics, pp. 479-484.

Cho, H.R., Niewiadomski, M. and Iribarne, J., 1989: A model of the effect of cumulus clouds on the redistribution and transformation of pollutants. Journal of Geophysical Research, 94(D10): 12895-12910.

Clapsaddle, C. and Lamb, D., 1989: The sorption behavior of SO2 on ice at temperatures between -30 C and -5 C. Geophysical Research Letters, 16(10): 1173-1176.

Grant, N.H. and Alburn, H.E., 1965: Fast reactions of ascorbic acid and hydrogen peroxide in ice, a presumptive early environment. Science, 150: 1589-1590.

Iribarne, J.V. and Barrie, L.A., 1995: The oxidation of S(IV) during riming by cloud droplets. Journal of Atmospheric Chemistry, 21: 97-114.

Lamb, D. and Blumenstein, R., 1987: Measurement of the entrapment of sulfur dioxide by rime ice. Atmospheric Environment, 21(8): 1765-1772.

Pruppacher, H.R. and Klett, J.D., 1997.: Microphysics of Clouds and Precipitation. Atmospheric and Oceanographic Sciences Library, 18. Kluwer Academic Publishers, Dordrecht, 954 pp.

Rutledge, S.A., Hegg, D.A. and Hobbs, P.V., 1986: A numerical model for sulfur and nitrogen scavenging in narrow cold-frontal rainbands 1. Model description and discussion of microphysical fields. Journal of Geophysical Research, 91(D13): 14385-14402.

Sato, K., Daimon, T., Takenaka, N., Bandow, H. and Maeda, Y., 1996: Decrease of solute in the aqueous solution in the freezing process. Proceedings from the NIPR Symposium on Polar Meteorology and Glaciology, 10: 138-148.

Skamarock et al., 2000: Numerical simulations of the 10 July STERAO / Deep Convection Experiment convective system: kinematics and transport. Journal of Geophysical Research, accepted.

Snider, J.R., Montague, D.C. and Vali, G., 1992: Hydrogen peroxide retention in rime ice. Journal of Geophysical Research, 97(D7): 7569-7578.

Takenaka, N. et al., 1996: Acceleration mechanism of chemical reaction by freezing: The reaction of nitrous acid with dissolved oxygen. Journal of Physical Chemistry, 100: 13874-13884.

Tao, W.-K. and Simpson, J., 1993: Goddard Cumulus Ensemble Model. Part I: Model description. TAO, 4(1): 35-72.

Valdez, M.P., Dawson, G.A. and Bales, R.C., 1989: Sulfur dioxide incorporation into ice depositing from the vapor. Journal of Geophysical Research, 94(D1): 1095-1103.

Wang, C. and Chang, J.S., 1993: A three-dimensional numerical model of cloud dynamics, microphysics, and chemistry 4. Cloud chemistry and precipitation chemistry. Journal of Geophysical Research, 98(D9): 16799-16808.

Wicker, L.J. and Wilhelmson, R.B., 1995: Simulation and analysis of tornado development and decay within a three-dimensional supercell thunderstorm. Journal of the Atmospheric Sciences, 52(15): 2675-2703.

MODIFICATION OF THE SIZE AND COMPOSITION OF CCN BY CLOUD PROCESSING OF MINERAL DUST PARTICLES AND THE EFFECTS ON CLOUD MICROPHYSICS

Yan Yin[1], Sabine Wurzler[2] *, Tamir G. Reisin[3] and Zev Levin[4]

[1]School of the Environment, University of Leeds, UK
[2]Institute for Tropospheric Research, Leipzig, Germany
[3]Soreq Nuclear Research Center, Yavne, Israel
[4]Department of Geophysics and Planetary Sciences, Tel Aviv University, Tel Aviv, Israel

1. INTRODUCTION

Measurements of aerosol composition in the Mediterranean reveal that sulfate is found in most aerosol particles. Among these, mineral dust particles coated with sulfate and other soluble substances are found (e.g. Fonner and Ganor, 1992). The amount of soluble material on the mineral dust particles was found to be related to their surface area, suggesting that the deposition process could be surface dependent. The source of this sulfate is from air masses descending from the industrial countries in Europe into the Mediterranean region or from DMS that is emitted from the Mediterranean Sea itself. The soluble coating of the mineral dust particles could significantly change their ability to serve as cloud condensation nuclei (CCN). Evidence for the activation of these giant CCN was observed during in–cloud measurements, where a few large drops containing both dust and sulfate were found (Levin et al., 1996). The processes responsible for the sulfate coating of dust particles are still not identified. There are a number of pathways that could explain the formation of sulfate–coated aerosols. One probable coating mechanism is the cloud processing of mineral dust particles. In it, mineral dust particles are collected by cloud drops that have been originally nucleated by sulfate or other soluble aerosol particles. Additional sulfate is added by gas scavenging and subsequent liquid phase oxidation. After the cloud evaporation, mineral dust particles coated with soluble material are released together with other cloud processed aerosols. Apart from warm cloud microphysics, the scavenging of mineral dust particles and of sulfate containing droplets by ice crystals, their melting and subsequent evaporation might be another possible coating mechanism. The above suggested microphysical processes involved in the coating of the mineral dust particles are schematically given in Fig. 1.

Numerical simulations, using a parcel model with detailed treatment of the microphysical processes (Wurzler et al., 2000) show that one possible path for the formation of the sulfate coating is through the interaction of clouds with dust particles. However the effects of these coated particles on rain development has not yet been studied. In this study we discuss the cloud's growth and the development of precipitation resulting from the changes in the CCN size distribution that occur due to the coating of the mineral dust particles. For this purpose we first use the parcel model to calculate the changes that occur in the size and composition of the dust particles as they go through clouds. We then use these results as the initial aerosol distribution in a 2D cloud model with detailed microphysics to study the precipitation formation processes. Results from calculations with these two models are described.

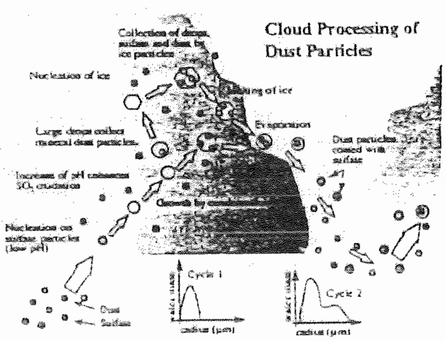

Figure 1: Schematic representation of the cloud microphysical processes leading to the sulfate coating of mineral dust particles (Wurzler et al., 2000).

2. DESCRIPTION OF THE MODELS

2.1 The Parcel Model

The basic dynamic frame work of the air parcel model is discussed in detail by Flossmann et al. (1985). The formulations for the detailed microphysical processes and for the scavenging of several aerosol types simultaneously present in the air are given by Flossmann et al. (1985), Flossmann and Pruppacher (1988) and Floss-

* *Corresponding author address:* Sabine Wurzler, Institute for Tropospheric Research, Permoserstrasse 15, 04303 Leipzig, Germany; e-mail:wurzler@tropos.de

mann (1991). The effects of the water soluble and insoluble fractions of the aerosols are discussed by Wurzler et al. (1995). This model was employed to evaluate the role of clouds in the coating process and to provide the initial conditions of the CCN for the 2D model.

2.2 The Two Dimensional Cloud Model

The basic dynamic framework of the 2D-cloud model is discussed in detail by Yin et al., (2000). The model is a slab symmetric cloud model with detailed microphysics of warm and cold processes. The warm microphysical processes included are: nucleation of CCN, condensation and evaporation, collision-coalescence, and binary breakup (Low and List kernel). The ice microphysical processes included are: ice nucleation (deposition, condensation-freezing, contact nucleation, and immersion freezing), ice multiplication (Hallett-Mossop mechanism), deposition and sublimation of ice, ice-ice and ice-drop interactions (aggregation, accretion and riming), melting of ice particles, and sedimentation of both drops and ice particles. All these microphysical processes are formulated and solved using the method of Multi-Moments (Tzivion et al., 1987; Reisin et al., 1996)

Three different types of ice are considered: ice crystals, graupel particles and snowflakes (aggregates of ice crystals). The radius resolution of each cloud particle type is given by 34 bins with mass doubling in each bin. The mass of the lower boundary of the first bin and the upper boundary of the last bin for both liquid and solid phases were 0.1598×10^{-13} and 0.17468×10^{-3} kg, which correspond to drop diameter of 3.125 and 8063 μm, respectively. The CCN spectrum is divided into 67 bins with a minimum radius of 0.0041 μm.

The grid size of the model is set to 300 m in both horizontal and vertical directions (separate numerical tests using grid sizes of 150 and 200 m showed that except for a two-minute delay in the cloud and rain initiation, the development of cloud properties such as liquid water content, maximum updraft, ice content, were similar to those reported in this paper). The width and height of the domain are 30 and 12 km, respectively. The time step for all the processes is 5 s except for diffusive growth/evaporation, where a shorter time step of up to 2.5 s is used.

3. INITIAL CONDITIONS

Three cycles through a cloud of a marine aerosol distribution including a tail of mineral dust particles were studied.

3.1 First cycle

For the initial aerosol distribution in the first cycle, the distribution observed by Hoppel et al. (1990) (see their Figure 7, curve 2) was chosen. A tail of dust particles was added to the particle size distribution (see Fig. 2, solid lines). The aerosol distribution was approximated using four lognormal function (three for Hoppel's distribution and one for the tail of dust particles).

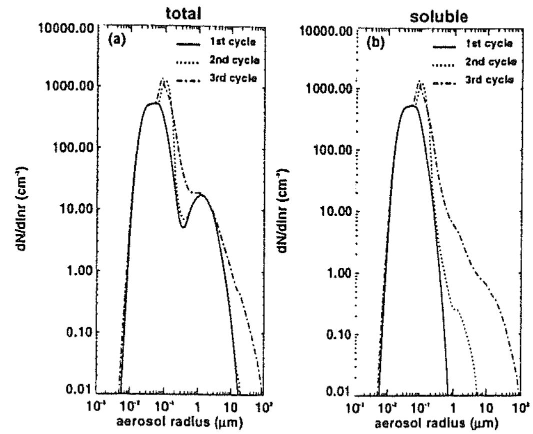

Figure 2: Initial conditions for three cycles of an aerosol distribution through a cloud (a) Total aerosol number distribution and (b) the number distribution of the aerosols containing water soluble material. Note that the initial distributions used for cycles 2 and 3 are the resulting distributions produced after evaporation of cycles 1 and 2, respectively (Wurzler et al., 2000).

3.2 Second and third cycles

The aerosol distribution resulting after cloud evaporation following the first and second cycles was used for initializing the second and third cycles, respectively. The number distributions of these aerosol distributions are displayed in Fig. 2 (2nd cycle: dotted lines, 3rd cycle: dashed dotted lines). These cloud processed aerosol distributions have been calculated with the entraining air parcel model.

For the 2D model a single–cell cloud with large instability was considered to be representative of one of the growing cells in a convection complex. A theoretical thermodynamic profile which produced a cloud with cloud base at 8-10°C and top at -25°C was used for the initial thermodynamic conditions. In order to initiate convection, a temperature perturbation of 2°C was applied for one time step at $t = 0$ at a height of 600 m, in the middle of the domain. The same initial aerosol distribution as in the parcel model was used for the first cloud. The second and third clouds were initialzed with the same thermodynamic profile. The aerosol distributions were those provided by the parcel model after the cloud processing. These aerosol spectra were fitted by superimposing four, five, and six lognormal distributions, for the first, second, and third cycle, respectively. The parameters of the distributions are given in Table 1.

4. RESULTS

Table 1: Parameters for the aerosol particle distributions: n_i= total number of aerosol particles per cubic centimeter of air, R_i = geometric mean aerosol particle radius in μm, σ_i = standard deviation in mode, i.

	Mode i	n_i	R_i	$\log\sigma_i$
cycle 1	1	350	0.028	0.15
	2	459	0.06	0.17
	3	50	0.1	0.21
	4	30	1.2	0.3
cycle 2	1	350	0.028	0.165
	2	459	0.06	0.17
	3	35	0.1	0.35
	4	620	0.105	0.1
	5	2	0.8	0.45
cycle 3	1	6050	0.024	0.39
	2	350	0.028	0.165
	3	459	0.06	0.17
	4	620	0.09	0.1
	5	60	0.11	0.65
	6	2.5	2.0	0.45

The results from the parcel model suggest that cloud processing of mineral dust particles in the presence of sulfate containing CCN and atmospheric trace gases is a possible pathway, which leads to the formation of the water soluble coating on mineral dust particles. As the number of cycles through the cloud increases the more large particles are formed, among which there are also coated mineral dust particles. The parcel model results suggest that the cloud processed mineral dust particles can lead to an enhanced production of precipitation sized drops (Wurzler et al., 2000). However, since a parcel model cannot adequately study precipitation due to its limitation, we use the 2D model to simulate the rain formation processes and how they are affected by the processed aerosol distribution calculated by the parcel model.

Figs. 3 and 4 show the model results after 40 minutes of simulation. Fig. 3 shows the distribution of the liquid water content obtained during the first (thick line) and the second (thin line) cycle. After 40 minutes in the first cycle only a narrow size distribution is formed with the largest drops still smaller than 100 μm near cloud top. In contrast, in the second cycle after 40 min, the cloud formed on the cloud processed aerosol has already developed precipitation sized drops (>1 mm). Fig. 4 shows the water mass distribution of the model cloud after the second (thick line) and the third (thin line) cycle of the aerosols through the cloud. The figure shows that in the third cycle the development of precipitation was even more efficient, producing larger drops in the cloud and rainfall on the ground after only 40 min.

Significant differences are also found in development of ice-phase precipitation particles. The results (not shown here) indicate that in the clouds formed on second and third cycle aerosols graupel particles developed earlier and reached higher water content than those in the cloud formed on the first cycle.

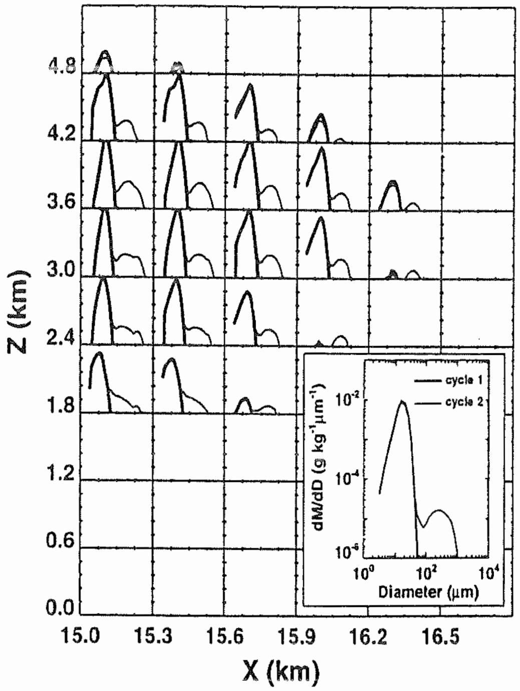

Figure 3: Mass concentration size distribution at different locations in the cloud after 40 min of simulation time. The thick lines represent the results obtained with the initial unprocessed aerosol distribution (Fig. 2, solid lines). The thin lines represent the results obtained with the aerosol distribution which had already undergone one cycle through the cloud (Fig. 2, dotted lines).

Fig. 5 shows the rainfall rate and rainfall amounts on the ground at the cloud center as a function of time for the three clouds. As can be seen, the cloud processing of the aerosol increases the rain formation efficiency of the cloud. Rain is produced faster and in larger amounts the more cycles the aerosols go through.

5. CONCLUSIONS

This work shows that: 1) Mineral dust particles get coated with soluble sulfate after passing through clouds. 2) The more cycles through the clouds, the more particles get coated and the larger is the mass that they accumulate. 3) These coated particles produce larger cloud drops and more efficient precipitation processes. 4) Rainfall resulting from such clouds is initiated earlier and in larger amounts than similar clouds not affected by the dust.

Acknowledgments

One of the authors (S.Wurzler) acknowledges the BMBF (AFS program, project 07AF214/9) as well as

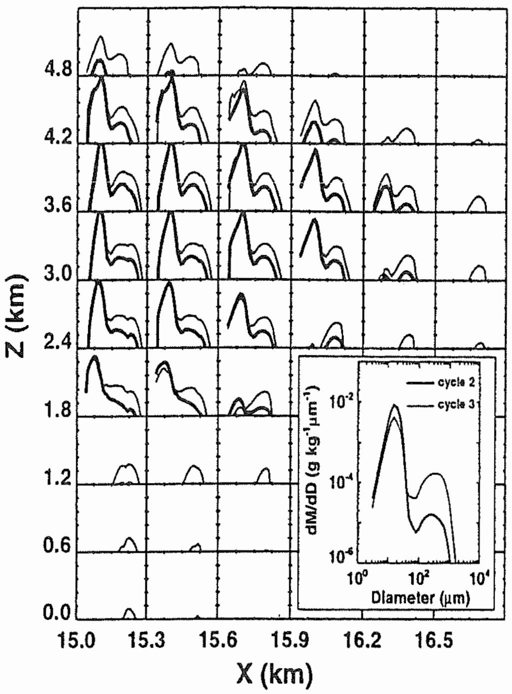

Figure 4: Mass concentration size distribution at different locations in the cloud after 40 min of simulation time.. The thick lines represent the results obtained with the aerosol distribution which had already undergone one cycle through the cloud (Fig. 2, dotted lines). The thin lines represent the results obtained with the aerosol distribution which had already undergone two cycles through the cloud (Fig. 2, dash dotted lines).

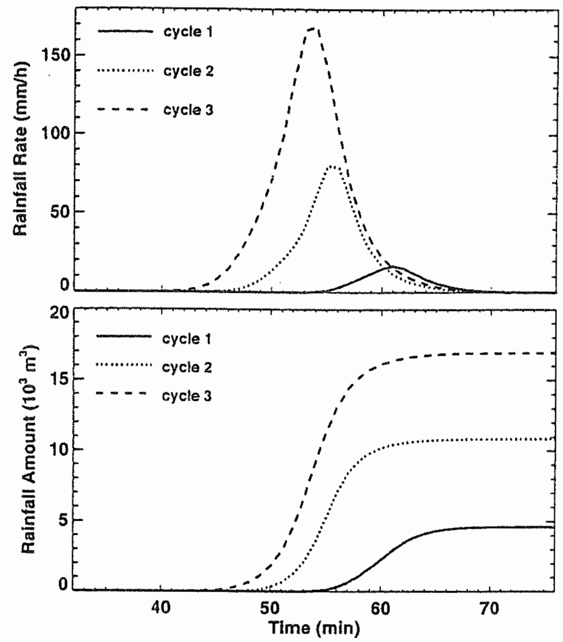

Figure 5: Rainfall rate (top) and rainfall amount (bottom) at cloud center as a function of time.

the Johannes Gutenberg–University for provid ing funding for the present study. Parts of this work were carried out under the sponsorship of the German–Israeli Foundation under contract I–544–156.08/97.

REFERENCES

Flossmann, A.I., W.D: Hall and H.R. Pruppacher, 1985: A theoretical study of the wet removal of atmospheric pollutants, Part I. *J. Atmos. Sci.*, **42**, 582–606.

Flossmann, A.I., H.R. Pruppacher and J.H. Topalian, 1987: A theoretical study of the wet removal of atmospheric pollutants, Part II. *J. Atmos. Sci.*, **44**, 2912–2923.

Flossmann, A. I., 1991: The scavenging of two different types of marine aerosol particles calculated using a two–dimensional detailed cloud model, *Tellus*, **43B**, 301–321.

Fonner, D., and E. Ganor, 1992: The chemical and mineralogical composition of some urban atmospheric aerosols in Israel, *Atmos. Environ.*, **26B**, 125–133.

Hoppel, W. A., J. W. Fitzgerald, G. M. Frick, R. E. Larson, and E. J. Mack, 1990: Aerosol size distributions and optical properties found in the marine boundary layer over the Atlantic Ocean, *J. Geophys. Res.*, **95**, 3659–3686.

Levin, Z., E. Ganor, and V. Gladstein, 1996: The effects of desert particles coated with sulfate on rain formation in the eastern Mediterranean, it J. Appl. Meteorol., **35**, 1511–1523.

Reisin, T.G., Z. Levin and S. Tzivion, 1996: Rain production in convective clouds as simulated in an axissymmetric model with detailed microphysics. Part II. Effects of variing drop and ice initialization. *J. Atmos. Sci.*, **53**, 1815–1837.

Tzivion, S., G. Feingold, and Z. Levin, 1987: A efficient numerical solution to the stochastic collection equation. *J. Atmos. Sci.*, **44**, 3139-3149.

Wurzler, S., A.I. Flossmann, H.R. Pruppacher and S.E. Schwartz, 1995: The scavenging of nitrate by clouds and precipitation, Part I. *J. Atmos. Chem.*, **20**, 259–280.

Wurzler, S., T.G. Reisin and Z. Levin, 2000: Modification of mineral dust particles by cloud processing and subsequent effects on drop size distributions. *J. Geophys. Res.*, **105**, D4, 4501–4512.

Yin, Y., Z. Levin, T. G. Reisin, and S. Tzivion, 2000: The effects of giant cloud condensation nuclei on the development of precipitation in convective clouds – A numerical study, *Atmos. Res.* (in press).

ESTIMATES OF THE CONTRIBUTION OF BELOW-CLOUD SCAVENGING TO THE POLLUTANT LOADINGS OF RAIN IN TAIPEI, TAIWAN, BASED ON THE OBSERVATIONS OF CLOUD CHESMITRY

Neng-Huei Lin and Chi-Ming Peng

Department of Atmospheric Sciences, National Central University, Chung-Li, Taiwan

1. INTRODUCTION

In northern Taiwan (see Figure 1), wet deposition of sulfates and nitrates has been assessed (Chen *et al.*, 1996) to be more than twice the maximum values observed in the eastern USA (NAPAP, 1991). High loadings of sulfates were found to be associated with frontal passages and northeast monsoon flows, especially during the winter seasons, indicating the possibility of the long-range transport of sulfur compounds. Under such weather conditions, low clouds (cloudbase can be as low as 600 m MSL) frequently cap the mountains in the very northern part of Taiwan. Upon formation, clouds are very efficient scavengers of air pollutants if they lead to precipitation subsequently. Thus, in this paper we use a semi-quantitative scheme to examine the relationship between the chemistry of clouds observed at the peak of Mt. Bamboo (see Figure 1) and the precipitation chemistry concurrently collected at ground level in Taipei City in order to assess the contribution of below-cloud scavenging of pollutants by raindrops to the chemical composition of rainwater.

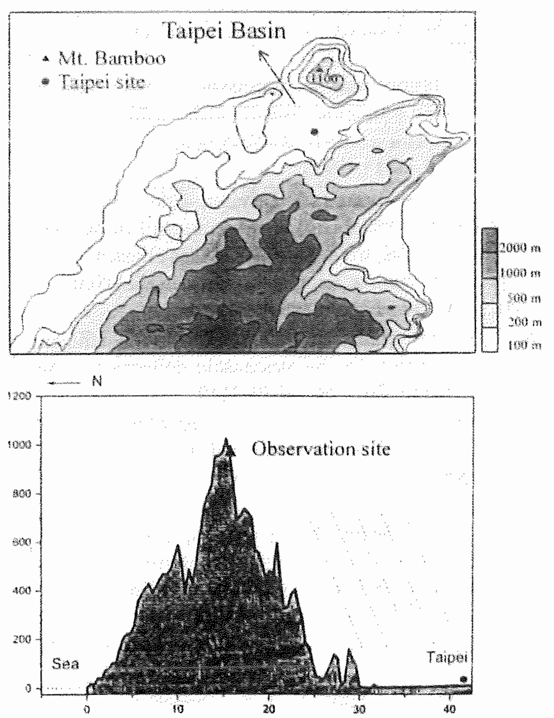

Fig. 1. (a) Location of the Mt. Bamboo site (marked as "▲") and Taipei site (denoted by "●") for collection of cloud water and rainwater, respectively, and (b) cross-sectional illustration of above two sites.

2. EXPERIMENTAL SETUP

The cloud water was collected at the peak (about 1100m MSL) of the Mt. Bamboo, as part of the Yang-Ming-Shan National Park, during the winter seasons (late January-early March) of 1996-1998 as the northeast monsoon flows prevailed. Figure 1 depicts the location of the experimental site (marked by "▲"). It is noted that the site is frequently immersed in clouds which form either due to frontal passage or topographic effects. The temperatures at our site were recorded as 9.0±3.7 ^{0}C during the field seasons. The lowest temperature recorded was near 0 ^{0}C. The wind speed, on average, was about 7.0 m s^{-1} and can reach as high as 20 m s^{-1}. Prevailing flows to the site are northerly. Therefore, during the northeast monsoon seasons, in consideration of its location and altitude (see Fig. 1), this site should be free from local pollutant. Therefore, we assume that the cloud water collected at our site should not be contaminated by local anthropogenic emissions such as sulfur and nitrogen compounds, when northerly flows prevail during the field seasons.

Cloud water was collected hourly at the roof of a building, about 4 m above ground level during the cloud events. We used the collector of ASRC (Atmospheric Science Research Center, State University of New York) type for cloud water collection. The pH of cloud water was measured immediately after collection. Thereafter, samples were refrigerated at 4 ^{0}C and shipped to National Central University for later chemical analysis. The cloud water was analyzed for ion concentrations of Cl^-, NO_3^-, SO_4^{2-}, NH_4^+, Na^+, K^+, Mg^{2+}, and Ca^{2+} using Ion Chromatography (Dionex-100). The H^+ was converted from the measured pH. The QA/QC protocol for chemical analysis was based on the recommendation by GAW/WMO (see Mohnen *et al.*, 1994). Additionally, collection of rainwater was also performed on a daily basis near downtown Taipei City using a wet/dry collector (Lin *et al.*, 1999). The location of the site is marked by "●" in Fig. 1. The sampling and analysis protocols of rainwater were based on the recommendations by the USA NADP/NTN. Detailed description and references can be found elsewhere (Lin *et al.*, 1999).

the peak of Mt. Bamboo may have become loaded with atmospheric pollutants primarily originating from long-range transport. When they grow and subsequently fall as raindrops, atmospheric pollutants can be scavenged the below the cloudbase. Thereby, chemical composition of rainwater is altered owing to the addition of local pollutants.

2 Estimates of Below-cloud Scavenging of Pollutants by Raindrops

As generally observed (Saxena and Lin, 1990) in cloud water and rainwater, ion concentrations for the former were usually higher than those for the latter. This difference results from the dilution effect of raindrops when they form from the growth of cloud droplets. Because sulfate particles are the most effective cloud condensation nuclei, the tiny cloud droplets in general contains relatively concentrated sulfates. In the course of the condensational growth of cloud, more sulfates are formed through heterogeneous oxidation of SO_2. Later, precipitation occurs as cloud droplets keep growing (*e.g.*, self-growth or collection by larger hydrometers) and become heavy enough to overcome the updrafts. Then, the rainwater would be expected to have lower ion concentrations than cloud water. Concurrently, below-cloud scavenging of air pollutants by falling raindrops will enhance the concentrations of these ions in rainwater. Nevertheless, the ionic concentrations in rainwater are still relatively low, compared with cloud water because of large volumetric ratio of raindrops to cloud droplets. Hence, we may estimate the dilution effect by comparing the concentrations of a tracer between rainwater and cloud water. Such a tracer, for instance, can be the Na^+ since its natural origin is from the ocean.

In this study, coincident sampling of cloud water at the peak of Mt. Bamboo and of rainwater at the ground level (see site description in Section 2) was performed through two different experiments. We assume that the clouds observed at our site preserved their chemical properties as they extend horizontally tens of kilometers to shelter the Taipei basin, as these clouds were well organized and distributed in accordance with the frontal passage. Thus, the dilution factor (*DF*) of a specific tracer *X* in cloud droplets with respect to raindrops can be obtained by calculating the ratio of the equivalent concentration of *X* in cloud water to that in rainwater:

$$DF = \frac{[X]_c}{[X]_r - [X]_p} \qquad (1)$$

where *c*, *r* and *p* denote the cloud water, rainwater and particle phase, respectively. The $[X]_p$ is due to the below-cloud scavenging of *X* in the form of aerosol particles by raindrops. The *X* can be the Na^+, which originates from the ocean. Therefore, neglecting the absorption of gaseous *i*, the portion ($f(i)$) of $[i]_r$, which results from below-cloud scavenging of a species *i* in the form of aerosol particles by raindrops, can be expressed as:

$$f(i) = 1 - \frac{[i]_c}{[i]_r} \bullet \frac{1}{DF} \qquad (2)$$

For simplicity, we neglect the contribution of Na^+-containing aerosols to raindrops. However, it is not necessarily the case that more or less, seasalt aerosols should have already existed in the air below the cloudbases above Taipei basin. Thus, the *DF* calculated by Eq. (1) is substantially underestimated since $[Na^+]_p$ is presumed to be zero. The *f* somewhat represents the contribution from local pollutants, whereas, the portion (*1-f*) is due to in-cloud scavenging. As along as our site is not contaminated by local sources, the latter portion of pollutants in rainwater can be attributed to long-range transport. This ideal situation is evaluated below.

According to the chemistry of cloud water and rainwater listed in Table 2, we calculate the *DF*, f(nss-SO_4^{2-}), $f(NO_3^-)$ and $f(NH_4^+)$ for 6 cases. The results are listed in Table 3. For Cases A and D2, nss-SO_4^{2-}, NO_3^- and NH_4^+ in rainwater are highly enhanced by below-cloud scavenging, resulting in relatively higher *f*, as shown in Tables 2 and 3. For the former event, their contribution to total ions increased from 15.7, 2.3, and 3.4% for cloud water to 23.0, 8.7 and 20.0% for rainwater, respectively. By contrast, seasalt ions decreased at least 50% both in their concentrations and contributions to total ions. Similar variations can also be seen in Case D2. The former event was more contaminated than the latter one. Case B had the highest concentrations of SO_4^{2-} and NO_3^- for both cloud water and rainwater among all cases. Meanwhile, excessive NH_4^+ over NO_3^- can only neutralize a part of the SO_4^{2-}, consequently, leading to the highest acidity as well. About half of [nss-SO_4^{2-}]$_r$ was attributed to below-cloud scavenging, compared with 2/3 of $[NO_3^-]_r$ and $[NH_4^+]_r$. By contrast, Case C had the largest concentrations of Na^+ and Cl^- among all cases, both accounting for around 60 and 40% of total ions for cloud water and rainwater, respectively. In this case, SO_4^{2-} still played a major role in controlling the acidity. The NO_3^- was evidently a minor component. It was primarily derived from in-cloud scavenging (1-*f* = 0.69), as well as nss-SO_4^{2-}.

As to Cases DI and D2, they were derived from cloud event D (see Table 1). For cloud water, seasalt and SO_4^{2-} were the principal ions for D1. However, the relative contribution of NH_4^+ to total ions increased from 9.6% for DI to 18.2% for D2 (see Table 2), and it became equivalent to seasalt on the second day (D2), indicating the relative enhancement of local sources, *e.g.* the biological products from the National Park. This situation was even more

3. RESULTS AND DISCUSSION

Table 1 lists the information of six cloud events observed at our site during which concurrent collection of rainwater in Taipei City was performed. All of these cloud events were associated with frontal passages. Event D is further divided into Cases DI and D2 in order to match the daily collection of rainwater because it last for more than 40 hours. Table 2 summarizes the chemistry of the cloud water and rainwater. The average values and their standard deviations for cloud water chemistry are based on hourly samples for each cloud event. The followings will present our quantitative analysis of both cloud and precipitation chemistry.

Table 1. Information on cloud events studied on this work.

Event	Start		End		Duration
	Time	Date	Time	Date	(hour)
A	0800	1/26/96	0800	1/27/96	24
B	1000	2/28/96	1800	2/28/96	8
C	0820	2/17/97	0620	2/18/97	22
D[a]	1600	2/4/98	0800	2/6/98	40
E	1730	2/15/98	2000	2/15/98	3.5

a. Event D last for 40 hours and was further divided into two cases D1 and D2 for later discussion since r ainwater collection is on a daily basis. The cut point between D1 and D2 was at 8:00, 2/15/98.

3.1 Chemical Composition of Cloud Water and Rainwater

As shown in Table 2, the average pH of the six cloud events ranged between 3.55-4.31, while it was between 3.82 and 5.89 for rainwater. In our case, the acidity of cloud water was generally higher than that of rainwater. Table 2 also lists the relative contribution of individual ions to total ions. Except for Case E, the principal components in cloud water were found to be seasalt (Na^+ and Cl^-) and SO_4^{2-}, each contributing 17-31%, 17-33% and 15-29% of total ions, respectively. The former two ions essentially originate from the ocean, while, in addition to natural sources, the later is converted from anthropogenic SO_4^{2-}. Meanwhile, excluding Case D2, NH_4^+ played a minor role, only accounting for less than 12% of total ions. Generally speaking, agricultural and industrial activities are the origins of NH_4^+. Hence, NH_4^+ can be thought of as an important indicator of local emissions. The cloud droplets collected at our site should be, to a lesser extent, contaminated by local sources. By contrast, for rainwater, SO_4^{2-} and NH_4^+ were the dominant ions, followed by seasalt and NO_3^-. According to Table 2, for all cases, relative contributions of NO_3^- and NH_4^+ to total ions in rainwater are significantly higher than those in cloud water, suggesting the below-cloud scavenging of local pollutants by raindrops. Meanwhile, the relative contribution of seasalt ions to total ions drops dramatically from cloud droplets to raindrops. This result further supports the addition of local pollutants to rainwater. Evidently, the cloud droplets forming at

Table 2. Statistical summary of cloud and precipitation chemistry measured at Mt. Bamboo and Taipei city, respectively. (Unit: rain in mm, LWC in g m^{-3}, ion concentration in $\mu eq l^{-1}$)

Case	Type		Rain	LWC	pH	Cl^-	NO_3^-	SO_4^{2-}	$nss\text{-}SO_4^{2-a}$	H^+	Na^+	NH_4^+	K^+	Mg^{2+}	Ca^{2+}	Sum
A	Cloud	μ		0.27	4.13	273.0	20.1	139.5	105.7	71.9	279.7	29.9	7.5	49.9	18.6	890
		σ			0.36	226.6	16.3	109.8	78.5	51.0	259.4	24.7	5.5	43.5	16.0	
		% of sum				30.7	2.3	15.7	11.9	8.1	31.4	3.4	0.8	5.6	2.1	
	Rain	μ	8.6		4.06	108.7	66.1	175.6	162.3	87.1	110.2	152.6	6.1	24.1	33.9	764
		% of sum				14.2	8.7	23.0	21.2	11.4	14.4	20.0	0.8	3.2	4.4	
B	Cloud			0.38	3.55	336.5	108.7	532.6	489.5	97.6	356.2	203.3	29.5	71.7	91.5	1827
					2.15	115.6	25.2	71.0	55.9	35.4	124.7	60.4	3.1	21.3	12.8	
						18.4	5.9	29.1	26.8	5.3	19.5	11.1	1.6	3.9	5.0	
	Rain		7.5		3.82	92.3	97.2	200.9	191.1	151.4	80.8	179.7	6.1	20.4	27.0	855
						10.8	11.4	23.5	22.3	17.7	9.4	21.0	0.7	2.4	3.2	
C	Cloud			0.21	4.02	488.6	42.8	228.4	183.1	87.3	374.1	78.1	15.5	90.0	63.8	1468
					0.18	412.9	29.9	158.2	121.6	37.5	302.3	38.6	8.5	64.3	46.8	
						33.3	2.9	15.5	12.5	5.9	25.5	5.3	1.1	6.1	4.3	
	Rain		9.9		4.00	174.3	28.7	162.5	139.8	100.0	187.4	84.2	10.1	41.9	42.9	832
						20.9	3.4	19.5	16.8	12.0	22.5	10.1	1.2	5.0	5.2	
D1	Cloud			0.22	4.15	164.5	24.8	150.7	132.2	72.7	153.0	62.7	7.0	15.0	6.1	656
					0.12	59.5	7.8	45.6	41.0	21.1	38.1	30.3	2.7	13.1	6.2	
						25.1	3.8	23.0	20.1	11.1	23.3	9.6	1.1	2.3	0.9	
	Rain		5.2		4.34	31.8	14.6	55.1	52.5	45.7	21.6	44.7	2.5	5.1	2.1	223
						14.3	6.5	24.7	23.5	20.5	9.7	20.0	1.1	2.3	0.9	
D2	Cloud			0.24	4.31	84.2	30.6	113.0	103.4	53.1	79.7	84.4	5.1	9.2	3.5	462
					0.19	76.4	17.1	58.5	50.4	22.1	66.2	49.9	2.3	8.8	1.7	
						18.2	6.6	24.4	22.3	11.5	17.2	18.2	1.1	2.0	0.8	
	Rain		7.6		4.68	10.2	10.6	37.6	37.2	20.9	3.4	34.7	1.9	0.7	0.3	120
						8.5	8.8	31.3	30.9	17.4	2.9	28.8	1.6	0.6	0.3	
E	Cloud			0.28	3.62	149.3	66.8	230.8	212.5	242.6	151.3	21.1	2.0	4.9	4.1	872
					0.09	53.3	22.0	24.7	18.1	50.2	54.4	4.7	0.1	2.0	1.0	
						17.1	7.7	26.4	24.3	27.8	17.3	2.4	0.2	0.6	0.5	
	Rain		2.5		5.89	48.7	35.9	78.1	73.9	1.3	34.8	134.9	5.8	6.7	5.8	352
						13.8	10.2	22.2	21.0	0.4	9.9	38.3	1.7	1.9	1.6	

a. $[nss\text{-}SO_4^{2-}]=SO_4^{2-} - 0.121*[Na^+]$

significant for rainwater. According to Table 3, it is observed that $f(NO_3^-)$ and $f(NH_4^+)$ have a gentle increase from DI to D2, while $f(nss\text{-}SO_4^{2-})$ increased almost by half in the second day. At the end of this frontal passage, the clouds became relatively cleaner (see the decrease in ion concentrations for Case D2 in Table 2), whereas local emissions relatively enhanced the sulfur compounds in rainwater. Unlike the above cases, rainwater for Case E had its pH > 5.6, the CO_2-equilibrated value, although the pH of cloud water was as low as 3.62, the second highest acidity among all cases. In this case, SO_4^{2-} and NO_3^- were significantly elevated, compared with Case A. Meanwhile, they were the major contributors to the acidity of cloud water. In addition, minor cations accounted for less than 4% of total ions. By contrast, for rainwater, excessive NH_4^+ over SO_4^{2-} and NO_3^- increased the alkalinity of rainwater (see Table 2). According to Table 3, it is found that for Case E NH_4^+ originated mostly from below-cloud scavenging (f = 0.96), whereas, most of $nss\text{-}SO_4^{2-}$ was attributed to in-cloud scavenging ($1\text{-}f$ = 0.66).

In summary, the *DF* varied between 2-23 for the above 6 cases. The $f(nss\text{-}SO_4^{2-})$, $f(NO_3^-)$ and $f(NH_4^+)$ ranged between 0.31-0.88, 0.25-0.88 and 0.54-0.96, respectively. Overall, most of $[NH_4^+]_r$ were evidently attributed to below-cloud scavenging, again reflecting their origins from local sources. Meanwhile, $[NO_3^-]_r$ was accounted for at least 75% by the same scavenging mechanism, except for Cases C and E. In contrast, a large portion of $[nss\text{-}SO_4^{2-}]_r$ resulted from in-cloud scavenging. In comparison with NH_4^+ and NO_3^-, relatively higher amount of $nss\text{-}SO_4^{2-}$ was obviously derived from long-range transport.

These results are dependent mainly on two assumptions, the horizontal homogeneity of the layer of clouds and no below-cloud scavenging of seasalts. The former assumption may be held unless strong entrainment occurs, especially near the proximity of cloud boundaries. For the latter, it is probably not true since in the winter northeast monsoon flows bring seasalt aerosols into the basin, later, accumulating in the air. For instance, if $[Na^+]_p/[Na^+]_r$ = 0.1, then *DF* will increase to 2.82 for Case A (around 11% increase). Consequently, $f(nss\text{-}SO_4^{2-})$, $f(NO_3^-)$ and $f(NH_4^+)$ increase slightly to 0.77, 0.89 and 0.93, respectively. Based on these two assumptions, those *f*s listed in Table 3 should represent the minimum contribution of below-cloud scavenging of the corresponding pollutants by raindrops.

4. CONCLUDING REMARKS

In this paper, we have demonstrated the usefulness of a simple and semi-quantitative scheme for estimating the effects of below-cloud scavenging of pollutants on the composition of rainwater collected on the ground level of Taipei City, based on the cloud chemistry observed at the peak of the Mt. Bamboo. In addition, we have also learned of a possibility of the long-range transport of sulfur compounds through frontal clouds. By contrast, the nitrogen compounds, including NH_4^+ and NO_3^- in rainwater collected in Taipei during the wintertime frontal passages, can be primarily attributed to local sources.

Table 3. Dilution factor (DF) and contribution (*f*) of below-cloud scavenging by raindrops to $nss\text{-}SO_4^{2-}$, NO_3^- and NH_4^+ in rainwater.

Case	*DF*	$f(nss\text{-}SO_4^{2-})$	$f(NO_3^-)$	$f(NH_4^+)$
A	2.54	0.74	0.88	0.92
B	4.41	0.46	0.75	0.74
C	2.00	0.31	0.25	0.54
D1	7.10	0.63	0.76	0.80
D2	23.17	0.88	0.88	0.89
E	4.35	0.34	0.57	0.96

Acknowledgements Our work was supported by the National Science Council of Taiwan and the Central Weather Bureau. The field experiments of cloud chemistry were performed with the help of many graduate and undergraduate students. The data of precipitation chemistry was provided by Prof. F.-T. Jeng, the Graduate Institute of Environmental Engineering, National Taiwan University.

REFERENCES

Chen, J.-S., N.-H. Lin, C.-M. Peng and F.-T. Jeng, 1996: Acidic deposition on Taiwan and associated precipitation systems. In Proceedings of International Conference on Acid Deposition in East Asia, Taipei, Taiwan, May 28-30, 1996.

Lin, N.-H., H.-M. Lee and M.-B. Chang, 1999: Evaluation of the characteristics of acid precipitation in Taipei, Taiwan using cluster analysis. Water, Air & Soil Pollut., **113**, 241-260.

Mohnen, V., J. Santroch and R. Vet, 1994: Report of the Workshop on Precipitation Chemistry Laboratory Techniques. Global Atmosphere Watch, World Meteorological Organization, WMO/TD-No. 685.

NAPAP (National Acid Precipitation Assessment Program), 1991: 1990 Integrated Assessment Report. U.S. Government Printing Office, Washington, D.C., 520 pp.

Saxena, V. K and N.-H. Lin, 1990: Cloud chemistry measurements and estimates of acidic deposition on an above cloudbase coniferous forest. Atmos. Environ., **24**, 329-352.

Estimation of the effect of operator splitting on detailed aerosol growth including multiphase chemistry

Frank Müller

Meteorological Institute, University Hamburg, D-20146 Hamburg, Germany

1. INTRODUCTION

Simultaneous numerical simulation of dynamical, micro-physical, and multiphase chemical processes is very time consuming in multi-dimensional models. Application of such numerical models with present day computer resources often requires a functional separation of the overall model and a separate sequential solution of the corresponding sub-problems. The application of the method of 'operator splitting' to solve 3D chemistry-transport-problems has been accepted for many years in the modeling of atmospheric chemical processes. Disadvantages, inherant to this method, are the creation of discontinuities of the spatial concentration distribution at the beginning of each 'chemical' time step (which lead also to an increase of the stiffness in the case of the chemical system) and splitting errors which add up to the discretization errors and other errors due to the numerical solution method.

Operator splitting is analogously applied to the complex micro-physical and multiphase chemical processes in clouds, too. The de-coupling of the corresponding processes is expected to cause strong deviations from the solution of the completely coupled system for both the micro-physical and the chemical particle properties. This would have further consequences for the life time of clouds, their optical properties, the deposition behavior, etc.

The aim of this study is a systematic investigation of the uncertainty/variability of the simulated cloud micro-physical and chemical parameters for the de-coupled modeling of the corresponding processes in cloud models and cloud modules of air quality models as a function of the de-coupling period. Special emphasis is given to the size of aerosols and cloud droplets, liquid water content, liquid phase concentrations and their size distribution as well as the resulting partitioning of trace gases between the corresponding phases.

2. MODEL DESCRIPTION AND MODEL SETUP

To investigate the effect of operator splitting between micro-physical and multiphase chemical processes a simple box model is employed. A relatively simple system of processes for a size distributed particle population is considered to determine a clear cause-effect relationship. Micro-physical processes are represented by condensation/evaporation while multiphase chemistry compiles the uptake of trace gases by particles and aqueous phase reactions.

For the exchange of volatile species between the aqueous and the gas phase the numerically more expensive flux formulation according to Schwartz (1986) is employed. Dissociation equilibria are assumed to be adjusted instantaneously as well as homogeneous concentration distributions within the drops. Table 1 summarizes the considered gas phase species and their diffusion coefficients $D_{g,i}$ and sticking coefficients a_i.

The chemical reaction mechanism follows essentially the work of Müller and Mauersberger (1994). Beside the mass transfer of the trace gases between the gas and the aqueous phase, it comprises the most essential oxidation pathways of S(IV) to S(VI) by O_3 and H_2O_2 in the liquid phase. The involved gas phase species have primary importance for the acidity development in the liquid phase.

Author's address: Frank Müller, Meteorological Institute, University Hamburg, D-20146 Hamburg, Germany; E-Mail.: frank.mueller@dkrz.de

Gas	$D_{g,j}$	a_j
O_3	0.15	0.52
HNO_3	0.13	0.11
H_2O_2	0.18	0.13
HCl	0.18	0.08
CO_2	0.16	0.0002
SO_2	0.13	0.13
NH_3	0.25	0.097

Table 1: Diffusion coefficients, $D_{g,j,}$ and sticking coefficients, a_j for the uptake of gaseous species.

The size dependent formulation of the change of water mass m_w by condensation/evaporation of water vapor accounts for the temperature effect due to the release/uptake of latent heat by the phase change of water vapor, the Kelvin effect, and the Raoult effect according to e.g. Pruppacher and Klett (1997), and Jacobson (1997). Activity effects are disregarded throughout this study assuming that all particles are highly diluted. This assumption, however, might be violated for the smallest particles during the first seconds of their growth. Essential details of the model can also be found in Müller and Mauersberger (1994).

In the case of mutual interaction of microphysical and multiphase chemical processes, the Equations are simultaneously solved with a Gear-solver (Hindmarsh, 1980). For the case of de-coupled processes, the corresponding Equations are sequentially solved with the same solver using the operator sequence:

$$\Delta x = L_{microphys} \cdot \Delta t * L_{chem} \cdot \Delta t$$

where L represents the corresponding operators, and x stands for the aqueous phase concentration, $c_{i,}$ and the partial presser,p_i. It is assumed that the de-coupling intervals of 0.01s, 0.1s, 1s, 10s, 100s, 200s, 500s and 1000s are representative for present day air quality models where dynamic and micro-physical/chemical processes are de-coupled as well. Hence, the box is regarded as 'open' with respect to the thermodynamic parameters temperature T, relative humidity RH, and pressure P. For the most part these parameters are mostly kept constant when applying the concept of operator splitting. With respect to the trace gases the box is considered to be 'closed' since trace gas concentrations are objects of the chemical processes. The initial conditions for both the considered trace gases and the thermodynamic parameters, given in Table 2, are chosen to represent average conditions in clouds.

The physico-chemical aerosol parameters are arbitrarily chosen for this study. The applied maritime aerosol distribution is constructed as the superposition of three log-normal distributions according to Jaenicke (1987). The size dependent distribution of the aerosol composition was arbitrarily selected. NaCl, $(NH_4)_2SO_4$, and SiO_2 are considered as initial aerosol components. For this study the considered particle size range is arbitrarily selected according to the critical particle radius for activation, r_c, at the given relative humidity, RH. The lower limit of the considered particle size range was set to a dry particle radius of r_c=7.4·10^{-5}cm.

Trace gas species	Concentration [ppb(v)]	Thermodynamic Parameter	Initial Value
H_2O_2	1	T	280
HNO_3	1	RH	100.1
NH_3	1	P	800
SO_2	5		
HCl	0.5		
CO_2	330		
O_3	50		

Table 2: Initial conditions for the box model simulations

3. Results

Starting with the micro-physical parameters of the particle population, Figure 1 shows the spectral evolution of the size dependent liquid water content, G_w, (top) and of the total mass of dissolved material, $G_{ap,d}$, in the particles (bottom) in the case of all indicated processes being considered simultaneously. Initial values for t=0 are shown.

With increasing simulation time both the water content attached to the particles and the content of soluble aerosol mass increase considerably in the smallest size ranges due to the higher mass transfer coefficients relative to the bigger particle sizes. In addition, sulfur oxidation by ozone and H_2O_2 increases the total mass of dissolved matter. The developing minimum in the total aerosol content results from the counteracting processes of dilution by water vapor uptake and redistribution of volatile compounds from the bigger particles to the smaller particles via the gas phase.

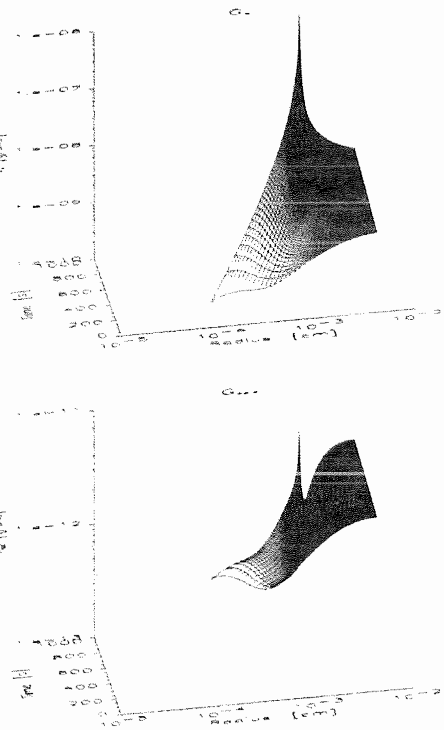

Figure 1: Spectral evolution of the liquid water mass density, G_w, (top) and the mass density of the total aerosol content (bottom), $G_{ap,d}$ for the case of simultaneous treatment of all processes.

Deviations from the results shown in Figure 1 due to varying de-coupling intervals are presented in Figure 2 and 3. The time evolution of the differences in size integrated total liquid water content (Figure 2) increase markedly for de-coupling intervals longer than 1s. This can be explained by the characteristic times of water vapor diffusion which is in the order of a magnitude smaller than 1s. A reduction of the de-coupling interval does not notably change the total liquid water content but the size dependent water content of the particles. With increasing de-coupling intervals between micro-physical and multiphase chemical processes the total water content is increasingly underestimated in the case of de-coupled treatment. The temporal evolution of the differences of total liquid water content within each single de-coupling interval reaches a maximum of about 5-8% after 300-500s simulation time.

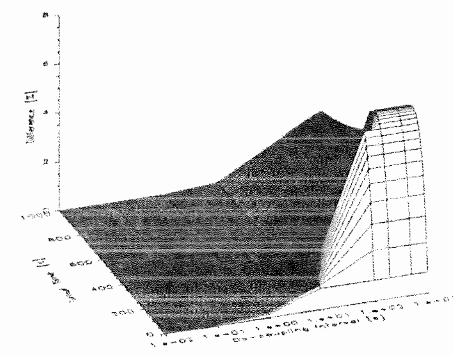

Figure 2: Percent difference of the liquid water content as a function of de-coupling interval and simulation time

This behavior can be explained as follows: At the beginning of the growth the counteracting Kelvin effect and Roalt (or solution) effect are of special importance for the smallest particles which are characterized by the highest rates of water vapor as well as trace gas uptake, respectively. In the case of mutual interaction of dilution by condensation of water vapor and multiphase chemical processes, condensation causes enhanced fluxes of trace gases due to reduction of the tráce gas specific saturation vapor pressure at the particle surface. This, in turn, regenerates the depression/reduction of the water vapor saturation ratio at the particle surface. In the case of de-coupled treatment the water vapor fluxes towards the particle surfaces decrease faster for longer de-coupling intervals due to rapid dilution since the mass of chemical substances in the individual particles is fixed during the micro-physical step. In these cases the Roalt effect rapidly loses impact on the drop specific condensation rate. This mechanism is of decreasing importance for bigger particles, and, hence of decreasing importance for increasing simulation time.

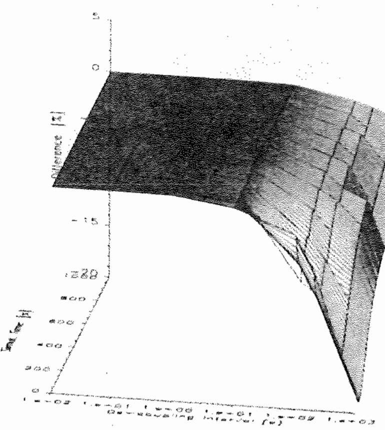

Figure 3: Evolution of the molar concentration difference of the total amount of chemical matter inside the particles as a function of simulation time and de-coupling interval

The behavior of the time evolution of the differences between mutual and de-coupled treatment of the processes with respect to total mass dissolved in the particles (Figure 3) is qualitatively different from that of total liquid water content . The total content of chemical matter inside the particles is increasingly overestimated with increasing de-coupling intervals while the overestimation decreases with increasing simulation time within each single de-coupling interval.

This behavior is caused by the fact that at the beginning of each chemical operator step during one de-coupling interval the concentration gradients between the corresponding gas and aqueous phase components, respectively, are very high due to the preceding micro-physical operator step. Compared to the completely coupled case this leads to higher fluxes of gaseous precursors towards the the particle surfaces which overcompensate the opposite effect due to the inverse flux-to-particle surface relationship. Additionally, the particle volume related sulfate production in the particles is enhanced by sufficient oxidant availability in the de-coupled case through the particles are somewhat smaller (about 3-8% in radius) in this case mainly during the very early simulation period. The decreasing importance of these effects with increasing simulation time is caused by the continuous depletion of the gas phase reservoir of precursor species which can also be seen in Figure 4.

4. Conclusions

The presented results indicate that de-coupling of condensation/evaporation and multiphase chemical processes for less then 10s generates no significant operating splitting errors compared to results of completely coupled simulations. For longer de-coupling intervals very strong deviations in the aqueous phase concentrations occur especially during the early phase of each de-coupling interval. Since the presented system is relatively simple further investigations are necessary to improve the understanding of non-linear interactions in more complex and, therefore, in more realistic systems.

5. References

Hindmarsh, A.C., 1980: LSODE and LSODI, Two new initial value ordinary differential equation solvers, ACM- SIGNUM Newsl. 15, no. 4, 10-11

Jacobson, M.Z,, 1997: Numerical techniques to solve condensational and dissolutional growth equations when growth is coupled to reversible aqueous reactions, Aerosol Sci. Technol. 27, 491-498

Jaenicke, R., 1987: Aerosolphysics and chemistry, in Landold-Börnstein Neue Serie, 46: Physical and chemical properties of the air, Springer Verlag, Berlin

Müller, F., Mauersberger, G., 1994: Case study on the interaction of size dependent multiphase chemistry and detailled microphysics, Atmos. Res., 32, 273-288

Schwartz, S.E.,1986: Mass-transport considerations pertinent to aqueous phase reactions of gases in liquid water clouds, in W. Jaeschke (ed.), Chemistry of multiphase atmospheric systems, NATO ASI Series, Series G: Ecological Science, Vol. 6, 415-472

Pruppacher, H.R., Klett, J.D., 1997: Microphysics of clouds and precipitation, Kluwer Academic Publishers, Dordrecht, pp 955

THE INDIRECT RADIATIVE FORCING OF ANTHROPOGENIC AEROSOL IN MIXED PHASE CLOUD

T.W.Choularton[1], V.T.J. Phillips[1], A.M. Blyth[2], J. Latham[1] and M.W. Gallagher[1]

[1]University of Manchester Institute of Science and Technology (UMIST), UK.
[2]New Mexico Institute of Mining and Technology (NMIMT), USA.

1. INTRODUCTION

In recent years much attention has been given to the parametrisation of liquid phase clouds in global climate models. Most clouds in the atmosphere, however, contain the ice phase and little attention has been given to attempts to parametrise the indirect effect in such clouds. As with water clouds there are two forms of the indirect effect. Firstly, the aerosol entering the cloud will affect the size distribution and hence the effective radius of the particles in the cloud. Secondly, the aerosol will also affect the efficiency of precipitation production in the clouds and hence the total water path in the cloud. The efficiency of precipitation process from ice and mixed phase cloud is generally high. Consequently it is argued that the first indirect effect is probably the most important.

The results from a model of mixed phase cloud are presented aimed at investigating the indirect effect of aerosol. The cloud model includes the effects of the activation of water droplets on cloud condensation nuclei, the formation of ice particles by primary nucleation processes, the Hallett-Mossop (H-M) process and the freezing of supercooled raindrops. Anthropogenic activity can affect both the number of cloud condensation nuclei available and the number of ice forming nuclei active in a given temperature range.

Model results are presented using a range of cloud condensation nuclei (CCN) activity spectra. Some results are shown below which make use of the Multi-Thermal Microphysical Model (MTMM) developed by Phillips, Blyth, Brown, Choularton and Latham described in this conference. These results are for simulations of convective clouds forming in the continental USA and investigate the sensitivity of the cloud microphysics to changes in the number of CCN. A wider range of results will be presented at the conference.

2. RESULTS FROM THE CCN SENSITIVITY TEST

Figure 1 shows the response of the precipitation rate at the ground to the change in aerosol concentration from C = 1000 /cm^3 to 3000 /cm^3, in the equation for the CCN activity spectrum $N = Cs^k$. Here, N is the number of CCN per unit volume activated at supersaturations less than s, and C and k are parameters determined by the airmass type. A value of $k = 0.8$ was used in both simulations. The simulation with the tripled aerosol concentration is hereafter referred to as the 'super-continental case'.

Corresponding author's address: T.W.Choularton, Department of Physics, UMIST, PO Box 88, Manchester M60 1QD, United Kingdom;
E-Mail: t.w.choularton@umist.ac.uk

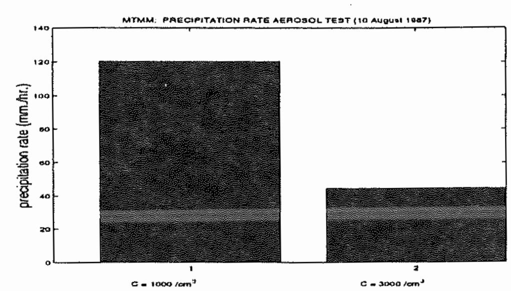

Figure 1. The precipitation rate at the ground for the control (left) and super-continental (right) cases.

It is evident that the precipitation rate decreases from 120 to 40 mm/hr when aerosol concentrations are tripled. Precipitation rates > 100 mm/hr are only produced by convective cloud, according to Rogers and Yao (1989).

Figure 2 confirms that the immediate effect of extra aerosol particles in the super-continental case is to reduce the time-averaged cloud droplet diameter by around 5 – 10 microns below the –15°C level. The level at which the mean cloud droplet diameter reaches the critical value of 25 microns for auto-conversion to rain has shifted from 2 to –14°C in the super-continental case. Furthermore, in the H-M generation region (-3 to –8 °C) at most levels the mean cloud droplet diameter is reduced to values less than 24 microns.

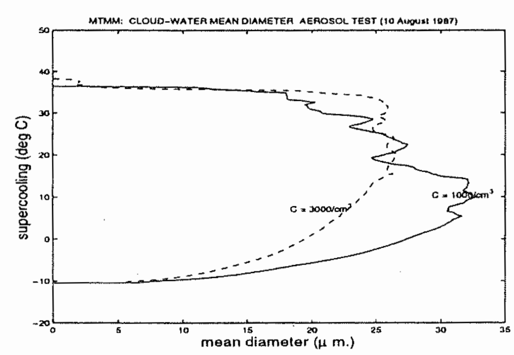

Figure 2. Vertical profiles of the mean cloud droplet diameter, for the control (full line) and super-continental (dashed line) cases.

Figure 3 shows the vertical profile of rainwater mixing ratio for both cases. The time-averaged mixing ratio of rain in the super-continental case is reduced by more than 50% compared to the control simulation. Below the freezing level, the value is 0.05 - 0.1 g/kg In the super-continental case compared to 0.2 – 0.7 g/kg in the control simulation. Moreover, the onset of rain is delayed by around 15 minutes in the super-continental case relative to the control simulation. This is evident from the evolution of the column-averaged mixing ratio of rain shown in Figure 4.

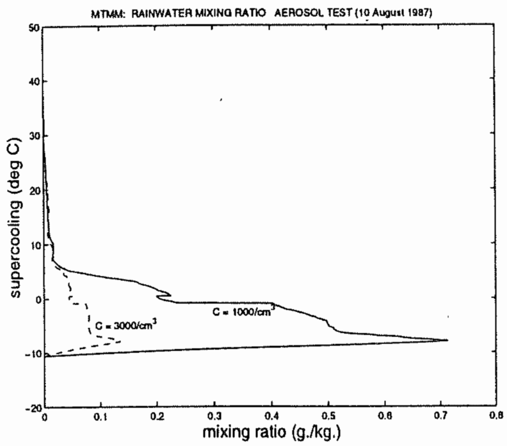

Figure 3. Vertical profiles of rainwater mixing ratio, plotted as in Figure 2.

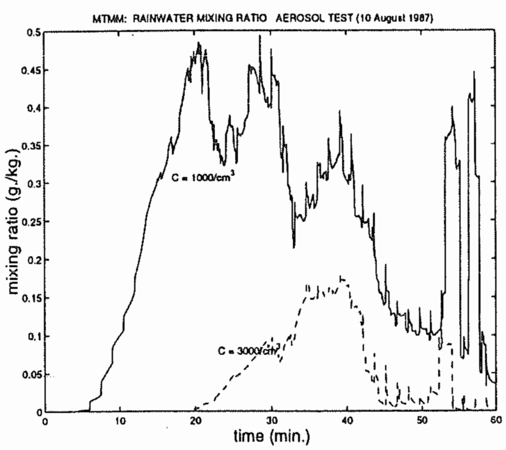

Figure 4. The time series of column-averaged mixing ratio for rainwater, plotted as in Figure 2.

Figure 5 shows the column-averaged mixing ratio of graupel. Graupel prevails in the total ice mixing ratio in both simulations. Significant values of graupel mixing ratio start one thermal later in the super-continental case compared to the control simulation. During the initial 45 minutes of both simulations, the graupel mixing ratio is suppressed by at least 50 % in the super-continental case relative to the control simulation. Nevertheless, the peak value of graupel mixing ratio realised at around 50 minutes is similar at around 2 g/kg in both simulations. Figure 6 illustrates evolution of the mixing ratio of snow. For most of the simulation, the mixing ratio of snow is significantly weaker in the super-continental case than in the control simulation.

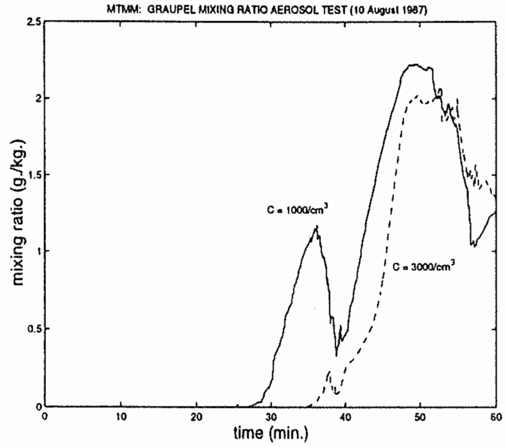

Figure 5. The time series of column-averaged mixing ratio for graupel, plotted as in Figure 2.

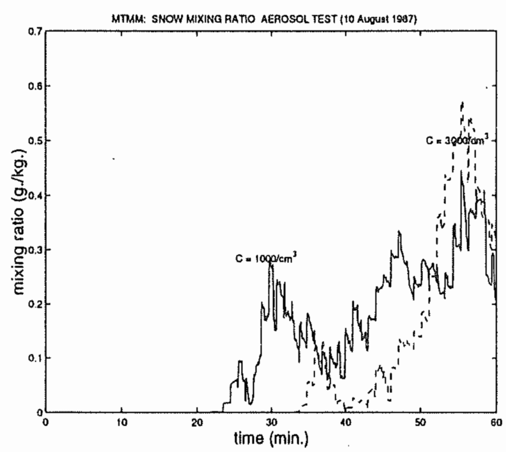

Figure 6. The time series of column-averaged mixing ratio for snow, plotted as in Figure 2.

Figure 7 shows the time-evolution of the column-averaged concentration of frozen drops and of H-M splinters. There is a delay in the onset of significant concentrations of frozen drops and H-M splinters of around 10 minutes in the super-continental case relative to the control simulation. Frozen drops in the super-continental case remain always at column-averaged concentrations reduced by more than 30% relative to the control simulation. Moreover, drop-freezing tends to occur at higher altitudes in the super-continental case than in the control simulation, further reducing the rates of H-M ice multiplication.

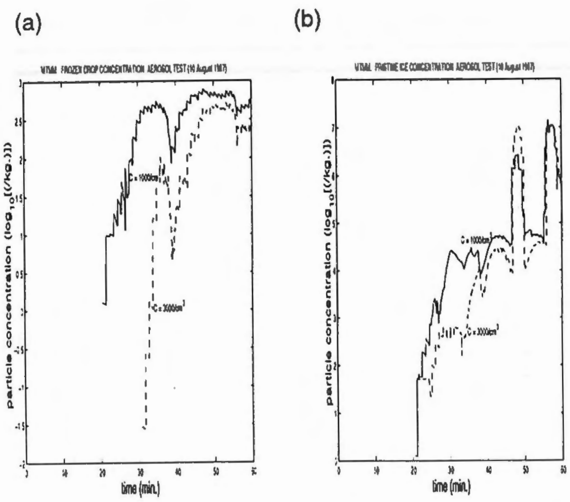

Figure 7. Time series of the column-averaged particle concentrations of (a) frozen drops and (b) H-M splinters, plotted as in Figure 2.

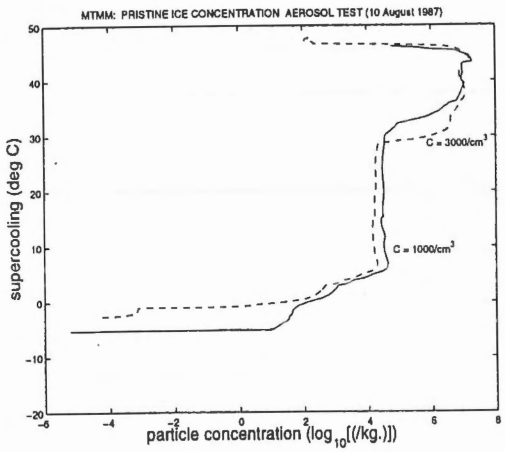

Figure 8. Vertical profiles of the pristine ice concentration, plotted as in Figure 2.

Figure 8 shows the response of the anvil ice concentration. There is an increase of 40% in the depth of the region of concentration > 1/cm^3 to around 2 km. in the super-continental case.

Figure 9 illustrates the change in mean ice diameter for all ice particles and for homogeneously frozen cloud droplets. In the mixed phase region, raindrop-freezing shifts towards colder temperatures in the super-continental case. Hence, H-M splinters emanate from levels nearer to the top of the H-M generation region. Thus, the mean ice diameter in the mixed phase region is suppressed slightly at all levels in the super-continental case. The decrease of mean ice diameter with height at levels above –20 ^{o}C reflects the detrainment of H-M splinters from the updraft at successive levels of dissipation of thermals, before riming can begin to convert these splinters to graupel.

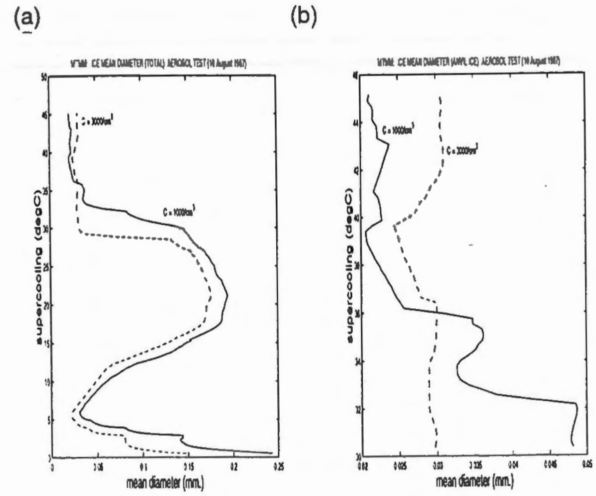

Figure 9. Vertical profiles of mean ice diameter for (a) all ice particles and (b) homogeneously frozen cloud droplets, plotted as in Figure 2. The averaging is weighted by particle concentration at each level.

At the anvil base, the mean diameter of cloud droplets is around 5 microns greater in the super-continental case relative to the control, due to the stronger riming rates in the control simulation. Thus, the anvil ice diameter is slightly larger in the super-continental case relative to the control.

3. DISCUSSION

The difference in graupel mixing ratio between the simulations decreases with time when glaciation is underway during the final 15 minutes of the simulation. As riming onto graupel is the dominant sink for cloud-water, and since large droplets have a larger collision efficiency than smaller droplets, the relatively strong glaciation in the control simulation significantly reduces the mean cloud-droplet diameter towards the values in the super-continental case at levels above –15 ^{o}C. This, in turn, causes less difference in rates of auto-conversion of cloud-water to rain and in rates of drop-freezing between the simulations once glaciation has started than earlier on.

The time-averaged mean value of cloud-droplet diameter is reduced from around 30 – 32 microns in the control simulation to 20 – 24 microns in the super-continental case at levels within the H-M generation region. This is expected to influence directly the rates of secondary ice production.

The response of the anvil ice concentration to aerosol concentration is somewhat limited by the fact that the anvil only starts to form less than 15 minutes before the end of the simulation. The increased vertical extent of anvil ice in the super-continental case is linked to a larger mean cloud droplet diameter at the anvil base than in the control simulation. The presence of relatively large cloud droplets at the anvil base in the less glaciated, super-continental case causes homogeneous freezing to start at slightly warmer temperatures relative to the control simulation.

4. CONCLUSIONS

Clearly, the increases in cloud droplet concentration and in aerosol concentration tend to reduce the average supersaturation, restricting the growth rates of cloud droplets. There is a strong dependence of the overall precipitation rate on the coalescence of cloud droplets to form rain. Thus, there is a significant reduction in the precipitation rate when the mean cloud-droplet diameter in the super-continental case is decreased.

Recent satellite observations from the Tropical Rainfall Measuring Mission (TRMM) documented by Rosenfeld (2000) have indicated that urban and industrial aerosol pollution causes a reduction in cloud particle size. A complete shut-off of precipitation from clouds with tops at temperatures of –10 °C is seen over polluted areas.

The MTMM results not only explain the TRMM observations in terms of a coalescence mechanism inhibited by aerosol pollution, but also there is support here for Rosenfeld's conclusion that aerosol emissions are likely to reduce directly the rates of secondary ice multiplication in clouds. Droplets in the –3 to –8 °C region must be larger than 24 microns in diameter if H-M splinters are to be emitted during riming. In the super-continental case, the cloud droplet diameter was reduced to values less than 24 microns in the H-M generation region. Recent simulations of the MTMM with this condition incorporated into the representation of secondary ice production will be presented at this conference.

Rates of raindrop-freezing in the super-continental case are weakened by the paucity of liquid drops, delaying the onset of glaciation. The reduction in growth rates of cloud droplets causes auto-conversion and drop-freezing to occur at higher levels in the cloud. The delay of 15 minutes in the peak of graupel mixing ratio in the super-continental case relative to the control simulation causes a similar delay in the appearance of H-M splinters. These differences in rates of glaciation between the simulations become less marked as glaciation progresses, however, owing to the weaker reduction of the mean cloud droplet diameter by the riming of graupel in the less glaciated super-continental case.

The weaker rates of glaciation and of rain formation in the super-continental case tend to cause more cloud droplets to survive to reach the anvil where they freeze, than in the control simulation. Cloud droplets are advected into the anvil region in the adiabatic cores of thermals in both simulations. A significant sensitivity of the size and production rate of ice particles in the anvil to aerosol concentrations is revealed in this paper. Consequently, there is a clear possibility of anthropogenic pollution altering the albedo of cirrus clouds created by the decay of storm systems.

4.1 <u>References</u>

Rogers, R.R., and M.K. Yao, 1989: *A short course in cloud physics.* Pergamon Press.

Rosenfeld, D., 2000: Suppression of rain and snow by urban and industrial air pollution. *Science*, **287**, 1793 - 1796.

ALTERATION OF CLOUD MICROPHYSICAL AND RADIATIVE PROPERTIES OF DUE TO HNO_3 CONTAMINATION

S.Ghosh and P.R.Jonas

Department of Physics, UMIST, PO BOX 88, Manchester M60 1QD,England

1. INTRODUCTION

It is generally accepted that the droplet concentration in clouds that are formed over sources of pollutants, are larger than in clouds formed in clean air and that these clouds have a correspondingly smaller droplet size for any given value of the liquid water content. Reduction in cloud droplet size can be achieved when the air passes over sources of condensable vapours like HNO_3 as well as over sources of cloud condensation nuclei (CCN). In this study we have examined the effect of 10 ppb of HNO_3 on the evolution of the droplet spectrum for the EUCREX (European Cloud Radiation Experiment) stratocumulus cloud. We have also done sensitivity tests at varying updraught speeds as well as CCN composition which show that the effect of the acid is most pronounced under low updraught speeds and for a CCN spectrum that includes NaCl as well as $(NH_4)_2SO_4$.

2. MODEL DESCRIPTIONS

We have used the UK Meteorological Office LES (Large Eddy Simulation) model with an optimised Kessler scheme in order to account for the effect of pollutants to obtain the distribution of the cloud liquid water. Since the LES model is not size-resolving, we used its dynamical outputs to run a parcel model to obtain the droplet spectrum. From an analysis of the synoptic conditions over the region of interest for the EUCREX cloud on 18 April 1994, we find a strong NE flow indicating that the incoming air could be contaminated by air pollutants (including HNO_3 from the continental air). Unfortunately, the HNO_3 concentration was not measured and for our studies we assumed it to be of the order of 10 ppb. The process of CCN activation is initiated in the model by invoking the Kohler theory with modifications to account for the reduction in the saturation vapour pressure due to the presence of the acid. Further details can be obtained from Ghosh et al. (2000) and the references therein.

Corresponding author's address: S. Ghosh, Dept. of Physics, UMIST, PO Box 88, Manchester, M60 1QD, England

3. RESULTS

In Fig. 1 we have shown the modelled 3D cloud liquid water content (LWC) after 4 hours of the LES simulation and Fig. 2 shows the corresponding drop-size distribution.

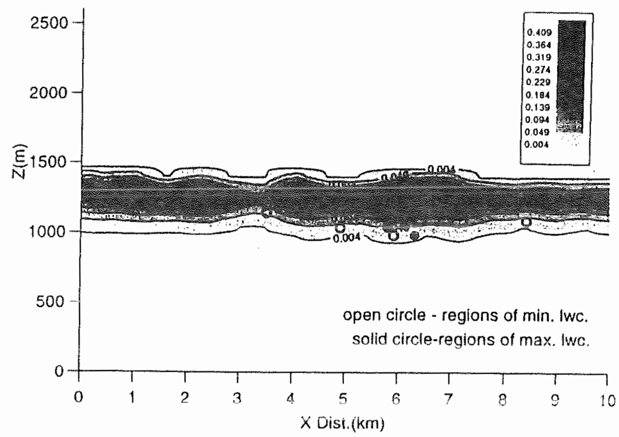

Figure 1. Modelled LWC (gm^{-3}) for the EUCREX cloud

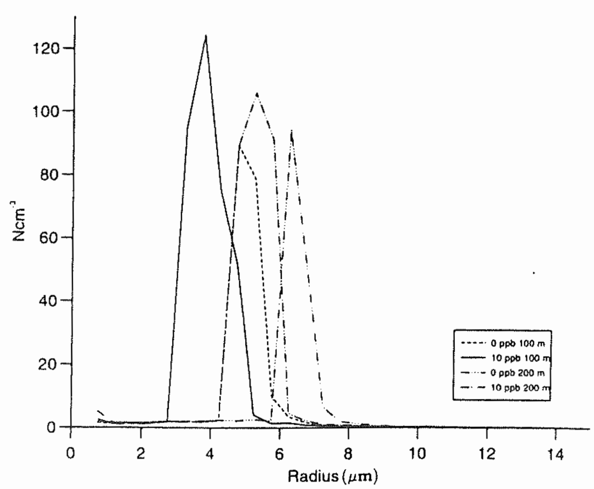

Figure 2. Droplet spectrum for the EUCREX cloud

We find that at 100 m above the cloud base the peak in the concentration distribution is at about 4.0 μm radius with the highest number density ~120 cm^{-3} for the run with 10 ppb HNO_3. When no acid is included the peak is observed at larger sizes at around 5.0 μm radius with a smaller number density ~90 cm^{-3}. A similar feature is also observed at 200 m above the cloud base and by comparing the spectra at these two levels we find that there are more of the larger drops towards the cloud top -a feature which is generally observed for stratocumulus clouds. The peak number density ~125 cm^{-3} at 4.0 μm radius is achieved only when 10 ppb of HNO_3 is introduced in the simulation. The range of predicted droplet sizes with radii between 4-7 μm is in broad agreement with the observations from Pawlowska and Brenguier (1996) although the maximum observed number concentrations were sometimes higher.

In Fig. 3 we show a comparison between the observed and modelled droplet effective radii. The measurements have been made on board the Merlin-IV with the Fast FSSP (Pawlowska and Brenguier 1996). From this figure it is clear that the modelled droplet effective radii agree reasonably well with the observations and the run which includes 10 ppb of HNO_3 is able to yield the observed smallest droplet effective radii close to 3 μm which are not predicted by the acid-free run.

In Fig. 4 we have shown the modelled optical depth and it is found that the acid-free simulations have about 7 % smaller optical depths than those which contained HNO_3. The overall optical depth variability agrees well with the POLDER (Polarisation and Directionality of the Earth's Reflectance) observations on board the ARAT aircraft and optical depths approaching the maximum observed value 60 could be attained in the model results only after 10 ppb of HNO_3 was introduced in the microphysical simulation.

The results presented above correspond to an initialisation with an assumed NaCl CCN spectrum. We have also done some further studies on the effect of HNO_3 on the evolution of cloud droplet spectra where we have used observed CCN spectra measured on 19 July 1997 during the Aerosol Characterisation Experiment-2 (ACE-2). Chemical analysis showed that in the small size category with aerosol radius smaller that 0.75 μm the aerosol composition was dominated by $(NH_4)_2SO_4$ and for the larger ones with radii greater than 0.75 μm the aerosol particles were mainly sea salt (NaCl)(A. Dore 1999; personal communication).

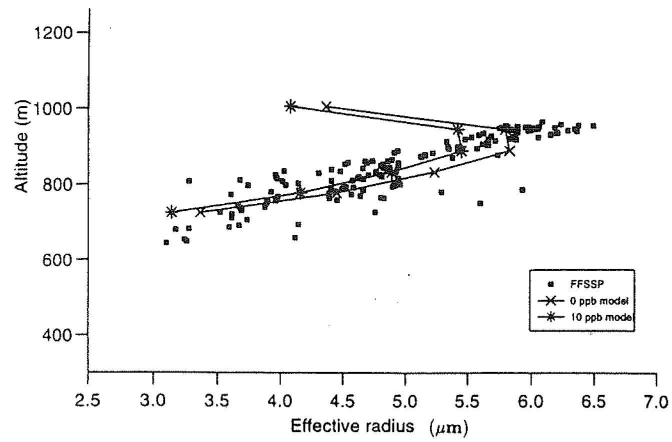

Figure 3. Comparison of modelled and observed droplet effective radii for the EUCREX cloud

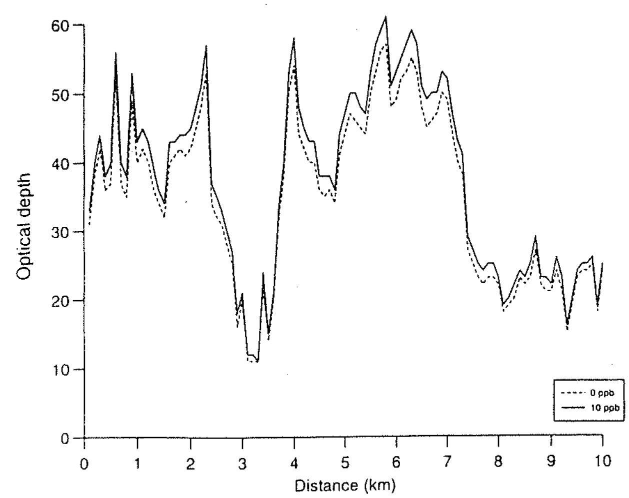

Figure 4. Modelled optical depths for the EUCREX cloud

The observed updraught speed for the ACE-2 case study was of the order of 0.95 ~ms^{-1} and the HNO_3 concentration were of the order of 5 ppt. Under these conditions the modelled drop-size distribution was insensitive to the presence of the acid. One of the main reasons for the relative insensitivity of the model run to the acid vapour is due to the the high updraught speed approaching 1 ms^{-1} when water saturation itself is high enough to activate a large fraction of the aerosol particles and the acid no longer plays any part in the activation process (Kulmala et. al. 1993).

Our sensitivity tests revealed that at large updraught speeds the drop-size distribution resulting from condensation upon a population of mixed nuclei composed of both soluble and insoluble components (as in this case with NaCl being less soluble than $(NH_4)_2SO_4$) is generally not much broader than that produced by condensation upon a population of pure NaCl nuclei. This conforms to the earlier Fitzgerald (1974) results.

These observations led us to perform further sensitivity tests with low updraught speeds and higher acid concentrations. The most interesting result that emerged from these tests was that with low updraught speeds the drop-size spectrum was sensitive to the acid concentration as well as to the CCN composition. This is shown in Fig. 5 where we find that when the updraught speed is 0.25 ms^{-1} and the HNO_3 concentration is 10 ppb there is a distinct shift of the spectrum towards smaller radii. In particular, at 200 m above the cloud base the shift towards smaller radii is accompanied with an increase in the number concentration. However, for the same updraught speed and acid concentration, when we alter the spectrum to a pure $(NH_4)_2SO_4$ spectrum we find that the cloud droplet spectrum is again insensitive to the acid concentration.

Since gaseous HNO_3 absorbed by cloud droplets result in the formation of many liquid phase species, it is important to quantify the time-dependence of N(V) in the cloud droplets with radii corresponding to the distribution with 10 ppb of acid shown in Fig. 5. Unfortunately, to date the ventilation factor for HNO_3 uptake is not known and modellers still use empirical relations applicable to water vapour (Pruppacher and Klett 1997, p 541). To overcome this difficulty we explicitly calculated this coefficient by developing a numerical model based on the solution of the time-dependent convective diffusive transport of HNO_3 into and around a falling spherical droplet and found that the actual ventilation was larger than the predictions

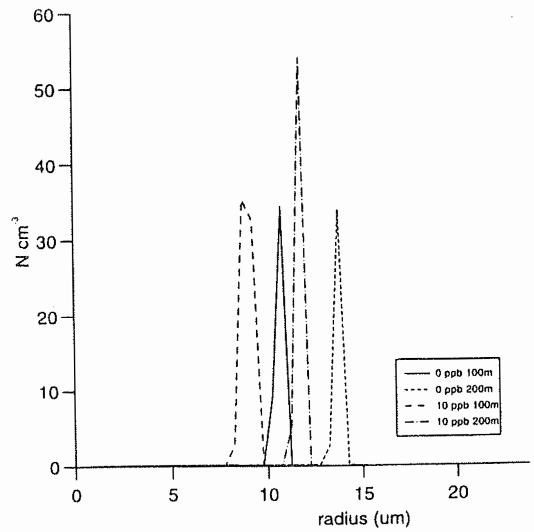

Figure 5. Droplet spectrum formed over mixed CCN at low updraught speed

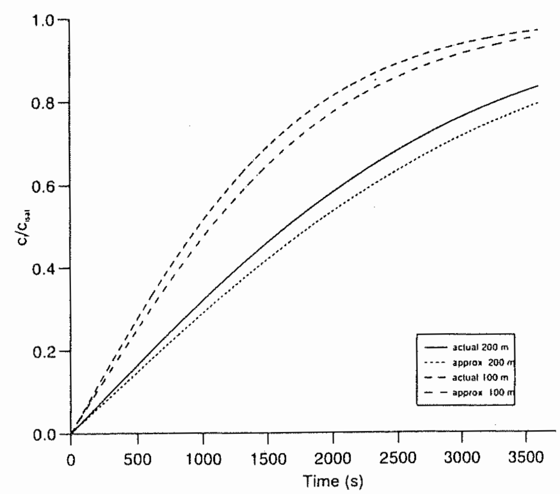

Figure 6. Time variation of N(V) in cloud droplets at different heights

from empirical relations. Then we used this coefficient to estimate the concentration of N(V) in the cloud droplets invoking standard methods (Pruppacher and Klett 1997). The results are shown in Fig. 6 where we have shown the time-variation of the N(V) normalised by the value at saturation ($c_l / c_{l,sat}$) and we find that while the relatively smaller droplets in the cloud interior are nearly saturated within an hour, the larger droplets closer to the cloud top are about 80%saturated. We also find that the predicted concentrations using the approximate values of the ventilation coefficient are lower than those obtained from the full calculation.

4. CONCLUSIONS

We have shown that air pollutants like HNO_3 can affect the process of CCN activation and alter cloud microphysical and radiative properties. Cloud optical depth and effective radii estimations based on the EUCREX case study showed that model simulations which included 10 ppb of HNO_3 better captured the observations than an acid-free run. Model sensitivity studies showed that the effect of HNO_3 was most pronounced at low updraughts speeds and for a mixed CCN spectrum comprising of $(NH_4)_2SO_4$ as well as NaCl rather than a pure $(NH_4)_2SO_4$ spectrum.
Finally, we also found that by using empirical values for water vapour ventilation and applying them to the process of HNO_3 uptake can lead to underpredictions in the estimation of N(V) concentrations within cloud droplets.

5. References

Fitzgerald, J.W., 1974 : Effect of aerosol composition on cloud droplet size distribution : A numerical study. *J. Atmos. Sci.,* **31**, 1358-1367

Kulmala, M., Laarksonen, A., Korhonen, P., Vesala, T., Ahonen, T., and J.C. Barrett 1993 : The effect of atmospheric nitric acid vapor on cloud condensation nucleus activation. *J. Geophys. Res.,* **98**, 22949-22958

Pawlowska, H., and J-L. Brenguier 1996 : A strudy of the microphysical structure of stratocumulus clouds. *Proc. 12th Int.Conf. on Clouds and Precipitation,* Zurich Switzerland, Vol. I, 23-26

Ghosh, S., Jonas, P.R., and R. Wood 2000 : Some impact of pollutants on the development and optical properties of stratocumulus clouds. *Quart. J. Roy. Meteorol, Soc.* (in press)

Pruppacher, H.R., and J.D. Klett 1997 : *Microphysics of clouds and precipitation.* Kluwer Academic Publishers, Dordrecht. 954 pp.

TROPICAL DEEP CONVECTION AND TROPOSPHERIC CHEMISTRY

Chien Wang and Ronald G. Prinn

Center for Global Change Studies and the Joint Program for the Science and Policy of Global Change, Massachusetts Institute of Technology, Cambridge, MA 02139, USA

1. INTRODUCTION

Tropical oceanic regions experience frequent deep atmospheric convection. These regions also possess the globally highest UV fluxes and mole fractions of water vapor, and thus the globally highest levels of OH. The combination of high OH levels and increasing influx of pollutants due to industrialization and biomass burning in tropical and subtropical latitudes lead us to ask how atmospheric composition in these regions may be changing. However, despite the increased emissions of pollutants in tropical lands, recent measurements have shown extremely low (< 10 ppb) O_3 mole fractions over tropical oceans in both the planetary boundary layer and, most interestingly, in the upper troposphere when deep convection occurs (Newell and Wu, 1985; Johnson *et al.*, 1990; Piotrowicz *et al.*, 1991; Kley *et al.*, 1996). Because O_3 is a greenhouse gas in the upper troposphere, perturbations to its mole fraction there have important climatic impacts. Previous studies have indicated that when deep convection exists, both downward transport of O_3-rich air from the lower stratosphere (e.g., Wang *et al.*, 1995; Poulida *et al*, 1996) and enhanced O_3 production due to transport of reactants from the lower troposphere (e.g., Pickering *et al.*, 1990) can increase mole fractions of O_3 in the upper troposphere. These results suggest that any mechanism that causes the loss of O_3 in the upper troposphere must be significant enough to compensate the increase of O_3 induced by these other processes.

Besides these puzzling anomalous lows in the O_3 distribution, observations also indicate that in the convective zones the mole fractions of water vapor in the lower stratosphere are often higher than those in the upper troposphere (e.g., Kley *et al.*, 1997). Whether the upward transport of ice crystals followed by their evaporation, or the upward and horizontal transport of water vapor causes this reversed profile is still unclear.

To elucidate the various possible impacts of deep convection on tropospheric chemistry over the tropical oceans, we have developed an integrated model including dynamics, radiative transfer, cloud and aerosol microphysics, gaseous and aqueous chemistry, and lightning and related NO production. We use observed trace chemical profiles combined with profiles derived from previous modeling results to initialize our model. We then carry out a set of simulations to study model sensitivity and enable detailed budget analyses. Our aim is to understand the net effects of different physical and chemical processes on the redistribution of chemical species during convection and to provide information for handling these processes in large-scale coarse-resolution model studies.

Corresponding author's address: Chien Wang, Massachusetts Institute of Technology, E40-269, 77 Massachusetts Avenue, Cambridge, MA 02139, USA; E-Mail: wangc@mit.edu.

2. MODEL AND NUMERICAL EXPERIMENTS

The model used in this study is a recently improved version of the cloud-resolving model by Wang and Chang (1993). The major change made to the original model is the integration of the dynamics-physics and chemistry submodels. This procedure avoids the duplication of the dynamics-physics submodel calculations in the chemistry submodel and the storage of the large amount of data needed for the off-line chemistry submodel simulations. The new integrated model provides the chemistry simulations with 'real-time' values of winds, temperature, turbulent and radiative fluxes, and microphysical conversion rates, and also allows inclusion of aerosols in both the dynamics-physics and chemistry submodels.

The dynamical prognostic equations in this model consist of the nonhydrostatic momentum equations, the continuity equations for water vapor and air mass density, the thermodynamic equation, and the equation of state (Wang and Chang, 1993). These equations are integrated in either two or three dimensions. Also included are prognostic equations for the mixing ratios (as well as number concentrations) of: cloud droplets (liquid droplets smaller than 200 microns in diameter); rain drops (>200 microns); ice crystals (single and aggregated); and graupel (heavily rimed ice particles) (Wang *et al.*, 1995). The microphysical transformations are formulated based on a "two-moment" scheme incorporating the size spectra of particles (Wang and Chang, 1993; Wang *et al.*, 1995). A radiation module based on Fu and Liou (1993) is used in the model. It is a δ-four-stream radiation model including a parameterization for ice-phase cloud layers.

The chemistry sub-model predicts atmospheric concentrations of 25 gaseous and 16 aqueous (in both cloud droplets and raindrops) chemical species, undergoing about 100 reactions as well as transport, and microphysical conversions. The equilibrium reactions on the surface of liquid particles are calculated using the mass-transfer method described in Wang and Chang (1993). Surface reactions on ice particles can be also included. In order to calculate lightning flash and resultant production of NO molecules, a parameterized lightning scheme based on cloud electricity and microphysics is included in the model. The concentrations of both cloud condensation nuclei (CCN) and ice nuclei (IN) are calculated incorporating transport as well as nucleation and precipitation scavenging in the model. The nucleation rates of cloud droplets and ice crystals are limited by the local concentrations of CNN and IN. Aerosol chemistry and physics can be easily incorporated to predict the concentrations of CCN.

The simulations are initialized using observed profiles of temperature, water vapor concentrations, and horizontal wind velocities from a deep convective event which occurred on March 8, 1993 (see Wang and Prinn, 1998) during the Central Equatorial Pacific Experiment (CEPEX, Ramanathan *et al.*, 1993). This event is a squall line system consisting of several isolated convective storms separated by about 20-50 km from each other. Since the dynamical interactions between different convective towers were not the focus point of this research, we chose to simulate a single storm rather than the entire group of them. The initial concentration fields for chemical species were derived from a 6-hour clear-sky integration of the model. These clear-sky calculations were initiated with an observed ozone sounding (Wang *et al.*, 1995) and with vertical profiles for other chemical species based either on observations (e.g., Thornton and Bandy, 1993; Thornton *et al.*, 1996) or on global model results (Wang *et al.*, 1998). The initial mole fractions of chemicals at the surface were 80 ppb for CO, 40 ppt for NO, 1750 ppb for CH_4, 50 ppt for SO_2, 50 ppt for dimethyl sulfide (DMS), and 360 ppm for CO_2, and are intended to represent clean atmospheric conditions.

The stratospheric portion of the initial CEPEX profile of water vapor mass mixing ratio was modified to be constant (10^{-4} g/kg). This is because we want to investigate whether convection can generate a relatively moist layer in the lower stratosphere. To determine whether the vertical transport of air from the ozone-poor boundary layer is responsible for the formation of the low ozone layer in the upper troposphere, the middle and upper tropospheric part of the initial ozone profile was also modified to have a constant ozone mole fraction (see Wang *et al.*, 1995).

Simulations have been done using both three-dimensional and two-dimensional versions of the model. The three-dimensional runs are designed to explore the importance of strong vertical transport of the chemical species including water vapor during the developing and mature stage of the convection, while the faster two-dimensional runs are designed to study the long term chemical consequences of the deep convection well after the convective event. Table 1 lists the assumptions made or processes included in a set of sensitivity runs of the model. In order to explore the influence of the NO production per flash on the chemical processes, two lightning runs have been carried out using different NO production rates. In both three-dimensional and two-dimensional runs, the tops of the simulated clouds are able to reach the tropopause within about one hour.

The spatial resolutions of the model in this study are 2 km horizontally and 0.5 km vertically. The model domain covers 240×160×25 km in the three-dimensional runs and 1000×25 km in the two-dimensional runs. Time steps for dynamics, microphysics, and transport of chemicals are all 5 seconds (0.5 second for sound-wave terms, cf. Wang and Chang, 1993). Time steps for radiation are 5 minutes in the first five hours and 10 minutes thereafter. For both gaseous and aqueous

Table 1. List of Relevant Simulations

Simulations	Cloud	Gas Chemistry	Aqueous Chemistry	Lightning
REF3D	Yes	Yes	Yes	No
NCH3D	Yes	No	No	No
REF2D	Yes	Yes	Yes	No
NC2D	No	Yes	No	No
LTN2D	Yes	Yes	Yes	Yes(1)
LTNH2D	Yes	Yes	Yes	Yes(2)
GAS2D	Yes	Yes	No	No

Notes: (1) uses NO production rate based on Price et al. (1997); (2) uses NO production rate based on Franzblau and Popp (1989).

chemistry, the time step is 30 seconds. All simulations started from noon local time. Integration times are 4 hours for the three-dimensional runs and 30 hours for the two-dimensional runs. Radiation-type lateral boundary conditions are used for the three-dimensional run, while periodic lateral boundary conditions, which maintain mass conservation, are applied in the two-dimensional runs.

3. RESULTS AND CONCLUSIONS

Our results suggest that the relatively high H_2O in the lower stratosphere is primarily formed by the direct upward transport of water vapor from below, rather than by upward transport of ice crystals followed by their evaporation. The high altitude increases in H_2O concentration, and enhancement of UV flux by upward reflection from the cloud anvils, then induces high OH concentration just above the cloud top. At the same time, OH concentrations inside or below the cloud are significantly lower than in the case of clear skies. Also, the downward transport of O_3-rich air from the lower stratosphere has been found to be very important for the O_3 mass budget in the upper troposphere. On the other hand, our simulations have shown that the upward transport of O_3-poor air from the boundary layer does not significantly decrease O_3 concentrations in the upper troposphere.

We find that gas phase production of some chemical species is changed by more than a factor of 2 due to convection. In addition, lightning production of NO is found to be very important. In the lightning runs, reduced UV fluxes inside and below the convective tower and anvils, as well as during the nighttime, combined with the massive production of NO molecules, leads to reductions of both NO_x and O_3. Before contributing to O_3 production, as much as 28% of the NO_x molecules produced by lightning have been converted to N_2O_5 and HNO_3 through reactions with O_3 and OH. Tropospheric O_3 in total is reduced through convection by up to 11% relative to the pre-convective state. The lowest O_3 mole fractions in the upper troposphere calculated in the lightning runs are slightly lower than 2 ppb, which is an 80% decrease from the initial O_3 mole fraction. Vertical profiles of O_3 from our two lightning runs agree quite well with O_3 observations in the upper troposphere, suggesting that lightning related O_3 loss in cloud anvil regions can help explain the occasional formation of an O_3-poor layer in the upper troposphere.

Although aqueous reactions are in theory very fast in producing sulfates, our study indicates that for the specific remote equatorial convection cases studied here, only about 9% of the dissolved SO_2 is converted to sulfates. As a result, the aqueous processes only contribute 21% to the total sulfate production inside the range of the two-dimensional model domain (~1000 km wide). Three processes have been identified as limiting the aqueous reactions: the much lower solubility of SO_2 relative to H_2O_2; the conversion of water to ice phase particles that terminates the aqueous chemistry; and the limited coverages and lifetimes of the liquid phase portions of the clouds. Our results suggest that global models that neglect these processes may overestimate aqueous sulfate production.

Our study address important issues including the formation of the observed H_2O-rich layer in the lower stratosphere, the transport and chemical causes of the observed O_3-poor layer in the upper troposphere, the impact of the convective tower and associated anvils on the gas phase and aqueous phase chemistry, and the chemical consequences of massive NO production by lightning. It has revealed the importance of considering interactions among convective cloud dynamics, cloud microphysics, radiation, and tropospheric chemistry. Deep convection influences tropospheric chemistry not only through vertical transport but also by changing UV fluxes (and thus the photochemical rates), by scavenging soluble species, and by producing NO molecules through lightning (which then changes the main chemical pathways). The formation of large amounts of ice phase particles can greatly change the relative efficiencies of gaseous and aqueous reactions and thus modify the changes in chemical properties induced by deep convection.

Many questions about the effects of deep convection on tropospheric chemistry remain unanswered. Our understanding could be further improved by including more detailed aerosol physics and chemistry as well as surface chemical processes in our models. Also our model simulations of lightning initiation and associated NO production would become more realistic if we include a more detailed description of atmospheric electric fields based on observational and laboratory data.

Acknowledgements

We thank Donald Locus for providing results on DMS and OH reactions and Dr. Qiang Fu for providing the radiation module. The observational data of the CEPEX experiment are kindly provided by the Center of Clouds, Chemistry, and Climate at the Scripps Institution of Oceanography. This research was supported by the NOAA Climate and Global Change Program grant GC97-474 to MIT, the MIT Joint Program on the Science and Policy of Global Change, and the NSF grant ATM-96-10145 to MIT.

References

Franzblau, E., and C. J. Popp, 1989: Nitrogen oxides produced from lightning, J. Geophys. Res., 94, 11089-11104.

Fu, Q., and K. N. Liou, 1993: Parameterization of the radiative properties of cirrus clouds. J. Atmos. Sci., 50, 2008-2025.

Johnson, J. E., R. H. Gammon, J. Larsen, T. S. Bates, S. J. Oltmans, and J. C. Farmer, 1990: Ozone in the marine boundary layer over the Pacific and Indian Oceans: latitudinal gradients and diurnal cycles, J. Geophys. Res., 95, 11847-11856.

Kley, D., P. J. Crutzen, H. G. J. Smit, H. Vömel, S. J. Oltmans, H. Grassl, and V. Ramanathan, 1996: Observations of near-zero ozone concentrations over the convective Pacific: Effects on air chemistry, Science, 274, 230-233.

Kley, D., H. G. J. Smit, H. Vömel, H. Grassl, V. Ramanathan, P. J. Crutzen, S. Williams, J. Meywerk, and S. J. Oltmans, 1997: Tropospheric water-vapour and ozone cross-sections in a zonal plane over the central equatorial Pacific Ocean, Q. J. R. Meteorol. Soc., 123, 2009-2040.

Newell, R. E., and M.-F. Wu, 1985: Simultaneous measurements of carbon monoxide and ozone in the NASA Global Atmospheric Sampling Program (GASP), Atmospheric Ozone, C. S. Zerefos and A. Ghazi (eds.), 548-552, D. Reidel, Dordrecht.

Pickering, K. E., A. M. Thompson, R. R. Dickerson, W. T. Luke, D. P. McNamara, J. P. Greenberg, and P. R. Zimmerman, 1990: Model calculations of tropospheric ozone production potential following observed convective events, J. Geophys. Res. 95, 14049-14062.

Piotrowicz, S. R., H. F. Bezdek, G. R. Harvey, M. Springer-Young, and K. J. Hanson, 1991: On the ozone minimum over the equatorial Pacific Ocean, J. Geophys. Res., 96, 18679-18687.

Poulida, O., R. R. Dickerson, and A. Heymsfield, 1996: Stratosphere-troposphere exchange in a midlatitude mesoscale convective complex, 1. Observations, J. Geophys. Res., 101(D3), 6823-6836.

Price, C., J. Penner, and M. Prather, 1997: NOx from lightning, 1. Global distribution based on lightning physics, J. Geophys. Res., 102, 5929-5941.

Ramanathan, V., R. Dirks, R. Grossman, A. Heymsfield, J. Kuettner, and F. P. J. Valero, 1993: Central Equatorial Pacific Experiment Design, Center for Clouds, Chemistry, and Climate, University of California, San Diego, 115 pp.

Thornton, D. C., and A. R. Bandy, 1993: Sulfur dioxide and dimethyl sulfide in the central Pacific Ocean, J. Atmos. Chem., 17, 1-13.

Thornton, D. C., A. R. Bandy, B. W. Blomquist, D. D. Davis, and R. W. Talbot, 1996: Sulfur dioxide as a source of condensation nuclei in the upper troposphere of the Pacific Ocean, J. Geophys. Res., 101(D1), 1883-1890.

Wang, C., and J. S. Chang, 1993: A three-dimensional numerical model of cloud dynamics, microphysics, and chemistry, 1. Concepts and formulation, J. Geophys. Res., 98, 14827-14844.

Wang, C., P. J. Crutzen, V. Ramanathan, and S. F. Williams, 1995: The role of a deep convective storm over the tropical Pacific Ocean in the redistribution of atmospheric chemical species. J. Geophys. Res., 100(D6), 11509-11516.

Wang, C., R. G. Prinn, and A. Sokolov, 1998: A global interactive chemistry and climate model: Formulation and testing, J. Geophys. Res., 103, 3399-3417.

Wang, C., and R. G. Prinn, 1998: Impact of the horizontal wind profile on the convective transport of chemical species, J. Geophys. Res., 103(D17), 22063-22071.

THE INFLUENCE OF CLOUD PROCESSES ON THE DISTRIBUTION OF CHEMICAL SPECIES FOR THE 10 JULY 1996 STERAO/DEEP CONVECTION STORM

Mary C. Barth[1], William C. Skamarock[1], and Amy L. Stuart[2]

[1]National Center for Atmospheric Research, Boulder, Colorado, USA
[2]Stanford University, Stanford, California USA

1. INTRODUCTION

Clouds are able to modify the distribution of chemical species in many ways. Through air motions associated with clouds, chemical species are transported from the boundary layer to the free troposphere. Highly soluble species may dissolve into the cloud water and rain and ultimately be deposited on the ground in the precipitation. Because of the interaction of the cloud hydrometeors, chemical species may be captured by the precipitating ice particles. Photolysis rates are altered by the scattering and attenuation of solar radiation. The cloud hydrometeors may serve as locations for aqueous and ice-phase reactions.

Deep convection is usually thought to transport insoluble chemical species from the boundary layer to the upper troposphere and to rain out highly soluble species. By using a non-hydrostatic, three-dimensional convective cloud model coupled to a simple chemical reaction mechanism, we examine the importance of aqueous chemistry, microphysical processes, and modified photolysis rates compared to transport on the spatial distribution of peroxide species (H_2O_2 and CH_3OOH).

2. MODEL DESCRIPTION

The cloud model used for the simulations is the three-dimensional, fully-compressible, non-hydrostatic COllaborative Model for Multiscale Atmospheric Simulation (COMMAS), which is derived from the Wicker and Wilhelmson (1995) model. This model uses a Van-Leer type, monotonic advective scheme (Wicker and Wilhelmson, 1995) to transport water vapor, cloud water, rain, cloud ice, snow, graupel or hail, and scalars. A second order Runge-Kutta time integration (Wicker and Skamarock, 1998) is used to advance the quantities in time. The ice microphysics parameterization is that described by Tao et al. (1993). For the simulations performed here, hail hydrometeor characteristics (ρ_h = 0.9 g cm^{-3}, N$_o$ = 4 × 10^4 m^{-4}) are used.

The model is configured to a 120 x 120 x 20 km domain with 121 grid points in each horizontal direction (1 km resolution) and 51 grid points in the vertical direction with a variable resolution beginning at 50 m at the surface and stretching to 750 m at the top of the domain. A description of the meteorological scenario and transport of passive tracers is found in Skamarock et al. (2000) for the 10 July 1996 STERAO storm. We initialize the model environment and the initiation of convection in the same manner as Skamarock et al..

The gas chemistry (Table 1) represents daytime chemistry of 15 chemical species. The aqueous chemistry (Table 1) is computed for the cloud water and rain assuming a pH of 4.5. This chemistry includes two photolysis reactions whose rates are 1.25 times the interstitial photolysis frequency (S. Madronich, 1996, personal communication). Most chemical species are initialized with values measured in the inflow region of the storm; other species are estimated from values found in the literature or from the July monthly-mean mixing ratio for northeastern Colorado calculated by the 3-dimensional global transport model, MOZART (Brasseur et al., 1998). The initial profile for H_2O_2 and CH_3OOH are noted in Figures 2 and 3.

The chemical mechanism is solved with an Euler backward iterative approximation using a Gauss-Seidel method with variable iterations. A convergence criterion of 0.01% is used for all the species.

3. RESULTS

In general, the simulated storm reproduces the structure and dynamics of the observed storm (Skamarock et al., 2000). Both the observed and simulated storm evolve from a multicellular convective system to a supercellular system. Here, results after 1 hour of integration are discussed. These results reflect the multicellular stage of the storm when there are three updraft cores. Previous simulations indicate that 75% of the air parcels had a residence time between 500 and 1200 seconds traveling from 4 km m.s.l. to 500 meters below the air parcel's maximum attained height in the updraft (Skamarock et al., 2000), and that 74% of the air parcels had a residence time in contact with liquid water between 400 and 800 seconds (Barth et al., 2000). This short residence time in contact with liquid water may limit the influence the liquid water has on the chemical species (via aqueous chemistry, separation of soluble and insoluble species, or washout).

Corresponding author address: Mary C. Barth, NCAR, P.O. Box 3000, Boulder, CO 80307-3000. Email: barthm@ucar.edu

Table 1. Chemical reactions depicted in chemistry module.

		k_{298}	$\frac{E}{R}$
		Gas-Phase Reactions	
$O_3 + h\nu$	$\rightarrow$ 2 OH	3.41×10^{-6}	
$NO_2 + h\nu$	$\rightarrow NO + O_3$	3.65×10^{-3}	
$H_2O_2 + h\nu$	$\rightarrow 2OH$	2.19×10^{-6}	
$CH_2O + h\nu + 2O_2$	$\rightarrow 2HO_2 + CO$	7.84×10^{-6}	
$CH_2O + h\nu$	$\rightarrow H_2 + CO$	1.48×10^{-5}	
$CH_3OOH + h\nu + O_2$	$\rightarrow CH_2O + HO_2 + OH$	1.66×10^{-6}	
$HNO_3 + h\nu$	$\rightarrow NO_2 + OH$	1.25×10^{-7}	
$O_3 + NO$	$\rightarrow NO_2 + O_2$	1.8×10^{-14}	1400.
$O_3 + OH$	$\rightarrow HO_2 + O_2$	6.8×10^{-14}	940.
$O_3 + HO_2$	$\rightarrow OH + 2O_2$	2.0×10^{-15}	
$NO_2 + OH + M$	$\rightarrow HNO_3 + M$	$k_o=2.6\times10^{-30}(\frac{T}{300})^{-3.2}$ $k_\infty=2.4\times10^{-11}(\frac{T}{300})^{-1.3}$	
$H_2O_2 + OH$	$\rightarrow HO_2 + H_2O$	1.7×10^{-12}	160.
$HO_2 + HO_2$	$\rightarrow H_2O_2 + O_2$	2.9×10^{-12}	-590.
$HO_2 + OH$	$\rightarrow H_2O + O_2$	1.1×10^{-10}	-250.
$OH + OH$	$\rightarrow O_3 + H_2O$	1.9×10^{-12}	240.
$OH + OH + M$	$\rightarrow H_2O_2 + M$	$k_o=6.9\times10^{-31}(\frac{T}{300})^{-0.8}$ $k_\infty=1.5\times10^{-11}$	
$HO_2 + NO$	$\rightarrow NO_2 + OH$	8.6×10^{-12}	-250.
$HNO_3 + OH$	$\rightarrow 0.89NO_2 + 0.89O_3 + 0.11\ NO$	1.0×10^{-13}	-785.
$CH_4 + OH + O_2 + M$	$\rightarrow CH_3OO + H_2O + M$	6.3×10^{-15}	1800.
$CH_3OO + NO + O_2$	$\rightarrow CH_2O + HO_2 + NO_2$	7.7×10^{-12}	-180.
$CH_3OO + HO_2$	$\rightarrow CH_3OOH + O_2$	5.6×10^{-12}	-800.
$CH_3OO + CH_3OO$	$\rightarrow 1.4CH_2O + 0.8HO_2 + 0.6HCOOH$	4.7×10^{-13}	-190.
$CH_2O + OH + O_2$	$\rightarrow CO + H_2O + HO_2$	1.0×10^{-11}	
$CH_3OOH + OH$	$\rightarrow 0.7CH_3OO + 0.3CH_2O + 0.3\ OH + H_2O$	7.4×10^{-12}	-200.
$CO + OH + O_2$	$\rightarrow CO_2 + HO_2$	2.4×10^{-13}	
$HCOOH + OH + O_2$	$\rightarrow HO_2 + CO_2 + H_2O$	3.2×10^{-13}	
$SO_2 + OH + M$	$\rightarrow SO_4^=$	$k_o=3.0\times10^{-31}(\frac{T}{300})^{-3.3}$ $k_\infty=1.5\times10^{-12}$	
		Aqueous-Phase Reactions	
$O_3 + h\nu + H_2O$	$\rightarrow H_2O_2 + O_2$	4.26×10^{-6}	
$H_2O_2 + h\nu$	$\rightarrow 2OH$	2.73×10^{-6}	
$H_2O_2 + OH$	$\rightarrow HO_2 + H_2O$	2.7×10^{7}	1700.
$HO_2 + O_2^-$	$\rightarrow HO_2^- + O_2$	1.0×10^{8}	1500.
$OH + HO_2$	$\rightarrow H_2O + O_2$	1.0×10^{10}	1500.
$O_3 + O_2^- + H_2O$	$\rightarrow OH + 2O_2 + OH^-$	1.5×10^{9}	1500.
$CH_3OO + O_2^- + H_2O$	$\rightarrow CH_3OOH + OH^- + O_2$	5.0×10^{7}	1600.
$CH_3OOH + OH$	$\rightarrow CH_3OO + H_2O$	2.7×10^{7}	1700.
$CH_3OOH + OH$	$\rightarrow CH_2(OH)_2 + OH$	1.9×10^{7}	1900.
$CH_2(OH)_2 + OH + O_2$	$\rightarrow HCOOH + HO_2 + H_2O$	2.0×10^{9}	1510.
$HCOOH + OH + O_2$	$\rightarrow CO_2 + HO_2 + H_2O$	1.6×10^{8}	1510.
$HCOO^- + OH + O_2$	$\rightarrow CO_2 + HO_2 + OH^-$	2.5×10^{9}	1510.
$HSO_3^- + H_2O_2 + H^+$	$\rightarrow SO_4^= + 2H^+ + H_2O$	$\frac{4.0\times10^7[H^+]}{1.+13[H^+]}$	4800.
$HSO_3^- + O_3$	$\rightarrow SO_4^= + H^+ + H_2O$	3.7×10^{5}	5530.
$SO_3^= + O_3$	$\rightarrow SO_4^= + O_2$	1.5×10^{9}	5280.

Reaction rates are of the form $k = k_{298}\exp[-\frac{E}{R}(\frac{1}{T} - \frac{1}{298})]$ unless otherwise noted. Units for first order reactions are s^{-1}, second order gas reactions $cm^3\ s^{-1}$, and second order aqueous reactions $M^{-1}\ s^{-1}$.

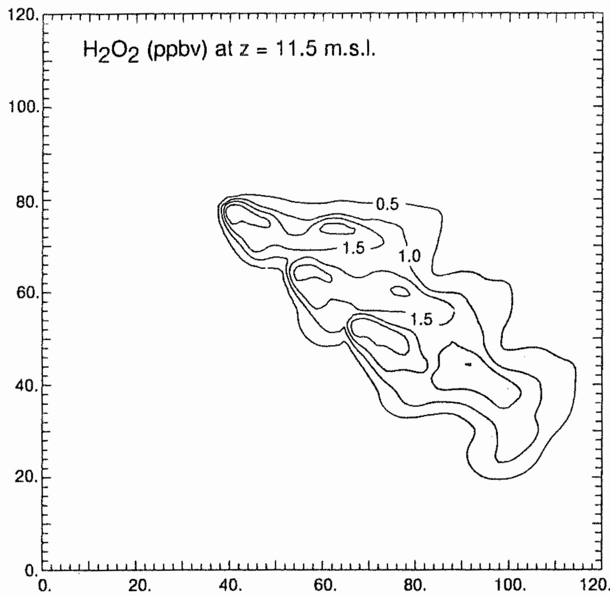

Figure 1. Passively transported H_2O_2 mixing ratio at z = 11.5 km m.s.l. and t = 3600 s.

The anvil, which had a northwest-southeast orientation, is composed primarily of snow and ice. Figure 1 shows a non-reactive H_2O_2 mixing ratio (i.e., the tracer is initialized with the H_2O_2 profile in Figure 2, but is merely transported during the simulation) at an altitude of 11.5 km (middle of the anvil). The multicellular nature of the storm is evident with mixing ratios of 2 ppbv reaching the anvil. The outflow region, marked in Figure 1 by the gray box, is analyzed to examine the effect aqueous chemistry and ice hydrometeors have on the peroxide species. Figures 2 and 3 show the average mixing ratio of H_2O_2 and CH_3OOH for the outflow region marked by the gray box in Figure 1. Besides the initial profile, results of 4 simulations are shown.

3.1 Transport

The transport-only simulation initializes all of the chemical species with their initial mixing ratios, but does not allow any chemistry or dissolution of the species. The species are only transported. Compared to the initial profile, H_2O_2 was transported from below 6 km m.s.l. to the region above 6 km m.s.l. and below 15 km m.s.l. CH_3OOH shows similar transport, except the region above 8 km m.s.l. and below 11 km m.s.l. where CH_3OOH is removed via transport.

3.2 Gas Chemistry

The gas chemistry only simulation transports the chemical species and calculates gas chemistry (no aqueous chemistry and no dissolution into liquid hydrometeors). Compared to the transport-only profile, H_2O_2 mixing ratios from the gas chemistry only simulation are generally higher above 6 km m.s.l., and are similar in value above 11 km m.s.l. CH_3OOH also shows this trend, indicating that the peroxy radicals, which produce the peroxides, are greater between 6 and 11 km m.s.l.

3.3 Aqueous Chemistry

The gas and aqueous chemistry simulation transports the chemical species, calculates gas and aqueous chemistry, but does not allow the ice to capture the dissolved chemical species. When riming occurs, it is assumed in this simulation that the dissolved chemical species degasses from the cloud water or rain. Compared to the gas-only profile, H_2O_2 mixing ratios from the gas and aqueous chemistry simulation are very similar. This is also the case for CH_3OOH. It is surprising that H_2O_2 does not show greater depletion due to aqueous chemistry, especially since SO_2 has mixing ratios of about 1 ppbv in the boundary layer. We could speculate that H_2O_2 is being produced in the aqueous phase (photolysis of O_3 and/or reaction of peroxy radical with superoxide), but SO_2 mixing ratios averaged in the area of the outflow of the storm are not depleted. Without a more detailed analysis, we can only assume that the short residence time in contact with liquid water (less than 800 seconds) is not sufficiently long enough to allow aqueous chemistry to proceed.

3.4 Microphysical Processes

The gas and aqueous chemistry with ice capturing tracers simulation transports the chemical species,

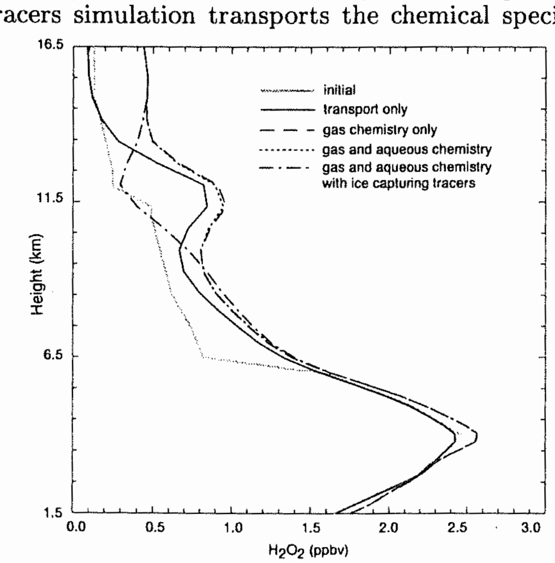

Figure 2. Average vertical profiles of total H_2O_2 mixing ratio for the passively transported, gas chemistry only, gas and aqueous chemistry with degassing when freezing occurs, and gas and aqueous chemistry with capture when freezing occurs at t = 3600 s in an area demarked by the gray box illustrated in Figure 1.

calculates gas and aqueous chemistry, and allows the ice to capture the dissolved chemical species. When riming occurs, it is assumed in this simulation that the frozen hydrometeor retains the chemical species and the chemical species moves with the frozen hydrometeor allowing it to precipitate. Compared to the gas and aqueous chemistry profile, H_2O_2 is substantially depleted in the outflow of the convection (10 to 14 km m.s.l.). CH_3OOH is also depleted, but not as much as H_2O_2. At z = 11.5 km m.s.l., H_2O_2 is depleted by 55-60% whereas CH_3OOH is depleted by 14%. These results are similar to those found by Barth et al (2000) for soluble tracers. Barth et al noted a 35% depletion for a tracer with a solubility similar to H_2O_2 and no depletion for a tracer with a solubility similar to CH_3OOH. Differences between these numbers may be due to this study allowing the solubility of the species to vary with temperature (solubility increases as temperature decreases) or may be due to the gas and aqueous chemistry that occur in this study.

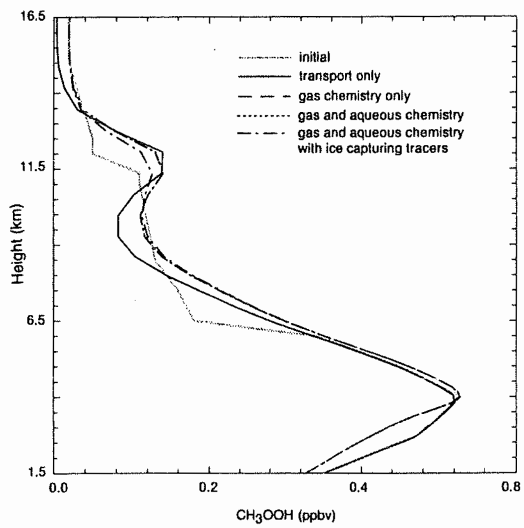

Figure 3. Same as Figure 2 except for CH_3OOH.

4. DISCUSSION

4.1 Scavenging Efficiency

Cohan et al (1999) determined the scavenging efficiency of soluble species from measurements of soluble and insoluble species obtained in the boundary layer, the convectively-influenced upper troposphere, and the upper troposphere unaffected by convection. They found that H_2O_2 has a scavenging efficiency of 55-70%. If we do the same calculation here for the simulation where gas and aqueous chemistry were predicted as well as transport and capture of the dissolved species by frozen hydrometeors, we find that H_2O_2 has a scavenging efficiency of 74% and CH_3OOH has a scavenging efficiency of 14%. These values can have quite a large uncertainty because both peroxides have a strong gradient in mixing ratio in the boundary layer.

4.2 Effect of the Cloud on Photolysis Rates

The influence of the storm upon photolysis rates has not yet been assessed, but we speculate that higher mixing ratios of H_2O_2 would be found in brighter regions of the storm (to the west and top) because hydroxyl and peroxy radicals would be enhanced in these regions.

5. ACKNOWLEDGMENTS

The National Center for Atmospheric Research is sponsored by the National Science Foundation. X.X. Tie is thanked for providing output for northeastern Colorado from the 3-d global chemistry transport model.

6. REFERENCES

Barth, M. C., A. L. Stuart, and W. C. Skamarock, 2000: The fate of soluble tracers in deep convection, in preparation.

Brasseur, G. P., D. A. Hauglustaine, S. Walters, P. J. Rasch, J.-F. Müller, C. Granier, and X. X. Tie, 1998: MOZART: A global chemical transport model for ozone and related chemical tracers, Part 1. Model Description, *J. Geophys. Res.*, **103**, 28,265-28,289.

Cohan, D. S., Schultz, M. G., Jacob, D. J., Heikes, B. G., and Blake, D. R., 1999: Convective injection and photochemical decay of peroxides in the tropical upper troposphere: methyl iodide as a tracer of marine convection, *J. Geophys. Res.*, **104**, 5717-5724.

Skamarock, W. C., J. Powers, M. C. Barth, J. E. Dye, T. Matejka, D. Bartels, K. Baumann, J. Stith, D. D. Parrish, and G. Hubler, 2000: Numerical simulations of the 10 July STERAO/Deep Convection Experiment convective system: Dynamics and transport, *J. Geophys. Res.*, accepted.

Tao, W.-K. and J. Simpson, 1993: Goddard cumulus ensemble model. Part I: Model description, TAO, **4**, 35-72.

Wicker, L. J. and W. C. Skamarock, 1998: A time splitting scheme for the elastic equations incorporating second-order Runge-Kutta time differencing, *Mon. Wea. Rev.*, , **126**, 1992–1999.

Wicker, L. J. and R. B. Wilhelmson, 1995: Simulation and analysis of tornado development and decay within a three-dimensional supercell thunderstorm, *J. Atmos. Sci.*, **52**, 2675-2703.

INSIGHTS INTO CLOUD PROCESSES FROM HIGHER RESOLUTION MEASUREMENTS OF CLOUD CHEMISTRY VARIATIONS BY DROP SIZE USING A NEW MULTI-STAGE CLOUD WATER COLLECTOR

Katharine F. Moore, Derek J. Straub, D. Eli Sherman, Jill E. Reilly, Jeffrey L. Collett, Jr.

Department of Atmospheric Science, Colorado State University, Fort Collins, CO 80523, U. S. A.

1. INTRODUCTION

Cloud drop chemistry is size-dependent which has important implications for atmospheric chemistry. Recent atmospheric models predict this size-dependence and are supported by experimental measurements at varying locations (examples include: Pandis et al. 1990; Lin and Chameides 1991; Ogren et al. 1992; Collet et al. 1993; Roelofs 1993; Bator and Collett 1997; Schell et al. 1997; Gurciullo and Pandis 1997; Collett et al. 1999). Drop chemistry depends upon a complex interaction of many factors including cloud dynamics and microphysics, atmospheric composition and competing gas and multi-phase reactions. Aqueous-phase processing is an essential transformation pathway for some important species, such as the oxidation of S(IV) to S(VI). Cloud processes impact these species' environmental fate by providing a reaction medium, serving as storage reservoirs for reactants, and affecting removal by deposition among other processes. While useful, bulk cloud water measurements do not capture important chemistry variations across the drop size spectrum. Size-resolved cloud water chemistry measurements help to provide the necessary information to more completely understand cloud processes and their impact on atmospheric chemistry.

2. THE NEW CSU 5-STAGE COLLECTOR

Recently a new active multi-stage cloud water collector was developed at Colorado State University (the CSU 5-Stage). As the name suggests, the CSU 5-Stage separates collected cloud water into five, independent fractions across the expected drop size spectrum. For a single collector, this represents an increase in available drop fractions from the two or three previously available (Collett et al. 1995; Demoz et al. 1996; Schell et al. 1997). The CSU 5-Stage's design is based upon the principles of cascade inertial impaction developed by Marple and co-workers (Marple 1970; Marple and Rubow 1986). As illustrated in the line drawing (Figure 1), the cloud drops are pumped into the first of five jet/impaction surface combinations (stages). Acceleration by the first jet causes the larger drops to be collected via inertial impaction on the downstream impaction surface as they cannot follow the flow streamlines. Moving through the "staircase-style" collector, the jets become progressively smaller, and the flow becomes faster. Increasingly smaller drops are thus collected. The design cut-size d_{p50}s for each stage are 30, 25, 15, 10 and 4 μm, respectively for Stage 1 ("V1") through Stage 5 ("V5"). A more thorough discussion of the CSU 5-Stage's design is given elsewhere (Moore et al. 1998).

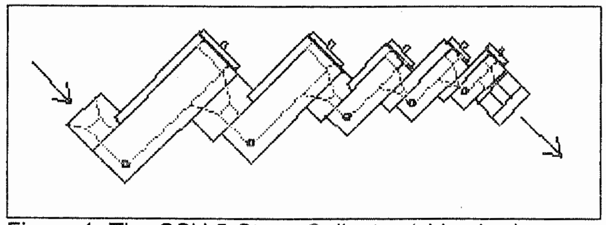

Figure 1: The CSU 5-Stage Collector (side view)

Calibration curves for the CSU 5-Stage were recently developed using both experimental laboratory and computational fluid dynamics modeling techniques (Straub and Collett 1999). They suggest that the overlap between the first two stages is greater than anticipated, but together their d_{p50} is approximately 25.5 μm. Stages 3, 4, and 5 are approximately as designed with d_{p50}s of 17.5, 10.5, and 4.5 μm, respectively. While useful, there are limitations to these calibration techniques. Therefore, the CSU 5-Stage's performance was also evaluated based upon field measurements.

3. FIELD PERFOMANCE VERIFICATION OF THE CSU 5-STAGE

3.1 Drop chemistry comparison between collectors

During July 1999 the CSU 5-Stage was operated as part of an integrated sampling campaign to measure orographic clouds upon the summit of Whiteface Mountain, NY. Over a period of approximately ten hours during the cloud event on July 17, five sets of samples were collected from the CSU 5-Stage as well as from a simultaneously operated single-stage Caltech Active Strand Cloudwater Collector version 2 (CASCC2) and a two-stage size-fractionating CASCC (sf-CASCC). The CASCC2 has a d_{p50} of 3.5 μm and the sf-CASCC has d_{p50}s of 23 μm ("large") and 4 μm ("small") (Demoz et al. 1996). Recent modeling work suggests the large sf-CASCC d_{p50} is closer to approximately 16 μm. Figure 2 compares ammonium concentrations between the three collectors for the measured (CASCC2) or derived

Corresponding author's address: Jeffrey L. Collett, Jr., Department of Atmospheric Science, Colorado State University, Fort Collins, CO 80523, U.S.A.;
E-Mail: collett@lamar.colostate.edu

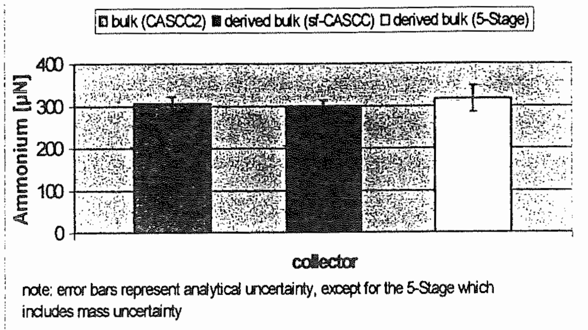

Figure 2: Comparison of bulk ammonium concentration by collector (Whiteface, 7/17/99, 6 - 7 am)

(sf-CASCC, CSU 5-Stage) "bulk" concentrations. The concentrations agree within two standard deviations suggesting that drop chemistry can be compared between the collectors. Although only ammonium is shown, these results are typical for all the major inorganic ions (NH_4^+, H^+, NO_3^-, $SO_4^=$) measured and for additional time periods.

3.2 Collected/measured water mass comparison

During the same July 17, 1999 event, the cloud liquid water content (LWC) was measured by a Gerber PVM-100 (Gerber Scientific, Inc., Reston, VA) and the cloud drop size distribution was measured by a PMS CSASP (PMS Inc., Boulder, CO). Figure 3 shows that as the measured cloud LWC increased during the event, the collected water volume in the samplers increased similarly. The CSASP's measured drop size distribution

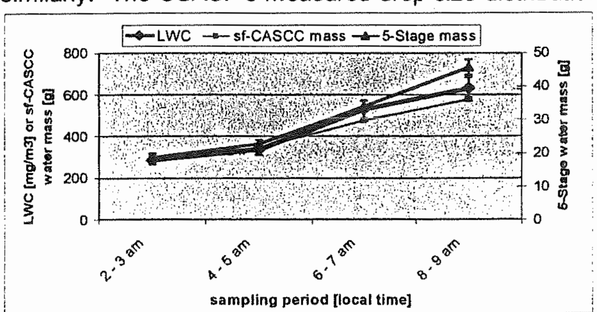

Figure 3: LWC compared to total water mass on the collectors (Whiteface, 7/17/99)

shifted towards larger drops during the same event. This shift is mirrored in the relative amounts of sampled water mass in the multi-stage collectors. As the event progressed, relatively more large drops were collected. Figure 4 shows the temporal evolution of the normalized collected water mass for the sf-CASCC and the CSU 5-Stage where the stages of the CSU 5-Stage have been grouped to match the cut-size between the two sf-CASCC fractions. Similar to the chemistry results in the preceding section, the sampled masses between the collectors agree to within approximately two standard deviations.

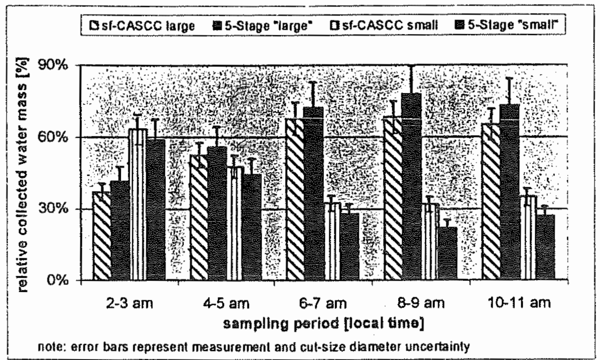

Figure 4: Temporal evolution of the normalized sf-CASCC and CSU 5-Stage sample volume distribution (Whiteface, 7/17/99)

4. INSIGHTS INTO SIZE-DEPENDENT DROP CHEMISTRY

The CSU 5-Stage has been operated in five field campaigns to date. Selected results from these campaigns illustrate the benefits of having its finer chemical resolution across the drop size range. In the figures that follow, please note that the CSU 5-Stage fractions are labeled sequentially "VI" (the largest stage/collected drop fraction) through "V5" (the smallest).

At Whiteface Mountain during July 1999, measurements from the sf-CASCC suggest that for the previously indicated major inorganic species, the chemistry is largely independent of drop size. Data from the CSU 5-Stage, however, suggests that there is size-dependence to the chemistry that was not previously discernible. For the representative example shown, the concentration variation measured by the CSU 5-Stage is up to 36% (Figure 5).

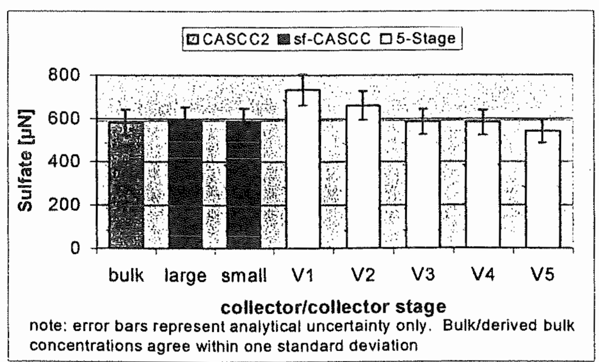

Figure 5: Sulfate concentration by collector/collector stage (Whiteface, 7/17/99, 6 – 7 am)

In Davis, CA during January 1999, the chemistry of urban-influenced radiation fogs was studied. Results from the sf-CASCC suggest that concentrations were generally enhanced in the small fraction for the same major inorganic species. This variation is up to a factor of ten in the representative ammonium example (Figure 6). The CSU 5-Stage captures this size-dependence and suggests that the actual variation may be on the order of twenty for its simultaneously collected sample.

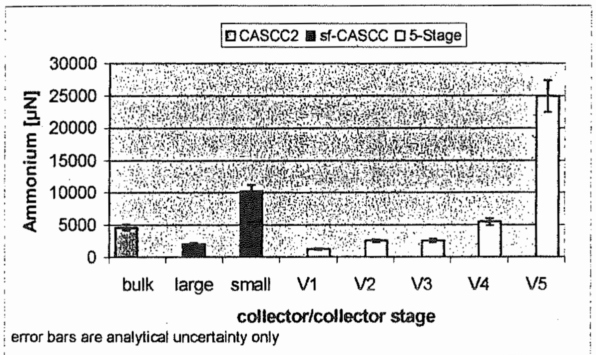

Figure 6: Ammonium concentration by collector/collector stage (Davis, 1/9/99, 7 – 9 am)

Data from the sf-CASCC has been used in earlier studies of San Joaquin Valley fogs to calculate the maximum potential aqueous-phase S(IV) to S(VI) oxidation rates (Hoag et al. 1999). At the relatively high pH of these fogs (approximately pH > 5), the non-linear O_3 and metal catalyzed auto-oxidation pathways can predominate. Hoag et al. (1999) suggested that using non-size-resolved cloud chemistry to calculate these rates can result in their significant underestimation by factors of 1.5 to 9. During January 1999 in Davis, CA drop pH measurements were in a similar range. For four sampled time periods, the maximum potential aqueous-phase S(IV) to S(VI) oxidation rates based upon the more finely resolved CSU 5-Stage chemistry range from 18 to 123% greater than those calculated based upon the mean drop chemistry. This is larger than the 8 to 81% increase predicted by calculations using the sf-CASCC data (Figure 7). Allowing for increased uncertainty in the CSU 5-Stage's pH measurements yields no worse than a 17% increase in the maximum potential oxidation rate. Recent work (Reilly et al. 2000) suggests drop mass transport limitations may be important in these calculations, and the maximum potential rate may not be achieved in actuality. However, it remains unclear how much this may impact calculations based upon the CSU 5-Stage's measured results.

One additional component of interest in the January 1999 Davis, CA fogs is aqueous-phase nitrite. Nitrite charge concentrations during some fog events were on the order of those for sulfate, making it one of the more important inorganic species measured. Interestingly the $NO_2^-{}_{(aq)}$ concentration pattern varies from those for the other major species with the large drops generally being relatively enhanced in concentration (Figure 8). Nitrite occult deposition rates likely vary from those for the major inorganic species due to the different drop size-dependence. As before, the finer resolution available using the CSU 5-Stage permits more accurate interpretation of the $NO_2^-{}_{(aq)}$ concentration as a function of time and size than previously possible. Preliminary results suggest the observed concentration differences between drops are a function of pH and that partitioning of HONO from the gas-phase may be responsible for nitrite's presence in the aqueous-phase.

5. ON-GOING WORK

A comparison of the physical and chemical measurements between the CSU 5-Stage and other cloud collectors and measurement devices continues for the January 1999 Davis, CA fog events. The additional information of actual drop size-dependent chemistry

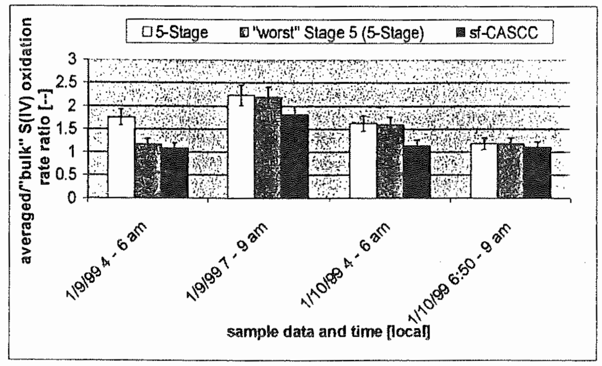

Figure 7: Relative enhancement of volume-averaged/"bulk" rates of in-cloud S(IV) oxidation by collector (Davis, 1/99)

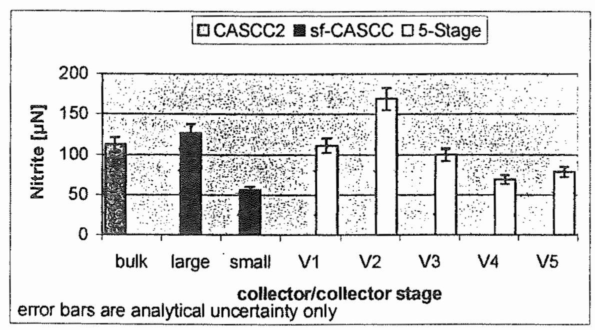

Figure 8: Nitrite concentration by collector/collector stage (Davis, 1/9/99, 7 – 9 am)

available from the CSU 5-Stage for the Whiteface and Davis campaigns continues to be evaluated. Of particular interest is how these new observational results may be interpreted in view of modeling studies (such as those by Pandis et al. 1990), and what that may suggest regarding the fog/cloud physical processes. In addition several case studies from the Davis, CA campaign use the CSU 5-Stage results, in addition to other concurrent measurements, to gain insight into the role fog processing has on local aerosol properties.

6. SUMMARY

The CSU 5-Stage cloud water collector separates cloud drops into more chemically distinct fractions than previously possible with a single collector. The CSU 5-

Stage measurements were compared to other co-located cloud water collectors and measurement devices in a field performance evaluation. The results suggest both that the CSU 5-Stage works largely as intended and that its results are consistent with the other cloud water collectors. Examples of the benefits of the CSU 5-Stage's enhanced resolution of drop size-dependent chemistry are shown. Its results suggest there is broader variation in species concentration than previously measureable. Continuing work will further evaluate the impact of these new observations to the understanding of cloud physical and chemical processes.

7. ACKNOWLEDGEMENTS

KFM is supported by the US Environmental Protection Agency Science to Achieve Results Graduate Fellowship U915364-01. Additional funding for this work was provided by the National Science Foundation under grants ATM-9509596 and ATM-9712603. Access to and assistance at the Whiteface Mountain and Davis, CA sites were provided by The Atmospheric Sciences Research Center, and UCDavis, respectively.

8. REFERENCES

Bator, A., and J. L. Collett, Jr., 1997: Cloud chemistry varies with drop size. *J. Geophys. Res.*, **102**, 28071-28078.

Collett, J. L. Jr., B. Oberholzer, and J. Staehelin, 1993: Cloud chemistry at Mt. Rigi, Switzerland: dependence on drop size and relationship to precipitation chemistry. *Atmos. Environ.*, **27A**, 33-42.

— , R. Iovinelli, and B. Demoz, 1995: A three-stage cloud impactor for size-resolved measurements of cloud drop chemistry. *Atmos Environ.*, **29**, 1145-1154.

— , K. J. Hoag, D. E. Sherman, L. W. Richards, 1999: Spatial and temporal variations in San Joaquin Valley fog chemistry. *Atmos Environ.*, **33** (1), 129-140.

Demoz, B., J. L. Collett, Jr., and B. C. Daube, Jr., 1996: On the Caltech Active Strand Cloudwater Collectors. *Atmos. Res.*, **41**, 47-62.

Gurciullo, C. S., and S. N. Pandis, 1997: Effect of composition variations in cloud droplet populations on aqueous-phase chemistry. *J. Geophys. Res.*, **102**, 9375-9385.

Hoag, K. J., J. L. Collett, Jr., and S. N. Pandis, 1999: The influence of drop size-dependent fog chemistry on aerosol processing. *Atmos. Environ.*, **33** (29), 4817-4832.

Lin, X., and W. L. Chameides, 1991: Model studies of the impact of chemical inhomogeneity on SO2 oxidation in warm stratiform clouds. *J. Atmos. Chem.*, **13**, 109-129.

Marple, V. A., 1970: A fundamental study of inertial impactors. Ph. D. thesis, University of Minnesota.

—, and K. L. Rubow, 1986: Theory and design guidelines. *Cascade Impactors: Sampling and Data Analysis*. J. P. Lodge, Jr. and T. L. Chan, Eds., American Industrial Hygiene Association, 79-101.

Moore, K., D. Straub, D. El Sherman and J. L. Collett, Jr., 1998: Development of a new five-stage active cloud water collector for size-resolved droplet sampling. American Meteorological Society, *Proceedings of the Conference on Cloud Physics*, Everett, WA, Amer. Meteor. Soc.

Ogren, J. A., K. J. Noone, A. Hallberg, J. Heintzenberg, D. Schell, A. Berner, I. Solly, C. Kruisz, G. Reischle, B. G. Arends, and W. Wobruck, 1992: Measurements of the size dependence of the concentration of non-volatile material in fog droplets. *Tellus*, **44B**, 570-580.

Pandis, S. N., J. H. Seinfeld, and C. Pilinis, 1990: Chemical composition deifferences in fog and cloud droplets of different sizes. *Atmos. Environ.*, **24A**, 7, 1957-1969.

Reilly, J. E., J. L. Collett, Jr., K. F. Moore, D. E. Sherman, C. Judd, M. Das, O. Rattigan, V. Dutkiewicz, and L. Husain, 2000: Field Investigations of the drop size-dependent rate of sulfate production in clouds and fogs. *This volume*.

Roelofs, G. J. H., 1993: A cloud chemistry sensitivity study and comparison of explicit and bulk cloud model performance. *Atmos. Environ.*, **27A**, 1957-1969.

Schell, D., W. Wobrock, R. Maser, M. Preiss, W. Jaeschke, H.-W. Georgii, M. W. Gallagher, K. N. Bower, K. M. Beswick, S. Pahl, M. C. Facchini, S. Fuzzi, A. Wiedensohler, H.-C. Hansson, and M. Wendisch, 1997: The size-dependent chemical composition of cloud droplets. *Atmos. Environ.*, **31**, 2561-2576.

Straub, D.J., and J. L. Collett, Jr., 1999: Numerical and Experimental Performance of Two Multi-Stage Cloud Collectors. *Colorado State University Department of Atmospheric Science Paper No. 676.*

ON ABILITIES OF NO3- IN SOLID PRECIPITATION PARTICIPATING IN LONG RANGE TRANSPORT (PART II)

T. Endoh[1], T. Takahashi[2], I. Noguchi[3], N. Tanaka[4],, S. Koga[5], and M. Wada[6],

[1],Institute of Low Temperature Science, Hokkaido University,
[2],Hokkaido University of Education, Sapporo,
[3],Hokkaido Institute of Environmental Science,
[4],Graduate School of Environmental Earth Science, Hokkaido University,
[5],National Institute for Resources and Environment and Resource Research
and
[6],National Institute of Polar Research

1. INTRODUCTION

It had been observed and marked that non-rimed snow crystals have preferentially higher concentration of NO_3^- ion than rimed snow crystals as reported by Takahashi etal. (1996). Such results are seen in coinciding to the results obtained in the laboratory experiments by Mitra etal. (1992) and Diehl etal. (1996). At that time, the component of NO_3^- in solid precipitation without frozen cloud droplets were considered to be taken by the atmospheric scavenging of an anthropogenic contamination of air in land breeze below cloud base. One of the reasons why they took place in these processes as their origin was thought that NO_3^- was brought in short range transport. To verify that, same kind of observation and sampling were carried out in a remote area, Moshiri where environmental atmosphere was extremely clean like in the polar region. The concentration of NO_3^- was however, not observed to be in the lower level expected but in the considerably greater values. Therefore, these results made us to consider about the abilities of NO_3^- in solid precipitation participating in long range transport like as SO_4^{2-} ion. To examine and verify these hypotheses, this study was carried out over the polar region i.e. one of the most remote area of the world.

2. METHODS

Solid precipitation particles were sampled with receiving directly as a natural snowfall with several clean-up containers in the center surrounded by a screening net wind-shelter avoiding not to be contaminated by drifting snow. Inside of the shelter, two instruments were installed i.e. a measuring system for snowfall rate with an electric balance and a recording system of snow particle shapes, sizes and species by a time lapse video microscopic camera. The environmental atmosphere was introduced from inlet pipes set in the outdoor and connected to an low volume air sampler and taken the aerosol particles and gaseous material by several stages of filter papers doped.

3. RESULTS

Solid precipitation particles were sampled in one of the most remote areas of the world, the arctic, Ny-Ålesund and analyzed chemically with some isotopic analyses. Environmental

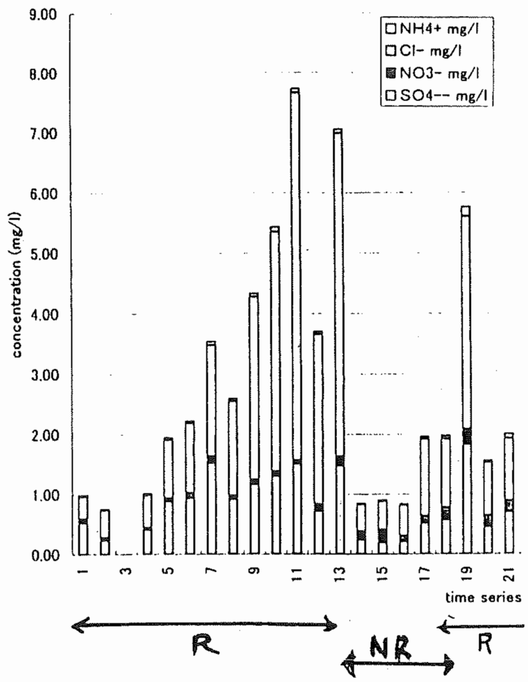

Fig.1 Temporal changes of chemical components in the solid precipitation in Ny-Ålsunde from December 1998 to January 1999. Lengths of solid columns and open ones below them are the concentration of NO_3^- and SO_4^{2-} ion respectively. R, NR: rimed and non-rimed snowfall duration.

atmosphere in the environmental atmosphere were also sampled by some doping filters with a system commercially called low volume air sampler and analyzed to the chemical components, species and concentration.

Over the whole duration of snow fall season, we have almost rimed snow crystals which had contained SO_4^{2-} ions predominantly as reported previously by Parungo etal. (1987). In very shorter period, non-rimed snow crystals were observed with north westerly which were thought to be brought by the air stream from sea ice covered ocean area where the supply of water vapor were not sufficient. Those samples of solid precipitation have been analyzed to contain much higher concentration of NO_3^- ions than the rimed snow crystals as shown in Fig. 1.

4. DISCUSSION

In the temporal changes of the concentration of relatively large aerosol particles shown in Fig.2, many abrupt changes were observed to have greater variations during the snowfall with inverse spikes forward the lower concentration. These may be considered clean air are pulled down and introduced at the surface by downdraft caused by snowfall corresponding to these negative spikes.

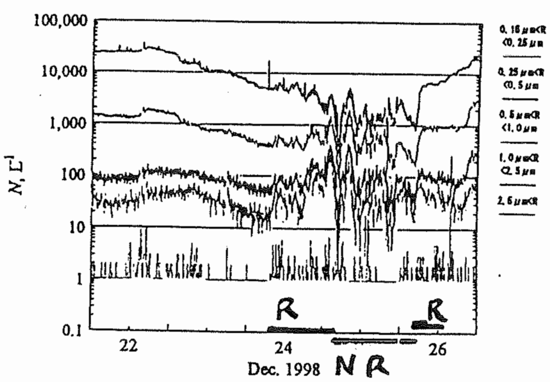

Fig. 2 Temporal change of size distribution of large aerosols measured by OPC . R ,NR: same as Fig.1

In the temporal changes of concentration of NO_3^- ions of gas vs. fine aerosols and fine vs. coarse aerosols of the environmental atmosphere shown in Figs.3 and 4 respectively during fall of non-rimed solid precipitation, noted depressions

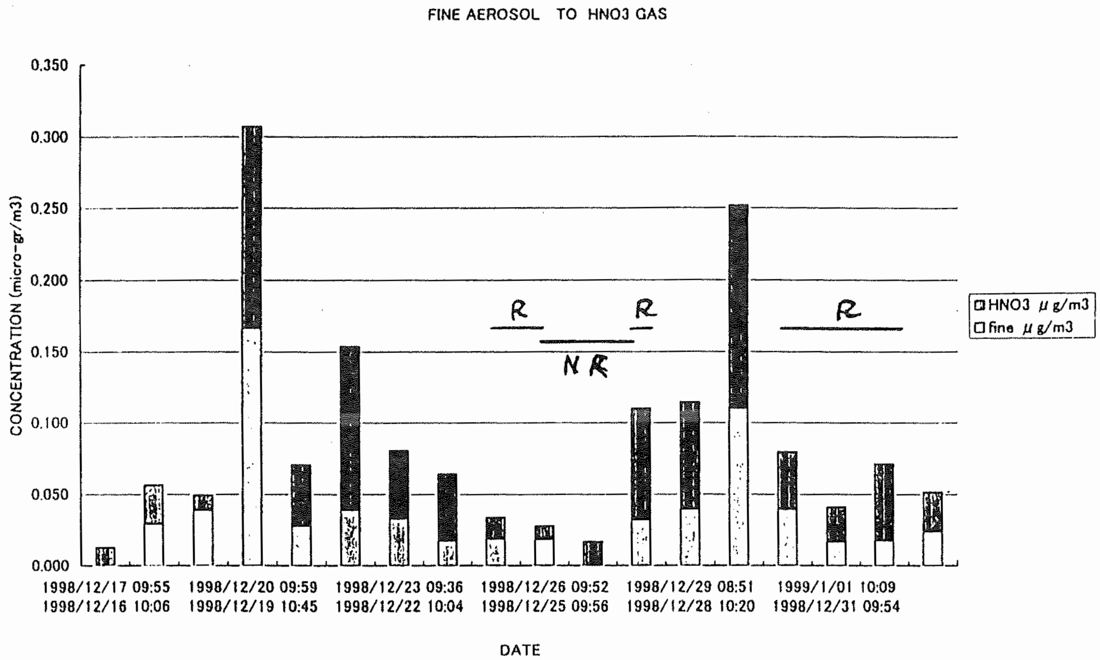

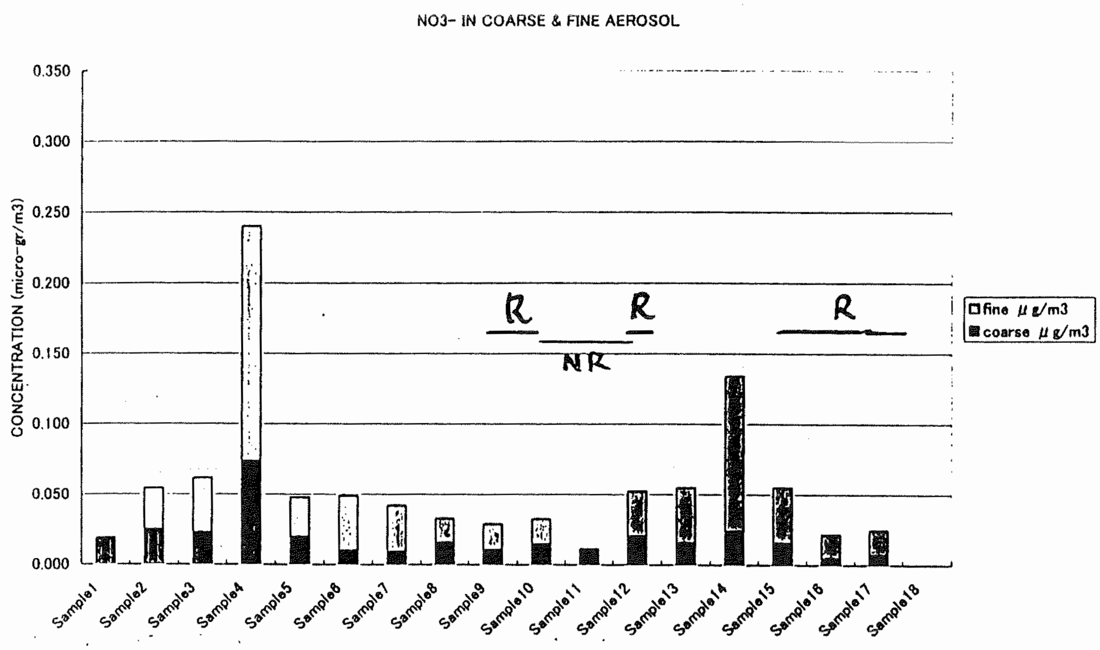

Fig. 3 (upper) Temporal changes of concentration of NO_3^- in gas and fine aerosols corresponding to solid and open columns. R,NR: same as Fig.1.

Fig. 4 (lower) Temporal changes of concentration of NO_3^- in fine and coarse aerosols corresponding to open and solid columns, respectively.

or losses were remarked in fine aerosol particles rather than those in HNO_3 gas coarse aerosols. Therefore, it may be considered that intake of NO_3^- to the interface of snow crystal particles take place more efficiently on some processes of fine aerosol scavenging mechanism than on those processes of physical absorption of gas or inertia coalescence of coarse aerosols.

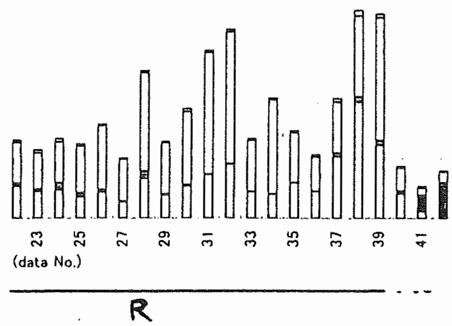

Fig. 5 Temporal change of chemical components in solid precipitation proceeding with Fig.1 with same axes and legend.

As shown in Fig. 5 which are followed as time series after the duration of Fig.1, on the way of a series of snowfall lasting for a long time, the concentration of NO_3^- in the precipitation were seen to decrease with the time lapse and arrive to the lowest value which is not detected ones till the end of the whole duration of the snowfall. These phenomena may be considered to suggest that the concentration of NO_3^- are decreasing in the atmosphere in the long range transport. These results made us to suspect that NO_3^- are consumed and lost along the migration in long range transport. On the other hand, NO_3^- in the environmental atmosphere were observed not to be in the lower values rather than that in the mid-latitude. These make us to uptake that NO_3^- in solid precipitation are considered in the worth of admiration in participating in the whole and casting in long lasting

5. CONCLUDING REMARKS

The remarked findings are summarized as followings.

- It may be recognized again and confirmed that rimed and non-rimed snow crystals have predominantly higher concentration of SO_4^{2-} and NO_3^-, respectively.
- In the period non-rimed snow crystals fall, noted depressions of NO_3^- were observed in temporal changes of fine aerosols among HNO_3 gas and coarse aerosols of the environmental atmpsphere.
- Therefore, it may be considered that some scavenging mechanisms are more predominantly efficient than those of gaseous absorption or coalescence of coarse aerosols for the intake mechanism of NO_3^- toward the ice interface.
- Concentration of NO_3^- in solid precipitation had been observed to decrease almost up to the value of the limit of detection within the time lapse in a long lasting snowfall.

References

Diehl K., Mitra S. K. and Pruppacher H. R., 1996: A laboratory investigation on uptake of SO_2, HNO_3 and HCl by 12th ICCP (Zurich), Proceedings of 12th ICCP(Zurich), 1047-1049.

Mitra S. K. , Diehl C. and Puruppacher H. R 1992: A laboratory study of the uptake of SO_2 and HNO_3 by snow crystals., 11th Intl. Conf. on Cloud and Precipitation, 851-854.

Parungo F., Nagamoto C. and Madel R., 1987: A study of the mechanisms of acid rain formation. J. Atmos. Sci. , 44, 3162-3174.

INVESTIGATION OF A WINTERTIME ACIDIC CLOUD EPISODE
IN THE NORTHERN COLORADO ROCKIES

Maria C. Meyer[1], Edward E. Hindman[1],
Stanley D. Gedzelman[1], and Teresa J. Bandosz[2]

[1]Earth and Atmospheric Sciences Department, [2]Chemistry Department
The City College of New York, New York City, NY 10031 USA

1. INTRODUCTION

Cloud physical and chemical measurements have been made at Storm Peak Laboratory (SPL) every winter since the winter of 1983/84 in an attempt to identify effects of air pollutants (Hindman, et al., 1994 and Hindman and Borys, 1998). SPL is located on the west summit of Mt. Werner near Steamboat Springs, Colorado at an elevation of 3210 m. At this elevation, the laboratory is frequently immersed in supercooled clouds during the winter. These clouds form when moist Pacific air masses rise upon encountering the Rocky Mountains. During the 1998 SPL expedition (10 - 24 January), observations were made, meteorological data were collected, and supercooled cloud droplets were captured and measured. Cloud water samples were tested for pH and anions. A 30-hour acidic episode was identified in an almost continuous, four-day, less acidic cloud event (Fig. 1). This paper will summarize the investigation of these cloud episodes.

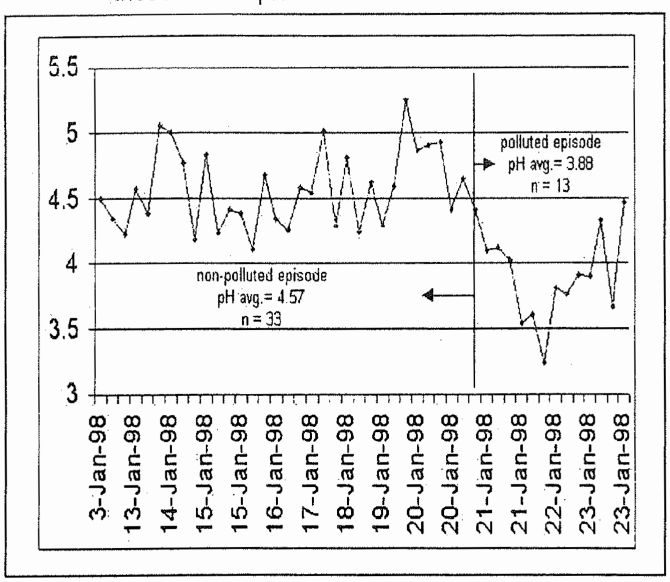

Figure 1: pH of cloud water identifying the less-acidic (non-polluted) and acidic (polluted) episodes.

Corresponding author address: Prof. Ward Hindman, Earth & Atmospheric Sciences, CCNY, Convent at 138th St., NYC, NY 10031 USA, hindman@sci.ccny.cuny.edu

2. METHODS

The measurements, collected every three hours during cloud events, included cloud droplet count, mean diameter of the droplets and liquid water content (using a Forward Scattering Spectrometer Probe), pH and conductivity of cloud water samples from a cloud sieve technique (Hindman, et al., 1992), condensation nucleus count and standard meteorological data. In the laboratory at CCNY, cloud water samples, returned frozen from SPL, were analyzed by liquid ion chromatography for chloride, nitrate and sulfate mass concentrations. The resulting physical and chemical properties of the acidic and less-acidic episodes are given in Table 1. It can be seen in the table, there was significantly more nitrate, chloride and droplets of smaller size in the acidic episode with similar liquid water contents, sulfate and CN in both episodes.

Table 1: Physical and chemical properties of the less-acidic and acidic episodes (+/- std. error)

Variable	Less-acidic	Acidic
Nitrate (mg/l)	1.7 (+/-) 0.16	3.73 (+/-) 0.52
Conductivity (umhos/cm)	19.37 (+/-) 1.54	34.21 (+/-) 3.85
Droplet count (cm ^-3)	74.7 (+/-) 9.22	131.03 (+/-) 17.16
Chloride (mg/l)	0.42 (+/-) 0.04	0.56 (+/-) 0.07
Droplet size (um)	13.11 (+/-) 0.53	9.44 (+/-) 0.54
Liquid water content (g/m^-3)	0.11 (+/-) 0.01	0.09 (+/-) 0.02
Measured pH	4.57 (+/-) 0.05	3.88 (+/-) 0.09
Sulfate (mg/l)	2.54 (+/-) 0.29	2.92 (+/-) 0.37
CN count (cm^-3)	709.96 (+/-) 107.02	800.49 (+/-) 203.43

The SPL cloud physical and chemical measurements were analyzed by building a multiple regression model to identify the variables which correlated best with variations in pH. Using the SPSS Forward Criterion Method, a method that allowed only variables with a 95% probability to enter the model, complete measurements from the historical SPL database were regressed. It was found that the most influential variables affecting changes in pH were, in order of importance, nitrate mass concentration, condensation nucleus count, and cloud droplet count. Further, to determine which anion was most influential in causing the pH variations, ionic mass concentration was stoichiometrically converted to molarity and regressed against pH. It was found that nitrate was the most important anion causing variations in cloud water pH sampled at SPL (Meyer, 2000).

Trajectories of air parcels arriving at SPL during the 1998 episodes were determined by accessing NOAA's HYSPLIT algorithm (Draxler and Hess, 1998) on the Internet. 48h horizontal back-trajectories were superimposed for the acidic episode and for the less-acidic background. Qualitative analysis revealed that the acidic episode's trajectories were primarily anticyclonic in curvature indicating the presence of a ridge of high pressure. In contrast, the less-acidic episode's trajectories varied between cyclonic and anticyclonic, suggesting a series of ridges and troughs indicating the presence of storms (Meyer and Hindman, 1999). The average pressure changes for the vertical components of the trajectories were calculated. It was found the air parcels rose, on average, only 43 mb during the acidic episode while the parcels rose 245 mb during the less-acidic episode consistent with the high pressure during the acidic episode and generally low pressure during the less-acidic episode.

The behavior of the air parcels during the last hour prior to arrival at SPL are illustrated in Figs. 2 and 3: the air parcels for the less-acidic episode were rising at both the 500 and 600 mb levels, conditions that would produce deep clouds and more precipitation; in contrast, air parcels for the acidic episode were rising at the 600 mb level but were sinking at the 500 mb level, conditions that would produce shallow clouds and less precipitation.

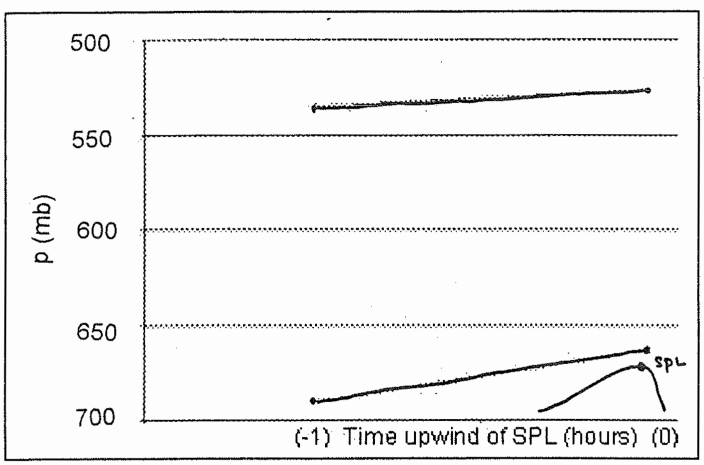

Figure 2: Average change in pressure of the air parcels for the less acidic event during the last hour prior to arrival at SPL.

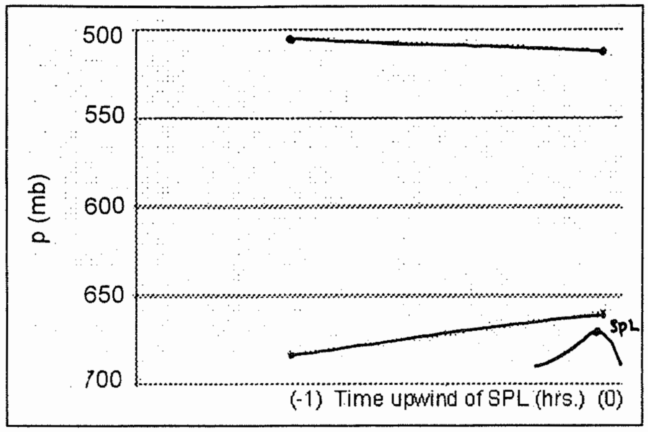

Figure 3: Average change in pressure of the air parcels for the more acidic event during the last hour prior to arrival at SPL.

The SPL snowfall measurements indicated substantially more precipitation during the less-acidic episode. Further, the results of trajectory analysis indicated the presence of predominantly low-pressure systems west of SPL associated with this episode. Thus, it was hypothesized that the air parcels arriving at SPL during the less-acidic episode were exposed to greater precipitation, hence resulting in "cleaner" clouds with higher measured pH of the cloud water samples.

To test this hypothesis, the period air parcels encountered precipitation on their way to SPL was determined. Hourly radar images from NOAA's NCDC web site were downloaded and superimposed on the corresponding backward horizontal trajectories, using the GIS program ArcView, for a select sample of trajectories representing the acidic and less acidic episodes. Figures 4 and 5 are sample radar images with superimposed trajectories during, respectively, the less-acidic and acidic episodes. Table 2 lists the amount of precipitation encountered by the air parcels on their way to SPL. It can be seen in the table, the parcels constituting the acidic episode experienced significantly less precipitation than the parcels during the less-acidic episode.

3. DISCUSSION

The cloud samples collected during the 1998 expedition to SPL revealed two distinct periods of higher and lower pH values. The two distinct periods were the most definite episodes found to date in the droplet physical and chemical data collected over the past 15 years at SPL. Hence, the episodes deserved further investigation.

It was found that nitrate was the dominant anion in the acidic episode (Table 1), a surprise since sulfate is, on average, the most

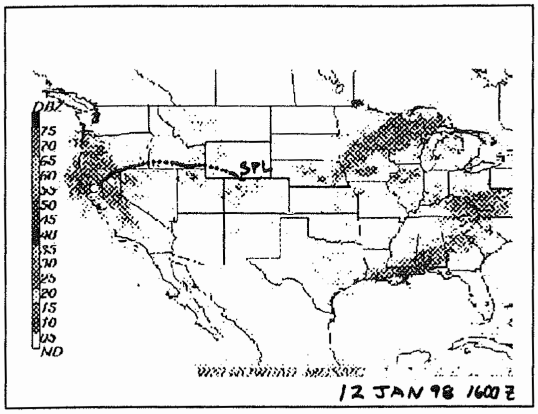

Figure 4: Sample radar image with superimposed backward horizontal trajectories for the less-acidic episode (The circled point indicates the position of the air parcel at the time of the radar images. This air parcel arrived at SPL on 14 January 1998 at 0200 MST).

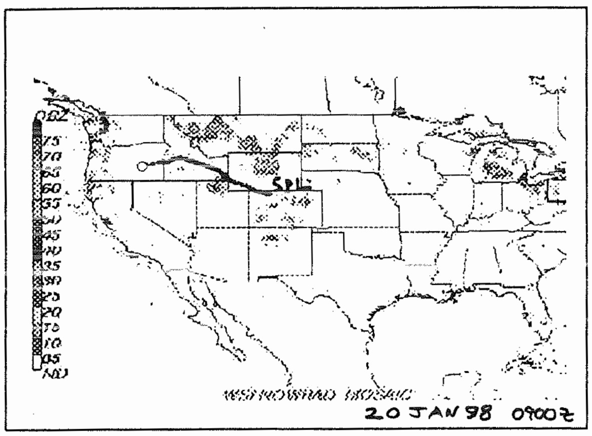

Figure 5: Sample radar image with superimposed backward horizontal trajectories for the acidic episode (The circled point indicates the position of the air parcel at the time of the radar image. This air parcel arrived at SPL on 22 January 1998 at 0200 MST).

Table 2: Comparison of total exposure time to precipitation between the less-acidic (non-polluted) and acidic (polluted) episodes.

Non-polluted sample events	Exposure time to precipitation	polluted sample events	Exposure time to precipitation
14 Jan 0200	51%	21 Jan 2000	10%
14 Jan 0800	26%	21 Jan 2300	10%
14 Jan 1100	28%	22 Jan 0200	0%
Averages	35%		7%

concentrated anion in the cloud water samples at SPL (Carter and Borys, 1993). This finding led to the multiple regression analyses of the SPL database. These analyses revealed the mass concentration of nitrate was the most important variable that related to variations in observed pH (Meyer, 2000). The importance of nitrate at SPL is not reflected in the eastern USA where sulfate is the dominant anion in cloud water samples. Sulfate was found to be the dominant anion in cloud water samples taken at Whiteface Mountain (Calvert, et al., 1985) and Leaitch, et al. (1996) also measured increased sulfate concentration in clouds over the North Atlantic. At Mount Mitchell, Saxena and Lin (1990) reported sulfate was the major anion influencing cloud chemistry.

The analyses of back-trajectories suggested meteorological conditions played an important role in defining the acidic and less-acidic episodes. The pronounced anticyclonic curvature, weakly rising air. presumably shallow clouds and low precipitation during the acidic event suggested that a high pressure system dominated the region upwind of SPL. The more cyclonic curvature, strongly rising air. presumably deep clouds and high precipitation during the less-acidic event suggested that a low pressure systems dominated the region upwind of SPL.

Analyses of the superimposed radar and trajectory images revealed the air parcels 48 hour journey to SPL during the acidic episode did, indeed, encounter less precipitation that those of the less-acidic episode: on average, three hours for the acidic episode and 15 hours for the less-acidic episode, or 7% of the time for the acidic episode and 35% of the time for the less-acidic episode (Table 2).

The air parcels during the acidic event encountered less cleansing on the way to SPL and vice versa for the less-acidic episode. This finding is consistent with a study at Whiteface Mountain that suggested cleansing due to thunderstorms: a tenfold increase in cloud water acidity was associated with dry air spells, or lack of precipitation events due to high pressure (Falconer and Falconer, 1980). These results imply higher pH values in cloud water at Whiteface occur when there is precipitation in the vicinity and vice versa.

4. CONCLUSIONS

An acidic cloud episode, containing large droplet number-concentrations and small droplet sizes and a less-acidic cloud episode, containing smaller droplet number-concentrations and larger droplet sizes (both episodes had similar liquid water contents) were detected during CCNY's January 1998 expedition to SPL. The episodes were explained by differences in atmospheric conditions upwind of SPL (assuming the upwind gas and particulate emissions were constant). An analysis of the trajectories of the air parcels arriving at SPL during the acidic episode revealed the parcels followed a anticyclonic path, the parcels were associated with weakly rising air, presumably shallow clouds and encountered few precipitation events; in fact, the air parcel with the lowest measured pH missed all precipitation events on its way to SPL. An analysis of the trajectories of the air parcels arriving at SPL during the less-acidic episode revealed the parcels followed a generally cyclonic path, the parcels were associated with strongly rising air, presumably deep clouds and encountered many precipitation events.

Variations in cloud water nitrate correlated best with variations in cloud water pH in spite of the fact that sulfate has been the dominant anion in SPL wintertime cloud water samples. A more detailed study, beyond the scope of the investigation reported here, will be required to explain this potentially important finding.

5. ACKNOWLEDGEMENTS

Thanks go to the members of the CCNY 1998 student-expedition SPL: John DiMartino, Jeff Gross and Joanne Roque. Thanks go to Steamboat Ski Corporation for mountain transportation and ski logistics and the Ramada Vacation Suites for providing first class accommodations. Dear thanks to Dr. Neal Phillip and the entire CCNY Environmental Engineering Lab, the CCNY EAS Department and the SPARS Lab at Hunter College. Support for this research was received from the New York City Alliance for Minority Participation in Science, Mathematics, Engineering, and Technology directed by Dr. N. Parker, and from PSC-CUNY Research Award 69229-00-29, Prof. E. Hindman, PI.

6. REFERENCES

Calvert, J. G., A. Lazrus, G. L. Kok, B. G. Heikes, J. G. Walega, J. Lind, C. A. Cantrell , 1985: Chemical mechanisms of acid generation in the troposphere. *Nature*, **317**, 27-35.

Carter, E. C., and R. D. Borys, 1993: Aerosol-cloud chemical fractionation: Enrichment factor analysis of cloud water. *J. Atmos. Chem.*, **17**, 277-202.

Draxler, R. R. and G. D. Hess, 1998: Description of the HY-SPLIT 4 modeling system. NOAA Technical Memo ERL ARL-224, Air Resource Laboratory, Silver Spring, MD U.S.A. (URL is http://www.arl.noaa.gov/hysplit.html)

Falconer, R. E. and P. D. Falconer, 1980: Determination of cloud water acidity at a mountain observatory in the Adirondack Mountains of New York State. *J. Geophysical Research*, **85**, 7465-7470.

Hindman, E. E., R. D. Borys, E. J. Carter, D. L. Mitchell, 1992: Collecting supercooled cloud droplets as a function of droplet size. *J. Atmos. Ocean Tech.*, **9**, 337-353.

Hindman, E. E., M. A. Campbell, R. D. Borys, 1994: A ten-winter record of cloud droplet physical and chemical properties at a mountaintop site in Colorado. *J. Appl. Meteor.*, **33**, 797-807.

Hindman, E. E. and R. D. Borys, 1998: Long-term cloud droplet measurements for climate-change studies. *World Resource Rev.*. **10**, 569-576.

Leaitch, W. R., C. M. Banic, G. A. Isaac, M. D. Couture, P. S. K. Liu, I. Gultepe, S. M. Li, L. Kleinman, P. H. Daum, J. I. MacPherson, 1996: Physical and chemical observations in marine stratus during the 1993 North Atlantic regional experiment: Factors controlling cloud droplet number concentrations. *J. Geophys. Res.,* **101**, 29,123-29,135.

Meyer, M. C. and E. E. Hindman, 1999: Pollution episode in a winter mountain cloud? In "*Ppts. Symposium on Interdisciplinary Issues in Atmos. Chem.*," Amer. Meteor. Soc., Boston, 113-116.

Meyer, M. C., 2000: Towards an Understanding of an Acidic Episode in the Northern Colorado Rockies, M. A. Thesis, CCNY, 91 pp.

Saxena, V. K. and N. H. Lin, 1990: Cloud chemistry measurement and estimates of acidic deposition on an above cloudbase coniferous forest. *Atmos. Environ.,* **24A**, 329-352.

A Detailed Resolved Cloud Physics/Chemistry Model for the Models-3/CMAQ

Qingyuan Song[1], Shawn Roselle[2], Jason Ching[2], Jonathan Pleim[2], Robin Dennis[2], Daewon Byun[2], Jeff Young[2], Kenneth Shere[2], Jerry Gipson[3], James Godowitch[2]

1. UCAR/EPA Scientific Visitor
2. ASMD, Air Resources Laboratory, NOAA
3. NERL, U.S. Environment Protection Agency

1. Introduction

Studies of atmospheric aerosol have received much attention because of their implication to climate change and public health. It has long been speculated that aerosols might impact climate by direct and indirect radiative forcings. Also, growing evidence has revealed that atmospheric aerosols, especially fine particulate matter (those less than 2.5 microns, e.g. $PM_{2.5}$), might be a great detriment and risk to human health. A National Ambient Air Quality Standard (NAAQS) for $PM_{2.5}$ has been promulgated by the U.S. Environmental Protection Agency (US EPA). With high costs associated with attaining these revised NAAQS, it is critical that a model with credible chemistry and physics packages is available to develop and assess emissions control plans so as to assure the effectiveness of control strategies and to optimize the cost of controls to meet the national objectives. Models-3/CMAQ, developed at US EPA, has been considered as a tool for such tasks (Byun and Ching, 1999).

Aqueous chemistry in cloud and rain, coupled with aerosol and gas-phase chemistry, is known to play an important and critical role in regional to urban scale air quality modeling. Clouds and precipitation can act as both sinks and sources of atmospheric aerosol. In-cloud oxidation of S(IV) by H_2O_2 and O_3 is the most efficient pathway for the conversion of SO_2 to sulfate. When cloud droplets evaporate, non-volatile chemicals can be released into air as particulate matter. On the other hand, when rain or snow precipitates to the ground, it functions as a terminal sink of atmospheric aerosols, including pre-existing CCN and scavenged below-cloud aerosols.

2. Purpose

The description of cloud physics and chemistry, especially convective clouds, are usually crude and highly simplified in air pollution models, because they are mostly sub-grid phenomena. In Models-3/CMAQ, an existing resolvable-scale cloud aqueous chemistry package was originally designed for sub-grid convective cloud chemistry simulations in large and regional air pollution cases (Walcek and Taylor, 1986). However, it is now also used in small urban scale cases. In the sub-grid scheme, there is no partitioning between cloud and rainwater, therefore, aqueous chemistry in clouds and rain, is combined into a single bulk-water calculation. An artificial cloud lifetime is set equal to the model advection time interval (i.e., the synchronization time-step, or SYN-T of CMAQ). Cloud physics and chemistry such as nucleation of CCN, oxidation of S(IV), and acid deposition are simulated during this artificial cloud lifetime. However, clouds are assumed to totally evaporate, and all chemicals in cloud water are released back into atmosphere at the end of each SYN-T. In regional or mesoscale air pollution simulations, the SYN-T and the cloud life-time of sub-grid clouds is about one hour that is somehow similar to a typical convective cloud lifetime. However, when CMAQ is used in urban scale air quality studies, i.e., 4-12 km resolution, an explicit, fully coupled aqueous chemistry model in Models-3/CMAQ becomes necessary since the SYN-T in such scales is considerably smaller than one hour. Therefore, the constraint of cloud lifetime to the SYN-T of CMAQ should be removed. We have developed a detailed cloud physics and chemistry algorithm for refinement of the formulation of cloud processor of CMAQ.

Corresponding author's current address:
Qingyuan Song, Ford Motor Company,
SRL Building, MD #3083, P.O. Box 2053,
Dearborn, MI, 48121; Email: qsong1@ford.com

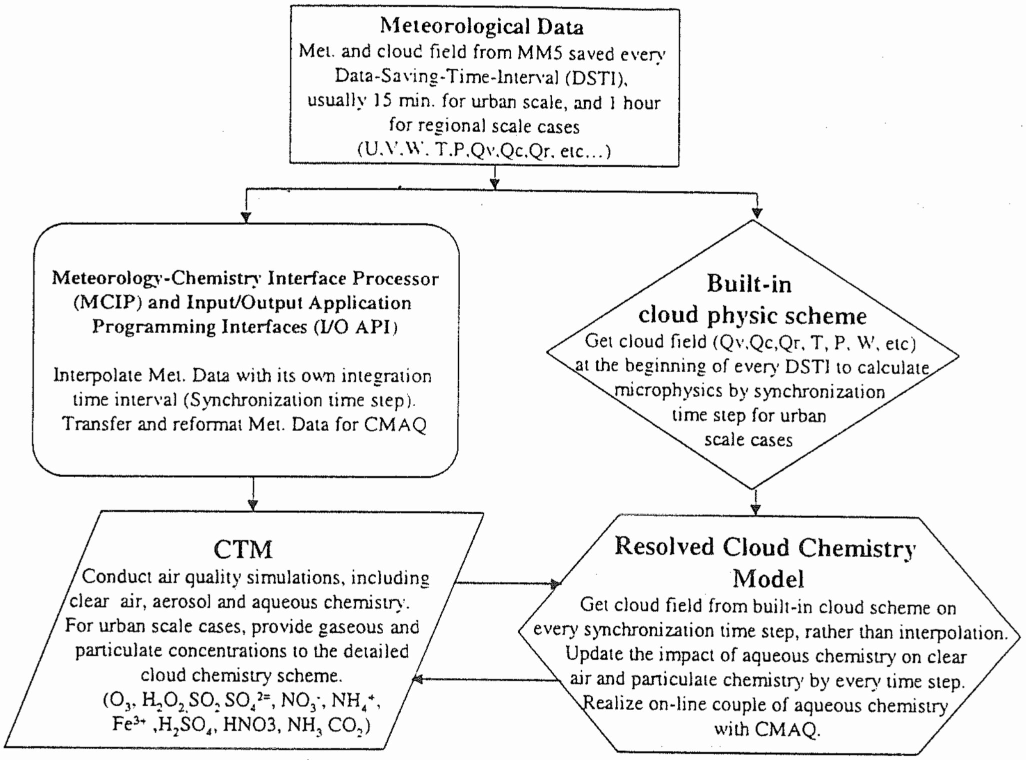

Fig.1 CMAQ system with the detailed cloud physics/chemistry model

3. Model description

This package is composed of two parts, a built-in cloud microphysics scheme and a cloud chemistry scheme. The meteorological input data of CMAQ (met. data), including cloud fields, are provided by the Mesoscale Meteorological Model version 5 (MM5). As shown in Fig. 1, these meteorological data are stored every Data-Saving-Time-Interval (DSTI). Due to the limitation of disk space, DSTI is much larger than real integration time-step of MM5 and CMAQ, which is usually 15 minutes for urban scale simulations and one hour for regional scale simulations. In CMAQ, met. data are interpolated linearly by the Meteorology-Chemistry Interface Process (MCIP) to the integration time-step (synchronization time-step) to drive the Chemical Transport Model (CTM).

3.1. Cloud microphysics scheme

Cloud chemistry is closely integrated with in-cloud microphysics. To describe in-cloud chemistry in a resolved way, cloud parameters such as air pressure (P), temperature (T), water vapor mixing ration (Qv), cloud water content (Qc), and rain water content (Qr) must be available. Aqueous chemicals are transferred between different hydrometeors by in-cloud microphysical processes, therefore the rates for microphysics processes such as auto-conversion, accretion and evaporation etc. are also needed. These processes are essential in the calculations of the mass budgets of species, chemical transport and pH value of cloud and rain water.

There are several resolved cloud physics schemes in MM5 that describe the microphysics needed by cloud/rain chemistry simulations (e.g. Hsie and Anthes, 1984; Reisner et al, 1998, etc). Ideally, CTM gets cloud fields directly from MM5 to simulate aqueous chemistry every time-step. In-cloud physics and associated chemistry are sensitive to thermal dynamics, hence they are highly variable and nonlinear. Cloud features such as Qc, Qr etc. can change significantly during one DSTI. The previous linear interpolation of CMAQ causes the loss of information of cloud microphysics such as auto-conversion, accretion, evaporation etc., and ultimately mass conservation problems.

An in-cloud microphysics scheme is implemented in CMAQ to minimize the inaccuracies and inconsistencies that result from interpolation. During each DSTI, cloud microphysics and hydrometeor budget, i.e., Qv, Qc, Qr are calculated independently in CMAQ based on the met. field at the beginning of a DSTI. Cloud fields for the built-in scheme are always updated by the MM5 output at the beginning of each DSTI. The scheme is based on warm cloud microphysics algorithm of Hsie and Anthes (1984) and Song et al (1998).

3.2 Cloud chemistry scheme

Chemical species in the new scheme are identical to the previous RAMD aqueous package. The detailed aqueous chemistry/physics mechanisms are based on the McGill Cloud Chemistry Model (MCCM) (Tremblay and Leighton, 1986; Song and Leighton, 1998).

The chemical species in the resolved cloud chemistry scheme of CMAQ are sulphur dioxide (SO_2), sulphuric acid (H_2SO4), nitric acid (HNO_3), ammonia (NH_3), ozone (O_3) and carbon dioxide (CO_2), and atmospheric aerosols such as NH_4^+, $SO_4^=$, NO_3^+, Fe^{3+}. Soluble gases such as SO_2, H_2O_2, CO_2 dissolve in cloud and rain water, and an equilibrium state between the aqueous and gaseous pollutants is established according to Henry's Law, while extremely soluble gases such as NH_3, H_2O_2 and HNO_3 are assumed to be totally dissolved into cloud water. Aerosols included in the scheme are hygroscopic, so all the PM at the accumulation mode are considered as CCN, and dissolve in the cloud water by nucleation at cloud base. After the dissolution and nucleation processes, aqueous chemical contents are carried along as the water substance is transformed from one category of hydrometeor to another with various microphysics processes. Pollutants are washed out by precipitation through both in-cloud and below-cloud scavenging. When the cloud or rain water evaporates, the non-volatile chemicals are released into atmosphere as new aerosol particles. These chemistry processes and associated cloud microphysics can be only described in such a detailed scheme.

4. Preliminary results

In this section, the time evolutions of the concentrations of HNO_3 and O_3 in different hydrometeors are depicted to demonstrate the transfer of chemicals with phase changes. A simple idealized cloud case is simulated with the same initial conditions as Song et al (1998). The cloud dynamic model requires as input the initial temperature and humidity profiles, the vertical profile of the horizontal wind and the surface pressure. These fields are assumed to be horizontally uniform over the domain of integration at the beginning. A convective system is initialized by a temperature impulse of 10 km x 10 km x 2 km along the x, y and z directions, within which the temperature increases from the ambient temperature T_0 to T_0 + 2°C at the center of the impulse by a Gaussian function. The domain size is set as 40km x 40km in the horizontal with a resolution of 1km, and 20km in the vertical with a resolution of 500m. The cloud lasts about one and a half hours. The cloud top reaches to around 10km at 30 min..

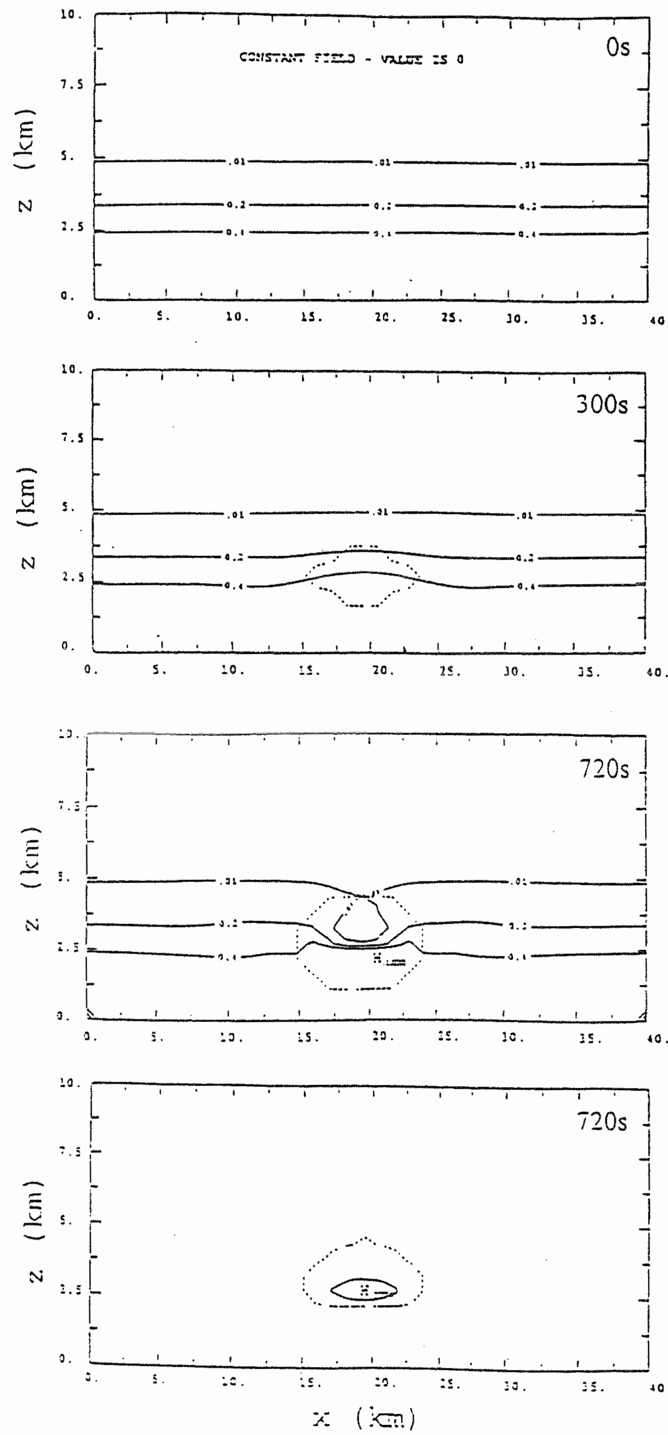

Fig. 2. HNO_3 Concentrations (ppb) in air and cloud at (a) 0s, (b) 300s, and (c) 720s; (d) HNO_3 in rain at 720s

The transfer processes for HNO_3 is shown in Fig. 2. All xz sections presented here are located at y = 20 km, which is roughly the center of the domain in the y direction. The dotted line identifies the cloud boundary taken as the 0.01 gm^{-3} contour. The time evolution of vertical sections of HNO_3 concentration at 0s, 720s, 1000s in air and cloud are depicted in Fig.2 a, b and c, where we can see the initial HNO_3 concentration has a constant value of 0.4 ppb below 2.5 km and decreases gradually to zero at 5 km. HNO_3 vapor is totally dissolved if there exists cloud water in a grid box. The interstitial concentration of HNO_3 is zero. Therefore, the concentration outside the cloud boundary is the gas phase HNO_3, while the concentration within cloud boundary represents cloud-dissolved HNO_3. As shown in Fig.2b, HNO_3 is advected and diffused upward mainly within the cloud volume with vertical convection during the early stage. However, after 720 s, with the formation of rain, the transfer of HNO_3 into precipitation and the scavenging by precipitation become significant. This is illustrated by the descent of the 0.2 ppb isopleth in Fig. 2c. In Fig 2d, the HNO_3 concentration in rain at 720 s, we can clearly see that the loss of HNO_3 from cloud (Fig. 2c) has been transferred to rain. The dotted lines in Fig. 2b,c identify cloud boundary. The one in Fig. 2d identifies the 0.1 g/kg mixing ratio of rain.

5. Summary

A resolved cloud physics/chemistry model is currently being incorporated into Models-3/CMAQ to simulate the impacts of cloud on aerosol and gaseous chemistry in urban scales. A cloud microphysics package is built in the CMAQ to simulate cloud processes so as to remove the crudeness of the linear interpolation adopted in previous approach. The aqueous chemistry is fully coupled with gaseous and particulate chemistry. The chemical species in the model include SO_2, H_2SO4, HNO_3, NH_3, O_3 and CO_2, and particulate species such as NH_4^+, $SO_4^=$, NO_3^+, Fe^{3+}.

An idealized cloud case has been used to test the resolved cloud chemistry model. The results demonstrate that the model is able to simulate the oxidation of S(IV) and the chemical transfer associated with cloud microphysics processes. The latter process can only be described in such a resolved scheme.

This new scheme also lays the groundwork for on-line coupling of cloud and aerosol physics and chemistry for future work.

6. Reference:

Byun, D.W. and J.K.S. Ching, 1999, Science Algorithms of the EPA Models-3 Community Multiscale Air Quality (CMAQ) Modeling System.

Hsie, E.-Y. and R. A. Anthes, 1984: Simulations of frontogenesis in a moist atmosphere using alternative parameterizations of condensation and precipitation. J. Atmos. Sci., 41, 2701-2716.

Reisner, J., R.J. Rasmussen, and R.T. Bruintjes, 1998: Explicit forecasting of supercooled liquid water in winer storms using the MM5 mesoscale model. Quart. J. Roy. Meteor. Soc., 124B, 1071-1107.

Song, Q., and H.G. Leighton, 1998: A parameterization of heterogeneous sulphate production for use in large scale models. J. Atmos. Rea., Vol. 47-48, June 1998, 555-572.

Song, Q., F. Kong and H.G. Leighton, 1998: A numerical simulation of the north-eastern Colorado hail storm of 24 June 1992. WMP Report 29, WMO/TD-No. 901, 55-60.

Tremblay, A. and H. Leighton, 1986: A three-dimensional cloud chemistry model. J. Clim. Appl. Meteorol., 25, 652-671.

Walcek, C, and G. Taylor, 1986: A theoretical method for computing vertical distributions of acidity and sulfate production within cumulus clouds. J. Atmos. Sci., vol. 43, No. 4, 339-355.

NUMERICAL STUDY OF SEVERAL IMPACTS OF CLOUD ON TROPOSPHERIC OZONE

Hui XIAO[1], Bin ZHU[2,1], Meiyuan HUANG[1], and Zihua LI[2]

[1] LAPC, Institute of Atmospheric Physics, Chinese Academy of Sciences, Beijing 100029, China

[2] Nanjing Institute of Meteorology, Nanjing 210044, China

1. INTRODUCTION

Ozone (O_3) is the key one of the chemical components in the troposphere and serves as both the product and participant of photochemical reaction therein. The change and distribution of ozone exert immediate effects on the lifetime and distribution of other species, e.g., SO_x, NO_x and OH radical, thereby influencing the composition and equilibrium of tropospheric chemistry (*cf.* Bojkov, 1988). Numerous observations have shown that substantial impact of cloud on the ozone concentration in the troposphere (e.g. Xiao *et al.*, 1993; Zhou *et al.*, 1993; Luo and Zhou, 1994) can be separated into three components: 1) cloud weakening or reflecting solar radiation flux that is responsible for the reduction or reinforcement of photochemical reaction, thereby changing O_3 concentration, which is called cloud effect on radiation (referred to this effect as factor A thereafter); 2) direct absorption (wet scavenging) of ozone and its precursors (*e.g.*, NO_x, *NMHC*) and free radicals (e.g. HO_x) by in-cloud liquid water, which is called cloud absorption effect (factor B); 3) steady reduction of ozone and its precursors in cloud liquid water due to aqueous phase chemical reaction, thus responsible for the change in gaseous-phase O_3 concentration, which will be referred to as in-cloud liquid phase chemical effect (factor C). Certainly, clouds also play an important role in transport of atmospheric pollutants.

Many efforts have been made at simulation of cloud impact on ozone (Chang *et al.*, 1987; Lelieveld *et al.* 1990; Carmichael *et al.*, 1991; He and Huang, 1996), but very little is known of quantitative research of the contribution of each of the above three factors to the ozone concentration, especially the roles of factors B and C in the concentration in all parts of cloud. This paper attempts to make quantitative research on the problem in terms of an elaborate coupled gaseous- and aqueous-phase chemistry model and to reveal the respective role of each of the three factors (A, B, C).

2. BRIEF DESCRIPTION OF THE MODEL

2.1 Chemistry Model

Corresponding author's address: Hui XIAO, Institute of Atmospheric Physics, Chinese Academy of Sciences, Beijing 100029, China; E-mail: hxiao@mail.iap.ac.cn

The effects of the three factors on ozone are investigated by the cloud chemistry box model developed, consisting of gaseous- and aqueous-phase chemical reactions with the inclusion of physical processes, *e.g.*, inter-phase transfer of species. The box model is formulated on the basis of the STEM-II model that is a famous three dimensional model of Eulerian transport and chemical reactions of atmospheric pollutants, developed by Professor Carmichael and his research group at the University of Iowa, USA (Carmichael et al., 1986, 1991).

2.2 Parameterization of Cloud Effect on Solar Radiation

The effects of cloud physical parameters on photolysis rates are parameterized as shown in the following (similar to Chang *et al.*, 1987).

$$j = j_{clear}[1+\alpha(F_{cld}-1)], \quad (1)$$

where j_{clear} is the photolysis rate in clear sky, α stands for cloud coverage and F_{cld} for the ratio of cloudy- to clear-sky photolysis coefficients and, with sun's zenith angle $\chi_0 \leq 60^0$ it has a range of forms, as shown below.

$$F_{cld} = 1+\alpha_i(1-t_r)\cos\chi_0 \quad \text{above the top of cloud (2a)}$$

$$F_{cld} = 1.4\cos\chi_0 \quad \text{upper part of the cloud (2b)}$$

$$F_{cld} = 1.6t_r\cos\chi_0 \quad \text{lower part of the cloud and below cloud base (2c)}$$

and for $\chi_0 > 60^0$ F_{cld} takes the values at $\chi_0 = 60^0$ for the different levels; α_i thereof has its values dependent on the photolysis reaction at different strength and t_r, representing energy transmission coefficient at ordinary light intensity, has the form

$$t_r = (5-e^{-\tau})/[4+3\cdot\tau\cdot(1-f)], \quad (4)$$

where f = 0.86 and τ is the optical thickness of cloud and in the form

$$\tau = 3Q_c\Delta Z_{cld}/(2\rho_w r), \quad (5)$$

in which Q_c signifies the in-cloud mean liquid water content, ΔZ_{cld} the mean depth of cloud, ρ_w the density of cloud liquid water, and r the average radius of cloud droplets. With these set, the photolysis rate will increase and decrease above the top of cloud and below its base, respectively, and differ in its change inside the cloud, depending on sun's zenith. The original parameterization scheme on this issue takes no account of the difference in photolysis rates vertically in cloud, which is actually vast between its upper and lower portions within a quite deep stratiform or cumulus cloud (>400 m in thickness) (see Hanson and Derr, 1987). Thus this study makes some special correction of the original scheme as follows: Eq.2b is still used for the upper part and Eq.2c used for the lower portion as well as below cloud base.

Table 1. Initial conditions for running the box model.

Species or elements	Initial value
NOx	5.5 ppb
C_3H_8	1.0 ppb
>C3 alkane	8.0 ppb
C_2H_4	1.5 ppb
>C2 alkene	1.5 ppb
HCHO	1.5 ppb
>C2 aldehyde	1.5 ppb
alkyl-benzenes	2.0 ppb
lumped ketones	1.5 ppb
Isoprene	1.5ppb
light intensity	time-dependent
Temperature	283°K
relative humidity	99% inside cloud 50% external to cloud
cloud liquid water content Q_c	Variant:0.09-1.44g/m^3
cloud thickness ΔZ_{cld}	Variant: 0 - 4000m
mean droplet radius r	Variant: 2.5 - 100μm
simulation starting time	6:00 a.m.

Table 2. Factors A, B and C involved in the experiments or not for analysis.

Experiment	1	2	3	4
factor A: cloud effect on radiation	no	yes	yes	yes
factor B: cloud absorption effect	no	no	yes	yes
factor C: liquid phase chemical effect	no	no	no	yes

3. Experimental Conditions and Methodology

Table 1 presents the initial conditions for the component analysis, based on the observational data from Lin'an atmospheric background station (Luo and Zhou, 1994). To differentiate the effects of the three factors on ozone, four experiments have been conducted as shown in Table 2. Exp.1 is taken as the control experiment for a clear sky without cloud influence; Exp.2 takes account of the impact of factor A on ozone concentration; Exp.3 of factors A and B; Exp.4 of all the three factors. Only some of the simulation results will be shown in the following section.

4. ANALYSIS OF CLOUD EFFECTS ON OZONE CONCENTRATION

4.1 In the Upper Part of Cloud

Liquid water is available in the upper part of cloud so that each of the mentioned three factors has impact on the ozone concentration. Fig.1 shows that radiation effects in this portion are weak, causing a reduction of only 1.5%. The role of cloud absorption is responsible for the decrease in the concentration and enhanced as Q_c grows, a variation that is almost linear. For Q_c > 0.7 g m^{-3}, the absorption effect is strong enough to compare with aqueous-phase chemical effect, which causes O_3 reduction inside the cloud and is intensified at rapidity with increasing Q_c, which represents the leading cause of ozone mitigation. Take Q_c = 0.36 g m^{-3} for example. The joint influence of the three factors is responsible for a 33.1% reduction, of which 28.0% is owed to liquid-phase chemistry, accounting for 84% of the total reduction. With Q_c having other values a similar situation would appear.

Fig.2 delineates that the radiation plays a very weak role. For the particle with radius r < 5μm, the absorption effect is most noticeable, making the liquid- phase chemistry rank the second. But, with increasing of r, the absorption effect weakens rapidly and the liquid-phase chemical impact becomes predominant. This is because at the same Q_c, r, if twice as small, will make the total absorption cross section per unit volume of cloud increase twofold as large. Following the inter-phase species transfer equation, besides, the total cloud-absorption per unit time and per unit volume will grow four times as high. Hence, for quite small or big droplet radius the pollutant absorption coefficient is higher or lower, compared to the consumption rates of aqueous-phase pollutants, *viz.*, the control of the ozone concentration decrease is aqueous-phase chemical (absorption) effect. Also, ones can observe from Fig.2 that both the aqueous-phase chemical and the joint impacts are mitigated rapidly with increasing of r and, particularly, for r > 50μm, each of the three factors exerts little influence only. This demonstrates that the smaller absorption coefficient of larger droplets gives rise to an insufficient supply of aqueous-phase pollutants, thereby causing weak consumption of radical species, ozone and its precursors in the aqueous-phase chemical process.

4.2 In the Lower Part of Cloud

The O_3 concentration in the lower part of cloud is under the joint effect of the three factors, which is similar to the upper portion simulations, except that sunlight flux is greatly reduced because of the cloud layer overhead. Fig.3 shows that with increasing of Q_c the concentration can be mitigated up to 90%, the radiation effect acting as the dominant reducer, next to it being liquid-phase

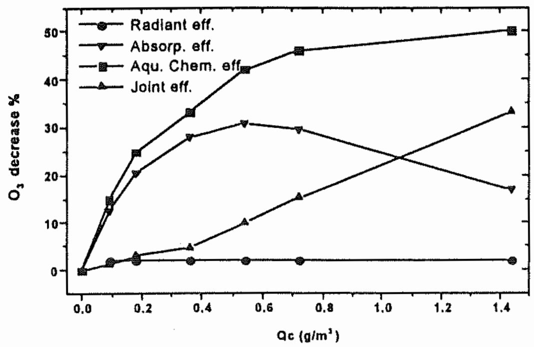

Fig.1 Ozone concentration changing as a function of Q_c compared to 100% for the upper part of cloud with mean cloud droplet radius r=10μm and cloud thickness ΔZ_{cld}=500m.

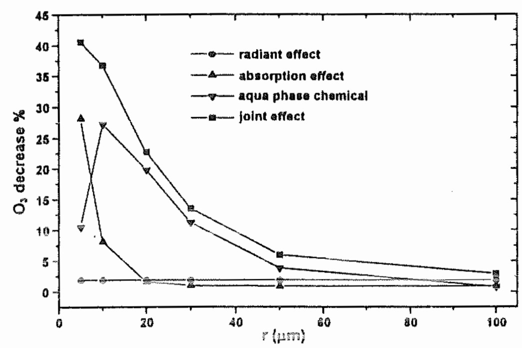

Fig.2 The same as in Fig.1 but for changing with r, where Q_c = 0.36 g m^{-3} and ΔZ_{cld} = 500 m.

chemical effect and the least important being the absorption effect. Fig.4 shows the percentage decrease in the concentration under the effect of one factor and all the three in combination at a range of r, indicating that cloud droplets with a smaller r is related to more loss of O_3, for which the radiation effect acts as the leading factor. This is due to the fact that at the same Q_c, a smaller r is responsible for greater optical depth of cloud. Likewise, the smaller the radius r, the greater the absorption effect – the role is likely to exceed that of liquid-phase chemistry. Fig.4 also illustrates that even at constant Q_c, the O_3 concentration in the lower part of cloud can be reduced by 10% - 90% for different r.

The upper part of cloud layer has great effect on the reduction of solar radiation with the thickness effect on the concentration portrayed in Fig.5. It is seen from Fig.5 that the deeper the cloud depth above, the more its loss and with a 4-km thickness, a reduction of >90% would occur just owing to radiation effect.

4.3 Integrated Effects of Cloud

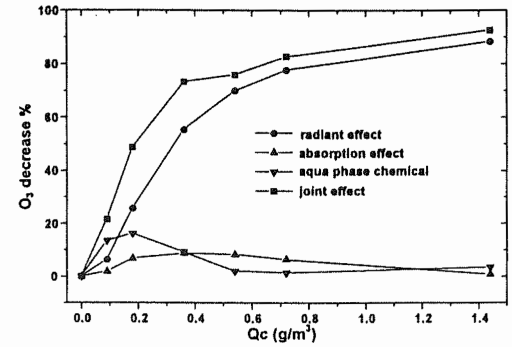

Fig.3 The same as Fig.1 but for the lower part of cloud.

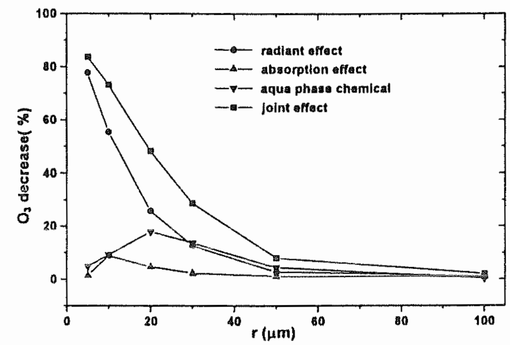

Fig.4 Like Fig.2 but for the lower part of cloud.

Take the concentration in the lower portion of cloud for example. Assuming cloud liquid water content to be 0.36 g m^{-3}, mean radius of could droplets to be 10μm and cloud depth above it to be 500m (other conditions can be seen in Table 1), ones made a comparison of these experiments, as shown in Fig.6. In Table 1 the curves denote the daily variation in O_3 concentration (ppb), and the almost maximum ozone concentration at 1800 Beijing time (BST) obtained in Exp.1 is taken as 100% in comparison to the results from the other three. Very little variation after 1800 BST is due to the fact that both dry deposition and source emission were not considered. One can see that the difference between Exps.1 and 2 is indicative of the effect of Factor A; between Exps. 2 and 3 for factor B; and between Exps. 3 and 4 for factor C. In this instance, factor A exerts maximum impact, thus reducing the concentration to 55.3% versus 100% from Exp.1; factor C to 9.1%; factor B to 8.8%.

Further analysis can know that in-cloud liquid water acts as a powerful scavenger of gaseous HO_2, leading to the fact that one of the key links of gaseous-phase photochemical reaction is enfeebled, resulting in noticeable decrease of gaseous ozone production.

Finally, this study also conducted some simulations to real cases and showed that the simulation results agree well with observations.

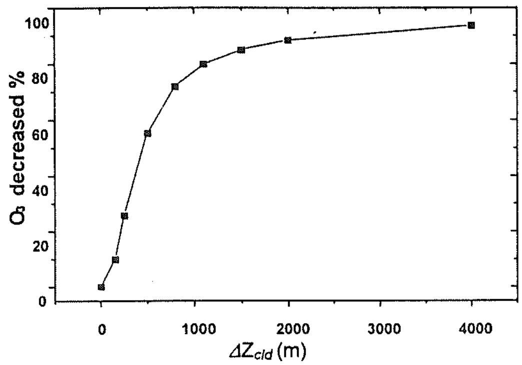

Fig.5 Like Fig.1 except for changing versus ΔZ_{cld}, with r = 10μm and Q_c = 0.36 g m^{-3}.

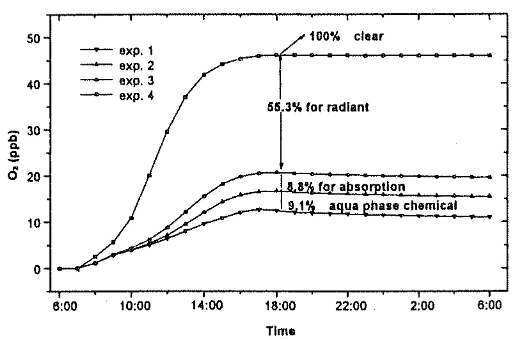

Fig.6 Factor analysis of cloud effects on ozone concentration with the initial conditions given in Table 1, but for Q_c of 0.36 g m^{-3} and mean radius of cloud droplets r = 10μm. The ozone concentration expressed in a unit of ppbv is given on the ordinate and the 24-h simulation given along the abscissa.

5. CONCLUDING REMARKS

1) There is noticeable difference in the effect on O_3 concentration in different portion of cloud between the three factors. In the upper portion of cloud the concentration is reduced owing chiefly to the liquid-phase chemical effect when r>10μm; the absorption effect becomes predominant for r <10μm; the radiation effect (negative in this case) plays a negligible role in the reduction. In the lower part of cloud, the radiation effect is the leading cause of the concentration decrease, next to it being the liquid-phase chemical effect. The absorption effect is normally unimportant for the cloud with r>20μm and Q_c<0.7g m^{-3}.
2) The cloud physical structure bears an intimate relation to the three factors. Inside the cloud, with increased Q_c and reduced r the radiation effect (negative role in this case) is enhanced. In general, the aqueous-phase chemical effect becomes prominent when r is quite small and the radiation effect is less intense.
3) The cloud water absorption of radical and soluble organic species and the aqueous–phase chemistry scavenging are the dominant causes of the cloud absorption and aqueous phase chemistry effects.

Acknowledgements. This research was supported by the Program of Major Scientific Projects of Chinese Academy of Sciences under Grant No. KZ951-A1-403-01 Chinese Natural Science Foundation under Grant No. 49675247, and the Foundation of the Institute of Atmospheric Physics, Chinese Academy of Sciences. The authors especially thank to Professor Gregory R. Carmichael and his research group at University of Iowa, USA, for use of their STEM-II model and for their kind help.

REFERENCES

Bojkov, R.D., 1988: Ozone changes at the surface and in the troposphere, in *Tropospheric Ozone*, edited by I.S.A. Isakse, D. Reidel, Hingham, Mass., 1988, pp. 83-96.

Carmichael, G.R., L.K. Peters, and T. Kitada, 1986: A Second Generation Model for Regional-Scale Transport/ Chemistry/ Deposition, *Atmos. Environ.*, 20, 183-186.

Carmichael, G.R., L.K. Peters, and R.D. Saylor, 1991: The STEM-II regional scale acid deposition and photochemical oxidant—I. An overview of model development and applications, *Atmos. Environ.*, 25A, 2077-2090.

Chang, J.S., R.A. Brost, I.S.A. Isaken, S. Middleton, W.R. Stockwell, and C.J. Walcek, 1987: A three-dimensional Eulerian acid deposition model: Physical concepts and formulation, *J. Geophy. Res.*, 92, D12, 14,681-14,700.

Hanson, H. P. and V. E. Derr, 1987: Parameterization of radiative flux profiles within layer cloud, *J. Atmos. Sci.*, 44, 1287-1295.

He, D.Y. and M.Y. Huang, 1996: A numerical study on tropospheric ozone over China, *Atmos. Environ.*, 30, 2449-2451.

Levieveld, J. and P.J. Crutzen, 1990: Influences of cloud photochemical processes on tropospheric ozone, *Nature*, 343, 227-232.

Luo, C. and X. J. Zhou, 1994: A regional model study of the variations and distributions of ozone and its precursors in eastern Asia and west Pacific, *Acta Meteorologica Sinica*, 8(2), 195-202.

Xiao, H., Z.L. Shen, M.Y. Huang, and Y.X. Wu, 1987: An observational study on atmospheric ozone in the lower troposphere and at the surface in southwest China, *Scientia Atmospherica Sinica*, 17(5), 622-628 (in Chinese).

Zhou, X.J., C. Luo, G.A. Ding, J. Tang, and Q.J. Liu, 1993: Preliminary analysis of the variations of surface ozone and nitric oxides in Li'an, *Acta Meteorologica Sinica*, 7, 287-294.

THE INFLUENCE OF CLOUDS ON THE OXIDIZING CAPACITY OF THE ATMOSPHERE

W. R. Stockwell[1] and C. J. Walcek[2]

[1]Division of Atmospheric Sciences, Desert Research Institute, Reno, NV 89512,
[2]Atmospheric Sciences Research Center, State University of New York at Albany, NY 12203

1. INTRODUCTION

The oxidizing capacity of the atmosphere affects the lifetimes of greenhouse gases and the flux of pollutants reaching the stratosphere. The oxidizing capacity of the atmosphere is determined by the concentrations of oxidants including ozone, hydroxyl radical (HO), hydroperoxy radical (HO_2) and hydrogen peroxide.

The effect of clouds on the oxidizing capacity of the atmosphere has been investigated through the use of a cloud chemistry model with coupled aqueous and gas-phase chemistry. The effect of clouds on actinic flux was calculated with a separate radiative transfer model. The model was used to simulate a number of atmospheric cases with and without clouds.

2. CALCULATION OF PHOTOLYSIS RATES

Photolysis rates for the model were derived from the two-stream radiative transfer model of Madronich (1987) which accounts for absorption of reactive photons by O_2 and O_3, scattering and absorption by aerosols, Rayleigh scattering, and ground albedo, Figure 1. Photolysis rates are usually lower than clear-sky values near the base of clouds, but can become greater than clear-sky values in the upper regions of clouds (Lelieveld and Crutzen, 1990; Madronich, 1987).

3. CHEMISTRY SIMULATIONS

The simulations were made with a model with coupled gas-phase and aqueous chemistry (Walcek et al., 1997). The integrated heterogeneous box model can simulate the chemistry of both cloudy and clear air over a wide range of pollutant concentrations.

Corresponding author's address: W. R. Stockwell, Division of Atmospheric Sciences, Desert Research Institute, 2215 Raggio Parkway, Reno, NV 89512-1095; E-Mail: wstock@dri.edu.

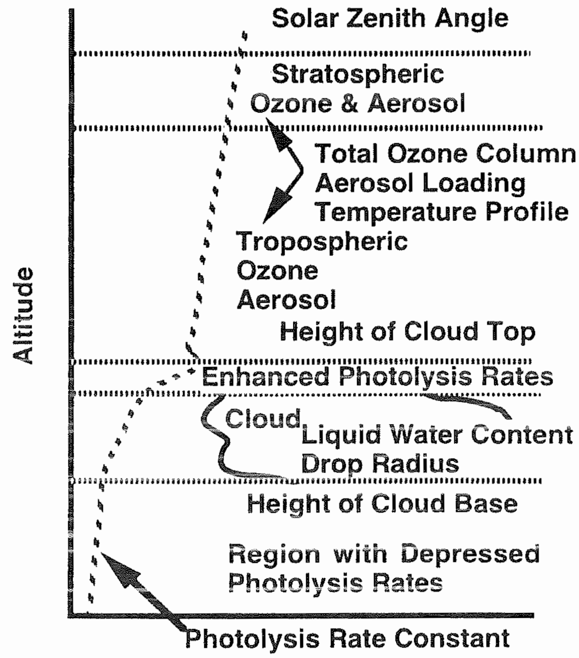

Figure 1. Factors that affect atmospheric photolysis rate parameters. The dashed line shows a typical photolysis rate constant as a function of altitude.

The gas-phase mechanism was based upon the mechanism of Stockwell et al. (1990) which was designed to simulate acid and oxidant formation over conditions ranging from clean remote atmospheres to polluted urban atmospheres in the troposphere. This gas-phase mechanism includes over 160 reactions among 60 constituents. The aqueous-phase chemistry mechanism includes over 70 aqueous-phase reactions and dissolution equilibria (Walcek et al., 1997). The mass-transfer of gas-phase constituents to cloud water was calculated by using the assumption that a mass-transfer limited equilibrium is maintained between the interstitial gas and the aqueous phase. The solution of the stiff rate equations was accomplished through the use of an exponentially-assisted, iterative integration technique of the total (gas + liquid phase) concentrations of all constituents. The steady-state approximation was used to calculate the concentrations of fast-reacting radical species in both phases.

The simulated cloud was based upon measurements made at Grünten, Germany (Junkermann et al., 1994). The Grünten is a relatively isolated mountain in the western Bavarian Alps. The measurements were made with an instrumented cable car system. The cable car system runs between 765 m a.s.l. and the summit at 1738 m a.s.l. on the northwesterly slope of the mountain. For most of its route the cable car is over 50 m above the ground level. Typical measurements include air, aerosol or cloud water sampling. Data for a typical relatively thin stratus cloud were used to calculate the droplet radius and optical depth for the simulations.

4. RESULTS

4.1 Effect of Clouds on Ozone Photolysis

Clouds had a large impact upon photolysis rates. We calculated ozone photolysis rates using the code of Madronich (1987) to examine the effect of clouds on photolysis rates. We choose the ozone photolysis reaction which produces O^1D because this reaction is the primary source of HO radicals in the troposphere. The figure shows the results for a 2 km thick homogeneous cloud, optical depth 75, with a cloud base at 1 km and a cloud top at 3 km altitude.

There is a large difference between the calculated photolysis rates with and without cloud, Figure 2. The clear air photolysis rate parameter is relatively constant with altitude. For the photolysis rate parameter with cloud the values are reduced below the cloud and within the lower third of the cloud. In the top half of the cloud and above the photolysis rate parameters are increased. This shows that clouds should affect the gas phase production rates of radicals. Photolysis rate parameters within the cloud are predicted to be highly variable and this would be expected to strongly affect the gas-phase and aqueous phase chemistry within the cloud.

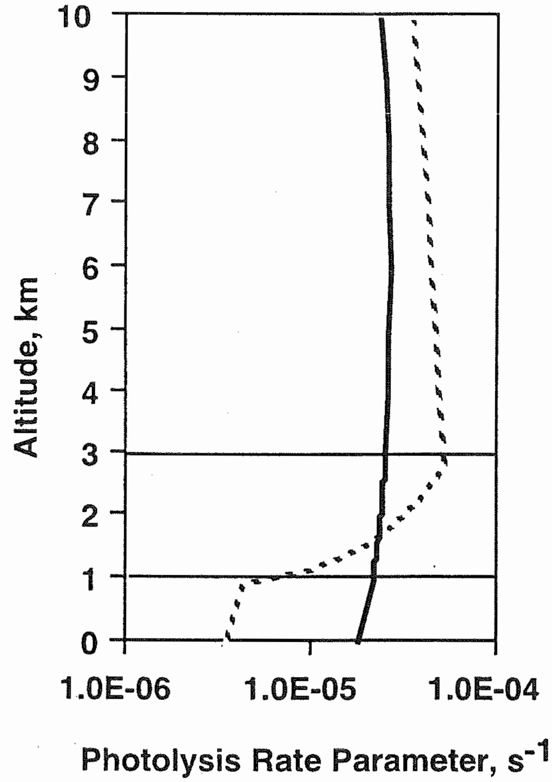

Figure 2. Photolysis rate parameters calculated for the photolysis of ozone to produce $O(^1D)$ excited oxygen atoms. The solid line is for clear sky while the dashed line is for cloudy conditions. The lower horizontal line at 2 km represents cloud base and the upper line at 3 km represents cloud top.

4.2 Effect of Clouds on Chemical Simulations

Clouds increase photolysis frequencies above cloud top and decrease them below. Clouds also strongly affect gas-phase chemistry by serving as a strong sink of HO_2 radicals. The gas-phase self reaction of HO_2 is important in the absence of clouds but scavenging of HO_2 by cloud water droplets is the dominate loss of HO_2 within clouds.

The simulations showed that clouds affect the ratio of HO_2 to HO, Figure 3, and the concentrations of HO_x (HO + HO_2), Figure 4, in the atmosphere through their effects on photolysis rates.

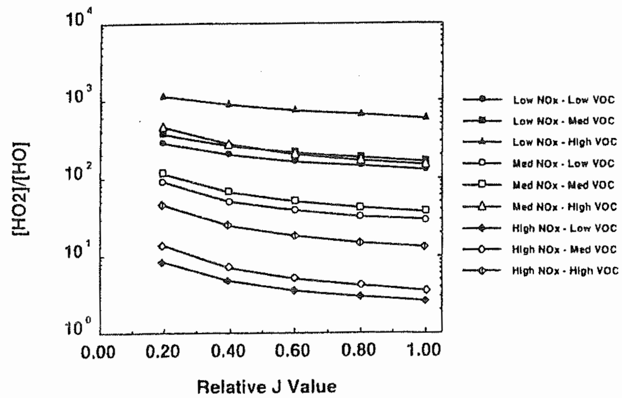

Figure 3. Effect of photolysis rate parameters on HO_2 to HO ratio for different mixing ratios of nitrogen oxides and volatile organic compounds.

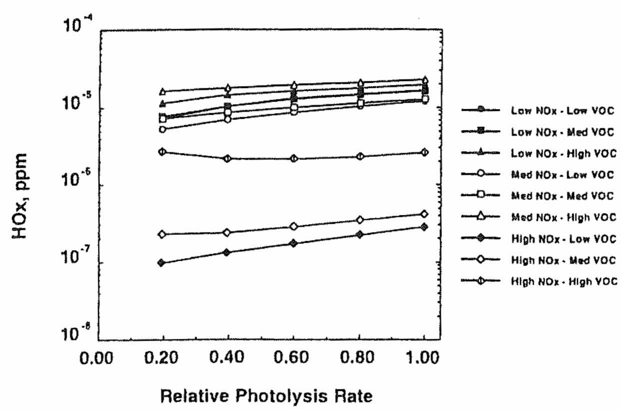

Figure 4. Effect of photolysis rate parameters on HO_x for different mixing ratios of nitrogen oxides and volatile organic compounds.

Below clouds photolysis rates are reduced. This reduction in photolysis rates increases the gas-phase HO_2 to HO ratio which reduces the oxidizing capacity of the troposphere near the Earth's surface. Any change in climate that increases the frequency of clouds will affect the troposphere's oxidizing capacity and its ability to remove many greenhouse gases.

It is possible that a positive feedback cycle between global warming and the oxidizing capacity of the troposphere will become established with very negative consequences for the environment.

4. REFERENCES

Junkermann, W., J. Dietrich, P. Wolf, W. Wieprecht, J. Slemr, G. Kolthoff and R. Niessner, 1994: Investigation of the vertical distribution of trace components in the lower troposphere using a cable car. *Proceedings of the EUROTRAC Symposium '94*, P. M. Borrell, P. Borrell, T. Cvitas, W. Seiler Eds., SPB Academic Publishing, Den Haag, pp 1156-1161.

Lelieveld, J. and P. J. Crutzen, 1990: Influences of cloud photochemical processes on tropospheric ozone. *Nature*, **343**, 227-233,

Madronich, S., 1987: Photodissociation in the atmosphere 1. actinic flux and the effects of ground reflections and clouds. *J. Geophys. Res.*, **92**, 9740-9752.

Stockwell, W.R., P. Middleton, J.S. Chang and X. Tang, 1990: The second generation regional acid deposition model chemical mechanism for regional air quality modeling. *J. Geophys. Res.*, **95**, 16343-16367.

Walcek C. J., H. -H. Yuan and W. R. Stockwell, 1997: The influence of aqueous-phase chemical reactions on ozone formation in polluted and nonpolluted clouds. *Atmos. Environ.*, **31**, 1221-1237.

APPLICATION OF A TRACER TECHNIQUE TO STUDY SULFUR DIOXIDE OXIDATION IN CLOUD DROPS AS A FUNCTION OF DROP SIZE

Jill E. Reilly[1], Katharine F. Moore[1], D. Eli Sherman[1], Jeffrey L. Collett Jr.[1], Christopher Judd[2], Mita Das[2], Oliver Rattigan[2], Vincent Dutkiewicz[2] and Liaquat Husain[2]

[1]Department of Atmospheric Science, Colorado State University, Fort Collins, CO, 80521, USA
[2]Wadsworth Center, NY State Department of Health, Albany, NY 12201 and Department of Environmental Health and Toxicology, School of Public Health, State University of New York, Albany, NY 12201, USA

1. INTRODUCTION

Aqueous phase oxidation of S(IV) in clouds and fogs is a major process leading to sulfate formation. Approximately 80 percent of global SO_2 oxidation is believed to occur in clouds (Lelieveld and Heitzenberg, 1992). Measurements have shown that the chemical compositions of cloud and fog drops vary with drop size (Bator and Collett, 1997). These differences can lead to the prediction of differential S(IV) oxidation across the drop size spectrum. Under conditions where oxidation by hydrogen peroxide is not the predominant pathway for the transformation of S(IV) into sulfate this is especially true.

The peroxide pathway is typically dominant over a range of relatively acidic conditions, but within this range the oxidation rate is independent of pH. In drops of higher pH, however, differential oxidation becomes important due to the increased role played by other, nonlinear, oxidation pathways. Even slight differences in pH, such as those measured between large and small drops in the same cloud/fog sample, can yield a large difference in oxidation rates when the ozone oxidation pathway is dominant. In both the ozone and metal-catalyzed autooxidation pathways, the oxidation rate is a non-linear function of the drop composition. Thus, taking drop size-dependent composition into account, a higher predicted oxidation rate is obtained for these pathways than by simply calculating the rate using average drop composition.

To quantify the rate of SO_2 oxidation as a function of drop size a tracer technique developed by Husain et al. (1989, 1992) is used in the current study to determine the amount of in-cloud/fog sulfate produced in two different drop size fractions. This was then compared with the expected rate of aqueous sulfate production calculated based on measured drop size-dependent composition and published oxidation rate laws. A comparison of the results provides an opportunity to demonstrate experimentally the existence of drop size-dependent sulfate production rates.

Corresponding author's address: Jill E. Reilly, Department of Atmospheric Science, Colorado State University, Fort Collins, CO 80523, USA; Email: jreilly@lamar.colostate.edu

2. EXPERIMENTAL DESIGN

Two field campaigns were launched cooperatively by Colorado State University (CSU) and State University of New York, Albany – Department of Health (SUNY-DOH) in an attempt to test the hypothesis that S(IV) oxidation varies with drop size in high pH radiation fogs where ozone is an important oxidant, but is independent of drop size in acidic clouds where oxidation is dominated by the hydrogen peroxide pathway. The purpose of the campaigns was to gather data that would enable both the prediction of size-dependent sulfate production rates from the cloud/fog composition, and also allow for the determination of the amount of sulfate produced in the cloud or fog by the tracer technique. The only source of the tracer, Se, in the cloud droplets is the scavenging of aerosols, whereas sulfate may be derived both from aerosol scavenging and *in situ* formation. Therefore, by comparing the SO_4/Se ratio in cloud/fog water to that in ambient aerosol the sulfate scavenged from aerosols is deduced and, by difference, the amount produced through in situ reaction (SO_{4in}) can be determined. This is expressed as

$$(SO_{4in})_{cw} = [(SO_4/Se)_{cw} - \alpha/\beta(SO_4/Se)_{aa}](Se)_{cw} \quad (1)$$

where α and β are the scavenging coefficients for SO_4 and Se aerosols and cw and aa denote cloud water and ambient aerosols, respectively. Previous field studies have shown that $\alpha/\beta = 1$, therefore measurement of the SO_4 and Se concentrations in cloud water and pre-cloud ambient aerosol enables a determination of SO_{4in} (Husain et al., 1991).

The sites chosen represent two distinct types of environments: Whiteface Mountain, NY and Davis, CA. Whiteface Mountain was chosen because it is generally a very acidic environment where S(IV) oxidation by the hydrogen peroxide pathway dominates aqueous phase sulfate production. Therefore, it is a site not likely to exhibit drop size-dependent sulfate production rates. The Whiteface Mountain field campaign took place throughout July of 1998 during which time there were six cloud interception events. Two measurement sites were operated to characterize the chemical composition of both the in-cloud and below-cloud air: a summit site at 1.6 km and a lower site at an elevation of 0.6 km on the mountain. Continuous measurements of aerosol samples, trace gas species (H_2O_2, SO_2 and O_3) and meteorological parameters were made at both sites throughout July. During cloud events, liquid water content measurements were made at the summit. Cloud samples were gathered by cloud collectors (a two-stage, size-fractionating Caltech Active Strand Cloudwater Collector (sf-CASCC) and a bulk Caltech Active Strand Cloudwater Collector (CASCC2)) positioned on the mountain summit. The sf-CASCC is designed to collect two different drop size fractions simultaneously (Demoz et al. 1996) . The small fraction primarily contains drops in the range 4 < d < 16 μm, while the large fraction primarily contains drops that have diameters greater than 16 μm. Once collected, the samples were immediately weighed, then the pH was measured. Aliquots were taken and appropriately preserved for later analysis of various trace species in the lab.

The radiation fogs typical of the second study site, Davis, California, tend to be more alkaline and therefore S(IV) oxidation is more likely to be dominated by the ozone pathway. This is a prime location for studying drop size dependent S(IV) oxidation and the resulting sulfate rate enhancement. Six radiation fog sampling events took place through late December and early January of 1998-1999 in a large field where the sf-CASCC and CASCC2 collectors were mounted on poles, approximately 3 m above the ground. Aerosol measurements were taken at the same site, with filters being run both before and after the fog events. The same gas and meteorological measurements were made in Davis as at Whiteface.

3. STUDY RESULTS

3.1 Drop composition and predicted S(IV) oxidation in Whiteface Mountain, NY clouds

The chemical compositions of the samples collected at Whiteface Mountain were fairly homogeneous with respect to drop size. The cloudwater was found to be acidic, with pH values in the range 2.8 to 4.7. The pH values also appear to remain constant across the drop size spectrum (Fig. 3.1.1). This homogeneity is also characteristic of the other inorganic ions and aqueous H_2O_2. One to one scatter plots of samples collected using the sf-CASCC show that there is little difference between large and small drop concentrations for most ions (e.g. sulfate Fig. 3.1.2). Overall, the variation in drop composition as a function of drop size is smaller in these clouds than we have observed in most other situations we have studied. The oxidation rates calculated from the Whiteface Mountain cloud compositions suggest that indeed hydrogen peroxide is the dominant oxidant here. Also, as expected, the predicted oxidation rates are nearly the same for both size fractions and the bulk samples. Ratios between the calculated rates in large and small drops, with some exceptions, are close to one.

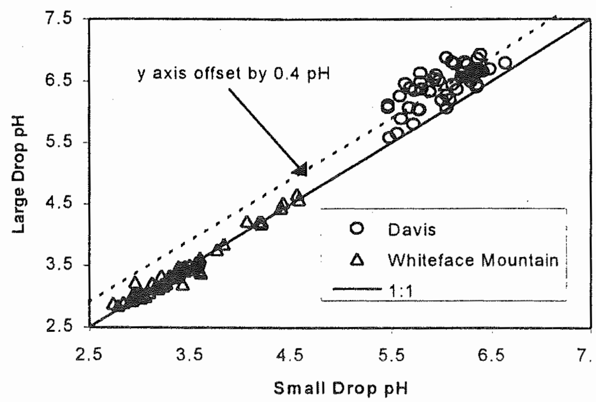

Figure 3.1.1: Comparison of pH in large and small drop sizes at Whiteface Mountain vs. Davis.

3.2 Drop composition and predicted S(IV) oxidation in Davis, CA fogs

The results from Davis, in contrast, show that the fog chemistry varies strongly with drop size. For Davis the drop size distribution heavily favors larger drops. As expected, the Davis fogs also tend to be more alkaline, with pH values on the order of 5.5-6.9 (Fig. 3.1.1). There was also a notable difference in the pH values between the small and large drop size-fractions collected using the sf-CASCC, with the large drops having pH values on average 0.4 units higher than the small drops. The inorganic ion concentrations also show enhancement in the small drops. On average the concentration of sulfate in the small fraction, for example, is approximately seven times the concentration in the large drop fraction (Fig. 3.1.2).

For these more alkaline fogs, dominance of the ozone oxidation pathway is predicted for most periods. A majority of the Davis fog events exhibit such high rates of S(IV) oxidation by ozone as to render the other S(IV) oxidation pathways insignificant. There are, however, a few early samples in the first event where

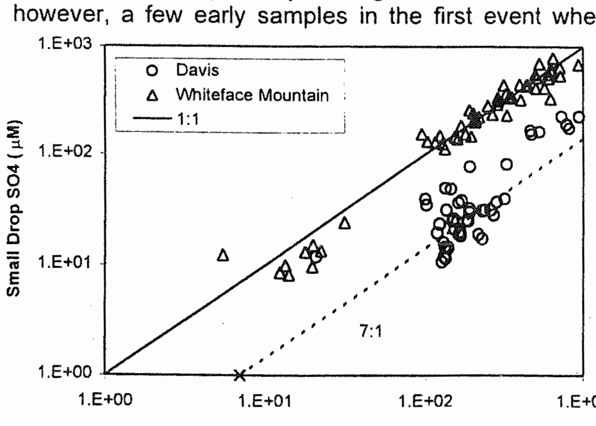

Figure 3.1.2: Comparison of sulfate in large and small drops at Whiteface Mountain, NY and Davis, CA.

peroxide appears to be the dominant S(IV) oxidant. This pathway quickly declines as the amount of available hydrogen peroxide is depleted, leaving the ozone oxidation pathway as the predominant means of sulfate production.

The calculated Davis fog S(IV) oxidation rates show that the pH differences between large and small fog drops, can make a large impact on the rate of S(IV) oxidation by ozone. The S(IV) oxidation rates predicted for the larger drops are typically much faster than those predicted for the smaller drops. Because of the non-linear nature of the oxidation rate equation, this also leads to a greater total oxidation rate for the case where independent drop compositions (corresponding to large and small drops) are considered than in the case where only bulk fog composition is considered. An oxidation rate enhancement factor can be calculated. This factor is defined as the total oxidation rate predicted using the size-differentiated fog drop composition divided by the total oxidation rate calculated from the bulk fog composition. The enhancement factor is a measure of how much faster S(IV) is predicted to be oxidized as a result of the drop size-dependence of fog composition. The enhancement factor values range from near one for the peroxide dominated samples from the first Davis fog event to over 2 for several samples taken in the later events.

3.3 Comparison of sulfate production determined from the tracer technique to predicted S(IV) oxidation rates

The ratios of oxidation rates predicted in the large and small fog/cloud drop fractions were compared to ratios of sulfate produced in large and small fog/cloud drop fractions as determined using the tracer technique. The tracer technique compares ratios of sulfate/selenium in pre-fog or below-cloud aerosol with those in the fog/cloud water in order to determine the amount of sulfate produced in the fog/cloud (Eq. 1). The results from Whiteface Mountain show that the amount of sulfate produced in the clouds is fairly uniform across the drop size spectrum (Fig 3.3.1). The ratio of in-cloud sulfate production between the large and small fractions is generally near one. This is consistent with the predicted oxidation rate ratios. Therefore, Whiteface Mountain does indeed represent a good control case for this study, exhibiting the expected behavior.

The tracer calculations of in-cloud sulfate production for the Davis fogs show a less uniform distribution over the drop size spectrum. The concentration of sulfate produced in the small drops is determined to be much larger than the concentration produced in the large drops. The ratio of large drop to small drop in-cloud sulfate production tends to be below one; in fact it is almost always less than 0.35.

These results are significantly different from the predicted S(IV) oxidation rate ratios. The ratios are shown for the early stages of three fog events sampled at Davis (see Figure 3.3.2). While the predicted oxidation rate ratios indicate there should be enhanced

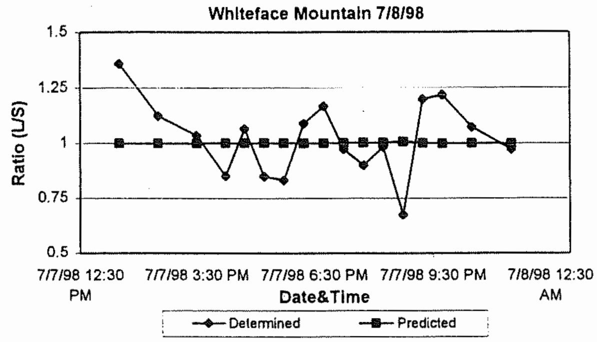

Figure 3.3.1: Comparison of the large/small ratios for one event at Whiteface Mountain for both the predicted rates and the tracer determined rates.

sulfate production in the large drops, the tracer results show enhanced production in the small drop fraction. There are only two samples for which the tracer-derived large/small drop ratio is over one, indicating increased production in the large drop fraction, while the predicted rates show ratios that are consistently over one. Further investigation into the physical reasons for this discrepancy is required.

One possible reason for the disagreement between the tracer-derived sulfate production ratios and those predicted based on drop composition could be caused by differential scavenging of sulfate and Se bearing aerosols in the fog. Extensive studies at Whiteface Mountain have shown that SO_4^{2-} and Se are scavenged with equal efficiencies. Nevertheless, aerosol particles at Davis may have different characteristics, resulting in differential scavenging. Therefore, we have examined size resolved aerosol fog samples collected at the Davis site using a Micro Orifice Uniform Deposition Impactor (MOUDI). The MOUDI samples were taken at the same time as the SUNY high volume aerosol samples and should therefore be representative of the air masses used in the tracer calculations. Examination of the chemical results shows that the size distributions of

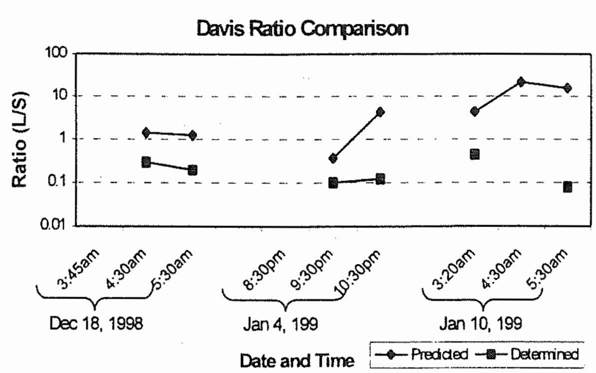

Figure 3.3.2: This figure shows a comparison of the large/small ratios for the CSU predicted rates and the tracer calculated SUNY values. The data is taken from the first few samples of three different events.

sulfate and Se are very similar, suggesting that both species should have similar fog scavenging efficiencies at Davis.

Another possible reason for the discrepancy between the predicted and tracer-derived sulfate production ratios could be that the sulfate production reaction rate is limited by one or more mass transport steps or by competition with another reaction (Seinfeld and Pandis, 1998). The rates predicted from Davis fog composition observations are extremely fast, generally on the order of 10^{-6} **M** s^{-1}, while the predicted Whiteface Mountain S(IV) oxidation rates are frequently less than 10^{-8} **M** s^{-1}. This is a result of the very fast reaction between ozone and dissolved S(IV) at high pH. Possible mass transport limitations to the overall rate of reaction include limits in transfer of gaseous reactants from the bulk gas phase to the drop surface, rates of interfacial mass transfer, and rates of aqueous phase diffusion of reacting species. Preliminary calculations suggest that the mass transport, particularly in the aqueous phase, is indeed important in limiting the oxidation rates. It appears that by including the limitations the ratio of large to small drop predicted oxidation rates is brought down considerably. This is an approach we are currently pursuing.

There is also the possibility that a competing reaction could account for the discrepancy between the predicted and tracer-derived oxidation rate ratios. The most likely reaction is the formation of hydroxymethanesulfonate (HMS), through the complexation of dissolved S(IV) and HCHO. Previous studies we have conducted of San Joaquin Valley fog chemistry (Rao and Collett, 1995) indicate this reaction can be important in samples that have a pH greater than 6 when there is ample HCHO present. Again preliminary calculations indicate that this complexation may play a role in limiting the production of sulfate, especially in large drops. This is another avenue currently being investigated.

Acknowledgements

This work was supported by the National Science Foundation (ATM-9712603) and the U.S. Environmental Protection Agency Science to Achieve Results Graduate Fellowship (U-915364-01). We would also like to thank Cort Anastasio and his group at UC Davis for the use of their sampling site.

References

Bator, A., Collett, J.L. Jr., 1997: Cloud chemistry varies with drop size. *Journal of Geophysical Research*, **102**, 28071-28078.

Demoz, B., Collett, J.L. Jr., Daube, B.C. Jr., 1996: On the Caltech active strand cloudwater collectors. *Atmospheric Research* ,**41**, 47-62.

Husain, L., 1989: A technique for determining In-Cloud Formation of SO4. *Geophys. Res. Lett.*, **16**, 57-60.

Husain, L., Dutkiewicz, V.A., 1992: Elemental tracers for the study of homogenous gas-phase oxidation of SO2 in the atmosphere. *Journal of Geophys. Res.- Atmos.*, **97**, 14635 – 14643.

Lelieveld, J., Heintzenberg, J., 1992: Sulfate cooling effect on climate through in-cloud oxidation of anthropogenic SO_2. *Science*, **258**, 117-120.

Rao, X., Collett, J.L. Jr., 1995: Behavior of S(IV) and Formaldehyde in a Chemically Heterogeneous Cloud. *Environ. Sci. Technol.*, **29**, 1023 – 1031.

Seinfeld, J.H., Pandis, S.N., 1998. Atmospheric Chemistry and Physics: From Air Pollution to Climate Change. Wiley-Interscience, New York.

IN CLOUD AND BELOW CLOUD NUMERICAL SIMULATION OF SCAVENGING PROCESSES AT SERRA DO MAR REGION, SE-BRAZIL

Gonçalves, F.L.T.[1], Malheiros, A. R. [1], Silva Dias, M. A. [1], Freitas, S. [1], Massambani O. [1]
[1] Dept. of Atmospheric Sciences, IAG/USP - São Paulo, Brazil

Mail Address: *Rua do Matão, 1226 -Cidade Universitária -USP-05508-900- São Paulo/Brazil*

1. INTRODUCTION

Air pollution and its removal processes have been recognised since many years as a topical problem in the whole world. Thus, with the preoccupation of mapping the sensitivity of ecosystems to acid deposition, a German-Brazilian ENV-3 Project was promoted, named: "Air Pollution and Vegetation Damage in the Tropics- The Serra do Mar as an example", in the Southeastern region of Brazil, addressing as the main objective all the physico-chemical parameters of the vegetation, soil, climate and effects of topography, to a global analysis submission. The project is an interdisciplinary approach of research concerned with the effects of air pollution on vegetation and soil, including fields such as meteorology, chemistry, biology and soil sciences.

Scavenging processes have been examined in many experimental and in theoretical studies. Herbert and Beheng & Herbert (1986) have developed initially a numerical model to study the aerosol collection. Gonçalves et al. (2000) have incorporated gas absorption in order to investigate the magnitude of the below cloud scaveging in this region. This modeling was parameterized in order to obtain the observed rainwater concentration variability, taking into account both gas and particle scavenging. The air concentration data were used as initial conditions into the modeling.

To help us evaluate the in cloud scavenging contribution as the first attempt described in Gonçalves & Massambani (1998), the RAMS (*Regional Atmospheric Mesoscale System*) as well as the weather radar data were used. RAMS can address the space and time evolution of the cloud microphysics and rainfall system which entered the study area. In particular the cloud water liquid content, with its respective cloud droplet spectra, and vertical dimensions of the clouds were analyzed because both parameters can describe the in cloud scavenging added to the nucleation scavenging.

2. EXPERIMENTAL SITE

The Serra do Mar study area is located around 23°S and 46°W near the coast of the Atlantic ocean. The chosen ground station was Paranapiacaba St, at about 800 m above sea level.

Corresponding author's address :Fábio L.T Gonçalves; Rua do Matão, 1226 -Cidade Universitária -USP-05508-900- São Paulo/Brazil; Email address: fgoncalv@model.iag.usp.br

The continuous monitoring of the rainfall structures was performed from the São Paulo Weather Radar, located 30 km NE of the study area, as it has been described in Vautz et al. (1995).

3. METHODOLOGY

The fractionated rainwater chemical analysis had been described in Vautz *et al.* (1995) and Gonçalves et al. (2000). The below cloud numerical modeling is also presented in Gonçalves et al.(2000), which includes the physical and mathematical descriptions proposed by Pruppacher & Klett (1997), Volken (1994), Seinfeld & Pandis (1998). The RAMS parameterizations and the new scavenging processes parameterization follow the considerations:

1- the Congonhas airport radiosonde was used as the input data for the RAMS modeling initialization. The initialization was homogeneous and the model run for 24 hours;

2-Topography and vegetation have been used to characterize the Serra do Mar as the modeling input. Vegetation parameterization used type 6 (evergreen broadleaf trees). Soil moisture was assumed 0.80 for all depths;

3-The cloud physical parameterization (type 3 from Flatau, 1989) has been used with the full microphysical module including ice phase. The cumulus parameterization from Molinari (1985), solar and terrestrial radiation parameterization from Mahler & Pielke (1977) was also used ;

4-The coarse grid specification was assumed one grid, 20 x 20 km, with delta z of 100 m, 1.2 vertical grid stretch ratio and 500 m maximum delta z for vertical stretch. Time step was assumed 20 s and 2 s the smallest time step ratio;

5-The grid point for the cloud water liquid content vertical profile, used for scavenging modeling, was chosen as close as possible to the Serra do Mar station;

6-The cloud water liquid content height (vertical profile) has been necessary to integrate the in cloud scavenging processes along its vertical distribution in order to obtain the cloud droplet spectra therefore the total mass removed per square meter.

7-the nucleation scavening was assumed to be 0.7 for sulfate, 0.8 for nitrate and ammonium, based on Seinfeld & Pandis (1998). The remaining interstitial aerosol was assumed to be scavenged through Brownian diffusion, through the RAMS cloud water profile simulations described in 1 to 6;

8- The aerosol spectra was assumed rural and urban (Whitby , 1980);

9- The convective profile of trace gas concentration was obtained with a parameterization of sub-grid scale convective transport of trace gases and aerosol particles associated to deep and moist convection systems for low-resolution atmospheric models. The parameterization is based on the 'top-hat' method, has been coupled to the cumulus parameterization scheme of RAMS-CSU model and used for long range transport studies of emissions associated to biomass burning over South America [Freitas et al., 1999].

4. RESULTS AND DISCUSSION

As discussed in Gonçalves et al. (2000) the March 92 events present a below cloud scavenging dominance. This result was based on the exponential decreasing of the rainwater concentration in the observed data set as well as in the modeled (from below cloud modeling) rainwater concentration. The correlation coefficients between modeled and observed concentrations are higher than 0.70.

However, the March 93 events present a different behavior which has been described in Gonçalves & Massambani (1998) with correlation coefficients smaller than 0.20. According to the Weather Radar data, during the March 15th 1993 event, a large rainfall pattern was advected towards east not affecting the study area by the heaviest rainfall rates. On the other hand, for March 16th, a smaller convective raincell was advected from NW, which presented heavy rainfall cores observed crossing the study area and with rainfall rates higher than 20 mm/h (Gonçalves & Massambani, 1998).

Therefore, the below cloud modeled and observed data set differences could be attributed to the in cloud scavenging contribution, supported by the Weather Radar maps described above, mainly at March 16th.

Trying to explain these differences, the RAMS simulations were used in order to investigate the in cloud contribution. The Weather radar maps were used to fit the best RAMS simulation as the observed rain systems.

The vertical cloud water content simulated profiles, shown in Figure 1, were used in order to obtain the cloud water droplet spectra. From the droplet spectra, the in cloud scavenging coefficient was calculated and consequently the gas and interstitial aerosol scavenged amount.

Figure 1 The vertical profile of the cloud water liquid content at 15/03/93 simulated by RAMS.

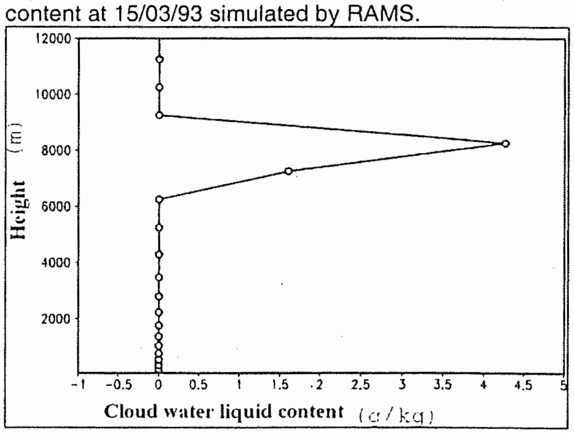

The time of the cloud formation from the RAMS simulation was also used to calculate the in cloud scavenging period as well as the cloud height (Figure 1).

The aerosol particle and gas vertical profiles, based on Freitas et al. (1999), were the most reasonable assumptions for deep convective transport in a Cumulus cloud which could reproduce the input concentrations, better than the vertical exponential decreasing assumption evaluated in Gonçalves & Massambani (1998).

The urban aerosol spectra were also the best fit to the observed rainwater concentrations, which were used in the in cloud and below cloud modelings. This result could be explained due to the origin of the rain systems, both over São Paulo City. Rural spectra present a significant decreasing after the second sample which it is not present in the observed rainwater concentration in the March 1993 case studies. Adding to this, the urban PM spectra presents a smoother decreasing which fits better to the observed data set (see Figures 2 to 4).

Figures 2, 3 and 4 show the below cloud and in cloud modeled rainwater concentrations compared to the observed concentration for the March 15th event.

The correlation coefficients, between both observed and modeled concentrations, are 0.44, 0.57 and 0.48 respectively to ammonium, nitrate and sulfate. The good agreement for nitrate is probably due its high solubility in rainwater, which fits best to the numerical modeling.

Figure 2, for NO_3^-, shows observed values higher than modeled concentrations. Opposite behavior has appeared for $SO_4^=$ (Figure 4). NH_4^+ concentrations present an intermediary behavior (Figure 3). The results also show constant rainwater concentrations rather different than the exponential decreasing. In accordant to Naik et al. (1994), it demonstrates an in cloud contribution, also especially for NO_3^-.

Figure 2. Nitrate scavenged in rainwater at March 16th Paranapiacaba St.

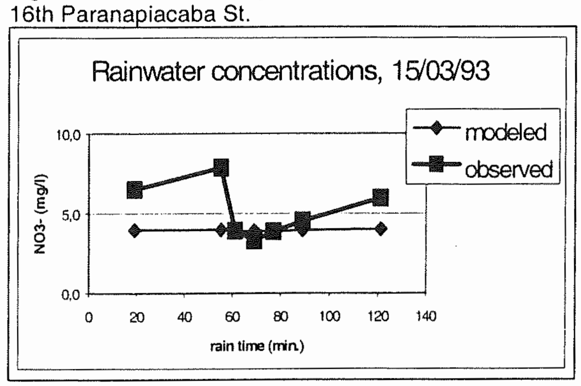

Figure 3 Amonium scavenged in rainwater at March 16th Paranapiacaba St.

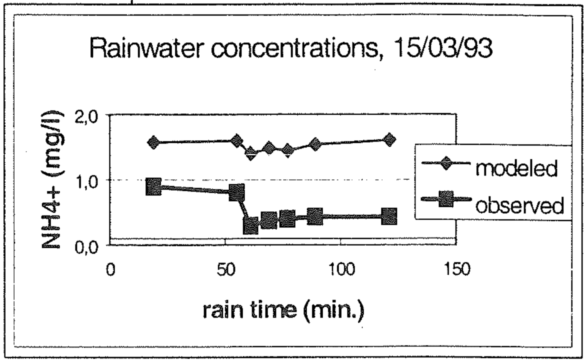

Figure 4 Sulfate scavenged in rainwater at March 16th Paranapiacaba St.

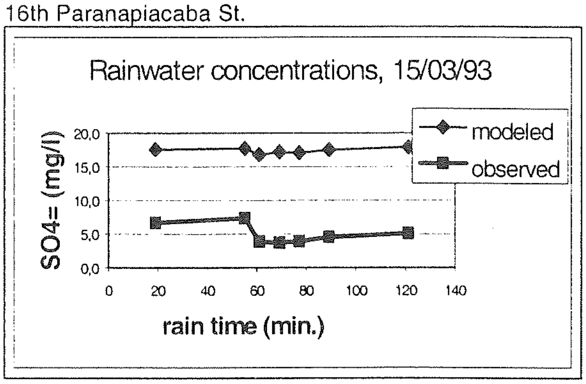

Comparing to Gonçalves & Massambani (1998) there is an increment of the modeled concentrations because of the in cloud contribution as expected. The explanation for the higher nitrate observed rainwater concentrations should be attributed to the vertical atmospheric nitrate convection over S. Paulo City. Other explanation should be that the nitrate has very high solubility to the cloud droplets. And, the input data used the Serra do Mar ground station data in which could not represent the actual nitrate amount in the atmosphere over S. Paulo.

On the other side, the explanation for the high modeled sulfate and ammonium rainwater concentrations should be attributed to the optimization of the assumptions in the modeling. These assumptions include mainly the highest concentrations in the vertical profile, pH acid to the sulfate (Walcek et al., 1981), no drop evaporation, high nucleation scavenging rate, no other chemical transformations and the highest scavenging coefficient calculations. All of these assumptions take the result as higher as possible increasing the modeled rainwater concentrations. Mass advection from S. Paulo could also explain the smaller concentrations in the in cloud atmosphere. In that case, Serra do Mar input data overestimate the particle initial concentrations over S.Paulo, opposite of nitrate. This assumption may be supported by the urban nitrate distributions, rather different of ammonium and sulfate (Seinfeld & Pandis, 1998).

6. CONCLUSIONS

The modeling result show a reasonable agreement to the observed data, at least the same magnitude of the rainwater concentration and similar curve shapes. Sulfate and ammonium present a total overestimation and nitrate the opposite. The overestimation could be explained by the optimization of the modeled assumptions as well as the S. Paulo advection. On the other hand, the nitrate behavior is probably due to its high solubility to the water and the particle distribution over S. Paulo urban area.

Acknowledgements: Financial support of the German Ministry for Education and Research, the Ministry of Science and Research of Northrhine-Westphalia, Frankfurt Environment Centre- ZUF (*Zentrum Unwelt Frankfurt*), ISAS, UFBAHIA, UFLONDRINA, *Centro Tecnológico e Hidráulico,* the *Secretaria do Meio Ambiente, CETESB* and the *Conselho Nacional de Desenvolvimento Científico e Tecnológico*, Brazil is gratefully acknowledged. We also thank Prof. Dr. Klaus Beheng from IMK (Germany), Dr. Maria C. Solci from U. E. Paraná (Brazil), Dr. Vania Tavares from U. F. da Bahia (Brazil) and Drs. W. Vautz, M. Schilling and Prof. Dr. D. Klockow from ISAS-Dortmund (Germany).

7. REFERENCES

Beheng, K.D. & Herbert, F. 1986. Mathematical studies on the aerossol concentraction in drops changing due to particle scavenging and redistribuition by coagulation. *Meteorol. and Atm. Phys.*, vol. 35, 212-219.

Flatau, P.J. 1989 "The CSU RAMS Cloud Microphysical module: General Theory and Code Documentation". Colorado St. Univ. Dep. Atm. Sci. Fort Collins, CO 80523. *Atmos. Sci.*, , 451, 88 pages.

Freitas, S. R., M. A. F. Silva Dias, P. L. Silva Dias, 1999. "Modeling the Convective Transport of Trace Gases by Deep and Moist Convection" submitted to Hybrid Methods in Engineering, Begell House.

Gonçalves F.L.T. & Massambani, O. 1998. "Atmospheric pollutant scavenging processes: a case study at Serra do Mar- SE Brazil." *Conference on Cloud Physics, 14th Conference on Planned and Inadvertent Weather Modification, Everett*, 109-111.

Gonçalves, F.L.T., Massambani O., Beheng, K.D., Solci-Palhares, Rocha, V., M.C., Schilling, M.,Vautz, W., Klockow, D. "Modelling and measurements of below scavenging processes in the highly industrialized region of Cubatão-Brazil" Accepted in the periodic *Atmos. Environ.* in November, 1999.

Molinari, J. 1985 "A general form of Kuo's cumulus parameterization." *Mon. Wea. Rev.*, 113, 1411-1416.

Mahler, Y. & Pielke, R.A., 1977. "A numerical study of the airflow over irregular terrain. "*Beitrage zur Physik der Atmosphäre*, 50, 98-113.

Molinari, J. "A general form of Kuo's cumulus parameterization." *Mon. Wea. Rev.*, 1985, 113, 1411-1416

Naik, M.S.; Khemani, L.T.; Momin, G.A.; Rao, P.S.P.; Safai, P.D. 1994. Variation in the ionic composition in convective showers in Pune, India. *Tellus*, vol.46B, 68-75.

Pruppacher, H.R. & Klett, J.D. 1997. "Microphysics of clouds and precipitation. Ed. Reidel Publ. Company, 714 pages.

Seinfeld, J.H. & Pandis 1998. Atmospheric and physics of air pollution. Ed.: J.Wiley & Sons, 1030 pages.

Vautz, W., Schilling, M., Gonçalves, F.L.T., Solci-Palhares, M.C.; Massambani, O., Klockow D. 1995. "Preliminar Analysis of Atmospheric Scavenging Processes in the Industrial Region of Cubatao, Southern Brazil." *Water, Air and Soil Poll.*, vol. 85,1973-1978.

Volken, M. A. 1994. A Model of Below-Cloud Scavenging of Aerosols and Trace Gases: Results and Observations. Thesis, Swiss Federal Institute of Technology, Switzerland, 157 pages

Walcek, C; Wang, P.K.; Toppalian, J.H.; Mitra, S.K. and Pruppacher, H.R. 1981. An experimental test of a theoretical model to determine the rate at which freely falling water drops scavenge SO_2 in air." *J. Atmos.Sci.*, vol.:38, pages: 339-355.

Whitby, K.T. 1980. The physical characteristics of the sulfur aerosols. *Atm. Environ.*,vol.12, 135-159.

ESTIMATING THE IMPACT OF NATURAL AND ANTHROPOGENIC EMISSIONS ON CLOUD CHEMISTRY

Lester Alfonso and G. B. Raga[1]

Centro de Ciencias de la Atmósfera, UNAM, Mexico City, 04510 Mexico

1. INTRODUCTION

It has been known for many years that clouds developing over the continents differ substantially in their precipitation efficiency from clouds developing under maritime conditions. The radically different cloud condensation nuclei (CCN) size distributions and compositions, play a clear role in warm precipitation development. A change in these CCN characteristics is expected to produce changes in rain development. In particular, enhanced CCN concentrations that could be produced either through natural (such as volcanic emissions) or anthropogenic processes, would be expected to inhibit rain production (Twomey, 1974, 1977; Albrecht, 1989). This effect has been observed in stratocumulus clouds and commonly named "ship tracks" (Radke et al., 1989). Nevertheles, it is not as straightforward to predict the impact on deep convective clouds.

A recent study by Rosenfeld (2000) presented evidence from Tropical Rainfall Measurement Mission (TRMM) satellite data that clouds developing near urban and industrial emissions have smaller droplet sizes and less precipitable water in them, for equivalent thermodynamic conditions. These results from Australia, Turkey and Canada, constitute further motivation to understand the links between dynamics-microphysics and chemistry of convective clouds developing in urban environments.

In the particular case of deep convection in Mexico City, Jauregui and Romales (1996) presented climatological trends of precipitation at the surface (utilizing a raingauge network distributed throughout the city) and indicated that the observed increase may be linked to the development of the urban heat island. Morfin and Raga (1998) used a 3-dimensional (3-D) cloud model with parametrized microphysics, and showed the importance of the orographic forcing in cloud development. Their results also indicated that the largest precipitation amounts fall up in the mountains, where there are virtually no surface observations against which to compare.

In this study we present preliminary results from a theoretical 1-dimensional (1-D) cloud model that includes detailed microphysics and inorganic chemistry. The study will continue to develop further, by incorporating chemical reactions for both inorganic and simple organics in an attempt to estimate the impact of urban emissions on precipitation development. Eventually, the results from the 1-D model will be adapted and included in the 3-D cloud model (discussed in Morfin and Raga, 1998).

2. NUMERICAL MODEL

A 1-D Eulerian model with detailed microphysics is used in this study, with the dynamical framework being based on Ogura y Takahashi (1971). The microphysical modules include droplet activation, condensation, coalescence and deposition, and the feedback between dynamics and microphysics is fully implemented.

The initial CCN are composed of ammonium sulfate, with sizes up to 1.0 μm. The microphysical algorithm for droplet evolution considers the development of drops up to 2.508 mm in diameter, similar to Takahashi (1975). The initial radius for cloud droplets is determined assuming that CCN grow under 100% relative humidity. The semi-explicit algorithm described by Clark (1973) is used for condensational growth. Since this algorithm uses an analytic solution for the supersaturation, it allows somewhat larger time steps than those used in explicit algorithms. Droplet evolution by condensation is computed with the Kovetz and Olund (1968) algorithm while growth by coalescence is calculated using the Berry and Reinhardt (1974) scheme.

The microphysical model in the 1D dynamical framework has been coupled to an aqueous phase chemistry model, for the prediction of pH evolution as a function of droplet size. The model closely follows Flossman et al. (1987), while aerosol mass and sulfate mass within droplets are based on Flossman et al. (1985). Aerosol and gas phase concentration evolution by condensation is implemented using the Kovetz and Olund algorithm, as described by Takahashi (1975). SO_2 difussion into droplets and S(IV) oxidation to S(VI) basically follows Flossman et al, (1987), but implementing an analytical equation for SO_2 difussion as in Pruppacher and Klett (1997). An oxidation rate of 5.0e-3 sec^{-1} was used in the simulations described here.

[1] Corresponding author's address: Graciela Raga, Centro de Ciencias de la Atmósfera, UNAM, Mexico City, 04510, Mexico; E-Mail: raga@servidor.unam.mx.

3. RESULTS

The sounding used was idealized, with a temperature gradient of -6ºK per kilometer constant up to 10km, where the tropopause is located. The relative humidity also has a constant gradient of -5% per km. Surface temperature was taken at 298ºK. Given this unstable sounding, the cloud that develops (cloudbase at about 1.0 km) has very large vertical velocities (up to 13 m/s). Afte only 15 minutes into the simulation the cloud is about 4 km deep and the maximum liquid water content reaches 3 g/kg.

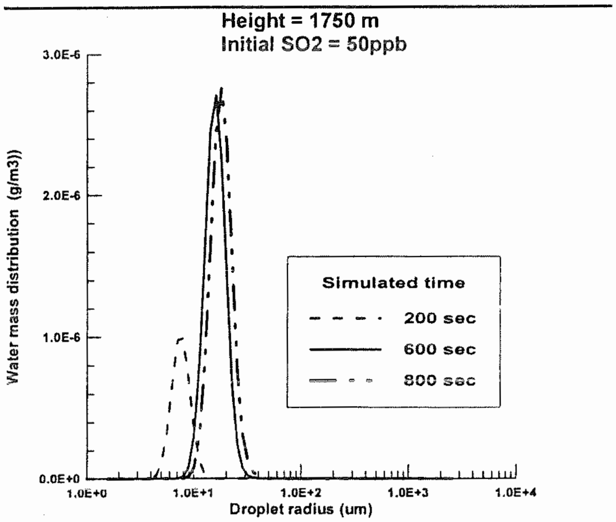

Figure 1. Water mass distribution as a function of droplet radius, for an incloud level of 1750 m above the surface. Three time periods are presented, after 200, 600 and 800 seconds of simulation. The initial SO_2 concentration was 50ppb.

Two initial ambient SO_2 concentrations were used: a) low background concentration (1ppb) based on other studies (e.g. Flossman et al, 1987) and b) high background concentration (50ppb). The latter would be associated with urban emissions in Mexico City (Raga et al, 1999) or with volcanic emissions. Measurements of ambient SO_2 were made in April-May 1999 about 10km from the rim of the active volcano Popocatepetl, located approximately 60 km SE of Mexico City. This volcano has been active since 1993, and currently constitutes the largest source of SO_2 in the world, about 10,000 tons per day on average (Delgado, personal communication). Baez et al (1997) collected cloud and rain water samples for ionic analysis, which provide some data to compare against the model results. Unfortunately, Baez et al (1997) did not make SO_2 measurements in 1994 and 1995, but since their sampling site was only a few kilometers from the sampling site in 1999, there is confidence in using the observed ambient SO_2 concentrations from the latter period.

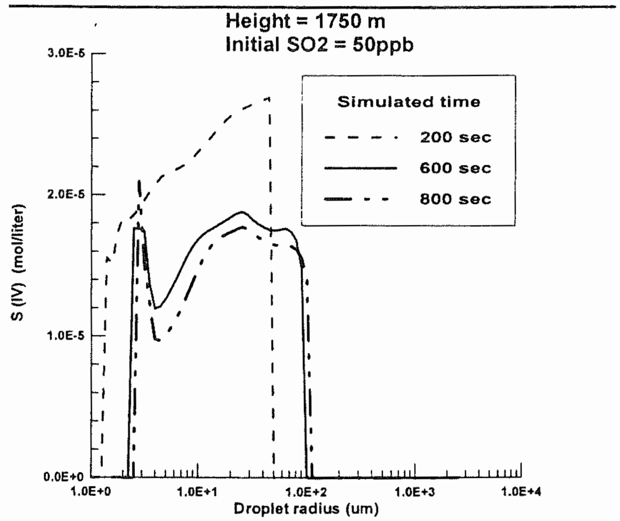

Figure 2. Same as Fig. 1, but for S(IV).

Figure 1 shows the water mass distribution for 3 different times in the simulation, at a height of about 750m above cloudbase. By 800 seconds, coalescence is only then starting to become important. Since the initial thermodynamic sounding is the same in both cases considered (low vs. high ambient SO_2), the water mass distribution for the low SO_2 is similar to the one presented in Fig. 1. Figures 2 and 3 resent the concentrations of S(IV) and S(VI) present in the droplets, as a function of droplet size. The onset of coalescence is evidenced by the increase in the respective concentrations for droplets larger than 30 μm. Initially S(VI) is maximum for the smallest droplets, and therefor the pH of those droplets is the most acidic.

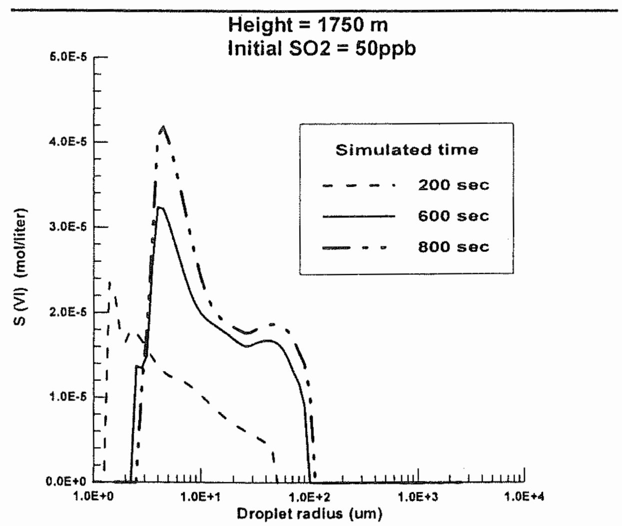

Figure 3. Same as Fig. 1, but for S(VI).

4. DISCUSSION

Figure 4 presents the variation of pH as a function of size for the 3 different time periods and for the same height above cloudbase discussed above. After only 200 seconds of simulation, the pH increases uniformly with droplet radius. For later periods, there is evidence of acidification for droplets larger than 3μm. At all times, the larger droplets are the most basic of the spectrum.

As mentioned above, Baez et al. (1997) collected cloud and rain water samples for about 10 days in 1994 and 1995, and the samples were then analyzed by ion cromatography to determine the concentration of the following ions: $SO_4^=$, Cl^-, NO_3^-, HCO_3^-, Na^+, K^+, Ca^{++}, Mg^{++}, NH_4^+. The pH and conductivity of the samples were also determined.

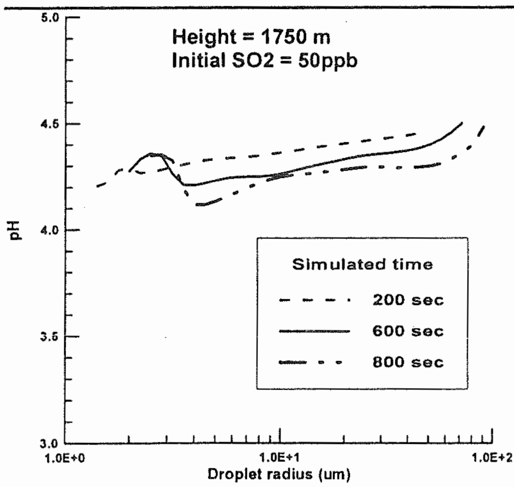

Figure 4. Same as Fig. 1, but for pH.

Figure 5 presents the pH for the case of low ambient SO_2 concentration. As expected, the pH in this case is much larger than thar presented in Fig. 4, by about a 22% for the largest droplets sizes. Again there is a minimum in pH for droplets of about 3μm, linked to the droplet spectral evolution.

The pH of cloudwater samples presented by Baez et al (1997) ranged from 4.68 up to 7.37. The model results are in reasonable agreement with the lower values presented by Baez et al (1997). About 64% of the samples obtained during that study have values of pH larger than 6.0. Based on the observed ambient SO_2 concentrations near the active volcano, the model produces much more acidic cloud droplets than the cloudwater samples obtained there. The results of Baez et al (1997) indicate that also NO_3^-, K^+ and Ca^{++} are present in large quantities in the cloudwater samples. Whenever Ca^{++} and NH_4^+ are present in approximately the same concentrations, then the sample is significantly acidic. In contrast, whenever Ca^{++} concentrations are much larger than NH_4^+, then the pH is larger than 6.0. It is therefore, possible that a large fraction of soil component was mixed in the cloudwater samples collected at the surface, which is not accounted for in the simulations.

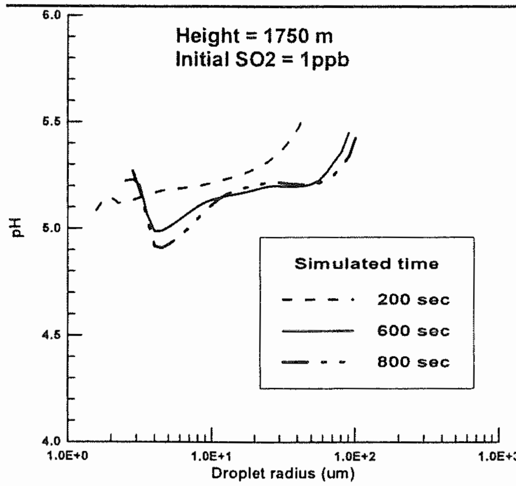

Figure 5. Same as Fig. 4, but for initial SO_2 concentration of 1ppb.

There are other aspects of the simulations that need to be noted, when comparing with observations. Firstly, the microphysical model does not allow for further activation of droplets after initialization. This could result in more SO_2 dissolving into larger droplets than would do otherwise. Also, it is important to note that the clouds sampled *may* have contained large amounts of ice present at higher levels. At present, the microphysical model does not consider ice formation and interaction with chemistry. Furthermore, there are no observations of NH_3 in the vicinity of the volcano, which could be present and thus, neutralizing the droplets.

Finally, it should be mentioned that there is a field campaign planned for this year's rainy season, with 2 observing periods (in July and October), during which gases, CCN and water samples will be collected and used to further validate the model.

5 ACKNOWLEDGEMENTS

This study was partially funded through grants from Papiit (# IN120898) and Conacyt (#27528-T).

6 REFERENCES

Albrecht, B., 1989: Aerosols, cloud microphysics and fractional cloudiness. Science, 245, 1227-1230.

Baez, A., R. Belmont, E. Azpra, M. Torres and H. Padilla, 1997: Cloudwater and precipitation chemistry at

Popocatepetl volcano: A high elevation site. J. Environ. Quality, 26, 253-258.
Berry, E. and R. Reinhardt, 1974: An analysis of cloud drop growth by collection: Part I. Double distributions. J. Atmos. Sci., 31, 1814-1824.
Clark T.L. Numerical modeling of the dynamics and microphysics of cumulus warm convection. *J. Atm. Sci.*, 1973, vol. 30, N 5, p.857-878.
Flossmann, A.E., W.D. Hall and H.R. Pruppacher, 1985: A theoretical study of wet removal of atmospheric pollutants. Part I: The redistribution of aerosol particles captured through nucleation and impaction scavenging by growing cloud drops. J. Atm. Sci., 42, 583-606.
Flossmann, A.E., Pruppacher, H. and J. Topalian, 1987: A theoretical study of the wet removel of atmospheric pollutants. Part II: The uptake and redistribution of $(NH_4)_2SO_4$ and SO_2 gas simultaneously scavenged by growing cloud drops. J. Atm. Sci., 44, 2912-2923.
Jauregui, E. and E. Romales, 1996: Urban effects on convective precipitation in Mexico City. Atmos. Environ., 30, 3383-3389.
Kovetz, A., and Olund, 1969: The effect of coalescence and condensation on rain formation in a cloud of finite vertical extent. J. Atmos. Sci., 26, 1060 -1065.
Morfin, J. and G.B. Raga, 1998: Modelling deep convective clouds over Mexico City. Proceeding of the Conference on Cloud Physics, Everett, USA, 17-21 August, 95-96.
Pruppacher and Klett, 1997: Microphysics of clouds and precipitation, Kluwer Academic Publishers. 954 pp.
Radke, L., J. Coakley and M. king, 1989: Direct and remote sensiing observations of the effects of ships on clouds. Science, 246, 1146-1149.
Raga,G.B., G. Kok, D. Baumgardner, A. Baez and I. Rosas, 1999: Evidence of volcanic influence in Mexico City aerosols. Geophys. Res. Lett., 26, 1149-1152.
Rosenfeld, D., 2000: Suppression of rain and snow by urban and industrial air pollution. Science, 287, 1793-1796.
Takahashi, T., 1975: Tropical showers in an axi-symmetric cloud model. J. Atm. Sci., 32, 1318-1330.
Twomey, S., 1974: Pollution and planetary albedo. Atmos. Environ., 8, 1251-1256.
Twomey, S., 1977: The influence of pollution on the shortwave albedo of clouds. J. Atmos. Sci., 34, 1149-1152.

ORGANIC AND INORGANIC SOLUTES IN FOG DROPLETS: A FULL CHARACTERISATION APPROACH

Stefano Decesari, Maria Cristina Facchini, Emanuela Matta, Sandro Fuzzi

Istituto di Scienze dell'Atmosfera e dell'Oceano – CNR, I-40129 Bologna, Italy

1. INTRODUCTION

The chemical composition of cloud/fog droplets derives from several concurrent physical and chemical processes taking place in the multiphase cloud system: a) nucleation scavenging; b) dissolution of trace gases into droplets; c) chemical reactions within cloud droplets; d) capture of interstitial aerosol particles by the droplets, although this is expected to be of minor importance.

Until recently, information on cloud chemical composition has been restricted to inorganic ions and a few low-molecular weight organic compounds. Some recent results have now shown that water soluble organic compounds (WSOC) (Facchini et al., 1999a) are also present in substantial amounts in cloud and fog droplets.

This paper presents some preliminary data on the chemical composition of both organic and inorganic species in fog water. The characterisation of WSOC in fog water was carried out following a new procedure recently developed by our group (Decesari et al., 2000).

2. FOG DROPLET SAMPLING

Fog droplet samples were collected at the field station of S. Pietro Capofiume, in the Po Valley (Northern Italy) in the period November 1998 – March 1999. The sampling of fog droplets was performed using an active string collector designed by Fuzzi ét al. (1997).

The instrument collects fog droplets suspended in an air stream created by a fan, by impacting them on cylindrical strings. Sampling flow rate is 17 m^3 min^{-1} and the collection efficiency is 43% of the actual fog liquid water content (LWC), with 50% cut-off calculated for each string of ca. 6 μm aerodynamic diameter (AED). It enables the collection of fog water up to 200 ml h^{-1}.

For the purpose of the present experiment, the fog collector was modified and all parts coming into contact with the fog droplets, including the sampling strings, were made out of stainless steel to avoid problems of artifact formation and adsorption on the surfaces for organic compounds. Collection was performed on an event basis.

Corresponding author address: S. Decesari, ISAO-CNR, Via Gobetti 101, Bologna, Itlay; E-Mail: s.decesari@isao.bo.cnr.it

3. CHEMICAL PROCEDURE

The collected samples were analyzed for inorganic ions by ion chromatography (IC) and the total WSOC was determined by a commercial Total Organic Carbon (TOC) analyser.

The speciation of WSOC was performed by a method consisting of a combination of three steps (Decesari et al., 2000). Ion exchange chromatography was first used to resolve the complex mixture of organic compounds in fog water into a few main classes of species (Fig. 1). The organic compounds were detected by measuring the UV absorption at 254 nm, preventing any significant interference from the co-eluting inorganic ions. Only nitrate significantly absorbs at 254 nm and is revealed by the detector. Three main classes of organic compounds were determined: a) neutral species; b) mono- and di-carboxylic acids; c) poly-carboxylic acids.

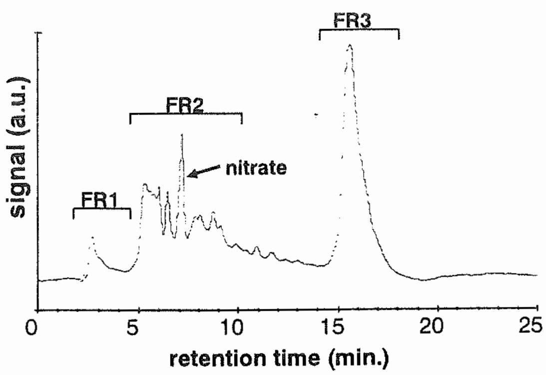

Figure 1. Chromatographic separation of the WSOC of a fog sample in three fractions performed on a DEAE anion-exchanger stationary phase. FR1: neutral species; FR2: mono- and di-carboxylic acids; FR3: poly-carboxylic acids. The nitrate peak also appears in the chromatogram.

TOC analysis was then used to determine the total carbon content in each class of organic compounds separated by the ion exchange chromatographic procedure.

Finally, proton Nuclear Magnetic Resonance (HNMR) allowed a characterisation of the main features of the organic compounds in each of the above classes (Fig. 2). On the basis of the HNMR characterisation we found that:

a) the neutral species are mainly polyols or polyethers;
b) the mono- and di-carboxylic acid fraction is mainly composed of hydroxylated aliphatic acidic compounds;
c) the polyacidic compounds are mainly unsaturated species of predominantly aliphatic character, with a minor content of hydroxyl-groups.

With the above procedure we were able to account for ca. 80% of the WSOC measured by TOC.

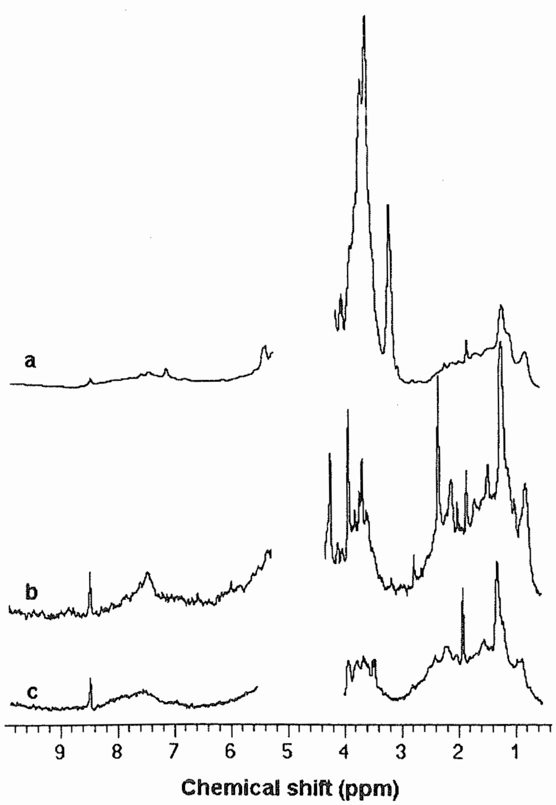

Figure 2. HNMR spectra of a) neutral species, b) mono/di-acids; c) polyacids, isolated from a Po Valley fog water sample. In the figure the horizontal axis refers to frequency shift of signals, compared to that of a reference (sodium 3-trimethyl-silyl-2,2,3,3-d_4-propionate). The 4.2-5.3 ppm region is not shown due to solvent interference.

4. RESULTS AND DISCUSSION

A total of 16 samples, characterized by a wide range of pH values (3.53 - 6.35) were collected during the sampling period. Collection was performed on an event basis; events typically lasted from four to 24 hours. Half of the samples were collected in January, which had an unusually high fog occurrence. It should be noted that in December fog events were also quite frequent the sub-freezing conditions made sampling impossible for most of the time.

Table 1. Statistics of the total solute composition of fog water in the Po Valley (winter 1998-1999). All data are expressed in $\mu g\ m^{-3}$. All inorganic species, formate, acetate and oxalate were measured by IC.

Chemical species	Minimum	Mean	Maximum
		Inorganic	
H^+	4.1E-05	1.2E-03	6.2E-02
Na^+	0.08	0.44	1.49
NH_4^+	3.5	7.5	18
K^+	0.15	0.30	0.73
Mg^{2+}	0.02	0.07	0.39
Ca^{2+}	0.17	0.82	4.4
Cl^-	0.29	0.86	1.9
NO_2^-	0.02	0.10	0.31
NO_3^-	6.0	13	36
SO_4^{2-}	3.3	7.3	23
		Organic	
Formate	0.05	0.71	4.9
Acetate	0.33	1.1	3.5
Oxalate	0.04	0.16	0.32
WSOC	6.7	10	29
Neutral compounds	1.9	3.3	9.9
Mono/di-acids	2.2	3.9	8.7
Polyacids	0.8	2.6	5.6

Table 1 shows a statistical summary of the whole data set on fog water chemical composition. Low molecular weight organic acids represent only a minor contribution to total organic acids in these samples. Acetate and formate are five to ten times less concentrated than total organic acids, and the concentration of oxalate is one order of magnitude lower.

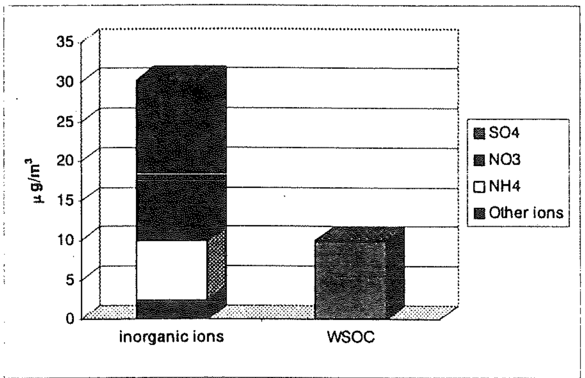

Figure 3. Average concentration in the samples of the major classes of water-soluble substances. Data are expressed in µg m^{-3} calculated by multiplying the measured concentrations in fog water by the fog liquid water content (LWC).

Fig. 3 shows the average concentration of inorganic and organic species in the collected fog samples. While the inorganic ions represent on average 75% of the total mass of solute, WSOC accounts for the remaining 25%, a significant fraction of the solute mass

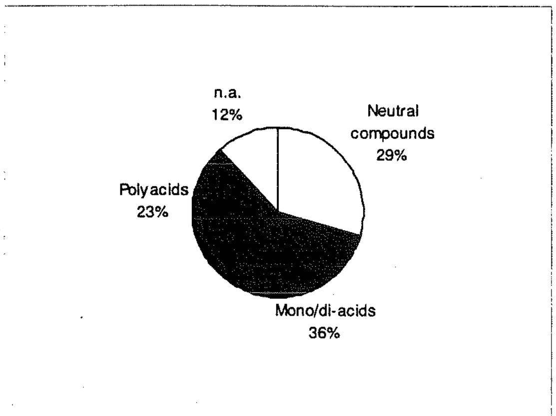

Fig.4. Percent distribution samples of water-soluble organic matter in Po Valley fog. Our speciation procedure accounted on average for 88% of WSOC mass.

The mass balance of WSOC is shown in Fig. 4. The three classes of compounds discussed previously were detected in all fog samples, and their relative contributions to WSOC was relatively constant. The "non analysed" WSOC can probably be attributed to volatile species which are lost during the fractionation procedure (Decesari et al., 2000).

5. CONCLUSION

The results presented here show that, although inorganic ions account for an average 75% of total fog water solution, the concentration of WSOC in the samples is by no means negligible. Acidic compounds are the dominant WSOC, accounting for an average of 59% of soluble organic species.

The presented methodology allows for the characterisation of both inorganic and organic components of fog/cloud samples, although the complex series of organic compounds can still not be characterised at the molecular level. Our methodology allows investigation of the role of WSOC in determining fog/cloud droplet properties (see e.g. Facchini et al., 1999b), which was not previously possible.

6. ACKNOWLEDGEMENTS

The present work was financed by the European Commission (EUROZEP Project ENV4-CT98-0785).

7. REFERENCES

Decesari, S., M.C. Facchini, S. Fuzzi and E. Tagliavini, 2000: Characterization of water soluble organic compounds in atmospheric aerosol: a new approach, *J. Geophys. Res.*, **105**, 1481-1489.

Facchini, M.C, S. Fuzzi, S. Zapoli, A. Andracchio, A. Gelencsér, G. Kiss, Z. Krivácsy, E. Mészáros, H.-C. Hansson, T. Alsberg and Y. Zebühr, 1999a: Partitioning of the organic aerosol component between fog droplets and interstitial aerosol, *J. Geophys. Res.*, **104**, 26821-26832.

Facchini, M.C., M. Mircea, S. Fuzzi and R. J. Charlson, 1999b: Cloud albedo enhancement by surface-active organic solutes in growing droplets, *Nature*, **401**, 257-259.

Fuzzi S., G. Orsi, G. Bonforte, B. Zardini, and P.L. Franchini, 1997: An automated fog water collector suitable for deposition networks: design, operation and field tests. *Water Air Soil Pollut.*, **93**, 383-394.

A CLOSURE EXPERIMENT ON THE AEROSOL ACTIVATION PROCESS

S. Guibert[1], J. R. Snider[2], and J. L. Brenguier[1],

[1] Météo-France, CNRM-GMEI (F); [2] University of Wyoming, DAS (USA)

1. INTRODUCTION

Cloudy-Column, as part of the second aerosol characterization experiment (ACE-2), is a closure experiment on the indirect effect of the aerosols on climate for marine boundary layer clouds (Brenguier et al. 2000). The aerosol indirect effect refers to possible changes of the cloud radiative properties due to anthropogenic modifications of the physical and chemical properties (APP) of the aerosols. The aerosol indirect effect is presently the most uncertain process in the evaluation of climate change. The cloud droplet number concentration (CDNC) is dependent upon the properties of a subset of the background aerosol, referred to as cloud condensation nuclei (CCN). CDNC thus varies with the origin of the air mass, from a few tens per cubic centimetre in a pure marine air mass, to more than 1500 cm^{-3} in a heavily polluted air mass. Changes of CDNC affect cloud precipitation efficiency (Albrecht, 1989) and its radiative properties (Twomey, 1977). The transformation of aerosols onto cloud droplet is referred to as the CCN activation process, which shall be parameterised in general circulation models (GCM).

This paper is concerned with a closure experiment on the activation process. The closure experiment aims at evaluating how accurate is the CDNC prediction derived from the APP measured in the boundary layer. The measured APP (input variable) is used to initialise the model of CCN activation for deriving a prediction of CDNC, which is then compared to the CDNC values measured in the cloud layer (control variable).

It has been recently reported that parameterizations of the activation process are overestimating CDNC (Chuang et al. 2000), though it is not clear yet if the discrepancies must be accredited to the parameterization itself, to the APP that are used for its initialisation, or even to instrumental errors in the measurements of input and control data. Our objective here is thus to test the model of the activation process before considering any parametrization. The tests are performed with data collected during the ACE-2 project in 1997 (Raes et al. 2000), using APP measured at the PDH ground station (Putaud et al. 2000), and CCN and cloud microphysical properties measured in situ with the Météo-France instrumented aircraft Merlin-IV (M-IV). The analysis includes 12 flights that have been performed between 18 June and 21 July, 1997. Some days were characterized by very clean marine air masses in the boundary layer, while some were significantly affected by anthropogenic pollution from Europe, providing mean values of CDNC from about *10* cm^{-3}, up to *250* cm^{-3}.

The model of the aerosol activation process is composed of two distinct calculation steps. The Köhler theory describes the hygroscopic properties of the aerosols. In particular, it provides the value of critical supersaturation S_c, associated to a critical particle radius r_c, that separates the stable and unstable regimes of particle growth. This is further referred to as the static step. The second calculation step, referred here to as the kinetic step, deals with the prognostic of the time evolution of supersaturation in a convective cell, and it depends on the vertical velocity of the cell w.

2. THE DATA SET

The 12 Cloudy-Column cases analysed here are summarized in Table I, with the corresponding date and flight number.

2.1 The aerosol data set

The APP have been measured at the Punta del Hidalgo (PDH) ground site, on the north-eastern coast of Tenerife (Putaud et al. 2000). They comprise the sub-micrometric aerosol composition at PDH, i.e. the ammonium to sulfate mole ratio, the aerosol mass loading and the relative abundance of each chemical species or category. The hygroscopic mass fraction, or water solubility, was evaluated as the ratio of the mass sum of all hygroscopic species divided by the total particulate mass. Particle size distributions were measured at *20%* relative humidity (*RH*).

2.2 Airborne measurements

The sampling flight pattern was generally a square of *60 km* side, with a diagonal oriented N-S, located N/NW of the Tenerife Island, with the southern corner at about *80 km* from PDH. Exceptions are on 20 June, 24 June, 7 July and 21 July, with flight tracks oriented SW/NE. The orientation and location of the flight tracks are indicated in Table I. The M-IV was equipped with two sets of instruments (Brenguier et al. 2000). On the fuselage, three PMS probes were

Corresponding author's address: S. Guibert, Météo-France, CNRM/GMEI, 42 av. Coriolis, 31057 Toulouse Cedex 01, FRANCE.
Email : guibert@cnrm.meteo.fr

installed for measurements of the particle size distribution at ambient humidity. Two of them are used here: the FSSP-300 for the particle diameter range *0.3-20 μm* (wet CCN and droplets) and the Fast-FSSP for the range *2.6-35 μm* (droplets). Inside the fuselage, four instruments were connected to a sampling inlet for measurements of the dry aerosol properties: Two CN counters for the total concentration of particles with diameters respectively larger than *5* and *10 nm*, a PMS-PCASP for the size distribution of particles in the diameter range *0.1-2 μm* and a CCN counter for measurements of the CCN activation spectra in the range of supersaturation between *0.2* and *1.6 %.*

3. CLOSURE METHODOLOGY

3.1 Input data quality assessment

PDH data are the most complete ones available on APP during ACE-2. However the instruments were sampling at a height of *55 m*, while most of cloud base altitudes observed with the aircraft were between *650* and *1400 m*. In addition, most of the flights were performed at a distance of *60* to *120 km* (up to *250 km* on 7 July) from PDH. This becomes significant with respect to the natural APP variability in the boundary layer. First of all, PDH dry aerosol measurements shall be compared to airborne measurements to estimate if the PDH data are representative of APP at the flight location. Airborne APP measurements are however limited. Only CN total concentration and the size distribution measured with the PCASP inside the aircraft can be used to compare with the PDH data. The aerosol dry size distribution measured with the PCASP is reported in Fig. 1, together with the PDH distribution.

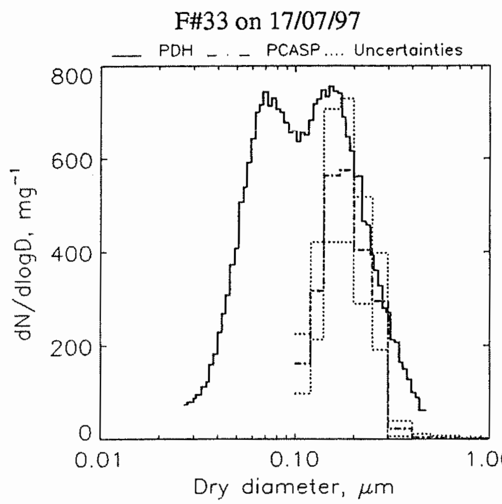

Fig. 1: Size distributions of dry aerosol measured at PDH (thick line) and on board the M-IV with the PCASP (dot-dashed line). The uncertainty range of the PCASP measurements is represented by dotted lines.

The agreement between the two data sets is summarized in Table I by the ratio RA_{100} of the airborne to PDH particle concentrations for particles with diameters in the range between *100* and *500 nm* (overlap range of the airborne and PDH measurements).For the cases A, E, I and J, the ratio varies between *1.07* (A) and *0.6* (I), with PDH concentrations between *114* (E) and *463* mg^{-1}. On 19 July (K), the ratio is much lower (*0.43*), but the analysis reveals that the aerosol properties were quite heterogeneous on this day, with larger concentrations in the South (PDH). In contrast, the ratio is much higher on 21 July (L) because the aircraft was flying downwind of the island.

3.2 Static closure experiment

The APP measured at PDH are then used to initialise the Köhler equation. The equilibrium size distributions of the hygroscopic particles are calculated at *87*, *92*, and *97 %* RH. Aircraft samples are selected below cloud base at an altitude where *RH* belongs to that range. The size distribution measured on board with the FSSP-300 is then compared in Fig. 2 to the PDH equilibrium size distributions at *87* and *97 % RH*.

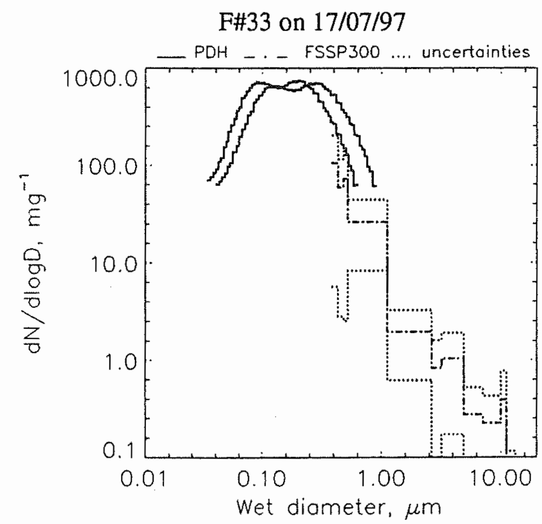

Fig. 2: Size distributions of wet aerosols derived from PDH measurements at 87 and 97 % RH (thick lines) and measured on board the M-IV with the FSSP-300 (dot-dashed line). The uncertainty range of the FSSP-300 is represented by dotted lines.

The agreement between the two data sets is summarized in Table I by the ratios $RH_{380,\ 430,}$ and $_{520}$ of the FSSP-300 concentration to the PDH one at *92 % RH*. The concentrations are obtained by cumulating the size distributions over the overlap diameter range, defined by the largest particle in the PDH equilibrium size distribution (slightly below *1 μm*) and the lower bounds of FSSP-300 size classes, at *380*, *430* and *520 nm* respectively. The agreement is poor with values of the ratio between *0.1* (RH_{520} in G) and *0.48* (RH_{380} in E). However, the overlap diameter range for the comparison corresponds to the upper classes of the PDH measurements and the first four classes of the FSSP-300, which are the most uncertain.

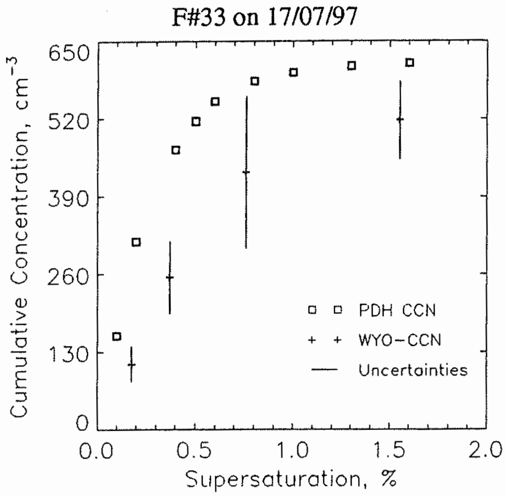

Fig. 3: CCN activation spectra derived from PDH measurements (square) and measured on board the M-IV with the CCN counter. The vertical bar illustrates the variability of the CCN measurements, with the mean value represented by a tick mark.

The CCN activation spectrum is also derived from the Köhler theory by assuming that the number of activated nuclei at a value of supersaturation S is equal to the number of particles with S_c smaller than S (equilibrium solution). Figure 3 shows an example of the comparison with the CCN activation spectrum measured on board the M-IV. The agreement between the two data sets is summarized in Table I by the ratios $RS_{2,\ 5,\ 8,\ 10}$ and $_{16}$ of the CCN counter to PDH derived CCN concentrations at *0.2, 0.5, 0.8, 1.0* and *1.6 %* supersaturation respectively. The agreement is also poor with values between *0.25* (RS_2 in G) and *1.48* (RS_{16} in A). The analysis in fact reveals that most of the CCN concentrations at low supersaturation for the polluted cases are overestimated by the Köhler prediction.

3.3 Kinetic closure experiment

Finally, the complete activation model is run. The difficulty at this point is to select a relevant value of vertical velocity to use for the convective updraft. CDNC can be measured accurately at about 100 m above cloud base, after all the droplets have reached a diameter larger than the Fast-FSSP sensitivity threshold. The value of vertical velocity measured at that level is not necessarily representative of the value encountered by the convective cell at the activation level. A statistical approach is applied to circumvent this obstacle. First, the probability density function of the vertical velocity *PDF(w)* is built from airborne measurements performed at cloud base. The model is run for various *w* values within the same range and the probability density function of the CDNC predicted values *Cp(w)* is derived. *PDF(Cp)* is then compared to the PDF of the CDNC values measured within the cloud layer *PDF(Cm).*

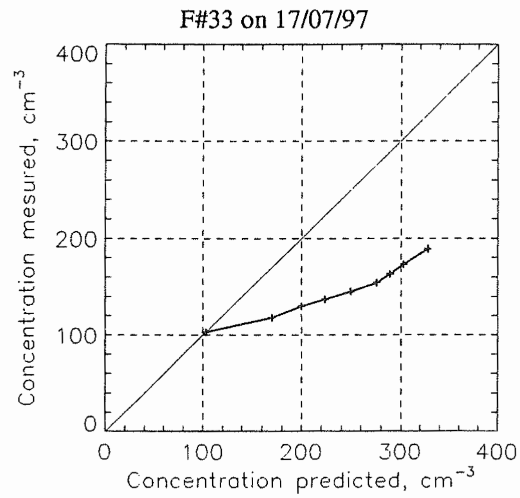

Fig. 4: 10 % percentiles of the CDNC cumulated distributions, measured in situ versus predicted from PDH APP measurements.

In Fig. 4, the 10 % percentiles of the predicted and of the measured cumulative distributions are compared. The agreement between the two data sets is summarized in Table I by the ratios $RP_{20,\ 50}$ and $_{80}$ of the measured CDNC distribution to the predicted one, at the *20, 50* and *80 %* percentiles respectively. This final test reveals that the predicted concentration is always overestimated with respect to the measured one, for both the pure marine and the polluted cases. For the *50 %* percentile, the discrepancy varies from a factor of *0.32* (A) to 0.59 (J), except for case D which shows a better agreement.

4. CONCLUSION

Snider and Brenguier (2000) have already concluded with the same procedure as in 3.3, but using the measured CCN spectra for initialisation of the activation model, that the predicted *PDF(Cp)* was comparable to the measured one. It follows that the source of the discrepancy reported here is likely to be related to the initialisation of the model with the APP measured at PDH. It is possible that the aerosol sampled at PDH is not representative of the aerosol at the flight level, but other hypotheses shall now be tested such as the aerosol partitioning into hygroscopic and non-hygroscopic chemical species.

5. ACKNOWLEDGMENTS

The authors acknowledge the contributions of the ACE-2 participants, and the support of Météo-France and the European Union under grants ENV4-CT95-0117 (Cloudy-Column) and EVK2-CT-1999-00340 (PACE).

6. REFERENCES

Albrecht, B. A., 1989: Aerosols, cloud microphysics, and fractional cloudiness. *Science*, **245**, 1227-1230.

Brenguier, J. L., P. Y. Chuang, Y. Fouquart, D. W. Johnson, F. Parol, H. Pawlowska, J. Pelon, L. Schüller, F. Schröder and J. R. Snider, 2000; An overview of the ACE-2 CLOUDYCOLUMN Closure Experiment. *Tellus.* **52B**, 814-826.

Chuang, P. Y., D. R. Collins, H. Pawlowska, J. R. Snider, H. H. Jonsson, J. L. Brenguier, R. C. Flagan, and J. H. Seinfeld, 2000: CCN Measurements during ACE-2 and their relationship to cloud microphysical properties. *Tellus.* **52B,** 842-866.

Putaud, J. P., R. Van Dingenen, M. Mangoni, A. Virkkula, H. Maring, J. M. Prospero, E. Swietlicki, O. H. Berg, R. Hillamo, and T. Mäkelä, 2000: Chemical mass closure and assessment of the origin of the submicron aerosol in the marine boundary layer and the free troposphere at Tenerife during ACE-2. *Tellus.* **52B,** 141-168.

Raes, F., T. Bates, F. McGovern, and M. van Liedekerke, 2000: The second aerosol characterization experiment (ACE-2): General overview, and main results. *Tellus.* **52B,** 111-125.

Snider, J. R., and J. L. Brenguier, 2000: Cloud condensation nuclei and cloud droplet measurements during ACE-2. *Tellus.* **52B,** 827-841

Twomey S., 1977: The influence of pollution on the shortwave albedo of clouds. J. Atmos. Sci., **34**, 1149-1152.

Date	*21/06/97*	*24/06/97*	*25/06/97*	*26/06/97*	*01/07/97*	*04/07/97*
Flight number	*#18*	*#19*	*#20*	*#21*	*#23*	*#24*
Flight letter	*A*	*B*	*C*	*D*	*E*	*F*
Flight track	*NE/SW*	*N/S*	*60 km square*	*60 km square*		*60 km square*
Position	*NW*	*N*	*N/NW*	*N/NW*		*N/NW*
Air masse	*intermediate*	*clean*	*clean*	*clean*	*clean*	*clean*
N_{mean}, cm^{-3}			*71*	*54*		
N_{PDH}/RA_{100}	*194 / 1.07*				*114 / 0.67*	
N_{PDH}/RH_{380}	*22 / 0.27*	*17 / 0.27*	*18 / 0.30*	*9 / 0.41*	*20 / 0.48*	*17 / 0.26*
N_{PDH}/RH_{430}	*12 / 0.22*	*11 / 0.24*	*11 / 0.30*	*5 / 0.37*	*11 / 0.46*	*10 / 0.24*
N_{PDH}/RH_{520}	*4 / 0.14*	*5 / 0.21*	*4 / 0.32*	*2 / 0.30*	*4 / 0.46*	*3 / 0.26*
N_{PDH}/RS_{2}	*163 / 1.10*	*89 / 0.64*	*95 / 0.94*	*65 / 0.52*	*97 / 0.78*	*88 / 0.56*
N_{PDH}/RS_{5}				*100 / 0.67*	*192 / 0.55*	*140 / 0.60*
N_{PDH}/RS_{8}	*328 / 1.33*	*182 / 0.94*	*177 / 1.00*			
N_{PDH}/RS_{10}				*154 / 0.85*	*389 / 0.46*	*254 / 0.95*
N_{PDH}/RS_{16}	*378 / 1.48*	*211 / 0.87*	*212 / 1.13*			
N_{PDH}/RP_{20}	*147 / 0.35*	*84 / 0.38*	*82 / 0.39*	*59 / 0.84*		
N_{PDH}/RP_{50}	*199 / 0.32*	*104 / 0.42*	*107 / 0.40*	*80 / 0.76*		
N_{PDH}/RP_{80}	*220 /0.34*	*117 / 0.52*	*124 / 0.48*	*93 / 0.77*		
Date	*07/07/97*	*09/07/97*	*17/07/97*	*18/07/97*	*19/07/97*	*21/07/97*
Flight number	*#26*	*#30*	*#33*	*#34*	*#35*	*#36*
Flight letter	*G*	*H*	*I*	*J*	*K*	*L*
Flight track	*SW/NE*	*60 km square*	*60 km square*	*60 km square*	*60 km square*	*SW/NE*
Position	*NE*	*N/NW*	*N/NW*	*NE*	*N/NW*	*W*
Air masse	*polluted*	*polluted*	*polluted*	*polluted*	*polluted*	*polluted*
N_{mean}, cm^{-3}		*245*	*111*	*179*	*130*	
N_{PDH}/RA_{100}			*312 / 0.60*	*463 / 0.64*	*422 / 0.43*	*181 / 2.17*
N_{PDH}/RH_{380}	*216 / 0.16*	*112 / 0.23*	*48 / 0.29*	*135 / 0.25*	*174 / 0.10*	*46 / 0.17*
N_{PDH}/RH_{430}	*150 / 0.13*	*74 / 0.21*	*31 / 0.26*	*101 / 0.22*	*132 / 0.08*	*30 / 0.15*
N_{PDH}/RH_{520}	*71 / 0.10*	*35 / 0.18*	*13 / 0.20*	*59 / 0.17*	*75 / 0.07*	*15 / 0.15*
N_{PDH}/RS_{2}	*913 / 0.25*	*404 / 0.56*	*287 / 0.38*	*450 / 0.30*	*438 / 0.36*	*181 / 0.31*
N_{PDH}/RS_{5}	*1508 / 0.63*	*568 / 0.83*				
N_{PDH}/RS_{8}			*533 / 0.81*	*755 / 0.73*	*627 / 0.49*	*252 / 0.70*
N_{PDH}/RS_{8}						
N_{PDH}/RS_{16}			*560 / 0.92*	*768 / 0.96*	*638 / 0.65*	
N_{PDH}/RP_{20}	*226 / 0.57*	*143 / 0.74*	*170 / 0.69*	*164 / 0.79*	*140 / 0.68*	*137 / 0.47*
N_{PDH}/RP_{50}	*383 / 0.56*	*306 / 0.49*	*250 / 0.58*	*284 / 0.59*	*272 / 0.54*	*187 / 0.50*
N_{PDH}/RP_{80}	*618 / 0.49*	*395 / 0.52*	*303 / 0.57*	*417 / 0.52*	*359 / 0.54*	*215 / 0.58*

Table I: Summary of the aerosol activation closure experiment

Observation of smoke and giant aerosol particles over Kalimantan and model results of the impact on warm cloud processes.

Jørgen B. Jensen[1], John Gras[1], and Ruth McDonnell[2].

[1]CSIRO Division of Atmospheric Research, Aspendale 3195, Victoria, Australia.
[2]Monash University, Clayton 3168, Victoria, Australia.

1. INTRODUCTION

With human development in remote areas, there may be large increases in the aerosol concentration as a result of forest clearing, agricultural practices, industrial emissions and urban development. Increases in aerosol particle concentrations have effects on both the precipitation formation (Warner and Twomey, 1967) and on the radiative properties of clouds (Twomey, 1977). In the clean tropics, a significant fraction of the total precipitation may fall from wholly warm clouds. The exact fraction is difficult to estimate, and it depends on location and season.

Growth of condensation drops on giant nuclei (dry radius, $r_d > 1$ μm), followed by these drops collecting smaller cloud droplets, is increasingly recognised as an important pathway for forming raindrops. When the concentration of aerosol particles (e.g. cloud condensation nuclei, CCN) increases, then more cloud droplets will be activated, and the average super-saturation will decrease. This results in slower condensation growth of drops formed on both giant nuclei and small CCN. Consequently all drops will have smaller sizes than they would have achieved in clouds formed clean air. When drops are smaller, they fall slower and they also have reduced collision efficiencies.

The purpose of the present study is to use measurements for a cumulus cloud growing over southern Kalimantan (Indonesian part of Borneo) to calculate the growth rate of all cloud droplets, including those formed on giant nuclei, for a small air volume ascending from below cloud base to a level 2 km higher. Measurements of giant nuclei in the inflow air of tropical cumulus clouds are very scarce. Those reported here for coastal Kalimantan in October 1998 were made from the AFTS F27 research aircraft, instrumented jointly by CSIRO and Meteorological Research Institute (Japan). This period was characterised by relatively clean, background air quality. In our model, the growth of droplets on all aerosol particles in a 1 litre air volume is calculated using a kinematic parcel model with condensation, entrainment and coalescence. The coalescence is calculated using Gillespie's (1975) stochastic coalescence model, which allows for the tracking of individual aerosol particles through condensation and coalescence events.

The aerosol observations, for all particle sizes, were used to calculate a "reference" case. In other model runs the same concentration of giant nuclei was used but the concentration of smaller particles ($r_d < 1$ μm) was varied. Giant nuclei were found to be predominantly sea-salt, for which the concentration will be independent of the increase in concentration of small particles induced by human activity.

2. OBSERVATIONS

2.1 Cloud observations

The cumulus cloud, see Fig. 1, was observed in the afternoon of 20 October 1998. Four penetrations were made between cloud top (3300 m) and cloud base (1700 m), followed by an ascent up into cloud base and a flight leg 170 m above the surface.

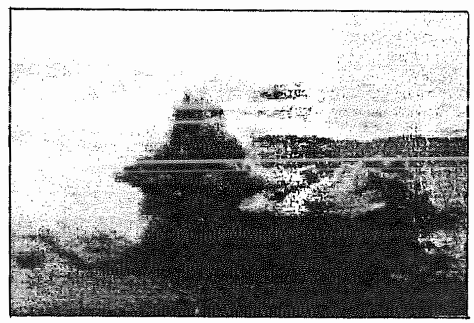

Figure 1. Photo of the study cloud from the side.

Cloud droplet concentration (N_c, $r < 20$ μm) and drizzle drop concentration (N_d, $r > 20$ μm) are shown for the 6 flight legs in Fig. 2. The drizzle drops concentration was calculated using the largest drops measured with the PMS FSSP probe and all the drops measured with the PMS 2D-C probe. The cloud activated about 650 cm^{-3}, see Figs. 2d and 2e. Small raindrops were found near cloud top, see Fig. 3, but no rain was observed below cloud base, possibly due to the cloud dissipating too rapidly.

2.2 CCN and giant nuclei observations

Measurements of aerosol particles below cloud base were made using a static cloud condensation nuclei counter operated at 0.5% supersaturation ($r_d \approx 0.02$ μm), a PMS ASASP sensor with 15 size bins between about 0.1 and 1.5 μm, and an impactor for larger aerosol particles.

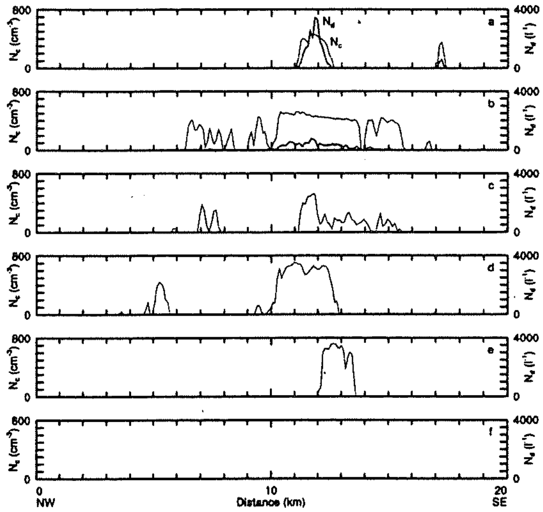

Figure 2. Cloud droplet concentration (N_c, r <20 μm, thin line) and drizzle drop concentration (N_d, r >20 μm, bold line).

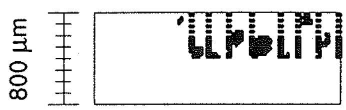

Figure 3. Examples of 2D-C images of drizzle drops for 20 October 1998. The vertical bars separate individual images of droplets which are seen as rounded "blobs". The probe had a limited viewing area due to an electronics problem. The largest drop has a diameter of about 200 μm.

The CCN counter measured about 2000 cm^{-3} during the lowest flight leg. For particles with sizes between those determined using the CCN counter and the ASASP (0.02 < r_d < 0.1 μm), concentrations were determined assuming a distribution shape the same as that observed for particles in remote marine air reported by Gras (1995).

The ASASP measurements were made at ambient relative humidity. We assume that the particles are solution drops, consisting of 50% ammonium-sulfate, $(NH_4)_2SO_4$ and 50% of insoluble material in an internal mixture. From the size bins of the ASASP probe and this chemical composition, we calculate the salt mass corresponding to each ASASP size bin (Jensen et al., 2000).

Larger aerosol particles (giant nuclei) were impacted on small polycarbonate slides, which were positioned outside the aircraft, perpendicular to the airflow, for a few minutes. The slides have a cross-sectional area of about 2 cm^2, which at an airspeed of 100 $m\,s^{-1}$ yields a sample volume of 20 $\ell\,s^{-1}$, or about 1 $m^3\,min^{-1}$. The impactor slides were typically exposed for 2 - 10 minutes, thus providing a reasonable estimate of the sizes and concentrations of giant nuclei occurring in the same concentrations as raindrops (e.g. 20 - 50 m^{-3} using the Marshall-Palmer distribution).

The giant nuclei were sized at 85% relative humidity (RH) using a microscope and video frame grabber; figure 4 shows an example. A clear majority of the Indonesian particles were solution drops when viewed at 85% relative humidity; this is consistent with sea-salt composition and not mineral dust. We calculate the mass in each giant nuclei by assuming that they consist of pure NaCl solution in equilibrium at 85% RH. The size distribution of the giant nuclei measured below cloud base is shown in Figure 5. The figure also shows the results from an un-exposed control slide, as well as Woodcock's (1953) measurements.

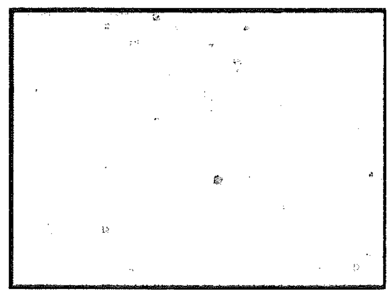

Figure 4. Example of an image of giant aerosol particles. The largest particle has a radius of 8 μm. There were typically 100 such images for each impactor slide.

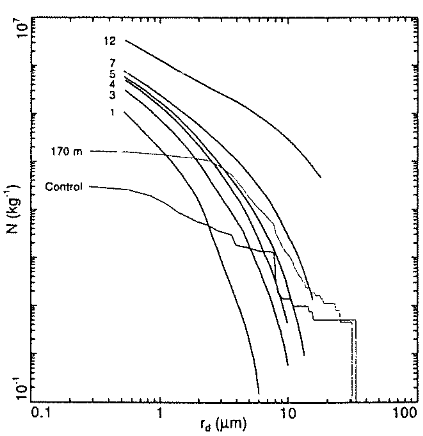

Figure 5. Cumulative distribution of concentration (N) of giant nuclei as a function of dry radius (r_d). The measurements were obtained on 20 October 1998 during a flight leg 170 m above the surface. The figure also shows as a control the cumulative distribution obtained from an un-exposed slide, and Woodcock's (1953) measurements as a function of Beaufort wind force (curves labelled 1 - 12).

Two features are immediately apparent from Fig. 5: (i) The exposed slide shows about a factor 10 more giant nuclei than does the un-exposed control slide, thus giving confidence in the procedure, and (ii) the observed spectrum follows Woodcock's (1953) curves well in the radius range of 4 - 15 μm. For sizes larger than 15 μm, the cumulative concentration is low and thus not well determined. For radii smaller than 2 μm the impaction efficiency is reduced (see e.g. Ranz and Wong, 1952).

In the range of 4 - 15 μm dry aerosol radius, the observed distribution falls between Woodcock's distributions for Beaufort wind force 5 and 7. These wind forces correspond to speeds higher than the aircraft-observed wind speeds (5 - 11 m s^{-1}) in the boundary layer. Woodcock's observations were taken over the ocean off Massachusetts and upwind of Hawaii. In the coastal zone of Kalimantan there are numerous giant nuclei with concentrations similar to Woodcock's observations. Two other slides were exposed later during the same flight at distance of more than 100 km inland, in air that had not been affected by the sea breeze of the day. Both samples showed virtually the same giant nuclei concentrations as the coastal sample. Air observed over Kalimantan would have been over land for about 24 hours if it had either advected inland from western Kalimantan or resulted from a local sea-breeze the previous day. This air retained its maritime giant aerosol character, although from a thermodynamic point of view the 1.5 km thick boundary layer was nearly continental in character.

3. MODEL CALCULATIONS

3.1 Model initial conditions

For the model runs to be presented here, the modelled cloud volume was restricted to 1 litre due to the computational requirements caused by the accurate coalescence scheme. This is smaller than required to make the calculation comparable with raindrops which typically occur in concentrations of 1 per 50 litre; nevertheless, the model is a powerful tool for comparing the strength of warm cloud processes in environments with different aerosol concentrations. The 1 litre sample volume also restricts the size of the largest aerosol particle which can be included; only particles occurring in 1 ℓ or larger concentrations are included. For the present giant nuclei distribution, this limits the largest of the modelled giant nuclei to 5 μm dry radius.

The model is initialised with a 1 m s^{-1} updraft speed. This is kept constant from 200 m below cloud base (1585 m MSL) to 3225 m MSL, where the parcel entrains environmental air in a mass-ratio of 2 parts cloud to 1 part environment. This entrainment fraction is roughly in accord with the thermodynamic properties of the centre of the top-most aircraft penetration of the study cloud. The entrainment event is specified as having classical homogeneous evaporation (Baker and Latham, 1979), and after completion of the evaporation, the cloud parcel ascends once again at 1 m s^{-1} until it reaches 3250 m MSL which was the level of the top-most cloud penetration.

The extended aerosol spectrum is shown in Fig. 6. In order to examine the sensitivity of the warm rain process to aerosol concentration, we define the "aerosol concentration factor" (*ACF*). The giant nuclei are assumed to be of marine origin, and their concentration remain unchanged for all runs. The sub-micrometer aerosol can increase due to biomass burning and other human activity. An aerosol concentration factor of unity corresponds to the spectrum shown in Fig. 6. An aerosol concentration factor of 2 implies that all the concentration values for aerosol radii less than 1 μm have been increased by a factor 2. Aerosol concentration factors less than 1 imply cleaner air than was observed on 20 October 1998. During the 1997 biomass burning period, the aerosol concentration was a factor of 10 - 40 higher than those shown in Fig. 6.

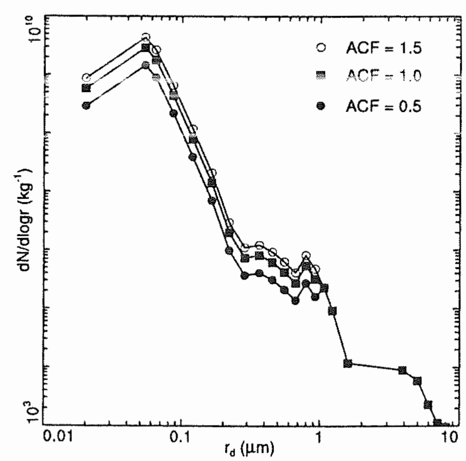

Figure 6. Size distribution of aerosol particles. Separate curves are shown for aerosol concentration factors in the range 0.5 - 1.5. The curve for ACF = 1.0 shows the observed spectrum.

3.2 Model results

The model was run with aerosol concentration factors 0.5, 0.7, 1.0 and 1.5. These correspond to a range from clean air to moderately polluted air. As a measure of the strength of the warm rain process, we take the sizes of the three largest drops. We focus on the largest drops since they are the only ones which contribute effectively to the precipitation flux.

Figure 7 shows the resulting drop sizes as a function of the aerosol concentration factor. The results show a marked decrease in the sizes of the largest drops as the

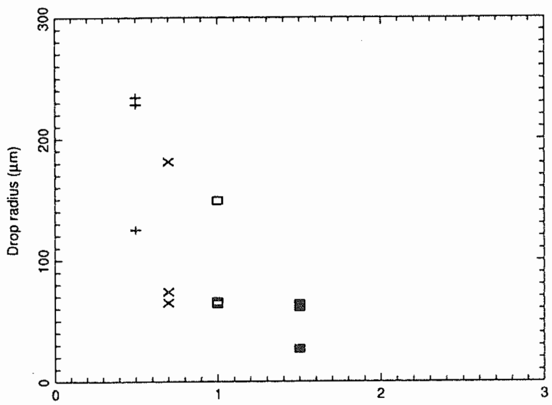

Figure 7. Drop radius for the three largest drops modelled at 3250 m altitude. These are shown as a function of the aerosol concentration factor (ACF). The reference case has ACF = 1.0.

aerosol concentration is increased. There is some variability from run to run which is caused by the stochastic properties of the coalescence scheme; ideally each concentration factor should be modelled with an ensemble of runs. The values shown in Fig. 7 are also based on just one updraft profile and final level; changing the updrafts and final altitude will result in different numerical results. Nevertheless the decrease in the sizes of the largest droplets as the aerosol concentration increases, see Fig. 7, demonstrates that the rate of formation of warm rain is extremely sensitive to modest increase in aerosol particle concentration, be it from biomass burning or other human activity.

Increasing the aerosol concentration from aerosol concentration factor 1 to 1.5 (a very modest increase) leads to a halving of the large drop radii. This radius decrease corresponds to a reduction in the drop volume of a factor 8. Secondly, the fall speeds of small raindrops (r = 40 - 600 μm) is approximately linearly dependent on drop size (Rogers and Yau, 1988); i.e. halving the dropsize leads to a halving of the fallspeed. Combining the effect of decreased drop volume and decreased fallspeed leads to a reduction in the formation of warm rain flux by a factor of 16, for a relatively small increase in the concentration of small aerosol particles of just 50%. For aerosol concentration factors of 10 - 40, as are observed during the 1997 fires, the warm rain process will be even slower. The tendency for slower development of the precipitation by coalescence is not surprising in view of Squire's (1952) ideas of the colloidal stability of clouds, but the calculated magnitude of the reduction of precipitation development is cause for concern for warm rain formation when aerosol particle concentrations increase.

The result is consistent with Rosenfeldt's (1999) finding for Kalimantan clouds with identical cloud top temperature, that the clouds growing in dense smoky air contained less precipitation than those growing in cleaner air. More importantly, it demonstrates that even the smaller scale fires used as a clearing and land management tool in Kalimantan and other tropical areas may well have a significant impact on warm rain formation, despite the presence of giant sea-salt nuclei.

ACKNOWLEDGEMENTS

Funding for PACE-5 and PACE-6 was provided by Science and Technology Agency (Japan), COSSA's Aircraft Program, CSIRO's Multi-Divisional Program for Climate Change, and AusAID as part of the Indonesian Government Sector Linkages Program (GSLP).

REFERENCES

Baker, M. B. and J. Latham, 1979: The evolution of droplet spectra and the rate of production of embryonic raindrops in small cumulus clouds. *J. Atmos. Sci.*, **36**, 1612-1615.

Gillespie, D. T., 1975: An exact method for numerically simulating the stochastic coalescence process in a cloud. *J. Atmos. Sci.*, **32**, 1977-1989.

Gras, J. L., 1995: CN, CCN and particle size in Southern Ocean air at Cape Grim *Atmos. Res.*, **35**, 233-251.

Jensen, J. B., S. Lee, P. B. Krummel, D. Gogoasa, J. Hudson, M. Harvey and J. Gras, 2000: Precipitation in marine cumulus and stratocumulus. Part II: Observations of entrainment, aerosol particles, cloud droplets and drizzle drops. To be submitted to *Atmos. Res.*

Ranz, W. E., and J. B. Wong, 1952: Impaction of dust and smoke particles on surface and body collectors. *Indust. and Eng. Chem.*, **44**, 1371-1381.

Rogers, R. R., and Yau, M. K., 1988: A short course in cloud physics, third edition. Pergamon Press, Oxford, U.K., 293 pp.

Rosenfeldt, D., 1999: TRMM observed first direct evidence of smoke from forest fires inhibiting rainfall. *Geophys. Res. Let.*, **26**, No 20, 3105-3108.

Squires, P.,1952: The growth of cloud drops by condensation. Part II. The formation of large cloud drops *Austral. J. Sci. Res., Ser. A*, **5**, 473-499.

Twomey, S., 1977: The influence of pollution on the shortwave albedo of clouds. *J. Atmos. Sci.*, **34**, 1149-1152.

Warner, J, and S. Twomey, 1967: The production of cloud nuclei by cane fires and the effect on the cloud droplet concentration. *J. Atmos. Sci.*, **24**, 704-706.

Woodcock, A. H., 1953: Salt nuclei in marine air as a function of altitude and wind force. *J. Meteor*, **10**, 362-371.

DETERMINATION OF PRECIPITATION RATES AND THUNDERSTORM ANVIL ICE CONTENTS FROM SATELLITE OBSERVATIONS OF LIGHTNING

A.M. Blyth[1], H.J. Christian Jr[2], K. Driscoll[2] and John Latham[3]

[1]Physics Dept, NMIMT, Socorro, New Mexico 87801

[2]ES43, NASA/MSFC, Huntsville, Alabama 35812

[3]MMM Division, NCAR, PO BOX 3000, Boulder, CO 80307-3000

INTRODUCTION

As a first step in the possible exploitation of satellite- borne lightning measurements (Christian and Goodman (1992), Christian, Blakesee and Goodman (1992)) made with NASA/MSFC devices, Baker, Christian and Latham (1995) developed a crude model of multiple lightning activity in thunderclouds, with a view to examining the hypothesis (supported by the research of Chauzy et al. (1985), Goodman, Buechler and Wright (1988), Goodman and Buechler (1990), Orville (1990), Williams et al. (1990) and others) that quantitatively definable relationships exist between lightning frequency f and thundercloud parameters such as precipitation rate (P), updraught speed (w), radar reflectivity (Z), cloud-width (W) etc. If such relationships are established, then measurements made with the OTD (Optical Transient Detector) or its successor, the LIS (Lightning Imaging Sensor), can be used to derive values of P, w, Z and other parameters; and the instrument could thus have significant forecasting or nowcasting importance. This preliminary work yielded the conclusion that over a wide range of conditions f was roughly proportional to the first power of the parameters Z and W (and also the ice crystal and graupel pellet concentrations); and, in some circumstances, to around the sixth power of w. The relationship between f and P depended critically on the extent to which the value of w deter- mined the location of the "balance level" in the thundercloud, i.e. the altitude at which the precipitation started to fall towards ground.

We reiterate here a point stressed by Baker et al., that their "model" cannot be regarded as a quantitatively adequate thunderstorm electrification model, but as rather a vehicle enabling sensitivity tests to be conducted into the possible relationships between f (which models have not computed hitherto, because of the complexity and unknown features of thunderstorm characteristics following the first lightning stroke) and the cloud parameters defined earlier. In these sensitivity tests each parameter was varied in turn the others being held constant thus making no concession to the fact that strong interdependencies exist between some of them. These workers considered that our current limited understanding of multiple lightning activity rendered premature the utilisation of a more comprehensive model; and indeed, that the simplicity of this first model (in which explicit cloud microphysics is retained) is helpful in identifying the separate sensitivities of f to the individual cloud parameters.

RELATIONSHIPS BETWEEN LIGHTNING ACTIVITY AND CLOUD ICE CONTENT

In this section we present some preliminary results concerned with possible relationships between lightning frequency f and total ice content I: and in particular the possibility that measurements of f might yield information on the ice crystal concentrations in the anvils of thunderclouds, a parameter of considerable climatological importance.

It is well established that thunderstorms - more specifically thunderstorm anvils - are an important source of ice particles in the upper atmosphere, and that such particles exercise a considerable influence on the radiative balance of the atmosphere.

A simple non-dimensional analysis indicates that f might be roughly proportional to thunderstorm non-precipitating ice content, I. This analysis, of course, is not identifiably associated with a particular region of a thundercloud, although it is most likely, in reality, to relate closely to the highest levels of the charging zone, since this is where the great preponderance of the charging occurs. Accordingly, it was decided to use a re-cently refined version of our model to examine the relationships between f and I at three separate locations: (1), the top of the charging zone; (2), throughout the charging zone, the lower level of which is at either 0C or -3C, according to whether ice is assumed to be created by either the primary nucleation mechanism or the Hallett-Mossop process; (3), the ice crystal anvil.

In the case of (1), our preliminary results indicate that for both glaciation mechanisms mentioned earlier f increases roughly linearly with I, as predicted by the dimensional analysis, and illustrated in Table 1. Such a dependence is not surprising, since the charging (resulting from rebounding collisions between ice crystals and growing graupel pellets) is principally concentrated near the balance level, and the charging rate per unit volume (which will determine the rate at which breakdown fields can regenerate after a lightning flash) depends on the numbers and sizes of ice crystals in this region.

Virtually identical results were obtained in the case of (2), which is as expected, since both the ice content and the charging rate in the charging zone increase rapidly as the altitude increases towards the highest region (the balance level).

In the case of (3), the value of I increased steadily with time, whereas the value of f tended to be roughly time-independent. This result is not surprising since, on our simple model, in which the dimensions of the anvil are fixed, its ice content increases linearly ly ly with time, whereas - once the cloud is fully developed - that in the charging zone remains roughly constant throughout much of the active period of lightning production.

Plots of f against J, the upward flux of ice crystals through the top of the charging zone into the ice crystal anvil of the model thundercloud indicate a relationship between these two parameters which is close to linear.

It follows from the above considerations that a fixed mass Mi of ice (in the form of non-precipitating crystals) can be associated with a single lightning stroke; and the preliminary computational work conducted to date suggests that a characteristic value for Mi is around 106 kg. This figure, emanating from a simplistic model and with no direct observational evidence against which to test it, cannot be regarded as accurate. The same statement must be applied to the crude calculations that follow. Our primary concern at this stage is simply to illustrate how it is possible, in principle, to derive characteristics of ice crystal anvils from satellite measurements of lightning. Detailed global-scale measurements of anvil characteristics are urgently required.

Taking the above-mentioned value for Mi, and assuming a figure of 40/s (as determined from OTD measurements) for the global lightning frequency fglob, we deduce that the global flux Jglob of ice crystals upwards into thunderstorm anvils is approximately 4.107 kg/s.

An estimate of the global ice crystal content Mglob present in thunderstorm anvils can be determined by noting that the rate of creation of cirrus crystals by thunderstorm activity (the product Mi.fglob) must be equal to Mglob/tanv, where tanv is a characteristic time defining anvil dissipation. Taking tanv_4 s, and the above-mentioned values of Mi and fglob, we obtain a global ice crystal thunderstorm anvil content Mglob of 4.1011 kg.

For an individual thunderstorm or a thunderstorm complex, the amount of ice (as crystals) introduced into the anvils is given simply by the product Mi.Ntot, where Ntot is the satellite-derived number of lightning strokes associated with the storm.

Further reinforcement of the hypotheses that simple relationships exist between F and P, and between F and I has emerged from the work of Driscoll (1999), who presented scatterplots illustrating simple log-linear relationships between lightning activity as measured by the satellite-borne

MSFC/NASA Lightning Imaging Sensor (LIS) and the brightness temperature T at both 85 and 37 GHz, measured by the TRMM Microwave Imager. The higher frequency corresponds to ice crystals in the anvil regions of thunderclouds, and the lower frequency principally to larger ice particles (characteristically graupel) at lower levels in the clouds. Driscoll reports that these relationships are consistent throughout the seasons in a variety of regimes, suggesting the existence of a global dependence between lightning activity and cloud ice content.

Much more data acquisition and analysis, together with computational improvement, are required in order to obtain more definitive and quantitative information on the question of the extent to which satellite measurements of lightning can provide estimates of large-scale and global upper level atmospheric ice crystal contents resulting from thundercloud activity. These first results, however, are encouraging, and if confirmed should be of climatological importance.

ACKNOWLEDGEMENTS

This work was supported by NASA/USRA.

REFERENCES

Baker, M.B., H.J.Christian and J.Latham (1995) "A computational study of the relationships linking lightning frequency and other thundercloud parameters" Quart J Roy Met Soc., 121, 1525-1548

Chauzy, S., Chong, M., Delannoy, A. and Despiau, S. (1985) The June 22 tropical squall line observed during COPT 81 experiment: Electrical signature associated with dynamincal structure and precipitation. J. Geophys. Res. 90, 6091-6098.

Christian, H.J. and Goodman, S. (1992) "Global observations of lightning from space". Proc. 9th Internat. Conf. on Atmospheric Electricity, St. Petersburg, 316-321.

Christian, H.J., R.J.Blakesee and S.J.Goodman (1992) Lightning imaging sensor for the earth observing system. NASA Tech. Memorandum 4350.

Driscoll, K. (1999) "A comparison between lightning activity and passive microwave measurements". Proc. 11th Internat. Conf. on Atmospheric Electricity, Guntersville, Alabama, 523-526.

Goodman S.J., D.E.Beuchler and P.D.Wright (1988) Lightning and precipitation history of a microburst-producing storm. Geophys. Res. Letters, 15, 1185-1188.

Goodman S.J. and D.E.Buechler (1990) Lightning-rainfall relationships. Proc. AMS Conf. on Operational Precipitation Estimation and Prediction, Anaheim, California, 1990.

Orville, R.E. (1990) Winter lightning along the East Coast.Geophys. Res. Lett., 17, 713-715.

Williams, E.R., S.G.Geotis, N.Renno, S.A.Rutledge, E.Rasmussen, T.Rickenback. "Hot Towers" in the tropics. Proc AMS Conf on Atmos. Elect., Alta, Canada, 1990.

ELECTROSCAVENGING AND CONTACT NUCLEATION IN CLOUDS WITH BROAD DROPLET SIZE DISTRIBUTIONS

Brian A. Tinsley

Center for Space Science, University of Texas at Dallas, Richardson, TX 75083-0688, USA

1. INTRODUCTION

The question of the importance of contact ice nucleation in clouds has been an unresolved issue for many years (Cooper, 1974; Young, 1974; Vali, 1974; Desher and Vali, 1992; Meyers et al., 1992). In their study of clouds with high and unexplained rates of ice production Hobbs and Rangno (1985) suggested that in these clouds, which had a broad droplet size distribution, the initial ice formation might be due to contact ice nucleation. Beard (1992) reviewed various ice nucleation processes and concluded that contact nucleation could be important at temperatures above about -10°C if the ice forming nuclei were of 'giant' size, i. e., greater than 1 μm in diameter. He also suggested another possible mechanism, not involving giant nuclei. When mixing and entrainment in clouds causes evaporation of electrically charged droplets the resulting aerosol particles (evaporation nuclei) are highly charged (losing only slowly the typically several hundred elementary charges retained from the droplets). We have shown (Tinsley et al., 2000) that the collection efficiencies for such charged nuclei are one or more orders of magnitude greater than for uncharged nuclei. We call this process electroscavenging.

Beard (1992) also noted that the evaporation nuclei are also likely to be effective as contact ice nuclei. This is because of their (temporary) retention of adsorbed sulfate and organic materials scavenged as vapors or solids by the droplet before evaporation (Garrett, 1978; Rosinski and Morgan, 1991), which increase the probability of ice nucleation occurring at contact. Thus it is of interest to estimate the importance of contact ice nucleation of electroscavenged evaporation nuclei relative to other forms of ice nucleation, such as deposition nucleation for various types of clouds.

2. CHARGES ON DROPLETS

There are extensive measurements showing typically several hundred elementary charges on droplets, generally positive at cloud tops and negative at cloud base for early stages of development of clouds (Pruppacher and Klett, 1997, sect. 18.4; MacGorman and Rust, 1998, ch. 2). When such charged droplets evaporate due to mixing processes, e. g., as at the tops of stratocumulus clouds, the relatively large droplet charge that is retained on the residual aerosol particles decays towards an equilibrium value. The decay can be approximated by an initial decay time constant of about 15 minutes (Tinsley et al., 2000). This allows time for electroscavenging to occur. Also, even at equilibrium a significant charge may be retained, depending on the sign and magnitude of the surrounding space charge density and the radii of the particles.

Corresponding author's address: Brian A. Tinsley, FO22, UTD, Box 830688, Richardson, TX 75083-0688, USA. E-mail: Tinsley@UTDallas.edu

3. MODELING OF CONTACT ICE NUCLEATION

To model contact ice nucleation rates, it is first necessary to determine the electroscavenging rate, i. e., the variation of collection efficiency as a function of the charges on and the radii of the particle and droplet. In addition, it is necessary to know the probability of ice nucleation at contact between the coated evaporation nucleus and the droplet. This is likely to be a function of temperature, size of nucleus, and the nature of the coating as well as of the substrate of original condensation nucleus material. Several of these factors depend on the history of the air mass and the type and droplet size distribution of the clouds.

Modeling carried out by Grover and Beard (1975) and Wang et al. (1978) focussed on a different range of parameters than relevant here; there were mostly very small charges on the particles and mostly very large charges on the droplets, as in equilibrium after redistribution of initial charging. Also, charges on particles of unlike sign to those on droplets were modeled, because it was assumed that the repulsion of like charges would prevent collection. However, it was shown by Tinsley et al. (2000) that while the repulsion of same sign charges is effective as a long range force, at short range the formation of an image charge of opposite sign just inside the surface in the conducting droplet can ensure collection. The flow of air past a falling droplet can bring the particle and droplet close enough so that the short-range attraction dominates. This is important, because in early cloud stages mainly charges of one sign (positive at cloud tops) are likely to be found on interacting particles and droplets.

The calculations of electroscavenging made by Tinsley et al. (2000) considered the electrical forces between droplets and particles separately from other forces. Here we include in a self-consistent treatment the phoretic forces due to gradients of temperature and vapor density around evaporating droplets, and the gravitational force on the particle. Fig. 1 is a

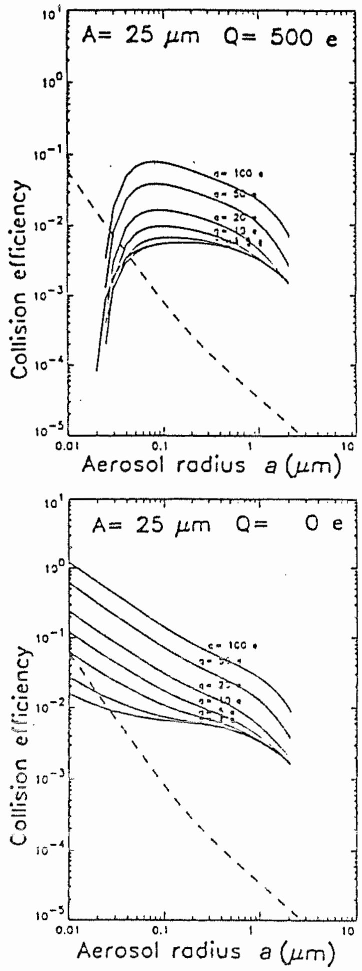

Fig. 1. Collision efficiency as a function of aerosol particle radius and charges of 1 to 100*e*; for 25 μm radius droplets with charge 500*e* (top) or 0*e* (bottom).

sample of the results for collection efficiencies *E(A,a,Q,q)*, for a droplet radius (*A*) of 25 μm, and charges (*q*) on the particle of 1 to 100*e*, with charges (*Q*) on the droplet of 500*e* and 0e, (where *e* is the elementary charge of 1.6×10^{-19} C). The particle radii (*a*) ranged from 0.01 μm to 2μm. The relative humidity was 98% and temperature -17° C and pressure 540 hPa. The effect of long range electrical repulsion is evident for *Q* = 500*e* and *a* less than 0.05 μm. Otherwise phoretic forces determine the lower limit on collection efficiencies.

4. RELATIVE RATES OF COLLECTION

Scavenging processes in clouds involve a summation over a distribution of droplet sizes and a distribution of aerosol particle sizes. The collection rate for a concentration n_A of droplets of radii *a* mixed with a concentration n_a of particles of radius *A* is given by:

$$R(A,a,Q,q)n_A n_a = \pi A^2 U_\infty(A)E(A,a,Q,q)n_A n_a \quad ....(1)$$

where U_∞ is the fall speed of the droplet. We show in Figure 2a curves for the above rate coefficient *R(A,a,Q,q)* as a function of droplet radius *A*, with curves for particle radii *a* ranging from 0.1 μm to 1.0 μm. The charge on the droplets was *500e* and the charge on the particles was 50*e*. The rapid decrease in the rate for *A* less than about 15 μm for all the curves is because U_∞ varies approximately as A^2 in that range, so that the rate coefficient varies approximately as A^4. This means that scavenging and contact nucleation are much less effective for droplets smaller than about 10 to 15μm radius than for droplets of larger size.

Figure 2b illustrates the difference between the droplet size distribution for high and low ice producing clouds observed by Hobbs and Rangno (1985). It can be seen that in high ice producing clouds the droplet size distributions extend appreciably past 10-15μm, whereas for the low ice producing clouds they do not. This is just what is to be expected for contact nucleation given the theoretical result of Fig. 2a.

The main difficulty with the original hypothesis of Hobbs and Rangno was that calculated rates were too low. However, when electroscavenging and the effects of surface coatings of the evaporation nuclei are taken into account, the discrepancies are greatly reduced, and contact nucleation again becomes an attractive explanation.

As noted earlier, the uncertainties preclude calculations of absolute contact nucleation rates, so we now estimate the ratio of the rates for contact nucleation versus deposition nucleation.

5. EFFECTIVENESS OF DIFFERRENT ICE NUCLEATION MODES

The variation of effectiveness of particles as contact ice nuclei, as compared to deposition or immersion or condensation-freezing nuclei, has been discussed by Beard (1992); Young (1993); and Pruppacher and Klett (1997 sect. 9.2.2). The latter review a number of experiments on clay mineral particles, a major component of atmospheric ice nuclei. Wind tunnel measurements made with relative humidity below 100% (saturation ratio $S_w < 1$) and other experiments were used to characterize the dependence of the activity of these particles in terms of activation mode and temperature. For the immersion and deposition modes the clay particles are inactive when warmer than -15°C to -9°C; whereas in the contact mode the threshold is -5°C to -2.5°C. The full nucleating activity in the immersion and deposition modes is at -30°C to -20°C; whereas for the contact mode the full activity is at -14°C to -6°C. In his review Young (1993, sect. 4.6 and 4.7) finds that the depression of temperature below 0°C (supercooling) required for activation of the deposition mode is roughly 2-3 times that required for contact freezing. The immersion thresholds are mostly even lower than the deposition thresholds. Condensation-freezing (which requires that the vapor be supersaturated with respect to water, or $S_w > 1$) has thresholds approximately the same as for contact nucleation. In his analysis of the properties of evaporation nuclei (collected outside of clouds and be effective ice forming nuclei in the deposition and

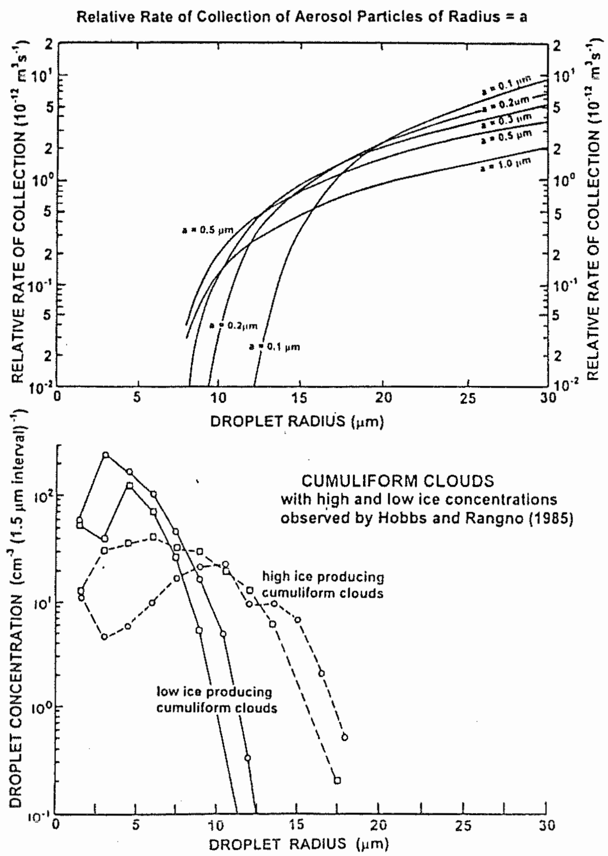

Fig. 2. (a) Relative rates of collection of aerosol particles as a function of droplet radius, for charges of 500e on droplets, and 50e on particles, for particle radii ranging from 0.1 to 1.0 μm. (b) Droplet size distributions in clouds with high or low ice production (adapted from Hobbs and Rangno (1985, Fig 3.)).

condensation-followed-by freezing modes. Thus it is reasonable to expect that they would also be effective as ice forming nuclei in the contact mode.

Observations of concentrations of atmospheric nuclei, effective as ice forming nuclei in different modes at different temperatures, were made by Cooper (1980). The same equipment was used to obtain similar data on AgI nuclei created in the laboratory. At temperatures from -20°C to -15°C the concentrations of both the atmospheric and the AgI particles active as contact nuclei were an order of magnitude greater than the concentrations active as deposition or immersion nuclei. At -10°C and warmer the concentrations were 30 to 100 times larger.

Pruppacher and Klett (1997, p. 340 - 341) discuss a number of possible explanations for this behavior, including that of Fukuta (1975a,b), who suggested that the difference is associated with the movement of the water-air interface relative to the surface of the contacting particle during the moment of contact. Fukuta pointed out that the rapid spreading of the water along the hydrophobic solid surface forces its local wetting, and thereby temporarily creates high interface-energy zones that can increase the likelihood of ice nucleation. The experiments of Abbas and Latham (1969) showed that freezing could be triggered in supercooled droplets merely by sudden disruption of them by impacting objects.

If the concentration of atmospheric ice nuclei effective in the contact mode as a result of electroscavenging is taken as n_{cn} and the concentration in the deposition mode is taken as n_{dn}, and we define the ratio $G = n_{cn}/n_{dn}$, then the above discussion would suggest that for temperatures of -10°C and warmer, a ratio of G = 30 would be conservative, and $G = 10^2$ reasonable. For the temperature range -15 to -20 °C G = 10 would be conservative, and G = 30 reasonable.

There is very little data available on ice nuclei particle size distributions, especially for the contact mode. The distributions evidently depend strongly on the source and on transport processes. From shipboard measurements in the equatorial Pacific ocean Rosinski et al. (1987) found that in the condensation-followed-by freezing mode (in supersaturated air) the ice nuclei present were sulfate bearing particles in the 0.05 to 0.15 μm radius range. Other aerosol particles present in the same locations generally showed a size distribution decreasing rapidly for a >0.5 μm. For this study we will confine ourselves to the effects of ice nuclei size distributions that are constant (in linear increments of radius) from 0.1 μm < a < 1.0 μm.

6. EVALUATION OF REALTIVE RATES OF ICE PRODUCTION IN CLOUDS

Ice formation can begin when the top of a cloud cools below 0 °C, either radiatively or by uplift. We consider clouds in which mixing and evaporation are taking place, with evaporation nuclei, which are assumed to be the main source of nuclei effective in contact and deposition modes, being mixed with supercooled cloud droplets. The saturation ratio is taken to be in the range $S_w < 1$, consistent with the mixing and evaporation, so that ice formation by the condensation-followed-by-freezing mode, requiring S_w < 1, is not effective. Also, because condensation has ceased by the time that the ice forming evaporation nuclei are mixed into the cloud, they do not act as condensation-freezing nuclei or as immersion nuclei, and only contact and deposition nuclei need be considered. We consider a time interval Δt during which the cloud cools through a small temperature range centered on a temperature T, during which all the deposition nuclei effective at that temperature are assumed to freeze. Then the number of these frozen nuclei is given by

$$N_{dn} = \Sigma_a n_{dn} = \Sigma_a n_{cn}/G \qquad \text{............(2)}$$

The number of frozen droplets formed from contact nucleation during that time is found by summing equation (1) over all droplet sizes and all particle sizes:

$$N_{cn} = \Sigma_A \Sigma_a \pi A^2 U_\infty(A) E(A,a,Q,q) n_A n_{cn} \Delta t \quad \text{...(3)}$$

We take n_{cn} as being constant with a over nine bins in Σ_a which we sum from a = 0.1μm to a = 1.0μm. Then the ratio of the concentration of frozen droplets to the concentration of frozen deposition nuclei N_{ct}/N_{dn} is given by:

$$N_{ct}/N_{dn} = G\pi\Sigma_A\Sigma_a A^2 U_\infty(A)E(A,a,Q,q)n_A n_{cn}\Delta t/\Sigma_a n_{cn}$$
$$= G\pi\Sigma_A\Sigma_a A^2 U_\infty(A)E(A,a,Q,q)n_A\Delta t/9 \quad ....(4)$$

and this result is independent of the concentration n_{cn}. We take Δt as 10^3 s, and values of $E(A,a,Q,q)$ from interpolation of our calculated values, samples of which are plotted in Figs 1 and 2a. We take the temperature range to be -15 to -20°C, and G = 30. We have estimated the value of N_{ct}/N_{dn} for a few relatively broad measured droplet size distributions. These are from Hobbs and Rangno (1985) Figs 9 and 17, and from Pruppacher and Klett (1997) Figs. 2.8(c), 2.9, 2.11(c) and 2.15(a). They are all maritime cumuliform clouds, except for Fig. 17 which is an average of a number of marine stratocumulus clouds, and Fig. 2.8(c) which is an average of four cumuli embedded in stratiform clouds in Montana. The values obtained for N_{ct}/N_{dn} were approximately 1,1,10, 2, 2, and 8.

Contact ice nucleation is likely to be the dominant nucleation process giving rise to ice precipitation from clouds for values of N_{ct}/N_{dn} only unity or greater, but also for those considerably less than unity. The reason is that while ice particles of any size can grow by vapor deposition, the frozen droplets of radii 10 - 20 μm from contact nucleation grow more rapidly than those of radii of order 1μm from deposition nucleation. In addition to a greater rate of adding mass by vapor deposition, the larger particles have much greater fall speeds and rates of riming and collision coalescence (Braham, 1986), and are more likely to give rise to secondary ice production.

Thus, these estimates, and the implications of figures 1 and 2 make a case that contact ice nucleation, responsive to the presence of electric charge in clouds, is the dominant mechanism for production of ice particles large enough for precipitation, for many clouds that are undergoing mixing and have broad droplet size distributions.

Acknowledgements

I thank K. Beard for many stimulating discussions. Support has been provided by NSF ATM9903424.

References

Abbas, M. A., and J. Latham, 1969: The electrofreezing of supercooled water droplets, *J. Met. Soc. Japan*, **47**, 65-74.

Beard, K. V. 1992: Ice initiation in warm-base convective clouds: An assessment of microphysical mechanisms, *Atmosph. Res.*, **28,** 125-152.

Braham, R. B, 1986:Coalescence-freezing precipitation mechanism, *10th Conf. Planned and Inadvertent Weather Modification,* Am. Meteor. Soc., Boston, 142-145.

Cooper, W. A., 1974: A possible mechanism for contact nucleation, *J. Atmos. Sci.*, **31**, 1832-1837.

Cooper, W. A., 1980: A method of detecting contact ice nuclei using filter samples, 8th. Intern. *Conf. Cloud Phys.,* Clermont-Ferand, France, 15-19 July, 1980, 665-668.

Desher, T., and G. Vali, 1992: Atmospheric concentrations of submicron contact-freezing nuclei. *J. Atmos. Sci.*, **49**, 773-784.

Fukuta, N., 1975a: A study of the mechanism for contact ice nucleation, *J. Atmos. Sci.* **32**, 1597-1603.

Fukuta, N., 1975b: Comments on 'A possible mechanism for contact ice nucleation', *J. Atmos. Sci.* **32**, 2371-2373.

Garrett, W. D. 1978: The impact of organic material on cloud and fog processes, *Pageoph.*, **116**, 316-334.

Hobbs, P. V., and A. L. Rangno, 1985: Ice particle concentrations in clouds, *J. Atmos. Sci.*, **42**, 2523-2549.

Grover, S. N., and K. V. Beard, 1975: A numerical determination of the efficiency with which electrically charged cloud drops and small raindrops collide with electrically charged spherical particles of various densities, *J. Atmos. Sci.,* **32**, 2156-2165.

MacGorman, D. R., and W. D. Rust, 1998: *The Electrical Nature of Storms*, Oxford University Press, Oxford.

Meyers, M. P., P. J. McDermott, and W. R. Cotton, 1992: New primary ice-nucleation parameters in an explicit cloud model, *J. Appl. Meteor.*, **31**, 708-721.

Pruppacher, H. R., and J. D. Klett, 1997: *Microphysics of Clouds and Precipitation*, 2nd rev. ed., Kluwer, Dordrecht.

Rosinski, J. 1995: Cloud condensation nuclei as a real source of ice forming nuclei in continental and marine air masses, *Atmosp. Res.*, **38**, 351-359.

Rosinski, J., and Morgan, G., 1991: Cloud condensation nuclei as a source of ice-forming nuclei in clouds, *J. Aerosol. Sci.*, **22**, 123-133.

Rosinski, J., P. L. Haggenson, C. T. Nagamoto, and F. Parungo, 1987: Nature of ice forming nuclei in marine air masses, *J. Aerosol Sci.*, **18**, 291-301.

Tinsley, B. A., R. P. Rohrbaugh, M. Hei, and K. V. Beard, 2000: Effects of image charges on the scavenging of aerosol particles by cloud droplets, and on droplet charging and possible ice nucleation processes, *J. Atmos. Sci.*, in press.

Vali, G., 1974: Contact ice nucleation by natural and artificial aerosols, Preprints, *Conf. on Cloud Physics,* Tucson, Amer. Meteor. Soc., 34-37.

Wang, P. K., S. N. Grover and H. R. Pruppacher, 1978: On the effects of electric charge on the scavenging of aerosol particles by clouds and small raindrops, *J. Atmos. Sci.*, **35**, 1735-1743.

Young, K. C. 1993: *Microphysical Processes in Clouds,* Oxford.

Young, K. C., 1974: The role of contact nucleation in ice phase initiation in clouds, *J. Atmos. Sci.,* **31**, 768-776.

2-D modelling of thundercloud microphysics, electric charge generation and lightning.

Katherine Miller[1], Alan Gadian[1], Clive Saunders[1], John Latham[2], and Hugh Christian[3],

Physics' Department, UMIST, UK., NCAR, Boulder, USA, Marshall Space Flight Center, Huntsville, USA

1. INTRODUCTION

A two-dimensional lightning frequency model is applied to two different case studies of thunderclouds; 9th July 1981, the CCOPE case, and 19th July 1991, the CaPE case. It is shown that although there is a strong link between updraft speed and lightning frequency, the relationship is not distinct; the initial environmental conditions, the updraft speed and the graupel number concentration, particularly significant, all have an effect Despite the limitations of the charge transfer parameterisations and the simple dynamical framework, the model is capable of reproducing a realistic cloud structure and lightning activity.

This study of the relationships between cloud microphysics, dynamics and lightning frequency follows from the one-dimensional work of Baker et al. (1995). Charging equations from laboratory experiments of Saunders et al. (1991) are applied. A computationally very simple and efficient two-dimensional stream function vorticity model is used to supply the dynamical framework, allowing fuller computation of the charge transfer parameterisation processes. A Lagrangian parcel approach is used to advect the associated cloud microphysical and electric charge characteristics.

Standard microphysical equations of Pruppacher and Klett, (1978) are used to calculate the saturated mixing ratios. A Fletcher(1969) primary ice spectra is used, and graupel is injected in three different sizes as defined by Charlton and List, 1972) and consistent with the observational data of Dye et al. (1986); the charging equations of Keith and Saunders (1990) for non-inductive charging generate the electric charge.

A simple two-dimensional streamfunction vorticity model (Sawyer, 1963 and Gadian, 1991) is used. The model uses a resolution of 200m, for 19.2km and 38.4km range in the horizontal and vertical directions respectively, and large enough to remove any boundary condition effects. Full details can be found in Miller(1997) The convection is initiated by a perturbations of 1^{0}C (temperature) and 2g/kg (relative humidity) in a central block, 1.2km in width and 0.4-1.4km in depth.

2. CCOPE CASE: DATA AND MODELLING.

The CCOPE case is a well documented storm (e.g. Dye et al., 1986) which is used for testing the model. Helsdon et al. (1987a, 1987b and 1992), who also use this case, highlight the problems of a two-dimensional study. However it is important to reiterate that the purpose of the model is to simulate multiple lightning model using a relatively computationally efficient dynamical framework.

On 19th July 1981 at 16:15MDT a single isolated storm is observed in south-eastern Montana. The observations monitored the particle characteristics, air motion and electrical properties and are used by Helsdon et al. (1987a, 1987b and 1992) and Norville et al. (1991) in their studies. Cloud tops of 11km, a weak wind shear with moderate instability compared with the wet adiabat are observed. A rapid electric field growth to 8-15kVm^{-1} is observed from 1630 to 1637, culminating in a single intra-cloud discharge at 16:37 (Tables 1 and 2). It takes only 7mins from the first signs of substantial field growth, for an electric field capable of producing lightning, to develop. A subsequent decrease in electric field is observed at 16:40, coinciding with the collapse of the updraught core. Observations indicate that the charge structure is classical in nature (that is, positive above negative charge). The negative charge is centred around the -20^{o}C temperature level (approximately 7km in height) but as the cloud begins to dissipate the negative charge centre progressively moves to lower levels

The model cloud develops quickly, especially between 15-31mins, and after 24mins ice appears The maximum liquid water is found between about 5 and 6.5km. By 33mins the cloud has attained a steady height of 9.8km and a cloud base of about 2.4km. After about 42mins there is a gradual fall of the balance level as the graupel falls in the subsiding updraughts. The graupel distribution is translated into radar reflectivity using the radar equation for graupel.

2.1 CCOPE data compared with modelling results.

The model replicates many major features of the storm, see Table 1. The largest discrepancy occurs in the

Alan Gadian, Physics Dept, UMIST, Manchester, M60 1QD, UK

cloud base heights, but this is probably due to the initialisation sounding (Helsdon and Farley, 1987a), and is not important for this electrification model. The aircraft observations avoid the central core of the storm and this reflects the lower measured vertical velocities and the field observations may have missed local high electric fields, the greatest observed being 15kVm^{-1}

Feature	CCOPE observations	Helsdon results	Model results
Cloud base ht.	3.8km (msl)	2.8km (msl)	3.2km (msl)
Maximum cloud top ht.	10.5km (msl)	11.6km (msl)	10.6km (msl)
Cloud top rise rate	5-7ms^{-1}	3-7ms^{-1}	5-15 ms^{-1}
Cloud width	6km	6km	6km
Maximum liquid water	2.50gm^{-3}	4.08gm^{-3}	3.1gm^{-3}
Max vertical velocity	15ms^{-1}	26ms^{-1}	23ms^{-1}
Max reflectivity	45dBz	60dBz	50dBz
Max electric field	15kVm^{-1}	400kVm^{-1}	300 kVm^{-1}

Table 1. Significant cloud characteristics

The time scale is meant to give an indication of the order of significant features rather than an exact time correspondence (Table 2). The liquid part of the cloud dries out too early and the graupel reaches the ground too late, but considering the model's simplicity, the agreement is good. Helsdon and Farley's model (1987a) gives better agreement, but their graupel reaches the ground before the lightning occurs

Feature	CCOPE 0bs. Times, MDT	Helsdon's times, MDT	Model, mins
Rapid growth	1620-1630	1620-1632	15-31
Graupel first appeared.	1626	1625	24
Liquid water decreases	1632	1630	26
Updraught decay starts	1632	1632	28
Cloud top ht is constant	1632	1634	31
Max.reflect-ivity / balance ht. level falls	1635	No data	39
First stroke of lightning	1637	1636	39
Graupel rea-ches ground	1640	1632	47

Tqble 2. Comparable timings for model and data.

The model lightning timing is in reasonable agreement with observation. The model produces two strokes rather than the one reported; this is not important as not only is it uncertain whether there is a second stroke of lightning. Primarily the model is only attempting to reproduce the general cloud features. The discharges (4.1C and 25.2C) are of the correct order of magnitude from similar observational studies of thunderstorms and an indication that the discharge process is reasonably simulated.

In general there is good agreement between the observational data and the model results and further endorsement of the model results is provided by a comparison with Helsdon et al. (1987a, 1992). The study shows that it is possible to reproduce the observed conditions with reasonable accuracy using a simple two dimensional model

3. CaPE CASE; MODELLING AND OBSERVATIONS

The second case study relates to the CaPE storm in Florida, on July 19th 1991, and is detailed in Breed (1993 and 1995). From a group of short lived convective cells, the most active member is chosen for study by a sail plane and King Air aircraft. The CCOPE storm, in contrast, is an isolated event and this dominates any intercomparison. In CaPE, the cloud base is lower and there is more moist air near the ground, but is much drier above cloud base. Table 3 gives a summary

Feature	CCOPE tephigram	CaPE tephigram
Stable layer begins	250mb	150mb
Ground temps	25°C	30°C
Expected condensation level	630mb	860mb
Temp. instability	2°C	10°C
Mixing ratio r_v at ground	7g/kg	16g/kg

Table 3 Comparison of CCOPE and CaPE tephigrams

The model produces a vigorous dynamical structure for the cloud, with the peak updraught occurring at about 13minutes with a value of 47ms^{-1} , with small down-draughts on either side of the core. As with the CCOPE case, the core updraught becomes disorganised. In the CaPE simulation only two intra-cloud lightning strokes occur as in the CCOPE case.

3.1 <u>CaPE data compared with modelling results.</u>

The limited observational data for the CaPE case has hindered detailed comparison but the numerical simulation has created a storm displaying vigorous characteristics, which agrees with the data provided. The model lightning activity (in agreement with observations) is minimal, in contrast to the hypothesis that dynamically more active storms produce more lightning. In Table 4, the significant cloud characteristics are summarised. As with CCOPE, the electric fields are much smaller than the model values.

Feature	CaPE Observation	Model results
Cloud base ht.	895mb (≈1.2km)	0.8km
Maximum cloud top ht	12km	10.8km
Cloud top rise rate	Approx. $2.2ms^{-1}$.	$2.3ms^{-1}$
Cloud width	Few km (3-4km near base, 2km above 8km)	4-5km
Maximum liquid water content	Approx. $4gm^{-3}$ at 4km (11:35)	$8gm^{-3}$
Max vertical velocity	$25ms^{-1}$ at 4.2km (11:37 EDT)	$47ms^{-1}$
Max electric field	$45kVm^{-1}$ at 6km (11:45 EDT)	$300kVm^{-1}$

Table 4 Cloud characteristics for CaPE case.

Timing correspondence between the observations and simulation data is presented in Table 5. The objective is to replicate the order of events. The basis of the timing correspondence is taken to be the time at which the cloud reaches 8km and the radar observations begin. In the simulation the graupel reaches the ground (32mins) after the first lightning stroke, but as with CCOPE this is later than expected.

Feature	CaPE observations, EDT	Model results model time
Cloud top at 8km	11:37	14mins
Liquid water content falls	11:38	14mins
Updraught decays	11.38	14mins
Time of maximum ht. of supercooled water tower.	11:39	16mins
Sudden rapid increase of electric field	11:43 7-24kV/m in 2mins	27mins 110-220kV/m in 1 min
Time of first lightning stroke	11:45	28mins

Table 5 Timing of events in CaPE and model cases

Again this simulation reproduces the cloud's features with reasonable accuracy . The CaPE storm is much more vigorous than the CCOPE case, and this suggests that there is not a strong link between updraught and lightning frequency.

4. LIGHTNING AND CLOUD PARAMETERS.

The one dimensional results of Baker et al. (1995) in contrast propose that the updraught speed is of primary influence on lightning activity. This section suggests that the graupel concentration is important. The two observational studies are not sufficient for a hypothesis, but are supported by model simulations. The CCOPE profile is primarily used to test changes in the model parameters, as there is a more comprehensive observational dataset. Initial conditions are modified to produce the changes in updraught.

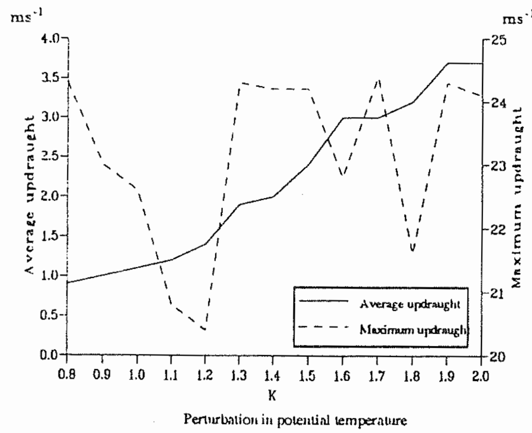

Figure 1. Variation of average updraught (left axis, bold line) and maximum updraught (right axis, dotted line) with varying perturbation in potential temperature forcing. CCOPE case.

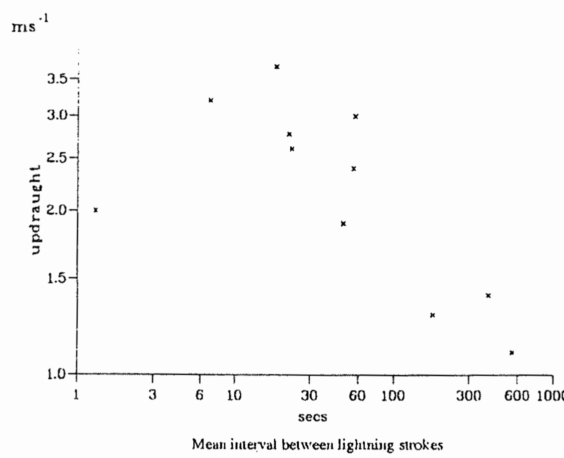

Figure 2 Variation of average updraught with mean interval between lightning strokes. CCOPE case. With the perturbation in potential temperature forcing varied.

The average updraught displayed a smooth curve which increased as the potential temperature forcing becomes larger (Figure 1). The effect of increasing the initial temperature perturbation from 0.8^0 to 2.0^0 C, produces only small increases in average water content, graupel content and ice content but does suggest that the variables are likely to be of only limited use as indicators of lightning frequency.

The variation of the average updraft with the mean interval between lightning strokes is displayed in. Figure 2, showing a trend between lightning interval and increasing average updraught. This is only a general relationship, since the largest averaged updraft does not produce the smallest interval between lightning strikes.

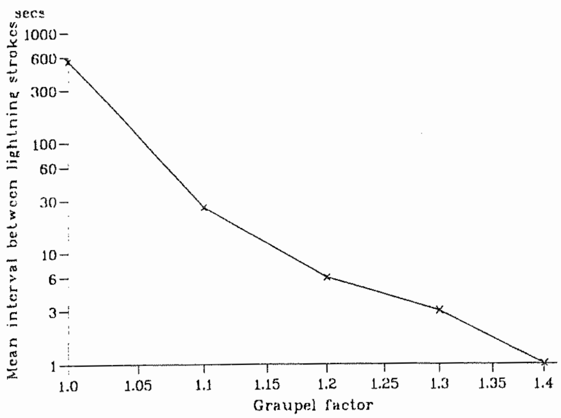

Figure 3 Mean interval between lightning strokes against graupel factor. Note the logarithmic scale on both axes. CCOPE case. Perturbation in potential temperature is *not* varied; only graupel concentration.

The effect of the variation of the number concentration of graupel particles is examined in Figure 3. The value of N_G, the graupel number concentration, is altered from a value of 1.0 to $1.4*10^5$, well within observed graupel concentrations. This figure suggests a dependency of lightning frequency on the graupel number factor. The effect of the graupel number concentration on lightning frequency is also tested using the CaPE profile. An identical range of graupel factor values again shows, a pattern of increasing frequency with increasing graupel factor. The dependency is not as emphatic as for the CCOPE case; the mean interval between strokes decreasing from 556s to 41s, for the graupel factor of 1.0 to 1.4, but is again monotonic.

5. CONCLUSIONS

A two dimensional model simulating multiple lightning activity in a single thundercloud is produced and compared with two observed storms of a different structure. The research suggests that the major factors controlling lightning frequency are the updraught strength and, perhaps more importantly, the graupel number concentration. More research must be carried out to build upon the findings here, but this study has engendered significant insights into the mechanisms leading to lightning generation

6. REFERENCES

Baker, M. B., Christian, H.J. and Latham, J, 1995: A computational study of relationships linking lightning frequency and other thundercloud parameters, Quart. Jou. Roy. Met. Soc, 121, 1525-48

Breed, D 1993: Electric Field Development and multiparameter radar measurements in a Florida storm AMS conf preprint (Dallas) 5A.4 190-2

Breed, D. 1995: Glaciation in the convective core of a Florida thunderstorm AMS conf. Preprint 5A.3 188-9

Charlton, R. B. and List, R, 1972: Hail size distributions and accumulation zones. J Atmos. Sci., 1182-93

Dye, J.E., Jones,J., Winn, W., Cerni, T., Gardiner, B., Lamb, D, Pitter, R. Hallett, J. and Saunders, C.P.R 1986: Early electrification and precipitation development in a small, isolated Montana cumulonimbus. J. Geo. Res. 91, 1231-47

Fletcher, N.H, 1969 The physics of rainclouds University Press Cambridge

Gadian, A. 1991, Lagrangian modelling of an atmospheric convective plume, Computer Modelling in the Envirnonmental Sciences, Clarendon Press. Ed D. Farmer

Helsdon, J. and Farley, R., 1987a: A Numerical modelling study of a Montana thunderstorm: 1, J. Geo. Res., 92, D5, 5645-5659

Helsdon, J. H. and Farley, R. D. 1987b: A numerical modelling study of a Montana thunderstorm: 2. Model results versus observations involving electrical aspects. J. Geo. Res. 92 D5, 5661-5675.

Helsdon, J., Wu G., and Farley, R., 1992: An intracloud lightning parameterization scheme for a storm electrification model, Jou. Geo. Res., 97, 5865-84

Keith, W.D. and Saunders, C.P.R.S. 1990: Further studies of the charging of graupel during ice interactions, Atmos. Res 25, 445-64

Miller, K. L. 1997, Numerical modelling of thundercloud electrification and lightning, Ph.D. Thesis, UMIST, Manchester M60 1QD

Norville, K., Baker, M. and Latham, J. 1991: A Numerical study of thunderstorm electrification: Model development and case study. J. Geo. Res. 96, 7463-7481.

Pruppacher, H. Klett, J. 1978, The microphysics of clouds and precipitation, D. Reidol

Saunders, C.P.R., Keith, W.D. and Mitzeva, R.P., 1991: The effect of liquid water on thunderstorm charging. Jou. Geo. Res., 96, 11007-17

Sawyer, J.S, 1963::A semi-lagrangian method of solving the vorticity advection equation, Tellus, XV, 4, 336-42

THE VELOCITY DEPENDENCE OF CHARGE TRANSFER IN GRAUPEL- ICE CRYSTAL COLLISIONS

Peter Berdeklis and Roland List[1]

Department of Physics, University of Toronto, Toronto, M5S iA7, Canada

1. INTRODUCTION

Basic experiments on graupel charging on objects attached to an arm rotating in a cold box have been carried out by Takahashi (1978) and Jayaratne et al (1983), as reviewed by Saunders (1993). These experiments showed substantial and unexplained differences in (charge) reversal temperatures. Takahashi's experiments have been carried out at relative speeds of 9 m s^{-1}, whereas Jayaratne et al used speeds of 3 m s^{-1}. Later Keith and Saunders (1992) found that the charge transfer was a strong function of velocity. At -12°C the positive charge transfers increased as $V^{2.5}$, and the negative charge transfers at -25°C increased as $V^{2.8}$.

In 1998 Berdeklis established a strong dependence of the charge transfer on the relative humidity at which the ice crystals used in the graupel collision experiment grew. This humidity effect was larger than that produced by the variations in temperature and liquid water content (see also Berdeklis and List, 2000). The new results were obtained in a new Triple Interaction Facility, TIF, which allowed a wider choice of experiment parameters. The effect of velocity for ice crystals grown at humidities near water saturation is the subject of this communication.

2. THE TRIPLE INTERACTION FACILITY, TIF

The TIF (Figure 1) consists of two parts, an icing wind tunnel (List et al, 1987) and a 7.1 m^3 ice crystal chamber, ICC. The operation of the facility is implied by the components: [1] tunnel fan; [2] heaters; [3] turning vanes; [4] pipe to vacuum pump; [5] cooling element; [6] access door; [7] double wall flaps; [8] perforated wooden board; [9] tunnel kettle; [10] ice crystal injection; [11] water injection; [12]

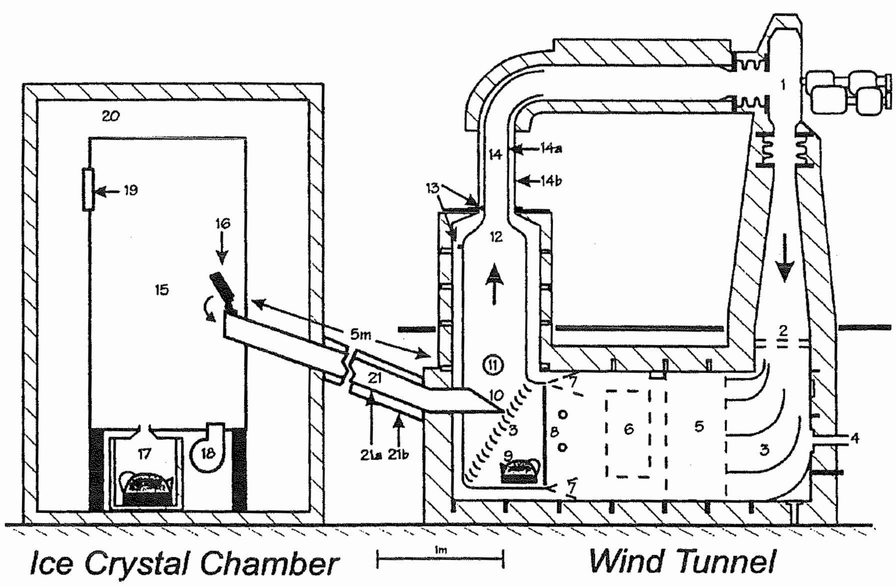

Figure 1. The Triple Interaction Facility. For explanation see text.

[1]Corresponding author's address: Roland List, Department of Physics, University of Toronto, Toronto, Ontario M5S 1A7, Canada; E-Mail: listr@netcom.ca

contraction; [13] pressure measuring nipples; [14] measuring section (a: inner wall; b: outer wall), [15] ice crystal growing chamber (2.4m x 2.4m x 1.2m); [16] pipe access door; [17] steam kettle in insulated can; [18] chamber fan; [19] chamber window; [20] cold room;[21] connecting pipe (a: ice crystal pipe; b: dry ice pipe). General aspects of TIFs have been outlined by List et al 1986.

Ice crystals were produced in the ICC by quickly inserting a liquid nitrogen cooled rod into a cloud of supercooled droplets. Ice crystals grew to sizes of ~80 µm, as determined by a special, for-laboratory-designed Particle Measuring Systems (PMS) 2-Dimensional Cloud Particle Grey-scale (2DCG) probe. The crystals were then sucked into the icing wind tunnel and mixed into a cloud of supercooled droplets. A cylindrical test particle, similar to the one in the whirling rod experiments of Takahashi (1978) and Jayaratne et al (1983), was used to simulate graupel. Charge transferred to the test particle during growth in the mixed cloud was measured as a current to ground through a shielded co-axial cable and a 500 MΩ resistor, using a Keithley 4½ digit, ±20,000 count picoammeter (model 485). State and experiment parameters were measured and recorded at 3Hz.

The ice crystal number concentration was calculated for every 10 s average of the 2-4 min duration of the electrically active "ice phase" of the experiment. The error associated with each number concentration estimate was also calculated, assuming a Poisson distribution and estimated errors for the depth-of-field calibration (Berdeklis, 1998).

The humidity in the ICC, which turned out to be the key parameter in controlling charging, was classified as close to water saturation (high), close to ice saturation (low) or intermediate, depending on the cloud droplet concentration observed in the ICC at the time of ice crystal initiation.

3. RESULTS

The experiments on the velocity dependence were carried out at a temperature of -16°C, a laboratory air pressure of ~101 kPa, an effective liquid water content of 0.5 g m^{-3}, and with ice crystals grown at ICC humidities close to water saturation (high). At velocities of 3, 4, and 6 m s^{-1} the charge transfer to the target particle was ~ -5 fC per ice crystal collision. At a velocity of 5.3 m s^{-1} a much stronger weighted average negative charge transfer of -16 fC was observed (Figure 2). This is an increase by a factor of ~ 3, representing a difference of nearly 5 standard deviations. In all these cases, the ice crystals were grown under nearly identical conditions.

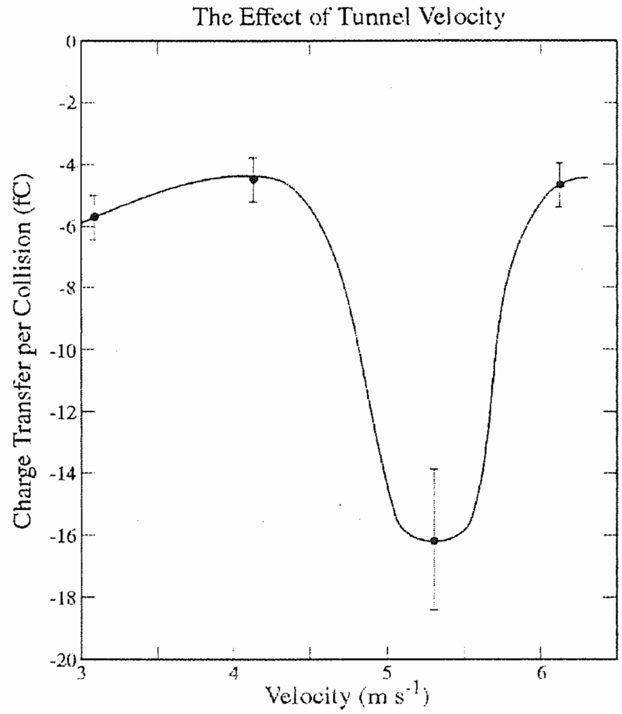

Figure 2. *Average charge transfer per collision of an ice crystal with the test graupel as function of relative velocity, at -16°C and a liquid water content of 0.5 g m^{-3}.*

4. INTERPRETATION AND COMMENTS

1) Two possible mechanisms have been offered by Berdeklis (1998) and Berdeklis and List (2000) to explain the velocity dependence of the charge generation: a dependence on target rime density or a neutralizing current (Iribarne, 1972) across the contact point of liquid-like layers. Neither mechanism, however, has been confirmed or rejected based on the limited data available.

2) Comparisons of the velocity dependence with that observed in earlier studies are consistent with a scenario of two competing charge mechanisms, each with a different velocity dependence. However, the velocity dependence observed previously suggests a possible sensitivity to relative humidity.

3) Dye et al (1986) found that 5 mm graupel had to be present in clouds before strong electric fields could develop. The approximate position of the early negative charge center in thunderstorms in

Alberta and Colorado hailstorms is close to a temperature of -16^{0}C and a pressure of 45 kPa. Under such conditions the terminal velocity of 5 mm graupel is ~ 5 m s^{-1} (List and Schemenauer, 1971). Thus, the present findings suggest a physical explanation for this link of strongest charge transfer in the high humidity region in and surrounding the updraft and graupel size. Smaller graupel have lower fall speeds, coupled with much lower negative charge transfers.

Acknowledgments

The authors owe special thanks to Drs. S. Cober and P. Joe from the Meteorological Service of Canada and Dr. Zheng Guoguang from the Chinese Meteorological Administration. The support by Dr. J. Day from NCAR was particularly appreciated. This work was carried out within a research program sponsored by the National Sciences and Engineering Research Council of Canada and the Canadian Meteorological Service.

References

Berdeklis, Peter, 1998: The ice crystal—graupel collision charging mechanism of thunderstorm electrification. Ph.D. thesis, Department of Physics, University of Toronto, 133 pp.

Berdeklis, Peter, and Roland List, 2000: The ice crystal—graupel collision charging mechanism of thunderstorm electrification. *J. Atmos.Sci*, **47,** (submitted).

Dye, J. E., J. J. Jones, W. P. Winn, T. A. Cerni, B. Gardiner, D. Lamb, R. L. Pitter, J. Hallett, and C. P. R. Saunders, 1986: Early electrification and precipitation development in a small, isolated Montana cumulonimbus. *J. Geophys. Res.*, **91**, 1231 - 1247.

Iribarne, J. V., 1972: The electrical double layer and electrification associated with water disruption processes. *J. Rech. Atmos.*, **6**, 265 - 281.

Jayaratne, E. R., C. P. R. Saunders, and J. Hallett, 1983: Laboratory studies of the charging of soft-hail during ice crystal interactions. *Quart. J. Roy. Meteor. Soc.*, **109**, 609 - 630.

Keith, W. D., and C. P. R. Saunders, 1990: Further laboratory studies of the charging of graupel during ice crystal interactions. *Atmos. Res.*, **25**, 445 - 464.

List, R., G.B. Lesins, F. Garcia-Garcia, and D.B. McDonald, 1987: Pressurized icing tunnel for graupel, hail and secondary raindrop production, *J. Atmos. Ocean. Technol.*, **4**, 454 – 563.

List, R. and R. S. Schemenauer, 1971: Free-fall behavior of planar snow crystals, conical graupel and small hail. *J. Atmos. Sci.*, **28**, 110 - 115.

List, R., J. Hallett, J. Warner and R. Reinking, 1986: "The future of laboratory research and facilities for cloud physics and cloud chemistry." *Bulletin Amer. Meteor. Soc.*, **67**, November, 1389-1397.

Saunders, C. P. R., 1993: A review of thunderstorm electrification processes. *J. Appl. Meteor.*, **32**, 642 - 655.

Takahashi, T., 1978: Riming electrification as a charge generation mechanism in thunderstorms. *J. Atmos. Sci.*, **35**, 1536 - 1548.

THE PRODUCTION OF NO_x BY LIGHTNING - RESULTS FROM EULINOX

H. Höller[1], H. Huntrieser[1], and C. Théry[2]

[1]Institut für Physik der Atmosphäre, DLR-Oberpfaffenhofen, D-82234-Wessling, Germany
[2] Département Mesures Physiques (DMPH), ONERA, F-92322 Châtillon Cedex, France

1. INTRODUCTION

Thunderstorms do very efficiently redistribute atmospheric trace gases between the boundary layer and the upper troposphere. Due to it's significance for ozone production the NO_x budget of the troposphere became an issue of increasing interest in recent years. The main inputs of NO_x to the middle and upper troposphere arise from vertical transports originating in the atmospheric boundary layer, from lightning in thunderstorms, due to transport from the stratosphere, and in-situ emissions of NO_x from aircraft (Levy et al., 1996).

The global lightning induced NO_x (LNO_x) source represents the largest uncertainty in the global NO_x budget, with estimates varying between 1 and 220 TgN/yr (Liaw et al., 1990). More recent model analysis and field experiments come up with more narrow ranges of 2 to 5 TgN/yr (Levy et al., 1996; Ridley et al., 1996). The strength and distribution of the LNO_x sources must be known, in particular, for assessments of the impact of aircraft NO_x emissions on the state of the atmosphere (Beck et al., 1992; WMO, 1995; Brasseur et al., 1996).

The European Lightning Nitrogen Oxides Project (EULINOX) addressed the questions raised above. The overall aims were to improve the knowledge of the role of lightning for NO_x production in mid-latitude thunderstorms and to investigate the distribution of NO_x sources on the European scale. These objectives were addressed by a field experiment and modeling studies both at regional scale (in Southern Germany) and at the scale of Western Europe. This paper focuses on the storm-scale aspects of LNO_x production.

2. FIELD EXPERIMENT SETUP

The EULINOX field experiment was performed during July 1998. A special observational area was selected close the DLR radar and airfield site near Munich in Southern Germany. The region was well covered by two weather radar systems (see Figure 1 for illustration). DLR's polarization diversity radar (POLDIRAD) and the Doppler radar of the German Weather Service (DWD) did enable dual Doppler analysis and the identification of different types of hydrometeors. Detailed three-dimensional lightning observations were performed by ONERA's VHF-interferometer (ITF). Two-dimensional flash localization was available from a lightning positioning and tracking system (LPATS).

Corresponding author's address: Hartmut Höller, Institut für Physik der Atmosphäre, DLR-Oberpfaffenhofen, D-82234-Wessling, Germany;
E-Mail: hartmut.hoeller@dlr.de.

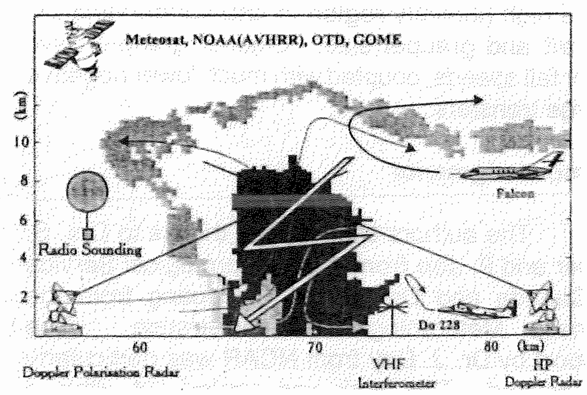

Figure 1. General design of the field experiment showing the principle measuring systems.

In-situ chemical and meteorological measurements were performed by two aircraft. The Falcon jet aircraft did penetrate thunderstorm anvils providing measurements of the trace gases NO, NO_2, CO, CO_2, and O_3. Concentrations of some of these constituents at low levels were measured onboard a Do228.

Additional meteorological data were available for the experimental period from operational systems like soundings or satellite observations. Moreover, a European radar composite was prepared from the available national and international composites.

3. THE 21 JULY 1998 SUPERCELL STORM

The radar and lightning structure of a storm along with the chemical measurements will be discussed based on the 21 July 1998 case study. On this day a cold front moved across Central Europe from west to east. Convective storms were associated with the frontal system. One of these storms developed over the Alps and then moved out of the mountains into the EULINOX experimental area. Rapid intensification of the storm was followed by a splitting of the main cell and a subsequent development of the southern storm into a supercell-like structure. Model simulations of this storm are presented by Fehr at al. (this volume).

3.1 Radar and Lightning Observations

After the supercell characteristics had formed the cell intensified further at about 17:45 UTC. At this time it was located within the optimum observation area for ITF lightning detection.

As an example of the typical radar and lightning structures, Figures 2 and 3 show a comparison of po-

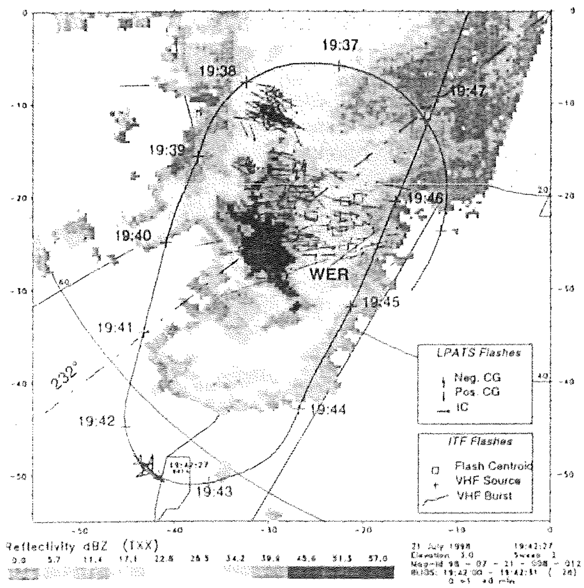

Figure 2. The supercell storm of 21 July 1998. POLDIRAD radar reflectivity at 17:42 UTC taken at 3° elevation. Falcon flight track with the position of the aircraft indicated at the time the radar scan was taken. ITF and LPATS flashes from a 45 s period are shown.

larimetric radar parameters and the flash characteristics as inferred from ITF and LPATS. At 40 km distance from POLDIRAD the radar scan height is about 2 km above ground thus representing low level features. The weak echo region (WER) and the hook echo extension towards the south can clearly be identified. The WER is most likely connected to the position of the main updraft of the storm. One consistent feature which can be noted from the ITF as well as from the LPATS flash locations is that the flashes occur preferentially in the regions located downwind (NE) of the main storm updraft.

Most of the flashes detected by the LPATS and the ITF were identified as intra-cloud (IC) flashes. This finding applies to longer periods of the storm development and thus has important implications for NO_x assessment. As described later in this paper, very high NO_x concentrations were found in this storm. This stresses the role IC flashes play for NO_x production.

The vertical sections shown in Figure 3 demonstrate a close connection between cloud microphysics and lightning. From the reflectivity scan it can be noted that discharges dominate in regions of moderate reflectivity values. The core of the storm (high reflectivity) is relatively flash-free as is the large anvil and the stratiform-like precipitation area at closer ranges. The hydrometeor classification scheme described by Höller et al. (1994) uses differential reflectivity (Z_{DR}) and linear depolarization ratio LDR for inferring hydrometeor type. From this analysis (shown in Figure 3c) it can be concluded that the VHF-sources are concentrated in the graupel region extending in the upper parts of the convective cell structures which are superimposed on large scale (supercell like) features.

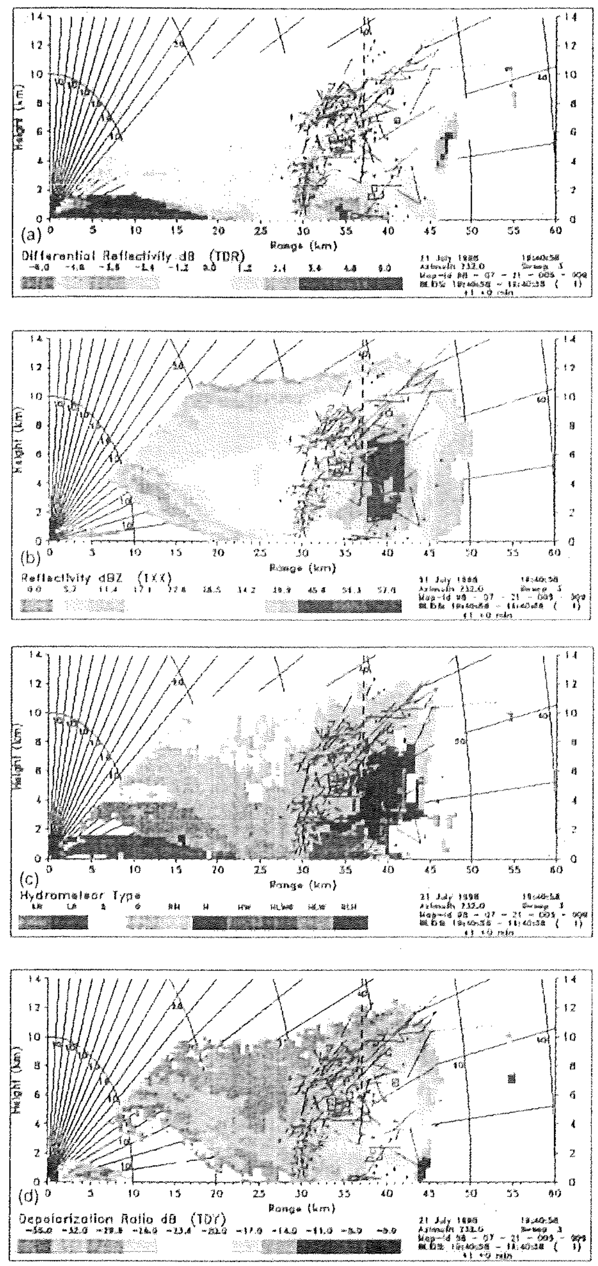

Figure 3. Vertical section of the supercell storm of 21 July 1998 at 17:41 UTC along the 232° azimuth from POLDIRAD as shown in Figure 2. ITF-flashes are plotted for 30 s interval around the nominal scanning time from an azimuth interval of ±10°. The Falcon aircraft is visible in all parameters shown at a range of 55 km and 9 km height SW of the storm. (a) Differential reflectivity, (b) reflectivity, (c) particle type (R: rain, G: graupel, S: snow, H: hail), (d) linear depolarization ratio.

3.2 Storm Structure and NO_x Measurements

The airborne measurements and the relation to radar and lightning structure within the supercell anvil will be

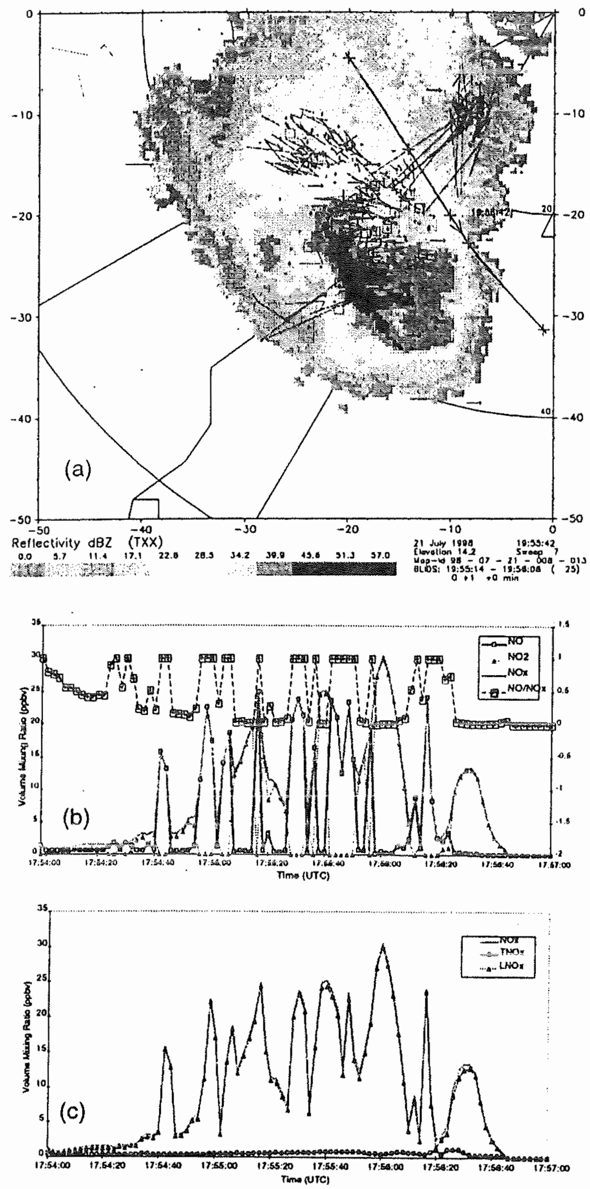

Figure 4. Radar, lightning and airborne measurements on 21 July 1998. (a) PPI scan of radar reflectivity at 14.2° elevation (9 km height at 37 km range) at 17:56 UTC, VHF-sources and LPATS strokes (symbols as in Figure 2 from within ±30 s around the radar scan time. Aircraft track during 3 min (17:54-17:57 UTC). (b) Time series of NO, NO_2, NO_x, and NO/NO_x (right ordinate) along the track shown in Figure 4a. (c) Lightning produced NO_x (LNO_x) and NO_x transported from boundary layer (TNO_x).

discussed here in more detail with respect to the assessment of NO_x production by lightning. As an example, Figure 4 shows a combined analysis from radar, lightning, and airborne measurements. The aircraft position was downwind (NE) of the main storm core at a height of 9 km. Lightning was still very active at this time, about 5-10 min after the phase of maximum intensity. Thus the generally high level of NO_x concentration can be explained. The mean NO_x concentration during the cloud penetration was 10 ppbv with peaks up to 30 ppbv. Such high concentrations have never been reported before from inside thunderstorm clouds. During LINOX (Huntrieser et al., 1998; Höller et al., 1999) maximum values were typically up to 4-5 ppbv. Dye et al. (1999) report NO maxima up to 19 ppbv measured during STERAO (Stratospheric-Tropospheric Experiment: Radiation, Aerosols and Ozone) in a Colorado thunderstorm.

For assessing the amount of NO_x produced from lightning two methods will be applied in the following (tracer and spike analysis). For tracer analysis the vertical profile of CO_2 is used to assess the contribution of boundary layer transport and mixing of cloud and environmental air to the total NO_x content measured in the anvil. The method assumes that the atmospheric vertical trace gas composition can be represented by only two layers with distinctly different concentrations (step-like profile): the boundary layer and the free atmosphere (Höller et al. 1999). The result of the analysis is that almost all of the NO_x concentration measured in the anvil originates from lightning (up to 90-95%, see Figure 4c).

The second method follows Stith et al. (1999). It is assumed that the NO plume is encountered perpendicular to its axis and in its center parts. Mean NO concentration is used for calculating the LNO_x production according to the plume size. The NO peaks from two penetrations of this storm result in a mean production rate of $6 \cdot 10^{22}$ molecules of NO per meter of flash which is about 25 times larger that the mean value found by Stith et al. (1999). Comparing the maximum values results in one order of magnitude larger production rates for the EULINOX penetrations.

These results underline the finding that the 21 July EULINOX storm was an electrically very active storm and a very effective LNO_x producer. Obviously, the spikes were due to IC flashes underlining the dominant role IC flashes can play with respect to NO_x production. This finding is in accordance with a similar result reported recently by Dye et al. (1999) for a Colorado storm.

These experimental results do support the new look upon the role this type of flash plays for overall NO_x production. Especially in global models it is usually assumed that IC flashes are 3 to 10 times less effective than CG flashes in producing NO_x. This assumption has been questioned recently by Gallardo and Cooray (1996) who claimed that IC and CG flashes dissipate similar amounts of energy and that they may be equally effective per discharge as NO_x producers. As a further consequence they indicated that the LNO_x source in global models had to be amplified in that case by a factor of 2.6. The present results give indication that this might be the case, but direct comparison of NO_x spikes from CG and IC flashes could not be obtained due to the lacking low level measurements.

4. DISCUSSION AND CONCLUSIONS

In this paper a detailed analysis of the 21 July 1998 EULINOX (supercell) storm was presented. In a multi-system approach the detailed physical and chemical structure of a severe storm event was investigated.

It was found that the position of the flashes in the main storm was predominantly downwind of the main updraft core in a region of intermediate radar reflectivity values. High reflectivity areas (core of the updraft) and low reflectivity areas (outer anvil) were relatively free of lightning sources. Most flashes were found in graupel or small hail regions as inferred from the polarimetric measurements. This stresses the role non-inductive charging processes (collisions of riming graupel particles with ice crystals) play for thunderstorm electrification.

In spite of the low number ground flashes (which were assumed in previous studies to be much more efficient NO_x producers than IC flashes) the highest ever reported NO_x contents within thunderstorms were measured in this storm. This results indicates an important finding of EULINOX: IC flashes are important for NO_x production in storms.

The high NO_x amounts found in the 21 July storm are not only caused by the large number of IC flashes but also the flash-specific NO_x production is very large. The values are well above all production rates found in previous campaigns (LINOX and STERAO). A possible explanation for this is the build-up of stronger electric fields especially due to the rapid growth phase of the storm.

The EULINOX results support recent findings from Gallardo and Cooray (1996) who showed that IC flashes dissipate equal or more energy than CG flashes, given the same amount of energy neutralized. They concluded that IC flashes may be equally effective as NO_x producers than are CG flashes. As a consequence they pointed out that the strength of the global lightning source used in 3D global model studies should be amplified by a factor of 2.6. The present results indicate that IC flashes can even be more effective NO_x producers than CG flashes. But up to now there is still insufficient knowledge about the energy distribution of the IC flashes.

EULINOX represents the first detailed investigation of NO_x production in storms in Europe. The above statements indicate that, in view of the large implications of the subject with respect to global climate problems, further efforts should to be undertaken in future experiments by following a similar combined measuring approach as during EULINOX.

5. ACKNOWLEDGEMENTS

The EULINOX project was sponsored by the Commission of the European Communities (CEC) within the Environment and Climate Program, contract ENV4-CT97-0409.

6. REFERENCES

Beck, J. P., C.E. Reeves, F.A.A.M. de Leeuw, and S.A. Penkett, 1992: The effect of air traffic emissions on tropospheric ozone in the northern hemisphere. *Atmos. Environ., 26A*, 17-29.

Brasseur, G.P., J.-F. Müller, and C. Granier, 1996: Atmospheric impact of NO_x emissions by subsonic aircraft: A three-dimensional model study. *J. Geophys. Res., 101*, 1423-1428.

Dye, J.E., B.A. Ridley , K. Baumann, W. Skamarock, M. Barth, M. Venticinque, E. Defer, P. Blanchet, C. Thery, P. Laroche, G. Hubler, D.D. Parrish, T. Ryerson, M. Trainer, G. Frost, J.S. Holloway, F.C. Fehsenfeld, A. Tuck, T. Matejka, D. Bartels, S. A. Rutledge, T. Lang, J. Stith and R. Zerr, 1999: An Overview of the STERAO - Deep Convection Experiment with Results for the 10 July 1996 Storm. *J. Geophys. Res.*, in press.

Gallardo, L., and V. Cooray, 1996: Could cloud-to-cloud discharges be as effective as cloud-to-ground discharges in producing NO_x? *Tellus, 48B*, 641-651.

Höller, H, U. Finke, H. Huntrieser, M. Hagen und C. Feigl, 1999: Lightning produced NO_x (LINOX) - Experimental design and case study results. *J. Geophys. Res., 104*, D11, 13911-13922.

Huntrieser, H., H. Schlager, C. Feigl, and H. Höller, 1998: Transport and production of NO_x in electrified thunderstorms: Survey of previous studies and new observations at midlatitudes. *J. Geophys. Res., 103*, 28,247-28,264.

Levy, II, H., W.J. Moxim, and P.S. Kasibhatla, 1996: A global three-dimensional time-dependent lightning source of tropospheric NO_x. *J. Geophys. Res., 101*, 22911-22922.

Liaw, Y.P., D.L. Sisterson, and N.L. Miller, 1990: Comparison of field, laboratory and theoretical estimates of global nitrogen fixation by lightning. *J. Geophys. Res., 95*, 22489-22494.

Ridley, B.A., J.E. Dye, J.G. Walega, J. Zheng, F.E. Grahek, and W. Rison, 1996: On the production of active nitrogen by thunderstorms over New Mexico. *J. Geophys. Res., 101*, 20985-21005.

Stith, J., J. Dye, B. Ridley, P. Laroche, E. Defer, K. Baumann, G. Hübler, R. Zerr, and M. Venticinque, 1999: NO signatures from lightning flashes. *J. Geophys. Res., 104*, 16081-16089.

WMO (World Meteorological Organisation), 1995: Scientific assessment of ozone depletion: 1994, Global Ozone Research and Monitoring Project, Rep. 37, Geneva.

ANALYSIS OF AIRCRAFT MEASUREMENTS OF DROP AND AEROSOL CHARGES IN WINTERTIME CONTINENTAL CLOUDS

Kenneth V. Beard[1], Jasbir S. Naul[1], Harry T. Ochs[1] and Cynthia Twohy[2]

[1]Department of Atmospheric Sciences, University of Illinois at Urbana-Champaign
[2]College of Oceanic and Atmospheric Sciences, Oregon State University, Corvallis

1. INTRODUCTION

Coalescence growth and freezing of supercooled drops by contact ice nuclei (IN) are important cloud microphysical processes that can be enhanced by cloud drop charge. Although cloud drop charges have been obtained from mountain tops and balloons, the origin and spatial distribution of cloud drop charge remains speculative because existing data lacks measure-ments of other cloud properties. The purpose of the drop charge measurements in the 1997-98 Lake-ICE and Snowband field projects was to obtain drop charges using the NCAR Electra in various clouds and cloud locations for analysis with concurrent measurements of drop spectra, liquid water content, updraft speed, as well as Doppler radar.

2. MEASUREMENTS

For the aircraft measurements of drop charge, the cloud drops were sampled using a counterflow virtual impactor (CVI). In the CVI input stream, drops of about 10-50 mm diameter were evaporated before entrance into the aircraft (Twohy et al. 1997). The drop residue was collected by an absolute filter electrometer having a sensitivity of 1 femto amp (10^{-15} A). The mean charge on the cloud drops was calculated from the flow-corrected CVI drop concentration (using a CN counter) and the electrometer flow rate. The mean drop size was initially obtained from the CVI drop concentration and the CVI condensed water content (derived from a Lyman-alpha hygrometer).

The mean charges on cloud drops were determined from the electrometer current, sample flow rates and CVI CN concentrations. Mean drop sizes were calculated from CVI condensed water contents and CN concentrations. Charges on aerosol particles were measured using an aft-facing inlet to help determine the character of the space charge at cloud edges and within clouds.

3. DATA

Preliminary data analysis revealed regions of both negative and positive charge on cloud drops within the lake-effect boundary layer clouds. Flights through growing cumuli near cloud top showed positive charge with the highest value near cloud edges, presumably originating from the excess positive space charge accumulating at cloud edges (see Fig. 1). The peak values of drop charge are over 200 electron units (e) for the CVI sampled cloud drops ($d \geq 10\mu m$) having mean diameters of 13-16 μm, concentrations of 300-400 cm^{-3} and condensed water contents of 0.3-0.5 gm m^{-3}.

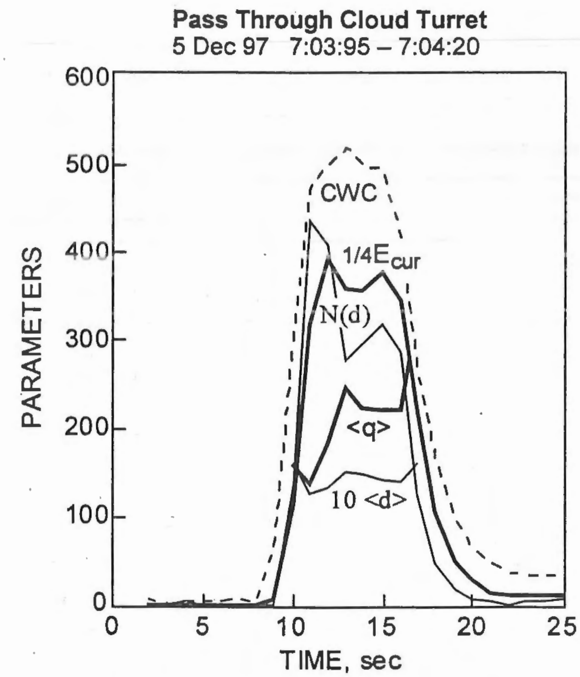

Fig. 1. Plot of CVI electrometer current (E_{cur}, pA) and mean drop charge (<q>, e) using cloud drop concentration (N, cm^{-3}) from CVI CN counts. Also shown are mean drop diameter (<d>, μm) and CVI condensed water content (CWC, mg m^{-3}).

Negative drop charges were obtained during an Electra flight climbing through cloud layer over Lake Michigan (Fig. 2). The drop charge has peak values of <q> = -110 to –140e for the CVI sampled cloud drops ($d \geq 10$ μm) with mean diameters increasing from 10 to 16 μm, concentrations from 20 to 115 cm^{-3} and condensed water contents from 0.02-0.20 gm m^{-3}.

Corresponding author: Ken Beard, Atmospheric Sciences, UIUC, 105 S Gregory St, Urbana, IL 61801
Email: k-beard@uiuc.edu

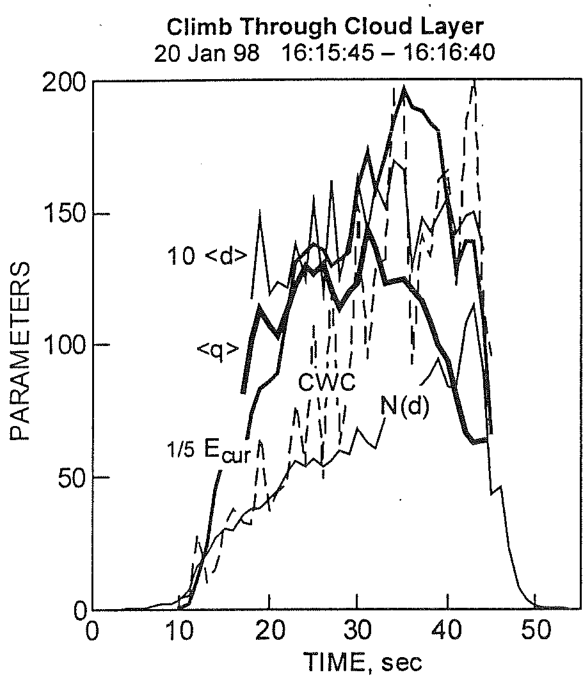

Fig 2. Plot of CVI electrometer current (E_{cur}, pA) and mean drop charge (<q>, e) using cloud drop concentration (N, cm^{-3}) from CVI CN counts. Also shown are mean drop diameter (<d>, μm) and CVI condensed water content (CWC, mg m^{-3}).

4. CONCLUSIONS

Preliminary data analysis of flights through stratocumulus clouds over Lake Michigan showed positive drop charges near cloud top with the highest values at cloud edges. The drop charges appear to have originated from space charge that accumulates at cloud edge because of different conductivities in clear and cloudy air. Negative drop charges were found below cloud top throughout the stratocumulus layer. The polarity may be associated with buoyant parcels that have ascended from cloud base where the space charge is negative. Descending, clear air parcels originating near cloud top should contain positive charges that can be evaluated from separate measurements of aerosol charge.

These data may be useful for studying effects of charge in promoting drop collisions and enhancing ice nucleation (e.g., see Beard 1992, Rosinski 1995, Tinsley et al. 2000). In addition, the charge polarity may serve as a tracer for the origin of cloudy and clear parcels, because charge is conserved and should remain unneutralized in the developing and mature stages of cumulus elements. During this time, mixing of clear and cloud air is incomplete and the charge cannot "relax" because the electrical conductivity is greatly reduced by the attachment of ions to cloud drops.

We hope to learn more about the origin of cloud particle charges using aircraft data such as particle type from the 2DC cloud particle optical array probe and vertical velocity. In addition, comparisons will be made with mountaintop and balloon measurements of cloud drop charges.

Acknowledgments The research reported here is based on work supported by the National Science Foundation under Grants ATM 95-05298 and ATM 94-21735. Any opinions, findings and conclusions or recommendations expressed in this material are those of the authors and do not necessarily reflect the views of the National Science Foundation.

4. REFERENCES

Beard, K. V., 1992: Ice initiation in warm-base convective clouds: An assessment of microphysical mechanisms. *Atmos. Res.*, **28**, 125–152.

Rosinski, J., 1995: Cloud condensation nuclei as a real source of ice forming nuclei in continental and marine air masses. *Atmos. Res.*, **38**, 351-359.

Tinsley, B. A., R. P. Rohrbaugh, M. Hei and K. V. Beard, 2000: Effects of image charges on the scavenging of aerosol particles by cloud droplets and possible consequences for droplet charging and ice nucleation. *J. Amos. Sci.* (in press).

Twohy, C.H., Schanot, A.J. and W.A. Cooper, 1997: Measurement of condensed water content in liquid and ice clouds using an airborne counterflow virtual impactor. *J. Atmos. Oceanic Technol.*, **14**, 197-202.

ICE PARTICLE MORPHOLOGY IN AN MCS: IMPLICATIONS FOR ELECTRIFICATION OF THE STRATIFORM AREAS.

R. A. Black[1], T. L. Schurr[2], and I. Winger[2]

[1]NOAA/AOML/HRD, Miami, FL., 33149
[2]NOAA/NSSL, Norman, OK 12349

1. INTRODUCTION

Mid-latitude Mesoscale Convective Systems (MCS) are copious producers of severe weather in the North American plains. In addition, cloud to ground lightning peppers the landscape for hours after the convective line passes. This leads to the speculation that charge separation processes may be occurring in the trailing stratiform areas. To investigate this, and to obtain better information about the nature of the precipitation in order to better measure rainfall accumulation, the Mesoscale Electrification and Polarimetric Radar Study (MEaPRS) was conducted in the spring of 1998.

Previous studies of the electric fields in and around MCS stratiform areas used ballon-borne electric field mills (Shepard et al, 1996). These studies showed that persistent layered charge distributions are common there, with the strongest fields occurring in the cloud at or above the melting layer. Unfortunately, these studies gave no hint of the origin of the observed fields. Other studies showed that positive polarity (lowering positive charge to ground) CG flashes are relatively common in the stratiform areas (Rutledge et. al, 1990), whereas negative polarity CG flashes predominate closer to the convective line (MacGorman and Morgenstern, 1998).

This result is significant, because most theories of thunderstorm electrification place the positive charge center near the top of the anvil (Williams et al., 1994). If positive CG flashes occur, there cannot be a strong negative screening layer between the positive charge center and the ground, or the strongest charge center nearest to the surface must be positive.

2. DATA

The data we report were obtained during the night of 8/9 June 1998 in a small MCS that formed along the Nebraska - Kansas border. Radar reflectivity maps were constructed from the operational WSR-88D radar data and/or the on-board radars of the NOAA WP-3D aircraft. No polarimetric radar data are available, as these storms were outside the range of the polarimetric radar.

Cloud and precipitation particle imagery was obtained from Particle Measuring Systems, Inc. (PMS) 2-Dimensional Optical Array Probes. A PMS 2D-Grey cloud probe (0.03 - 1.92 mm) provided Greyscale images, and the PMS 2D-P monoprobe (0.2 - 6.4 mm) provided number concentrations and precipitation water content. These data were reduced using the methods described by Black and Hallett (1986). Ice water content was computed assuming equivalent circle area diameters and a bulk ice density of 0.1 g cm^{-3}.

Cloud water content was provided by both a PMS King LWC probe, and a Johnson-Williams (JW) LWC meter. These devices are somewhat sensitive to ice particles (Gardiner and Hallett, 1985), so they do not provide an unambiguous cloud LWC measure when such particles are present. Electric fields were obtained from a pair of rotating vane field mills mounted on the fuselage of the aircraft. These data were reduced as in Black and Hallett (1999). Only the vertical component was measured.

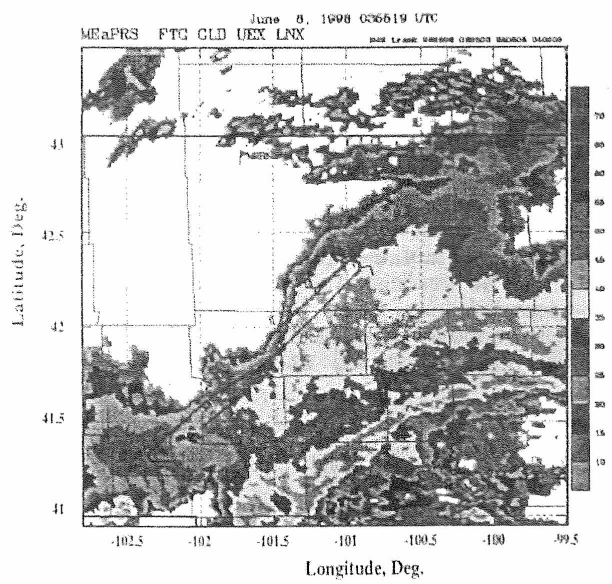

Figure 1. Composite PPI from the nearest NEXRAD radars at 03:50Z when the P-3 was at 3.0 km AGL (-2°C) in the Southern Nebraska MCS. The direction of flight is given by the arrow. The black line is the flight path from 0330 - 0400 UTC.

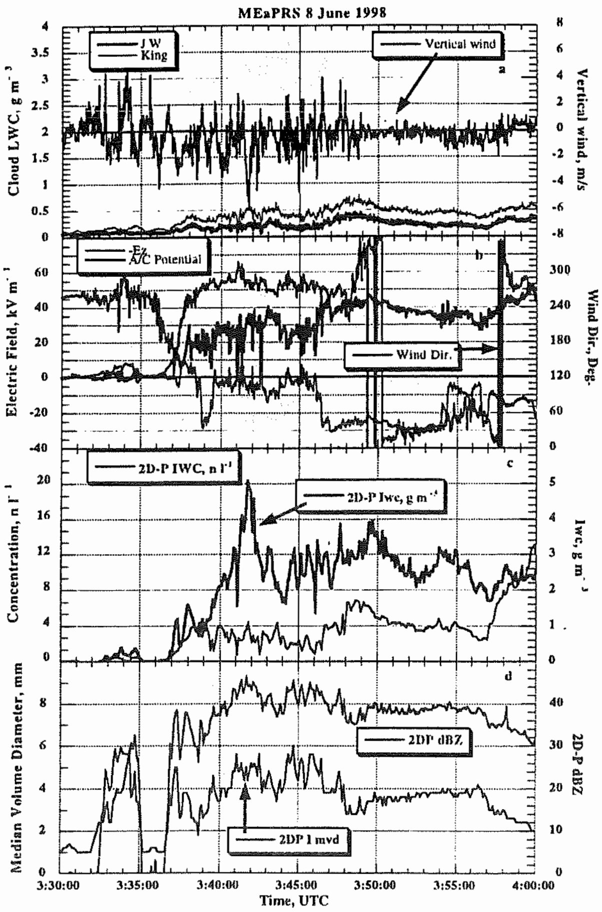

Figure 2. a) Vertical wind and cloud LWC. b) Electric field and wind direction. Note: the inverse of the electric field component is plotted. c) Ice particle number concentration and water content computed from the 2D-P imagery. d) Ice particle median volume diameter and computed radar reflectivity.

3. RESULTS

Figure 1 shows the radar reflectivity during a pass at ~2500 m AGL through the stratiform area northwest of the convective line. The dark line is the path of the WP-3D from 0330:00 to 0400:00 UTC; the arrow shows the direction of the flight. Henceforth, all times are UTC. Radar reflectivites were observed to be 35 - 40 dBZ at this time. This pass ended at 0357:00 and was just above the melting level, with a mean temperature of -2°C. The 2-D particle image data (not shown) during this time showed that the precipitation particles were predominately irregular snow with equivalent circle diameters up to 6.4 mm in low concentrations of 3-5 l^{-1} and IWC of ~3-5 g m^{-3}.

No cloud water is present anywhere during this pass, and the air was turbulent (Fig. 2a) where the large ice particles were most numerous. Reflectivites computed from the 2-D size distributions were around 40 dBZ, reasonably consistent with that from NEXRAD. (Fig. 2a). The JW and King water contents were uncorrellated with the vertical velocity, consistent with ice particle impacts. Note in this and subsequent plots that the largest vertical winds tend to occur during turns - those winds are probably erroneous.

Vertical electric field (E_z) was small to moderate, mostly below 20 kV/m, except for an abrupt increase in the magnitude of E_z at 0348, and a similar decrease at 0356 (Fig. 2b). The abrupt increase was correlated with the number concentration, but the subsequent decrease was not. As A_z did not change abruptly at these times, the field change is assumed to be real. The wind speed decreased from 18 m s^{-1} to 6 m s^{-1} and the direction also changed from WNW to NNE, then back to WNW, or toward the convection.

Ice water content and number concentration are shown in Fig. 2c, and the computed radar reflectivity and median volume diameter is shown in Fig. 2d. The dominance of the large snowflakes is shown by these plots. The median volume diameter (MVD) varied irregularly from 1 mm to 5-6 mm, and the highest reflectivity and IWC occurred where the number concentration was small.

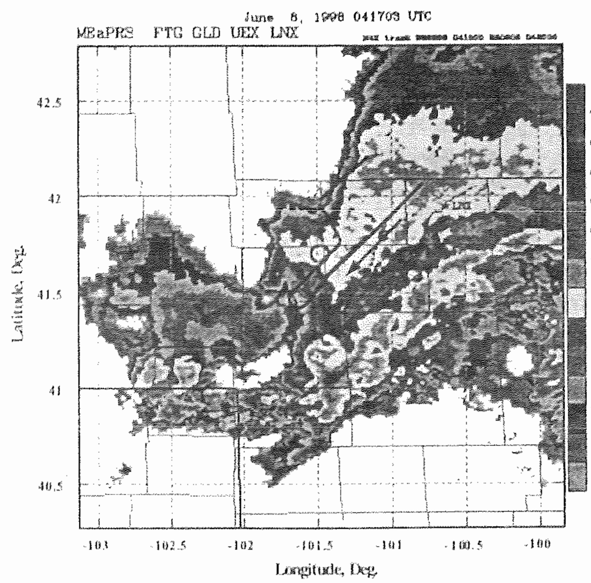

Figure 3. As in Fig. 1, but for 04:20Z, when the P-3 was at 3.8 km AGL (-8°C). The flight track from 0400 - 0430 is shown

The next pass we discuss was at 3.8 km AGL and a temperature of -8°C. Radar (Fig. 3) showed slightly lower (20-35 dBZ) reflectivity at this altitude, and the wind directions varied from WNW to S. Vertical winds (Fig. 4a) were mostly ± 2 m s^{-1}, and no cloud LWC was present. Electric fields during this pass (Fig. 4b) were from 0 - 20 kV m^{-1}, proportional to the equivalent field from charge on the aircraft. Irregular snow in concentrations of ~8 l^{-1} again dominated the 2-D imagery. Peak concentrations of ~16 l-1 (mostly small particles) occurred near the beginning of the pass at 04:02 and in the middle at 04:15 (Fig. 4c). Large particles (Fig. 4d) were somewhat more numerous near the end of the pass where the radar

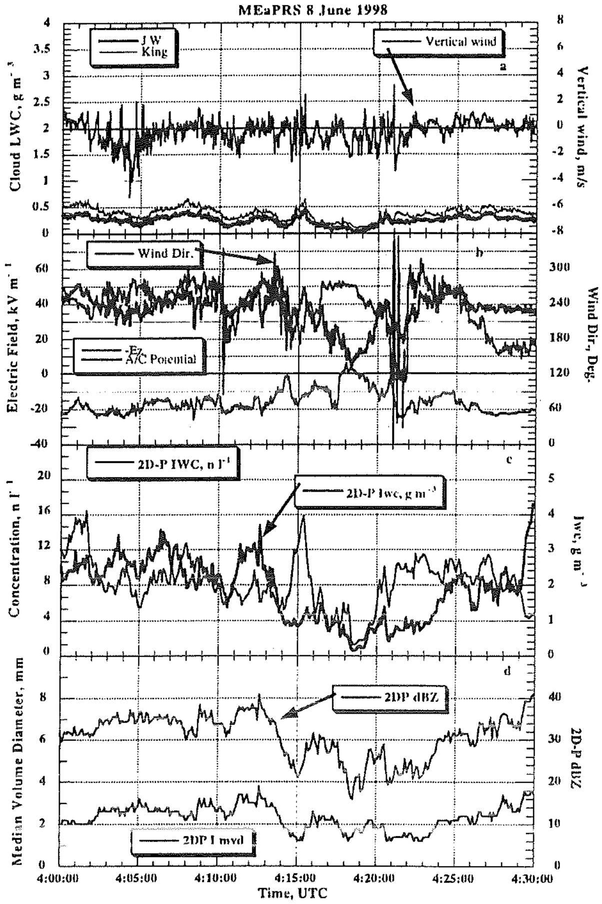

Figure 4. As in Fig. 2, but for the period 0400-0430 UTC with the aircraft at 3.8 km AGL (-8°C).

showed ~40 dBZ reflectivity. Again, IWC from the 2D-P varied from 1-3 g m^{-3}, and the King and JW probes showed no evidence of supercooled cloud LWC.

The highest pass took place at about 5 km AGL at a temperature of about -12°C. At this level, vertical winds were small (Fig. 6a), the 2D-P showed that the particles were fairly uniform in size in concentrations of 12 - 15 l^{-1}, with computed IWC of 3-4 g m^{-3} (Fig. 6c). The maximum particle sizes were 3-4 mm in diameter with a MVD of ~2 mm, compared with 6-6.6.4 mm with MVD of 3-4 mm at the lowest altitude. Radar reflectivity (Fig. 5 and Fig. 6d) was reasonably steady at ~30 dBZ throughout the pass. E_z was also constant at ~15 kV m^{-1} and uncorrelated with the charge on the aircraft(Fig. 6b). Wind direction was predominately from the south (away from the convection), except near the start of the pass at 05:00, when it was from the west. Since the winds at this level were predominantly blowing away from the convection, whereas winds during the lower passes were predominantly blowing with a component toward the convective line, it is pertinent to ask where the ice particles originated.

This question is partially answered by the Doppler radar plot shown in Figure 7. These data show the hydrometeors advecting from right to left above the melting layer, and from left to right at and below that level. Since the convective line was to the right at this time, the particles are clearly coming from there. Later, we will produce 3-D wind fields from these data to clearly show the advection patterns around this MCS.

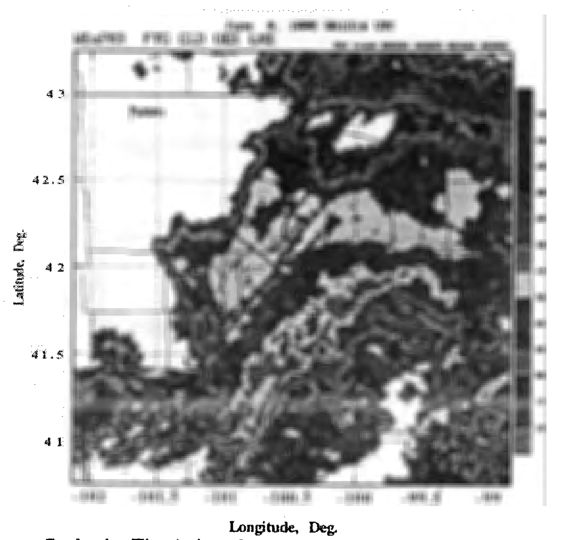

Figure 5. As in Fig.1, but for 0519, with the aircraft at 5.0 km AGL (-12°C). The Doppler cross-section was from the line segment marked $\overline{ab}$.

4. Summary

The observations presented here are fully consistent with the idea that the ice particles in the stratiform area are advecting from the convective line, metamorphosing and aggregating as they fall. Radar reflectivity and median volume diameter decreased with height above the melting layer, whereas number concentrations increased. IWC computed from the size distributions was about constant with height. This indicates that little mass was added to the ice particles by vapor diffusion during their residence in the stratiform cloud. The bulk ice particle density of 0.1 g cm^{-3} used in the computation of water content was about right, as shown by the good agreement between the computed reflectivity and that provided by NEXRAD.

Conditions favored for charge separation include graupel, supercooled cloud water, and vapor grown ice crystals (Saunders and Peck, 1998), although the quantities of these items that are needed for electrification is disputed (e. g. Williams and Zhang, 1996). No evidence of supercooled cloud water, no graupel, and few crystals with identifiable habits were encountered anywhere. Thus, this stratiform area was an unlikely place to find substantial electric field, but the moderate fields encountered are indicative of a cloud that could conduct lightning.

Updraft speeds were uniformly less than 4 m s^{-1}, and no sustained drafts wider than ~1.5 km were encountered. Electric fields were relatively uniform, and the polarity did not change with altitude. As we are unable

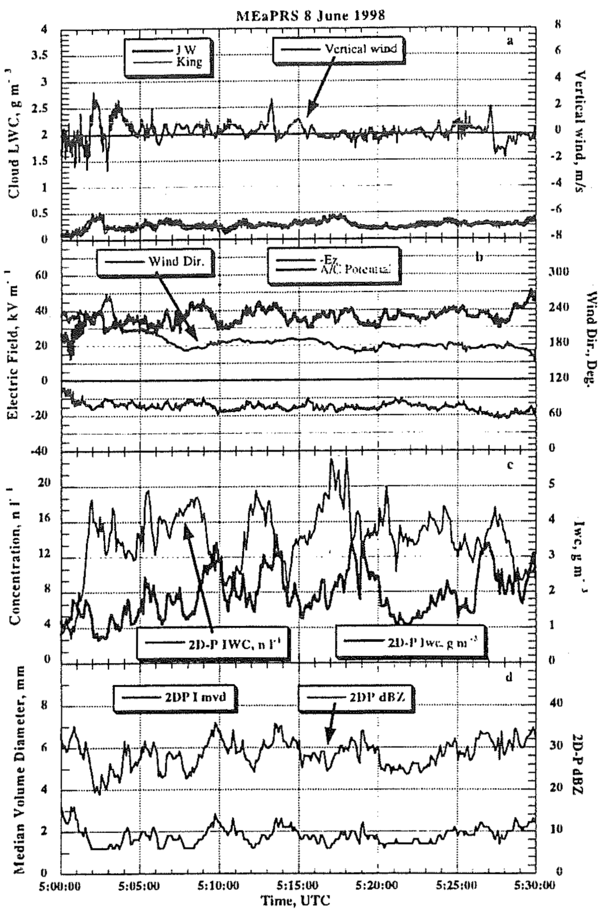

Figure 6. As in Fig. 2, but for the pass at 5.0 km AGL (-13°C).

to remove the effects of charge on the aircraft, we cannot be certain that the observed electric field component is real, but also, these data are consistent with the layered charge structure observed by Shepard et al. (1996) and others, with the exception that the strongest electric field (positive polarity) observed by the WP-3D was substantially above the melting level.

5. REFERENCES

Black , R. A. and J. Hallett, 1999: Electrification of the hurricane. J. Atmos. Sci., **56**, 2004-2028.

Black, R. A. and J. Hallett, 1986: Observations of the distribution of ice in hurricanes. J. Atmos. Sci., **43**, 802-822.

Gardiner, B. and J. Hallett, 1985: Degradation of in-cloud forward scattering spectrometer probe measurements in the precence of ice particles. J. Atmos. Ocean. Tech., **2**, 171-180.

MacGorman, D. R. and C. D. Morgenstern, 1998: Some characteristics of cloud-to-ground lightning in mesoscale convective systems J. Geophys. Res., **103,** 14011-14023.

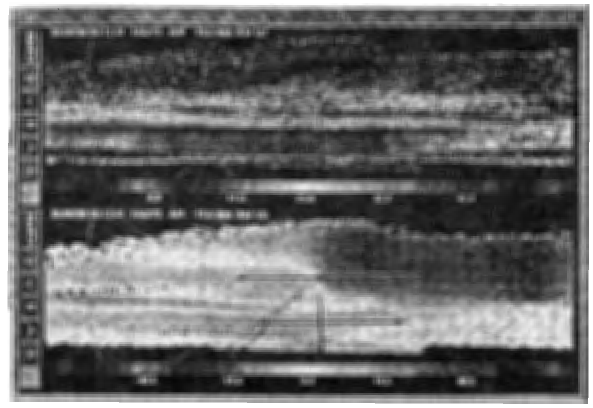

Figure 7. Doppler cross-section of the stratiform area from the position marked in Fig. 5. Reflectivity is in the top panel, and Doppler speed in the lower. The arrows denote the direction taken by the hydrometeors.

Rutledge, S. A., C. Lu, and D. R. MacGorman, 1990: Positive cloud-to-ground lightning in mesoscale convective systems. J. Atmos. Sci., **47**, 2085-2100.

Shepherd, T. R., W. D. Rust, and T. C. Marshall, 1996: Electric fields and charges near 0°C in stratiform clouds. Mon. Wea. Rev., **124**, 919-938.

Saunders, C. P. R. and S. L. Peck, 1998: Laboratory studies of the influence of the rime accretion rate on charge transfer during crystal/graupel collisions. J. Geophys. Res, **103**, 13949-13956.

Williams, E., R. Zhang, and D. Boccipio, 1996: Density of rime in laboratory simulations of thunderstorm microphysics and electrification J. Geophys. Res., **101**,, 29715-29719..

Williams, E., R. Zhang, and D. Boccipio, 1994: Microphysical growth states of ice particles and large scale electrical structure of clouds. J. Geophys. Res., **99**, 10787-10792.

FORMATION OF ELECTRIC CHARGES IN MELTING LAYER

A.V. Kochin

Central Aerological Observatory, Dolgoprudny, Moscow Region, 141700 RUSSIA

1. INTRODUCTION

The mechanisms for generation of electric charges in clouds have been intensively studied in many countries for a long time, which is an indication of both scientific and applied importance of the subject. The majority of theoretical models describe processes in cumulonimbus clouds. Models dealing with nimbostratus clouds are few and more of a qualitative nature. They do not offer any reliable quantitative estimates of the observed effects.

However, the electric charges are being generated not only in Cb but also in Ns. Moreover, about 80% of the electric discharges to the aircraft occur in Ns clouds (Brylev et al., 1989). This is not an indication of a large electric activity of Ns clouds but, rather is a result of the fact that any flying in vicinity of the cumulonimbus clouds is prohibited because of strong vertical drafts inside them.

Thus, development of a model to explain electrification of the Ns clouds is viewed as an urgent task. Besides, one can reasonably assume that, similar to precipitation development in Ns and Cb, the generation of the electric charges in different types of clouds is based on some common principles, but also has specific features resulting from peculiarities of the given cloud type. Hence, the model should be also valid for explanation of the processes in cumulonimbus clouds.

2. ORIGIN OF ELECTRIC FIELD IN CLOUDS

Any model intended for description of electric charge formation and origin of the electric field in the clouds should explain two phenomena, which could be called micro- and macroscale partitioning of the charges.

At the stage of the charge microscale partitioning, the electrically neutral hydrometeors (droplets, snow flakes, hailstones) are charged by elementary electrification mechanisms. For example, a rapid freezing of a droplet is accompanied by breaking small pieces off the ice cover, which could be electrically charged. In response, the initially neutral droplet acquires an equal charge of the opposite sign. Similarly, the air current overflowing a melting graupel pellet, blows off small charged droplets thus charging the graupel pellet with a charge of the opposite sign. A large number of electrification mechanisms have been examined (Mason, 1971; Muchnik, 1974).

However, no significant electric fields are induced because the carriers of charges of different signs are close to each other and mutually compensate for the induced electric fields.

After the microscale partitioning is completed, the charges of different signs should gather in relatively small and spatially separated areas, with the concentration of charges of a given sign exceeding that of the opposite sign (i.e., a macroscale charge partitioning).

3. A PHENOMENOLOGICAL DESCRIPTION OF THE PROPOSED MODEL

This paper suggests a mechanism for generation of electric charges within clouds. According to this mechanism

-the microscale partitioning of electric charges takes place within the low melting layer due to breaking of large droplets emerging from melting ice particles,

-the macroscale partitioning is induced by different rates of gravitational sedimentation of the different charge carriers,

-the emerging electric field increases the charge generation rate in the course of the microscale partitioning.

3.1 <u>Large droplet formation and breaking</u>

Precipitation particles form from the water vapour mainly in the cold part of the cloud. Then, the ice particles (snow flakes, snow aggregates, graupel pellet) fall down into warm area and turn into droplets thus forming a so called melting

Corresponding author's address: A.V. Kochin , CAO, Pervomaiskaya 3, Dolgoprudny, Moskow region, 141700 Russia, E-mail: alexkochin@mtu-net.ru

layer. Its vertical extension is several hundred metres.

A distance covered by a falling ice particle before its total melting is approximately proportional to a cubic root of the particle mass (Kochin, 1994). In the low melting layer the largest ice particles will be transformed into largest droplets. Drops which diameter exceeds 4 mm are unstable and tend to break into a large number of smaller droplets. The process is as follows. A droplet with an initial diameter of 4-5 mm grows to 40-50 mm, transforming its shape to that of parachute. Then the parachute top breaks into a large number of small droplets, while its bottom yields a few large ones (Mason, 1971). If the ice particle spectrum contains crystals, which produce drops exceeding 4 mm in diameter, these drops will break. The radar observations have proved droplet breaking in the low melting layer in Ns and Cb (Kochin, 1994).

3.2 Electric charge generation

A rain droplet in the electric field behaves as a conducting sphere and polarises in response to electric field strength. This is why breaking of a large droplet in the electric field produces electrically charged fragments (Mason, 1971). The upper part of the break droplet transforms into small droplets with electric charges, which sign corresponds to that of the vertical component of electric field. The lower part of the droplet transforms into large droplets with charges of the opposite sign.

Usually the vertical component of the Earth's electric field is negative, so the small and large drops will be charged negatively and positively, respectively. The values of the forming charges are proportional to the field strength (Mason, 1971). Thus, a microscale partitioning of charges takes place.

3.3 Macroscale partitioning

Macroscale partitioning of the charges occurs due to different falling velocities of the carriers of charges of different signs. Since the velocities of small droplets are smaller, their concentration in the vicinity of the melting layer will be much greater than concentration of the large droplets. Thus, a negatively charged region forms there.

As the distance from the melting layer increases, the concentration of small droplets declines. This results in a relative growth of large droplet concentration and inception of a positively charged region at some distance below the melting layer.

3.4 Enhancement of charge generation

Initial large droplets break in the Earth's electric field (~150 V/m) and then the drop fragments (small and large droplets) leave the layer where the drops are breaking. After that, the electric field in this layer is controlled by interaction of negatively charged small droplets and positively charged large droplets. The small droplets induce a field which sign coincides with that of the Earth's field; a contribution of small droplets into the resulting field will be greater since they are closer to the droplet breaking layer. Hence, the electric field strength in that layer grows up. The value of the breaking charge is proportional to the field strength. Thus, a positive feedback arises which will lead to a continuos growth of the field strength because each subsequent portion of droplets breaks in a stronger electric field and produces a larger charge than the previous one.

4. QUANTITATIVE ESTIMATES OF ELECTRIC FIELD STRENGTH GROWTH

The above description of a charge generation mechanism presents only the basics of the proposed model. In order to give quantitative estimates one needs to derive an equation describing the charge generation process with an account of the affecting factors, i.e. vertical and horizontal extension of the droplet breaking layer, ice particle size distribution, vertical draft velocity within the melting layer, etc.

This equation was derived and numerical simulations of electric field strength growth were made by using of the vertical draft velocity and precipitation rate as variables. Ice particle distribution was taking in accordance with Rogers (1976).

The length of the path of a particle before melting is expressed as a linear function in accordance with Kochin (1994)

$$L(d) = 100d \quad (1)$$

where d and L(d) are given in mm and m, respectively. The horizontal dimention of the droplet breaking layer was taking 300 m in accordance with radar data.

5. RESULTS OF NUMERICAL SIMULATIONS

The numerical simulations show that in the course of time the vertical profile of the field strength assumes a complicated shape of varying sign, caused by the vertical extension of the droplet breaking layer. In general, the maximum field strength grows up as precipitation enhances. Depending on the vertical draft velocity the maximum field strength in the melting layer can either be a monotonous function of time or have an oscillating nature, with the charge generation rate reaching maximum in the downdrafts with velocities of 0.5 - 1 m/s.

Temporal variation of the maximum electric field strength E_{max} in a downdraft with a velocity of 0.5 - 1 m/s is perfectly described by (for I>5mm/h, t>60s)

$$E_{max} = 250\exp\left[0.01\frac{I^2-20}{I^2}t\right] \quad (2)$$

where E_{max} is expressed in V/m, I is precipitation rate, mm/h, t is time, sec.

The results of numerical simulations have also shown that

i) within updrafts or weak (less than 0.3 m/s) downdrafts the electric field strength is about 300 - 3000 V/m, with the maximum values only slightly depending on precipitation rate and having a spatial and temporal variability of charge sign;

ii) maximum electric field strength is attained in a layer with temperature +2°C;

iii) when the downdraft velocity is 0.5 - 1 m/s the charge generation rate is the largest and electric field strength growth rate increases as precipitation enhances. In this case the electric field strength reaches values of 10^5- 10^6 V/m after 15 min of raining at a rate of 10-15 mm/h.

6. COMPARISON WITH EXPERIMENTAL DATA

The experimental data on electrical activity of the Ns clouds are in good agreement with the theoretical results:

- typical electrical field strength in Ns clouds coincides with the model results according to item i) (Brylev et al., 1989);

- maximum frequency of lightening strokes to aircraft is observed at a level with temperature +1°C (Brylev et al., 1989) ;

- according to estimates by different investigators the electric discharging begins when electric field strength reaches 10^5 - 10^6 V/m (Mason, 1971) which requires precipitation rate at least 10 mm/h for more than 15 min.

7. ON FEASIBILITY OF PROPOSED MECHANISM IN CB CLOUDS

Apart from others, the proposed mechanism is likely to contribute to electrification of Cb clouds as well. This belief is supported by the fact that the model also agrees with the experimental data on the electrical activity of the Cb clouds.

According to the model results, under a near zero updraft velocity the electric field strength attains a value of 300 - 3000 V/m with no further build-up of the electric field strength. In strong updrafts the electric field strength varies within a range -300 - +300 V/m. This corresponds to the observed values in the non-lightening convective clouds.

In order that the field strength, typical of the thunderstorm, is achieved, it is essential that the precipitation area coincides with the downdrafts.

Usually, an updraft concentrates in the centre of the thunderstorm while downdrafts occupy the cloud periphery. The lower part of the cloud converges the horizontal air currents as the upper part is a region of divergence. In accordance with the proposed model, the charges are to generate on the cloud's periphery. The area of charge generation, comprising individual cells, forms a narrow ring or a sickle. This phenomenon has been already discovered from the experiments (Williams, 1989) but failed to be explained theoretically.

Besides that, the following phenomena should be observed near the melting layer:

- a fast change of value and sign of the hydrometeor's charge;

- maximum values of charges on hydrometeors .

Both effects have been found during aircraft spiral descents on the periphery of thunderstorm (McCready and Proudfit, 1965).

Two-charge clouds are most frequent to occur, with positively charged upper parts and negatively charged middles (Mason, 1971). So, one may believe that positive charges are descending, captured by updraft and carried to the cloud top. A similar process is observed in Cb clouds during the hailstone growth, namely, the large rain droplets are carried to the cloud top. Studies of the hail clouds have shown (Muchnik, 1974) that the hailstone growth is accompanied by a strong radio emission, typical of the thunderstorm inception and development stages, a fact that supports this belief.

In 10-15 min from start of precipitation, the positive charges, captured by updraft, will reach the cloud top. By that time the field strength will build-up to 10^5 - 10^6 V/m, resulting in lightening activity development.

In case of a sharp enhancement of downdrafts in a precipitating cloud the change of electric field sign within the melting layer is possible. The reason is that at the early stage of development the field sign is oscillating, so an increase in charge generation rate can "fix" the sign of field, which existed at the moment of the downdraft enhancement. As a result, an opposite (as compared to described above) distribution of cloud charges emerges, something which has been proved by observation (Mason, 1971).

8. OUTLOOK FOR FURTHER STUDIES

The described model, however, fails to account for several factors, which strongly affect the charge generation rate.

There is a process, similar to droplet breaking, taking place in the melting layer and capable of generating charges. The thing is that the peripheral branches of melting snow crystals subject to breaking off. If this process is taking place in the electric field, the charged fragments emerge, similar to charge partitioning during droplet breaking. However, this process has not been studied in detail and there are only preliminary theoretical estimates of its effectiveness. Based on these results, a quantitative estimation of electric field growth rate has been made from the model equation (5). It has been found that under exponential ice particle size distribution the crystal destruction provides a fast growth of the electric field up to 10^3 V/m and its further oscillations.

If the ice particle size spectrum is transformed to a monodispersal one, the described process can lead to field strength values of 10^5 - 10^6 V/m even in a light precipitation (about 1-3 mm/h). Another possibility is charge generation in precipitating winter-time warm frontal clouds. This situation can provoke formation of a thin layer with positive temperatures, resulting in the same effect as produced by a transformation of the particle size spectrum to a monodispersal one.

Besides, as soon as the electric field strength reaches 10^4 - 10^5 V/m, the smaller droplets become unstable and begin breaking, thus giving birth to additional charge carriers.

As the electric field strength exceeds 10^5 V/m, another factor comes into play, i.e. the electrostatic interaction becomes comparable with the aerodynamical drag effect. This can alter the falling velocity of charged droplets.

A detail analysis of these processes is the next stage in the proposed model improvement.

9. CONCLUSION

In conclusion, one has to mention that despite a satisfactory agreement between obtained theoretical results and the experimental data, special experiments are needed for model verification. The experiment should include registration of starting moment and rate of the droplet breaking (e.g., with radar methods) and measurements of electric field strength. Such an experiment will allow to conclude whether physical bases for the proposed model are correct.

10. ACKNOWLEDGEMENT

The author is grateful to I. L. Bushbinder and V. L. Kuznetsov for useful discussions and also to V.R. Megalinsky and colleagues from the Central Aerological Observatory for their assistance in conducting the experiments.

REFERENCES

1. Brylev G.B., S.B. Gashina, B.F. Evteev and I.I. Kamaldina, 1989. Kharacteristiki electricheski aktivnyh zon v sloistoobraznyh oblakah.- Leningrad, Hydrometizdat, 158 p.p.
2. Kochin A.V., 1994. Radiolokatsionnie issledovania microphysicheskih protsessov v polose tayania .- Meteorologia i hydrologia, No 10, p.p 34 - 40
3. Mason B. J., 1971. The physics of clouds.- Clarendon Press, Oxford, 671 p.p.
4. Muchnik V.M., 1974. Fizika grozi.- Leningrad, Hydrometeoizdat, 352 p.p.
5. Rogers R.R., 1976. A short course in cloud physics.- Pergamon Press, 232 p.p.
6. McCready J.B. and A. Proudfit, 1965. Observations of hydrometeor charge evolution in thunderstorm.- Quart. J. Roy. Met. Soc., V.91, No 387, p.p. 44 - 53
7. Williams E.R., 1989. The tripole structure of thunderstorms.- J. Geoph. Res., v. 94, No 11, p.p. 13151 - 13179

OBSERVATIONAL- AND MODELING-BASED ANALYSIS OF PASSIVE TRACER AND LIGHTNING-PRODUCED NOx TRANSPORT IN THE 10 JULY 1996 STERAO STORM

W. C. Skamarock, J. Dye, E. Defer, M. Barth, J. Stith, B. Ridley

National Center for Atmospheric Research,*
Boulder, Colorado

1. INTRODUCTION

Production of NOx by lighting represents the largest uncertainty in the global NOx budget, with estimates varying by over two orders of magnitude (Liaw et. al. 1990). Here we present an NOx budget for the 10 July STERAO storm that contains estimates of the time varying production rate of NOx by lightning along with total lightning NOx production over the lifetime of the storm. These budgets are produced by combining meteorological and chemical observations from aircraft in the anvil outflow with lightning channel length data produced by the ONERA interferometer and with an analysis of a 3D cloud model simulation. This study is unique in that the aircraft data are used to calculate a flux of NOx out into the anvil, and this flux is related directly to a time history of the lightning channel length production; typically, estimates of NOx production by lightning have been produced by using estimates of NO production per lightning flash and multiplying this production rate by the total number of observed flashes.

2. NOx FLUX ANALYSIS

The 10 July STERAO storm developed along the southern portion of the border between Wyoming and Nebraska over a locally elevated topographic feature known as the Cheyenne Ridge. Through most of its lifetime (from approx 2200 to 2500 GMT) the convective system consisted of multiple cells aligned along a NW-SE axis. Storm inflow at low levels was from the south and west, and anvil outflow was to the SE in the lower and middle parts of the anvil (from 6.5 to 10.5 km MSL) and towards the east above approximately 12.5 km. The orientation and growth of the anvil is dictated by the upper level winds, which were northwesterlies turning to westerlies above 12.5 km, and the slow storm movement relative to these upper level winds (approximately 5 m/s towards the SSE, Skamarock et al 2000). At later times the storm consisted of a single strong cell (with supercell characteristics) that propagated at a somewhat higher speed to the south.

Extensive observations of the storm were obtained from a variety of observational platforms (see Dye et al 2000). Of particular interest for this study, NO measurements were taken on the the North Dakota Citation aircraft, which spent its flight time in the vicinity of the storm between 7 to 12 km MSL. Figure 1 shows the projection of the Citation flight track, between 2313 and 2440 GMT, on the horizontal plot of radar reflectivity at 2400 GMT and 10.5 km MSL. The Citation aircraft mapped out the anvil structure during this time period by traversing the anvil in horizontal passes, approximately perpendicular to the long axis of the anvil, at elevations starting at approximately 11.8 km (close to the anvil top) and ending at approximately 6.8 km.

Both satellite photos and radar reflectivity (see Skamarock et al 2000, fig 5) suggest that the evolution of the storm from a line of convective cells to a single supercell occurred somewhat after the period in which the Citation observations in the anvil were taken. A parcel detraining from the updraft cores would take around 45 minutes to reach the analysis plane based

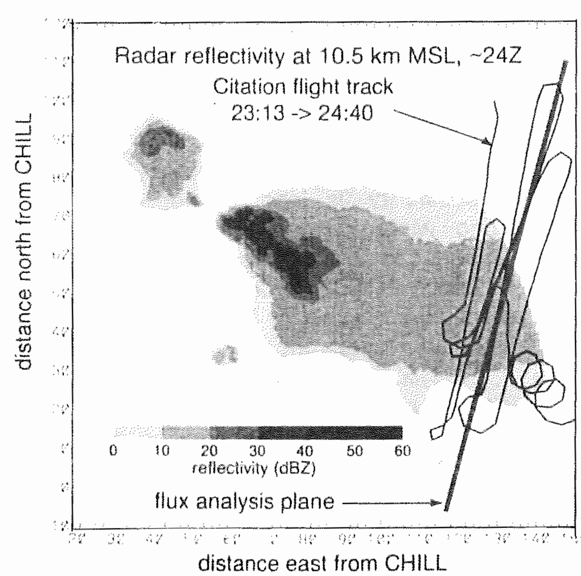

Figure 1. Horizontal cross section of radar reflectivity at 10.5 km MSL. The analysis plane is shown in the thick gray line and the black line is the aircraft flight track.

* The National Center for Atmospheric Research is sponsored by the National Science Foundation.

Corresponding author address: Dr. William C. Skamarock, NCAR, P.O. Box 3000, Boulder, CO 80307-3000. email: *skamaroc@ucar.edu*

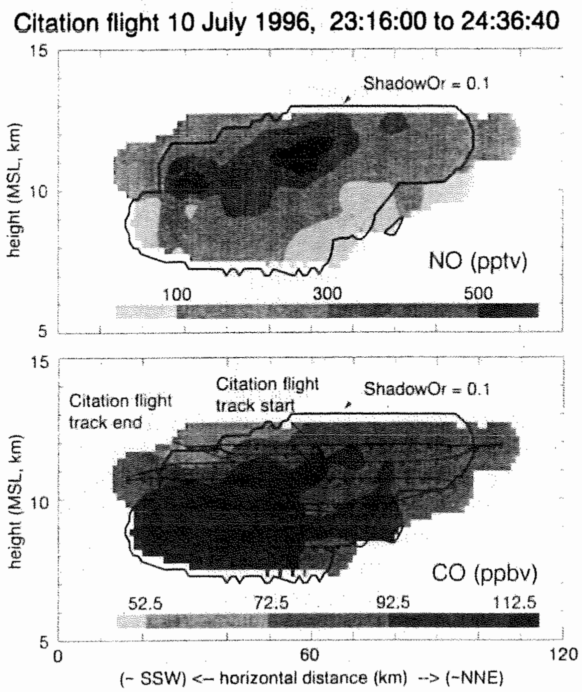

Figure 2. Objective analysis of NO and CO using the Citation flight data. The flight track is shown in the CO plot.

on the mean upper level winds, thus the aircraft was sampling anvil air from the multicellular period of the storm, from approx 2230 GMT to 2400 GMT.

Figure 2 depicts the Citation aircraft track projected perpendicularly onto the vertical flux analysis plane (shown in Figure 1) using 30 s averages of the aircraft position; these mean locations are shown as circles along the flight track. The analysis plane moves with the storm at the system velocity (u,v) = (1.5,-5.5) m/s where u is towards the east and v is towards the north (see Skamarock et al 2000). Observations from the Citation aircraft are averaged over the 30 s intervals and likewise projected onto the analysis plane, and include the horizontal winds (u,v), NO, and CO.

For calculating fluxes and for plotting, the projected observations are analyzed onto a regular grid using an objective analysis procedure similar to that developed by Cressman (1959). In this application, we represent a variable as the sum of a reference state and a perturbation, $\phi = \phi_o(z) + \phi'$, where the reference state represents the undisturbed (pre-convective) environment. On the regular grid at points (z_a, x_a), we calculate the objectively analyzed value $\phi_a = \phi_o(z)+\phi'_a$ by computing the perturbation value ϕ'_a using

$$\phi'_a = \frac{\sum_{i=1}^{K} w_i\left(\phi_{obs} - \phi_o(z)\right)}{\sum_{i=1}^{K} w_i}$$

Flux Analysis	cross section area [10^5 m^2]	mass flux per unit area [kg/s/m^2]	CO flux per unit area [10^{-5} moles/s/m^2]	NO_x flux per unit area [10^{-8} moles/s/m^2]
Analyzed (Citation data)	315	5.9	1.9	4.5 (NO) 5.8 (NO_x) (NO_x = 1.3 • NO)
Simulation Time [s]				
3600	109	6.7 (1.13)	1.9 (0.99)	2.4 (0.41)
4200	177	6.6 (1.11)	1.9 (0.90)	2.2 (0.38)
4800	193	6.5 (1.09)	1.9 (0.99)	2.2 (0.38)
5400	232	6.6 (1.11)	1.9 (0.99)	2.3 (0.40)
6000	238	6.5 (1.09)	1.9 (0.99)	2.2 (0.38)
6600	187	6.6 (1.11)	2.0 (1.02)	1.9 (0.33)
7200	119	6.5 (1.09)	2.0 (1.02)	2.0 (0.34)
average of the four times	180	6.6 (1.11)	1.9 (0.99)	2.2 (0.38)
		(fraction of analyzed flux per unit area)		

Table 1: Flux analysis for the observations and the simulation.

where

$$w_i = \frac{1-d^2}{1+d^2}, \text{ if } d^2 < 1,$$
$$w_i = 0, \text{ if } d^2 \geq 1,$$

$$d^2 = \left(\frac{x_a - x_{obs}}{x_r}\right)^2 + \left(\frac{z_a - z_{obs}}{z_r}\right)^2,$$

the summation K is over all the observations, x_r and z_r define the radius of influence of the observation on the analyzed values, and we use x_r = 5 km and z_r = 1.5 km. The results of the analyses are not sensitive to values of x_r and z_r, and the primary constraint on the values are that they be significantly greater than half the height difference between flight levels for z_r (> 1/2 km), and significantly greater than half the horizontal distance between time-averaging locations.

Figure 2 presents the results from the objective analyses for NO and CO. The data is contoured only where observations have contributed to the values. The NO and CO fields extend somewhat more than a km above and below the highest and lowest flight track observations. We have no data in these regions, and the values represent an extrapolation. The fields possess much structure, and the structures differ substantially. The NO analysis shows isolated maxima located above 10 km MSL while the CO analysis shows somewhat less-isolated maxima located below 10 km MSL. Two factors likely contribute to the different structures; the pre-convective vertical distributions of NO and CO differ (higher CO levels extend well beyond the PBL top compared to NO), and NO is also produced by lightning.

To compute fluxes of mass, NO and CO through the anvil on the analysis plane, we use the plane-perpendicular velocities analyzed from the aircraft data (not shown) along with the analyzed NO and CO and a reference density profile. We define the anvil area as that lying within the 0.1 particles per liter contour in the ShadowOr analysis. The fluxes are given in Table 1.

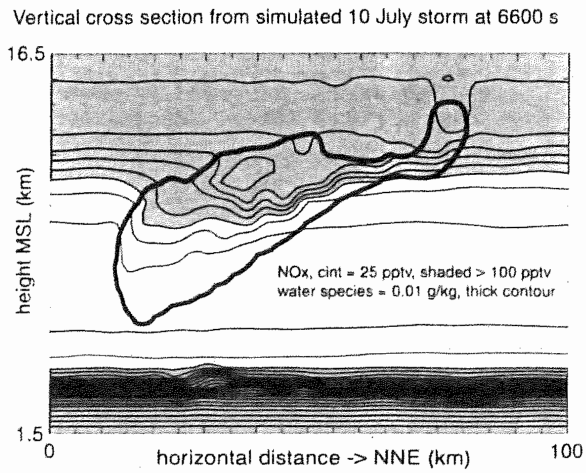

Figure 3. Vertical cross section of NOx and water species in a position similar to the analysis cross section.

3. CLOUD MODEL SIMULATION

A 3d cloud model simulation of the 10 July storm is described in Skamarock et al (2000). We have included NOx as a tracer in this simulation, using a profile derived from aircraft observations and a sounding composited from observations. There is no lightning source of NOx in the model. Figure 3 shows an outline of the model cloud and precipitation field and NOx and can be compared with the observational analysis NO in figure 2. The simulated anvil cross sectional area is significantly smaller than that observed, averaging less than 2/3 the observed area between 1 and 2 h in the simulation.

For quantitative comparison, we have normalized the observed and simulated fluxes by the anvil cross-sectional area; these normalized fluxes are presented in Table 1. The simulated fluxes are given at ten minute intervals between 1 h and 2 h. The simulated storm transitions to a supercell somewhat after 2 h in the simulation, and the observed storm transitions to a single supercell around 0100 GMT 11 July. The observations used to compute the fluxes span a little over an hour starting at approximately 2315 GMT, that is, somewhat before the observed storm transitioned to a supercell. Thus the averaging period for the observations is similar to the flight time used in the observational analysis, and the simulated and observed storms are in at similar points in their evolution to a supercell.

The normalized mass and CO fluxes compare well, although the simulated normalized mass flux is consistently higher than the observed flux. This difference could be attributed to errors in the initial wind profile or errors in the convective simulation. The average normalized NOx flux (we use a photostationary state assumption and NOx = 1.3*NO) differ dramatically. The observed normalized flux is approximately 2.6 times larger than the simulated flux. From this we conclude that approximately somewhat over 60 percent of the observed NOx flux out the anvil can be attributed to lightning generated NOx. This results in an average of approximately 11.5 moles/s of NOx produced by lightning (anvil area X NOx flux per unit area X 0.62) fluxing out through the anvil in the observation period.

4. LIGHTNING AND NOx PRODUCTION

During the STERAO field program, the ONERA lightning interferometer was used to map the three dimensional lightning channel paths in the observed convective storms. The capabilities of the instrument and the analysis of the data for the 10 July storm are described in Defer et al (2000). The 10 July storm produced mostly IC lightning as opposed to CG lightning, and there were almost no CG flashes during the analysis period (2230-2400 GMT). Also, the P3 aircraft did not find evidence of enhanced NOx values at low levels, and the simulations show that boundary layer NOx was transported primarily into the anvil by the convective updrafts; other simulations having NOx sources representing lightning production also show the lightning produced NOx being transported out into the anvil. Thus the NOx production rates presented next are based on the assumption that all lightning-produced NOx appears in the anvil outflow.

4.1 *Lightning NOx Production Rate*

For the 10 July storm, the lightning-channel-length production per unit time, and the flash rate, is given in figure 4. Both the flash rate and channel length production vary significantly over the lifetime of the storm. These two measures of lightning activity are not always well correlated; for example the large peak at approximately 2320 in the flash rate that does not correspond to a particularly large peak in channel length production.

The average lightning channel length production over the period 2230 GMT to 2400 GMT is approximately 10^4 m/s. Using the analyzed production rate for NOx given in the previous section, we estimate that the average amount of NOx produced per meter path length over this period is approximately 1.15×10^{-3}moles/m NO_x or (4.7×10^{-5}kg/m or 6.9×10^{20} molecules/m). Similarly, the average flash rate over the period from 2230 GMT to 2400 GMT was 0.26 flashes per second, which leads to in an NOx production rate of 2.7×10^{25}molecules/flash.

These estimates of NOx production rates per meter channel length and per flash fall within the other NOx production rate estimates produced using entirely different approaches. Stith et al (1999) analyzed flight track NOx peaks from the STERAO storms on 9, 10 and 12 July 1996. In that study, individual NO anomalies (above a measured background) were fit to a simple model of lightning-generated NO plumes. Using the

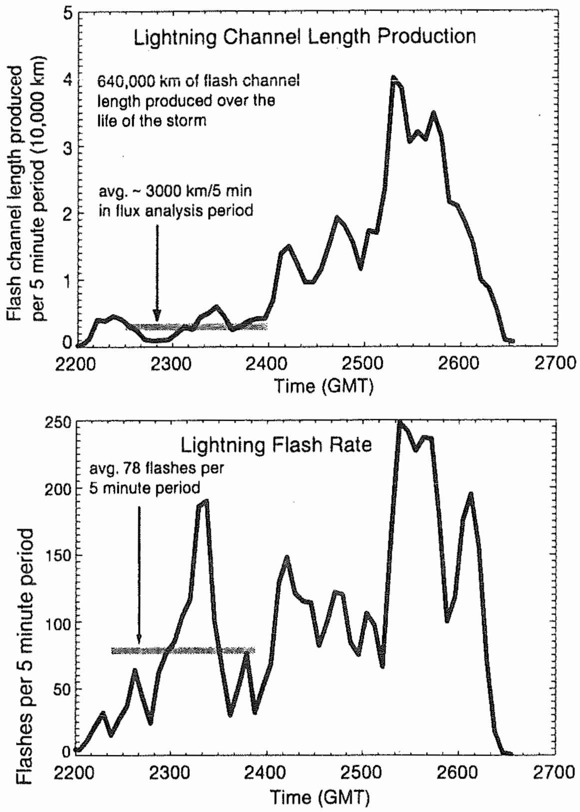

Figure 4. Lightning channel length production and flash rate for the 10 July STERAO storm

model, they estimate that between 2×10^{20} and 10^{22} molecules of NOx per meter were produced in the plumes that they sampled. Our estimate (6.9×10^{20} molecules NO per meter), which integrates the NOx over the storm outflow and uses measurements of total lightning channel length, is in the lower end of the Stith et al range. Wang et al (1998) found between 5×10^{20} and 3×10^{21} molecules of NOx were produced for lightning generated in the laboratory with currents between 10 to 30 kA at sea level. Again our estimate is in the lower end of the range.

Lawrence et al (1995), in a study that combined theory and laboratory and observational analyses, found that between 0.5 to 300×10^{25} molecules of NO are produced per lightning flash. Our estimate of 2.7×10^{25} molecules per flash falls on the lower end of the Lawrence et al range.

4.2 *NOx Storm Budget*

The ONERA lightning interferometer data span the entire lifetime of the 10 July storm. The total NOx produced by lightning in the storm can be estimated by multiplying the the NOx production rate per unit flash or the production rate per meter lightning channel length by the total number of flashes or the total channel length produced over the lifetime of the storm. Using the total lightning channel length ($\sim$ 640,000 km) and the NOx production rate per meter ($\sim 1.15 \times 10^{-3}$ moles/m) we compute a net production of $\sim 7.4 \times 10^5$ moles of NOx. Using the total number of flashes ($\sim$ 5340) and the NOx production rate per flash ($\sim 2.7 \times 10^{25}$) we compute a net production of $\sim 2.4 \times 10^5$ moles of NOx. The discrepancy between these estimates is the result of the change in the average flash-channel length; at later times the flash channel were on average longer than during the observation period used to compute anvil NOx flux, and the flash rate produces a lower NOx production estimate.

5. Acknowledgments

We would like to thank all those who participated in the STERAO field campaign and subsequent data analysis. This work is partially supported by NOAA CGCP award NA76GP00400.

REFERENCES

Cressman, G.P., 1959: An operative objective analysis scheme. *Monthly Weather Review*, **87**, 367-374.

Defer, E., et al, 2000: Lightning activity for the 10 July 1996 storm during the STERAO-A experiment. In preparation.

Dye, J. E., et al, 2000: An overview of the STERAO/Deep Convection Experiment with example results from the July 10th storm. accepted *J. Geophys. Res.*

Lawrence, et al, 1995: Lightning and atmospheric chemistry: The role of atmospheric NO production, in *Handbook of Atmospheric Electrodynamics, Vol 1*, edited by H. Holland, CRC Press, pp 189-202.

Liaw, Y.P., D.L. Sisterton, and N.L. Miller, 1990: Comparison of field, laboratory and theoretical estimates of global nitrogen fixation by lightning. *J. Geophys. Res.*, **95**, 22489-22494.

Skamarock, W. C., et al, 2000: Numerical simulations of the 10 July STERAO/Deep Convection experiment convective system: Kinematics and transport. accepted. *J. Geophys. Res.*

Stith, J., et al, 1999: NO signatures from lightning flashes. *J. Geophys. Res.*, **104**, 16081-16089.

Wang, Y., A.W. Desilva, G.C. Goldenbaum, and R.R. Dickerson, 1998: Nitric oxide production by simulated lightning: Dependence on current, energy, and pressure. *J. Geophys. Res.*, **103**, 19149-19159.

STUDY OF LIGHTNING INDUCED NO_x IN A CLOUD-SCALE THUNDERSTORM MODEL

Thorsten Fehr, Hartmut Höller, and Heidi Huntrieser

Institut für Physik der Atmosphäre, DLR Oberpfaffenhofen, D-82230 Wessling, Germany

1. INTRODUCTION

Nitrogen oxides, $NO_x = NO+NO_2$, play a fundamental role in the tropospheric and stratospheric chemistry. Their concentration and distribution control the ozone (O_3) and hydroxy (HO_x) budget, and thus play a significant role in the climate-relevant radiative forcing and the oxidation ability of the atmosphere.

Source	Emission $Tg(N)yr^{-1}$	Uncertainty $Tg(N)yr^{-1}$
Fossil fuel combustion	22	13 – 31
Biomass burning	7.9	3 – 15
Soil microbial production	7.0	4 – 12
Lightning	**5.0**	**2 – 20**
Stratospheric decomposition of N_2O	0.6	0.4 – 1
Ammonia oxidation	0.9	0.6
Aircraft	0.6	0.5 – 0.8
Total	44	23 – 81

Table 1: Summary of source estimates and uncertainties (cf. Lee et al., 1997).

To estimate the effect of man-made and natural NO_x emissions on the future development of the climate, the three-dimensional and temporal distribution must be quantified. While some sources are known within a reasonable range for global climate modeling, the contribution of lightning induced NO_x (LNO_x) can only be estimated with large uncertainties (Tab. 1).

In thunderstorms, the LNO_x produced in a lightning channel is instantaneously transported by the wind field, while at the same time ground emissions of NO_x can be lifted to the anvil almost undiluted. It is extremely difficult to observe the NO_x transport near a storm core experimentally. High resolution cloud-scale numerical modeling offers an approach to quantify the LNO_x production and redistribution.

Corresponding author's address: Thorsten Fehr, Institut für Physik der Atmosphäre, Deutsches Zentrum für Luft- und Raumfahrt (DLR) Oberpfaffenhofen, D-82234 Wessling, Germany; E-Mail: Thorsten.Fehr@DLR.de

2. LIGHTNING-NO_x-PARAMETERIZATION

The spatial and temporal resolution of a cloud model is far too coarse to resolve the lightning channel with approx. 10 cm radius, 0.3 s duration, and a temperature of 20 000 K. To overcome this restriction, the LNO_x produced in the channel is represented by Lagrangian particles, whose trajectories are integrated with the cloud-model time step, each "carrying" a certain amount of NO_x.

The parameterization of the lightning activity, type, and NO_x production is based on Price and Rind (1992, 1993) and Pickering et al. (1998).

The parameterized lightning frequency F is a function of the maximum vertical velocity w_{max} alone:

$$F = 5\times10^{-6}\, w_{max}^{4.54} \quad , \qquad (1)$$

with F in flashes s^{-1} and w_{max} in m s^{-1}.

For the ratio β between cloud-to-cloud (IC) and cloud-to-ground (CG) flashes Price and Rind (1993) found:

$$\beta = 0.021 Z_{fr}^4 - 0.648 Z_{fr}^3 + 7.493 Z_{fr}^2 - 36.54 Z_{fr} + 63.09 \quad , \qquad (2)$$

where Z_{fr} denotes the cloud depth above freezing level in km.

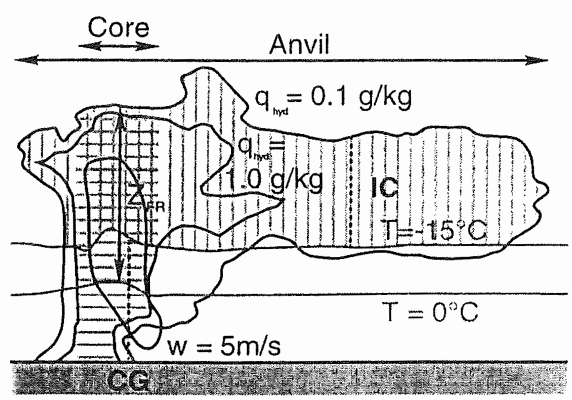

Figure 1: Parameterization of lightning position. The horizontally/vertically hatched region denotes the storm core/anvil.

The position and geometry of an individual flash relative to the storm core is a critical and not well known parameter. For the parameterization, cloud regions having total hydrometeor mixing ratios q_{hyd} above 1 g kg^{-1} (approx. 40 dBZ) and simultaneously lying between 0°C and −15°C, CG lightning can be initiated running vertically downward in a straight line (Fig. 1). IC lightning can develop in the complete anvil, which is defined by a threshold of 0.1 g kg^{-1} and temperatures below −15°C. The IC lightning channel runs vertically through the complete anvil. The horizontal position of a flash, IC or CG, in its "permitted" region is determined by a random process.

Following Price et al. (1997), the LNO_x production of a single CG flash was set to 6.7×10^{26} molecules, while for IC flashes 10% of the CG value was assumed. The LNO_x production depends linearly on atmospheric pressure. In the model, a CG flash consists of 500, an IC flash of 50 Lagrangian particles, each carrying equal amounts of NO_x.

The Lagrangian particle model for the representation of lightning induced NO_x was introduced to the PennState/NCAR Mesoscale Model 5 (MM5).

3. THE JULY 21, 1998 SUPERCELL STORM

3.1. The EULINOX Project

In Summer 1998, several European organizations were involved in the field campaign of the European Community EULINOX (European Lightning Nitrogen Oxides Experiment) project. A major objective of the project was to understand and quantify the contributions of lightning induced NO_x to the composition of the atmosphere over Europe (Höller and Schumann, 2000).

Among others, the experimental tools involved airborne in-situ trace gas measurements, including thunderstorm anvil penetrations, and 2D lightning detection by an LPATS (Lightning Positioning and Tracking System) system. The DLR polarimetric Doppler radar POLDIRAD supplied high resolution data on cloud development on a regional scale. In addition, radiosonde, dropsonde, ground based and airborne measurements provided standard meteorological data.

On July 21, 1998 a supercell development was observed over the German alpine foreland. Airborne chemical, radar and lightning measurements covered most of the storm development, and combined with other meteorological observations this storm represents a unique dataset for cloud-scale lightning and transport studies.

3.2. Cloud-Scale Model Study

Using the meteorological data from aircraft, dropsonde, radiosonde, and ground based measurements a composite sounding of the thermodynamic situation ahead of the July, 21 thunderstorm was compiled.

The values of CAPE and CIN reach 1343 J kg^{-1} and −37 J kg^{-1} respectively. The wind profile leads to a kinetic shear energy of 52.7 J kg^{-1}. This results in a Bulk Richardson Ri_B number of 25.5 , indicating a moderate supercell development from thermodynamic considerations, which is supported by observations. This profile is used to initialize an idealized version of the MM5, reducing the systems complexity by neglecting orographic effects and large scale forcing.

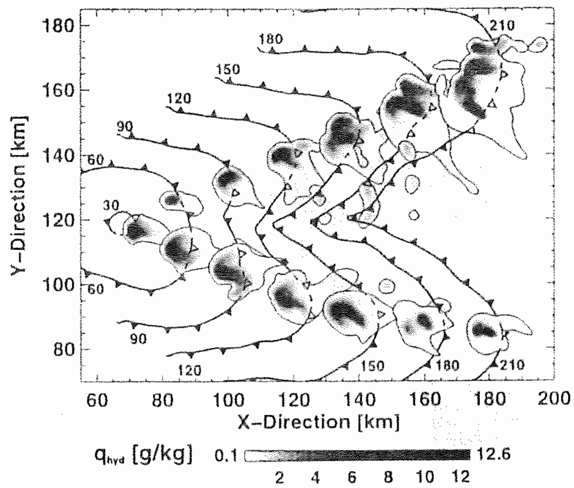

Figure 2: Evolution of storm in 4.11 km height. The solid line denotes q_{hyd}=0.1 g kg^{-1}. The surface gust front is indicated by barbed lines and labeled with the corresponding model time (min).

The model domain has a horizontal resolution of 1 km and consists of 50 vertical levels between ground and approx. 20 km height, 11 levels below 2 km and 12 levels above the tropopause. The size of the domain is 130×130 km^2. The model time step is set to two seconds. The microphysics scheme includes cloud water, rain, cloud ice, snow and graupel. Following the initialization of convection by a "hot bubble" in the boundary layer, the model runs for 3.5 hours. The storm development at mid-level is presented in Fig. 2, showing the total hydrometeor mixing ratio every 30 min.

Half an hour after convection was initialized, the storm consists of a single cell, that splits in a left-moving multicell and right-moving supercell storm during the following 30 min.

The supercell dominates the storm development in the first two hours. The maximum updraft velocity remains above 30 m s^{-1} during this period, reaching values close to 50 m s^{-1}, while the maximum supercell downdraft velocities remain above 25 m s^{-1}. The anvil reaches up to 12 km above ground with a maximum overshooting of approximately 2 km. The development of the horizontal "S"-shape cloud structure shown in Fig. 2 between 60 and 120 min results from the development of strong vertical vorticity. After two hours the quasi steady-state of the supercell rapidly decayed and the storm began to dissipate.

The parameterized lightning activity leads to a total of 6325 IC and 1206 CG flashes during the active stage of the supercell. 1 000 000 Lagrangian particles are emitted and followed individually. This results in a total LNO_x production of 28.7 t(N), 66% coming from CG lightning.

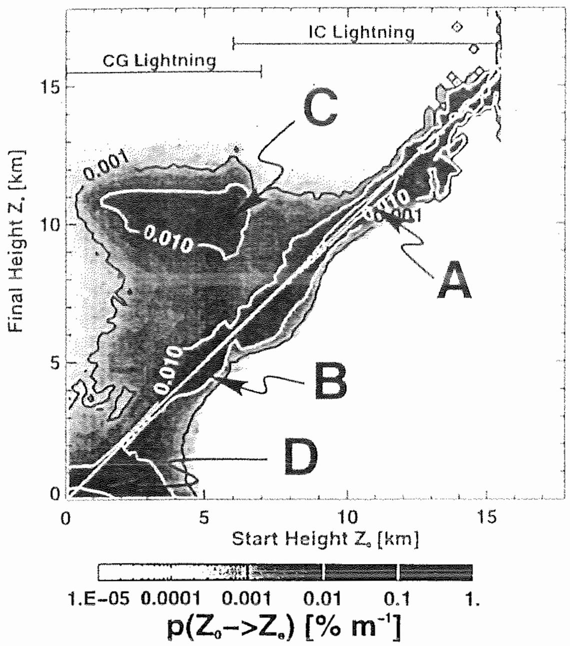

Figure 3: Probability density p_{z0ze} for the LNO_x transport at model time t=110 min.

Due to transport in the storm, the resulting domain mean vertical LNO_x-profile is "C"-shaped, with pronounced maxima of 1.3 and 1.0 ppbv in anvil levels and near the ground, and a well-defined minimum of 0.1 ppbv in 3 km. The probability density p_{z0ze} to find a particle that was emitted in a height Z_0+dZ in Z_e+dZ is given in Fig. 3.

Four regions of increased probability can be identified:

A: IC emissions in storm regions with little vertical movement. The particles are mainly advected horizontally.

B: Caused by CG lightning emissions in regions with little vertical motion.

C: Transport of mid-level CG particles into the anvil caused by strong updrafts.

D: Transport of mid- and low-level CG particles to the ground by downdraft motion.

The low values of p_{z0ze} for Z_0<4.5 km between 2 km<Z_e<9 km result from the positioning of CG lightning close to the thunderstorm core, where strong up- and downdraft motion dominate.

A vertical slice though the thunderstorm core is shown in Fig. 4. The LNO_x concentration in the vicinity of the storm core reaches 10 ppbv. The accumulation of NO_x in the anvil is pronounced and exceeds 5 ppbv in isolated regions.

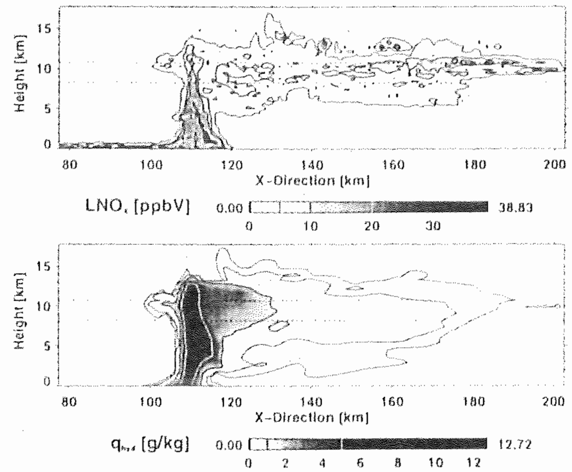

Figure 4: Vertical cross sections through the storm core. Top: LNO_x with 0.15, 5.0 and 10 ppbv contour lines. Bottom: q_{hyd} with 0.01, 0.1, and 5.0 g kg^{-1} contour lines.

3.3. Comparison with Observations

The supercell simulation shows many similarities with the radar observations, including translation speed and direction, cloud top and overshooting height, as well as a hook echo like low-level precipitation field.

Except for the convection initialization period and the following 30 min, the CG lightning frequency detected by the LPATS and the modeled CG activity have similar magnitudes and time evolution, suggesting that at least for the mature stage of the supercell, the parameterization gives reasonable results.

In order to compare the model data to airborne NO_x-observations, the Lagrangian particle distribution was interpolated on a 333 m grid, which corresponds to the resolution of the airborne NO_x-measurements. Taking the actual height and the radar reflectivity along the aircraft path during an anvil penetration into account, an artificial flight through the model anvil was defined. The resulting NO_x time series are given in Fig. 5.

The width of the "NO_x"-anvils and the absolute values of the NO_x signal are comparable, as well as its spiky nature.

In order to calculate global or thunderstorm NO_x production rates from aircraft anvil penetrations, many experimentalists use an approach proposed by Chameides et al (1987):

$$P_{gl} = \langle NO_x \rangle \times F_c \times S \times C, \quad (3)$$
$$P_{ts} = \langle NO_x \rangle \times F_c \times T_{ts} \times C_{ts}, \quad (4)$$

where P_{gl} and P_{ts} denote the global and storm NO_x production respectively, $\langle NO_x \rangle$ the mean NO_x concentration during the penetration, S the total number of active storms at any instant, T_{ts} the total time of storm activity, and C, C_{ts} conversion factors. Using the model data this approach can be tested.

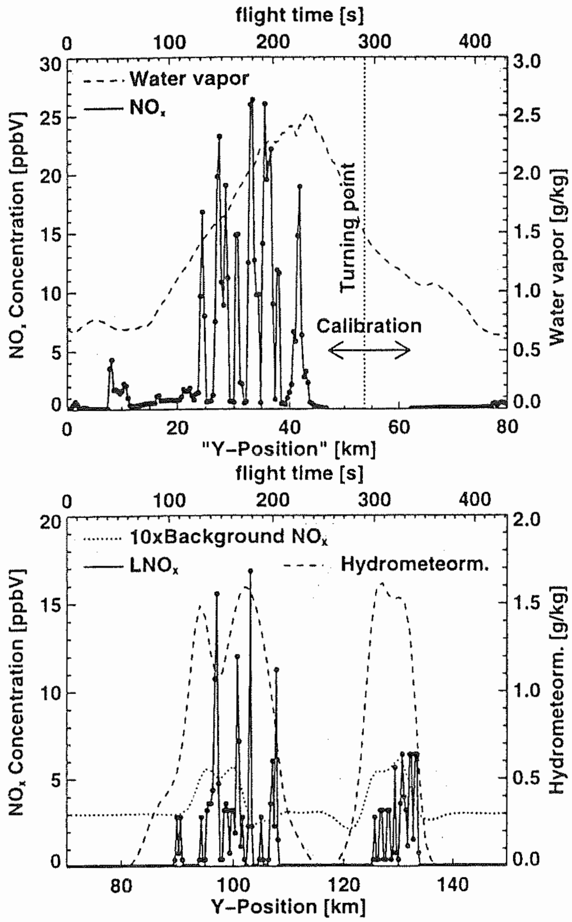

Figure 5: NO_x profiles of anvil penetrations. Top: During EULINOX on July, 21 in 8.8 km height. Bottom: Simulated flight through model anvil in 8.7 km height.

If applied to the model profile, Eqs. (3) and (4) yield 67±33 Tg(N) yr^{-1} and 5.7±1.0 t(N). In case the anvil penetrations are performed in 11 km instead of 9 km height (cf. Fig. 4), these values almost triple, reaching values of 171±90 Tg(N) yr^{-1} and 14.7±3.4 t(N). This clearly shows the sensitivity to height. The total LNO_x found in the model anvil is 15.7 t(N). This value implies, that an anvil penetration in higher altitudes, would result in more reliable production rates. Since aircraft measurements are commonly restricted in height, the model analysis can help scale the experimental results.

4. CONCLUSIONS

Although the presented LNO_x-parameterization is only a first guess approach, which does not conform to all observations in detail, the following conclusions can be drawn:

- The Lagrangian particle model combined with the LNO_x-parameterization can be used to study the LNO_x distribution in an isolated thunderstorm.
- The comparison between experimental and model derived CG lightning frequencies and aircraft anvil penetrations indicate that the parameterization is reasonable and can be used for further refinement.
- The model can give valuable information on the sensitivity of experimental analysis procedures.

New experimentally derived LNO_x-parameterizations based on radar, 3D lightning, aircraft and satellite data can be tested in this model environment. Further model investigations will expand our knowledge on lightning induced NO_x and its impact on the global and regional climate.

5. ACKNOWLEDGEMENTS

The EULINOX project was sponsored by the Commission of the European Communities (CEC) within the Environment and Climate Programme, contract ENV-CT97-0409.

6. REFERENCES

Chameides, W. L., D. D. Davis, J. Bradshaw, M. Rodgers, S. Sandholm, and D. B. Bai, 1997: An estimate of the NO_x production rate in electrified clouds based on NO observations from the GTE/CITE 1 fall 1983 field operation. J. Geophys. Res., **92**, 2153–2156

Höller, H., and U. Schumann (eds.), 2000: EULINOX—Final Report, Commission of the European Communities, Contract No. ENV4-CT97-0409, European Commission, Brussels, Belgium

Lee, D. S., I. Köhler, E. Grobler, F. Rohrer, R. Sausen, L. Gallardo-Klenner, J. G. J. Olivier, F. J. Dentener, and A. F. Bouwman, 1997: Estimates of the global NO_x emissions and their uncertainties. Atmos. Env., **10**, 1735–1749

Pickering, K. E., Y. Wang, W.-K. Tao, C. Price, and J.-F. Müller, 1998: Vertical distribution of lightning NO_x for the use in regional and global chemical transport models. J. Geophys. Res., **103**, 31 203-31 216

Price, C. and D. Rind, 1992: A simple lightning parameterization for calculating global lightning distributions. J. Geophys. Res., **97**, 9919–9933

Price, C, and D. Rind, 1993: What determines the cloud-to-ground fraction in thunderstorms? Geophys. Res. Lett., **20**, 463–466

Price, C., J. Penner, and M. Prather, 1997: NO_x from lightning, 1. Global distribution based on lightning physics. J. Geophys. Res., **102**, 5727–5941

A MODELING STUDY OF THE EARLY ELECTRICAL DEVELOPMENT IN TWO THUNDERSTORMS.

R. Mitzeva[1*], C. Saunders[2] and N. Samardjiev[1]

[1]Department of Meteorology, Faculty of Physics, University of Sofia, Sofia-1164, Bulgaria
[2]Department of Physics, UMIST, Manchester M60, 1QD, United Kingdom

1. INTRODUCTION

The goal of the work is to study the effect of cloud dynamics and microphysics on the electrical structure in the early stage of thunderstorm development. Two different cloud cases were simulated using a one-dimensional cloud model with parameterization of microphysical processes and the non-inductive charging mechanism of electrification.

2. MODEL DESCRIPTION

According to the model, convective clouds are composed of active and non-active cloud masses (Andreev et al.,1979). The active mass is modeled by successive ascending spherical thermals, while the non-active cloud region is formed by thermals that have previously risen and stopped at their convective levels. One can speculate that the ascending thermals represent the updraft region of convective clouds, while non-active masses represent the environment of the updrafts. The model uses bulk microphysical parameterizations with five classes of water substance - water vapor, cloud water S_c, rain S_p, cloud ice S_{cf}, and graupel S_{pf}. Precipitation fallout is calculated in the same manner as in Cotton (1972), and comprises that portion of rain drops S_R and graupel S_{rf}, which have terminal velocities greater than the updraft speed. Cloud electrification is parameterized based on laboratory data for non-inductive charge transfer of rebounding collisions between ice crystals and graupel in the presence of cloud droplets, following Brooks et al. (1997). The sign and magnitude of the charge per crystal separation event depends on the crystal size, the impact velocity, and the rime accretion rate. For the purposes of modeling cloud electrification in the regions free of cloud droplets (LWC =0) it is assumed that charge q acquired by graupel per separation event is q = -0.01fC. Ice crystals and graupel in the ascending thermals, together with falling graupel are the charge carriers in the model cloud. It is assumed that graupel capture of ice crystals and growth by autoconversion conserves the (average) charge on the crystals (from earlier interactions) when it becomes the initial graupel charge and is added to the total graupel charge density. The reduction of charge density in ascending thermals due to entrainment is taken into account. The charging rate per unit volume of model cloud is calculated as in Mitzeva and Saunders (1990). The net charge density in ascending thermals, Q_T is established by summing the charges on the ice crystals Q_{cr} and on the ascending graupel Q_{gr}. The net charge density in the non-active part of the cloud is the sum of the charge on falling graupel and on the ice crystals present.

3. THE CLOUD CASE STUDIES

The model has been run using temperature and moisture profiles observed on July 19, 1981 during the CCOPE experiment near Miles city, Montana (hereinafter denoted as the CCOPE cloud) and on June 29, 1989 during NDTP at Bismark ND, (hereinafter denoted as the NDTP cloud). In CCOPE, an isolated small cumulus cloud with maximum updraft speeds between 10-15 m s^{-1} was observed. During the early stage of CCOPE cloud electrification (Dye et al., 1986) negative charge accumulation was observed near 7 km (-20°C), with positive charge located above negative charge. The NDTP case was a large mesoscale convective system with updraft greater than 30 m s^{-1} that developed over much of North Dakota. There is no available information for the distribution of the electric field in the NDTP cloud. It is reported (Helsdon, 1990) that a high percentage of positive cloud to ground lightning was observed during NDTP on 28 June 1989.

4. NUMERICAL SIMULATIONS AND RESULTS.

Since the model in this study is one-dimensional, it can be used for the simulation of the small isolated CCOPE cloud but it is not appropriate for large mesoscale convective systems. So, the model simulates only one of the isolated thunderstorm cells, which developed on June 29, 1989 during NDTP.

The parameters necessary for the numerical simulations by the model (the thermal radii and

* Corresponding author's address: Rumyana Mitzeva
Dept. of Meteorology, Faculty of Physics, University of Sofia, 5 J. Bourchier Blvd., Sofia - 1164, Bulgaria;
E-mail: rumypm@phys.uni-sofia.bg

velocity at cloud base, the time interval between the ascending thermals, their number and the turbulent diffusion coefficient in the non-active cloud mass) were taken in the range of real values in such a way that the cloud top height and lifetime of the model cloud agree with observations.

Table 1. Maximum net charge density Q_T, max charge density on graupel Q_{gr}, and on crystals Q_{cr} in one of the ascending thermals. Z and T are the corresponding height above ground level and the temperature in the ascending thermals.

	CCOPE	NDTP
Q_T (nCm^{-3}) Z (km) T (°C)	-3.0/+ 4.3 6.7/ 11.4 -19.6/ -57.7	-6.8 /+ 0.03 12.2 / 6.3 -68.0 / -11.9
Q_{gr} (nCm^{-3}) Z (km) T (°C)	-2.1/+ 0.02 6.7/5.9 -19.6/ -13.4	-7.09 /+ .015 12.1/7.0 -68.0/ -18.4
Q_{cr} (nCm^{-3}) Z (km) T (°C)	-0.5/+ 4.5 8.0/8.5 -30.4/ -32.0	-0.1/+ 0.7 8.7/13.4 -32.0/ -79.0

We are primarily interested in how the cloud dynamics and microphysics affect the polarity of charge regions and the heights of the charge center in the updrafts of the simulated clouds, that is why only the microphysical and electrical features of the ascending thermals (updraft cloud region) were considered.

The results presented in Fig 1a and in Table 1 show that the maximum total (net) negative/positive charge density is situated higher/lower in the NDTP cloud (Z=12.2/6.3km) in comparison with the CCOPE cloud (Z=6.7/11.4 km). There are also significant differences in their magnitudes. The maximum values of simulated water substances (cloud water, rain, cloud ice and graupel) for both cloud cases are rather close (see Table 2). The two clouds however differ in the magnitude and height of the maximum updraft speeds - see Fig. 2 and Table 2. There are also differences between the heights at which the maximum values of water substances are reached - the maximum values of water substances were established at higher levels in the NDTP cloud, which has a higher updraft speed (see Table 2).

The results showed that the vertical charge density distribution in the updrafts of the simulated CCOPE cloud, as a whole, fit the classical charge tripole model - lower positive charge density with maximum magnitude Q_T = 0.02 nC m^{-3} at 5.8 km (-12°C), followed by a negative charge region with max charge density Q_T = -3.0 nC m^{-3} at 6.7 km (-19.6°C) and positive charge above the negative charge region with maximum Q_T = 4.3 nC m^{-3} at a height near the cloud top. In the updraft of the simulated NDTP cloud, one can recognize mainly two charge regions: a lower positive charge region with maximum charge density Q_T = 0.3 nC m^{-3} at 6.3 km (-11.9°C), above which the extended negative charge region is observed with maximum charge density Q_T = -6.8 nC m^{-3} at 12.2 km. 100-200 m below cloud top the weak positive region is observed. The analysis reveals that in both the

Table 2. Maximum values of updraft speed W and water substance -S_c, S_p, S_{cf}, S_{pf}, S_R and S_{rf} in one of the ascending thermals. Z is the corresponding height above cloud base in the ascending thermals.

	CCOPE	NDTP
W ($m.s^{-1}$) Z (km)	14.1 5.2	29.5 7.65
S_c ($g.m^{-3}$) Z (km)	1.34 2.1	1.42 3.0
S_p ($g.m^{-3}$) Z (km)	0.2 2.37	0.3 3.55
S_{cf} ($g.m^{-3}$) Z (km)	1.08 4.75	0.87 5.85
S_{pf} ($g.m^{-3}$) Z (km)	0.22 2.8	0.24 3.4
S_R ($g.m^{-3}$) Z (km)	0.016 2.7	0.000
S_{Rf} ($g.m^{-3}$) Z (km)	0.1 2.87	0.06 4.05

simulated clouds (CCOPE and NDTP), graupel pellets are the main carriers of negative charge in the ascending thermals (Fig.1b). However the main negative charge center is situated at higher level in the NDTP cloud than in the CCOPE cloud because in the NDTP cloud much graupel, Spf, resides in the ascending thermals to a higher level due to the very high updraft speeds (see Fig. 3). The crystals in both simulated clouds carry negative charge in the lower cloud region and positive charge in the upper levels (Fig. 1c). The total charge density in the updrafts of the CCOPE cloud is positive at heights with temperatures lower than -30°C because of the very high positive charge residing on the ice crystals. In the simulated updraft of the NDTP cloud the ice crystals carry smaller charges than in the CCOPE cloud. One of the possible explanations for this difference is a higher ice crystal concentration in the updraft of the CCOPE cloud than in the NDTP cloud.

It is also necessary to mention that the negative charge density increases with height in the simulated

NDTP updraft region free of cloud droplets; this is a consequence of our assumption that the separated charge transfer per crystal/graupel collision event at LWC=0 is q = -0.01 fC.

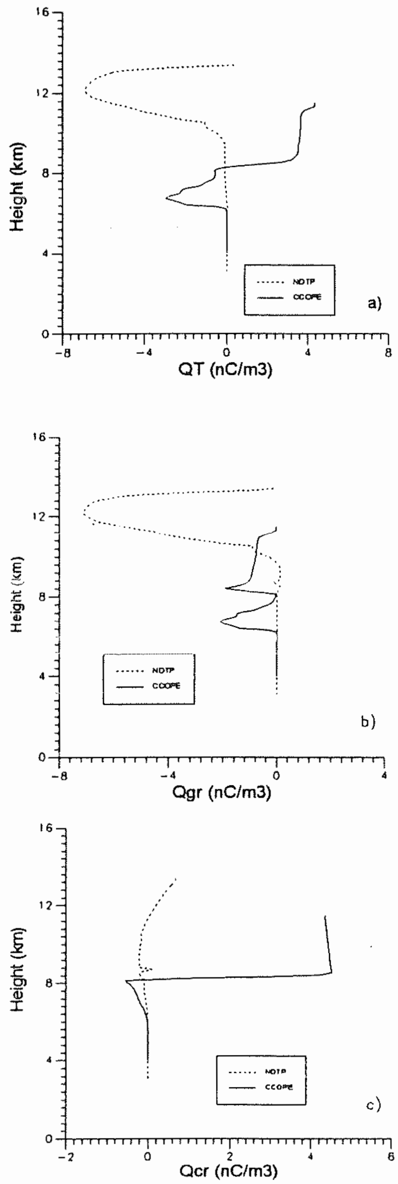

Figure 1: Charge density as a function of height in updraft region: a) net charge QT; b) charge carried by graupel Qgr; c) charge carried by crystals. Height is above ground level.

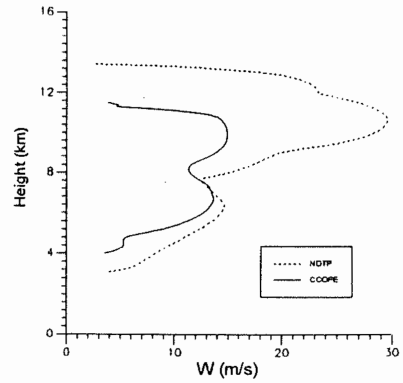

Figure 2: Updraft speed

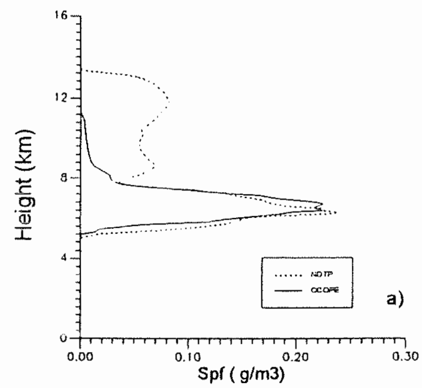

Figure 3: Graupel in the ascending thermals. Height is above ground level.

5. CONCLUSIONS

The present study demonstrates the significant effect of cloud dynamics and microphysics on the charge density profiles in the updrafts of convective clouds. The numerical simulations show that the main center of negative charge is higher (at colder temperatures) in updraft regions with stronger updraft speeds, which is in agreement with field observation analysis in Stolzenburg et al., 1998. In the frame of the parameterizations used for cloud electrification modeling, different charge distributions can be formed depending on the ice crystal concentrations and on the impact speeds of interacting particles. The results point out the effect of charge transfer in regions free of cloud drops on the charge distribution in convective clouds having high updraft velocity and a very cold cloud top height, so it is worthwhile for more laboratory investigations of charge transfer at LWC=0 to be carried out.

6. ACKNOWLEDGEMENTS

This work is supported partially by the Royal Society and the Science Foundation of Sofia University (grant 301/99).

7. REFERENCES

Andreev, V.,Syrakov D. And Mitzeva, R.,1979: Modeling of convective cloud formation as successive ascending thermals. Bulg. Geophys. J.,1, 3-9.

Brooks M., C. P. R. Saunders, R. P. Mitzeva and S. L. Peck, 1996: The effect on thunderstorm charging of the rate of rime accretion by graupel. J. Atmos. Res, 1997: 43, 277-295.

Cotton W., 1972: Numerical simulation of precipitation development in super-cooled cumuli - Part II. Mon. Wea. Rev., 100, 764 - 784.

Dye J., J. Jones, P. Winn, A. Cerny, B Gardiner, D Lamb, L. Pitter, J. Hallett and C. P. R. Saunders, 1986: Early electrification and precipitation development in a small isolated Montana thunderstorm. J. Geophys. Res., 91, 1231 – 1247.

Helsdon J., 1990: Analyses of a high positive flash frequency in severe storm (28.06.89) from the North Dakota Thunderstorm Project, 1990 Conf. of Atmos. Electricity, Kananaskis Provinsial Parc, Alberta, Canada, Oct 1990, 744-747.

Mitzeva R. P. and Saunders C. P. R., 1990: Thunderstorm charging: Calculations of the effect of ice crystal size and graupel velocity. J. Atmos. Terr. Phys., 52, 241-245.

Stolzenburg M., D. Rust and T. Marshall, 1998: Electrical structure in thunderstorm convective regions. 3. Synthesis. J. Geophys. Res., 10,:14097-14108.

DISTRIBUTION OF CONVECTIVE CLOUDS AND LIGHTNING DISCHARGES AT THE EARTH SURFACE IN KAKHETI REGION OF GEORGIA

A.G. Amiranashvili[1], V.A. Amiranashvili[1], T.N. Bibilashvili[2], Z.A. Chumburidze[2], T.G. Gzirishvili[1], R.I. Doreuli[1], A.G. Nodia[1], F.A. Khorguani[1], Yu.M. Kolesnikov[1]

[1]Institute of Geophysics of Georgian Academy of Sciences, Tbilisi, 380093, Georgia
[2]Tbilisi State University, 3., Chavchavadze Ave., Tbilisi, 380028, Georgia

1. INTRODUCTION

Georgia belongs to one of thunderstorm-active regions of the world. Therefore the study of thunderstorms in Georgia has always drawn a particular attention. However, these investigations were mainly based on visual observations on thunderstorms on a network of meteorological stations. Multi-year instrumental observations on the number of lightning discharges were carried out only at the station Dusheti 60 km to the North from Tbilisi (Gunia, 1960; Dvali et al., 1977).

From 1978 till 1984 in Kakheti Region of Georgia the Institute of Geophysics of Georgian Acad. Sci. together with the main Geophysical Observatory (St. Petersburg) and the anti-hail service of Georgia carried out large-scale weather modification experiments on thunderstorm clouds. A considerable amount of material was collected on the radar and electric characteristics of convective clouds Amiranashvili et al., 1988. These and Earlier radar investigations of clouds allowed to estimate the distribution fields of the convective cloudiness and cloud-to-ground lightning discharges on the territory of Kakheti.

2. METHODS

The observations on convective clouds were carried out continuously by means of four radars functioning on the wavelength 3.2 cm in the warm season of the year from 1967 till 1989. From 1978 till 1984 using a ground network of electrostatic fluxmeters were determined also the coordinates of cloud-to-ground lightning discharges and their intensity N_g. Between the values of N_g and the maximum radar echo hight of clouds H_m the following dependence was derived: $N_g \approx 5.2 \cdot 10^{-4} \cdot H_m^{3.27}$ min^{-1}, where H_m is in kilometers. The mentioned relation and the information on the convective cloudiness over the whole territory of Kakheti allowed to estimate the degree of the occurence of lightning discharges in the mentioned area.

The investigated territory was divided into 269 squares wit an area 25 km^2 each (the total area – 6725 km^2). In each square the mean multi-year (for 1972-1976) number of thunderstorm clouds Q (according to the radar criterium of the thunderstorm-dangerousity of clouds) with H_m more than 6.0 km and also the time during which these clouds stayed in the square were determined. Then with allowance to the mentioned formula the mean seasonal number of cloud-to-ground lightning discharges in squares was estimated.

Corresponding author's address: Avtandil Amiranashvili, Geophysics Institute of Georgian Academy of Sciences, 1., M. Aleksidze Str., Tbilisi 380093, Georgia;
E-Mail: vazha@excite.com

3. RESULTS

Fig. 1 presents the distribution of the mean seasonal number of convective clouds with the maximum radar echo height more than 6.0 km over the territory of Kakheti, while Fig.2 – the density of cloud-to-ground lightning discharges.

An analysis of the material showed:

The seasonal number of clouds over the squares varies from 3 (for a location elevation H from 0.156 to 0.3 km above the sea level) to 35 (for a location elevation 1.3 - 1.5 km). The mean values of Q have a tendency of increasing with a location elevation. For locations with elevations from 0.156 to 0.3 km above the sea level (1225 km^2) there are at the average 8.6 ± 4 convective clouds per square per season. For locations with H from 0.3 to 1.1 km (4500 km^2) there are at the average 11.5 ± 5 clouds, while for locations with H from 1.1 to 1.857 km (1000 km^2) – 16 ± 9 clouds. At the average for the investigated territory over a 25 km^2 square in the warm

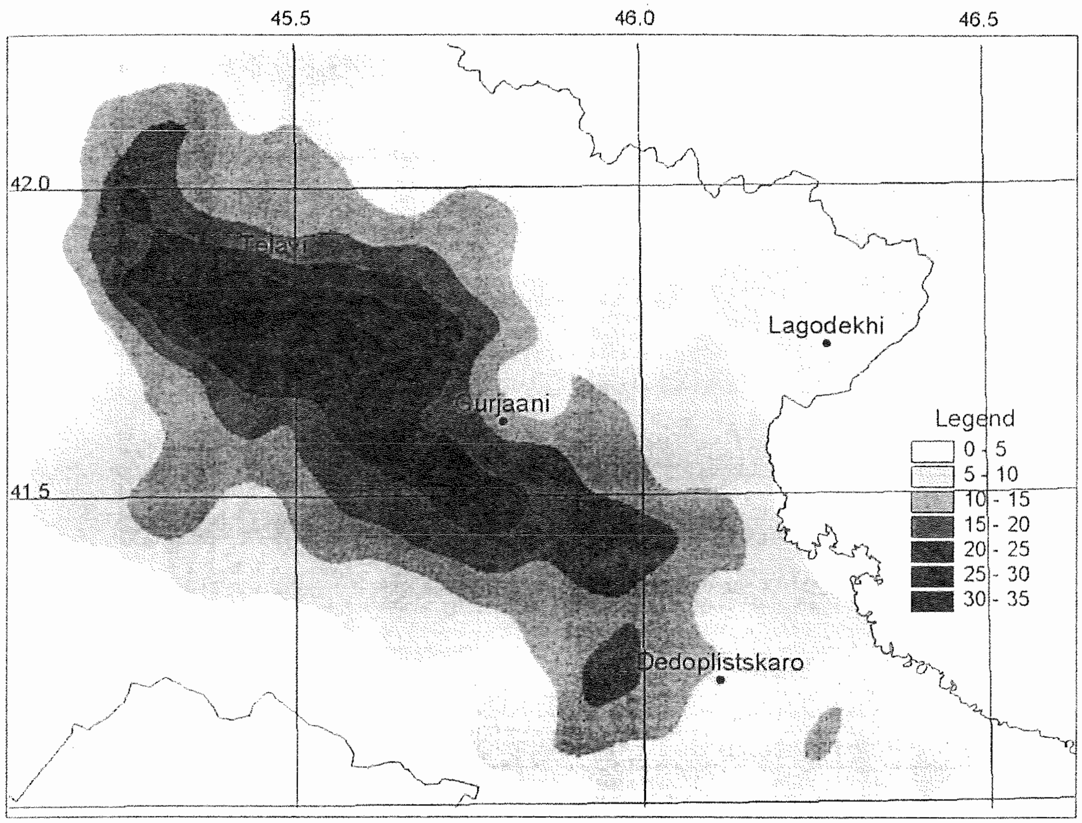

Fig. 1

The distribution of the mean seasonal number of convective clouds with $H_m > 6.0$ km over the territory of Kakheti according to the data of 1972 – 1976 (per 25 km^2)

season of the year 11.7 ± 5.6 convective clouds were observed with $H_m > 6.0$ km.

The minumum number of cloud-to-ground lightning discharges per season in Kakheti amounts to 13 (for H from 0.156 to 0.3 km), the maximum – to 377 (for H from 1.5 to 1.7 km). At the average N_g depending on a location elevation varies from 47 (for H from 0.156 to 0.3 km) to 215 (for H from 1.5 to 1.7 km) and is satisfactorily described by the empiric expression: $N_g \approx 42.1 \cdot \exp(0.978 \cdot H)$. At the average for the territory of Kakheti per 25 km^2 there are 90 lightning discharges.

The main contribution in the thunderstorm activity of Kakheti Region is made by clouds with the maximum radar echo from 8 to 12 km (about 87%); more than a half of the lightning discharges is produced by clouds with H_m from 9 to 11 km.

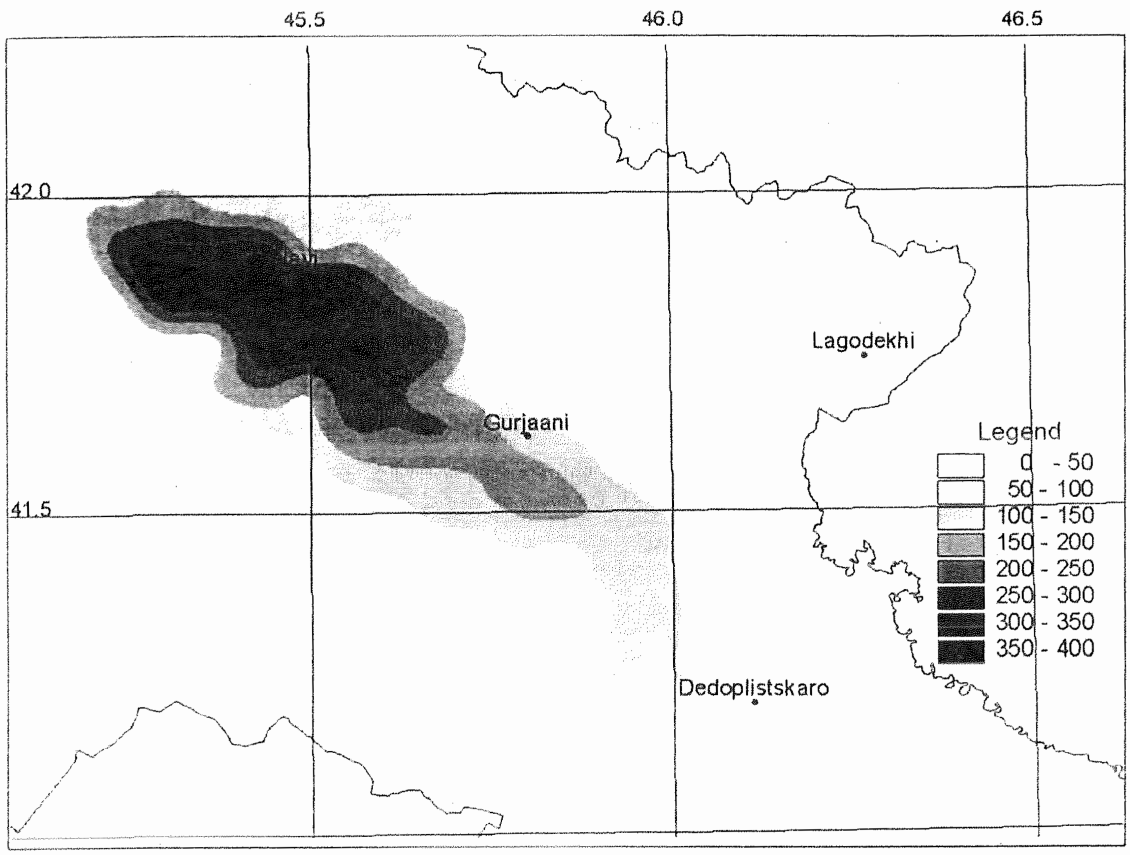

Fig. 2

The distribution of the mean seasonal number of cloud-toground lightning discharges (per 25 km^2) for the territory of Kakheti

4. REFERENCES

Amiranashvili, A.G., Gzirishvili T.G., Nekhotina L.M., Trofimenko L.T., Bogachuk V.S., 1988: Investigation of the Variations of Electrical and Radar Parameters of Thunder Clouds, Proc. VIII Int. Conf. on Atmospheric Electricity, Uppsala, Sweden, 388-391.

Dvali, E.R., Kalaijeva L.L., 1977: Results of Instrumental Observations on Thunderstorm Activity in Dusheti and Radionovka, Proc. ZakNIGMI, Iss. 54(60), Leningrad, Gidrometeoizdat, 137-139 (in Russian).

Gunia, S.U., 1960: Thunderstorm Processes in the Transcaucasia, Leningrad, Gidrometeoizdat, p. 155 (in Russian).

STUDIES ON THE CHAIN OF ICE PHASE PROCESSES IN HAILSTORMS WITH COLDER AND WARMER CLOUD BASES

Yanchao HONG[1], Hui XIAO[1], Peng FAN[2], and Hongyu LI[1]

[1]Institute of Atmospheric Physics, Chinese Academy of Sciences, Beijing 100029, China
[2]Meteorological Bureau of Shaanxi Province, Xi'an 710015, China

1. INTRODUCTION

The microphysical processes and mechanism of hailstone formation and growth in hailstorms are the basis of study on hail suppression. In this paper, we studied the chain of ice-phase processes consisting of hail embryos and hailstones using our 3-D numerical hailstorm model with non-hydrostatic and fully elastic equations we had developed (Hong *et al.*, 1999a,b). This model contains more detailed double-parameter (i.e., specific content Q and specific concentration N) and bulk-water parameterized microphysics for water vapor, cloud drops, rain drops, ice crystals, snowflakes, graupels, frozen drops, and hailstones. Two typical cases of hailstorms, one with a warmer and another one with a colder cloud base, were selected on this issue. The farmer case occurred on 8 July 1997 (referred to as Hailstorm 97708 thereafter) in Xunyi Hail Suppression Experimental Base located in the north of Shaanxi Province. The later, named Hailstorm 97709, was observed in Pingliang Experimental Base in the east of Gansu Province on 9 July 1997. Compared with the atmospheric stratiform of Hailstorm 97708, the one of Hailstorm 97709 has a 4°C colder cloud base and lower temperature almost at every level. Main results on the formation mechanism and growth pattern of hailstones existing in the two hailstorms are specially given below based on the simulations.

Corresponding author's address: Yanchao HONG, Institute of Atmospheric Physics, Chinese Academy of Sciences, Beijing 100029, China;
E-mail: hxiao@mail.iap.ac.cn

2. HAILSTORM 97708 WITH A WARMER CLOUD BASE

Formation zones and growth patterns of every kind of hydrometeor, particularly of graupels and frozen drops that can be converted to hailstones, are essential to studies on the mechanism of hail formation that is the basis of artificial suppression of hail.

Production of peak contents of hailstones has a relation to levels of their source areas. Based on the simulation of Hailstorm 97708 (some of the simulation results are shown in Figure 1), there is just one maximum of mass production rate of its hydrometeors during the early period of the storm. The maximum contents of graupels, frozen drops and hailstones appear at the height of about 6.0km during the first 20 minutes. Therefore, the zone at about 6.0km height should be the area of hail-embryo production and hailstone formation. After 24th minute the height of hail formation goes down to 4.0km, and it meets to the heights of lower-level maximums of graupels and frozen drops. There is intensely hail shooting on the ground at 28th minute.

Production of peak contents of hailstones also has a strong relation to their main growth pattern. Figure 1 gives the vertical distributions of mass production rates of

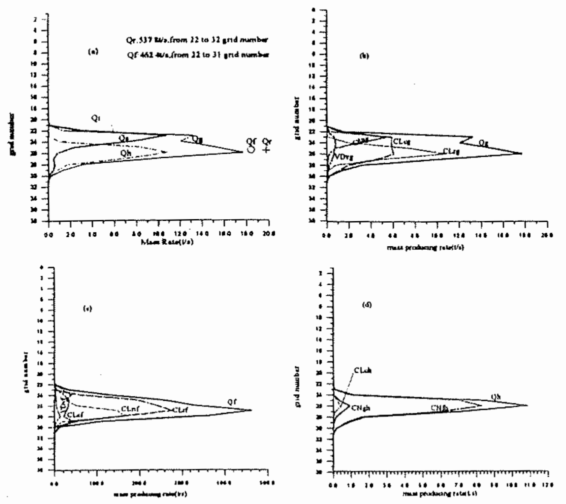

Figure 1. Mass production rates (ton/s) of particles at the 16th minute of the simulating Hailstorm 97708. Ordinate gives the vertical grid numbers, with a grid size of 500m.

hydrometeors in Hailstorm 97708 at 16th minute that is the key period of time for hail formation and growth.

Figure 1a indicates that there are typically layered structures in the vertical distributions of the mass producation rates of the hydrometeors. At 16th minute, the autoconversion of snowflakes (Figure 1b) contributes to the formation of graupels (CNsg). Its maximum has a height of 7.5km. Graupels grow greatly by means of their collection with cloud droplets (CLcg) and rain drops (CLrg). Because the height of the maximum mass production rate is about 6.0km for raindrops, the level is also suitable for graupel growth. For frozen drops, the collection of raindrops with ice crystals is essential to their formation (Figure 1c). The height of its maximum producation rate depends on that of raindrops. At the level of 6.0km, super-cold raindrops are so many that frozen drops grow rapidly by their collection. Figure 1d shows that hailstones are formed mainly by autoconversion of frozen drops (CNfh). Autoconversion of graupels to hailstones (CNgh) plays less important role. The maximum rate of the formation and growth of hail is located at 6.0km height which is based on CNfh. The collection rate of cloud water by hailstones is lower due to short time after hailstones emerge. From above we can see that source areas of all kinds of ice-phase particles are connected with their main microphysical processes of formation and growth. Graupels and frozen drops grow mostly by collecting super-cold raindrops. And raindrops are essential to hail formation and growth before a hailstorm grows maturely. The areas of hail embryos and hail formation and growth are located at the level of 6.0km.

The processes of formation and growth of hailstones vary greatly at different stages of a developing hailstorm. Figures 2a and 2b show respectively the mass production rates of graupels and frozen drops at 24th minute.

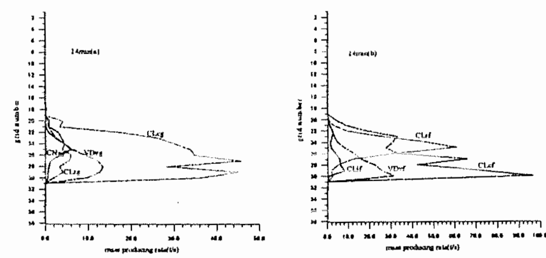

Figure 2. Mass production rates (t/s) of particles at variant stages of Hailstorm 97708.

3. HAILSTORM 97709 WITH A COLDER CLOUD BASE

For Hailstorm 97708 with a warmer cloud base, the strongest hail shooting on the ground occurred at 28th minute, while it turned up at 31st minute for Hailstorm 97709. At 25th minute, just three minutes before the shooting time in Hailstorm 97708, about 97 percent of the total hail embryos result from frozen drops, but only 66.5 percent in Hailstorm 97709 at 28th minute, also just three minutes before its hail shooting time. Some comparisons are given in Figure 3a for Hailstorm 97708 and in Figure 3b for another one. At 24th minute graupels converted from snowflakes, grow mainly by collecting cloud water (see Figure 2a), while their growth is from collecting raindrops at 16th minute (Figure 1b). Growth pattern of frozen drops is similar to that of graupels, and the role that vapor deposition on frozen drops (VDvf) plays in their growth comes to be important. The reason is that at different stage of developing storms there are different microphysical processes occurred.

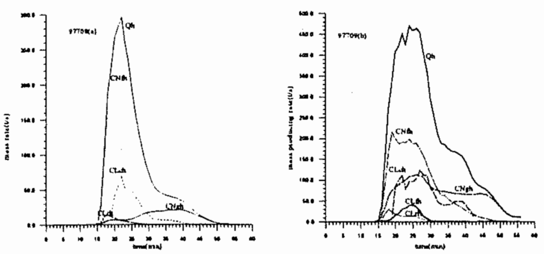

Figure 3. Change of the mass production rates of hailstone with time. (a) is for Hailstorm 97708 and (b) for Hailstorm 99709.

From Figure 3 we notice clearly that autoconversion rate of frozen drops to hailstones (CNfh) in both hailstorms is much higher than that of graupels (CNgh) and has almost the same amount for the two storms, but CNgh in Hailstorm 99709 is over three times higher than that in Hailstorm 97708. Hence, the contribution of graupels to hailstones in the hailstorm with a colder cloud base is more important than that in the hailstorm with a warmer cloud base. Field census shows that hailstones dropping from Hailstorm 97708 have small sizes only about 6 mm, while the size of some hailstones dropping from Hailstorm 97709 amounts to 30 mm in diameter. The simulating maximum kinetic energy flux of hail shooting on the ground is about 2.0 J/s.m^2 for the former storm and 4.0 J/s.m^2 for the later, indicating that our 3-D hailstorm model has the ability to well simulate real cases of hailstorm.

Table 1. Change of ratio values in Hailstorm 97709 compared with those in Hailstorm 97708

Ice crystal	Qi ↓	NUvi* ⇑	VDvi° ↓
	Pci ⇓	CLci° ↓	
Snow	Qs ↓	Cnis* ↑	VDvs° ↑
	Clris* ↓	CLcs° ↑	CLii ↑
Graupel	Qg ↑	CNig ⇑	CNsg* ↓
	VDvg° ↓	CLcg° ↑	CLig° ↓
	CLrg°⇑		
Frozen drop	Qf ↓	Clrif* ↓	VDvf° ↑
	CLcf° ↓	CLif ↓	CLrf° ↑
	NUrf ⇑		
Hailstone	Qh ↑	CNgh* ⇑	CLch° ↑
	CLih ↓	CLrh ↑	CLsh° ↓
	CLfh ↑	CLgh ⇑	CNfh* ⇓

Note: * , stands for main production process. ° , main growth process. ↑ , increasing. ⇑ , great increasing.

To investigate the effect of a storm cloud base with lower temperature put on hail formation and growth, we introduced here some ratio values to illustrate the part of every microphysical process played. Table 1 shows their changes in Hailstorm 97709 compared with those in Hailstorm 97708.

From Table 1 some conclusions can be simply drawn about particles and the chain of ice phase processes existing in a hailstorm such as,

(1) Most of graupels are converted from snow. They grow to be hail embryos after collecting much cloud water;

(2) Not similar to graupels, frozen drops grow by means of super-cold raindrop collection. They are formed mainly by collection of ice crystals and snowflakes with super-cold raindrops. The process gets stronger if temperature of environment and cloud base is lower.

(3) Hailstones come both from graupels and frozen drops. Hail embryos in a hailstorm with a warmer cloud base are converted mostly from frozen drops. While proportion of hail embryos converted from graupels gets to rise in a hailstorm with a colder cloud base.

4. CONCLUSION AND DISCUSSION

Two kinds of hailstorms with a colder and a warmer cloud base respectively are simulated here by using our 3-D hailstorm numerical model. The chain of ice-phase processes consisting of ice crystals, hail embryos, and hailstones and the roles of warm cloud processes played in hail formation and hail growth, are studied in detail. The results show that formation and growth modes of hail embryos and hailstones are remarkably different in the two kinds of hailstorms. Mass collection rates of ice crystals by graupels (CLig), and cloud droplets by frozen droplets (CLcf) and by hailstones (CLch) are respectively greater than those of rain drops by graupels (CLrg), frozen droplets (CLrf) and hailstones (CLrh) in the colder cloud base hailstorm, while it is opposite in the kind of hailstorm with a warmer cloud base. Producation rate of hailstones converted from graupels (Rgh) in a warmer cloudbase hailstorm is much higher than that in a colder base hailstorm. In the kind of hailstorm with a colder base the main part of hail embryos is frozen droplets, and the conversion rate of hailstones from frozen droplets (Rfh) is as much as Rgh in the warmer cloud base hailstorm.

Based on analyses above, it can be marked that plentiful super-cold rain water is very important in the formation and growth of hail embryos and hailstones. Intense hail shooting can hardly occur without it. In a hailstorm with a warmer or colder cloud base there are different levels of maximum amounts of formation and growth for all particles. Studies on the mechanism of micriophysical processes existing in a hailstorm, the chain of ice-phase processed consisting of ice crystals, hail embryos, and hailstones, are vital to hail suppression in practice. In fact, seeding in time at the layer between 5.5km and 6.0km, the best heights introduced in the paper of Hong and Fan (1999b), we achieved efficiently outcomes as we had expected. And the level is just best suitable for hail formation and growth. Analysis here is limited and more work should also be done to find their functions and effects on each other of those microphysical processes further.

Acknowledgements. This work was supported by Chinese National Scientific Key Program 96-020-01-07, Chinese Natural Science Foundation under Grant No. 49675247, China Heavy Rainfall Experiment and Study (CHERES) under Grant No. G1998040907-02-03, and the Foundation of the Institute of Atmospheric Physics, Chinese Academy of Sciences.

REFERENCES

Hong Y.C. and P. Fan, 1999a: Numerical Simulation Study of Hail Cloud—Part I: The numerical model, Acta Meteor. Sinica, 13,2,188 - 199

Hong Y.C. and P. Fan, 1999b: Numerical Simulation Study of Hail Cloud—Part II: Mechanism of hail formation and hail suppression with seeding. Acta Meteor.Sinica, 13,3, 331 - 346

Kong F.Y., M.Y. Huang, and H.Y. Xu, 1990: 3-D Numerical Simulation of Ice Phase Processes in Convective Cloud (1): The model and parameterization of microphysical processes, Sci. Atmos. Sinica, 14, 441 - 453 (in Chinese).

THREE-DIMENSIONAL HAIL CATEGORY NUMERICAL SIMULATION OF HAIL FORMATION PROCESSES

Meiyuan Huang Xueliang Guo Hui Xiao and Ling Zhou

Institute of Atmospheric Physics, Chinese Academy of Sciences, Beijing, 100029, China

1. INTRODUCTION

It is believed that a better understanding of the microphysics of hail growth might lead ultimately to better prediction and suppression of hailstorm. There are two significant unreasonable descriptions with hail/graupel parameterizations in the current hail/graupel parameterization models: the first is that graupel and hailstones are assumed to be distributed by an inverse exponential size distribution function and the second is that growth rates are based on mass weighted mean terminal velocities. The errors caused by these assumptions are particularly large when the size ranges of hydrometeor types such as hail can vary significantly over the spectrum. Some researchers have noted that the size distribution functions for hail/graupel are very difficult to formulate as the slope intercepts and slopes of these distributions tend to vary rapidly in both time and space (Cheng and English,1983).

This study was inspired by the need for more reasonable descriptions of size distribution and terminal velocities for hailstone and graupel. Results shown here are parts of those simulated by a three-dimensional hail/graupel category model.

2. MODEL DESCRIPTION

A three-dimensional compressible non-hydrostatic cloud model in which hail/graupel is divided into 21 size categories was used (Guo,1997). The basic equations in the standard Cartesian coordinates (x, y, z) are:

$$\frac{du}{dt}+C_p\overline{\theta_v}\frac{\partial\pi'}{\partial x}=D_u \qquad (1)$$

$$\frac{dv}{dt}+C_p\overline{\theta_v}\frac{\partial\pi'}{\partial x}=D_v \qquad (2)$$

$$\frac{dw}{dt}+C_p\overline{\theta_v}\frac{\partial\pi}{\partial z}=f_w+D_w \qquad (3)$$

$$\frac{d\pi'}{dt}+\frac{\overline{C}^2}{C_p\overline{\rho}\overline{\theta_v}^2}\frac{\partial\overline{\rho\theta_v}u_j}{\partial x_j}=f_\pi+D_{\pi'} \qquad (4)$$

$$\frac{d\theta}{dt}=Q_{fm}+Q_{ce}+Q_{ds}+D_\theta \qquad (5)$$

$$\frac{dq_x}{dt}=-D_{q_x}+W_{q_x}+I_{q_x}+\frac{\partial}{\partial x_3}(\rho_0V_xq_x) \qquad (6)$$

where

$$f_\pi=-\frac{R_d}{C_v}\pi'\frac{\partial u_j}{\partial x_j}+\frac{C^2}{C_p\theta_v^2}\frac{d\theta_v}{dt} \qquad (7)$$

$$f_w=g\left(\frac{\theta'}{\overline{\theta}}\right)+0.608q_v{}'-q_c$$
$$-q_i-q_r-q_s-\sum_{I=1}^{L_h}q_h(I)) \qquad (8)$$

D_u, D_v, D_w, D_θ and $D_{\pi'}$ are the turbulent fluxes of u, v, w, θ and π', respectively. Q_{fm}, Q_{ce} and Q_{ds} are the latent heating / cooling terms due to melting / freezing, condensation/evaporation, and deposition/ sublimation produced by microphysical processes, respectively. V_x is the terminal velocity of a hydrometeor q_x, where q_x is one of mixing ratio of water vapor q_v, cloud water q_c, rain water q_r, cloud ice q_i, snow q_s, and hail/graupel category water content $q_h(I)$ $(I=1,21)$. Cloud ice number concentration N_i is also included in the model.

The model domain is on a standard spatially staggered mesh system. A conventional Time-Splitting Integration Technique same as that proposed by Klemp and Wilhelmson (1978) was also used in this

Corresponding author's address: Meiyuan Huang, Institute of Atmospheric Physics, Chinese Academy of Sciences,Beijing,100029, China;
E-mail: hmy@linux2.iap.ac.cn

model. The spatial difference terms are second-order accuracy, except for the advection term that has fourth-order accuracy. All other derivatives are evaluated with second-order centered differences. A radiation boundary scheme was used for the lateral boundaries while the top and bottom boundaries are assumed as a wall. The model also includes a conventional first-order closure for subgrid turbulence and a diagnostic surface boundary layer based on Monin-Obukhov similarity theory. The haill/graupel size distribution is not prescribed but is predicted through mass-category technique proposed by Berry (1967).

3. MODEL INITIALIZATION

Simulation of the hailstorm was initiated based on the rawinsonde soundings taken from Colorado on 22 July 1976 during National Hail Research Experiment (Foote and Wade,1982). The domain size for the simulation was 36 x 36 km in the horizontal and 19 km in the vertical. The grid intervals were $\Delta x = \Delta y = 1$ km, $\Delta z = 0.5$ km. A thermal bubble placed in the center of model domain with size of 8 x 8 km in the horizontal and 2 km in the vertical was used to initiate convection. The peak temperature perturbation in the center of thermal bubble was 1.5 K.

4. RESULTS

The multi-cellular storm was at least qualitatively well simulated in this study. In response to the initial conditions, a strong single cell formed quickly. Rain and hail were beginning to reach ground at about 24 min and 40 min, respectively. With the development of the storm, it started to enter a well organized stage. A lot of new cells periodically developed in response to forcing by the intensifying gust front. The multi-cellular structure formed in this stage is evident in XZ vertical cross-section plot of vertical velocities (Fig.1). The wind field suggests that there were one strong main updraft cell with maximum updraft as large as 30 m/s and two sub-updraft cells

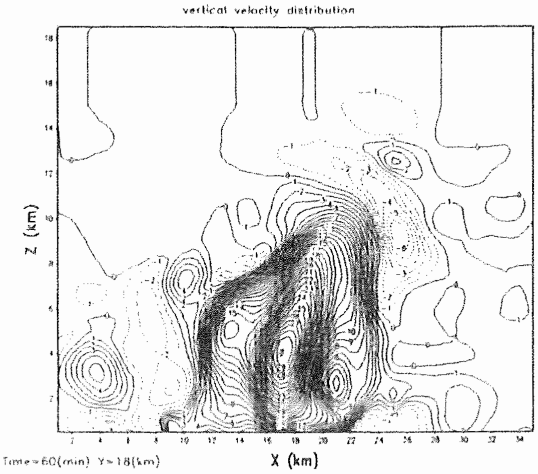

Fig.1 XZ field of velocity component W through region of higher hail water content at 60 min.

with maximum updraft of 16 and 8 m/s, respectively.

In order to understand the hail formation and growth in hail category model, the behavior of the different hydrometeor types will be discussed in here. Fig.2 and Fig.3 show the fields of cloud water and cloud ice in the XZ cross-section, respectively. Cloud water is found mainly in region of updraft while cloud ice is mainly found in upper region (above 8 km) of maximum updraft in the mature stage cell. The prediction of cloud base (3.5-4.0 km MSL) and the height of cloud top (12-13 km MSL) are very well comparing with the observed values (3.6 km and 13 km). Little of cloud ice can be found in the anvil.

Rain water exits primarily below the melting level (3.5 km) due to the melting of hails (Fig.4). A relatively low rain water region between 8 km and 3.5 km produced by auto-conversion of cloud water exits above the freezing level remained unfrozen as an important source of formation and growth of snow and hail/graupel.

Field of snow in XZ cross section is presented in Fig.5. It is shown that the snow mainly distributes in the cold upper portion of updraft and in the anvil. The snow in these regions could be considered to be unrimed crystals, larger rimed snow crystals.

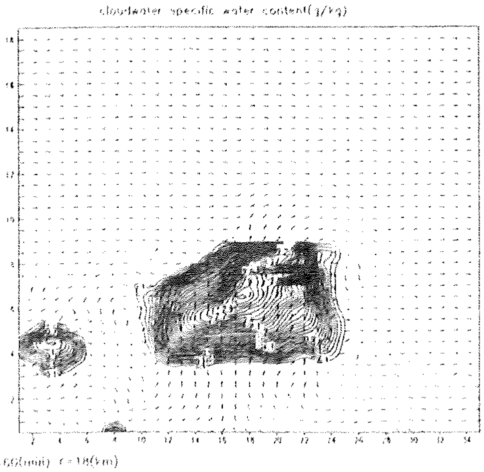

Fig.2 XZ field of cloud water mixing ratios through region of higher hail content at 60 min.

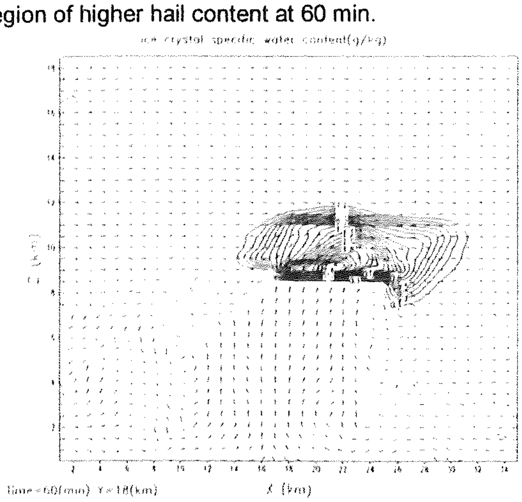

Fig.3 Same as Fig.2 except for cloud ice.

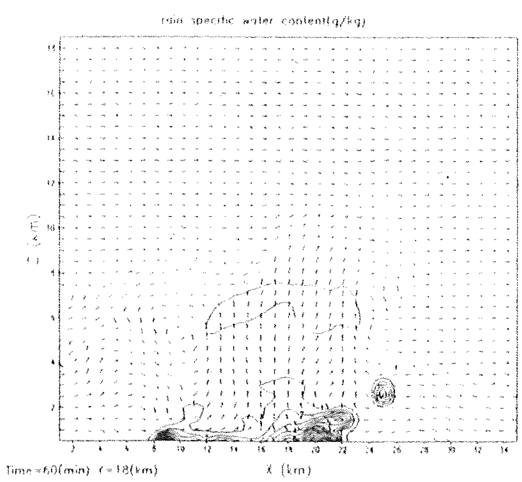

Fig.4 Same as Fig.2 except for rain water.

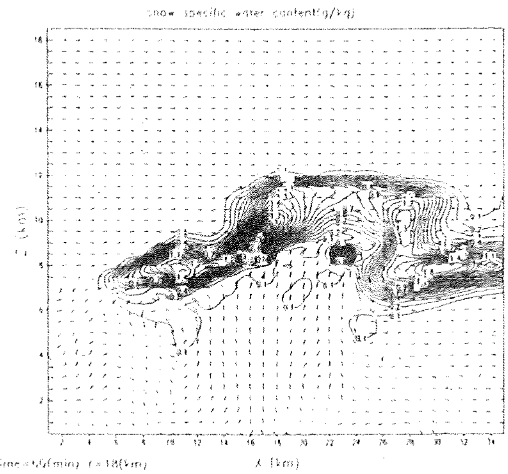

Fig.5 Same as Fig.2 except for snow.

Snow became abundant shortly after the presence of cloud ice in the simulation. Amounts of snow exceeded 2.5 g/kg near the main updraft. It is worthy noted that secondary maximums of snow also developed at the top of the younger cells caused by gust front. Snow aggregates at the top of these gust front cells were prime candidates to further grow into larger hailstones if they remained in regions of heavy riming, and are transported downstream into the main updraft again. In the model, snow formed primarily by the freezing of very small raindrops and by the conversion from collision between cloud water and cloud ice based on the Bergeron-Findeisen mechanism. Snow played an important role in the production and growth of small hail and graupel in the simulation.

Field of hail/graupel in XZ cross section is shown in the Fig.6. It shows that the vaulted structure, the upshear and downshear overhang regions of hail are evident at 60 min of simulation. This extension of the overhang structure were mainly produced by firstly the divergent updraft outflow and secondly the formation of new cells above the gust front. This kind of overhang structure can provide a favorite condition for embryos of hail to grow up larger hail as they fall back into the storm inflow or into new cells forming on the gust front.

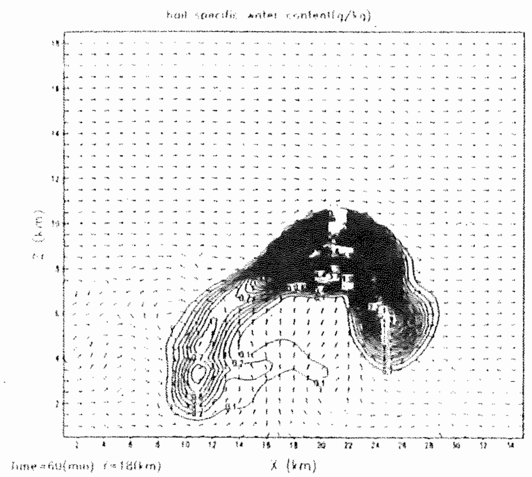

Fig.6 Same as Fig.2 except for hail and graupel.

Because the updraft of new subcells was much less than that of main cell (Fig.1), it could not support large-size hail. Therefore some of relatively larger hails fell from the subcells while some of small hails may reenter main updraft to continue their growth. From this simulation, It is likely that recycling growth of hails did occur in at least the multi-cellular hailstorm.

Due to limitation of page numbers, only simple comparison of maximum vertical velocities presented by Hail Category Model and Hail Parameterization Model is shown in Fig.7. The cloud simulated by HPM collapsed much quicker than that by HCM. According to observation, the storm lasted for more than two hours. Therefore, the results of HPM are not so reasonable .

5 . CONCLUSIONS

A three-dimensional hail category cloud model with detailed hail microphysics was used to simulate a multi-cellular hailstorm in this study. It was found that the most of simulated features such as obvious structure of vault and long overhang anvil are well consistent with available observations. This study shows that snow played a very important role in the microphysics of hail growth, which is consistent with observations that many of the graupel and hailstone embryos were formed from heavily rimed aggregates and snow crystals.

The fact that hail fell mainly from the anvil regions suggests that the recycling growth of hail could occur in the multi-cellular hailstorm.

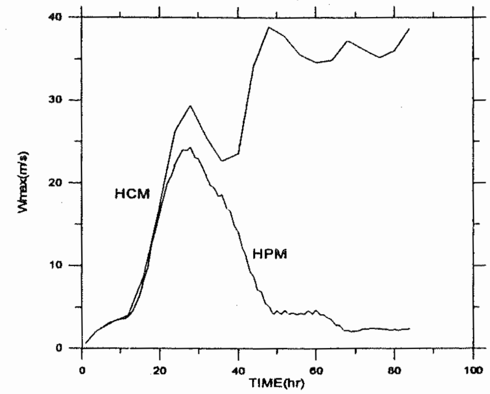

Fig.7 Comparison of W_{max} from HPM and HCM

Acknowledgments: This work was supported by the Chinese Natural Science Foundation under Grants 49675247 and Chinese National Scientific Key Program 96-020-01-07

REFERENCES

Berry, E.X., 1967: Cloud droplet growth by collection. *J. Atmos. Sci.*, **24**, 688-701.

Cheng, L., and M. English,1983: A relationship between hailstone concentration and size. *J. Atmos. Sci.*, **40**, 204-213.

Guo, X. L.,1997: The studies on three-dimensional hail category numerical simulation of hail formation and hailfall processes, *Ph.D Thesis*, Institute of Atmospheric Physics, Chinese Academy of Sciences.

Klemp, J.B., and R.B. Wilhelmson, 1978: the simulation of three-dimensional convective storm dynamics. *J. Atmos. Sci.*, **35**,1070-1096.

Foote, G.B., and C.G.Wade,1982: Case study of a hailstorm in Colorado. Part I: Radar echo structure and evolution. *J. Atmos. Sci.*,**39**, 2826-2846.

WEEKLY DISTRIBUTION OF HAILFALLS AND HAILSTONE SIZE DISTRIBUTIONS IN SOUTHWESTERN FRANCE

J. Dessens[1], R. Fraile[2] and J.L. Sanchez[2]

[1]Laboratoire d'Aérologie, Université de Toulouse, France
[2]Laboratorio de Física de la Atmósfera, Universidad de León, Spain

1. INTRODUCTION

There is a popular belief in the agricultural region around Toulouse, France, that hailfalls are more severe during weekends. In fact, the insurance data in the department of Haute-Garonne show that crop losses due to hail are higher on Saturdays, Sundays, and public holidays than during the working days, but the statistical significance of the difference has never been proved. On a physical point of view, this possible effect of air pollution on hailfalls recalls the finding by Dettwiller and Changnon (1976) that there is a sharp drop in precipitation amounts on weekends in Paris. The hypothesis of hailstorm mitigation by inadvertent weather modification recently received a stronger support with the observation of weekly cycles in lower-troposphere pollution, precipitation and tropical cyclones in the coastal NW Atlantic region (Cerveny and Balling 1998).

The availability of a data file of some 2500 point hailfall measurements made from 1989 to 1999 in a large area of southwestern France now gives the opportunity to check this possible unbalance in the weekly distribution of hailfalls. The results will show that there is really a physical difference between the characteristics of hailfalls on weekends and working days in the inland area of southwestern France.

2. HAILPAD DATA

The hailpad network was installed by the ANELFA (Association Nationale d'Etude et de Lutte contre le Fléaux Atmosphériques) in 1987-1989 in nine departments of southwestern France. The network reached its present structure for the hail season of 1989, and it consisted, in 1999, of 840 hailpad stations spread over an area of about 40000 km^2 (Fig. 1). Five departments are bordering the Atlantic Ocean (482 stations), while the other four departments are located inland (358 stations). The hailpad material, the calibration and the data processing are described in Dessens and Fraile (1994). The pads are scanned and the images processed automatically, except for the areas of some pads which exhibit overlapping dents. For these confused parts of pads, the visual interpretation of the technician remains necessary.

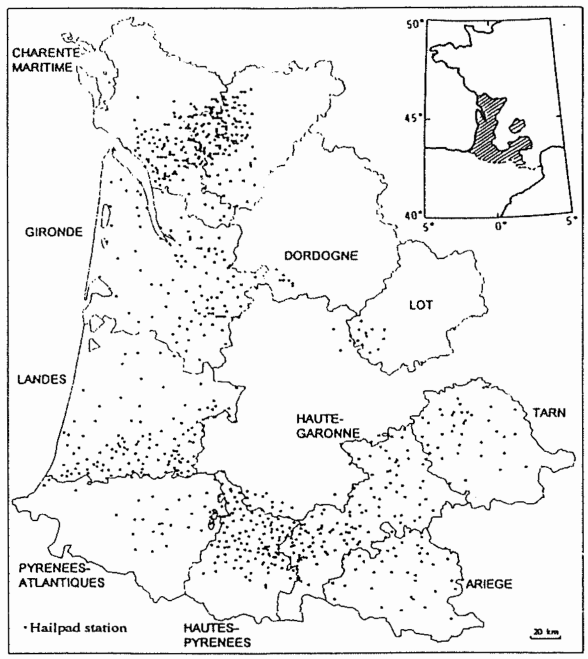

FIG. 1: Map of the ANELFA hailpad network in southwestern France in 1999.

From 1989 to 1999, the number of hailpad stations has increased from 577 to 840, with a mean number of 774 exposed pads per year. During this period, 2481 pads have been impacted by hailstones on 429 hail days. Only the 1790 hailpads hit by at least one hailstone of 1-cm diameter or more were processed, all hailstones larger than 0.5 cm being counted on these pads. The remaining 691 hailpads, which are relative to non-damaging hailfalls, will be processed shortly with the automatic system now available.

Corresponding author's address: Jean Dessens, Centre de Recherches Atmosphériques, 65300 Campistrous, France; E-Mail: desj@aero.obs-mip.fr

TABLE 1. Inland departments. Weekly distribution of the number of hailpads impacted by hailstones, of the number of hailpads impacted by hailstones larger than 1 cm diameter, and of the number of hailstones of different sizes per hailpad.

	SUN	MON	TUE	WED	THU	FRI	SAT
Pads impacted	164	237	175	193	228	188	244
- per hail day	5.29	4.65	3.98	4.11	4.47	4.09	5.08
Pads impacted by hailstones ≥ 1 cm	115	167	129	136	183	141	186
- per hail day	5.00	4.51	5.16	3.78	6.53	4.86	5.63
Hailstones ≥ 0.7 cm per hailpad (m^{-2})	1603	1080	1357	1112	1255	1301	1474
- ≥ 0.9 cm -	767	428	507	427	494	519	701
- ≥ 1.1 cm -	376	171	181	174	194	230	355

This set of data will be considered in the next section for a study of the weekly distribution of hailfalls.

3. WEEKLY DISTRIBUTION OF HAILFALLS

A possible effect of air pollution on the physics of hailstorms should be more pronounced in the inland departments than in the departments which are boardered, to the west, by the Ocean (storms coming in general from SW). The hail data collected in the four departments of Ariège, Haute-Garonne, Hautes-Pyrénées and Tarn will then be first considered.

Table 1 summarizes the data relative to the 1429 hailpads collected during the 1989-1999 hail seasons, 1057 of them having been impacted by hailstones larger than 1 cm and then processed. Nothing special appears on Saturday and Sunday concerning the hailfall frequencies, but when the intensity of hailfalls is considered, it is clear that the number of hailstones larger than 0.7 cm is more important on Sundays and Saturdays. The difference increases when only the hailstones larger than 0.9 or 1.1 cm are counted. The number of hailstones larger than 1.1 cm is about twice larger on weekends than during the rest of the week.

These results lead to computing the hailstone size distributions relative to the two parts of the week, and to testing if they are statistically significant.

4. HAILSTONE SIZE DISTRIBUTIONS

For each impacted hailpad, the number of hailstones is summed up in 2-mm diameter classes, from 0.5 to 1.7 cm, and in 4-mm classes above 1.7 cm. Table 2 gives the mean number of hailstones per hailpad in the different classes for the two periods of the week. Large hailstones are significantly less numerous in the working day hailfalls. The Mann-Whitney U Test, applied in each range of diameters for the two sub-samples, indicates that the difference in the sample means is statistically significant at the 0.05 level in all the ranges above 0.9 cm.

TABLE 2. Mean hailstone numbers (m^{-2}) in different diameter ranges for two samples of hailfalls relative to the two periods of the week.

Range (cm)	MON to FRI 1021 hailfalls	SAT and SUN 406 hailfalls
0.5-0.7	1471	1302
0.7-0.9	550	588
0.9-1.1	210	268
1.1-1.3	81.1	128
1.3-1.5	31.1	63.2
1.5-1.7	13.1	31.8
1.7-2.1	8.9	28.3
>2.1	3.9	15.4

A computation of the exponential form of the two distributions can be made without the first diameter class (0.5-0.7 cm), for which the number of hailstones is not determined with sufficient precision by the hailpad method, and without the classes above 1.5 cm, for which the number of hailstones per hailpad is low. The results obtained with the numbers of hailstones in the 0.7-1.5 cm diameter range gives the following exponential forms:

$N_D = 126{,}120\ e^{-4.78\,D}$ for Monday to Friday,

$N_D = 56{,}250\ e^{-3.71\,D}$ for Saturday and Sunday,

with N_D in $cm^{-1}\ m^{-2}$ and D in cm.

Fig. 2 gives a graphical representation of these distributions.

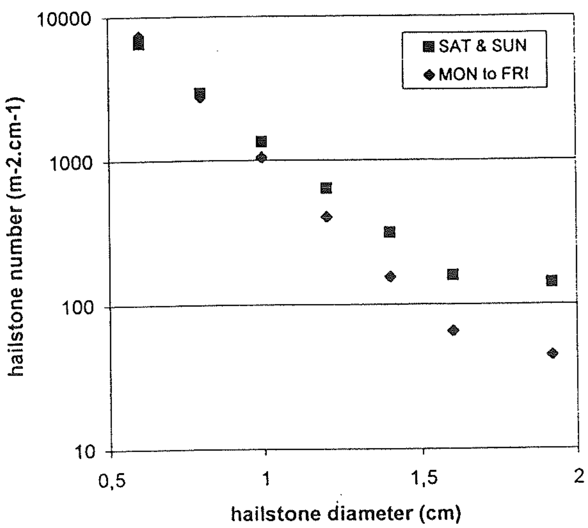

Fig. 2: Hailstone size distributions for weekends and working days in four inland departments of southwestern France.

For each of the 1429 hailpads that received hail impacts, the parameter λ of the exponential distribution was calculated. By applying the Mann-Whitney test with a significance level of 0.05, it has been proved that the λ parameter is significantly different in the sample of weekend days than in the sample of the rest of the days.

The same analysis applied to the five Atlantic departments does not give any significant results. For example, the number of hailstones larger than 0.9 mm is maximum on Sundays (1123 per pad), but Saturdays (839) receive less hailstones than Tuesdays (1020) and Fridays (985).

5. PHYSICAL HYPOTHESIS AND CONCLUSION

The relative maximum concentration in large hailstones observed on Saturdays and Sundays in the inland departments of southwestern France, but not in the Atlantic ones, suggests that an anthropogenic pollution subject to daily variations could be efficient in reducing hailfall severity during the week's working days. Several studies, recently reviewed in Cerveny and Balling (1998), show that weekly fluctuations in air pollution and in meteorological processes are observed in different parts of the world, and they confirm that human activities may influence the weather and the climate. Another example of man-induced change in meteorological events is given by Rosenfeld (1999) who showed that warm rain processes in convective tropical clouds infected by heavy smoke from forest fires are practically shut off, and that rain suppression due to air pollution may also prevail in the extra-tropics.

Among the activities which may influence the cloud physical processes in the hailstorms of the Toulouse area, road transport appears to be the main source of variable pollution in this moderately industrialized region. Statistics made on the main roads entering this town indeed show a decrease of about 40% in the traffic during weekends. Moreover, a French regulation nearly stops all truck traffic on Saturdays and Sundays. Most of the industrial and agricultural activities are also reduced on weekends. Lopez et al. (1982) have observed a strong decrease in the concentration of Aitken nuclei on Sundays and on public holidays in June 1976 in the Toulouse downtown. It is also probable that the concentrations in CCN (Cloud Condensation Nuclei) and IFN (Ice Forming Nuclei) are reduced on weekends.

Finally, air pollution appears to have the same effect as silver iodide seeding with ground generators (Dessens 2000): in the more seeded hailfalls, the number of hailstones with diameters larger than 0.7 cm is decreased, while the number of small precipitation elements (melted or not) is increased.

This rare beneficial effect of air pollution deserves to be checked with more hail seasons in the data file, and with measurements in other parts of the world.

Acknowledgements

We are grateful to Mr J.L. Serin, Direction Départementale de l'Equipement, for data and comments about road traffic in the Toulouse area.

References

Ceverny, R.S., and R.C. Balling, 1998 : Weekly cycles of air pollutants, precipitation and tropical cyclones in the coastal NW Atlantic region. *Nature* **394**, 461-563.

Dessens, J., 1998: A physical evaluation of a hail suppression project with silver iodide ground burners in southwestern France. *J. Appl. Meteor.* **37**, 1588-1599.

Dessens, J., and R. Fraile, 1994: Hailstone size distributions in southwestern France. *Atmos. Res.* **33**, 57-73.

Dessens, J., and R. Fraile, 2000: The effect of silver iodide seeding on hailstone size distributions. *J. Wea. Mod.* **32** (under printing).

Dettwiller, J.W., and S.A. Changnon Jr, 1976: Possible urban effects on maximum daily rainfall at Paris, St Louis and Chicago. *J. Appl. Meteor.* 15, 517-519.

Lopez, A., J. Fontan and P. Boulard, 1982: Mesure de l'intensité de la source de noyaux d'Aitken en site urbain. Influence des différentes composantes. *Atmos. Environ.* **16**, 283-292.

Rosenfeld, D., 1999: TRMM observed first direct evidence of smoke from forest fires inhibiting rainfall. *Geophys. Res. Let.* **26**, 3105-3108.

A NUMERICAL SIMULATION OF THE PRODUCTION OF HAIL AND RAIN IN SUPERCELLS

S. C. van den Heever and W.R. Cotton

Colorado State University. Ft. Collins, Colorado

1. INTRODUCTION

The influence of microphysical processes on the dynamics of severe storms has been the focus of several numerical simulations and observational studies recently. Based on their numerical simulations, Brooks et al. (1994) hypothesize that differences in the distribution of precipitation within supercells, which occur as a result of differences in storm-relative winds, cause changes in the low-level mesocyclone genesis. Rasmussen and Straka (1998) suggest that storm propagation, low-level mesocyclone genesis and decay, and even the midlevel mesocyclone rotation depend in varying degrees on the position and strength of the low-level horizontal buoyancy gradients which themselves are dependent on the precipitation distribution within the storm.

Ice processes are recognized to play an important role in the dynamics of convective storms. For example, latent heat released as a result of condensation onto ice particles can result in a much warmer cloud thereby increasing its potential for growth. Johnson et al. (1993) performed numerical simulations to determine the role of ice in a highly glaciated supercell storm. They conducted two simulations. In the first simulation only liquid water microphysics was used, while ice microphysics was included in the second. They found from their simulations that the inclusion of ice has a significant impact on the dynamics, kinematics, thermodynamics, and distributions of water within the storm, particularly at the lower model levels. General supercell characteristics were observed in both simulations, however, they tended to be better developed and longer-lived in the ice simulation. The surface precipitation was more concentrated in the liquid water simulation producing a faster moving gust front. This gust front cuts off the moisture supply resulting in the storm's demise. In the ice simulation, the precipitation was less concentrated, the gust front slower moving and the storm longer-lived.

The goal of the work presented here is to further investigate using numerical simulations, the influence that ice processes have on convective storm dynamics. In particular, the impact that changing the mean hail diameter has on supercell storm dynamics will be examined.

Corresponding author's address: Susan C. van den Heever, Colorado State Univ., Dept. of Atmospheric Science, Ft. Collins, CO 80523-1371; FAX: 970-491-8449; email: sue@cloud9.atmos.colostate.edu

2. MODEL SETUP

The model utilized for these simulations is the Regional Atmospheric Modeling System (RAMS) developed at Colorado State University. A single grid with a grid spacing of 1km and 140 by 170 points in the horizontal was used. The vertical grid spacing is variable and the model top stretches to approximately 23 km. Convection was initiated using a warm (3 K perturbation), moist (20% perturbation) bubble. The model was homogeneously initialized using a sounding from a previous RAMS simulation of the 26 April 1991 tornado outbreak. Surface friction is turned off while Coriolis force is turned on. The single-moment microphysics module in which mixing ratios are predicted was used for the results presented here. The bulk microphysical species include vapor, cloud droplets, rain, pristine ice, snow, aggregates, graupel and hail, the distributions of which are exponential. Simulations using a mean hail diameter of 3mm, 5mm, 1cm and 2cm were performed. Apart from the mean hail diameter, the model runs were otherwise identical.

3. RESULTS

3.1 Storm Morphology

Examination of the storm tracks of the 3mm and 2cm mean hail diameter simulations show significant differences in the storm development and morphology (Fig. 1). In the 3mm simulation (Fig. 1a), the left moving storm (LM) dies after about 35 minutes of simulation time, whereas the LM in the 2cm simulation (Fig. 1b) exists for at least 2 hours. Johnson et al (1993) also observed in their simulations that the presence of ice had an impact on the LM storm dynamics, the LM dying slightly earlier in the no-ice case than in the ice simulation. The right moving storm (RM) in the 3mm simulation travels faster than that in the 2cm simulation. The 2cm RM is a relatively steady storm, maintaining its structure and strength for the duration of the simulation, however, the RM in the 3mm simulation is somewhat unbalanced and undergoes what appears to be storm-splitting later on in the simulation. The 5mm and 1cm simulations represent the transition stages in the storm development and characteristics between the 3mm and 2cm cases for all of the results presented below.

The cold pool is significantly stronger in the 3mm than in the 2cm case (Fig. 2) due to the greater evaporative cooling that occurs as a result of the larger hail surface area exposed in the 3mm case. Temperatures vary about 12°C across the cold pool in the 3mm simulation (Fig. 2a) while only varying about 4°C in the 2cm

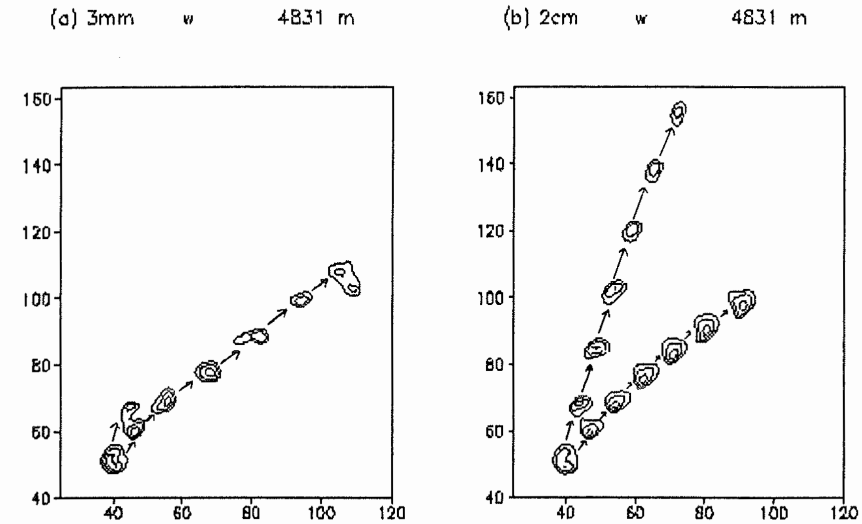

Figure 1: Storm tracks of the 3mm (a) and 2cm (b) simulations. Field shown is vertical velocity at 4831 m AGL. Contour interval is 10 m/s starting with 10 m/s. Storm positions are shown at 20, 35, 50, 65, 80, 95 and 110 minutes starting at the south-west corner. Axes are distance from the grid origin in km for all figures.

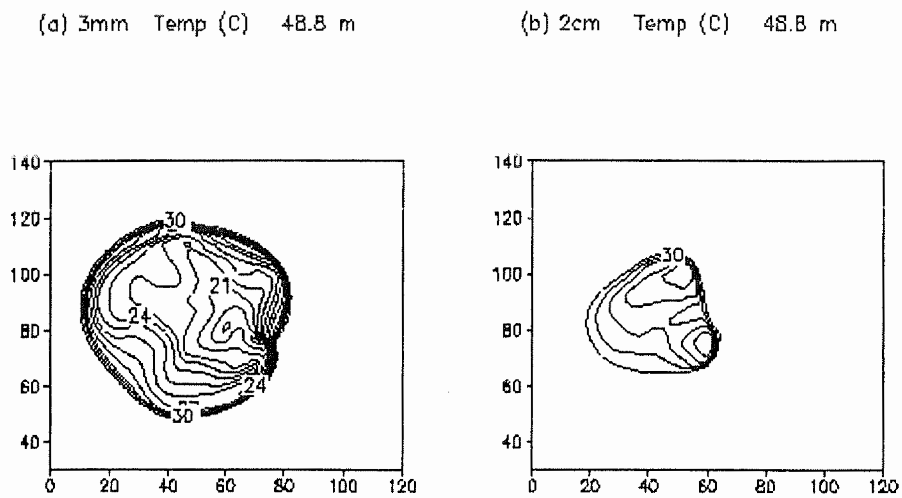

Figure 2: Temperature (°C) after 65 minutes at 48.8 m AGL for the 3mm (a) and 2cm (b) simulations (thin lines). Contour interval is 1°C.

simulation (Fig. 2b). The cold pool is more extensive in the 3mm simulation as a result of the colder, denser, and hence faster moving air. The gust front in the 3mm simulation is moving ahead of the storm in the upper-levels. This rapid movement of the gust front away from the storm cuts off the supply of moisture and positively buoyant air from the RM storm causing the observed weakening and unbalanced nature of the storm. In the 2cm simulation the upper-level storms stay at the leading edge of the cold pool resulting in the strong, quasi-steady RM supercell that is observed throughout the simulation. The factors causing the rapid decay of the LM storm in the 3mm simulation, as well as the splitting of the RM storm later in the simulation are currently under investigation. A more rapid gust front movement also occurred in the no-ice simulation compared with the ice simulation of Johnson et al. (1993). It is therefore apparent that hail size and the associated rates of evaporative cooling have a significant impact on the cold pool dynamics and resultant storm strength, balance and morphology.

3.2 Hail Distribution With Respect To The Updraft

In the 2cm simulation hail mixing ratios of about 1.5 g/kg are observed at the ground (Fig. 3b), however, in the 3mm case, the hail is insufficiently large to withstand the effects of melting and only traces of hail occur at the

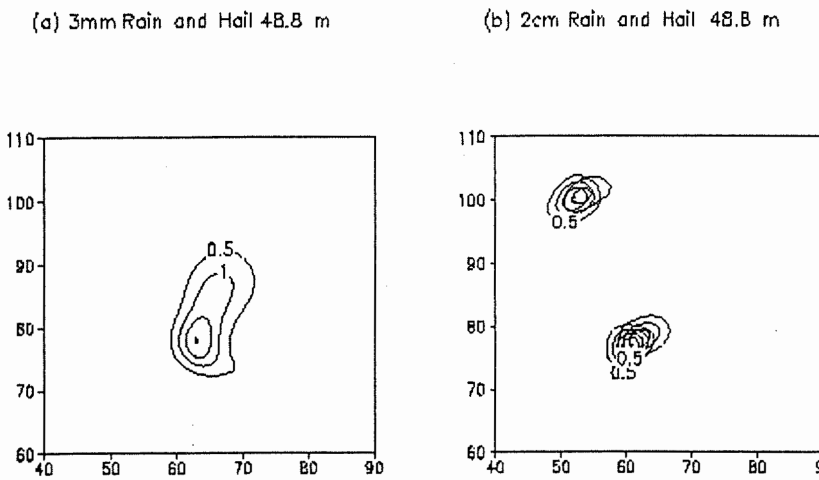

Figure 3: Rain (thin lines) and hail (thick lines) mixing ratios after 65 minutes at 48.8 m AGL for the 3mm (a) and 2cm (b) simulations. Contour intervals are 0.5 g/kg starting at 0.5 g/kg.

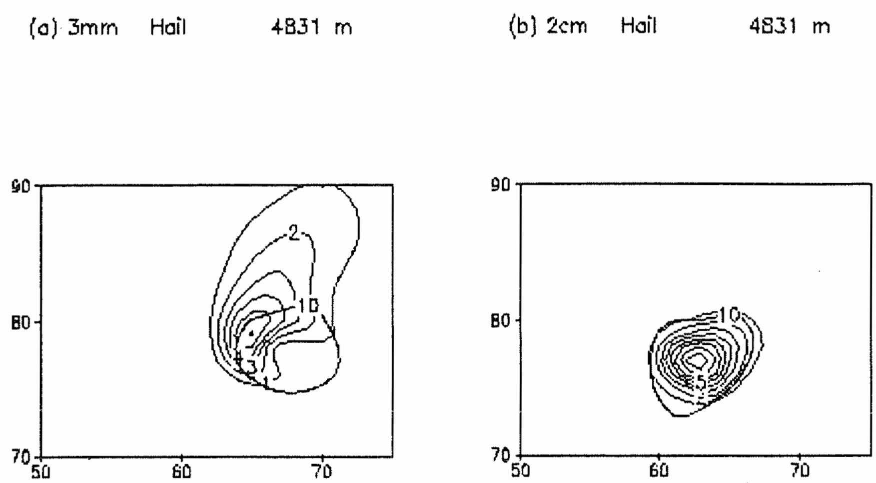

Figure 4: Hail mixing ratios (thin lines) and vertical velocity (thick lines) after 65 minutes at 4831 m AGL for the 3mm (a) and 2cm (b) simulations. Contour intervals are 1 g/kg starting at 1 g/kg for hail. Only the10 m/s contour interval is shown for the vertical velocity.

lowest model level (Fig. 3a). The rain mixing ratio is slightly higher in the 2cm simulation, however, rain occurs over a much greater area in the 3mm run. In the 2cm case, the rain and hail distributions are closely located at the lowest model level. Hail is co-located with the vertical updraft at mid-levels in the 2cm simulation (Fig. 4b). In the 3mm case, however, hail may be found as far as 10 km away from the updraft core (Fig. 4a). A hook is also apparent in the 3mm hail field (Fig. 4a). The smaller hail sizes in the latter case allow for the distribution of hail further away from the updraft compared with the larger hail sizes in which such transport is limited and the hail is found closer to the updraft. The surface distribution of the microphysical species can also be attributed to the transportability of the hail species (Fig. 3a,b), the larger area of rain in the 3mm case resulting from the melting of the more widely distributed hail. Smaller hail sizes therefore result in more rapid melting, further distribution of the hail from the updraft, more extensive although slightly less concentrated rainfall distributions at the surface and a more intense cold pool. Hail distribution with respect to the updraft in the 2cm case is similar to that in a high-precipitation supercell, while the displacement of the hail further away from the updraft in the 3mm case is more like the distributions found in a classic supercell (Doswell and Burgess, 1993; Rasmussen and Straka, 1998). Hail size may therefore be one of the factors determining the type of supercell produced.

3.3 Hail-Vorticity Relationship

Low-level vorticity values for the RM as a function of time are shown for the various mean hail diameters in Figure 5. It is apparent from this graph that as the mean hail diameter increases the vorticity of the RM decreases. Vorticity values drop toward the end of the smaller hail simulations when storm splitting occurs but strengthen again following the splitting. The vorticity for all of the hail diameter cases follow a similar trend of increasing to mesocyclonic values later in the simulation following an initial spike in the values around 20 minutes (Fig. 5). The same relationship between hail size and vorticity values has been observed in simulations using the candycane-type hodograph shown in Brooks et al. (1994). This relationship may help to explain why High Plains thunderstorms often produce large quantities of hail but are not frequent tornado producers. It may also aid in explaining the failure of the Hays storm to produce a tornado in spite of appearing so similar to the Garden City storm that did produce a tornado (Wakimoto and Cai, 2000). The Hays storm produced softball size hail.

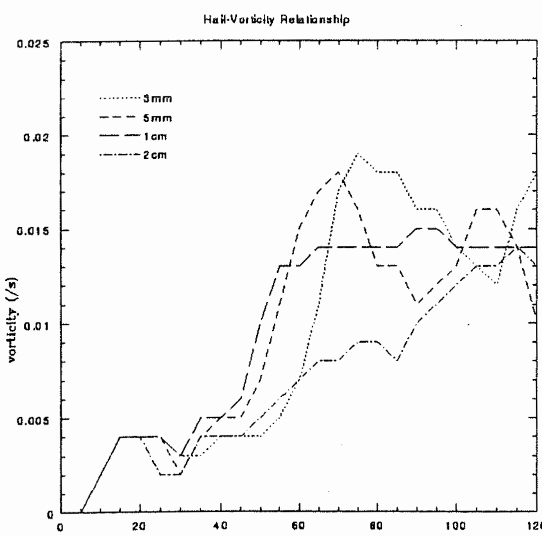

Figure 5: Low-level vorticity values of the RM storm for varying mean hail diameters as a function of time.

4. CONCLUSIONS

Numerical simulations have been performed in which the mean hail diameter was varied from 3mm to 2cm. These simulations show that such variations appear to have a significant impact on supercell dynamics and morphology. Smaller hail sizes result in a stronger, more expansive, more rapidly moving cold pool. The RM is less steady with smaller hail sizes than with larger hail. This can be attributed to the movement of the cold pool. The LM is a significantly longer-lived storm in the larger hail size cases. Hail is distributed further from the updraft in the smaller hail size simulations, whereas the hail and updraft are almost co-located in the larger hail runs. This results in a more expansive, although slightly less intense distribution of rain at the surface in the smaller hail cases. In the smaller hail runs the hail is too small to withstand the impact of evaporation and only a trace of hail is observed at the ground level. The distribution of hail with respect to the updraft is similar to high-precipitation supercells when the mean hail diameter is large, but is more like the classic supercell as the hail diameter decreases. Finally, the simulations reveal that as the hail diameter increases the low-level vorticity of the RM decreases. Such a relationship may have significant implications for the development of supercells and tornadoes, and the forecasting of this development.

5. ACKNOWLEDGEMENTS

This research was supported by the National Science Foundation under grant No. ATM-9900929. Thanks are extended to Brenda Thompson for help with the preparation of this manuscript.

6. REFERENCES

Brooks, H.B., C.A. Doswell III, and R.B. Wilhelmson, 1994: The role of midtropospheric winds in the evolution and maintenance of low-level mesocyclones. *Mon. Wea. Rev.*, **122**, 126-136.

Doswell, C.A., and D.W. Burgess, 1993: Tornadoes and tornadic storms: A review of conceptual models. *The Tornado: Its Structure, Dynamics, Prediction, and Hazards, Geophys. Monogr.*, Amer. Geophys. Union, 161-172.

Johnson, D.E., P.K. Wang, and J.M. Straka, 1993: Numerical simulations of the 2 August 1981 CCOPE supercell storm with and without ice microphysics.. *J. Appl. Meteor.*, **32**, 745-759.

Rasmussen, E.N., and J.M. Straka, 1998: Variations in supercell morphology. Part I: Observations of the role of upper-level storm-relative flow. *Mon. Wea. Rev.*, **126**, 2406-2421.

Wakimoto, R.M., and H. Cai, 2000: Analysis of a nontornadic storm during VORTEX 95. *Mon. Wea. Rev.*, **128**, 565-592.

Towards the physical explanation for different growth regimes of hailstones

Anatolij R. Karev
Republic Hydrometeorological Service of Macedonia, Skupi b/b, 1000 Skopje, Macedonia

1. INTRODUCTION

One of the first theoretical investigations of the thermodynamic (TD) part of the hailstone accretion problem, which was made by Schumann (1938) and worked out by Ludlam (1958), distinguished two different regimes of icing. These regimes called "wet" and "dry" were the modes with and without water film on an ice surface respectively. They were distinguished by using the macroscopic heat balance calculation for the condition at which the surface temperature of hailstones reaches $0^{o}C$. This boundary was called by List (1965) the "Schumann-Ludlam limit". An analogical approach considering $0^{o}C$ as a reference point for distinction of the solid and liquid water states on the icing surface was developed for aircraft icing (Messinger, 1953), with the introduction of the so-called "freezing factor" to explain the wet mode. This last approach, in turn, was the basis for the TD part of many atmospheric icing models with runback water (originally: Lozowski et al., 1983;), and many aircraft icing models (for example: Al-Khalil et al., 1992). Generally, three ice growth processes mentioned, i.e. hailstone growth, aircraft icing and in-cloud icing of atmospheric structures, use the same mentioned solution for the TD part and are very similar in that sense. The distinctions they have concern the features of motion in each case, resulting in corresponding addition or neglect of some terms in the heat balance equation or more complex description of already existing terms. For example, in the case of aircraft icing characterizing with high speed air flow, there are three additional terms to the usual terms in the heat balance equation: kinetic energy of incoming droplets, aerodynamic heating, and conduction through the ice, which is noticeable only in the beginning of process. In the case of hailstone growth, in turn, the characterizing features are: the noticeable effect of water shedding (Carras and Macklin, 1973); the effect of spongy ice formation; the complex aerodynamic motion in cloud, including its spin and nutation/precession (Kry and List, 1974; Stewart and List, 1983); the various shapes of hailstones (Macklin, 1977) and their various surface roughness (Browning, 1966). The effect of changeable density of the growing ice layer (Macklin, 1962; Kachurin and Gashin, 1968) in dry mode of icing could be considered as a common feature for all ice growth processes.

Another important component of the calculation of the ice growth process, which could be considered as a common feature, is the dynamic part. It consists of the aerodynamic theory of aerosol particle flow around the streamlined body for the potential airflow with or without separation (originally: Langmuir and Blodget, 1946; and Levin, 1953). Although application of this theory to the complex aerodynamic motion of the hailstones requires its revision, only the improvement of TD part will be examinated here, in the light of new experimental data and already existing theories.

2. SUPERCOOLING AT THE INTERFACES

2.1 Experimental evidences

The series of experiments (List et al. (1989); Garsia-Garsia and List (1992); Greenan and List (1995)), confirmed that the Schumann-Ludlam limit cannot be reached. The temperature of the water film in all experiments was always below $0^{o}C$, and its certain longitudinal and latitudinal distribution was observed, depending of the applied mode of motion of the hailstone (spin, nutation), and TD/dynamic conditions. We suppose, that the fact of negative temperature of water film in so-called wet regime may also be the case for other icing processes. Thus, this fact also imposes to present other physical explanation for the distinction of wet and dry regimes for icing processes.

2.2 Determination of supercoolings

It should be noted that the meaning of $0^{o}C$ in the macroscopic consideration is only as the highest point over which ice/water transition never occurs. The real point of transition depends on many factors: the bulk amount of water considered, the way of its cooling, contact with other surfaces or solid phase, fluctuation of TD parameters (TD noise) etc. In the microscopic consideration, the Gibbs-Thompson's effect is very appreciable for curved surfaces like small aerosols or dendrite shapes on the solid/liquid interface, moving the transition temperature in the direction of negative temperatures. Moreover, the fast-proceeding processes in *Cb* clouds should be considered as strictly irreversible with supercooling at the ice/water interface (Kachurin, 1990). The temperature of the surface of water film in that case should always be lower than the temperature at the ice/water interface, in order that temperature gradient in the film may contribute to the heat transfer from the ice/water interface to the skin surface (Karev, 1993a). Schumann-Ludlam's approach can be used exclusively for the case of hailstone melting in the warm layers of atmosphere (Mason, 1970), but not in the case of their growth.

Thus, let us consider two supercooling: Δ at the ice/water interface, which is the driving force for ice growth under supercooled water film, and δ at the surface of the supercooled water film. δ is higher than Δ, and there is strict relation between them through the conductive/convective transfer in water film. A usual heat balance equation could be written for the δ determination. The most important terms in this equation are: convection/conduction in the film (equal to the latent heat realized), convection/conduction with airflow, evaporation/sublimation, and heating of incoming aerosol particles (Karev, 1993a). Generally, in the case of water shedding, the last term should include two parts: the first one for the portion remaining on the

Corresponding address: akarev@meteo.gov.mk

surface and participating in ice growth, and the second one for the portion leaving the surface, participating in that way only in the heat exchange, but not in the mass transfer. The temperature of the first part is not equal for a general case with the temperature of the second part. A usual Stefan's condition should be written for the ice/water interface (released latent heat with the convection /conduction term in film) keeping in mind that there is supercooling (Δ) at this interface, which determines the corresponding ice growth velocity: V=f(Δ). Depending of the mechanism, which has been chosen for the explanation of the solid/liquid growth velocity (2-D embryos nucleation, dislocation growth or linear growth) (see for example: Hillig,1959; Hillig and Turnbull,1956; Chalmers, 1982), this relationship can be very different.

3. KINETICO-DYNAMIC THEORY

Kachurin (1962), choosing linear velocity growth, $V_1=A{\cdot}\Delta^B$, were A and B are constants (Hillig and Turnbull, 1956) for this explanation of ice growth, and taking into account the dynamics of the thin water shear-driven film on advanced icing surfaces with the Couette approximation (Levich, 1962), developed the theory of icing of flat surfaces of aircraft. In this theory distinction of the wet and dry regimes is not at all connected to 0°C. Quite the contrary, the theory reported negative temperatures of the surface of water film covering the icing surface. In this maybe unique theory, the regimes of crystallization corresponded only to the dynamic regime of the supercooled water film flow.

In the laminar flow of supercooled water film, when only conduction through it was taken into account, the reaction of the interface against the initial perturbations of some TD parameters, resulting in corresponding change of thickness of film, was always unstable. It consisted of the further changes of water film thickness in the same direction. In the case of its decrease, the reaction resulted in very fast disappearance of the film. In the case of its increase, the result consists of the fast thickening of film until it reaches a stable turbulent flow.

A completely different reaction was found in the case of turbulent flow of the supercooled water film on an ice surface. Each perturbation of TD parameters, manifesting themselves by the changes of thickness, was smoothed over, getting back the thickness to its initial value.

These reactions mean absence or unsteady thickening of the supercooled water film in the case of its laminar flow and continually its presence in the case of turbulent flow with const thickness for given TD condition. After the TD part, i.e. calculations of δ, was revised, the theory was applied to the calculation of a cylinder icing at low flow velocity (Kachurin et al., 1974). In the original work the temperature of the surface of water film was taken close to temperature of medium, taking into account fast aircraft speeds. Moreover, it was found that the parameter, which was originally proposed for the distinction of regimes h_{eq} –equilibrium water film thickness, could be successfully used for the determination of the density of growing ice layer. It was done by its comparison with its critical value h_{cr}, determining the boundary between two regimes (Kachurin and Gashin, 1968, Kachurin, 1990). In the works mentioned this parameter was compared with Macklin's parameter (Macklin, 1962), and some of its advantages were presented.

4. FURTHER DEVELOPMENT

Further development and improvement of the theory is related with its utilization for icing of spherical and cylindrical objects (Gvelesiani, 1968, 1970). Gvelesiani (1972) also proposed the method for the determination of the thickness of water film on the surfaces of bodies with various shapes. Karev (1993b), using Gvelesiani's main conclusions, obtained new equations for basic parameters, characterizing the process among which is the thickness of the supercooled water film. Since thickening of the film is limited by the outer dynamic conditions of the flow, the regime of water shedding was determined with the introduction of the theoretical coefficient of liquid water content (LWC) realization *(Rl)*. It presents the portion of LWC, which stays at the ice layer surface and which participates in icing process. This coefficient is related to experimentally determined net collection efficiency E_{net} (Garsia-Garsia and List, 1992) through the regular collection efficiency (E_{col}): $E_{net}=Rl\,E_{col}$. Rl is determined by the comparison of two Δ: one (Δ_H) from the heat balance equation for δ, and the second (Δ_M) from the mass balance equation. Since this way was connected to the determination of max water film thickness for given thermodynamic conditions by numerical solution of partial differential equation (Karev, 1993b)), later, it was improved and simplified (Karev and Kachurin, 1994) by introducing real supercooling at the ice/water interface (Δ_R). The latter is equal to one or the other of two previously mentioned supercoolings correspondingly, before and after the point characterizing the beginning of the shedding process at the TD diagram.

5. CURRENT DEVELOPMENT

Several experimental results and theoretical works will be presented below, which have been taken into account for the further development of Kachurin's kinetico-dynamic theory and its various applications in atmospheric icing and atmospheric physics (Karev and Lozowski, 2000).

5.1 Heat and mass exchange description

Taking into account temperature differences of shedding droplets and supercooled film, and to avoid some difficulties in heat balance calculation (δ), a utilization was proposed of the data on heat exchange of the bodies of different shapes with aerosol flow (Karev, 1993a; Karev and Kachurin, 1994). These are abundant in the literature. Nevertheless, when all the results for supercooled film temperature on the hailstone, with real motion simulation, became available (Greenan and List, 1995), they are used to obtain new relationships between the Nusselt number and all TD parameters included in the realization of the process.

5.2 Ice growth velocity

When speaking about the experimental results related to the growth rate of ice crystals in supercooled water or aqueous solution, one should strictly divide them into three groups: crystal growth in capillary tubes, growth in unconfined quiescent water or aqueous solution, and growth in flowing water under forced convection. Only the results from the third group can be used in this case. Fernandez and Barduhn (1967) appeared to be the first to propose a theoretical model for ice crystal growth in flowing supercooled water. The model proposed that the growth rate in the faster growth direction - basal plane (*a*-axis) is determined only by the rate of transfer of latent heat from crystal growth by forced convection in flowing water. Growth rate of the *c*-axis (perpendicular to basal plane) was not investigated in that work. Water flow was taken to be normally the growing crystal in the direction opposite to its growth. Since their last experiments with shear-driven melt confirmed the initial proposal that dendrites strive to grow towards the upstream direction (Huang et al., 1993), and very pronounced dependence on the forced convection ones again is registered (Lee et.al., 1993), the formula proposed by Fernandez and Barduhn seems to be very appropriate in case of forced convection: $V_2 = A_1 \cdot u^{B1} \cdot \Delta^C$, A_1, B_1 and C are constants, u is the velocity of water film flow. In that way the growth rate directly corresponded to the temperature field and dynamics of motion. In previous variant of the model, connection with dynamics was indirectly through the temperature field changes. The only limitation of that formula relates to cases with very slow water motion, when natural convection plays a significant role (Kallungal and Barduhn,1977), and the splitting of dendrite observed at small supercooling (Koo et al.,1991), but it does not apply to this case.

In fact, to have a stricter solution, the growth velocity would be treated more completely as a vector sum of the velocity in basal plane, where the growth determined by the transfer of latent heat by forced convection, and the velocity in the normal direction, where the growth presumable determined by dislocation mechanism: $\vec{V} = \vec{V}_1 + \vec{V}_2$. Levi (1970) was the first to realize that, however, without taking into account forced convection. Thus, the question of alignment of crystals arises.

5.3 Orientation of crystals and turbulence in the flow

The clearest situation is with wet growth: there is much experimental evidence of fast alignment of the c-axis normal to the growth direction (Levi and Aufdermaur, 1970; Levi et al., 1970). Moreover, in oceanography, Weeks and Gow (1978,1980) and Langhorne and Robinson (1986) have obtained results that give evidence of alignment of the *c*-axis with the direction of motion. Langhorne and Robinson are the first to explain the differences in morphology, drawing on Yaglom's and Kader's (1974) turbulence theory. However, in our opinion, applicability of these results requires revision, since in Yaglom's and Kader's case the main heat transfer was considered from the wall, not from protrusions. In this case heat transfer is considered exactly from the "protrusions" (i.e. dendrites). Having this fact in mind, the turbulent heat exchange between ice and water layers is explained in the model. We were able to find similar (with some exceptions) explanations of turbulent exchange between ice and water layers in oceanography (Omstedt, 1990; McPhee, 1990).

The dry growth mode is a more complex situation. Also Rye and Macklin (1975) reported that probability of droplet reorientation for given TD conditions depends on droplet and surface temperature and on the inclination of the c-axis of substrate, after Levi's and Prodi's results (1983) this question still remains open. Three different relationships are verified of crystal size (radius) with TD parameters in the model: two experimental - Levi and Aufdermaur (1970), Rye and Macklin (1975), and one theoretical.

The laminar boundary layer is treated with Blasius' solution (Schlichting, 1968) for flat surface and with the simplified Falkner-Skan's solution for the flow with pressure gradient, for the turbulent flow an eddy diffusivity conception is introduced.

6. FORMS OF OUTPUT WITH NEW ALGORITHM

The same reactions (unstable and stable) were found on the initial perturbation as in the depicted original model (Part 3). The following explanation could be given of the unstable reaction in the laminar regime of supercooled water film motion using the theory of solidification in the case of equiaxed growth (Kurz and Fisher, 1986 p.50). In both cases the growth of solid/liquid interface and heat flow are in the same direction. A perturbation, in this case it is a decrease or increase of thickness, in the case of equiaxed growth it is a protuberance or cavity on the solid/liquid interface, makes the temperature gradient steeper or gently sloping, and the interface accelerates or slows down. The stable reaction of the supercooled water film can be explained by the very fast adjustment of the turbulent flow through the film to "new" conditions by changing eddy diffusivity for heat (ε_H) with the thickness ($\varepsilon_H \sim h^2$) (Levich, 1962). In other words, presence of the turbulence in the supercooled water film is a determining factor of its stable existence in the natural medium with fluctuating TD parameters and its persistence to corresponding TD changes.

For the moment the model gives output in the form of calculated ice growth (crystal growth) rate depending on input TD parameters. There are 4 regimes correspondingly to the dynamics of water film flow: viscous indifferent, viscous reacting, turbulent without shedding, and turbulent with shedding. The crystal size, growing ice layer density, water film thickness ranges in the regime of its existence are also calculated with the growth mode. The main algorithm can be found (Karev, 1993a; Karev and Kachurin, 1994).

7.FURTHER CONSIDERATIONS

Despite of the improvements presented, the model is still far from ideal, to simulate all particularities of hailstone motion. We have completely avoided here the question of sponginess of ice, although the utilization of the equation for dendritic ice growth could provide answers on that question (Blackmore and Lozowski, 1996). The following improvements should be made in the future: introduction of the influence of corona discharge on the heat and mass transfer in the shedding mode; introduction of the wave motion. Greenan and List (1995) reported this regime at the equator of hailstone. The waves will have the same influence on the airflow as the dendrites on the water flow (Malamatenious et al., 1994; Langhrne and Robinson, 1986). The great challenge will be to modify the dynamic part, taking into account spin/nutation of hailstones.

References:

Al-Khalil, K.M., Keith,T.G.Jr.:, and K.J. De Witt,1992: Development of an improved model for runback water on aircraft surfaces, AIAA paper 92-0042.

Blackmore, R.Z., and E.P., Lozowski, 1996: A freshwater spongy spray icing model with surficial structure, 7th Int.Worksh.Atmos. Icing Struct., 33-38.

Browning, K. A., 1966: The lobe structure of giant hailstones. Quart. J. Roy. Meteor. Soc., 92 , 1-14.

Carras, J. N., and W. C. Macklin, 1973: The shedding of accreted water during hailstone growth. Quart. J. Roy. Meteor. Soc., 99, 639-648.

Chalmers,B.,1982:Principles of solidification, Krieger Publ. Company, 320.

Fernandez, R., and Barduhn, A.J., The growth of ice crystals, Desalination, 1967, Vol.3, P.330-342.

Garsia-Garsia, F., and R. List, 1992: Laboratory measurements and parametrizations of supercooled water skin temperatures and bulk properties of gyrating hailstones. J. Atmos. Sci., 49, 2058-2073.

Greenan, B.J.W., and R. List, 1995: Experimental closure of the heat and mass transfer theory of spheroidal hailstones. J. Atmos. Sci., 52, 3797- 3815.

Gvelesiani, A.I., 1968: On ice accretion growing in the flow of supercooled water aerosol on surfaces of different shapes, Soobsh.Akad. Nauk GSSR, 51, 63-68.

Gvelesiani, A.I., 1970: Some problems of the evolution of hailstones particles, Ph.D. Thesis, Tbilisi.

Gvelesiani, A.I., 1972: On settled thickness of liquid water film on the surfaces of hailstones with various shapes, Trudy Inst.Geoph. Akad.Nauk GSSR, 28, 174-178.

Hillig, W.B., and Turnbull, D., 1956: Theory of crystal growth in undercooled pure liquids, J.Chem.Phys., 24, 914.

Hillig, W.B., 1959: Kinetics of High Temperature, Technology Press, MIY, 127.

Huang, T., Liu, Sh., Yang, Y., Lu, D., and Y., Zhou, 1993: Coupling of Couette flow and crystal morphologies in directional freezing, 128, 167-172.

Kachurin, L.G., 1962: Towards the aircrafts icing, Izv. Akad. Nauk SSSR, Ser. Geophys., 6, 823-832.

Kachurin, L. G., and L. I. Gashin, 1968: On the density and structure of ice growing in supercooled aerosol flow. Izv. Acad. Nauk. SSSR, Phys. Atmos. Ocean, 4, 93-96.

Kachurin, L.G., 1990: Physical principles of influencing at the atmospheric processes, Gidrometeoizdat, Leningrad, 463.

Kallungal, J.P., and A.J., Barduhn, 1977: Growth rate of an ice crystal in subcooled pure water, AIChE J., 23, 294-303.

Karev, A., 1993a: Thermodynamic and Radar Properties of Water Skins Covering Growing Hailstones, Meteorol. Gidrol., N2, 46-52.

Karev, A., 1993b:Thermodynamic and radiolocation properties of icing surfaces, Ph.D. Thesis, Sankt-Petersburg.

Karev, A., and L.G., Kachurin, 1994: Radar reflectivity of hailstones band as a function of environment's thermodynamic parameters. VI WMO Sci.Conf.Cloud Phys. Wea.Mod., 1, 177-180.

Karev, A., Lozowski, E.P., .:2000: A kinetic of advanced crystallization of shear-driven supercooled liquid skin: contribution to the icing models with runback water, To be submitted to J. Atmos. Sci.

Koo, K.-K., Ananth, R., and W.N., Gill, 1991: Tip splitting in dendritic growth of ice crystals, Phys. Rev., A., 44, 3782-3790.

Kry, P.R., and R. List, 1974: Angular motions of freely falling spheroidal hailstone models. Phys.Fluids, 17, 1093-1102.

Kurz, W., and D.J., Fisher, 1986: Fundamentals of solidification, Trans Tech Publ., 244.

Langhorne, P.J., and W.H., Robinson,1986:Alignment of crystal in sea ice due to fluid motion, Cold Reg.Sci.Tech., 12, 197-214.

Langmuir, J., and Blodgett, K.B., 1946: A mathematical investigation of water droplet trajectories.Army air forces techn. Report 5418.

Lee, Y.W., Ananth, R., and W.N., Gill, 1993: Selection of a length scale in unconstrained dendritic growth with convection in melt, J.Cryst.Growth, 132, 226-230.

Levi, L., 1970: Interpretation of the orientation of ice dendrites growing from supercooled water, J.Glaciol., 9, 55, 109-117.

Levi, L., and A.N., Aufdermaur, 1970: Crystalographic orientation and crystal size in cylindrical accretion of ice, J.Atmos.Sci., 27, 443-452.

Levi, L., Achaval, E., and A.N., Aufdermaur, 1970: Crystal orientation in a wet growth hailstone, J.Atmos.Sci.,27, 512-513.

Levi, L., and F., Prodi, 1983: Effects of Growth temperatures and surface roughness on crystal orientation of ice accreted in a dry regime, J.Atmos.Sci., 40, 1281-1299.

Levich, V.G., 1962: Physicochemical Hydrodynamics, Prentice-Hall, Inc., 700.

Levin, L.M., 1953: On deposition of particles from the flow on the obstacles, Dokl. Akad. Nauk SSSR, 91, 1329-1332.

List, R., 1965: The mechanism of hailstone formation. Int.Conf. on Cloud Phys., Tokio, Japan Metor. Agency, 481-491.

List, R., Garsia-Garsia, F., Kuhn, R., and B., Greenan, 1989: The supercooling of surface water skins of spherical and spheroidal hailstones, Atmos. Res., 24, 83-87.

Lozowski, E. P., Stallabrass, J.R., and P. F. Hearty, 1983: The Icing of an Unheated, Nonrotating Cylinder. Part I: A simulation Model, J. Climate Appl. Meteor., 22, 2053-2062.

Ludlam, F.H., 1958: The hail problem. Nibula, 1, 12-96.

Macklin W.C., 1962: The density and structure of ice formed by accretion. Quart. J. Roy. Meteor. Soc., 88, 30-50.

Macklin, W.C., 1977: The characteristics of natural hailstones and their interpretation. Hail: A Review of Hail Science and Hail Suppression. Meteor. Monogr. 16, Amer. Meteor. Soc., Boston, 65-88.

Malamatenios, Ch., Giannakoglu, K.C., and K.D., Papailiou, 1994: A coupled two-phase shear layer/liquid film calculation method.Formulation of the physical problem and solution algorithm, Int.J. Multiphase Flow, 20, 593-612.

Mason, B.J., 1971:The Physics of clouds, Clarendon Press, 672.

McPhee, M.G., 1990: Small-scale processes, in: Polar Oceanography, A. Physical Science, Ed.: Smith Jr.,W.O., Academic Press, Inc., 287-334.

Messinger, B.L., 1953:Equilibrium Temperature of an Unheated Icing Surface as a Function of Air Speed, J. Aero.Sci., 20, 29-42.

Omstedt, A., 1990: A coupled one-dimensional sea ice-ocean model applied to a semi-enclosed basin, Tellus, 42A, 368-382.

Rye, P.J., and W.C., Macklin, 1975: Crystal size in accreted ice, Quart.J.R.Met.Soc., 101, 207-215.

Schlichting, H., 1968: Boundary-Layer Theory, McGrow-Hill Book Company, 748.

Schumann, T.E.W., 1938: The theory of hailstone formation. Quart. J. Roy. Meteor. Soc. 64, 3-21.

Stewart, R.E., and R. List, 1983: Gyrational motion of disks during free fall. Phys. Fluids, 26, 920-927.

Weeks, W.F., and Gow, A.J., 1978: Preffered crystal orientations in the fast ice along the margins of the Arctic Ocean, J.Geophys.Res., 83, C10, 5105-5121.

Weeks, W.F., and Gow, A.J., 1980: Crystal alignments in the fast ice of Arctic Alaska, J.Geophys.Res., 85,C2, 1137-1146.

Yaglom, A.M., and Kader, B.A., 1974: Heat and mass transfer between a rough wall and turbulent fluid flow at high Reynolds and Peclet numbers, J.Fluid Mech., 62, 601-623.

A NUMERICAL EXPERIMENT RESEARCH ON HAIL FORECAST OVER A COMPLEX TERRAIN

Zhou Ying[1] Cheng Guangde[2] Huang Haojun[1]

[1] Weather Modification Office of Guizhou Province, Guiyang, 550002, P. R .China

[2] Meteorological Bureau of Guizhou Province, Guiyang, 550002, P. R. China

1. INSTRUCTION

Hail is a disastrous weather system that usually develop in a small spatial scale and very short period of time. The complex lower boundary conditions usually are critical for the development of such a weather. Forecast of such small scale weather system is usually very difficult. The purpose of this study is using numerical method to do some case studies in order to improve the hail weather forecast in Guizhou area, a province in southwest China which is a plateau mountain area on the southeast extension of Tibetan Plateau and where hail weather occurs very frequently in the Spring and Summer.

In the study, a three-dimensional dynamical numerical model over complex terrain is first designed to simulate initial disturbance resulting from the thermodynamic and dynamic nonuniformity of underlying surface. On the basis of the initial disturbance, a completely elastic three-dimensional hail cloud numerical model is used to forecast the hail weather

Corresponding author's address: Zhou Ying, Weather Modification Office of Guizhou Province, No.124, Cuiwei Lane, xinhua Road, Guiyang, 550002, P. R .China;

E-mail: zhouy1@21cn.com

2. STRUCTURE OF MODELS

2.1 Three-dimensional dynamical model (model Ⅰ)

2.1.1 Basic equation group

The equation group of this model is

$$\frac{du}{dt} = -\theta\frac{\partial\pi}{\partial x} + fv + g\frac{\bar{Z}-H}{H}\cdot\frac{\partial Z_g}{\partial x} + Fu \quad (2.2.1)$$

$$\frac{dv}{dt} = -\theta\frac{\partial\pi}{\partial y} - fu + g\frac{\bar{Z}-H}{H}\cdot\frac{\partial Z_g}{\partial y} + Fv \quad (2.2.2)$$

$$\frac{\partial u}{\partial x} + \frac{\partial v}{\partial y} + \frac{\partial \bar{w}}{\partial \bar{z}} - \frac{1}{H-Z_g}\left(u\frac{\partial Z_g}{\partial x} + v\frac{\partial Z_g}{\partial y}\right) = 0 \quad (2.2.3)$$

$$\frac{\partial\pi}{\partial\bar{z}} = -\frac{H-Z_g}{H}\cdot\frac{g}{\theta} \quad (2.2.4)$$

$$\frac{d\theta}{dt} = F_\Phi \quad (2.2.5)$$

here, $Z_g = Z_g$ (x, y), is topographic height.

$\pi = C_p$ (P/1000) $^{R/C_p}$, is Exner function of atmospheric pressure.

F_Φ is turbulence diffusion item, Φ represent u, v, w and θ .

2.1.2 Initial condition and boundary condition

(1) Initial condition

The wind field is directly input by the numerical integral result of basic equation (2.1.1)-(2.1.4), their initial condition is given by meteorological data.

(2) Boundary condition

The inflow boundary condition calculated by wind field is given by meteorological data.

2.1.3. numerical method

The time step and integral step are decided by the stability of calculation. Generally, in stable condition, time step is 10s, calculate 360 steps (1 hour), in neutral or unstable condition, time step is 3-5s, calculate 720-1200 steps (1 hour).

2.2 Three-dimensional hail cloud model (model Ⅱ)

The model include 18 predictands, they are velocity component u, v, and w, non-dimensional atmospheric pressure π, potential temperature θ, specific water content of vapour, cloud water, rain, ice, snow, graupel and hail Q_v, Q_c, Q_r, Q_i, Q_s, Q_g, Q_h, specific content of AgI X_S, specific density of rain, ice, snow, graupel and hail N_r, N_i, N_s, N_g, and N_h.

2.2.1 Control equation group

The control equation group of this model is

$$\frac{du}{dt}+C_p\bar{\theta}_v\frac{\partial\pi}{\partial x}=D_u \qquad (2.2.1)$$

$$\frac{dv}{dt}+C_p\bar{\theta}_v\frac{\partial\pi}{\partial y}=D_v \qquad (2.2.2)$$

$$\frac{dw}{dt}+C_p\bar{\theta}_v\frac{\partial\pi}{\partial z}=g\left(\frac{\theta'}{\bar{\theta}}+0.608Q_v-Q_t\right)+D_w \qquad (2.2.3)$$

$$\frac{d\pi'}{dt}+\frac{\bar{C}^2}{C_p\bar{\rho}\bar{\theta}_v^2}\frac{\partial\bar{\rho}\bar{\theta}_v u_j}{\partial x_j}=-\frac{R_d}{C_v}\pi'\frac{\partial u_j}{\partial x_j}+\frac{C^2}{C_p\theta_v^2}\frac{d\theta_v}{dt}+D_{\pi'} \qquad (2.2.4)$$

$$\frac{dQ_x}{dt}=S_{Qx}+D_{Qx}+\frac{1}{\bar{\rho}}\frac{\partial}{\partial z}\left(\bar{\rho}Q_xV_x\right) \qquad (2.2.5)$$

$$\frac{dN_x}{dt}=S_{Nx}+D_{Nx}+\frac{1}{\bar{\rho}}\frac{\partial}{\partial z}\left(\bar{\rho}N_xV_x\right) \qquad (2.2.6)$$

$$\frac{dX_s}{dt}=S_{Xs}+I_{Xs}+D_{Xs} \qquad (2.2.7)$$

$$\frac{d\theta}{dt}=Q_{lv}+Q_{il}+Q_{iv}+D_\theta \qquad (2.2.8)$$

2.2.2 Initial condition and boundary condition

(1) Boundary condition

The lateral, up and down boundary condition are considered in the model.

(2) Initial condition

Initial environment field $\bar{u}$, $\bar{v}$, $\bar{\theta}$, $\bar{\pi}$, $\bar{Q}_V$ can be determined by sounding data . The initial disturbance field of potential temperature is related to convection start mode.

2.2.3 Numerical evaluation technique

In the model, the numerical evaluation technique of the standard spatial staggered mesh system and the time step separation is adopted, the technique of smooth operation, absorbing layer on top boundary and parallel moving of simulation field is applied.

3. NUMERICAL EXPERIMENT

3.1 Field experiment

From April 5 to July 30,1999, these two numerical models were used to forecast the hail weather in the numerical region. The sounding data on 08^h is used to simulate the initial disturbance resulting from the thermodynamic and dynamic nonuniformity of underlying surface by model I every day. If the initial disturbance exists, model II starts to simulate the development of cloud and forecast hail weather. Table 1 is the comparative analysis of hail shooting days.

Table 1 The comparative analysis of hail shooting days

item	result
initial disturbance days	11
forecast hail days	10
actual hail shooting days	8
accuracy	75%

It can be seen from table 1 that the prediction accuracy of hail is high. The models can not only forecast hail but also determine total hail shooting amount, direction of hail shooting and maximum hail diameter. In this paper, the production process of hail cloud on April 9 and June 4, 1999 are analyzed in detail.

3.2 Model verification

For verifying the numerical method, meteorological data in 1997 and 1998 were used to calculate the rate of failure to forecast. Several forecast methods such as the numerical model, Emagram and scatter diagram are compared in the end. It can be proved that the numerical forecast method is the best way.

4. CONCLUSION

4.1 By simulating initial disturbance according to topographic condition and development of hail cloud according to microstructure of cloud, the total hail shooting amount, direction of hail shooting and maximum hail diameter over a hill can be forecasted.

4.2 Compared with the methods of Emagram and scatter diagram, the accuracy of numerical model is high.

RERERENCES

Farley, R. D and H. D. Orville, 1986: Numerical modeling of hailstorms and hailstone growth. Part I: Preliminary model verification and sensitivity tests. *J. Clima. Appl. Meteor.*, 25, 2014-2036.

Farley, R. D, 1987: Numerical modeling of hailstorms and hailstone growth. Part II: The role of low-density riming growth in hail production. *J. Clima. Appl. Meteor.*, 26,234-254.

Farley, R. D, 1987: Numerical modeling of hailstorms and hailstone growth. Part III: Simulation of an Alberta hailstorm-Natural and seeded cases. *J. Clima. Appl. Meteor.*, 26,789-912.

Farley, R. D., P. Nguyen and H. D. Orville., 1994: Numerical simulation of cloud seeding using a three-dimensional cloud model. *J. Wea. Mon.*, 26, 113-124.

Kong Fanyou, Huang Meiyuan，Xu Huaying，1990: Three-dimensional numerical simulation of ice phrase microphysics in cumulus cloud （I）: model build and cold cloud parameterization. Chinese Journal of Atmospheric Sciences. 14（4）: 441-453.

Hong Yanchao，1998: A 3-D hail cloud numerical seeding model. Acta. Meteorologica. Sinca.，56(6): 641-651.

MODELLING OF SEVERE PRECIPITATION EVENTS IN NORTH-EASTERN ITALY

Wolfram Wobrock[1], Andrea Flossmann[1], Jutta Thielen[1] and R. Farley[2]

[1]Laboratoire de Météorologie Physique, Université Blaise Pascal/CNRS/OPGC
Clermont-Ferrand (France)
[2]Institute of Atmospheric Sciences, South Dakota School of Mines and Technology
Rapid City, South Dakota (USA)

1. INTRODUCTION

The North of Italy, and in particular the region of Friuli, is known for its devastating and repeated hail falls causing much damage to the agricultural community (Morgan, 1973).

Thus, at the research centre of *Cervignano del Friuli* in North Italy much research on hail falls has been conducted over the past decades. A hail pad network has been implemented and a precipitation radar is operational to study the severe storms.

The present work is aimed at investigating the performance of current state of the art mesoscale models to simulate severe hail storms. As the dynamic framework the three-dimensional, non-hydrostatic cloud physics model of Clark and co-workers has been used. The model in its usual form contains a Kessler type bulk water warm rain microphysics and a Koenig/ Murray ice parameterization. We have used this basic version of the model. In addition, we have replaced the microphysical code with the spectral hail module developed by Farley and Orville (1986). The spectral module discretises the precipitating ice phase into 21 different ice categories ranging from 100 μm to nearly 7 cm in diameter.

Both model configurations have been applied to the meteorological situation observed on 10 Sept 1993 in Friuli. The severe hailfall for this case was documented by the hail pad network.

Below, the two microphysical approaches used will be detailed as well as some results of their application to the 10 Sept 1993 case which were compared to the observations of the hail pad network.

2. MODEL DESCRIPTION:

2.1 The 3-D dynamic framework

Corresponding author's address: Andrea Flossmann, LaMP; Univ. Blaise Pascal/CNRS/OPGC ; 24, avenue des Landais ; F-63177 Aubière Cedex ; France; E-Mail: A.Flossmann@opgc.univ-bpclermont.fr.

The dynamic framework employed in the present study is the three-dimensional model developed by Clark and co-workers (e.g. Clark, 1977, 1979; Clark and Farley, 1984; Clark and Hall, 1991).

The model is a set of finite-difference approximations to the anelastic, nonhydrostatic fluid dynamics equations with expansion of system variables around profiles of an idealized atmosphere with constant stability. A terrain-following vertical coordinate transformation allows for treatment of realistic, complex topography. Subgrid-scale processes are parameterized using a first-order closure scheme. The finite-difference formulation of the model employs a second-order algorithm for momentum components combined with a second-order accurate positive definite advection transport algorithm for thermodynamic and moisture variables. The resulting algorithm for the evaluation of the entire system of model equations is second-order accurate in time and space.

2.2 The K-M microphysics

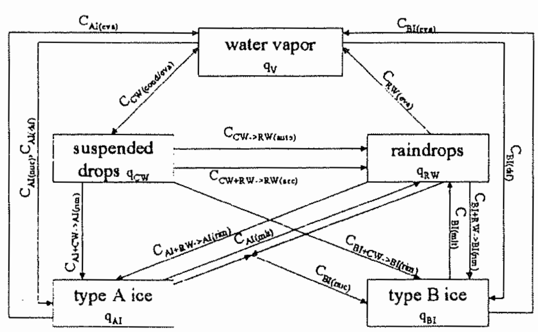

Fig.1: Scheme of the K-M parameterization

The original microphysics in the Clark model uses bulk parameterizations for both the water and the ice phase. The water phase is parameterized according to a modified form of the Kessler (1969) scheme. In this scheme, condensed water exists as cloud- and rainwater. The ice phase parameterization closely follows the work of Koenig and Murray (1976). This parameterization allows two types of ice particles, ice crystals initially formed by heterogeneous ice nucleation or ice splintering processes due to riming (type A) and ice particles (graupel) initially formed by freezing of raindrops (type B). Consequently, five categories of water substance have to be taken into account in the equations for the conservation of heat, water and ice substance. The categories are V: water vapor, CW: suspended drops, RW: raindrops, AI: type A ice, BI: type B ice. The interaction between the different categories is schematically displayed in Fig.1.

When detainling the rates the "C" refers to mass conversion and the "P" to number conversion rates.

The condensation/evaporation rate of cloud liquid water ($C_{CW(con/eva)}$) is determined by a saturation adjustment. The cloud water is converted to rain water using Berry's autoconversion formulation (1967) with N=300 cm^{-3} and D_d=0.26. The rainwater accretion $C_{CW+RW\to RW(acc)}$ and the evaporation rate of raindrops in subsaturated regions $C_{RW(eva)}$ are given in Clark (1979).

The terms concerning the Koenig-Murray scheme are described in detail in Koenig and Murray (1976) and Bruintjes et al (1994). Each ice particle category A or B is represented by two variables, namely, the mixing ratio and the number density which are related by defining an average particle mass by the following expression

$$N_{AI/BI}m_{AI/BI} = q_{AI/BI}\overline{\rho}$$

Type A ice is nucleated by heterogeneous ice nucleation process.This can occur whenever the air is saturated with respect to liquid and the temperature is below 0°C or whenever the air is supersaturated with respect to ice and the temperature is below –12°C. This process increases the number of type A particles, and assuming that each of the newly generated particles has a mass of 10^{-14}kg also the mixing ratio ($C_{AI(nuc)}$).

The formation of type B ice occurs when raindrops freeze due to a collision between a type A ice crystal and a raindrop at temperatures below 0°C. This results in the loss of one type A particle and one raindrop for each type B ice particle that is formed. The average mass of the type B particle equals the sum of the masses of the two colliding particles ($C_{BI(nuc)}$).

The diffusional and riming growth of the ice particle is treated in four different growth regimes following the simplifications of Bruintjes et al (1994).For growth regime 3 and 4 it is assumed that riming first depletes the raindrops (RW), and only after q_{RW}=0 the suspended drops are consumed.

Ice particles will melt as soon as they fall or are advected into a region where the ambient temperature is warmer than 0°C ($C_{AI/BI(mlt)}$). If the average mass of the particle is less than 10-8g, melting occurs instantaneously. When the mass exceeds this threshold, the change in mass due to melting is calculated after Bruintjes et al (1994). During melting it is assumed that the size of the average ice particle does not change but that the number concentration of ice particles decreases. It is also assumed that all melted ice is converted to rainwater.In addition, to determine the magnitude of heat transfer only the latent heat of melting is considered, while the heat capacity of the hydrometeors is neglected. Equally, type A and B ice particles evaporate in sub-saturated air ($C_{AI/BI(eva)}$).

2.3 The F-O microphysics

In order to be able to calculate more explicitly the evolution of hail in the cloud we have also used the explicit hail category model detailed in Farley and Orville (1986) and Farley (1987). This model employs a bulk microphysical formulation for the liquid phase q_{CW} and q_{RW} and the non precipitating ice particles q_{CI} as detailed in Lin et al (1983).

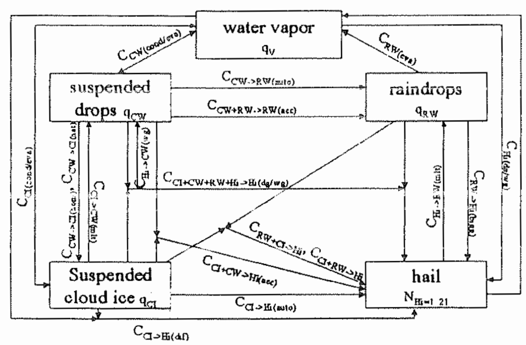

Fig.2: Scheme of the F-O parameterization

In the original paper of Lin et al (1983) the precipitating ice phase is treated in a bulk form. This part is replaced by a spectral representation consisting of 21 logarithmically spaced categories ranging in diameter from 100 μm to 6.95 cm. We refer to all these precipitating ice particles as "hail" although, technically, only category 14 and larger qualify as such. The six size categories cover a range of particle density from a mean of 0.35 g cm^{-3} in the first category to 0.85 g cm^{-3} in the sixth category. Larger particles have a constant density of 0.9 g cm^{-3}.The interaction between the different categories is schematically displayed in Fig.2.

This microphysics code has been implemented into the Clark et al model in place of the original K-M microphysics.

$$
\begin{aligned}
\overline{\rho}\frac{N_{Hi}}{dt} = {} & \vec{\nabla}\bullet\left(\overline{\rho}K_H N_{Hi}\right) - \frac{\partial}{\partial z}\left(\overline{\rho}\overline{V}_{THi}N_{Hi}\right) \qquad i = 1 \ldots 21 \\
& +\overline{\rho}\left(P_{RW\to Hi(bigg)} + P_{RW+CI\to Hi} + P_{CI+RW\to Hi}\right) \\
& +\overline{\rho}\left(P_{CI\to Hi(auto)} + P_{CI+CW\to Hi(acc)} + P_{CI\to Hi(dif)}\right) \\
& +\rho P_{CI+CW+RW+v+Hi\to Hi(dg/wg)} \\
& -\rho P_{Hi(eva)} - \rho P_{Hi\to RW(mlt)}
\end{aligned}
$$

The condensation/evaporation rate of cloud liquid water ($C_{CW(con/eva)}$) is determined by a saturation adjustment following Orville and Kopp (1977). The cloud water is converted to rain water using Berry's autoconversion formulation (1967)($C_{CW\to RW(auto)}$). The rainwater accretion $C_{CW+RW\to RW(acc)}$ and the evaporation rate of raindrops in subsaturated regions $C_{RW(eva)}$ are given in Lin et al (1983). If the temperature is colder than –40°C, homogeneous nucleation ($C_{CW\to CI(hom)}$) will occur. Between 0 and –40°C, cloud water and cloud ice can co-exist. The transformation between the two reservoirs is based on a Bergeron process ($C_{CW\to CI(het)}$). If the temperature is warmer than 0°C, the cloud ice is assumed to instantaneously melt back to cloud water ($C_{CI\to CW(mlt)}$). The cloud water will condense or evaporte ($C_{CI(cond/eva)}$). The treatment of the terms is detailed in Lin et al (1983).

The precipitating ice particles are created via different mechanisms. The first one is the freezing of rain drops. These frozen drop embryos are created via the probabilistic freezing of rain according to Bigg ($P_{RW\to Hi(bigg)}$), and/or the contact freezing of rain due to collision of raindrops with cloud ice crystals ($P_{CI+RW\to Hi}$). The cloud ice involved in this interaction process makes only a very small mass contribution to the precipitating ice field ($P_{RW+CI\to Hi}$) The distribution of the formed precipitating ice particles to the categories is accomplished by applying a relative weight per category determined from a differential form of the Bigg freezing equation as detailed in Farley and Orville(1986).

The second mechanism generates small graupel sized ice particles from cloud water and cloud ice. Cloud ice can aggregate ($C_{CI\to Hi(auto)}$), can grow by vapor diffusion ($C_{CI\to Hi(dif)}$) or collide with cloud water ($C_{CI+CW\to Hi(acc)}$) to form graupel particles. These are distributed among the first six hail categories using a modified Marshall-Palmer distribution (Farley and Orville, 1986).

These processes add number and mass to the individual hail categories, but, do not, however, include a transport from one hail category to another. This transport is calculated through the hailstone growth equations.

Growth of the ice particles is based on the wet and dry growth concepts applied to the continuous accretion process. Determination of the proper growth mode is based on the calculation of the equilibrium temperature of the hailstone (ice particle) surface. This equilibrium surface temperature is solved iteratively under the assumption that no heat is stored in the particle and, thus, all heat added from all sources must balance.

As long as the surface temperature is below 0°C the ice particle is in the dry growth regime. It grows by accretion of cloud water ($C_{CW\to Hi(dg)}$), cloud ice ($C_{CI\to Hi(dg)}$) and water vapor diffusion ($C_{Hi(dg)}$). If the surface temperature exceeds 0°C the ice particle is in the wet growth regime ($C_{CW\to Hi(wg)}$, $C_{CI\to Hi(wg)}$, $C_{Hi(wg)}$). and the excess of water which cannot be frozen is usually shed as cloud water ($C_{Hi\to CW(wg)}$). Dry and wet growth regimes yield an individual mass growth rate *dm*$_{Hi}$*/dt*. The individual growth rates are then used to calculate changes in the number concentration of the ice particles through:

$$
\frac{dN_{Hi}}{dt} = -\frac{\partial}{\partial m}\left(N_{Hi}\frac{dm_{Hi}}{dt}\right)
$$

Thus, the categories can grow one into another, but, do not interact, as, e.g., in a stochastic coalescence process. The hail particles will evaporate in subsaturated air ($P_{Hi(eva)}$) and melt at temperatures warmer than 0°C ($P_{Hi\to RW(mlt)}$) according to the rates specified in Farley and Orville (1986).

3. RESULTS

The model has been applied to the situation of the 10 Sept. 1993 and the terrain of the area of Friuli. The domain covers 110*110 km^2 with a grid resolution of 900m. In the vertical a telescopic grid has been used with a resolution of 50m close to the surface and 300m in higher levels. The model was initialized with the sounding observed at 12:00 UTC at Udine and was driven by an imposed diurnal evolution of the surface heat and moisture flux, distinguishing 3 different types of terrain (sea, valley, mountain) via the Bowen ratio.

The results obtained with the K-M parameterization ware compared with the results from the F-O parameterization.

In general the simulations show a closer agreement of the detailed hail parameterization and the observations. The hail cells develop earlier and are more vigorous. Furthermore, with the K-M parameterization the hail cells develop mainly over the mountainous area to the north while the F-O parameterization allows the formation of intense hail cells also in the plains. There, the main damage to the agricultural community has been observed. However, the presence of hail cells over the mountains during that day cannot be excluded due to the fact that no observations were made in this region.

Fig. 3 and 4 illustrate the distribution of the solid hydrometeors after 180 min of model time. In general, the number distribution of the hail pad counts modelled with the F-O parameterization agrees quite well with the observations of the hail pad network (Fig.5).

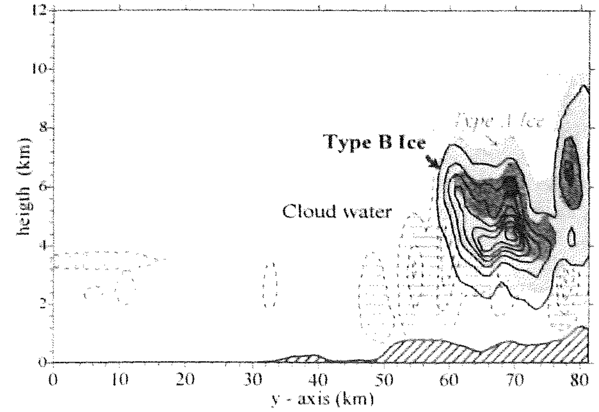

Fig.3: 2-D cross section through one modelled cloud band using the K-M parameterization

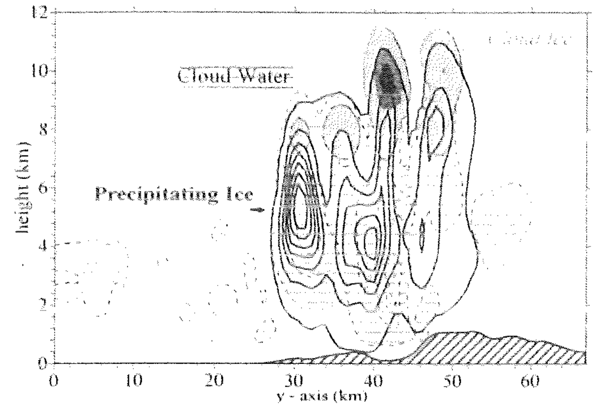

Fig.4: 2-D cross section through one modelled cloud band using the F-O parameterization

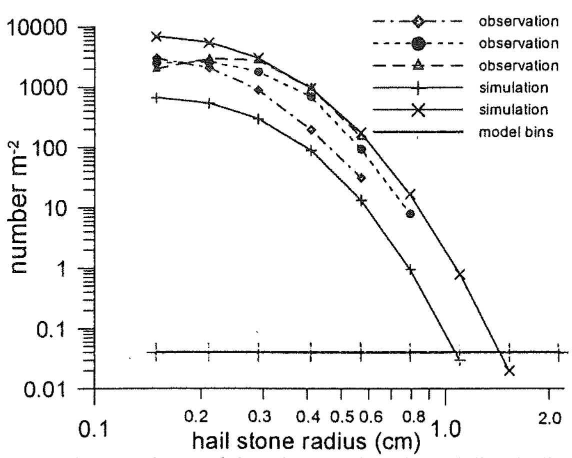

Fig.5: Comparison of the observed and modelled hail pad counts

4. ACKNOWLEDGEMENTS

The authors acknowledge with gratitude the financial support provided by the Centro Servizi Agrometeorologici per il Friuli-Venezia Guilia (C.S.A.) in Cervignano del Friuli (Italy) under the responsibility of G.M. Morgan Jr. The calculations have been done on the CRAY C98 and C94 of IDRIS (CNRS) under project no. 940180.

5. REFERENCES

Berry, E.X., 1967: Cloud droplet growth by collection. *J. Atmos. Sci*, **24**, 688-694.

Bruintjes, R.T., T. L. Clark and W.D. Hall, 1994: Interactions between topographic airflow and cloud/precipitation development during the passage of a winter storm in Arizona. *J. Atmos. Sci.*, **51**, 48-67.

Clark, T.L., 1977: A small scale dynamic model using a terrain-following coordinate transformation. *J. Comput. Phys.*, **24**, 186-215.

Clark, T.L., 1979: Numerical simulations with a three dimensional cloud model: Lateral boundary condition experiments and multi-cellular severe storm simulations. *J. Atmos. Sci.*, **36**, 2191-2215.

Clark, T.L and R.D. Farley, 1984: Severe downslope windstorm calculations in two and three spatial dimensions using anelastic interactive grid nesting: A possible mechanism for gustiness. *J. Atmos. Sci.*, **41**, 329-350.

Clark, T.L., and W.D. Hall, 1991: Multi-domain simulations of the time dependent Navier-Stokes equations: Benchmark error analysis of some nesting procedures. *J. Comput. Phys.*, **92**, 456-481.

Farley, R.D., 1987: Numerical modeling of hailstorms and hailstone growth. Part III: Simulation of an Alberta hailstorm-natural and seeded case. *J. Climate Appl. Met.*, **26**, 789-812.

Farley, R.D., and H.D. Orville, 1986: Numerical modeling of hailstorms and hailstone growth. Part I: Preliminary model verification and sensitivity tests. *J. Climate Appl. Met.*, **25**, 2014-2035.

Lin, Y-L., R.D. Farley, and H.D. Orville, 1983: Bulk parameterization of the snow field in a cloud model. *J. Climate Appl. Met.*, **22**, 1065-1092.

Kessler, E., 1969: On the distribution and continuity of water substances in atmospheric circulations. *Meteor.Monogr.*, **10**, 32.84pp

Koenig, L.R. and F.W. Murray, 1976: Ice-bearing cumulus cloud evolution: Numerical simulation and general comparison against observations. *J. Appl. Met.* **15**, 747-762.

Morgan G.M. Jr., 1973. A general description of the hail problem in the Po Valley of northern Italy., *J. Appl. Met.*, **12**, No.2, 338-353

STUDY OF HAIL DENSITY PARAMETERIZATIONS

N.E. Castellano[1], O. B. Nasello[1] and L. Levi[2]

[1]Facultad de Matemática, Astronomía y Física, Universidad Nacional de Córdoba, Argentina
[2]Consejo Nacional de Investigaciones Científicas y Tecnológicas , Argentina

1. INTRODUCTION

The literature shows that different parameterizations have been used to represent the density of accreted ice as a function of environmental conditions, in models where the evolution is simulated of hail in convective clouds or of ice deposits grown on structures in cold regions. In most cases the density ρ has been represented as a function of the Macklin's parameter $X = rV/T_s$, where r is the median volume droplet radius, V the droplet impact speed, calculated either on the stagnation point or as an average on the collector surface, and T_s the surface temperature. When $\rho < 0.9$ g/cm^3, an expression has been used of the type $\rho(X) = \boldsymbol{a}(X)^{\boldsymbol{b}}$; however, there is not a general coincidence as for the values assigned to the constant parameters ***a*** and ***b***. Actually, these have been empirically evaluated in laboratory experiments (Macklin, 1962; Pflaum and Pruppacher, 1979; Prodi et al., 1986), where significantly different $\rho(X)$ curves have been obtained. As a consequence, calculations of the accreted ice density in simulated conditions have not been always performed using the same expressions. For instance, many authors using the Macklin's parameterization (Nelson, 1983; etc.) have performed simulations of hailstone trajectories. However, other ones have applied that proposed by Pflaum and Pruppacher (among them, Heymsfield, 1983; etc.) or that proposed by Levi and Lubart (1991) (Masuelli et al, 1998; etc.). Also, in convective cloud models including hail growth microphysics, Farley (1987) applied the Macklin's parameterization while Straka (1989) that of Pflaum and Pruppacher. Similarly, variations of the used $\rho(X)$ expression can be found in models where the growth of accreted ice on electric cables or airplane wings is simulated.

Levi et al. (1999) showed how the application of different $\rho(X)$ expressions could largely affect the internal structure, size and free fall speed of simulated hailstones. Thus, it is necessary to analyze the usual parameterizations in order to unify criteria for a convenient use in simulation models of the different empiric $\rho(X)$ parameterizations.

In the present work a study will be performed of the causes that have determined the different empirical representations proposed for $\rho(X)$. In the discussion, also the different methods used to measure the density will be considered and the effects of the collector shape on the observed behavior will be analyzed.

Corresponding author's address: Nesvit Castellano, Fa.M.A.F.- Universidad Nacional de Córdoba, Ciudad Universitaria, CP 5000, Córdoba, Argentina.; E-Mail: nesvit@roble.fis.uncor.edu

2. PRESENTATION AND DISCUSSION OF $\rho(X)$ PARAMETERIZATIONS

2.1 Summary of existing parameterizations

The main conditions used in wind tunnel experiments performed to provide accreted ice density parameterizations are summarized in Table 1. In the first column the author's names are synthetically represented (Macklin, 1962, (M); Heymsfield and Pflaum, 1985, (HP); Prodi and Levi, 1987, (PL); Prodi et al., 1991, (PLNL)). In subsequent three columns we indicate: the collector geometry (cylinder or sphere) and the variation range of the Stokes number (K) and of the Reynolds number R_e. In column 5, the words "mean" or "local" represent the type of the used density measurement method. In the first case the density was measured as an average, which necessarily included possible voids formed by surface roughness. In the second, X-ray transparence measurements were performed in selected regions inside the initial, more uniform accreted layer or inside lobes, frequently occurring at larger deposit thickness. In the last column the adjusting parameter has been indicated as X when, following Macklin (1962), the droplet impact speed was calculated on the stagnation point ($X=rV_o/T_s$), as X^* when the average impact speed normal to the collector surface was used. ($X^*=rV_{imp}/T_s$).

Notice that the latter parameter was introduced by Pflaum and Pruppacher (1979) (PP), who studied rime formed on spherical frozen drops, and was subsequently corrected by Heymsfield and Pflaum (1985) (HP) who modified the expression of V_{imp}.

Author	Geometry	K	Re	Density	Adjust param.
M	Cylinder	0-17	200-15,000	Mean	X
HP	Sphere	3-10	24 - 200	Mean	X^*
PL	Cylinder	>4	1,800-20,000	Local	X
PLNL	Cylinder	0-3	1800-7500	Local	X

Table 1: Summary of main characteristic of experiments related to density of accreted ice.

In Table 2 the $\rho(X)$ or $\rho(X^*)$ equations proposed by different authors are presented. It can be seen that the values of the constants ***a*** and ***b*** vary significantly from one to other series of experiments, but that the largest shift from the original Macklin's curve is represented by the $\rho(X^*)$ curve. It must be noted, however, that $\rho(X^*)$ can not be actually compared with the other curves because of the different definition of the parameters X and X^* and because of the different shape of the collectors. Consequently, in order to overcome this difficulty, in the present work, a study has been performed of the relation existing between X and X^*, as a consequence of their dependence on V_o and V_{imp} respectively. In the discussion, also the effect of changing the collector shape from a sphere to a cylinder has been considered.

Taking into account the results of this analysis a new representation has been performed of the different experimental points in a ρ-X plane.

Autor	ρ [g/cm^3]	
M	$0.11\ (X)^{0.76}$	$X \leq 17$
	0.917	$X > 17$
HP	$0.30\ (X^*)^{0.44}$	$0.3 < X^* < 1.5$
PL	$0.28\ (X)^{0.6}$	$3 < X \leq 7$
	0.917	$X > 7$
PLNL	$0.2\ (X)^{0.5}$	$0.5 < X < 7$

Table 2: Parameterizations obtained from experiments belong to different author.

2.2 Relationship between V_{imp} and V_o on a sphere

In order to compare X^* and X for a sphere, expressions for V_{imp}/V_∞ have been derived from the equation proposed by Rasmussen and Heymsfield (1985), for Re=300, while V_o/V_∞ has been calculated using the results of Langmuir and Blodgett (1946).

The relationship V_{imp}/V_o has been represented in Fig. 1 as a function of the Stokes number, K. It can be seen that, for $K<1$, V_{imp}/V_o increases with K, but that, above this limit it approaches a limit value $V_{imp}/V_o = 0.63$, which can be considered attained at about K=2. Thus, since the PP experiments were carried out for $K>3$, it can be written

$$X = (V_o/V_{imp})X^* = (1/0.63)X^* = 1.59\ X^* \qquad (1)$$

This means that, when $\rho(X^*)$ is given, the derived curve for $\rho(X)$ can be obtained by shifting the variable on the horizontal axis by more than 50% of its initial value.

2.3 Geometry of the collector

The V_{imp}/V_o ratio has been calculated above for the sphere. However, Table 1 shows that most studies on accreted ice density were performed using cylinders as collectors, the only exception being represented by the PP experiments. It is consequently also necessary to determine the relationship between the values of X on the cylinder (X_{cyl}) and on the sphere (X_{sph}). With this purpose, calculations of these parameters have been performed, for given values of the air temperature T_a, liquid water contents L_{wc} and the median volume droplet radius r. The calculations have been made by adjusting flow velocity and collector radius so to obtain the same values for the numbers R_e and K on both the cylinder and the sphere. From these data, the mean surface temperature T_s and impact speed V_o were derived and used to obtain the value of X. The simulations were carried out for R_e varying from 50 to 10,000 and $0<K\leq100$. The assumed air temperatures were -5, -10, -20°C and the liquid water contents 0.5, 1.0, 2.0 g/m^3.

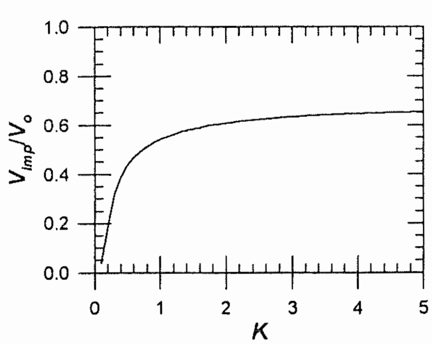

Figure 1: Relationship between the average radial impact speed on a spherical surface, V_{imp}, and the impact speed on the stagnation point of the same surface, V_o, as a function of K.

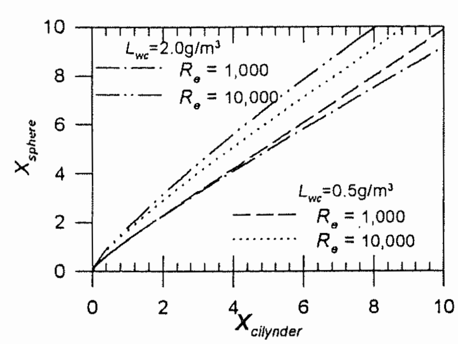

Figure 2: Examples of curves for X_{sph} as a function of X_{cyl}, for the same values of R_e, K and T_a (= -10°C).

An example of the results obtained is given in Fig. 2, where curves have been drawn of X_{sph} as a function of X_{cyl}, for T_a=-10°C, R_e = 1,000 and 10,000 and, for each R_e, two values of L_{wc} of 0.5 and 2 g/m^3. It can be seen that the studied effect increases with R_e. The curves for R_e=1,000 run rather near the diagonal of the coordinate plane, thus indicating that the correction required when the $\rho(X)$ curves obtained for the cylinder are applied to the sphere (or reciprocally) is small and it would become rapidly negligible when R_e decreases below this value.

The slope of the curves for R_e = 10,000 is larger and indicates that X_{sph} increases more rapidly than X_{cyl}, showing that the change of the collector geometry should be taken into account for large R_e values. This observation could be important, for instance, when the Macklin' s results obtained on the cylinder are applied to approximately spherical atmospheric ice particles of rather large size and free fall speed. In the present case the correction from X_{sph} to X_{cyl} has been calculated for the results of HP, to make it possible to represent them with a $\rho(X)$ curve comparable with those obtained by the other authors on cylindrical collectors. Using average values of T_a and L_{wc} and values of R_e in the experimental range (50<R_e<200), it was found

$$X_{cyl} = 0.96\, X_{sph}^{1.06}$$

Taking into account the discussion in 2.2 and 2.3, it can be shown that, instead of the $\rho(X^*)$ equation given in table 2, the HP results can be represented by

$$\rho(X) = 0.26X^{0.42} \tag{2}$$

Despite the relatively small variation of the coefficients ***a*** and ***b***, this fact shows that a non negligible error would be performed, if the results of these authors were represented by the given $\rho(X^*)$ equation but using X_{cyl} as a parameter. It can be seen for instance that, when the parameter X_{cyl} is used in Eq.(2) the formation of solid ice with ρ=0.91g/m^3 is reached at X_{cyl}=20, while, if the original $\rho(X^*)$ equation were used, the same density would be attained for X_{cyl}=13, where Eq.(2) gives ρ=0.77g/m^3. Thus, the change of the parameterization could have not negligible effects on the results of hail growth simulation.

3. ANALYSIS OF THE RESULTS AND CONCLUSIONS

In Fig. 3 all experimental data of Macklin (1962), Heymsfield and Pflaum (1985), Prodi and Levi (1987) and Prodi et al. (1991) are represented as a function of the only variable X, defined as the Macklin's parameter for cylinders. The experimental points were obtained as a digital reproduction of the experimental data presented by the authors in their original papers. Although digitalization could have carried out some difference between reproduced and exact experimental points, it is worth noting that, when those derived from the works of HP, PL and PLNL are used, the same values of the adjusting parameters proposed by the authors are obtained.

From the analysis of the experimental data, it can be concluded that:

- There is a large scattering of the results represented in the ρ-X plane, suggesting that some other parameter in addition to X should be considered to establish the relation between the ice density and the environmental conditions.

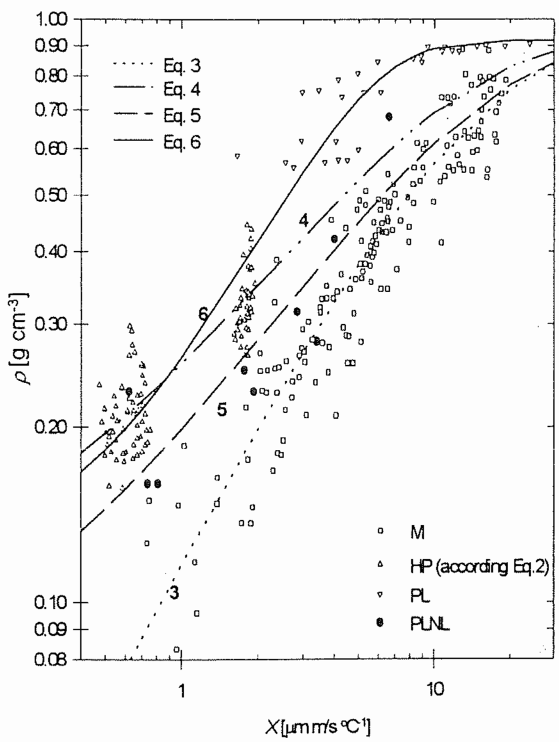

Figure 3. Experimental data for ρ as a function of X_{cyl}, according different authors and curves for ρ(X) derived from Eq. (3), (4), (5) and (6).

- Among the experimental points obtained by different authors, those given by HP and PL are located above the average. Although this behavior could be assigned, in the case of PL results, to the fact that the internal instead of the average density was measured, the same explanation can not be given for the HP results. On the other hand, it must be noted that the deposits grown by PL did not present pronounced lobes, so that, according to the authors, the average density could not have been more than 20% below the internal one. It can be worth noting that both series of experiments were performed with K>3.

- The results obtained by Macklin for the mean density represent a low limit of the scattered points. An accurate analysis of the total range of experimental conditions used by this author indicates that the possible range of K variations was: $K<2$ for $X<2$; $K<4$ for $2<X<5$; $K<17$ for $X>5$.
- The experimental points given by PLNL were distributed along a curve that could represent the superior limit of the Macklin's results. They were obtained by local density measurements, with $K<3$. The authors also show that, as pronounced lobes could be observed on most deposits, experimental points representing mean density would have been approximately located along the Macklin's curve.

The comparison of all these results shows that, for a given X, ρ decreases with K, as already noted by PLNL and by Jones (1990). Taking these considerations into account, the different groups of experimental points in Fig. 3 have been represented by different adjusting curves where the range of variation of K and the measurement method (mean or local) are taken into account. The following $\rho(X)$ expressions are proposed:

For the mean density:

$$K<4 \quad \rho = 0.917(1\text{-Exp}[-(0.096\, X)^{0.85}] \qquad (3)$$

$$K>4 \quad \rho = 0.917\text{-}0.813 \text{ Exp}[-(0.138X)^{0.78}] \qquad (4)$$

For the internal density

$$K<4 \quad \rho = 0.917\text{-}0.800 \text{ Exp}[-(0.270X)^{1.23}] \qquad (5)$$

$$K>4 \quad \rho = 0.917\text{-}0.854 \text{ Exp}[-(0.104)^{0.78}] \qquad (6)$$

The above parameterizations are thought to be useful to reduce the time needed for calculations in cloud simulation programs. The corresponding curves are represented in Fig.3. Among them, curve (3) adjusts the experimental points of Macklin and differs from Macklin's curve by less of 5% for $X<8$. For larger values of X it approaches the bulk ice density $\rho = 0.917$ g/cm^3 gradually, thus representing the experimental results better than the original curve, which was extrapolated up to attain, at X=17, this value of ρ and was kept constant for $X>17$. Curve (4) represents the behavior derived from Eq.(2) for $0.5<X<10$,with an error <2%. Similarly, curves (5) and (6) represent, with about the same error, the behavior resulting from the equations proposed by PLNL and by PL respectively.

4. REFERENCES

- Farley R. D., 1987: "Numerical modeling of hailstorms and hailstone growth. Part II: The role of low-density riming growth in hail production". J. Climate Appl. Meteor., 26, 234-254.
- Heymsfield A. J., 1983: "Case study of a hailstorm in Colorado. Part IV: Graupel and hail growth mechanisms deduced trough particle trajectory calculations". J. Atmos. Sci., 40, 1482-1509
- Heymsfield A. J. and Pflaum J. C., 1985: "A Quantitative of the accurancy of technique for calculating graupel growth". J. Atmos. Sci., 42, 2264
- Jones K. F., 1990: "The density of natural ice accretions related to nondimensional icing parameters". Q. J. R. Meteorol. Soc., 116, 477-496
- Langmuir I. and Blodgett K.B., 1946: "Mathematical investigation of water droplet trajectories". Tech. Report N° RL-224, U. S. Air Force, Wash. D.C.
- Levi L. and Lubart L., 1991: "Analysis of hailstones from a severe storm and their simulated Evolution". Atmos. Res., 26, 191-211
- L. Levi, N.E. Castellano, O.B. Nasello y F. Prodi, 1999: "Requirements for low density riming and two stage growth on atmospheric particles". Atmospheric Research, Vol 50, pp 21-35
- Macklin W.C., 1962: "The density and structure of ice formed by accretion". Quart. J. Roy. Meteor. Soc., 88, 30-50.
- Masuelli S., M. Pulido, M. Scavuzzo, and G. Caranti, 1998: Graupel trajectories and charging: a new numerical approach for cloud electrification studies. Q. J. R. Meteor. Soc., 124, 1329-1341.
- Nasello O.B. and Castellano N.E., 1998: "On the search for representative drag coefficient law to be used in hail trajectory simulations". Atmospheric Research, Vol 47-48, pp 87-96.
- Nelson S. P., 1983: "The influence of storm flow structure on hail growth". J. Atmos. Sci., 40, 1965-1983
- Pflaum J. C. and Pruppacher H. R. 1979: "A wind tunnel investigation of the growth of graupel initiated from frozen drops". J. Atmos. Sci., 34, 680-689.
- Prodi F., Levi L. and Pederozli P., 1986,b: "The density of accretedice". Q.J.R. Meteorol. Soc., 112, 1081-1090.
- Prodi F. and Levi L., 1987: "Density and surface structure of ice accretions". J. de Physique, 48, C1, 383-388.
- Prodi F., Levi L., Nasello O. B. and Lubart L., 1991: "Morphology and density of ice accreted on cylindrical collectors at low values of impactation parameter Part II: Rotating deposits". Q. J. R. Meteorol. Soc., 117, 783-801.
- Rasmussen R. M. and Heymsfield A. J., 1985: "A generalized form for impact velocities used to determine graupel accretional densities". J. Atmos. Sci., 42, 2275-2279.
- Straka, J.M., 1989: "Hail growth in a highlyglaciated central High Plains multicellular hailstorm". Ph. D. Diss., Dep. Meteorology, University of Winsconsin, Madison, 413pp.

5. ACKNOWLEDGEMENTS

This work was partially supported by CONICOR, CONICET and SeCyT-UNC, Argentina. We are grateful to Jose Barcelona for his technical assistance.

SOME CHARACTERISTICS OF HAIL PROCESSES IN THE KAKHETI REGION OF GEORGIA

A.G. Amiranashvili[1], V.A. Amiranashvili[1], R.I. Doreuli[1], T.V. Khurodze[2], Yu.M. Kolesnikov[1]

[1]Institute of Geophysics of Georgian Academy of Sciences, Tbilisi, 380093, Georgia
[2] Institute of Computational Mathematics of Georgian Academy of Sciences, Tbilisi, 380093, Georgia

1. INTRODUCTION

Kakheti Region of Georgia is known by its hail activity. In this region cansiderable territories are occupied by agricultural areas (vineyards, vegetable cultures, etc.). Therefore, the investigation of hail processes in this region has always drawn a particular attention both in the practical and scientific aspects. From 1967 till 1989 an anti-hail service was functioning here. This service collected a considerable amount of information on radar characteristics of convective clouds. Simultaneously the Geophysiscs Institute of Georgian Academy of Scinces was carrying out scientific investigations in this field. Methods for the radar diagnostics of the hail-dangerousity of clouds (in particular by means of the complex parameter of the hail-dangerousity of clouds) were developed, the fields of hail-dangerousity in the region, the directions and velocities of the movement of hail-dangerous clouds, etc. were built Gagua,1980, Salukvadze,1973, Doreuli,1996.

This paper represents a continuation of the mentioned investigations.

2. METHODS

The observations on convective clouds were carried out continuously using four three centimeter radars. The observational data for 1972-1976 were analysed. The investigated territory was broken into 334 equal squares with 25 km^2 area each. In each square the mean annual potential of the expected hail cases was calculated, which represents the following expression: $N=n \cdot K$, where K – the mean value of the complex radar hail-dangerousity parameter of clouds; n – the mean number of hail-dangerous clouds. K represents the measure of the hail probability and varies from 0 to 1. Clouds with $K \geq 0.41$ were considered hail-dangerous. The maximum elevation of the radar reflectivity H_m of such clouds in Kakheti is usually more than 9.0 km.

The data of 16 meteorological stations in Kakheti on the number of hail days P, and also the data on the total number of convective clouds Q with $H_m > 6.0$ km and the number of cloud-to-ground lightning discharges per square N_g (Amiranashvili et al., 2000) were also used for the analysis.

3. RESULTS

Fig.1 presents the distribution of the mean annual potential of expected hail cases N for the territory of Kakheti. As it follows from this figure the values of N on the territory of the investigated region are distributed nonuniformly. Depending on a location elevation the values of N in the 25 km^2 squares vary from 0.4 to 6.1 per year.

Table 1 presents the data on the statistical characteristics of the investigated parameters for the 16 squares, where the meteorological stations are located. As it follows from this table the mean value of the potential of expected hail cases according to the radar observations N practically coincides with the mean multi-year (more than 40 years) number of hail cases P, detected by the meterological stations. This indicates a high representativity of the radar regioning of the territory of Kakheti according to the hail-dangerousity degree.

The share of hail-dangerous clouds and hail cases in the 16 squares in the total number of clouds with $H_m > 6.0$ km amounts at the average to about 20% and varies for N/Q from 6.5 to 63% and for P/Q from 9.3 to 53%.

Table 2 presents the data on the correlations among the investigated parameters for the 16 squares. As it follows from this table the correlation of the number of cloud-to-ground lightning discharges with N and P is weak, lower than the significance level. Considerably higher is the negative correlation of N_g with the ratios N/Q and P/Q. Also the correlation of Q with

Corresponding author's address: Avtandil Amiranashvili, Geophysics Institute of Georgian Academy of Sciences, 1., M. Aleksidze Str., Tbilisi 380093, Georgia;
E-Mail: vazha@excite.com

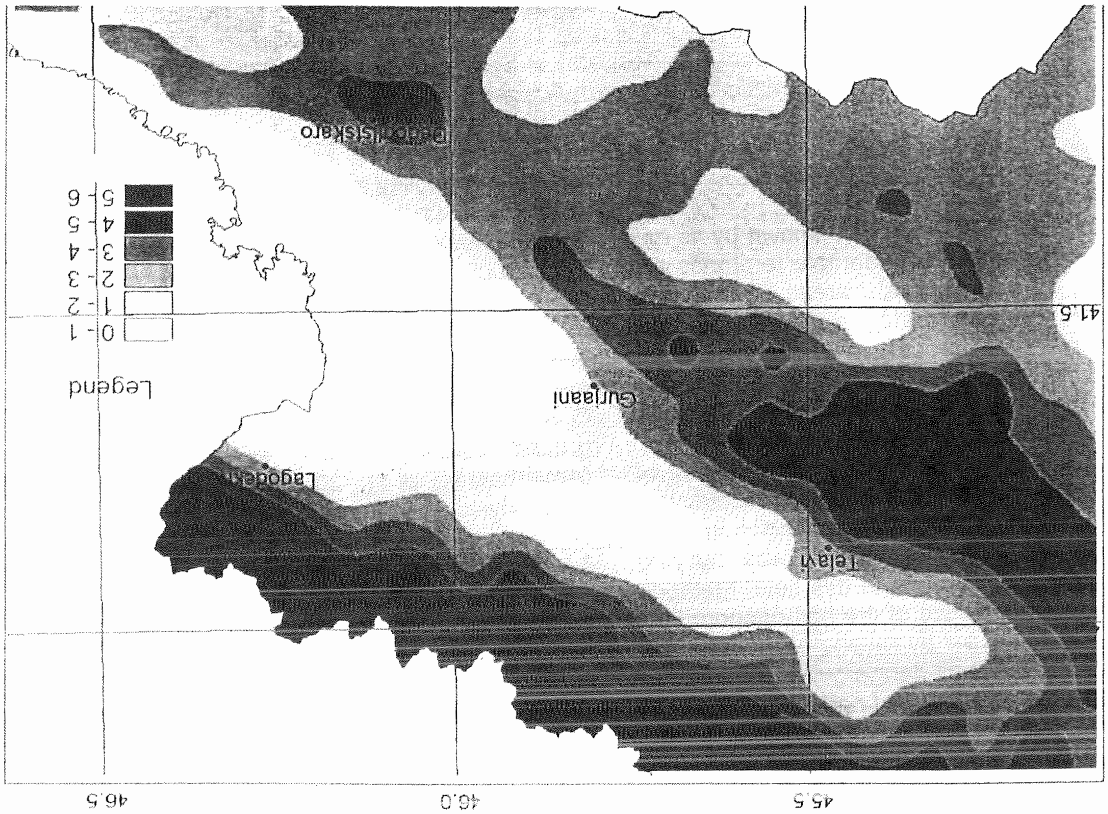

Fig.1
The distribution of the mean annual potential of expected hail cases in Kakheti

Table 1

The statistical charcteristics of the investigated parameters for the 16 squares where the meteorological stations are located

Parameter	P	N	N_g	Q	P/G	N/Q
Min	1.2	0.8	30	6.2	0.093	0.065
Max	3.7	4.4	175	24.8	0.529	0.629
Mean	2.2	2.3	94	13.7	0.19	0.20
Stand. dev.	0.69	0.91	42	5.7	0.12	0.15
Var.Coef.%	31.3	39.5	44.7	41.6	63.2	75

and P is low, while with N/Q and P/Q – high. A high correlation is between the actual and expected hail cases too. Below the corresponding linear regression equations are given for the mentioned parameters:

$$N = 0.1 + 1.003 \cdot P$$
$$P/Q = 0.32 - 0.0014 \cdot N_g$$
$$N/Q = 0.35 - 0.0015 \cdot N_g$$
$$P/Q = 0.38 - 0.136 \cdot Q$$
$$N/Q = 0.43 - 0.163 \cdot Q$$

The first of these equations indicates the actual equality of the expected (N) and actual (P) numbers of hail cases. The following four equations show that the share of hail clouds in the total number of convective clouds with $H_m >$ 6.0 km is inversly proportional to the number of cloud-to-ground lightning discharges N_g and the total number of clouds Q in the squares. In other

Table 2

Correlations among the investigated parameters for the 16 squares where the meteorological stations are located. The minimum significant value of correlation with a 95% confidence level amounts to ±0.43.

	P	N	N_g	Q	P/Q	N/Q
P	1.0	0.76	0.25	0.09	0.63	0.58
N		1.0	0.15	-0.10	0.67	0.77
N_g			1.0	0.95	-0.50	-0.43
Q				1.0	-0.66	-0.63
P/Q					1.0	0.97
N/Q						1.0

words, in locations with intensive lightning discharges and a large number of convective clouds the share of clouds reaching the hail state decreases. This is possibly related to processes of self-seeding of clouds with ice-forming nuclei, additionally arising in clouds due to the modification of inactive aerosols by ozone, generated by discharges. Another reason for this may be an intensive formation of nitrate and sulphate condensation nuclei in clouds, considerably changing their microphysical properties towards an increase of the small-disperse fraction of the size spectrum of droplets Amiranashvili et al., 1991, Amiranashvili at al., 1996.

4. REFERENCES

Amiranashvili, A.G., Gzirishvili T.G., 1991: Aerosols and Ice Crystals in Atmosphere, Tbilisi, Metsniereba, p. 113 (in Russian).

Amiranashvili, A.G., Abesalashvili L.Sh., Supatashvili G.D., 1996: Results of Rain Water Chemical Content Investigation in Alazani Valley, Proc. 12 th Int. Conf. on Clouds and Precipitation, Zurich, Switzerland, vol. 2, 1066-1069.

Amiranashvili, A.G., Amiranashvili V.A., Bibilashvili T.N., Chumburidze Z.A., Gzirishvili T.G., Doreuli R.I., Nodia A.G., Khorguani F.A., Kolesnikov J.M., 2000: Distribution of Convective Clouds on the Earth Surface in Kakheti Region of Georgia, Proc. 134 Int. Conf. on Clouds and Precipitation.

Doreuli, R.I., 1996: The Impact or Region Relief on Some Characteristics of Hail Processes, Proc. 12 th Int. Conf. on Clouds and Precipitation, Zurich, Switzerland, vol. 1, 196-199

Gagua, V.P., 1980: Hail, In: Dangerous Hydrometeorological Phenomena in the Caucasus, Edited by G.G. Svanidze and Ya.A. Tsutskiridze, Leningrad, Gidrometeoizdat, 137-150 (in Russian)

Salukvadze, T.G., 1973: Radar Characteristics of Hail Clouds with Allowance of their Seasonal Variation, Proc. of the Institute of Geophysics of Georgian Acad. Sci., vol. 32, Tbilisi, Metsniereba, 129-138 (in Russian).

CHARACTERISTIC PARAMETERS OF THE THUNDERSTORMS IN LEÓN (SPAIN) AS OBSERVED BY A C-BAND RADAR

R. Fraile, A. Castro, J.L. Sánchez, J.L. Marcos, J.T. Fernández

Laboratorio de Física de la Atmósfera, Universidad de León, 24071 León, Spain

1. INTRODUCTION

The high frequency of thunderstorms in the province of León (northwest of Spain), especially during the summer, and the damages on the crops caused by hail have led the authorities to promote and support research projects on these meteorological phenomena.

Since 1985, a wide range of data has been collected. These data include information obtained on the ground (by means of a hailpad network, a network of voluntary observers, and the meteorological parameters measured), as well as variables of the atmosphere in high levels (from satellite images, radiosondes, meteorological radar).

One of the research lines that has been followed is the characterization of thunderstorms and of their internal structure according to the type of precipitation and the size of the hailstone. A study of this type becomes necessary, since the characteristics of the thunderstorms vary depending on the orographic conditions of the region where they develop and the zones they cross (Simmons, 1984).

This paper will analyze the development of the thunderstorms detected by the radar that have crossed the study area on hail days. The variables used are the ones that have been previously employed in this kind of analysis (Castro et al., 1992).

2. DATA COLLECTION

The study zone (Fig. 1) and the network of voluntary observers are described in previous papers (for example Sánchez et al, 1994). The observers provided information about the time at which the thunderstorm occurred, whether there was any hailfall in their zone, and the size of the biggest hailstone found. The network of observers provided thus data about the type of precipitation that a certain storm originated while crossing the study area. It is therefore possible to establish a classification of thunderstorms: with hailfall and with no hailfall. Any type of solid precipitation will be called *hail*, without taking into account its size. It should nevertheless be remembered that the term hail usually designates the solid precipitation of more than 5 mm in diameter (OMM, 1992).

A meteorological C-band radar was used to study the thunderstorms. This radar has 250 kW and has a range of more than 140 km. Each of the 224 thunderstorms that crossed the study zone was analyzed in order to determine their values for the following radar variables:

- ZMAX: maximum reflectivity factor (expressed in dBZ) detected in the storm when it crossed the area.

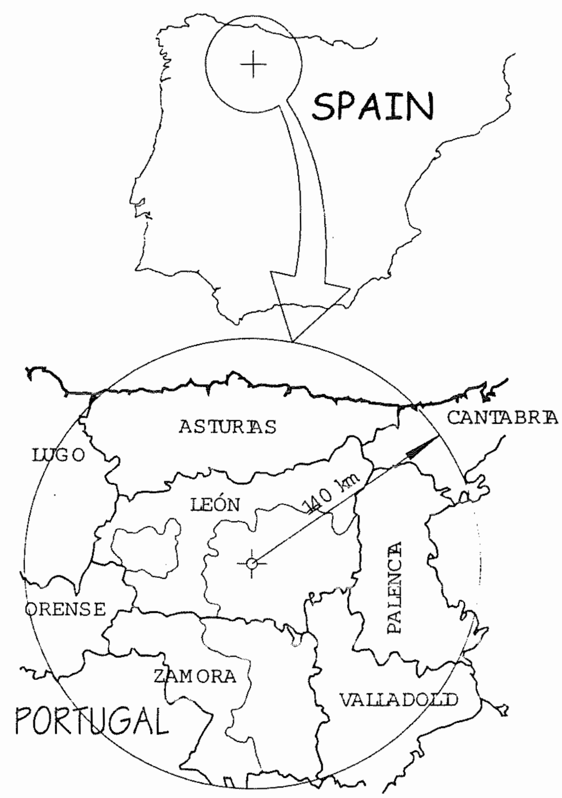

FIG.1. Study zone and range of the meteorological radar.

- HZMAX: altitude in kilometers of the point where the maximum reflectivity factor is located.
- HTOPZMAX: maximum altitude in kilometers reached by the 10 dBZ contour of the storm. It is determined considering the vertical cross section (RHI) at the moment of maximum intensity.
- HMAX: maximum altitude in kilometers of the 10 dBZ contour detected in the storm when it crossed the study zone.
- T45: duration of the active life of the storm, with a maximum reflectivity in the cloud mass of more than 45 dBZ. It is expressed in minutes.
- DIS: distance covered by the storm, expressed in kilometers, from the moment when it was first detected by the radar until the moment in which the echo disappeared.
- VEL: speed at which the storm moves in km/h.

3. HAILSTORMS AND HAILSTONE SIZES

Almost 30% of the 224 storms detected by the radar that were crossing the study zone originated hail precipitation in that area. The methodology employed to assign a storm the label *with hail* is based on a detailed comparison of the spatial and temporal location of the storms (with the radar) and every one of the hailfalls (information provided by the observers).

Table 1 shows, for each variable, the size of the sample analyzed, the mean value, and the standard deviation. The difference in the sizes of the samples is due to the fact that the amount of known data is often different for each variable. Thus, for DIS and VEL the reason is that the stationary storms have not been taken into account in these variables. There was one stationary storm with hail and 13 with no hail, which represents 6.25% of the total. This percentage is similar to the one found in the Central High Plains (Colorado) by Knight et al. (1982), but it is lower than the percentage obtained in the central part of the Ebro Valley (Northeast Spain) by Castro et al. (1992), who found 14% of stationary storms.

The data shown in the table are clearly different for storms with hail and storms with no hail. Nonetheless, in order to determine whether these differences are significant, the Kruskal-Wallis homogeneity test was applied. The value of the statistic *H* has been added to the table, and the last column on the right indicates whether the difference between the sample with hail and the sample with no hail is significant (s) or non-significant (ns).

It was observed that:

— All the non-mechanical variables (ZMAX intensity, HZMAX maximum precipitation zones, HMAX and HTOPZMAX maximum vertical developments) that characterize hailstorms are significantly different from those of the storms with no hail.

— Mechanical variables: the distance covered (DIS) and the duration of the storm (T45) are different, but the speed at which the storms move (VEL) is similar.

— All the variables reached higher values in the case of hailstorms, than in the case of storms with no hail precipitation.

TABLE 1. Characterization of storms with hail/no hail. Comparative study of samples with the Kruskal-Wallis test.

VARIABLES	HAILSTORMS			STORMS WITHOUT HAIL			K-W. TEST	
	N_i	X	σ	N_i	X	σ	H	s/ns
ZMAX (dBZ)	66	50	5.5	158	43	6.9	41.2	s
HZMAX (km)	66	2.3	1.5	130	1.8	1.6	7.6	s
HTOPZMAX (km	66	10.1	2.3	130	9.3	2.1	7.8	s
HMAX (km)	66	11.3	2.4	130	9.8	2.1	17.0	s
DIS (km)	65	90	54	145	58	40	19.9	s
VEL (km)	65	28	13	145	32	16	2.4	ns
T45 (min)	66	114	146	158	23	41	17.0	s

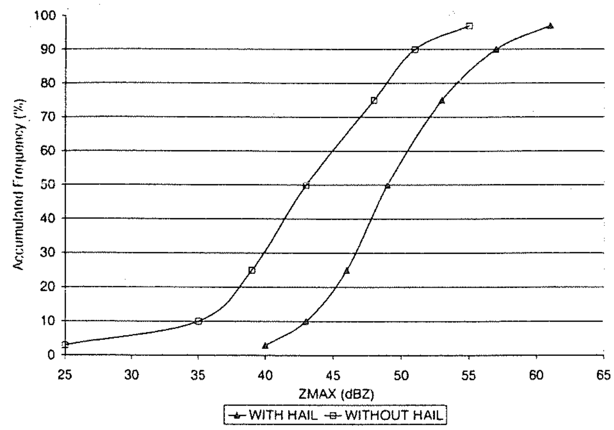

FIG 2. Distribution of accumulated frequencies of the maximum reflectivity factor variable for storms with and without hail.

When representing the accumulated frequency of the ZMAX variable for storms with and without hail (Fig. 2) the result found was very interesting, since 20% of the hailstorms did not reach 45 dBZ. This fact does not fit with the criterion that a storm must surpass 45 dBZ for at least 5 minutes, a criterion established by Knight et al., (1982), Mather and Treddenick (1976) or Waldvogel, (1987). This finding would rather support the theory by Sand (1976) and Carte and Held (1978), since it does not accept the level of 45 dBZ as the lower threshold of intensity for the presence of hail in a storm.

We will now analyze the hailstorm variables obtained by the radar, according to the size of the hailstones found on the ground. The sizes have been classified into four groups B, O, P, Q, R, as shown in Table 2. Table 2 also includes the mean values of the variables for each type of precipitated hailstone, and the statistic *H* from the Kruskal-Wallis test. The purpose is to determine whether there are differences between the 5 groups of hailstorms.

TABLE 2. Characterization of hailstorms according to hailstone size. Application of the Kruskal-Wallis test to the 5 samples of each variable: B [graupel], O [r ≤ 5 mm], P [5< r ≤ 10 mm], Q [10 < r ≤ 20 mm] and R [r > 20 mm].

Variables	HAIL SIZE											
	B N_i=8		O N_i=9		P N_i=30		Q N_i=12		R N_i=7		K.- W. TEST	
	X	σ	X	σ	X	σ	X	σ	X	σ	H	s/ns
ZMAX	46	5	48	5	50	5	53	5	54	4	13	s
HZMAX	2.2	0.8	2.1	1.1	2.3	1.7	2.1	1.5	3.0	2.0	1	ns
HTOPZMAX	8.9	3.0	9.1	1.8	10.0	1.9	10.7	2.0	12.6	2.2	12	s
HMAX	10.[illegible]	2.7	10.0	2.1	11.0	1.9	12.0	2.2	12.8	3.1	10	s
DIS	68	52	103	57	91	51	93	63	84	57	2	ns
VEL	27	12	29	11	32	14	27	14	18	10	6	ns
T45	55	67	59	81	107	163	150	159	224	130	12	s

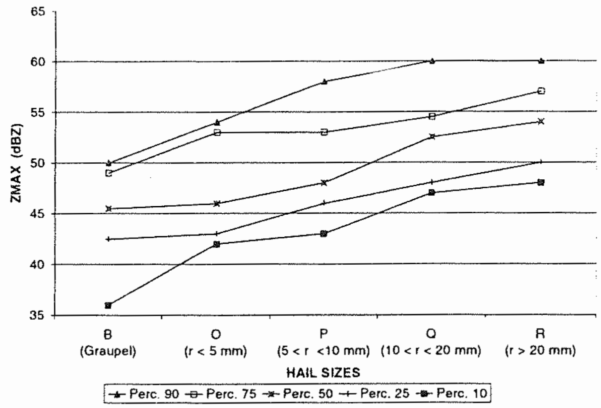

FIG. 3. Percentiles of the variable 'maximum reflectivity factor' for the 5 groups of hail sizes.

TABLE 3. Characterization of hailstorms, according to the type of storm. The table shows the results of applying the Kruskal-Wallis test for each variable, in order to determine the differences according to the type of storm. Group I, unicell; Group II, multicell; Group III, supercell (unicell) and Group IV, supercell (multicell).

	HAILSTORM TYPES									
VARIABLES	Group (I) Ni=14		Group (II) N_i=25		Group (III) N_i=3		Group (IV) N_i=24		K.-W. TEST	
	x	σ	x	σ	x	σ	x	σ	H	s/ns
ZMAX	45	4	48	3	53	7	54	4	32.7	s
HZMAX	1.7	1.2	2.3	1.5	3.2	2.4	2.5	1.6	2.9	ns
HTOPZMAX	8.7	2.4	9.8	1.7	12.1	2.3	11.2	2.2	11.7	s
HMAX	9.6	2.0	10.7	1.8	13.4	0.7	12.7	2.4	18.2	s
DIS	51	33	92	46	150	110	103	53	10.9	s
VEL	26	8	32	16	38	3	24	12	6.8	ns
T45	11	16	72	71	71	50	197	129	36.7	s

Considering the last column in Table 2, the following conclusions may be drawn:

– Neither the altitude of the activity zones, nor the speed, nor the distance covered vary significantly with the size of the hailstones.

– The bigger the reflectivity factor, the bigger the size of the hailstones. This relationship with the size is similar with the vertical development and the duration of the storms

Moreover, the detailed study of the K-W test has shown that the major differences are found between storms precipitating hailstones of slightly different sizes (groups B-R, O-Q, O-R and P-R). In the rest of the pairs the differences are not significant.

In order to visualize the differences between the storms according to the size of the precipitated hailstones the percentiles of the variables are represented next to the hailstone size. Thus, Fig. 3 shows that in 80% of the cases the maximum reflectivity factors of storms with hailstones of size O are between 42 and 54 dBZ. In contrast, if the size is R, the reflectivity factor varies between 48 and 60 dBZ.

In the study area 90% of the hailstorms had their most active zones below 4.6 km. During the moments of maximum storm activity the top of the cloud masses surpassed 14 km in 30% of the storms that precipitated hailstones of size R. Another important characteristic is that the duration of the active life of the storm increases with the size of the hail precipitated.

4. THE STRUCTURE OF HAILSTORMS

Following a classification proposed by Fankhauser and Mohr (1977), and also employed by Castro (1992), the storms have been divided into groups according to their internal structure:

- unicellular (group I), which represent 21.2% of the total;
- multicellular (group II), 37.9%;
- supercells with a unicellular character (group III), 4.5%;
- supercells with a multicellular character (group IV), 36.4%.

It can be observed that the supercellular storms (groups III and IV) represent 40.9% of the total, which indicates that the study zone is affected by severe thunderstorms during the summer. These data contrast with the ones found by Castro (1992) in the Ebro Valley, where only 7% of the storms were supercellular.

Table 3 shows the characteristics of the storms in the different groups. The Kruskal-Wallis test (right half of the table) has shown that there are no significant differences between the storm groups neither in the altitudes of maximum reflectivity, nor in the speed at which the storms move. Trying to determine between what pairs of groups there are differences, it may be concluded that the supercellular storms (groups III and IV) behave similarly, independently of the number of cells they are made of. They may thus be considered within the same group.

In the central part of the Ebro Valley the storms of these two groups (Castro 1989) present a similar intensity, vertical developments and duration, although their speed and the distance covered is limited by the orography of the area. Chaudhry et al. (1996) have also found differences between the storms of two neighboring geographic areas in Brazil. The study zone in León presents less orographic accidents, and the circumstances are therefore different. Thus, the distinction between groups III and IV can be obliterated in the case of hailstorms in the study zone. Both groups will be called henceforth supercells.

It is necessary to highlight the fact that the supercells are more intense and their active life lasts longer than in the case of multicells. Multicells, on the other hand, are more intense and last longer than unicells. The upward drafts are not significantly different between unicells (I) and multicells (II).

5. HAILFALLS

Is there any correlation between the size of the hailstones and the characteristics of the hailstorms that originated the hailfall? We have associated each hailfall with the parameters of the hailstorm that originated it. These parameters are obtained by the vertical cross sections (RHI) of the clouds carried out with the radar.

It was found that when the hail was smaller than 5 mm, or of an unknown size, the reflectivity factor of the cloud was below 45dBZ, on average. For the other sizes, the mean reflectivity values were below 50dBZ for hail size P (between 5 and 10 mm) and hail size Q (between 1 and 2 cm). In the case of hail size R (more than 2 cm) the mean reflectivity value was over 50dBZ. This leads us to confirm the interrelation between the reflectivity factor and the size of the hailstones.

It was also observed that during a hailfall the zones of maximum reflectivity are, generally, below 2.5km for all hail sizes, except for group R, where it is located at an altitude of 4km. The altitude of the top of the cell shows an important correlation with the size of the hailstones: the diameter of the hailstones increases with the altitude of the top of the cell. Nevertheless, the hailstones of unknown sizes present a particular feature in spite of the low reflectivity of the clouds that originated them.

After having established the differences between storms with and without hail, the results we have just presented are another approach to the analysis of hailstorms. However, this analysis does not offer general characteristics, but others that are possibly much more interesting, namely the characteristics of the hailstorms at the very moment when the hailstones were being precipitated, without considering the previous development of the storm. This fact explains the clear relationships between variables such as the reflectivity factor or the altitude of the storm, and the hailstones found on the ground.

As expected, the storms originating hail precipitation presented high reflectivity factors. However, in order to determine whether a convective cell contains hailstones or not, more variables are necessary apart from the ones used in this paper, such as for example the variables provided by a polarization radar (Reinking et al., 1996) or other variables (Liao and Sallen, 1994; Ulbrich and Atlas, 1998). Nonetheless, the results presented here improve our knowledge of the structure of those storms that actually led to hail precipitation.

ACKNOWLEDGMENTS

The authors would like to thank Noelia Ramón for the translation of this paper.

REFERENCES

Carte, A.E. and G. Held, 1978: Variability of hailstorms on the South African Plateau. *J. Appl. Meteor.*, **17**, 365-373.

Castro, A., J.L. Sánchez, R. Fraile and J.L. de la Madrid, 1989: Análisis de la estructura del valle medio del Ebro. *Boletín de Sanidad Vegetal-Plagas,* **15,** 149-160.

Castro, A., J.L. Sánchez and R. Fraile, 1992: Statistical comparison of the properties of thunderstorms in different areas around the Ebro-Valley (Spain). *Atmos. Res.,* **28,** 237-257.

Fankhauser, J.C. and C.J. Mohr, 1977: Some correlation between various sounding parameters and hailstorm characteristics in Northeast Colorado. *Proc. 10th Conf. On Severe Storms,* Omaha, Nebr., Amer. Meteorol. Soc., 218-225.

Chaudhry, F.H., A.G. Andrade Filho and R.V. Calheiros, 1996: Statistics on tropical convective storms observed by radar. *Atmos. Res.,* **42,** 217-227.

Knight, A.C., P. Smith and C. Wade, 1982: Storm types and some radar reflectivity characteristics. In "The National Hail Research Experiment", vol 1, Colorado Associated University Press, Boulder, CO, 282 pp. (81-93).

Mather, G.K. and D. Treddenick, 1976: An observed relationship between the height of the 45 dBz contours in storm profiles and surface hail reports. *J. Appl. Meteor.,* **15,** 1336-1340.

Liao, L. and K. Sassen, 1994: Investigation of relationships between Ka-band radar reflectivity and ice and liquid water contents. *Atmos. Res.,* **34,** 231-248.

Reinking, R.F., S.Y. Matrosov and R.T. Bruintjes, 1996: Ice and liquid hydrometeor identification with elliptical polarization radar. Applications to precipitation enhancement. Preprints 13th Conf. On Planned and Inadvertent Weather Modif., Atlanta, Feb 1996, Amer. Meteor. Soc., Boston 172-179.

Sánchez, J.L., A. Castro, J.L. Marcos, M.T. de la Fuente and R. Fraile, 1994: Criteria for a remote ground generator network in León (Spain). *J. Wea. Mod.,* **26,** 83-88.

Sand, W.R., 1976: Observations in hailstorms using the T-28 aircraft system. *J. Appl. Meteor.,* **15,** 641-650.

Simmons, A.J., 1984: The treatment of orography in numerical weather prediction models. Report of the seminar on progress in numerical modelling and the understanding of predictability as a result of the Global Weather Ex. WMO, 43 (II): 57-65.

Ulbrich, C.W. and D. Atlas, 1998: Rainfall microphysics and radar properties: Analysis methods for drop size spectra. *J. Appl. Meteor.,* **37,** 912-923.

Waldvogel, A., L. Klein, D.J. Musil and P.L. Smith, 1987: Characteristics of radar-identified big drop zones in Swiss hailstorms. *J. Climate Appl. Meteor.,* **26,** 861-877.

WMO, 1992: *International Meteorological Vocabulary,* WMO, 784 pp.

EMBEDDED CONVECTION, SUPERCOOLED LIQUID WATER AND AIRCRAFT ICING

Thomas Hauf[1] , Susanne Stingl[1] and Franz Schröder[2]

[1]Institut für Meteorologie und Klimatologie, University of Hanover, D-30419 Hanover, Germany
[2]Institut für Physik der Atmosphäre, DLR Oberpfaffenhofen, D-82230 Weßling, Germany

1. INTRODUCTION

The metastable thermodynamic state of supercooled liquid water in clouds is a still not well understood field in cloud physics and is of significant relevance for aviation safety as aircraft may accrete substantial amounts of ice while flying through a supercooled cloud. The ice accretion rate depends on the liquid water content but also on the drop size distribution. As a result of recent accidents, the current world-wide scientific discussion focuses on the role of supercooled large drops (SLD) having diameters of 50 to 500 µm and even more. These drops seem to be the cause of the accidents as aircraft are not certified for these drop sizes. SLD are assumed to grow by pure coalescence processes. The conditions under which SLD form and their role to observed aircraft icing is not fully understood yet. Here we report from in-situ measurements under the special conditions of embedded convection when also severe aircraft icing was observed. The measurements are described and a simple physical picture is developed as a guide to the understanding of the complex situation.

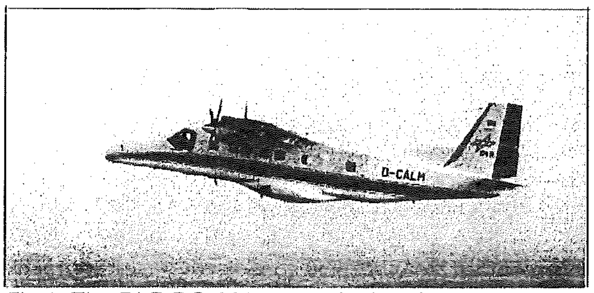

Fig.1: The DLR DO-228 research aircraft.

2. THE EURICE EXPERIMENT

In March 1997 a flight campaign was performed in Southern Germany with an DO-228 instrumented research aircraft (Fig. 1). The flights were part of the European funded project EURICE on aircraft icing. The aircraft was equipped with two optical scattering spectrometers (FSSP 100-ER, range 5-95 µm, FSSP 300, range 0.4-20 µm) to measure drop size and an optical array probe (OAP-2D-C, range: 20-750 µm) to determine shape and phase of the particles, together with a temperature sensor and a Johnson-Williams liquid water probe. Ice accretion on the wing and on an exposed cylinder (Fig. 7) was documented with video cameras. A ground-based Doppler and polarization radar monitored the clouds during the flights. Altogether eight flights were performed. During five of them supercooled clouds were sampled while one flight was in a 'warm' cloud with temperatures above zero. The other two flights were test flights. The measurements were made near Munich, Germany between March, 15 and 27. The flight pattern consisted of vertically staggered straight and horizontal flight legs of approximately 50 km length. Number of legs per flight ranged between 5 and 12. After an initial sounding through the entire depth of the cloud the latter was surveyed from above with penetrations of overshooting tops, if present. Then the cloud was probed from top to base. Temperatures below cloud base were above zero, so that in case of severe performance degradation due to icing the aircraft could descend and thaw off the accreted ice. This happened once. Weather during the flight campaign was dominated by a nearly stationary weather pattern with strong advection of cold and humid air from the North Sea to Central Europe. Mostly stratus clouds prevailed, often with embedded convection. Occasionally gravity waves were observed which could be identified by the regular wave-like undulations of the upper cloud deck or by the banded cloud structure. The latter cloud type was found during the 'warm' flight. Clouds in general were shallow. Cloud bases ranged between 1000 and 2000 m MSL, while cloud tops were found between 2000 m and 3400 m. Some clouds had an inclined base or top or both.

Fig. 2: Upper stratus cloud deck with an overshooting top of an embedded convective cell on March 24.

Corresponding author's address: Thomas Hauf, Institut für Meteorologie und Klimatologie, Universität Hannover, Herrenhäuserstraße 2, D-30419 Hannover, Germany

3. MEASUREMENTS

3.1 The flights

In the following, we show results from the two flights on March 15 and 24 only. Results from the other days, except for the 'warm' cloud, do not differ with respect to the conclusions.

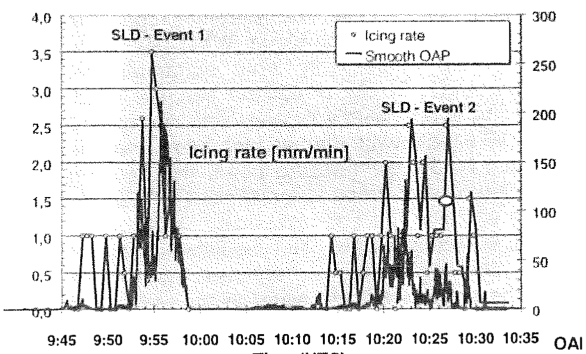

Fig.3: Ice accretion rate on the cylinder (left axis) and number of OAP trigger events (right axis) on March 15

3.2 Supercooled large drops

On March 15 a stratus cloud with embedded convection covered Southern Germany. Cloud base was at 2300 m AGL and cloud top at 3300 m with a temperature of –10°C. It should be noted that the embedded convection can only be identified by its overshooting tops when flying aloft (c.f. Fig. 2) or with a C-band radar (c.f. Fig. 5). Visually, while flying, one notices only one big stratus cloud. In Fig. 3 the time series of the icing rate and the number of trigger events for the optical array probe OAP-2DC is shown. The latter quantity is a measure of the number of large particles and seems to be well correlated with the ice accretion rate. Values of the latter were derived visually from the video records of the ice cylinder (c.f. Fig. 8) with a resolution of 0.5 mm. Maximum values of 3.5 mm/min can be found during SLD-events.

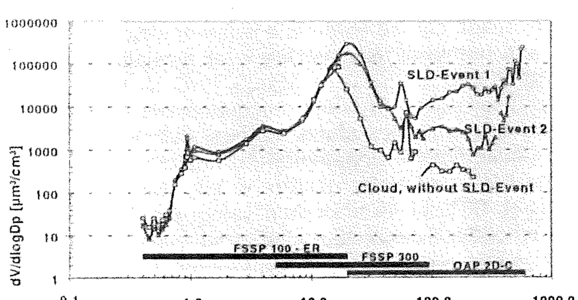

Fig. 4: Cloud drop volume distribution on March15 for two SLD-events and total cloud without SLD.

Generally, high icing rates and large drop can be found on spatial scales ranging between 500 m and 5 km. On March 15, two SLD events occurred. For these two events we determined the drop particle distribution from the measurements of all three cloud probes (Fig. 4). The spectral distribution, here shown as a volume distribution, is typical for a mixed phase cloud. A maximum is found at about 20 µm which represents the normal cloud drops in a stratus cloud. Towards larger drop sizes the distribution decreases and has a minimum at about 60 µm. During the two SLD events significantly more drops can be found there. It should be noted that the OAP 2DC probe does not automatically discriminate between solid and liquid particles. A visual discrimination, however, is possible (c.f. Fig. 6).

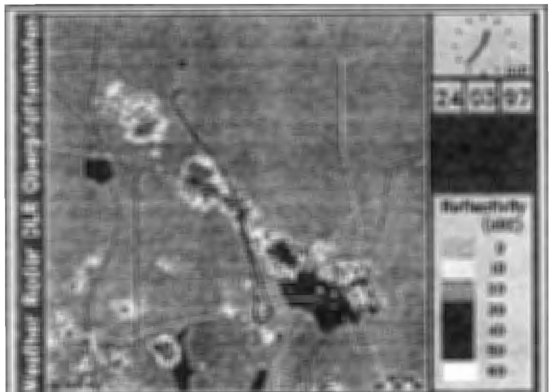

Fig. 5: Spatial radar reflectivity pattern (ppi) and flight path at the time of measurements

The increase of the distribution for particles larger than 100 µm is, therefore, due to both solid particles (graupel, snow flakes, ice crystals) and liquid drops. Of course, only the liquid drops contribute to the observed ice accretion. In summary, during SLD-events both the number density of solid and liquid particles increases significantly. The obvious question is, why are SLD and ice accretion maximum confined to these SLD-events.

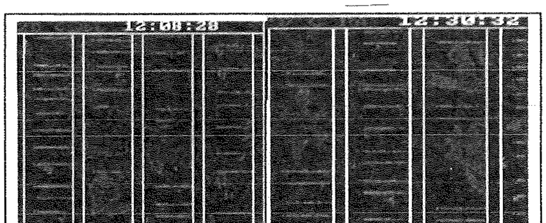

Fig. 6: Images of cloud particles taken near cloud top (right plate) and at 2200 m (right plate).See text for details.

3.3 Embedded convection and SLD

To answer this question we use the radar observations. On March, 15 no radar coverage was provided but radar was active on March, 24. A C-band radar is sensitive only for particles much larger than 100 µm and thus does not detect the normal cloud drops prevailing in a stratus cloud with a maximum at 20 µm. If the flight track is superposed on a radar reflectivity horizontal cross section (ppi) it can be seen that the aircraft crossed a cloud with precipitation-sized particles (Fig. 5). Checking now the icing rate and the OAP 2DC trigger events, similar as in Fig. 3, it becomes clear that the SLD events occur when the aircraft traverses a convective cell. The horizontal scale of such a convective cell is on the order of several kilometers. As the aircraft does not always pass through the center of the cell, aircraft traverses can be smaller. Assuming a true airspeed of 80 m/s, the exposure times for an aircraft to SLD ranges between 6 and 60 seconds.

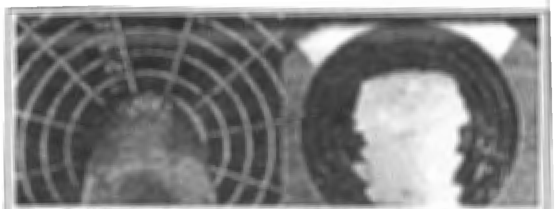

Fig. 7: View of the ice cylinder from top. Individual frozen drops recognizable on the right picture

3.4 Cloud particle types

Looking at cloud particle images taken with the OAP cloud probe (Fig. 6) one recognizes individual ice crystals (hexagonal structure), graupel (round structure but strictly spherical), needles, and drops. The latter can be identified by their diffraction pattern which gives them a 'hole' in the center. Right plate of Fig 6 is taken at 2700 m near cloud top, while the left plate in the lower part of the cloud at 2200 m. The horizontal length of one image is 800 µm. Horizontal lines represent trigger pulses. Size of the liquid drop is approximately 200 to 300 µm maximum, while solid particles can exceed 1 mm in size. Liquid particles, therefore, seemed to be limited in growth. In the lower part of the cloud, ice particles are more rimed and the crystal structure is less pronounced though still recognizable. In summary, convective cells have both liquid and solid particles at all levels.

3.5 Hypothetical SLD formation in embedded convection

How can the occurrence of supercooled large drops be explained? A simple hypothesis is developed as outlined in Fig. 8. Generally, two growth processes can be found in any precipitating cloud. The dominant one in mid-latitudes is the graupel process. Cloud drops grow in size while being carried upward in a cloud. At subzero temperatures drops start to freeze. Together with ice crystals which grow directly from the gas phase they fall and collect the still liquid drops. The latter freeze and the falling graupel grows continuously. The second process is the pure coalescence process. Liquid particles collide and remain together as a still liquid drop. As this process is the dominating rain producing process in the tropics, it is referred to also as the 'warm rain process'. Both processes are found in the convective clouds during the flights. The SLD, therefore, just represent the 'warm rain' process at subzero temperatures. Drops form through pure coalescence. Where do the drops form ? The measurements show quite clearly, that the highest liquid water content and the highest portion of liquid particles can be found close to the cloud top. Our measurements also point to the existence of a thin and liquid outermost shell of the cloud of several decameter depth in agreement with Rauber and Tokay (1991, in the following referred to as RT91). We, therefore, conclude that SLD form in that part of the cloud. What favors the production of SLD, respectively what enhances the 'warm rain 'process?. Three conditions can be listed. Natural glaciation of the cloud increases with decreasing temperature. RT91 showed that at high temperatures with values just below the freezing point, the freezing rate for the ensemble of drops is insufficient to glaciate them all. This explains the often observed liquid outermost shell of a stratus cloud. This insufficient natural glaciation at high temperatures becomes even more important, if the supply of liquid water in the updraft of the convective cell is strong due to the vigor of the

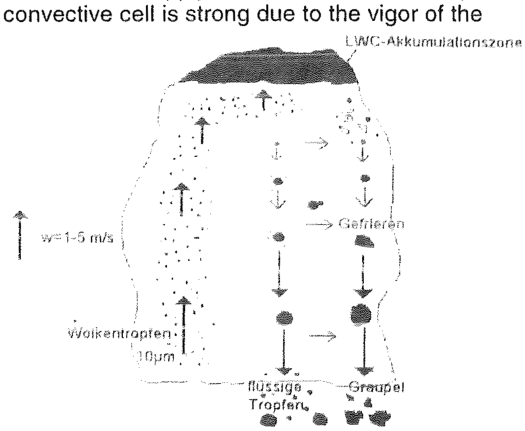

Fig.8 Sketch of principal processes in the mixed phase convective cell. Upward motion of cloud drops (left), falling of liquid drops grown by coalescence (middle) and falling solid particles (right). While falling some of liquid drops freeze, presumably by collision, thus limiting the maximum drop size to 200 –300 µm.

convection. Updraft velocities are estimated to 5 m/s. Vigorous convection can be found in a weather situation where cold and humid air is advected over a relatively warm land as it was the case in March 1997. A third favorable condition is the fact that the convective cells were embedded in a stratus cloud. Without this humid and cloudy environment entrainment of ambient air would reduce the liquid water content in the main updraft typically to 60% of its maximum value. As, however, for an embedded cloud saturated air is mixed into it, the liquid water content cannot be lowered by this process. In summary, insufficient glaciation of the rapidly vertically transported high amounts of liquid water near cloud top enhances the coalescence growth path of liquid drops. This hypothesis has to be confirmed by a deeper analysis of the existing data and by new flights under similar conditions.

Our measurements also point to the existence of a thin and liquid outermost shell of the cloud of several decameter depth in agreement with RT91. We, therefore, conclude that SLD form in that part of the cloud. What favors the production of SLD, respectively what en-

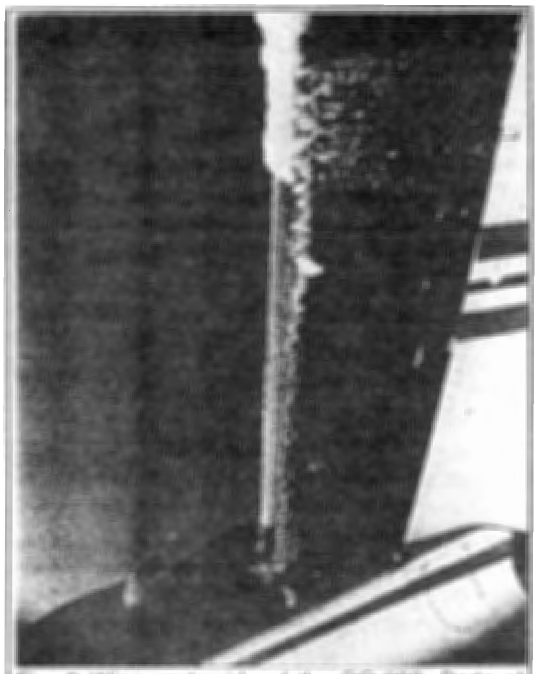

Fig. 9 Wing underside of the DO-228. Parts of the accreted ice could not be removed by the pneumatic boots. Note the frozen SLD up to 60 cm away from the leading edge.

hances the 'warm rain 'process?. Three conditions can be listed. Natural glaciation of the cloud increases with decreasing temperature. RT91 showed that at high temperatures with values just below the freezing point, the freezing rate for the ensemble of drops is insufficient to glaciate them all. This explains the often observed liquid outermost shell of a stratus cloud. This insufficient natural glaciation at high temperatures becomes even more important, if the supply of liquid water in the updraft of the convective cell is strong due to the vigor of the convection. Updraft velocities are estimated to 5 m/s. Vigorous convection can be found in a weather situation where cold and humid air is advected over a relatively warm land as it was the case in March 1997. A third favorable condition is the fact that the convective cells were embedded in a stratus cloud. Without this humid and cloudy environment entrainment of ambient air would reduce the liquid water content in the main updraft typically to 60% of its maximum value. As, however, for an embedded cloud saturated air is mixed into it, the liquid water content cannot be lowered by this process. In summary, insufficient glaciation of the rapidly vertically transported high amounts of liquid water near cloud top enhances the coalescence growth path of liquid drops. This hypothesis has to be confirmed by a deeper analysis of the existing data and by new flights under similar conditions.

3.6 Ice accretion and SLD

Significant ice accretion occurred during the SLD events whenever the aircraft traverses one convective cell. Ice accretion is strongest near cloud top with 3.5 mm/min but still significant at lower levels. Type of icing was rime and also glace. Quite interesting, individual drops can be identified on both the cylinder (Fig. 7, right plate) and the wing underside (Fig. 9). On March 24 the amount of accreted ice was such that a performance loss of 30 % occurred and the plane could not maintain its flight height and had to descent. Fig. 9 also shows that ice accreted also on parts of the wing which are not protected by the pneumatic boots. The video recording of the ice accretion on the cylinder provides an unique data set for the study of ice formation.

4. CONCLUSIONS

Supercooled large drops SLD were found in convective cells which were embedded in a stratus cloud. In these embedded convective clouds SLD form by coalescence. The SLD formation process is enhanced through the suppression of the natural glaciation process. Vigorous convection, warm cloud top temperatures, and an ambient stratus cloud favor the SLD formation process. Embedded convection is one type of weather conditions where we assume that SLD can generally be found. Convective cells which are embedded in a stratus cloud are hazardous as a pilot while flying in the cloud does not recognize visually the convective cell. Whenever the aircraft passes through a cell the amount of accreted ice increases. This can happen e.g. during holding patterns. Hazardous cells, however, can be identified by conventional weather radars. Together with observations or forecasts of the cloud type, cloud base, cloud top and cloud top temperature, a warning can be issued and the hazardous air spaces can be avoided. Currently such improved forecasting schemes are under development.

References

Rauber, R. M. and A. Tokay, 1991:"An Explanation for the Existence of Supercooled Water at the Top of Cold Clouds. J. Atmos. Sci., Vol. 48, 1005 - 1023.

GENERATION OF STRONG DOWNDRAFTS BY EVAPORATION OF DROPS FALLING IN "ENERGY TOWERS"

Shalva Tzivion[1] *, Zev Levin[1] and Tamir G. Reisin[2]

[1]Department of Geophysics and Planetary Sciences, Tel Aviv University, Tel Aviv, Israel
[2]Soreq Nuclear Research Center, Yavne, Israel

1. INTRODUCTION

The worldwide demand for energy increases very rapidly, while natural energy resources are continuously being depleted. Presently, 89% of the United States and 80% from the world's energy sources come from fossil fuels (Cassedy and Grossman, 1999). The combustion of such fuels pollutes the air, land and water, ultimately affecting our health.

Downdrafts generated by the evaporation of drops falling in a relatively dry and hot air are common in the atmosphere and are known as "microbursts". Measurements and numerical modeling of these phenomena (Proctor, 1988; Feingold et al., 1991) reported downdrafts that may reach as much as 25 m s^{-1}.

Based on this natural phenomenon Philip Carlson (1975) suggested to pump water from a lake or a sea to the top of an "Energy Tower" and disperse the water in the form of small drops with radius of several hundred microns. The evaporation of the falling drops in the relatively warm and dry environment would cool the air in the tower and produce a convective flow downward. At the bottom of the tower he suggested to place a turbine to transform the kinetic energy into electric energy.

Assuming a homogeneous cooling of the air in the tower, he calculated the air density and the pressure difference between the inside and outside at the bottom of the tower. Using Bernouli's equation he then calculated the kinetic energy of the outflowing air. He showed that for a tower with a height of 1000 m and a radius of 50 m a net energy of about 70 MW could be produced.

Later on, a one dimensional steady state model was developed (Guetta, 1993) for calculating the flow in such an "Energy Tower". The authors concluded that an "Energy Tower" with a height of H_T = 1000 m, radius R_T = 200 m and with a height of diffuser (the opening at the base of the tower through which the air exists and where the turbines must be placed) – ΔH_{diff} = 100 m can generate an average net energy of about 360 MW (see Fig. 1 for a schematic representation of the tower).

* *Corresponding author address:* Prof. Shalva Tzivion, Department of Geophysics and Planetary Sciences, Tel Aviv University, Tel Aviv 69978, Israel; e-mail: tzivion@storm.tau.ac.il

It must be emphasized that these studies have some very basic limitations. The first one is related to the flow inside the "Energy Tower" that was calculated as a laminar homogeneous flow. For towers exceeding 100 m in radius the flow will definitely be non-homogeneous, extremely turbulent with Reynolds numbers larger than 10^8 and with very complex boundary conditions. Because of inherent limitations of one dimensional models, calculations of the flow and energy output from an "Energy Tower" with such dimensions could lead to large errors of even hundreds of percent.

The second limitation is related to the calculation of the evaporation process. Since the driving force of the "Energy Tower" is the evaporation of the drops, this process must be calculated with great accuracy. However, the methods used to calculate the evaporation process in the mentioned studies were very simple. They assumed that the size distribution of drops falling from the tower's top is homogeneous. Consequently, their calculations of the total mass of water evaporated were based on the evaporated mass of one drop multiplied by the number of drops. In reality, inside the tower the size distribution of the drops is heterogeneous and changes with height and radial distance. Therefore, the process of evaporation in an "Energy Tower" must be studied on the basis of a common solution to the diffusion equation with respect to the drop size distribution and an equation with respect to the saturation deficit. In addition, since drops with different sizes fall with different velocities, gravitational collision and collection of drops is expected to occur. This also influences the evaporation of the drops.

2. THE MODEL

In order to correctly and accurately calculate the flow of the air and the drops in an "Energy Tower" with large dimensions, an axisymmetric numerical model was developed based on the solution of the Navier-Stokes differential equations for turbulent flow and integro-differential kinetic transfer equations for calculating the drops evaporation, collection - breakup and sedimentation processes. A detailed description of the set of equations, the turbulence parameterization, the microphysical processes and numerical methods used in the model can be found in former publications (Tzivion et al., 1987, 1988, 1989, 2000; Feingold et al., 1988; Reisin et al., 1988). As

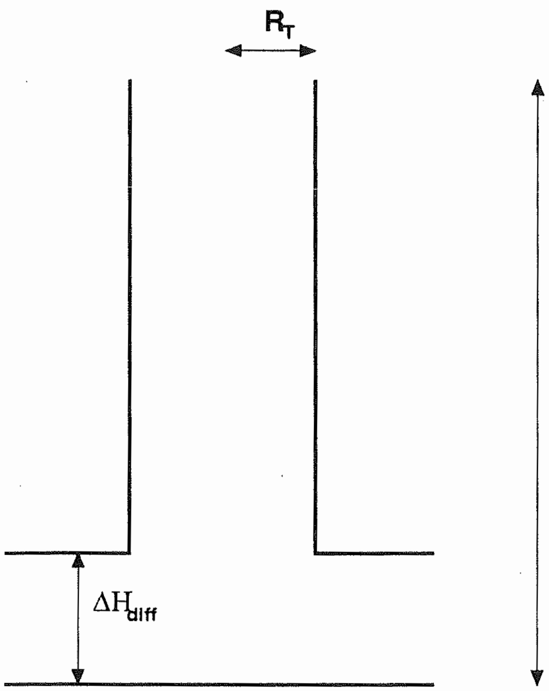

Figure 1: Schematic representation of a cross section of the "Energy Tower"

boundary conditions, non-slipping solid walls that are thermally isolated from the environment are assumed. At the walls the vertical and horizontal flows become zero. It is assumed that no exchange of heat, moisture or momentum between the tower and the environment exists. These assumptions imply that in the present work, issues related to the interactions between the tower and the environment are not addressed.

From the model, the size distribution of the drops and the air speed, temperature, humidity and pressure are calculated at every grid point in the domain. Using these parameters integral parameters are calculated such as: the air mass that flows through the top of the tower and out of its bottom through the diffuser, $M_{air,in}(t)$ and $M_{air,out}(t)$, respectively; the water mass that inflows the tower at its top and outflows through the diffuser, $W_{in}(t)$ and $W_{out}(t)$, respectively.

In order to evaluate the performance of an "Energy Tower" the following parameters are defined:
a) The *pumping energy*: the energy needed to lift the water from the bottom to the top of the tower:

$$PE = gH_T W_{in}(t) \quad (1)$$

where g is the acceleration of gravity.
b) The *kinetic energy of the outflowing air*:

$$KE(R_T, \Delta H_{diff}, t) = 2\pi R_T \int_0^{\Delta H_{diff}} \rho_{air}(R_T) u(R_T) \frac{V^2(R_T)}{2} dz \quad (2)$$

Here $V = \sqrt{u^2 + v^2}$, u, w are the radial and vertical velocities, respectively, and ρ_{air} is the air density. The dependence of these variables on (z,t) is implicit.
c) The *net energy*:

$$NE = KE(R_T, \Delta H_{diff}, t) - PE \quad (3)$$

d) The loss of internal energy of the air in the tower by the cooling of the evaporating drops:

$$\Delta QAIR = c_v \Big[T(H_T) M_{air}(H_T, t) - 2\pi R_T \int_0^{\Delta H_{diff}} \rho_{air}(R_T) u(R_T) T(R_T) dz \Big] \quad (4)$$

here, c_v is the specific heat at constant volume, $T(H_T)$ and $T(R_T)$ are the absolute temperatures at the top of the tower and at the diffuser, respectively. Their dependence on (z,t) is implicit. The first term represents the internal energy of the air entering the top of the tower and the second term is the internal energy of the outflowing air through the diffuser.

More than 200 numerical experiments were conducted in order to determine the optimal parameters of the "Energy Tower" needed in order to obtain the maximum net energy. In order to maintain the accuracy of the numerical method, the same resolution, in space and time, was used throughout all the simulations. For towers with $H_T \geq 800$ m the radial grid size was $\Delta r = 20$ m, the vertical grid size was $\Delta z = 30$ m and the time step was $\Delta t = 0.1$ s. For towers with $H_T < 800$m we used: $\Delta r(H_T) = \left(\frac{H_T}{800}\right) \times 20\text{m}$, $\Delta z(H_T) = \left(\frac{H_T}{800}\right) \times 30\text{m}$ and $\Delta t(H_T) = \left(\frac{H_T}{800}\right) \times 0.1\text{s}$. Tests were conducted in which the spatial and time resolutions were increased by a factor of two. The differences in the results were smaller than 5% while computation times increased by a factor of ten.

3. RESULTS

For the above mentioned initial and boundary conditions and numerical model parameters very stable numerical solutions were obtained. In all the following cases the flow in the "Energy Tower" reached a very stable and stationary flow. The time to reach this stationary condition varied from 12 min to 30 min depending on the parameters of the Energy Tower. Although the model is time dependent, only the results that are obtained when the stationary flow is reached are presented here. Based on physical considerations it was found that the largest net energy is obtained for the following relationships of geometrical parameters: $R_T = H_T/2$ and $\Delta H_{diff} = H_T/4$. In general, total mass was conserved in all the numerical simulations, and mass losses were less than 0.5%. Total energy was also conserved, with losses less than 3%.

Fig. 2 show the dependence of the kinetic, pumping and net energies on the height of the tower, for the above geometrical parameters. The mixing ratio of the drops at the top of the tower is $LW = 6$ g kg^{-1} and the average radius of the sprayed drops is r_{dr}=40 μm The temperature at the tower's bottom is 30 °C and the relative humidity at its top is 30%. Fig. 2 shows that with these optimal parameters it is possible to obtain a considerable amount of net energy - 560 MW even with a height of only H_T = 400 m. When HT increases the net energy grows very rapidly and for H_T = 880 m it reaches a value of 11500 MW. However, in this case the water amount that must be lifted to the top of tower and then dispersed as drops can reach 120 m^3 s^{-1}. This is a huge amount of water that may be difficult to realize technically. Therefore, in the subsequent numerical experiments a limit to the height of the tower was set to only H_T = 800 m. Under these conditions the amount of water needed is only about 78 m^3 s^{-1}.

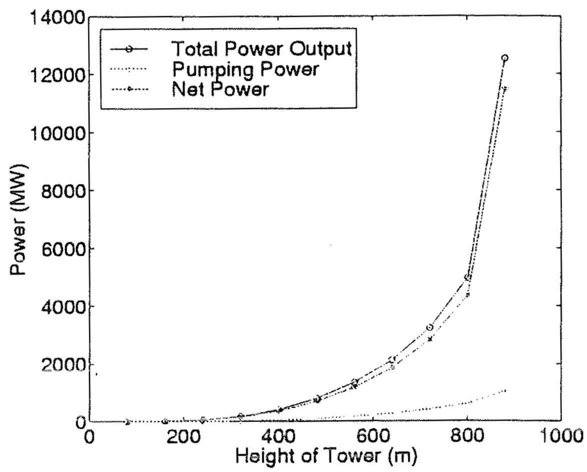

Figure 2: Dependence of the kinetic, pumping and net energies on the height of the tower - H_T, when $R_T = 0.25H_T$ and $\Delta H_{diff} = 0.125H_T$. In this cases $r_{dr} = 60\mu m$, $LW(H_T) = 8gkg^{-1}, T(Z=0) = 30°C$ and $\Gamma = 0.7°/100m$.

Fig. 3 shows the dependence of the maximum pressure difference between the center of the tower and the diffuser as well as the dependence of the inflow and outflow velocities, on the height of the tower. When the height of the tower increases from 80 m to 880 m, the maximum inflow velocity increases from 15.6 to 70.4 m s^{-1} and the corresponding maximum outflow velocity increases from 10.5 to 46.3 m s^{-1}. At the same time the pressure difference is enhanced from 130 to 2630 Pa. It must be emphasized that the reduction in the temperature due to cooling only weakly depends on the height of the tower. A temperature drop of -12.5 °C is almost always obtained as long as the other parameters are kept the same as in the figure.

In Fig. 4 the dependence of the kinetic, pumping and net energies on the radius of the sprayed drops are shown. Here, the height of the tower is kept at 800 m. The figure shows that the optimal drop radius is 40 μm. It must be emphasized that the net energy dramatically decreases when the radii of the sprayed drops decrease below 30 μm

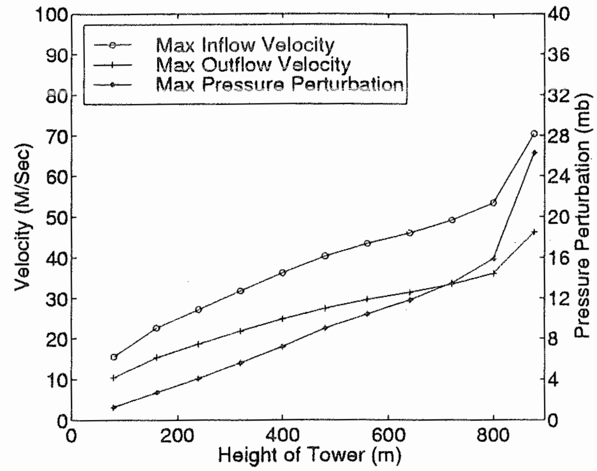

Figure 3: Dependence of the maximum pressure difference between the center of the tower and the diffuser, as well as the dependence of the maximum inflow and outflow velocities on H_T. All other parameters as in Fig.2.

(using the same input water mass). This is because the smaller drops evaporate rapidly (more numerous drops - larger surface area) saturating the air in the tower and preventing further evaporation.

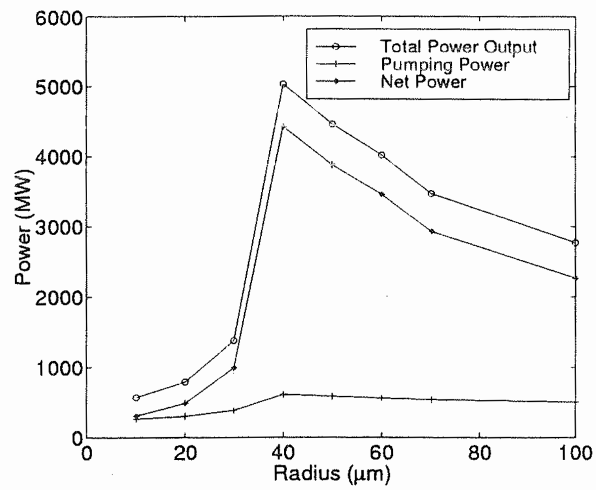

Figure 4: Dependence of the kinetic, pumping and net energies on the average radius of the sprayed drops, r_{dr} when H_T=800 mn R_T=400 m and ΔH_{diff}=200m. All other parameters as in Fig. 2

Varying the environmental relative humidity at the top of the tower from 20% to 90% decreases the net energy from 4423 MW to 793 MW. When the temperature at the bottom of the tower varied from 10 °C to 40 °C the net energy increases from 2317 MW to 4980 MW. Also, it was found that the net energy only weakly depends on the vertical gradient of temperature. These results show that even for relatively high humidity or low temperature it is possible to obtain a considerable amount of net energy.

4. CONCLUSIONS

The calculations indicate that the idea to produce energy from the evaporation of falling drops in relatively warm and dry climate could be realistic.

A set of optimal geometrical and physical parameters for which the net energy could be larger than 4000 MW and in some cases may reach up to 11500 MW is presented. Much smaller towers could also produce some energy and could be used as prototypes to test the extent of accuracy of the numerical model and the feasibility of the project without making major investments in full size towers.

The production of energy through the use of "Energy Towers" can reduce the dependence of many countries on oil. This could also help reduce international conflicts that arise from the deficiency in energy resources. At the same time the essential reduction of utilization of oil and coal for obtaining energy will considerably decrease the emissions of CO_2 and other greenhouse gases into the atmosphere and thus help in reducing the dangers of climate warning. Through the production of electricity by means of "Energy Towers" many countries could find it easier to comply with their international commitment (Kyoto, 1997) to reduce greenhouse gases.

Acknowledgments
Special thanks are due to Zipi Rosen and Sara Rechavi for their help with the programming, and the testing of the model. We also want to thank Rachel Duani for typing of the manuscript.

REFERENCES

Carlson P., 1975: Power generation through controlled convection (Aeroelectric Power Generation), Invention No. 3, 894-393.

Cassedy, E.S. and P.Z. Grossman, 1999: Introduction to Energy - Resources, Technology and Society. *Cambridge University Press.*

Feingold, G., S. Tzivion and Z. Levin, 1988: The evolution of raindrop spectra. Part I: Stochastic collection and breakup. *J. Atmos. Sci.*, **45**, 3387–3399.

Feingold, G., S. Tzivion and Z. Levin, 1991: The evolution of raindrop spectra. Part III: Downdraft generation in an axisymmetrical rainshaft model. *J. Atmos. Sci.*, **45**, 315–330.

Guetta R.,1993: Energy from dry air – a model of air flow and droplets evaporation in the chimney. Ph.D. Thesis, Technion, Technological Institute of Israel, Haifa, Israel.

Proctor, F.H., 1988: Numerical simulations of an isolated microburst. *J. Atmos. Sci.*, **45**, 3137–3160.

Reisin, T., S. Tzivion Z. Levin and G. Feingold, 1988: Numerical simulation of an Hawaiian convective cloud with a high resolution axisymmetric model. *Proc. Second WMO Int. Cloud Modeling Workshop*, Toulouse, France, 231–235.

Tzivion, S., G. Feingold and Z. Levin, 1987: An efficient numerical solution to the stochastic collection equation. *J. Atmos. Sci.*, **44**, 3139–3149.

Tzivion, S., G. Feingold and Z. Levin, 1989: The evolution of raindrop spectra. Part II: Collisional colection/breakup and evaporation in a rainshaft. *J. Atmos. Sci.*, **46**, 3312–3327.

Tzivion, S., T. G. Reisin and Z. Levin, 1999: A numerical solution of the kinetic collection equation using high grid resolution: a proposed reference. *J. of Comput. Phys.*, **148**, 527–544.

Tzivion, S., Z. Levin and T. G. Reisin , 2000: Numerical simulation of axisymmetric turbulent flow in "Super Power Energy Towers". *J. Comp. Fluid Dynamics*, **9**, No1.

MEFFE
SATELLITE AND COMBINED SATELLITE-RADAR TECHNIQUES IN METEOROLOGICAL FORECASTING FOR FLOOD EVENTS: RESEARCH ACTIVITIES AND RESULTS

F. Prodi[1,2], F. Porcú[2], S. Natali[2], C. Caracciolo[2], D. Capacci[1], S. Dietrich[3], A. Mugnai[3], G. Panegrossi[3,4], F. S. Marzano[5], E. Kubista[6], W. L. Randeu[6], P. Simpson[7], J. Goddard[7], L. Schanz[8], P. Bauer[8], S. Hacker[9], S. Bakan[10], D. Taurat[10], C. Klepp[10], C. Wunram[10], J.P.V. Poiares Baptista[11]

[1]Institute ISAO-C.N.R., Clouds and Precipitation Group, Bologna, Italy
[2]Department of Physics, University of Ferrara, Ferrara, Italy
[3]Institute IFA-C.N.R., Rome, Italy
[4]University of Wisconsin-Madison, Dept of Atmospheric and Oceanic Sciences, Madison,Wisconsin
[5]University of L'Aquila, Dept. of Electric Energy, L'Aquila, Italy
[6]Joanneum Research, Graz, Austria
[7]RCRU/RAL, Didcot, U.K.
[8]DLR, Cologne, Germany
[9]DLR, Oberpfaffenhofer, Germany
[10]Max-Plack-Institut fuer Meteorologie, Hamburg, Germany
[11]ESA/ESTEC, Norwjik, The Netherlands

1. INTRODUCTION

The risk management process implies a sequence of: 1) a long term meteorological forecasting (up to 7-10 days, done by Global Circulation Models); 2) a short term forecasting (up to 72 hours, done by Limited Area Models, LAM); 3) a very short term forecasting by observational tools (satellites and radar). A skilled rainfall rate forecast to minimize loss of life and economic damage is therefore important.
The MEFFE project (a IV Framework Projet) was conceived to produce improvements in rainfall intensity estimates for mitigating the risk of flood events using nowcasting techniques (meteorological satellite sensors, combined satellite-radar data and numerical models). The main goal was achieved by: 1) better knowledge of meteorological systems generating different flood events; 2) coupling satellite data, radar data and numerical Limited Area Models; 3) improving MW and VIS-IR algorithms for precipitation retrieval; 4) improving weather numerical models (LAM and Cloud Mesoscale) that combine surface and upper air measurements, and radar-satellite data; 5) defining the characteristics of Nowcasting procedures for rainfall rate intensity.

2.FLOODS IN EUROPE: STATISTICS, CLASSIFICATION AND CONCEPTUAL MODELS

2.1 Estimated social costs of the floods in Europe

Our estimates based on Munich Re-Insurance report, count 461 flooding events (flood and flash-flood) with significant losses, that killed 974 people and damaged environment and structures for about 27 billions of Euro. Floods affect all the European countries, but in two regions flooding is more frequent: coastal areas in the Western Mediterranean and the alpine region. The occurrence of a flood episode is always the product of meteorological and hydrogeological factors, but we focused on the meteorological factors and defined some features present in the cloud systems, related to some of the most severe flood episodes.

Corresponding author's address: Franco Prodi, Institute ISAO-C.N.R., Clouds and Precipitation Group, Via Gobetti, 101, 40129, Bologna, Italy, E-mail: f.prodi@isao.bo.cnr.it

2.2 Five years flood climatology in Europe

More than twenty major floods in Europe between 1992 and 1996 have been identified and classified from the meteorological point of view using satellite data and conventional meteorological data, in order to outline the synoptic and mesoscale features most favorable to floods occurrence in Europe (Porcù et al., 1997). The cloud systems are classified depending on the location of the low pressure, the upper air situation, the depth of the depression, the horizontal pressure gradient and the cloud types in the cyclonic structure. Only the most catastrophic events are considered with high human life losses and economic losses. The detailed analysis shows that in 20 out of 22 cases some degree of cyclogenesis was responsible for the flood-leading cloud systems. The maximum degree of cyclogenesis is reached in cold months (5 cases), while in the warm season the score is lower and deep convection is always present.

2.3 Austrian Flood Search Engine

An Internet based (Java Script) interactive data base information system has been developed, that provides a detailed information on all the strong flood event selected. The software uses various symbols to show the location of floods on the map of Austria. The symbols provide information on the 'amount of economical damage' the flood has caused. The software tools allow the definition of a time period that shall be used for the review and/or the selection of predefined areas. Furthermore for each of the flood events a reference to the corresponding newspaper article is given.

3. RADAR DATA PROCESSING

It was necessary to define operation procedures for the two radars of the Project in order to meet specific needs of integrating with SSM/I microwave sensors data.

3.1 Graz Hilmwarte radar (Joanneum Research)

A number of data retrieval and conversion programs were developed. Moreover a new display software has been developed which runs under WindowsNT and

Windows9x. Some means for 3-dimensional viewing of the data were also provided. A total number of 56 precipitation events simultaneous with SSM/I were recorded. Radar derived products (rain-fall intensity, raindrop size distribution, ice mass density, as well as flags for the type of precipitation, clutterflags, indication of melting layer conditions) were produced. A program was also developed which converts the radar data from a spherical coordinate system into a cartesian grid.

3.2 Chilbolton radar (RCRU/Rutherford Appleton Laboratory)

Also this radar was utilized to produce surface rainfall maps from radar observations timed to coincide with SSM/I satellite overpasses. The polarisation capability of the radar was used to estimate rainrate from Reflectivity and Differential Reflectivity Measurements. The polarisation data enabled DSD parameters in rain to be derived. LDR was used to identify hydrometeor phase, and thus differentiate between regions of rain, ice cloud, and melting layer during stratiform conditions. The Chilbolton radar was also used to generate vertical sections through rain regions. A list of severe weather events that occurred in the southern UK during 1995 and 1996, was produced from information compiled by the UK Tornado and Storm Research Organisation.

4. COMPARISON OF SATELLITE-DERIVED RAIN RATES AND RADAR MEASUREMENTS

The availability of high quality research radar data from different sites in Europe (i.e. Chilbolton, UK; Graz-Hillmwarte, Austria; and Oberpfaffenhofen, Germany) in combination with operational radar network data, like the Central European Weather Radar Network (CERAD) is a useful means for the development and validation of rainfall algorithms.

4.2 Satellite Estimates of Precipitation. The River Oder Flooding case

Most parts of Europe received substantially precipitation below average in the first months of 1997, but floods resulted mainly from two periods of very heavy rainfall: 4-7 July and 17-21 July.

Two reference algorithms were used for the identification using both SSM/I and SSM/T2 data. Additionally, a simple SSM/I scattering algorithm and a combined SSM/I - SSM/T2 precipitation algorithm were utilized over the central European region covered by the CERAD network. While the identification of the areas with higher rain rates shows an adequate agreement, the determination of rain rates fails totally for the simple scattering algorithm. The combined SSM/I & SSM/T2 algorithm shows a good agreement in rain screening as well as in the determination of absolute values.

4.3 Handling the Surface Emissivity Problem

A further enhancement of the algorithm performance can be reached taking the soil emissivity explicitly into account. The emissivity model used requires information about the soil wetness, soil temperature, its roughness, vegetation coverage, and the exposition of each individual area relative to the satellite's viewing direction. While vegetation coverage and area exposition can be deduced from Normalised Differential Vegetation Index data and Digital Elevation Models respectively the other parameters have to be derived from the satellite measurements themselves. An iterative variation process is used. This technique utilises the rather low atmospheric influence in the 19 GHz channel of the SSM/I for the estimation of the parameters, which, after an appropriate adaptation to higher frequencies, are used in the simulation of the soil emissivity at 85 GHz. This procedure suffers still from the extrapolation of the emissivity model.

5. RADAR-CALIBRATION OF SATELLITE RETRIEVALS.

Two reference algorithms were used for the identification of precipitating areas (rain screening). Additionally, a simple SSM/I scattering algorithm was utilized over the central European region covered by the Austrian radar network. While the identification of the areas with higher rain rates shows an adequate agreement, the determination of lower rain rates fails totally for the simple scattering algorithm. The additional use of the precipitation classes as used for the radar network data shows a further degradation of the SSM/I product compared to the radar network. The additional use of the Ferraro-screening technique leads to a much better discrimination of the raining areas, but with much too high rain estimates and a reduced dynamical range in its structures. The intercomparison with radar measurements interpolated on the SSM/I scan structure allows a simple correction in bias and slope of the rain rate distribution.

6. RADAR/ INFRARED METEOSAT SYNERGY FOR PRECIPITATION ESTIMATES

High-quality radar rainfall maps and infrared satellite rainfall estimations, computed by Negri-Adler-Wetzel technique (Negri et al., 1984) have been compared for three cyclonic precipitating events, occurring on 2-4/10/1992, 7-9/10/1993 and 14-15/11/1996 over Northern Italy. The results show discrepancies in terms of root mean square difference between radar and satellite. If integrated over the whole study area: for the 92 case this could be satisfactory, given the higher mean precipitation values, but it is not so for the 96 case, where lower rainfall was measured. The quantitative use of IR precipitation data as input to rainfall-runoff models has to be limited to large basins (some ten-thousand km^2), characterized by large response time.

The main source of error in the NAW procedure, applied to stratified, mid-latitude cloud systems, is in the choice of numerical values for the nominal rainrates to be assigned to the different areas. We introduced (Porcú et al, 1999) a calibration technique (RTC) that make use of radar data over a defined calibration area to compute, for every satellite slot, actual rainrates, to be used in the NAW scheme. This technique markedly reduced the overestimation of the NAW in the three cases.

7. MULTISENSOR OBSERVATION OF DEEP CONVECTIVE CLOUDS

7.1 Microwave/IR approach

The use of the 19 GHz data from SSM/I is recognised to be a valuable tool in the detection of the rain layer in clouds over the sea, given the low emissivity of water, but its use over land was not considered by most of the rain retrieval algorithms, given the sensitivity to the differences in soil emissivity, that often mask the rain signal. Recent studies (Porcù et al., 1998) shown that the use of 19 GHz over land can be made possible for precipitation layer analysis, if the layer itself is "thick" enough to mask the land contribution to the signal. In presence of intense, mature, convective systems it is possible to localise the rain layer by using the Polarisation corrected temperature (PCT) at 19 GHz.

7.2 Multiparametric radar/Microwave precipitation retrieval

The use of polarisation difference over the land for three cases of different nature has been investigated: Poldirad (14/07/1997, strong convective event), Graz (10/07/1997, convective event) and Chilbolton (27/06/1997, stratified event). The correlation between vertical and horizontal polarisation Tbs differences at 85 and 19 GHz and ZH and ZDR as measured by the available radar has been evaluated. The radar domain has been classified in three rain classes by means of the ZH values: no rain (0<ZH<20 dBZ), moderate rain (20<ZH<30 dBZ) and heavy rain/hail (ZH>30 dBZ). The 19 GHz polarisation differences decrease when Zdr increase. On the contrary, 85 GHz channels Tb differences are not related to Zdr variations. At 85 GHz the increase of Zdr results in an average increase of the polarisation difference from the satellite; this implies a rather strong correlation between rain layer at the ground (as seen by radar) and the ice layer on the top of the cloud as seen at 85 GHz.

8. IFA PASSIVE MICROWAVE-BASED PRECIPITATION RETRIEVAL ALGORITHM

The algorithm is based on the use of a cloud-radiation database, whose cloud portion is generated by means of the time-dependent, three-dimensional, cloud-mesoscale model. The first version has been basically developed at Florida State University (FSU) (Mugnai et al., 1992). The second version has been developed by the Istituto di Fisica dell'Atmosfera (IFA) and the University of Rome "La Sapienza" (IFA-SAP algorithm). Its main features are: 1) it is suitable for retrieving instantaneous precipitation, thus it is appropriate for flash flood; 2) rain rates are physically derived through a fallout equation; 3) it exhibits very good performance in terms of processing time; 4) it allows to obtain quantitative information on the uncertainty variance associated with a given retrieval; 5) A quantitative information on the variance associated with a given retrieval is made available; 6) It is based on a physical scheme.
The cloud model used in this study is the University of Wisconsin Non-hydrostatic Modeling System (Tripoli, 1992). It is a three-dimensional, non-hydrostatic mesoscale cloud model that incorporates explicit microphysical processes involving liquid and frozen hydrometeors. Three different simulations of the same of the Genova flood event of 27/09/92 event have been performed. Several sensitivity studies, as well as comparisons with corresponding SSM/I measurements TBs and sensitivity studies have been performed.

9. FRONTS CHARACTERISATION BY MEANS OF SSM/I DATA

Tools for screening rain events and for the classification of frontal systems connected to these events were provided. Rain screening can be used for the investigation of the history of events that have caused flash floods. Front classification could be used as an information source for the development of conceptual models. His investigations show that there is a close correlation of the horizontal gradient of the IWV, the rain detected by SSM/I, and the position of cold fronts.

9.1 Classification of frontal systems

The following atmospheric parameters, that can be retrieved from SSM/I measurements over the sea, are useful indicators for frontal systems (Katsaros et al., 1989): Integrated Water Vapour (IWV), Liquid Water Content (LWC), Ice Water Content (IWC) and rain-rate (Bauer and Schlüssel, 1993); Water Vapour content of the marine Boundary Layer (BLWV) (Schulz et al., 1993). Additionally, the polarisation difference at 85.5 GHz can be used to gain information on the amount of scattering particles in the atmosphere.
Frontal characterisation parameters
It was verified that the horizontal distribution of the atmosphere's WV and the precipitation of 7 case studies, are the most suitable indicators for the position of cold fronts.
85 GHz polarisation difference
It was found that usually a good overview of the atmospheric water particle amount can be gained from the consideration of the differences of the brightness temperatures at 37 GHz and 85.5 GHz between vertical and horizontal polarization.
SSM/I-ECMWF data set
The data set (North Atlantic area, November 1992), has been investigated to find a measure of the quality of front detection and front localization, including only one case with considerable rain rates, and to go even deeper into details on various front types.

9.2 Cloud System Tracking

All previously discussed schemes for rain identification are only valid over the sea surface. The main problem is to perform a transition of the schemes to the land surface.
Cases covered by the RAL-radar observations were examined. Using Meteosat and SSM/I data, it was proved that severe rain events are not strictly connected to fronts but might occur as convective rain in the cold air mass behind the cold front as well. Thus, a careful investigation of the individual set off of the tracking procedure is needed. Cloud clusters are very well

detected by this synergistic method and may be tracked throughout longer sequences of Meteosat imagery. Thus, the spatial and temporal gap underlying the SSM/I procedure alone, is closed, while the strict relation between the tracked cloud clusters to heavy rain events needs detailed investigation.

10. USE OF METEOSAT AND SSM/I DATA FOR TROPOSPHERIC WATER VAPOUR RETRIEVAL

The capabilities of multi-sensor water vapor (WV) observations for identification and classification of fronts and air masses in northern Atlantic and Mediterranean areas were explored. Data from the METEOSAT 6.3 μm channel has been used: the distribution of WV mean content in the layer between 600 and 300 hPa for cloudless area was retrieved. Multi-frequency data from SSM/I are used to estimate the distribution of WV mean content in lowest 500 m of the troposphere and the distribution of total WV content in the troposphere.
The multisensor approach allows an estimate of the vertical profile of water vapor in the troposphere in three layers over the sea under clear sky conditions. A semi-quantitative analysis of the moisture field was made, especially in presence of frontal structures when WV gradients are present and marked dry intrusion can be identified as important part of the cyclonic structure. Vertical moisture sections can be useful in identifying and classifying frontal structures with two clear limitations: Meteosat retrievals work only over cloud free areas and SSM/I works only over the sea.

11. ASSIMILATION OF SATELLITE DATA ON A LIMITED AREA MODEL

The new idea for the implementation of a new assimilation method is the existence of an attractor. A new assimilation method has been implemented and tested. It is based on the minimization of a cost-function modified with respect to the one used in the classical 4D-VAR. In practice, the function, which provides the distance from observation data, is calculated only in the subset described by Lyapunov vectors corresponding to non-negative exponents. The new algorithm is able to give optimal estimates already for smaller assimilation times. Secondly, the minimization of the cost-function is obtained analytically and this strongly simplifies the numerical implementation. The technique can be used to assimilate every kind of observables into the model and the initial conditions obtained are automatically on the attractor. That is to say, there are no problems related to the initial transient.

12. CONCLUSIONS

Results from rainfall rate estimate techniques based on individual sensors and their combinations have demonstrated that a significant improvement in performance is obtained by the use of microwave passive sensors (in our case from SSM/I sensors). They can provide useful information by proper combination with ground-based radar or radar networks. In turn radar determined and model calculated hydrometeor volumes enhance the possibilities of microwave sensors. This procedure cannot be operational and so cannot be of advantage for risk management operation until microwave sensors have full time-space coverage of the risk areas. Therefore the Space agencies should plan and very rapidly implement a mission based on a constellation of polar satellites hosting MW sensors (and possibly one active millimetric sensor: rain-radar). On one side, work on improving radar estimates and radar networking should be continued, while, at the same time, the great advantage of surveillance from space, and of a new continental center providing the flood warning service should be considered.
The existing risk management structure inside MHS or Civil Protection structures should be integrated with the new nowcasting procedure recommended by this project, combined with more classical procedures. Radar networking should be structured with flood forecasting and rainfall rate estimates (center resources management) as primary goal. This could improve SSM/I radar or IR radar estimates.

13. REFERENCES

Bauer, P., P. Schlüsse,l 1993: Rainfall, total water, ice water and water vapour over sea from polarized microwave simulations and SSM/I data, JGR, 98, pp 20737-20760.

Katsaros, K. B., I. Bhatti, L. A. McMurdie, G. W. Petty, 1989: Identification of atmospheric fronts over the ocean with microwave measurements of water vapor and rain. Weather and forecasting, 4,pp 449-460.

Mugnai, A., E.A. Smith and X. Xiang, 1992: Passive microwave precipitation retrieval from space: A hybrid statistical-physical algorithm. Specialists Meeting on Microwave Radiometry and Remote Sensing Applications, Boulder, Colorado, USA, E.R. Westwater, Ed., NTIS, Springfield, VA, USA, 237-244.

Negri, A.J., Adler, R.F. Wetzel, P.J., 1984: Rain estimation from satellite: an examination of the Griffith-Woodley technique. J. Climate Appl. Meteor., 23: 102-116.

Porcù F, Prodi, F., Franceschetti, S. and Pasetti, S., 1997: Short term climatology of cloud systems leading to flood events in Europe (1992-1996). 1997 Meteorological Satellite Data Users' Conference, 29 Sep-3 Oct 1997, Brussels, Belgium 461-466.

Porcù F., S.Dietrich, A.Mugnai, S.Natali, F.Prodi e P.Conway, 1998: Satellite multi-frequency observation of severe convective systems in the Mediterranean. J. of the Phys Chem of the Earth (B), 24, 643-648.

Porcù F., M. Borga, and F.Prodi, 1999: Rainfall estimation by combining radar and infrared satellite data for nowcasting purposes. Meteorol Appl, 6, 289-300.

Schulz, J., P. Schlüssel, H. Graz, 1993: Water vapour in the atmospheric boundary layer over oceans from SSM/I measurements, Int. J. of Remote Sensing, 14, 2773-2789.

Tripoli, G.J., 1992: A nonhydrostatic model designed to simulate scale interaction. Mon. Wea. Rev., 120, 1342-1359.

USE OF A MIXED-PHASE MICROPHYSICS SCHEME IN THE OPERATIONAL NCEP RAPID UPDATE CYCLE

John M. Brown[1], Tatiana G. Smirnova[1,2], Stanley G. Benjamin[1]

and

Roy Rasmussen[3], Greg Thompson[3] and Kevin Manning[4]

[1]NOAA/Forecast Systems Laboratory, Boulder Colorado USA
[2]Cooperative Institute for Research in the Environmental Sciences
[3]NCAR/Research Applications Program
[4]NCAR/Mesoscale and Microscale Meteorology Division

1. INTRODUCTION

Over the past few years, scientists at NCAR (National Center for Atmospheric Research) and NOAA (National Oceanic and Atmospheric Administration) have been collaborating to apply mixed-phase, bulk microphysics schemes to short-range operational numerical weather prediction. An important motivation for this work (under partial sponsorship of the Federal Aviation Administration) is to provide better guidance to the Aviation Weather Center of NCEP (National Centers for Environmental Prediction, part of the USA National Weather Service) for preparation of their icing forecasts.

2. BRIEF DESCRIPTION OF THE SCHEME

The particular scheme that is the subject of this paper is "Option 4" described in Reisner *et al* (1998, hereafter R), but with some modifications and enhancements. The original development of the scheme was motivated by a need to improve forecasts of inflight icing. The Reisner *et al* study developed a three-level bulk microphysical scheme, with each level introducing increasing complexity. Option 3 (lowest level) only predicted mixing ratios of cloud water, rain, ice and snow. Option 4 added the ability to predict number concentration of ice and mixing ratio of graupel, as well as introducing a variable N_0 of snow into the scheme.The highest-level scheme was a two-moment scheme that added the ability to predict number concentrations of snow and graupel in addition to that of ice. All four schemes use the Marshall-Palmer inverse-exponential particle-size distribution for rain, snow and graupel.

These schemes were run for observed icing cases occurring during the Winter Icing and Storms Project (WISP, Rasmussen *et al.* 1992) with the Penn State/NCAR Mesoscale Model (MM5, Grell *et al.* 1994) and were shown to produce reasonable predictions of supercooled liquid water for two well-observed cases. Based on these favorable results it was decided to implement this scheme into the Rapid Update Cycle (RUC) model.

Corresponding author address: John M. Brown, NOAA/Forecast Systems Laboratory, Mail Code R/E/FS1, 325 Broadway, Boulder CO 80303 USA E-Mail: jmbrown@fsl.noaa.gov

3. OPERATIONAL APPLICATION

The Rapid Update Cycle (RUC, Benjamin *et al.* 1999) is a four-dimensional atmospheric data assimilation and coupled land-atmosphere prediction system run at the National Centers for Environmental Prediction. The name RUC derives from its use as a vehicle for rapid updating and dissemination of analyses and very short term forecasts: analyses and forecasts are produced every hour by combining the latest 1-h model forecast with data received during the hour since the data cutoff for the previous analysis. Three-hour forecasts are produced every hour and 12-h forecasts every 3h. A distinctive aspect of the atmospheric component of RUC is its use of a hybrid sigma-isentropic vertical coordinate. Further, the forecast-model code has been written such that physics routines from MM5 can be easily adapted to run in RUC.

As mentioned above, it was decided to implement option 4 of the Reisner microphysics scheme into the Rapid Update Cycle operational system. This option was chosen because it was the lowest order scheme that produced reasonable forecasts in the Reisner *et al* study, allowing for an acceptably small impact on the operational system. In order to avoid having to "spin-up" clouds and precipitation at the start of each forecast, the 1-h forecast of the liquid and solid hydrometeor mixing ratios from the previous hour's run are passed into the next analysis without modification. (A real-time satellite-based cloud analysis is under development but will not be discussed at this conference.)

4. RECENT MODIFICATIONS

Operational experience with the initial implementation of the option 4 microphysics in RUC, corroborated by real-time forecasts and case-study simulations using MM5, revealed a number of unexpected behaviors. These included:

1) excessive graupel at both high levels (temperatures below -25° C) even when vertical motions are weak, and also just above the melting layer;

2) lower than expected amounts of supercooled liquid water;

3) unrealistically high cloud-ice number concentrations approaching $10^8/m^3$;

4) unrealistically small snow mixing ratios.

Careful reexamination of the code as well as use of a 2-dimensional version of MM5 capable of running either Reisner option 4 or a detailed microphysics code [companion paper by Rasmussen and Geresdi (2000), this conference] has led to a number of improvements to the code that have addressed these problems. In addition, the use of 10-min time steps in the operational implementation of Reisner option 4, necessary to meet operational run-time requirements on NCEP's old C90 Cray computer, was found to be a major contributor to graupel build-up.

Major changes to option 4 of R that address the above problems include the following.

1) Abandonment of the Fletcher curve (Fletcher, 1962) for ice nucleation as a function of temperature in favor of a more recent curve proposed by Cooper (1986) that leads to less aggressive ice nucleation at colder temperatures.

2) For both vapor deposition on snow and graupel, and for riming of snow or graupel by collection of supercooled cloud water, the assumed particle size distributions of both snow and graupel have been modified to a Gamma distribution in order to reduce the number of small particles. Further, as described in R (Eq A.43; Ikawa and Saito, 1991), there formerly was an explicit time-step dependence in the expression describing the rate of graupel formation as result of riming on snow. This is now replaced by a procedure of Murakami (1990) that is independent of time step: if depositional growth of snow is larger than riming growth, all riming growth of snow goes to augment snow, whereas if riming growth of snow exceeds depositional growth, riming growth of snow goes to augment graupel.

3) Extensive revision was made to calculations of cloud-ice number concentration to make this more consistent with mixing-ratio changes and to properly account for riming of cloud ice.

4) In order to more accurately simulate the production of supercooled drizzle droplets, a major icing hazard, through the collision-coalescence process in supercooled cloud layers, the zero intercept for the size distribution of raindrops has been increased from $0.8*10^6$ to 10^{10} m^{-4} for rain water mixing ratios less than 0.1 g/kg and the autoconversion threshold from cloud water to rain water changed to 0.35 g/kg based on comparison to detailed simulations of freezing-drizzle formation.

5) Numerous other changes have been introduced to improve internal consistency.

6) We are investigating the efficacy of lookup tables in reducing computation time.

5. RESULTS

At this writing (April 2000), the revised option 4 of Reisner *et al* as implemented into RUC is undergoing further testing. We anticipate that by the time of the conference an upgraded, higher-resolution version of the RUC, including the revised option 4, will be operational at NCEP. In our poster we will show comparison runs illustrating the impacts of these and other changes from the older operational version used since 1998.

6. ACKNOWLEDGEMENTS

This research is in response to requirements and funding by the Federal Aviation Administration. The views expressed are those of the authors and do not necessarily represent the official policy of the U. S. government.

7. REFERENCES

Benjamin, S.G., J.M. Brown, K.J. Brundage, D. Kim, B.E. Schwartz, T. Smirnova, and T.L. Smith, 1999: Aviation forecasts from the RUC-2. Preprints, Eighth Conference on Aviation, Range, and Aerospace Meteorology, Dallas TX. Amer. Meteor. Soc., 486-490.

Cooper, W. A., 1986: Ice initiation in natural clouds. AMS Meteor. Monograph, 21, [R. G. Braham, Jr., Ed.], Amer. Meteor. Soc., Boston, 29-32.

Fletcher, N. H., 1962: The Physics of Rainclouds. Cambridge University Press, 386 pp.

Grell, G., J. Dudhia, and R. Stauffer, 1994: A Description of the Fifth-Generation Penn State/NCAR Mesoscale Model (MM5). National Center for Atmospheric Research Technical Note NCAR/TN-398+STR, 138pp.

Ikawa, M., and K. Saito, 1991: Description of a non-hydrostatic model developed at the Forecast Research Department of the MRI. Technical Reports of the Meteorological Research Institute Number 28.

Murakami, M., 1990: Numerical modeling of microphysical and dynamical evolution of an isolated convective cloud--the 19 July 1981 CCOPE cloud. J. Meteorol. Soc. Japan, **68**, 107-128.

Rasmussen, R. M., and I. Geresdi, 2000: Freezing drizzle and supercooled large droplet (SLD) formation in stably stratified layer clouds: Results from detailed microphysical simulations and implications for aircraft icing. International Conference on Clouds and Precipitation, Reno NV, this volume.

Rasmussen, R. M., *et al.*,1992: Winter Icing and Storms Project (WISP). Bull. Amer. Meteorol. Soc., 73, 951-974.

Reisner, J., R. M. Rasmussen, and R. Bruintjes, 1998: Explicit forecasting of supercooled liquid water in winter storms using the MM5 model. Quart. J. Roy. Meteorol. Soc., **124**, 1071-1107.

Simulation of a Severe Snowstorm over the Black Hills with the Operational Multi-scale Environment Model with Grid Adaptivity (OMEGA)

YI JIN, R. A. SARMA, D. P. BACON, T. J. DUNN, N. N. AHMAD, Z. BOYBEYI, S.G.GOPALAKRISHNAN, M. S. HALL, P. C. S. LEE, R. MADALA, D. MAYS, M. D. TURNER, AND T. WAIT

Center for Atmospheric Physics
Science Applications International Corporation
McLean, VA 22102, USA

1. INTRODUCTION

Accurate precipitation forecasting has been a challenging task for meteorologists over the past decades (Olson 1995). It was suggested that the slow progress in precipitation forecasting skill was partially due to the inability of the NWP model to explicitly simulate mesoscale precipitation systems (Moore and Blakley 1988). Difficulties in forecasting precipitation can increase dramatically when frontal precipitation is influenced further by the topography (Williams *et al.* 1992; Houze 1993; Doyle 1997).

In the current study, the Operational Multiscale Environment Model with Grid Adaptivity (OMEGA) is employed to simulate a Black Hills snowstorm case with variable synoptic environment and localized high precipitation centers. There was as much as 24-mm water-equivalent snowfall observed in the Black Hills during 8-11 April 1995 (Farley 2000). This Black Hills case has been chosen specifically to test the microphysics package of OMEGA and to evaluate OMEGA's performance in forecasting frontal systems and a localized severe snowstorm in a region with complex terrain features.

2. MODEL DESCRIPTION

OMEGA, a fully non-hydrostatic three-dimensional simulation system for real-time weather and hazard forecasting, is based on an adaptive unstructured triangular prism grid that is referenced to a rotating Cartesian coordinate system (Bacon *et al.* 2000). Operationally oriented, OMEGA includes a bulk water microphysics scheme, which involves an interchange between water vapor, cloud droplets, ice particles, rain drops, and snow flakes (Lin *et al.* 1983). One important feature of OMEGA is that the unstructured grid allows for an increase in local resolution to better capture topography and the important physical features of the atmospheric circulation and cloud dynamics.

Corresponding author's address: Yi Jin, Center for Atmospheric Physics, MS 2-3-1, Science Applications International Corporation, 1710 Goodridge Drive, McLean, VA 22102, USA; E-Mail: jin@apo.saic.com.

3. SYNOPTIC OVERVIEW

During the period of 8-11 April 1995, a stationary front of large spatial extent slowly crossed the eastern two-thirds of the US. An initially weak high-pressure center in south-central Canada developed into a massive

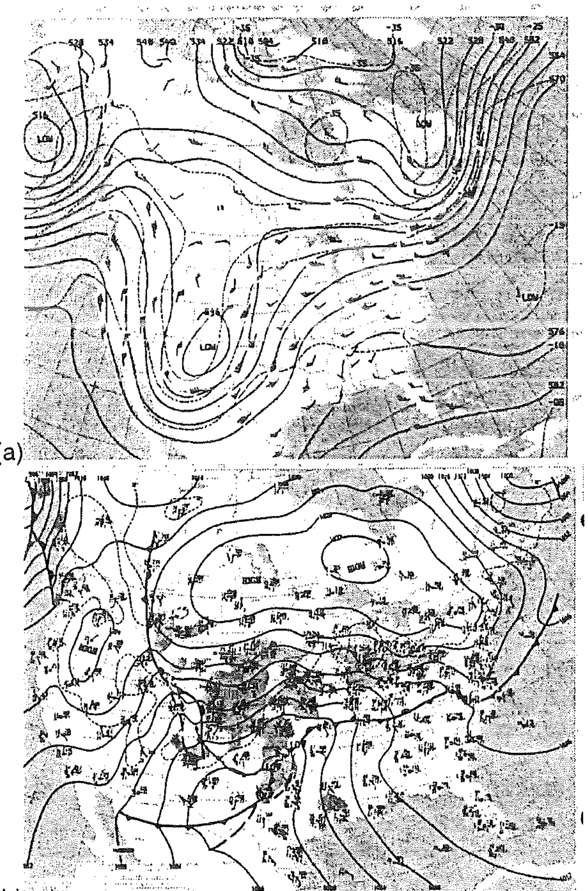

(a)

(b)

Figure 1 NWS 500-mb (top) and surface (bottom) analysis for 1200 UTC 10 April 1995.

system, occupying a vast area of southern Canada by 1200 UTC 10 April (Figure 1b).

The 500-mb observational analysis shows that there was zonal flow over the US on 8 April. In the course of the next 72 hours, a weak ridge formed over North and

South Dakota, ahead of a rapidly deepening trough to the southwest. The westerly polar-jet along the southern edge of the deepening trough had a maximum speed of 75 kt initially and it strengthened to 95 kt over central Texas by 1200 April 10 (Figure 1a). Corresponding to the 500-mb trough, a surface low-pressure center developed in the central US. A wide band of precipitation associated with the fronts extended from the central to the northeastern US. Snowfall persisted from 9 to 11 April in the Black Hills.

4. OMEGA RESULTS

Two simulations have been performed for this case: Test 1 and Test 2. Both simulations have the model top at 16.5 km and 33 vertical levels. The 12-hourly ETA analysis was used to produce the initial fields and boundary conditions. The domain for Test 1 covers an area from 110W to 90W longitude, and from 35N to 50N latitude at a relatively coarse resolution (30-60 km). The results from Test 1 indicates that OMEGA captures the synoptic systems very well, including the surface fronts, the large precipitation band, and the 500-mb trough and ridge systems.

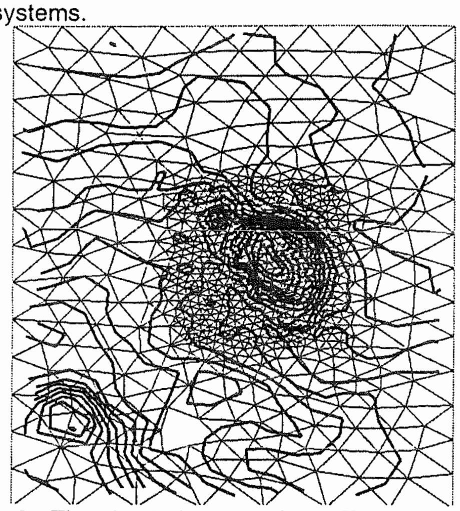

Figure 2. The simulation domain for Test 2. Terrain is contoured at 100 m intervals (thick lines)

The simulation domain for Test 2 covers a smaller area (106.5W-102W; 41.5N-46.5N, Figure 2), focusing on the area surrounding the Black Hills at a higher resolution (5 to 10 km). This test is designed to examine in more detail the precipitation fields, which are compared with the detailed precipitation observations. The following discussion concentrates on the Test 2 results only.

4.1 Test 2: High Resolution Simulation

The observed and simulated 4-day total precipitation is shown in Figures 3a and 3b, respectively. The quantitative comparisons between the observed and simulated values are summarized in Table 2. Precipitation centers H1, H3, and H4 are captured by OMEGA near the observed location with the amount very close to the observations. Precipitation accumulated at H6 in the simulation has a value (13.5 mm), compared reasonably well with the observed value (11 mm) near the observed location although it is shifted to the east by about 15 km in the simulation.

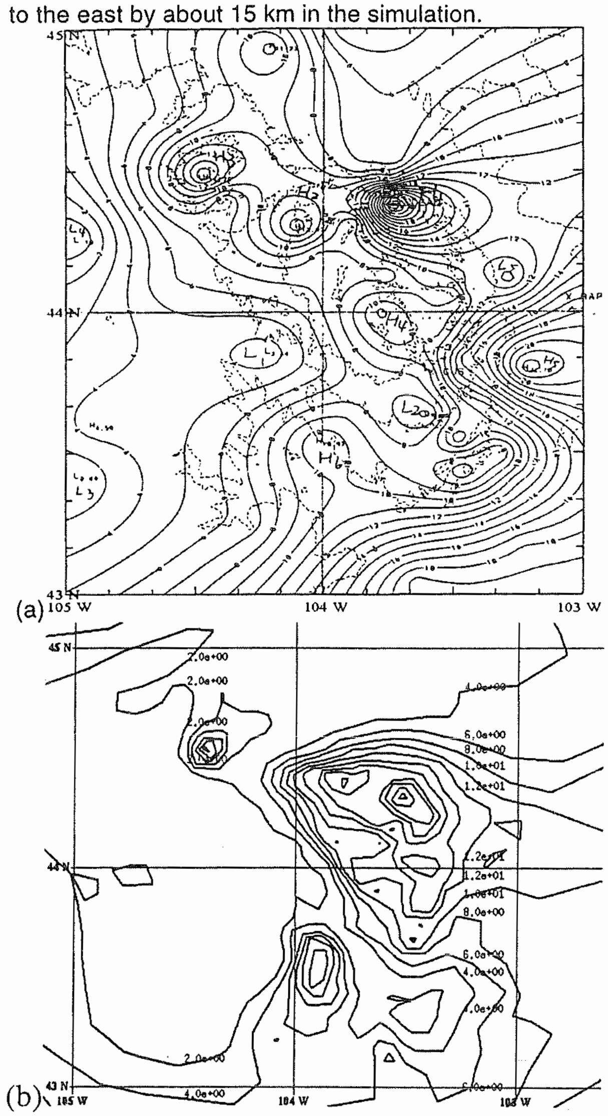

Figure 3. Observed (a) and simulated (b) four-day total precipitation fields (mm).

Precipitation center H2 in the simulation results, however, has too high precipitation (20 mm compared to the observed 14 mm) and is displaced by about 40 km to the east of the observed center. The model does not capture precipitation center H5, at all. This precipitation maximum is part of the wide precipitation band observed to the north of the front. It is very possible that the small domain of Test 2 does not have enough information about the large frontal system. This argument is supported by the fact that Test 1 with the much larger domain captured H5, a 24-mm accumulated precipitation center at the right location. The

Table 1. Comparison of observed and simulated storm-total precipitation (mm) in the Black Hills region during April 8-11, 1995.

Center	Location	Observed	Simulated
H1	44.36N, 103.75W	24.41	25.3
H2	44.25N, 104.10W	13.97	20.1
H3	44.50N, 104.50W	14.78	12.5
H4	44.00N, 103.80W	11.00	12.2
H5	43.80N, 103.30W	22.70	9.9
H6	43.50N, 104.00W	10.97	13.5

comparisons clearly indicate that for the majority of large precipitation centers in the Black Hills, OMEGA predicts the accumulated precipitation amounts and locations at a high level of accuracy.

4.2 Microphysical Processes

During the simulated snowstorm event, the cloud droplet and rain fields remain zero and hence the microphysical processes are related to water vapor, ice particles, and snowflakes only. For precipitation center

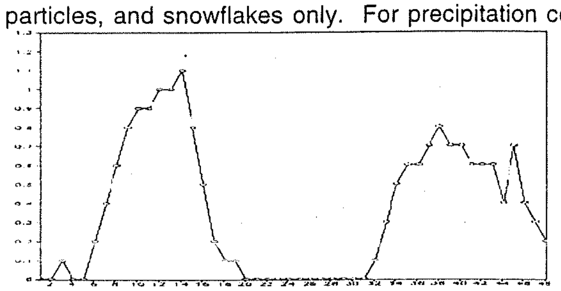

Figure 4. Simulated precipitation rate (mm h^{-1}) for H1. Time in hours since 1200 UTC April 9.

H1, the hourly precipitation rate shows two peaks: one from 1800 to 2300 UTC 10 April and the other from 2000 UTC 10 April to 1200 UTC 11 April (Figure 4). The most significant contribution to the snow formation is from the snow deposition process at the order of 10^{-7} to 10^{-6} s^{-1} with two peaks corresponding to those in the precipitation rates. The collection process of ice particles by snow occurs only for a short period during the first peak with a maximum of 10^{-7} s^{-1} near the surface. Positive ice deposition (vapor converted to ice) at a maximum rate of 10^{-7} s^{-1} process takes places at mid levels during the second precipitation peak. The ice deposition process is probably initiated by the ice nucleation at levels above starting about 4 hours earlier with a maximum of $2x10^{-7}$ s^{-1}. The time evolution of latent heat release shows a distribution remarkably similar to that of the snow deposition, with a maximum of $5x10^{-3}$ K s^{-1} during the first peak of precipitation rate at low levels while the latent heating/cooling from the other processes has negligible effects.

The time evolution of hourly precipitation at center H6 shows a single peak around 2200 and 2300 UTC on 10 April. The OMEGA simulation has about 60% of the total precipitation accumulated from 1800 UTC on 10 April to 0000 UTC on 11 April. As with precipitation center H1, the snow deposition process is more active (at least one order of magnitude greater) than the other microphysical processes. The latent heating from the snow deposition also dominates the latent heat release fields.

4.2 Dynamical Processes

Vertical cross-sections are constructed to display the airflow near precipitation centers H1 and H6. Our discussion here focuses on the airflow near H6.

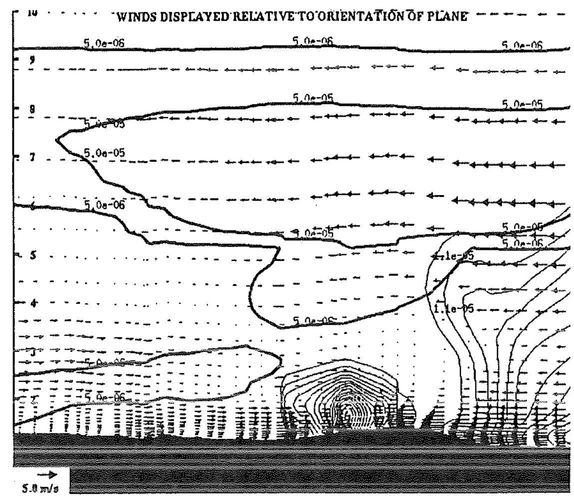

Figure 5. OMEGA Test 2 vertical cross-section from (43.5N, 105W) to (43.5N, 103W) valid for 1800 UTC 10 April 1995. Shown are the wind vectors in the plane, the precipitation concentration (thin lines) and contours indicating cloud concentration greater than $5x10^{-6}$ kg m^{-3} (thicker lines).

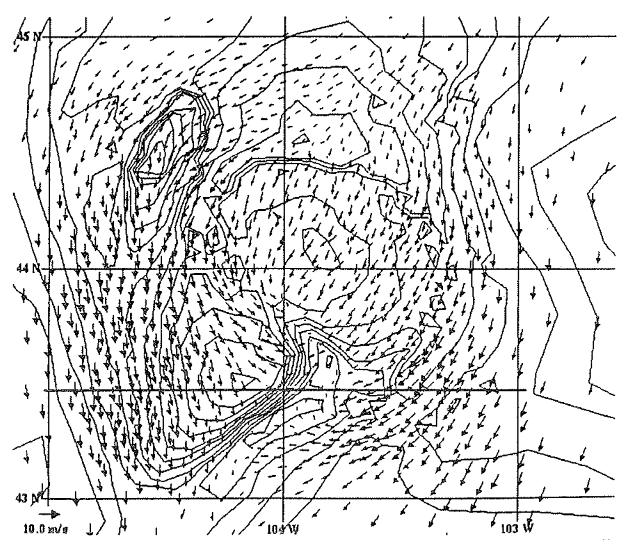

Figure 6. OMEGA Test 2 results valid for 1800 10 April, showing the surface wind vectors and water vapor fields (contoured). The thicker line shows the location of the vertical cross-section in Figure 5.

The flow across center H6 is illustrated in a west-east oriented vertical cross-section along the 43.5N latitude shown in Figure 6 at 1800 UTC 10 April (Figure 5). There is an elevation of about 1 km in terrain from East to West. The low-level winds are rather weak (3-4 m s^{-1}), and the two air streams converge near the top of the mountain, where the maximum snow concentration is present below the maximum ascent. A plan view of this area showing the water vapor contours and surface wind vectors (Figure 6) indicates that the convergence zone seen in the vertical cross-section results from the downstream convergence between the returning flow from the northerly flow deflected around the mountain and the flow across the mountain.

An important parameter to examine for the flow over mountains is the Froude number (Fr =U/NH, where U is the upstream wind; N the buoyancy frequency; and H the terrain height). When Fr<1, low-level flow can be blocked by the obstacle (Smith 1979). For the current case, Fr=U/NH=0.23. Part of the low-level northeasterly flow is deflected around the mountain. The other part of the flow continues to the southwest across the Black Hills. A partial blocking scenario is established in the Black Hills, similar to that simulated by Smolarkiewicz and Rotunno (1989). It is noteworthy that a stagnation point forms when the lateral deflected flow around the mountain meets the flow across the mountain on the lee-side of the mountain. Strong convergence occurs and hence upward motions are triggered there due to the partial blocking effect. However, precipitation is enhanced significantly only after the lower layers are destabilized when the surface heating starts around 1200 UTC 10 April. As mentioned above, 60% of the total precipitation is accumulated during the 6 hour period after 1800 UTC in A simulation.

A sensitivity test without the Black Hills terrain further supports the conclusion that localized centers of high precipitation in the Black Hills are due to the terrain forcing. This sensitivity test produced only 4 mm accumulated precipitation while the baseline simulation reproduced the 24 mm observed values. This study validates the cold water-ice microphysics of OMEGA and demonstrates its ability to forecast severe weather events at a high level of accuracy. It also demonstrates the power of such a simulation tool for understanding the microphysical and dynamical processes which govern these events.

5. ACKNOWLEDGEMENT

This work was supported by the Defense Threat Reduction Agency (DTRA) under contracts DNA001-95-C0130 and DTRA 01-99-C-0007. The authors would like to thank our Program Manager Mr. Ron Meris for his support. We would also like to thank Prof. Richard Farley of the South Dakota School of Mining and Technology and Dr. Qingyun Zhao of Navy Research Laboratory for their contributions to this work.

6. REFERENCES

Bacon, D. P., N. N. Ahmad, Z. Boybeyi, T. J. Dunn, M. S. Hall, P. C. S. Lee, R. A. Sarma, and M. D. Turner, 2000: A dynamically adapting weather and dispersion model: the Operational Multi-scale Environmental Model with Grid Adaptivity (OMEGA). *Mon. Wea. Rev.* (In press).

Doyle, J. D., 1997: The influence of mesoscale orography on a coastal jet and rainband. *Mon. Wea. Rev.*, **125**, 1465-1488.

Farley, R. D., D. L. Hjermstad, and H. D. Orville, 2000: Numerical simulation of a four-day early spring storm period in the Black Hills. *J. Appl. Meteor.* (in press).

Houze, R. A., 1993: Cloud Dynamics, Academic Press, 573pp

Lin, Y-L., Farley, R. D., and Orville, H. D., 1983: Bulk parameterization of the snow field in a cloud model. *J. of Clim. and Appl. Meteor.*, **22**, 1065.

Moore, J. T., and P. D. Blakley, 1988: The role of frontogenetical forcing and conditional symmetric instability in the Midwest snowstorm of 30-31 January 1982. *Mon. Wea. Rev.*, **116,** 2155-2171.

Olson, D. A., N. W. Junker, and B. Korty, 1995: Evaluation of 33 years of quantitative precipitation forecasting at NMC. *Wea. Forecasting,* **10,** 498-511.

Smith, R. B., 1979: The influence of mountains on the atmosphere. *Adv. Geophys.*, **21**, 87-230.

Smolarkiewicz, P. K., and R. Rotunno, 1989: Low Froude number flow past three-dimensional obstacles. Part I: Baroclinically generated lee vortices. *J. Atmos. Sci.*, **46,** 1154-1164.

Williams, R. T., M. S. Peng, and D. A. Zankofsi, 1992: Effects of topography on fronts. *J. Atmos. Sci.*, **49,** 287-305.

ELECTRICAL WIRE ICING AND THE MICROSTRUCTURE OF CLOUDS AND FOGS: EVIDENCE FROM HEAVY ICE AREA IN SICHUAN

Hesheng Zhou and Jianxi Liu

Sichuan Institute of Meteorology, Chengdu, Sichuan, 610072, P. R. China

1. INTRODUCTION

High and cold mountain area in Daliangshan, Sichuan is one of the heaviest icing areas in China. Heavy icing causes tremendous damages to wires used by industries such as electricity and telecommunication. Therefore, to study icing strength and its physical features has considerable practical implications. Basing on the electrical wire icing theory and using electrical wire icing data collected from observational spots, Guanri Tan analyzes the relationship between the thickness of ice of glaze, rime and mixed icing and the height from the ground. He finds that the ratio of the thickness of the ice from two height levels is a power function of the ratio of the two heights(1). In order to investigate the icing strength of high voltage electrical wires and its features, electricity engineers set up observational spots along the electricity transmission routes in Daliangshan mountain area, using a small glaze frame to study the icing strength. They also built the special ice observational station (the 2835 station, hereafter) at 2835 meters above the sea level (ASL hereafter) in heavy icing areas and set up four levels of electrical wires to investigate altitudinal variations of the icing strength. From January to March 1989, we investigated the microphysical features of the icing in some observational spots and obtained some important results.

2. THE ICE EXTREMUM AND ITS FEATURES IN DALIANGSHAN MOUNTAIN AREA

The heavy icing phenomenon in Daliangshan mountain area can be largely explained its meteorological conditions. The meteorological data from 1983 to 1990, collected at the 2835 station, show that (1) the lowest local temperature is –15.6 ^{0}C and the mean is 5.1^{0}C; (2) the annual largest precipitation is 1373.0 mm and the mean is 1303.0 mm; (3) the largest mean 10 minute wind speed is 22.7 m/s and the mean is 3.2 m/s; (4) annually, there are 234 precipitation days, 77 snowing days, 308 foggy days, 53 glaze days and 85 rime days.

2.1 The relation between the icing extremum at ice observational spots and the topographic and altitudinal characteristics of those spots

Along the 300 kilometer electricity transmission route, 12 ice observational spots were established. Wires with 28 mm diameter were set 2 meters above the ground along east-west and south-north directions. a small glaze frame was used to observe the icing phenomenon and the results show that the ice extremum along east-west direction is consistently larger than that along south-north direction. The results are reported in table 1. It shows that the ice extremum is topologically distributed. The heaviest wire icing occurred at the narrow and deep drought, secondly heavy at the windward and the lightest at the lees. The ice extremum is related to temperature. In general, below 0^{0}C, the higher the temperature is, the heaviest the ice is. Wind speed has significant influence on the ice extremum also. When the wind speed is high, the ice extremum is usually low. Even when the ice extremum is the largest, the wind speed is not high, only 2.2 m/s. The highest wind speed is only 4.2 m/s and there are three stationary wind records. The mean wind speed is less than 1.5 m/s. As far as the altitude is concerned, the variation of the ice extremum according to the change in altitudes is conditional upon topological changes. The higher the altitude is, the lower the ice extremum at the narrow and deep draught is, but the higher the ice extremum at the windward and the lee. The most severe icing is observed at No. 12 observational spot (No.12, hereafter), a narrow and deep draught (ice weight of 24200 g/m, density 0.39 g/cm^3, temperature –1.0^{0}C, north wind, wind speed 2.2 m/s and altitude 2081 meters ASL.).

Corresponding author's address: Hesheng Zhou
Sichuan Institute of Meteorology, Chengdu,
Sichuan, 610072, P. R. China
E-Mail: zhouhs@mail.sc.cninfo.net

Table 1 The ice extremum for ice observational spots (1984-1990) (2)

Observational Spots	Altitude (ASL)	Ice Weight (g/m)	Density (g/cm^3)	Temperature (^0C)	Wind Direction	Wind Speed (m/s)
1	2830	3600	0.22	–6.4	NE	2.4
2	2923	1680	0.17	–7.8	N	1.2
3	2940	4400	0.16	–7.8	NE	1.5
4	2994	5824	0.26	–5.0	W	4.2
5	2872	4160	0.20	–6.2	NE	0.6
6	2848	3360	0.20	–6.3	NE	0.7
7	3031	1120	0.19	–6.5	NE	1.2
8	2939	2576	0.49	–4.9	S	2.0
9	2511	9768	0.35	–5.8	C	-
10	2470	3040	0.38	–4.6	C	-
11	2476	1736	0.49	–6.0	C	-
12	2081	24200	0.39	–1.0	N	2.2

1. Lee 2. The wide and shallow draught 3. Windward 4. The narrow and deep draught
5. Windward 6. Lee 7. Hillside 8. Hillside 9. The narrow and deep draught 10. Windward
11. Lee 12. The narrow and draught

2.2 The relation between the ice extremum at the 2835 station and the height above ground and meteorological conditions

In order to investigate the variation of icing strength on electrical wires according to the variation of their heights above the ground, four levels of wires were set up at the 2835 station, their heights are 2 meters, 9 meters, 16 meters and 23 meters respectively. On each level, there are four groups of wires, with wire diameter 4 mm, 11 mm, 19 mm and 28 mm respectively, along east-west and south-north directions. Consecutive 8 years of ice and meteorological investigations showed that the extreme icing always occurred on east-west direction. Table 2 shows the results.

Table 2 The ice extremum for the 2835 station (1983-1990) (2)

Year	Level	Wire Diameter (mm)	Ice Weight (g/m)	Ice Density (g/cm^3)	Temperature (^0C)	Wind Direction	Wind Speed (m/s)
1983	2	28	5923	0.11	-9.0	C	-
1984	3	28	3112	0.13	-10.6	SW	1.2
1985	3	28	8308	0.22	-1.9	NW	2.7
1986	3	19	5744	0.18	-3.3	SW	1.2
1987	3	28	3480	0.30	-1.0	NNE	2.7
1988	3	19	3452	0.28	-9.4	SE	1.0
1989	3	19	11772	0.19	-6.6	ENE	0.6
1990	4	28	3744	0.16	-5.4	NNE	1.9

Table 2 shows that, among consecutive 8 years of investigation, the extreme icing occurred on the third level, which was 16 meters above the ground, in 6 years (75% of the total observations). The extreme icing occurred on level 2, which was 9 meters above the ground, and level 4, which was 23 meters above the ground, once individually. No extreme icing occurred on level 1, which was 2 meters above the ground. The ice extremum does not monotonically increase with the increase of the height above the ground. The ice extremum varies dramatically from year to year. The highest ice extremum occurred in 1989 with ice weight 11772 g/m. The lowest ice extremum occurred in 1984 with ice weight only 3112 g/m. The former is 3.5 times heavy of the latter. When the extreme icing occurred, wind speed was typically low, usually less than 2.7 m/s. Wind direction is not necessarily orthogonal to the direction of the wires and temperature is usually no lower than –10.0 ^{0}C.

3. THE CLOUD AND FOG MICROPHYSICAL FEATURES AND METEOROLOGICAL CONDITIONS IN DALIANGSHAN MOUNTAIN AREA

From January to March 1989, we carried out gradational investigations for the cloud and fog microphysical features and meteorological conditions of Daliangshan mountain area. The investigations were conducted at levels 1 (2 meters above the ground), 3 (16 meters above the ground) and 4 (23 meters above the ground) of the 2835 station and at No. 12 (2 meters above the ground). The sampling period was 0.1 second to get droplets. During the observation period, we collected 245 droplet spectrum samples totally, of which 97% were distributed in single peak shape. Super-cooling cloud drops were the major components of cloud and fog, and ice particles were seldom observed. Usually the sampling took 15 to 40 seconds to observe the liquid water content by the absorbed water method. Totally there were 686 liquid water samples. Among them, those collected at the 2835 station were collected from the middle of clouds with temperature under 0^0C (the mean was -7.2^0C) and mean relative humidity 92%. At No. 12, we collected the samples from the bottom of clouds with mean temperature -2.5^0C. The frequency for temperature to below 0^0C was 75% and the relative humidity was 98%.

3.1 The average droplet spectrum distribution and the variation of microphysical parameters

We took the average droplet spectrum from level 1 of the 2835 station and No. 12 and their distributions largely follow Khrgian-Mazin distributions.

$$n(r) = ar^2 e^{-br} \qquad (1)$$

In equation (1): n(r) is the number density, n(r)dr is the number of droplets per unit volume of radii between r and r+dr ; r is the radius of droplets; a and b are parameters determined by experience data.

Based on droplet spectrum collected from levels 1, 3 and 4 of the 2835 station and No.12, we computed N_m (the mean total number of droplets per unit volume) and r_m (the mean radius) for the droplets at each spot. Using equation (1) we can simulate the experience parameters a and b, and then use the droplet spectrum distribution function simulated for each spots to compute W_m (the mean liquid water content per unit volume) and r_w (the radius of cloud drops that contributes most to the liquid water content). The values of those parameters are reported in table 3.

Table 3. Cloud and fog microphysical parameters from each spot

Spots	a(10^{12}/cm^6)	b (10^4/cm)	N_m (/ cm^3)	r_m (um)	W_m (g/m^3)	r_w (um)
level 1	36.230	0.588	356	5.1	0.441	8.5
level 3	40.301	0.588	396	5.1	0.490	8.5
level 4	36.544	0.566	403	5.3	0.559	8.8
No. 12	129.738	0.714	712	4.2	0.492	7.0

Table 3 shows that the values of the cloud and fog microphysical parameters for the 2835 station and No.12 are significantly different. The mean total number of droplets per unit volume of the former is twice as large as that of the latter. Although the liquid water content is similar for two spots, but the mean radius of cloud drops and that of droplets contributing most to the liquid water content for the former are 1.2 times of those for the latter. At the 2835 station, droplet number, liquid water content, mean radius of droplets and that of droplets contributing most to the liquid water content increase slightly as the height (above the ground) of the sampling locations increase. These results are consistent with the finding that the electrical wire icing strength increases as the height (above the ground) of the wire increases[1].

3.2 The relation between liquid water content and temperature

Taking averages of the observed liquid water content by the absorbed water method at the 2835 station and No.12 under different temperatures, we find that super-cooling liquid water content in cloud and fog is closely related to the temperature.

Liquid water content is positively related to the temperature. The temperature is largely linearly related to the logarithmic values of liquid water content. This relation can be described by equation (2).

$$W = ae^{bt} \qquad (2)$$

In equation (2): W is the liquid water content (g/m^3); a (g/m^3) and b (l/^{0}C) are experience parameters; t (^{0}C) is the temperature

Basing on the liquid water content and temperature data collected from the three levels at the 2835 station and using equation (2), we get equation (3).

$$W = 0.241e^{0.128t} \qquad (3)$$

Applying temperature data in equation (3), we calculate liquid water content. The deviation of the estimated values from the observed data is within 10% of the observed values. Liquid water content measured by the method absorbed water is smaller than the calculation results based on droplets pectrum. This difference is attributed to different sampling methods and sample volumes.

4. CONCLUSION

Our study of the electrical wire icing extremum, cloud and fog microphysical parameters and meteorological conditions in Daliangshan mountain area, Sichuan, China suggests the following:

1. The persistence of weather systems is the primary factor that determines electrical wire icing. The more persistent the weather systems are, the longer the wires are exposed in super-cooling cloud and fog and the more severe the icing is. To generate severe icing, the super-cooling cloudy and foggy weather usually persists for several days.

2. The ice extremum varies dramatically from year to year. In our consecutive 8 years of observation, we find that the ice extremum in the most severe icing year is 3.5 times of that of the lightest icing year.

3. Topographical features have significant impacts on the strength of icing. In super-cooling cloud and fog, the ice extremum is the largest at narrow and deep draught.

4. In super-cooling cloud and fog, cloud and fog particles are usually in liquid form. Mean droplet spectrum is approximately khrgian-Mazin distributed. Mean droplet density is hundreds of particles per cm^3 with mean radius 5 μ. The water content is exponentially related to the temperature.

5. Comparing the droplets collected from the 2835 station and those from No.12, we find that the mean total number of droplets per unit volume of the former is twice as large as that of the latter. At the 2835 station, mean drop radius and liquid water content increase as the height of the platform increases. This result is consistent with the finding that the strength of the electrical wire icing increases as the height of the wires increases.

5. ACKNOWLEDGEMENT

Field investigation in high and cold mountain area is a very hardy job. The ice observational spots are scattered along 300 kilometers. To collect the data is a difficult and even dangerous task. We are deeply grateful to our respectable colleagues who work yearly in that area.

6. REFERENCE

1. Guanri Tan, 1982, On the micro-climatological characteristics of icing on wires. ACTA METEOROLOGICA SINICA, 40, 1, 13-22, (in Chinese).

2. Southwestern institute of electricity, department of energy, 1991, Research report of Huangmaogeng ice observatory heavy icing route and anti-icing experiments, (inChinese).

3. Jingshang Zou, et al., 1982, The foundation of atmospheric physics, 138-141, Meteorological Press (in Chinese).

4. Sichuan institute of meteorology, 1989, Gradient observation of cloud, fog and meteorological conditions in Huangmaogeng heavy icing area, (inChinese).

EVALUATION OF A MIXED-PHASE CLOUD SCHEME'S ABILITY AT FORECASTING SUPERCOOLED LIQUID WATER IN CLOUDS

Paul A. Vaillancourt[1], André Tremblay, Stewart G. Cober and George A. Isaac

Meteorological Service of Canada, Dorval, Québec, Canada

1. SUPERCOOLED WATER

The presence of supercooled liquid water (SLW) in clouds is very common as shown by the numerous PIREP's reporting icing of various intensities. For example, Brown et al. (1997) counted over 14000 icing reports over a two-month period in the winter of 1994. There is also an abundance of more detailed observations of SLW made in a cloud physics research context either from research aircraft or remote sensing. For example, Isaac et al. (1998) presents an overview of the Canadian Freezing Drizzle Experiments (CFDE) I, II and III during which many aircraft measurements of SLW in both maritime and continental conditions were made with a special focus on environments containing drizzle sized supercooled droplets. The abundance of these observations suggests that liquid water may be present in most cold clouds (if temperature >≈ -20°C) at some point during their evolution.

There are three conditions for the formation of supercooled water. The temperature must be below zero, the relative humidity with respect to water must reach saturation and if solid phase is present, the condensate supply rate must exceed the ice crystal mass diffusional growth rate. Once formed, the fate of the supercooled cloud droplets can take several paths. In certain conditions, the SLW drops can grow by collision-coalescence to drizzle or rain sized drops. For example, both Politovich (1989) and Cober et al. (1996) observed drizzle in shallow stratiform cloud systems with relatively warm cloud tops (> -15°C). The clouds can become glaciated if seeded with ice crystals sedimenting from an ice cloud at higher altitudes. The SLW can move into a region where primary or secondary ice production becomes more active. More research is necessary in order to understand how fast and under what conditions these various freezing mechanisms can glaciate a cloud region composed of SLW.

2. WHY STUDY SLW?

The formation and lifetime of SLW in clouds is important to study because of two potential impacts on human activity. The first one is aircraft icing which can cause serious loss of aircraft performance capability and may result in accidents. The second impact on human activity is through its role in the generation of freezing precipitation(FP). For example, the ice storm of January 1998 that hit densely populated regions of Ontario and Québec caused 22 deaths and $1 billion-plus in damages.

Supercooled drizzle or raindrops may originate either from the melting of solid hydrometeors in a warm air layer (classical mechanism) or may involve the liquid phase only (non-classical mechanism). In the latter case, the process of collision-coalescence is thought to be the main process by which the cloud droplets grow to drizzle or raindrop size.

Several studies (Huffman and Norman 1988, Strapp et al. 1996) have examined sounding data at stations all over North America to determine the relative importance of these two mechanisms. These studies found that, depending on geographic location, between 30 and 75 percent of FP events could be attributed to the non-classical mechanism.

3. OBJECTIVES

This research is part of the ongoing effort of the Meteorological Service of Canada at providing useful and reliable forecasts of aircraft icing and freezing precipitation. The actual operational microphysical scheme provides only information on the presence or absence of SLW in clouds. To improve upon this, Tremblay et al. (1996) developed the mixed phase scheme (MXP). This scheme solves prognostically for the total water content while diagnostically solving for its partition between the solid and liquid phase depending on the condensate supply rate. This scheme has been successfully validated against satellite, radiosondes and surface observations (Tremblay and Glazer 2000). In order to validate other aspects of this scheme and to provide guidance for its further improvement, point by point comparisons of dynamical, thermodynmical as well as microphysical variables between in-situ aircraft data and model data were made.

More specifically, this research is aimed at answering the following questions:

1. Is the dynamical model providing the proper input for the microphysical scheme?
2. Is the MXP scheme forecasting the position and phase of clouds, as well as the cloud water content properly, in particular for supercooled water?

[1] Paul Vaillancourt, Meteorological Service of Canada, Dorval, Quebec, H9P 1J3, Canada
e-mail: paul.vaillancourt@ec.gc.ca

3. In mixed phase conditions, does the MXP scheme reproduce the observed climatology of the partition between solid and liquid water?

4. DATASET

We will make use of research aircraft data from two field experiments, CFDE I and CFDE III. CFDE I was conducted during March 1995 out of St. John's, Newfoundland. This campaign comprised 12 research flights for a total of 60 hours of data. Eleven of these flights were selected for comparison with the model simulations. CFDE III was conducted out of Ottawa from December 1997 to February 1998. This campaign comprised 26 research flights for a total of 105 hours of data. Ten of these flights were selected for comparison with the model simulations. The flights selected were those that were the longest and contained the most cloudy data points. Information on the research aircraft and its instrumentation can be found in Isaac et al. (1998).

The data used were 15 second averages, representing a length scale of ≈ 1.5 km. For the 21 flights selected, this represents a total of ≈ 21000 data points. The histogram presented in Fig. 1 shows the number of data points of each cloudy type observed as well as modeled (discussed in the next section). Approximately half of the observed data points were clear skies (twc < .02 g/kg). Out of the observed cloudy data points, approximately 36% contained only ice crystals, 28% contained only SLW (pure SLW), 28% contained both SLW and ice crystals (mixed) and 8% contained warm liquid (temperature > 0°C). Furthermore, approximately 27% of the cloudy points contain droplets larger than 100 microns in diameter. This percentage increases to 40% if the data points

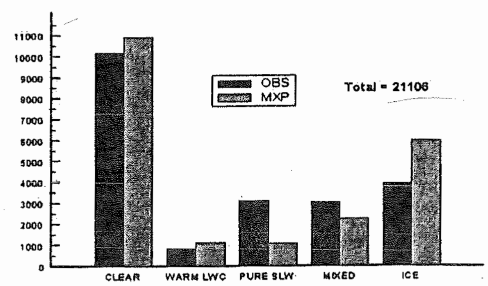

Figure 1: Histogram of cloud types

containing only ice crystals are excluded. The aircraft data, as well as other data such as radar or soundings when available, were carefully examined to determine the origin of the SLW for each data point where SLW is present. For a minimum of 75% of such data points, the SLW cannot be imputed to the supercooling of melted ice crystals. Furher details on phase assessment and differerences between CFDE I and CFDE III can be found in Cober et al. (2000).

5. MODEL AND EXPERIMENTAL PROCEDURE

The MXP scheme is used within a dynamical model comprising a full physics package. We use the fully compressible, three-dimensional, non-hydrostatic, semi-implicit, semi-Lagrangian MC2 (Mesoscale Compressible Community) model (Benoit et al. 1997). All simulations were 24-hour long runs initialized at 0 UTC from the CMC (Canadian Meteorological Center) analysis. The grid resolution was 35 km, the timestep was two minutes and 40 vertical levels were used. The simulated domain for the CFDE I cases comprised the north-east portion of the North American continent as well as part of the North Atlantic ocean. The simulated domain for the CFDE III cases comprised most of the North American continent.

The basis of the evaluation of the model performance is a point by point comparison of each pertinent variable along the real and "virtual" aircraft trajectories. The model is fed the aircraft trajectory in terms of the latitude-longitude points. For each of these points the model calculates the closest grid point. During its execution, the model outputs specified variables (e.g. temperature, total water content ...) at all vertical levels and every timestep for all such grid points. After model execution, the virtual aircraft trajectory is constructed by choosing, for every observed data point, the closest available model data point in terms of time, pressure level and latitude-longitude position.

It should be noted that such a comparison constitutes a very severe test for a NWP model. Given that the effective resolution of the initial conditions provided by the analysis is of the order of 100 kilometers (directly related to the density of the observation network and the data assimilation technique), we cannot expect the timing and position of the modeled meteorological systems to be exact.

6. RESULTS

The results of the comparison of the 21 real and virtual flights are now presented. Fig. 2 shows the aircraft trajectory (top panel) as well as a comparison of the observed (middle panel) and modeled (bottom panel) cloud types along the trajectories shown on altitude vs time plots for the March 3rd 1995 flight. The definition of the symbols identifying the cloud types shown in the three panels can be found on the botton panel. The aircraft flew out of St John's Newfoundland into the cloudy region ahead of an approaching warm front. A low pressure system was located about 500 kilometers south of Newfoundland. The aircraft first flew north-east where it sampled some ice clouds that were approximately 3000 m deep. It then turned and flew south west until a point south of the Avalon peninsula. During this leg the aircraft sampled some ice clouds and encountered a few areas of mixed phase conditions at time ≈ 350 min.. The aircraft then flew along an east-west direction. In the western portion of this leg the aircraft again encountered ice clouds. However, in the eastern portion it sampled some sustained mixed phase conditions near the surface at time ≈ 425 min.. The aircraft then gained altitude and encountered some pure SLW below a 1000 m deep warm layer (time ≈ 440 and 460 min.). At approximately 460 min., the aircraft turned

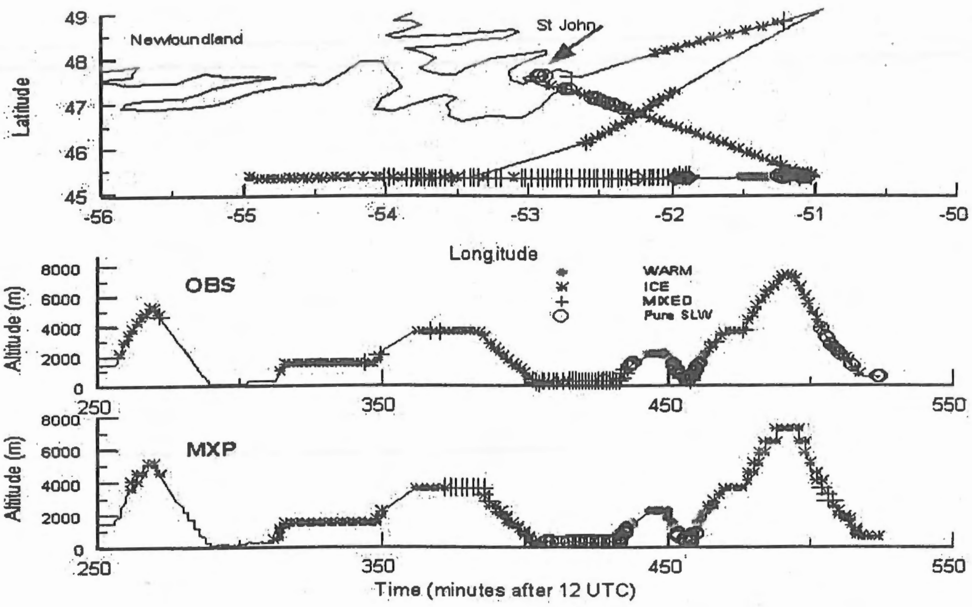

Figure 2: Aircraft trajectory, observed and modeled cloud types.

to fly north west where it sampled some pure SLW clouds on its approach towards St John's.

The comparison of the middle and botton panel shows that, for this case, the model has done a satisfactory job in terms of the position and phase of clouds. However, several differences can be seen. For example, around 425 min., the aircraft saw mixed phase conditions near the surface whereas the model produced pure SLW. Around 500 min. the aircraft sampled pure SLW while the model produced mixed phase.

Such qualitative comparisons were made for other measured variables, i.e temperature, wind speed, dew point temperature , total water content (TWC), solid water content (Qi), liquid water content (Qw) and SLW for all flights. More details on one particular flight (January 15th 1998) can be found in this volume (Tremblay et al. 2000). In general, we found that for approximately half the flights, the observation-model comparison is very encouraging. In several instances, there is clearly a timing difference between the observed and modeled meteorological situation that can explain a failed comparison.

Results over all flights will now be presented in a more quantitative and comprehensive manner. Fig. 1 shows the number of data points of each cloudy type observed as well as modeled. What is immediatly apparent in this figure is that the model under predicts the number of points where SLW can be found. It also over predicts the number of points where ice is found. Table 1 presents various statistics for the important variables. The first line gives the linear correlation between the observed and modeled variables, the two following lines gives the model and observed means respectively. The mean is calculated over the number of data points indicated lower in the table (Sample). Also included in the table is the mean error (bias), the mean absolute error (mean of the absolute value of the difference between the observed and modeled variable). For the water content variables, the number of points where the water content is non-zero is indicated. The correlation for the temperature, wind and dew point temperature is in general very good. The bias for temperature is negligible whereas there is a small negative bias (model is drier) for the dew point temperature. The correlations for the water contents are much smaller but still statistically significant given the large number of data points. The correlation for solid water content is much better than the correlation for liquid water content or supercooled liquid water content. Note also that the TWC is over-predicted essentially because the Qi is over-predicted almost by a factor of two. Eleven out of the twenty one cases have a correlation greater than 0.3 for TWC.

The performance of a NWP model is dependent on many aspects (e.g., initial conditions, resolution, physical parameterizations). In order to improve our microphysical scheme, we have made efforts to identify weaknesses which can be specifically imputed to it rather than to some other aspect of the complex NWP model. Fig. 3 shows the liquid water content as a function of solid water content for all data points which contain both (mixed). The lower left portion shows observed data points (circles) while the upper right portion shows the model data points (triangles). It can be seen that the microphysical scheme has difficulties producing larger values of liquid water content. These can be crucial for aircraft icing forcasts. Simulations with other more complex microphysical schemes have led us to the conclusion that this a problem inherent to Kessler

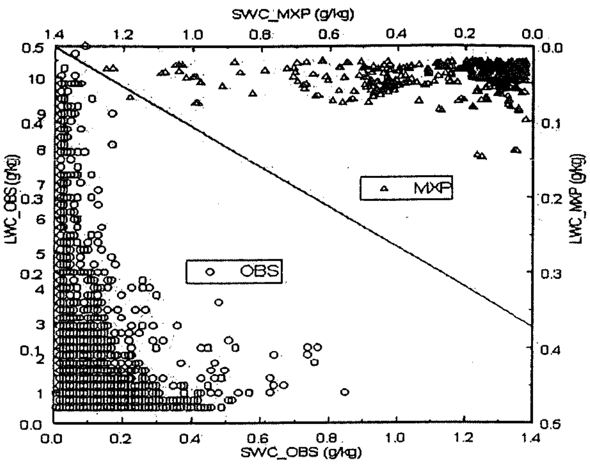

Figure 3: LWC vs SWC for mixed phase cloud type.

Table 1: Statistics for temperature, dew point temp., solid, liquid, total and supercooled water contents.

	T	TD	Qi	Qw	TWC	SLW
Correlation	0.97	0.87	0.355	0.139	0.285	0.116
Mean_MXP	-7.51	-11.64	0.062	0.016	0.078	0.011
Mean_OBS	-7.83	-10.61	0.031	0.037	0.068	0.033
Mean error	0.32	-1.03	0.031	-0.021	0.010	-0.022
Mean abs err	1.60	3.70	0.056	0.041	0.081	0.036
Sample	22221	22221	21076	21076	21076	21076
N_MXP			8331	4565	10632	3439
N_OBS			6966	7002	10925	6153

type parameterizations of rain water. Furthermore, by examining histograms of the fractional ice water content (Qi/TWC) for all mixed phase data points, it can be seen that for most observed data points the liquid phase is dominant while for most modeled data points the solid phase is dominant.

7. CONCLUSIONS

Even though the point by point comparison of the aircraft and model data is a very severe test given the possible errors in the initial conditions and the disparity in temporal and spatial resolution, we found the results very encouraging for about half the flights simulated.

We found that the model has more facility at predicting ice rather than water clouds. The model under predicts the presence and the quantities of SLW. Furthermore, where mixed phase is present in the model, the ice phase dominates rather than the liquid phase as in the observations.

8. ACKNOWLEDGMENTS

The authors would like to acknowledge the financial support of the National Search and Rescue Secretariat, Transport Canada, and Boeing. Measurements were made by the technical and scientific staff of MSC and the National Research Council of Canada (NRCC) using the NRCC Convair-580 research aircraft.

9. REFERENCES

Benoit R., M. Desgagne, P. Pellerin, S. Pellerin, Y. Chartier and S. Desjardins, 1997: The Canadian MC2: A semi-lagrangian, semi-implicit wideband atmospheric model suited for finescale process studies and simulation. *Mon. Wea. Rev.*, **125**, 2382-2415.

Brown B. G., G. Thompson, R. T. Bruintjes, R. Bullock, and T. Kane, 1997: Intercomparison of in-flight icing algorithms. Part II: Statistical verification results. *Wea. Forecasting*, **12**, 890-914.

Cober S. G., J. W. Strapp, and G. A. Isaac, 1996: An example of supercooled drizzle drops formed through a collision-coalescence process. J. Appl. Meteor.,35,2250-2260.

Cober S. G.,G.A. Isaac, A. V. Korolev, and J.W. Strapp, 2000: Assessing the relative contributions of liquid and ice phases in winter clouds. *13th International Conference on Clouds and Precipitation*, Reno, Nevada.

Huffman G. J. and G. A. Norman, 1988: The supercooled warm rain process and the specification of freezing precipitation. *Mon. Wea. Rev.*, **116**, 2172-2182.

Isaac G. A., S. G. Cober, A. V. Korolev, J. W. Strapp, and A. Tremblay, 1998: Overview of the Canadian Freezing Drizzle Experiment I, II and III. *Proceedings of the AMS annual Conference on Cloud Physics*, Everett, Washington, 447-450.

Politovich M. K., 1989: Aircraft icing caused by large supercooled droplets. *J. Appl. Meteor.*,**28**,856-868.

Strapp J. W., R. A. Stuart, and G. A. Isaac, 1996: A Canadian climatology of freezing precipitation and a detailed study using data from St John's, Newfoundland. *Proceedings of the FAA International conference on Inflight Aircarft Icing*, Volume II. 45-56. DOT/FAA/AR-96/81,II.

Tremblay A. and A. Glazer, 2000: An improved modeling scheme for freezing precipitation. *Mon. Wea. Rev.*, **128**, 1289-1308.

Tremblay A., A. Glazer, W. Yu and R. Benoit, 1996: A mixed-phase cloud scheme based on a single prognostic equation.. *Tellus*, **48A**, 483-500.

Tremblay A., P. A. Vaillancourt, S. G. Cober, and G. A. Isaac, 2000: Verification and sensitivity experiments for the mixed phase scheme forecasts.- Preliminary results. *13th International Conference on Clouds and Precipitation*, Reno, Nevada.

THE USE OF A SET OF 3-D NONHYDROSTATIC NUMERICAL MODELS WHEN SOLVING THE PROBLEMS RELEVANT TO THE AIRCRAFT FLIGHTS SAFETY, AND STUDY OF THE FORMATION OF FOG, CLOUDS, AND PRECIPITATION

V.G.Bondarenko and G.W.K. Moore
University of Toronto, Department of Physics
60 St. George Street, Toronto, Ontario, Canada M5S 1A7
e-mails:vbond@atmosp.physics.utoronto.ca; moore@atmosp.physics.utoronto.ca

1. HAZARDOUS WEATHER EVENTS

One of the causes of aircraft accidents is weather conditions unfavourable for air traffic. From information published by ICAO, unfavourable weather conditions were a direct cause of aviation accidents in 6-20 percent of cases out of the total number of accidents over a long time period. If we take also into account such accidents where the weather was an indirect cause , then the contribution of meteorological factors will amount to 30% and even more. Next to thunderstorms, ice is probably the weather hazard of greatest concern to pilots, especially those who spend a lot of time at relatively low altitudes.

A major part of aviation accidents (ICAO) occurring when aircraft came close to the ground were accounted for weather conditions in 66% of cases.

Such phenomena as fogs and low clouds are considered hazardous weather events since the conditions become most unfavourable for aircraft landings and take-off. Sharp temperature contrasts and ordered airflow motions in complex terrain lead to the formation of fogs along the slopes and orographic clouds which affect the safety of aircraft flights in a mountain area. Thus the problem on aviation safety in complex terrain should be solved by taking into account the combination of interacting dynamical and radiation factors, the processes governing the formation of clouds, fogs and precipitation which affect the aircraft flight.

The NTSB lists 40 to 50 accidents resulting annually from airframe ice; approximately the same number stem from induction system ice (Aircraft Icing,1998). The effect of snowstorms should be mentioned as it accounts for 6% of accidents due to weather conditions. Other weather events are responsible for 1 or 3 percent of aircraft accidents.

Hazardous weather events have been the subject of numerous accident prevention programs and field experiments. At the present time, efficient techniques including measurement technologies and analysis methodologies, as well as numerical weather modeling techniques have been developed at NCAR,USA, and CAO, Russia . Warning and prediction of icing conditions processes of fog and cloud formation, prediction of cloud ceiling and visibility quantitative detection and forecasts of snowfall have been extensively studied by many researchers , e.g. Mazin (1957), Khvorostyanov(1983), Kondratiev et al.(1992),Clark and Hall(1979), Rasmussen et al. (1998), Stoelinga and Warner (1999).

Moore and Peltier(1989); Moore (1996);Renfrew et al. (1999) have studied the Polar Low systems and precipitation regimes. Bernstein et al.(1997)developed the methodology of analysis the relationship between above-mentioned hazardous weather events. A 3D numerical model have been developed to simulate the dynamics of the thermal and orographically inhomogeneous Planetary Boundary Layer(PBL), and microphysics of clouds and precipitation , Bondarenko (1992, 1998).

2. MODELS DESCRIPTION

A set of 3D nonhydrostatic simulation model incorporate the following units:

i/ dynamics of the thermally and orographically inhomogeneous PBL;

ii/ hydrothermodynamics and microphysics of fogs, clouds and precipitation;

iii/ heat and moisture exchange with the underlying surface, and transport of heat in soils;

iv/ longwave and shortwave radiation transfer;

v/ transport and sedimentation of aerosols in a turbulent flow.

The model equations are solved in curvilinear coordinates connected with the relief profile (the relief function $X_3=\delta(X_1, X_2)$ is introduced).

$$\frac{\partial u_1}{\partial t}+div_a \bar{u} u_1+u_3\frac{\partial u_1}{\partial x_3}= =-\frac{\partial \pi'}{\partial x_1}+\frac{\partial \pi'}{\partial x_3}\delta_{x_1}+F_{u_1}+f_c(u_2-u_{20})+\frac{D u_{10}}{Dt}; \quad (1)$$

$$\frac{\partial u_2}{\partial t}+div_a \bar{u} u_2+u_3\frac{\partial u_2}{\partial x_3}= =-\frac{\partial \pi'}{\partial x_2}+\frac{\partial \pi'}{\partial x_3}\delta_{x_2}+F_{u_2}-f_c(u_1-u_{10})+\frac{D u_{20}}{Dt}; \quad (2)$$

$$\frac{\partial u_3}{\partial t}+div_a \vec{u} u_3+\tilde{u}_3\frac{\partial u_3}{\partial x_3}= =-\frac{\partial \pi'}{\partial x_3}+\lambda_s\theta'+F_{u_3}; \quad (3)$$

$$\frac{\partial u_\alpha}{\partial x_\alpha}=0;\ \tilde{u}_3=u_3^d-u_1\delta_{x_1}-u_2\delta_{x_2} \quad (4)$$

In Equations (1) through (4) the following symbols have been used: u is the 3-D wind vector; θ the average potential temperature; π' describes a deviation from background pressure (π_0); u_0, V_0 are horizontal components of the background wind; div_a the horizontal advection operator; $\delta_{x_1}, \delta_{x_2}$ are tangents of the relief's slope on the x and x coordinates; f_c is the Coriolis parameter, F_u are the Reynolds stresses, where $F_u \sim D_x$.

When describing the evolution of a three-phase hydrometeor system, the following particle types are considered: cloud and rain droplets, ice crystals and agglomerates (tiny pellets of snow and snow flakes).

In the formulated model for detailed description of the polymodal particle spectra the distribution of liquid and solid particles in size and mass is given through superposition of the gamma and exponential distributions (a short series).

$$F_i = F_{1i} + F_{2i} + F_{3i} \tag{5}$$

Thus, the liquid water (and ice crystal) phase in the model is divided into three categories: F_{1i} describes the generation of droplets and crystals, F_{2i} is the cloud water (ice content) and F_{3i} is the rainwater (or sedimenting ice crystals) falling through the air.

When making the parametrization, let us assume that the cloud drop (or ice crystal) spectra are approximated by a gamma-distribution of particles on sizes F_{j1}, or masses F_{j2} $(j=1,2)$. The distribution functions may be written

$$F_{ji}(r_{ji}) = \frac{N_{ji}\,\beta_{ji}^{\alpha_{ji}}\, r_{ji}^{\alpha_{ji}-1}}{\Gamma(\alpha_{ji})} \exp(-\beta_{ji} r_{ji}), \tag{6}$$

The equations of the thermohydrodynamics are supplemented with the transport equations for each of the categories of hydrometers - for droplet/crystal concentration N_{ji}, liquid water/ice mass q_{Lji}, and an additional equation for calculating average radii of droplets r_{1i}.

Equations for the supersaturating vapor density over pure water (S1), solutions (S 1s) and crystals (S 2) are solved.

$$\frac{\partial S_i}{\partial t} + P_i S_i + Q_i = 0, \quad P_i = P_i(\tau_i^{-1}),\ Q_i = Q_i(q_{si}) \tag{7}$$

where q_{s1}, q_{s2} are saturating humidities, $\tau_i^{-1} = 4\pi D N_i r_i \beta_i K_f$ is the time of phase relaxation of droplet and crystals, K_f are the correction coefficients.

The rate of transformation of cloud particle spectra may be expressed as

$$\frac{\partial R_L^P}{\partial t} = pK_i S_i \beta_i^{2-p_i}\frac{\Gamma(\alpha_i+p_i-2)}{\Gamma(\alpha_i)} + p_i K_i b_i \beta_i^{5-p_i}\frac{\Gamma(\alpha_i+p_i-5)}{\Gamma(\alpha_i)} \tag{8}$$

3. NUMERICAL MODELLING

Weather conditions favourable for the formation of fogs and clouds, and precipitation have been analyzed.

I/ Cloud/Fog Structure and Precipitation Rate

In the first series of numerical runs a study was made of the evolution of clouds and fogs in an orographically inhomogeneous PBL under the influence of airflow dynamics and radiative flux divergence.

Run 1.1. The effect of an airflow passes over individual dome-like circular hill on cloud and fog formation has been studied. Airflow motion regimes are considered with small Frud numbers Fr, when the flow moves around an obstacle ($Fr = u/NH_p$, where $N = \sqrt{g(\gamma_a - \gamma)/T_0} \sim 10^{-2}$ s-1 is the Brunt-Väisäla frequency), and hence, Fr ranging between 0.5 and 1.0.

The length of a wave resulting from streamlining of the flow around the hill is $\lambda_0 = 2\pi/(N/u) \cong 4 - 5$ km.

The deformation of the wind field leads to the formation of a secondary maximum of upward motion behind the obstacle (Fig.1.1). Airflow features result in the formation of cloud and fog caps on the windward side of the obstacle and of elevated cloudiness behind it in the upward branch of the gravity wave (Fig. 1.2). The long-wave cooling shifts from the earth's surface to the upper boundaries of the cloud/fog layers,and the cooling rate reaches -2, -4 K/hr, resulting in a increase of LWC q_L to 0.15 - 2.2 g/kg due to a positive feedback between R_L and q_L, which raises the upper boundaries of the cloud/ fog layers.

Run 1.2. Using 3D non-hydrostatic model meso-circulation in broken terrain and cloud/fog formation in a mountainous area where the Alma-Ata airport is situated (in the foothills of the northern slopes of the Tien Shan) have been studied .

When the surface wind has a southern component, the area where an airport is located is in the lee of the mountain ridge. This fact determines the nature of mountain-valley circulation: downward orographic flows of the order of -20, -40 cm/sec are localized along the downwind slope, while upward flows (of 25 cm/sec, Fig. 1.3) above the layer of wind reversal H_R form a closed circulation cell above the ridge slopes.

Defant has found the thickness of drag wind layer, H_R to be proportional to the square of the slope wind maximum

$$u_r^2 = \frac{g H_R}{\mu}\,\frac{\theta_1 - \theta}{\theta_1}\sin\alpha \tag{9}$$

The field of condensate that forms when a cold mountain air is mixing with the air in the valley, is seen to form at the foot-hills and is extending in the horizontal up to 5 or 10 km (Fields of liquid water contents inside the fog are shown in Fig. 1.4).

A detailed calculation of the microstructure of hydrometeors in Run 2 allows to estimate the liquid and ice precipitation rate, and obtain the qualitative visibility forecasts .

Meteorological visibility range L may be expressed as (Baranov, (1991))

$$L = \frac{3.91}{2\pi}\left[N_1\bar{R}_1^2 + 2N_2\bar{R}_2^2 \Big/ \left(\frac{2.5}{R_2}\left(\frac{6M_2}{\pi\rho_2 N_2}\right)^{1/3} - 3\right)\right]^{-1} \tag{10}$$

In a series of numerical experiments, model calculations were performed in orders to understand better processes of fog glaciation , propagation of the areas of artificial glaciation and those of improved visibility under various meteorological regimes of the PBL, which allowed to specify geometric sizes of the cleared areas, to compare them with the observations made during experiments on fog dispersal and once the models verified, to apply them for the purposes of methodological support of fog dispersal operations in a number of airports, Bondarenko (1998b).

II/ Aircraft Icing.

The problem relevant to the aircraft icing in the flight and ice on the ground may be solved using three-phase numerical model which incorporates the parameterized microphysics of fog/clouds and precipitation.

Examples of the transformation of ice crystal spectra associated with the diffusional growth of crystals are presented in Fig.1.5 , Bondarenko (1998a).

III/ This report describes the role of a previous stage of the outlined Aviation Safety Program analysing Polar Low events as a combination of the risk factors for aircraft flights. In order to study characteristic features of Polar Lows, a set of numerical models have been used, Bondarenko(1992,1999). The models treat the following processes in detail:

3.1. The dynamic regime of the Polar Lows, including: Wind Shear, Turbulence, and Influence of Orography.
3.2.Cloud/Fog system and Precipitation of polar front (Snowfalls, Cloud Boundaries, and Visibility Forecasts).
3.3. Aircraft Icing in the flight, and on the ground.

An example of analysed Polar Low structure is limited to published data of the Labrador Sea Deep Convection Experiment (1998), Renfrew et al.(1999). Polar Lows Cases were selected to provide :

i/ differentiation of the types of Polar Lows(stable, moving, evolution of Lows, Fig.2.1, 2.4);
ii/separation of Low zones:locations of cyclone quadrants (warm, cold sectors, fronts, dryline, main low, Fig.2.2);
ii/an analysis of surface precipitation and clod/fog frontal structure (Fig. 2.2).

4. RESEARCH AND DEVELOPMENT PLANS

In subsequent research we will utilize in-situ data (including satellite images, aircraft C-130 data (Fig. 2.3), and R/V Knorr measurements) for model initialization, qualitative model verification , and estimation of the factors of risk to aircraft in flight.

5. ACKNOWLEDGMENTS

We wish to express our appreciation to Professor V. Khvorostyanov for the collaboration and valuable discussion of the first results of work.

REFERENCES

Aircraft icing, 1996: a safety project- AOPA, Air Safety Foundation, 22 p.

Baranov A.M., 1991: Atmospheric visibility and flight security. - Leningrad, Gidrometeoizdat, 206 p.

Bernstein B.C.,Omeron T.F.,McDoough F.,Politovich M.K., 1997: Relationship between aircraft icing and synoptic-scale weather conditions. Weath.&Forecast., 12, 742-761.

Bondarenko V.G.,1992: Simulation of aerosol transport in an orographically inhomogeneous atmospheric boundary layer (mountain-valley circulation) by use of a 3-D non-hydrostatic model. Hemisphere Publ. Co, vol.3, 1335-1340.

Bondarenko V.G., 1998a: Study of a three-phase system hygrothermodynamics and reevaluate of the role on sublimation stage of crystal growth in supercooled fogs. Proc. of First Conf.on Fog and Fog Collection, Vancouver, 369-372.

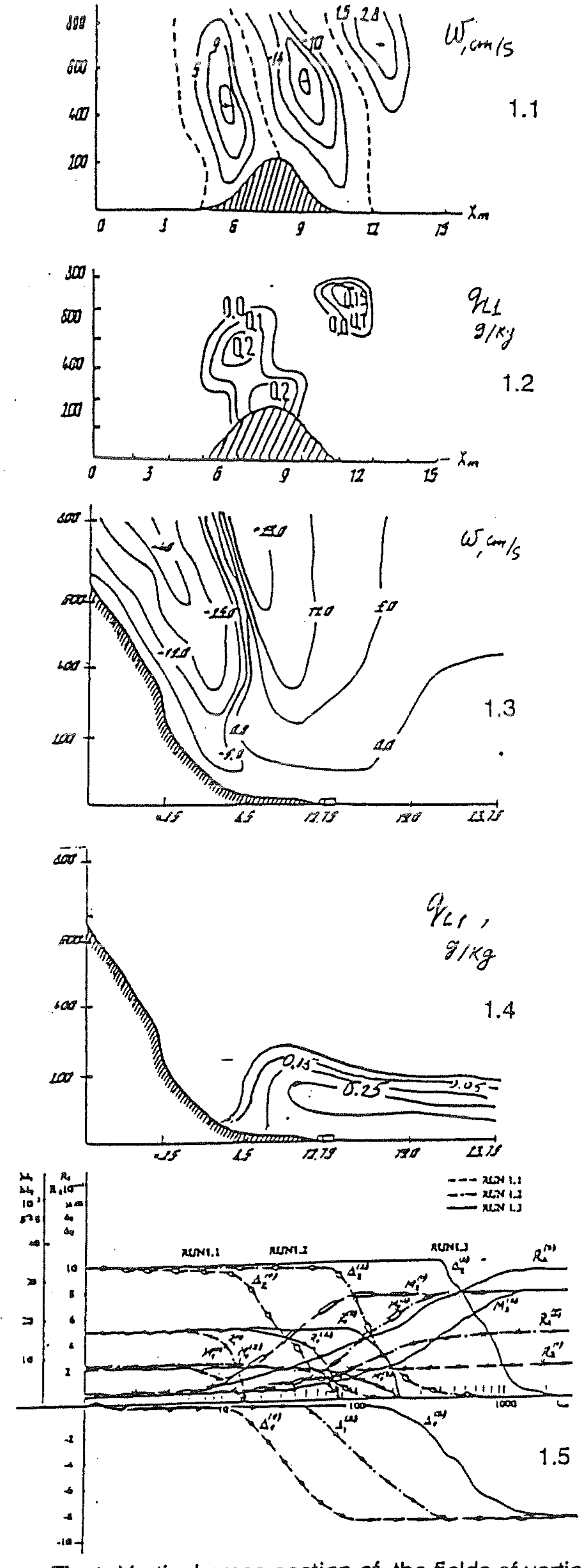

Fig.1. Vertical cross-section of the fields of vertical motions W (1.1), LWC (1.2), mountain-valley circulations in foothill in the Alma-Ata region (1.3), LWC in airport area (1.4); transformation of the hydrometeor spectra -crystallization of supercooled droplets(1.5) .

presented in Fig.1.5 , Bondarenko (1998a).

III/ This report describes a previous stage of outlined Aviation Safety Program in the part of analysis of a Polar Low events as a combination of the risk factors for the aircraft flight.

In order to study characteristic features of a Polar Lows, a set of numerical models have been used, Bondarenko(1992,1999). We use described models that treats in details:

3.1. The dynamic regime of the Polar Lows, including: Wind Shear, Turbulence, and Influence of Orography.

3.2.Cloud/Fog system and Precipitation of an polar front (Snowfalls, Cloud Boundaries, and Visibility Forecasts).

3.3. Aircraft Icing in the flight, and on the ground.

An example of analyse of Polar Low structure is limited to published data of the Labrador Sea Deep Convection Experiment (1998); Renfrew et al.(1999). Cases of Polar Lows was selected to provide :

i/the differentiation of the types of Polar Lows(stable, moving, evolution of Lows, Fig.2.1, 2.4);

ii/separation of Low zones:locations of cyclone quadrants (warm, cold sectors, fronts, dryline, main low, Fig.2.2);

ii/an analyse of surface precipitation and clod/fog frontal structure (Fig. 2.2).

4. RESEARCH AND DEVELOPMENT PLANS

In subsequent research we will utilize in-situ data (including satellite images, aircraft C-130 data (Fig. 2.3), and R/V Knorr measurements) for model initialization, qualitative model verification , and estimation of the factors of risk to aircraft in the flight.

5. ACKNOWLEDGMENTS

I must to express my gratitude to Professor V. Khvorostyanov for the scientific supervising and valuable discussion of the first results of work.

REFERENCES

Aircraft icing, 1996: a safety project- AOPA, Air Safety Foundation, 22 p.

Baranov A.M., 1991: Atmospheric visibility and flight security. - Leningrad, Gidrometeoizdat, 206 p.

Bernstein B.C.,Omeron T.F.,McDoough F.,Politovich M.K., 1997: Relationship between aircraft icing and synoptic-scale weather conditions. Weath.&Forecast., 12, 742-761.

Bondarenko V.G.,1992: Simulation of aerosol transport in an orographically inhomogeneous atmospheric boundary layer (mountain-valley circulation) by use of a 3-D non-hydrostatic model. Hemisphere Publ. Co, vol.3, 1335-1340.

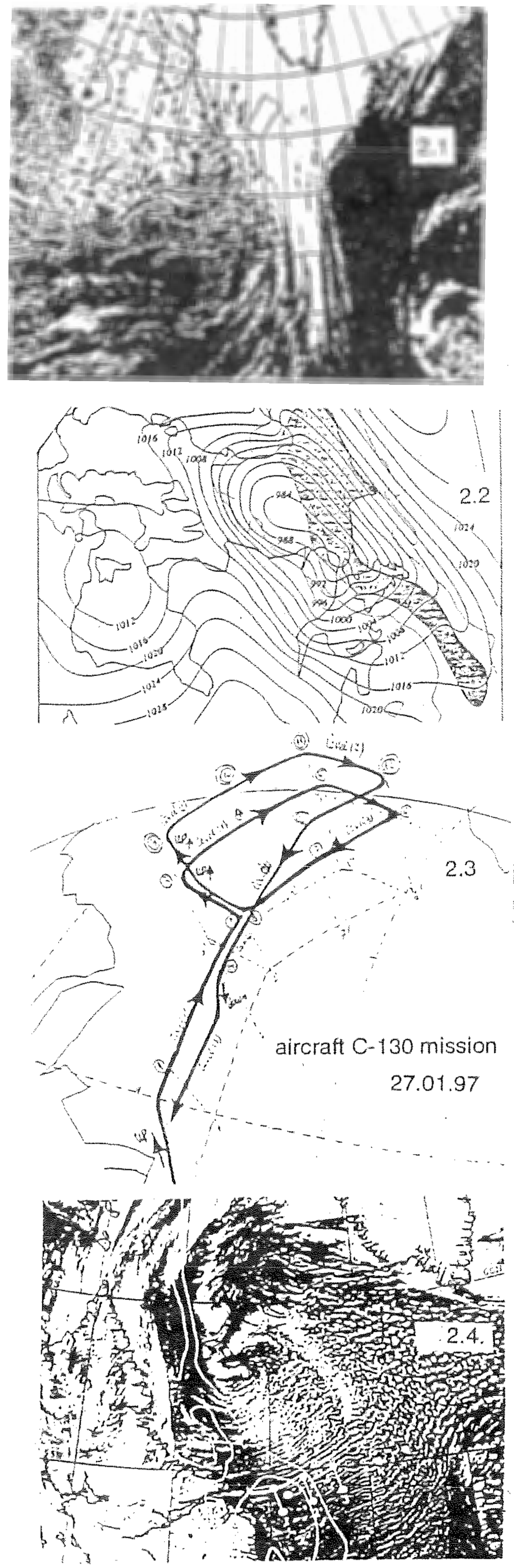

Fig. 2. IR satellite images of Labrador Sea region (27.01. 1997, 2.1), (08.02.1997, 2.4); surface pressure ,precipitation f ields, and sectors of Polar Low (27.01.1997, 2.2); the flight track of the 27.01.97 aircraft C-130 mission (2.3).

[1]OVERVIEW AND RESULTS FROM THE MEXICAN HYGROSCOPIC SEEDING EXPERIMENT

R. T. Bruintjes, D. W. Breed, V. Salazar, M. Dixon, T. Kane, G.B. Foote and B. Brown

National Center for Atmospheric Research, P.O. Box 3000, Boulder, CO 80307, USA

1. INTRODUCTION

In response to severe drought conditions in the early 1990's in the north of Mexico a scientific program, Program for the Augmentation of Rainfall in Coahuila (PARC) was started to evaluate the viability of increasing rainfall through cloud seeding techniques. A four-year program consisting of physical studies and a randomized seeding experiment following the South African hygroscopic seeding experiments was started in 1996. The program was conducted in the State of Coahuila in the north of Mexico bordering central Texas, with mountain ranges of the Sierra Madre Oriental dominating the central and western regions of the state. Elevations in the northeastern plains are around 220 m while mountain ridges in the central and southeastern parts of the state rise to over 3500m. During the field effort in 1996 (July-October), the emphasis was on establishing the infrastructure and operations procedures for collecting data to assess weather conditions and cloud characteristics in Coahuila. The goal was to evaluate the cloud microphysical characteristics of the clouds in Coahuila and how they compared with the South African clouds. Following the 1996 field season, an experimental design was written, based largely on the work and results in South Africa (Mather et al., 1997), and a randomized seeding experiment, utilizing hygroscopic seeding material released at cloud base, was conducted in 1997 and 1998 (July-September). Physical studies were continued within the constraints of the randomized experiment.

2. RESEARCH COMPONENTS

The primary tool for nowcasting and for quantitative evaluation of the seeding experiment was a 5-cm wavelength weather radar. The TITAN software (Dixon and Weiner, 1993) was used for the display of radar data and aircraft position in real-time for the purpose of directing operations. TITAN was also used as the automated evaluation software, defining the experimental unit and producing time-series of storm properties for use in analysis. The aircraft used in the project was a Piper Cheyenne (PA-31T) twin-engine turboprop airplane, equipped with wing-mounted racks carrying 24 hygroscopic flares and a basic cloud physics package

Microphysical measurements indicated similar cloud droplet size distributions and CCN spectra to those found in the Highveld region of South Africa. Convective storms in Coahuila have the classic characteristics of air-mass thunderstorms formed under weak upper-level flow. Of the 1085 storms tracked in 1996, the median storm duration (reflectivities greater than 30 dBZ) was 0.6 hr with 90% lasting less than 1.4 hr. The storms generally consisted of a few to several small cells. The median size of storms (i.e., maximum area of 30 dBZ during storm lifetime) was 35 km^2 and median cloud top heights were 9.1 km AGL. Storms also tended to be slow-movers. Ninety percent of the storms had speeds of 5 m s^{-1} or less, and over 50% were 2 m s^{-1} or less.

3. EXPERIMENTAL DESIGN

The objectives of the Program for the Augmentation of Rainfall in Coahuila (PARC) were to: a) determine whether there is an effect on rainfall from seeding, and if so, understand the time history of such effects, the time-integrated effect produced, and the probable cause; and b) test the concepts of the South African experimental approach in a different environment. The operational procedure for PARC followed the South African technique of introducing hygroscopic seeding material in updrafts at cloud base during the developing stage of a storm. The same flare design that was used in the South African experiment (manufactured by Swartklip) and pilots with experience in seeding in South Africa were used in PARC.

The randomization procedures were also the same as used in the South African experiment. The experimental unit is defined as the storm measured by the radar and tracked by TITAN, using a 30-dBZ threshold, for a time period of 20 min prior to decision time to 60 min after decision time. When the storm did not yet have an initial identifiable echo as tracked by TITAN, the period was defined as the time when the echo was first detected by TITAN to the time when TITAN no longer detected it. The TITAN tracking and analysis is fully automated to avoid the possibility of bias based on knowledge of the seed/no-seed decision. TITAN produces time series of storm properties for use in the analysis. As suggested from the results of the South African experiment, the time-series response

[1] Corresponding author's address: Roelof T. Bruintjes, Research Applications Program, NCAR, P.O. Box 3000, Boulder, CO 80307; E-Mail: roelof@ucar.edu

variables include precipitation flux, total storm mass, storm mass above 6 km MSL, and storm area. Radar-estimated precipitation measurements use a Marshall-Palmer Z-R relationship applied to a composite of maximum reflectivities at any height in the storm, which minimizes any range bias.

The hypothesis to be tested for each time-series response variable is that the value of the variable is larger for seeded cases than for non-seeded cases during the time period 10 to 60 min after decision time. The null hypotheses are for no differences in response variables for the seeded and non-seeded cases. The time-series variables were tested using the first three quantiles of the distribution of values for seeded and non-seeded cases. These variables were tested at 5-minute intervals from 10 to 60 minutes after decision time. A re-randomization technique was used to test the statistical significance of the differences in the quantile values of the time-series response variables at the specified times.

4. STATISTICAL RESULTS

A total of 99 cases were included in the experiments during the 1997 and 1998 seasons. Of these storms, 47 were seeded and 52 were not seeded. Initial examination of the cases indicated that 5 storms did not qualify as experimental units. In particular, two seeded cases and one non-seeded case did not have a TITAN storm track due to radar problems. In addition, two seeded cases had no aircraft GPS data and had intermittent radar data. Eliminating these five cases left 43 seeded and 51 non-seeded storms (total of 94 cases).

The results are summarized in Figures 1 and 2. Figure 1 shows the percentage of active cases as a function of time before and after seeding. It is evident that seeded cases tend to live longer than unseeded cases.

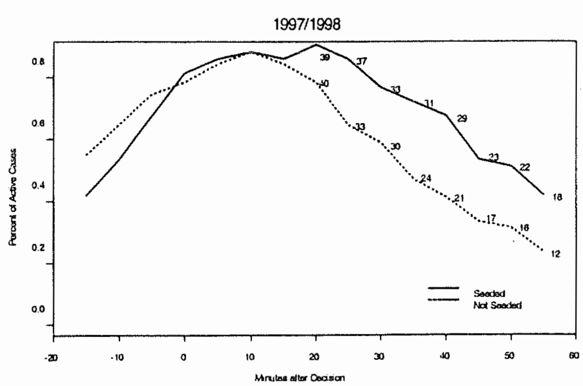

Figure 1: Percentage of active cases as a function of time after seeding for seeded (solid line) and unseeded cases (dashed line). The numbers at each time interval after 20 minutes indicate the number of active cases in each category.

Including all of the valid storms, Figure 2 shows the results of the quantile analysis for precipitation rate (flux). The Precipitation Flux was calculated using a Marshall-Palmer Z-R relation relationship where Z is the reflectivity and R the rainfall rate. Three pairs of curves are shown, one for each quantile. The quantile plots in Figure 2 clearly shows the effects of seeding. By 15 minutes after decision time, all three quantile values of Precipitation Flux are larger for the seeded storms than for the non-seeded storms and remain larger throughout the time period of the analysis. Re-randomization tests indicate that the differences are statistically significant after 30 minutes, especially for the 2nd and 3rd quantiles. In many instances the seeded storms have precipitation rates of up to a factor of two larger than the non-seeded storms.

One of the main objectives of the Coahuila program was to determine if the South African results could be replicated in another area of the world. Many past programs in the world failed when attempts were made to replicate previously successful programs.

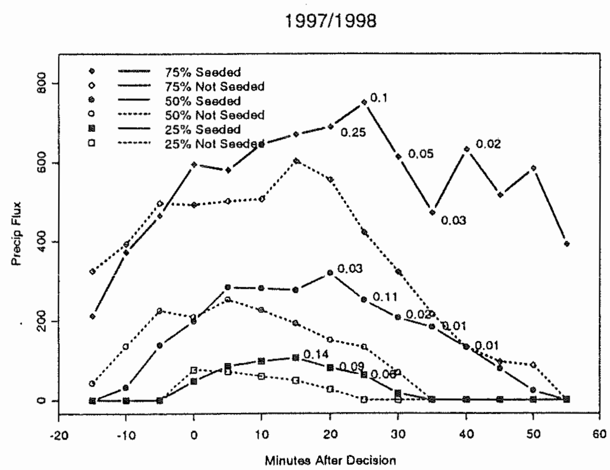

Figure 2: Quantile values of Precipitation Flux ($m^3 s^{-1}$) versus time after "decision time" for seeded and non-seeded cases. Precipitation Flux is the total rate of precipitation estimated for the storm at the specified time. 1st quantile is the value of Precipitation Flux that is larger than the value for 25% of the storms; 2nd quantile value exceeds the value for 50% of the other storms; and 3rd quantile value exceeds the value for 75% of the storms. The numbers on the plot indicate the statistical significance of the differences between the seeded and non-seeded storms for each quantile as determined by the re-randomization tests.

Figure 3 displays a comparison of the rain mass in seeded (solid lines) and non-seeded (dashed lines) cases for the three different quantiles as a function of time after "decision time" for the South African (dark lines) and Coahuila (gray lines) experiments. The rain mass is computed by integrating the rain flux for every minute for the period of the analyses. The differences in both the South African and Coahuila experiments were statistically significant after 20 minutes and remained significant for the remainder of the period. It is clear that the results from both experiments are in good agreement. The main difference is that the storms in South Africa tended to live longer than the storms in Coahuila. The reason for this difference is that the atmospheric environmental winds in South Africa are stronger than in Coahuila providing for better organization of the storms. However, the differences between the seeded and unseeded storms are remarkably similar. The agreement in the results for the two regions provide additional confidence that the results were not obtained by chance but that seeding produced a real difference in the development of precipitation in the clouds.

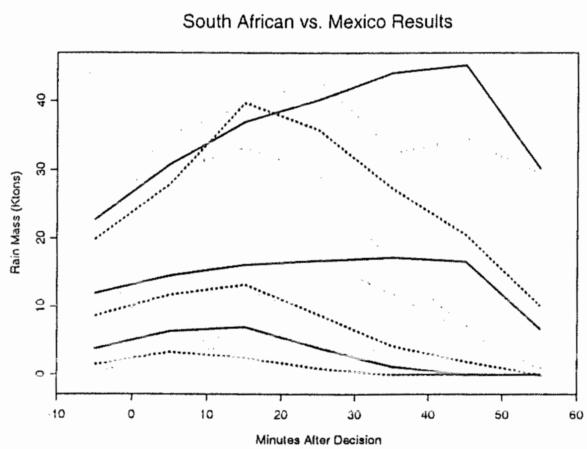

Figure 3: Quantile values of Rain Mass (Precipitation Flux integrated per minute) versus time after "decision time" for seeded and non-seeded cases for the South African (dark lines) and Coahuila (gray lines) experiments. Rain Mass is the Precipitation Flux integrated over 1-minute intervals. 1^{st} quantile is the value of Rain Mass that is larger than the value for 25% of the storms; 2^{nd} quantile value exceeds the value for 50% of the other storms; and 3^{rd} quantile value exceeds the value for 75% of the storms.

The results from additional analyses (not shown here) indicate of a positive effect of seeding, in terms of precipitation flux, rain mass above 6 km, rain area, lifetimes of the storms, the integrated area of precipitation, and the total precipitation. These results are also very similar to those found in the South African experiment (Mather et al., 1997). This fact is encouraging, especially because the timing as well as the magnitude of the seeding effects corresponds well to the South African results.

Re-randomization tests indicate that most of the observed differences are statistically significant at the 95% level specified in the Experimental Design document. However in some instances statistical significance was not reached. Thus, a small possibility exists that the apparent seeding effects may be the result of chance. Data from further field seasons should help to extend these results and establish statistical significance. Nevertheless, the results are very encouraging.

It is important to note that the number of cases (94cases) is still marginal for any statistical analysis. The South African experiment consisted of approximately 150 cases. The PARC program was planned for four years and the fourth year would probably have provided a sufficient number of cases. However, due to funding problems the fourth year of the experiment could not be completed. Therefore, being cautious is important if interpreting the results as unambiguous proof of success.

5. PHYSICAL INTERPRETATION

The principle of enhancing the coalescence process via hygroscopic seeding is dependent on three important parameters: the chemistry (hygroscopicity), size and concentrations of the particles produced from the flares or large particle salt seeding. In addition, the effectiveness of seeding will also depend on the natural background particles and their characteristics with regard to the same parameters especially with respect to hygroscopic flare seeding.

Seeding with hygroscopic flares involves seeding summertime convective clouds below cloud base with pyrotechnic flares that produce small salt particles (about 0.5 μm diameter) in an attempt to broaden the cloud droplet spectrum and accelerate the coalescence process. The burning flares provide larger CCN (>0.3 μm diameter) to the growing cloud, influencing the initial condensation process and allowing fewer CCN to activate to cloud droplets. Mather et al. (1997) showed measurements of the broadening of the cloud droplet spectra in a seeded cloud. The assumption was that the larger artificial CCN would inhibit the smaller natural CCN from nucleating, resulting in a broader droplet spectrum at cloud base. The fewer cloud droplets grow to larger sizes, and are often able to start growing by collision and coalescence with other cloud droplets within 15 minutes (Cooper et al., 1997), initiating the rain process earlier within a typical cumulus cloud lifetime of 30 minutes. The question still remains if the broadening of the droplet spectra or the provision of a large particle tail would initiate the coalescence earlier. In recent measurements in Argentina (Fig. 4) it was found that the droplet concentrations stayed constant but that seeding provided an additional tail to the cloud droplet spectra. The measurements were obtained approximately 500 m above cloud base while another aircraft was conducting seeding just below cloud base. However, in either case it is expected that the coalescence process would be enhanced. Another important question is how the effects of seeding would mix through the cloud volume. Cooper et al. (1997) suggested that drizzle drops could play an important role in this respect.

Numerical calculations by Reisin et al. (1996) and Cooper et al. (1997) support the hypothesis that the formation of precipitation via coalescence might be accelerated by the salt particles produced by the flares. These studies also found that for clouds with a maritime cloud droplet spectra hygroscopic seeding with the flares will have no effect, since coalescence is already very efficient in such clouds. However, the results from the calculations should be interpreted with considerable caution because they oversimplify the real process of precipitation formation. Cooper et al. (1997) allude to some of the shortcomings in the calculations related to mechanisms that broaden cloud droplet size distributions, sedimentation, and the possible effects on ice phase processes.

These hypotheses would physically explain the statistical results until about 30 minutes after seeding. However, the statistical results indicate that seeding still produces a significant effect beyond 30 minutes in both the South African and Mexican cases. This may indicate a dynamic response in the cloud system that carries the effects of seeding beyond the initial production of precipitation. Bigg (1997) has also suggested a dynamic response. Bigg suggested that the initiation of precipitation started at a lower height in the seeded clouds than in the unseeded clouds and that a more concentrated downdraft resulted closer to the updraft. The surface gust front was thereby intensified and its interaction with the storm inflow enhanced convection.

It is extremely important to obtain a better understanding of the both microphysical and dynamical responses before the statistical results can be accepted as unambiguous proof of success. A coordinated scientific field effort would be needed to address the above questions. A recent WMO sponsored workshop in Mexico was the first step in organizing such an effort.

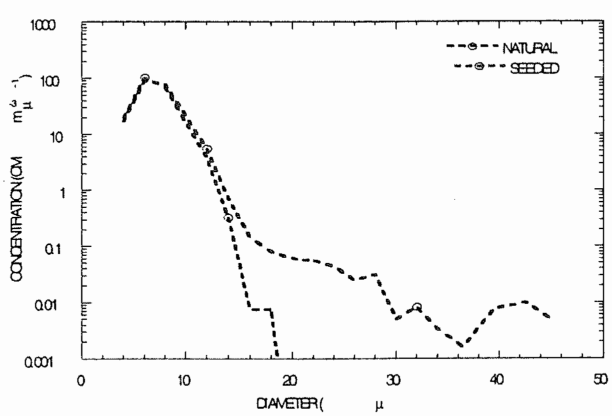

Figure 4: Droplet size spectra in natural and seeded part near cloud base. Concentrations are in $cm^{-3}\mu m^{-1}$ and diameter in μm.

6. CONCLUSIONS

The PARC program was originally planned for four years. However, due to financial problems only three years of the program could be completed. Although the statistical tests already show positive results, caution should be taken in interpreting the results as final proof that this technique could provide additional water resources.

The next step in a future program would be to move from storm-based results to possible area effects. The ultimate goal of all activities is to develop viable methods that will have a positive effect on the threatening water situation facing large parts of the world. "Acceptable" proof of positive seeding effects on storm-scale rainfall (as an experimental unit) is a prerequisite to higher area rainfall. The total seeding effect on all seeded storms' rainfall should also quantitatively match the area effect. It is important that future studies include the assessment of storm increases in rainfall on area rainfall and the resources necessary to implement an operational program that would have a substantial impact on area rainfall.

7. ACKNOWLEDGE MENTS

The research was sponsored by the State of Coahuila in Mexico with financial support from Altos Hornos de Mexico (AHMSA).

8. REFERENCES

Bigg, E.K., 1997: An independent evaluation of a South African hygroscopic cloud seeding experiment, 1991-1995. *Atm. Res.*, **43**, 111-127.

Cooper, W.A., R.T. Bruintjes, and G.K. Mather, 1997: Some calculations pertaining to hygroscopic seeding with flares. *J. Appl. Meteor.*, **36**, 1449-1469.

Dixon, M. J., and G. Wiener, 1993: TITAN – Thunderstorm Identification, Tracking, Analysis, and Nowcasting – a radar-based methodology. *J. Atmos. Oceanic Tech.*, **10**, 785 – 797.

Mather, G.K., D.E. Terblanche, F.E. Steffens and L. Fletcher, 1997: Results of the South African Cloud-Seeding Experiments Using Hygroscopic flares. *J. Appl. Meteor.*, **36**, 1433-1447.

Reisin, T., S. Tzivion, and Z. Levin, 1996: Seeding convective clouds with ice nuclei or hygroscopic particles: A numerical study using a model with detailed microphysics. *J. Appl. Meteor.*, **35**, 1416-1434.

OBSERVATIONS OF THE ROLE OF COALESCENCE ON RAINFALL AMOUNTS FROM TROPICAL CONECTIVE CLOUDS

William L. Woodley[1] and Daniel Rosenfeld[2]

[1]Woodley Weather Consultants, Littleton, Colorado
[2] Inst. Of Earth Sciences, the Hebrew University of Jerusalem, Jerusalem, Israel

1. INTRODUCTION

Convective cells around the world, comparable in size and stature, vary in the amount of rain they produce. The average rain volumes produced by convective cells of the same height increase as one progresses through the following locations: South Africa (Rosenfeld and Gagin 1989), Texas (Rosenfeld and Woodley, 1989; 1993), Israel (Rosenfeld and Gagin, 1989), Florida (Gagin, et al., 1985) and Thailand (this paper). One is left with the impression, therefore, that the rain production from convective cells is related somehow to their coalescence efficiency, since the effect of coalescence on the initiation and development of rain is known to be less important in South Africa (Mather et al, 1997) than in Thailand (this paper).

Unfortunately, observations relating coalescence to the production of rain from convective rain cells and cloud systems are unavailable. The goal of this study, therefore, is to help fill this void by examining volume-scan radar data of convective cells and cloud systems that developed over northwest Thailand prior to and during the Southwest Monsoon, clouds with mixed-phase processes that extend well above the freezing level. The results are partitioned into categories representing conditions with a rapid onset of coalescence and conditions with slower coalescence activity. This was done using observations of the presence or absence of detectable raindrops on the windshield of an aircraft as it penetrated the updraft of growing convective towers, 200 - 600 m below their tops to establish the categories.

2. EXPERIMENTAL AND DATA ANALYSIS PROCEDURES

A randomized, cold-cloud, rain enhancement experiment was carried out during 1994-1998 in the Bhumibol catchment area in northwestern Thailand (Woodley et. al., 1999a,b). During the course of this experimentation an Aero Commander seeder aircraft flying at about the –8°C level (about 6.5 km MSL), made passes the updrafts of vigorous, growing convective cells, 200 - 600 m below their tops. Each treatment pass of the seeder aircraft, involving the ejection or simulated ejection of silver iodide flares, was made into a new vigorous, growing convective cell; none was penetrated more than once. The observations made during these passes provide the basis for classifying the coalescence activity in the clouds.

Corresponding author's address: William L Woodley, Woodley Weather Consultants, 11 White Fir Court, Littleton, CO 80127; E-Mail: Woodley@compuserve.com.

The radar used in the experiments was the AARRP (Applied Atmospheric Research Resources Project) 10-cm, Doppler radar located in Omkoi, northwest Thailand. It was used in volume-scan mode to monitor and record, in 5-min intervals, the three-dimensional structure of convective precipitation entities. The radar was calibrated to the same reference throughout the experiments. Therefore, in addition to the electronic calibration, a re-calibration of the radar data was done to ensure the same ground clutter intensity on each day during periods without anomalous propagation. Reference was also made to solar intensity in the re-calibration process, mainly to check its validity and stability. Rain intensities (R) were calculated from the reflectivity (Z) by using the Z-R relationship, $Z = 300R^{1.5}$, on the 2-km altitude (cloud base) reflectivities. This Z-R relationship was obtained early in the Thai research from a comparison of data from the radar with that from a rain gage network installed in the project area.

The 3-D reflectivity matrices are divided into reflectivity cells that are tracked with time (Rosenfeld, 1987). Instantaneous properties of each cell are calculated for each 5-min radar scan, including peak and average reflectivity, area, echo top height at a 12 dBZ threshold, and rain flux. Lifecycle properties are also determined, including total rain volume and maximum echo top height. Total rain volume is obtained by integrating the rain intensity in space and time over the whole lifecycle of the rain cell.

In order to obtain the best representation of the full lifecycle of the cells, including the mature and dissipating stages, a long-tracking algorithm was used (Rosenfeld and Woodley, 1989). In long tracking, cell tracking is continued (forced) through all mergers and splits. A long-track cell is terminated only after it is determined that it is dying, as quantified by the relationship of its current properties to its historical maximum.

The analyzed long-tracked cells for this study are the 392 cells on 42 days that were penetrated and measured by the seeder aircraft and the radar, respectively, but were left unseeded as controls.

3. CLASSIFICATION OF THAI CLOUDS

Observations of the presence or absence of detectable raindrops on the windshield of the project AeroCommander seeder aircraft as it penetrated the updraft of growing convective towers at about the $-8^{\circ}C$ level (about 6.5 km MSL), was used as a measure of coalescence activity in the clouds. This was by viewing the flight videotapes made by a camera mounted in a forward-looking position on the right side of the cockpit in the seeder aircraft. The auto-focus feature of the camera ensured that it focused on the windshield during the cloud penetration and outside on the cloud field when the aircraft exited the cloud.

Since the cloud penetrations were made in strong updrafts (often > 5 m s^{-1}) about 200 – 600 m below cloud top, the visible impacts on the aircraft windshield were interpreted as raindrops originating below the aircraft. The strong updrafts assured that at least the smaller raindrops formed below the penetration level would rise with the updraft. Later comparisons with the cloud physics instruments showed that these impacts were associated with 2DC images of particles larger than about 150 microns. The rounded spherical shapes of these images and the penetration level temperature suggested that they were supercooled raindrops, or at most unrimed frozen drops.

If at least one cloud pass on a given day had detectable raindrops, it was classified as a day on which there was a rapid onset of coalescence, hereafter referred to as a day with convective cells and cloud systems having strong coalescence activity or a Category 2 coalescence day. Conversely, if none of the cloud passes on a given day had detectable raindrops, that day was classified as one with slower coalescence activity, hereafter referred to as a day with convective cells and cloud systems having weak coalescence activity or a Category 1 coalescence day.

4. FIRST-ECHO DEPTH ANALYSIS

To gain further insight about the coalescence activity partition, the mean first-echo cloud depth for all qualifying cells receiving treatment on each day was calculated and related to it. The mean first-echo cloud depth is defined as the difference between mean first-echo heights (FEH) and measured cloud-base height for the day. Only the cells existing at the time of the first aircraft pass were considered for the first-echo height analysis. Cloud base was measured from aircraft on each of these days, allowing for the calculation of first-echo depths.

The results are supportive of the coalescence partition. The mean first-echo cloud depth is smaller for cells with strong coalescence activity than cells with weak coalescence activity, i.e., 3.50 km vs. 4.28 km, respectively. This difference has a P-value of 0.01 using a one-sided "t" test, assuming unequal variances.

5. RESULTS

Maximum echo height at a threshold of 12 dBZ (HMAX) vs. rain volume (RVOL) relationships were derived for the Category 1 and Category 2 coalescence categories. It was found that RVOL increases with increasing echo height and that cells with strong coalescence activity produce more rain volume per echo height than cells with weak coalescence activity.

The overall lifetime cell results are presented in Table 1. Moving from left to right within each table subdivision are listed the averages of a particular cell property for the two coalescence partitions. Next come the ratios of the mean cell properties and their rerandomization P-values. All P-values provide an indication of the strength of a particular result and are not an indication of statistical significance.

Cells with strong coalescence activity produce twice as much rain volume as cells with weak coalescence activity. They are also more reflective, have greater rain-volume rates, last longer and are more clustered with other cells; however, the echo areas and top heights are little different. Taken collectively, these results imply that the rain production efficiency of convective cells is related to their coalescence efficiency with rain production increasing with increasing coalescence activity.

Table 1
Radar-Estimated Properties of Convective Cells as a Function of Coalescence Category

Cell Property	Cat. 2	Cat. 1	SR	P Value
RVOL (10^3 m^3)	267.86	130.59	2.05	0.016
HMAX (km)	10.29	10.05	1.02	0.388
ZMAX (dBZ)	46.73	41.74	1.12	0.014
AMAX (km^2)	54.21	53.82	1.01	0.464
RVRMAX (10^3 m^3 h^{-1})	565.71	395.60	1.43	0.072
RRMAX (mm h^{-1})	7.84	5.12	1.53	0.004
NCMAX	25.05	10.53	2.38	0.010
DUR. (min)	49.41	32.57	1.52	0.002

The larger RVOL from Category 2 cells is likely due to enhanced drizzle and raindrop formation which, in turn, results in a more efficient mixed-phase precipitation-development processes (Johnson, 1987, Pinsky et al, 1998) when these drops freeze and the growth of large graupel is accelerated. These results for Thai tropical convective cells are consistent with the finding that weak coalescence was associated with inefficient ice-phase precipitation development and reduced precipitation in both deep tropical clouds (Rosenfeld and Lensky, 1998 and Rosenfeld, 2000a), and in much shallower extratropical clouds (Rosenfeld, 2000b).

The ratios and differences in volumetric rainfall between coalescence categories as a function of maximum echo top height (Hmax) for the convective cells are plotted in Figure 1. It can be seen that the difference in rain volume produced by convective cells with strong coalescence and those produced by convective cells with weak coalescence increases as Hmax increases. Although the rain-volume ratios are impressively high for the shallow convective cells, in which condensation-coalescence is the dominant precipitation mechanism, the volumetric rain differences are rather small. On the other hand, for the deep convective cells, in which mixed-phase precipitation development processes are dominant, the rain-volume ratios are lower but still physically significant; and they are associated with volumetric rain differences that are important to the overall rainfall of the area. For example, deep tropical cumulonimbus cells (all cells with Hmax > 10 km) that exhibit a rapid onset of coalescence produce 1.99 times more rain volume than cells with slower coalescence activity with a P-value of 0.002, the volumetric rainfall difference being 253 x 10^3 m^3 per cell with a P-value of 0.026.

The analyses were then extended to the scale of the Thai floating target area, the convective cloud systems in which the individual treated (but not seeded) long-track cells reside. These results are presented in Table 2. They are similar to those for the individual long-track cells (Table 1). The rain volumes are larger because of the larger scale of the convection, but the sense of the results is the same as for the individual cells. Convective cloud systems containing cells with strong coalescence activity produced more than twice as much average rain volume as convective cloud systems having cells with weak coalescence activity.

6. CONCLUSIONS

This study shows the importance of coalescence in determining the rain production from convective cells. The results indicate that the difference in rain volume production between convective cells exhibiting a rapid onset of coalescence and those with slower coalescence activity increases with maximum echo top height. For the deep convective cells, the sizable rain volume differences are associated with rain volume ratios that average about a factor of two.

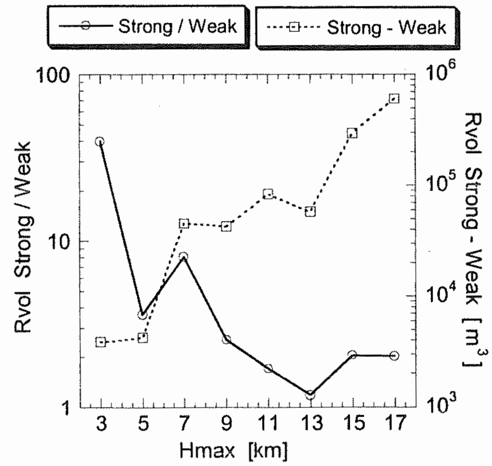

Fig. 1. Mean rain-volume differences and ratios of mean rain volumes vs. max precipitation echo top height for cells growing on days with weak coalescence activity and on days with strong coalescence activity. The data are plotted at the center point of 2-km intervals of max echo top height.

Table 2
Radar-Estimated Properties of Convective Cloud Systems as a Function of Coalescence Category

Cell Property	Cat. 2	Cat. 1	SR	P Value
RVOL (10^3 m^3)	6204.41	2631.78	2.36	0.000
HMAX (km)	10.07	10.76	0.94	0.181
ZMAX (dBZ)	41.40	36.04	1.15	0.008
AMAX (km^2)	658.66	536.81	1.23	0.193
RVRMAX (10^3 m^3 h^{-1})	3763.26	2221.04	1.69	0.006
RRMAX (mm h^{-1})	10.16	9.13	1.11	0.210
TNCELL	30.15	29.11	1.04	0.433
DUR. (min.)	320.394	259.222	1.24	0.037

The rainfall from convective cloud systems with strong and weak coalescence activity also differed by a factor of 2. Therefore, it can be concluded that area tropical rainfall in northwestern Thailand under conditions of weak coalescence activity can be less than half of that under conditions of strong coalescence activity, even for deep cumulonimbus clouds.

7. ACKNOWLEDGEMENTS

Our thanks to our many Thai colleagues for their many years of work on the cold-cloud and warm-cloud seeding experiments that resulted in the data used in this study. We are indebted especially to Khun Song Klinpratoom and Khun Somchai Ruangsuttinaruparp for the hours they spent viewing the videotapes of the cloud passes.

8. REFERENCES

Gagin, A., D. Rosenfeld and R.E. Lopez, 1985: The relationship between height and precipitation characteristics of summertime convective cells in south Florida. J. Atmos. Sci., **42**, 84-94.

Johnson, D.B., 1987: On the relative efficiency of coalescence and riming. J. Atmos. Sci., 44, 1671-1680.

Mather, G. K., D. E Terblanche, F. E Steffens, and L. Fletcher, 1997: Results of the South African cloud-seeding experiments using hygroscopic flares. J. Appl. Meteor., **36**, 1433-1447.

Pinsky M. B., A. P. Khain, D. Rosenfeld, and A. Pokrovsky, 1998: Comparison of collision velocity differences of drops and graupel particles in a very turbulent cloud. Atmos. Res., **49**, 99-113.

Rosenfeld, D., 1987: Objective method for tracking and analysis of convective cells as seen by radar. *J. Atmos. Oceanic Technol.*, **43**, 422-434.

Rosenfeld, D., and A. Gagin, 1989: Factors governing the total rainfall yield of continental convective clouds. J. Appl. Meteor., **28**, 1015-1030.

Rosenfeld D. and W. L. Woodley, 1989: The effects of cloud seeding in West Texas. J. Appl. Meteor., **28**, 1050-1080.

Rosenfeld D. and W. L. Woodley, 1993: Effects of cloud seeding in West Texas: Additional results and new insights. J. Appl. Meteor., **32**, 1848-1866.

Rosenfeld D. and I. M. Lensky, 1998: Spaceborne sensed insights into precipitation formation processes in continental and maritime clouds. Bull. Amer. Meteor. Soc., **79**, 2457-2476.

Rosenfeld, D., 2000a: TRMM first observed direct evidence for smoke from forest fires inhibiting rainfall. Geophys. Res. Let., **26**, 3105-3108.

Rosenfeld D., 2000b: Suppression of Rain and Snow by Urban and Industrial Air Pollution. Science, **287**, 1793-1796.

Woodley, W.L., D. Rosenfeld, W. Sukarnjanaset, P. Sudhikoses, S. Ruangsuttinaruparp and W. Khantiyanan. 1999a: The Thailand cold-cloud seeding experiment: 1. Physical-statistical design. Proc. Of 7th WMO Conf. on Wea. Mod., 16-22 Feb., 1999, Chiang Mai, Thailand.

Woodley, W.L., D. Rosenfeld, W. Sukarnjanaset, P. Sudhikoses, S. Ruangsuttinaruparp and W. Khantiyanan, 1999b: The Thailand cold-cloud seeding experiment: 2. Results of the statistical evaluation. Proc. of 7th WMO Conf. on Wea. Mod., 16-22 Feb. 1999, Chiang Mai, Thailand.

THE ANALYSIS OF RAIN CONVERSION EFFICIENCY AND CLOUD SEEDING POTENTIAL IN CLOUD BY GROUND-BASED REMOTE SENSING DATA

Wu Bo, Duan Ying, Wu Zhihui and Qi zuohui

Weather Modification Office of Hebei Province
No.178, Tiyu South Street, Shijiazhuang, P.R. China
Email: hbwmo@pblic.sj.he.cn postal code: 050021

Abstract

In this paper, the data of continuous vertical integral liquid water content (LWC) during from April to June of 1992 to 1994 obtained by a ground-based dual-channel microwave radiometer in Hebei province area of China are used to analysis the rain conversion efficiency of the precipitus stratiform cloud system and cloud seeding potential.

The analysis results indicate that the cloud seeding potential decrease with the increase of rain intensity, about 50% liquid water cannot be converted to rainfall through natural precipitation mechanism in most precipitating stratiform cloud over Hebei province area. Thus it can be regarded that this kind of stratiform cloud system has the cloud seeding potential.

1.Introduction

The method of using ground-based microwave remote sensing to detect atmospheric vapor and liquid water distribution was originated from the United States of America in the early 1980. Hill(1982) reported his results of using microwave radiometer to monitor cloud water distribution characteristics. Super and Holrogdl (1985) reported their results of super cooled Liquid water in Colorado cloud with microwave radiometer. Heggli etal. (1987) successfully monitored the liquid water distribution characteristics of winter storm cloud system in western USA with microwave radiometer. Warner et al.(1988) made comparison between results of Liquid water content (LWC) by microwave radiometer and the results by airborne particle measurement system(PMS).

Chain started atmospheric microwave remote-sensing research and design of radiometer in the late 1970s. In the late 1980,China produced its won microwave radiometer and put into field experiment use.

From April to June in 1992~1994,using the new generation dual-Channel ground-based microwave radiometer made by Peking University, the comparatively systematic observational study was conducted in Hebei province airplane artificial precipitation enhancement field experiments. Duan et al

(1996) studied atmospheric integral vapor and Liquid water distribution characteristics, based on the continuous microwave radiometer observational data in Hebei province.

Furthermore, You et al.(1994) used the observational data in Chinese Academy of Meteorological Sciences, combining the cloud Liquid water content data detected by airplane PMS, it discussed the conversion efficiency of cloud water to precipitation and studied cloud water resource condition and seeding potential. Based on the preceding work, this paper further discusses the correlation between cloudy atmosphere vertical integral water content and rainfall intensity, the rainfall conversion efficiency and artificial cloud seeding potential.

2. Data collecting

The basic data of this research are obtained by dual-channel co-antenna ground-based microwave radiometer in Shijiazhuang, Cangzhou, Gucheng of Hebei province, from April to June of 1992 to1994. In the observational period, the microwave radiometer was installed at the above three sites. In order to get the continuous data of vapor and Liquid water content in cloud, from 1993 to 1994, when rain occurred, a parachute-like cover was put on microwave radiometer to use 45° angle observation method.

The information of atmospheric vapor, Liquid water brightness temperature was put into the indoor computer system through cable, so as to obtain the real time atmospheric vapor, Liquid water continuous data. During the three years observation period, total 734 hours vapor observation data are obtained, which are under the condition of clear, cloudy and rainy. The cloudy and rainy data are 589 hours. Otherwise, the rainfall data in the corresponding period were collected as well. The related data of vapor and Liquid water collected is the following (Table).

The data of Atmospheric vapor Liquid water obtained by microwave radiometer

Weather condition	Data sample(h)	Sample content
Clear	145	Vapor data
Cloudy	534	Vapor and liquid water data
Rainy	55	Vapor and liquid water data

3.The analysis of rain conversion efficiency and cloud seeding potential

The key index of artificial cloud seeding is the conversion efficiency. The probability of artificial rain enhancement is determined by cloud water condition in raining cloud. For this reason it is important to quantitatively evaluate the rain conversion efficiency and furthermore the seeding potential of artificial precipitation enhancement. The conversion efficiency of natural rain can be defined as the ratio of cloud Liquid water to ground rain by natural process, $E = L_{rain} / L$. Where L is the integral Liquid water content in vertical cloud, it can monitor continuously by the microwave radiometer, only if the rain content L_{rain} in air column in the corresponding time is obtained, the natural rain conversion efficiency E can be estimated. The rain content in air column can be reflected in ground rain intensity I and its variation, so it can be referred through ground rain intensity. Based on the airplane observation, the rain content below 0° C level increases linearly with the decrease of height(you et al.1994), so the ground rain intensity can be used to evaluate ground layer rain water content w($w = 70I^{0.85}$), and to further evaluate the rain water content L_{rain} in air column and estimate the conversion efficiency of natural rain based on $E = L_{rain} / L$(you et al.1994). It is obvious that the computed 1- E can denote the potential of cloud seeding, in other words, 1 – E can be used as a quantitative index of cloud seeding.

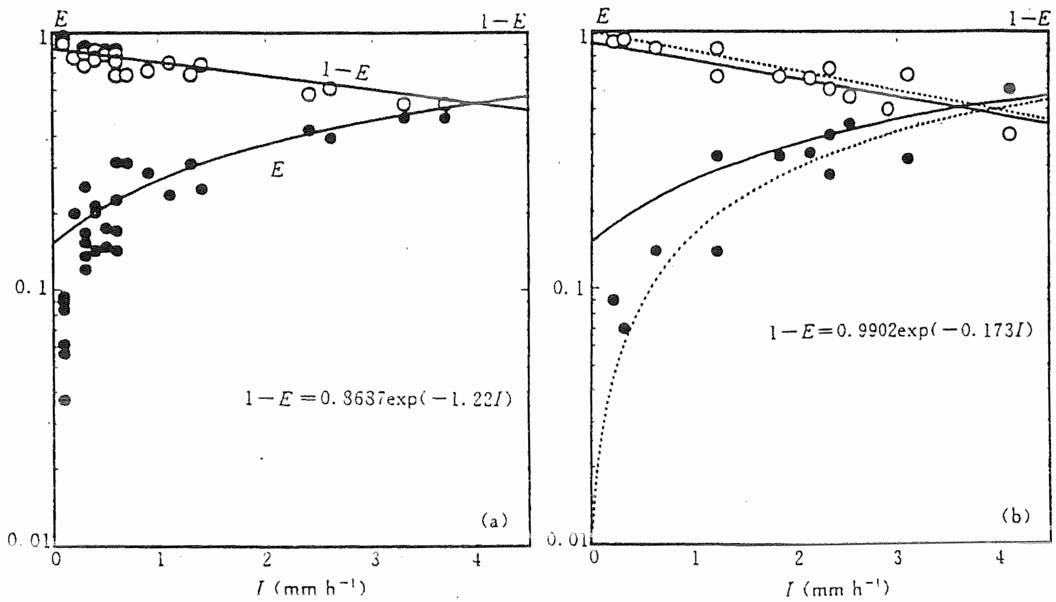

Figure of E – I correlation and (1-E) -I correlation

Solid line is observed results by microwave radiometer.

Solid line is observed results by airplane PMS.

Figure b gives the fitting relations between the estimated E value (or 1-E) by ground rain intensity I value and L value observed by the microwave radiometer in Beijing region. The relation of E (or 1-E) with I using airplane PMS real time monitoring data combined with rain intensity data also is given in Fig b (you et al.1994). Figure a is the results of observational data by microwave radiometer and corresponding rain intensity data analysis in Hebei province. In order to reduce the retrieval error of L caused by large particle scattering, only the data of rain intensity less than 4mmh^{-1} are used (Drake and Warner, 1988). Comparing the two figures, we can see that the results of the two sites are nearly the same, The figure shows that with the increase of rain intensity, the cloud seeding potential decreases. But in most cases of fitting, 1 – E value is larger than 0.5, this shows that in most precipitating stratiform cloud over Hebei province, the liquid water in cloud converted to rain by natural process is only a small portion, thus it can be regarded that this kind of stratiform cloud has the cloud seeding potential.

References

Drake. J. F. and Warner. J., 1988: A theoretical study of the accuracy of tomographic retrieval of cloud Liquid water with an airborne radiometer , J . Atmos , Ocean. Tech., 5: 844 - 857.

Duan Ying et al.,1996: An analysis for the precipitation structure of the stratiform cloud system in North China,12th International Conference on Cloud and Precipitation,19-23 August, 1996, Zurich, Switzerland.

Heggli, M. et al., 1987: Field evaluation of a dual-channel microwave radiometer designed for measurements of integrated water vapor and cloud Liquid water in the atmosphere, J .Atmos. Ocean.Tech.,4:204-213.

Hill,G.E., 1982: Evaluation of the Utah operational weather modification program, Final Report, NOAA, Contract Na81RA C00023,UWRL/A-82102, Utah state university.

Mason,B.J., 1978: Cloud physics. Translated by Institute of Atmospheric Physics, Chinese Academy of Sciences, China press, Beijing, 625-627 (in Chinese).

Super, A.B. and Holrogdl, E.W., 1985: Characteristics of super-cooled Liquid water, Episodes over the Gard Mesa, Colorado, papers presented at the Fourth WMO Scientific Conference on Weather Modification, WMO/TD, No. 53, 391 - 399.

Warner, J. And Drake, J. F., 1988: Field tests of on airforce remote sensing technical for measuring the distribution of liquid water in convection cloud, J. Atmos. Ocean. Tech., 5:833-843.

You Laiguang et. al., 1994: Study of cloud water content with a dual channel microwave radiometer in Beijing, Sixth WMO Scientific Conference on Weather Modification, Paestum, Italy.

Zhao Bolin and Yin Hong, 1980: The principle and experiment of microwave remote-sensing of atmospheric stratification, Scentia Sinica, 874-882.

Zhou Xiuji, 1982: Atmospheric Microwave Radiometer and Remote Sensing Theory, China Meteor. Press , Beijing (in Chinese).

NUMERICAL STUDY OF HAIL SUPPRESION BY AGI SEEDING

Wen Jifen[1, 2] Li Zihua[1] Zhou Ying[2]

[1]Nanjing Institute of Meteorology, 2002#,Nanjing, 210044,China
[2]Guizhou Weather Modification Office, Guiyang, 550002,China

1. INTRODUCTION

Cloud seeding activities for hail suppression using cannon are carried out In Weining, the western area of Guizhou province of China. In the area the hailstone affects the agrarian production seriously, and causes substantial damages to agriculture every year. One of the main characteristics of the zone is that the hailstorms are those which originate after the noon; it is relatively easy to find that the reflectivity measured by the radar reach values of over 40 dbz.

The purpose of hail suppression is to affect the micro-physical structure of hailstorm by inducing artificial freezing nuclei to the clouds. The principle of hail suppression by seeding is to produce a large of ice crystals by inducing artificial freezing nuclei to the supercooled clouds to consume supercooled water, so hail growth is restrained because of no enough water. According to this principle, some numerical simulations for supercooled cloud seeding are done. It is very important to study mechanisms of hail suppression by seeding using the three-dimensional model of hailstorm because hailstorms have three-dimensional structure. Especially in China, hail suppression work is blind and has no objective criterion on selecting seeding methods.

In this paper, using the three-dimensional fully elastic numerical model of hailstorm developed by Institute of Atmospheric Physics(IAP),a hailstorm occurred in Weining, Guizhou province of China on 28 April 1998, is simulated seeding by AgI and no seeding for this hailstorm. This study can supply optimal seeding scheme, it is beneficial to development of hail suppression.

2. MODEL

The model contains more detail bulk-water parameterized microphysics, including forty-six warm and ice phase micro-physical processes such as condensation (sublimation), collection, nucleation, multiplication, melting, melting-evaporation and auto-conversion. The model contains vapor、cloud water、rain、cloud ice、snow、graupel and hail. The simulation area moves with the simulation hailstorm simultaneously to enable the hailstorm located in the central area of the simulation area. The time-splitting numerical integral technique is adopted to improve computation efficiency of fully elastic model. The model contains eighteen equations which predict motion field, atmospheric pressure, temperature, mixing ratios (vapor, cloud water, rain, cloud ice, snow, graupel, hail and AgI particles), concentrations of rain and ice phase particles. The standard spatially staggered mesh system is used in the model where three components of velocity are located in normal boundary center of mesh unit and others in the center of mesh unit. Radiation lateral and rigid top boundary conditions are adopted and sponge zone is added in the top boundary to restrain vertical fluctuation of internal gravity wave. The influence of underlying surface ignored, the value of turbulent exchange item is assumed to zero. The model uses the fourth order difference scheme for advection terms and second order leapfrog scheme for time terms and other space terms. The formation mode of initial convection includes thermodynamic disturbance and humidity disturbance et. al. The mechanisms by which AgI can produce the ice phase are as follows:1)Deposition nucleation: by converting vapor to solid at ice supersaturation.2)Contact freezing nucleation(including immersion freezing nucleation):by converting cloud water and rain to cloud ice and graupel.

3. NUMERICAL STUDY

The numerical study of hail suppression by AgI shows that the principle of hail formation and growth conforms to the theory of accumulation zone. The basic theory of hail suppression by seeding is "competitive principle". A series of

Address: Wen Jifen, Nanjing Institute of Meteorology, P.O.2002, Nanjing, 210044, China

seeding experiments are done to seek optimal seeding methods.

3.1 Simulation of hail cloud

The seeding and natural (no seeding) experiment is a simulation of moist convection initiated by a warm, moist bubble. The integration domain is 36 km in both horizontal directions and 14.0 km in vertical, with grid intervals $\triangle x=\triangle y=1000$m and $\triangle z=500$m. The sounding data is used as the initial fields of temperature, moisture and velocity. To initiate disturbance, a warm moist bubble is inserted in the center of the domain at a height of 2 km. The initial impulse is 12km wide and 4km deep, with a maximum disturbance temperature of 2.5℃. Fig.1 shows Vertical cross section of total water content in natural simulation through the center of hail cloud at t = 2, 7,10,16 min. The hail cloud derived

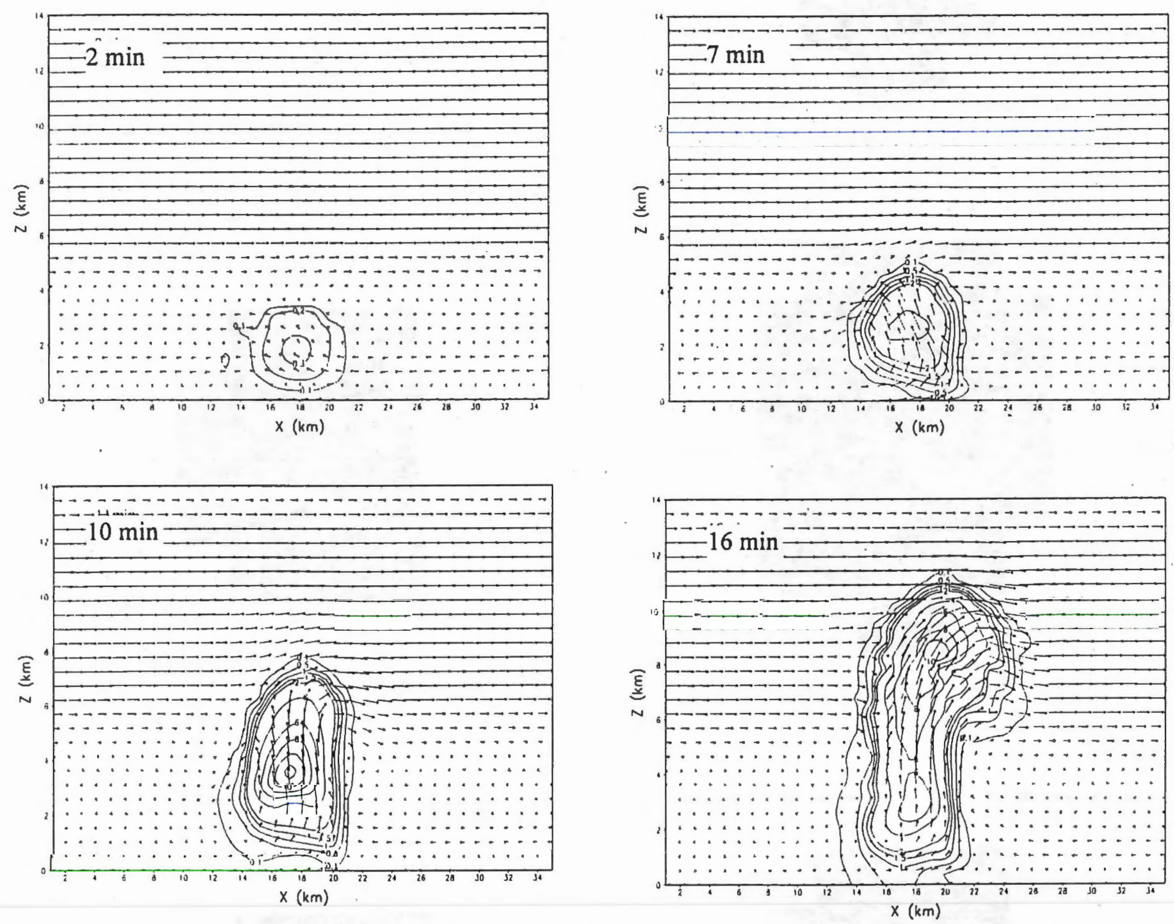

FIG.1. Vertical cross section of total water content in natural simulation through the center of hail cloud at t=2,7,10,16 min

from simulation is similar to that measured by radar (radar map omitted). From Fig.1, it can be seen that the center of water content of hail cloud is located 2km high at two minutes from the beginning of the developing hail cloud and it is becoming higher with the developing hail cloud. Seven minutes later, it is 3.5km high, ten minutes, 4 km. Then sixteen minutes later, the hail cloud becomes weaker. In addition, during the period of hail cloud developing, the total water content is always located in the maximum updraft area. In simulation, the top of hail cloud reach 11.0 km high, the body of hail cloud leans southwest, hail shooting begin on surface at ten minutes, the total hailfall on surface is 150.37 ton, and the maximum radium of hailstone is 5.85mm.

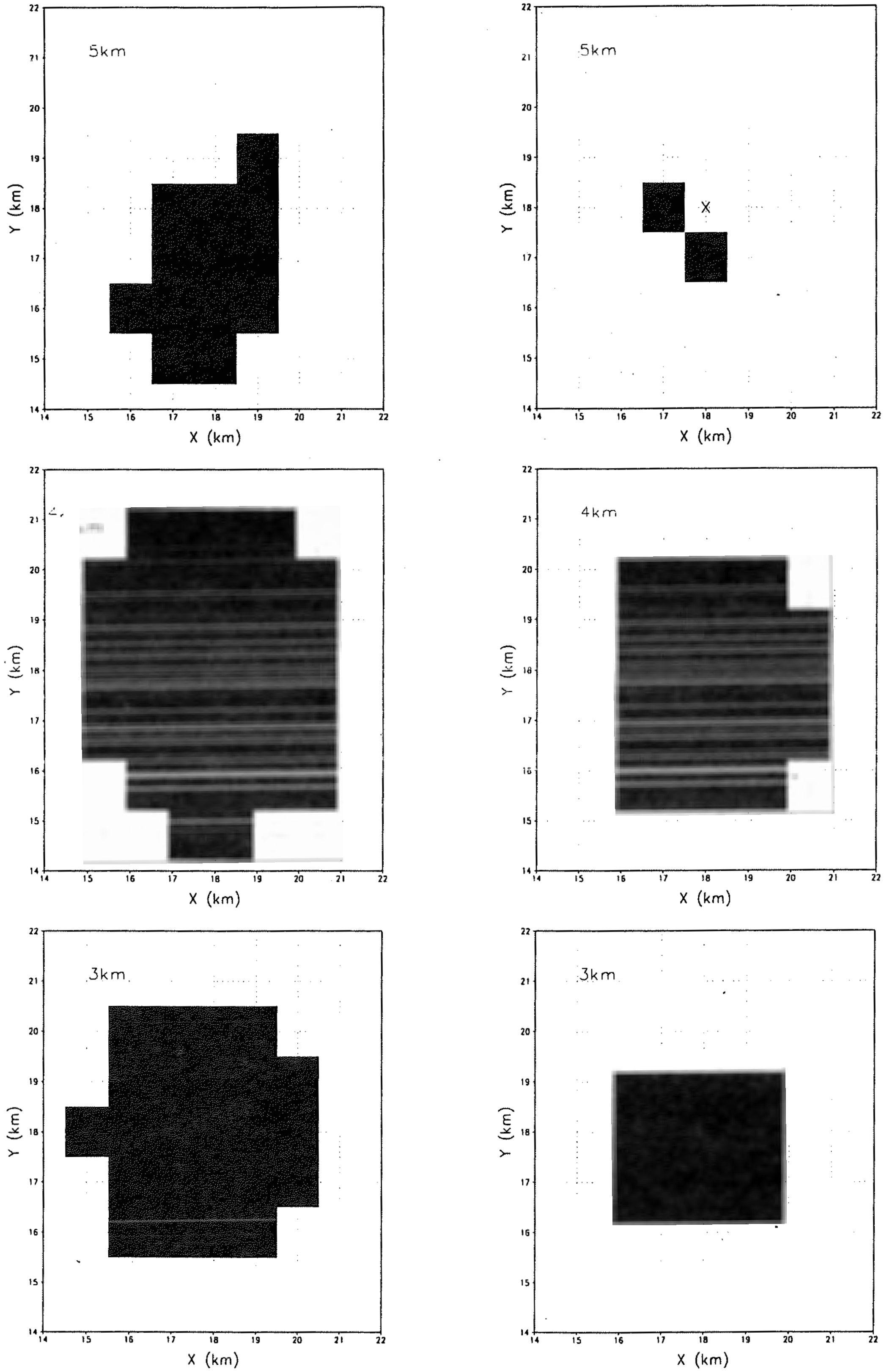
5km
5km
4km
3km
3km
Y (km)
X (km)

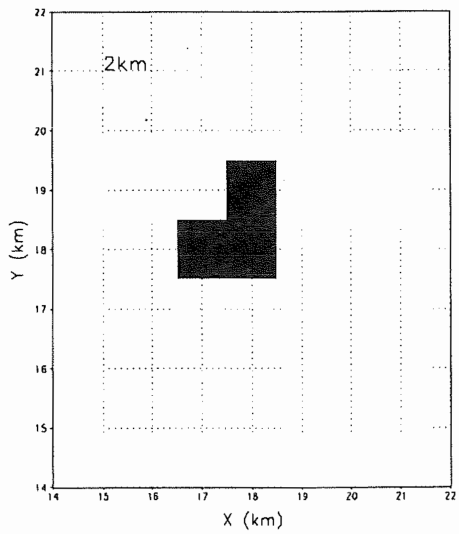

Fig.2 simulation of hail suppression by AgI seeding at two minutes (different height, different location and different amount of seeding agents, 300g in maps of left column, 50g in right, shadow area denotes E>50%)

3.2 Simulation of hail suppression

On the basis of the simulation of hail cloud on 28 April 1998, A series of experiments simulated seeding by AgI for this hail cloud has been done. In this paper, the seeding effect (E) is defined by the percentage of decreasing of hailfall on surface.

The simulation of hail suppression are shown in Fig.2, from which it can be seen the seeding effect at second minute at height 2km, 3km, 4km, 5km and 6km separately (shadow area denotes E>50%). Shown as Figure 2, seeding activities with different height, or different site, or different amount of agents can all get the effect more than 50%. For the same seeding agents, the shadow area increases with height from 2km to 4km, while decreases from 4km to 6km. But it is possible for the total hailfall to increase at height 6km. The shadow area extends to southwest, it has the consistency with the hail cloud southwest leaning. At the same height, the shadow area by 300g AgI seeding is larger than that by 50g. The hail suppression can be taken with the best effect of 88%. Because AgI taken by cannon only reach 3-5km high, it can be obtained that the seeding activities for hail suppression with cannon have certainly reached good effects in Weining, Guizhou province of China.

The simulation results of hail suppression by AgI seeding with cannon are as follows: 1)It explains effect of hail suppression with cannon. 2) The seeding is made at 5-8 minutes before hail shooting, the optimal seeding position is located at 3-4km height in the updraft area. 3) Other things being equal, the effect of hail suppression increases with amount of AgI.

Acknowledgements

The author thanks Guizhou Weather Modification Office for supplying sounding information.

References

Hong Yanchao, 1999: Study on mechanism of hail formation and hail suppression with seeding, ACTA METEOROLOGICA SINICA, Vol.57, No.1, 30-44.

NUMERICAL STUDY ON THE EFFECT OF HAIL-CLOUD CATALYSIS

Zhou Yuquan[1], Cheng Baojun[2], Li Zihua[2] and Huang Meiyuan[3]

[1]Henan Meteorological Administration, Zhengzhou 450003, P.R.China
[2]Nanjing Institute of Meteorology, Nanjing 21004, P.R.China
[3]Institute of Atmospheric Physic,Chinese Academy of Sciences, 100029, P.R.China

1. INTRODUCTION

At present hail suppression in China is dominantly by seeding, through arrays of artilleries or rockets, AgI inside hail clouds for affecting their microphysics to check hails from growth, for which the principle is based on the study of a belt of water accumulation in the cloud (Cheng Baojun, 1999). However, the following problems arises. Is such a belt available? Is the catalysis of the cloud valid if it does have the belt? When should the operation begin and to what part will AgI shells be sent? To reduce blind operation it is necessary to undertake numerical study in order to make all these problems clear. With the development of three-dimensional (3D) hail cloud models and computer technologies we are allowed to investigate them in terms of numerical experiments.

Since the 1980s, numerical study on AgI catalysis of cold cloud has been widely performed. Huang et al. (1994) and Hong (1999) made approach to the physical mechanisms for catalysis mitigation of hails with the aid of Kong (1990) 3D hail cloud model for a case study on catalysis experiment. In this work we present our numerical simulation, using a 3D hail cloud model developed by the Institute of Atmospheric Physics, Academia Sinica, of the hail-bearing cloud, known as 98721 (for July 21, 1998, the same below) of Henan province, followed by catalysis, thereby bearing out the existence of a belt of water accumulation inside the cloud whereupon the physical mechanism was examined for hail suppression by catalysis of the belt.

2. THE 3D HAIL CLOUD MODEL

For details of the model, see Hong Yanchao (1998).

3. NUMERICAL STUDY OF HAIL CLOUD PHYSICS

On July 21, 1998 an intense hailfall occurred in northern Henan (named 98721 event). Radar measurements showed the cloud-body echoes to be ~13 km high and ~15 km wide. And we conducted numerical study of the event based on radar soundings from Zhengzhou at 1300 BST of the day.

To facilitate research we set the meridional (zonal) wind to be the x (y) direction along the simulation area, covering horizontal (vertical) grid length of 1 (0.5) km (totalling in 36 (38) gridpoints at the horizontal (vertical) scale of 35 (18.5) km, with big (small) timestep of 10 (2) sec. in the run. We adopted the technique of storm's core-dependent simulation zone to make the hail cloud always inside and set the initial disturbance to have a 5-km radius, 4-km depth, central maximum potential temperature difference of 1° and the run time of 1 hr.

The profiles of the initial environmental field are given in Fig.1. We see therefrom that the hailfall took place in summer with high temperature at surface; the 20° cloud-base is 1.5 km above ground; the wind is 40 m s^{-1} at 200 hPa, becoming homogeneous at <10 m s^{-1} in general below 300 hPa.

Fig.2 reveals the physics of the target hail event, indicating that initial cloud emerges at a 2.5 km altitude at minute 4, followed by its developing, water content increasing and cloud top growing; at minute 12 the top rises to 10 km height; the 0° isotherm located in the predominant updraft zone is normally at 5.5 km height,

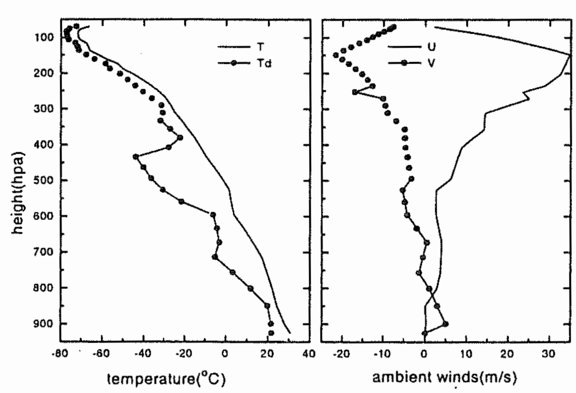

Fig.1. Simulation of the 98721 hailfall event with the temperature (a, solid line), dew point (a, dotted), meridional (b, full line) and zonal wind (b, dotted).

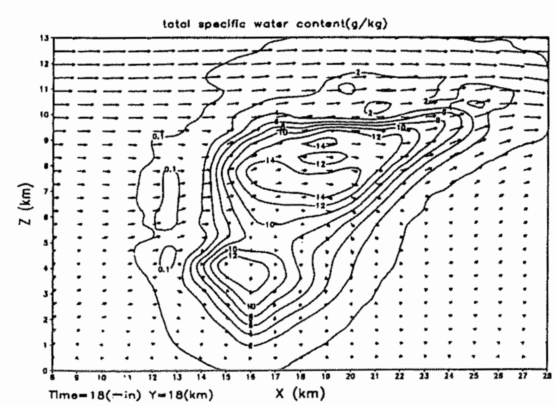

Fig.2. Temporally varying total liquid water content and flow field of the 98721 hail cloud.

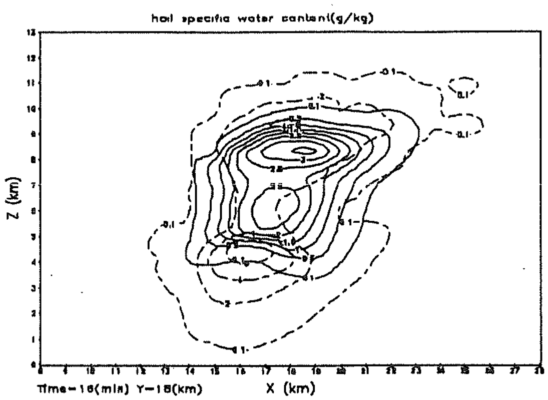

Fig3. Temporally varying total liquid water content(dotted line) and hail specific water content (solid line)of the 98721 hail cloud.

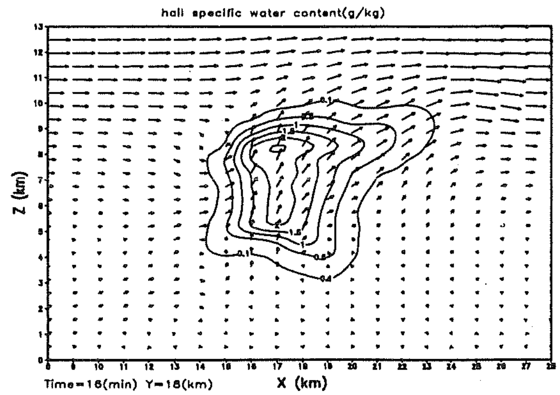

Fig.4. Specific content of hails at minute 16 from seeded cloud .

maximizing at 6 km; a water accumulation belt of >10 g kg^{-1} is between 5 to 8 km altitude, centered at 22 g kg^{-1} in the height of 6.5 km inside a negative temperature zone, where can be seen the genesis of hails at ~7 km elevation overhead; at minutes 14~16, as the center of the accumulation zone rises, so does the hail genesis band, and hails are growing fast with the consequence that the center of hail bearing is step by step coinciding with that of the water accumulation belt; at minute 18 the cloud top reaches its maximal height of 13 km and hails begin to fall and a big-value core of water content appears around a 4-km altitude; as seen from the flow field, subsidence flow shows up in the middle and lower levels of the cloud body but updraft is maintained at the higher and mid levels; at minute 24 the cloud body gets considerably weakened after hails fell and the plume is elongated ahead; at minute 36 the main body at mid and lower levels is disintegrated, only with the plume kept, so that the hail cloud has changed into stratocumulus.

initiated in the negative temperature zone at the slightly higher level ahead of the accumulation band.

To sum up, we have found a zone of liquid water accumulation above a major updraft in the study cloud where the maximal water content exceeds 20 g kg^{-1}, and hail genesis is initiated in a negative temperature belt above the accumulation by way of raindrop freezing and coalescence, followed by both belts lifted together and finally two centers (one for the water accumulation and the other for hail growth) coinciding gradually; in hail shooting another precipitation center emerges at lower levels of the cloud body. Simulation shows that rainfall (hailfall) accumulated at ground arrives at 433 (226) tons, surface maximal single-point precipitation (hailfall) at 6.8 (7.4) mm and maximal hailfall kinetic energy at 112 Jm^{-2}.

4. EXPERIMENT WITH AGI CATALYSIS

Seeding AgI by means of artilleries resulting in nucleation rate is given by eq.(1):

$$Na(\Delta T)=\begin{cases}0 & \Delta T<4^{\circ}\mathrm{C}\\ 10^{6}\exp\left(-0.009\Delta T^{3}+0.324\Delta T^{2}-1.900\Delta T+4\right) & 4^{\circ}\mathrm{C}\le\Delta T<18^{\circ}\mathrm{C}\\ 5\times10^{5}\exp\left(-0.009\Delta T^{3}+0.324\Delta T^{2}-1.900\Delta T+4\right) & 18^{\circ}\mathrm{C}\le\Delta T<20^{\circ}\mathrm{C}\\ 9.9\times10^{15} & \Delta T\ge20^{\circ}\mathrm{C}\end{cases}\qquad(1)$$

where the nucleation rate Na(•T) is in units of g^{-1} and •T= T_0 – T. The mechanism for nucleus formation under consideration are the nucleation 1) by contacting and freezing, 2) by sublimation and 3) by condensation and freezing. Owing to the icing around AgI particles, the density of hydrogenic particles and that of ice crystals experience a change for which the microphysical processes are 1) ice crystals from cloud droplet freezing, 2) graupels from raindrop freezing and 3) sublimation of vapor over artificial ice cores into crystals, etc.

The authors made 38 operations of the 98721 hail cloud at different time, locality and dose. Evidence suggests that the operation is effective if done 1~3 min before hail genesis and best if catalysis occurs slightly above the zone of water accumulation and the hail mitigation is bigger, the greater the AgI dose. It is noted

Results present the maximum and locality of updraft, liquid water and hail contents in the research cloud, showing that the maximal flow and water content are always in the central part; before hail genesis the center of aqueous water content is over the flow, entering a negative temperature overhead as the cloud develops and increasing its value; 1 min before the maximal water content is reached, hails are produced by freezing supercooled water above the core of water content and grow fast as a function of the increase of water content. During the ascent the center of hail growth is coinciding little by little with that of the water accumulation belt after which the water content is a bit reduced.

To make clear the relation between hail growth and water accumulation zone we prepared a diagram of the distribution of liquid water content (dotted line) and hail content (solid) in Fig.3, indicating that hail is formed in the region of >10 g kg^{-1} water content, and the growth is

Table 1. Production of particles from main microphysical processes under the action of catalysis at minute 16.

ice crystal	Tqi	TNUvi	Tpci	TCLci	TVDvi	THNUci	TNUxai	Tni
	576.9/465.4	25.5/23.7	0.44/0.22	0.26/0.19	371.1/287.8	177.8/153.7	2.23/0.0	22.3/22.252
	TNNUvi	TNPci	TNHNUci	TNNUxai				
	20.0/19.96	15.0/14.64	22.3/22.25	18.4/0.0				
snowflake	TQs	TCNis	TCLcs	TCLis	TCLrs	TCLris	TVDvs	TNs
	34.0/25.7	5.34/4.82	1.53/1.16	7.02/5.33	0.13/0.17	16.3/11.8	3.51/2.46	15.62/15.425
	TNCNis	TNCLii	TNCLris					
	15.51/15.358	14.83/14.406	14.76/14.406					
graupel	TQg	TCLig	TCLcg	TCLrg	TCLrig	TCLrsg	TVDvg	TNg
	1333/1294.7	81.4/49.7	100.6/54.8	754.9/802.5	294.8/304.5	70.3/45.6	94.7/77:1	15.17/15.07
	TNCNig	TNCNsg	TNCLrig	TNHNUrg	TNNUrg	TNNUrsg		
	12.36/12.43	13.85/13.7	15.12/15.03	13.6/14.75	12.15/12.13	10.8/13.31		
hail	TQh	TCNgh	TCLih	TCLch	TCLsh	TCLgh	TCLrh	TNh
	192.9/216.5	156.6/177.4	0.158/0.11	2.27/1.04	0.02/0.01	17.66/19.17	16.13/18.76	12.101/12.159
conversion	Pis(10^{-7})	Pig(10^{-11})	Psg(10^{-2})	Pgh(10^{-3})				
	1.62/1.27	11.48/15.06	1.698/1.88	0.853/1.23				

Note: 1) the numerator and denominator represent, respectively the seeded and unseeded cloud; 2) for each of the rows the top and bottom lines the mass (Kg) and number (10^{x}), in order, with TQ and TN denoting total mass (total number) of the particles; 3) Pxy shows the proportion of the conversion of x-kind particles in their total into a y-kind.

$$AgI \Rightarrow \begin{Bmatrix} 24\% & 32.3\% \\ TQ_i \uparrow & TQ_s \uparrow \\ TN_i \uparrow & TN_s \uparrow \\ 0.22\% & 1.3\% \end{Bmatrix} \Rightarrow \begin{Bmatrix} 23.8\% \\ P_{ig} \downarrow \\ P_{sg} \downarrow \\ 9.68\% \\ NCL_{rig} \uparrow \\ 0.6\% \end{Bmatrix} \Rightarrow \begin{Bmatrix} 3\% \\ TQ_g \uparrow \\ TN_g \uparrow \\ 0.66\% \end{Bmatrix} \Rightarrow \begin{matrix} 30.7\% \\ P_{gh} \downarrow \end{matrix} \Rightarrow \begin{Bmatrix} 11\% \\ TQ_h \downarrow \\ TN_h \downarrow \\ 0.48\% \end{Bmatrix} \Rightarrow \begin{matrix} 18.7\% \\ TH \downarrow \end{matrix}$$

Fig.5 The mechanism for hail number change

that opposite results will follow if a wrong catalysis scheme is adopted. Fig.4 depicts the hail distribution in a seeded cloud at minute 16 with catalysis carried out 3 min before hail genesis, i.e., at minute 9 and AgI of 300 g sent to the center of water accumulation zone at 5 km height. Fig.3 and 4 portray that the number of hails in the cloud get greatly reduced after catalysis. Table 1 illustrates the totals of ice phase particles from dominant microphysical processes under catalysis at minute 16, indicating that after catalysis the number of ice crystals and snowflakes are vastly increased but due to the tiny growth of their mass, the mean mass and size from catalysis are reduced, leading to significant drop of their conversion to graupels p_{ig} and p_{sg}. In fact, graupels come lasrgely from supercooled raindrop colliding with ice crystals (Clrig).

From Table 1 we see that the Clrig process after catalysis augments conspicuously the number of graupels in contrast to small growth of mass so as to greatly reduce the conversion of graupels into hails (P_{gh}). Based on our catalysis experiment, the total hailfall is decreased by 24.4% at ground and maximal single-point hailfall by 18.7% and in contrast rainfall is augmented.

A diagram(Fig.5) based on Table 1 is presented to denote the mechanism for hail number decrease from catalysis with up- and downward arrows showing the increase and decrease of hails.

5. CONCLUDING REMARKS

Artificial catalysis is responsible for a large increase of ice crystals and snowflakes in the cloud that collide and are combined with supercooled raindrops in such a way as to augment the number of graupels (as hail's embryo), thus reducing the volume of such raindrops so as to check the conversion of graupels into hails and suppress hail growth by means of coalescence with supercooled raindrops. In this way the number and mass of hails falling onto ground are mitigated.

REFERENCE

Hong Yanchao, 1998, A 3-D hail cloud numerical seeding model, Acta Meteoro. Sinca, vol.56, 641-651

_____, 1999, Study on mechanism of hail formation and hail suppression with seeding, Acta Meteoro. Sinica, vol.57, 30-44

Huang Yan et al., Numerical experiments on hail suppression by AgI seeding, Scientia Atmos. Sinica, vol.18, 1994, 612-622

Kong Fanyou et al., Three-dimensional numerical simulation of ice phase microphysics in cumulus clouds, part•: model establishment and ice phase parameterization, Scientia Atmos. Sinica, vol.14, 1990, 441-453

INTERACTIONS OF DEEP CUMULUS CONVECTION AND THE BOUNDARY LAYER OVER THE SOUTHERN GREAT PLAINS

Steven K. Krueger*, Steven M. Lazarus, and Yali Luo
University of Utah, Salt Lake City, Utah

Kuan-Man Xu
Colorado State University, Fort Collins, Colorado

1. INTRODUCTION

We are using observations and cloud-resolving model simulations to better understand the interaction between deep cumulus convection and the boundary layer over the southern Great Plains of the United States. The observations are from a 29-day DOE ARM (Dept. of Energy Atmospheric Radiation Measurement program) Single Column Model (SCM) Intensive Observation Period (IOP) that took place at the ARM Southern Great Plains (SGP) site during June and July 1997.

The site is a 365 km (north-south) by 300 km (east-west) area (110,000 km^2) that extends from south-central Kansas to central Oklahoma. The SGP site includes a Central Facility (CF) and four Boundary Facilities (BFs). Each of the four BFs is located near the mid-point of one side of the rectangle that bounds the site, as shown in Fig. 1.

The SCM IOP observations included temperature, humidity, and wind profiles from radiosondes launched at 3-hourly intervals from the CF and the four BFs, surface turbulent and radiative fluxes, rainfall rates based on a combination of radar and rain gauge measurements, top-of-atmosphere radiative fluxes, cloud amounts, and cloud fraction profiles obtained from a cloud radar. The surface turbulent fluxes were measured every thirty minutes by 10 EBBR (Energy Balance Bowen Ratio) stations located at the CF and several of the Extended Facilities.

The ARM Data and Science Integration Team processed the observations using a constrained variational analysis technique (Zhang and Lin 1997) in order to obtain estimates of the advective tendencies of temperature and water vapor averaged over the SCM domain, an area that corresponds approximately to the SGP site. These estimates, along with those of the surface turbulent fluxes and the radiative heating rate profile, make it possible to perform diagnostic studies of the the interaction between convection and the boundary layer, as well as simulations of this interaction using cloud-resolving models (CRMs). We are undertaking both approaches.

A similar set of measurements was collected at the ARM program's Southern Great Plains site during a 17-day SCM IOP during the summer of 1995, processed in the same way to obtain estimates of the large-scale advective tendencies, and then used as input to simulations of this period by eleven different SCMs and one CRM (Ghan et al. 2000). The simulation by the CRM is in several respects in better agreement with the observations than are the simulations by the SCMs. However, even the CRM-simulated temperature and water vapor profiles had relatively large rms errors and low correlations with observations in the boundary layer (Xu and Randall 2000). Compared with simulations

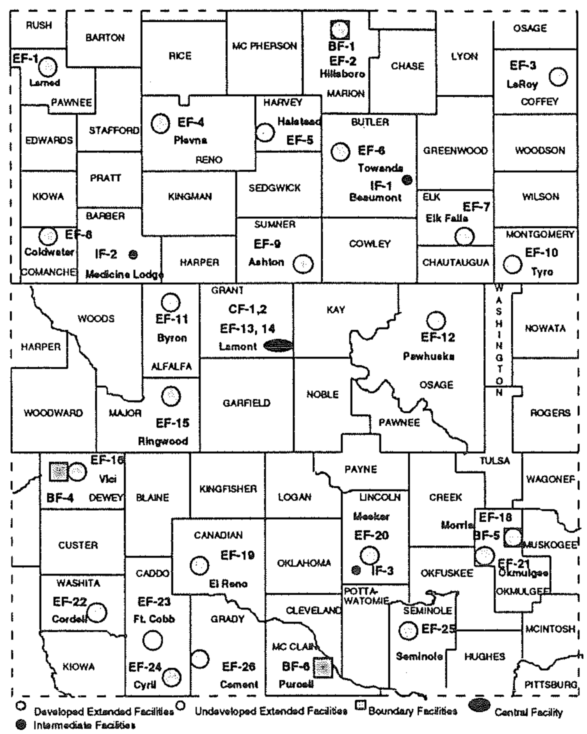

Figure 1: Map of the ARM Southern Great Plains site.

of convection during GATE (GARP [Global Atmospheric Research Program] Atlantic Tropical Experiment), Xu and Randall showed that the Southern Great Plains simulations exhibit much larger temporal variations of surface fluxes, deeper boundary layers, and a predominance of cumulus downdraft effects below 800 hPa.

We simulated the 29-day summer 1997 SCM IOP with the 2D UCLA/CSU CRM, the same CRM that was used for the 17-day 1995 summer SCM IOP. The CRM has been described by Krueger (1988), Xu and Krueger (1991), and Xu and Randall (1995). The CRM's dynamical framework is anelastic. The model includes a third-moment turbulence closure, a three-phase bulk microphysics parameterization, and an interactive radiative transfer code. The third-moment turbulence closure consists of 35 prognostic equations for the second and third moments, and a diagnostic equation for the turbulence length scale.

The CRM simulations for both IOPs used prescribed, time-varying surface turbulent fluxes based on observational estimates. For the summer 1995 SCM IOP simulation and one of the two summer 1997 SCM IOP simulations, the radiative heating rate profile was calculated by the CRM's radiative transfer code. The other summer 1997 SCM IOP

* *Corresponding author address:* Department of Meteorology, University of Utah, Salt Lake City, UT 84112. E-mail: skrueger@met.utah.edu

simulation used prescribed, time-varying estimates of the radiative heating rate profile based on the ECMWF NWP model.

2. CUMULUS EFFECTS IN THE BOUNDARY LAYER

The large-scale *apparent heat source* due to cumulus convection and turbulence is

$$Q_1 - Q_R \equiv L(c-e) - \frac{\partial}{\partial z}(F_s)_{\mathrm{Cu}} - \frac{\partial}{\partial z}(F_s)_{\mathrm{turb}}, \qquad (1)$$

and the large-scale *apparent moisture sink* due to cumulus convection and turbulence is

$$Q_2 \equiv L(c-e) + L\frac{\partial}{\partial z}(F_q)_{\mathrm{Cu}} + L\frac{\partial}{\partial z}(F_q)_{\mathrm{turb}}, \qquad (2)$$

where Q_R is the large-scale radiative heating rate, c is the condensation rate, e is the evaporation rate, $(F_s)_{\mathrm{Cu}}$ and $L(F_q)_{\mathrm{Cu}}$ are the fluxes of sensible and latent heat due to cumulus convection, and $(F_s)_{\mathrm{turb}}$ and $L(F_q)_{\mathrm{turb}}$ are the fluxes of sensible and latent heat due to turbulence.

For simplicity, will assume that the turbulent flux profiles are linear with height above the surface, z, at all times, and that the fluxes due to cumulus convection vanish at the surface. Then

$$(F_s)_{\mathrm{turb}}(z) = F_s(0)(1 - z/h), \qquad (3)$$

and

$$(F_q)_{\mathrm{turb}}(z) = F_q(0)(1 - z/h), \qquad (4)$$

for $z \leq h$, where h is the boundary layer depth. For $z > h$, $(F_s)_{\mathrm{turb}}(z) = (F_q)_{\mathrm{turb}}(z) = 0$. With (3) and (4), the turbulent flux convergences that appear in (1) and (2) are simply

$$-\frac{\partial}{\partial z}(F_s)_{\mathrm{turb}} = F_s(0)/h \qquad (5)$$

and

$$-L\frac{\partial}{\partial z}(F_q)_{\mathrm{turb}} = LF_q(0)/h \qquad (6)$$

for $z \leq h$, and zero for $z > h$.

Substitute (5) and (6) into (1) and (2) and solve for the cumulus effects in the boundary layer:

$$L(c-e) - \frac{\partial}{\partial z}(F_s)_{\mathrm{Cu}} = Q_1 - Q_R - F_s(0)/h \qquad (7)$$

and

$$L(c-e) - L\frac{\partial}{\partial z}(F_q)_{\mathrm{Cu}} = Q_2 - LF_q(0)/h. \qquad (8)$$

The cumulus effects in the boundary layer are due to rain evaporation and cumulus transport. We can isolate the cumulus transport by differencing (7) and (8):

$$-\frac{\partial}{\partial z}(F_h)_{\mathrm{Cu}} = Q_1 - Q_R - Q_2 - F_h(0)/h, \qquad (9)$$

where $F_h \equiv F_s + LF_q$ is the flux of moist static energy.

The ARM variational analysis provides Q_1 and Q_2. In addition, we have observational estimates of Q_R, the surface fluxes, $F_s(0)$ and $LF_q(0)$, and the boundary layer depth (see next section). Therefore, we can (in principle) estimate the cumulus effects in the boundary layer using (7) and (8). The CRM simulations can be analyzed analogously.

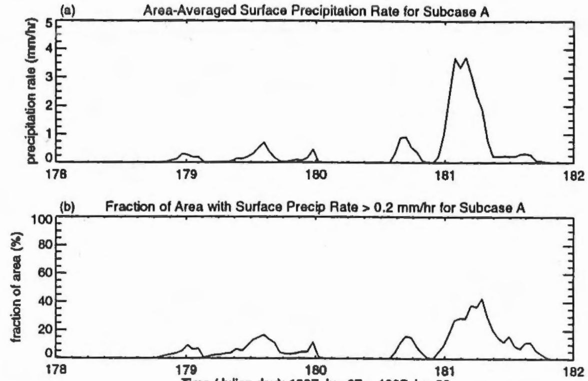

Figure 2: For subcase A of the summer 1997 SCM IOP: (a) hourly surface precipitation rate averaged over the SCM domain; (b) fraction of SCM domain with hourly surface precipitation rate > 0.2 mm hr^{-1}.

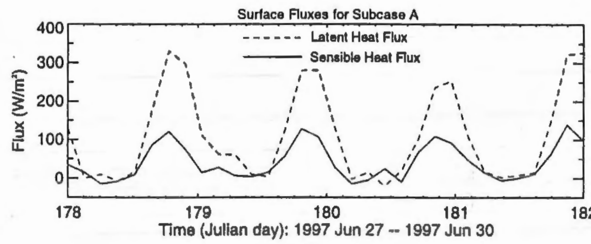

Figure 3: For subcase A of the summer 1997 SCM IOP: 3-hourly surface sensible and latent heat fluxes averaged over the SCM domain.

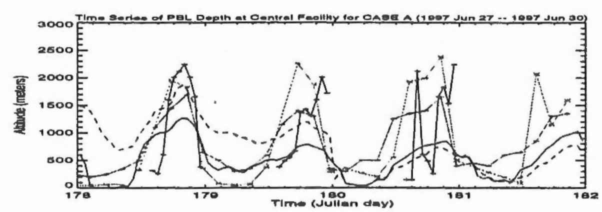

Figure 4: The boundary layer depth for subcase A of the summer 1997 SCM IOP estimated observationally at CF by the 915 MHz profiler (black line with +), the Heffter algorithm (light gray line with *), and visual inspection of the potential temperature profile (dark gray line with +). Also shown are the boundary layer depths obtained from the CRM simulations with interactive radiative heating (black line) and prescribed radiative heating (dashed black line).

3. BOUNDARY LAYER DEPTH ESTIMATES

In the summer 1997 SCM IOP CRM simulations, the boundary layer depth was diagnosed as the minimum of (1) the depth of the subcloud turbulent layer (the layer below cloud base where the turbulence kinetic energy is greater than 0.125 $\mathrm{m}^2\ \mathrm{s}^{-2}$), (2) twice the height of the LCL for the lowest layer air, and (3) 4000 m.

We used three observational estimates of the boundary layer depth:

1. 915 MHz profiler at three sites: CF (Central Facility), IF-1 (Beaumont, KS) and IF-2 (Medicine Lodge, KS) (see Fig. 1).

2. Heffter (1980) algorithm applied to 3-hourly radiosonde profiles of potential temperature at CF.

3. Visual inspection 3-hourly radiosonde profiles of potential temperature at CF.

3.1 *915 MHz Profiler*

All estimates are the result of an automated routine that is far from foolproof. In particular,clouds can have an effect and poorly defined boundary layers are difficult to detect. Early morning values often represent an elevated layer that is not a capping inversion. It is likely that the differences in estimated boundary layer depths between the three sites indicate significant real differences.

3.2 *Heffter Algorithm*

We estimated the boundary layer heights from the potential temperature profiles measured by radiosondes using a method suggested by Heffter (1980) and described by Marsik et al. (1995).

Each potential temperature profile is examined for the existence of a layer that meets the following two criteria: (1) $d\theta/dz > 0.005$ K m^{-1} and (2) $\theta_{top} - \theta_{base} > 2$ K, where θ_{top} and θ_{base} are the potential temperatures at the top and bottom of this layer. The boundary layer top is then defined as the top of this layer.

Problems with this method include overestimating the boundary layer height for surface-based inversions and difficulty in identifying the boundary layer top during the morning and evening transition periods.

3.3 *Results*

Figures 2 and 3 show the surface precipitation rate and fractional area, and the surface sensible and latent heat fluxes, all averaged over the SCM domain, for a 4-day period (subcase A) during the summer 1997 SCM IOP. Figure 4 shows the boundary layer depth for the same time period: estimated observationally at CF and obtained from the CRM simulations.

The boundary layer depths from the CRM simulations and observations for the first half of the summer 1997 SCM IOP are shown in Fig. 5, while those for the second half of the IOP are shown in Fig. 6. Panel (a) in each figure shows the observationally estimated boundary layer depths at CF, while panel (b) shows the profiler estimates from the three sites.

4. PLANS

1. Diagnose cumulus thermodynamic effects on the boundary layer in the CRM simulations. The CRM provides each term in (1) and (2) directly.

2. Diagnose cumulus thermodynamic effects on the boundary layer in the CRM simulations using (7) and (8) and analogs of the SGP observations: 3-hourly profiles and boundary layer depths at 5 locations about 100 km apart.

3. Compare the approximated turbulent flux profiles used in the observational analysis, (3) and (4), to the CRM turbulent flux profiles.

4. Diagnose the cumulus effects on the boundary layer from the observations for two simplified situations: (a) the nocturnal boundary layer affected by precipitating convection, and (b) the clear sky daytime boundary layer.

ACKNOWLEDGMENTS. This research was supported by the Environmental Sciences Division of the U.S. Department of Energy under grants DE-FG03-94ER61769 and DE-FG03-95ER61968 as part of the Atmospheric Radiation Measurement Program. The computations were performed at the National Energy Research Supercomputer Center, Livermore, CA. The 915 MHz profiler data were provided by Richard Coulter (ANL). The precipitation data were provided by Ric Cederwall (LLNL).

REFERENCES

Ghan, S. J., D. Randall, K.-M. Xu, R. Cederwall, D. Cripe, J. Hack, S. Iacobellis, S. Klein, S. Krueger, U. Lohmann, J. Pedretti, A. Robock, L. Rotstayn, R. Somerville, G. Stenchikov, Y. Sud, G. Walker, S. Xie, J. Yio, and M. Zhang, 2000: A comparison of single column model simulations of summertime midlatitude continental convection. *J. Geophys. Res.*, **105** (D2), 2091–2124.

Hefter, J.L., 1980: Air resources laboratories atmospheric transport and dispersion model. NOAA Tech. Memo. ERL ARL-81, 24pp.

Krueger, S.K., 1988: Numerical simulation of tropical cumulus clouds and their interaction with the subcloud layer. *J. Atmos. Sci.*, **45**, 2221–2250.

Marsik, F.J., K.W. Fischer, T. D. McDonald, and P.J. Samson, 1995: Comparison of methods for estimating mixing height used during the 1992 Atlanta Field Intensive. *J. Appl. Meteor.*, **34**, 1802–1814.

Xu, K.-M., and S.K. Krueger, 1991: Evaluation of cloudiness parameterizations using a cumulus ensemble model. *Mon. Wea. Rev.*, **119**, 342–367.

Xu, K.-M., and D. A. Randall, 1995: Impact of interactive radiative transfer on the macroscopic behavior of cumulus ensembles. Part I: Radiation parameterization and sensitivity test. *J. Atmos. Sci.*, **52**, 785–799.

Xu, K.-M., and D. A. Randall, 2000: Explicit simulation of midlatitude cumulus ensembles: Comparison with ARM data. *J. Atmos. Sci.*, **57**, in press.

Zhang, M.H., and J.L. Lin, 1997: Constrained variational analysis of sounding data based on column-integrated budgets of mass, heat, moisture and momentum: Approach and application to ARM measurements. *J. Atmos. Sci.*, **54**, 1503–1524.

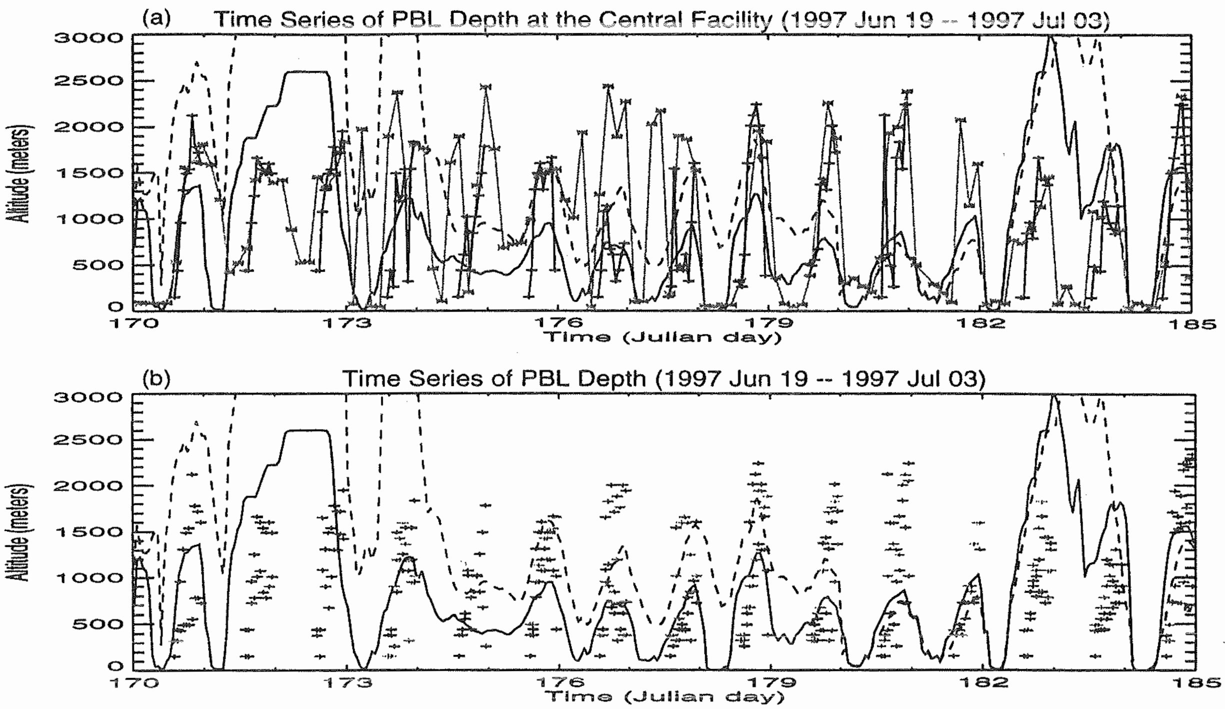

Figure 5: Boundary layer depths from the CRM simulations and observations for the first half of the summer 1997 SCM IOP. Both (a) and (b) show the boundary layer depths obtained from CRM simulations with interactive radiative heating (solid black line) and prescribed radiative heating (dashed black line). Also shown in (a) are the boundary layer depths estimated observationally at CF by the 915 MHz profiler (black line with +), and the Heffter algorithm (light gray line with *); and in (b), the 915 MHz profiler at CF (black +), Beaumont (dark gray +), and Medicine Lodge (light gray +).

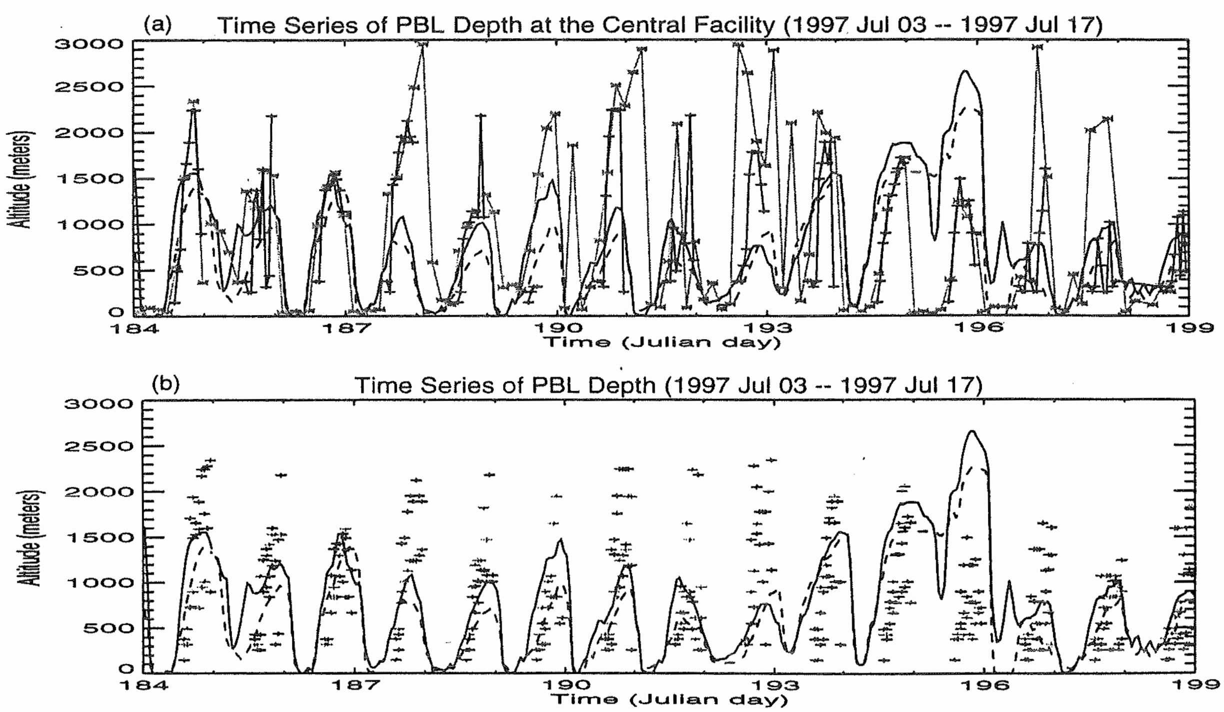

Figure 6: Same as Fig. 5 except for the last half of the summer 1997 SCM IOP.

HEATING DISTRIBUTION BY CLOUD SYSTEMS DERIVED FROM DOPPLER RADAR OBSERVATION IN TOGA-COARE IOP

Tomoki Ushiyama[1], Masayuki Kawashima[2], and Yasushi Fujiyoshi[2]

[1]Frontier Research System for Global Change(FRSGC), Tokyo, 105-6791, Japan
[2] Inst. Low Temperature Sci. Hokkaido Univ., Sapporo, 060-0819, Japan

1.INTRODUCTION

Latent heat release by cloud systems is the major energy source for the atmospheric circulation in the tropics. Its appropriate estimate is crucial for not only the tropical atmospheric circulation but also the global climate system. Therefore, we investigated the heating profiles of various types of convective cloud systems observed during TOGA-COARE IOP '92-'93 (Tropical Ocean and Global Atmosphere- Coupled Ocean Atmosphere Response Experiment, Intensive Observation Phase) at Manus island, P.N.G. And discussed the mechanism that controls the heating profiles of cloud systems. The result which we got will be greatly and also useful for the derivation of latent heat release by using precipitation radar data of TRMM (Tropical Rainfall Measuring Mission) launched in 1997.

2.DATA

Observations by two 3.2 cm wavelength ground-based Doppler radars, omegasonde, and raingauges were carried out at Manus island, Papua New Guinea (2°S, 147°E) from Nov. 1992 to Jan. 1993 during the TOGA-COARE IOP (Uyeda et al.,1995). The two Doppler radars were operated for 66days to obtain three-dimensional wind field. The omegasondes were launched at least 4 times a day. Because of trouble of the sensor, humidity data was not measured at Manus site from 1 to 24 Dec., 1992. For this period, data at Kavieng (2.5°S, 151°E) is used. To evaluate the synoptic scale atmospheric conditions, GMS T_{BB} (Geosynchronous Meteorological Satellite, Temperature of Black Body), in 0.1°×0.1° resolution and at 1-hour interval, and GANAL (Global analysis by Japan Meteorological Agency) in 1.875° ×1.875°resolution at 12-hour interval are utilized.

3.METHOD

To investigate heating profiles by cloud systems, Q_1 (apparent heat source) and other thermodynamic properties are calculated from three-dimensional system relative wind fields and hydrometeor fields.

An equation deriving Q_1 is the modified version of that from Yanai et al.(1973) as follows.

$$\begin{aligned} Q_1 &\equiv \pi_0\frac{\partial\theta_0}{\partial t}+\frac{\pi_0}{\rho_0}\nabla_H\cdot(\rho_0\overline{\mathbf{V}}\,\theta_0)+\frac{\pi_0}{\rho_0}\frac{\partial(\rho_0 w_0\,\theta_0)}{\partial z} \\ &= \frac{L_{c/s}}{c_p}\overline{(C-E)}+Q_R-\frac{L_f}{c_p}\overline{M}-\frac{\pi_0}{\rho_0}\frac{\partial\overline{(\rho_0 w'\theta')}}{\partial z} \end{aligned}$$

where π the the non dimensional pressure, ρ the air density, g the gravitational acceleration, z the height, ∇_H the horizontal derivative operator, $\mathbf{V}$ the horizontal wind vector, Q_R the total radiative heating, L the latent heat of condensation, C/E the condensation/ evaporation rate. Subscript 0 denotes the environmental profile that assumed as same as sounding observation.

We calculate Q_1 by substituting latent heating rate, melting rate, and vertical eddy heat flux divergence at the right hand side of the equation. The latent heating rate and melting rate are calculated from advection equation of hydrometeors derived from radar reflectivity. Vertical velocity and potential temperature perturbation in eddy heat flux convergence term are derived from multiple Doppler synthesis and thermodynamic retrieval technique as same as Roux et al.(1993), respectively.

To evaluate the two distinctive precipitation processes, convective and stratiform rain process, we partition the echo area into convective part and stratiform part. The partitioning technique by Steiner et al.(1995) is invoked in this study.

4.RESULTS AND DISCUSSION

16 cloud systems with reliable wind field of their main part of development has been observed are selected for analysis. These cases are shown in table 1 with duration of observed life, ratio of convective/ stratiform raindrop mixing ratio in 3km height, average surface rainfall rate (mm/h), maximum echo top height (km), CAPE (J/kg), relative humidity (%) of 700 to 400 hPa level, and vertical shear (U_{850hPa}

[1]Tomoki Ushiyama, Frontier Research System for Global Change, Tokyo, 105-6791, Japan, ushi@frontier.esto.or.jp.

Table 1: List of analyzed cases. Each column indicates date, duration, ratio of c/s raindrop mixing ratio, rainfall rate, echo top height, CAPE, relative humidity in mid troposphere, and vertical shear.

Date	Du	C/S	RR	ET	CAPE	RH	Shear
14Dec	3.0	(0.01)	1.8	11.5	555	79	14.6
16Dec		(0.06)	0.8	12.5	507	76	6.9
18Jan		0.17	1.2	14	1775	74	−4.7
18Dec	6.5	0.19	0.8	10.5	1021	30	14.4
21Dec	9.0	0.21	1.3	11	820	82	14.8
11Dec	5.0	0.28	1.1	9.5	1100	66	12.6
27Nov	9.2	0.39	0.6	10	905	68	12.4
24Nov	7.2	0.41	1.1	12	766	42	2.5
27Dec		0.63	1.1	7	1182	64	29.4
29Dec	5.0	1.04	1.6	13	620	50	8.5
10Jan	3.2	1.62	2.0	7	2255	45	9.7
09Dec	4.7	1.72	1.8	13	2167	66	11.9
07Dec	4.7	1.92	1.4	18	3142	63	5.3
13Jan	6.0	2.05	2.3	13.5	1847	51	−5.9
04Jan	3.2	2.81	2.8	15	2389	55	8.3
19Dec	1.5	(4.75)	4.3	15	1785	53	14.7

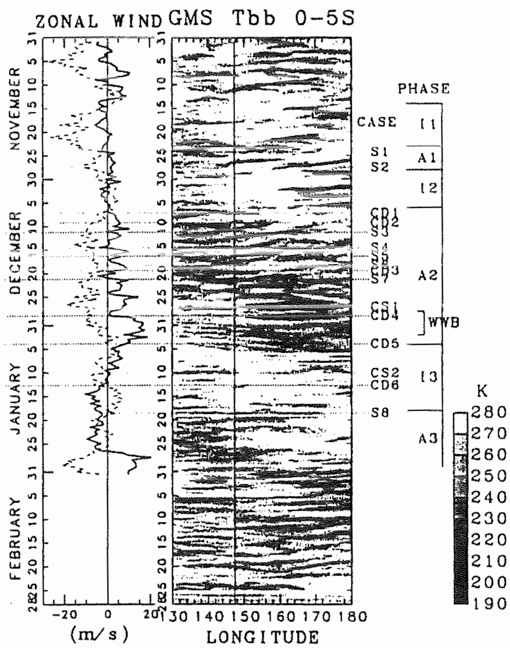

Figure 1: Time-longitude diagram of GMS T_{BB} (temperature of black body) field averaged in equator to 5 S. Marks on the right side of figure indicates convective systems ($S1 \sim S8, CD1 \sim CD4, CS1 \sim CS2$) and MJO phase (inactive phase: $I1 \sim I3$ and active phase $A1 \sim A3$).

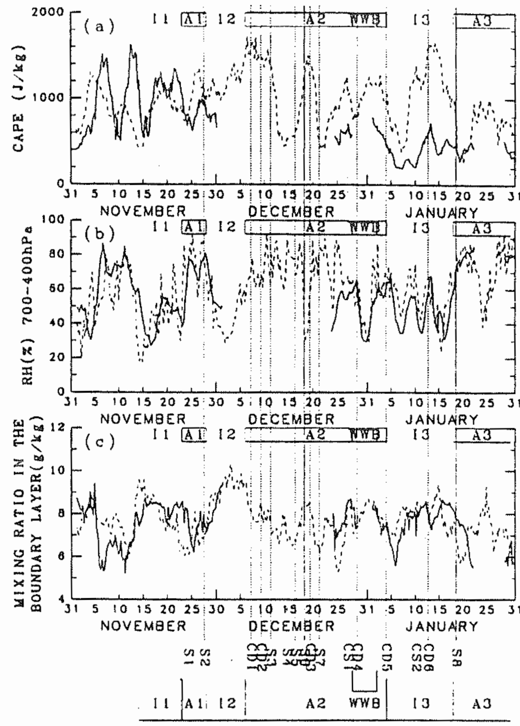

Figure 2: Large scale environmental condition in the observation period. In these panels, these variables are calculated from in-situ radiosonde Manus (solid line) and from Kavieng (broken line). (a) 2-day running mean-ed CAPE. (b) Relative humidity between 700hPa to 400hPa. (c) Water vapor mixing ratio in the boundary layer. Marks under the panels are same as Fig. 1.

$-U_{200hPa}$ m/s) before the system development. Cloud systems in this table is arranged by its ratio of C/S raindrop mixing ratio. Cases with C/S ratio over unity are defined as convective type cases, and others are stratiform type cases.

In this equatorial region, environmental condition is strongly affected by Madden Julian Oscillation (MJO). In this observation period, two clear MJOs passed over the observation area in December 1992 and late January to February 1993 as in Fig. 1. We define active (A1∼A3) and inactive (I1∼I3) phases associated with MJO as in right side of Fig. 1. An active phase in late November (A1) is not associated with MJO, but with a westward propagating cloud cluster. S1∼S8, CD1∼CD6 and CS1∼CS2 in the right side in Fig. 1 indicate selected cloud systems, stratiform, deep convective, and shallow convective cases, respectively. All stratiform cases appear in active phases, and convective cases appear in both active and inactive phases. Fig. 2 shows variation of CAPE, mid tropospheric relative humidity, and mix-

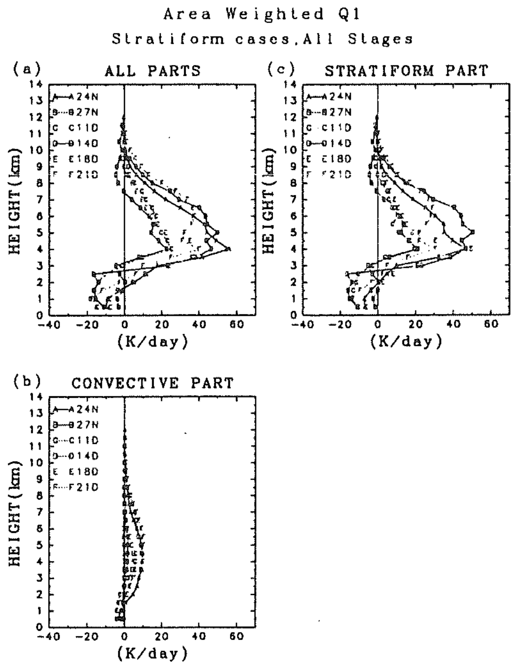

Figure 3: Area weighted average profiles of Q_1 for each partitioned part.(a) all parts, (b) convective part, and (c) stratiform part. These profiles are average in their all life stages.

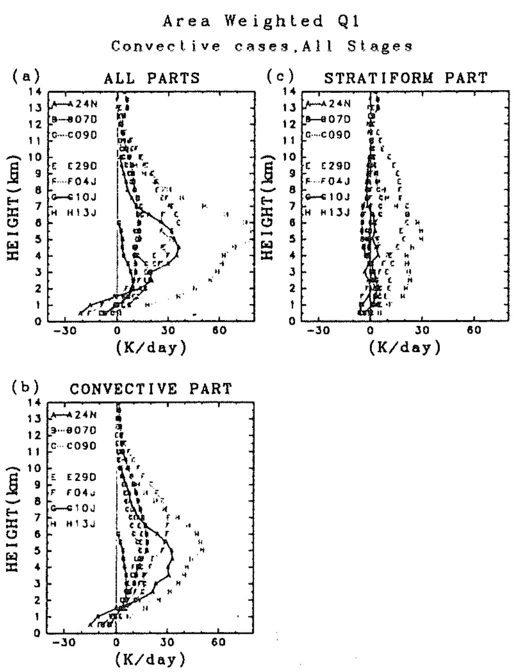

Figure 4: Same as figure 3 except for convective cases.

ing ratio in boundary layer associated with the phase of MJO.

In Fig. 3, Q_1 profiles of various stratiform type cloud systems are indicated. They heat middle troposphere and cool the lower troposphere (below 3km height). Shapes of the heating profiles are coincided with each other. Heating rate in their convective part has little contribution. The profiles of heating rate shows 24Nov., 14Dec., 21Dec. cases have larger heating rate compare with 27Nov., 11Dec., 18Dec. cases. When we pay attention to two couple of cases in December (A2 phase), 11Dec., 14Dec. and 18Dec., 21Dec., following cases have larger heating rate than preceding cases. It is considered that after the development of preceding cases, atmosphere become humid and following case can develop much more, even though CAPE and vertical shear do not show favorable condition for cloud system development. In 18Dec., dry air intrude in this region as shown in Fig. 2(b), and remove the favorite condition for the stratiform type cloud system to develop. In Fig. 2, sudden recovery of CAPE and boundary layer water vapor are also shown. They show the favorite condition for the convective type cloud system to develop again. Actually, strongest convective type cloud system appears in 19Dec.

In Fig. 4, Q_1 profiles of convective type cloud systems are shown. In this figure, dominant heating levels and heating rates depend on the cases. However, the shapes of the heating profile in convective part (panel b) suggests that there are two certain types of heating profiles. One (24Nov., 09Dec., 10Jan.) effectively heats the lower troposphere (maximum in 3~4km), and another (07Dec., 29Dec., 04Jan., 13Jan.) effectively heats middle troposphere (maximum around 5~7km). The cases with the heating profile like latter one show highly consistent heating profile with each other when they are normalized by surface rainfall rate (not shown). Panel (c) suggests their stratiform part has also considerable contribution for the total heating. We would like to give attention to the cases appeared in the active phase of MJO (A2 phase) to consider the relation of heating profiles with the phase of MJO. There are four cases, 07Dec., 09Dec., 29Dec., and 04Jan., which heat middle to upper troposphere. Two cases appeared in the beginning of active phase, 07Dec., and 09Dec., show weaker heating rate compare with the two cases appeared in the end of active phase (29Dec. and 04Jan.). CAPE show higher value in the beginning of active phase, however, the vertical shear show large value in the end of active phase. In their mature stage, maximum updraft show same

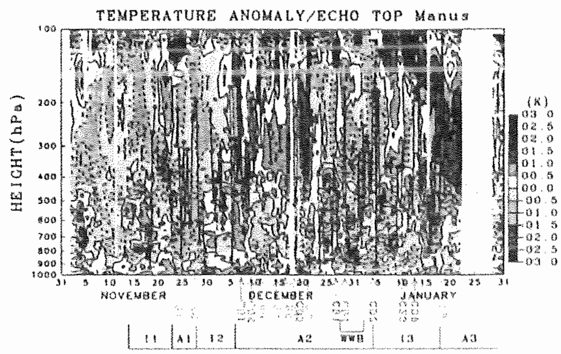

Figure 5: Time height cross section of temperature anomaly (contour and shading) with the echo top height (solid line and black circles). Contour lines in broken lines show negative value. Marks on abscissa are cloud systems and MJO phases, same as Fig. 1.

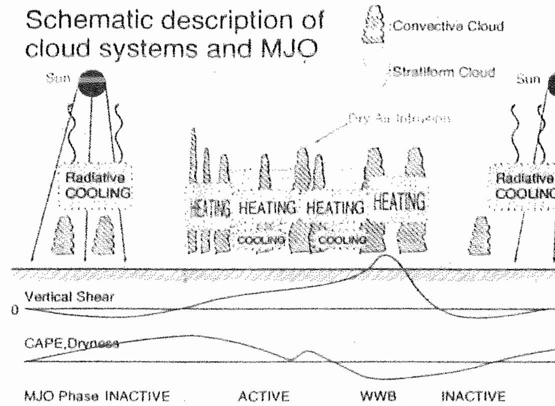

Figure 6: Schematic figure of cloud systems associated with the phase of MJO. The width of cloud picture indicates the amount of heating.

range of speed. However, the mid tropospheric humidity is extremely low in the beginning of active phase. This dry atmospheric condition seems to be the reason of weak heating effect in the beginning of active phase. Entrainment of dry air may have an important effect to restrict the quick development of the cloud systems.

Figure 5 shows time height cross section of temperature anomaly from sounding observation with echo top height at Manus island. In the active phase of MJO (A2, A3), the height of positive temperature anomaly rises as the echo top heights rise. In the end of December, westerly wind bursts and the height of temperature anomaly and echo top drops in this period. As in the beginning of January, echo top height does not always agree with temperature rise, which is considered that the heating effect of cloud systems is not dominant in this period. However, in the main part of the active phase, the sounding data in this figure is in consistent with the heating effects of clouds retrieved from Doppler radar data. Especially, the stratiform cloud systems heat the atmosphere dominantly in the active phase of MJO.

5.SUMMARY

We study heating profiles of various types of convective cloud systems associated and not associated with the active phase of MJO. The heating rate and its profiles are different according to the phase of MJO as schematically shown in Fig.6. The most important factor related to the heating rate is the relative humidity in the middle troposphere. Besides, the change of the relative humidity is well linked with the type of the cloud systems, that is convective and stratiform type.

6.ACKNOWLEDGEMENTS

This work was performed under the TOGA-COARE, and radar observation was performed by J-COARE at Manus island. The authors would like to special thank TCIPO and P.N.G. national weather service for their great effort to providing this experiment.

7.REFERENCE

Roux,F., V.Marecal and D.Hauser, 1993: The 12/13 January 1988 narrow cold-frontal rainband observed during MFDP/FRONTS 87. Part I: Kinematics and thermodynamics. *J. Atmos. Sci.*, **50**, 951-974.

Steiner,M., R.A.Houze Jr. and S.E.Yuter, 1995: Climatological characterization of three- dimensional storm structure from operational radar and rain gauge data. *J. Appl. Meteor.***34**1978-2007

Uyeda,H. el.al.,1995:Doppler radar observations on the structure. and characteristics of tropical clouds during TOGA- COARE IOP in Manus, Papua New Guinea: Outline of the observation. *J. Meteor. Sci. Japan*, **73**, 415-426

Yanai,M., Esbensen,S. and Chu,J.-H.,1973: Determination of bulk properties of tropical cloud clusters from large-scale heat and moisture budgets. *J. Atmos. Sci.*, **30**,611-627

PHYSICAL PROPERTIES OF OVERCAST CLOUDS OBTAINED FROM VIRS AND TMI MEASUREMENTS

Bing Lin[1], Patrick Minnis[2], and Bruce Wielicki[2]

[1]Hampton University, Hampton, VA23668
[2]NASA Langley Research Center, Hampton, VA23681

1. INTRODUCTION

Clouds play important roles in the Earth's climate. They affect both shortwave and longwave radiation. Over the tropical western Pacific warm pool, warm sea surface water and convergent winds generate strong atmospheric convection, which heats upper troposphere and regulates sea surface temperature over the region. For large spatial and long time scales, the only effective technique to monitor clouds over oceans is satellite. The Tropical Rainfall Measuring Mission (TRMM) is the only satellite so far that single platform provides visible (VIS), infrared (IR), and microwave (MW) measurements. Studies (Lin et al. 1998) found that the combination of VIS/IR/MW observations could be used to retrieve cloud physical properties, especially for cloud systems with cirrus on the top and stratiform clouds below.

Because particle size of cirrus clouds is generally much less than MW wavelength and ice has minimal absorption in MW spectrum, the radiation measured by MW radiometer mainly depends on cloud water, water vapor, and surface properties. VIS/IR measurements, on the other hand, are sensitive to the micro/macro-physics of both water and ice clouds. Thus, cloud properties, such as cloud layering, liquid water path (LWP), optical depth, particle size, height, and cloud cover, can be estimated from the combined VIR/IR/MW satellite data (Lin et al. 1998a & b). This study will use the VIS/IR/MW measurements of VIRS and TMI on-board of TRMM satellite to retrieve cloud properties.

2. DATA AND METHODS

The TRMM satellite has a low (350km) altitude, circular orbit with a 35° inclination angle. The data used in this study was obtained during January 1998. The VIRS is an AVHRR-like five channel imaging spectroradiometer with bands in the wavelength range from 0.6 to 12μm. The spatial resolution is about 2.1km at nadir view. TMI is a 9-channel, passive thermal microwave radiometer. It measures radiances at frequencies of 10.65, 19.35, 21.3, 37.0, and 85.5 GHz (hereafter referred to as 10, 19, 21, 37 and 85 GHz for short). The vertically (v) and horizontally (h) polarized measurements are taken at all frequencies, except at 21 GHz where TMI, like SSM/I, only has a vertically polarized channel. The spatial resolution varies from about 4.6×7.2 km^2 at 85 GHz to 9.1×63.2 km^2 at 10 GHz. The details of the instruments can be found from Kummerow et al. (1998).

The retrievals of current study are all from rain-free conditions. The rain/no rain decision is made using TMI 37GHz polarization difference with a threshold of 37K, which is the same as that used in Lin and Rossow (1994). The algorithm developed to estimate cloud liquid water path (LWP) and temperature (Tw) using TMI data is based on the method for SSM/I measurements (Lin et al. 1998a). Since Tb values at 85 GHz channels have significantly different Tw characteristics from those of 37GHz channels, combining the observations of 37 and 85 GHz channels, we can estimate LWP and Tw values simultaneously. The cloud top temperature (Tc) and optical depth (τ) are retrieved from VIRS. Particle size for water clouds is estimated using the following equation: $r_e = 1.5LWP/(\rho_w\tau)$, where ρ_w is water density.

Corresponding author's address: Bing Lin, MS 420, NASA Langley Research Center, Hampton, VA 23681; E-Mail: B.Lin@larc.nasa.gov.

3. RESULTS

The matched data sets for VIRS and TMI pixels show that the frequency of overcast clouds varies in all FOV scales of TMI channels. At the scale of the FOV of TMI 37 GHz channels (~16 km), about 53% of the overcast cases are warm clouds (Tc > 273.15K), and the others are cold. For these overcast clouds and at larger spatial scales (~63km; or FOV of 10GHz channels), very few cases are detected multi-layered by VIRS, indicating the overcast clouds (or the top layers of the clouds if they are multi-layered) have horizontal scale length ≥ 60km. Vertically, the retrievals of VIRS LWP, Tc, TMI LWP and Tw show that these overcast clouds have very complicated structure. Multi-layered cases (~30%) are frequently observed.

Figure 1 shows the histogram of LWP values estimated from TMI and VIRS (the left panel is for 45°S to 45°N, while right panel is for 20°S to 20°N). Since the samples over tropics for TRMM are much more than over midlatitudes, the quasi-global statistics are similar to those of tropics. Although a lot of warm clouds have low water amount (< 0.05mm), some of them have large values (> 0.2mm). The means are around 0.06mm. Comparing VIRS and TMI LWP retrievals, this study finds that warm clouds generally have much more column liquid water than cold clouds (~0.01mm). The total water amounts for cold clouds (~0.15mm) are larger than those of warm clouds. Ice water contributes significantly to the totals. The distribution of Tw determined by TMI (Figure 2) is

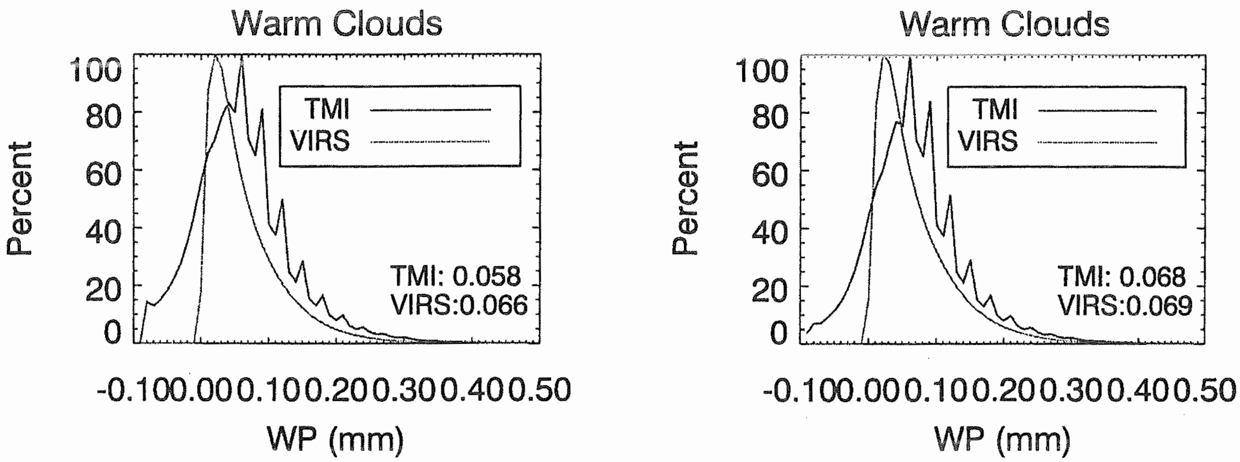

Figure 1: Histograms of LWP for warm overcast clouds.

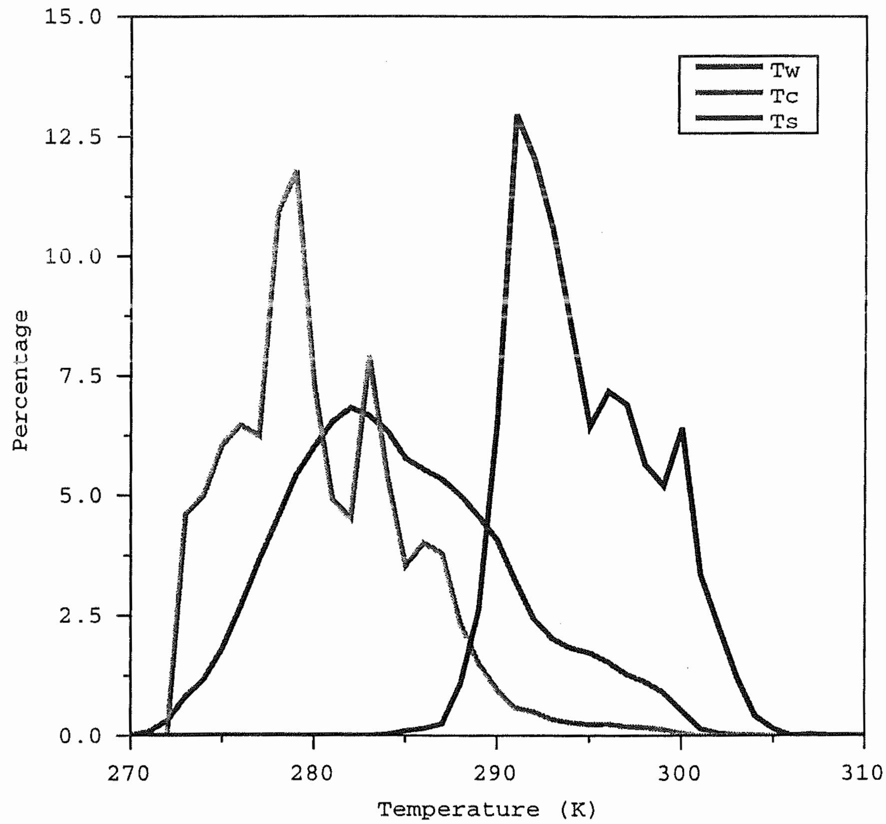


```
Mean Tw = 284.6649 Std = 5.976768
Mean Tc = 280.3620 Std = 4.765409
Mean Ts = 294.6388 Std = 3.738696
```

Figure 2: Histograms of Tc, Tw, and Ts.

similar to that of VIRS Tc for warm overcast clouds except it is warmer and broader due to deep penetration of microwave radiation to clouds and multi-layered clouds. The uncertainties in Tw retrievals also contribute some of the broadening (Lin et al. 1998a). The estimated particle size is about 16μm, which could be overestimated due to underestimation in optical depth.

4. DISCUSSION

This study discusses the micro/macro-properties of overcast clouds using TRMM data. This study, along with previous results for SSM/I data, shows that the combination of visible, infrared, and microwave satellite measurements gives us a great potential for monitoring the multi-layered cloud systems with ice on the top of water over large spatial and long time scales, especially over tropical oceans.

Acknowledgements

The authors thank G. Gibson, Ben Ho, and Y. Hu for their many suggestions. This research is part of the Clouds and the Earth's Radiant Energy System under the NASA Earth Observing System. The authors gratefully acknowledge support from NASA under grant NAG-1-1963. The Distributed Active Archive Center at NASA Goddard Space Flight Center provides VIRS and TMI data.

References

Kummerow, C., W. Barnes, T. Kozu, J. Shiue, and J. Simpson, 1998: The tropical rainfall measuring mission (TRMM) sensor package, J. Atmos. Oceanic Tech., 15, 809-817.

Lin, B. and W.B. Rossow, 1994: Observations of cloud liquid water path over oceans: optical and microwave remote sensing methods, J. Geophys. Res., 99, 20907-20927.

Lin, B., B. Wielicki, P. Minnis, and W. Rossow, 1998a: Estimation of water cloud properties from satellite microwave, infrared and visible measurements in oceanic environments, I: microwave brightness temperature simulations, J. Geophys. Res., 103, 3873-3886.

Lin, B., P. Minnis, B. Wielicki, David R. Doelling, Rabindra Palikonda, David F. Young, and T. Uttal, 1998b: Estimation of water cloud properties from satellite microwave, infrared, and visible measurements in oceanic environments. II: Results, J. Geophys. Res., 103, 3887-3905.

QUANTIFYING CLOUD TEXTURE AND MORPHOLOGY USING GENERALIZED SCALE INVARIANCE

J.-B. Addor,[1] S. Lovejoy,[1] and D. Schertzer[2]

[1]Physics, McGill University, Montréal, Québec, H3A 2T8, Canada
[2]LMM, CNRS, Université Pierre et Marie Curie, F-75252 Paris, France

1. INTRODUCTION

Using various isotropic scaling analysis techniques (including isotropic energy spectra) we established on nearly 1000 cloud images (spanning the range 0.5m to 5000km) that cloud radiance fields are accurately (multi) scaling (Stanway 2000, Lovejoy et al. 2000, Sachs et al. 2000). Since cloud morphology and type obviously vary significantly from image to image (even within images), we anticipate that the latter are determined by the scale by scale (differential) anisotropy associated with anisotropic (nonself-similar) scaling.

Schertzer and Lovejoy 1985 introduced the formalism for describing anisotropic scale invariance: "Generalized Scale Invariance" (GSI). It involves a group of scale changing operators which are quantified by their generator. In this report, we describe a new GSI analysis technique called the local scale invariant generator (LSIG) technique and test it out on infra red and visible channel AVHRR satellite pictures of clouds. The linear approximation to GSI (quantified by 4 parameters) yields a scale invariant characterization of local cloud texture. We find that this scale invariant texture varies considerably (apparently stochastically) from one region of a cloud to another and discuss the implications for objective classification of clouds and multifractal cloud simulations. By making systematics linear approximations with the new technique, we show how the (stochastic, nonlinear) infinitesimal generator of the anisotropy can be estimated.

2. THE ELEMENTS OF GENERALIZED SCALE INVARIANCE

To be completely defined, GSI needs three basic elements which can be summarized as follows:

- A unit ball B_1 whose "frontier" defines all the unit vectors.
- A scale changing operator T_λ which transforms the scale of vectors by scale ratio λ; with B_1, T_λ yields all the balls, all the vectors. T_λ is the rule relating the statistical properties at one scale to another and involves only the scale ratio (there is no characteristic "size"). This implies that T_λ has certain properties. In particular, if and only if $\lambda_1\lambda_2 = \lambda$, then

  $$T_{\lambda_2}T_{\lambda_1}B_1 = T_{\lambda_1}T_{\lambda_2}B_1 = T_\lambda B_1 = B_\lambda.$$

  i.e., T_λ is a one parameter multiplicative group:

  $$T_\lambda = \lambda^{-G_{\text{op}}},$$

  where G_{op} is an operator called the "infinitesimal generator". When G_{op} is a matrix, we have linear GSI, when the matrix is diagonal we have self-affine geometry, when G_{op} is the identity, self-similarity.
- A measure of scale for each elementary ball. This could be taken as the usual area or volume (a Lebesgue measure). These elementary balls can then be used to produce anisotropic coverings and hence for arbitrary sets to define anisotropic Hausdorff measures, in this way, any set can be measured (integrated).

3. STRUCTURE FUNCTION ANALYSIS OF DATA

A convenient way to characterize the scaling and anisotropy is via structure functions; for simplicity we consider only the usual second order case:

$$\begin{aligned} S(\vec{x}) &= \left\langle \left(f(\vec{x}+\vec{x'}) - f(\vec{x'}) \right)^2 \right\rangle \\ &= 2\left(\left\langle f(\vec{x'})^2 \right\rangle - \left\langle f(\vec{x}+\vec{x'})f(\vec{x'}) \right\rangle \right), \end{aligned}$$

where the angle brackets indicate averaging over an ensemble of clouds fields with identical anisotropies

[1]Corresponding author's address: S. Lovejoy, Physics department, McGill University, 3600 University St., Montréal, Québec, H3A 2T8, Canada; E-mail: lovejoy@physics.mcgill.ca.

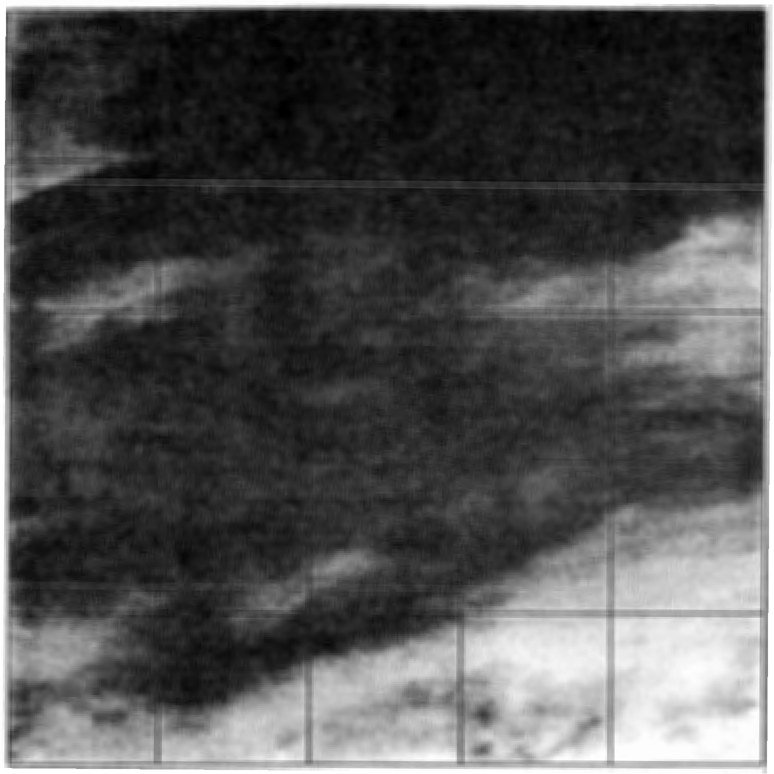

Figure 1: The infra red cloud image

The infra red cloud image (in a flat land area) used for the analysis. The picture is divided in 5x5 blocs (shown) for all the analysis.

(here replaced by spatial averaging). The isotropic scaling tested in Stanway 2000 is equivalent to:

$$S(T_\lambda \vec{x}) = \lambda^{-\xi} S(\vec{x}),$$

with $T_\lambda = \lambda^{-1}$ (i.e. G_{op} = identity). It was found that, although ξ varied from one image to another, that, on the ensemble, for IR imagery, $\xi = .48$, but varied between 0.3 and 0.8 on individual images. Although the SIG technique was applied to the spectral energy density, it turns out that the mathematically equivalent real space technique (using structure functions) is advantageous not least because it easily permits generalization to study of the anisotropy of moments of arbitrary order (the spectrum is a second order moment). In figure 1, the infra red channel of a cloud image, can be considered as a random field and the structure function can be computed on it. To investigate the spatial variations of the images statistics, it has been divided into 25 blocks, 64 by 64 pixels each, shown in figure 1. The using contour lines figure 2 shows the structure functions calculated on the corresponding blocks. The first comment is that the isotropic ξ parameter of these structure functions is nearly the same on each block ($\xi = .28 \pm .01$), indicating that the isotropic scaling is quite robust. The second observation is that there is no obvious trend in the anisotropy. Comparing figure 1 and 2 however, we see that the anisotropy in S is clearly linked to variations in texture. For example, the structure functions in the second row show a dominating horizontal pattern that can be explained, on the corresponding row of figure 1, by the upper part of the blocks being dark opposed to the clear lower part, with a very sharp separation line. The same phenomenon can be observed for the two last blocks of the fourth row and for the second and the third blocks of last row. The pattern of the remaining blocks of figure 2 is also elliptical, but with a much smaller horizontal component. The differences between blocks indicate a strong spatial variability in the anisotropy. This significant spatial variability brings into question the basis of previous methods which assumed only slow variations. As we were searching for a scaling characterization of the

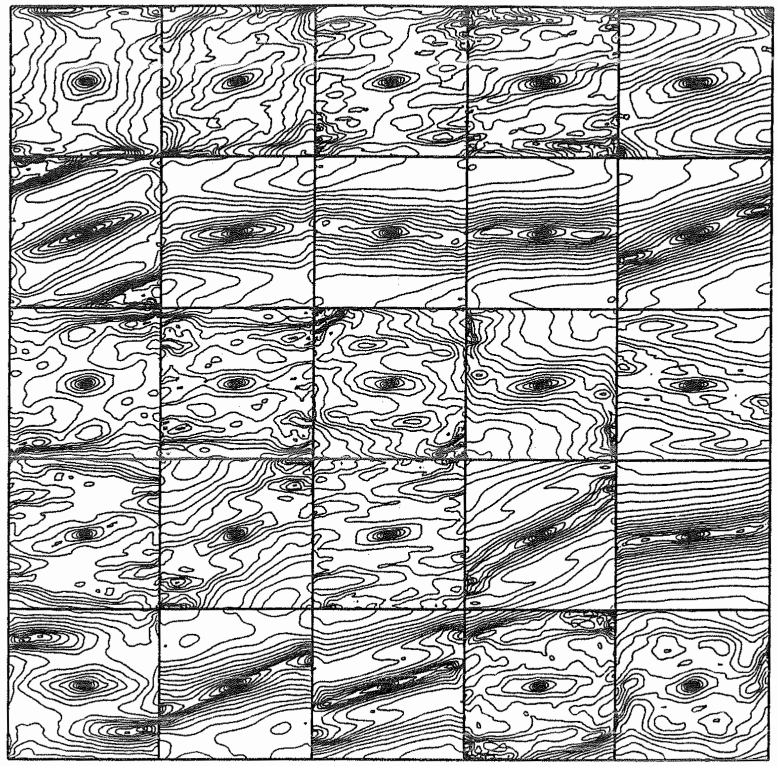

Figure 2: The infra red structure functions calculated on each bloc

anisotropy of the structure function and as we required that the same characterization would be valid for all the blocks constituting the whole image, we see that we will have to take into account the apparently stochastic spatial variability in the anisotropy which will require stochastic generators; see below. Further work will have to focus on a stochastic description not only of the cloud fluctuations themselves, but also of their anisotropies.

4. DIRECT ESTIMATE OF GSI GENERATORS THE LSIG TECHNIQUE

In Pflug et al. 1993, the first technique for estimating the generator of the scale changing operator was described. This method had the significant drawback of requiring simultaneous estimates of the parameters describing the unit ball as well as linear approximation to the generator (a total of at least 7 parameters). Lewis et al. 1999 describe a significant improvement, the Scale Invariant Generator technique (SIG) which directly estimates the 4 parameters of the generator. Although the SIG technique was a significant improvement, the optimum parameter estimation was barely tractable even on fast computers and required enormous statistics (256x256 points) and assumptions about the small variations of parameters across the region of interest. Finally there was no simple way of generalizing the method to stochastic nonlinear GSI. In the following we describe a further improvement, where we transform the generalized scaling relation into a partial differential equation involving the generator. From there a simple linear regression is performed. Since the solution for the optimum parameters is analytic it is extremely computationally efficient. In addition, the generator can be allowed to be random since "no stringent" smoothing requirements are necessary.

To see how this works we need to define T_λ for a nonlinear (e.g. and here, stochastic) G_{op}. When G_{op} is a matrix, the exponentiation necessary for T_λ can be defined using series expansions, but more generally, for nonlinear GSI, it is defined by:

$$\frac{dT_u}{du} = -G_{\mathrm{op}}T_u; \qquad u = \log\lambda.$$

Operation of this on a unit vector shows that $G_{\mathrm{op}} = \vec{g}(\vec{x}) \cdot \nabla$, where the "infinitesimal transformation" $\vec{g}$

satisfies

$$\frac{d\vec{x}}{du} = \vec{g}(\vec{x}).$$

We can now suppose that S is symmetric with respect to generalized scale changes, i.e.:

$$S\left(T_\lambda \vec{x}\right) = \lambda^{-\xi} S(\vec{x}):$$

where ξ is the exponent of the second order structure function. Since for any function F

$$F\left(e^{uG_{op}}\vec{x}\right) = e^{uG_{op}} F(\vec{x})$$

Therefore, applying this to the scaling of the structure function we obtain:

$$S\left(e^{uG_{op}}\vec{x}\right) = e^{uG_{op}} S(\vec{x}) = e^{-u\xi} S(\vec{x})$$

Hence, taking $u = \epsilon$ (small) and expanding the exponent, keeping first order terms:

$$\vec{g} \cdot \nabla\sigma(\vec{x}) = \xi; \qquad \sigma = -\log S$$

Taking $\xi = 1$ loses no generality since it is equivalent to using a different GSI system with $\vec{g}$ rescaled by ξ. If this is done, then we obtain the standard form:

$$\vec{g} \cdot \nabla\sigma(\vec{x}) = 1$$

This therefore is a partial differential equation for σ, which can be used to estimate $\vec{g}$. On small enough regions (which in principle can be as small as 2x2 pixels), we make the linear approximation:

$$\Delta g_i(\Delta\vec{x}) \approx \mathbf{G}_{ij}\Delta x_j$$

where $\mathbf{G}$ is the a matrix, i.e.:

$$\frac{\partial g_i}{\partial x_j} \approx \mathbf{G}_{ij}$$

$$\Delta\vec{x} \cdot \mathbf{G} \cdot \nabla\sigma = 1$$

5. ESTIMATING G

The basic technique is now straightforward. From S, we calculate the gradient fields $\nabla\sigma = \left(\frac{\partial\sigma}{\partial x}, \frac{\partial\sigma}{\partial y}\right)$ and seek the optimum G e.g. the values which minimize the mean square error:

$$E^2 = \sum_{i=1}^{N^2} \left(\vec{x}_i G \nabla\sigma(\vec{x}_i) - 1\right)^2$$

The sum is over all the points in $\Delta\vec{x}$ space (denote $\vec{x}$ for convenience). In the example here, the region over which we estimate $\vec{g}$ is 64x64 but could be made smaller. The minimization is easy to perform analytically (it only involves the inversion of a 4X4 matrix). We can now estimate $G_{ij} \approx \frac{\partial g_i}{\partial x_j}$ at nearly the same resolution as the data, and then integrate to obtain the infinitesimal $\vec{g}(\vec{x})$.

6. CONCLUSION

LSIG method allows to measure deviations from isotropy on different parts of a typical cloud satellite image. Contrasting with the nearly spatial constancy of ξ = TrG (TrGis the "trace" of $\mathbf{G}$), the anisotropic GSI parameters $\mathbf{G} - \mathbf{1}\mathrm{Tr}\mathbf{G}$ ($\mathbf{G}$ with the trace removed) exhibit strong spatial variations, without any clear trend. These results suggest further work to reconstitute the "infinitesimal" $\vec{g}$.

REFERENCES

Levis, G.M., S. Lovejoy, D. Schertzer, and S. Pecknold, 1999: The scale invariant generator technique for quantifying anisotropic scale invariance. *Computer & Geosciences*, **25**, 963–978.

Lovejoy, S., J.D. Stanway, and D. Schertzer, 2000 (submitted): Direct evidence of atmospheric cascade dynamics from 1 to 20,00 km. *Science.*

Pflug, K., S. Lovejoy, and D. Schertzer, 1993: Generalised Scale Invariance, differential rotation and cloud texture. *Journal of Atmospheric Sciences*, **50**, 538–553.

Schertzer, D., and S. Lovejoy, 1985: Generalized scale invariance in turbulent phenomena. *Physico-Chemical Hydrodynamics Journal*, **6**, 623–635.

Stanway J.D., 2000: Multifractal analysis of cloud radiances from 5000km to 1 km. *Master's of Science Thesis, McGill University.*

EVOLUTION OF A MESO- α -SCALE CONVECTIVE SYSTEM ASSOCIATED WITH A MEI-YU FRONT

Biao Geng[1*], Kazuhisa Tsuboki[1], Takao Takeda[1], Yasushi Fujiyoshi[2] and Hiroshi Uyeda[3]

[1]Institute for Hydrospheric-Atmospheric Sciences, Nagoya University, Japan
[2]Institute of Low Temperature Sciences, Hokkaido University, Japan
[3]Division of Earth and Planetary Sciences, Graduate School of Sciences, Hokkaido University, Japan

1. INTRODUCTION

During the IOP of GAME/HUBEX (the GEWEX Asian Monsoon Experiment/Huaihe River Basin Experiment) in 1998, a long-lived meso- α -scale convective system (MCS) associated with a Mei-Yu front in China was well observed. The MCS formed and persisted from the early morning of June 29 till the morning of June 30. It was composed of several meso- β -scale precipitation clusters which often appeared in band structure. By using data from conventional radar, Doppler radar, special upper-air sounding and surface network, this paper will investigate the structure and evolution of the MCS.

2. EARLY DEVELOPMENT STAGE

This stage was from about 0000 LST to 0800 LST on June 29. The MCS moved eastward at this stage. As shown in Fig. 1a, convective rainbands developed along a direction from southeast to northwest. It is noted that stratiform echoes began to develop to the east of convective echoes. A west-east vertical section through the stratiform area derived from a Doppler radar (Fig. 1b) indicates that a region of enhanced reflectivity appeared at an altitude of 4.5 km in the vicinity of 0°C melting level. Under the melting level, middle-level airflow descended from east to west. This easterly middle-level inflow was first observed in the stratiform area at an altitude of about 4.0 km and gradually descended into the surface. It reached the surface at about 0800 LST, when surface temperature dropped considerably.

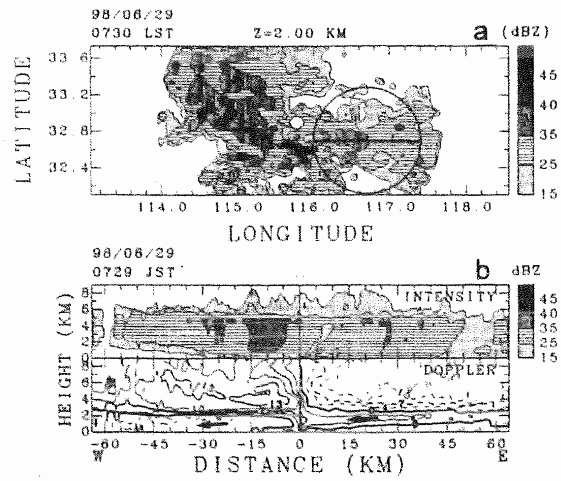

Fig. 1. (a) Horizontal distribution of radar reflectivity observed by the conventional radar at 0730 LST on June 29. Circle indicates the coverage of the Doppler radar. (b) Vertical cross sections of radar reflectivity and Doppler velocity observed by the Doppler radar along a line shown in (a), with positive (solid lines) and negative (dashed lines) Doppler velocities toward and away from the Doppler radar, respectively.

3. MATURE AND DECAYING STAGES

During the mature stage from about 0800 LST to 2000 LST on June 29, the movement of the MCS became stagnant. After 2000 LST, the MCS began to decay. At the decaying stage, the system moved southward.

As shown in Fig. 2a, convective rainbands tended to be orientated from west-southwest to east-northeast during the mature and decaying stages. Meanwhile, stratiform precipitation developed mainly to the northeastern portions of

* Current affiliation: Inst. for Global Change Research/FORSGC

* Corresponding author address: Biao Geng, Inst. for Global Change Research/FORSGC, SUMIMOTO HAMAMATSU-CHO BLDG. 4F, 1-18-16 Hamamatsu-cho, Minato-ku, Tokyo 105-0013, Japan

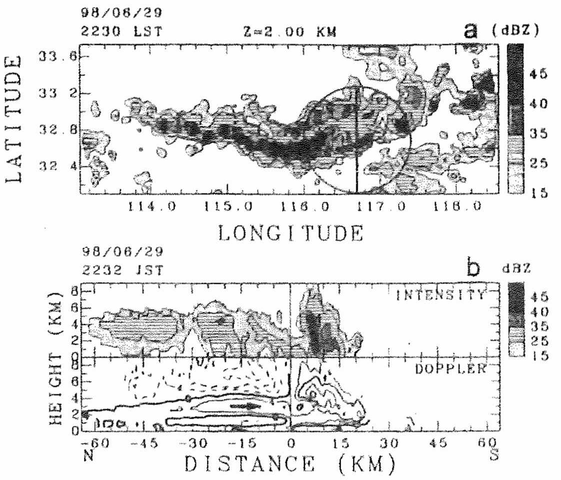

Fig. 2. Same as Fig.1, except for 2230 LST on June 29.

rainbands during the mature state and to the northern portions of rainbands during the decaying stage. Figure 2b shows a north-south vertical section from the Doppler radar. As before, bright band appeared in the stratiform region. Instead of the easterly middle-level inflow during the early development stage, northerly middle-level inflow was observed under the bright band during the mature and decaying stages. The northerly middle-level inflow also formed at an altitude of 4.0 km at first. It reached the surface at about 2000 LST on June 29. The arrival of the northerly middle-level inflow at the surface also accompanied the sudden decrease in surface temperature. Meanwhile, it is also seen from Fig. 2b that low-level airflow entered the system from the leading line of convection, extended up in the convective region, and moved more horizontally into the stratiform region over the bright band.

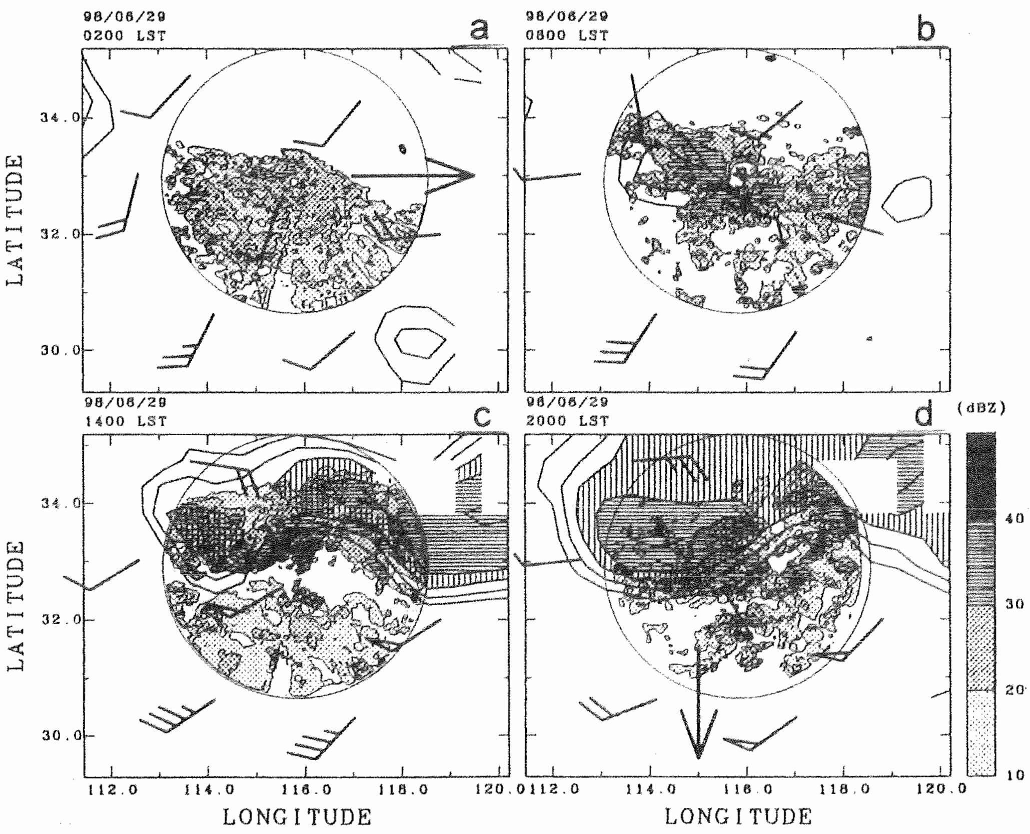

Fig. 3. Evolution of radar reflectivity at an altitude of 2.0 km (dotted), equivalent potential temperature at the surface (contoured every 2°K with the outside contour being 354°K), and horizontal winds derived from radiosonde data at an altitude of 3.0 km (wind bars). Vertically and horizontally hatched area represents equivalent potential temperature between 348°K and 350°K and below 348°K, respectively. Arrows indicate the movement of the MCS. Circle is the coverage of the radar.

4. DISCUSSION AND SUMMARY

The evolution of stratiform precipitation would have been related to the development of vertical vorticity. We have shown that during the early development of the MCS, stratiform precipitation was mainly found in the eastern portions of convective rainbands in the MCS. As shown in Fig. 3a, vertical vorticity at low to middle levels was negative during the early development stage. A middle-level mesoscale cyclone developed from about 0800 LST (Fig.3b). The development of stratiform precipitation to the northeastern and northern portions of convective rainbands corresponded to the increase in the positive vertical vorticity at low to middle levels (Figs.3c, d). As suggested by Houze et al. (1989), the development of stratiform precipitation would have been associated with the supplies of ice particles from convective regions through the gently ascending front-to-rear flow such as seen in Fig. 2b. The trajectories of these particles would have been influenced strongly by the development of vertical vorticity in the MCS, which would be responsible for the formation of stratiform precipitation in different portions of the MCS at different stages.

We have shown that there existed close relationship between the development of stratiform precipitation in different portions of the MCS and the development of middle-level inflow into the MCS from different directions. It was found that the middle-level inflow developed gradually in the area where stratiform precipitation became established. This fact suggests that the formation of the middle-level inflow would be related to processes internal to the MCS.

The propagation of the MCS seemed dependent on the development of cyclonically rotated cold pool associated with the middle-level inflow. The MCS propagated eastward during the early development stage (Fig. 3b). As a cold pool developed in the eastern portion (Fig. 3b), the movement of the MCS became stagnant. The intensified cold pool extended to the northeastern portion and the MCS was stationary during a period of 12 hours (Fig. 3c). Finally, after the stronger cold pool moved to the northern portion (Fig. 3d), the MCS began to propagate southward.

References

Houze, R. A., Jr., S. A. Rutledge, M. I. Biggerstaff, and B. F. Smull, 1989: Interpretation of Doppler weather-radar displays in midlatitude mesoscale convective systems. Bull. Amer. Meteor. Soc., 70, 608-619.

SPATIAL-TEMPORARY VARIATIONS OF TOTAL AND LOWER LAYER CLOUDINESS OVER THE GEORGIAN TERRITORY

A.G. Amiranashvili[1], V.A. Amiranashvili[1], T.G. Gzirishvili[1], Yu.M. Kolesnikov[1], K.A. Tavartkiladze[2]

[1]Institute of Geophysics of Georgian Academy of Sciences, Tbilisi, 380093, Georgia
[2] Institute of Geography of Georgian Academy of Sciences, Tbilisi, 380093, Georgia

1. INTRODUCTION

As it is known the cloudiness represents one of main factors determining the climate formation and change. Therefore studies of long-term cloudiness trends with purpose of predicting their effect on the climate change become quite important. Such investigations in Georgia were started by V.G. Khorguani (e.g. Khorguani et al. (1996)). This work represents a continuation of the mentioned investigations.

2. METHODS

The following characteristics of cloudiness were considered Mazin et al. (1989): Total (G) and lower (g) cloudiness. A unit of cloudiness amount corresponds to a sky visible above 15^{O} from the horizon, by 10% covered by clouds. To lower cloudiness belong lower layer clouds with an upper vertical elevation limit at 2000 m and a lower - at the Earth's surface respectively, and also cumulus clouds with the bases at a lower cloudiness level regardless of their upper limit levels. To total cloudiness belong all clouds observed simultaneously. The mean monthly visual observation data on cloudiness at 46 meteorological stations of Georgia from 1936 till 1991 were analysed. The stations were located at elevations from 0 to 2850 m above the sea level. 28 stations were in Western Georgia, 18 of them - in Eastern Georgia. Missing observational data were recovered using the method of expanding of random functions into orthogonal vectors, Obukhov (1960). The accuracy of the recovered data for G amounted at the average to 75%, while for g – to about 65%.

Corresponding author's address: Avtandil Amiranashvili, Geophysics Institute of Georgian Academy of Sciences, 1., M. Aleksidze Str., Tbilisi 380093, Georgia;
E-Mail: vazha@excite.com

For each station the coefficients of linear trends $y=a\cdot(t-1935)+b$ were calculated, where y is a value of G or g, t – years, $1936 \leq t \leq 1991$. The data analysis showed that with a probability not worse than 90% according to Student's criterium changes in the mean annual values of G and g in the cold and warm seasons of the year take place if the variations of cloudiness are heigher than ± 0.5 per 100 years according to the calculated linear trends.

3. RESULTS

The data on total and lower cloudiness over the Georgian territory and their variation tendencies are presented in Fig. 1-4 and Tables 1 and 2.

As it follows from Fig. 1 and 2 and Table 1 the regimes of total and lower cloudiness in Western and Eastern Georgia do not differ much from each other both in the warm and cold seasons of the year. The variability characters of the mean annual values of G in Western and Eastern Georgia are also similar. In the cold season in both parts of the country negative trends of G prevail. In the warm season in Western Georgia at most stations (46%) positive trends of G are detected, while in Eastern Georgia at most stations (56%) there are no trends.

Lower cloudiness trends in Western Georgia at the average per year and in the cold season are mainly negative, while in the warm season – positive. In Eastern Georgia for all seasons of the year clear positive trends are observed for g. for the whole territory of Georgia at the average per year and in the warm season at most stations trends of G were not detected.

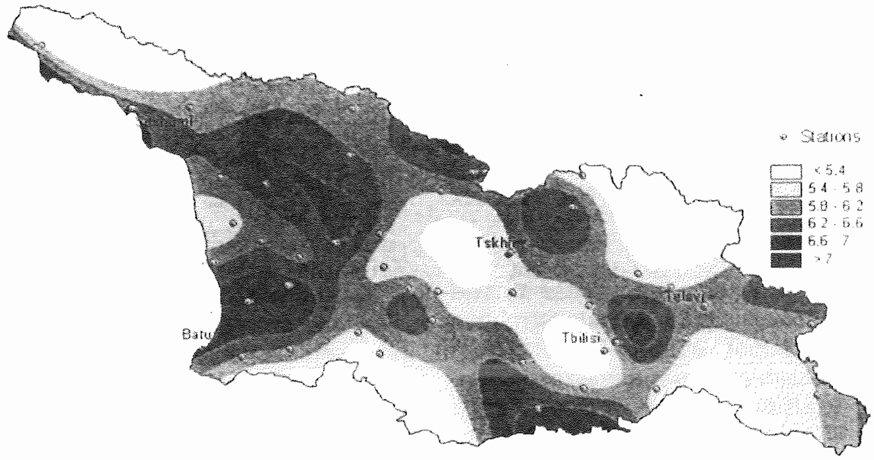

Fig. 1

The distribution of the mean annual values of total cloudiness over the territory of Georgia (averaged for 1936-1991)

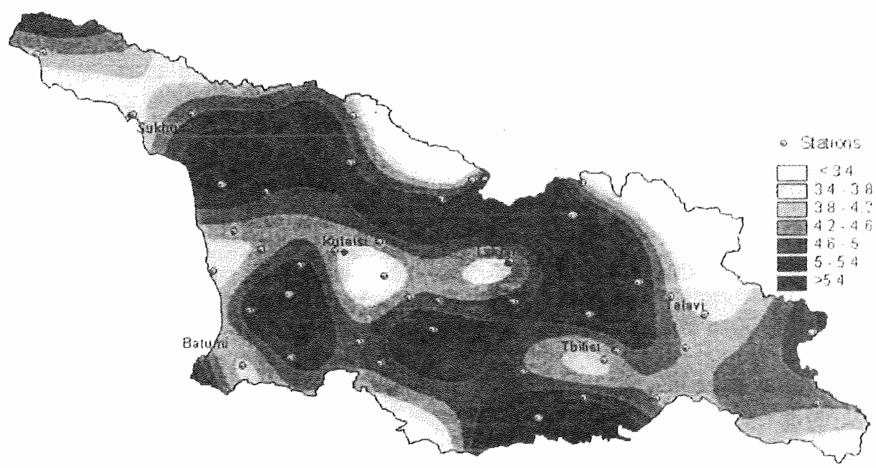

Fig.2

The distribution of the mean annual values of lower cloudiness over the territory of Georgia (averaged for 1936-1991)

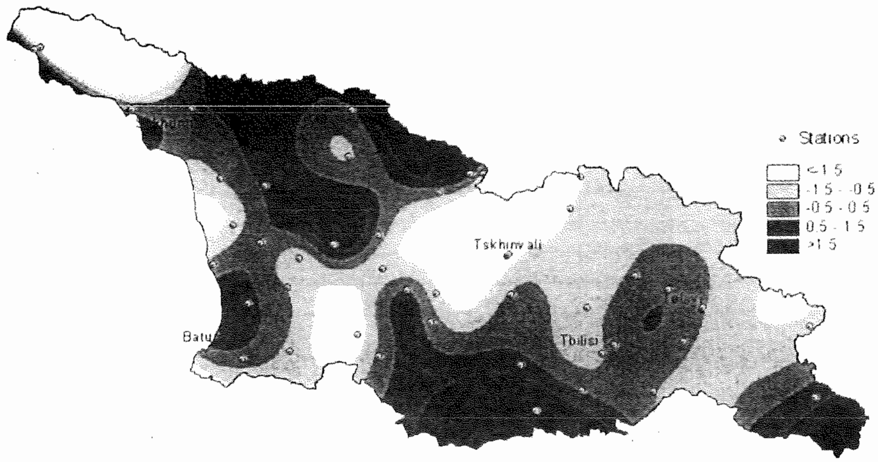

Fig.3

The variability of the mean annual values of total cloudiness over the territory of Georgia
(a unit per for 100 years)

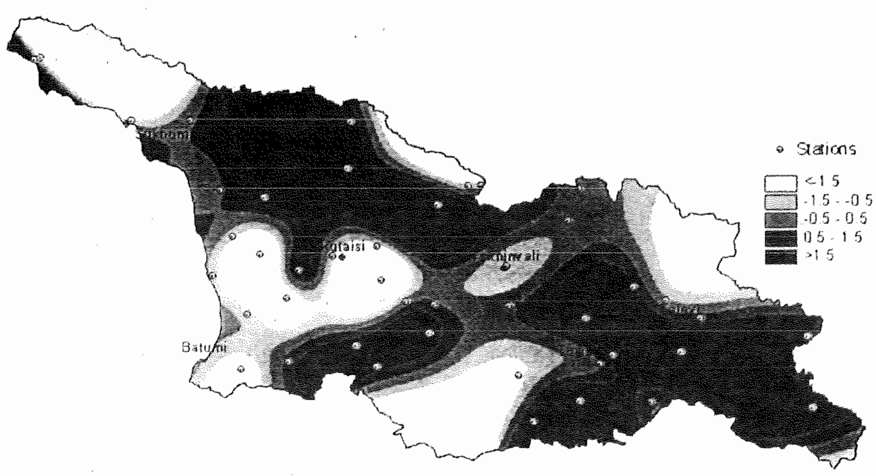

Fig.4

The variability of the mean annual values of lower cloudiness over the territory of Georgia
(a unit per for 100 years)

Table 1

Statistical characteristics of total and lower cloudiness in Georgia

Region	Cloud. type	Year		Cold season		Warm season	
		Mean	St. dev.	Mean	St. dev.	Mean	St. dev.
Western Georgia	G	6.2	0.34	6.4	0.50	6.0	0.40
	g	4.4	0.56	4.3	0.67	4.4	0.63
Eastern Georgia	G	6.0	0.43	6.1	0.56	5.8	0.52
	g	4.6	0.58	4.6	0.69	4.5	0.66
Whole territory	G	6.1	0.39	6.3	0.54	5.9	0.46
	g	4.5	0.57	4.4	0.68	4.4	0.64

Table 2

Occurence of total and lower cloudiness trends in Georgia
(% with reference to the number of stations)

Region	Cloud. type	Year			Cold season			Warm season		
		Trend			Trend			Trend		
		(+)	(-)	(0)	(+)	(-)	(0)	(+)	(-)	(0)
West. Georg.	G	21	36	43	11	50	39	46	18	36
	g	39	47	14	36	43	21	50	43	7
East. Georg.	G	22	39	39	17	56	27	27	17	56
	g	61	11	28	56	28	16	72	6	22
Whole territ.	G	22	37	41	13	52	35	39	17	44
	g	48	32	20	43	37	20	59	28	13

The data also show that in the cold season at most stations negative trends of G are detected. As regards lower cloudiness, for the whole territory of Georgia at most stations in all seasons positive trends are observed (Fig. 4 and Table 2). In the future it is planned to continue the investigations of total and lower cloudiness in Georgia using a more considerable number of meteorological stations.

4. REFERENCES

Khorguani, V.G., Gvazava R.A., 1996: Secular Regime of Cloudiness in Georgia, Proc. 12 th Int. Conf. on Clouds and Precipitation, Zurich, Switzerland, vol. 2, 1024-1025.

Mazin, I.P., Khrgian A.Kh., 1989: Handbook of Clouds and Cloudy Atmosphere, Leningrad, Gidrometeoizdat, p. 647 (in Russian).

Obukhov, A.M., 1960: On Statistically Orthogonal Expansion of Empiric Functions, Izv. AN SSSR, Ser. Geophys., N3, 432-439 (in Russian).

THE LIFE-CYCLE OF HIGH CLOUDS

Martin Köhler[1] and Brian Soden[2]

[1]European Center of Medium-Range Weather Forecasting, Reading, RG2 9AX, UK
[2]Geophysical Fluid Dynamics Laboratory, Princeton, New Jersey, 08542, USA

1. INTRODUCTION

High clouds play an important role in the radiation budget of the Earth. Yet, their evolution is poorly documented quantitatively and the dominant mechanisms for their maintenance are not well established. Of particular interest are the following problems:

- *life-time of high clouds* They have been believed to last for up to days (Randall 1989) and be advected over thousands of kilometers.
- *spatial evolution of high clouds* - in terms of horizontal and vertical cloud fraction, and cloud cell scale.
- *total upper tropospheric water budget* - cloud water and water vapor.
- *sensitivity of high cloud life-cycle* - to solar radiation, land vs. ocean, tropics vs. mid-latitudes, large-scale vertical velocity, environmental static stability, environmental relative humidity.

Boer and Ramanathan (1997) focused on the tracking of mesoscale convective systems, with emphasis on the effect of spatial scale.

In this paper, a simple tracking algorithm is used to quantify the typical life-time of hig clouds as well as the anvil spreading time-scale.

2. METHODOLOGY

Our analysis is based on geostationary observations of infra-red brightness temperature ($T_{11\mu m}$) from GOES-7, a measure highly sensitive to high cloudiness. The resolution is 1 hour and 8 km, the time period is August 1987, and the spatial region spans from the equator to 30 degree North and from the Western Pacific to the Central Atlantic.

High clouds are tracked from one hour to the next by selecting the displacement yielding the highest time-lagged cross-correlations of $T_{11\mu m}$ with the original box (368km^2 or 46^2 pixels). The procedure is consecutively repeated to produce cloud tracks of 4 days. See Soden (1998) for details of this tracking method applied to the water vapor channel.

For the analysis of the resulting cloud tracks we define two variables:

- *high cloud fraction*: fraction of pixels with $T_{11\mu m}$ < 250 K. An optically thick cloud with that $T_{11\mu m}$ would be mostly in the ice phase.
- $mean(T_{11\mu m})_{cld}$: using the above high cloud definition. This variable is mostly a function of the cloud optical thickness τ and the cloud top temperature $T_{cld,top}$. Assuming that the cloud top temperature is approximately constant during each track, the $mean(T_{11\mu m})_{cld}$ becomes a function of the ice water path (*IWP*) only ($\tau \sim IWP$).

3. PRELIMINARY RESULTS

A mean life-time of high clouds can be estimated from a large sample of tracks. First, only tracks, whose $mean(T_{11\mu m})_{cld}$ peaked below 230 K, were chosen. Those 354 tracks are then synchronized around their peak (Fig. 1). The mean evolution exhibits a ~4 hr creation e-folding time-scale and a ~5 hr decay time-scale. Fig. 2 shows the identical tracks, but plots high cloud fraction. The corresponding time-scales are ~7.5 hr and ~9.5 hr for creation and decay.

The mean peak in cloud fraction (Fig. 2) lags the peak in $mean(T_{11\mu m})_{cld}$ by ~1.5 hr. We attribute that lag to the anvil spreading time-scale. When repeating the analysis with a cloud definition threshold of 270 K (instead of 250 K), and therefore detecting thinner clouds, the time-lag increases to ~2.5 hr (not shown). This is consistent with the assumption that the anvils become thinner while spreading.

Corresponding author address:
Martin Köhler, Shinfield Park, Reading, RG2 9AX, UK; e-mail: martin.koehler@ecmwf.int.

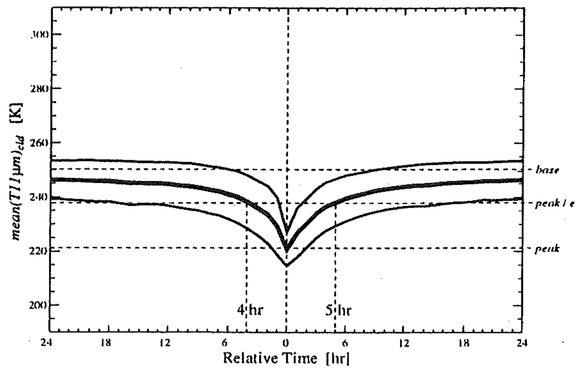

FIG. 1. Statistics of 354 high cloud evolutions of cloud mean 11μm brightness temperatures, selected to all have minima below 230 K and synchronized to all peak at t=0. The central thick line corresponds to the mean evolution and the thin lines represent the intrinsic variability (sample standard deviation).

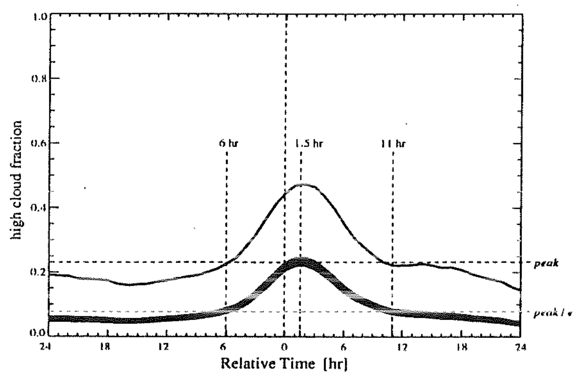

FIG. 2. Same high cloud evolutions as in Fig. 1, but plotting high cloud fraction. Note the approximately 1.5 hour later peak compared to Fig. 1.

The effect of solar radiation on the evolution of individual high cloud systems was investigated by synchronizing their evolution with the daily cycle (not shown). Over land we found a minimum in cloud fraction and maximum in $mean(T_{11\mu m})_{cld}$ in the morning (10am) and the opposite in the afternoon (6pm). This effect can easily be understood in terms of cumulus detrainment being more active in the afternoon in response to surface heating.

Over oceans, the observed maximum in high cloud fraction in the afternoon (3pm) is less obvious. Possible explanations include the daily cycle in sea surface temperature (~1 K) and the rising of high clouds due to solar heating and the related adiabatic cooling.

5. SUMMARY AND DISCUSSION

Two main results emerged from the study of the Lagrangian evolution of high cloud fraction and mean 11μm brightness temperature:

- E-folding time-scale for creation and decay of high clouds are around 4-7 and 5-9 hours respectively.

  Note that both parts of the evolution are governed by quite different mechanisms (e.g. deep convective detrainment vs. cloud layer scale mixing, falling of ice crystals, radiative cooling). It is therefore expected for the two corresponding time-scales to be rather independent.

  The high cloud fraction was found to peak about 1-3 hours after the peak in mean 11μm brightness temperature, which can be interpreted as the peak in ice water path.

  This time-scale may be understood as an estimate of the time anvil take to spread, while decaying in optical thickness below a corresponding threshold.

In completion of this study, the water vapor channel will be used to estimate the upper tropospheric water vapor in the environment of the high clouds. Beside radiative effects and large-scale motion, we expect the mixing of cloudy and dry air to play a dominant role in the determination of high-cloud life-times.

Acknowledgments: We like to thank Leo Donner, Stephen Klein, Isaac Held, Bjorn Stevens and V. Ramanathan for valuable comments. This research was partly supported by a visiting scientist fellowship at the Geophysical Fluid Dynamics Laboratory.

REFERENCES

Boer, E. R. and V. Ramanathan, 1997: Lagrangian approach for deriving cloud characteristics from satellite observations and its implications to cloud parameterization. *J. Geophys. Res.*, **102** (D17), 21383-21399.

Randall, D. A., 1989: Cloud Parameterization for Climate Models: Status and Prospects. *Atmos. Res.*, **23**, 345-362.

Soden, B. J., 1998: Tracking upper tropospheric water vapor radiances: A satellite perspective. *J. Geophys. Res.*, **103** (D14), 17069-17081.

NUMERICAL STUDY THE STRUCTURE OF THE CLOUD-CYCLONE SYSTEM FORMED OVER NORTH ATLANTIC IN THE FASTEX REGION AND PASSED OVER UKRAINE IN JANUARY 1997

Pirnach, A.[1], A.Belokobylski, G.Dukel, S. Krakovskaia

Ukrainian Hydrometeorological Research Institute, Kiev, Ukraine

1. INTRODUCTION

The field operations of the Fronts and Atlantic Storm Track Experiment (FASTEX) have take place in January and February 1997. FASTEX is a cooperative research program involving scientists from many countries, research institution, and scientific community (see Thrope and Shapiro, 1995). The primary objectives of FASTEX are intended to advance the scientific understanding nessesary to enable detailed diagnosis and prediction of the life cycles and effects of eastern Atlantic storms and their associated cloud and precipitation systems.

This paper presents an investigation of the cloud and precipitation fields associated with western cyclone moved toward Ukraine from North Atlantic during Intensive Observation Period (IOP) of FASTEX on January 12, 1997 (IOP-2 experiment).

The planned primary mission of this experiment was the cold frontal rainband study on an active portion of the cold front extending from an open wave that is being tracked as Low 11. The approach of Low 12 from the west is expected to lead to the further development of the cyclone.

3-D nowacasting and forecasting numerical models developed in Ukrainian Hydrometeorological Research Institute were used for the study. Transformation of air mass moved from the FASTEX region toward Ukraine was studied. Rawinsonde, aircraft, radar observations and appropriate synoptic charts were used as initial data for investigation and simulation of frontal and cyclone cloud systems passed over different regions. The evolution of cloud systems moved over Great Britain, France and Ukraine was simulated. The model runs have to represent the response of the weather over Ukraine to cyclone formation processes over North Atlantic. A system of two warm fronts was observed in response to it over Ukraine.

Influence on cloud and precipitation development of different dynamical and microphysical conditions was investigated and comparison between the natural and modeled frontal cloud systems was performed.

2. A SHORT DESCRIPTION OF THE RESEARCH METHODOLOGY

A set of cloud resolving models with explicit microphysics has been developed at UHRI for the simulation of various types of frontal cloud systems. For the simulation 3-D version of model was selected and further improved. The formation and development in space and time of atmospheric state and the clouds' rainbands were simulated by integration of a full thermodynamic equation set, which included primitive equations for air motion, water vapour content, temperature transfer, the continuity and thermodynamic state equations. The additional integro-differential equations for the supersaturation with respect to water and ice were used. Cloud microphysics is considered explicitly by solving the kinetic equations for the droplet and crystal size distribution functions. The size distribution functions of the cloud and precipitation particles are formed due to cloud condensation nucleation, ice nucleation, growth (evaporation) by deposition, freezing, riming, collection by raindrops of cloud drops (see Buikov, 1978, Krakovskaia and Pirnach, 1998, Pirnach, 1976, 1987, 1998, Pirnach and Krakovskaia,1994). Parameterisation of droplet and ice nucleation is used (Buikov, 1978, Hobbs et al.,1977, Twomey, 1959, Valy, 1975).

3. INVESTIGATION OF THE ATLANTIC REGION CLOUD SYSTEMS

The main focus of this study is the intercomparison of the different modeled objects with each other and the observations. Of particular importance to this study is the prediction of time development of rainbands with different properties.

Synoptic charts, sounding data, satelite data and reports of precipitation at the surface and other observational data for these events were included into modeling. The used additional rawinsondes that were launching from ships

Corresponding author's address: Anne M. Pirnach, Ukrainian Hydrometeorological Research Institute, 37 Nauki Avenue, Kiev, 03028, Ukraine; E-Mail: hanna@ozsol.kiev.ua.

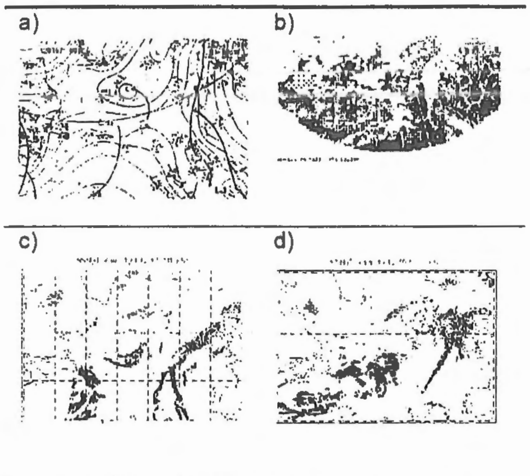

Figure 1. Surface analysis of weather during the IOP-2 Experiment over North Atlantic region on 12 January 1997. Reconstruction, based on data supplied via the Internet from the FASTEX Central Archive: a) surface map at 0000 GMT on 12 January; b) satellite image (mosaic IR data) at 1200 GMT on 12 January; c) regions with intensive rain at time 1500 GMT on 12 January; d) as c) at 0300 GMT on 13 January.

into the FASTEX region and series of dropsondes greatly improved the model initialization and allow to capture adequately the clouds and rainbands of not significant scales for the regular rawinsonding.

The models were initialized with regular rawinsondes, special sounding from ships and aircraft dropsondes data at 1200 GMT on 12 January 1997 (t=0, initial calculation time for the North Atlantic region) from FASTEX data archives. On 12 January 1997 the pressure lows situated in vicinity the Greenland coast to Northwest of the investigated region (Fig.1a). These lows forced the further developing of cyclone that moved in eastward and defined the weather over north Europe and Ukraine in particularly during 12-15 January.

The most interesting events were connected with the cold front located in eastern part of investigated Atlantic region and had length of a more 2000 km. The cloud cover of this front is well identified from satellite imaginary (see Fig.1b). The same an extensive cloud cover existed in vicinity of pressure lows. The large precipitation areas located in these regions.

3.1 A NUMERICAL STUDY THE DIFFERENT SCALE COLD FRONT RAINBANDS

Models with regular, nested and stretched grids were used for modeling of different weather events into Atlantic area. The coarsest grid had a 200 km grid increment covering the area shown into Fig.2 (first row). The origin co-ordinate point is (lon, lat)=(0,50°).

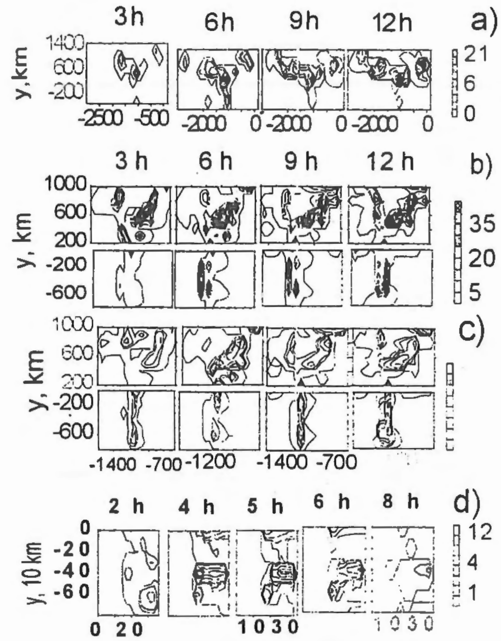

Figure 2. Computed rainband space and time development over North Atlantic. a) sum of z-integrals of liquid water and ice content presented as precipitation rate, mm/h, for most coarse grid; b) as a) for frontal region with regular grid; c) precipitation rate for the frontal region, mm/h; d) precipitation rate, mm/h, for westernmost rainband with finest nested grid in southern part of frontal system. Original coordinate point of nested grid corespond to x=-1165 km for the frontal regular grid, xs=3 km.

Numerical simulation with this grid allows to construct a large picture of a cloud cover over Atlantic region at initial time (t=0, 1200 GMT) and next 12 h of its time development. The most intensive cloudiness was connected with the cold front and pressure lows.

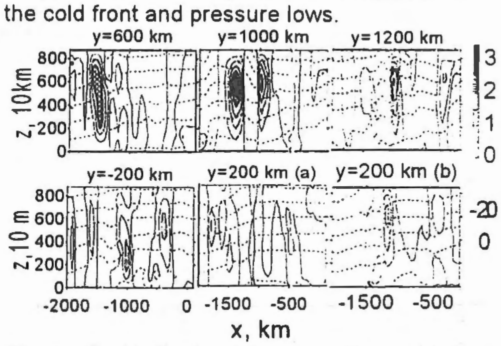

Figure 3. Vertical sections of the cold front along y-axis: (a) at t=0; (b) at t=12 h and y=200 km. Solid line contoured updraft motions, cm/s (number near scale). Dashed line indicated temperature, °C (number near line).

A regular grid for front region had interval for y-axis (directed from south to north) ys=100km, for x-axis it was xs=50 km (see Figs.2-3). For the non regular grid the coarse grid had xs=ys=100 km. The finest nested grid had a grid space xs=3 km presenting a cold front small rainband on latitude of France. Vertically each model used 36 levels with 250 m spacing.

The study focuses on meteorological events of January 12-13, 1997 examining a sequence of mesoscale and microscale processes that occurred during a cold frontal passage through FASTEX observation network in the middle latitude of North Atlantic. This frontal wave persisted for many hours, producing the bands of updraft motion of different nature that produced patterns and appearing rainbands of different features and scales. The evolution a some from them was modeled and presented in Fig.2-5.

The space and time distribution of temperature and vertical motions at t=0 and t=12h at y=200 km shown in Figs.3. The north part of the frontal cloud system is mainly shown in this picture. Section y=200 km at initial time crossed the central band located between the north and south bands with higher cloud moisture (see Fig.2). After t=5h this band was captured by the eastern flank of a large south rainband.

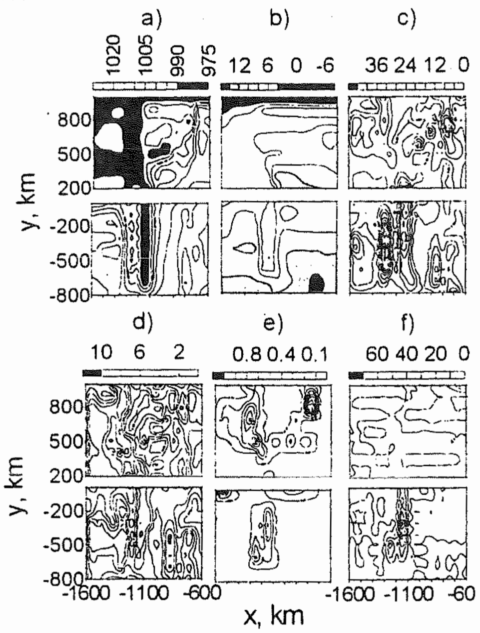

Figure 4. Forecasting for t=12 h, 0000 GMT 13 January. Simulated fields of the: (a) surface pressure, hPa; (b) temperature, °C; (c) z-peaks of updraft motion, cm/s; (d) thickness of updraft columns, km; (e) z-peaks of water content, g/kg; (f) ice concentration, g^{-1}.

As it can see from Fig.3-4 the features of the frontal cloudiness clearly varied along the front. North part frontal cloud system was more large and varied. Furthermore, it is connected with cloud system produced by the low pressure region. Both these events (cold front and pressure lows) persisted many hours forcing and complementing each other.

The features of the south part cloudiness are very different. There were two rainbands evident in Figs.3-4. The easternmost rainband was associated with a pre-frontal line, and the westernmost one was apparently associated with the surface position of the front. The width of each line varied from very thin (>5 km) to 20 km. The calculated space and time development of the western rainband presented by Fig.2, the last row. The most intensive period of this one life coinsided with 2<t<6 hs. In this time interval precipitation intensity exceeded 5 mm/h. After t=7 h this band began to degenerate and the easternmost rainband developed rapidly. It clearly indicated into Figs.2-4. Distribution of vertical motion at 12h presented the band of convective updrafts (Fig.3b) accompanied the easternmost small rainband with heavy rainfall. The peak of precipitation rate was depicted in this rainband and reached 12 mm/h.

3.2 FEATURES OF CLOUD DEVELOPMENT OVER GREAT BRITAIN AND FRANCE

The cloud cover over Great Britain was determined by outward environment. The cold front from west and pressure low from north and northeast produced the cloudiness that spread slowly and cover the whole country.

The surface high pressure over France not allows the propagation of fronlal features into the country. Only separate clouds were detected near coast line and over the Bay of Biscay.

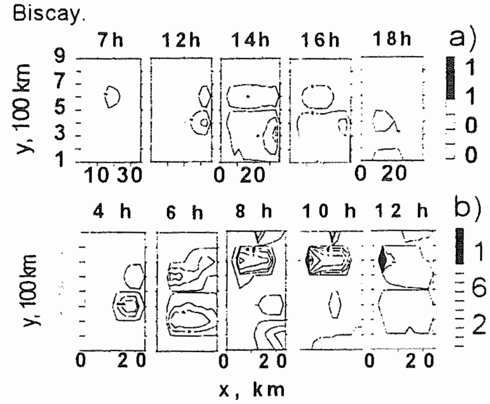

Figure 5. Time and space development of small rainbands over the Bay of Biscay: (a) precipitation rate for a light precipitable rainband; (b) as (a) for rainband with heavy rainfall.

Two small rainbands were modeled in this region. One from them was detected at -721 <x< - 757 and presented in Fig.5a at different time of its development. This band was non-convective and non strongly precipitable.

A finest nested grid was used for second rainband presented by Fig.5b with xs=2 km and –712 <x< -736 km. This band maintained many hours and produced heavy rainfall reached 12 mm/h after 8 h of its development.

4. WEATHER EVENTS OVER UKRAINE CONNECTED WITH WESTERN CYCLONE

A main influence on the weather of Ukraine had the developing low pressure that transformed into a large cyclone over north Europe and defined the weather of north Ukraine during 12-15 January. The cyclone forced the developing of two warm fronts. These fronts determined the cloud cover accompanied them during 13 January (Fig.6).

The 3-D diagnostic and prognostic models were initialized with regular rawinsondes data at 1200 GMT on 13 January 1997. It should be noted that initial data for modeling supplied by regular aerologic sounding were no sufficient to reproduce the small rainbands. Therefore, the regular grid with xs=50 and ys=100 km spacings was selected for modeling. It let to reproduce the spread rainband only. Two widespread rainbands accompanied these fronts forced a cloud cover and precipitation over north part of country. The severe weather was observed 12-14 January.

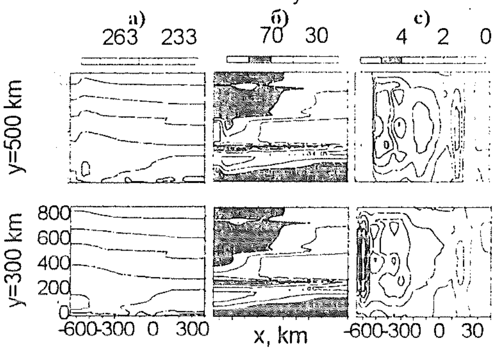

Figure 6.. *Vertical sections of warm fronts (from west to east) at t=0 and different y. (a) temperature, °K; (b) humidity, %; (c) vertical motion, cm/s.*

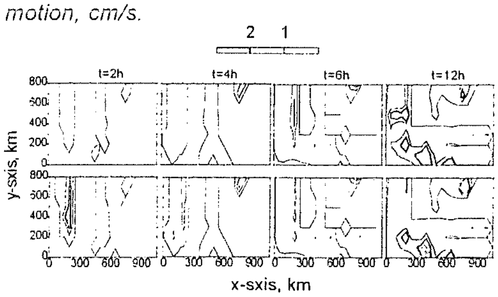

Figure 7. *Time development of: (a) cloud budget, mm/h; (b) precipitation rate, mm/h.*

A spread cloud cover observed on 13 January. Fig.7 presented precipitation development during first 12 h. Two spread rainbands maintained for a long time. The size and configuration of cloudiness non-always coincided with real one. A lack of information in initial time not allows a perfectly reproducing of real atmospheric processes. The modeling these events allows to restore a reasonably real picture of their time development notwithstanding the evident lack of sounding information.

Major differences between the simulated and observed fields concern the less large precipitation contours in initial time and the fact that more large convective region developed in south region connected with southwestern air mass intrusion.

5. CONCLUSION

This study is the next in turn aimed at developing analyses coupling observational and numerical approaches to study mesoscale and microscale of precipitating systems. Using observation obtained during the FASTEX field project, the mesoscale and microscale structure of cloud systems connected with the cold front and developing low pressure over Atlantic region on 12 January and response on these events the weather on Great Britain, France and Ukraine was investigated by numerical modeling.

The widespread and smaller scale rainbands were subjected for modeling using the nested and stretched grid of different scales.

The weather element features (common and different) for various regions of the investigated area were discussed. Comparison between the time development features of rainbands connected with different weather events and their locations was performed.

ACKNOWLEDGEMENTS

Many thanks are due to Dr.D.Parsons at NCAR, who helped to supply the original meteorological fields.

REFERENCES

Buikov, M. 1978. Numerical simulation of stratiform clouds. Obninsc, 68pp.

Hobbs, P., Bowdle, D. and Radke, L, 1977. Aerosol over High Plains of the United States. Res. Rep. XII, 143pp.

Krakovskaia, S., Pirnach, A., 1998. Theoretical study of the microphysical structure of mixed stratiform frontal clouds and their precipitation. J. Atmos. Res., 47-48: 491-504.

Pirnach, A., 1976. Influence on mixing cloud microstructure of a collection by solid precipitation particles of cloud drops. Trudy UHRI, 144: 20-24

Pirnach, A., 1987. Numerical Simulation of frontal cloud system taken into account dymanics and microphysics processes (3-D models). Trudy UHRI, 221: 71-82.

Pirnach, A., Krakovskaia, S., 1994. Numerical studies of dynamics and cloud microphysics of the frontal rainbands. J. Atmos. Res., 33: 333-365.

Pirnach, A., 1998. Construction and application of the various numerical models for study the cloud dynamics and structure of the frontal rainbands. J. Atmos. Res., 47-48:355-376.

Twomey, S., 1959. The nuclei of natural cloud formation. Part II, The supersaturation in natural clouds and the variation of cloud drop concentration, Geofis. Pura Appl., 43: 243-249.

Valy, G., 1975. Remarks of the mechanism of atmospheric ice nucleation. In: Proc. VIII ICN. Gidrometeoizdat, Moscow, pp. 265-269.

ENSO IN HIGHLY REFLECTIVE CLOUD: A FRESH LOOK

David W. Martin[1], Christopher C. Collimore[2] and Matthew H. Hitchman[2]

[1]Space Science and Engineering Center, University of Wisconsin-Madison, Madison, WI, 53706, USA
[2]Department of Atmospheric and Oceanic Sciences, University of Wisconsin-Madison, Madison, WI, 53706, USA

1. INTRODUCTION

Suspecting a particular modulation of the troposphere, recently we looked for long records of tropical deep convection. In a modified form, Highly Reflective Cloud (Garcia 1985; also see Grossman and Garcia 1990) became a prime candidate. However, a time series of these data led us to question the adequacy of the record for depicting deep convection. Supposing that the record could not possibly reflect the modulation in question if it did not at least contain the most robust of the climate signals in tropical deep convection, we devised a test of the modified HRC for the presence of the El Niño/Southern Oscillation (ENSO).

2. HIGHLY REFLECTIVE CLOUD

HRC records 17 years of cloud clusters (organized deep convection). Using visual and infrared images from U.S. National Oceanic and Atmospheric Agency (NOAA) or from Defense Meteorological Satellite Program polar-orbiting satellites, for each day the 18,360 1° x 1° boxes between 25.5°N and 25.5°S were assigned to one of two states: cloud-cluster (highly reflective cloud) or not. HRC was subjectively identified according to cloud brightness, size, appearance, texture, cloud-top temperature and the local cloud climatology. With allowances for variable numbers of days in a month and for missing data, daily occurrence was aggregated to monthly count.

Dividing the year into six bi-month seasons (Jan-Feb, Mar-Apr, ... Nov-Dec), Hastenrath (1990) studied the annual cycle in HRC. In the context of the annual cycle, he also related HRC to a Southern Oscillation Index involving the gradient of surface pressure between Tahiti and Darwin. One of these relational analyses yielded maps of seasonally-correlated HRC and SOI.

Subsequently, using empirical orthogonal functions, Waliser and Zhou (1997) documented and repaired a flaw in the HRC record stemming from variable equatorial crossing times. They remapped the corrected HRC data to a 2° x 2° grid and (at each grid point) subtracted the annual cycle. To our knowledge, no one has composited either old or new records of HRC by the phases of ENSO.

Corresponding author's address: Space Science and Engineering Center, 1225 West Dayton Street, Madison, WI, 53706, USA; E-Mail: dave.martin@ssec.wisc.edu.

After acquiring the new record (via ftp; see http://terra.msrc.sunysb.edu/home.html), we remapped the HRC anomaly values to the 5° x 5° grid of NASA's record of Outgoing Longwave Radiation (OLR) (ERBE Project 1996), our primary record of tropical deep convection. Hereafter, unless otherwise indicated, "HRC" refers to the Waliser/Zhou record of HRC anomaly remapped to the NASA OLR grid.

3. TEST

In addition to ENSO as *sine qua non,* the test rests on two premises. First, we could, indeed, treat ENSO as a series of bipolar (El Niño or La Niña), aperiodic events which are phased to the annual cycle. Second, if composited separately for El Niño and La Niña, tropical Pacific rainfall should reflect any ENSO signal in HRC. These premises led in turn to two hypotheses. H_1 postulates that HRC contains no signal of ENSO. Denying H_1, H_2 postulates that the ENSO signal in OLR exceeds that in HRC.

We used maps on the Home Page of the NOAA Climate Diagnostics Center (CDC) (at http://www.cdc.noaa.gov/ENSO/enso.description.html) to locate the Niño/Niña dipole in Pacific rainfall. Rainfall in these maps was estimated from the NOAA record of OLR (M. Hoerling, personal communication). Cueing on the CDC maps, as Region we selected 120°E to 160°W, 15°S to 15°N. Consisting of 96 5° x 5° boxes, or cells, Region encompasses the rain dipole. Along the 160°E meridion we divided Region into east and west "Blocks". Consisting of 48 cells, each Block contains one end of the rain dipole. Nominally, the period of the study matched that of the HRC record, January 1971 through December 1987.

Cell-by-cell, for Region we chose to composite HRC over a long period (approaching or exceeding a year) centered on December. Each "Event" (El Niño or La Niña) consisted of a set of "Cases". To identify Cases, we deferred to NOAA's Climate Prediction Center, which (at http://www.cpc.ncep.noaa.gov/products/analysis_monitoring/ensostuff/ensoyears.html) lists cold and warm episodes by season since 1950. To qualify, a Case had to reach moderate or strong intensity and last two or more consecutive seasons. Applying these criteria to the HRC period of the table of episodes yielded two full (and one partial) La Niña Cases and three full El Niño Cases. Applying the selection criteria to the HRC/OLR overlap period yielded one La Niña Case and two El Niño Cases. By beginning month and ending month, Table 1 lists Cases.

TABLE 1. Cases.

Event	HRC Only beginning	HRC Only ending	HRC vs OLR[1] beginning	HRC vs OLR[1] ending
La Niña	1/71	8/71	---	---
	4/73	8/74	---	---
	4/75	8/76	7/75	5/76
El Niño	4/72	8/73	---	---
	4/82	8/83	7/82	5/83
	4/86	8/87	7/86	5/87

[1] Overlap period begins Jul 1975 and ends Dec 1987.

4. RESULTS

4.1 HRC Only

Except for the first La Niña (Table 1), a Case ran for 17 months. To address H_1, we examined the data in three ways. First, cell-by-cell, separately for each Case and each Block, we converted HRC to a binary value: zero, if negative; one, if positive. (In the regridded data set there were no zero values). Then, by Case and Block, we counted ones and zeros. From contingency tables of observed counts we constructed contingency tables of expected counts. Assuming equal probabilities of positive and negative values, through the chi-squared distribution, for each table we calculated the probability of the observed pattern occurring by chance.

We expected that during El Niño negative values of HRC anomaly would favor the west Block; during La Niña, the east Block. Conversely, during El Niño positive values of HRC anomaly would favor the east Block; during La Niña, the west Block. Table 2 confirms this pattern. Values of chi-squared calculated from Table 2 indicate a very, very small probability of such a pattern occurring by chance.

In the second of the three views of the data, by Block and by Event we calculated simple moments of the values. As in the binary analysis described above, in the averages we expected a dipole pattern: negative in the west Block during El Niño; negative in the east Block during La Niña. Especially for the west Block during La Niña, average values proved to be small (Table 3). Nevertheless, Table 3 confirms the expected pattern.

TABLE 2. Counts of positive and negative values by Block for El Niño Cases and La Niña Cases. Observed (top). Expected (bottom). For the left hand side of the table chi-squared equals 214; for the right hand side, 119. Each value is significant at the 0.1% level.

	west Block negative	west Block positive	west Block sum	east Block negative	east Block positive	east Block sum
El Niño	1660	788	2448	1225	1223	2448
La Niña	929	1087	2016	1336	680	2016
sum	2589	1875	4464	2561	1903	4464
El Niño	1420	1028	2448	1404	1044	2448
La Niña	1169	847	2016	1157	859	2016
sum	2589	1875	4464	2561	1903	4464

TABLE 3. Average values of HRC anomaly.

Event	Block west	Block east
El Niño	-0.50	0.38
La Niña	0.20	-0.37

In the last of the three views of the data, Case-by-Case, for each cell we averaged HRC. Then, weighting the 1970 Case according to its abbreviated period, by Event we averaged the Cases. If the record contained an ENSO signal, the La Niña map of HRC should resemble the CDC map of La Niña rainfall anomaly; similarly, for the El Niño maps. Across Region for La Niña Fig. 1a shows a tripole dipping toward the east-southeast (the primary axis) and toward the east-northeast (the secondary axis). Across Region for El Niño Fig. 1b shows a dipole dipping toward the west-northwest. To a surprising degree our HRC maps resemble CDC's rain maps.

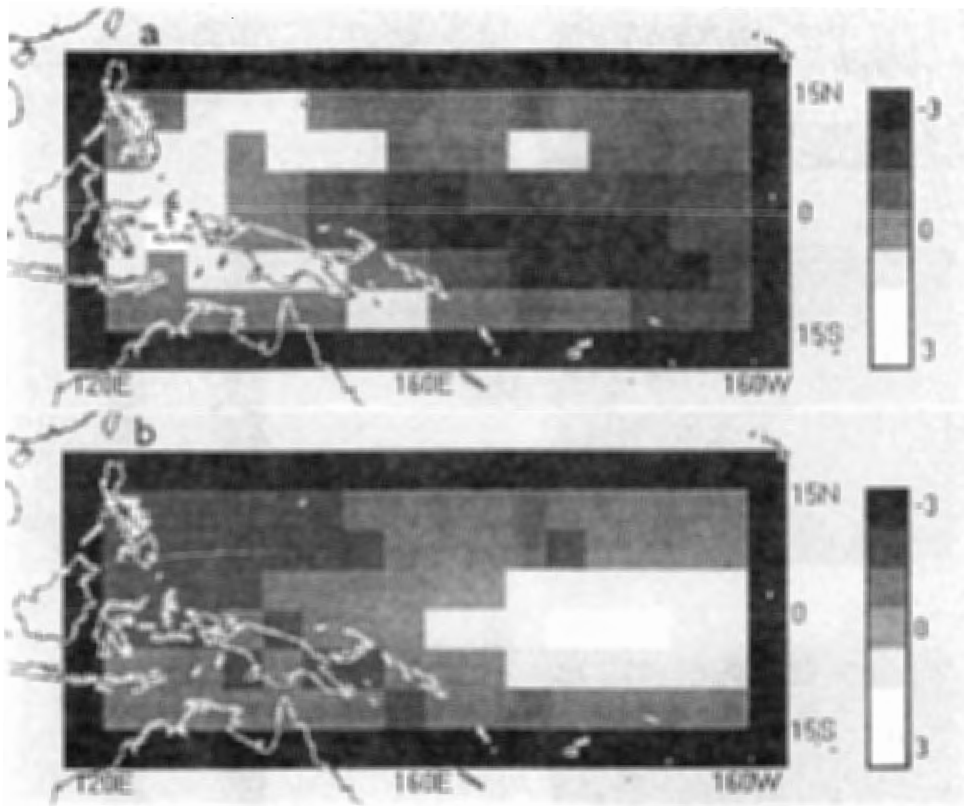

FIG. 1. Average of HRC anomaly (Waliser/Zhou record) for Region. Units of counts. A positive count (bright shade) represents more cloud clusters; a negative count (dark shade), fewer.
(a) La Niña (range of -2.9 to 1.7); (b) El Niño (range of -1.1 to 1.7).

4.2 <u>HRC versus OLR</u>

Within the overlap period only one La Niña occurred. To accommodate the truncation of this Case (an absence of overlap data before July 1975), for the comparison of HRC and (NASA) OLR data we limited the length of a Case to 11 months. With this definition of period, two El Niños occurred (Table 1). Because the OLR data existed as raw rather than anomaly values, for each of these three Cases we converted the HRC data within Region from anomaly to raw values.

Subjectively, across the full record HRC had seemed noiser than OLR. However, the results reported in Section 4.1 indicated a strong ENSO signal in HRC. Furthermore, using the original record, Waliser et al. (1993) concluded that as a measure of tropical deep convection HRC matched (if not exceeded) OLR. Thus we anticipated a stronger ENSO signal in HRC than in OLR.

A calculation of mean values by Event and Block (Table 4) repeats the pattern found for HRC-only (Table 3). As expected, in OLR the calculation gives exactly the opposite pattern. To facilitate comparisons of differences between means, we define "normalized difference" as the Event difference for a Block divided by the mean for both Blocks. This "Region mean" includes each of the three Cases and weights the Cases equally. By this measure the ENSO signal in HRC far exceeds that in OLR.

TABLE 4. Comparison of Event means.

Data-base	Statistic	Block west	Block east
HRC[1]	mean (Niño)	2.3	3.0
	mean (Niña)	3.3	2.2
	difference (Niño-Niña)	-0.97	0.79
	normalized difference[2]	-0.36	0.29
OLR[3]	mean (Niño)	244	237
	mean (Niña)	231	254
	difference (Niño-Niña)	13	-17
	normalized difference[2]	0.055	-0.070

[1] Except for normalized difference, units of counts.
[2] Difference (Niño-Niña) divided by sample-weighted mean for Region.
[3] Except for normalized difference, units of $W\ m^{-2}$.

For each dataset we also constructed a difference map (Niño minus Niña). In contrast to Fig. 1, for each map the gray scale was matched to the range of the differences it portrayed. For HRC (Fig. 2a) the difference map implies a noisier signal than that in either of the two Event maps (Fig. 1). However, consistent patterns indicate that the sample in the HRC/OLR test adequately represents the "population" in the HRC-only test.

For OLR (Fig. 2b) the difference map reveals a smoother signal than that in HRC. Especially for the eastern end of the dipole, it implies a broader response. Otherwise, the difference patterns closely resemble one another.

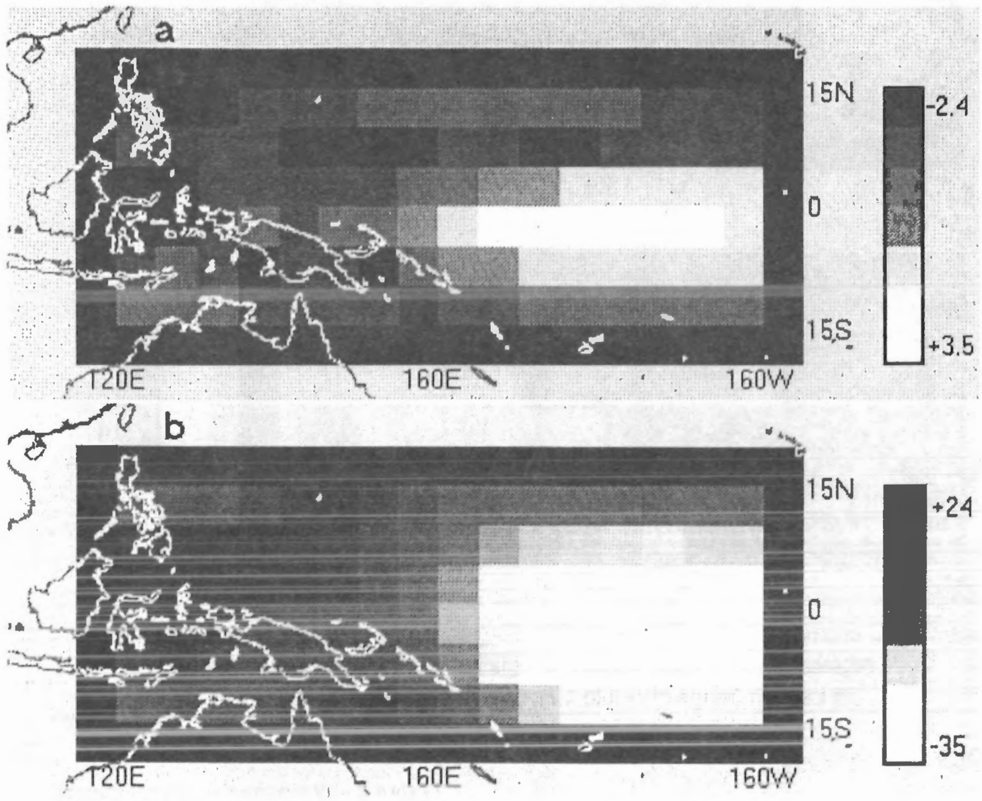

FIG. 2. As for Fig. 1, except difference values rather than raw values and HRC/OLR overlap Cases rather than full-HRC Cases. La Niña composite is subtracted from El Niño composite. HRC (top); OLR (bottom). For both datasets dark shades represent diminished convection; bright shades, enhanced convection. However, only for HRC do dark shades represent negative values. HRC differences ranged from -2.4 to 3.5 counts; OLR differences, -35 to 24 W m^2.

5. CONCLUSION

We have presented results from a two-part test of the robustness of the convective signal in the HRC record. Decisively, the test shows an ENSO signal in HRC. It suggests a stronger ENSO signal in HRC than in OLR. These results encourage us to examine the HRC record for evidence of the original modulation.

6. ACKNOWLEDGEMENTS

Duane Waliser supplied the HRC data; Kathryn Bush and Dale Bess, the OLR data. Under Grant ATM-9812429, the US National Science Foundation supported this study.

7. REFERENCES

ERBE Project: 1996 Earth Radiation Budget Experiment (ERBE) Langley DAAC Project Document, Langley DAAC User and Data Services Office. <http://charm.larc.nasa.gov/ GUIDE/campaign_documents/erbe_project.html>

Garcia, O., 1985: *Atlas of Highly Reflective Clouds for the Global Tropics: 1971-1983.* U. S. Department of Commerce, Washington, D.C., xii, 365 pp.

Grossman, R. L., and O. Garcia, 1990: The distribution of deep convection over ocean and land during the Asian summer monsoon. *J.Climate*, **3**, 1032-1044.

Hastenrath, S., 1990: The relationship of highly reflective clouds to tropical climate anomalies. *J. Climate*, **3**, 353-365.

Waliser, D. E., and W. F. Zhou, 1997: Removing satellite equatorial crossing time biases from the OLR and HRC datasets. *J. Climate*, **10**, 2125-2146.

Waliser, D. E., N. E. Graham and C. Gautier, 1993: Comparison of the Highly Reflective Cloud and Outgoing Longwave Radiation datasets for use in estimating tropical deep convection. *J. Climate*, **6**, 331-353.

REGIONAL DIFFERENCE OF RELATION BETWEEN UPPER-LEVEL CLOUD AREA AND PRECIPITABLE WATER CONTENT

Sento Nakai[1]

[1]National Research Institute for Earth Science and Disaster Prevention, Tsukuba 305-0006, Japan

1. INTRODUCTION

Upper-level cold clouds are the most easily recognizable features in infrared satellite imagery. An organized convection generate a variety of anvil clouds from single storm to MCC (Maddox, 1980), which sometimes cause heavy rainfall. Tropical cyclones and mid-latitude frontal systems are also distinctive features and have a great deal of influence to daily weather and radiative forcing. So, investigating the characteristics of upper-level cloud is important for clarifying the climatic effect of clouds and for disaster prevention.

Nakai and Kawamura (1998) analyzed thirty pairs of nearly simultaneous GMS-4 IR and SSM/I data, when cloud cluster existed within the data area. They showed that the cloud clusters appeared within the area where precipitable water (PW) was more than 50mm. Upper-level cloud can be related to water vapor flux convergence, not directly to water vapor amount in the lower troposphere. However, if large PW is related with low-level convergence and local instability, it can be an indicator of upper-level cloud generation in a certain condition. In this study, more general relation between upper-level cloud amount and low-level moisture is investigated over ocean around east Asia using satellite data. Meridional variation of the relation will be emphasized.

2. DATA AND ANALYSIS METHOD

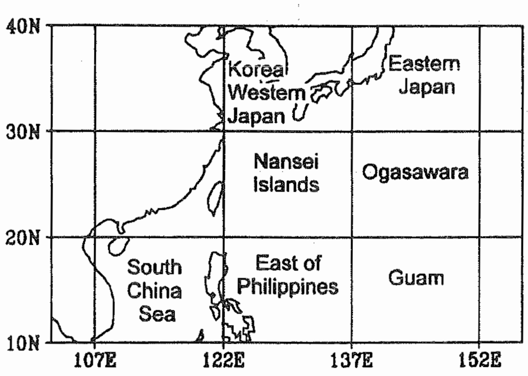

Fig. 1 Subareas of analysis.

Corresponding author's address: Sento Nakai, National Research Institute for Earth Science and Disaster Prevention, Tsukuba 305-0006, Japan; E-mail: saint@ess.bosai.go.jp

Upper-level cloud area was calculated from hourly GMS-5 IR1 (10.5 μ m$-$11.5 μ m) TBB. Upper-level cloud was defined by TBB less than -30°C. PW retrieved from SSM/I data was used for low-level water vapor amount. Analysis area is over ocean around east Asia and divided into several subareas (Fig. 1) for which upper-level cloud amount was calculated. Analysis period is a 97-day period from 29 April to 3 August 1996. 'Humid region' was defined by PW more than 50mm. An area of less PW was called 'dry region' for convenience. An example of Upper-level cloud distribution and humid/dry region in the analysis area is shown in Fig. 2. Daily mean cloud amount was calculated for each of humid/dry region of all subareas.

First, both TBB and PW data were converted on the same latitude-longitude coordinate. Noisy TBB data was excluded and data lack (78 among 2328) was treated as 'no observation', even though it was because of local receiving problem. A sequence of data from 01UT to 00UT on the next day were considered as one-day data. It is because data of 00UT is, usually, observed between 2332UT and 2357UT on the day before. SSM/I PW data is available zero to six times a day for a single geographical point. We took average of one-day PW data to get 'daily' PW, however, it sometimes represent a single time on a day because of low time resolution of SSM/I. It may cause some error on TBB-PW relation, however, we assumed in this analysis that the change of PW within a day is not

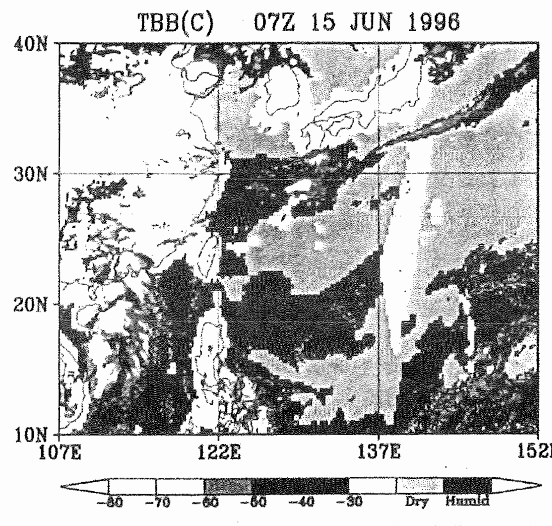

Fig. 2 An example of upper-level cloud distribution indicated by TBB less than -30°C. Dry and humid regions are indicated out of the cloud area.

significant.

We compared a single 'daily' PW with twenty-four hourly TBB distributions. Each subarea was divided into humid region and dry region. Subarea-mean daily upper-level cloud amount *Auc* was defined by

$$Auc(k) = \frac{1}{24}\sum_{t=1}^{24}\left(Suc(t,k)/Sa(k)\right)$$

for each day. *Suc(t,k)* is number of grid points occupied by upper-level clouds at which PW category was *k* at *t* UT. *Sa(k)* is number of grid points at which PW category was *k*. *k*=1 and 2 indicates dry and humid region, respectively.

3. RESULTS

Time series of upper-level cloud amount *Auc* is shown in Fig. 3. *Auc* of humid region (*Auc*(2)) was much larger than that of dry region (*Auc*(1)) in tropical subareas located between 10°N and 20°N (South China Sea, east of Philippines, Guam). The difference between *Auc*(1) and *Auc*(2) was not found in midlatitude subareas located between 30°N and 40°N (Korea/western Japan, eastern Japan). In subtropical subareas located between 10°N and 20°N (Nansei Islands, Ogasawara), *Auc* characteristics were different between before and after early June (day 40). *Auc* in midlatitude subareas showed no difference between humid region and dry region from April to early June. A clear change occurred around day 40 (7 June), and *Auc* of humid region became much larger than that of dry region. Subareas in the same latitudinal belt showed similar characteristics.

Ratio of *Auc*

$$Ruc = Auc(2)/Auc(1)$$

was calculated to show the difference between humid and dry regions clearly. For clear longitudinal difference was not seen, only one panel is shown for each latitude belt. In tropical western Pacific (Fig.4, lower panel), *Ruc* is much larger than unity from May to middle July. Humid region has sometimes one order larger *Auc* than dry region of the same subarea. It suggests that upper-level cloud amount had two regimes corresponding to the PW regimes. Little dry region appeared in late July, when high *Auc* appeared in humid regions of all of three tropical subareas (Fig. 3).

Ruc is close to unity in midlatitude subareas (Fig.4, upper panel). It indicates that upper-level cloud appeared regardless of low-level moisture represented by PW. It suggests that the upper-level cloud formation process was different from that of tropical subareas, although neglecting the change of PW in a day may cause *Ruc* somewhat closer to unity.

The change of *Ruc* in early June (day 40) is apparent in subtropical subareas (Fig.4, middle panel). Before day 40, Ruc of Nansei Islands was close to unity. It rarely fell below 2 after day 40. Scattergram of *Auc* is shown in Fig. 5. Least-square fitting to

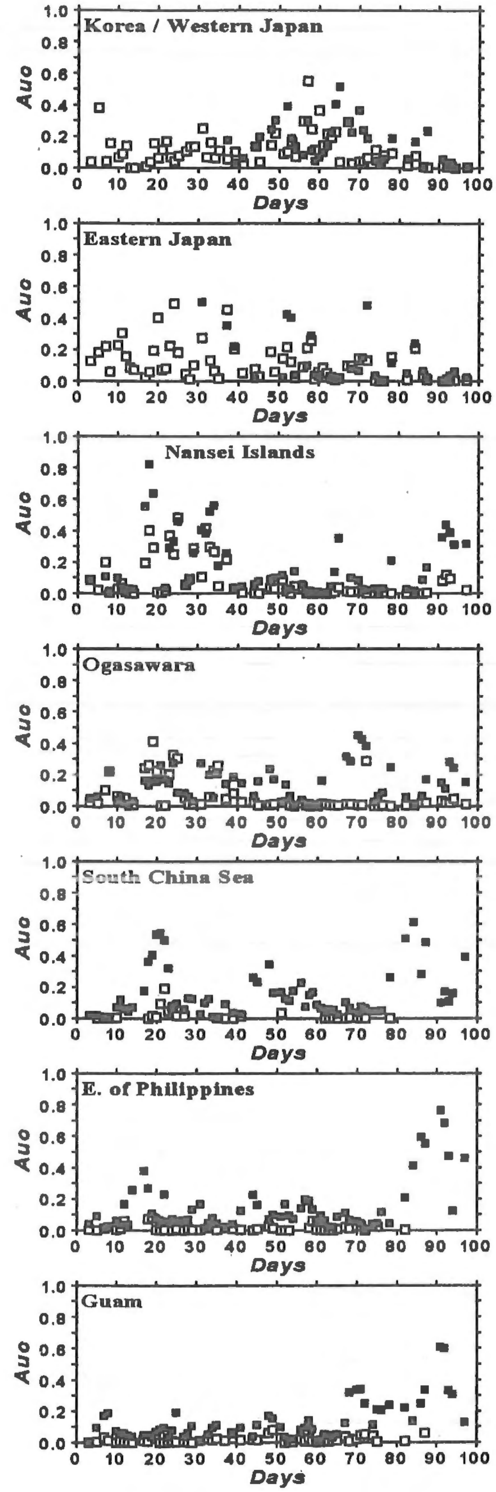

Fig. 3 Time series of *Auc* for seven subareas. Open and solid squares indicate dry (*Auc*(1)) and humid (*Auc*(2)) region, respectively. Days in abscissa is from 29 April to 3 August 1996.

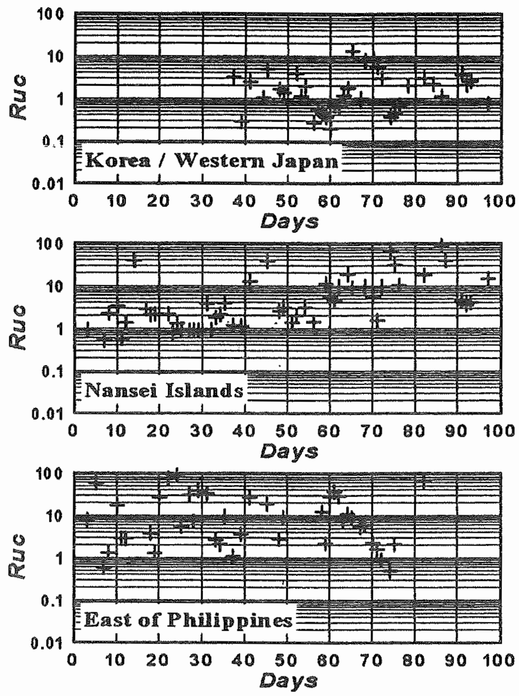

Fig. 4 Time series of *Ruc* for selected subareas. Days in abscissa is from 29 April to 3 August 1996.

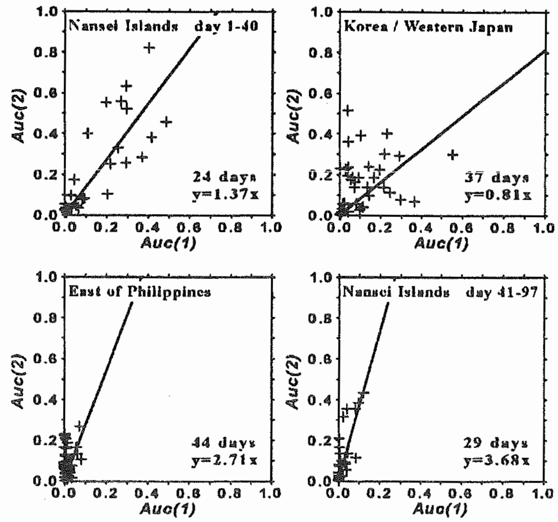

Fig. 5 Scattergram of daily mean upper-level cloud amount of humid region *Auc*(2) to that of dry region *Auc*(1) for three subareas. Before and after early June are drawn in separate panels for subarea 'Nansei Islands.'

Auc(2) = *a Auc*(1) indicates the similarity of day 1-40 of Nansei Islands to midlatitude (Korea / western Japan), and of day 41-97 to tropics (east of Philippines). The former *a* was near unity and the latter *a* was more than 2.5.

4. DISCUSSIONS

In this study, all upper-level clouds were analyzed regardless of cloud system. Considering that subtropical cloud clusters had a tendency to appear in humid regions (Nakai and Kawamura, 1998), large *Ruc* may indicate that the dominant process of upper-cloud formation is organized convections. It is consistent with the result that large *Ruc* appeared in tropics and subtropics after early June. The clear change of *Ruc* in subtropical subregions suggests that the seasonal transitions of Baiu front is accompanied by the change of prevailing high cloud formation process.

Cloud systems appeared in midlatitude subareas were synoptic scale lows, Baiu fronts, cloud clusters and decaying typhoons. A cloud cluster is sometimes change into a Baiu frontal depression around Japan (Ninomiya et al., 1988). The environment of this area is characterized by strong baroclinicity, which affects the characteristics of the cloud systems (Takeda and Iwasaki, 1987; Ninomiya et al., 1988; Hirasawa et al., 1995). It is considered that the baroclinic environment made upper-level cloud formation independent on low-level moisture, leading to small *Ruc* in midlatitude subareas.

Appearance of extremely dry air in the lower- and mid-troposphere is known as 'dry intrusion' in the tropical warm pool region. The dry air masses were formed by horizontal advection from subtropics (Numaguti et al., 1995; Sheu and Liu, 1995; Yoneyama and Fujitani, 1995; Johnson et al., 1996; Mapes and Zuidema, 1996). Yoneyama and Parsons (1999) concluded that the dry intrusion was induced by midlatitude processes. The dry intrusion affects convective activity (Mapes and Zuidema, 1996), and bring tropics 'drought periods' with few deep clouds as mesoscale convective systems. Rainy periods and drought periods are two regimes on moisture profile and cloudiness in the tropical warm pool region (Brown and Zhang, 1997). The dry air may advect both from winter and summer hemispheres (Yoneyama and Parsons, 1999). We made hourly composite maps as shown in Fig. 1 for 97 days of analysis period. Time series of the composite map suggests that the large *Ruc* may reflect the moisture and cloudiness regimes affected by processes in higher latitudes.

5. SUMMARY

An analysis using satellite data was made on environmental conditions for the development of cloud systems. A comparison was made between GMS upper-level cloud amount and SSM/I precipitable water over ocean around and to the south of Japan (10°N−40°N, 107°E−152°E) during a 97-day period in Baiu season of Japan. Cloud amount was calculated for each of PW category (humid and dry regions) divided by a threshold of precipitable water.

The characteristics of upper-level cloud amount showed meridional variations. Upper-level cloud amount had much larger value in humid region than in dry region in tropical subareas. PW and upper-level cloud amount expressed two regimes of tropical air, possibly affected by advection from higher latitudes. Almost no relation was found between PW category and upper-level cloud amount in midlatitude subareas, where environmental condition is strongly baroclinic. Subtropical subareas showed seasonal transitions in upper-level cloud type around early June.

Precipitable water expresses the moisture mainly of lower troposphere, and is different from water vapor flux convergence that can be directory related to convective activity.. However, moisture regimes are reflected to upper-level cloud amount in lower latitudes where organized convection is responsible to the formation of upper-level clouds. The moisture regime is considered to represent total environment controlling convective activity.

Acknowledgments. This work was done as part of the Japanese Cloud-Climate Study (JACCS) projects. SSM/I PW data were produced and provided by Remote Sensing Systems and sponsored, in part, by NASA's Earth Science Information Partnerships (ESIP): a federation of information sites for Earth science; and by the NOAA/NASA Pathfinder Program for early EOS products; principal investigator: Frank Wentz.

REFERENCES

Brown, R. G., and C. Zhang, 1997: Variability of midtropospheric moisture and its effect on cloud-top height distribution during TOGA COARE. J. Atmos. Sci., **54**, 2760-2774.

Hirasawa, N, K. Kato and T. Takeda, 1995: Abrupt change in the characteristics of the cloud zone in subtropical East Asia around the middle of May. J. Meteor. Soc. Japan, **73**, 221-239.

Johnson, R. H., P. E. Ciesielski, and K. A. Hart, 1996: Tropical inversions near the 0°C level. J. Atmos. Sci., **53**, 1838-1855.

Maddox, R. A., 1980: Mesoscale convective complexes. Bull. Amer. Meteor. Soc., **61**, 1374-1387.

Mapes, B. E., and P. Zuidema, 1996: Radiative-dynamical consequences of dry tongues in the tropical troposhere. J. Atmos. Sci., **53**, 620-638.

Nakai, S. and R. Kawamura, 1998: Prevailing scale of cloud clusters appeared in Baiu cloud zone: June 1992 case. *International Symposium: Meso-scale Water Cycle and Heavy Rainfall in East Asia Extended papers*, February 2-4, 1998, Nagoya.

Ninomiya, K., T. Akiyama and M. Ikawa, 1988: Evolution and fine structure of a long-lived meso- -scale convective system in Baiu frontal zone. Part I: Evolution and meso- -scale characteristics. J. Meteor. Soc. Japan, **66**, 331-350.

Numaguti, A., R. Oki, K. Nakamura, K. Tsuboki, N. Misawa, T. Asai and Y. Kodama, 1995: 4-5-day-period variation and low-level dry air observed in the equatorial western Pacific during the TOGA-COARE IOP. J. Meteor. Soc. Japan, **73**, 267-290.

Sheu, R.-S., and G. Liu, 1995: Atmospheric humidity variations associated with westerly wind bursts during Tropical Ocean Global Atmosphere (TOGA) Coupled Ocean Atmosphere Response Experiment (COARE). J. Geophys. Res., **100**, 25759-25768.

Takeda, T. and H. Iwasaki, 1987: Some characteristics of meso-scale cloud clusters observed in East Asia between March and October 1980. J. Meteor. Soc. Japan, **65**, 507-513.

Yoneyama, K., and T. Fujitani, 1995: The behavior of the dry westerly air associated with convection observed during the TOGA COARE R/V Natsushima Cruise. J. Meteor. Soc. Japan, **73**, 291-304.

Yoneyama, K. and D. B. Parsons, 1999: A proposed mechanism for the intrusion of dry air into the tropical western Pacific region. J. Atmos. Sci., **56**, 1524-1546.

CASE STUDY ON A SLOW-MOVING LONG-LIVED MESO-α-SCALE CLOUD CLUSTER FORMED ALONG THE BAIU FRONT

Yasutaka Wakatsuki*and Takao Takeda

Institute for Hydrospheric-Atmospheric Sciences, Nagoya University, Nagoya, 464-8601, JAPAN

1 INTRODUCTION

A long-lived oval-shaped meso-α-scale cloud cluster was observed on July 6-7, 1996 over the East China Sea. It was stationary off the west coast of the Kyushu District, the westernmost part of Japan Islands. Meso-α-scale cloud clusters along Baiu front have been studied by several authors. Ninomiya et al. (1988 a,b) and Iwasaki and Takeda (1989) found that the meso-α-scale cloud cluster consisted of meso-β-scale convective systems and, its stagnation and maintenance were attributed to the successive formation of new meso-β-scale convective systems in the upwind side (west side) of the cloud cluster.

Ishihara et al. (1995) studied the structure of an intense meso-β-scale convective system in a oval-shaped cloud cluster formed around the west coast of the Kyushu District by dual Doppler radar observation. They pointed out that dry rear-inflow at middle levels and convective scale updraft in the front side of the system ware its characteristic features.

In this paper, the multi-scale structure of the meso-α-scale cloud cluster is studied to clarify its stagnation and maintenance processes, forcusing on the structure of the environmental atmosphere and the periodical development of meso-β-scale convective systems in the cloud cluster.

2 DATA

Data used in this study are as follows: the infrared channel data of GMS-5 (*Geostationary Meteorological Satellite*), the data of Tanegashima radar of the Japan Meteorological Agency(JMA), the data of dual-doppler radar of Nagoya University and Meteorological Research Institute(MRI), JMA. Tairajima and Choufumaru radio-sonde data are also used.

*Corresponding author's address: Yasutaka Wakatsuki, Institute for Hydrospheric-Atmospheric Sciences, Nagoya University, Furo-cho, Chikusa-ku, Nagoya, 464-8601, Japan; E-mail: waka@ihas.nagoya-u.ac.jp

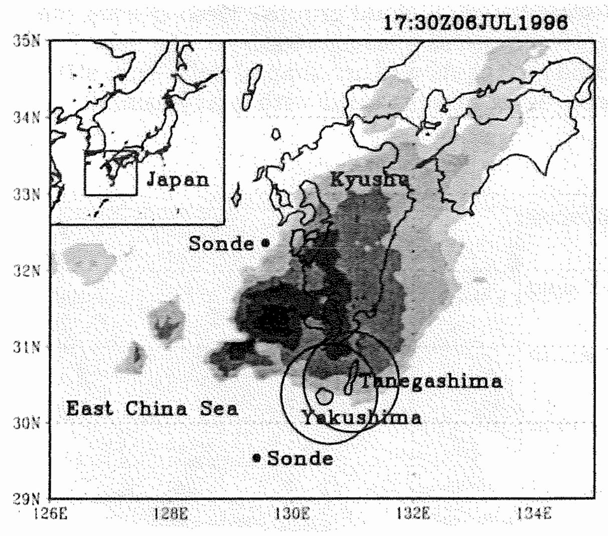

Figure 1 Map of an area around the meso-α-scale cloud cluster. Shade is T_{BB} distribution in the cloud cluster. Two circles are Doppler radar observation ranges. Two dots are radio-sonde observation point.

3 RESULTS OF ANALYSIS

3.1 Distribution of meso-β-scale convective systems in a meso-α-scale cloud cluster.

The meso-α-scale cloud cluster was generated at about 12 UTC, July 6 on the west side of the Kyushu District over the East China Sea. The cloud cluster developed drastically after its generating, as seen in Fig. 2, minimum T_{BB} reached about -78°C. This means that convective clouds developed very deeply in the cloud cluster. The life time of the cloud cluster was about 18 hours. It was stagnant over the Kyushu District and a large amount of rainfall more than 300mm/day was observed in a narrow area.

The cloud cluster was consisted of meso-β-scale low T_{BB} cloud groups. The movement of the cloud groups shown in Fig. 2 as solid lines. That cloud groups formed in the upwind side of the cloud cluster with about 5 hours period, and moved eastward in the cloud cluster. The cloud cluster was stagnant by the persistent generation of new meso-β-scale low T_{BB} cloud groups are observed in the upwind side(west side) of the cloud cluster.

Meso-β-scale echo groups was observed by Tanegashima radar in the cloud cluster(Fig.3). It is to be noted that meso-β-scale intense radar echo groups ware generated periodically in the western part of the cloud cluster with period of 1-3 hours. They showed a band-shaped structure in the central part of the cloud cluster and an intermittent intensification with period of 5 hours in association with the movement of meso-β-scale low T_{BB} cloud groups. Meso-β-scale convective systems corresponded to the low T_{BB} cloud groups showed arc-shaped radar-echo structure, being accompanied with heavy rainfall.

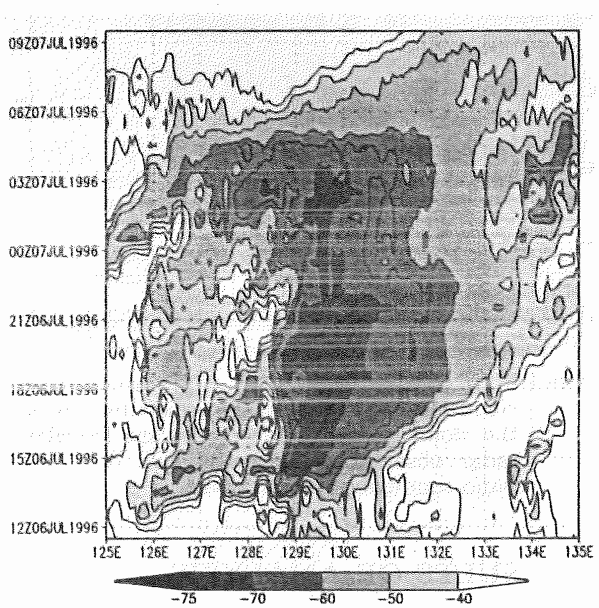

Figure 2 Longitude-time cross section of minimum T_{BB} in the latitude zone of 30 to 35N obtained from GMS infrared imagery. Solid lines indicate the movement of meso-β-scale low T_{BB} cloud groups.

3.2 Structures of two types of meso-β-scale convective systems

Several meso-β-scale convective systems in the cloud cluster were observed by dual-doppler radar in the later stage. Two arc-shaped meso-β-scale convective systems developed in the Doppler radar region at 22 UTC, July 6 and 03 UTC, July 7, respectively. Simultaneously, these convective systems correspond to the second and third meso-β-scale arc-shaped intense echo groups and low T_{BB} cloud groups, respectively. Between these arc-shaped convective systems, four band-shaped meso-β-scale convective systems were observed in

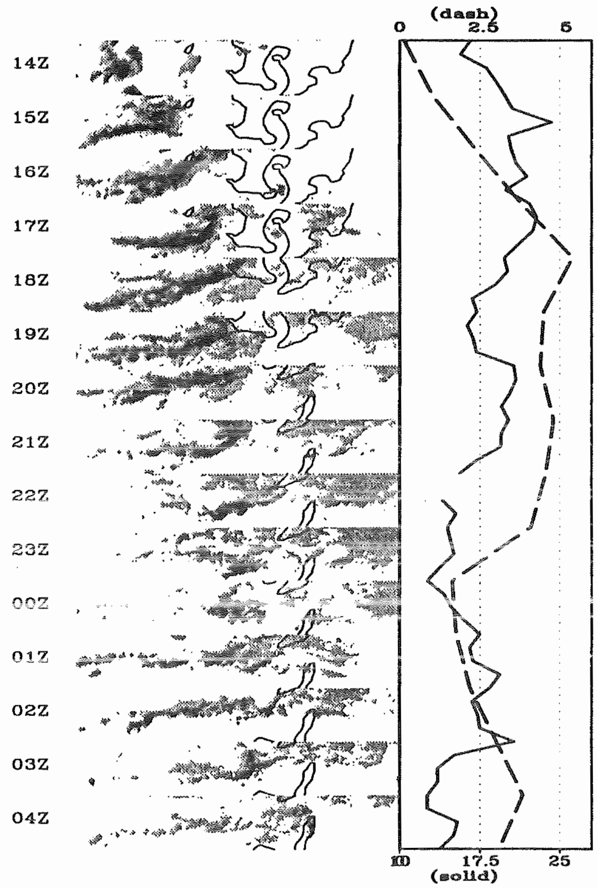

Figure 3 Time Variation of radar-echo distribution (left panels). Time variation of averaged-radar echo intensity in the intense($\geq$10mm/h) rainfall area (solid line; unit is mm/h) and the area of T_{BB} below -60°C (dashed line; unit is 10^4km^2) associated with the cloud cluster.

the doppler radar observation range. In Fig. 4, arc-shaped convective systems were deeper and more intense than other convective systems. The former systems developed above 10km. The top height of the band-shaped convective system was about 7km.

Warm and moist air advection toward northeast was significant around the band-shaped convective systems at the lowest level(Fig.4),(Fig.5). The direction of the band was parallel to low-level wind and vertical wind shear at low and middle levels(Fig.6). Strong dry westerly winds ware remarkable above the convective systems and descended mainly in the downwind side(east side) of the convective systems(Fig.4),(Fig.7). In Fig. 4, band-shaped convective system became deeper after the second arc-shaped convective system disappeared. This variation was accompanied with the variation of the level of downdraft at middle and upper levels.

In the arc-shaped convection system, inflow from the rear side of the convective system at about 3km level was strong(Fig.7). The rear-inflow was accompanied with strong downdraf, and caused intense convergence along the leading edge against southwesterly wind at low level. It is suggested that the rear-inflow contributed to the development of downdraft by evaporating cooling. Updrafts existed in the domain from low level convergence zone to the top level rear side of the system, and stronger than that of the band-shaped convective systems. The relative wind velocity of the rear-inflow was extremely strong as that at other levels. The rear-inflow might be accelerated by the deep and strong updraft. This structure is similar to squall-line while this arc-shaped convective system was slow moving.

4 SUMMARY

An oval-shaped, long-lived meso-α-scale cloud cluster was observed on July 6-7, 1996 over the East China Sea. It was stationary for 18 hours off the west coast of the Kyushu District. The cloud cluster was stagnant over the Kyushu District, a large amount of rainfall more than 300mm/day was observed in a narrow area.

It was consisted of meso-β-scale convective systems which ware generated with 1-3 hours period. Its stagnation and maintenance were attributed to the successive development of new meso-β-scale convective systems in the upwind side(west side) of the cloud cluster. Meso-β-scale convective systems ware organized as band-shaped convective system in the central part of the cloud cluster. They showed periodical intensification as arc-shaped meso-β-scale convective systems with 5-hour period. Rear-inflow was significant at middle and low levels in the arc-shaped convective systems and it caused intense conver-

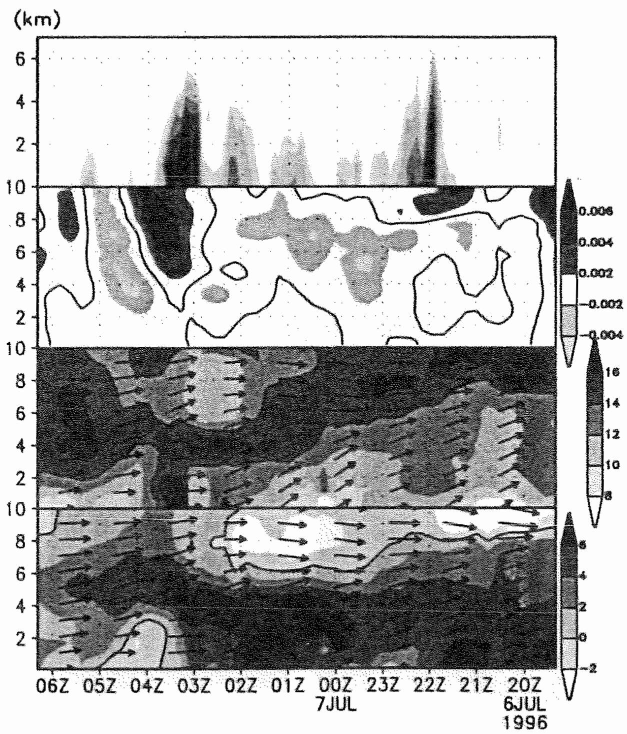

Figure 4 Time variations of vertical profiles of intense($\geq$39dBZ) radar echo area (km^2) and wind velocity above Doppler radar site estimated by extended multi-VAD method (m/s).

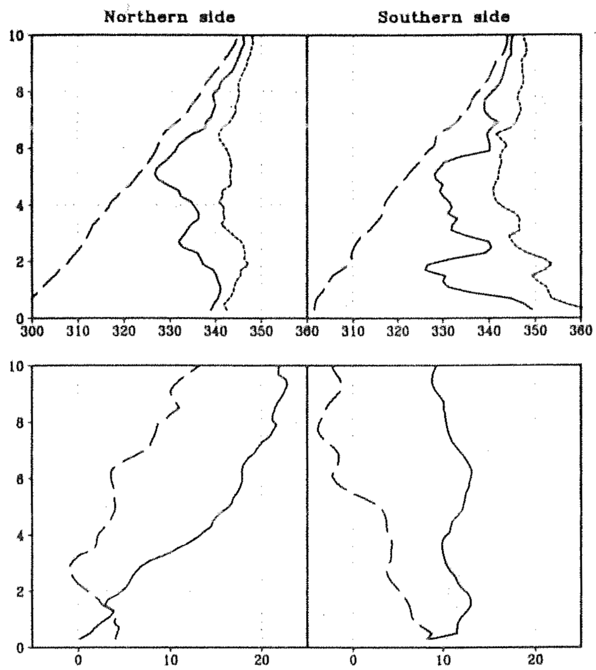

Figure 5 Sonding profiles in the south and north part of the cloud cluster at 00 UTC. Parameters are potential temperature (dashed), equivalent potential temperature (solid), saturated equivalent potential temperature (dotted; K) and wind profile(u:solid,v:dashed; m/s).

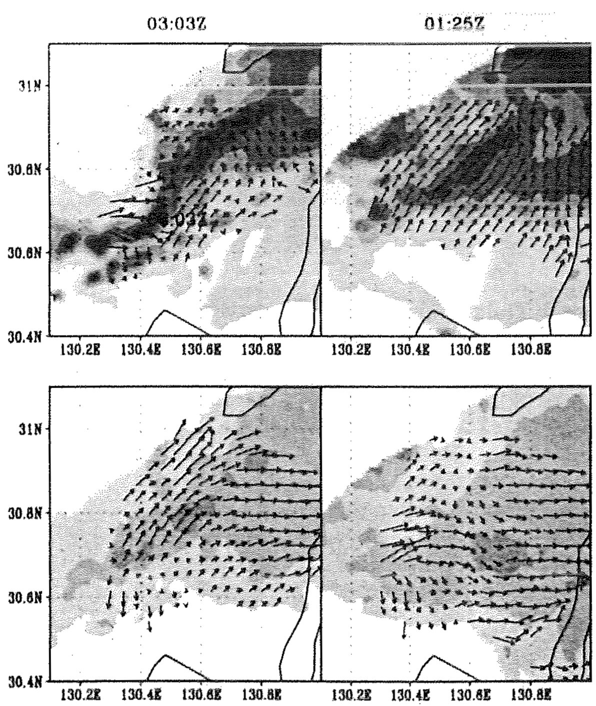

Figure 6 Horizontal distributions of radar echo intensity and wind in band and arc-shaped meso-β-scale convective systems (dBZ,m/s). The upper panel is at 1km level and the lower one is at 7km level.

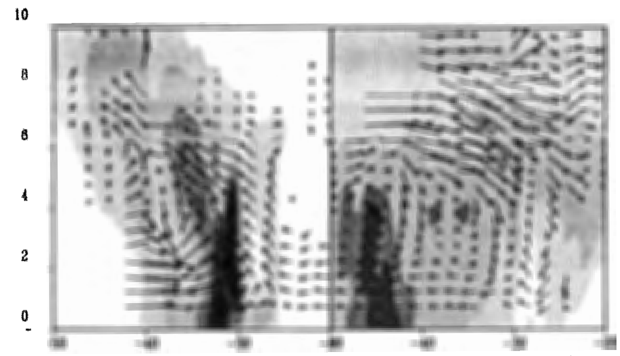

Figure 7 Vertical distributions of radar echo intensity and wind in band and arc-shaped meso-β-scale convective systems.

gence along the leading edge. In the later stage, the evolution and development of band-shaped meso-β-scale convective systems ware associated with low-level southerly winds. The generation and development of band-shaped convective systems would have been related to southerly warm air advection at low levels. In the arc-shaped convective systems, dry rear inflows at low and middle levels would have been important to development of the deep convection. The periodical generation and development of these two types of convective systems might have maintained the meso-α-scale cloud cluster.

References

Ishihara, M., Y. Fujiyoshi, A. Tabata, 1992:, Dual Doppler Radar Analysis of an Intense Mesoscale Rainband Generated along the Baiu Front in 1988: Its Kinematical Structure and Maintenance Process. J. Meteor. Soc. Japan, **73**, 139.

Iwasaki, H., and T. Takeda, 1992:, Behavior of Cumulonimbus-Cloud Groups in a Slow-Moving Meso-Scale Cloud Cluster over the Ocean. J. Meteor. Soc. Japan, **67**, 575.

Ninomiya, K., T. Akiyama, M. Ikawa, 1988 a:, Evolution and Fine Structure of a Long-Lived Meso-α-Scale Convective System in Baiu Frontal Zone. Part I: Evolution and Meso-β-scale Characteristics J. Meteor. Soc. Japan, **66**, 331.

Ninomiya, K., T. Akiyama, M. Ikawa, 1988 b:, Evolution and Fine Structure of a Long-Lived Meso-α-Scale Convective System in Baiu Frontal Zone. Part II: Meso-γ-scale Characteristics of Precipitation J. Meteor. Soc. Japan, **66**, 351.

WATER VAPOR AND CLOUD LIQUID WATER CONTENT SOUNDED BY DUAL-BAND MICROWAVE RADIOMETER IN XINXIANG CITY HENAN PROVINCE

Li Tielin and Zheng Hongwei

Weather Modification Center of Henan Province Meteorological Bureau,
Zhengzhou, 450003, China

1. INTRODUCTION

The water vapor and cloud water content were sounded using a dual-band microwave radiometer for researching the developing feature of vertical integration water vapor (V) in the troposphere and liquid water content (L) in cloud during the period of 1998.3-1999.11. The working wave-length of radiometer are 8*mm* (31.65GHz) and 1.25cm (23.75GHz). The distributing features and developing patterns of water vapor and water liquid in the atmosphere is an important part in the physical research of clouds and precipitation. The microwave radiometer has received more and more attentions because it could timely and automatically sound water vapor and liquid water in the air and record the vapor contents continuously.

In the early 1980s, the remote sounding technology on the based microwave was made remarkable progress in China. Zhao Bailin and others used the radiometer at 1.35cm wave-length to sound the stratification of atmospheric humidity and the vapor content and its deviation was only 3 percent when compared with that sounded by radiosonde. Wei chong and others have showed that the radiometer of 8.6mm wave-length had a wide sounding range and high precision, it can basically be used in the sounding clouds.

Outside China much research has been done in using microwave rediometer to sound the atmosphere and the character of cloud and precipitation. In 1984, Mark Hegg Li performed the consecutive tracking sounding for the distribution of water liquid in the winter storm cloud system in the Mount Nevada in the western United States. In 1988, Warner conducted research on microwave radiometer's precision in sounding the liquid water and proved its feasibility. Achievements above mentioned show that ground based microwave radiometer is an effective tool in sounding features of atmosphere and cloud and precipitation.

The procedure and results of the research are given in detail in this paper.

Li Tielin, Weather Modification Center of Henan Province Meteorological Bureau, Zhengzhou, 450003, China ; E-Mail:litielin@public2.zz.ha.cn

2. CACULATION METHODS

The total amount of microwave radiation from the atmosphere and cloud sounded by the microwave radiometer usually can be expressed by microwave brightness temperature(T_B). For non-scattering atmosphere, presuming the atmosphere level is in balance, T_B got from the atmospheric microwave transition equation is:

$$T_B(\theta,\upsilon) = T_\infty \exp[-\int_0^\infty \alpha \sec\theta dz] + \int_0^\infty T(z)\alpha \exp[-\int_0^z \alpha \sec\theta dz]\sec\theta dz \quad (1)$$

Where V is Vapor water content and L is liquid water content, then:

$$V = \int_0^\infty \rho_v(z)dz \quad (2)$$

$$L = \int_{Z2}^{Z1} \rho_\lambda dz \quad (3)$$

Where V is equal to the vertical integration of vapor density ρv from the ground to atmosphere. L is equal to the vertical integration of liquid water density. Where $z1$ is altitude of cloud bottom and $z2$ is that of cloud top.

Two methods can be adopted in the calculation of the total integration water vapor content in the atmosphere. One is sounding the brightness temperature of atmosphere microwave radiation with single-band microwave radiometer at 23.75GHz, as can be calculated in a simplified theory model as follows:

$$V = \int_0^\infty \rho_{H_2O}(z)dz \approx \frac{T_B - T_C}{(\overline{T} - T_C)\alpha_m} \quad (4)$$

where ρv is vapor density, T_B is the brightness temperature sounded with radiometer, T_C is the brightness temperature of the cosmic radiation, 2.7K for 23.75GHz frequency,

$$\alpha_m = 2V^2(\frac{300}{T_0})^{1.5}\Delta V[\frac{300}{T_0}e^{-644/T_0}$$
$$\times\frac{1}{(v^2-494^2)+4v^2\Delta v^2}+1.2\times10^{-6}] \quad (5)$$

$$\Delta v = 2.85(\frac{P_0}{1013})(\frac{300}{T_0})^{0.626}[1+0.018\frac{\rho_{H2O}T_0}{P_0}] \quad (6)$$

$$\overline{T} = \frac{\int_0^\infty T(2)\rho_{H2O}(z)dz}{\int_0^\infty \rho_{H2O}(z)dz} \approx \alpha T_0 + b\rho_{H2O}(0) \quad (7)$$

where V is frequency of microwave radiometer, P_0 is the pressure on the ground, T_0 is ground temperature, $\rho H2O(0)$ is ground vapor density and *a*, *b* is empirical coefficient of regression.

The other method we adopt for calculating V is sounding the brightness temperature of atmospheric microwave radiation with dual-band microwave radiometer at 23.75GHz and 31.65GHz and calculating in a return statistic model. As we know, if V(vapor content) mounts up , $T_B(\theta, \upsilon)$ received by microwave radiometer will mount up too, and approximation linear relation exists between them. And this is the very theoretical base of calculating the value of V with a statistical inversion method. The lineal model we adopt is:

$$V = A_0 + A_1T_{B1} + A_2T_{B2} \quad (8)$$

Considering that T_B and V are not completely of lineal relations, we therefore adopt the nonlinear model and introduce into the square and mixing terms. That is:

$$V = A_0' + A_1'T_{B1} + A_2'T_{B2} + A_3'T_{B1}^2 + A_4'T_{B2}^2 +$$
$$A_5'T_{B1}T_{B2} + A_6'P_0 + A_7'Q_0 + A_8'T_0 \quad (9)$$

where T_{B1} *and* T_{B2} *are* respectively the brightness temperatures of atmospheric radiation sounded by radiometer at wave-lengths of 21.75 GHZ and 31.65GHZ.

We adopt lineal model and non-lineal model in the calculating of *L*(liquid water content in cloud) :

$$L = B_0 + B_1T_{B1} + B_2T_{B2} \quad (10)$$

$$L = B_0' + B_1'T_{B1} + B_2'T_{B2} + B_3'T_{B1}^2 + B_4'T_{B2}^2 +$$
$$B_5'T_{B1}T_{B2} + B_6'P_0 + B_7'Q_0 + B_8'T \quad (11)$$

where T_{B1} and T_{B2} are the atmosphere radiometer brightness temperatures sounded by radiometer at wave-length of 21.75GHZ and 31.65GHZ.

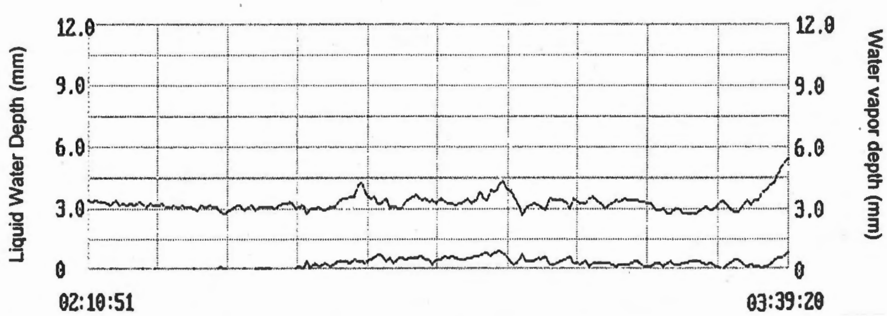

Fig 1 Integrated liquid water and vapor depths as measured by microwave radiometer on 23-24 April 1999. this is a example of shear line cloud system sounding.

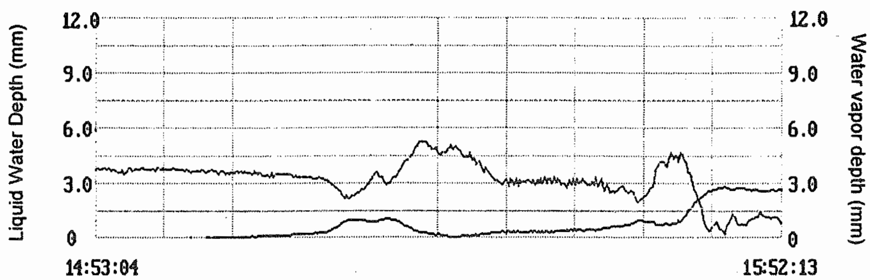

Fig 2 Integrated liquid water and vapor depths as measured by microwave radiometer on 18 August 1999. this is a example of cold front cloud system affecting the area .

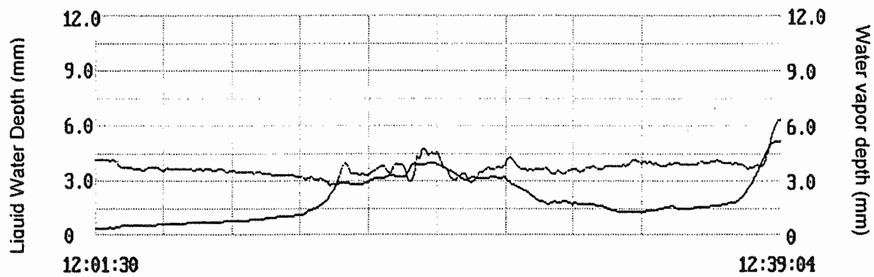

Fig 3 Integrated liquid water and vapor depths as measured by microwave radiometer on 8 September 1999. this is a example of thunderstorm affecting the area .

3. SOUNDING RESULTS

We have performed the consecutive tracking observation on water vapor (V) in the atmosphere and liquid water content (L) in cloud during different weather systems affecting the area. Comparing the *V* value sounded by microwave radiometer with that sounded by radiosonde, the standard deviation is 1.46mm to 2.81*mm* and the mean relative deviation is 7%. The change range of L value is within 0.01mm to 0.28*mm* and the mean value is 0.13mm in clouds while it is not raining. The *L* value has a large change range of 0.35mm to 1.30mm while it is raining. In general, precipitation occurs when *L* value is over 0.4mm.There are phenomena of rapid accumulating and increasing of *L*.

3.1 Case study

Fig 1 to 3 demonstrate the development of *V* and *L* affected by different weather systems. Fig 1 is one example of shear line cloud system sounding.

During Apr.23-24, 1999, Henan province of China was affected by 700hpa shear line. It rained in a large area in Henan province. After 0000 (all time are UTC) on Apr.23, the shear line cloud system spreaded slowly eastward and influenced the whole province. The cloud layer thick over the sounding station since early morning. There are phenomena of rapid accumulating and increasing of *L* sounded by microwave radiometer, when it is about to rain. And we can see from the fig that *L* value showed some small change after 0210. At 0243, sporadic rain drops were observed in the station and *L* value increased sharply to 0.5mm. Afterward, with the stop of the sporadic rain, the *L* decreased. At 0336, a light rain was observed and *L* value mounted up rapidly to 0.8mm.

Fig 2 is a example of cold front affecting the area. On August 18,1999, a cold front moved from the northwest to the southeast and affected Henan province of China. As the cold front cloud system moved closer to the sounding station, L accumulated and mounted up with the thickening of cloud. At 1523, there were sporadic raindrops on the earth and L mounted up to 0.5mm.

Fig 3 is a example of thunderstorm affecting the area. When the sounding station was affected by a convective cloud, *L* sounded by microwave radiometer increased rapidly and was obviously bigger than that of stratiform cloud.

3.2 Acknowledgements

Thanks to Cheng Xianhai, Ren kang, Guo li, Li hu and others from China Research Institute of Radiowave Propagation for their kind helping during the writing of the paper.

4. REFERENCES

Zhao Bolin, Yin hong, and Li huixin and others, 1980: The principle and experiment of atmospheric stratification by microwave sounding, *Chinese science*, 9. 874-882.

Zhou Xiuji, 1982, The atmospheric microwave radiometer and sounding principle, Beijing: Weather press.

Weichong, Linhai, and Qi Miaoxin, 1982, The sounding liquid water in the cloud by dual-band ground radiometer at wave-length of 8.6mm and 3.2cm, *Atmospheric science*, 6(2), 195-201.

Heggli mark, Rauber Robert M and Snider J.B.,1987: Field evaluation of a dual-channel microwave radiometer designed for measurement of integrated water vapour and cloud liquid water in the atmosphere, *J. Atmos. Technol.*, 4, 204-213.

Warner J and Fdrake J, 1988: Field fests of an airforce remote sensing technique for measuring the distribution of liquid water in convective cloud, J. Atmos. Ocear. Technol., 5, 833-843.

Sheppard. B. E., R. E. Stewart, G. A. Isaac, and T. B. Low, 1991: Nonlinear optimal estimation of temperature and integrated water vapor and liquid using a ground-based microwave radiometer in coastal winter storms. *J. Atmos. Oceanic Technol.*, 8, 812-825.

Belay B. Demoz, Arlen W. Huggins, Joseph A. Warburton, and Richard L. Smith, 1993: Field performance of a spinning-reflector microwave radiometer, *J. Atmos. Oceanic Technol.*,10, 420-427.

Hill, G. E., 1991: measurement of atmospheric liquid water by ground-based single frequence microwave radiometer. *J. Atmos. Oceanic Technol.*, 8, 685-690.

Wei, C., H. G. Leighton, and R. R. Rogers, 1989: A comparison of several radiometer methods of deducing path-integrated cloud liquid water. *J. Atmos. Oceanic Technol.*, 6, 1001-1012.

DYNAMICAL AND MICROPHYSICAL INTERACTIONS WITHIN FRONTAL CLOUD

Claire M. Kennedy[1], Peter R. Jonas[1] and Philip R. A. Brown[2]

[1]Department of Physics, UMIST, Manchester, UK
[2]Meteorological Office, Bracknell, UK

1. INTRODUCTION

Studies of frontal rainbands have emphasised a requirement of a better understanding of the influence of precipitation processes upon the dynamical structure (Cox 1998). It has been postulated that evaporation of snow plays a major role in frontal dynamics (Clough and Franks 1991). Barth and Parsons (1996) suggest the that ice phase may play a crucial role in maintaining frontal systems whereby pronounced cooling within the air mass due to sublimation and melting of frozen hydrometeors causes an increase in the intensity of the system. Studies by Carbone (1982) and Rutledge (1989) reveal the importance of melting ice phase microphysics in enhancing the stability of the system.

More recently research has concentrated on the role of latent heat transfers and dynamics and specifically on the role of ice in the Clough-Franks (CF) mechanism. Simulations of frontal precipitation systems focusing on the effects of melting snow on surface frontogenesis reveal melting snow may enhance baroclinicity (Szeto and Stewart 1997).

One of the findings of the GEWEX Cloud System Study (GCSS) Working Group 3 is the poor representation of mid-level clouds by larger-scale models. Using the UK Meteorological Office Large-Eddy Simulation (LES) model we specifically focus on mid-level clouds and associated rainbands within the frontal region of FASTEX IOP 16. By simulating these processes at a high resolution it may be possible to clarify the role of microphysics within a dynamical framework with consequent implications for larger-scale modelling

.2. THE MODEL

The numerical model used for this research is the UK Meteorological Office Large-Eddy Simulation Model (Version 2). The microphysics scheme predicts the mass mixing ratios of snow, graupel, rain, ice cloud and liquid cloud. Also incorporated within the scheme is a 'double-moment' representation of hydrometeors which represent both the mass and number concentration of each hydrometeor (Swann 1996). The model was run in 2 dimensions at high-resolution (200m up to 500 hPa and 500m thereafter) with a domain of size 12km x 50km. Forced large-scale ascent was imposed above 1000m with random heat perturbations added to lower levels of the model to initiate convection.

3. CASE STUDY - FASTEX IOP 16

There have been a number of major meteorological programs focusing on extratropical storms during the last few decades. The most recent study is the Fronts and Atlantic Storm-Track Experiment (FASTEX) which focused on the life cycles of cyclones evolving over the North Atlantic Ocean during January and February 1997. Intensive Observing Period 16 is characterized by a fast moving (29 ms $^{-1}$), rapidly deepening frontal wave secondary cyclone over the northeastern Atlantic. The model was initialized using temperature, humidity and wind profiles from the 08:00Z dropsonde launched from the C-130 aircraft on February 17th 1997. The air was saturated throughout the atmosphere with the exception of a small section centered around 550 hPa. Data from the Valencia 09:00Z sounding was used to initialize the model above 450 hPa. The windspeeds and direction reveal little variation throughout the atmosphere.

4. RESULTS

Figure 1 below reveals the distribution of cloud ice and liquid cloud (20 hours). Cellular structures are evident on scales of a few kilometers and are seen to decay on timescales of approximately 2 hours.

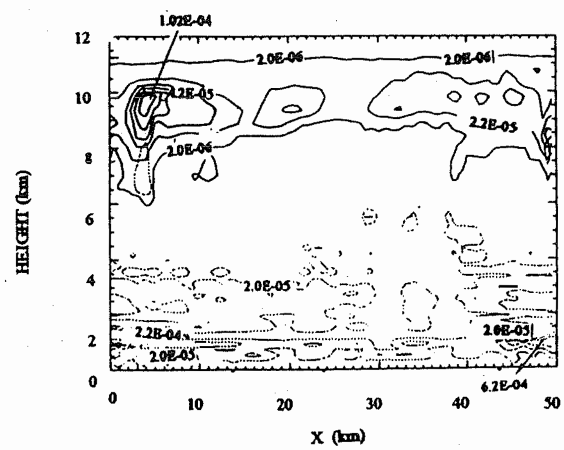

Figure 1: Hydrometeor mixing ratios (kg/kg) at 20 hours - cloud ice (solid) and liquid cloud (dashed). [cloud ice max = 1.11E-04, liquid cloud max = 7.4E-04]

Corresponding author's address:
Claire M. Kennedy, Department of Physics, PO Box 88, UMIST, Manchester, M60 1QD, UK.
E-Mail: claire@cloud2.phy.umist.ac.uk.

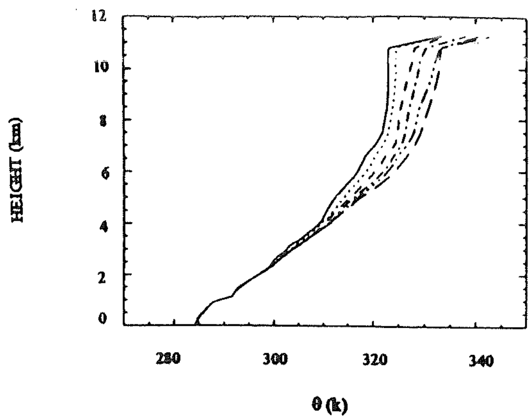

Figure 2: θ profile over time [10 hrs (solid), 13 hrs (dot), 16 hrs (dash), 19 hrs (dot-dash), 22 hrs (dash, dot, dot, dot), 25hrs (large dash)].

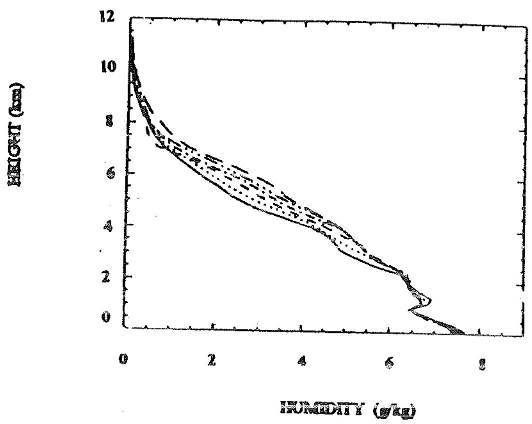

Figure 3: Humidity profile over time [10 hrs (solid), 13 hrs (dot), 16 hrs (dash), 19 hrs (dot-dash), 22 hrs (dash, dot, dot, dot), 25hrs (large dash)].

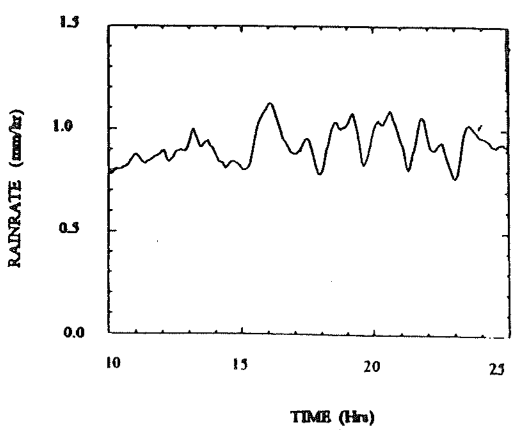

Figure 4: Rainrate (mm/hr) over time.

Figures 2–4 reveal the atmosphere is changing over time becoming increasing warm and moist in the mid-levels. Of importance are the fluctuations in the rainrate after 18 hours (figure 4) which appear to be of a similar frequency to the decay of the cellular features in figure 1. Such oscillations suggest the importance of small-scale substructures within the larger cloud formations.

Future work will focus on the small-scale features evident in mid-level clouds. By comparing these high-resolution results concerning cloud structure and the distribution of ice and water with the larger-scale models, the reasons for global model defects can be investigated with implications for cloud parameterization discussed.

ACKNOWLEDGMENTS

This work was supported by the Natural Environment Research Council and the UK Meteorological Office.

REFERENCES

Barth, M. C., and D. B. Parsons, 1996: microphysical processes associated with intense frontal rainbands and the effect of evaporation and melting on frontal dynamics. *J. Atmos. Sci.*, **53**, 1569-86.

Carbone, R., 1982: A severe frontal rainband. Part I: stormwide hydrodynamic structure. *J. Atmos. Sci.*, **39**, 597-611.

Clough, S. A., and R. A. A. Franks, 1991: The evaporation of frontal and other stratiform precipitation, *Q. J. R. Meteorol. Soc.*, **117**, 1057-1080.

Cox, G. P., 1988: Modelling precipitation in frontal rainbands. *Q. J. R. Meteorol. Soc.*, **114**, 115-127.

Rutledge, S. A., and P. V. Hobbs, 1988: The Mesoscale and microscale structure and organisation of clouds and precipitation in midlatitude cyclones. XII: A diagnostic modelling study of precipitation development in narrow cold-frontal rainbands. *J. Atmos. Sci.*, **41**, 2949-2972.

Swann, H., and P. R. A. Brown, 1996: Development and Validation of a double-moment microphysics scheme for simulating cumulus clouds. *Proceedings of the 12th International Conference on Clouds and Precipitation*, 19-23 August 1996, Zurich, Switzerland.

Szeto, K. K., and R. E. Stewart, 1997: Effects of melting on frontogenesis. *J. Atmos. Sci.*, **54**, 689-702.

MICROPHYSICAL PROPERTIES OF MIDLATITUDE CIRRUS CLOUDS OBTAINED FROM IN SITU MEASUREMENTS WITH HYVIS OBSERVATIONS DURING JACCS FIELD CAMPAIGN

Narihiro Orikasa, Masataka Murakami, Mizuho Miyao, Shoji Asano

Meteorological Research Institute, Tsukuba, Ibaraki 305-0052, Japan

1. INTRODUCTION

Upper-level cirrus clouds, which occur over globally widespread areas, play a significant role in the earth's radiation budget (e.g., Liou 1986). The radiative properties of these clouds depend critically on their microphysical properties, such as the sizes, shapes, and number concentrations (e.g., Stephens et al. 1990). In order to investigate the microphysical processes in cirrus clouds, airborne PMS imaging probes have been frequently used for measuring the size distributions. However, it is still difficult to accurately measure small ice crystals of sizes less than 50 μm. The images of small ice particles (<50 μm) are acquired by using airborne impactors (e.g., replicators), but their collection efficiencies are not well-studied. The airborne instruments used for in situ measurements provide us useful information to understand the relationship between the microphysical and radiative properties of cirrus clouds. However, there have been limited measurements of cirrus cloud microphysical parameters, because of their high location in the troposphere, which requires special research aircraft specified for a high-altitude flight.

Balloonborne instruments have a clear advantage over the difficult conditions of high-altitude locations. Hydrometeor videosonde (HYVIS) by Murakami and Matsuo (1990) is one of the balloonborne instruments for microphysical measurements. The new version of the HYVIS has been developed to measure the vertical distributions of ice particles in cirrus clouds (Orikasa and Murakami 1997). We have successfully acquired imagery of cirrus ice crystals observed by about 30 launches of the new HYVIS, through the Japanese Cloud and Climate Study (JACCS) program. This project was conducted from Tsukuba (36.0N, 140.1E), Japan, possessing a ground-based observation system which involves the combined special sonde (HYVIS + radiation sonde) system, a cloud lidar, a windprofiler, and various types of ground-based radiometers (Asano et al. 1994).

In this paper, we present some observational results by using the HYVIS and also characterize the microphysical properties of midlatitude cirrus mainly associated with warm and stationary fronts of synoptic-scale lows.

Corresponding author address: Narihiro Orikasa, Meteorological Research Institute, Tsukuba, Ibaraki 305-0052, Japan; E-mail: norikasa@mri-jma.go.jp

2. INSTRUMENTS AND DATA OVERVIEW

The HYVIS has two video cameras with different magnifications to take pictures of particles larger than about 7 μm. It collects the particles on a 35-mm wide leader film over which silicone oil is applied. The sampling volume is approximately 1 Ls^{-1}. Collection efficiencies derive from Ranz and Wong (1952) were estimated as unity for all particles larger than 10 μm (Orikasa and Murakami 1997).

Each particle detected by the HYVIS was classified visually according to its crystal habit and maximum dimension (D). Ice water content (IWC) was calculated based on habit-dependent diameter to mass equations (Murakami and Matsuo 1990). Projected cross-sectional area (*Ac*) was obtained using habit-dependent dimension to area conversions given in Mitchell et al. (1996). Cloud optical depth in cirrus was calculated by integrating extinction coefficients from cloud base to cloud top; the extinction coefficients were obtained based on the reasonable assumption that the extinction efficiency equals 2 within measured ranges of ice particle size. The projected area was not measured because of lack of appropriate software to analyze automatically the analog image data. The result in this paper may be improved by using the measured values on projected areas.

Microphysical measurements of cirrus clouds were carried out using the new HYVIS over the Tsukuba area, Japan, between 1994 and 1999. These clouds were high-level ice clouds generally associated with midlatitude fronts of synoptic-scale lows in spring to early summer seasons (mostly in May and in June). There were no direct aircraft measurements and no radar data available. However, some general features of sampled clouds could be obtained using various ground-based remote sensing instruments data, for example, by a sunphotometer, the windprofiler, and the cloud lidar.

3. MICROPHYSICAL MEASUREMENTS AND ANALYSIS

3.1 Ice Crystal Habits

Ice crystal shapes were identified from the HYVIS

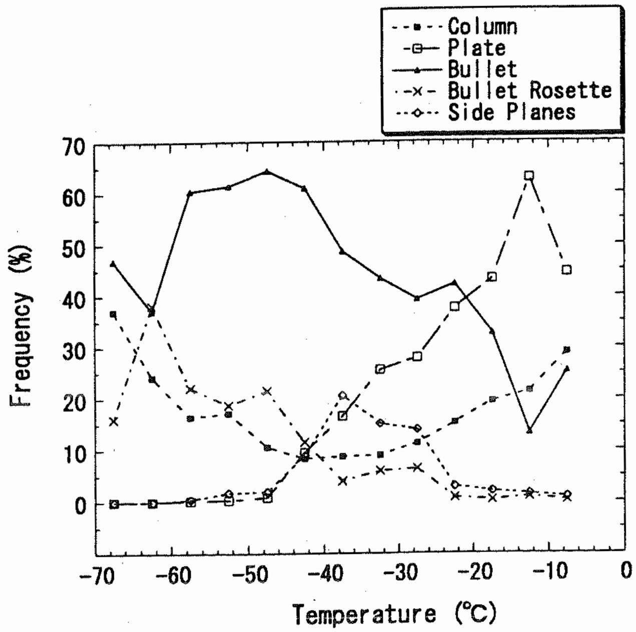

Fig. 1. Percent frequency of ice-crystal habits as a function of temperature.

image data. The percent frequency of the habits had a significant dependence on the temperature, as shown in Fig. 1. The dominant crystal type was bullet at temperatures colder than –30 ℃, with bullet rosettes as the second-most common type at temperatures colder than –40 ℃. The frequency of single plate crystals had a significant tendency to increase with increasing temperature when the temperature was warmer than –50 ℃.

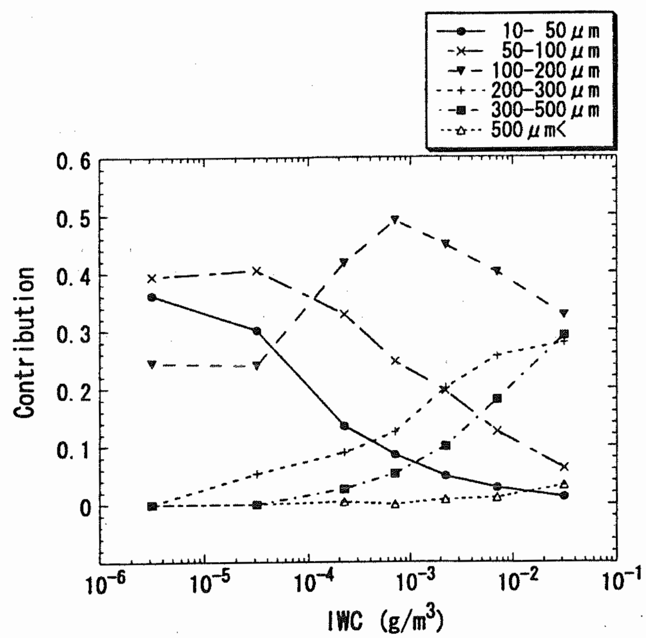

Fig. 2. Averaged contribution of ice crystals in different size ranges to the total IWC for every 250m-thick cloud layers.

Examining a similar figure for the frequency in several ranges of IWC (not shown), bullet type was most dominant in every ranges of the IWC. About 40% of all ice crystals were occurred at IWCs between 10^{-3} and 5×10^{-2} gm^{-3}; nearly half in that IWC range were bullet type of ice crystals.

3.2 Contributions of Particles Different in Size to IWC and *Ac*

What amount the smaller or larger particles contribute of total microphysical and radiative parameters may be needed for determining cloud radiative properties. However, few studies have been obtained in cirrus clouds (McFarquhar and Heymsfield 1996; Heymsfield and McFarquhar 1996).

The number distributions of ice crystals sampled by the HYVIS usually peak between 10 and 50 μm. Figure 2 shows averaged contributions of particles in six different size ranges to the total IWC which was calculated for every 250m-thick cloud layers. The contributions of small particles (in the ranges of 10 to 50 μm and of 50 to 100 μm) were found to decrease with increasing IWC, while the contributions of larger particles (>200 μm) became more substantial with larger IWCs.

Moreover, the contributions to the total *Ac* of ice crystals had the similar tendency to those to the total IWC (figure not shown). Since the IWC is weighted between D^2 and D^3 while *Ac* weighted between $D^{1.5}$ and D^2, contributions due to the smaller particles were more significant at large *Ac* than at large IWCs.

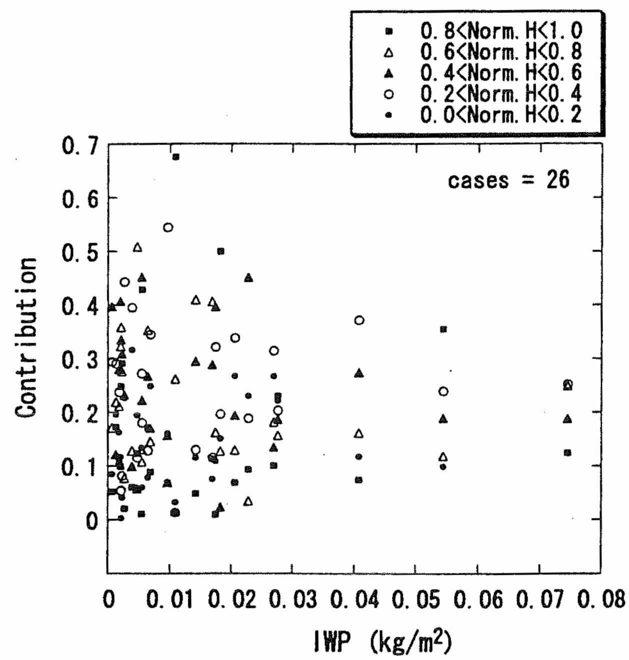

Fig. 3. Contribution of ice crystals in different sub-layers normalized by the cloud thickness, to the total IWP of each ice cloud.

3.3 Contributions of particles in different sub-layers to IWP and τ_{ext}

Figure 3 shows which sub-layers contribute most to ice water path (IWP) of every ice clouds observed by 26 HYVISs. Each cloud was divided into five sub-layers as shown in Fig. 3, normalized by the cloud thickness. For thin clouds, the contributions were widely scattered, because clouds often had multi-layer structures with some sublimation regions inside the cloud. Although some clouds had the largest contributions to the IWP at the upper-most sub-layers, the lower-half portion of the clouds except lower-most sub-layers typically had more IWCs.

Examining a similar figure for τ_{ext} (not shown), there was a large amount of scatter; in particular, the contributions in upper-most cloud sub-layers to the τ_{ext} were highly variable. That means that it should be highly desirable to know the vertical distributions of hydrometeors when the optical properties of total cirrus cloud are estimated.

3.4 Location in Cloud with Maximum Ice Crystal Concentration

In general, many studies have shown that the ice crystal number concentration decreases from near cloud top to cloud base; further, ice particles are nucleated in the upper portion of the cloud, grow in ice

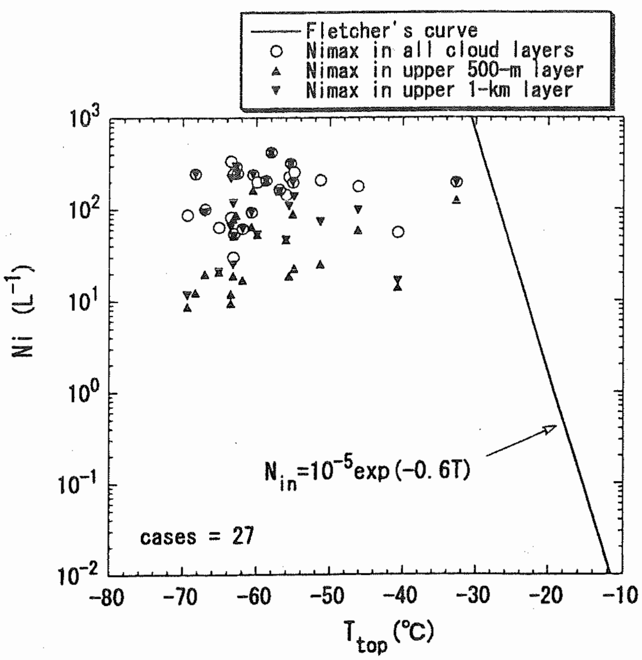

Fig. 4. Maximum ice-crystal concentration measurements as a function of cloud top temperature. ○ shows the maximum concentration in all cloud layers; ▼ and ▲ refer to the maximum concentrations in the upper 1-km and 500-m of cloud layers, respectively. Fletcher's ice-nucleus curve is also shown for reference (solid line).

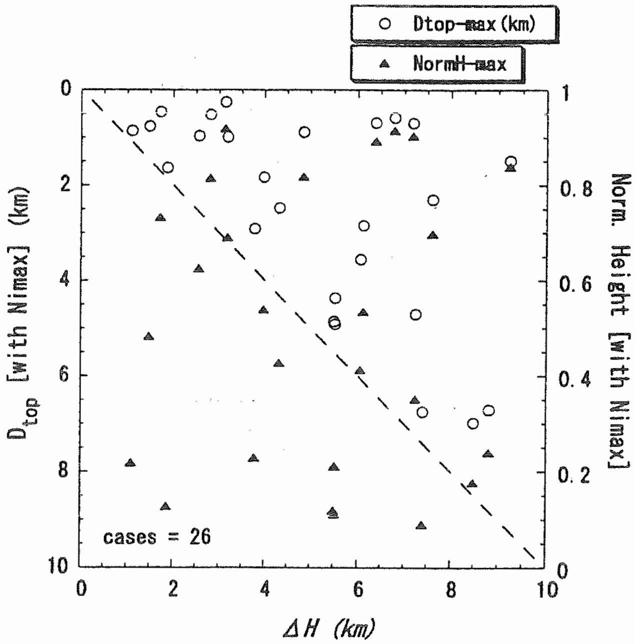

Fig. 5. Geometrical height (○) from cloud top and relative height (▲) with maximum ice-crystal concentration occurred, as a function of cloud depth. Dashed line shows ΔH = Dtop.

supersaturated regions and sublimate near cloud base, which arise from fallout of ice crystals (Heymsfield and Miloshevich 1995).

Figure 4 compares the HYVIS measurements of the maximum concentration in all cloud levels to the Fletcher's (1962) curve and to the maximum concentrations in the upper 1-km or 500-m of high. One of the strongest features is that the maximum ice concentrations did not have as strong dependence on the temperature as the Fletcher's formulation. Another strong feature is that cirrus clouds generated by synoptic-scale forcing had the maximum ice concentration of the order of 10 to 100 L^{-1}.

To examine in more detail where the maximum ice concentration occurred in the vertical structures of ice clouds, figure 5 shows both geometrical height from cloud top and relative height with the maximum ice concentration occurred as a function of cloud depth. Nearly half of the clouds were found to have a maximum concentration in the upper-half portion of the cloud. However, in the remainder of clouds, the maximum concentrations appeared at the middle levels or near the cloud base.

Thermodynamic instability could be one of the reasons why the maximum ice concentrations sometimes occur in the lower portion of clouds. In the lower clouds, the lapse rates of equivalent potential temperatures were highly variable compared with in the upper levels (figure not shown); rawinsonde measurements sometimes indicated convective instability near cloud base.

4. CONCLUSIONS

On the basis of our in situ microphysical measurements using the balloonborne HVYIS, we presented some characteristics of midlatitude cirrus clouds associated with synoptic-scale depressions.

The results of ice crystal measurements by the HYVIS showed detailed microphysics in cirrus clouds; this equipment had reliable measurements especially for small ice crystals less than 100 μm, compared to conventional airborne imaging probes. The following general tendencies were observed in our HYVIS datasets during the JACCS program:

1) Ice crystal habits exhibit a temperature-dependent tendency: the most common shapes were bullets at temperatures colder than –30 ℃ and plate crystals became dominant at temperatures warmer than –20 ℃; at temperatures below –40 ℃, the second-most common habits were bullet rosettes.

2) Small ice crystals (<100 μm) were found to have a decreasing contribution with increasing total IWC and *Ac*. Large particles (>200 μm) became more substantial at larger IWCs. The contributions of particles ranging from 100 to 200 μm in size were most dominant at IWCs above about 10^{-4} gm^{-3} and at *Ac* above about 10^{-2} mm^2L^{-1}.

3) Analysis of contributions of sub-layers to the total cloud parameters such as IWP or τ_{ext} shows that their contributions were widely scattered especially for thin clouds; this scatter results from multi-layer cloud structures with some sublimation regions included.

4) Maximum ice-crystal concentrations near the cloud top did not exhibit a strong temperature-dependence. The cirrus clouds observed by the HYVIS, mainly generated by synoptic-scale forcing, had typically ice concentrations of the order of 10 to 100 L^{-1}.

5) Maximum ice concentrations were sometimes observed at the base of cirrus clouds; thermodynamic instability is likely responsible for this observational results. However, additional measurements and further investigations are needed to confirm the findings.

Acknowledgements. Some of this work was carried out when N. Orikasa is a visiting scientist at NCAR/MMM on leave from MRI, Japan. The authors express their sincere thanks to Dr. Andrew J. Heymsfield for useful discussion and kindly reviewing this paper. The HYVIS observation was assisted by the JMA TATENO Aerological Observatory, Tsukuba. The JACCS program was supported by the Science and Technology Agency of Japanese Government.

5. REFERENCES

Asano, S., JACCS/MRI Research Group, 1994: Japanese Cloud Climate Study (JACCS): Research plan and preliminary results. *Preprint of the 8th Conf. Atmos. Radiation*, Nashville, TN, U.S.A., Amer. Meteor. Soc., 282-284.

Fletcher, N. H., 1962: *Physics of Rain Clouds*. Cambridge University Press, 386 pp.

Heymsfield, A. J., and G. M. McFarquhar, 1996: High albedos of cirrus in the tropical Pacific warm pool: Microphysical interpretations from CEPEX and from Kwajalein, Marshall Islands. *J. Atmos. Sci.*, **53**, 2424-2451.

Heymsfield, A. J., and L. M. Miloshevich, 1995: Relative humidity and temperature influences on cirrus formation and evolution: Observations from wave clouds and FIRE Ⅱ. *J. Atmos. Sci.*, **52**, 4302-4326.

Liou, K. N., 1986: Influence of cirrus clouds on weather and climate processes: A global perspective. *Mon. Wea. Rev.*, **114**, 1167-1199.

McFarquhar, G. M., and A. J. Heymsfield, 1996: Microphysical characteristics of three anvils sampled during the Central Equatorial Pacific Experiment. *J. Atmos. Sci.*, **53**, 2401-2423.

Mitchell, D. L., A. Macke, and Y. Liu, 1996: Modeling cirrus clouds. Part Ⅱ: Treatment of radiative properties. *J. Atmos. Sci.*, **53**, 2967-2988.

Murakami, M., and T. Matsuo, 1990: Development of the hydrometeor videosonde. *J. Atmos. Ocean. Tech.*, **7**, 613-620.

Orikasa, N., and M. Murakami, 1997: A new version of hydrometeor videosonde for cirrus cloud observations. *J. Meteor. Soc. Japan*, **75**, 1033-1039.

Ranz, W. E., and J. B. Wong, 1952: Impaction of dust and smoke particles on surface and body collectors. *Ind. Eng. Chem.*, **44**, 1371-1381.

Stephens, G. L., S. C. Tsay, P. W. Stackhouse, and P. J. Flatau, 1990: The relevance of the microphysical and radiative properties of cirrus clouds to climate and climatic feedback. *J. Atmos. Sci.*, **47**, 1742-1753.

ANALYSIS ON THE MACROPHYSICS AND MICROPHYSICS STRUCTURE OF COLD FRONT CLOUD SYSTEM IN THE SPRING AND AUTUMN AND ITS PRECIPITATION CHARACTERISTICS IN HENAN PROVINCE

Li Tielin and Zheng Hongwei

Weather Modification Center of Henan Province Meteorological Bureau,
Zhengzhou, 450003, China

1. INTRODUCTION

The macrophysics and microphysics structure of cold front cloud system in the spring and autumn and its precipitation characteristics have been analyzed in the paper; by using of multiple scale sounding data obtained during clouds and precipitation sounding research plan in Henna implement period from 1997.9 to 1999.10. During the sounding program, the main instruments were as follows: a set of satellite cloud picture receiving instrument for receiving a set of four-band satellite cloud picture data each hour; a Doppler radar at wave-length of 5cm, two weather radar at wave-length of 5cm and five weather radar at wave-length of 3cm for consecutive tracking sounding of precipitation cloud system during the experiment; a plane equipped with PMS particle observation system (FSSP-100, 2D-C, 2D-P) for go-through-cloud sounding of cold front cloud system; a raindrop disdrometer (GBPP-100) for observing raindrop size distribution characteristics; a dual-band ground based microwave radiometer for sounding water vapor content in the atmosphere and the integrated liquid water content in the cloud; a lightning fixed-location meter for monitoring the lightning in unsteady precipitation.

2. MACROPHYSICS STRUCTURE

The cold front is a weather system which visits Henan province frequently in the spring and the autumn. It usually causes a province-scale precipitation. The ground cold front usually influences Henan province from the three directions of the west, the middle and the east. When cold air travels southward from the east or the middle direction, strong precipitation often occurs. The sectional structure of this kind of weather system is that the ground-850hpa is a thicker layer of east wind and the thickness of negative temperature layer and saturation layer in the cloud is between 2 and 4 kilometers. When cold air influences the Henan province from the west direction, local scattered shower occurs due to poor water vapor content in the atmosphere.

According to radar, radiosonde and plane go-through cloud soundings, there are mainly two arrangement patterns of the meso-scale zonality radar echo in the cold front cloud belt. One is the short zonality radar echo which goes parallel to the direction of cold front with a belt-length of 30 to 60 kilometers. The other is some undulatus radar echo zone which goes approximately vertical to cold front with their interval of 15 to 30 kilometers. Its spreading direction is near to that of the southwest air current in 850hpa.

The width of the cold front cloud belt often goes from 100 to 230 kilometers and the altitude of its echo top is usually between 4 and 9 kilometers. The altitude of the strong convection echo cell in the cloud belt can reach as high as 14 kilometers. The echo intensity in the cold front cloud belt is usually 15 to 30 dBz and the maximum echo intensity is 45 dBz. The echo top temperature is usually -6℃ to -17℃ and the minimum is -26℃. The structure of precipitation clouds behind the front in the vertical direction are mainly separate seeding cloud and feeder cloud (57%) . The temperature in the seeding cloud top is usually lower than -16℃. The mean cloud top height is 5695 meters. It is a mixing cloud where supercooled water droplet and ice crystal coexist.

3. MICROPHYSICS STRUCTURE

Influenced by macroscopic environment, seasons and other factors, the microphysics structure in cold front cloud system varies greatly. Three sounding cases are given as follows:

Li Tielin, Weather Modification Center of Henan Province Meteorological Bureau, Zhengzhou, 450003, China; E-Mail: litielin@public2.zz.ha.cn

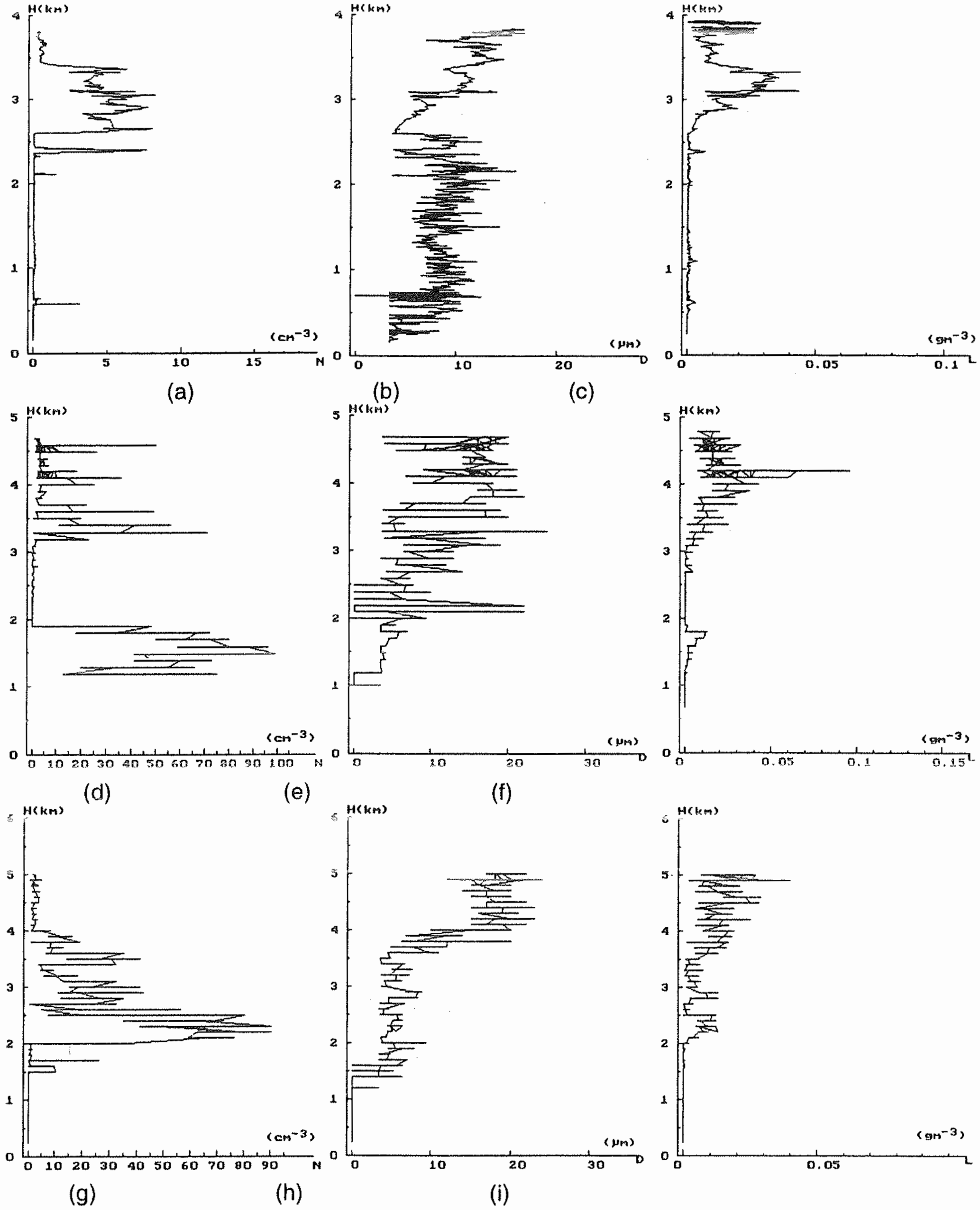

Fig 1: The distribution chart of microphysics feature values with altitude.

Case A is the precipitation process on Oct. 13,1998. A plane equipped with PMS particle observation system took two sorties: once at 0031-0235(UT) with a flight altitude of 4000 to 4500 meters, the other time at 0345-0605(UT) with a flight altitude of 3800 to 4200 meters. The altitude of cloud top is about 5800 meters. According to FSSP-100 sounding, the cloud particle concentration is mainly 10^5-10^6/m^3 with the maximum of 3×10^7/m^3 and water content is 0.01-0.05g/m^3. Particle diameter is usually 10-20um with the maximum of 35um. Fig. 1. a-c is distribution chart of feature values with altitude.

Case B is the precipitation process on Apr.11, 1999. The flight sounding time is at 0210-0235(UT) with flight altitude of 3800 to 4800 meters. The altitude of cloud top is 6800 meters and zero-temperature level in the cloud is about at 3100 meters. As shown by sounding results, the cloud layer is multiple-layer one and the ice-crystal concentration is somewhat lower in the stratiform ice-water mixing clouds. According to FSSP-100 sounding, the cloud particle diameter is usually 6-20um. The cloud particle concentration is mainly 10^6-10^7/m^3 with the maximum of 1.5×10^8/m^3 at 3000 to 4800 meters. Water content in the cloud is a bimodal spectrum with the maximum of 0.12g/m^3 at 4200 meters (see Fig. 1. d-f).

Case C is the precipitation process on Apr. 26, 1999. Fig. 1. g-i are a distribution chart with altitude of cloud particle concentration, water content and cloud particle diameter sounded by FSSP-100. At 4 to 5 kilometers inside the cloud, the particle is smaller with concentration and bigger with diameter, so its water content is bigger. Things are on the contrary in the lower layer . It tells that water content in the cloud is mainly linked with the cloud particle diameter.

4. RADIOMETER SOUNDING RESULTS

The water vapor and cloud water content were sounded using a dual-band microwave radiometer for researching the developing feature of vertical integration water vapor (V) in the troposphere and liquid water content (L) in cloud during cold front cloud system affecting the area. The working wave-length of radiometer are 8*mm* (31.65*GHz*) and 1.25*cm* (23.75*GHz*). Comparing the *V* value sounded by microwave radiometer with that sounded by radiosonde, the standard deviation is 1.43mm to 2.95*mm* and the mean relative deviation is 8%. The change range of L value is within 0.01mm to 0.26*mm* and the mean value is 0.14*mm* in clouds while it is not raining. The *L* value has a large change range of 0.32mm to 1.65mm while it is raining. In general, precipitation occurs when *L* value is over 0.4mm. There are phenomena of rapid accumulating and increasing of *L*. Fig. 2. is a case sounded by microwave radiometer.

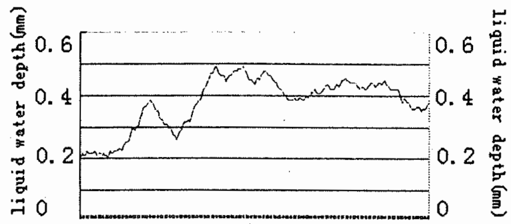

Fig. 2. Integrated liquid water depth as measured by microwave radiometer on 23-24 April 1999

5. RAINDROP SIZE DISTRIBUTION

We have observed precipitations in different parts of cold front cloud system with GBPP-100 ground raindrop disdrometer. And we performed a simultaneous sounding of cold front cloud belt structure by using satellite cloud picture, 714-CD radar, radiosnode and recording pluviometer. The interval of the raindrop disdrometer sampling is 10 to 30 seconds. Using the data above mentioned, we performed a comprehensive analysis of the raindrop size distribution characteristics from different parts precipitation in cold front cloud system.

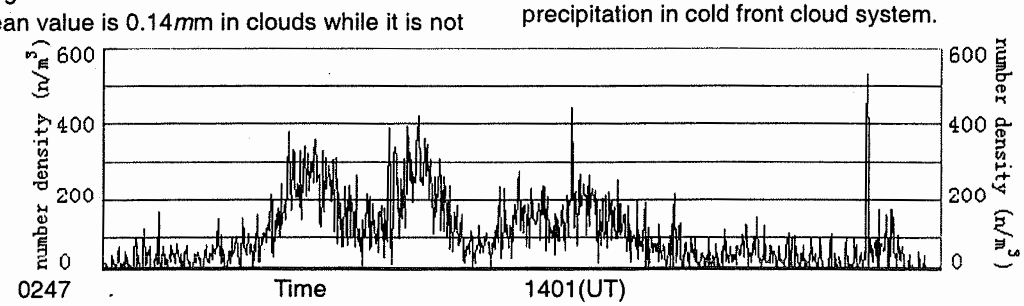

Fig. 3. A. The developing chart for raindrop total mount density (N_t) with time

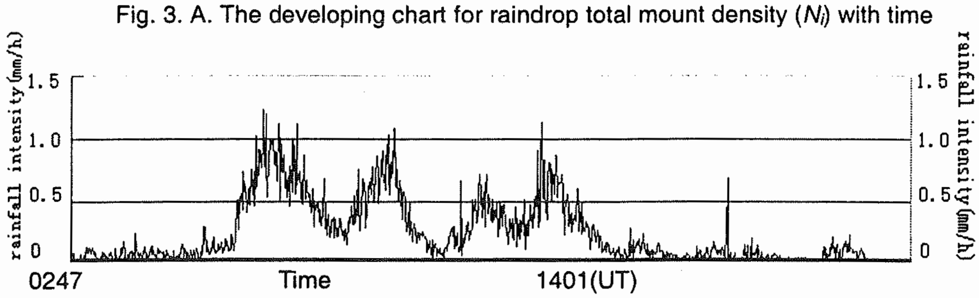

Fig. 3. B. The developing chart of rainfall intensity I with time

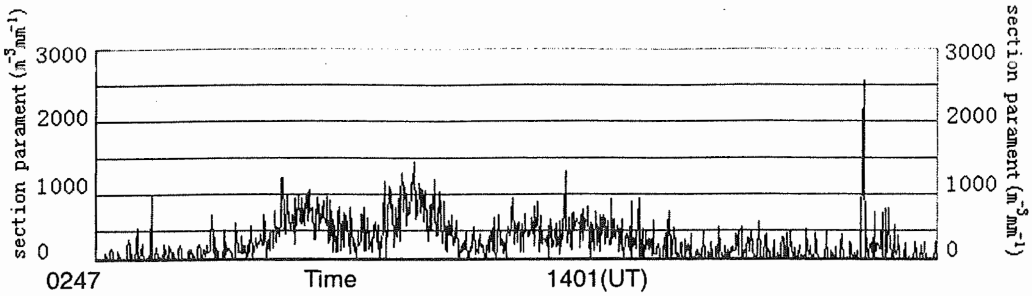

Fig. 3. C. The developing chart for raindrop size distribution section parameter (N_O) with time.

Raindrop size distribution types in cold front precipitation can be divided into four ones: A-1, B-1, B-2 and B-3 type. A-1 is descent type, that is, raindrop number density N_i decreases monotonously with the increase of raindrop diameter D_i. B-1 type is that N_i decreases with the increase of D_i, after a peak value, it decreases monotonously, as we call it unimodal distribution type. Correspondingly, B-2 type and B-3 type are bimodal spectrum and multimodal spectrum. N_i has two or more peak values respectively at large raindrop diameter interval.

The raindrop size distribution of convectional rain belt in the cold front cloud system usually have a feature of large raindrop diameters interval and are mainly B-2 type and B-3 type. The raindrop size distribution of the stable precipitations behind front are usually A-1 type and B-1 type. The adopting of the exponential law and □-function respectively fits the function of A-1 type and B-1 type raindrop size distribution density with which we analyzed the correlation between the slope parameter of raindrop size distribution and precipitation intensity and the developing of section parameter (N_O) with time . The raindrop size distribution feature values of precipitation in different parts of cold front rain belt have been analyzed in the paper.

Fig. 3. A-B is raindrop size distribution feature value developing chart of precipitation of cold front with time on Sep. 18.1999, in which A for developing chart for raindrop total mount density (N_i), B for developing chart of rainfall intensity and C for developing chart for raindrop size distribution section parameter (N_O) with time. These are observing results of sheet cloud precipitation in cold front rain belt. It is thus clear that raindrop size distribution has the nonuniform feature.

6. REFERENCE

Wang Pengfei and Li Zihua, 1989: The microphysics of Clouds, Beijing, Weather press.

You laiguang and Liu Yubao, 1989: The synoptic structures and microphysical processes of precipitation systems in winter in Urumqi area, Xinjiang, WMO/TD No. 269, 65-68.

You laiguang, 1994: A study of cloud physics and seedability of artificial precipitation with particle measuring system, *The study of technology on cloud physics and artificial precipitation*, Beijing, weather press.

Sun Yuwen, Analysis of the microphysical structure of a cold frontal system in spring and the conditions for artificial precipitation, *The study of technology on cloud physics and artificial precipitation*, Beijing, weather press.

ON THE RADIATIVE FORCING BY CONTRAILS

[1]P. Wendling, F. Schröder, [1]R. Meerkötter,
[1]M. Degünther and [2]R. Sussmann

[1]Deutsches Forschungszentrum für Luft- und Raumfahrt,
Institut für Physik der Atmosphäre, Oberpfaffenhofen, Germany
[2]Fraunhofer-Institut für Atmosphärische Umweltforschung,
Garmisch-Partenkirchen, Germany

1. INTRODUCTION

Air traffic influences the atmosphere through the emission of various gases and particles (Schumann, 1994). Among these, water vapour and aerosol particles acting as cloud nuclei are of special interest because they support cloud formation. When the temperature is cold enough contrails form directly from the emitted water vapour. They are short-lived when formed in dry air but persist and develop into extended cirrus cloud layers when the ambient relative humidity exceeds ice saturation. Individual contrails may persist for hours and develop into cirrus clouds that look like those formed naturally (Minnis et al., 1998).

Contrails with a line-shaped structure can well be identified in satellite pictures. According to an analysis of Bakan et al. (1994) and Mannstein et al. (1998) line shaped contrails cover 0.5% to 2% of parts of Europe and the Eastern North Atlantic. Based on an analysis of meteorological and aircraft fuel consumption data, the global coverage due to contrails can be estimated to be 0.1% (Sausen et al., 1998). Further studies on the radiative effects of contrails that make use of these results indicate that the computed global mean radiative forcing by line-shaped contrails is 0.02 Wm^{-2} with the expected growth of air traffic 0.1 Wm^{-2} in 2050 (Minnis et al.,1999). At northern latitudes, the zonal mean forcing is five times larger than the global mean. Applying radiative-convective models, an additional cirrus cloud cover of 0.5% may increase the surface temperature in northern midlatitudes by less than 0.1 K (Liou et al., 1990; Strauss et al., 1997). Though this effect appears to be small contrails may play a larger role in modifying the climate in future in view of the fast growth rate of air traffic.

All the previously mentioned studies had to make assumptions on the radiative properties of contrails which might differ considerably from those of cirrus clouds because aircraft emissions induce more and smaller ice particles in fresh contrails for a given ice water content (Kärcher et al., 1996). We therefore present measurements of the microphysical and radiative properties of fresh contrails in order to better characterize and understand the radiative forcing of contrails.

2. MEASUREMENTS

During the national campaign 'CONTRAIL'96' in situ-measurements were carried out from aircraft in southern Germany between 9 April and 3 May 1996 in order to characterize the microphysical and radiative properties of contrail clouds. For this purpose the german research aircraft Falcon was equipped with a set of optical spectrometers (FSSP-300, FSSP-100) both mounted at outside wing stations of the aircraft. These instruments allowed the determination of ice crystal concentration and size in a diameter range from 0.4 to 32 μm. It was shown by Gayet et al. (1996) that the FSSP sondes can be reliably applied in the presence of small particles. The procedure for the data evaluation during the 'CONTRAIL'96' campaign is described in detail by Schröder et al. (2000).

Measurements of shortwave radiative fluxes were made by upward and downward looking standard Eppley pyranometers which measure

Corresponding author's address: Peter Wendling, DLR, Institut für Physik der Atmosphäre, D-82230 Wessling, Germany

the integrated hemispherical radiation flux density in the wavelength interval from 0.3 to 3.0 μm. Upward directed longwave fluxes were measured by an Eppley PIR-pyrgeometer and downward directed fluxes by a pyrgeometer of the type described by Foot (1986). Both instruments use a coated silicon dome for blocking the solar radiation and measure the radiation fux density in the spectral range from 3 to 50 μm. Details of the calibration of the instruments, data evaluation and correction methods are described by Saunders et al. (1992).

The thermodynamic properties of the atmosphere were deduced from the meteorological sensor set of the Falcon previously described by Busen et al. (1997).

In addition to the research aircraft Falcon a scanning backscatter lidar was operated on ground by the Fraunhofer Institut für Atmosphärische Umweltforschung (IFU), Garmisch-Partenkirchen. The IFU bistatic backscatter lidar (Freudenthaler, 1995) consists of a Nd-Yag laser (550 mJ pulse energy at 532 nm, beam divergence < 0.5 mrad), a 52 cm diameter Cassegrain telescope with chopper, two photomultipliers and four channels of analog sampling. It is combined with a CCD camera oriented parallel to the laser axis. The lidar is operated in single shot mode with a 10 Hz repetition rate and a range resolution of 3 m. Integration of the whole system on a two-axis scanning mount with a pointing accuracy that exceeds the laser beam divergence allows for tracking and cross-sectional measurements of contrails. For this purpose, the horizontal drift speed of the contrail (typically 20 m/s) is preestimated from al lidar sounding (altitude) and video image analysis (angular velocity). Based on these data the lidar-CCD-camera mount is computer controlled to track the drifting contrails.

3. RESULTS

We report on the results obtained on 23 April 1996 in the area west of Munich between 47.9°N, 9.5°E and 48.9°N, 11°E. The backscatter lidar on ground was located at 48.3°N, 10.7°E, 500 m asl. The meteorological conditions were favorable for the formation and persistence of contrails at altitudes of 11 to 12 km. In order to have a good control of the age of the contrails it was decided to investigate contrails that were produced by the research aircraft Falcon itself. The flight strategy to measure microphysical and radiative contrail properties consisted in flying one minute above (vertical distance from contrail top about 30 m), one minute inside and one minute below the contrail (vertical distance from contrail base about 30 m). Three contrails originating from the exhaust of the Falcon could be measured on 23 April 1996 in addition to one contrail of a Boeing 747 just passing the experimental area. We were able to make measurements on contrails of different age ranging from 3 minutes (Boeing 747) to 14 minutes (Falcon).

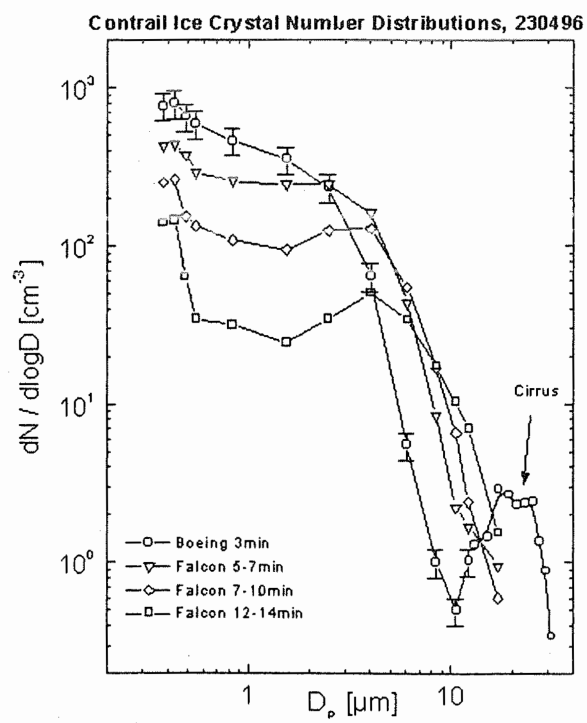

All contrails were located at altitudes between 11 and 11.5 km corresponding to a temperature range from -58°C to -64°C.

Fig. 1 Measured ice particle size distributions in four contrails of different age on 23 April 1996 in Southern Germany (temperature range -58°C to -64°C)

A representative selection of ice crystal number size distributions in contrails of different age is shown in Fig. 1. Fresh contrails in the jet phase typically start developing from a narrow ice crystal mode close to 1 μm mean diameter (Schröder et al., 2000). With increasing time the size distribution broadens and the number concentration decreases due to dilution with the ambient air from about 240 cm^{-3} (3 min age) to 30 cm^{-3} (12 - 14 min age). The broadening of the spectra during aging could result from mixing processes inside the contrail that lead to a superposition of crystal modes with different mean sizes formed due to spatial variations of humidity and temperature. In the vicinity of the 3 minute Boeing contrail natural cirrus occurred showing up in Fig. 1 as a peak centered around a particle diameter of 20 μm. This mean particle size is typical for young cold cirrus in midlatitudes (Schröder et al., 2000).

In the following we will concentrate on the second measured contrail which is denoted in Fig. 1 by the 7-10 min case. The measured ice particle size spectrum corresponds to an average of about 20 seconds. At the time of the aircraft measurements (11:36:00 - 11:41:00 UTC) this contrail was 200 m wide and extended vertically from 11300 m to 11600 m as is shown by the lidar backscatter measurements from ground. Further, during the in situ-sounding of the contrail a thin cirrus layer with an optical thickness of 0.03 at 0.532 μm was present at an altitude between 12 300 and 12 400 m. Approximately one minute before carrying out the aircraft measurements the lidar performed a scan along the cross section of the contrail. By applying the shadow calibration technique (Ruppersberg and Renger, 1991) the optical depth along 15 lidar pointing directions could be derived. As shown in Fig. 2 the optical depth in z-direction varies along the contrail cross section from about 0.05 to 0.25, still indicating the original structure of two vortices. The two curves in Fig. 2 are obtained by taking different background targets for the retrieval of the optical depth, thus giving a certain measure for the uncertainty of the values.

The radiation flux changes arising from the contrail were measured by taking one minute averages on flight legs approximately 30 m above and below the contrail as well as at one level within the contrail during the time interval from 11:36:00 to 11:41:00 UTC. Note, that during this time a thin cirrus layer was present at about 12 km. As a reference for the calculation of the radiative forcing we determined the corresponding fluxes during non-contrail conditions by setting the downwelling fluxes equal to those when the contrail was present and taking the upwelling fluxes from the measurements below the contrail. All considered measurements took place at local noon so that no correction with respect to sun elevation was necessary. Considering the level just at the top of the contrail we obtained for the change in radiation budget of the troposphere (system atmosphere/ground below contrail top) a loss of 5 W/m^2. The albedo effect in reducing solar input to the system is larger in this special case of a contrail with very small particles than the gain by the reduced longwave emission to space. This is in agreement with the study of Lyzenga (1973). On the other hand, it was shown by Strauss et al. (1997) and Meerkötter et al. (1999) that more aged contrails which contain larger particles tend to heat the earth/atmosphere system. Further results of radiation transport calculations will be shown in order to demonstrate this transition from cooling to heating.

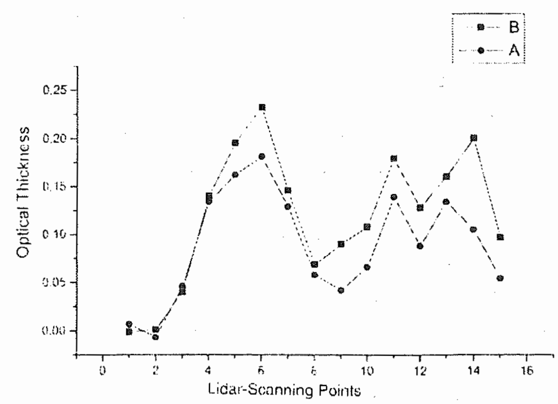

Fig.2 Optical thickness (0.532 μm) of the 7 - 10 min aged contrail of Fig. 1 along the contrail cross section determined from ground-based lidar backscatter measurements at 11:37 UTC

4. References

Bakan, S., M. Betancor, V. Gayler, and H. Grassl, 1994: Contrail frequency over Europe from NOAA-satellite images. Ann. Geophys., 12, 962-968

Busen, R., R. Baumann, A. Petzold, F. Schröder, and U. Schumann, 1997: Aircraft measurements on the formation and dilution of contrails. DLR-Mitteilung 97-04, 11pp. (available from reinhold.busen@dlr.de)

Foot, J.S., 1986: A new pyrgeometer. J. Atmos. Oceanic Technol., 3, 363-370

Freudenthaler, V., F. Homburg, and H. Jäger, 1995: Contrail observations by bround-based scanning lidar: Cross-sectional growth. Geophys. Res. Lett., 22, 3501-3504

Gayet, J.-F., G. Febvre, and H. Larsen, 1996: The reliability of the PMS FSSP in the presence of small ice crystals. J. Atmos. Oceanic Technol., 13, 1300-1310

Kärcher, B., Th. Peter, U.M. Biermann, and U. Schumann, 1996: The initial composition of jet condensation trails. J. Atmos. Sci., 53, 3066-3083

Liou, K.N., S.C. Ou, and G. Koenig, 1990: An investigation on the climatic effect of contrail cirrus, in 'Air traffic and the environment - background, tendencies and potential global atmospheric effects', Ed. U. Schumann, Proc. DLR Int. Coll., Bonn Germany, Springer Verlag, Berlin, 1990

Lyzenga, D.R., 1973: Environmental effects of aircraft condensation trails. Dissertation, University of Michigan, 94 pp.

Mannstein, H., R. Meyer, and P. Wendling, 1999: Operational detection of contrails from NOAA-AVHRR-data. Int. J. Remote Sens., 20, 1641-1660

Meerkötter, R., U. Schumann, D.R. Doelling, P. Minnis, T. Nakashima, Y. Tsushima, 1999: Radiative forcing by contrails. Ann. Geophys., 17, 1080-1094

Minnis, P, D.F. Young, D.P. Garber, L. Nguyen, W.L. Smith, Jr., and R. Palikonda, 1998: Transformation of contrails into cirrus during SUCCESS. Geophys. Res. Lett., 25, 1157-1160

Minnis, P., U. Schumann, D.R. Doelling, K. M. Gierens, and D. W. Fahey, 1999: Global distribution of contrail radiative forcing. Geophys. Res. Lett., 26, 1853-1856

Ruppersberg, G.H., and W. Renger, 1991: Invertierung der Lidarsignale von Cirrus und Kondensstreifen unter Nutzung des Schattenwurfes. DLR-Forschungsbericht, 91-07 (available from peter.wendling@dlr.de)

Saunders, R.W., G. Brogniez, J.C. Buriez, R. Meerkötter, and P. Wendling, 1992: A comparison of measured and modeled broadband fluxes from aircraft data during the ICE '89 field experiment. J. Atmos. Oceanic Technol., 9, 391-406

Sausen, R., K. Gierens, M. Ponater, and U. Schumann, 1998: A diagnostic study of the global distribution of contrails: Part I: Present day climate. Theor. Appl. Climatol., 61, 127-141

Schröder, F., B. Kärcher, C. Duroure, J. Ström, A. Petzold, J.-F. Gayet, B. Strauss, P. Wendling, and S. Borrmann, 2000: On the transition of contrails into cirrus clouds. J. Atmos. Sci., 57, 464-480

Schumann, U., 1994: On the effect of emissions from aircraft engines on the state of the atmosphere. Ann. Geophys., 12, 365-384

Strauss, B., R. Meerkötter, B. Wissinger, P. Wendling, M. Hess, 1997: On the regional climatic impact of contrails: microphysical and radiative properties of contrails and natural cirrus clouds. Ann. Geophys., 15, 1457-1467

NUMERICAL SIMULATION OF THE WARM-SEASON FRONTAL CLOUDS OVER UKRAINE

A.V.Belokobylski and A.M. Pirnach

Ukrainian Hydrometeorological Research Institute, Kiev, 03028, Ukraine

1. INTRODUCTION

The attempt to apply the 3-D nowacasting and forecasting models that have been developed in UHRI for study of the winter frontal cloud systems was carried out for numerical simulation of warm-season frontal clouds (see Pirmach 1987, 1998, Palamarchuk and Pirnach, 1992, Krakovskaia and Pirnach 1994, 1998 etc). Three-dimension numerical models with detail description of an evolution of cloud particles (drops, crystals, cloud and ice nuclei, etc.) are used to study the microphysical processes into widespread and convective frontal clouds. Primitive approach of equations was used to simulate dynamical and thermodynamic processes. An evolution of the processes of condensation, nucleation, sublimation, freezing, sedimentation, droplet collection by raindrops and ice particles, etc was calculated with aid of set equations for particle size distribution functions.

To accomplish these objective, two different synoptic situations were simulated, both of them associated with heavy precipitation. One of them (Case 1) presented sinoptic situation accompanied a squall line that forced some vigorous events into western Ukraine on 23 June 1997. In second case (Case2), a cloud system accompanied the passage over Ukraine a diving cyclone. These study were devoted to the mesoscale and convective scale circulation associated with active cold frontal systems, leading to the well-known large cloud cover and to smaller scale bands. The dynamical and microphysical features of the widespread cloud system and rainbands of heavy rainfall were objected herein study.

The bands of heavy rainfall that frequently accompanied the passage of cold front in middle laltitude were subject many investigation (Brouning and Harrold, 1970, Hobbs, 1981, Hobbs and Persson, 1982, McBeen and Stewart, 1991, Barth and Parsons, 1995, Locatelli et all, 1995, Pirnach, 1998 etc) Probably, it will be interesting the short description of squall-line and line heavy rainfall connected with cold fronts that forced a severe wather over Ukraine.

2. FEATURES OF OCCLUDED FRONTAL CLOUD SYSTEM DEVELOPMENT. *Case 1*

A frontal wave connected with a western cyclone moving over a north border of Ukraine was accompanied by the heavy precipitation, showers and thunders. The widespread occluded frontal system and the rainband of heavy precipitation was object of this investigation. The weather state on 23 June 1997 at 12 00 GMT modeled as initial data by 3-d diagnostic model. As zero coordinate point the Meteorological Proving Graung of UHRI (Kr. Rog) was selected. The space lengths in direction normal to front (from west to east) (xs) and along front (ys) were 50km and 100 km respectively. They let to clearly indicate the spread mesoscale features and rainband only.

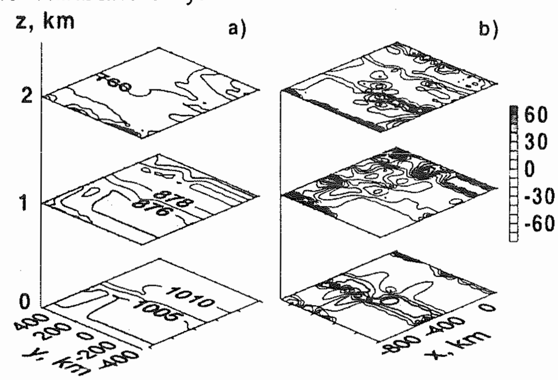

Figure 1. 3-D fields of pressure, hPa (a), and vorticity $10^{-6} s^{-1}$ (b), for 1200 GMT on 23 June 1997

Figs 1-2 show the time and space distribution of the pressure, temperature, vertical motion and vertical vorticity in initial time. Shallow pressure low and band of contra clockwise helical motion clearly depicted from Fig.1 were located in western and central part of the grid box. The regular rawinsondes into Ukraine were used for diagnostic modeling. They had not found a fine structure of squall line. But forecasting modeling with using set of equation for cloud evolution allow to restore a some features of this event and the widespread cloud band and rainband of heavy rainfall between them. The coordinate system was supposed moving eastward with middle velocity of 12 m/s. As shown in Fig.2b the modeling with regular grid detected the band of widespread updraft motion in western edge of

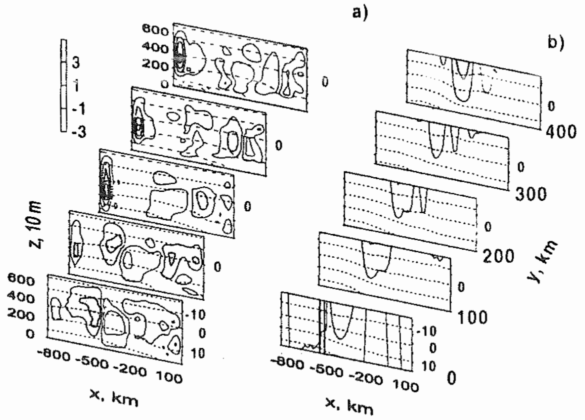

Figure 2. Distribution of vertical motion (solid lines, numbers near scale are cm/s) and temperature (°C) in initial time, t=0 (a), and after 5h development, t=5h (b). Two bold vertical lines at y=0 in (b) define the region of nested grid, -552<x<-522. The calculated time t=0 correspond of 1200 GMT.

the positive vertical vorticity location and the band of widespread cloud was located in this region (see Fig.3).It was almost non-precipitable. A collection of ligtly precipitation elements and cells of convective precipitation appeared from time to time.

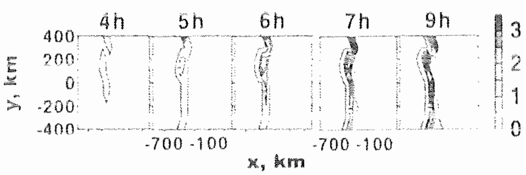

Figure 3. Cloud cover presented by a sum of water and ice content z-integrals. Numbers near scale show the sum as precipitation intensity, mm/h

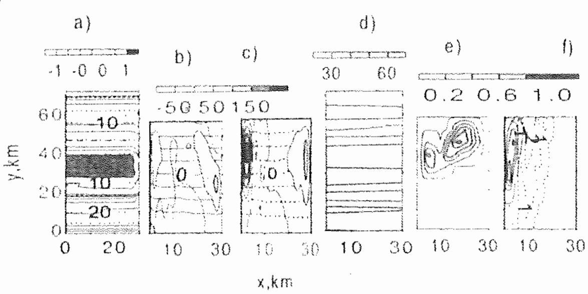

Fig.4. Vertical cross-sections of the thermodynamical and microphysics characteristics into precipitation core (y=200km): Vertical motion (solid line, shaded area), and temperature (dashed lines) at t=0 (a), t=3h(b), t=9h (c); numbers near scales means cm/s and number near lines means °C; relative humidity, % (d) at t=0; liquid water content, g/kg (solid line) and ice concentration, g^{-1}, at t=3h(e) and t=9h (f).

The band of convective clouds and heavy rainfall was identified at 552<x<522 km on western flank of a shallow pressure low. The nested grid with xs=2km and stretched grid with xs=100km was fitted. Fig.4 illustrated the vertical distribution of the dynamical and microphysics features in region of precipitation core. The dry air with relative moisture no exceeded 70% and small vertical velocity (less 1cm/s) was found at t=0. The 3-hours development of the widespread rainband produced the cores of the strong updrafts and heavy rainfall on its western edge. The two region of convective vertical motion reached 2m/s was found at the 3-hs time cloud development. These regions maintained to the t=9h and produced convective clouds. Two cores of water content at t=3h and liquid water and ice content cores after t=4h shown into Fig.4.

A spatial distribution of surface pressure, potential temperature and vorticity in an initial calculated time clearly indicated a gap in these elements between the centers of precipitation core at y=200 and y=400 km (see Fig.5). Vertical distribution of potential temperature at y=200 km shown the atmospheric stability in this region. Higher gradients of presented elements only predicted future disturbance in atmosphere state.

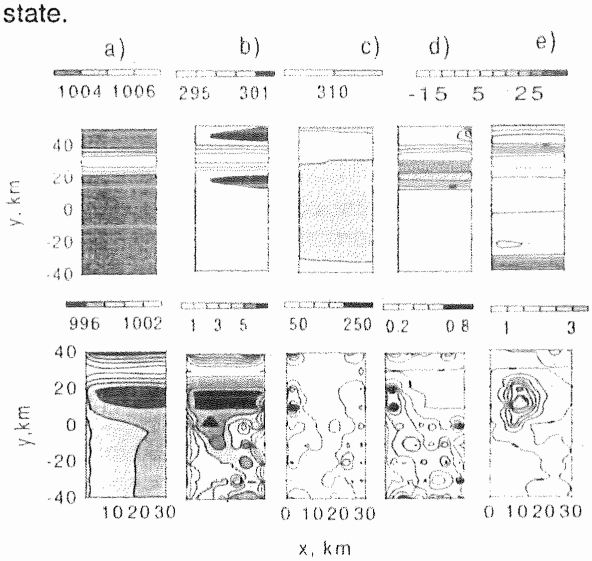

Figure 5. Horizontal cross-sections of small rainband features: First row: t=0, a) surface pressure, hPa; b) and c) potential temperature, ° K, at z=0 and z=3 km; d) and e) vertical vorticity $10^{-6}s^{-1}$, at z=0 and z=3 km. Second row: t=6h, a) surface pressure, hPa; b) height of a cloud top, km; c) highest updrafts, cm/s, in z-columns; d) highest means of liquid water content, g/kg, in z-columns; e) highest ice concentration means, g^{-1}, in it.

As it can be see from Fig.5 a sallow pressure low and lowering in temperature produced two band of updraft motion, two liquid water content cores and ice concentration and precipitation cores in vicinity of y=200km. In north part of the

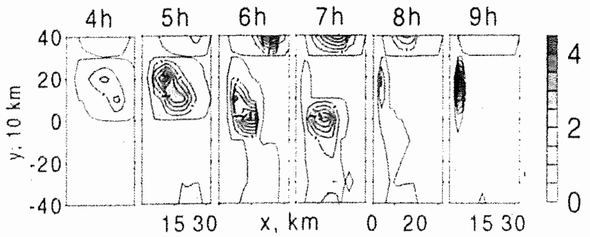

Figure 6. Time and space development of precipitation intensity in rainband with nested grid in the coordinate system moving with velocity of 12 m/s. x=0 for nested grid respect x= -552 for regular grid. Numbers near the scales are precipitation rate, mm/h.

nested grid box at y=400 km a similar precipitation core was found. The updraft motion in last core reached 3 m/s. A band of convective clouds produced the heavy rainfall. Precipitation rate reached 5 mm/h in precipitation cores (see Fig.6). After t=7h the rainband began to weaken and decrease in area and organization and had degenerated into a collection of lightly precipitable elements after t=9h.

3. THE CYCLONE CLOUD SYSTEM AND ITS PRECIPITATION CORE DEVELOPMENT. *Case2*

On 29 September 1995 the north-south-oriented pressure trough with cold front located in central Ukraine. By this way the cyclone moved rapidly in north direction during 29-30 September 1995. A large air of cloud and precipitation accompanied it on September 30. The structure and evolution of cloud systems into this cyclone have been a subject of modeling. As initial data the state of atmosphere on 30 September 1995 at 00 GMT was selected. Fig.7 show surface distribution of the temperature, pressure at t=0, 0000 GMT on 30 September 1995 . The regular couple of updraft and downdraft cells, lowering of temperature into regular updraft region and increasing of temperature and pressure gradients forced the a weadspread rainband located along cold front and precipitation cores with heavy precipitation in it (see Fig.7-8). In this case for regular grid the space length in direction normal to front (from west to east) (xs) and along front (ys) were 50 and100 km respectively. They let to indicate the large cloud system that accompanied a cyclone moving along cold front. The zones of instability were identified into rainbands. They likely forced forming convective cells and convective bands and modified the stratiform precipitation. Ahead of front the fall

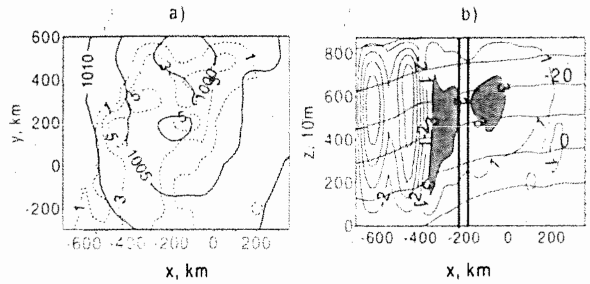

Figure 7. Case 2. 30 September 1995. Surface features (a) and vertical cross-sections (b) at the time t=0 (0000 GMT; a)pressure, hPa (solid lines), temperature °C (dashed lines); b) temperature, °C (dashed lines, vertical motion, cm/s(solid lines) at y= 300 km; two vertical bold lines the nested grid box.

temperature was very fast and precipitation was very heavy. Vertical motions reached 70cm/s and produced heavy precipitation that reached in several time interval to 10 mm/h presenting the convective cells that appeared from time to time in several regions of cloud systems.

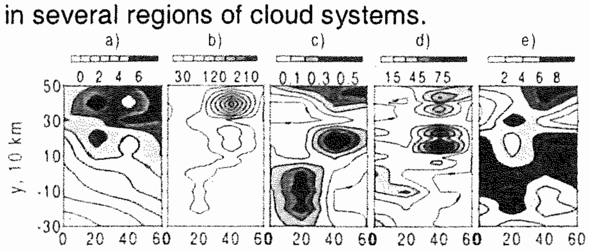

Figure 8. Cloud feature at t=2h in frame of nested grid x=0 for nested grid corresponds -250km for regular grid. Horizontal cross-sections: temperature °C(a); highest updraft motion, cm/s(b); highest water content, g/kg(c); highest ice concentration, g^{-1}, in z-columns(d); updraft motion column deep, km(e).

Precipitation cores was found near x=-250km. Three peaks of precipitation have been clearly identifed in this region. The special attenation was devoted to central core (y=200km) (see Fig.8). The nested grid for it of 50 km wide with the grid interval xs=5 km was constructed. The resolution for stretched grid was xs=ys=100. The maximal vertical motion (of 3 m/s) and precipitation intensity exceeded 15 mm/h were identified in the nothern precipitation core(y=400 km). But the convective cells appeared in other regions too. For example, near y=200 km the heaviest precipitation was detected of 10 mm/h at t=3h (see Fig.8).

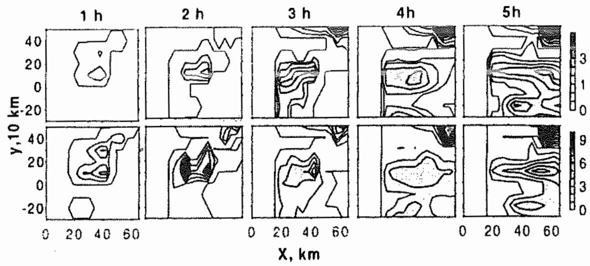

Figure 9. Time and space development of precipitation intensity in rainband with nested grid in the coordinate system moving with velocity of 13 m/s. First row presented a run without coagulation. Second row presented coagulation. The numbers near the scales are precipitation rate (mm/h).

The numerical experiments for different mechanism of precipittation formation was performed. An impact on precipitation core development of collection of precipitating particles with cloud droplets shown into Fig.9. The precipitatin cores time development has similar structure for both runs but coagulation processes clearly increased precipitation intensity.

A number of simulation of widespread and convective cloud bands for warm-season and winter cloud systems have studied the impact on the development of clouds and precipitation by different microphysical processes (such as sublimation, collection, riming, etc) and thermodynamical conditions (such as surface pressure, temperature and updrafts). Study of the different mechanisms of cloud and precipitation formation has shown that every such mechanism is important but the extent of influence is different for winter and summer clouds.The sublimation processes may be sufficient for to realize all precipitable moisture for winter processes and for warm-season cloud systems the coagulation processes are necessary for ealization this moisture.

4.CONCLUSIONS

3-D numerical models with detail description of an evolution of cloud particles (drops, crystals, cloud and ice nuclei, etc) are fitted to study the microphysical processes into widespread and convective frontal clouds. The nowacasting and forecasting models of a warm-season frontal clouds was constructed for two cases of the severe weather connected with cold fronts passed over Ukraine. The inner structure of the widespread and small convective rainbands was analyzed.

Numerical experiments for different warm rain production mechanisms (sublimation and droplet collection by raindrops and ice particles) were conducted. A comparison between different conditions for cloud and precipitation formation for the warm and cold seasons appears that the sublimation processes may be sufficient for to realize all precipitable moisture for winter processes and for warm-season cloud systems the coagulation processes are necessary for realization this moisture.

6. ACKNOWLEDGEMENT

Special thanks are due to Prusov V. and Romanjuk A. at UHRI for supplying the original meteorological fields.

7. REFERENCES

Barth, M., Parsons, D.: Microphysical processes associated with intense frontal rainbands and the effect of evaporation and melting on frontal systems. J. Atmos. Sci., 53, 1589-1586.

Browning, K. A., Harrold, T. W., 1970: Air motion and precipitation growth at a cold front. Quart. J. Roy. Meteor. Soc., 96, 369-389.

Hobbs, P., 1981: Mesoscale structure in midlatitude frontal systems. Proc. JAMAP Symp., Hamburg, August, 1-8.

Hobbs, P., Persson, O., 1982: The mesoscale and microscale structure and organization on cloud and precipitation in midlatitude cyclones. Part V: The substructure of narrow cold-frontal rainbands. J. Atmos. Sci., 39, 280-295.

Locatelli, J., Martin, J., Hobbs, P., 1995: Development and propagation of precipitation cores on cold fronts. J. Atmos. Res. 38, 177-206.

McBean, G., Stewart, R., 1991: Structure of frontal system over the Northeast Pacific ocean. Mon. Wea. Rev., 119, 997-1013.

Palamarchuk, L., Pirnach, A., 1992: Study of internal structure of frontal sones with help of three-dimensional numerical models. Trudy UHRI, 243, 107-124.

Pirnach, A., 1987: Numerical simulation of frontal cloud systems taken into account dynamics and microphysics processes (3-D models). Tr. UHRI, 221, 81-83.

Pirnach, A., 1998: Construction and application of the various numerical models for study the cloud dynamics and structure of the frontal rainbands. J. Atmos. Res., 45-47, 356-375.

Pirnach, A., Krakovskaia, S., 1994: Numerical studies of dynamics and cloud microphysics of the frontal rainbands. J. Atmos. Res., 33, 333-365.

OBSERVED TRENDS IN THE VERTICAL VARIABILITY OF CIRRUS MICROPHYSICAL PROPERTIES

Larry M. Miloshevich and Andrew J. Heymsfield

National Center for Atmospheric Research,
Boulder, Colorado

1. INTRODUCTION

Parameterizations for the vertical distribution of cloud microphysical and radiative properties are needed to accurately represent clouds in numerical models and to improve cloud property retrievals from remote sensor measurements. Cloud parameters such as effective particle radius retrieved from multispectral radiance measurements are typically single values that represent a weighted average of contributions from the entire cloud column. Expressions for the vertical distribution of ice crystal sizes and cross-sectional areas (from which effective radius is derived) may allow single-parameter retrievals to yield a vertical profile that is reasonable in at least a statistical sense. Such techniques will become increasingly important as retrievals from global satellite measurements are used as inputs to large-scale models and for development of long-term global climatologies.

Cirrus properties such as ice-water content, ice-mass flux, or cloud albedo are typically derived from measured or parameterized size distributions, where crystal masses, terminal velocities, and optical extinction are calculated using relationships to crystal diameter that may or may not consider the crystal habit (shape). Treatment of ice crystal shape is critical for accurately calculating crystal mass, fallspeed, and cross-sectional area, yet crystal shape is usually neglected or treated crudely relative to the importance of crystal size. We represent crystal shape in terms of the "area ratio," which is the ratio of a crystal's projected cross-sectional area to the area of a circumscribed circle having the crystal's maximum diameter (i.e., the fraction of the circle that would be covered by the crystal). This study determines the dependence of area ratio (A_r) on maximum crystal diameter (D) and on fractional height within the cloud column (Z_f, where Z_f=0 is cloud base and Z_f=1 is cloud top), using ice crystal data from the NCAR balloon-borne Formvar replicator (Miloshevich and Heymsfield 1997). The replicator is a cloud sampling instrument that collects ice crystals larger than 20 μm and preserves them as plastic replicas. These data are digitized at a resolution of 5 μm and correlated with simultaneous radiosonde data.

Corresponding author address: Larry Miloshevich, NCAR, P.O. Box 3000, Boulder, CO; E-Mail: milo@ncar.ucar.edu

2. CONCEPTUAL CIRRUS LAYER-MODEL

Replicator data were analyzed at height intervals of approximately 100 m in two synoptically-generated cirrus clouds (i.e., not anvil or orographic cirrus) that were sampled during the 1991 NASA/FIRE-II experiment. Ice crystals that represent the variation of crystal characteristics in the vertical are shown for one of the profiles in Figure 1. The ice crystal sizes and shapes in almost all of the 10 existing replicator profiles from synoptically-generated cirrus show similar general trends that ice crystal size increases from cloud top

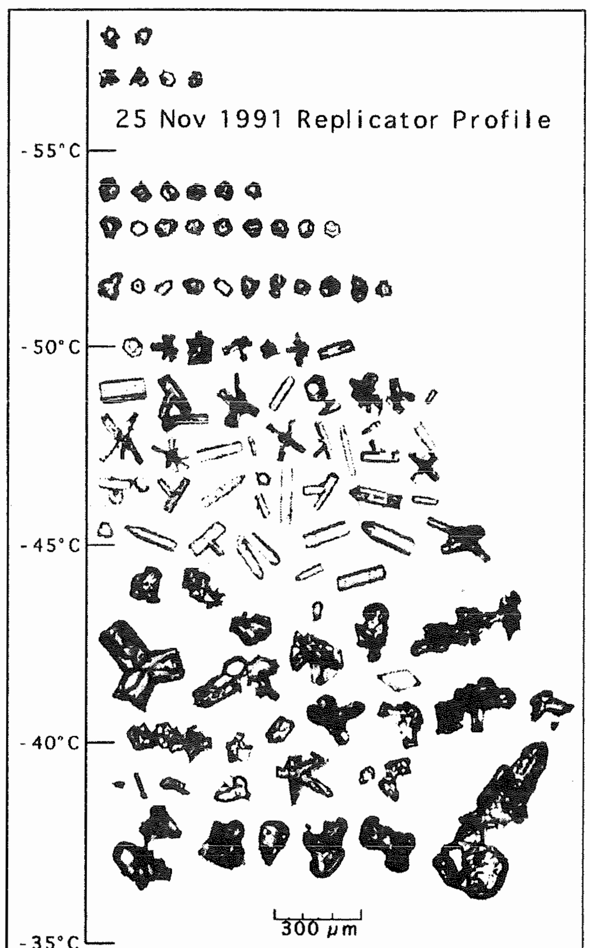

Figure 1. Temperature profile of characteristic ice crystals from a cirrus cloud sampled by the replicator on 25 November 1991 during the NASA/FIRE-II experiment.

downward, ice crystal shapes in the upper portion of the cloud are pristine and sharp-edged, and crystals become more rounded in the lower portion of the cloud. Heymsfield and Miloshevich (1995) proposed a "three-layer conceptual model" that relates the dependence of cirrus microphysical properties on height within the cloud column to fundamental cirrus processes including ice nucleation, crystal growth and sublimation, and crystal breakup and aggregation. The uppermost "nucleation layer," where ice crystals nucleate in ice-supersaturated air, is characterized by small and relatively round crystals with pristine shapes, sharp edges, and high area ratios. The "growth layer," where crystals grow as they fall with increasing terminal velocities through ice-supersaturated air, is characterized by pristine crystal shapes with lower area ratios, and crystal sizes that increase with distance downward in the cloud. The "sublimation layer," where crystals sublimate in ice-subsaturated air in the lower portion of the cloud, is characterized by crystals whose edges become more rounded and size decreases with distance downward in the cloud, and aggregation is more prevalent than at higher levels.

3. AREA RATIO–DIAMETER RELATION

Ice crystals in the digitized replicator data are identified using image analysis software that measures ice crystal cross-sectional area directly (by counting pixels), and determines the maximum crystal diameter from a best-fit ellipse to the crystal. Figure 2 shows the area ratio as a function of diameter for all crystals analyzed from the 25 November 1991 profile, with curves that show the mean A_r and its standard deviation in 20 μm size bins. The distinct trend that A_r decreases with increasing crystal diameter is represented by an exponential fit to the binned data, which decreases smoothly from A_r=0.79 at the smallest sizes to A_r=0.25 for 500 μm crystals. The standard deviation of the A_r data is about $\pm$0.2 at all sizes. The second analyzed replicator profile, from 5 December 1991, shows an $A_r(D)$ dependence that is nearly identical to the 25 November case (Figure 3), although the cloud top temperature is about 10°C colder. The best estimate of $A_r(D)$ for these mid-latitude, synoptically-generated cirrus is given by the average of the two cases:

$$A_r(D) = C_0 \cdot e^{C_1 \cdot D}, \quad \text{where} \qquad (1)$$

C_0=0.8043, C_1=−0.00230, and D is given in μm.

4. HEIGHT-DEPENDENCE OF $A_R(D)$

Figure 1 and the conceptual cirrus model suggest that the crystal population evolves in a downward direction as crystals that nucleated near the cloud top experience ventilated crystal growth, aggregation, breakup, and sublimation, all of which likely affect the mean area ratio. The height-dependence of the $A_r(D)$ relationship for the 25

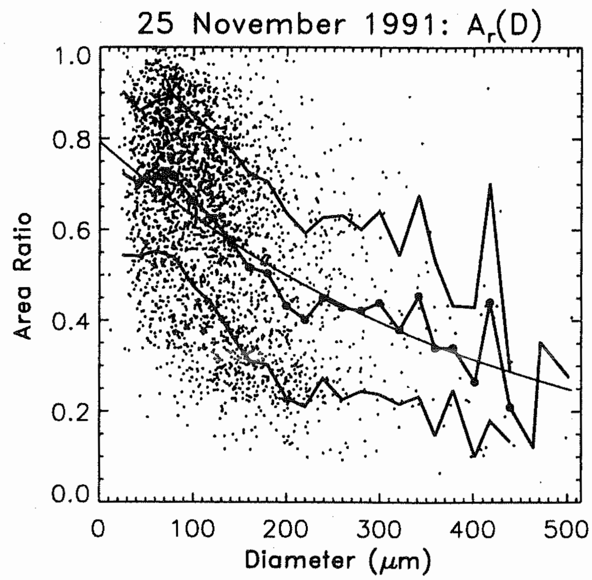

Figure 2. Area ratio versus maximum crystal diameter for 3113 ice crystals analyzed at 28 height levels from the 25 November 1991 replicator profile. The jagged curves show the mean and standard deviation of the data in 20 μm diameter bins. The smooth curve is an exponential fit to the bin averages. The cloud base and cloud top temperatures are -31°C and -54°C.

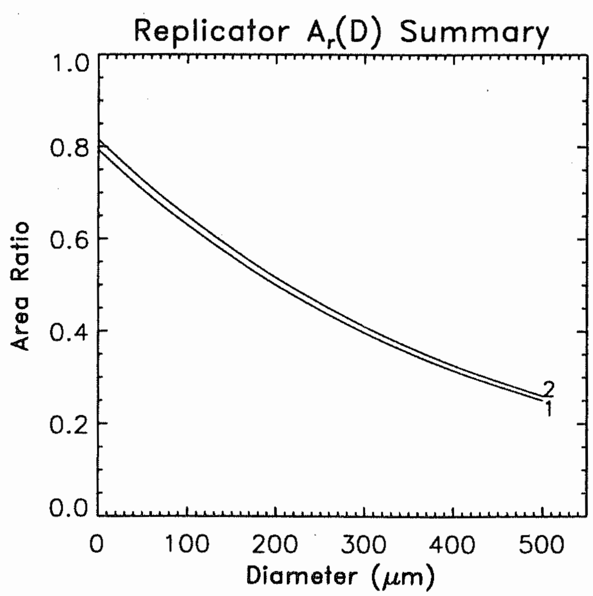

Figure 3. The $A_r(D)$ exponential fits as in Figure 1 for both replicator profiles ('1'=25 Nov. 1991; '2'=5 Dec. 1991).

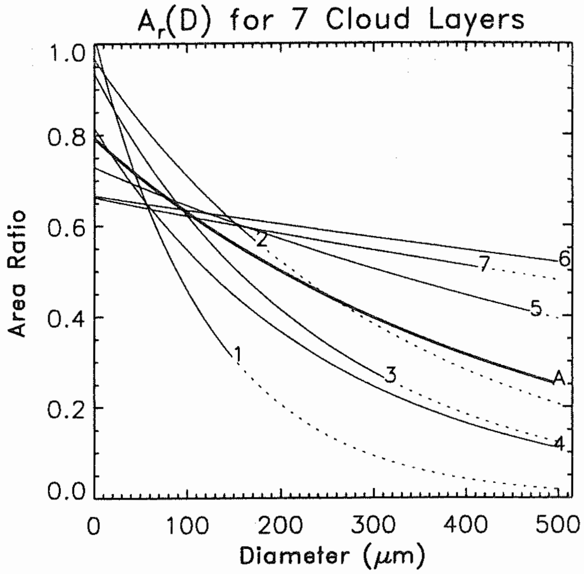

Figure 4. $A_r(D)$ exponential fits for each of seven equal-thickness cloud layers from the 25 November replicator profile. Level 1 is the top one-seventh of the cloud column, level 7 is the bottom one-seventh of the cloud column, and 'A' is the fit for the entire cloud depth from Eq. (1). The dashed portion of each curve is an extrapolation of the fit beyond the largest crystal at each level.

November profile is indicated in Figure 4, where analysis as described for Figure 2 was performed for each of seven equal-thickness cloud layers. The exponential fits that describe $A_r(D)$ for each layer show systematic trends with height in the cloud column. The intercept parameter, C_0, decreases downward in the cloud from about 1.0 (i.e., round) near cloud top to 0.67 near cloud base. The slope parameter, C_1, is less steep in the lower portion of the cloud (levels 5-7) than in the upper portion. Crystals larger than about 200 μm are considerably more round in the lower portion of the cloud than crystals of the same size at higher levels, possibly due in part to crystal sublimation in ice-subsaturated air and the consequent rounding of crystal edges. Figure 4 also shows that the diameter of the largest ice crystals at each level (the rightmost end of each solid curve) increases from cloud top downward to the mid-cloud levels, showing that the size distribution broadens with increasing distance below the cloud top, consistent with the idea that crystals nucleate at cloud top and grow in ice-supersaturated air as they fall.

The height-dependence of the $A_r(D)$ fits can be expressed in terms of a height-dependence for the intercept and slope coefficients, C_0 and C_1. Figure 5 shows the height-dependence of C_0 and C_1 for the 25 November profile, in terms of the fractional height within the cloud column (Z_f). The solid lines in Figure 5 were determined subjectively by choosing values that best represent the data at height intervals of 0.1, where the coefficients at the cloud boundaries are chosen based on similar analysis but with greater vertical resolution. It is clear that $A_r(D)$ depends systematically on height within the cloud column, and information is lost if the constant values of C_0 and C_1 from Eq. (1) are taken to represent the entire cloud depth.

The height-dependence of C_0 and C_1 were similarly determined for the 5 December 1991 replicator profile (Figure 6, labeled '2'). The coefficients for the two profiles are very similar, with

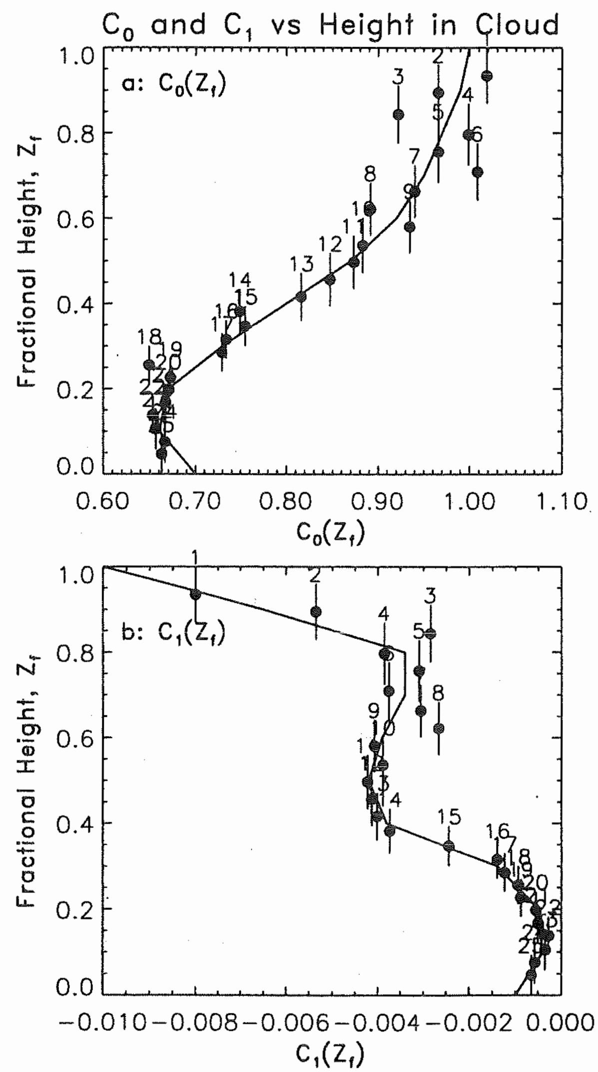

Figure 5. Height-dependence of the coefficients C_0 (Panel a) and C_1 (Panel b) for the 25 November profile, in terms of the fractional height within the cloud column (Z_f, where Z_f=0 is cloud base and Z_f=1 is cloud top). Each dot shows the coefficient for the height interval indicated by the corresponding vertical bar. The solid lines are estimates of the coefficients at height intervals of 0.1.

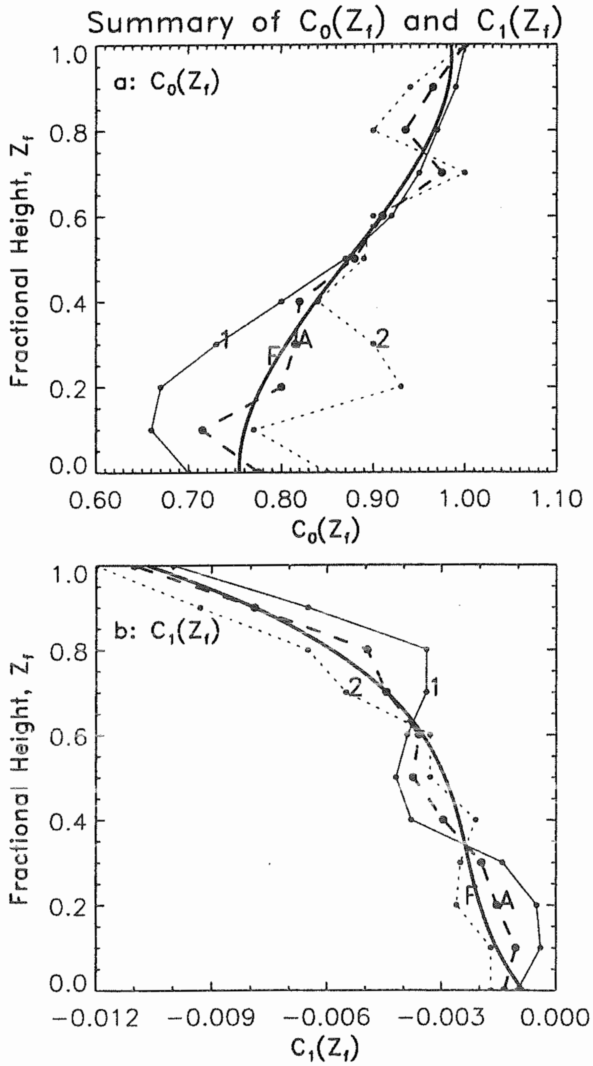

Figure 6. Height-dependence of the coefficients C_0 (Panel a) and C_1 (Panel b) for both replicator cases ('1'=25 Nov. 1991; '2'=5 Dec. 1991), at fractional height intervals of 0.1 as described in Figure 5. The average of both cases ('A'), and a polynomial fit to the average ('F') are also shown.

the exception of C_0 near the cloud base. The best estimate for the height-dependence of C_0 and C_1 is the polynomial fit ('F') to the average of both clouds ('A'). Then A_r is given by Eq. (1) with $C_0 = 0.7543 - (0.01205 \cdot Z_f) + (0.7590 \cdot Z_f^2) - (0.5168 \cdot Z_f^3)$, and $C_1 = -8.444 \times 10^{-4} - (8.832 \times 10^{-3} \cdot Z_f) + (1.980 \times 10^{-2} \cdot Z_f^2) - (2.079 \times 10^{-2} \cdot Z_f^3)$.

5. DISCUSSION AND FUTURE WORK

This study has used in-situ microphysical data to determine the mean dependence of an ice crystal shape parameter, the area ratio, on crystal diameter and on fractional height within the cloud column. The smallest crystals near cloud top are nearly round ($C_0 \approx 1.0$), possibly because little crystal growth has occurred since nucleation, whereas the smallest crystals at lower levels in the cloud are less round, possibly due to processes such as crystal breakup and sublimation. The slope parameter, C_1, decreases with distance downward in the cloud, possibly a reflection of lower supersaturations in the region below cloud top that result from vapor depletion by crystal growth. The aspect ratio (width/length) of columnar crystals and the individual elements of rosette crystals is an inverse function of the supersaturation (i.e., crystals grow longer and thinner when the supersaturation is high and crystal growth is rapid), so the area ratio may decrease more steeply with increasing crystal diameter near cloud top than at lower levels where the supersaturation is lower and crystal aspect ratios are presumably higher.

These data and results apply only to mid-latitude, continental, synoptically-generated cirrus with cold cloud top temperatures. Trends in the area ratio and other crystal characteristics may differ in environments where different physical processes are most important. We have conducted preliminary analysis of microphysical data from airborne imaging probes acquired during Lagrangian spiral descents in cirrus sampled during the NASA/FIRE-I experiment with warmer cloud top temperatures than those presented here, and in cirrus anvils sampled during the NASA/TRMM experiments. These data suggest that the $A_r(D, Z_f)$ relationships depend on both the cloud top temperature and on whether the cloud is a cirrus anvil or a synoptically-generated cirrus.

6. ACKNOWLEDGMENTS

This study was supported by NASA/EOS (grant S-97894-F), and NASA/FIRE-III (grant L55549D).

REFERENCES

Heymsfield, A.J., and L.M. Miloshevich, 1995: Relative humidity and temperature influences on the formation and evolution of cirrus: Observations from wave clouds and FIRE II. *J. Atmos. Sci.*, **52**, 4302-4326.

Miloshevich, L.M., and A.J. Heymsfield, 1997: A balloon-borne continuous cloud particle replicator for measuring vertical profiles of cloud microphysical properties: Instrument design, performance, and collection efficiency analysis. *J. Atmos. Oc. Tech.*, **14**, 753-768.

Observations in cirrus clouds during the INCA Southern Hemisphere campaign

J. Strom[1], U. Schumann[2], J.-F. Gayet[3], J. Ovarlez[4], F. Flatoy[5], M. Kulmala[6], O. Schrems[7], P. Minnis[8], Susana B. Diaz[9], Beatriz Milicic[10], Victor Valderama[11], Eligio Amthauer[12], Jan Pettersson[13], F. Arnold[14]

Funded by the European Union (Fifth Framework Programme)

[1]Stockholm University (Sweden), [2]Deutsches Zentrum für Luft- und Raumfahrt (Germany), [3]University Blaise Pascal (France), [4]Centre National de la Recherche Scientifique (France), [5]Norsk institutt for luftforskning (Norway), [6]University of Helsinki (Finland),
Associated partners
[7]Alfred Wegener Institute (Germany), [8]NASA, Langly Research Center, (USA), [9]CADIC (Centro Austral de Investigationes Cientificas), (Argentina), [10]UNPA (Universidad National de la Patagonia Austral), (Argentina), [11]Universidad de Magellanes, Punta Arenas (Chile), [12]Universidad de Conception (Chile), [13]University of Gothenburg (Sweden), [14]Max-Planck-institut fur Kernphysik, Heidelberg (Germany)

1. INTRODUCTION

The impact of anthropogenic emissions on climate change and on changes of the air composition, in particular ozone, was the topic of several recent assessments by the IPCC (1996, 1999), and the WMO/UNEP (1999). It is still the topic of the ongoing third IPCC Climate Assessment. The assessments have shown so far that cirrus clouds are important in influencing the radiative forcing and air chemistry. However, the estimated values of radiative forcing and ozone changes with a certain probability are within large ranges of potential best estimates, and one cannot exclude that future assessments will result in strongly different values because of yet incomplete scientific understanding. This is the case in particular for assessing the impact of aviation induced aerosols and contrails on cloud cover changes. In fact, the IPCC-Aviation report of 1999 states that the key uncertainty which has to be overcome in the future for better assessing the climate impact from aviation is the knowledge of contrail and aerosol impact on cirrus cloudiness.

The aim of the project INCA (Interhemispheric Differences in Cirrus Properties From Anthropogenic Emissions) is to study the aerosol and cirrus properties in the Southern and Northern hemispheres in order to understand the impact of aerosols on cirrus properties.

2. PROJECT STRATEGY

The overall strategy is to compare observations made in one of the cleanest regions available (west of Punta Arenas, 53°S, Chile) to observations made in air strongly affected by anthropogenic emissions near the North Atlantic Flight Corridor (west of Shannon, 53°N, Ireland).

The measurement campaigns are performed in both hemispheres during the same year, at equivalen seasons, using the same measurement strategy and instrument payload. The measurements are performed using the DLR Falcon research aircraft and with ground-based LIDAR. In addition, support are provided from chemical and meteorological forecast models and remote sensing satellites as well as ECMWF analysis (A. Dörnbrack, DLR).

The aircraft payload can be devided into four groups:

1) Microphysical properties, mainly observed using PMS-probes. A Polar Nephelometer is used to measure the crystal phase function.
2) Trace gas measurements of CO, O_3, NO, NOy and H_2O to characterize the airmass.
3) Ambient and interstitial aerosol properties are measured using several different techniques to characterize: number, size, thermal properties, morphology, chemistry, and light absoption.
4) Residual aerosol properties (particles remaining after evaporated crystals sampled by a CVI) are observed using an identical setup as for ambient or interstitial aerosols.

3. SOUTHERN HEMISPHERIC CAMPAIGN

The first campaign took place from 13 March to 20 April 2000, with four weeks in Punta Arenas, Chile. Ten scientific mission flights, which typically lasted 3.5 hours, were conducted in various cloud conditions ranging from thin wispy clouds and frontal cirrus, to intense lee-wave driven lenticular clouds. The campaign was just recently finished and results must be regarded as highly preliminary. However, some important results can already now be identified.

The instruments generally worked very well and a very good correspondence in observed cloud properties using different techniques was observed. For instance, the crystal number density observed by the PMS-FSSP-300 and the CVI (Counterflow Virtual Impactor) presented an almost perfect match.

By combining the information from CPC, DMPS, and OPC a composite size distribution of the residual aerosol between 0.01 to 3.5 μm diameter can be generated. With a one-to-one correspondence between the residual particles and crystal number density, the residual particles can be considered as the ice nuclei on which the crystals formed. The measurements west of Punta Arenas show that the mode of the residual particles is located in the Aitken mode around 30 to 80nm diameter. Previous measurements over Germany

(Strom et al, 1997) show that the mode is shifted towards larger sizes and located around 100 nm diameter in the more polluted environment.

One explanation for this can be the very low number density of aerosol particles present in the remote free troposphere in the Southern Hemisphere. In the Northern Hemisphere where the aerosol particles are more abundant, ice nucleation is quenched before the really small particles have a chance to be incorporated into crystals.

By differentiating the NOy signal from a forward facing and rearward facing inlet, the uptake of NOy by cold clouds can be inferred. The enhancement of crystals in the sample line of the forward facing inlet (caused by the non-isokenetic sampling) give the possibility to observe even small quantities of NOy in the crystals. Preliminary NOy data suggests a temperature dependence in the uptake over the observed temperature range from about –25 to –65°C. Trace gases in the region otherwise presented extremely low levels and put forth a real challenge for the experimental groups.

Besides measuring the total number density of aerosol particles, the number density after heat treatment to 125 and 250°C was also measured. This is a simple but very effective way to gain insight into the composition of the aerosol. Comparison of the data from the thermal denuders when measuring inside and outside of clouds show an enhancement of the least volatile particles (particles remaining after heating the sample air to 250°C) in the cloud particles compared to the ambient aerosol. Incorporating the aerosol size distribution into the analysis suggests that the least volatile particles are mainly associated with particles in the accumulation mode or larger. Measurements performed during the ferry flight from Germany (via Iceland, North America, and Central America) to Punta Arenas show that the fraction of particles remaining after heat treatment to 250ºC is largest in the tropics and less in the Southern Hemisphere compared to the Northern Hemisphere. This suggests a potential sensitiveness that could result in an interhemispheric difference in the cloud properties.

Asymmetry factors derived from the Polar Nephelometer measurements show a reduction in this parameter with altitude. Close to the top of cold cirrus the distribution of values is very narrow and around 0.79, which suggests quasi-spherical ice particles of sizes less than about 25 μm diameter. We can say that the particles are really ice because the shape of the scattering phase function gives no evidence of liquid water. Lower down into the cirrus cloud where temperatures are warmer the distribution of asymmetry values becomes much broader with values down to 0.75. This indicates larger irregular shaped particles that probably grew rapidly in the ice supersaturated air.

Humidity measurements performed by a cryogenic frostpoint mirror show that commonly the observed cirrus clouds were saturated with respect to ice. However, many occasions where the atmosphere was ice saturated without the presence of a cloud was also observed.

The observations performed during the Southern Hemisphere campaign of the INCA project will be compared with observations performed during the second campaign in the Northetrn Hemisphere, which is planed for September/October 2000 in Shannon, Ireland.

Corresponding author's address: Johan Ström, Institute of Applied Environmental Research, Air pollution Laboratory, Stockholm University, Frescativägen 54, S-106 91 Stockholm , Sweden; E-mail: johan@itm.su.se

4. Acknowledgements

The INCA team acknowledges the funding support by the European Union and by the institutes of the associated partners.

5. References

IPCC, 1996: *Climate Change 1995 - The Science of Climate Change* [J.H. Houghton et al. (eds.)]. Cambridge University Press, Cambridge, 572 pp.

IPCC, 1999: *Aviation and the Global Atmosphere, Special Report* [J.H. Houghton et al. (eds.)]. Cambridge University Press, Cambridge, in press.

Ström, J., B. Strauss, F. Schröder, T. Anderson, J. Heintzenberg, P. Wendling, 1997: In-situ observations of microphysical properties of young cirrus clouds. *J. Atmos. Sci.*, 54, 2542-2553.

WMO, 1999: *Scientific Assessment of Ozone Depletion: 1998.* Report No. 44, Global Ozone Research and Monitoring Project, World Meteorological Organisation, Geneva, Switzerland, 732 pp.

IN SITU MEASUREMENTS OF MID-LATITUDE AND TROPICAL CIRRUS CLOUDS

Carl G. Schmitt, R. Paul Lawson and Bradley A. Baker

SPEC Incorporated, Boulder, Colorado

1. INTRODUCTION

Cirrus clouds regularly cover 20-30% of the globe (Takano and Liou 1995). Cirrus, composed mainly of small ice crystals, can have a positive or negative net cloud radiative forcing depending on the cirrus cloud cover (Stephens et al. 1990). Numerical calculations by Fu and Liou (1993) indicate that cirrus with small effective particle diameters and small ice water path (IWP) have a warming influence. As the IWP increases the solar albedo increases sufficiently to give a net cooling effect. Cirrus with large crystals generally have a net warming effect. Direct knowledge of the particle size distributions and concentrations will provide a better understanding of the impact cirrus have on climate.

The only previous measurements giving high-definition images of particles required the use of replicators or impactors which typically contain contamination from the media and artifacts due to particle breakup (Poellet et al. 1999). The cloud particle imager probe (CPI) developed by SPEC Inc collects digital high-definition images of cloud particles and processes them on the fly. Post processing allows objective particle shape analysis of particles as small as 30 μm.

In this paper we present particle concentrations, size distributions, ice water contents and particle habit classification of cirrus from a variety of geographic locations. Tropical cirrus and decaying anvils were sampled frequently by the NASA DC-8 during the KWAJalien Experiment (KWAJEX) project in the South Pacific. Mid-latitude cirrus has been sampled over Utah and Oklahoma by the SPEC Learjet for the Earth Observing System (EOS) project. Arctic cirrus was sampled by the National Center for Atmospheric Research (NCAR) C-130 during the NASA FIRE Arctic Cloud Experiment (FIRE.ACE) project.

2 OBSERVATIONS

1.1 Arctic Cirrus

Arctic cirrus was sampled multiple times by the NCAR C-130 during the FIRE.ACE project. Cirrus was mainly sampled during ferry flights between Fairbanks and the polar ice cap. Figure 1 shows example cloud properties from one such ferry flight.

Corresponding author's address: Carl Schmitt, 5401 Western Ave Ste. B, Boulder CO, 80301 e-mail: cschmitt@specinc.com

The particle size distribution has a peak near 40 μm is dominated by particles that are spheroidal in appearance. A second, more broad mode centered around 400 μm, consists mainly of bullet rosettes.

Particle habit classification shows that the bulk of the particles observed were spheroidal, although not exactly spherical. The CPI maximum sample volume per frame is approximately 0.2cm^3. Sample volume is a function of the square of the particle size (Lawson and Cormack, 1995). Corrections to the sample volume for small particles will increase the small mode of the CPI particle size distribution to approach that of the FSSP. The bullet rosettes, because of their larger size, dominate the ice water mass in the cloud.

IWC in most arctic cirrus ranged between 0.0 and 0.05 g/m^3. Particle concentrations on a larger scale rarely exceeded 50 per liter.

2.2 Mid-Latitude Cirrus

The SPEC Learjet has conducted research flights over the University of Utah's Facility for Atmospheric Remote Sensing (FARS) site as well as the Atmospheric Radiation Program Cloud and Radiation Testbed (ARM-CART) site in Oklahoma in 1998, 1999, and 2000. An example from a March 1, 2000 research flight is shown in figure 2.

The CPI particle size distribution is distinctly bi-modal. The small mode centered near 40 μm was dominated by small, spheroidal in appearance, particles. The larger mode in the cpi size distribution consisted of bullet rosettes and is centered near 300 μm.

Particles habit classification shows a high concentration of spheroidal particles. The spheroidal particles again exist in extremely high concentrations on a local scaleand are interspersed with individual larger bullet rosettes (see Baker et al 2000 in this volume). Irregular particles (aka. others) are also prominent. Bullet rosettes and irregulars dominate the ice water mass.

IWC over time generally stayed below 0.025 g/m^3. Particle concentrations rarely exceeded 20/L.

2.3 Tropical Cirrus

Tropical cirrus was sampled by the NASA DC-8 during the KWAJEX field project in the summer of 1999. During KWAJEX, the DC-8 flew several missions over a two month period sampling the upper regions of tropical convection. On several occasions the DC-8 encountered natural cirrus while ferrying between areas of convection. Additionally, decaying anvils were often

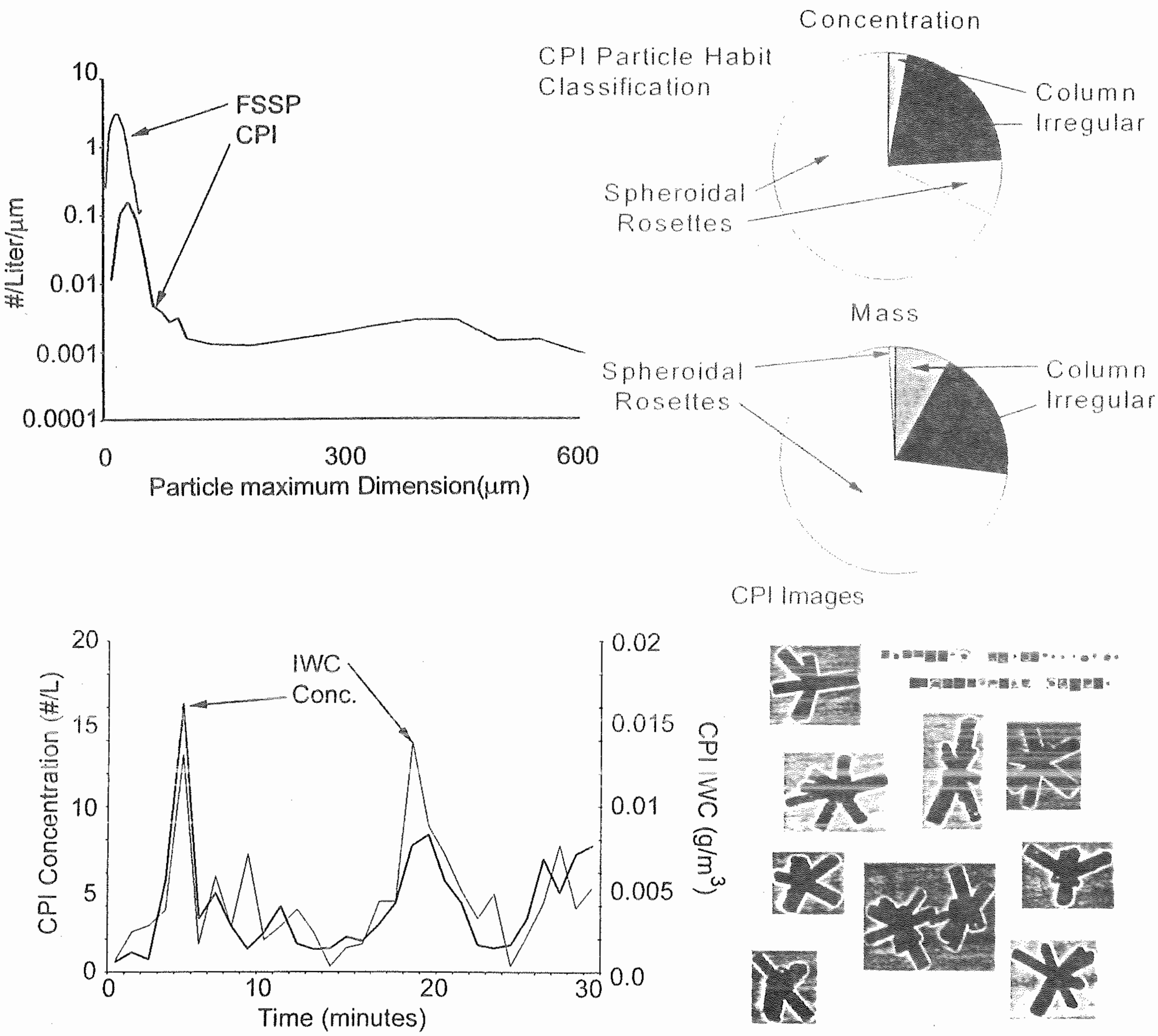

Figure 1. Example of cirrus data collected during the FIRE.ACE project on May 15, 1998. The altitude was 6,500 meters and the temperature was –45.

sampled as storms reached the end of their life-cycle. These decaying anvil clouds are thought to provide the seeds of future tropical cirrus.

Figure 3 is an example of the properties of "natural" cirrus sampled by the DC-8 on July 30, 1999. The particle size distribution shows a mono-modal size distribution. The peak of the size distribution is at 20 μm. Particles larger than 400 μm are rare.

Particles habit classification shows that in addition to the abundance of small spheroidal particles, there is a distinct lack of bullet rosettes. Irregularly shaped particles, which can be thought of as anvil debris, are high in concentration and dominant in mass. Tropical cirrus again, appear to be very inhomogeneous, with small particles clumped together. CPI frames often contain multiple particles showing the high local particle concentrations.

Average particle concentrations often exceeded 50/L. IWC in the tropical cirrus observed was very low due to the small sizes of the particles in general. Average concentrations in tropical anvils (not shown here) were much higher, sometimes exceeding 5 cm^{-3}

3 DISCUSSION

The data shown here suggest that particle shapes in arctic cirrus and mid-latitude cirrus appear to be similar in nature. Both show bi-modal size distributions

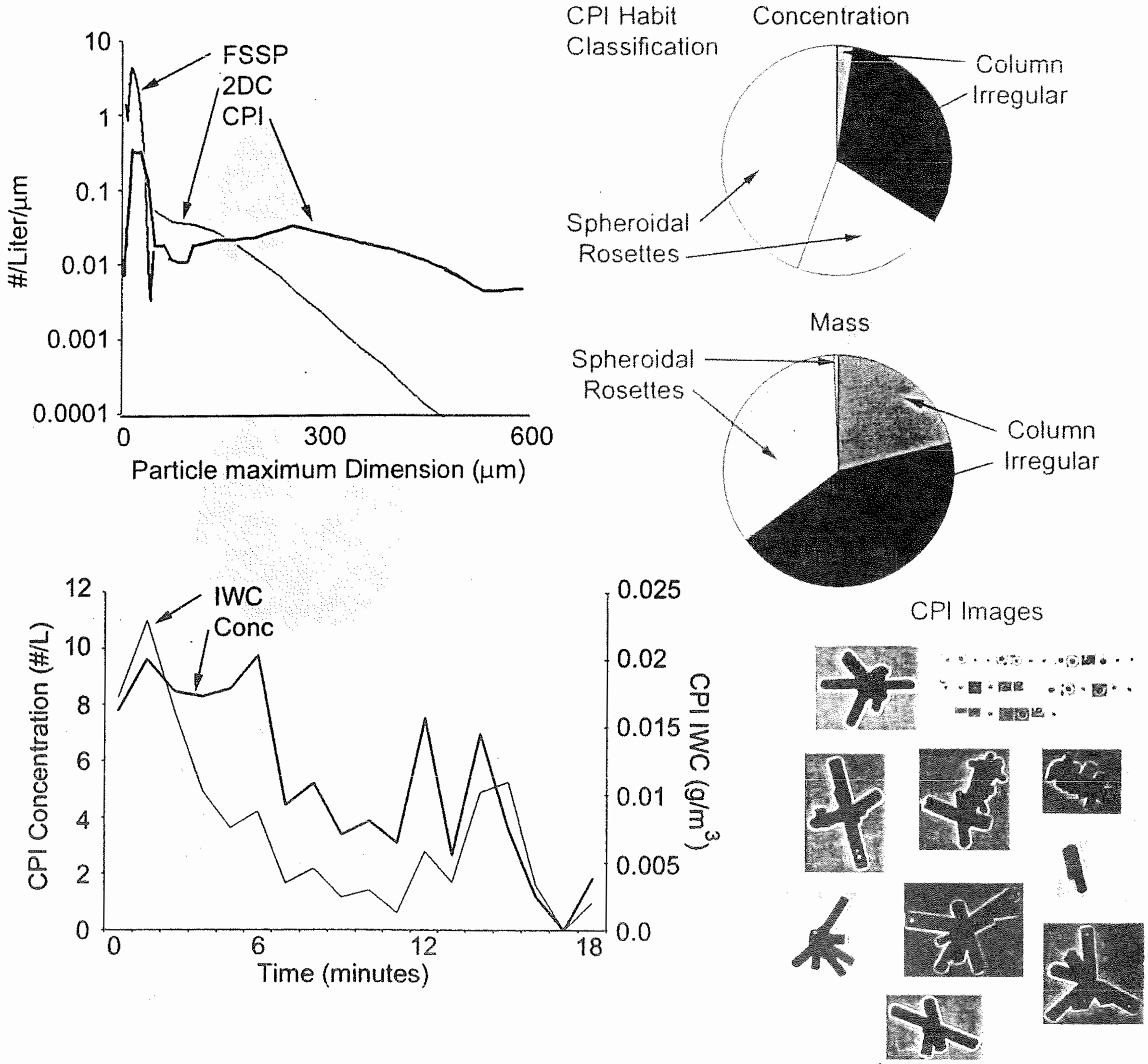

Figure 2. Example of cirrus data collected on March 1, 2000 in Oklahoma. The altitude was 8800 meters and the temperature was –42 C.

and high percentages of bullet rosettes. The large number of bullet rosettes implies crystal growth at cold temperatures. Both also show high concentrations of small spheroidal (in appearance) ice particles less than 50 µm in size.

Initial analysis of data from KWAJEX suggests that tropical cirrus is distinctly different from its cousins to the north. Few bullet rosettes were observed in tropical cirrus, suggesting that the particles in tropical cirrus may have formed at warmer temperatures (lower altitude) and then been carried aloft by convection. The abundance of irregularly shaped particles would indicate that these cirrus clouds are made mainly of tropical anvil debris.

All of the observed cirrus clouds showed an abundance of very small, spheroidal (in appearance) particles. These particles often were found clumped together. The CPI often observed up to 20 particles in a frame giving a local concentration of more than 100/cm^2.

4 ACKNOWLEDGEMENTS

This work has been supported by NASA FIRE contract NAS1-96015, NASA EOS contract (from the Univ. of Utah) 98-0-3, and DOE contract 354593-A-Q5. We would also like to thank pilot Bill Harris and Rainbow Chaser, LLC, owner of the Learjet operated by SPEC.

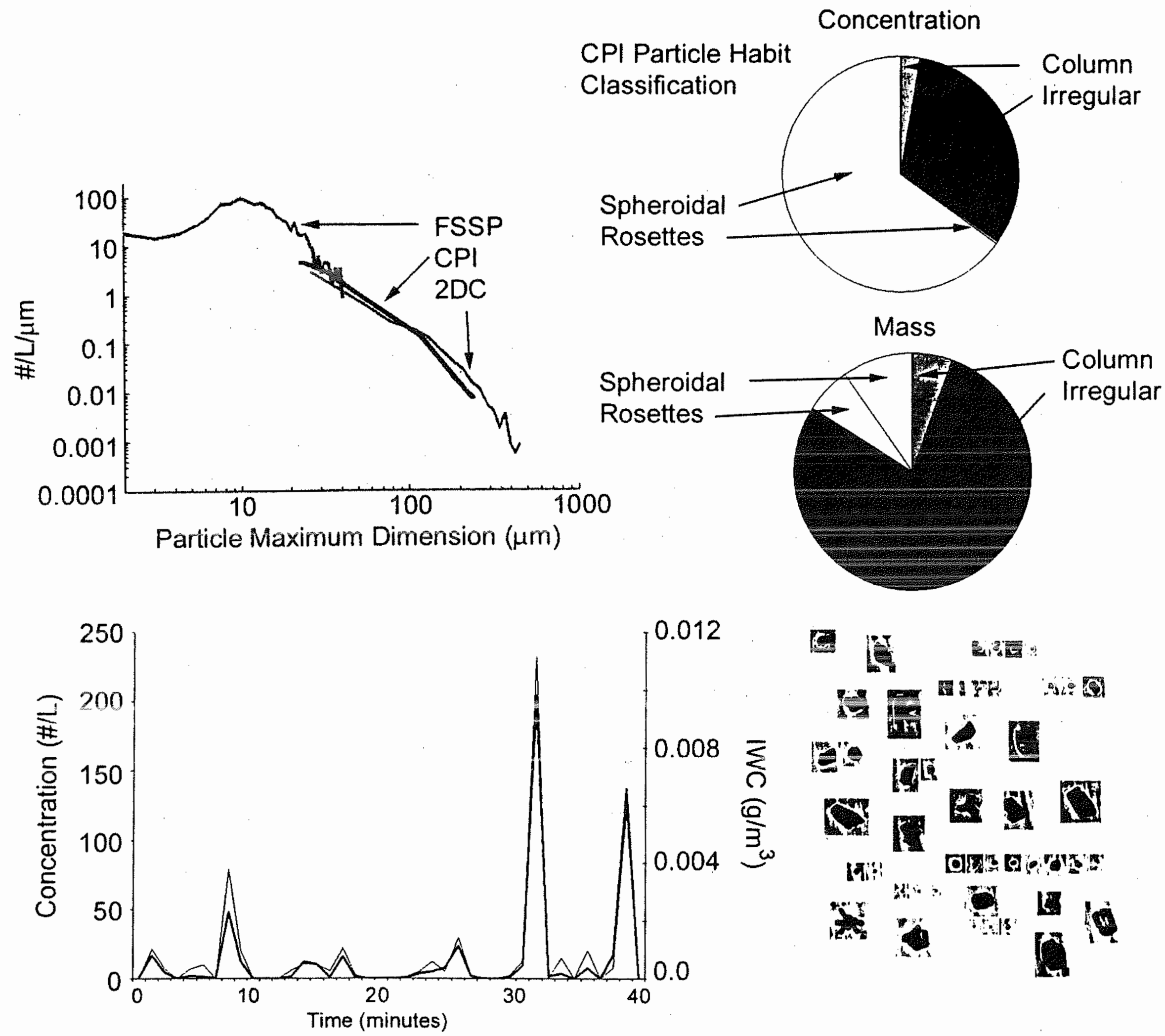

Figure 3. Example of cirrus sampled during the KWAJEX project on July 30, 1999. The altitude was 11850 meters and the temperature was –54 C.

5 REFERENCES

Baker, B., Lawson, R. P., Schmitt, C. G., 2000: Clumpy cirrus. Proceedings 13th International Conference on Clouds and Precipitation, 14-18 August, Reno, NV.

Fu, Q., Liou, K. N., 1993: Parameterization of the radiative properties of cirrus clouds. J. Atmos. Sci. 50, 2008-2025.

Lawson, R. P., Cormack, R. H., 1995: Theoretical design and preliminary tests of two new particle spectrometers for cloud microphysics research. Atmos. Res., 35, 315-348.

Poellot, M. R., Arnott, W. P., Hallett, J., 1999:In situ observations of contrail microphysics and implications for their radiative impact. J. Geo. Res. 104, 12077-12084.

Stephens, G. L., Tsay, S. C. Jr., Flatau, P. J., 1990: The relevance of the microphysical and radiative properties of cirrus clouds to climate and climatic feedback. J. Atmos. Sci. 47, 1742-1753.

Takano, Y., Liou, K. N., 1995: Radiative transfer in cirrus clouds. Part III: Scattering by irregular ice crystals. J. Atmos. Sci., 52, 818-837.

INTERACTION OF MICROPHYSICS AND RADIATION IN THE EVOLUTION OF CIRRUS CLOUDS

Yu Gu and K. N. Liou

Department of Atmospheric Sciences, University of California, Los Angeles
Los Angeles, CA 90095, U.S.A.

1. INTRODUCTION

Ubiquitous cirrus clouds play an important role in the radiation field of the earth-atmosphere system, and hence the earth's climate. However, fundamental understanding of the mechanisms for their formation and dissipation is still extremely limited and has received substantial scientific attention of late (Liou 1992). Cirrus clouds are a dynamic and thermodynamic system that involves the intricate coupling of microphysics, radiation, and dynamic processes (Gultepe and Starr 1995). Moreover, cirrus clouds are frequently finite and highly inhomogeneous based on satellite and replicator sounding observations (Ou et al. 1995; Heymsfield and Miloshevich 1993). We have developed a two-dimensional (2D), time-dependent numerical model, including detailed ice microphysics, second-order turbulence closure, and a three-dimensional (3D) radiative transfer model based on a modified diffusion approximation, to study the interaction of various physical processes in the evolution of cirrus clouds.

2. A TWO-DIMENSIONAL CIRRUS CLOUD MODEL

The basic dynamic and thermodynamic equations governing the shallow convection motions in the x-z plane, including ice crystal size distribution evolution, are described in Gu and Liou (2000). The radiative heating is computed from a radiative transfer scheme that is based on the delta-four-stream approximation developed by Liou et al. (1988) for nonhomogeneous cloudy atmospheres. The incorporation of non-gray gaseous absorption is based on the correlated k-distribution method developed by Fu and Liou (1992). In this method, the cumulative probability of the absorption coefficient in a spectral interval is used to replace wavenumber as an independent variable. Using the correlated k-distribution method, 121 spectral calculations are required for each vertical profile to cover the entire solar and infrared spectra.

The single-scattering properties for hexagonal ice crystals are computed from the parameterization using a mean effective size (D_e) to represent the ice crystal size distribution given by

$$D_e = \int D \cdot DLn(L) / \int DLn(L)dL. \qquad (1)$$

Based on physical principles, the extinction coefficient normalized by ice water content (IWC), the single-scattering albedo, and the expansion coefficients in the phase function may be expressed by a simple polynomial form in terms of $1/D_e$. The single-scattering parameterization is performed for six solar and twelve IR bands. Based on parameterization, the radiation program is driven by two parameters: IWC and D_e.

The time rate of change of mass for an individual ice crystal can be obtained from the classical mass growth theory, including the conservation of water mass and total energy at the ice crystal surface in the form

$$\frac{dm}{dt} = AS - BH_R, \qquad (2)$$

where S represents a term associated with the ice saturation ratio and the surface free energy of ice, A and B are coefficients related to the thermal and mass diffusivities, and H_R denotes the radiative heating effect on the ice crystal surface.

The heating due to radiation on the ice crystal surface must be the product of the absorption cross section and the net radiative flux density and can be expresses as follows:

$$\begin{aligned} H_R &= \int_0^\infty \sigma_{a,\lambda}[m(L)][F_\lambda^+ + F_\lambda^- - 2\pi B_\lambda(T)]d\lambda \\ &\cong \bar{\sigma}_a[m(L)][F^+ + F^- - 2\sigma T^4], \end{aligned} \qquad (3)$$

where F^+ and F^- are the upward and downward net radiative fluxes, $\pi B_\lambda(T)$ is the Planck function at the temperature T. For simplicity of calculations, we use a mean absorption cross section of an ice crystal $\overline{\sigma_a}$ which can be determined from the parameterization equations presented in Fu and Liou (1993).

Since the temperature in the present model ranges from -20°C to -40°C and since no liquid water is considered, only the heterogeneous deposition nucleation is taken into account according to the effective ice nuclei (IN). The number concentration of effective INs increases with increasing supersaturation over ice S_i in the form

$$N_{IN} = CS_i^k, \qquad (4)$$

where C and k are certain constants which are obtained from Huffman (1973). The effective INs nucleate immediately, implying that the presence of effective INs is the same as the creation of new ice particles. The nucleation process is terminated when the saturation ratio begins to decrease.

For the solution of ice crystal size distribution, we divide the crystal length spectrum into a finite number of intervals (bins). A partial differential equation can then be expressed for each bin and solved numerically. The mean mass of the ice crystals of each size group can be calculated based on the empirical relationship given by Ramaswamy and Detwiler (1986).

· Corresponding author's address: Yu Gu, Department of Atmospheric Sciences, University of California, Los Angeles, Los Angeles, CA 90095; E-mail: gu@atmos.ucla.edu.

3. RADIATION AND ICE MICROPHYSICS

Vertical profiles of the differences of horizontally averaged $\overline{IWC}$, latent heat, and the saturation ratio at four time steps between simulations with and without radiation are shown in Fig. 1. Inclusion of the radiation effect enhances the latent heat release in the cloud generation region after t = 10 min, implying that the deposition and hence the rate of net formation is enhanced. Moreover, the sublimation process in the lower area is also strengthened after t = 40 min. The corresponding supersaturation ratio decreases (increases) in the cloud formation region (the region below) due to radiation effects, revealing that radiation enhances both deposition and sublimation. Evidently, radiation appears to enhance stability during the maintenance and dissipation periods of the cirrus cloud evolution. The simulated $\overline{IWC}$ is also larger during the cloud formation period when radiation is included. However, less $\overline{IWC}$ occurs in the cloud generation region after t = 40 min with radiative processes included in the model. This surprising result may be explained by the effects of radiation on ice crystal growth as detailed in the following.

Figure 2 presents the effects of radiation on ice crystal size distributions. Radiative cooling tends to increase the number densities of larger ice crystals. This can be explained from Eq. (2), in which radiative cooling contributes to the growth of ice crystals. According to the diffusional growth equation, when radiative cooling is present at the cloud top (i.e., $H_R < 0$), the radiation effect contributes more significantly to the diffusional growth of ice crystals with larger cross sections. The cloud-scale updraft speeds with a maximum value of about 15 cm s^{-1} are now smaller than the fall speed of larger ice crystals. These ice crystals then fall to the lower drier level where the diffusional mass growth becomes negative because subsaturation occurs. The radiative heating in the lower part of the cloud then tends to strengthen the sublimation process, leading to smaller number densities of ice crystals with sizes less than 300 m in the subcloud region after t = 40 min. The corresponding larger fall speeds result in less $\overline{IWC}$ in the cloud generation region, but more in the subcloud region during the maintenance period. Because more sublimation occurs when radiation is included at t = 40 min, the corresponding $\overline{IWC}$ becomes less after t= 60 min (Fig. 1a). The ranges of size spectra become narrower when radiation is not included in the model.

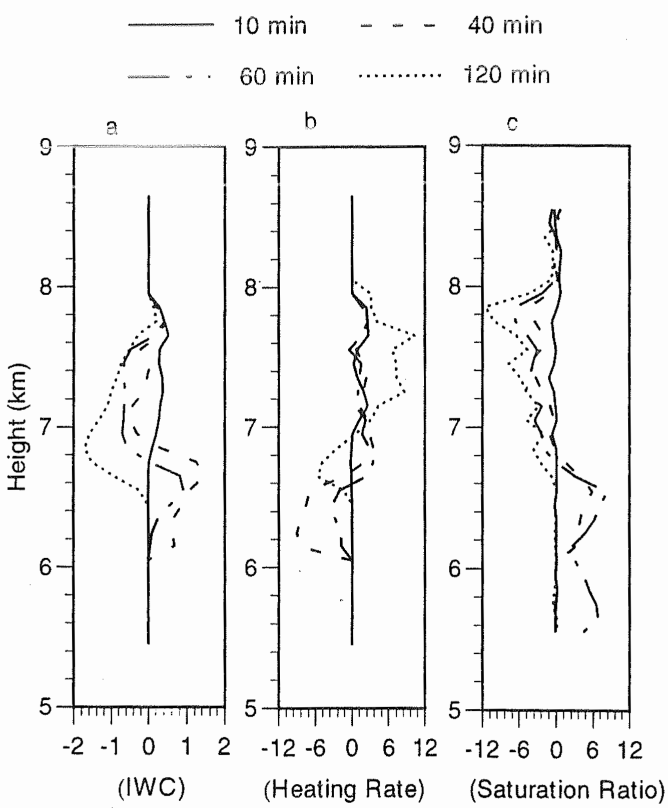

Fig. 1 Differences (with radiation minus without radiation) of the vertical profiles of the horizontally averaged (a) IWC, (b) the heating rates due to phase change, and (c) the saturation ratio at four time steps.

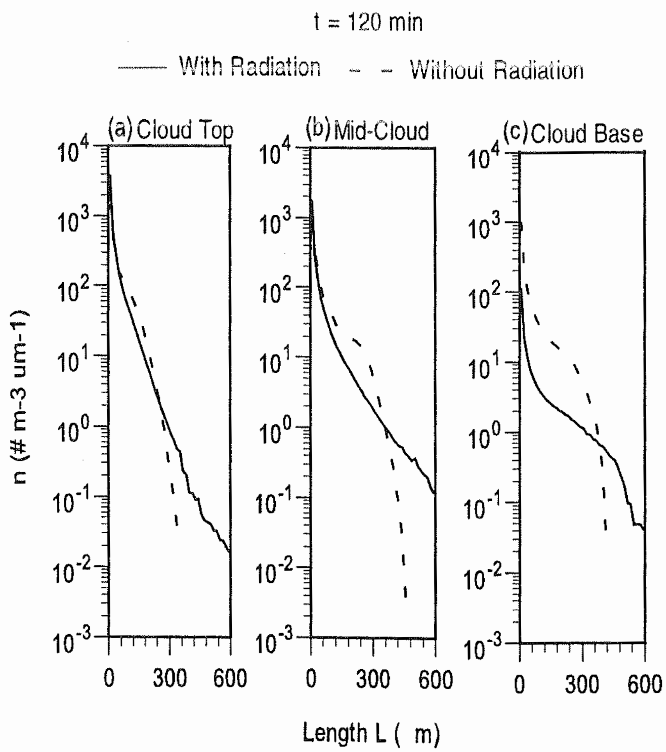

Fig. 2 Ice crystal size distributions at different altitudes: (a) cloud top, (b) mid-cloud, and (c) cloud base, at t = 120 min for simulations with (solid) and without (dashed) radiation.

4. CLOUD INHOMOGENEITY EFFECTS ON RADIATIVE TRANSFER

The general equation governing the transfer of diffuse intensity, I, can be expressed in the form

$$-\frac{dI(s,\Omega)}{\beta_e(s)ds} = I(s,\Omega) - J(s,\Omega). \qquad (5)$$

The source function which is produced by the single scattering of the direct solar irradiance, multiple scattering of the diffuse intensity, and emission of the cloud, can be written as follows:

$$J(s,\Omega) = \frac{\varpi(s)}{4\pi} P(s;\Omega,\Omega_0) F_{\odot} e^{-\tau_s} + \frac{\varpi(s)}{4\pi} \int_{4\pi} I(s,\Omega')P(s;\Omega,\Omega')d\Omega' + [1-\varpi(s)]B(T). \qquad (6)$$

Applicability of the source function to solar and thermal infrared regions is dependent on wavelength.

By expanding the phase function and the intensity in terms of spherical harmonic functions and by taking four terms in the expansion in a manner presented in Liou (1992), the following 3D inhomogeneous diffusion equation can be derived in the form

$$\nabla \cdot (\nabla I_0^0/\beta_t) - 3\alpha_t I_0^0 = -F_t + \Omega_0 \cdot \nabla(F_t g/\beta_t), \qquad (7)$$

where $\beta_t = \beta_e(1-\varpi g)$, $\alpha_t = \beta_e(1-\varpi)$, and

$$F_t = \begin{cases} 3\beta_e F e^{-\tau_s}/4\pi, & \text{Solar} \\ 3\beta_e(1-\varpi)B(T), & \text{IR} \end{cases}.$$

In these equations, all the variables are functions of the coordinate (x, y, z); I_0^0 is the first component of the intensity expansion; β_t and α_t are terms associated with single-scattering properties; g is the asymmetry factor; F_t is associated with the direct solar radiation and emission of cloud, respectively, depending on wavelength; and the last term in Eq. (7) vanishes for IR bands. The solution requires the imposition of the boundary conditions such that the incident diffuse flux at each surface is equal to a constant. We use the successive over-relaxation method to calculate I_0^0 at each grid point. Once I_0^0 is determined, the diffuse intensity and flux can then be obtained. To increase computational accuracy, we have applied the similarity principle for radiative transfer to each grid point such that $\beta_e^* = \beta_e(1-\varpi f)$, $\varpi^* = \varpi(1-f)/(1-\varpi f)$, and $g^* = (g-f)/(1-f)$. The fractional energy in the diffraction peak of the phase function f is taken to be $\varpi_4/9$, where ϖ_4 is the fourth moment in the phase function expansion. Calculations of the single-scattering properties are usually tedious and time consuming. For this reason, we follow the parameterization approach developed by Fu and Liou (1993) in determining the single-scattering properties.

To investigate the horizontal inhomogeneity, we use the optical depth and mean effective ice crystal size retrieved from the AVHRR data. Moreover, the extinction coefficient varies in the vertical and can be estimated from the ice crystal data determined from the replicator sounding. By combining the satellite and replicator sounding data, a 3D IWC and D_e field can be constructed (Liou and Rao 1996). For the homogeneous

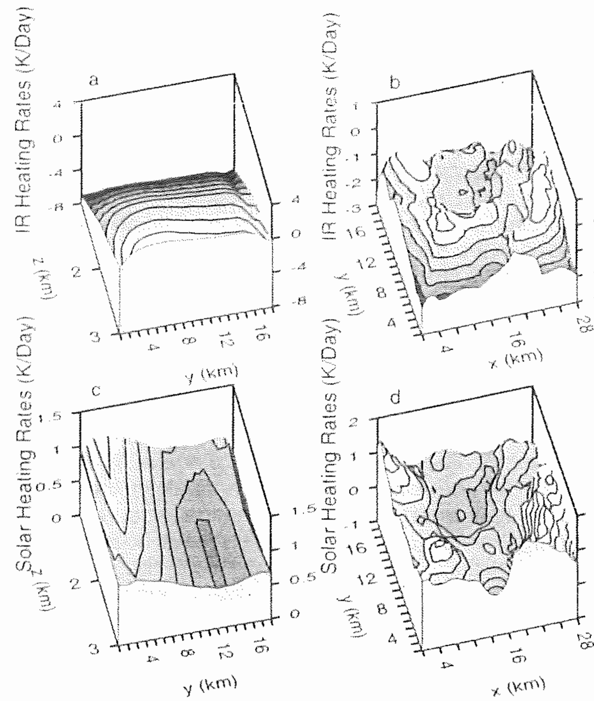

Fig. 3 3D images of differences in IR and solar heating rates between inhomogeneous and homogeneous cloud layers.

condition, mean single-scattering parameter values were used in the calculations. The solar zenith angle in this case is about 60°. Figure 3 displays the differences in the averaged heating rates in the x-y and y-z planes between inhomogeneous and homogeneous clouds. In the x-y plane, the patterns correspond to the variabilities of the horizontal extinction coefficient (or IWC) field . More solar heating and IR warming are found in the area with larger extinction coefficients, while less solar heating and more IR cooling are shown in the area with smaller extinction coefficients. In the y-z plane, stronger IR cooling at the cloud top and a slightly more IR warming at the bottom are displayed in the inhomogeneous case. This is associated with smaller extinction coefficients in the upper part of the cloud and larger values in the lower part of the inhomogeneous cirrus cloud. For solar radiation, more heating is found in the inhomogeneous case in the whole y-z plane.

5. SUMMARY

A two-dimensional numerical model with explicit ice microphysics module, turbulence closure, and advanced radiative transfer scheme has been developed to investigate the interaction of radiative processes and ice microphysics and their effects on the formation of cirrus clouds. Radiative processes begin to play an important role once a sufficient amount of ice water is produced in the atmosphere. Radiative cooling provides an impetus to the growth of ice crystals at the cloud top through its effect on individual ice crystals, while radiative heating enhances the sublimation of ice crystals in the lower region. Radiatively-forced processes play an important role during the evolution of ice crystal size distributions. The action of radiative heating and cooling increases the number densities of large ice particles but reduces the small ones in the lower level. When radiative properties are included in the model, larger ice crystals and larger fall speeds lead to less ice in the cloud generation region. The simulated size spectra become narrower when radiation is not included in the model.

A radiative transfer model based on the diffusion approximation approach has been developed to simulate the transfer of radiation in 3D inhomogeneous cirrus clouds. The extinction coefficient, single-scattering albedo, and asymmetry factor are functions of the wavelength and spatial position, and can be parameterized in terms of IWC and mean effective ice crystal size. The delta-function adjustment is used to account for the forward diffraction peak in the phase function to enhance the computational accuracy. For inhomogeneous cases, upwelling and downwelling fluxes illustrate patterns associated with the extinction coefficient field. Moreover, the cloud inhomogeneity plays an important role in determining heating rate distributions for both solar and IR radiation.

We are presently in the process of incorporating the 3D inhomogeneous radiative transfer program in the cirrus cloud model to further investigate feedbacks and interactions between radiation and ice microphysics.

Acknowledgment. This research has been supported by AFOSR Grant F499620-98-1-0232, NSF Grant ATM-9907924, and DOE Grant DE-FG03-00ER62904.

REFERENCES

Fu, Q., and K. N. Liou, 1992: On the correlated k-distribution method for radiative transfer in nonhomogeneous atmosphere. *J. Atmos. Sci.*, **49**, 2139-2156.

Fu, Q., and K. N. Liou, 1993: Parameterization of the radiative properties of cirrus clouds. *J. Atmos. Sci.*, **50**, 2008-2025.

Gu, Y., and K. N. Liou, 2000: Interactions of radiation, microphysics, and turbulence in the evolution of cirrus clouds. *J. Atmos. Sci.* (accepted and in press).

Gultepe, I., and D. O'C. Starr, 1995: Dynamical structure and turbulence in cirrus clouds: aircraft observations during FIRE. *J. Atmos. Sci.*, **52**, 4159-4182.

Heymsfield, A. J., and L. M. Miloshevich, 1993: Overview of microphysics and state parameter measurements from FIRE-II. *Proc. Conf. on FIRE Cirrus Science Results 1993*, Breckenridge, CO, NASA, 1-4.

Liou, K. N., Q. Fu, and T. P. Ackerman, 1988: A simple formulation of the δ-four-stream approximation for radiative transfer parameterizations. *J. Atmos. Sci.*, **45**, 1940-1947.

Liou, K. N., 1992: *Radiation and Cloud Processes in the Atmosphere: Theory, Observation, and Modeling*. Oxford University Press, New York, 487pp.

Liou, K. N. and N. Rao, 1996: Radiative transfer in cirrus clouds. Part IV: On cloud geometry, inhomogeneity, and absorption. *J. Atmos. Sci.*, **53**, 3046-3065.

Ou, S. C., K. N. Liou, Y. Takano, N. X. Rao, Q. Fu, A. J. Heymsfield, L. M. Miloshevich, B. Baum, and S. A. Kinne, 1995: Remote sounding of cirrus cloud optical depths and ice crystal sizes from AVHRR data: Verification using FIRE II IFO measurements. *J. Atmos. Sci.*, **52**, 4143-4158.

Huffman, P. J., 1973: Supersaturation spectra of AgI and natural ice nuclei. *J. Appl. Meteo.*, **12**, 1080-1082.

Ramaswamy, V., and A. Detwiler, 1986: Interdependence of radiation and microphysics in cirrus clouds. *J. Atmos. Sci.*, **43**, 2289-2301.

A MULTI-SCALE SIMULATION OF FRONTAL CLOUDS ASSOCIATED WITH AN ARCTIC LOW-PRESSURE SYSTEM

M. K. Yau

Dept. of Atmospheric & Oceanic Sciences, McGill University, Montreal, Quebec, H3A 2K6, Canada

1. INTRODUCTION

In the Canadian north, Arctic low-pressure systems occur about once a week during the cold season. Generally, their precipitation rates are quite low. However, their frequency of occurrence suggests that they may affect significantly the water and energy budgets in the region. Hanesiak et. al (1997) analysed the internal structure and the organization of precipitation associated with the warm front in such a storm that occurred on September 30 1994 during BASE (Beaufort Arctic Storm Experiment). They made use of measurements gathered by aircraft, satellite, and surface observations.

In this study, we simulated the cloud system associated with this Arctic low which passed over the southern portion of the Beaufort Sea. The simulation employs the Canadian Mesoscale Community Model (MC2) with four nested grids having grid sizes of 20km, 10km, 5km, and 3 km respectively. Our focus is to compare the simulated fine scale structures with the analysis and to determine the mechanism for the organization of the banded cloud structure in the occluded front.

2. THE MC2 MODEL

The MC2 model is a non-hydrostatic model based on the Navier-Stokes equations (Benoit et al. 1997). It utilizes the terrain following Gal-Chen coordinate system on a polar stereographic projection. The prognostic variables are u, v, w, $\ln(p/p_o)$, T, q_v, q_c, q_r, q_i and q_g, where p_o is a reference pressure of 1000 hPa, q_v, q_c, q_r, q_i and q_g are respectively the mixing ratio for water vapor, cloud water, rain water, ice/snow and graupel particles. The numerical method used is the semi-implicit semi-Lagrangian scheme.

The model has a comprehensive physics package. It includes planetary boundary layer processes based on turbulent kinetic energy, implicit vertical diffusion, and a surface layer scheme using similarity theory. The surface temperature over land is predicted via the force restore method. The diurnal cycle associated with solar and infrared fluxes over ground is modulated by diagnostic clouds. The solar and infrared schemes in the radiation package of the model are fully interactive with the clouds.

For the 20km and 10 km runs, a Kuo type deep cumulus parameterization is used and the total precipitation is the sum of the convective and stratiform precipitation. For the 5km and 3km simulations, clouds and precipitation are generated entirely by an explicit microphysics scheme (Kong and Yau 1997).

The total number of grid points for the different grid sizes are: 281x281x25 (20km), 160x224x25 (10km), 301x341x25 (5km), and 340x440x25 (3km). A 30-h simulation, from 18 UTC September 29 to 00 UTC October 1, was made for the 20km and 10km grid mesh. The 5-km grid mesh was run for 24 h (00 UTC September 30 to 00 UTC October 1). A 10-h simulation, from 14 UTC September 30 to 00 UTC October 1, was made for the 3-km grid mesh.

3. RESULTS

Fig. 1 shows the synoptic analysis at 0000 UTC 1 October 1994. An occluded front extends from the center of the low and a warm front lies south of Banks Island. The enhanced NOAA-12 infrared imagery valid at 2041 UTC 30 September (Fig. 2) depicts a cloud head around the low center, banded cloud structures in the regions of the occluded front, and warm and cold frontal cloud bands. The model simulated well the time evolution of the central pressure and the storm track (not shown). Of particular interest is that at a resolution of 3 km, many of the fine-scale structures of the cloud system are reproduced. Fig. 3 shows the sum of the ice content at 700 and 550 hPa valid at 2200 UTC 30 September. The simulated features agree well with the enhanced IR satellite imagery. The detailed structure of the cloud head, and the fine structures of the cloud bands in the occluded front are illustrated by the vertical velocity at 600 hPa

Corresponding author's address: M.K. Yau, Dept. of Atmospheric & Oceanic Sciences, McGill University, Montreal, Quebec, H3A 2K6, Canada; E-Mail: yau@rainband.meteo.mcgill.ca.

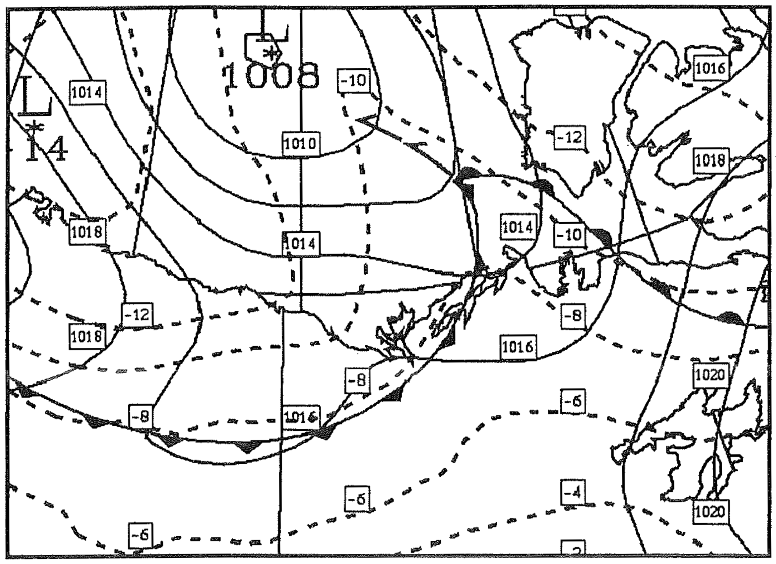

Fig. 1. Analysis of BASE Arctic low-pressure system at 0000 UTC 1 October 1994. Solid contours denote isobars in hPa. Dashed lines depict isotherms in degrees centigrade. The positions of the warm, cold, and occluded fronts at 85-kPa are marked by special symbols.

Fig. 2. Enhanced infrared NOAA-12 imagery valid for 2041 UTC 30 September 1994.

Fig. 3. Sum of the ice mixing ratios at 85-kPa and 55-kPa simulated by the model with a grid size of 3 km, valid for 2200 UTC 30 September 1994.

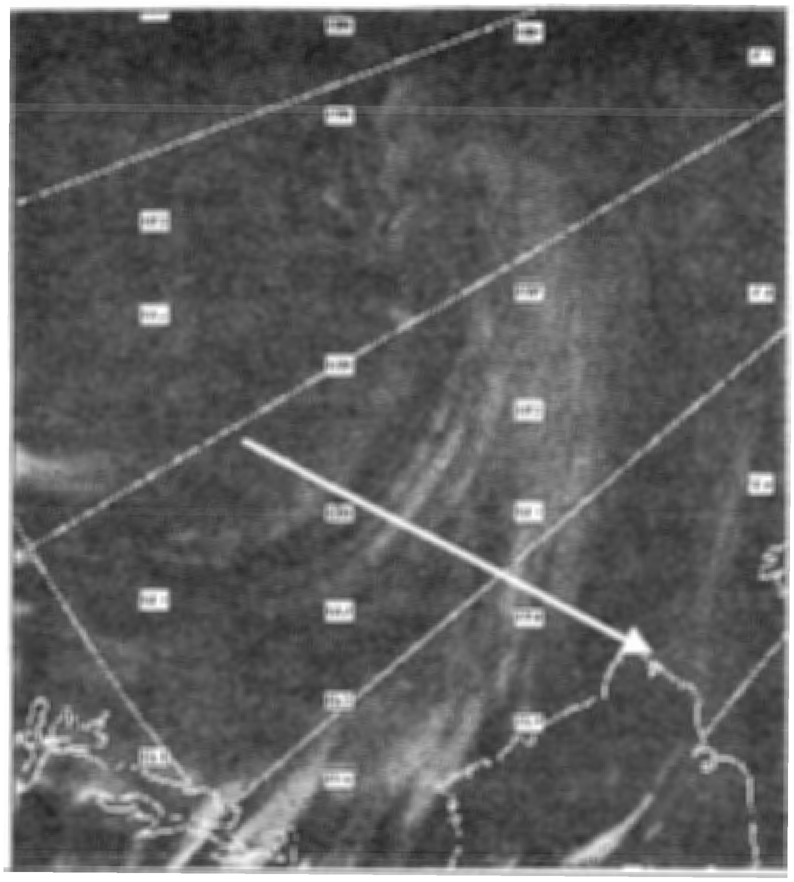

Fig. 4. Simulated vertical velocity at 60-kPa valid for 2200 UTC 30 September 1994

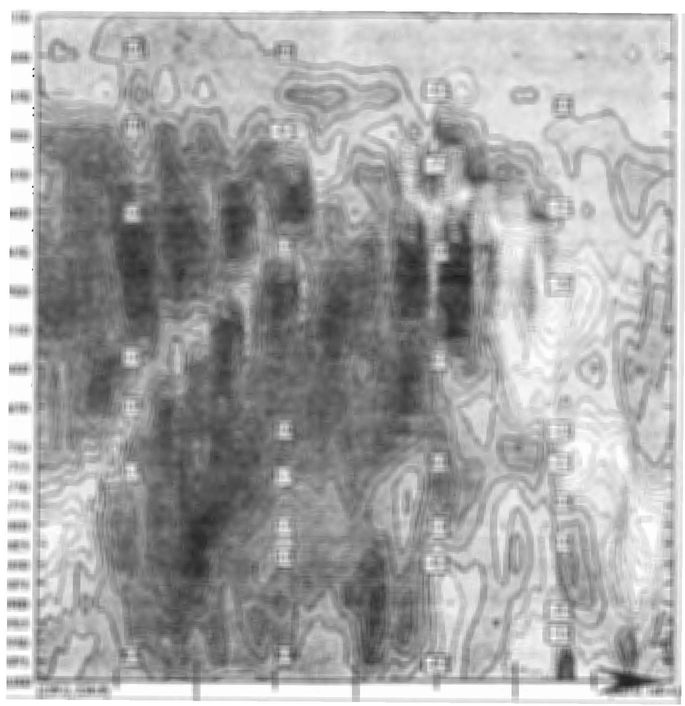

Fig. 5. Vertical section of vertical velocity along the line indicated by the arrow in Fig. 4.

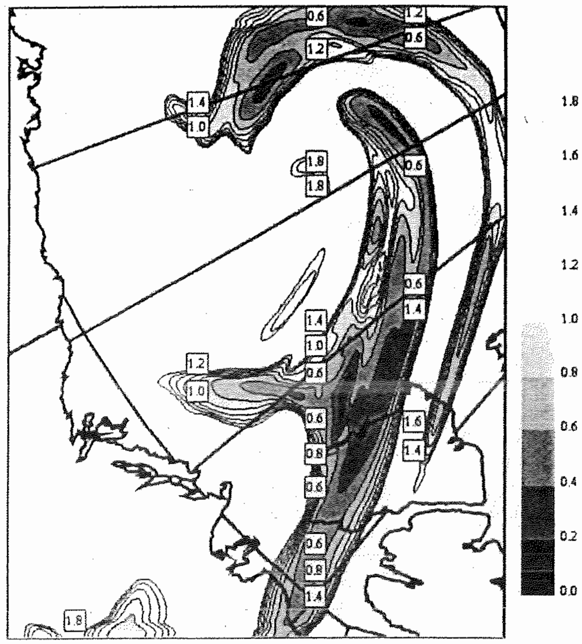

Fig. 6. Richardson number at 50-kPa simulated by the model valid for 2200 UTC 30 September 1994.

(Fig.4). The agreement with the satellite measurement is good.

Fig. 5 depicts the vertical section of vertical velocity along the line indicated by the arrow in Fig. 4. Substantial downward motion occurs on the front edge of the storm. Further analysis (not shown) indicates that the subsiding motion occurs in a dry slot and is accompanied by significant amounts of sublimation.

The pattern of vertical motion indicates updraft cells spaced about 30 km apart in the occluded front. To determine the mechanism for their formation, we plotted in Fig. 6 the Richardson number (R_i) at 50-kPa at 2200 UTC 30 September 1994. Emanuel (1983) showed that symmetric instability occurs when $R_i < 1$ and the length scale L of the unstable motion is

$$L \sim \frac{HN\sqrt{R_i}}{f}$$, where H is the vertical scale of

the unstable motion, N is the Brunt-Vaisalla's frequency, and f is the Coriolis parameter. Using $H\sim1$ km from Fig. 5, $N\sim10^{-2}\ s^{-1}$ and $f\sim1.4\times10^{-4}\ s^{-1}$, L can be calculated for different values of R_i as

R_i	L(km)
0.1	23
0.2	32
0.5	50

An inspection of Fig. 6 shows that a substantial region of the occluded front has $R_i < 1$ with some areas with values smaller than 0.2. Therefore symmetric instability offers a possible explanation for the occurrence of cloud and precipitation bands.

4. CONCLUSION

A high-resolution numerical model simulated successfully the Arctic low-pressure system of September 30, 1994. As verified against various observations and the best analysis, the high-resolution run (3km-grid size) simulates quite well the thermal and kinematics structure and the cloud and precipitation fields associated with the warm front and the occluded front. Symmetric instability is shown to be a likely candidate to organize the bandedness in the cloud and precipitation fields.

5. REFERENCE

Benoit, R., M. Desgagne, P. Pellerin, S. Pellerin, Y. Chartier, and S. Desjardins, 1997: The Canadian MC2: A semi-Lagrangian, semi-implicit wideband atmospheric model suited for finescale process studies and simulation. ***Mon. Wea. Rev.***, ***125***, 2382-2415.

Emanuel, K.A., 1983a: The Lagrangian parcel dynamics of moist symmetric instability. ***J. Atmos. Sci.***, ***40***, 2368-2376.

Hanesiak, J. M., R. E. Stewart, K. K. Szeto, D. Hudak, H. G. Leighton, 1997: The structure, water budget, and radiational features of a high-latitude warm front. ***J. Atmos. Sci.***, ***54***, 1553–1573.

Kong, F.-Y. and M.K. Yau, 1997: An explicit approach to microphysics in MC2. ***Atmos.-Ocean.*** ***35***, 257-291.

CIRRUS PARCEL MODEL COMPARISON PROJECT PHASE 1

Ruei-Fong Lin[1]*, David O'C. Starr[2], Paul J. DeMott[3]
Richard Cotton[4], Eric Jensen[5], and Kenneth Sassen[6]

[1]Universities Space Research Association, Greenbelt, MD, USA
[2]Laboratory of Atmosphere, NASA/GSFC, Greenbelt, MD, USA
[3]Dept. of Atmospheric Sciences, Colorado State University, Fort Collins, CO, USA
[4]Meteorological Research Flight, Hants, UK
[5]NASA/Ames Research Center, Moffett Field, CA, USA
[6]Dept. of Meteorology, University of Utah, UT, USA

1 INTRODUCTION

The Cirrus Parcel Model Comparison (CPMC) is a project of the GEWEX Cloud System Study Working Group on Cirrus Cloud Systems (GCSS WG2). The primary goal of this project is to identify cirrus model sensitivities to the state of our knowledge of nucleation and microphysics. Furthermore, the common ground of the findings may provide guidelines for models with simpler cirrus microphysics modules.

Table 1: Simulation identifiers.

W [m/s]	*0.04*	*0.2*	*1*
HN-ONLY	Ch004	Ch020	Ch100
	Wh004	Wh020	Wh100
ALL-MODE	Ca004	Ca020	Ca100
	Wa004	Wa020	Wa100
HN-λ-fixed		Ch020L	
		Wh020L	

We focus on the nucleation regimes of the warm (parcel starting at $-40°C$ and 340 hPa) and cold ($-60°C$ and 170 hPa) cases studied in the GCSS WG2 Idealized Cirrus Model Comparison Project [*Starr et al.,* 2000]. Nucleation and ice crystal growth were forced through an externally imposed rate of lift and consequent adiabatic cooling (Table 1). The background haze particles are assumed to be lognormally-distributed H_2SO_4 particles. Only the homogeneous nucleation mode is allowed to form ice crystals in the HN-ONLY runs; all nucleation modes are switched on in the ALL-MODE runs. Participants were asked to run the HN-λ-fixed runs by setting $\lambda = 2$ (λ is further discussed in section 2) or tailoring the nucleation rate calculation in agreement with $\lambda = 2$[1]. The depth of parcel lift (800 m) was set to assure that parcels underwent complete transition through the nucleation regime to a stage of approximate equilibrium between ice mass growth and vapor supplied by the specified updrafts.

2 MODEL DESCRIPTIONS

Five parcel modeling groups participated in the CPMC (Table 2). Hereafter, we will refer to these models as the C, D, J, L, and S models, respectively, as denoted in the table.

The estimate of the nucleation rate of ice in solution droplets, J_{haze}, remains an active research area. J_{haze} was computed using either (1) the modified classical theory approach (model J) or (2) the effective freezing temperature approach (hereafter, T_{eff} models, models C, D, L, S).

The T_{eff} models attempt to directly link measured J_{haze} to nucleation rates of equivalent-sized pure water droplets J_w via the effective freezing temperature, which is defined as

$$T_{eff} = T + \lambda \Delta T_m, \qquad (1)$$

such that $J_{haze} = J_w(T_{eff})$ as introduced by *Sassen and Dodd* [1988]. In (1), ΔT_m is the equilibrium melting point depression (positive valued), which depends on solute wt%, and λ is an empirical coefficient to account for additional suppression/enhancement of nucleation temperature due to

*Corresponding author's address: Ruei-Fong Lin, USRA, NASA/GSFC, Code 913, Greenbelt, MD, 20771; E-Mail: lin@climate.gsfc.nasa.gov

[1]Note that $\lambda = 2$ agrees approximately with data presented by *Koop et al.* [1998].

Table 2: Participant cirrus parcel models.

Organization *Investigator*	*UKMO* *Cotton (C)*	*CSU* *DeMott (D)*	*ARC* *Jensen (J)*	*GSFC* *Lin (L)*	*U. Utah* *Sassen (S)*
Bin characteristic[a]	discrete	continuous	continuous	continuous	particle tracing
Haze size[b]	r_{eq} or $\frac{dr}{dt}$	r_{eq}	r_{eq}	r_{eq}	r_{eq} or $\frac{dr}{dt}$
λ	1.5	1.5	varying[c]	1.0	1.7
deposition coef. β_i	0.24	0.04	1	0.1	0.36
References	*Spice et al.* [1999]	*DeMott et al.* [1994] *DeMott et al.* [1998]	*Jensen et al.* [1994] *Tabazadeh et al.* [1998]	*Lin* [1997]	*Sassen and Dodd* [1988] *Sassen and Benson* [2000]

[a] Discrete vs continuous binning indicates if assuming that all particles have exactly the same size in a given size bin or a certain distribution of particle sizes is allowed in a bin.
[b] r_{eq} vs. $\frac{dr}{dt}$ denotes either using the equlibrium-sized haze approximation or computing the diffusional growth of haze particles explicitly.
[c] See section 2 for detailed discussion.

non-ideal interaction between ions and condensed water. Although *Sassen and Dodd* [1988] noted that an average λ for different solutions was around 1.7, values for specific solutions may range from 1 to 2.5.

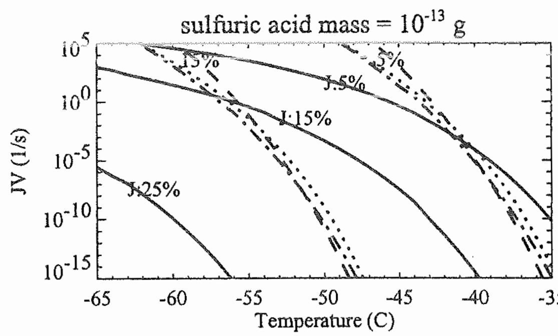

Figure 1: $J_{haze}V$ vs. temperature for solute wt% 5, 15 and 25%. Solid, dashed, dash-dotted, dotted curves denote models J, C, S, models D and L (same curves), respectively, for $\lambda = 2$.

In model J, recent direct data on ice/solution surface tension was incorporated and activation energy was inferred from recent laboratory measurements of J_{haze} for H_2SO_4 particles following *Tabazadeh et al.* [1997] and *Koop et al.* [1998]. This approach to determine J_{haze} can be interpreted as a T_{eff} scheme with varying λ (Figure 1). The intrinsic λ varies inversely with solute wt% and temperature. Also, the differences in the sensitivity of $J_{haze}V$ (V is the volume of the particle) to solute wt% between these two approaches may lead to systematic differences in the freezing haze size distributions. Nucleation rate data over a wide range of values, e.g., data points beyond critical freezing conditions, are needed to diminish the inconsistency between the two approaches.

Little constraint was imposed on formulating heterogeneous nucleation because theoretical and experimental understanding are still quite poor. Models C and L employ ice saturation ratio dependent parameterizations of activated IN following *Spice et al.* [1999] and *Meyers et al.* [1992], respectively. These parameterizations are expected to represent a maximum heterogeneous nucleation impact.

Haze particles of the given H_2SO_4 aerosol distribution are subject simultaneously to heterogeneous and homogeneous nucleation in models D and S. The number concentration of the activated IN in model D is computed following *DeMott et al.* [1998] based on field experiment data. This treatment was expected to yield the most conservative estimate of IN in cirrus. Model S computes the activated freezing nuclei using T_{eff} dependent Fletcher equation [*Sassen and Benson,* 2000], where parameters were set to yield the most favorable conditions for heterogeneous nucleation.

Participants either assumed that haze particles are in equilibrium with the environment or computed the diffusional growth of haze particles directly (Table 2). The diffusional growth rate of haze particles more or less exponentially decreases with temperature as caused by water vapor saturation pressure. The response time scale to the deviation from equilibrium can be considerably greater than one model time step in a swift updraft in a cold environment. Therefore, large haze particles may become more concentrated than the corresponding equilibrium-size particles in such conditions. This may result in considerable delaying of haze growth in models C and S (Table 2) and affect ice particle formation rate.

3 RESULTS AND DISCUSSIONS

As we proceed to describe the results and differences between models, it must be noted that the benchmark is not necessarily the median or the average of model results. The predicted N_i (ice number concentration) at 800 m above the starting point is compared (Fig. 2). In the HN-ONLY cases, to a first order approximation, the logarithm of N_i increases quasi-linearly with the logarithm of updraft speed. The predicted N_i by models D, S and L are close; N_i by models J and C form the lowest and highest bounds in the six cases, respectively.

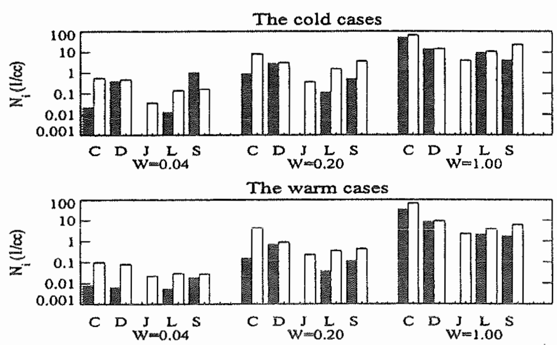

Figure 2: N_i predicted vs imposed updraft speed. The unfilled and filled bars denote HN-ONLY and ALL-MODE, respectively.

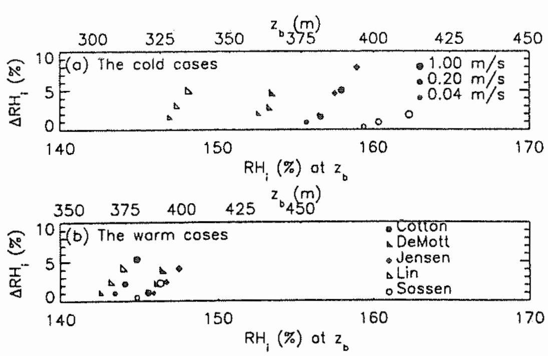

Figure 3: The RH_i at cloud base z_b ($N_i = 1$ liter^{-1}) and the corresponding ΔRH_i, defined as the difference between peak RH_i and RH_i at z_b (the HN-ONLY cases).

Cirrus initiation occurred over a narrower range of altitude and RH_i (relative humidity over ice) in the warm HN-ONLY cases than in the cold cases (Fig. 3). The increasing sensitivity of the cloud base RH_i as temperature decreases in the four T_{eff} models is primarily caused by λ.

Heterogeneous nucleation is a possible explanation of the discrepancy between the observed threshold RH_w for cirrus formation and the theoretically derived threshold RH_w (relative humidity over water) for homogeneous nucleation of H_2SO_4 or $(NH_4)_2SO_4$ solution particles; e.g., [*Heymsfield and Miloshevich,* 1995]. Cirrus properties are affected by the dominant nucleation mode in cloud initiation because of the distinct characteristics of the two modes.

The cloud base height, RH_i and peak RH_i in the ALL-MODE cases (not shown) vary even more because of our respective unbounded choices of heterogeneous nucleation. The impact of heterogeneous nucleation on lowering N_i, peak RH_i, and cloud formation altitude is extremely sensitive to the onset conditions for nucleation and the subsequent ice particle formation rate. With heterogeneous nucleation, the peak RH_i is lower in all but the case Wa100 by model S. The predicted N_i is reduced in all but the case Ca004 by model S.

We now discuss the results of the HN-λ-fixed simulations. The nucleation regimes of Wh020L and Ch020L take place within the temperature range of -43.2 to -44.2°C and -63.2 to -64.2°C, respectively. The effect of temperature variation on nucleation rates within this 1°C range is secondary, compared to the evolution of haze solute wt%. Thus, it is justified to analyze and visualize results according to the $z - z_b$ coordinate (Fig. 4).

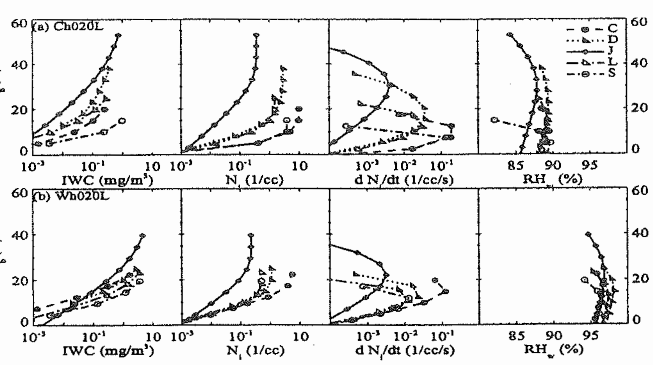

Figure 4: Ice water content (IWC), N_i, ice particle formation rate $\frac{dN_i}{dt}$, and RH_w as functions of $z - z_b$.

The triggering RH_w range was reduced significantly, to less than 2% in Wh020L and 5% in Ch020L in comparison to 3% and 8% in Wh020 and Ch020. The predicted N_i is only marginally affected.

At the beginning of the nucleation stage in Wh020L, ice particle formation rates by the four T_{eff} models are close. However, models C and D reach much larger RH_w that leads to larger instantaneous nucleation rates, and maintain the peak ice formation rate longer than the other two models.

Quite contrarily, the N_i curves of models D and L in Ch020L distinctly separate from those of models C and S. This grouping incidentally coincides with the grouping according to the haze size specifications. Large haze particles are more concentrated than the corresponding equilibrium values in models C and S. Yet, the nucleation regime in model S was not sustained as long as in model C; a similar finding is noted when comparing results of model D and L. The results of model J feature slow ice particle formation rate, long nucleation duration, and broader freezing haze number distribution.

The above results indicate that nucleation duration time and the maximum nucleation rate achieved are the two key components in determining the final N_i. These two factors are sensitive to the growth rates of small ice crystals, which under the influence of the kinetic effect are sensitive to the deposition coefficient, β_i. It was found that varying β_i from 0.04 to 1 (Table 2) would result in about a factor of 4~5 (Wh020L) and 9~12 (Ch020L) variation in N_i by models C and L.

4 SUMMARY

Results of Phase 1 of CPMC projects show that the predicted cloud properties strongly depend on updraft speed. Significant differences are found in the predicted N_i. Detailed examination revealed that the homogeneous nucleation formulation, aerosol size specification, ice crystal growth (especially the specification of the deposition coefficient for ice) and water vapor uptake rate were the critical components. These results highlight the need for new laboratory and field measurements to infer the correct values for critical quantities in the cirrus regime.

No attempt was made to scrutinize the causes of differences in ALL-MODE simulations due to the substantial differences in formulation of heterogeneous nucleation. Nevertheless, it was confirmed that the expected effect of a heterogeneous nucleation process is to decrease N_i and the RH_i required for cloud initiation. Clearly, new measurements of ice nuclei activation in cirrus conditions are warranted.

CPMC Phase 1 was conducted based on a single CCN distribution. Phase 2 of the CPMC, now underway, examines the effects of varying aerosol distributions. Sensitivity of model results to CCN composition is indirectly made by altering λ.

5 ACKNOWLEDGMENT

The U.S. DOE ARM Program and NASA Radiation Sciences Program have provided direct support (RFL and DS) for this GCSS project. We thank support from NSF-ATM9632917 (PJD), NASA's Stratospheric Aerosol and Gas Experiment (EJ), NSF-ATM9528287 (KS) and DOE grant DEFG0394ER61747 (KS).

6 REFERENCES

DeMott, P. J., M. P. Meyers, and W. R. Cotton, Parameterization and impact of ice initiation processes relevant to numerical model simulations of cirrus clouds, *J. Atmos. Sci.*, *51*, 77-90, 1994.

DeMott et al., The role of heterogeneous freezing nucleation in upper tropospheric clouds: Inferences from SUCCESS, *Geophys. Res. Lett.*, *25*, 1387-1390, 1998.

Heymsfield, A. J., and L. M. Miloshevich, Relative humidity and temperature influences on cirrus formation and evolution: Observations from wave clouds and FIRE II, *J. Atmos. Sci.*, *52*, 4302-4326, 1995.

Jensen et al., Microphysical modeling of cirrus 1. Comparison with 1986 FIRE IFO measurements, *J. Geophys. Res.*, *99*, 10,421-10,442, 1994.

Koop et al., A new optical technique to study aerosol phase transitions: The nucleation of ice from H_2SO_4 aerosols, *J. Phys. Chem.*A, *102*, 8924-8931, 1998.

Lin, R.-F., 1997, A numerical study of the evolution of nocturnal cirrus by a two-dimensional model with explicit microphysics, Ph.D. thesis, 199 pp., Pennsylvania State University, Aug. 1997.

Meyers, M. P., P. J. DeMott, and W. R. Cotton, New primary ice-nucleation parameterizations in an explicit cloud model, *J. Appl. Meteor.*, *31*, 708-721, 1992.

Sassen, K., and G. C. Dodd, Homogeneous nucleation rate for highly supercooled cirrus cloud droplets, *J. Atmos. Sci.*, *45*, 1357-1369, 1988.

Sassen, K., and S. Benson, Ice nucleation in cirrus clouds: A model study of the homogeneous and heterogeneous modes, *Geophys. Res. Lett.*, *27*, 521-524, 2000.

Spice et al., Primary ice nucleation in orographic cirrus cloud: A numerical simulation of the microphysics, *Quart. J. Royal. Met. Soc.*, *125*, 1637-1667, 1999.

Starr et al., Comparison of Cirrus Cloud Models: A Project of the GEWEX Cloud System Study (GCSS) Working Group on Cirrus Cloud Systems, this conference, 2000.

Tabazadeh, A., E. J. Jensen, and O. B. Toon, A model description for cirrus cloud nucleation from homogeneous freezing of sulfate aerosols, *J. Geophys. Res.*, *102*, 23,845-23,850, 1997.

THE COMPARISON OF CLOUD-RESOLVING SIMULATIONS OF CIRRUS WITH OBSERVATIONS

Philip R.A.Brown[1] and Paul R.Field[1]

[1]The Met.Office, Met.Research Flight, DERA, Farnborough, GU14LX, UK.

1. INTRODUCTION

Working Group 2 of the GEWEX Cloud System Study (GCSS) is intercomparing cloud-resolving models (CRMs) of cirrus, with the intention that they should subsequently guide the development of improved parametrizations of cirrus for use in large-scale climate and numerical weather prediction models. In this paper, we report idealized simulations of cirrus obtained using one of the models participating in this comparison. The simulations differ principally in the methods used to describe the primary nucleation of ice crystals.

The ability of a CRM to achieve the correct ice mass contribution from larger particles has an important bearing on the ice fallout rate from the cloud, and hence has a significant impact on the time evolution of the simulated cloud and its response to external forcing. We, therefore, examine the partitioning of total ice mass between small ($D \leq 500$ μm) and large particles, both from direct measurements and through its impact on millimetre-wave radar reflectivity. The behaviour of the simulations is compared with that seen in in-situ particle size measurements and in ground-based vertically-pointing radar. The impact of the different nucleation methods on the simulated cloud fractional coverage is also examined.

Since the CRM simulations are based on idealized cirrus scenarios, the observations reported here do not provide direct validation of the model behaviour. Rather, they illustrate techniques that may be utilized in a future GCSS case study, which will be based on an actual observed case. The comparisons also show how the observations might be used to determine the realism, or otherwise, of alternative CRM simulations using, for example, different representations of key processes such as primary ice nucleation.

2. THE CLOUD-RESOLVING MODEL

The model is a version of the Met.Office Large-Eddy Simulation (LES) model that was originally developed for studies of turbulent transport in the atmospheric boundary layer (Mason 1989). For the present study, it has had added a three-phase, bulk-water microphysics parametrization (Swann 1998) and a two-stream broadband longwave radiation code (Edwards and Slingo 1996). The microphysics scheme describes the evolution of total water (vapour plus liquid), cloud ice and snow. Liquid water is diagnosed as the excess total water above saturation mixing ratio w.r.t. water at the ambient temperature and pressure. Each of the two ice species is represented by two prognostic variables (number concentration and mass mixing ratio). Cloud ice is assumed to have an exponential size distribution whilst snow has a modified gamma distribution with a shape factor of 2.5.

Two methods for the primary nucleation of cloud ice are available. The first uses a parametrization of the activity of heterogeneous IN given by Meyers et al. (1992), which is given by:

$$N_I = 1000\exp(-0.639 + 0.1296 S_I) \quad (1)$$

where N_I is in m^{-3} and S_I is the supersaturation w.r.t. ice (%). The second is a simple representation of the homogeneous freezing of liquid cloud droplets. Explicit models of this process (Spice et al. 1999) show that it occurs very rapidly when droplets are activated at temperatures around –40 C. The present model allows the diagnosis of liquid water at all temperatures. For values colder than –38 C, this liquid is then frozen within one time step. This acts as a source of ice crystal number provided that the latter remains below the droplet number concentration, which is a fixed parameter in the model and set to 100 cm^{-3}. The autoconversion of ice to snow is allowed to begin when the mass-mean diameter of the cloud ice reaches a threshold of 500μm.

The simulations described in the present study were performed as part of the Idealized Cirrus Model Comparison (ICMC) project, which was organized by Working Group 2 of GCSS. Further information on this project is given by Starr et al. (2000) and can also be obtained from:
http://eos913c.gsfc.nasa.gov/gcss_wg2/

The model is initialized with horizontally uniform vertical profiles of potential temperature and relative humidity. The profiles have a region between 8 and 9 km altitude that has a relative humidity of between 100 and 120% w.r.t. ice and is neutrally-stable with respect to ice saturated ascent. A cooling rate of 25.3 K day^{-1} is applied to the region between 7 and 10 km for the first four hours, reducing to zero thereafter. The magnitude of this cooling is equivalent to that generated by large-scale ascent at 0.03 ms^{-1}. The potential temperature profile is set such that that the

[1] Corresponding Author's address: The Met.Office, Meteorological Research Flight, Y46 Building, DERA, Farnborough, GU14 0LX, UK. E-mail: prabrown@meto.gov.uk

imposed cooling does not create any further instability outside the 8-9 km region during the 4-hour period. Random initial temperature perturbations of ±0.01 K are applied to the 8-9 km region in order to initiate turbulent motion.

3. OBSERVATIONAL METHODS

3.1 Aircraft Microphysical Measurements

The data that are utilized in the present study are taken from Lagrangian spiral descents, in which the aircraft maintains a continuous turn drifting with the wind and descending at 1 ms^{-1}, commencing at or near the top of frontal cirrus cloud bands around the UK. They are described in more detail by Field (2000).

The measurements are taken from PMS Optical Array Probes (OAP), the 2D-C measuring in the size range 25-800μm and the 2DP 200-6400μm. Particle size measurements are converted to ice mass using

$$m = cD^d \qquad (2)$$

where m is in kg and D is the particle diameter in m. In the present study, values of c and d used were 0.03 and 2, respectively. Particle size spectra and the contributions to the total ice mass are averaged over one orbit of each spiral descent.

3.2 Radar

Hogan et al. (2000) describe the use of dual-wavelength radar measurements for the retrieval of ice particle size information. For a population of particles, the radar reflectivity is given by:

$$Z_E = \int C(D)K(D)N(D)D^6 dD \qquad (3)$$

where D is the particle diameter, $K(D)$ accounts for the effect of the particle density on its dielectric constant and $C(D)$ is the ratio of Mie- to Rayleigh-scattering for a particle of given diameter and density. The dual-wavelength ratio (DWR) is defined as the ratio of reflectivities made at two different radar wavelengths. Using measurements at wavelengths of 8mm (35GHz) and 3mm (94GHz) from the radar facility at Chilbolton, England, Hogan et al. (2000) show that DWR (= $Z35$ / $Z94$) does not commonly exceed about 4dB.

4. RESULTS

The time-evolution of W_{max} (the maximum vertical velocity occurring within the domain) and the vertically integrated water paths of cloud ice and snow are shown in Figure 1, for two simulations that use homogeneous and heterogeneous ice nucleation, respectively. These will subsequently be referred to as experiments HOM and HET.

In run HOM, cloud first forms at around 90 minutes, when the imposed cooling has brought gridpoints within the 8-9 km altitude range to saturation w.r.t. water. There is then a spin-up period of approximately

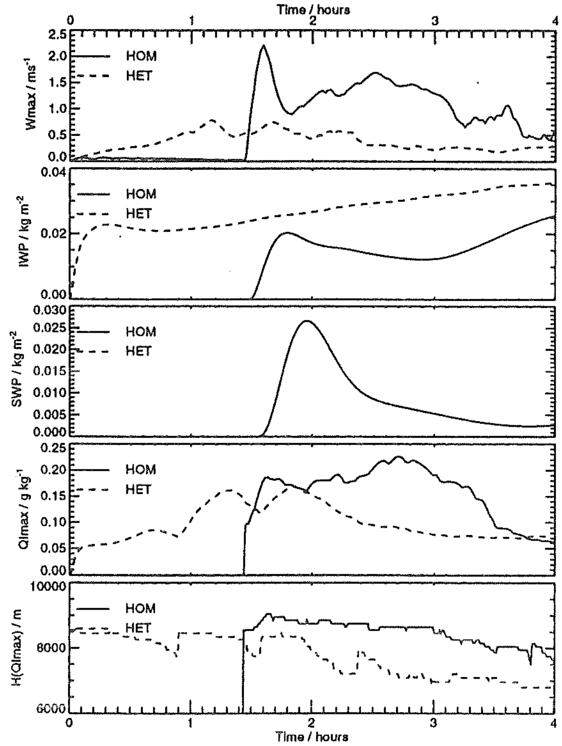

Figure 1. Time-series showing, from top to bottom, the maximum vertical velocity within the model domain (Wmax) the vertically-integrated water paths of cloud ice (IWP) and snow (SWP), the local maximum of cloud ice within the domain (QI_{max}) and the altitude at which it is located ($H(QI_{max})$). Data are shown for two model experiments, the first having only homogeneous nucleation active (HOM) and the second also having heterogeneous nucleation (HET).

20 minutes duration during which time W_{max} reaches a peak and the integrated water paths of cloud ice (IWP) and snow (SWP) rise rapidly as the ice supersaturation in the cloud layer is removed. In run HET, cloud forms at the start of the run, as cloud ice is nucleated in the initial ice supersaturation, and IWP again rises rapidly as this supersaturation is removed. However, there is no formation of snow in this run, implying that the cloud ice does not reach the required threshold diameter of 500μm. After about 130 minutes, run HET maintains a higher total ice water path than HOM but its values of W_{max} are significantly lower.

Differences in the evolving vertical profiles of the mean total ice content, IWC, (i.e. cloud ice plus snow) are shown in Fig.2. Both simulations evolve towards a state in which the peak IWC occurs near the cloud base, as noted in earlier cirrus simulations (eg. Starr and Cox, 1985). Notable differences between the two simulations are the higher IWC values in HOM between 2 and 3 hours and 8 to 9km altitude and the sharper cutoff in IWC at cloudbase in HET.

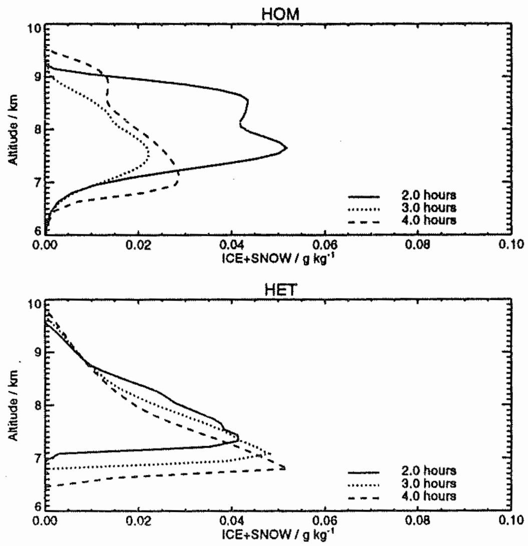

Figure 2. Vertical profiles of the total (ice + snow) water content at 2, 3 and 4hr during the evolution of HOM and HET runs.

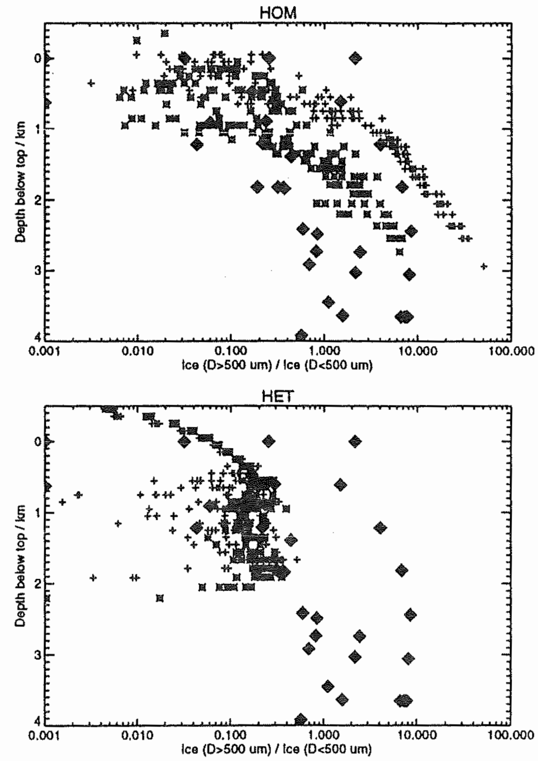

Figure 3 Data points show the ratio of ice mass contained in particles larger than 500 μm to that in particles smaller than 500 μm and are plotted as a function of depth below cloud top. The large filled symbols are from in-situ measurements in a number of different cirrus cases. Model data are shown at times of 2hr (+) and 3hr (*) for runs HOM (upper plot) and HET (lower plot) assuming that cloud-top remains at 9km altitude throughout.

4.1 Ice Mass Partitioning

At each model grid point, the parametrized size spectra of cloud ice and snow may be evaluated using the prognosed values of mass and number concentration for each species. The total ice mass due to all particles smaller and larger than 500 μm in diameter may then be determined. The in-situ data are shown in Fig.3 together with model results from the HOM and HET simulations.

4.2 Simulated Radar Properties

Values of *C(D)* and *K(D)* in (3) were calculated using a Mie-scattering code provided by R.Hogan (personal comm.). This uses the parametrized size spectra together with the mass-size relations specified for cloud ice and snow in the model, and assumes that the particles are quasi-spherical and a mixture of solid ice with air inclusions. Vertical profiles of the simulated values of maximum 94GHz reflectivity, $Z94_{max}$, and *DWR* are shown in Fig.4.

HOM shows larger values of both $Z94_{max}$ and *DWR* than HET. This is consistent with its production of more mass in the snow category, creating larger mean particle sizes. *DWR* for run HOM exceeds 8dB at 110 minutes, which is well in excess of the typical range for observed values of 0-4dB. At 180 minutes, *DWR* has fallen to around 5dB at the base of the cloud layer. In contrast, run HET generates values of *DWR* that are less than 2dB throughout.

5. DISCUSSION AND CONCLUSIONS

Although the observations of large- to small-particle ice mass contribution have a large scatter, they suggest that the model results from HOM at 3hrs have a somewhat better agreement than at 2hrs. In particular, the rate of increase of large particle mass with depth below cloud top appears to be too rapid. In contrast, large particle mass in the HET run appears to be too low throughout the run.

The simulated *DWR* from run HOM at 2hrs has values that are well in excess of the observations of Hogan et al. (2000) for a cloud of similar depth. At 3hr, there is somewhat better agreement with DWR_{max} of around 4dB in association with $Z94_{max}$ of -6dBZ. The HET run maintains lower values of both these parameters throughout and does not approach the values of DWR_{max} seen in observations.

Taken together, these results suggest that the peak of snow formed immediately following cloud formation in HOM is probably spurious. In this run, nucleation

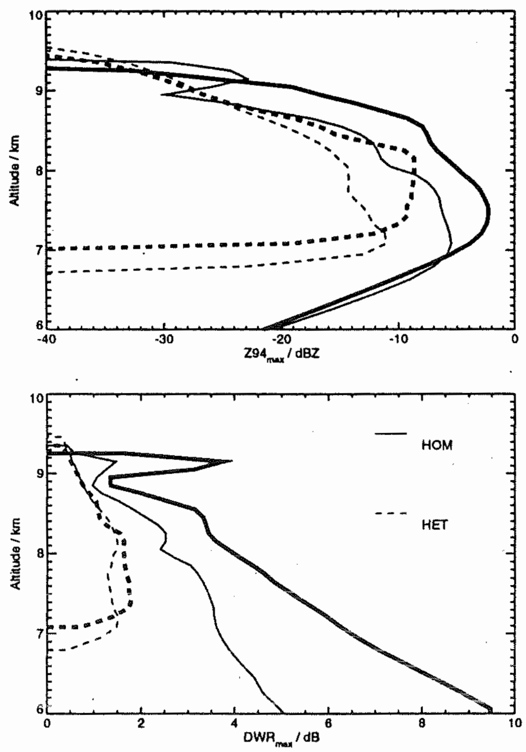

Figure 4 Vertical profiles of the maximum 94 GHz radar reflectivity (Z94max - upper plot) and maximum dual-wavelength ratio (DWRmax - lower plot). Results are shown for times of 2hrs (thick lines) and 3hrs (thin lines) in the HOM (solid) and HET (dashed) model runs.

can only occur in regions that have achieved saturation w.r.t. water. The use of random initial temperature perturbations on the grid scale ensures that saturation brought about by the

uniform cooling of the domain tends to occur initially in regions which have a horizontal scale comparable with that of the grid. This leads to sharp gradients in the ice number concentration. It appears that numerical diffusion of these concentration gradients can lead to the attribution of mass-mean cloud ice diameters that exceed the 500 μm threshold for the onset of autoconversion to snow, which can then grow further by deposition and accretion of cloud ice. In the HET run, the initial ice concentrations (approx. 10^5 kg^{-1}) are much less than those of the HOM run (approx.10^8 kg^{-1}). They are, however, much more uniform over the domain and this problem does not occur. It is planned to provide the model with a new parametrization of homogeneous freezing based on results from a 1-d parcel model (Spice et al. 1999, Cotton et al. 2000), with a view to improving this aspect of model behaviour.

Another feature of the HOM run which contrasts with that seen in observations is the relatively slow decrease in maximum radar reflectivity towards the cloud base. This suggests that the ice mass contained in larger, more rapidly-falling snow particles is not evaporating sufficiently rapidly when it falls into sub-saturated air. The behaviour of the HET run appears to be better in this respect.

This study illustrates how the availability of both in-situ particle size measurements and, ideally, dual-wavelength radar measurements in a future case study can be used to guide the improvement of the model's microphysics scheme. Since the information about mean particle sizes that is provided by *DWR* measurements can also be obtained from in-situ data, the availability of dual-wavelength radar is not crucial. It does, however, provide a more representative view of the evolving vertical structure of the cloud than can be obtained from aircraft measurements at a single level.

REFERENCES

Cotton,R.J., P.R.Field and D.W.Johnson (2000) Ice nucleation in orographic wave clouds: a model-observation comparison of an isolated wave cloud. 13th Int.Conf. on Clouds and Precip., Reno. *This volume.*

Edwards,J.M. and A.Slingo (1996) Studies with a flexible new radiation code. Part I. Choosing a configuration for a large-scale model. Quart.J.R.Meteorol.Soc., **122**, 689-719.

Field,P.R. (2000) Bimodal ice spectra in frontal clouds. Quart.J.R.Meteorol.Soc., **126**, 379-392.

Hogan,R.J., A.J.Illingworth and H.Sauvageot (2000) Measuring crystal size in cirrus using 35- and 94-GHz radars. J.Atmos.Oceanic Technol., **17**, 27-37.

Mason,P.J. (1989) Large-Eddy simulation of the convective atmospheric boundary layer. J.Atmos.Sci., **46**, 1492--1516.

Meyers,M.P., P.J.DeMott and W.R.Cotton (1992) New primary ice nucleation parametrizatons in an explicit cloud model. J.Appl.Met., **31**, 708--721.

Spice,A., D.W.Johnson, P.R.A.Brown, A.G.Darlison and C.P.R.Saunders (1999) Primary ice nucleation in orographic cirrus clouds: a numerical simulation of the microphysics. Quart.J.R.Meteorol.Soc., **125**, 1637-1667.

Starr,D.O'C. et al. (2000) Comparison of Cirrus Cloud Models: A Project of the GEWEX Cloud System Study (GCSS) Working Group on Cirrus Cloud Systems. 13th Int.Conf. on Clouds and Precip., Reno. *This volume.*

Swann,H.A. (1998) Sensitivity to the representation of precipitating ice in CRM simulations of deep convection. Atmos.Res., **47**, 415-435.

STRATOSPHERIC INFLUENCE ON UPPER TROPOSPHERIC * TROPICAL CIRRUS

Matthew T. Boehm and Johannes Verlinde

Department of Meteorology, The Pennsylvania State University, University Park, PA 16802

1. INTRODUCTION

Thin cirrus layers have frequently been observed near the tropical tropopause. These clouds extend several hundred to more than a thousand kilometers horizontally and persist for time periods of several hours to several days before dissipating. Because of their ubiquitous nature and location in the very cold tropical upper-troposphere and above the very warm tropical ocean, tropical cirrus clouds play a major role in Earth's radiation budget (Liou 1986). Despite their impact on the climate of the Earth, relatively little is known about tropical cirrus processes. Studies are hampered by a lack of detailed observations, a result of the location of these clouds at very high altitudes in relatively remote regions.

In a recent article we described results of a series of model runs designed to test the hypothesis that cloud circulations associated with radiative destabilization of the cirrus layer are responsible for the maintenance of high tropical cirrus (Boehm et al. 1999). In spite of significant differences in cloud circulation strength among the model runs performed, very little difference was found in the ability of the modeled clouds to maintain themselves against the processes of sedimentation and evaporation. When normalized by the initial value, the ice water path of each of the modeled clouds decayed at a similar rate, leading to the conclusion that an internal dynamics-microphysics-radiative transfer mechanism is not sufficient for maintaining tropical cirrus over the periods observed. We hypothesized that a source of large-scale rising motion is required to form and maintain cirrus layers near the tropical tropopause.

Tropical waves are an important source of rising motion near the tropical tropopause. Waves which are well documented in the tropical upper troposphere include mixed Rossby-gravity waves and Kelvin waves (Tsuda et al. 1994; Shimizu and Tsuda 1997; Wikle et al. 1997). It has been suggested that these tropical waves may play a role in the formation and maintenance of cirrus layers near the tropical tropopause (Jensen et al. 1996). Here we present observational evidence that tropical waves play an important role in the life cycle of tropical cirrus.

*Article submitted to Geophysical Research Letters

Corresponding author's address: Matthew T. Boehm, Department of Meteorology, The Pennsylvania State University, University Park, PA 16802; e-mail: boehm@essc.psu.edu

2. OBSERVATIONS

The Department of Energy (DOE) Atmospheric Radiation Measurement (ARM) program maintains two Atmospheric Radiation and Cloud Stations (ARCS) in the tropical western Pacific (TWP) (Mather et al. 1998). The ARCS, located on Manus Island and Nauru, are equipped with a broad range of instruments for evaluating the radiation budget of the tropical atmosphere. In this paper we use Nauru ARCS (0.5° S, 166.9° E) radiosonde temperature and wind profiles and a time series of micropulse lidar cloud profiles. In particular, we focus on data obtained during Nauru99, a field experiment conducted during the summer of 1999 at Nauru.

Radiosondes are launched from Nauru at least 4 times each day during Intensive Operational Periods (IOPs) such as Nauru99 and twice each day otherwise. Data are obtained into the lower stratosphere from most of the radiosondes, providing a view of temperature and wind fluctuations near the tropopause. Radiosonde data have previously been used to detect waves near the tropopause (e.g. Tsuda et al. 1994; Hamilton 1997).

The MPL provides a nearly continuous record of the clouds that pass over the site (Mather et al. 1998). The MPL at Nauru, with 30 m vertical resolution data averaged over 1 minute time intervals, is very effective at detecting thin cirrus layers near the tropopause, making it a very useful instrument for studying these clouds. However, the MPL is unable to detect cirrus when lower clouds attenuate the signal and for a short period around local noon due to noise from the sun passing overhead. Therefore, the MPL does not always detect cirrus when it is present. This should be taken into account when analyzing MPL data.

3. PROCEDURE AND RESULTS

To test the hypothesis that tropical waves play a role in the life cycle of tropical cirrus, observations of tropical waves and cirrus occurrence near the tropopause were combined. This was accomplished by superimpos-

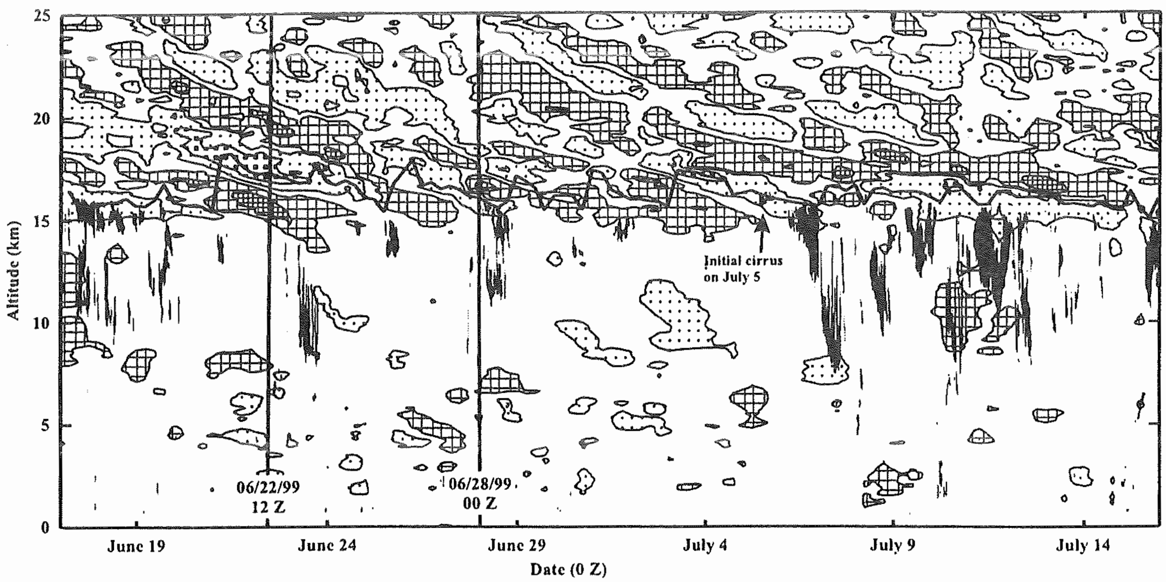

Figure 1: Lidar and radiosonde data from the DOE ARM Nauru99 Field Experiment showing the correlation between stratospheric waves and upper tropospheric cirrus. The background contours and shading are radiosonde observations of temperature deviations from the mean for the period (see Figure 3 for mean profile). The cross-hatching represents positive perturbations while the speckling represents negative perturbations, with contours at -4 K, -1 K, +1 K, and +4 K. The solid shading superimposed on the temperature perturbations shows clouds detected by micropulse lidar data, while the superimposed solid line shows the minimum temperature detected in each sounding. The vertical lines mark the times represented by the individual soundings in Figure 3.

ing cloud data obtained from the lidar on a time series of profiles of temperature perturbations obtained from radiosonde data. The result is shown in Figure 1.

The time series of profiles of temperature perturbations makes up the background contour field in Figure 1. It was constructed by fitting temperature data from each of the radiosondes (4 per day from 17 June 1999 through 15 July 1999) to a regularly spaced profile with 50 m spacing, combining the individual profiles into a time-altitude grid, calculating the period average at each altitude, and finally calculating the temperature perturbation at each time-altitude point from the period average at that altitude. Tropical waves are visible as perturbations in the temperature field descending from the lower stratosphere with periods of several days and amplitudes up to 8° C.

A cloudmask algorithm developed by Clothiaux et al. (1998) uses MPL data to construct a mapping of cloud occurrence. We have superimposed cloudmask data on the temperature perturbation field in Figure 1. In this figure we can distinguish between two types of cirrus: thin cirrus layers in the upper troposphere at altitudes up to around 16 km and lower, thicker anvil cirrus. Careful inspection reveals that upper tropospheric thin cirrus formation occurs exclusively in the cold phases of the waves descending from the lower stratosphere. A good example is seen during the first week of July. After clear conditions form the 2nd through the 4th, cirrus develops as the cold phase of a wave descends to 16 km on the 5th. As the wave continues its descent through the 6th and 7th, the cirrus gradually descends as well. Note that the break in the cirrus around 0 Z on the 6th corresponds to midday, when the cloud signal was lost in the noise.

The solid line in Figure 1 marks the altitude of the minimum temperature, sometimes called the cold point, in each of the soundings. The cold point has sometimes been used to define the tropopause in the deep tropics (Highwood and Hoskins 1998). During the period shown, the cold point closely follows the cold portions of the waves descending from the lower stratosphere, with a cycle of gradual descent followed by a rapid rise when the next wave descends to an altitude of 17-18 km. The cold point also closely corresponds to cirrus occurrence, nearly always lying above the highest cirrus by an altitude of less than 1 km. Cirrus clouds tend to occur only when the cold point descends to an altitude of about 16 km, suggesting a possible lack of sufficient moisture for cirrus formation at higher altitudes.

To further visualize the relationship between cirrus near the tropopause and negative temperature perturbations, Figure 2 shows a histogram of temperature perturbations coinciding with cloud occurrences above 15 km. With few exceptions, the temperature perturbations are negative, with a peak in cloud occurrence when the temperature perturbation is about -2° C, verifying

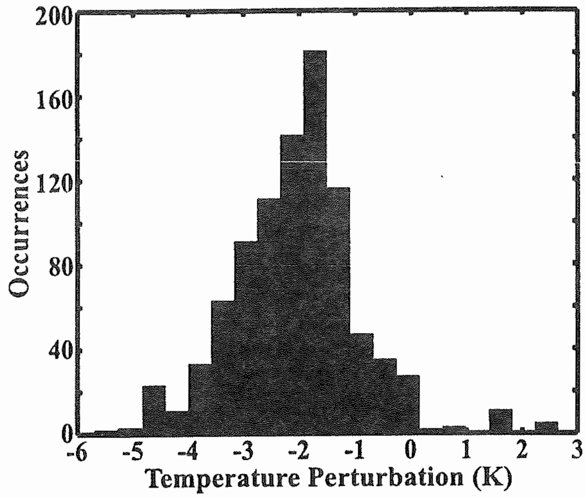

Figure 2: Histogram of temperature perturbations coinciding with cloud occurrences above 15 km.

the close relationship between cirrus and negative temperature perturbations near the tropopause.

4. DISCUSSION

A number of types of planetary waves have been observed near the tropical tropopause, with more than one type often present at a time. The identification of the types of waves present at any given time requires detailed analyses that are beyond the scope of this letter. We only describe the waves present during Nauru99. The observed waves have periods of 3-5 days in the temperature and zonal wind fields and about half as long in the meridional wind field. Moreover, the amplitudes of the zonal wind perturbations are twice as large as the meridional wind perturbations. The 3-5 day period is consistent with periods observed for Rossby-gravity waves in the equatorial lower stratosphere, although the zonal wind and temperature perturbations are higher than those observed for Rossby-gravity waves and are more consistent with those observed for Kelvin waves; however, the periods of observed Kelvin waves are several times the observed periods (Andrews et al. 1987). We have not attempted to positively identify the types of waves present during Nauru99 since this is beyond our objective for this paper.

In addition to leading to cirrus formation, the waves we have observed descending from the stratosphere play a role in determining the structure of the tropical tropopause. The processes that determine the properties of the tropical tropopause are complex and not well understood (Reid and Gage 1996). In fact, a meaningful, physically based, definition for the tropical tropopause has not been agreed upon (Highwood and Hoskins 1998). These authors argue that the conventional lapse rate tropopause definition has little physical meaning in the tropics. The difficulty in defining the tropopause is compounded by the considerable day-to-day variability in tropopause height and temperature and by the frequent occurrence of double tropopauses in which the cold point tropopause is significantly higher than the lapse rate tropopause (Reid and Gage 1996).

Our results show that there is an intricate relationship between fluctuations in tropopause height and temperature and the presence of stratospheric waves. This relationship is consistent with observations that tropopause properties are generally uniform over large areas of the tropics (Reid and Gage 1996). Thus we conclude that large-scale processes are likely responsible for the variability in tropopause properties. However these results do not help to provide a meaningful definition for the tropical tropopause. Rather, they help to confirm the complexity of this region.

To illustrate the variability observed in the tropopause properties during Nauru99, Figure 3 shows the mean temperature profile for the period along with two individual profiles. Notice that significant variability occurs above 15 km, with only minor variability at lower levels, as expected based on the the temperature deviations plotted in Figure 1. The profile for 22 June at 12 Z has a double tropopause structure, with the conventional lapse rate tropopause at around 15 km and a much colder cold point tropopause at around 17 km. Referring to this time in Figure 1, it is apparent that this structure is caused by the descent of a strong stratospheric wave. The lower tropopause corresponds to the warm perturbation associated with the wave,

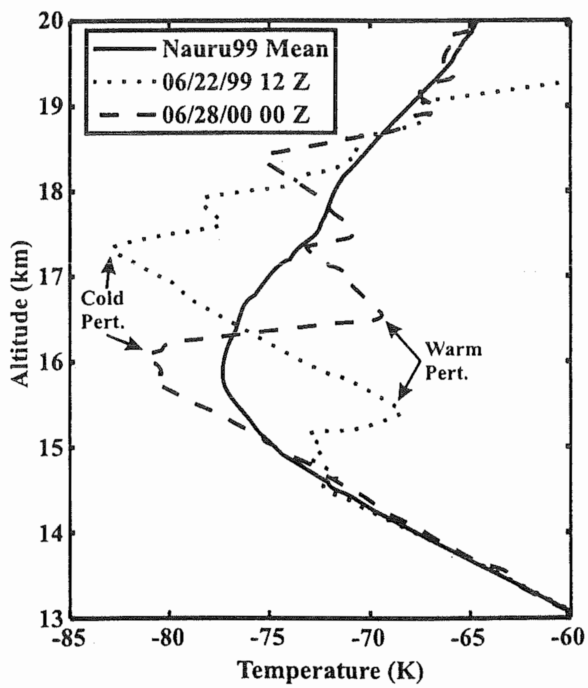

Figure 3: Temperature profiles illustrating the variability in tropopause properties during Nauru99. The solid line shows the period mean, and the dotted and dashed lines show individual soundings. The arrows point to warm and cold temperature perturbations associated with tropical waves.

while the upper tropopause corresponds to the cold perturbation associated with the wave. Cirrus clouds were not observed at this time.

In contrast, the profile for 28 June at 0 Z has a single well-defined tropopause around 16 km. In this case, the lapse rate and cold point tropopauses are equivalent. Referring to this time in Figure 1, note that it corresponds to a situation where a cold perturbation is the lowest perturbation near the typical tropopause altitude. The cold perturbation raises the tropoause by significantly cooling a layer found in the stratosphere of the mean profile, thus raising the altitude at which the temperature begins increasing with altitude. Cirrus clouds were observed near the tropopause at this time.

5. CONCLUSIONS

Observations have revealed the frequent presence of cirrus layers near the tropical tropopause. In a recent article we showed that an internal dynamics-microphysics-radiative transfer mechanism is not sufficient for maintaining these cirrus layers and proposed that large-scale rising motion is required to explain the life cycle of tropical cirrus. Data from the DOE-ARM Nauru99 experiment were used to investigate this hypothesis by looking for a correlation between planetary scale tropical waves and cirrus occurrence. Radiosonde data revealed waves descending into the upper troposphere from the lower stratosphere. Cirrus cloud occurrence coincided with the cold phases of these waves. Moreover, the tropical tropopause location was closely associated with these waves.

This study reveals the close association between upper tropospheric cirrus and large-scale dynamics. These data suggest that tropical cirrus cannot be studied in isolation from planetary scale forcing. Moreover, this limited dataset suggests a possible way to predict the occurrence of tropical cirrus through monitoring stratospheric wave activity.

ACKNOWLEDGEMENTS

We gratefully acknowledge Eugene Clothiaux for providing the cloudmask algorithm and results and the Nauru99 field crew for the measurements. MTB was supported by a NASA Earth System Science Fellowship. This work was supported in part by a grant from the Department of Energy under the Atmospheric Radiation Measurement program (DE-FB02-90ER6L071).

REFERENCES

Andrews, D. G., J. R. Holton, and C. B. Leovy, 1987: *Middle Atmosphere Dynamics*. Academic, Orlando, Flor., 489 pp.

Boehm, M. T., J. Verlinde, and T. P. Ackerman, 1999: On the maintenance of high tropical cirrus, *J. Geophys. Res.*, **104**, 24,423-24,433.

Clothiaux, E. E., G. G. Mace, T. P. Ackerman, T. J. Kane, J. D. Spinhirne, and V. S. Scott, 1998: An automated algorithm for detection of hydrometeor returns in micropulse lidar data, *J. Atmos. and Oceanic Technol.*,**15**, 1035-1042.

Hamilton, K., 1997: Observation of an ultraslow large-scale wave near the tropical tropopause, *J. Geophys. Res.*, **102**, 13,457-13,464.

Highwood, E. J., and B. J. Hoskins, 1998: The tropical tropopause, *Q. J. R. Meteorol. Soc.*, **124**, 1579-1604.

Jensen, E. J., O. B. Toon, L. Pfister, and H. B. Selkirk, 1996: Dehydration of the upper troposphere and lower stratosphere by subvisible cirrus clouds near the tropical tropopause, *Geophys. Res. Lett.*, **23**, 825-828.

Liou, K.-N., 1986: Influence of cirrus clouds on weather and climate processes: A global perspective, *Mon. Weather Rev.*,**114**, 1167-1199.

Mather, J. H., T. P. Ackerman, W. E. Clements, F. J. Barnes, M. D. Ivey, L. D. Hatfield, and R. M. Reynolds, 1998: An atmospheric radiation and cloud station in the tropical western Pacific, *Bull. Am. Meteorol. Soc.*, **79**, 627-642.

Reid, G. C., and K. S. Gage, 1996: The tropical tropopause over the western Pacific: Wave driving, convection, and the annual cycle, *J. Geophys. Res.*, **101**, 21,233-21,241.

Shimizu, A., and T. Tsuda, 1997: Characteristics of Kelvin and gravity waves observed with radiosondes over Indonesia, *J. Geophys. Res.*, **102**, 26,159-26,171.

Tsuda, T., Y. Murayama, H. Wiryosumarto, S. W. B. Harijono, and S. Kato, 1994: Radiosonde observations of equatorial atmosphere dynamics over Indonesia I. Equatorial waves and diurnal tides, *J. Geophys. Res.*, **99**, 10,491-10,505.

Wikle, C. K., R. A. Madden, and T.-C. Chen, 1997: Seasonal variation of upper tropospheric and lower stratospheric equatorial waves over the tropical Pacific, *J. Atmos. Sci.*, **54**, 1895-1909.

RADIATIVE INFLUENCES ON THE STRUCTURE OF CIRRUS CLOUDS USING A LARGE EDDY SIMULATION (LES) MODEL

J. Steven Dobbie and Peter Jonas
Dept. of Physics, UMIST
Manchester, M60 1QD, England

ABSTRACT

This work focuses on the interplay between microphysical structure and radiaton in cirrus clouds. We look at the effect that radiation has on the development and evolution of structure in cirrus clouds, and we also see how inhomogeneous microphysics affects a cloud's evolution.
The work is based on three LES runs. The first run is with no radiation, the second run is with radiation switched on and a homogeneous effective ice crystal size, and the third run is again with radiation but with an inhomogeneous assignment of ice crystal effective size in the vertical. For the cases studied, we find that the clouds with and without radiation tend to diverge in their morphological structure quite substantially within 30 minutes of a base run. The sensitivity of cloud inhomogeneity in time to the vertical treatment of ice particle size is much less pronounced, but the cloud morphology is still very similiar.

1. INTRODUCTION

Cirrus clouds have a substantial role in influencing climate through their interaction with solar and terrestrial radiation (Ramanathan and Collins, 1991). Climate is found to be very sensitive to the radiative properties of cirrus clouds (Stephens et al., 1990). However, the treatment of cirrus clouds in large scale models, such as GCMs, is inadequate due to the often highly inhomogeneous structure and microphysics of these clouds. Dealing with the layer radiative properties is inherently difficult.

There has been previous work on the radiative effects of inhomogeneous cirrus clouds (for example, Chylek and Dobbie, 1995), but not for realistic cloud shapes. In this work, we will generate realistic cirrus clouds using a Large Eddy Simulation (LES) model and investigate the effects of inhomogeneous shape and distribution of microphysics. To complement this, we look at the magnitude of the role in which radiative heating and cooling takes in the development and evolution of cirrus clouds by running simulations with and without radiative transfer.

2. LARGE EDDY SIMULATION MODEL

This present version of the LES model (Derbyshire et al., 1999) is based on an original code by P. Mason (for example, see Mason and Callen, 1986; or Mason, 1989). The early versions of the LES code were successful in modeling a variety of boundary layer problems (Mason and Thomson, 1987; Mason and Derbyshire, 1990; MacVean, 1993). The more recent versions have been equipped to handle a wide range of microphysical processes, and so the model has been applied to a wider range of atmospheric problems (for example, MacVean, 1993).

The LES simulation seeks to resolve the large scale turbulent motions, which contain most of the turbulent energy and are responsible for most of the turbulent energy transport. The smaller eddies, which are responsible for dissipation of kinetic energy, are parameterized (Derbyshire et al., 1999). The UK Met. Office's LES model has evolved into a model that is able to handle a variety of warm cloud microphysical processes (cloud droplets, rain, etc.). The version of the LES that we use is also capable of handling ice microphysics (including homogeneous nucleation).

The LES model used in this study was recently ported to a personal computer (Pentium 200) running the Linux operating system. And to it, a radiation model, based on a model by Fu and Liou (1992), has been installed. Included in the radiative transfer scheme is the effects of cirrus cloud ice particles, water cloud (none in this work), water vapour, Rayleigh scattering, aerosols (none in this work), ozone, nitric acid, carbon dioxide, and methane. The reason for using this radiation model is that it uses state-of-the-art ice crystal optical properties.

We are running the LES in 2-D at the moment, but the simulations are easily extended to 3-D. We use a 2-D which accommodates 100 grids in the horizontal dimension and 64 in the vertical. The vertical grids are not equally space, unlike the horizontal grids, and have been chosen so as to provide resolution of about 100 meters within and near the cirrus cloud region. The resolution near the surface and at the top of the simulated atmosphere is more coarse. The simulation space in the vertical extends from the surface to 20 km and the horizontal extent is 10 km.

The various runs performed in this work are all started from a base run. The base run is 2 hours long and has been initialized in a way similar to the cirrus clouds in the GCSS WG2 case. A cooling of a layer by 0.0002931 degrees C per second for the first two hours between the heights of 7 and 10 kms is imposed. The cooling is linearly decreased to zero above (to 10.5 km) and below (to 6 km) this region. Cirrus clouds begin to develop a little after 90 minutes. The clouds at first are numerous, isolated, and dispersed along in the horizontal, initially between 8 and 9 kms. The cloud develops by 110 minutes to nearly cover the whole horizontal extent, and it begins to spread above and below the 8 to 9 km region. By two hours, the cloud is almost completely extended across in the horizontal and it extends from 7 to 9.2 kms in the vertical. All of the runs and comparisons in this work begin

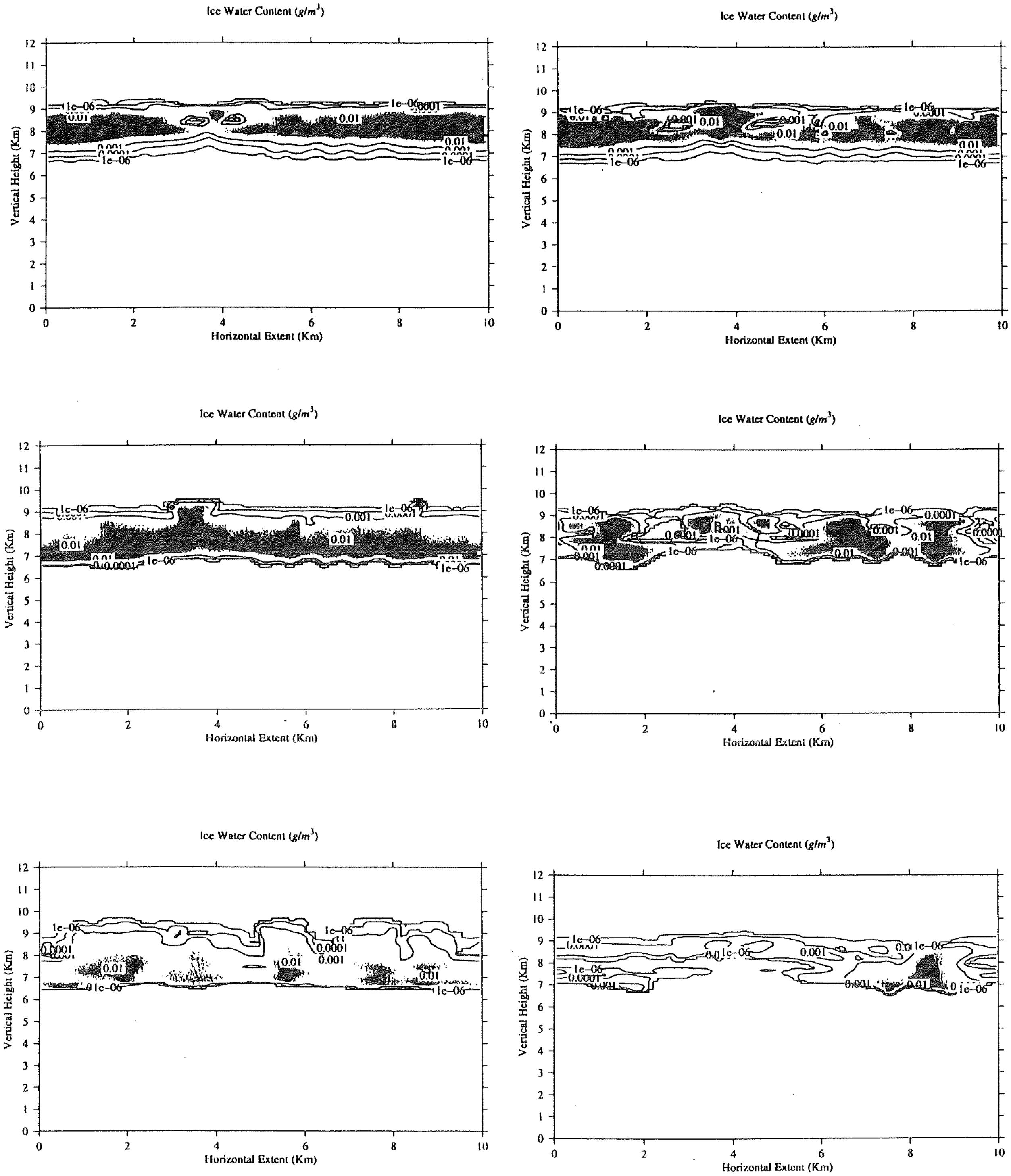
Ice Water Content (g/m^3)
Vertical Height (Km)
Horizontal Extent (Km)

Figure 1

from this two hour basis run.

3. RADIATION AND CLOUD EVOLUTION

Three simulations are performed in this work, all beginning from the two hour basis run and were run for four additional hours of simulation time. The first run was performed with no radiation. The second was performed with radiation and with a homogeneous ice crystal effective size of 30 microns assigned to all cirrus cloud. The third run was performed again with radiation switched on, but now the ice crystal size was varied in the vertical. The choice of the vertical variation was from observations from the FIRE 1991 campaign (Dec 25). The effective size was set to a maximum of 45 microns at 8.5 (middle of cloud) and was inversely decreased to 25 microns above (10 km) and below (6 km) the cloud.

Shown in Figure 1 are three plots of the evolution of the ice water content of the simulated cirrus cloud. The plots on the left are for simulations without radiation and the plots on the right have radiation included. The top row of plots are after 2.5 hours of simulation time (half an hour after the base run), the middle row of plots are for 3.5 hours of simulation time, and the lower plots are after 5 hours of simulation time. From the top row, we see that the cloud is essentially one single layer for both cases. The no radiation case (left) is seen to be horizontally smooth in ice water content. There are two regions of ice water content up to 0.01 g/m^3 which extend either side of the 4 km horizontal dimension. The top right plot (which includes radiation) is observed to be less smooth in its horizontal distribution of ice water content (IWC), and it is evident that the region of high IWC (0.01 g/m^3) is horizontally broken up. Evidently, radiation is causing more turbulence in this layer and causing isolation of the high IWC cells. Most of the differences appear around the 8 km vertical height. This is where the cirrus cloud first developed and where the crystals are most numerous (number concentration plots are not shown).

The middle plots are seen to be similar to the upper plots in that the no radiation case (left) is more horizontally stratified than the plot on the right. And, the simulation with radiation (right) shows much more structure and more regions of isolated cells of high IWC. The middle left plot shows a cloud top with the start of isolated plumes extending into the layer above 9 km. Excluding the plumes, the middle left plot is still very stratified. The middle right plot is less stratified, but has no sign of plumes extending into the layer above cloud-top. The majority of the turbulence is within or at cloud-base for the middle right plot. The cloud base, however, is much less stable and we can see that regions of high IWC comprise the lowest levels, below the cloud base seen in the top right plot. The low IWC values at cloud base are now seen at higher altitudes as compared with the top right plot.

The bottom two plots show a cloud that is dissipating. It is observed that the cloud with radiation is dissipating earlier than the cloud without radiation effects. The bottom right plot shows a cloud that still has a cloud top around 9 km but its base is depleted in IWC in many regions. The region of high IWC is small, as much of the ice has sublimated. The no radiation case (bottom left) shows a cloud in which the cloud-top has asended slightly to 9.5 km in a number of areas at cloud top. The within cloud IWC is greatly depleted and little is left of that high IWC band around 7 km. The cloud base is now very stratified.

Shown in Figure 2 (a), (b), (c), and (d) are the top of the atmosphere reflectances as a function of horizontal dimension. Plots (a) and (b) are for a simulation time of 130 minutes (10 minutes after the base run). Plots (c) and (d) are for a simulation time of 3.5 hours. The plots (a) and (c) are for simulations with radiation in which the effective ice crystal size is fixed at 30 microns for all the cirrus cloud. Plots (b) and (d) are for simulation with radiation in which the effective ice crystal size is inversely decreased from a maximum value at a vertical height of 8.5 km of 45 microns to a value of 25 microns above (10.5 km) and below the maximum. For a fixed time, the IWC is the same for both simulations. Plots (a) and (b) show that the reflectivities are very similar in shape ten minutes past the basis simulation run. The shapes are similar but plot (a) has a higher average reflectivity compared to plot (a) by about 8%. This is because the high ice water contents around 8.5 km are assigned larger effective ice crystal sizes (nearer to 45 micron) than plot (a). The smaller ice particles reflect more into the upward hemisphere and so result in a slightly higher reflectance.

Plots (c) and (d) of Figure 2 show that by 1.5 hours after the base run the reflectances are quite different in their variability along the horizontal dimension. Even with these visible differences, the average reflectivities are still in fairly close agreement (10.5%). As the simulations progressed, the absolute differences between the simulations disappeared since the clouds were progressively dissipating.

4. CONCLUSIONS

We see from the plots shown in Figure 1 that radiation has quite an effect on the morphology and evolution of cirrus clouds. It affects the stability of the cloud top and base, it affects the distribution of ice water content throughout the layer, and affects the dissipation of the cloud. Thermal infrared heating of the base of the cloud was causing the bottom of the cloud to be less stable and causing it to dissipate more rapidly than the no radiation case. Radiative cloud top cooling was acting to cool the top of the cloud, and it was possibly counteracting the generation of turbulence there from latent heating due to sublimation (vapour to ice). This may explain why the simulation without radiation had a cloud top that progressed into the layer above (plumes). Release of absorbed radiation within the regions of high ice water content increased turbulence within the cloud, and this acted to break up the stratiform distribution of ice water content in the radiation simulation cases. The two different radiation simulations, treated in this work, showed substantial differences in time for the variation in reflectivity in the horizontal. However, this variability did not greatly affect either the TOA average reflectivity (10%) or the morphology of the distribution of ice water for the radiation inclusive cases.

This work forms only a preliminary basis and future work will seek to validate and quantitatively assess the above conclusions.

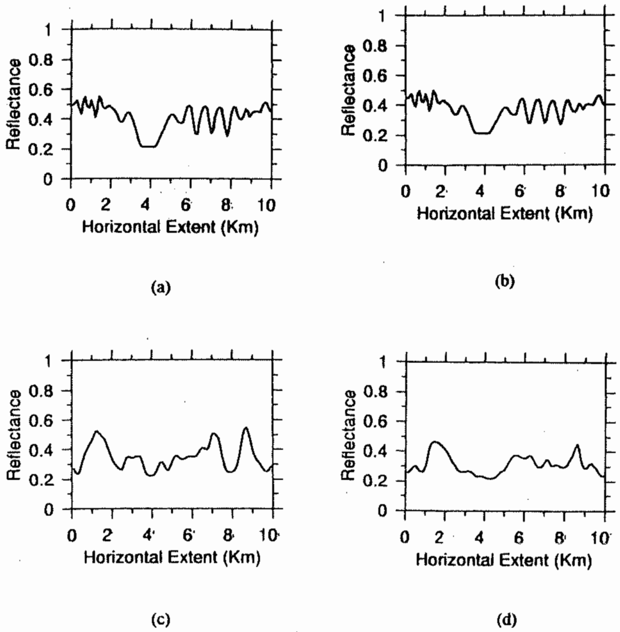

Figure 2

ACKNOWLEDGMENTS

Thanks to Phil Brown (Met. Office) and Malcolm MacVean for the present version of the LES model and for help in becoming familiar with the model (JSD). Thanks to Q. Fu for supplying his radiation routine.

REFERENCES

Chylek, P., and J. S. Dobbie, Radiative transfer through inhomogeneous cirrus clouds: Monte Carlo calculations. J. Atmos. Sci., Vol. 52, pp. 3512-3522, 1995.

Derbyshire, S. H., A. R. Brown, and A. P. Lock, The Meteorological Office large-eddy simulation model. Turbulence and Diffusion Note No. 213, Oct. 1999.

MacVean, M. K., A numerical investigation of the criterion for cloud-top entrainment instability. J. Atmos. Sci., Vol. 50, pp. 2481—2495, 1993.

Mason, P., and N. S. Callen, On the magnitude of the subgrid-scale eddy coefficient in large-eddy simulations of turbulent channel flow. J. Fluid Mech., Vol. 162, pp. 439—462, 1986.

Mason, P., and S. H. Derbyshire, Large-eddy simulation of stably-stratified atmospheric boundary layer. Quart. J. Roy. Meteorol. Soc., Vol. 113, pp. 413—433, 1987.

Mason, P., Large eddy simulation of the convective boundary layer. J. Atmos. Sci., Vol. 46, pp. 1492—1516, 1989.

Mason, P., and D. J. Thomson, Stochastic backscatter in Large-eddy simulations of boundary layers. J. Fluid Mech., Vol. 242, pp. 51—78, 1992.

Stephens, G. L., Si-Chee Tsay, P. W. Stackhouse Jr., and P. J. Flatau, The relevance of the microphysical and radiative properties of cirrus clouds to climate and climate feedback. J. Atmos. Sci., Vol. 47, No. 14, pp. 1742—1753, 1990

HIGH RESOLUTION SIMULATIONS OF RADAR REFLECTIVITY AND LIDAR BACKSCATTERING FROM SUBTROPICAL CIRRUS CLOUDS: COMPARISON OF OBSERVATIONS AND RESULTS FROM A 2D/3D CLOUD RESOLVING MODEL

Angela Benedetti and Graeme L. Stephens

Department of Atmospheric Science, Colorado State University, Fort Collins, CO, 80523, USA

1. INTRODUCTION

As part of the ARM–UAV (Atmospheric Radiation Measurement Unmanned Aerospace Vehicle) Program, a field campaign took place over the Pacific (Kauai, Hawaii, 22N–160W) during Spring 1999 (Stephens *et al.*, 2000). Two research aircraft were flown with the mission of observing clouds using various active and passive instruments, such as a Cloud Detection Lidar, a W–band Cloud Radar, radiometers and spectrometers. Data were collected from April, 28 to May, 18. One of the main objectives of the campaign was to obtain accurate and multi–instrument measurements of cirrus clouds.

Cirrus are ubiquitous and long–lived high clouds. As such they are radiatively very significant. Due to their relative inaccessibility and constitutional complexity, they present major challenges to modelers and observers.

The motivation for this study is to better understand the characteristics of subtropical cirrus clouds using the available information from the ARM–UAV Kauai experiment in conjunction with the use of a Cloud Resolving Model (CRM) and to test our current capability of modeling cirrus clouds.

2. DESCRIPTION OF CRM FEATURES

The model used has full dynamics, radiation and bulk microphysics and its heritage is the Regional Atmospheric Modeling System (RAMS, Walko *et al.*, 1995). The cloud mycrophysics module predicts the mixing ratios of relevant hydrometeor categories. For the simulation reviewed here only pristine ice (small ice crystals), snow (bigger unaggregated ice crystals) and aggregates were included. Rain, graupel and hail were inhibited, being less likely present in a subtropical cirrus cloud. Hydrometeors in each category are assumed to be distributed according to a generalized γ distribution. Nucleation, vapor deposition growth, collection and sedimentation processes are all simulated.

Corresponding author's address: Angela Benedetti, Department of Atmospheric Science, Colorado State University, Fort Collins, CO, 80523, USA; E-Mail: angela@atmos.colostate.edu

The radiation scheme in RAMS is a two–stream model with 3 bands in the shortwave and 5 in the longwave. The required inputs for the radiation routine, such as optical depth, single scattering albedo and asymmetry parameter are computed based on the microphysical properties of the hydrometeors. The computed heating rates are passed back to the microphysics and dynamics modules so that there is full coupling between all the components of the model.

3. SYNTHETIC RADAR AND LIDAR OBSERVATIONS FROM CRM FIELDS

The model calculates mixing ratios of the various ice species for the whole model domain and at selected times throughout the simulation. Mixing ratios can be converted into total Ice Water Content (IWC). The IWC is then converted into radar reflectivity, Z and lidar backscattering, β. The conversion to radar reflectivity is straightforward if we assume a power law relationship between IWC and Z,

$$Z = aIWC^b \qquad (1)$$

where we used values of coefficients a and b from Sassen and Liao (1994).

The conversion to lidar backscattering is more involved and the approach we took can be described as *empirical.* Following Platt *et al.* (1998), (henceforth, P98), it is possible to obtain an estimate of the cloud backscatter to extinction ratio at the lidar wavelenght, k, via the LIRAD method. This method makes use of radiometric information on cloud emittance and cloud infrared optical depth in order to obtain an estimate of k. Since cloud emittance is a function of cloud temperature, k is also a function of temperature. Table 3. in P98 provides empirically derived values of backscattering to extinction ratio for various temperature intervals, along with best–fit coefficients from a linear interpolation. These coefficients were used along with the temperature field provided by the CRM to compute the appropriate values of k.

Multiple scattering effects can be accounted for by introducing a multiple scattering coefficient, η. We assumed this coefficient to be unity on the basis that at longer lidar wavelengths (1053 nm for the Cloud Detection Lidar, used in the Kauai field experiment), the effects of multiple scattering are reduced. Cloud visible optical depth was computed from the total IWC and the average effective radius.

Molecular backscattering was calculated using the Rayleigh approximation. For consistency, values of background atmospheric density were computed from the model pressure and temperature fields.

3.THE ARM–UAV SPRING 1999 EXPERIMENT

The ARM–UAV program established in 1991 has been pivotal in demonstrating how measurements from unmanned aircraft platforms can contribute to our understanding of cloud microphysical and radiative processes.

The Spring 1999 campaign, operated from the Pacific Missile Range Facility, Kauai, Hawaii, was designed as a two aircraft cirrus cloud experiment. The stratospheric aircraft Altus II was flown above cloud top in formation with the Twin Otter flown below cloud base.

The Altus II payload provided measurements of spectral and broadband radiative fluxes, spectral radiances and lidar backscattering from the Cloud Detection Lidar (CDL). The Twin Otter provided similar radiometric measurements as well as radar reflectivity from the NASA JPL/University of Massachusett's 94 GHz Airborne Cloud Radar (ACR).

An example of radar reflectivity and lidar backscattering data for April, 30, 1999 is shown in figure 1.

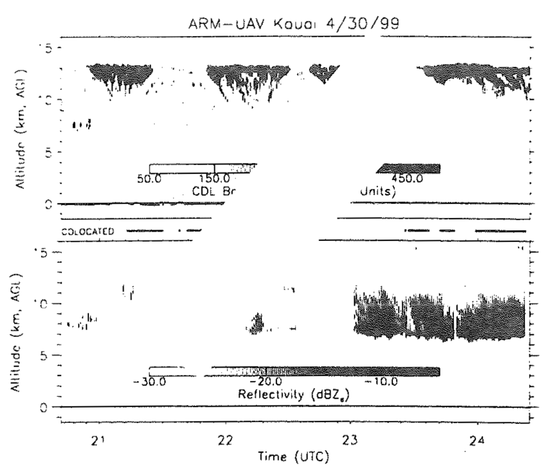

Figure 1: Lidar and radar cirrus observation for April, 30, 1999.

It's useful to note that lidar and radar measurements perfectly complement each other. The radar misses the signal from small ice crystals residing at cloud top, which is captured by the lidar. On the other hand the lidar signal gets attenuated rapidly going downward from cloud top, due to the presence of larger crystals and aggregates.

4. THE CASE STUDY

4.1 Synoptic overview

The cirrus case chosen for this study consisted of a single layer cloud observed on the 30th of April 1999. The synoptic analysis for that day pointed out that an upper level low located about 1500 km north of Honolulu was deepening and moving slowly to the southwest. A trough extended from the upper level low southwest to a second low near the dateline. The second low had isolated thunderstorms associated with it, and due to the west to southwest winds aloft, cirrus clouds thrown off from the tops of the thunderstorms were advected over the observation area.

Visible images from GOES 10 at 2200UTC and 000UTC respectively (figs. 2 and 3) show the cirrus layer being advected over the study region.

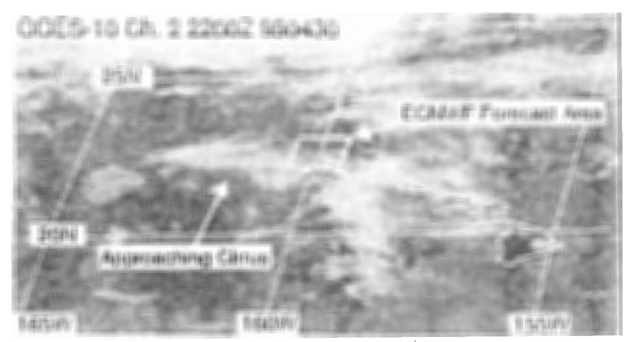

Figure 2: GOES 10 visible image at 2200UTC on April, 30, 1999. Courtesy of Steve Miller.

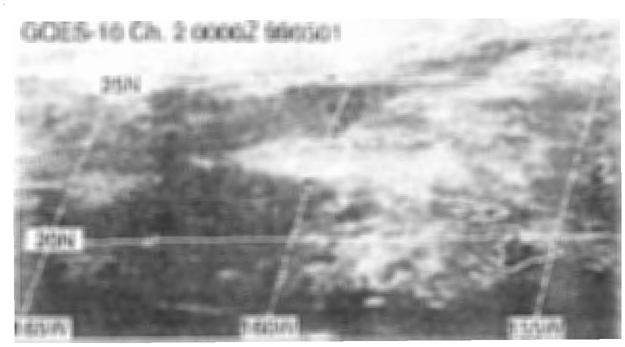

Figure 3: GOES 10 visible image at 000UTC on May, 1, 1999. Courtesy of Steve Miller.

The lidar and radar cross sections shown in figure 1 confirmed the presence of a relatively deep cirrus layer between 7 and 14 km, which was deepening over time at around 2200UTC and 000UTC.

4.2 Implementation of the CRM simulations

The CRM domain consisted of a single grid, centered at 22.5N and 160.25W, 80 km long and few kilometers wide, representative of a cross section along the study area at an angle of roughly 45 degrees with the flight track. The model resolution was 400 m in the horizontal and variable in the vertical from 400 m in the Boundary Layer to 50 m at cloud levels. The configuration of the model run was 3D, but due to the the fact that the total number of grid points in the zonal (x–) direction was much greater than the number of grid points in the meridional (y–) direction, the results must be regarded as 2D. Thus it is impossible to establish a one–to–one comparison between observations and model fields. Nevertheless, if we assume horizontal homogeneity in the cloud field, it's still meaningful to compare the simulated fields with the measurements, especially in a domain average sense.

The initial thermodynamic fields (pressure, temperature, specific humidity and wind speed) were specified from the ECMWF forecast over the study area. The initial profiles were assumed to be horizontally homogenous. A large scale forcing of roughly 3 $cm\, s^{-1}$ representative of an average vertical velocity as given by the ECMWF analysis, was implemented throughout the simulation. This forcing featured the large–scale advection of cloudy air mass over the model domain, otherwise absent in the CRM due to the fact that the ECMWF fields were only given at the initial time and not updated during the course of the simulation. Without this forcing, it was verified that the CRM produced a much shallower cloud which did not thicken over time as the observations were showing.

5. COMPARISON BETWEEN MODEL AND OBSERVATIONS

Portions of the flight level data shown in figure 1 are reproduced in figures 5 and 4 along with the simulated radar reflectivity and lidar backscattering.

As anticipated, the model simulations of cloud variability do not match the observations in any quantitative detail. Besides the fact that the model cross–section and the data cross-section are not directly comparable as mentioned in the previous section, there are a number of other reasons why the structure of the predicted cloud differs from the observed cloud. The model initialization is horizontally homogeneous as is the forcing applied to the model during the simulation and, as such, it lacks of any mesoscale structure. Despite these obvious deficiencies, encouraging qualitative agreement of the modeled and the observed fields was found.

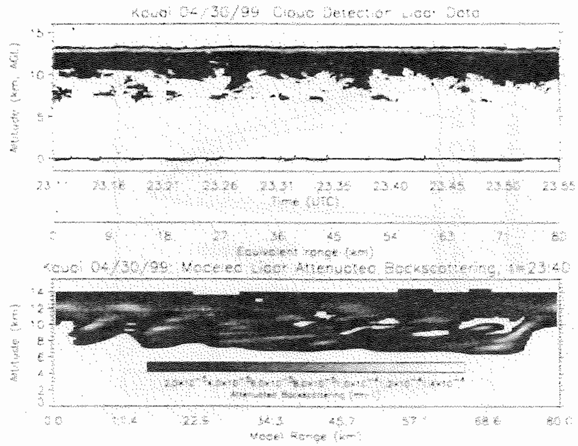

Figure 4: Observed versus modeled lidar backscattering.

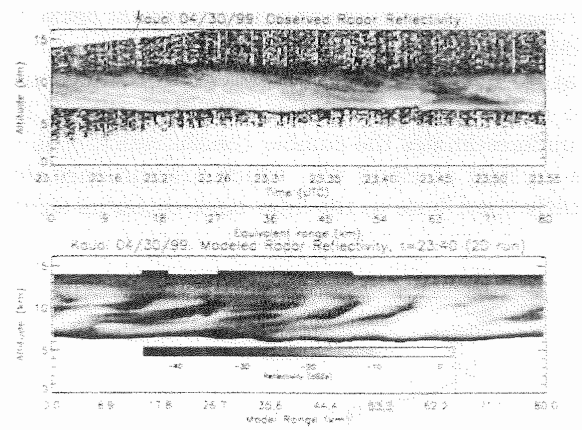

Figure 5: Observed versus modeled radar reflectivity.

More quantitatively meaningful is the comparison of the domain averaged model results with the average of the observations. Figure 6 shows the vertical profile of the measured radar reflectivity, averaged along the flight track over the period of time from 2311 and 2389UTC, along with average profiles derived from the ECMWF and the CRM Ice Water Content. The comparison shows a good degree of similarity betweeen both the ECMWF and CRM profiles and the profiles measured by the ACR.

Figure 7 shows a similar comparison for the av-

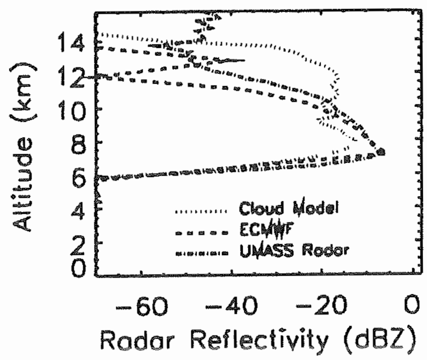

Figure 6: Domain averaged radar reflectivity: comparison betweeen observations, ECMWF and CRM results.

erage lidar backscattering profiles. The lidar is fully attenuated below 11 km and the agreement betweeen modeled and observed backscattering is worse than that for the radar. One possible explanation is that the model produces realistic bulk IWC values, but it underestimates the number concentration of small ice crystals at cloud top, which are the ones that mostly contribute to the lidar backscattering signal.

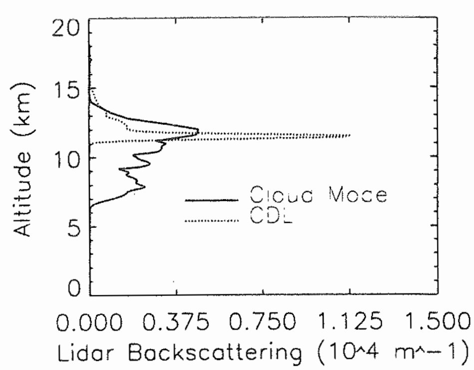

Figure 7: Domain averaged lidar backscattering: comparison betweeen observations and CRM results.

6. CONCLUSIONS

A study was conducted to test the capability of a Cloud Resolving Model to reproduce the observed characteristics of subtropical cirrus clouds as derived from radar and lidar measurements in the context of the ARM–UAV Spring 1999 field experiment over Kauai, Hawaii.

Results were shown for various fields which include the modeled radar reflectivity and lidar attenuated backscattering for the simulated cloud. Average profiles of radar reflectivity and lidar backscattering were also shown.

Comparisons with measurements show a good agreement between the modeled and the observed fields for the domain averaged profiles and the probability distribution functions. Quantitative comparisons are made difficult by the absence of mesoscale forcing in the model and the spatial dislocation between model and measurement cross–sections. Despite these inadequacies, when properly forced, the CRM seems capable of capturing the average features of the observed cirrus.

These results are relevant to the cloud modeling community in view of quantitative estimates of the performance of the models and for an error analysis. The results also demonstrate the usefulness of multisensor measurements of cloud properties in conjunction with numerical models to improve our knowledge of microphysical and radiative properties of cirrus clouds.

7. ACKNOWLEDGMENTS

The useful advice and material help of Steve Miller are gratefully acknowledged. This research was performed under NASA grants NCC5-288 and NAG5-6637.

REFERENCES

Platt. C.M.R., Young S.A., Manson P.J., Patterson G.R., Marsden S.C., and R.T. Austin, 1998: The optical properties of equatorial cirrus from observations in the ARM pilot radiation opbservation experiment, *J.Atmos.Sci.*, **55**, 1977–1996.

Sassen K. and L. Liao, 1994: Investigation of relationships between Ka–band radar reflectivity and ice and liquid water contents, *Atmos.Res.*, **34**, 231–248.

Stephens G.L., Ellingson R.G., Vitko J. Jr, Bolton W., Tooman T.P., Valero F.P.J., Minnis P., Pilewskie P., Phipps G.S., Sekelsky S., Carswell J.R., Miller S.D., Benedetti A., McCoy R.B., McCoy R.F. Jr, Lederbuhr A. and R. Bambha, 2000: The Department of Energy's Atmospheric Radiation Measurement (ARM) Unmanned Aerospace Vehicle (UAV) Program. Submitted to *B.Amer.Meteorol.Soc.*, February, 21 2000.

Walko R.L., Cotton, W.R., Meyers M.P. and J.Y. Harrington, 1995: New RAMS cloud microphysics parameterization. Part I: the single moment scheme. *Atmos.Res.*, **38**, 29–62.

ICE CLOUD DIABATIC PROCESSES AND MESOSCALE STRUCTURE IN FRONTAL ZONES

R.M. Forbes

Joint Centre for Mesoscale Meteorology, The Met. Office, U.K.

1. INTRODUCTION

There is clearly a need to understand the interactions between cloud microphysics and mesoscale structure in order to improve microphysical parametrizations in Numerical Weather Prediction (NWP) models. Microphysical processes can provide a significant source of latent heating and cooling in mid-latitude cyclones and this paper looks at the importance of one of these processes, ice evaporation, in determining mesoscale structure in developing frontal systems.

The hypothesis is that diabatic cooling due to the evaporation (and melting) of ice has a significant dynamical effect in frontal situations. Some authors have suggested that cooling from ice evaporation is an important mechanism for the enhancement of frontogenesis and rainband formation (Rutledge 1989, Clough and Franks 1991, Marecal and LeMaitre 1995). Others have shown the importance of cooling due to melting ice in frontal zones (Szeto et al. 1988, Szeto and Stewart 1997). It can be inferred from these and other studies that to forecast the development of mesoscale structure correctly, NWP models require a microphysical parametrization that produces an appropriate distribution of diabatic cooling. The dynamical importance of ice evaporation in mid-latitude cyclones needs to be better understood as well as the sensitivity of mesoscale structure to the formulation of the microphysics parametrization.

A microphysics parametrization sensitivity study is performed here using the Unified Model at mesoscale resolution (12km). Case studies are taken from the Fronts and Atlantic Storm Track Experiment (FASTEX), a major observational campaign over the North Atlantic during early 1997 (Joly et al. 1997). The effect of diabatic cooling due to ice evaporation in mid-latitude cyclones is investigated and a series of model experiments are performed to identify the sensitivity of cyclone development to terms in the parametrized microphysics scheme; the ice evaporation rate and ice particle terminal velocity. Results for FASTEX Intensive Observing Period (IOP) 16 are presented and the mechanisms for the sensitivity are discussed.

Corresponding author's address: Richard M. Forbes, JCMM, Meteorology Building, University of Reading, Reading,RG6 6BB,UK; E-mail:rmforbes@meto.gov.uk

2. MODEL DESCRIPTION

The sensitivity studies were performed with version 4.5 of the Unified Model (Cullen 1993) including a mixed-phase precipitation microphysics scheme (Wilson and Ballard 1999). The horizontal resolution was 0.105º (approximately 12km) with a rotated-pole limited area domain covering much of the North Atlantic. The model had 45 levels with a mid-troposphere resolution of about 25hPa. The initial field and lateral boundary conditions were taken from a coarser resolution model (50km) operational at the time of FASTEX. Using the analysis and boundary conditions from a lower resolution model ensures that all the higher resolution mesoscale structure in the sensitivity experiments develops during the forecast.

The Wilson and Ballard (1999) large scale cloud and precipitation scheme is a bulk microphysics scheme with prognostic liquid/vapour and ice variables. Figure 1 shows the four water variables used in the scheme and the transfer processes described by physically based equations.

3. THE FASTEX IOP 16 CASE STUDY

FASTEX IOP 16 was characterized by a fast moving rapidly deepening frontal-wave cyclone that developed in a pre-existing baroclinic zone. The system developed multiple fronts with associated cloud heads emerging from beneath the polar front cloud band. The reference 18 hour forecast of the system agrees well with observations on the synoptic scale but there are significant differences in the mesoscale structure.

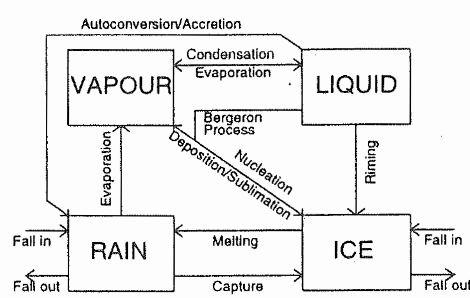

Figure 1 Schematic of mixed-phase precipitation scheme (from Wilson and Ballard, 1999).

4. RESULTS

4.1 Dynamical Impact of Ice Evaporative Cooling

To investigate the role of ice evaporative cooling in the development of the IOP 16 cyclone, a model experiment is performed in which the cooling due to evaporating ice is turned off (i.e. the ice is still allowed to fall and evaporate but the evaporation has no diabatic cooling effect). Although this is an unphysical experiment it highlights the importance of this process on the mesoscale dynamics of the system.

The results show only small differences in the track of the low (50km difference in position after 18 hours) and in the low centre depth (2hPa) but larger differences in the mesoscale structure. Figure 2 shows a plan view of the vertical velocity at 800hPa and the surface precipitation rate for the reference model forecast and the forecast with no ice evaporative cooling after 18 hours. The effect of the cooling is most significant in the cold frontal troughs. In particular the main cold frontal trough-ridge-trough structure is very weak without evaporative cooling (Fig. 2b).

Figure 3 shows a vertical cross section across the low centre and trough to the north-west (along the line marked in Fig. 2) with the heating/cooling rate due to ice deposition/evaporation in the reference forecast

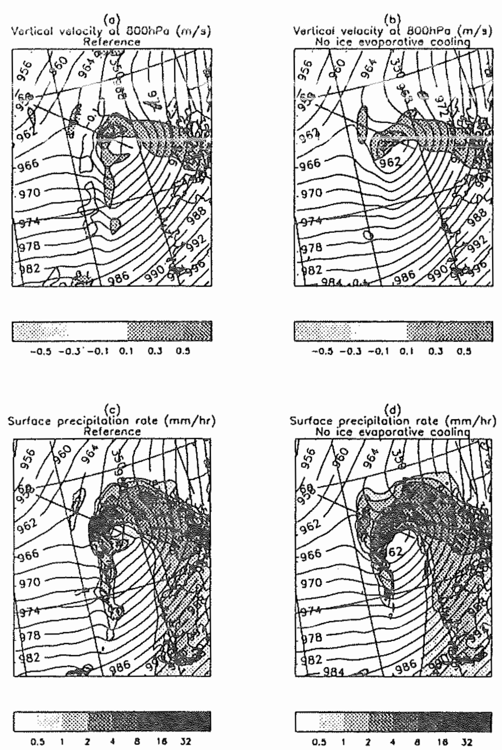

Figure 2 *Plan view of vertical velocity at 800hPa and surface precipitation rate for the reference forecast and the forecast with no evaporative cooling after 18 hours.*

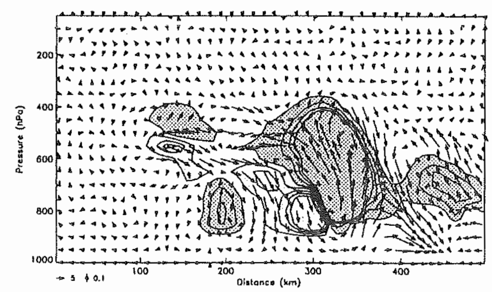

Figure 3 *Vertical cross-section (along the line marked in Fig. 2) showing the ice evaporation rate (light shading) and ice deposition rate (dark shading) from the reference forecast (contours at 0.2, 0.6, 1.0 and >1.4 K/hr). Arrows show the wind difference (m/s) between the reference and the no evaporative cooling forecast.*

and the wind vector difference between the two model forecasts. In the region of evaporative cooling there is strong descent in the reference forecast which extends to the surface and diverges to produce two regions of increased convergence either side. This low-level convergence acts to reinforce the initial updraught (at 350km) as well as strengthen the secondary frontal updraught (at 200km). Along the length of both the cold and warm fronts the downdraughts below the frontal cloud bands are significantly weaker or non-existent in the forecast with no ice evaporative cooling. This supports the hypothesis that ice evaporation does play an important role in the formation of mesoscale structure and can lead to the enhancement of frontal rainbands.

To investigate the relative importance of melting a similar experiment with the cooling due to melting ice turned off was performed. However, for this cyclone the effects on the mesoscale structure were much weaker and less coherent.

The ice evaporative cooling sensitivity experiment illustrates that changes to the microphysics parametrization that affect the amount of evaporative cooling will change the mesoscale dynamics of the system through the mechanism described. Such changes to the microphysics parametrization are investigated in the following sections.

4.2 Sensitivity to Ice Deposition/Evaporation Rate

The rate of change of mass of a single ice particle due to vapour deposition or evaporation can be written as

$$\frac{\partial m}{\partial t}=\frac{4\pi C(S_i-1)F}{\left(\frac{L_s}{RT}-1\right)\frac{L_s}{k_aT}+\frac{RT}{Xe_{si}}} \qquad (1)$$

where C is the capacitance term, $(S_i\text{-}1)$ is the supersaturation of the atmosphere with respect to ice, F is the ventilation coefficient, R is the gas constant for water vapour, L_s is the latent heat of evaporation of ice, X is the diffusivity of water vapour in air, e_{si} is the saturated vapour pressure over ice and k_a is the thermal conductivity of air at temperature, T. The ice particles are assumed to be spheres so the capacitance, C, is equal to the particle radius, $D/2$. The rate equation is integrated over the ice particle size spectrum to give a bulk rate of change of ice mixing ratio.

The main uncertainties in Equation (1) are in the assumption of the sub-gridscale heterogeneity, and the capacitance and ventilation terms which depend on ice crystal habit. The model does not represent different habits (all ice crystals are assumed to be spherical), so these two terms are likely to introduce some error into the model. The ventilation coefficient, F, is dependent on the terminal velocity and length scale of an ice crystal. For an ice particle with a length scale of 1mm, the ventilation coefficient can differ by a factor of up to two depending on the assumption of crystal habit (Hall and Pruppacher, 1976). For example, bullet rosettes have twice the ventilation coefficient of dendrites, partly due to the higher terminal velocity but also to the higher characteristic length scale. The capacitance term, C, also depends on the length scale and morphology of an ice crystal and can vary by a factor of two between bullet rosettes and columns, essentially because of the larger diameter to mass ratio.

Each of these factors will vary with location (both horizontally and vertically) but it is conceivable that there is also a systematic error in the parametrization of the ice deposition/evaporation rate equation and therefore reasonable to look at the sensitivity of the model to changes to this term. Two integrations in which the deposition/evaporation term is multiplied by 0.5 and 2.0 are performed to investigate this sensitivity.

The results show the largest sensitivity in the system to be in the cold front trough-ridge-trough structure (Figure 4). As the multiplication factor in the deposition/evaporation rate is increased the low

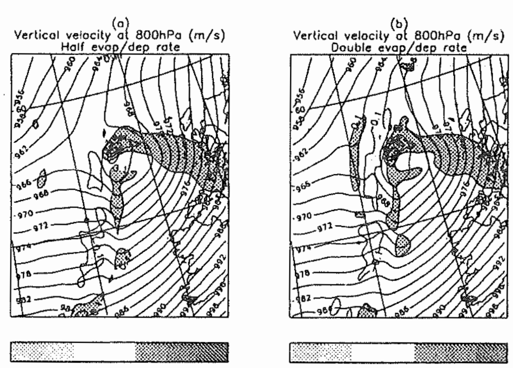

Figure 4 *Plan view of vertical velocity at 800hPa for the forecasts with half and double the deposition/evaporation rate after 18 hours.*

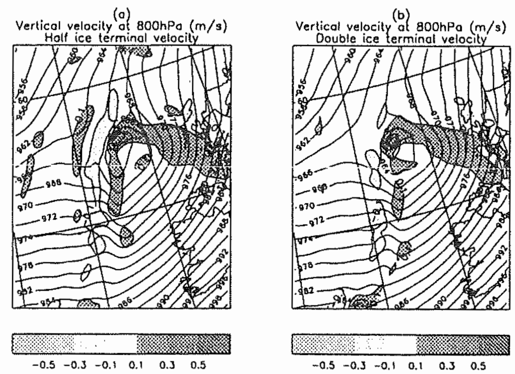

Figure 5 *Plan view of vertical velocity at 800hPa for the forecasts with half and double the ice terminal velocity after 18 hours.*

centre and frontal updraughts are slightly stronger, but the most significant difference is in the increased strength of the downdraught beneath the primary cold front and the substantial increase in the development of the secondary cold front to the west.

4.3 <u>Sensitivity to Ice Particle Terminal Velocity</u>

The fall speed of an ice crystal, v, is parametrized in the model as a function of ice crystal diameter, D:

$$v(D) = cD^{d} \qquad (2)$$

where $c = 25.2m^{0.473}\,s^{-1}$ and $d = 0.527$ at a pressure of 1000hPa, and the mass, m, is defined as

$$m(D) = aD^{b} \qquad (3)$$

where $a = 0.069$ kg m^{-3} and $b = 2.0$. The bulk (mass-weighted) fall speed is calculated for each grid point by integrating the above equations over the ice crystal spectrum. Ice crystal fall speed strongly depends on the morphology of an ice particle and there can be significant sub-grid scale variability and a wide spectrum of particle sizes and crystal types falling at different fall speeds. For example the fall speed of ice crystal columns can be up to four times that of dendrites of a similar size (Heymsfield 1972; Kajikawa 1972). The present bulk parametrization in the model does not include the crystal habit or the sub-grid variability in a detailed way and there is certainly scope for improving the fall of ice in the model. To investigate the sensitivity of the model to ice crystal fall speed two integrations are performed in which the coefficient, c, is halved and doubled.

The results show a similar magnitude and pattern of sensitivity to the deposition/evaporation rate equation experiment. As the terminal velocity is reduced, the cold front trough-ridge-trough structure weakens substantially (Figure 5). The direct impact of the change in the ice particle terminal velocity is the change in the amount of ice. The ice content behaves as expected from the mass flux divergence argument; if the ice production term remains the same then doubling the terminal velocity results in roughly half the amount of ice in the model. The deposition/evaporation rate (Eqn. 1) depends on the amount of ice in a grid box, so doubling the terminal velocity will result in reduced deposition and evaporation rates. This leads to reduced ascent in the updraughts and reduced descent in the downdraughts. The consequence of this is to modify the development of the frontal flows through the mechanism described in section 4.1.

5. CONCLUDING DISCUSSION

The aim of this work is to understand the importance of ice evaporative cooling on frontal system mesoscale dynamics and identify the issues for microphysical parametrization development in mesoscale NWP models. It is shown that ice evaporation beneath sloping frontal updraughts has a significant impact on the development of frontal rainbands for a rapidly developing mid-latitude cyclone during FASTEX IOP 16. Plausible variations to the ice deposition/evaporation rate and ice particle terminal velocity in the microphysical parametrization affect the amount of evaporative cooling and lead to significant differences in the evolution of the frontal bands. Some of the issues and directions for future work are highlighted below:

- The purpose of this study is to determine and understand the sensitivity of the model forecasts to aspects of the microphysical parametrization. If this is combined with the identification of systematic errors in the forecasting of mesoscale structure in mid-latitude cyclones by validation against observations, then this may provide enough information to refine the parametrization to improve forecasting of such systems

- The generality of the results for FASTEX IOP 16 first needs confirming and further case studies showing the sensitivity to microphysical parameters are required. These will be performed for other FASTEX IOPs.

- Heating from condensation immediately ahead of a front and cooling from evaporation behind are important in maintaining the density contrast across the front, and can lead to enhanced frontogenesis. Slantwise potential vorticity sheets generated by the heating/cooling dipole may also play a role in the maintenance and formation of frontal bands and the occurrence of symmetric instability will be affected by these diabatic processses. The relative importance of these mechanisms in mid-latitude frontal zones will be investigated.

Study of the interactions between microphysical processes and mesoscale dynamics brings together work on cloud processes, forecasting and weather system dynamics and provides physical insight into the development of mesoscale structure in mid-latitude cyclones. It is essential to understand these interactions to improve the microphysical parametrizations in the current generation of NWP models.

Acknowledgements

The author would like to thank Nigel Roberts, Humphrey Lean and Peter Clark at the Joint Centre for Mesoscale Meteorology for valuable discussions on the observational and modelling aspects of the IOP 16 case study.

References

Clough, S. A., Franks, R. A. A., 1991: The evaporation of frontal and other stratiform precipitation. *Quart. J. Roy. Meteor. Soc.*, **117**, 1057-1080.

Cullen, M. J. P., 1993: The unified forecast/climate model. *Meteor. Mag.*, **122**, 81-94.

Hall, W. D., and Pruppacher, H. R., 1976: The survival of ice particles falling from cirrus clouds in subsaturated air. *J. Atmos. Sci.*, **33**, 1995-2006.

Heymsfield, A. J., 1972: Ice crystal terminal velocities. *J. Atmos. Sci.*, **29**, 1348-1357.

Joly, A., et al., 1997: The Fronts and Atlantic Storm-Track Experiment (FASTEX): Scientific Objectives and Experimental Design. *Bull. Amer. Meteor. Soc.*, **78**, 1917-1940.

Kajikawa, M., 1972: Measurement of falling velocity of individual snow crystals. *J. Meteor. Soc. Japan*, **50**, 577-584.

Marecal, V., Lemaitre, Y., 1995: Importance of microphysical processes in the dynamics of a CSI mesoscale frontal cloud band. *Quart. J. Roy. Meteor. Soc.*, **121**, 301-318.

Rutledge, S. A., 1989: A severe frontal rainband Part IV: precipitation mechanisms, diabatic processes and rainband maintenance. *J. Atmos. Sci.*, **46**, 3570-3594.

Szeto, K. K., Lin, C. A., Stewart, R. E., 1988: Mesoscale circulations forced by melting snow. Part I: Basic simulations and dynamics. *J. Atmos. Sci.*, **45**, 1629-1641.

Szeto, K. K., Stewart, R. E.,1997: Effects of melting on frontogenesis. *J. Atmos. Sci.*, **54**, 689-702.

Wilson, D. R., Ballard, S. P., 1999: A microphysically based precipitation scheme for the UK Meteorological Office Unified Model. *Quart. J. Roy. Meteor. Soc.*, **125**, 1607-1636.

MICROPHYSICAL FEATURES IN TROPICAL CLOUDS

J. Stith, J. Dye, A. Heymsfield[1] and C. A. Grainger[2]

[1]National Center for Atmospheric Research, Boulder, CO
[2]University of North Dakota, Grand Forks, ND

1. INTRODUCTION

Airborne data on cloud particle types and sizes were collected in convective and stratiform clouds during three Tropical Rainfall Measuring Mission (TRMM) field campaigns. The locations for the campaigns were Eastern Florida (September 1998), Rondonia, Brazil (January and February 1999) and Kwajalein, Marshall Islands (August and September 1999). In this paper we describe some of the major microphysical features of the convective and stratiform regions and compare the results from the different areas.

The airborne measurement program was designed to obtain data on the location, sizes and types of hydrometeors, so that the algorithms used to determine rainfall from the TRMM satellite could be evaluated and improved. One of the major goals of the TRMM program is to use the satellite-measured rainfall in the tropics to predict the vertical heating profile. The Goddard Cumulus Ensemble Model (GCE) is used to derive vertical profiles of hydrometeors and to relate this information to the profile of vertical heating rate (Tao, et al., 1990 and references therein). These vertical hydrometeor profiles are also used for passive microwave rainfall retrievals (Kummerow, 1998).

Below we briefly describe the instruments and measurement strategy, present examples that illustrate the characteristics of convective and stratiform regions, and discuss the results in light of the TRMM program.

2. INSTRUMENTATION AND MEASUREMENT STRATEGY.

Aircraft instrumented for in situ cloud physics measurements were used during the TRMM field campaigns to measure hydrometeors at various altitudes. Sampling was conducted in regions sampled by Doppler radar, the TRMM satellite, and by remote sensors on the NASA DC-8 and ER-2 aircraft.

Corresponding author address: Jeffrey Stith, NCAR, Box 3000, Boulder CO 80303. Stith@ucar.edu.

In this paper we present measurements from the University of North Dakota Citation aircraft, which was used during each of the three campaigns. Future analyses of TRMM data will include combined data from all the TRMM cloud physics aircraft, and a fourth TRMM field campaign in Texas during 1998.

The Citation was equipped with a rather complete set of instruments for measuring cloud particle types and sizes. These included a Cloud Particle Imager (CPI) and a High Volume Particle Sampler (HVPS) from SPEC Inc. A set of Particle Measuring Systems (PMS) instruments included a FSSP-100, a 2DC (32 micron diode spacing), a 1DC (Kwajalein) and a 1DP (Florida and Brazil). The Citation also carried an INS/radome gust probe for wind and turbulence measurements and standard sensors for liquid water (PMS version of King liquid water instrument), temperature, dewpoint, pressure and location (GPS and INS). This paper presents the results from the PMS probes. Data from the CPI and HVPS are presented in this conference in Heymsfield et al (this conference). Work is currently in progress to merge and compare the data from the various probes.

Aircraft flight patterns included spiral ascents and descents (see Heymsfield, et al, this conference) and horizontal legs stepping up or down through different temperatures. These patterns were flown in both convective and stratiform regions, although spirals were mostly limited to stratiform cloud regions.

3. RESULTS

3.1 Convective Cloud Regions

Table 1 presents some examples of the measurements made in convective clouds associated with several of the case studies during the field campaigns. Convection was classified as strong if updrafts were measured in excess of 10 m s^{-1} and moderate otherwise. (Because only precipitating clouds were sampled, weak convection was not sampled.)

Table 1. Examples of Tropical Convective Cloud Features

Date	Location	Type	Temp. Range (°C)	Peak Liquid Water (g m^{-3})	2DC Conc. ($liter^{-1}$)	FSSP Conc. (cm^{-3})	Precipitation Particle Observations
14 Sept. 1998	Eastern Florida	Strong	-5 to -12	1.3 at -5 °C	280 at –10 °C	234 at –7 °C	Supercooled large (mm) Drops and partially rimed small drops
26 Jan. 1999	Brazil	Strong	+6 to -2	3.4 at +6 °C	205 at -2 °C	463 at +6 °C	Drizzle Drops
13 Feb. 1999	Brazil	Strong	-5 to -12	1.0 at –5 °C	115 at -5 °C	220 at -10 °C	Rimed frozen large (mm) droplets
23 Feb. 1999	Brazil	Moderate	-7 to -18	1.2 at –7 °C	306 at –18 °C	187 at -7 °C	mm Graupel
19 Aug. 1999	Kwajalein	Moderate	+4 to -23	1.0 at 0 °C	310 at -11 °C	NA	Aggregates and particles with various amounts of riming

Only a few of the potential case studies have been examined to-date; however, several features are evident in this limited sample. The highest liquid water contents were observed at temperatures warmer than freezing and reached just over 3 g m^{-3}. Significant liquid water (above 0.5 g m^{-3}) was observed at temperatures below freezing (as cold as –10 °C), but it did not persist for long, as most colder cloud regions with liquid water glaciated quickly, or had developed precipitation. In the stronger storms frozen droplets were commonly observed in mm size ranges. These were identified by nearly round shapes in the 2DC imagery. These most likely became graupel as riming progressed. For the 14 Sept. case, raindrops were observed at –8.5 °C. The moderate clouds exhibited fewer or smaller images that might be classified as frozen droplets. A higher proportion of aggregates was found in the Kwajalein case than in stronger convection.

Droplet concentrations similar to typical continental clouds were observed at warmer temperatures in Brazil. At colder temperatures, droplet concentrations were less, but these lower values were usually found in the presence of precipitation, suggesting that significant numbers of droplets may have been removed by accretion. In all cases examined to-date, precipitation free regions were scarce and limited to warmer temperatures or small regions of the cloud. This is consistent with the expected rapid collision coalescence process.

An example of the development of precipitation is given by the measurements made on 26 January 1999 in Brazil (Figures 1 and 2). These measurements were made near the top of growing turrets that were part of a developing line associated with a strong convective storm with radar reflectivity greater than 50 dBZ.

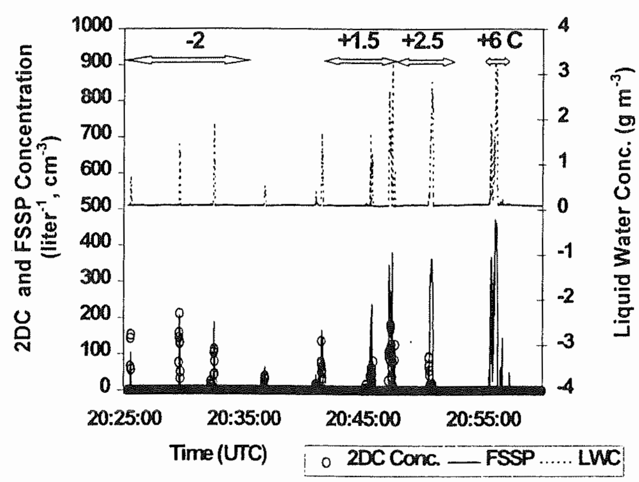

Figure 1. The concentrations of liquid water, cloud droplets (FSSP), and large particles (2DC) near the top of a Brazilian convective cloud on 26 January, 1999. A maximum updraft of 15 m s-1 was measured at 20:50:46

Droplet concentrations and liquid water were highest during the pass at + 6 °C, where large particles (as measured by the 2DC) were nearly absent. At the colder temperatures the larger particles were evident and liquid water and small cloud droplets had decreased. Examination of the 2DC imagery (Fig. 2) revealed that drizzle droplets had formed between + 6 °C and 1.5 °C, and had grown slightly at – 2 °C. Thus, for this cloud, the development of drizzle took place between +6 and 1.5 °C.

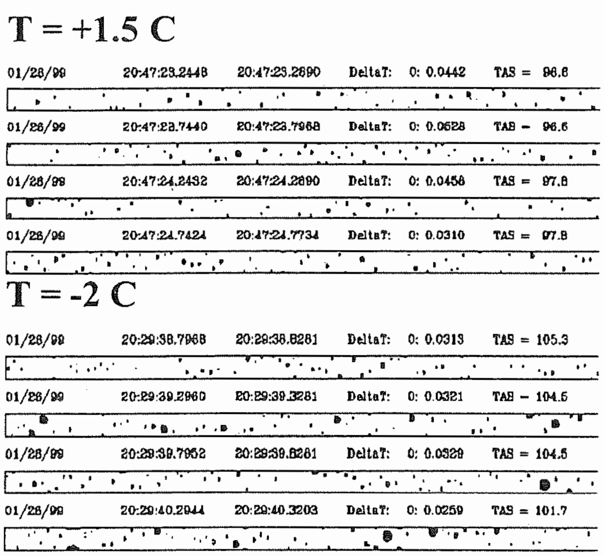

Figure 2. Examples of 2DC imagery illustrating the development of drizzle sized droplets on 26 January 1999 in Brazil. The distance between the bars is 1.024 mm.

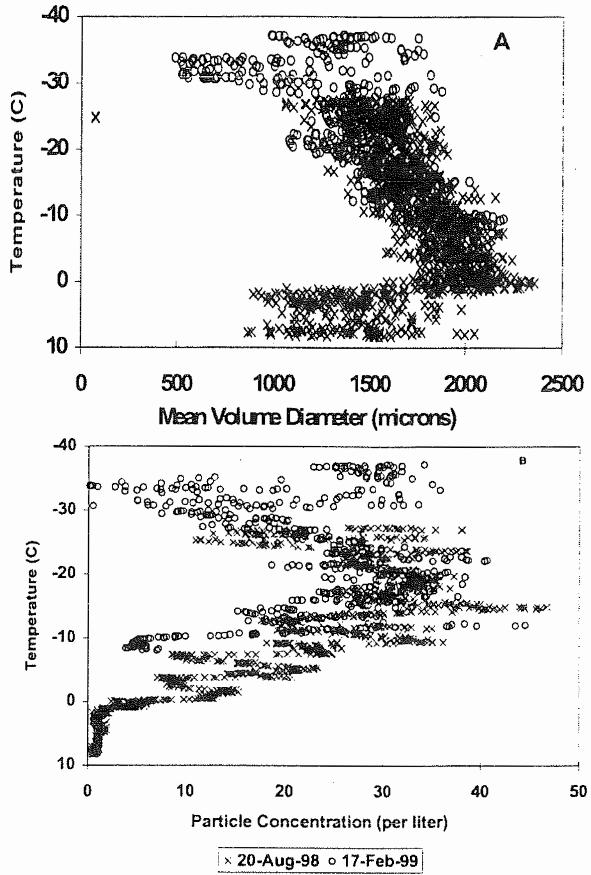

Figure 3. The mean volume diameter (a) and concentrations (b) of particles larger than 300 microns on 20 August 1998 (Florida) and 17 February (Brazil). Spirals through the cloud were used to collect the data.

3.2 Stratus Clouds

Spirals through stratiform regions were used to develop vertical profiles of hydrometeors. An example of the results from two spirals on 20 August 1998 and 17 February 1999 is given in Figure 3. Both of these clouds were stratiform anvils associated with major convective storms. Steady growth of precipitation size particles is evident proceeding from colder to warmer temperatures, until particles melt below the freezing level (Fig. 3 a) The highest concentrations of precipitation sized particles is observed in the middle regions of the cloud between –10 to –25 °C (Fig. 3. b). Contrary to the model results of Tao, et al (1990), as discussed below, aggregates were the primary particle type, with some individual crystals also observed in the upper portions of the cloud. Significant liquid water was not observed. Graupel was not found in the 2D images.

4. DISCUSSION

Tao et al. (1990) used a composite sounding from three GATE squall-type Mesoscale Convective Systems as input to the GCE. The model output provided vertical profiles of hydrometeors for convective and stratiform regions, which was then used to derive vertical heating profiles. Their results are reproduced in Fig. 4. The techniques described in Heymsfield et al. (this conference) were used to determine mass mixing ratios of precipitation particles. These were then smoothed by a 150 s moving average. These observations are compared with the total mass mixing ratio from Tao et al. in Fig. 5.

The comparison between the observations and the model are reasonably good, given the uncertainties in estimating mass concentration from the image data. However the major particle type in the simulation was graupel, a species that

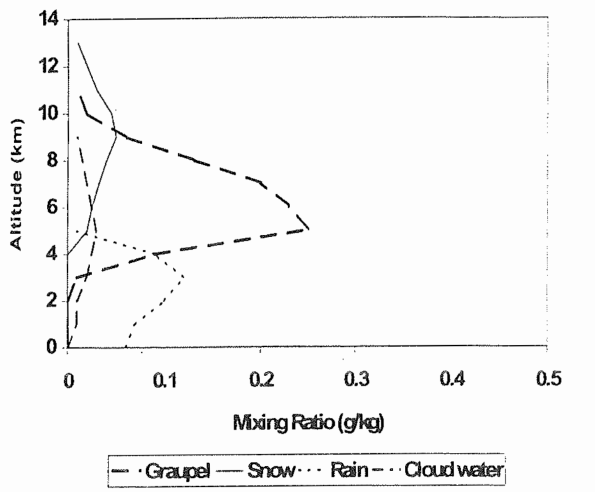

Figure 4. The modeled mixing ratios of hydrometeors for the Mature Anvil stratiform case of Tao et al. (1990).

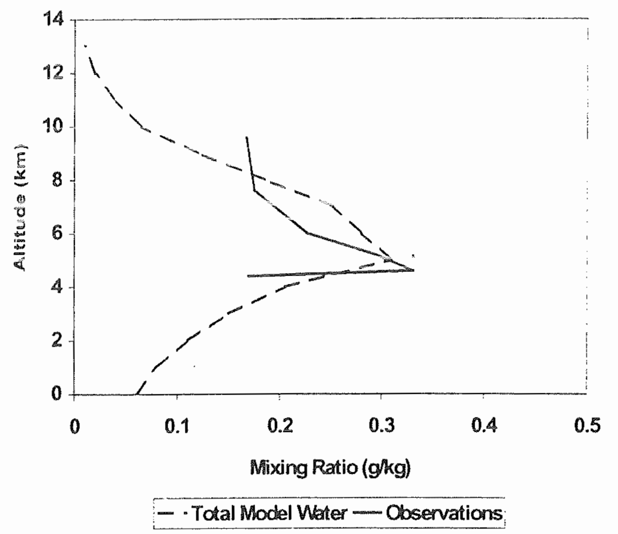

Figure 5. Comparison of the total hydrometeor mixing ratio from the model data in Fig. 4, against mixing ratios estimated from the measurements on 17 August. Most of the mass above the freezing level in the observations was due to aggregate snowflakes.

was not found in significant numbers in the observations for 17 Feb., 20 Aug. or a third stratiform case in Kwajalein on 28 Aug, 1999. The particle type not only affects the computation of vertical heating rate, but also plays an important role in the passive microwave precipitation retrievals used in TRMM.

The liquid water instrument was not able to resolve the concentrations of liquid water predicted by the model, due to interference from ice particles; however a Rosemount icing detector, did not detect significant supercooled water.

The mean sizes and concentrations of precipitation in anvils associated with convective storms on 20 Aug. and 17 Feb. showed rather similar profiles (Fig. 3). The presence of aggregates and low liquid water in these anvil clouds is similar to observations made elsewhere in tropical regions (e.g. Houze and Churchill, 1987; McFarquhar and Heymsfield, 1996). This suggests that the profiles of hydrometeors in Tao et al (1990), may contain too high a percentage of graupel and cloud water for their mature anvil (Fig. 4) or their decaying anvil (not shown) stratiform cases. This is likely to significantly affect the rainfall retrieval algorithms and the calculation of vertical heating.

Future work will combine data from the various probes and instrument platforms for the rest of the TRMM cases, to develop more robust microphysical characterizations of tropical clouds and to improve the TRMM hydrometeor profiles for convective and stratiform clouds.

5. ACKNOWLEDGEMENTS

Thanks are due to Steve Spears and the field crew for help in data collection. The data collection was supported by the TRMM program office through NASA cooperative agreement NCC5-193. The National Center for Atmospheric Research is sponsored by the National Science Foundation.

REFERENCES

Houze, R. A. and D. D. Churchill, 1987: Mesoscale organization and cloud microphysics ina a Bay of Bengal depression, *J. Atmos. Sci*,., **44**, 1845-1867.

Kummerow, C, 1998: Beamfilling errors in passive microwave rainfall retrievals. *J. Appl. Meteor.*, **37**, 356-370.

McFarquhar, G. M and A. J. Heymsfield, 1996: Microphysical characteristics of three anvils sampled during the central equatorial pacific experiment. *J. Atmos. Sci.*, **53**, 2401-2423.

Tao, W. K., J. Simpson, S. Lang. M. McCumber, R. Adler and R. Penc, 1990: An algorithm to estimate the heating budger from vertical hydrometer profiles. *J. Appl. Meteor.*, **29**, 1232-1244.

REMOTE SENSING OF TROPICAL STORM ANVILS – DETECTION OF STRONG COOLING AT ANVIL CLOUD BASE

C. M. R. Platt, R. T. Austin[1], S. A. Young[2], and A. J. Heymsfield[3].

[1]Colorado State University, Fort Collins, Colorado, 80523.
[2]CSIRO, Atmospheric Research, Aspendale, 3195, Australia.
[3]National Centre for Atmospheric Research, Boulder, Colorado

1. INTRODUCTION.

The aim of the CSIRO/University of Massachusetts (UMASS) component of the Maritime Continent Thunderstorm Experiment (MCTEX, Keenan et al., 2000) was to observe cirrus clouds and to determine their optical properties by the Lidar/radiometer (LIRAD) method. During the experiment, several thunderstorm anvils were also sampled. Infrared emittances were calculated by the methods described in Platt et al. (1998) and previous papers.

This paper describes and interprets some observations and analyses of an anomalous phenomenon of depressed emittance at cloud base. The experiment took place on Melville Island, Tiwi islands, Northern Territory Australia and is described in Platt et al. (2000a). Lidar (0.532 μm), IR radiometry (10.86±0.5 μm), microwave water vapour radiometry and millimetre radar (33 and 94 GHz) were used to sample the clouds. The instruments were sited close together and all sounded in the vertical.

2. OBSERVATIONS AND RESULTS.

Several anvils were observed on different days to drift over the site and subsequently dissipate. The most striking observation was that the calculated IR emittance had maximum values lying between 0.8 and 0.9, even when the anvil was known from lidar returns to be extremely attenuating to visible and IR radiation.

The above phenomenon was interpreted as a cooling near cloud base due to strong evaporation. The emittance was calculated from local radiosonde temperature and humidity data taken about 3 hours apart.

Corresponding author address: 47 Koetong Parade, Mt. Eliza, VIC, 3930, Australia. Email: mplatt@net2000.com.au

The emittance depression was converted into a corresponding temperature decrease, ΔT_m, below the radiosonde temperature, T_a:

$$\Delta T_m = T_a - f(\varepsilon_\lambda, T_a) \qquad (1)$$

Where ε_λ was observed (depressed) spectral emittance and f represents the measured brightness temperature. Values of ΔT_m from (1) for an anvil on November 27,1995,are shown in Figure 1. The cooling is seen to be quite appreciable. In order to assess whether this cooling was possible

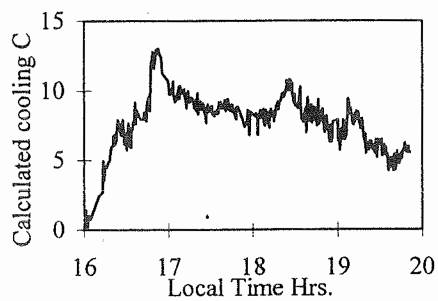

Figure 1. Temperature reduction ΔT_m at cloud base compared to radiosonde temperature.

physically, a simple model of evaporation into sub-saturated air, and subsequent moistening to saturation was used. The calculations gave the values shown in Figure 2. The measured values are seen to be somewhat greater than those predicted, but they are of the right order. Two reasons for the differences might be the lack of representativeness of the radiosonde humidity below cloud base, and the effects of cooling on atmospheric buoyancy with further descent, leading to Mammata.

Now some anvil emittance data taken previously at a site near Darwin (125 km SE of the MCTEX site) with the LIRAD method (Platt et al, 1984) gave very similar results, with maximum emittance in the 0.7 to 0.9 regions at anvil cloud base. Figure 3 shows emittance histograms for the Darwin results. It was observed that the anvils in the region of maximum emittance, were strongly attenuating to lidar pulses.

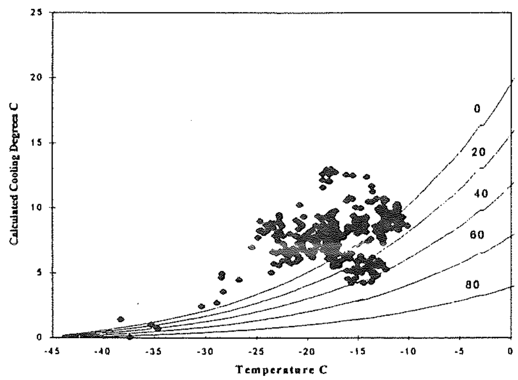

Figure 2. Calculated cooling (full lines) and observed cooling (points) at anvil cloud base.

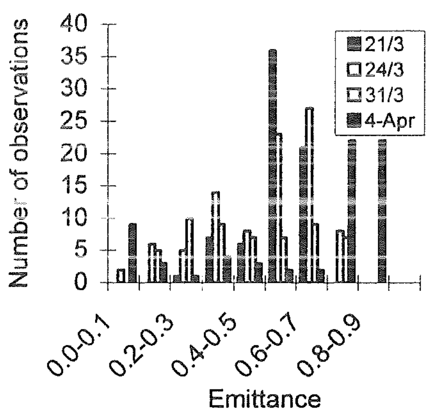

Figure 3. Histogram of numbers of observations of various values of emittance on anvil cloud bases measured in Darwin (Platt et al., 1984)

It was also found that profiles of radar reflectivity at 95 GHz from the anvil of November 27 indicated a rapid fall-off near cloud base. Using the maximum reflectivity as a measure of maximum ice water content (Sekelsky et al., 1999), it can be shown that the radar data yielded similar magnitudes of cooling, at least within a factor of two.

The observed cooling near anvil cloud base has been predicted for years, but to the authors' knowledge, has never been observed directly.

Full details of the method will appear in Platt et al. (2000b). Future LIRAD observations of the thermal environment at anvil base, particularly those made remotely, from US Department of Energy Atmospheric Radiation Measurement (ARM) sites, will give a better understanding of the storm anvil hydrological and convective cycles.

3. ACKNOWLEDGMENTS

The U. S. Department of Energy, Office of Health and Environmental Research, Grant No's DE-FG02-92ER61373 and DE-FG03-9461748, funded the field observations and part salaries.

4. REFERENCES.

Keenan, T., and Co-authors, 1994: Science Plan for the Maritime Continent Thunderstorm experiment (MCTEX). BMRC Research Rep. 44, BMRC, Melbourne, Victoria, Australia, 61 pp. [Available from Bureau of Meteorology, BMRC, P. O. Box 1289k, Melbourne, Victoria 3001, Australia].

Platt, C.M.R., A.C. Dilley, J.C. Scott, I. J. Barton, and G.L. Stephens, 1984: Remote sounding of high clouds, V: Infrared properties and structure of tropical thunderstorm anvils. *J. Clim. and Appl. Meteor.*, **23**, 1296-1308.

Platt, C. M. R., S. A. Young, P. J. Manson, G. R. Patterson, S. C. Marsden, R. T. Austin and J. Churnside, 1998: The optical properties of equatorial cirrus from observations in the ARM Pilot Radiation Observation Experiment. *J. Atmos. Sci.*, **55**, 1977-1996.

Platt, C. M. R., R. T. Austin, S. A. Young, and G. R. Patterson, 2000a: LIRAD observations of tropical clouds in MCTEX. Part I: Optical properties and parameterisation of tropical cirrus. *J. Atmos. Sci., (Submitted for publication).*

Platt, C. M. R., R. T. Austin, S. A. Young, and A. J. Heymsfield, 2000b: LIRAD observations of tropical cirrus clouds in MCTEX. Part III. Optical properties and base - cooling in dissipating storm anvil clouds. *J. Atmos. Sci., (Submitted for publication).*

Sekelsky, S. M., Ecklund, W. L., Firda, J. M., Gage, K. S., and McIntosh, R. E., 1999: Particle size estimation in ice-phase clouds using multi-frequency radar reflectivity measurements at 95 GHz, 33 GHz, and 2.8 GHz. *J. Appl. Meteor.*, **38**, 5-28.

KINEMATIC AND MICROPHYSICAL STRUCTURES OF HURRICANE BOB (1991) DETERMINED FROM A 1.3-KM-RESOLUTION NUMERICAL SIMULATION

Scott A. Braun, Joanne Simpson, and Wei-Kuo Tao

NASA/Goddard Space Flight Center, Greenbelt, MD, USA

1. Introduction

Numerical simulations of tropical cyclones are being conducted at increasingly higher grid resolution, often reaching horizontal grid spacings of ~5 km (Liu et al. 1997; Braun and Tao 2000). While use of this grid scale removes the necessity for parameterizing the effects of cumulus clouds, it is still not fully adequate for resolving cloud-scale processes. In this study, we present a simulation of Hurricane Bob (1991) that uses a horizontal grid spacing of 1.3 km, which is typical of grid spacings used in most cloud-resolving models. Basic kinematic and thermodynamic structures are described.

2. Model Setup

The PSU—NCAR mesoscale model MM5 was used to conduct a 72-h simulation of Hurricane Bob using a 36-km grid. Initial and boundary conditions for this grid were obtained from ECMWF analyses. High-resolution simulations were conducted by using 1-h output from the 36-km grid to provide initial and boundary conditions for the 12 and 4-km grids beginning at hour 48 of the 72-h control run. The 1.3-km grid was active between 62-68 h. Physics options for the fine-grid simulations include the Betts-Miller cumulus parameterization (12-km grid), the Goddard Cumulus Ensemble (GCE) model cloud microphysics, and the Burk-Thompson PBL scheme.

3. Results

Figure 1 shows the simulated radar reflectivity at t=66 h (4 h into the 1.3-km grid simulation). The simulation produces a strong eyewall, with a radius of about 40 km, and a principal rainband extending from north to east at a radius of about 90 km. Considerable small-scale structure is apparent, particularly in the rainband, which is composed of many small convective elements.

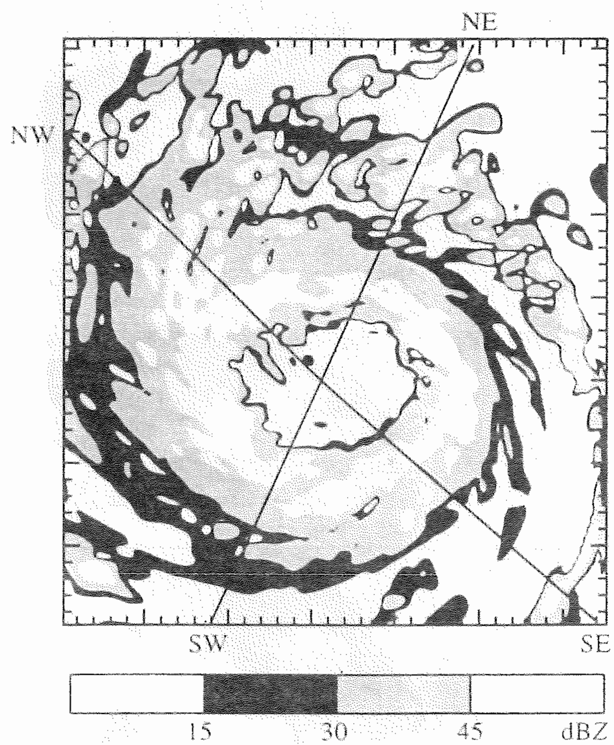

Figure 1. Simulated radar reflectivity at 66 h and 1 km MSL. Solid lines indicate locations of cross sections. Tick marks are drawn every 5 grid points (~6.7 km)

Vertical cross sections (Fig. 2) extending from the center (see Fig. 1) are examined in order to describe the variability of vertical motions and precipitation structure around the storm. The cross section to the NE (Fig. 2a) cuts through both the eyewall and the principal rainband. Updrafts in the eyewall extend from the boundary layer to the upper troposphere, with peak values slightly greater than 4 m s^{-1} near 3 km. In the rainband, vertical motions exceed 4 m s^{-1} and are accompanied by strong convective downdrafts. Reflectivities exceeding 45 dBZ extend upward to 5 km in the eyewall and about 8 km

Corresponding Author: Scott A. Braun
NASA/GSFC, Code 912, Greenbelt, MD 20771, USA. Email: braun@agnes.gsfc.nasa.gov

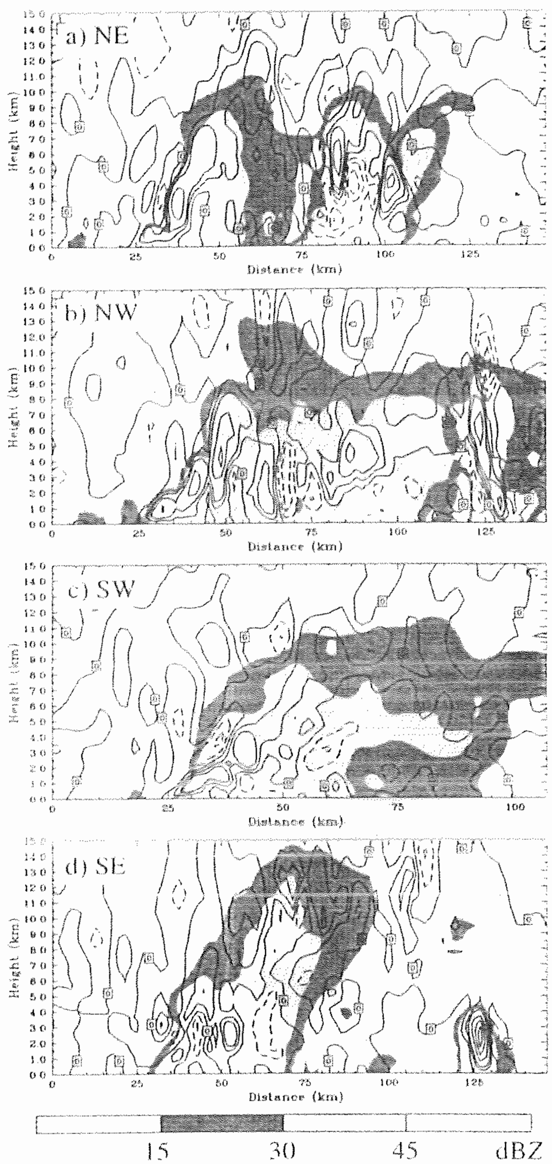

Figure 2

Figure 2. Vertical cross sections of reflectivity (shaded) and vertical velocity, w, (contours, 1 m s^{-1} intervals for $w < 2$ m s^{-1} and 2 m s^{-1} intervals for $w > 2$ m s^{-1}).

in the rainband. In the NW cross section (Fig. 2b), vertical motions in the eyewall are up to 6 m s^{-1}. Near a radius of 125 km, a strong convective rainband tilts upshear (in terms of the radial velocity component), with strong downdrafts at upper and lower levels. Between the eyewall and the convective band, the precipitation is a mix of convective and stratiform precipitation. Some of this stratiform rainfall is likely from advection of hydrometeors from the principal rainband to the north and east of the center. To the SW

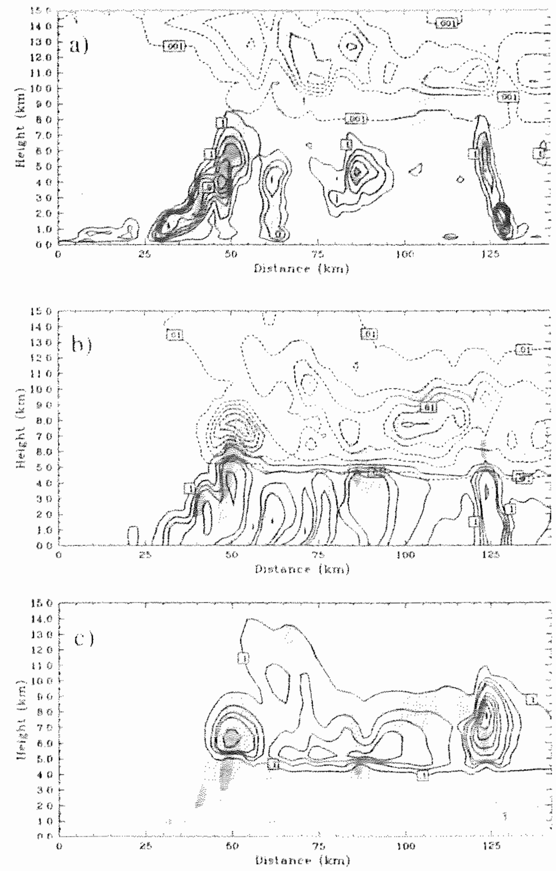

Figure 3. Vertical cross sections of (a) cloud water and cloud ice, (b) rain and snow, and (c) graupel mixing ratios for the NW cross section. Contour intervals are 0.05 g kg^{-1} for cloud ice and 0.2 g kg^{-1} for cloud water and snow. For rain and graupel, the contour interval is 0.5 g kg^{-1} for values less than 2 g kg^{-1}, and 1 g kg^{-1} for larger values. Light shading indicates $w > 2$ m s^{-1}, dark shading $w > 4$ m s^{-1}.

(Fig. 2c), strong vertical motions are confined to the eyewall mostly below 5 km. Significant stratiform precipitation is evident outside the eyewall. Finally, in the SE cross section (Fig. 2d), vertical motions are more disorganized and tend to be strongest at upper levels. The precipitation structure shows relatively shallow, intense reflectivities just inside very deep, but weaker echoes. A very shallow warm-rain band is seen near a radius of 125 km and represents the tail of the principal rainband.

Details on the structure of the hydrometeor fields in the NW and SE cross sections are shown in Figs. 3 and 4, respectively. In the NW cross section, cloud water mixing ratios are coincident with areas of strong vertical motions and are largest in the eyewall and in the outer rainband. Much

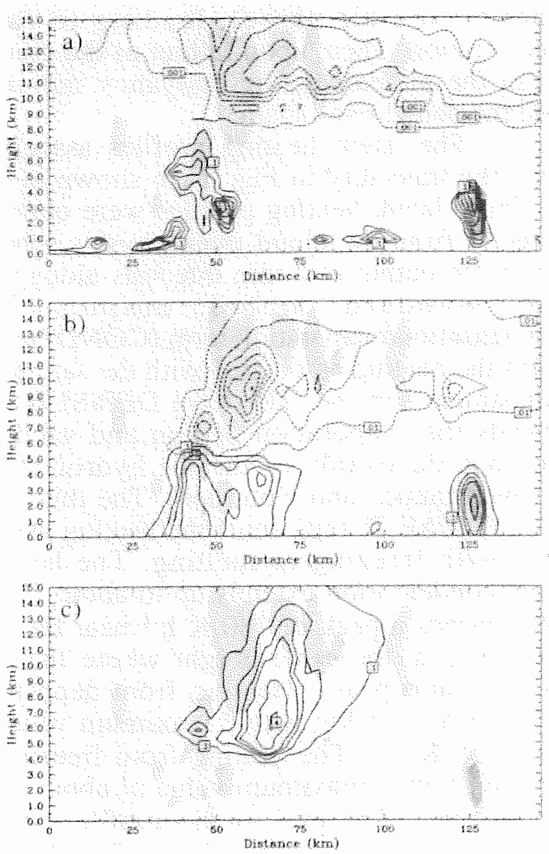

Figure 4. Same as Fig. 3, but for the SE cross section.

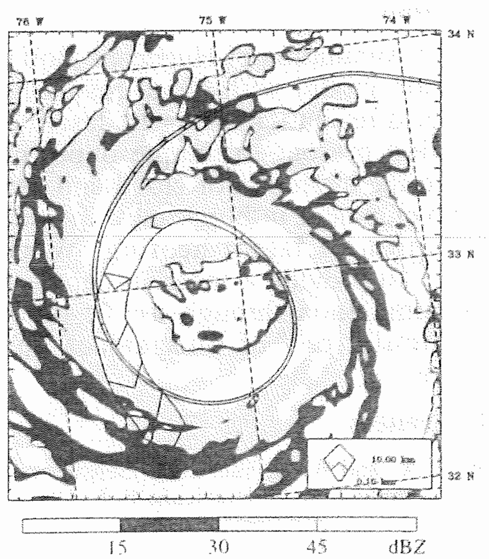

Figure 5. Air parcel trajectory depicting air motion relative to the moving storm overlaid on 0.25 km reflectivity field (as in Fig. 1) at 66 h. The width of the arrow is proportional to the height of air parcel. Tick marks along the trajectory are drawn every 15 min. Tick marks along the axes are drawn every 5 grid points (~6.7 km).

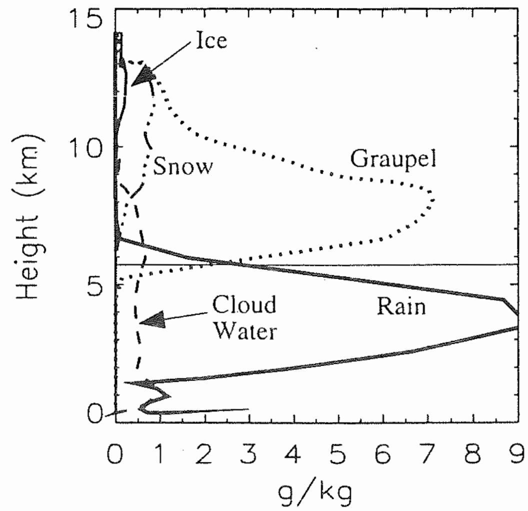

Figure 6. Vertical profiles of hydrometeor mixing ratios from the ascending portion of the trajectory in Fig. 5. The horizontal line indicates the freezing level.

of the rain (Fig. 3b) in the eyewall is generated from warm rain processes, although rapid conversion to snow (Fig. 3b) and graupel (Fig. 3c) occurs with the strong updraft near 50 km. The outer convective band also produces significant graupel. Snow mixing ratios are largest near 100-115 km, just inside the convective band; the moderate vertical motions and lack of cloud water suggests growth of snow by deposition, as is common in stratiform precipitation regions. Melting of graupel contributes to the rainfall between the eyewall and convective band.

In the SE cross section (Fig. 4), cloud water is generally confined to the updrafts in the eyewall and the shallow outer rainband. Much of the rain inside of 70 km appears to be produced by warm rain processes, with some conversion to graupel and snow near 45 km. The secondary rain maximum near 60-65 km apparently forms from melting graupel. The large amount of graupel is not associated with significant vertical motion and must therefore have been produced upwind and advected around to this side of the storm. The maximum in snow is inward of the graupel region and is coincident with an area of upward motion, suggesting growth by deposition in addition to advection by the storm circulation.

The development of precipitation can be further examined by calculating air parcel trajectories. An example is given in Fig. 5, in which the arrow indicates the trajectory rela-

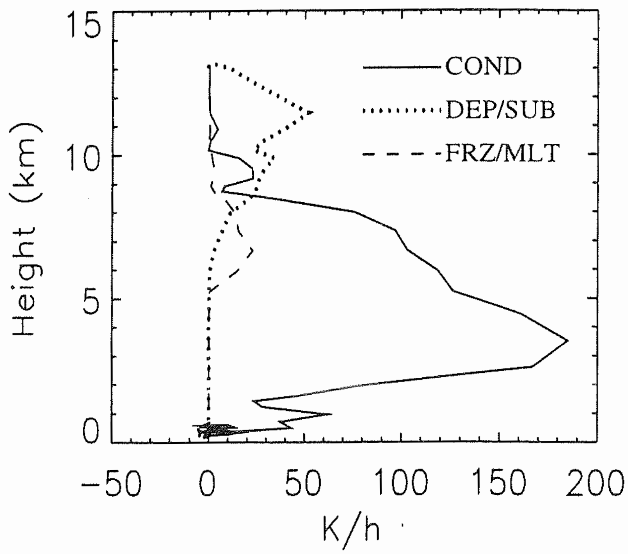

Figure 7. Latent heating rates for cloud condensation/evaporation (COND), rain evaporation, snow and graupel deposition/sublimation (DEP/SUB), and freezing and melting (FRZ/MLT) following the ascending portion of the trajectory.

tive to the storm motion at 66 h. The trajectory was calculated using model output every 2 min. In this example, the air parcel originates in the boundary layer well to the northeast of the eyewall, circles around the western side of the storm, and crosses through the eyewall on the southeastern side. The air parcel rises rapidly on the northwestern side of the storm and then moves outward from the center to the south at an altitude of about 14 km.

Hydrometeor mixing ratios were calculated following the trajectory and are shown for the ascending portion of the trajectory in Fig. 6. As the air parcel rises, cloud water generated by condensation gets rapidly converted to rain by collection processes. Ascent above the freezing level leads to rapid conversion of rain to graupel as well as additional growth of graupel by accretion of cloud water. Cloud water is present up to about 10 km MSL (approximately the –25°C level). Snow is mostly concentrated above the 8-km level.

Many trajectories (not shown) indicate a substantial impact of the graupel concentrations on the vertical motion of the rising air. In many cases, the vertical motion is substantially reduced at the level where graupel mixing ratios peak and then increased again at higher levels. Such behavior suggests that water loading by graupel temporarily reduces the buoyancy of the air parcel, leading to rapid deceleration. Then, upon fallout of the graupel from the air parcel, the buoyancy increases and the parcel rises again.

The latent heating profiles associated with the trajectory in Fig. 5 are shown in Fig. 7. These latent heating profiles were obtained directly from the cloud microphysics scheme and were output at 2 min intervals along with the standard model output. The condensation/evaporation term (COND) represents the heating associated with the saturation adjustment scheme. The term DEP/SUB represents the evaporation of rain and sublimation and deposition of the ice hydrometeors (snow, graupel, and cloud ice). The third profile (FRZ/MLT) represents the heating associated with freezing or melting. The heating from condensation extends up to about 10 km and reaches a peak of 180 K h^{-1} near the 3.5-km level, at the same height where the rain mixing ratio peaks. Heating from deposition peaks near 11.5 km with a maximum value of about 55 K h^{-1}. The heating from freezing is smaller, with a maximum value of about 12 K h^{-1} near the 7-km level. In this profile, there is no cooling from melting, suggesting that the rain developed from warm rain processes along this trajectory.

4. Summary

A simulation of Hurricane Bob using a mesoscale model with cloud-resolving horizontal grid resolution has been described. The simulation presents a unique opportunity to examine the evolution of cloud and precipitation development in hurricanes, including the distribution of latent heating. Work is in progress to provide a more in-depth analysis of the simulation through use of trajectories and calculations of budgets of heat and moisture.

5. References

Braun, S. A., and W.-K. Tao, 2000: Sensitivity of high-resolution simulations of Hurricane Bob (1991) to planetary boundary layer parameterizations. *Mon. Wea. Rev.* (conditionally accepted).

Liu, Y., D.-L. Zhang, and M. K. Yau, 1997: A multiscale numerical study of Hurricane Andrew (1992). Part I: Explicit simulation and verification. *Mon. Wea. Rev.*, **125**, 3073-3093.

Numerical Simulations of TOGA COARE, GATE and PRESTORM Convective Systems: Sensitivity tests on Microphysical processes

W.-K. Tao, Y. Wang, S. Lang, B. Ferrier and J. Simpson
Laboratory for Atmospheres
NASA/Goddard Space Flight Center
Greenbelt, MD 20771

(301) 614-6269
Email: tao@agnes.gsfc.nasa.gov

Abstract

The 3D Goddard Cumulus Ensemble (GCE) model was utilized to examine the behavior and response of simulated deep tropical cloud systems that occurred over the west Pacific warm pool region, the Atlantic ocean and the central United States. The periods chosen for simulation were convectively active periods during TOGA-COARE (February 22, 1993), GATE (September 4, 1974) and PRESTORM (June 11, 1985). The TOGA COARE convective event was also part of the GEWEX Cloud System Study (GCSS) WG4 model intercomparison (Case 1). We will examine differences in the microphysics for both warm rain and ice processes (evaporation/sublimation and condensation/deposition), Q1 (Temperature), Q2 (Water vapor) and Q3 (momentum both U and V) budgets for these three convective events from different large-scale environments. The contribution of stratiform precipitation and its relationship to the vertical shear of the large-scale horizontal wind will also be examined. New improvements to the GCE model (i.e., microphysics: 4ICE two moments and 3ICE one moment; advection schemes) as well as their sensitivity to the model results will be discussed.

1. INTRODUCTION

The interactions of thunderstorms and mesoscale convective systems with their environment is an important link in a chain of regional- and global-scale processes responsible for monsoons, the Baiu frontal depression, tropical cyclones, El Nino-Southern Oscillation (ENSO) events (i.e., super cloud clusters-SCCs and westerly wind bursts-WWBs) and other climate variations (*e.g.*, 30-60 day intra-seasonal oscillations). Convective systems play a crucial role in the earth radiation budget, and interact with ocean and land surface processes. Computer models provide essential insights into the dynamics of convective cloud systems and their interactions with their surroundings. Numerical models are also used in the development and refinement of spaceborne retrievals.

A cloud-resolving model (Goddard Cumulus Ensemble Model - GCE model) is being used to study the physical and dynamical processes associated with mesoscale convective systems in various geographical locations. The GCE model has been used to understand the following: **i)** the effects of land- and ocean-surface processes on precipitation processes and their roles in the hydrologic cycle and regional climate variations; **ii)** the water and energy cycles and their roles in the tropical climate system; **iii)** the vertical redistribution of **ozone** and trace constituents by individual clouds and well organized convective systems over continental scales; **iv)** the relationship between the vertical distribution of cloud-scale and mesoscale diabatic heating (latent heating) and the antecedent conditions of the pre-storm environment; **v)** the complex interactions between storm-scale diabatic heating and the environment, and their net effect on mesoscale divergence; **vi)** the validity of assumptions used in the representation of cloud processes in climate and global circulation models; **vii)** the representation of cloud microphysical processes and their interaction with radiative forcing over tropical and midlatitude regions.

In this paper, we will examine differences in the microphysics for both warm rain and ice processes (evaporation/sublimation and condensation/deposition), Q1 (Temperature), Q2

(Water vapor) and Q3 (momentum both U and V) budgets for these three convective events from different large-scale environments. The contribution of stratiform precipitation and its relationship to the vertical shear of the large-scale horizontal wind will also be examined. New improvements to the GCE model (i.e., microphysics: 4ICE two moments and 3ICE one moment; advection schemes) as well as their sensitivity to the model results will be also discussed.

2. Goddard Microphysics Schemes

The tool used in this study is the three-dimensional version of the Goddard Cumulus Ensemble (GCE) model. The equations that govern cloud-scale motion (wind) are anelastic by filtering out sound waves by neglecting the local variation of air density with time in the mass continuity equation (see Tao and Soong, 1986 for a description of the anelastic assumption and cloud motion equations). The subgrid-scale turbulence used in the GCE model is based on work by Klemp and Wilhelmson (1978), and Soong and Ogura (1980). In their approach, one prognostic equation is solved for subgrid kinetic energy, which is then used to specify the eddy coefficients. The effect of condensation on the generation of subgrid-scale kinetic energy is also incorporated in the model (see Tao and Soong, 1986 for details). The cloud microphysics include a parameterized Kessler-type two-category liquid water scheme (cloud water and rain), and a parameterized Lin *et al.* (1983) or Rutledge and Hobbs (1984) three-category ice-phase scheme (cloud ice, snow and hail/graupel) (see Tao *et al.*, 1993 for a description of the cloud microphysics). Shortwave (solar) and longwave (infrared) radiation parameterizations are also included in the model [see Section 2.1(a) for details]. All scalar variables (potential temperature, mixing ratio of water vapor, turbulent coefficients, and all five hydrometeor classes) use forward time differencing and a positive definite advection scheme with a non-oscillatory option (Smolarkiewicz and Grabowski, 1990). The dynamic variables, u, v, and w, used a fourth-order accurate advection scheme and leapfrog time integration.

(a) Three Ice Scheme

A two-class liquid and three-class ice microphysics scheme developed and coded by the Goddard Mesoscale Modeling Group (Tao and Simpson, 1993) was mainly based on Lin *et al.* (1983) with additional processes from Rutledge and Hobbs (1984). In addition, the Goddard microphysics scheme has several minor modifications. The modifications include: (1) the option to choose either graupel or hail as the third class of ice (McCumber *et al.* 1992). Graupel has a low density and a large intercept (i.e., high number concentration). In contrast, hail has a high density and a small intercept (low number concentration). These differences can affect not only the description of the hydrometeor population, but also the relative importance of the microphysical-dynamical-radiative processes. (2) the saturation technique (Tao *et al.* 1989): This saturation technique is basically designed to ensure that supersaturation (subsaturation) cannot exist at a grid point that is clear (cloudy). This saturation technique is one of the last microphysical processes to be computed. It is only done prior to evaluating evaporation of rain and snow/graupel/hail deposition or sublimation. Without considering ice in the mixed phase saturation technique more cloud water is generated (Braun *et al.* 1999). (3) Another difference is that all microphysical processes (transfer rates from one type of hydrometeor to another) are calculated based on one thermodynamic state. This ensures that all processes are treated equally. The opposite approach is to have one particular process calculated first modifing the temperature and water vapor content (i.e., through latent heat release) before the second process is computed.

(b) Four Ice Scheme

An improved microphysical parameterization called 4ICE has been developed and implemented into the GCE model (Ferrier 1994; Ferrier *et al.* 1995), which combines the main features of previous three-class ice schemes by calculating the mixing ratios of both graupel and frozen drops/hail. Additional model variables include the number concentrations of all ice particles (small ice crystals, snow, graupel and frozen drops), as well as the mixing ratios of liquid water in each of the precipitation ice species during wet growth and melting for purposes of accurate active and passive radiometric calculations. The scheme also includes the following: (1) more accurate calculation of accretion processes, including partitioning the freezing of raindrops as sources of snow, graupel and frozen drops/hail; (2) consideration of rime densities and riming rates in converting between ice species due to rapid cloud water riming; (3) incorporation of new parameterizations of ice nucleation processes, the rime splintering mechanism using laboratory data, and the aircraft observations of high ice particle concentrations; (4) shedding of liquid water from melting ice and from excessive amounts of water accumulated on supercooled frozen drops/hail; (5) preventing unrealistically large glaciation rates immediately above the freezing level by explicitly calculating freezing rates of raindrops and freezing rates of liquid water accreted onto supercooled ice; (6) introducing fall speeds and size distributions for small ice crystals; (7) calculating radar reflectivities of particles with variable size distributions and liquid water coatings from Rayleigh theory; (8) basing conversion of particle number concentrations between hydrometeor species on preserving spectral characteristics of particle distributions rather than conserving their number concentrations (important). The 3-D GCE 4ICE scheme was recently coupled with the positive definite advection scheme, substantially reducing the decoupling of mixing ratios and number concentrations caused by advection errors, and resulting in a significant improvement in model performance.

3. Results

A well-organized tropical oceanic squall system, observed during TOGA COARE on February 22, 1993 (Jorgensen *et al.*, 1995; LeMone *et al.*, 1995), was chosen to quantify the effect of microphysics on the development and structure of the squall system. The GCE model was initialized with a sounding provided by Dr. LeMone and was integrated for 12 hours. The corresponding CAPE (Convective Available Potential Energy) and vertically integrated water vapor content for this squall line's environment were 1418 $m^2\ s^{-2}$ and 6.049, respectively. Tropical oceanic convective systems are typically associated with a moderate CAPE and very moist environmental conditions. The convection is initialized in the model by a cool pool (4.8 ^{0}K of cooling over 10 minutes) in the middle of the computational domain. In the GCE model simulations, a stretched vertical coordinate (height increments from 70 to 1150 m) with 31 grid points was used to maximize resolution in the lowest levels of the model. A total of 170 by 140 grid points was used in the horizontal with 1500 m resolution.

Figure 1 shows surface rainfall using the 4ICE scheme and 3-ICE scheme for a TOGA COARE squall line. Both GCE model simulated squall lines produced an asymmetric arc shape convective system. Stratiform rain developed faster and covered a larger area (as well as have a higher percentage over 7 hours of integration) in the 3ICE scheme than its counterpart in the 4ICE scheme. For example, the stratiform percentage is 33% and 27%, respectively, for the 3ICE and 4ICE schemes over 7 hours of simulation. Also, the maximum vertical velocity is about 20-25 m/s and freezing rain (hail), not graupel, is produced in the 4ICE scheme. In addition, the hydrometeor structures are quite different between these two schemes even though the same initial conditions are applied.

Acknowledgement

The author is supported by the NASA Headquarters physical climate program, the NASA TRMM, and the interdisciplinary program of EOS. The author is grateful to Dr. R. Kakar for his support of this research. Acknowledgment is also made to NASA/Goddard Space Flight Center for computer time used in this research.

Fig. 1 Surface rainfall simulated by the 3-D GCE model for a TOGA COARE squall line (February 22, 1993). The left panels (at 4, 6 and 7 h into the simulation) are from the 4ICE scheme while the right panels are from the 3ICE scheme. Vertical profiles of various hydrometeors in the convective and stratiform regions simulated from the 3ICE and 4ICE scheme.

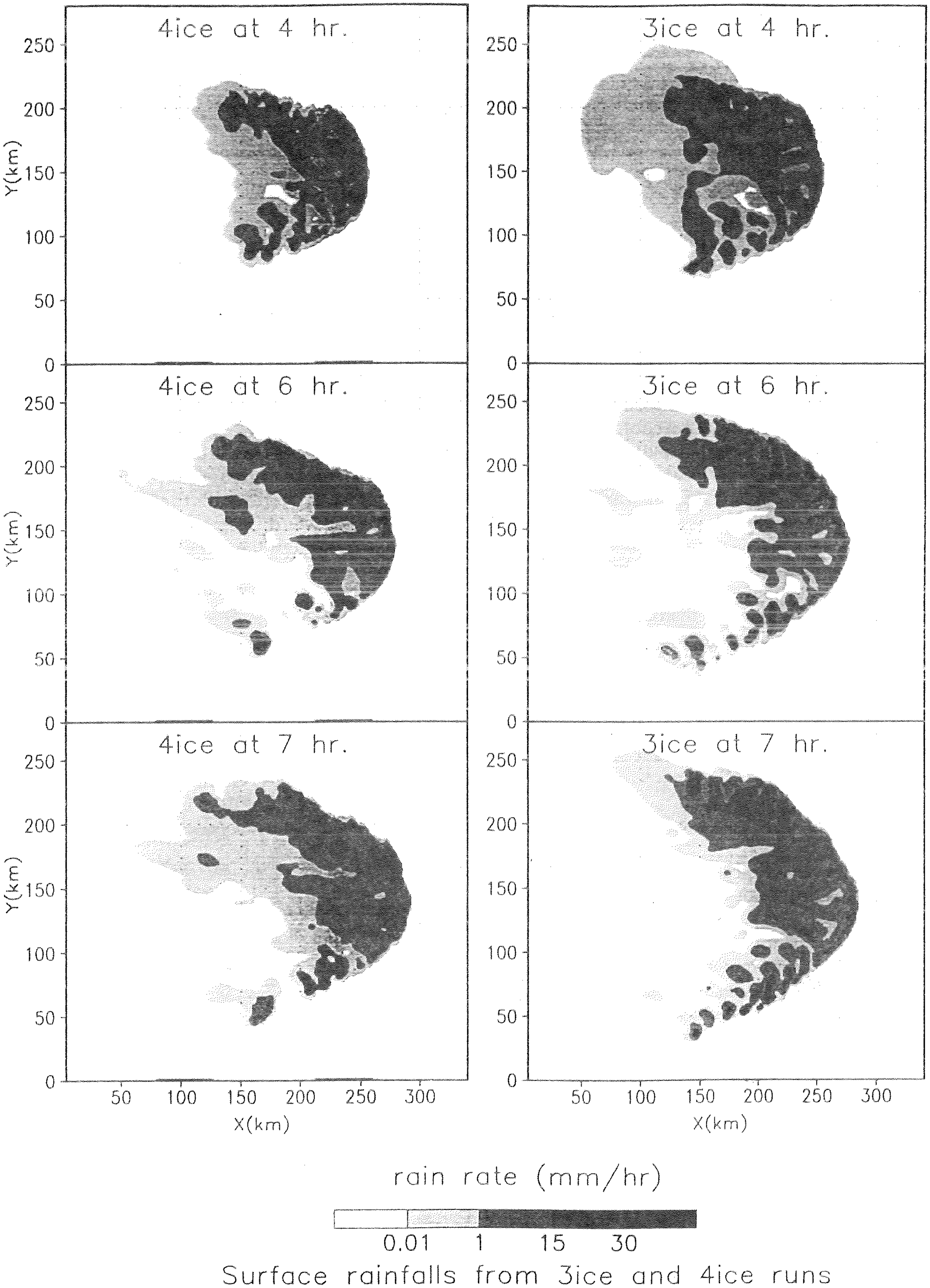
4ice at 4 hr.
3ice at 4 hr.
4ice at 6 hr.
3ice at 6 hr.
4ice at 7 hr.
3ice at 7 hr.
Y(km)
X(km)
0
50
100
150
200
250
300
rain rate (mm/hr)
0.01
1
15
30
Surface rainfalls from 3ice and 4ice runs

STRUCTURAL CHARACTERISTICS OF CONVECTIVE MESOSCALE SYSTEMS OVER THE AMAZON

L. M. V. Carvalho[1] and C. Jones[2]

[1]Dept. Atmospheric Sciences, IAG, University of Sao Paulo, Sao Paulo, SP, 05508-900, Brazil
[2]Institute for Computational Earth System Sciences, UCSB, City, CA, 93106-3060, USA

1. INTRODUCTION

Convective systems in the Earth's atmosphere occur in wide spectra of time and space scales and play important roles in the distribution of energy, momentum and mass in the general circulation In particular, mesoscale convective systems (MCS) can be broadly defined as cloud systems associated with ensembles of thunderstorms with contiguous precipitation areas. Satellite methods that identify and track the structural properties of MCS can provide valuable information on the dynamical mechanisms involved in their life cycle including the interaction between the MCS and the large-scale circulation. The purpose of this paper is to introduce a new methodology to identify structural properties of MCS. We discuss different approaches to compute some structural parameters of clouds and their applicability for the identification of different stages of intensification and decaying of MCS. Furthermore, as it will be shown by examples, this new simple and efficient automated satellite tracking methodology allows the identification of splitting and merging systems as they occur during their life cycles.

2. DATA

As an application of the present satellite tracking methodology, we focus our attention on two distinct days of the Wet Season Atmospheric Mesoscale Campaign (WETAMC) of the Large Scale Biosphere-Atmosphere Experiment (LBA). This field experiment, which was realized from December 1998 through February 1999 in the Brazilian state of Rondônia in the Amazon basin, was a joint scientific venture with the ground validation component of the Tropical Rainfall Measurement Mission (TRMM). The two days analyzed correspond to distinct regimes of low level winds (Rickenbach et al., 2000): February 15, with predominantly easterly regime and February 24, with an extensive band of westerlies extending along the Andes towards the Brazilian central high plane, with a NW-SE orientation.

3. MAXIMUM SPATIAL CORRELATION TRACKING TECHNIQUE (MASCOTTE)

The method uses as input fields brightness temperature T_B from GOES-8 satellite images. These images have horizontal resolution of 4 km and are separated every one-hour. Convective systems are identified in the satellite images whenever regions of $T_B \leq 235$K. This threshold allows to investigate clouds that are mostly associated with anvil regions and embedded in areas of active deep convection. In order to test the skill of our method and emphasize the tracking of MCS with long life cycles, we consider systems with horizontal radius $R \geq 100$km (see Machado et al. ,1998). These limits of brightness temperature and horizontal area in our methodology imply that the life cycle of a given MCS begins when the convective system has $T_B \leq 235$K *and* $R \geq 100$km. The end of the life cycle, on the other hand, occurs when $T_B > 235$K *or* $R < 100$km. Our characterization of MCS life cycles and their structural properties is defined as the maximum spatial correlation tracking technique (hereafter *MASCOTTE*). Our basic hypothesis is that the spatial correlation between regions defined by two different cloud systems in different times is a simple and powerful method to identify the evolution of spatial patterns associated with MCS. The basic steps involved in the method are as follows.

1. We consider that N satellite images of T_B are available with time interval ΔT. In this work, ΔT is taken to be 1 hour. However, as it is shown later, the method is successful for ΔT intervals up to three hours. For each satellite image at time t_m, $0 \leq t_m \leq N$, regions of MCS are identified according to the criteria $T_B \leq 235$K *and* $R \geq 100$km. Regions that do not meet the threshold criteria are set to an arbitrary value. We consider that at time t_m there is N_{tm} MCS identified.

---

[1] Leila M. Vespoli de Carvalho
DCA/IAG/University of Sao Paulo, SP, Brazil, 05508-900
E-mail: leila@model.iag.usp.br

2. For each time t_m and each MCS, structural properties are computed. These include: the horizontal area (A), perimeter (P), mean and variance of T_B, minimum T_B and fractional convective area $C = 100\ (A_{TC}/A)$, where A_{TC} is the area within the MCS such that $T_B \leq 210$K.
3. In addition, spatial properties are computed for each MCS at each time t_m. The spatial coordinates of the center of gravity (X_{CG}, Y_{CG}).
4. The orientation of the MCS is computed in two ways. First, a straight line is fitted to the ($X_i, Y_i, i=1,N_P$) pixel coordinates by least squares criterion and the counter-clockwise angle between the east-west direction and the straight line is recorded. However, as it will be discussed in the next section, a satellite method that relies in this definition of orientation can oftentimes obtain quite misleading results, depending on the geometrical structure of the MCS. In contrast, a new way of computing the orientation is proposed. We consider a given MCS in which the array of pixel coordinates is given by ($X_i, Y_i, i=1,N_P$). The means $\overline{X}$ and $\overline{Y}$ are first subtracted from the vectors X_i and Y_i and an Empirical Orthogonal Function (EOF) is computed on the covariance matrix determined by X' and Y' perturbations. The result of this operation is a pair of eigenvalues and eigenvectors that explain the total variance of the geographical coordinates of the given MCS. Consequently, a second orientation is computed as the counter-clockwise angle between the east-west direction and the direction of the first eigenvector.
5. Another important property to characterize the structure of MCS is the eccentricity, which in our method is defined by the ratio of the norms $\|EOF2\|/\|EOF1\|$, where $EOF2, EOF1$ are the second and first eigenvectors, respectively.
6. Once the above structural properties are computed for each MCS in each satellite image, the tracking of individual MCS is performed in the following way. At time t_m there is N_{tm} MCS in the satellite image. The k^{th} MCS ($1 \leq k \leq N_{tm}$) is first isolated in the image, which has a size of I_{CxL}, where C (=1332) and L(=860) are the number of pixels in the east-west and north-south direction respectively. The new image at time t_m with a single MCS is then transformed into a one-dimensional vector $V_k(t_m)$, whose dimension is CxL. We then consider the next satellite image at time t_{m+1} and identify the M_{tm+1} MCS. Each j^{th} MCS at time t_{m+1} is isolated and their images are transformed into one-dimensional vectors $V_j(t_{m+1})$ ($1 \leq j \leq M_{tm+1}$). Spatial correlation is then computed between the vector $V_k(t_m)$ and all the $V_j(t_{m+1})$ vectors. All the MCS at the satellite image at time t_{m+1} with positive correlations with the k^{th} MCS at the image t_m are identified and considered candidates for the evolution of the k^{th} MCS. The MCS at the image t_{m+1} with maximum spatial correlation is defined as the MCS at time t_{m+1} in which the k^{th} MCS at time t_m has evolved to. The process is repeated for all MCS at time t_m and starts again for the next satellite image at time t_{m+1}.

The splitting of an MCS at time t_m is identified by the MASCOTTE method when more than one convective system with positive and high spatial correlation is observed at time t_{m+1} followed by the decreasing of area. MASCOTTE continues the tracking of MCS with the assumption that the propagation is now defined by the most correlated convective systems in subsequent satellite images. MASCOTTE also maps the position of any part of the splitting cell in order to follow its life cycle until it decays, which usually happens in a short period. Furthermore, due to the definition of MCS using the T_B threshold, merging of high clouds is also frequently observed, which is in fact related to the connection of anvil regions. At this point, it is difficult to identify the main cell because its life cycle is determined by the interaction of more than one MCS. However, the merging is characterized in MASCOTTE by positive spatial correlation, since the identity of a tracked MCS is kept as it merges to another one. These situations can be clearly identified during the life cycle when the spatial correlation decreases and the horizontal area increases in two consecutive satellite images.

For the thresholds considered, we know: duration of each system; total number of systems in the N images, number of splits and merges, as well as the structural properties described above.

4. MCS PROPERTIES USING MASCOTTE

4.1 Structural properties for the entire events

Some properties of the MCS obtained with MASCOTTE are summarized in the Table-1 for the two case studies. These properties suggest that the westerly regime is characterized by a relative increase in the number of MCS and duration of life cycle, though the mean and maximum area of MCS are statistically very similar in both events. The observation of enhancement of convection over the Amazon during the Westerly Regime have been obtained by radar in Rondônia, Brazil (Rickenbach et al, 2000). Fig. 1 shows the variability of number of systems according to the time of the day, indicating the importance of the diurnal cycle and nocturnal cloudiness for the westerly regime. The diurnal distribution of the number of MCS seems to be consistent with the results of Rickenbach et al. (2000b).

Table-1 Basic Statistics for the life cycles of MCS in the two events: number of life cycles, total of splits and merges, mean duration, the maximum area mean area averaged for all life cycles ($T_B \leq 235K$ and $R \geq 100km$). *Merges are not considered.

	Feb-15 **Easterly**	Feb-24 **Westerly**
*N of life cycles	63	75
Total of Splits	15	20
Total of Merges	9	12
* Mean duration	3.0 ± 2.0h	4.0 ± 3.0 h
Avg. Max. area	117,363 km^2	113,459 km^2
Mean area	83,865 km^2	88,262km^2

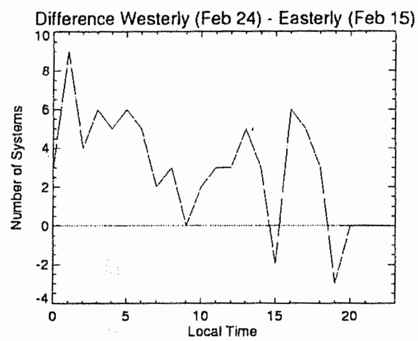

Fig. 1. Time difference of total number of MCS

The mean trajectories of the systems are shown in Fig. 2. The row indicates the mean direction of the MCS propagation. The X symbol shows the beginning of the trajectory.

The most important difference in the direction of propagation of MCS observed in these two events occurs approximately between –5 to –12 S and –40 to –65 W (which covers the S-Pol and TOGA radar domain). In this region, systems propagate from W-E for the Westerly regime in opposition to the Easterly, consistently with the low-level wind pattern (to be discussed in details in the conference). The distribution of the orientation of the MCS according to the definition described in the item 5 is shown in Fig. 3. Angles of the first eigenvector larger than 90° indicate the NW-SE predominant orientation of the cloud tops, which is consistent with the predominant direction of high-level winds (not shown).

All parameters described in the items 1- have been computed for these two events. The importance of these parameters and how they change during the life-cycle of a MCS will be discussed in details in the conference.

4.2. Examples of life cycles of MCS

Figure 4 illustrates an evolving MCS observed for February-15 for which both merging and splitting occur in different phases of the MCS life cycle. This MCS was observed during 3 hours before the merging. After that, this system could be tracked for more 10 hours until a new merging occurred. In the example of Fig. 4, only the images of the MCS at by the time of the first merge and first split are shown. It is worth noticing the left side preference for the propagation of splitting cells relatively to the motion of the MCS.

Fig. 5 shows examples of how the orientation of a MCS and eccentricity are obtained with the use of the EOF. Also, it is indicated the difference between the method of least squares (LS) applied in Machado et al (1998). These examples illustrate how the orientation of the MCS obtained by LS can very often be misleading. At the top and bottom of each frame, two structural parameters are shown: eccentricity and the perimeter fluctuation. This last one was obtained after removing the trend (or fractal dimension of the set of MCS), which is obtained from the fit between the logarithm of perimeters and areas (Lovejoy, 1982). The resulting set represents the fluctuation (Fluc) of the perimeter and can be interpreted as a measure of the fragmentation of an evolving MCS. Increasing/decreasing magnitudes of Fluc indicate increase/decreasing of fragmentation of MCS.

5. SUMMARY

Examples of application of MASCOTTE have been presented for the characterization of structural properties of the MCS over the Amazon. A more complete examination of the life cycle of the MCS and the complexity of forms in the context of distinct large-scale regimes is already in progress.

7. Acknowledgments

This research was supported by FAPESP.

8. References

Lovejoy, S. 1982: Area-Perimeter relationship for rain and cloud areas, Science, 216-185-187.

Machado, L. A.T., W. B. Rossow, R. L. Guedes, and A. W. Walker, 1998: Life cycle variations of mesoscale convective systems over the Americas. *Mon. Wea. Rev.*, **126**, 1630-1654.

Richenback, T. and co-authors, 2000: Evolution of convective systems in contrasting large-scale regimes from radar and infrared satellite data during the TRMM-LBA field campaign in Rondônia, Brazil. AMS 25th Conference on Hurricanes and Tropical Meteorology, Ft. Lauderdale FL, USA, May 2000.

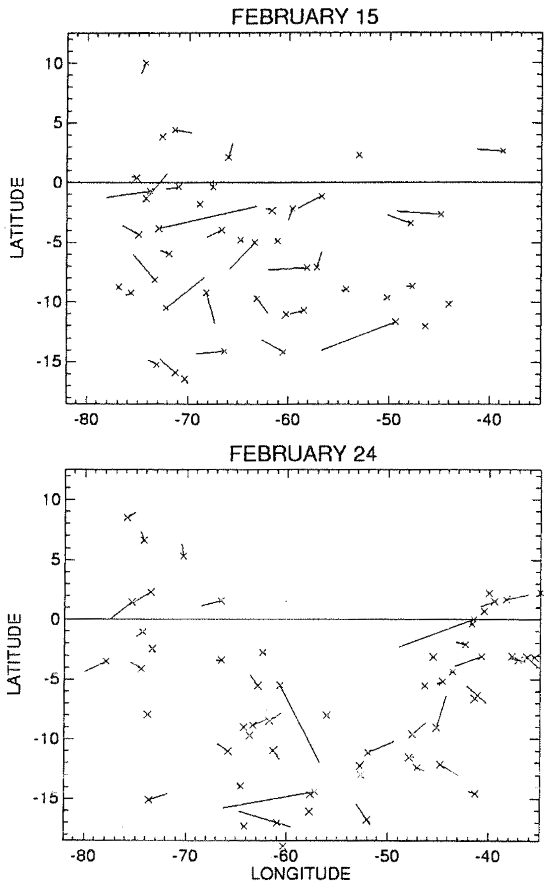

Fig. 2 Trajectories of MCS

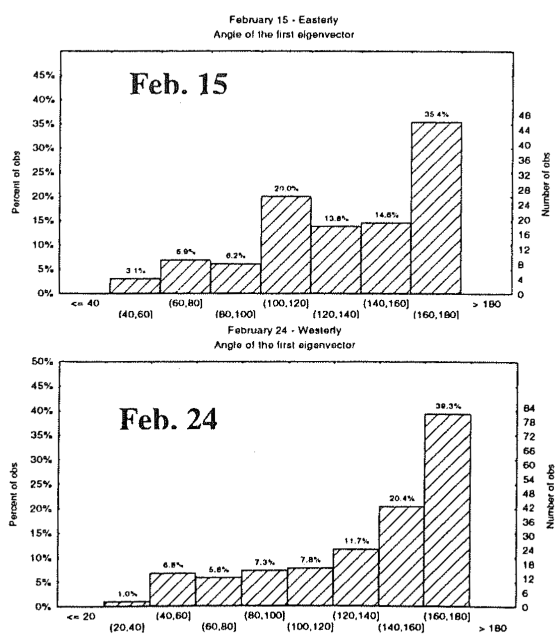

Fig.3 Distribution of EOF-1 Angle

Fig. 4. Examples of Merging and splitting during the life cycle of a MCS.

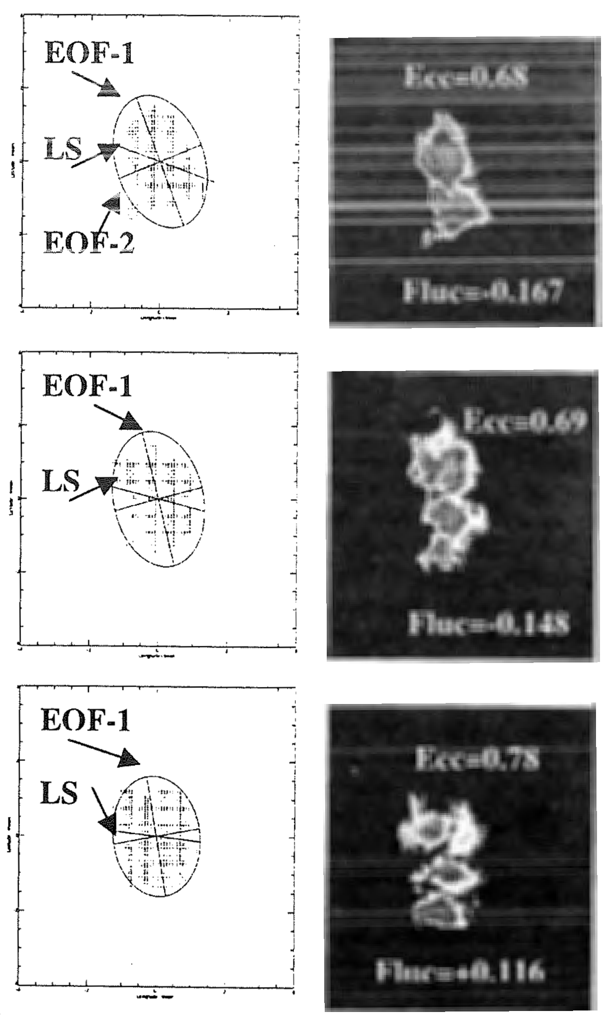

Fig. 5. Examples of orientation, eccentricity (ecc) and perimeter fluctuation (fluc) for a evolving MCS.

STRUCTURE OF A SQUALL LINE OBSERVED OVER THE CHINA CONTINENT DURING THE GAME/HUBEX INTENSIVE FIELD OBSERVATION

Kazuhisa Tsuboki,* Biao Geng and Takao Takeda

Institute for Hydrospheric-Atmospheric Sciences, Nagoya University
Nagoya, 464-8601, JAPAN

1. INTRODUCTION

The energy and water cycle in the subtropical monsoon region of the East Asia is characterized largely by Baiu/Meiyu front in summer. It is one of subtropical fronts and a unique subsystem of the Asian monsoon. Various scale of cloud/precipitation systems are formed in this frontal zone and play major role in the energy and water cycle in the zone. One of purposes of GAME/HUBEX (GEWEX Asian Monsoon Experiment/ Huaihe River Basin Experiment) is to study the evolution of a mesoscale cloud system.

The intensive field observation (IFO) of GAME/ HUBEX was performed in the Huaihe River Basin, China during the period from 11 June 1998 to 22 July 1998. During IFO, a significant squall line was observed by three Doppler radars.

Houze et al. (1989) showed a conceptual model of the kinematic, microphysical, and radar-echo structure of a mid-latitude squall line. Its characteristic features are the convective line with a trailing stratiform precipitation, the rear-inflow, the front to rear flow and a gust front. Biggerstaff and Houze (1993) showed a vertical motion and trajectory of precipitation particles within a mid-latitude squall line. They found a transition zone between the convective line and a mesoscale stratiform precipitation zone. Johonson and Hamilton (1988) found the pre-squall mesolow in front of a squall line, the mesohigh just behind the convective line and a wake low within the stratiform precipitation area. It is not clear that these characteristic features are found in the squall line which developed in the monsoon environment.

The purpose of this study is to clarify the structure of the squall line developed over the China Continent. We made data analysis of the three Doppler radar observation during the IFO of HUBEX and a numerical simulation using a cloud resolving model.

*Corresponding author's address: Kazuhisa Tsuboki, Institute for Hydrospheric-Atmospheric Sciences, Nagoya University, Furo-cho, Chikusa-ku, Nagoya, 464-8601, Japan; E-Mail: tsuboki@ihas.nagoya-u.ac.jp

2. ENVIRONMENTAL CONDITION

The squall line was observed around 10 UTC, 16 July 1998. The local time of the observation site was advanced for 8 hours to UTC. The squall line, therefore, developed in the late evening as a part of diurnal variation of convective activities due to strong solar radiation.

The synoptic condition of the squall line development is found in the JMA (Japan Meteorological Agency) Global Objective Analysis (GANAL). The height field in Fig. 1 shows a mesoscale low, whose horizontal scale was about 1000 km, was located around the observation sites. A westerly or a southwesterly was prevailed at Fuyang (indicated by 'Fy' in the figure) and Shouxian ('Sx') at 850 hPa. The relative humidity at Fuyang and Shouxian was larger than 80 % at this level.

The mesoscale low had a significant lower-level convergence and its vorticity extended from the surface to 350 hPa. The squall line is considered to be developed in a favorable environment of the lower-level convergence and the positive vorticity associated with the mesoscale low.

A sounding at Fuyang at 1119 UTC, 16 July 1998 showed that the stratification was convectively unstable below 750 hPa. CAPE of this profile was 1720 J kg^{-1}. The troposphere was highly humid below 500 hPa and a dry layer was present between 500 hPa and 350 hPa. The humid condition is one of the characteristics of the environment. Wind direction was almost westerly throughout the troposphere. Wind speed was about 7~8 m s^{-1} below 700 hPa and 11~12 m s^{-1} between 650 and 500 hPa. The vertical wind shear was not so strong.

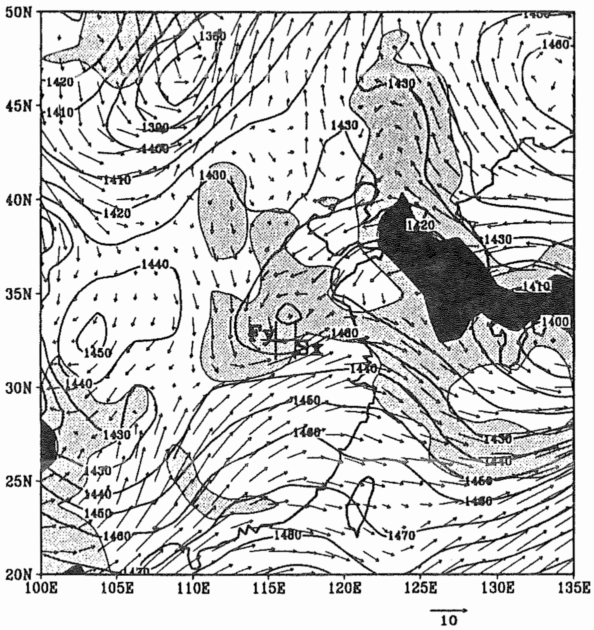

Figure 1: Height (meter), Relative humidity (lightly shaded areas mean larger than 80 % and darkly shaded larger than 90 %) and horizontal wind (arrows; the scale is shown at the bottom of the figure) at a level of 850 hPa at 1200 UTC, 16 July 1998 obtained from the JMA GANAL. The location of Fuyang observatory is indicated by 'Fy' and that of Shouxian by 'Sx'.

3. DOPPLER RADAR OBSERVATION

The squall line was formed outside of the Doppler radar observation range and approached the radars from the southwest around 10 UTC, 16 July 1998. It passed over the radars at 1130 UTC and moved northeastward with decaying. The squall line extended from the northwest to the southeast with a width of a few tens kilometers. CAPPI display of radar echo showed that the squall line consisted of intense convective cells and its leading edge was clear (Fig.2). Most convective cells were located along the leading edge. Some of cells reached to a height of 17 km. After the squall line passed over the radar sites, a stratiform precipitation was extending behind the convective leading edge.

The vertical cross section of echo intensity observed by RHI scan normal to the squall line showed that the convective cell at the leading edge was reached to a height of 8 km and a weaker echo extended to about 16 km in height behind the convective cells (Fig.3a). Doppler velocity showed that a strong forward flow was present whose velocity was larger than 13 m s^{-1} at a level of 4 km (Fig.3b). This is a significant rear-inflow to the squall line. The axis of the maximum of the rear-

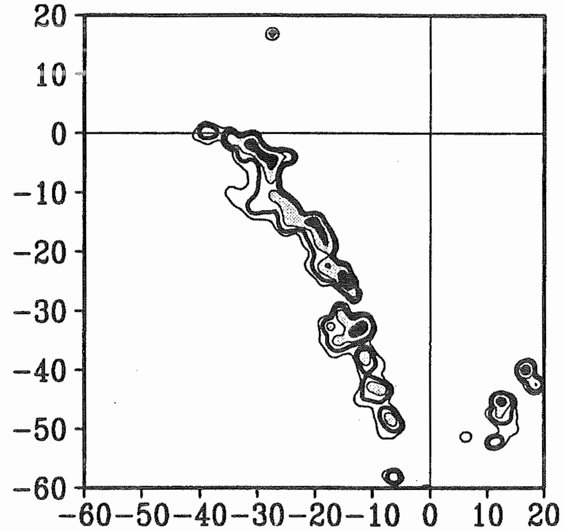

Figure 2: CAPPI display of echo intensity at a level of 2 km observed by the Feng-tai Doppler radar at 1057 UTC, 16 July 1998. The darkly shaded areas indicate echo intensity is larger than 38 dBZ, lightly shaded areas larger than 34 dBZ, thick contour lines are 30 dBZ and thin contour lines 25 dBZ.

inflow was descended behind the leading edge. Another maximum of forward flow was present below a height of 2 km. In the upper levels, a negative Doppler velocity which was indicated by shadings means a rear-ward flow. The axis of the rear-ward flow was inclined to the rear of the squall line. The lower-level convergence at the leading edge and the upper-level divergence behind the leading edge were significant.

Time-distance cross section shows that the squall line moved almost at a constant speed of 11 m s^{-1} during the observed period (Fig.4). Individual convective cells developed at the leading edge and was almost stationary. New cells developed successively in front of the older cells. Consequently, the squall line moved to the northeast. Some of the convective cells occasionally developed higher than 8 km.

4. SIMULATION EXPERIMENT

Fovell and Ogura (1988) performed a numerical experiment of a squall line. They found a self-maintaining squall line with a periodical intensification. A simulation experiment is effective to examine the dynamic structure and evolution of the squall line. We, therefore, made a simulation experiment of the observed squall line using a cloud resolving model in a two-dimensional geometry with a horizontal grid size of 500 m. In this study, we used the Advanced Regional Prediction System (ARPS) developed by the Center for Analysis and Prediction of Storms (CAPS), the

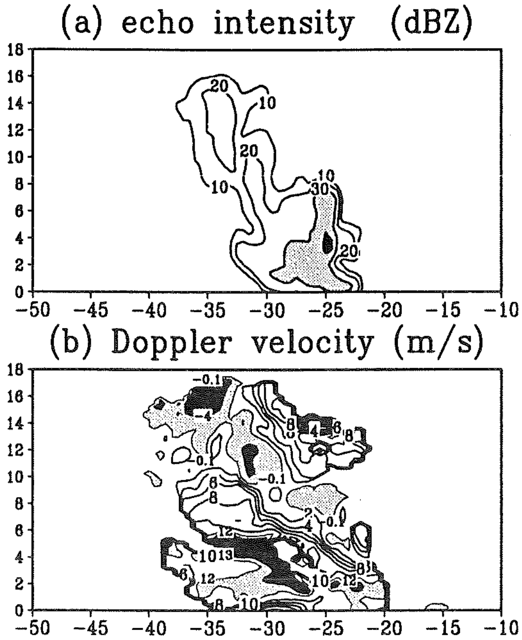

Figure 3: RHI display of (a) echo intensity and (b) Doppler velocity at an azimuth of 235° at 1100 UTC, 16 July 1998. The darkly shaded areas indicate velocity is larger than 13 m s^{-1} or −4 m s^{-1}, lightly shaded areas larger than 12 m s^{-1} or −0.1 m s^{-1}.

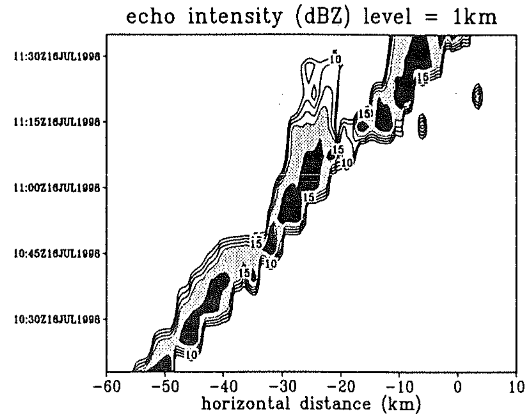

Figure 4: Time-distance cross section of echo intensity at an azimuth of 235° at a height of 1 km composited from RHI scans.

University of Oklahoma.

The basic field of the simulation was the Fuyang sounding at 1119 UTC, 16 July 1998. An initial perturbation was given by a negative buoyancy thermal bubble whose maximum perturbation temperature was −4°C.

The vertical cross section of the simulated squall line (Fig.5) showed a similar structure to the observed squall line. The horizontal velocity (Fig.5a) has two maximum of forward flow to the leading edge. One was present at a height of 4 km and its maximum was accelerated and descended to the leading edge. The other was located near the surface. Consequently, the lower-level convergence at the leading edge was intense. An axis of negative velocity was inclined to the rear of the squall line with height and the upper-level divergence was also intense. This structure is similar to the observed Doppler velocity pattern shown in Fig.3b.

The vertical cross section of precipitation mixing ratios (Fig.5b) also shows similar structure to the radar echo structure (Fig.3a). This shows successive formation of convective cells from the leading edge to the rear. A new cell developed at the leading edge and included precipitation of rain. With development of the cell, precipitation of ice phase became significant. The distributions of snow, graupel, and rain of the oldest cell indicate that snow was produced in the uppermost part of the cell and developed into graupel. Then, rain was produced by melting of graupel. As a result, vertical cross section of precipitation was inclined as observed by the Doppler radars.

The perturbation temperature (Fig.5c) shows a cold air was present at the surface, whose maximum perturbation temperature was −3°C. The cold air was produced by evaporation cooling of rain. This was a driving force to form the squall line and controlled the movement of the squall line.

The time-distance cross section of the rain mixing ratio and the surface temperature perturbation (Fig.6) shows that the surface front moved at a speed of about 13 m s^{-1}. Convective cells developed successively along the surface front. Individual cells were almost stationary while the squall line moved as a result of the successive development of convective cells. This is similar to the observed squall line (Fig.4).

5. SUMMARY AND CONCLUSIONS

A significant squall line was observed by Doppler radars during the intensive field observation of HUBEX. The squall line was formed within the circulation of a mesoscale low.

The squall line was maintained for longer than two hours. On the basis of the Doppler radar observation, this study revealed the echo structure and the characteristics of the flow field of the squall line. The squall line was composed of intense convective cells along the leading edge. After it passed over the radar, a stratiform region was observed behind the convective leading edge. The squall line was tilted to the up-share side. The rear-inflow was significant at a height of 4 km with a maximum velocity of 13 m s^{-1}. The squall line advanced as a result of the successive development of convective cells at the leading edge.

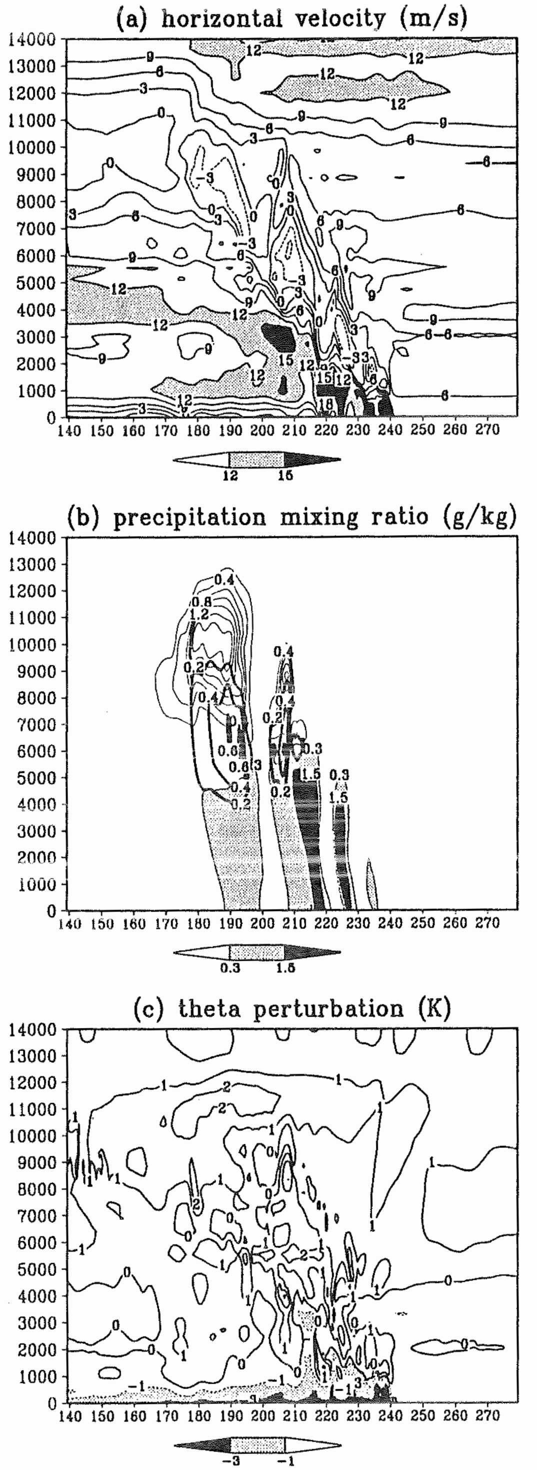

Figure 5: Vertical cross sections of the simulated squall line at 1700 UTC, 16 July 1998. (a) horizontal velocity (m s^{-1}), (b) precipitation mixing ratio (this lines are mixing ratio of snow; g kg^{-1}, thick lines of graupel; g kg^{-1} and shadings of rain; g kg^{-1},), and (c) perturbation of potential temperature (K).

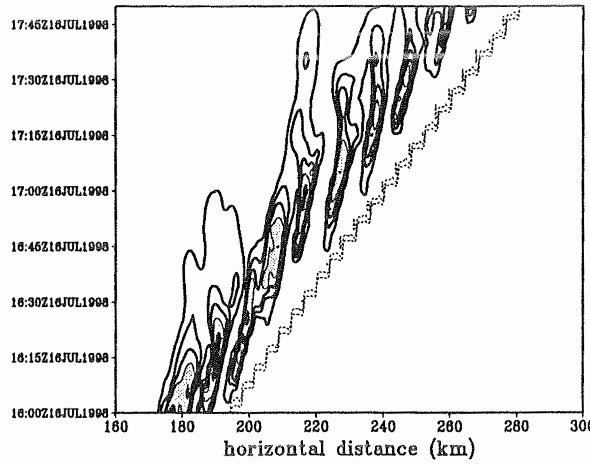

Figure 6: Time-distance cross section of rain mixing ratio at a level of 1000 m and surface front (dashed lines) obtained from the simulation experiment.

We made a simulation experiment of the squall line using ARPS in the two-dimensional geometry. The simulation showed a similar squall line to the observed one. The flow structure showed that two maxima of rear-inflow; one was present at a level of 4 km and the other was near the surface. The squall line was forced to move by the surface cold air mass. At the leading edge, convective cells successively developed. As a result, the squall line advanced while individual cells were almost stationary.

Acknowledgements

This study is a part of the GAME/HUBEX project which was carried out by the collaboration between China and Japan. We would like to express our sincere thanks to Professor Y. Ding of the National Climate Center, China Meteorological Administration. The simulation experiment was made using ARPS developed by CAPS, University of Oklahoma. CAPS is supported by the National Science Foundation and the Federal Aviation Administration through combined grant ATM92-20009.

References

Biggerstaff, M. I., and R. A. Houze, Jr., 1993: Kinematics and microphysics of the transition zone of the 10–11 June 1985 squall line. *J. Atmos. Sci.*, **50**, 3091–3110.

Fovell, R. G., and Y. Ogura, 1988: Numerical simulation of a midlatitude squall line in two dimensions. *J. Atmos. Sci.*, **45**, 3846–3879.

Houze, R. A., Jr., S. A. Rutledge, M. I. Biggerstaff, and B. F. Smull, 1989: Interpretation of Doppler weather-radar displays in midlatitude mesoscale convective systems. *Bull. Amer. Meteor. Soc.*, **70**, 608–619.

Johnson. R. H., and P. J. Hamilton, 1988: The relationship of surface pressure features to the precipitation and airflow structure of an intense midlatitude squall line. *Mon. Wea. Rev.*, **116**, 1444–1472.

HIGH ALTITUDE OBSERVATIONS OF ICE IN TROPICAL CONVECTIVE CLOUDS

David E. Kingsmill * and John Hallett

Desert Research Institute, Reno, NV

1. INTRODUCTION

Tropical clouds play a key role in the global energy balance, influencing both solar/terrestrial radiation and latent heating. The microphysical composition of these clouds is an important factor in determining how these interactions take place. Previous microphysical studies of tropical clouds have focused on the low to midlevels of precipitating convection at temperatures greater than –25 °C (e.g., Black and Hallett 1986; Houze and Churchill 1987; Yuter and Houze 1997) and on mid- to high-level cirrus at temperatures less than –25 °C (e.g., Griffith et al 1990; Heymsfield and McFarquhar 1996; McFarquhar and Heymsfield 1996). There are only limited microphysical observations of ice particles at high altitudes (i.e., a few km below the tropopause) in tropical convective clouds, and those are mainly in the transition regions between convective and cirrus clouds.

Observations from the Kwajalein Experiment (KWAJEX), operated in the vicinity of the Marshall Islands during July-September 1999, provide an opportunity to fill this gap in our understanding of tropical convective cloud microstructure. The primary motivation for KWAJEX was to support the needs of the NASA Tropical Rainfall Measuring Mission (TRMM). TRMM requires more detailed information about the microstructure of tropical convective clouds to more accurately retrieve rainfall estimates from spaceborne microwave remote sensors. KWAJEX attempted to address this need by obtaining simultaneous microphysical measurements at many levels in the same convective cloud or cloud system. Three aircraft were used for this purpose: the University of Washington Convair, the University of North Dakota Citation, and the NASA DC8. The Convair and Citation focused on sampling the low to midlevels of convective clouds, especially near the melting level (~5 km). In contrast, the DC8 focused on sampling the upper levels of convective clouds (~10.5 to 12.5 km). Almost 35 hours of in-cloud microphysical observations were collected on 27 different flights, with most of the data in the temperature range of –42 to –62 °C (Fig. 1). Since this is the region of most relevance to our study, we focus on these observations.

The DC8 was equipped with five different microphysical instruments during KWAJEX. A Cloud Particle Imager (CPI, Lawson et al. 1998) was mounted on top of the fuselage while a Cloudscope (Hallett et al.1998), FSSP, 2DC, and 2DP were mounted in wing-tip pods. The latter three probes are upgraded versions of the originals first designed by PMS (Knollenberg 1970). Droplet Measurement Technologies (DMT Inc., Boulder, CO) performed the modifications, which were primarily directed at improving the speed of the electronics. These upgrades allow the probes to operate with little, if any dead time and to perform more effectively at high aircraft speeds. On the DC8, this latter feature is particularly relevant since the aircraft normally cruises at speeds of about 200 m s^{-1}.

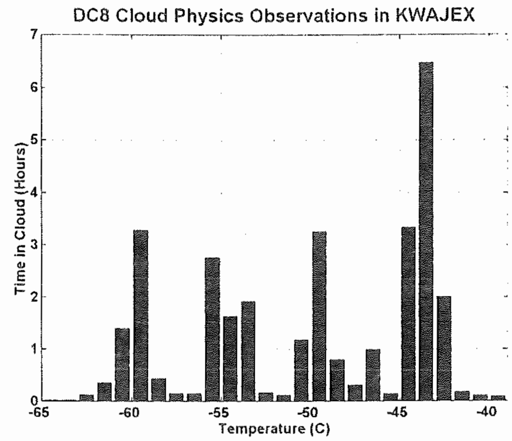

Figure 1. Temperature distribution of in-cloud microphysics observations from the DC8 during KWAJEX

Our first analysis objective is to characterize the microphysical mean state and variability of convective clouds sampled by the DC8 during the entire period of KWAJEX. In this study we simplify the task by focusing on data from just the 2DC probe, which has a 64 diode array, 1 bit of image depth (i.e., a mono-probe), a size range of 25-1550 μm and a resolution of 25 μm. The analysis is further simplified by sizing images only in the direction orthogonal to the diode array and rejecting images that occult either end diode. As a result of the last constraint, the entire-in technique (Heymsfield and Parrish 1978) for computing sample volume is employed.

2. DC8 OBSERVATIONS

A size spectra incorporating all DC8 2DC observations in the temperature range of –42 to –62 °C is shown in Fig. 2. This composite spectrum was calculated by taking averages of every relevant 5-second spectrum. Worthy of note is the lack of any apparent reduction in concentration at the small size end of the distribution due to electronic roll-off (Baumgardner and Korolev 1997). This result can likely be attributed to the faster electronics associated with this probe (response time < 0.1 μs) compared to previous versions of the 2DC that have response times

*Corresponding author address: David E. Kingsmill, Desert Research Institute, 2215 Raggio Parkway, Reno, NV 89512-1095; email: davidk@dri.edu

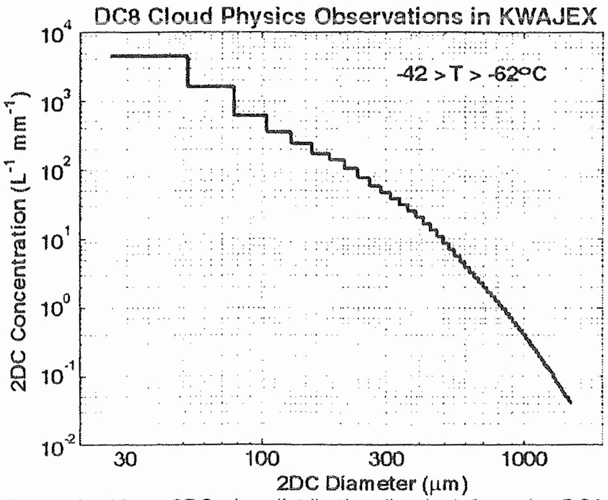

Figure 2. Mean 2DC size distribution (log-log) from the DC8 during KWAJEX for the temperature range of –42 to –62 °C.

of about 0.4 μs. Although a standard depth of field versus size relationship (Heymsfield and Parrish 1978) was used in these calculations, no aircraft airspeed corrections were applied. Overall, the spectrum shows similarities to those derived by McFarquhar and Heymsfield (1996) for cirrus anvils over the central Pacific. One indicator of this similarity is the distinct change in slope of the spectrum at about 400-500 μm.

To examine the variability embedded within individual 5-second spectra, we make use of two derived parameters: the total concentration and mean volume diameter. Total concentration is the sum of all concentrations within the 2DC size range multiplied by the bin width (25 μm). Mean volume diameter is the fourth moment of the distribution divided by the third moment of the distribution, which is in effect a volume weighted mean particle size. Frequency distributions of these parameters are shown in Figs. 3 and 4. Temperature is used as one means to stratify the data. The bounds of these stratifications (-42 to –47, -47 to -52, -52 to –57, and –57 to –62 °C) are based on the four peaks in sampling frequency seen in Fig. 1. In addition, total concentration and mean volume diameter are stratified against each other. Looking at all of the data for these parameters, it is clear that small values of total concentration (Fig. 3a) and mean volume diameter (Fig. 4a) dominate the distribution. Total concentration is restricted to small values (< 750 L^{-1}) when mean volume diameters are less than 250 μm (Fig 3b). The distribution of total concentration is spread over a wider range of values when mean volume diameters are larger (Figs 3c-d), but the frequency peaks are still on the small valued end. As temperature decreases, there is a tendency for less frequent occurrence of total concentrations greater than 1000 L^{-1} (Figs 3e-h). However, even at the lowest temperatures, 2000-3000 L^{-1} total concentrations occur occasionally. The distribution of mean volume diameter also shows some interesting trends. As total concentration increases, the mode of the distribution increases from 100 to 500 μm, the occurrence of mean volume diameters greater than 1000 μm becomes more frequent and the occurrence of mean volume diameters less than 300 μm becomes less frequent (Figs 4b-d). Mean volume diameters greater than 1000 μm tend to occur most frequently at the warmest temperatures (Figs. 4e-h).

Although large total concentrations and mean volume diameters occur infrequently in the dataset, they are important to characterize because they likely represent the areas of most intense convection aloft and

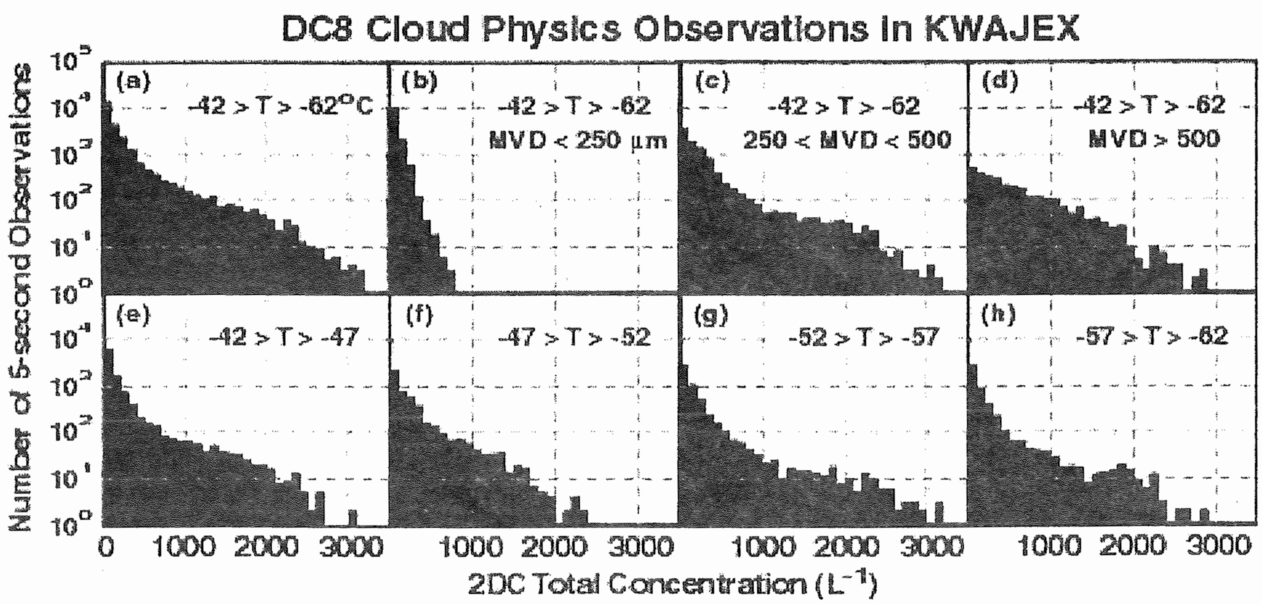

Figure 3. Various histograms showing logarithmic frequency of occurrence for 2DC total concentration (L^{-1}). (a) All observations in the temperature range of –42 to –62 °C, (b) same as (a) except for mean volume diameters less than 250 μm, (c) same as (a) except for mean volume diameters between 250-500 μm, (d) same as (a) except for mean volume diameters greater than 500 μm, (e-h) all observations in the temperature ranges of –42 to –47 °C, -47 to –52 °C, -52 to –57 °C, and –57 to -62°C, respectively.

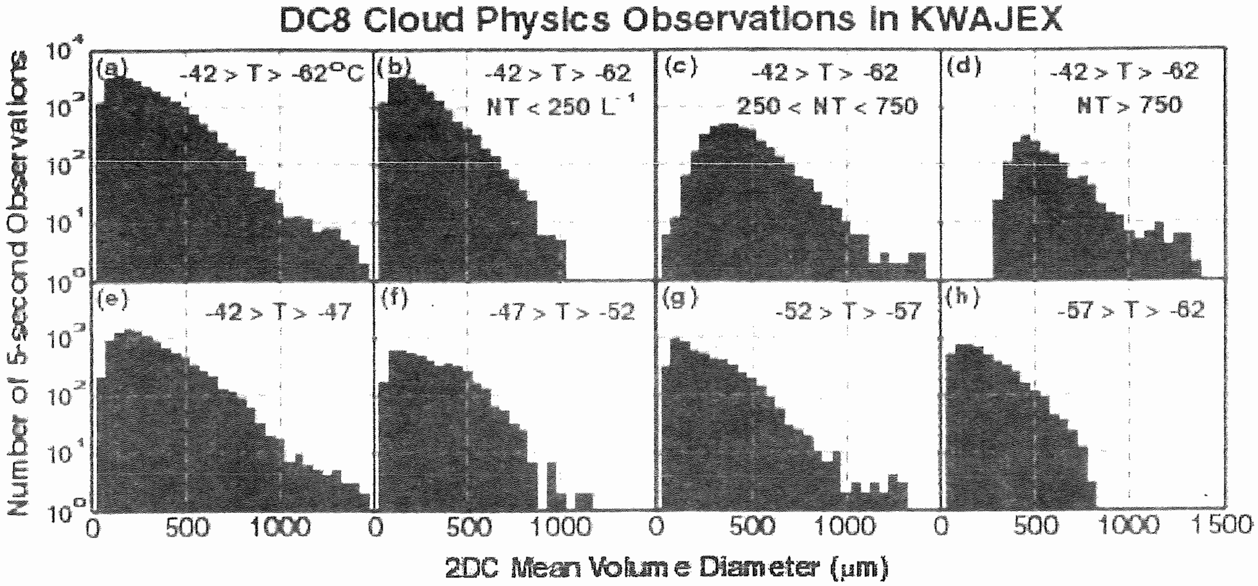

Figure 4. Various histograms showing logarithmic frequency of occurrence for 2DC mean volume diameter (μm). (a) All observations in the temperature range of –42 to –62 °C, (b) same as (a) except for total concentrations less than 250 L^{-1}, (c) same as (a) except for total concentrations between 250-750 L^{-1}, (d) same as (a) except for total concentrations greater than 750 L^{-1}, (e-h) all observations in the temperature ranges of –42 to –47 °C, -47 to –52 °C, -52 to –57 °C, and –57 to -62°C, respectively.

heaviest precipitation at the surface. These are regions of great relevance to TRMM. In this light we examine two specific examples where large total concentrations and/or large mean volume diameters were encountered. The DC8 was sampling relatively small (~10-20 km diameter) but intense convective cells in both cases. The time series on 10 September 1999 (Fig. 5) has two periods with mean volume diameters greater than 750 μm. The first of these is associated with large total concentrations (~222313 UTC) whereas the second is not (~222516 UTC). Particle habit in both instances is dominated by aggregates (Fig. 6) with the latter appearing less rimed than the former due to the more porous character of the images. The time series on 19 August 1999 (Fig. 7) has two periods with mean volume diameters exceeding 900 μm, both of which are associated with total concentrations of almost 2000 L^{-1}. Particle habit for both periods appears to be composed of heavily rimed aggregates and/or graupel due to the lumpy, non-porous, and sometimes quasi-spherical appearance of the images.

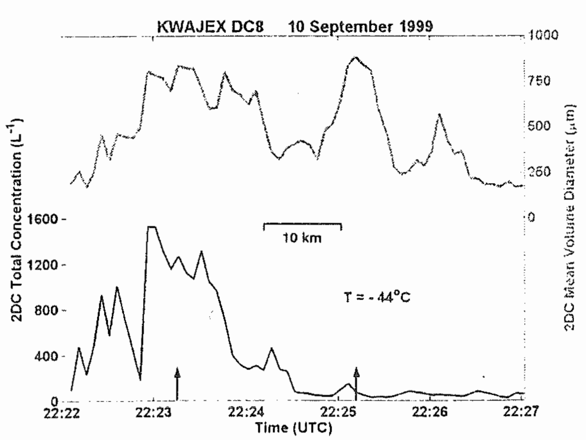

Figure 5. Time series of 2DC total concentration (black, lower) and mean volume diameter (gray, upper) for a DC8 flight segment on 10 September 1999 during KWAJEX. Arrows represent times of images shown in Fig. 6.

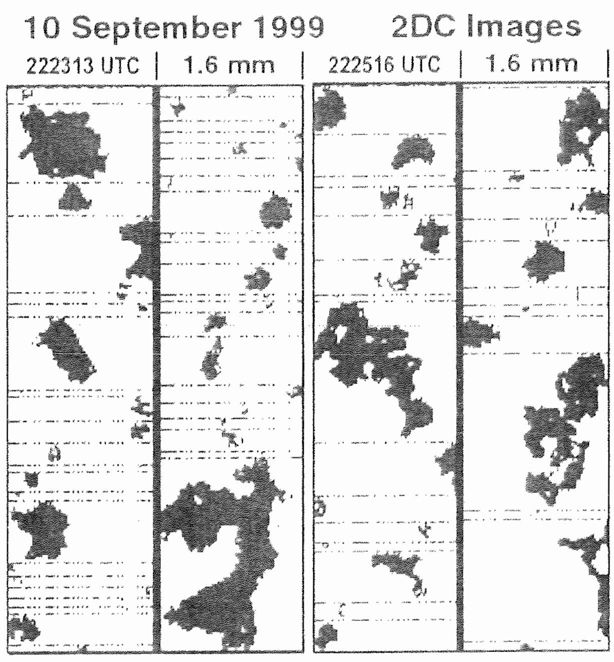

Figure 6. Selected 2DC images at 222313 and 222516 UTC for a DC8 flight segment on 10 September 1999 during KWAJEX. Each column of images is 1.6 mm wide.

3. SUMMARY

This study has focused on analysis of microphysical data collected at high altitudes in tropical convective clouds. Small ice particle sizes and small number concentrations were most frequently observed. However, larger ice particle sizes and larger number concentrations were occasionally detected, sometimes in the form of aggregates and graupel. Future work will involve better characterizing these regions, including statistical discrimination of ice particle habits, derivation of ice water contents, and a critical assessment of the assumptions used to make these calculations. Intercomparisons of these parameters with radar and radiometer measurements will also be employed to provide a better context for cloud structure.

ACKNOWLEDGEMENTS

The authors would like to thank the crew of the NASA DC8 for their assistance in mounting the microphysical instruments on the aircraft and for their skill in executing the flight strategies desired by the science team. This research was sponsored by NASA grant NAG5-7973.

REFERENCES

Baumgardner, D., and A. Korolev, 1997: Airspeed corrections for optical array probe sample volumes. *J. Atmos. Oceanic Technol*, **14**, 1224-1229.

Black, R. A., and J. Hallett, 1986: Observations of the distribution of ice in hurricanes. *J. Atmos. Sci.*, **43**, 802-822.

Griffith, K. T., S. K. Cox, and R. G. Knollenberg, 1980: Infrared radiative properties of tropical cirrus clouds inferred from aircraft measurements. *J. Atmos. Sci.*, **37**, 1077-1087.

Hallett, J., W. P. Arnott, R. Purcell, and C. Schmidt, 1998: A technique for characterizing aerosol and cloud particles by real time processing. *PM2.5: A fine particle standard*, Long Beach, CA, Air and Waste Management Association, Pittsburgh, PA.

Heymsfield, A. J., and G. M. McFarquhar, 1996: High albedos of cirrus in the tropical Pacific warm pool: Microphysical interpretations from CEPEX and from Kwajalein, Marshall Islands. *J. Atmos. Sci.*, **53**, 2424-2451.

Heymsfield, A. J., and J. L. Parrish, 1978: A computational technique for increasing the effective sampling volume of the PMS two-dimensional particle size spectrometer. *J. Appl. Meteor.*, **17**, 1566-1572.

Houze, R. A., Jr., and D. D. Churchill, 1987: Mesoscale organization and cloud microphysics in a Bay of Bengal depression. *J. Atmos. Sci.*, **44**, 1845-1867.

Knollenberg, R. G., 1970: The optical array: An alternative to scattering or extinction for airborne particle size determination. *J. Appl. Meteor.*, **9**, 86-103.

Lawson, R. P., A. V. Korolev, S. G. Cober, T. Huang, J. W. Strapp, and G. A. Isaac, 1998: Improved measurements of the drop size distribution of a freezing drizzle event. *Atmos. Res.*, **47**, 181-191.

McFarquhar, G. M., and A. J. Heymsfield, 1996: Microphysical characteristics of three anvils sampled during the Central Equatorial Pacific Experiment. *J. Atmos. Sci.* , **53**, 2401-2423.

Yuter, S. E., and R. A. Houze, Jr., 1997: Measurements of raindrop size distributions over the Pacific warm pool and implications for Z-R relations. *J. Appl. Meteor.*, **36**, 847-867.

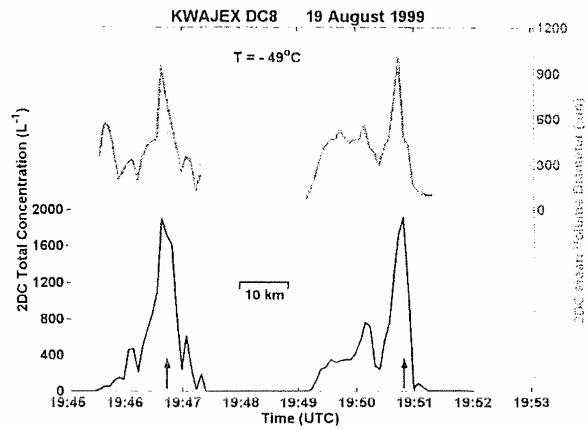

Figure 7. Time series of 2DC total concentration (black, lower) and mean volume diameter (gray, upper) for a DC8 flight segment on 19 August 1999 during KWAJEX. Arrows represent times of images shown in Fig. 8.

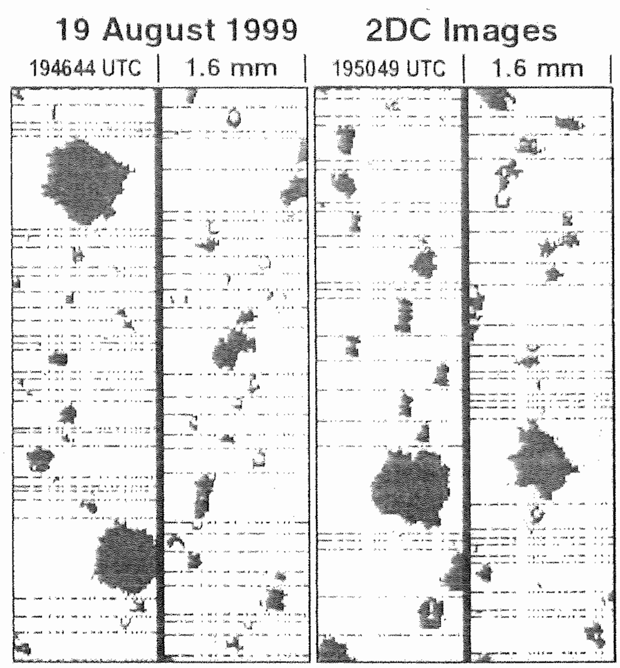

Figure 8. Selected 2DC images at 194644 and 195049 UTC for a DC8 flight segment on 10 September 1999 during KWAJEX. Each column of images is 1.6 mm wide.

MULTISENSOR ANALYSIS OF CONVECTION IN MEDITERRANEAN CYCLONES

Federico Porcú[1], Franco Prodi[1,2], Stefano Natali[1], Davide Capacci[2] and Clelia Caracciolo[1]

[1]University of Ferrara, Dept. of Physics, Ferrara, I-44100, Italy
[2]ISAO-CNR, Clouds and Precipitation Group, Bologna, I-40129, Italy

1. INTRODUCTION

A recent climatological study (Trigo et al., 1999) has shown that the cyclonic activity is a key feature of the meteorology of the Mediterranean basin during the whole year. In particular, during warm months, short-living cyclones (averaged lifetime about 30 hours) rise from well known birthplaces (Gulf of Genoa, Gibraltar area, Atlas Mountains are the most effective) and affect the weather in the Mediterranean area.

Following a different approach Porcú et al. (1997) have shown that very often such cyclones force convective initiation and development. Moreover those episodes are responsible for the most severe rainfall events, sometimes related with flood/flash-flood occurrence in coastal and continental areas. The combination of long-lasting, moderate precipitation with heavy showers is the most common mechanism originating such floods.

The cloud systems related to the cyclonic structure often develop over the sea: the scarcity of conventional observation available in the Mediterranean basin makes satellites preferred points of view for a detailed study of these events.

A complete analysis will include the use of ECMWF fields to assess the larger scale setting: in particular we'll consider the presence and intensity of Potential Vorticity Anomalies (PVAs) related to the cyclonic depression. PVAs are suspected to be precursor of heavy rainfall episodes (Massacand et al., 1999). A further approach will be developed including combined SSM/I-Meteosat water vapour retrieval over cloud-free areas, in order to evaluate the potential of convective initiation.

In this work we present preliminary results of a multi-sensor, multi-frequency analysis of convective patterns in cyclonic structure. We modified a cloud classification algorithm originally developed for visible-infrared (VIS-IR) data (Porcù and Levizzani, 1992) including also microwave radiances, to increase the informative content of the classification. In particular the SSM/I brightness temperature at 85 GHz is used together with the equivalent black body temperature as measured by the Meteosat infrared channel.

2. METHODOLOGY

The aim of this work is to investigate convective patterns embedded in cyclonic cloud bands and/or forced by the cyclonic flow, and evaluate the capabilities of a pure remote sensing approach to the study of convection.

We used a clustering algorithm originally developed for working in a two dimensional radiances' space: the two-dimensional histogram is constructed and a classifier is used to find clusters of radiances (each one refers to a cloud class) by minimising a similarity function to perform a partition of the histogram and therefore classify the cloudy scene.

Usually, the VIS-IR classification resolves rather reliably most of the isolated convective clouds, large enough to be observed at the Meteosat ground resolution (about 5x7 km in the Mediterranean basin). In case of convective cells cluster or cells embedded in thick stratified cloud shields, the method is not able to distinguish convective cores from other thick cold clouds. The use of Brightness Temperature at 85 GHz (85Tb) data would resolve this shortcoming, given the low sensitivity of the microwave data to clouds without a thick ice layer.

At VIS and IR wavelengths clouds are opaque bodies if thicker than few hundred meters: the radiance measured by the Meteosat sensors are reflected (VIS) or emitted (IR) from the top of the cloud. Convective clouds appear as very bright spots in both channels in the updraft area, surrounded by a warmer cloud shield, usually related to the anvil; the thinning of the stratified anvil is often recognised by VIS data: at this wavelength cirrus are optically semi transparent. On the other side at microwave wavelength cloud droplets weakly interact with the radiation: in particular at 85 GHz the scattering dominates on absorption and the radiometer primarily measures the presence of scattering particles, e.g. ice.

The variability of the soil emissivity makes the classification of cloud-free or thin (in the microwave) cloud areas more difficult than the VIS-IR case. Nevertheless, in region covered by thick clouds (the focus of out study), the classification seems appropriate and directly related to physical cloud structure. The classification can be seen as a starting point of a more complete analysis that will include PVA analysis and satellite water vapour retrieval.

We compared VIS-IR and 85Tb-IR classification for convective cases evaluating differences between the two images, then we applied for the whole period the IR-85Tb scheme to more than 40 images. Two examples are presented in this work.

The results show potential in understanding of the convective patterns, especially if embedded in cyclonic cloud bands, as it is common at mid-latitude.

Corresponding author's address: Federico Porcú, University of Ferrara, Dept. of Physics, Ferrara, I-44100, Italy; E-Mail: porcu@fe.infn.it.

3. DATA AND ALGORITHMS

We considered one-month data from 27/08/1998 to 26/09/1998: in this period 6 cyclones developed in the Mediterranean basin and a considerable number of convective events were detected. Our basic database was the ISAO-CNR Meteosat data archive (for VIS-IR dataset) and the SSM/I data were available through a co-operation with the Global Hydrology and Climate Center, University of Alabama, Huntsville/NASA.

METEOSAT infrared images (IR: 10.5-12.5 μm) were calibrated and converted to Equivalent Black Body Temperature (EBBT) accordingly with EUMETSAT calibration coefficients. Visible data (VIS: 04-0.9 μm), available from 06:00 UTC to 19:30 UTC, are normalised with the solar elevation angle and converted to albedo.

The SSM/I is a seven-channel, four-frequency, linearly polarised, passive microwave radiometric system, which measures atmospheric, oceanic, and terrain microwave brightness temperatures at 19.35, 22.235, 37.0, and 85.5 GHz. It is carried aboard Defense Meteorological Satellite Program satellites (DMSP), launched into a near polar, sun-synchronous orbit. The data used in this study are extracted from sensors placed on F-13 and F-14 satellite.

Meteosat and SSM/I data were carefully co-located: only images with a maximum time lag lower than 5 minutes were selected. Moreover a parallax correction was applied to the SSM/I descending orbit, where the displacement between polar (SSM/I) and geostationary (Meteosat) apparent position of the cloud is maximum (about 1.5 85GHz pixel, as showed in Porcù et al., 1999). Finally SSM/I images were remapped onto the Meteosat grid by a simple nearest neighbour procedure.

Original classification algorithm was based on a simple clustering technique applied to bi-dimensional histogram derived from METEOSAT VIS and IR sensor counts. The resulting partitioning of the histogram consists of several classes, each characterised by a centre that defines the radiative signature of the cloud (or no-cloud) class. The algorithm is iterative: starting from an initial partition, a different partition is generated in each step and then kept or rejected after controlling. In order to decide whether or not a new partition is to be kept, a similarity function characterising the partition is evaluated. This function is minimised to obtain the best possible partition.

Two modifications are considered in this work. First we decided to work in the temperature space, instead of counts (or radiances) space: this makes the dynamics of the EBBT lower for colder pixels, given the logarithmic dependence of the EBBT from the radiance. The second was to introduce the 85Tb axis to replace the VIS in the histogram.

The replacement of the VIS with the 85Tb in order to perform classification on a 85Tb-IR temperature space poses technical problems in modifying the algorithm, because of the different sensitivity and dynamics of the visible and microwave channels. The number of total classes found by the algorithm is generally higher if the 85Tb-EBBT space is used. Moreover, different emissivity of the soil can influence the classification even pixel covered by optically thin clouds at 85 GHz that can be differently classified, depending on the background (sea or land). This effect is more effective if Tb at horizontal polarisation is used, especially due to the great emissivity difference of the sea.

4. RESULTS

4.1 Comparison between IR-VIS and IR-SSM/I classification

The physical significance of the microwave channels plays a key role in the cloud classification results. The improvement of the performances of the new method is more evident in scenes where convective cores are embedded in thick cyclonic cloud band. Indeed in scene with isolated convective systems the performances of the two methods are very similar.

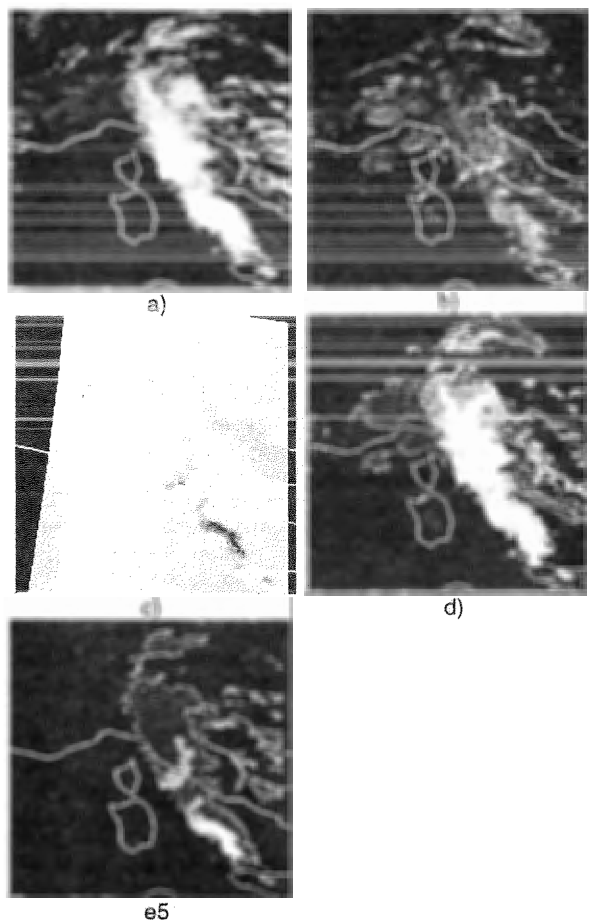

Figure 1: 25/09/1998 08:20 UTC: a) METEOSAT Infrared image, b) Visible and c) SSM/I 85 GHz vertical polarisation; cloud classification by d) VIS-IR method and e) by Tb85-IR method.

As an example, we consider the situation occurred on 25/09/98 08:20 UTC: a large cloud band approaches the Italian west coast from the Mediterranean. Images from METEOSAT IR and albedo correct VIS and from SSM/I 85GHz vertical polarisation of the same scene are shown in figure 1(a, b, c). VIS-IR classified image is shown in figure 1d and the 85Tb-IR one in figure 1e.

The VIS-IR algorithm identifies in the same class (white class) thick cloud areas, without discriminating between the most active convective areas and other cold and thick cloud shields. On the other side, the 85Tb-IR approach allows such discrimination: convective cores are isolated (white class) and a squall line structure, in the southern part of the image, is revealed embedded in more stratified cloud types (light grey, medium grey). Looking at the METEOSAT sequence, the arc-shaped light-grey class, in the centre of the image, represents older, decaying cells (lower ice content, but very cold in the IR); this is also confirmed by the large surrounding anvil (medium grey class).

The southern squall line is relatively younger: the convective portion (white class) is large and very cold in both EBBT and 85Tb fields; the anvil (medium grey) is less extended. This squall line will last for more than four hours. Lower level stratiform over north-west Italy is classified in the same way with both schemes.

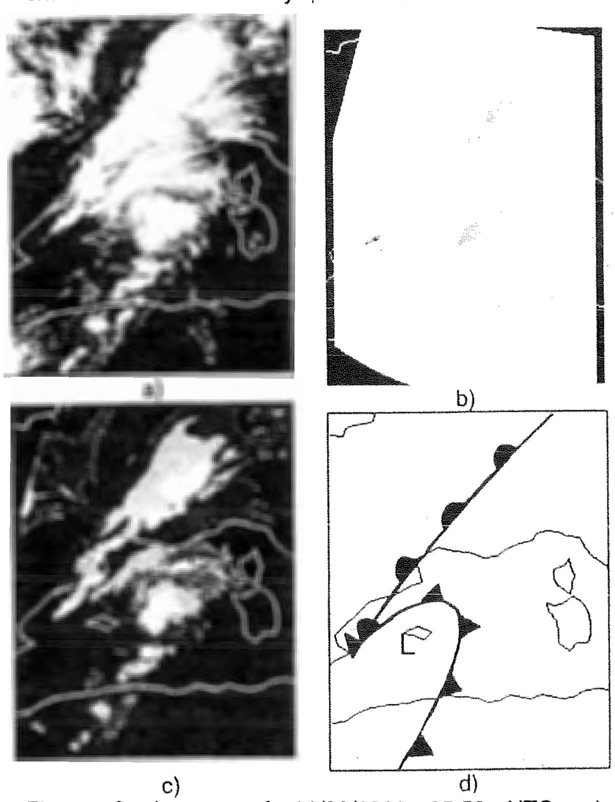

Figure 2: images of 11/09/1998 05:50 UTC: a) METEOSAT IR, b) SSM/I 85 GHz vertical polarization, c) 85Tb-IR cloud classification, d) sketch of the fronts and low location.

4.2 Application of SSM/I-IR method

A typical case of convection related to cyclonic development in the Mediterranean is shown in Figure 2. The mesoscale setting, sketched in figure 2d, shows a well-defined cyclonic structure, derived from an instant occlusion generated from extratropical cyclone interacting with continental European orography. This cyclone induces a secondary pressure minimum placed near the Balearic Island originated few hours before our images, as a perturbation of a polar front.

Comparing the satellite images two cloud systems related with the warm and cold fronts can be identified.

The classified image shows peculiar cloud patterns. In the warm sector scattered convection follows the frontal surface; the size and the life stage of the cells increase from the south to the north. Alongside the warm front, convection is still present with a considerable extent, but it is embedded in large, stratified cloud shield with thinner ice layer but very cold top. Convection is also detected near the occlusion.

5. CONCLUSIONS AND FURTHER WORK

A classification algorithm working with METEOSAT IR and VIS data has been adapted to include SSM/I microwave data. In order to evaluate the information improvement introduced by the microwave, a case with complete information dataset has been deepened. An effective improvement in the convective cores identification has been observed, mainly in systems with complex cloud structure. Cloud structures identified by the classification are in agreement with other observations.

Investigation based on conventional fields (e.g. potential vorticity) and satellite water vapour retrieval will be faced with such kind of classification for a better understanding of Mediterranean cyclones.

6. ACKNOWLEDGEMENTS

The SSM/I data were provided by the Global Hydrology and Climate Center, University of Alabama, Huntsville/NASA. This work is funded by the EU project MEFFE (satellite and combined satellite-radar techniques in meteorological forecasting for flood events) of the IV Framework Program, under contract ENV4-CT96-0281, and the Italian GNDCI (National group for the prevention of hydrogeological disasters).

6. REFERENCES

Massacand, A., H. Wernli and H.C. Davies, 1998: Heavy precipitation on the Alpine southside: an upper level precursor. Geoph Res. Lett., 25, 1435-1438

Porcù, F. and V. Levizzani, 1992: Cloud classification using METEOSAT VIS-IR imagery. Int. J. Remote Sensing, **13**, 5, 893-909.

Porcù , F., F. Prodi, S. Franceschetti, S. Pasetti, 1997: Short term climatology of cloud systems leading to floods in Europe (1992-1996). The 1997 Meteorological Satellite Data Users' Conference, 29 Sep-3 Oct 1997, Brussels, Belgium 461-466.

Porcù, F., S. Dietrich, A. Mugnai, S. Natali, F. Prodi and P. Conway, 1999: Satellite multi-frquency observations of severe convective systems in the Mediterranean. Phys. Chem. Earth (B), **24**, 6, 643-648.

Trigo, I.F., T.D. Davies and G.R.Bigg, 1999: Objective climatology of cyclones in the Mediterranean region. J. of Climate, 12, 1685-1696.

Vertical Transport of Momentum within and Surrounding Isolated Cumulus Clouds

Paul B. Bogner and Gary M. Barnes

Department of Meteorology, University of Hawaii at Manoa, Honolulu, Hawaii

1. INTRODUCTION

Organized cumulus convection, in the form of squall lines and mesoscale convective complexes, is observed to alter the shear of the horizontal wind by way of large momentum transports induced by the storm circulation (LeMone et al., 1984, Wu and Yanai, 1994). However, at the smaller scales, comparatively little is known about the vertical transport of momentum within "ordinary" isolated cumulus clouds. This is the result of the limitations of past observing platforms and the difficulty in obtaining detailed observations from clouds that evolve and decay on short time scales (8-20 min). Consequently, previous studies describing aspects of cumulus cloud lifecycles (Warner 1977, Stith 1992, Barnes 1995) are limited to sampling one altitude numerous times, or one pass each, at varying altitudes.

The Convection and Precipitation/ Electrification Experiment (CaPE), conducted during the summer of 1991 near Cape Canaveral, offers the opportunity to probe clouds with two highly maneuverable, well-equipped King Air aircraft, both of which execute coordinated patterns for a nearly simultaneous penetration of a cloud at different altitudes. This allows for a detailed analysis of the vertical transports in momentum within and surrounding the cloud as a function of the cloud's lifecycle.

2. DATA AND SAMPLING STRATEGY

We are currently studying a subset of 12 clouds, encompassing 122 passes, that occurred on 5 days: July 18 and 26, and August 3, 9, and 10 of 1991. The aircraft data are supported by an upper-air sounding network of 10 stations as well as an automated surface mesonet comprised of 47 stations to aid in the determination of the environmental stability, shear and surface forcing.

Corresponding author address: Paul B. Bogner, Department of Meteorology, University of Hawaii at Manoa, Honolulu, HI 96822

The aircraft sampled the clouds using either a rosette or bow-tie pattern (Fig. 1a, b).

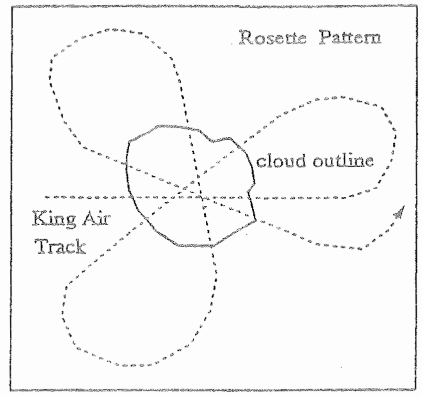

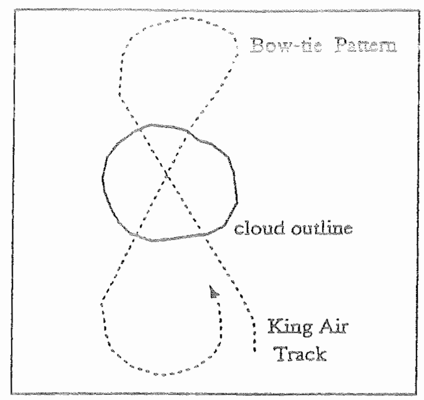

Fig. 1. Plan view of aircraft sampling patterns (a) the rosette and (b) the bow-tie.

The rosette pattern allows sampling on all sides of the cloud, enabling the determination of fields normal and parallel to the mean wind. The bow-tie pattern would essentially retrace and sample the same track through the target cloud.

The cloud edges are determined using the forward-scattering spectrometer probe (FSSP), which is designed to measure the smallest particles (0.5-47 μm). Figure 2 (a, b, lower panel) represents the FSSP time series of liquid water content for a target cloud sampled by both aircraft. More information on the CaPE dataset and sampling strategies can be found in Barnes et al. 1996.

3. Goals

We will present trends in the vertical transport of momentum as a function of cloud lifecycle along with comparisons between the aircraft sampling levels. Findings will be discussed in light of the previous work on various conceptual models of cloud growth and mixing. Relationships between vertical velocity, liquid water content and wind speed will be explored.

We will address the following issues:

1) Do updrafts (downdrafts) preferentially transport lower (higher) momentum air?
2) How would the diagnosed momentum transports change the environmental shear?
3) Does the magnitude of the momentum transfer increase or decrease with height or age of cloud?
4) Observations by Perry and Hobbs (1996) indicate that moisture haloes around the cloud grow in horizontal scale as the cloud ages. Is this phenomenon recognizable in the momentum field?
5) Does the transfer of momentum within the cloud yield important evidence, which leads one to support or reject any of the conceptual models for cumulus?

4. PRELIMINARY RESULTS

The time series of vertical velocity, liquid water content and wind speed (Fig. 2 a, b) shows the evolution of all three quantities. The environmental conditions on 10 Aug. 1991 show moderate conditional instability (CAPE =1600 J kg^{-1}) and low wind shear (a change of only 4.4 m s^{-1} within the lowest 6 km). The peak winds were 10 – 12 m s^{-1} from the west/southwest between 2-3 km and decreasing with height. Aircraft passes are made at 3960 and 4570 m within this cloud.

The vertical velocity signature is consistently upward for the first two passes (pass two of the lower aircraft missed the updraft). By the third pass, both levels are seeing strong edge downdrafts around the core updraft as the cloud has reached maturity. These gradually work their way toward the center and result in the collapse of the updraft by pass four, completing the transition to downdraft for the remainder of the cloud lifespan. The liquid water content has a peak in the early passes when the updrafts dominated and then a gradual decline in water content (a combination of rainout and evaporation). The evolution of momentum for this cloud is particularly interesting. The lower aircraft shows a consistently strong peak (5-7 m s^{-1}) in the horizontal wind speeds even after transition to downdraft. The upper aircraft sees comparatively little wind speed variation; a maximum occurs during the third pass and quickly fades thereafter. The horizontal wind speeds observed by the lower aircraft are consistent with the winds 1 km below the sampling level.

It is important to point out that these results will differ for different sampling levels. For example, other clouds on this day were sampled at much lower altitudes, 1800 and 2400 m (not shown). At these levels, which are below the soundings wind maximum, the transport of momentum is in contrast to that described above. The updrafts carry lower momentum air and the downdrafts carry higher momentum air consistently.

By subtracting the wind speed within cloud from the environmental wind speed, we can calculate the average perturbation created by the cloud at each level. Fig. 3 shows only the perturbation wind velocities at the two sampling levels. As described earlier, the lower aircraft is sampling higher momentum during all passes (except the last pass) with the maximum on the first pass of 3.1 m s^{-1} and consistently 1.5-2 m s^{-1} until the last pass when lower momentum air is sampled. The peak perturbations within each pass are significantly larger as seen in fig. 2b, where increases of 6-7 m s^{-1} are observed. The upper aircraft perturbations are significantly smaller with the mean perturbations only 0.5 – 1 m s^{-1} for most of the cloud except for the maximum 2.3 m s^{-1} during the third pass. We are currently dividing the cloud into the updraft and downdraft components to see not only the individual capabilities of each to transport momentum but also to determine if the cloud mean gives an adequate representation of the signal.

Scatter plots comparing the vertical velocity, liquid water content and wind speed indicate that there is a strong relationship between the liquid water content and the vertical velocity at both levels. Strong updrafts tended to have higher liquid water contents than downdraft air.

For the lower aircraft, there is a persistent relationship between liquid water content and wind speed. This relationship is largely due to the consistent nature of the momentum signal. The relationship between vertical velocity and wind speed is a little more complex and is dependent on the stage of the cloud's life.

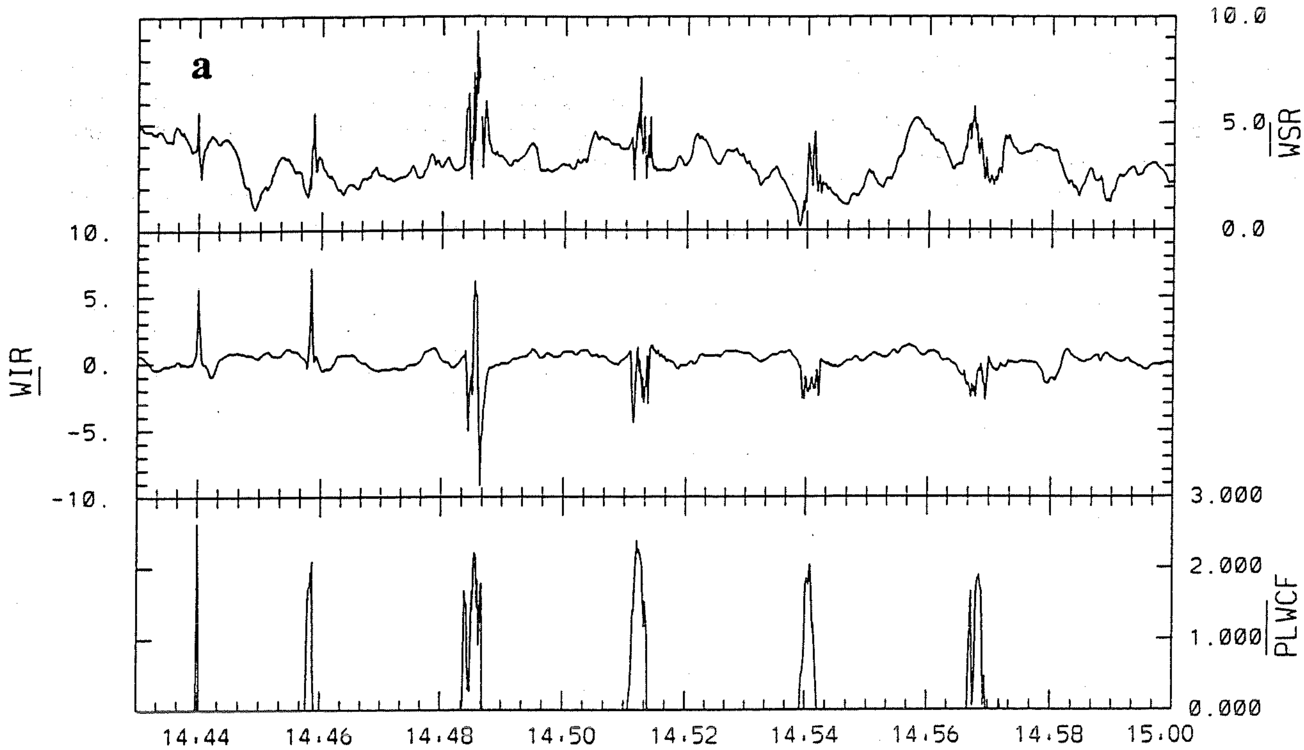

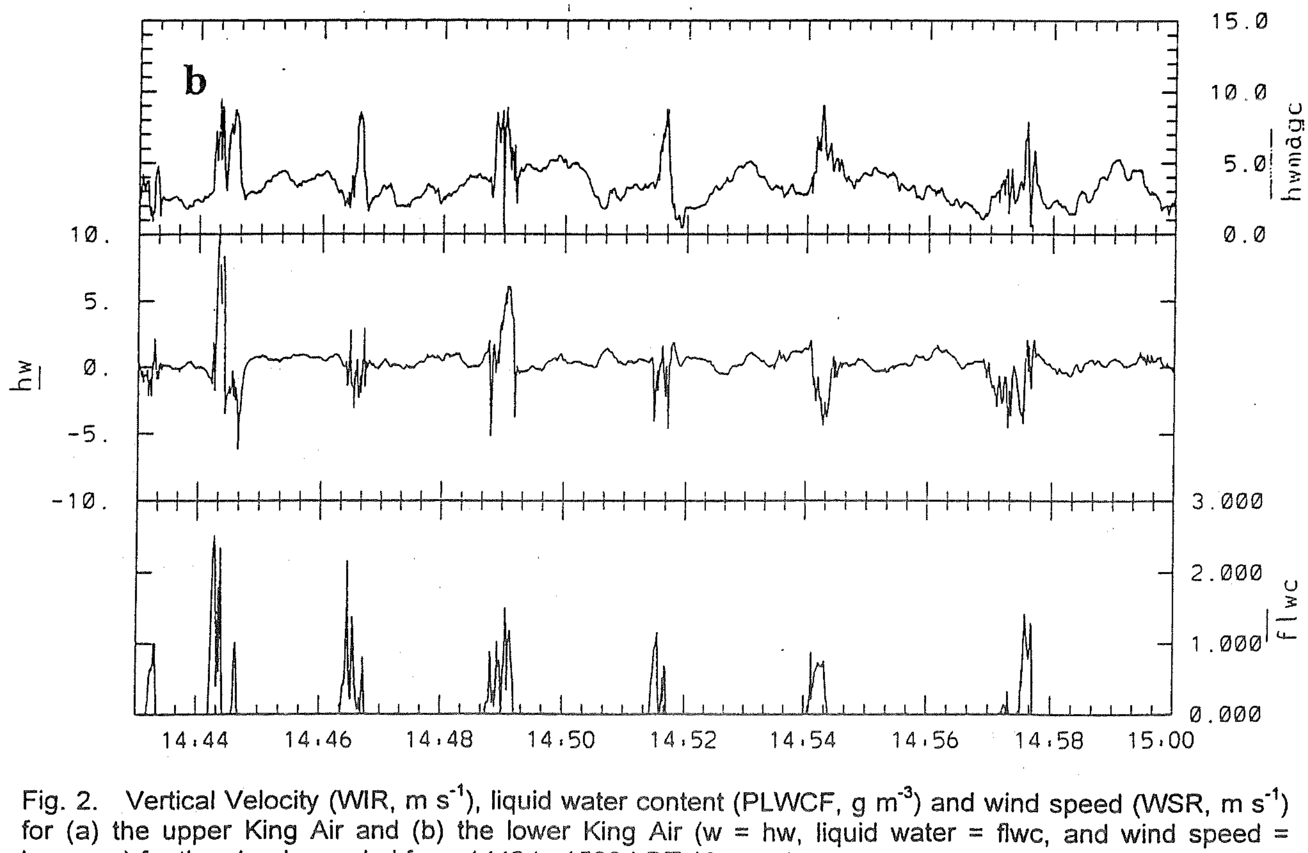

Fig. 2. Vertical Velocity (WIR, m s^{-1}), liquid water content (PLWCF, g m^{-3}) and wind speed (WSR, m s^{-1}) for (a) the upper King Air and (b) the lower King Air (w = hw, liquid water = flwc, and wind speed = hwmagc) for the cloud sampled from 1443 to 1500 LDT 10 Aug.1991.

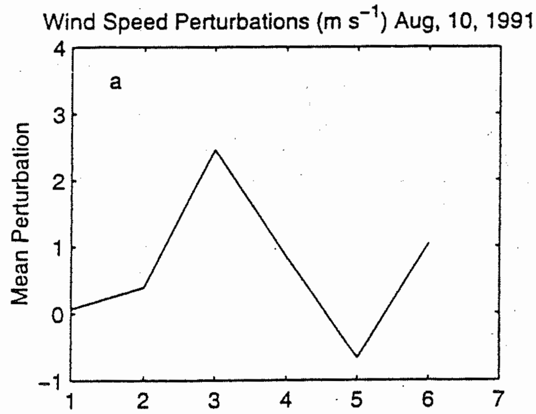

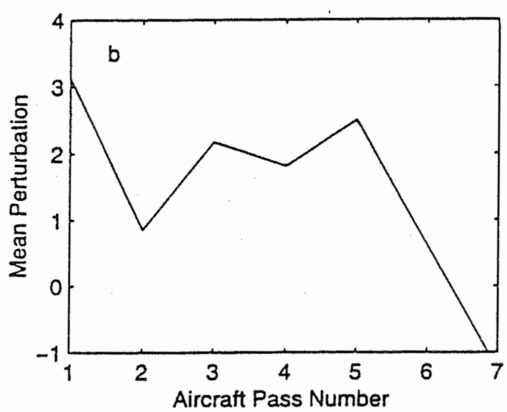

Fig. 3. The mean velocity perturbations (cloud – environment) in m s^{-1} for (a) the upper King Air and (b) for the lower King Air. The x-axis indicates the number of the aircraft pass through the cloud.

For this cloud, there is a tendency for a better correlation to occur in the early updraft stages and during the later stages when downdrafts were dominant. During the mature stage (pass 3 and the collapse of the updraft in pass 4) there is virtually no relationship between wind speed and vertical velocity, mostly because of the high variability in the vertical velocity signal.

The upper aircraft differs in that vertical velocity and wind speed show a poor correlation within the initial updraft passes because there is no wind speed maximum present. Thereafter, a weak but persistent correlation is present from the mature stage to dissipation. There is a poor correlation between the liquid water content and wind speed for all passes.

5. DISCUSSION

Although only one cloud is presented, this cloud is representative of a subset of those sampled during CaPE. The cloud is in a low shear environment with moderate conditional instability. The transport of momentum observed is in such a manner as to decrease the shear, or down gradient. Other passes through clouds sampled on this day at lower altitudes showed a down gradient transport, but with the updraft and downdraft transports opposite those of the upper level. Therefore, it is vital to know how the shear is oriented within the environment with respect to the sampling level as the transports can contrast significantly.

At this point, it is unclear exactly how important the vertical shear within the environmental profile is to the vertical transport of momentum. Is the shear simply a source of higher or lower momentum air for updrafts or downdrafts to displace or does it help to generate horizontal momentum by tilting of the buoyant updrafts? We will be evaluating cases that have shears larger and smaller than the case presented to determine how the differing shear profiles modulate the transport of momentum.

6. REFERENCES

Barnes, G.M., 1995: Updraft evolution: A perspective from cloud base. *Mon. Wea. Rev.*,**123**, 2693-2715.

Barnes, G.M., J. C. Fankhauser, and W. D. Browning, 1996: Evolution of the vertical mass flux and diagnosed net lateral mixing in isolated convective clouds. *Mon. Wea. Rev.*, **124**, 2764- 2784.

LeMone, M. A., G. M. Barnes, and E.J. Zipser, 1984: Momentum flux by lines of cumulonimbus over the tropical oceans. *J. Atmos. Sci.*, **41**, 1914-1932.

Perry, K., and P. Hobbs, 1996: Influences of isolated cumulus cloud on the humidity of their surrounding. *J. Atmos. Sci.*, **53**, 159-174.

Stith, J., 1992: Observations of cloud-top entrainment in cumuli. *J. Atmos. Sci.*, **49**, 1334-1347.

Warner, J., 1977: Time variation of updraft and water content in small cumulus clouds. *J. Atmos. Sci.*, **34**, 1306-1312.

Wu, X and M. Yanai, 1994: Effects of vertical wind shear on the cumulus a transport of momentum: observations and parameterization. *J. Atmos. Sci.*, **51**, 1640-1660

MICROPHYSICS OF A CENTRAL TROPICAL PACIFIC STRATIFORM PRECIPITATION MELTING LAYER

Paul T. Willis [1] and Andrew J. Heymsfield [2]

[1] NOAA/AOML/CIMAS, Miami, FL 33149
[2] NCAR/MMM, Boulder, CO 80302

1. INTRODUCTION

Since the beginning of the attempts to use radar as a quantitative tool for the measurement of precipitation, the bright band has been a troublesome source of error. A major objective of the TRMM satellite borne radar has been to measure vertical heating profiles in tropical convective systems. The stratiform precipitation regions, and the presence of the bright band, is of particular importance in these systems, because the stratiform region heating profiles are dynamically significant, extensive in areal coverage, and significantly distinct from the convective precipitation heating profiles. The coexistence of ice and liquid water in the melting regions, the attenuation occurring at microwave frequencies, as well as the very complex microphysical processes interacting, make microwave measurements taken through the melting layer difficult to interpret. The hydrometeor size distributions through the melting layer are important because of the effects on the transmission of radiation at microwave frequencies. In addition, the melting layer is potentially dynamically significant, because the diabatic cooling due to the microphysical process of melting is restricted to a very narrow layer beneath the 0 deg. C level. Horizontal variations in precipitation rate can result in pressure perturbations, and wind field perturbations (Heffernan and Marwitz, 1996).

The purpose of this study is to present preliminary results from an observational case study of a tropical oceanic melting layer obtained during the KWAJEX campaign in August of 1999. Several advances in airborne microphysical instrumentation make this case particularly exciting. The HVPS, which was utilized in concert with the more widely used PMS imaging probes, provides an adequate sample volume for observing the low concentrations of very large hydrometeors typically present during melting. The CPI instrument, though best suited for quantitative measurement of smaller cloud particles, provides very detailed looks at a small sample of large hydrometeors through the melting layer.

Aggregation and breakup are now recognized as important processes associated with the melting process. Barthazy, Henrich, and Waldvogel (1998) find strong evidence in Switzerland for aggregation of hydrometeors within the upper part of the melting layer, and breakup within the lower part. Our previous observational bright band study (Willis and Heymsfield, 1989), based on an advecting spiral descent through an MCS trailing stratiform region, found that the radar bright band maximum is due to a very few very large aggregates that survive to temperatures a little warmer than 0 deg. C. A continuing question in melting layer studies has been to quantify the importance of aggregation during the conversion from snow to rain. In this preliminary study we present size distributions through the melting layer. Breakup during melting also occurs to varying degrees at times during the melting process (Drummond, et al., 1996), and it is difficult to determine the relative magnitudes of each, when both are occurring during the melting process. With this newer suite of instruments we plan to pay very close attention to hydrometeor size, hydrometeor water mass, hydrometeor fall velocity distributions, particle number flux densities, and mass flux and mass conservation through this melting layer. In this study we present a first look at the hydrometeor size distributions through this melting layer.

Corresponding author: Paul T. Willis, NOAA/AOML/HRD
4301 Rickenbacker Cswy, Miami, FL 33149
willis@aoml.noaa.gov

2.0 DATA

The sampling aircraft was the University of North Dakota (UND) Citation cloud physics aircraft. The measurements were taken during the NASA KWAJEX field campaign on 19 August 1999. The flight pattern was an advecting spiral descent, first utilized by Lo and Passarelli (1982), where the descent rate is adjusted to match the fall speed of the hydrometeors through the descent. The aircraft is allowed to drift with the horizontal wind flow. The sampling starts with a volume of hydrometeors, and samples their evolution along their trajectory to, and through the melting layer. So, ideally we sample the same volume of particles during their lifetime, alleviating samling problems and homogeneity. The NASA DC-8 aircraft was making passes above the Citation and the ARMAR radar obtained vertical profiles of radar reflectivity in the vicinity of the Citation spiral, but not precisely at the spiral location.

The instruments utilized on the UND Citation in sampling the microphysical data presented herein include the Particle Measuring Systems (PMS) 2DC imaging cloud probe, sampling cloud particles to about 1 mm, and extrapolated to 3 mm using edge techniques. The large precipitation hydrometeors were sampled with the Stratton Park Engineering Corp. (SPEC) High Volume Particle Sampler (HVPS), which has a sampling width of 5 cm, a resolution of 200 microns, and a sample volume of nearly one cubic meter per second of flight track. The NASA/JPL airborne rain mapping radar (ARMAR) operates at 13.8 GHz (Ku band), the same frequency as the TRMM satellite borne radar, and normally scans +/- 20 degrees across track.

3.0 OBSERVATIONS

The onset of melting is very close to 2240/00. Fig. 1 shows the hydrometeor size distributions measured by the HVPS above, and through the melting layer. The data presented are 120 s averages, and so represent a sample volume of over 100 m3. at each time interval. The dimension of the hydrometeors plotted is the maximum dimension in mm. The Marshall-Palmer size distribution for 10 mm/hr of rain is plotted as a solid line. The melting, and or breakup, of the very largest aggregates is not complete by this time (+6.0C), but the rainfall rate below the melting layer is clearly about 7 mm/hr. This will give a reflectivity of about 36 dBZ when melting is complete.

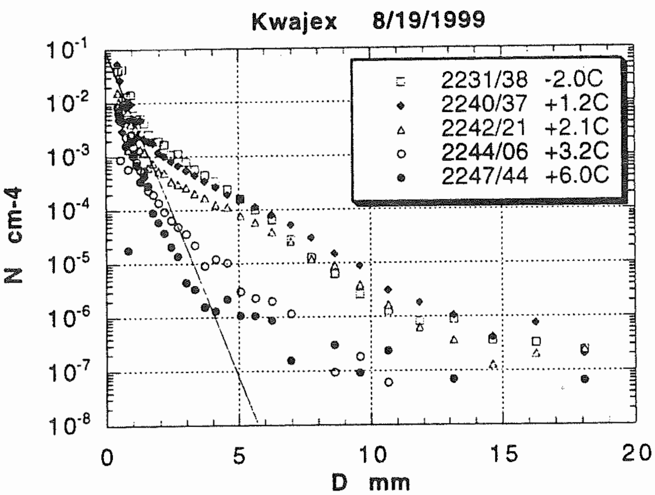

Fig. 1 Hydrometeor size distributions through the melting layer, maximum dimension from HVPS data.

3.1 Hydrometeor Size Distributions

The hydrometeor size distributions clearly track the microphysical processes operative on the trajectory through the melting process. Just above the melting layer (-2C) there has been considerable aggregation of the ice hydrometeors., as there are a fair number of aggregates present of dimension 1 cm, and larger. But look what happens shortly after the onset of melting (1.2C) in the upper part of the melting layer. The distributions show a depletion of particles less than 5 mm, and a large increase in the number of hydrometeors from 1mm to 1.5 cm. If we assume these are all water spheres of the indicated dimension in the distribution at +1.2C, which they most definitely are not, the reflectivity would be of the order of 65 dBZ. This is clearly not plausible, as they are not water spheres, but are still largely irregular ice. Then as melting progresses (2.1C) the entire distribution shifts lower, but a few very large aggregates (>1.2 cm) remain. These few remaining very large aggregates are apparently sufficient to keep the reflectivity (Z) quite high. Then by 2244/06 (+3.3C) the melting is very well developed. and the distribution is approaching a rain spectrum at sizes less than 4 mm. Then by (+6.0C) the rain distribution is well formed, but a very few giant aggregates remain. Also, it appears that the concentrations at sizes less than 1 mm may have increased, possibly due to breakup (collision breakup).

Fig. 2 presents data from the 2DC PMS cloud particle imaging probe. A general lowering of the concentration in these size ranges as melting progresses is indicated in these data. The data, which are for slightly different time intervals than those of Fig. 1, do not clearly show the breakup upon final melting. This will be investigated in more detail later.

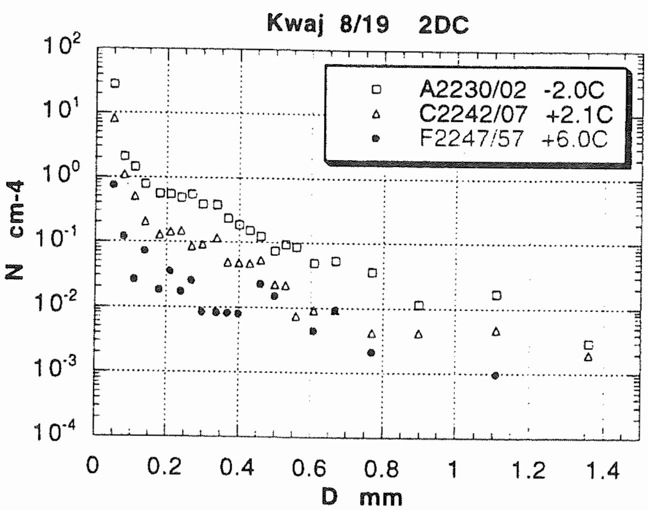

Fig. 2 Size distributions from PMS 2DC cloud imaging probe.

3.2 ARMAR Radar Profiles

Fig. 3 and Fig. 4 present two near vertical profiles of reflectivity measured in the vicinity of the spiral, but not precisely coordinated with it. Since the spiral descent follows the trajectory of the evolving particle volume, no instantaneous vertical profile is going to match this slantwise trajectory. Fig. 3 has a Z below the melting layer of about 25 dBZ, probably slightly low based on the rain distributions measured. The profile of Fig. 4, with 35 dBZ below the melting layer is probably a better match. The Z profiles above the onset of melting are different in the two profiles, probably indicative of horizontal inhomogeneity.

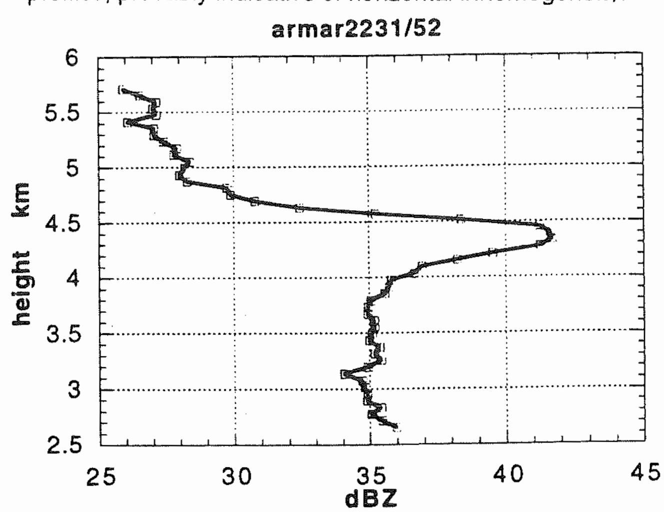

Fig. 3 DC-8 ARMAR vertical profile of radar reflectivity. Courtesy of S Durden - JPL

The profile of Fig. 4 shows slower aggregation above the melting layer, then very much enhanced aggregation below the onset of melting.

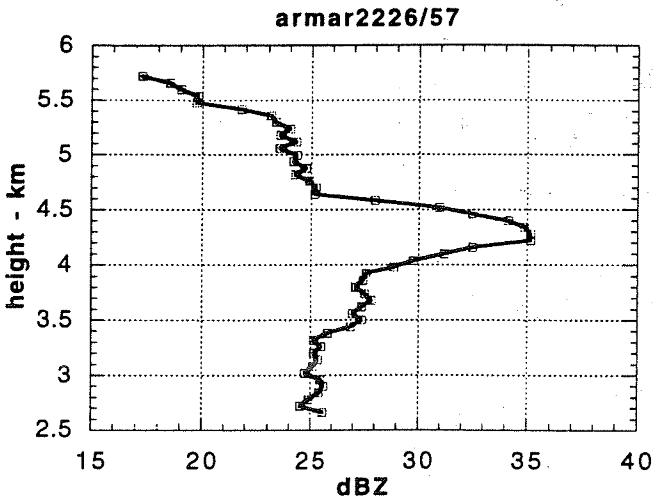

Fig. 4 DC-8 ARMAR vertical profile of radar reflectivity.

3.3 Hydrometeor Images

In this section we will show a small sample of images for three temperature levels from each of the three primary instruments used. Fig. 5 shows three sets particle images from the PMS 2DC probe. The dimension of the images can be gaged as the vertical dimension of each image strip is just under 1 mm. The first temperature clearly shos the small particles starting to melt, and the predominance of large ice aggregates. As melting progresses, the smaller particles are nearly all spheres, and large, probably denser aggregates remain. Then in panel c millimeter size hydrometeors are melted, but somelarger ice probably remains.

In Fig. 6 a sample of images for three temperatures form the HVPS are presented. The height of each image strip is 5 cm. The same progression of melting is apparent, and was quantified in the size distributions of Fig. 1. Fig. 7 presents a small sample of images from the SPEC Cloud Particle Imager. The black and white images shown here do not do justice to the original images, but they do indicate the complexity of the aggregation, regrowth of ice sites and the melting. The image of the nearly completely melted aggregate of large dimension is amazing. Tthat the hydrometeor can maintain its ice dimension that long without breaking up is astounding.

4.0 DISCUSSION AND CONCLUSIONS

For us these data are an exciting look at the details and complexity of the melting process. It is particularly significant that we now have an adequate sample volume to look at the small concentrations of large partially melted aggregates that are responsible for the radar bright band. The size distributions agree with the anlysis of Barthazy, et al., (1998). This is just a preliminary cursory look at the data of this case, and future work will focus on mass continuity and particle and mass fluxes through the melting layer, as well as microwave characteristics.

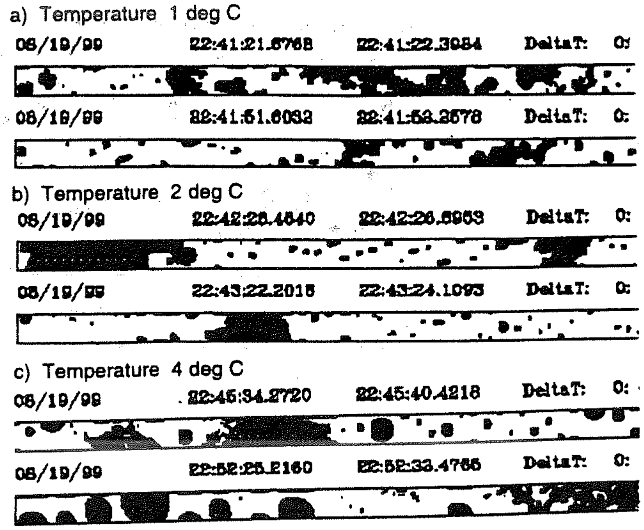

Fig. 5 PMS 2DC cloud probe images matching temperature levels of Fig. 1. The size scale is 0.8mm from the bottom to the top of each image strip.

In many respects this melting layer is very different from the one we previously analyzed. The previous one was very definitely in a layer of pronounced mesoscale ascent, and this one is probably a more passive melting, without a continuing supply of cloud condensate.

References

Barthazy, E., W. Henrich, and A. Waldvogel, 1998: Size distribution of hydrometeors through the melting layer. Atmospheric Research 47-48, 193-208.

Drummond, F, R. Rogers, S. Cohn, W. Ecklund, D. Carter, and J. Wilson, 1996: Anew look at the melting layer. J. Atmos. Sci., 53, 759-769.

Heffernan, E., and J. Marwitz, 1996: The front range blizzard of 1990. Part II:Melting Effects in a convective band. Mon. Wea. Rev., 124, 2469ff

Lo, K., and R. Passarelli, 1982: A new sampling technique for quantitative sampling of snow growth. J. Atmos. Sci., 39, 697-706.

Willis, P. T. and A. J. Heymsfield, 1989: Structure of the melting layer in mesoscale convective system stratiform precipitation. J. Atmos. Sci. 46,2008-2025.

a) HVPS images - Temperature 1 deg C

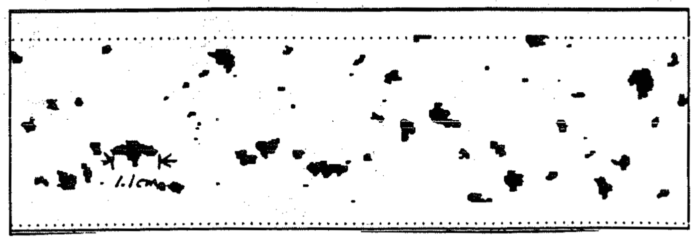

b) HVPS images - Temperature 2 deg C

c) HVPS Images - Temperature 3+ deg C

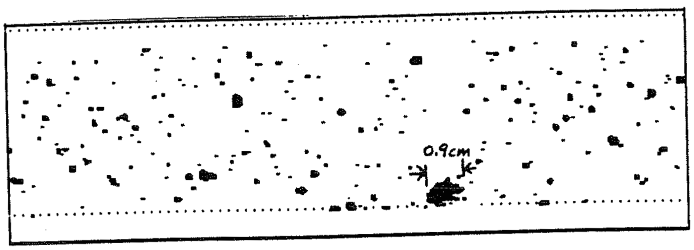

Fig. 6 HVPS images matching temperature levels of Fig. 1.
The size scale is 5cm from the bottom to the top of each image strip.

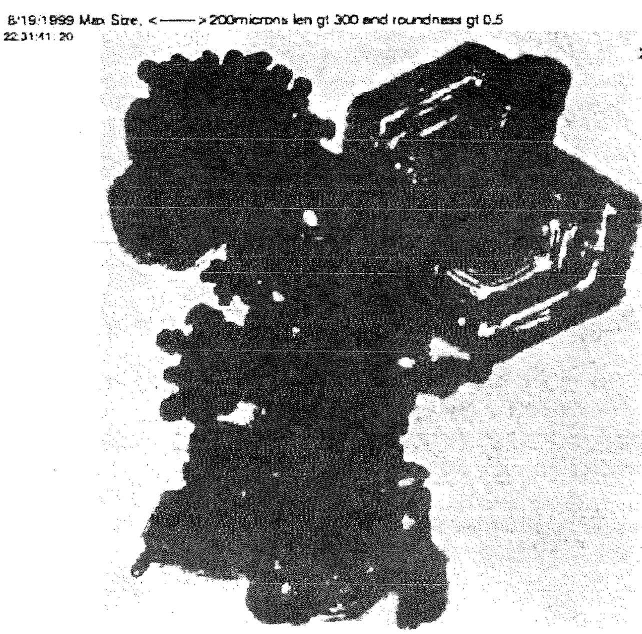

Fig. 7 CPI images from two temperatures all to the same scale - 200 microns indicated by <------>. a) left aggregates from -2 deg C; b) right melted particle from +7 C.

CHARACTERISTICS OF VORTEXES ACCOMPANYING CONVECTIVE CLOUDS OVER THE TIBETAN PLATEAU DURING THE GAME-TIBET IOP

Jun'ichi Horikomi[1], Hiroshi Uyeda[1], Hiroyuki Yamada[1], Ryuichi Shirooka[2], Shuji Shimizu, Hideyuki Fujii, Ken'ichi Ueno and Liping Liu

[1]Graduate School of Science, Hokkaido University, Sapporo 060-0810, Japan
[2]Hokkaido National Aguricultural Experiment Station, Sapporo 062-8555, Japan

1 INTRODUCTION

It was known that there is a lot of convective activity over the Tibetan Platau after the onset of a monsoon and the influence of this activity on energy and water cycle of the Asian monsoon has been dicussed. But because of the difficulty of obtaining information about the clouds over the Tibetan Plateau, however, there have so far been few studies of the internal structures of clouds.

Only one observation using the meteorological radar (X-band, non-Doppler type) has been carried out on the central region of the Tibetan Plateau. It was carried out in the summer of 1979 as part of the QXPMEX (Qinghai-Xizang Meteorological Experiment) project. In the report of that project, Zhang et al. (1988) showed that there was diurnal variation in the echo-top height derived from hourly-cycled RHI (Range Height Indicator) scans and the small but deep convective cells developed during the daytime. But little information related to the development process and the internal structures of precipitating clouds was collected in that observation.

To acquire this information, a Doppler radar observation was carried out at Naqu in 1997 during the preliminary observation period (POP) of the GAME-Tibet project (Yamada et al., 2000). This project is one of the regional projects in the GAME (GEWEX Asian Monsoon Experiment). The observation gave us three-dimensional information about the interior of clouds, information with the spatial and temporal resolution needed for documenting cloud development. Not only the diurnal variation of the convective clouds, but also vertical signature of the convective clouds was identified in this observation.

In 1998 a three-dimensional X-band Doppler radar was installed in the grassland of the central region of the Tibetan Plateau in the same place as the observation in 1997, and successive observations were carried out from 27 May to 19 September. In order to show the features of convective clouds over the Tibetan Plateau, we extracted convective regions from the reflectivity data objectively. Moreover, since the observation period includes the day of the monsoon onset, we could investigate the difference between the convective clouds before and after monsoon onset. The convective clouds over the Tibetan Plateau were accompanied by vortexes, and the funnel cloud was also observed. we show the results of our analysis of those vortexes.

2 METHOD OF ANALYSIS

The volume data of reflectivity, obtained from 10 steps of PPI (Plain Position Indicator) scan data; covered a 120 km x 120 km grid, centered on the Naqu radar site (31.38N, 91.93E, h=4500 m), and a depth of 16 km (from 4.5 to 20.5 km ASL). The grid spacing was 1.0 km horizontally and 0.5 km vertically.

To identify the convective area of the echo objectively, we used an algorithm (Steiner's method) developed by Steiner et al. (1995) and selected the 'medium' boundary of the mean background reflectivity and convective radius. The grid reflectivity data at 7.5 km ASL (3.0 km AGL) was also used in the analysis; here no effect of bright band to reflectivity was included as the height of the melting layer was below 6.0 km ASL (1.5 km AGL).

To detect a mesoscale vortex, we chose a method for recognizing vortex patterns in a Doppler velocity field that uses the following four vortex indentification criteria introduced by Donaldson(1970): a) there is significant tangential shear of the radial velocity in a quasi-horizontal plane where the sum of the angular diameter and the elevation angle of observation is less than 30°, b) tangential shear persists for at least half the period reqired for one vortex resolution ,c) the vertical extent of the shear pattern exceeds the horizontal diameter, and d) the qualitative shear pattern is invariant during a viewing angle change approaching or exceeding 45°. From the inverse pair of radial velocity peaks in Doppler velocity fields, the vorticity ζ can be calculated by the following equation,

$$\zeta = 2(V_{r1} - V_{r2})/\Delta d \qquad (1)$$

where V_{r1} and V_{r2} are respectively the muxmum radial velocities toward and away from the radar reflectivity, and Δd is the distance between the velocity peaks.

3 RESULTS

There were big differences between convective clouds before and after the monsoon onset. Yamada et al. (2000) reported the daily maxima of the echo-top height and echo area at 7.5 km ASL during the period from 30 May to 17 September 1998. The echo-top height of 10 dBZ exceeded 14 km ASL almost every day after 13 June. From this data, the monsoon onset of 1998 was recognized to be 13 June.

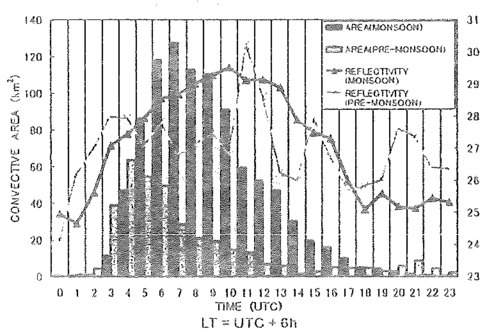

Figure 1: Diurnal variation of averaged reflectivity and echo area before and after the onset of the monsoon.

To clarify the differences in convective activity between the pre-monsoon period (before 13 June) and the monsoon period (after 13 June) we show in Fig.1 the averaged echo area and reflectivity for the convective region identified using Steiner's method.

During the IOP, convective clouds formed and developed in the daytime and decayed at night. In the daytime the area of after the monsoon onset is more than two times larger than that before the monsoon onset and the reflectivity after the onset is stronger than that before onset. The peak of the echo area in the pre-monsoon period is at 04 UTC, which is three hours earlier than that in the monsoon period. The first peak of reflectivity in the pre-monsoon period is one hour earlier than the peak of the echo area and is seven hours earlier than the peak of the reflectivity in the monsoon period. This early peak could be explained by the convection in the pre-monsoon, which is much shallower than that of the monsoon period, reaching the mature stage very early.

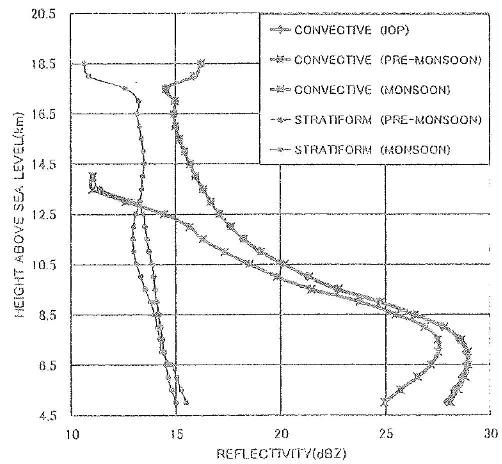

Figure 2: Vertical profile of reflectivity for convective and stratiform echos for before and after the monsoon and averaged vertical profile of reflectivity in convective echo during the IOP.

We also compared the convective clouds before and after monsoon onset from other viewpoints. The vertical profile of reflectivity is shown in Fig.2. The echo-top height during the monsoon is taller than that of the pre-monsoon and the reflectivity during the monsoon is stronger than that of the pre-monsoon, especially above 12 km ASL.

The difference between the heights of convection during the pre-monsoon and the monsoon period can be explained by the differences in the vertical structure of ecvironmental conditions as shown in Fig.5. Figure. 5 indicates that the large specific humidity at the lower altitudes is high after 13 June and that until 12 June there is a very strong easterly wind above 10 km. The high specific humidity, namely a large amount of vapor. and weak vertical shear through the troposphere during the monsoon period enabled

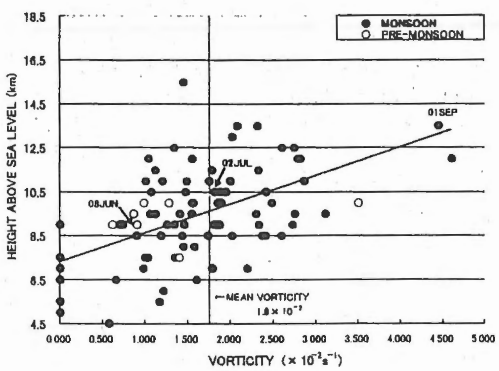

Figure 3: Relation between the daily maximum vorticity and the echo-top height of the associated convective cloud (> 30dBZ). Open and solid circles indicate, respectively, before and after the monsoon onset. Mean vorticity of the daily maximum vorticities is shown by vertical solid line. Three marked vortexes correspond to the three profiles shown in Fig.4

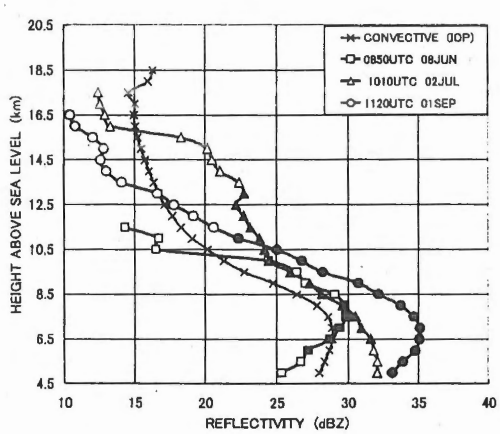

Figure 4: Vertical profiles of reflectivity for convective echos at 0850 UTC 8 June (open square), 1010 UTC 2 July (open triangle) and 1120 UTC 1 September (open circle) 1998 (refer to Fig.3). The altitudes at which the vortex is recognized are shown by solid symbols. Averaged vertical profile of reflectivity for convective echo during the IOP is shown by cross marks.

the tall convection to reach to the tropopause.

In spite of the convective clouds observed over the Tibetan Plateau being small (but strong), many vortexes accompanied them, and some funnel clouds were also observed. The relation, during the IOP between the daily maximum of vorticity identified in the Doppler velocity pattern and the height of the corresponding echo is plotted in Fig.3. A vorticity pattern was recognized on most of the days: 78 of the total 106 observation days, 71 of 90 after the monsoon onset and 7 of 16 before the monsoon. Vorticity and echo-top height during the IOP was positively correlated and the vorticity of the pre monsoon period was smaller than the mean of the daily maximum vorticity (1.8×10^{-2}), except on one day.

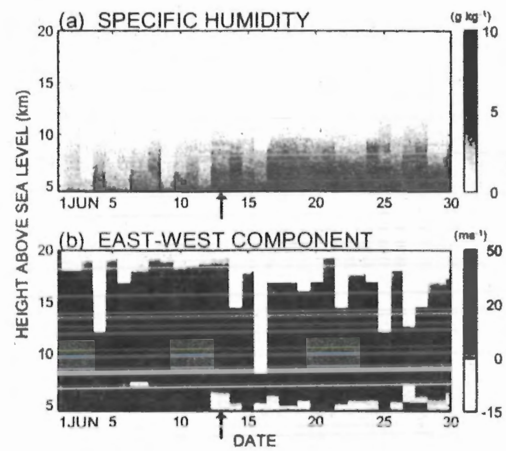

Figure 5: Time series of vertical profile of (a) specific humidity and (b) east-west component of wind at 11UTC from 1 to 30 June 1998. The arrow shows the day of monsoon onset (13 June).

In Fig.4 the vertical profiles of the reflectivity of the convective area for three cases shown Fig.3 are shown with the profile for the IOP. Although the vortex pattern at 0850 UTC on 8 June, before the monsoon onset, was in shallow layers (up to 8 km ASL), the vortex patterns on 2 July and 1 September were respectively in deep layers up to 13 km and up to 11 km.

The reflectivity profile of the strongest convective cell during the IOP (from 0830 UTC to 1010 UTC in 17 July) is shown in Fig.6. Although a strong vortex was not observed on this day, a very strong convective cloud was observed from devel-

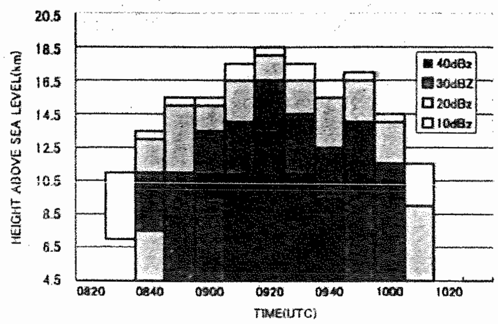

Figure 6: The reflectivity profile of the strongest convective cell during the IOP from 0830 UTC to 1010 UTC in 17 July.

opment to mature stage, the reflectivity core of this convective cell is observed at height of 9 km ASL. Because the melting layer at radar site is below 6 km ASL, the convective core existed above 0°C level. This indicates the presence of graupel particles in the convective core.

4 DISCUSSION AND CONCLUSIONS

Doppler radar observations were carried out in the suburbs of Naqu city (4500 m ASL) in the central part of the Tibetan Plateau from 27 May to 19 September 1998 during the GAME-Tibet IOP. Convective clouds formed and developed in the daytime and decayed at night. The echo-top height and convective area, extracted objectively from grid data of radar reflectivity, were larger after the monsoon onset than before the onset. Furthermore, many vortexes associated with the convective clouds (identified in Doppler velocity fields) were observed in the daytime. The strongest vorticity of a given day during the observation period showed a positive correlation with the appearance of the maximum echo-top height (> 30 dBZ) of the convective clouds. The daily maximum vorticity after the monsoon onset was larger than that of the pre monsoon period. Figure. 5 indicates the cause of vortex generation. After the monsoon onset, the easterly wind near the ground and the higher westerly wind formed a vertical wind shear and the horizontal vortex was tilted by the strong updraft formed by solar heating. Thus a vertical vortex formed.

The reflectivity profile (Fig.2) indicates that the median lapse late of the convective area for the 3 km interval above the freezing level - that is, between 0°C and -20°C - was 2.4 dBZ km^{-1} after the monsoon onset and 1.1 dBZ km^{-1} before it. The small lapse late indicates the uplifting of large precipitation particles, such as graupel and hail. according to Zipser and Lutz (1994) and Donaldson (1961), the lapse late of a squall line and hail storm are respectively 1.5 dBZ km^{-1} and 1.3 dBZ km^{-1}. In spite of low temperature in the Tibetan Plateau, the convective clouds over it show the same convective activity shown by convective clouds in other areas, especially after the monsoon onset.

ACKNOWLEDGMENTS

We would like to thank the members of the GAME-Tibet observation group for their cooperation in the observations. Thanks are also due to Dr. Nobuhiko Endo for providing sounding data.

REFERENCES

Donaldson, R. J. Jr., 1961: Radar refrectivity profiles in thunderstorms. *J.Meteor.*, **18**, 292-305.

Steiner, M., R. A. House Jr, and S. E. Yuter,1995: Climatological characterization of three-dimensional storm structure from operational radar and rain gauge data. *J. Appl. Meteor.*, **34**, 1978-2007.

Yamada, H., H. Uyeda, S. Simizu, R. Shirooka, L. Liu, K, Ueno, H. Fujii, and T. Koike, 2000: Doppler radar observation on the characteristics and structures of the convective clouds developed on the central Tibetan Plateau during the GAME-Tibet preliminary observation period. *J. Meteor. Soc. Japan* (submitted)

Zhang, J., B. Zhu, F. Zhu, D. Weng, G. Sun, J. Lu, Y. Peng and Y. Wang,1988: *Advance in the Qinghai-Xizang plateau meteorology, The Qinghai-Xizang Plateau Meteorological Expariment (1979) and Resarch.* Science Press, Beijing, 268pp., (in Chinese).

Zipser, E. J., and K. R. Lutz, 1994: The vertical profile of radar reflectivity of convective cells :A strong indicater of storm intensity and lightning probability? *Mon. Wea. Rev.*, **122**, 1751-1759

THE 3-D MODEL CHARACTERISTICS OF Cb CLOUD WHICH MOVES ALONG A VALLEY

Mladjen Ćurić, Dejan Janc, Vladan Vučković and Dragana Vujović

Institute of Meteorology, University of Belgrade, YUGOSLAVIA

1. INTRODUCTION

The development of Cb clouds in orography conditions is treated only sporadic in literature (e.g. Cotton et al.,1982; Knupp and Cotton,1982a,b). The number od studies (experimental, theoretical and model) is small. The central Serbia has very specific orography intersected by numerous river vallies flanked by mountains and hills on their sides. The air often has the great humidity in lowest 2-3 km. On the base of numerous radar data and the observations on the ground, Ćurić (1980;1982) concluded that the Zlatibor plateau and the Western Morava valley (Western Serbia) are extremely interesting for formation and development of an isolated Cb cloud which moves along the valley flanked by orography on its sides. He developed the conceptual model of the development of a such cloud. According to this model, the cloud formed on the mountain plateau would come down from a plateau into a valley when the environmental mid-tropospheric wind is nearly parallel with valley and the low-level air motion is from the opposite direction. A strong downdraft will occur since the land slopes down to a valley. The local low pressure and the forced lifting of a warm air above the cold air amplify the warm air motion toward the mountain side and the strong updraft associated with the nose of a cold air in front of a cloud occurs. The height of the nose of the cold air shows the characteristic oscillations with time. On the nose, the new daughter cloud can form. Ćurić and Janc (1992) concluded that such Cb cloud behaviour appear only for isolated clouds.

The model simulations of Cb clouds in orography conditions are treated by one-dimensional time dependent and two-dimensional models. In papers of Ćurić and Janc (1987;1988;1993) and Ćurić et al. (1999) , the effect of orography is treated through the forced lifting vertical component which is a positive branch of a sinusoidal curve. Orville and Kopp (1977) treated the orography as a traingle obstacle in their two-dimensional model. The three-dimensional model simulations of Cb clouds in the complex orography are not numericaly treated. The primary aim of this paper is to verify the results of Ćurić (1980;1982) by help of the ARPS three-dimensional mesoscale model.

Corresponding author's address:Mladjen Ćurić, Institute of Meteorology,University of Belgrade. P.O.B. 368, Belgrade Yugoslavia; E-mail: curic@rudjer.ff.bg.ac.yu

2. MODEL

The model used the three-dimensional mesoscale model (ARPS) developed by CAPS (Center for Analysis and Prediction of Storms) in Oklahoma University. It is designed for prediction of small and convective scales (Droegemeier et al.,1991; Droegemeier et al.,1992; Johnson et al.,1994). The ARPS is the non-hydrostatic model for the limited area. It contains the Navier-Stokes equations, the equations for potential temperature, mass (pressure), water substance (six categories), turbulent kinetic energy (TKE) and state equation. These equations are written in curvelinear coordinates which match the orography. The coordinate system is uniform and ortogonal in the horizontal plane.

The radiation lateraly boundary condition is used for u i v components. No slip conditions are applied for top and bottom boundaries. The phase velocity of Orlansky (1976) is calculated in great time step and it is averaged in vertical direction. Such calculated phase velocity is then used in small time steps. The model uses the soundings data as the initial input values for temperature, humidity, pressure, wind velocity and direction. The reference state is homogeneous in horizontal direction, while the thermal bubble is used as the initial perturbation.

The model equations are numericaly integrated in the 112 km×112 km×16 km region with grid steps of 1000 m in x and y directions and 500 m along the z-axes. The leap-frog scheme is used for integration of non-acoustic wave modes with great time step of 6 s. The small time step is 2 s. The horizontal and vertical advections of momentum and scalars are treated by fourth and second order accurancy schemes. The surface fluxes are not calculated. The isotropic filtering of acoustic wave divergence is used. The turbulent closure scheme 1.5 is included. The Coriolis force is neglected. The original ARPS data for orography given for the mid-latitude region of USA are replaced with those for the region of Western Balkan and Serbia.

3. RESULTS OF EXPERIMENTS

The integration domain as well as the physical chart of this region are derived from the model. The selected integration domain consists of the Western Morava valley (mean height above sea level 300 m), as well as the mauntainous region westerly from it, which is an important region for isolated Cb clouds formation. Between Požega and Čačak, the Western Morava valley is wide only a few hunderd meters (Ovčar-Kablars' cliff). Under such conditions the Cb clouds move under forcing above the mountains (Ćurić,1982). The wider region of the Western Morava valley is presented in Fig. 1.

We select the local sounding of 13th June 1982. (00 of local time) when the Cb cloud with moderate precipitation rates was observed. The air was moist up to 11.3 km height. At the surface, the relative humidity was 65% and then oscillates with height up to 5.9 km. At 4.2 and 5.9 km heights it attains the values of 100%. The low-level wind is typicaly SE, and it blows along the Western Morava valley toward the mountains. At 4 km height, the wind is from NW direction. The local conditions are favourable for Cb cloud formation according to

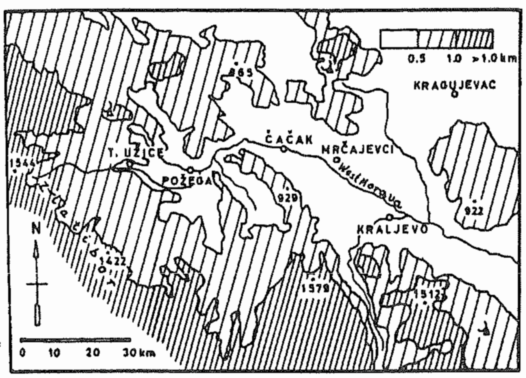

Fig. 1. Contour map of Western Morava valley.

Knupp and Cotton (1982a,b). The wind in the mid-troposphere is nearly parallel with the valley, while the air moves from the opossite direction at low-level heights. Then, the Cb cloud comes down into the valley (Ćurić,1982). The wind intensity in the wind shear level (0-2 km) is 6-7 ms^{-1},and between 2-9 km 11-17 ms^{-1}. The temperature perturbation is placed at the upper left corner of the integration domain NW from Požega (Fig. 1), with the initial potential temperature excess of 5 $^{\circ}$C at 1.5 km height.

The model cloud is formed after t=15 min of integration time and it starts to move toward the Western Morava valley. As important characteristics of a such cloud are taken the patterns of reflectivity factor (in dBZ) in x-y plane as it can be seen from the Figs. 2 and 3 for t=30 and 75 min of integration time. For t=75 min, the radar reflectivity factor attains its maximum of 55.4 dBZ.

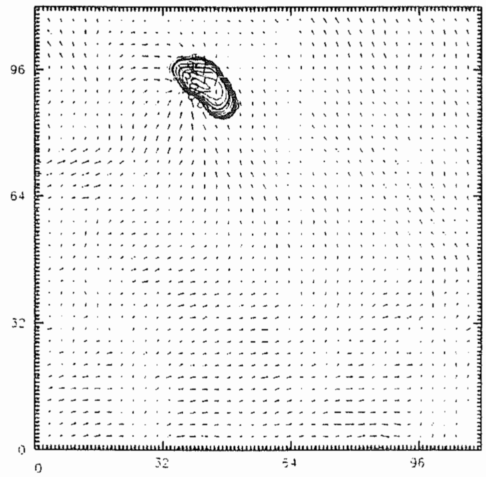

Fig. 2. Reflectivity factor contours of 10 dBZ and wind (m / s) in x-y plane. The axes are given in km for t=30 min.

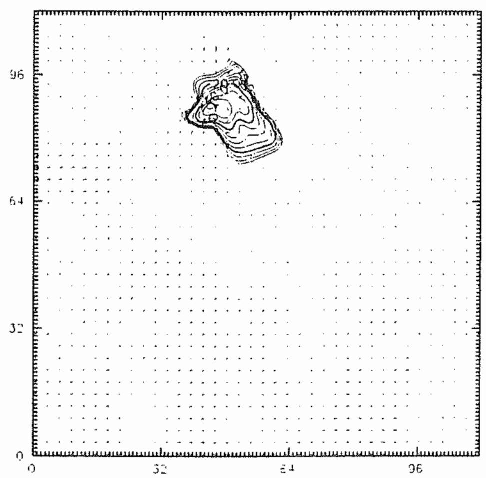

Fig. 3. As in Fig. 2. but for t=75 min.

As can be seen, the Cb cloud developes very intensively during its motion towards the Western Morava valley. In order to illustrate the oscillatory character of the nose of the cold air in front of the Cb cloud we select two figures for t=60 min and t=105 of integration time.

From Fig. 4 , we detect clearly the nose of the cold air in front of the main cloud, when the cold air increases its height. Above it, the vertical velocity perturbation due to the forced lifting of the warm air is observed (maximum of 27.6 m/s). In Fig. 5., the height of the cold air decreases and it spreads out in a

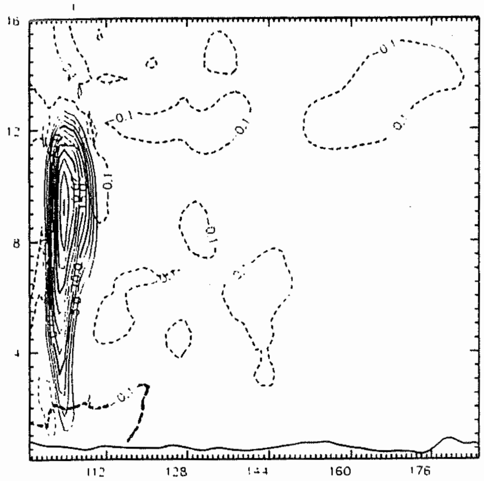

Fig. 4. The potential temperature perturbation (° C, the isoline of -0.1 ° C is only shown) and vertical velocity perturbation (m/s) in the vertical plane along the Cb cloud motion for t=45 min of integration time. The nose of the cold air is presented by dash line.

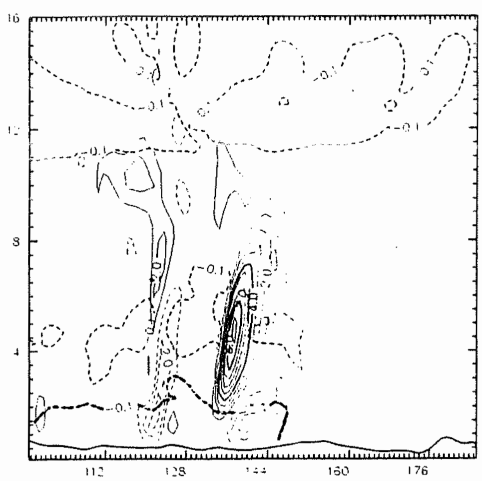

Fig. 5. As in Fig. 4. but for t=75 min.

valley direction. The forced vertical lifting of the warm air is observed but with smaller maximum value (9.43 m/s) than in Fig. 4, because of the smaller cloud intensity. Such distribution of the vertical velocity with respect with the nose of the cold air lead to the daughter cloud generation.

4. CONCLUSIONS

We simulate the isolated Cb cloud development in orography conditions by help of the ARPS three-dimensional meso scale model. We have simulated some characteristics of an isolated Cb cloud which forms and moves in the Western Serbia from the Zlatibor plateau toward the Western Morava valley. Our experiments clearly show that a such cloud cannot be developed without great humidity and strong wind shear in low-level atmosphere where the mid-tropospheric wind is nearly parallel to the valley direction. Some features of such clouds presented by the conceptual model of Ćurić (1982) are well simulated as the oscillatory character of the nose of the cold air in front of the main cloud and the forced lifting of the warm air above it . The reflectivity factor shows the tendency to attain its maxima values in the valley.

References

Cotton,W.R., R.L. George, and K. R. Knupp,1982: An Intense, Quasi-Steady Thunderstorm over Mountainous Terrain. Part I: Evolution of the Storm-Initiating Mesoscale Circulation. *J. Atmos. Sci*.,39,328-342.

Ćurić,M.,1980: Dynamics of a cold air outflow from the base of the thunderstorm. A simple model. *J. Rech. Atmos.*,14,493-498.

Ćurić,M.,1982: The development of the cumulonimbus clouds which move along a valley. In: *Cloud Dynamics* (eds. Agee,E.M., Asai,T.). Dordrecht: D. Reidel,259-272.

Ćurić,M.,and D. Janc,1987: On the influence of entrainment and forced lifting on some products of a 1-D model of a Cb cloud. *Atmos. Res*.,21,151-169.

Ćurić,M.,and D. Janc,1988: A forced 1-D convective cloud model. *Meteorol. Atmos.Phys*.,39,51-62.

Ćurić,M.,and D.Janc,1992: Mountain influence on the areal characteristics of types of convective precipitation. *Theor. Appl. Climatol*.,45,71-76.

Ćurić,M.,and D. Janc,1993: Predictive capabilities of a one-dimensional convective cloud model with forced lifting and a new entrainment formulation. *J. Appl. Meteor*.,32,1733-1740.

Ćurić,M.,D. Janc, and V. Vučković, 1999: Verification of the improved capability of a 1-D forvced time-dependent cloud model with truncated hail spectrum. *Meteorol Z*.,N.F.8, *Meteorol Z*., 145-154.

Droegemeier,K.K., M. Xue, P.V. Reid, J. Straka, J. Bradley III, and R. Lindsay,1991: The Advanced Regional Prediction System (ARPS) version 2.0, Theoretical and numerical formulation. CAPS Report No. CAPS91-001,55 pp.

Droegemeier,K., and coauthors,1994: Weather prediction: A scalable stormscale model. *High*

Performance Computing. G.W. Sabot, Ed., Addison Wesley, 45-92.

Johnson,K.W., J. Bauer, G.A. Riccardi, K.K. Droegemeier, and M. Xue, 1994: Distributed Processing of a Regional Prediction Model. *Mon. Wea. Rev.*,122, 2558-2572.

Knupp,K.R., and W.R. Cotton,1982a: An Intense, Quasi-Stready Thunderstorm over Mountainous Terrain. Part II: Doppler Radar Observations of the Storm Morphological Structure. *J. Atmos. Sci.*,39,343-357.

Knupp,K.R., and W.R. Cotton,1982b: An Intense, Quasi-Stready Thunderstorm over Mountainous Terrain. Part III: Doppler Radar Observations of the Turbulent Structure. *J. Atmos. Sci.*,39,343-357.

Orlanski,I.,1976: A simple boundary condition for unbounded hyperbolic flows. *J. Comput. Phys.*,21,251-269.

Orville,H.D., and F.J. Kopp,1977: Numerical Simulation of the Life History of Hailstorm. *J. Atmos. Sci.*,34,1596-1618.

OBSERVATIONS AND MODELING STUDIES OF FLORIDA CUMULUS CLOUDS

Harry T. Ochs III[1,2], Neil F. Laird[1,2], and Robert M. Rauber[2]

[1]Illinois State Water Survey, 2204 Griffith Drive, Champaign, IL 61820
[2]Department of Atmospheric Sciences, University of Illinois Urbana-Champaign

1. INTRODUCTION

One of the simplest hypotheses to explain the onset of precipitation is the existence of very large (> 20 µm diameter) wettable or soluble nuclei that, when carried through cloud base, can almost immediately begin to collect cloud droplets. According to the extensive measurements of Woodcock in Hawaii, giant salt particles can often occur in significant concentrations. Woodcock's observations in the presence of modest surface winds of 5-10 ms^{-1} show concentrations at elevations of cloud base (0.7-0.9 km) in the range of 100-1000 m^{-3} for salt particles with masses > 1 ng (corresponding to NaCl particles with diameters > 10 µm).

We have tested the ultra-giant nuclei hypotheses using the Ochs and Yao (1978) parcel model. Data from observations are used as input for the model calculations. Concentrations of cloud droplets produced in the model are compared with those actually measured during the Small Cumulus Microphysics Study (SCMS) and the computed model radar reflectivities are compared with radar observations prior to the onset of precipitation based on Rayleigh scattering.

2. OBSERVATIONS

Data from the NCAR C130 FSSP and 260X optical array probes were composited for the entire SCMS field program when the aircraft was below 600 m (typical cloud base elevation). The resulting clear air spectra are shown in Fig. 1 for the period when the aircraft was between 200 and 400 m and 400 and 600 m above sea level. Figure 1 shows a broad distribution of particles below cloud base extending to sizes > 300 µm diameter. These particles are probably solution droplets containing sea salt.

Figure 2 shows C130 liquid water contents from the FSSP and the 260X for cloud passes (in one second intervals) on a single day. Also plotted are the estimated values of adiabatic liquid water content and the estimated uncertainty in the adiabatic liquid water content as a function of height. The data indicates that many small cumulus cores have near adiabatic liquid water contents.

Figure 3 shows a vertical cross section of x-band (3 cm) reflectivity at 15:24:21-15:24:28 UTC on 5 August,1995. The contours in the cloud are labeled from -20 to -5 dBZ with 5 dBZ steps. This figure depicts the cloud at the time when –5 dBZ reflectivity was first observed.

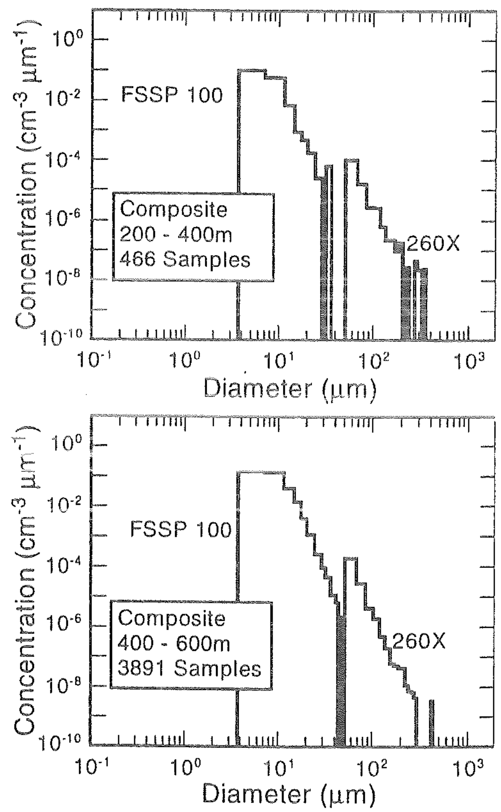

Figure 1. Haze particle distributions below cloud base.

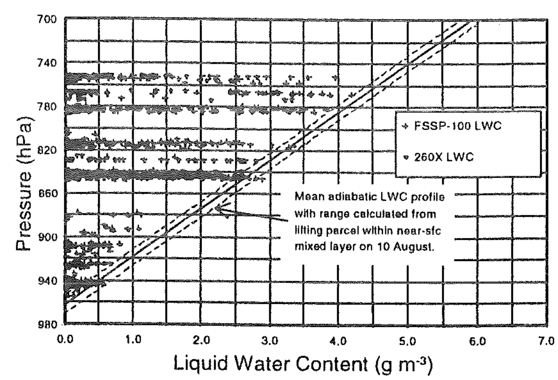

Figure 2. Observed liquid water contents.

Corresponding author: Harry Ochs, Illinois State Water Survey, 2204 Griffith Dr., Champaign, Illinois 61820, USA; E-Mail: h-ochs@uiuc.edu

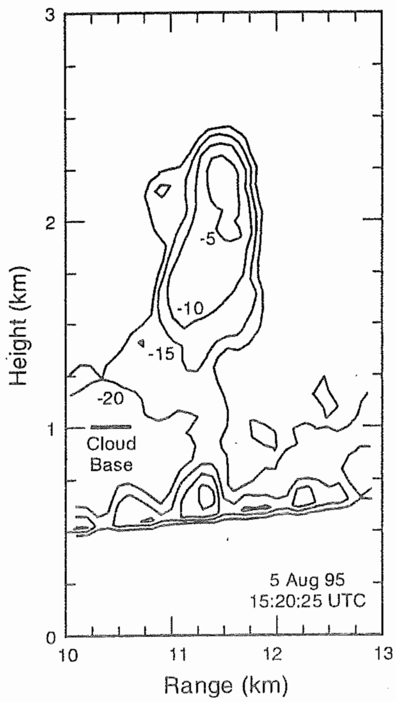

Figure 3. Vertical cross section of radar reflectivity.

Cloud base was at about 1 km MSL. The base of the -5 dBZ reflectivity contour is slightly less than 1 km above cloud base.

2. MODEL INITIALIZATION

Details of the parcel model structure and numerical techniques are found in Ochs and Yao (1978) and in Ochs (1978). The CCN were assumed to be composed of NaCl and had a distribution that corresponded with the observed haze particle distributions just below cloud base. Figure 4 shows the clear air haze particle distributions just below cloud base and the model predicted particle distributions at 90 and 95% RH. An assumed updraft speed of 1.8 ms^{-1} was used below cloud base to produce the distributions in Fig. 4. The vertical velocity increased to about 3.0 ms^{-1} at 1 km above cloud base. This updraft profile was derived from average updrafts observed in developing Florida cumulus clouds during SCMS. As the parcel was adibaticaly lifted both condensation and collection were calculated. Collection efficiencies based on laboratory measurements were used (Beard and Ochs 1984). A closed adiabatic parcel was chosen because the aircraft observations from Fig. 2 showed that adiabatic liquid water contents were possible in the SCMS clouds.

3. CALCULATIONS AND COMPARISON WITH OBSERVATION

The model was run using the complete CCN spectra. The identical calculation was repeated with the initial spectra truncated at 100, 40, 20, and 10 μm diameter. Ultra Giant CCN are defined as having a minimum size of 20 μm diameter. Figure 5 shows the evolution of radar reflectivity factor for these four model simulations.

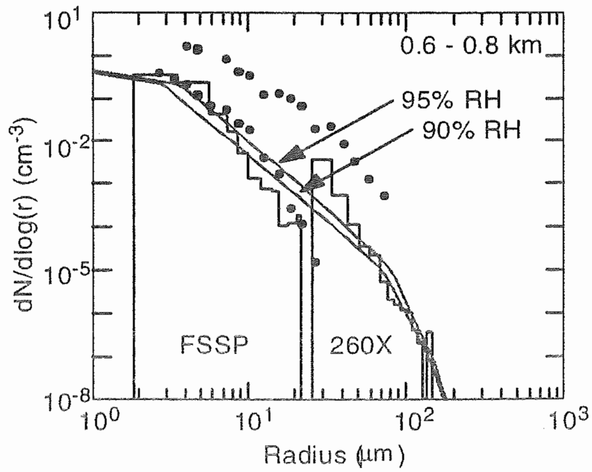

Figure 4. Comparison of clear air haze particle distributions just below cloud base and computed distributions.

Figure 5 shows that the parcel containing the complete CCN spectra developed a -5 dBZ reflectivity at about 500 m above cloud base while the observed cloud (Fig. 3) had the base of the -5 dBZ contour slightly less than 1 km above cloud base. The parcel without any ultragiant CCN developed a -5 dBZ reflectivity at about 1 km above cloud base. The parcel with CCN truncated at 10 μm was unable to match the observed onset of precipitation. Any mixing with environmental air would retard precipitation development such that, in the absence of ultragiant CCN, other processes such as inhomogeneous mixing (Baker and Latham 1979) must be evoked. These calculations suggest that ultragiant CCN are a viable explanation for the onset of precipitation in SCMS clouds.

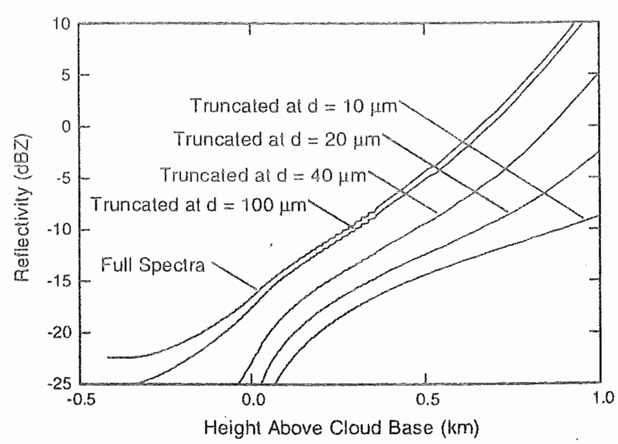

Figure 5. Calculated evolution of radar reflectivity factor.

Acknowledgements. This research was supported by the National Science Foundation under grant NSFATM 9634660.

REFERENCES

Baker, M. B., and J. Latham, 1979: The evolution of droplet spectra and rate of production of embryonic raindrops in small cumulus clouds., J. Atmos. Sci., 36, 1612-1615.

Beard, K. V., and H. T. Ochs, 1984: Collection and coalescence efficiencies for accretion, *J. Geophys. Res.*, **89**, 7165–7169.

Ochs, H. T., 1978: Moment-conserving techniques for warm cloud microphysical computations. Part II. Model testing and results. *J. Atmos. Sci.*, **35**, 1959-1973.

Ochs, H. T., and Yao, 1978: Moment-conserving techniques for warm cloud microphysical computations. Part I. Numerical techniques. *J. Atmos. Sci.*, **35**, 1947-1958.

MICROPHYSICAL INFLUENCE ON SUPERCELLULAR LOW-LEVEL MESOCYCLONES

Brian J. Gaudet* and William R. Cotton

Colorado State University
Fort Collins, Colorado

1 INTRODUCTION

A supercell can be defined as a cumulonimbus possessing a persistent mesocyclone over much of its depth (Doswell and Burgess 1993). The origin of the vorticity associated with this mesocyclone can be attributed to the tilting of environmental horizontal vorticity by the storm's updraft (Weisman and Klemp 1982). However, numerical modeling studies suggest that the formation of near-surface vorticity by supercells requires a separate mechanism such as the tilting of vorticity baroclinically generated by the supercell itself (Klemp and Rotunno 1983), although the presence of vertical vorticity in the environment due to mesoscale surface boundaries could also be important (Atkins et al. 1999). Any factors which alter the evaporative cooling within the supercell can influence the evolution of the low-level vorticity (Brooks et al. 1994; Gilmore and Wicker 1998).

Johnson et al. (1993) found that the inclusion of ice microphysics in a numerical model had a large influence on the evolution of a supercell. The presence of a hail category distributed hydrometeors over a larger area, causing the gust front generated by the storm to be less intense. The storm was able to remain quasi-steady state whereas in a simulation without ice microphysics the surging gust front cut off the inflow of low-level moist air.

There are a number of well-observed supercells in the literature that have been characterized by softball-sized hail but an absence of a typical supercell tornado (Blanchard and Straka 1998; Wakimoto and Cai, 2000). Because of this, we are interested in using the Regional Atmospheric Modeling System (RAMS) to examine the influence of hail size on supercell and low-level vorticity evolution.

*Corresponding Author Address, Department of Atmospheric Science, Colorado State University, Fort Collins, CO 80523

2 STUDY

In this study, RAMS was used to simulate the evolution of a supercell thunderstorm in a horizontally-homogeneous environment. A warm, moist bubble was placed in the initialization to trigger convection. The model environment was based on a sounding extracted from the simulation of Grasso (1996) of the Red Rock tornado of 26 Apr 1991. The latter simulation utilized a horizontally-heterogeneous environment; the sounding used in the current study came from a region just east of the dryline in Grasso (1996), near the location of the tornadic vortex that developed in his study (see Figure 1).

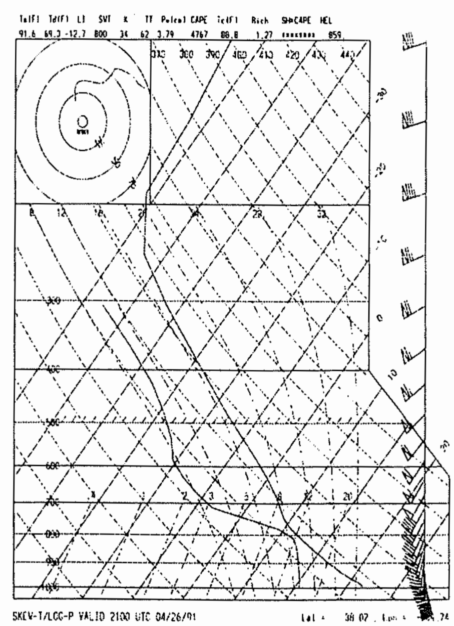

Figure 1: Initial sounding for simulations

The current study uses 150 grid points in both horizontal directions, with a grid spacing of 500 m. There are 35 grid points in the vertical direction, with grid spacings increasing from 40 m near the surface to 2000 m near model top. In the vertical direction the first grid point is located below the ground, so the lowest atmospheric grid point is about 20 m above the surface.

Simulations were performed with and without surface friction. RAMS uses a semislip lower boundary condition based on the equations of Louis (1979). The friction simulations in this study use a roughness length of 0.05 m.

After the storm velocity of motion was determined in a preliminary simulation, the simulations under study were performed after the mean storm velocity was subtracted from the model winds at initialization, in order to keep the storm within the grid. The resultant simulation should then be the same as what would be seen in the initial simulation from a reference frame moving at the mean storm velocity with respect to the grid. However, since the grid in the initial simulation is assumed to be stationary with respect to the ground, the surface stress calculations are performed using the winds prior to subtraction.

The model microphysics is described in detail in Walko et al. (1995). The mixing ratios of water vapor, total water substance, and six condensed water species are predicted: rain, snow, pristine ice, aggregates, graupel, and hail. The mixing ratio of cloud water is diagnosed by condensing out all water vapor exceeding the saturation vapor mixing ratio; the concentration of cloud droplets is specified at the start of a model run (for these simulations, 300cm^{-3}). Nucleation schemes are used to predict the number concentration of pristine ice. For the other species of condensed water, the mass-weighted mean diameter of the species is specified by the user. In these simulations the default hydrometeor sizes were used except for the hail category, for which the mean diameter was increased from 3 mm to 2 cm.

3 RESULTS

By 2700 s of simulation time, the convection initiated by the warm bubble divides, and the rightward-moving storm consistently exhibits vertical vorticity greater than 0.01s^{-1} within the updraft above cloud base (around 2 km). Vorticity at the lowest model level concentrated along the leading edge of a gust front developing to the west of the convection.

In the absence of surface friction, it was generally found that increasing the size of the hail category decreased the amount of low-level vorticity generated by the storm. Refer to van den Heever and Cotton (this volume) for more details on the effects of smaller hail sizes. Increasing the hail size beyond 2 cm was not found to produce large difference in storm morphology. With this mean diameter, most of the hail falls in a shaft near the core of the storm updraft, whereas for smaller hail diameters more of the hail has a chance to be advected away from the updraft core.

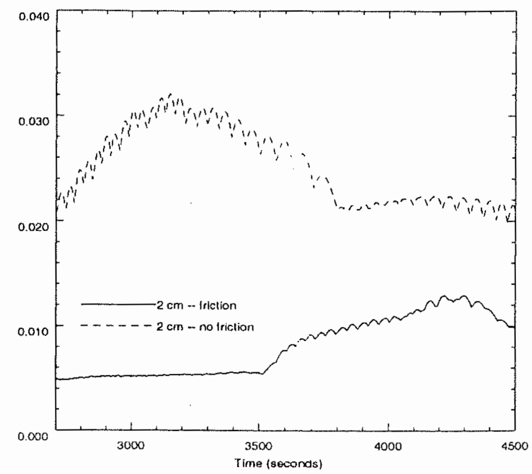

Figure 2: Relative vertical vorticity (s^{-1}) vs. simulation time at 20 m above the surface for friction and no friction simulations. Hail diameter is set at 2 cm.

For the 2 cm hail case, after storm splitting occurs the maximum near-surface vorticity is consistently higher in the no-friction simulation than in the friction simulation (see Figure 2). The near-surface vorticity in the friction simulation shows a late peak to the conventional mesocyclone threshold, but still remains below the value in the no-friction case. However, the maximum vorticity along the gust front for the no-friction case occurs at the lowest model level; in the case with surface friction, the maximum vertical vorticity along the gust front occurs 1 km above the surface, and at 3600 s (not shown) reaches a value of 0.024s^{-1}. The differences in surface vorticity values are not simply due to a reduction in the surface wind speed; in fact, the maximum surface winds associated with the gust front are stronger in the friction simulation.

In the simulations a low-level downdraft is seen to form on the west (upshear) side of the hail shaft, and it surges eastward underneath the hail shaft. The region of maximum surface vorticity forms on the leading edge of the gust front associated with this downdraft. In the case without surface friction, the gust front shows more of a tilt in the vertical, and is able to surge farther away from the hail shaft, towards the inflow sector of the storm.

4 CONCLUSIONS

The vertical structure and intensity of low-level vorticity in supercells appears to be quite sensitive to hail diameter as well as the surface friction representation used in a numerical model. Larger hail sizes may inhibit the formation of vorticity at the surface not only through decreased baroclinicity due to lesser evaporative cooling, but by creating concentrated downdrafts in regions unfavorable for vorticity concentration. Further testing of the effects of surface friction on low-level vorticity is required.

5 ACKNOWLEDGMENTS

This work was supported by the National Science Foundation under grant ATM9900929.

6 REFERENCES

Atkins, N.T., M.L. Weisman, and L.J. Wicker, 1999: The influence of preexisting boundaries on supercell evolution. *Mon. Wea. Rev.*, **127**, 2910-2927.

Blanchard, D.O., and J. Straka, 1998: Some possible mechanisms for tornadogenesis failure in a supercell. *Preprints, 19th Conf. Severe Local Storms*, Minneapolis, MN, American Meteorological Society, 116-119.

Doswell, C.A., and D.W. Burgess, 1993: Tornadoes and tornadic storms: a review of conceptual models. *The Tornado: Its Structure, Dynamics, Prediction, and Hazards, Geophys. Monogr. 79*, Amer. Geophys. Union, 161-172.

Gilmore, M.S. and L.J. Wicker, 1998: The influence of midtropospheric dryness on supercell morphology and evolution. *Mon. Wea. Rev.*, **126**, 943-958.

Grasso, L.D., 1996: Numerical simulation of the May 15 and April 26, 1991 tornadic thunderstorms. Ph.D. dissertation, Colorado State University, Dept. of Atmospheric Science, Fort Collins, CO 80523, 151 pp.

Johnson, D.E., P.K. Wang, and J.M. Straka, 1993: Numerical simulations of the 2 August 1981 CCOPE supercell storm with and without ice microphysics. *J. Appl. Met.*, **32**, 745-759.

Klemp, J.B., and R. Rotunno, 1983: A study of the tornadic region within a supercell thunderstorm. *J. Atmos. Sci.*, **40**, 359-377.

Louis, J.F., 1979: A parametric model of vertical eddy fluxes in the atmosphere. *Bound.-Layer Meteor.*, **17**, 187-202.

Wakimoto, R.M., and H. Cai, 2000: Analysis of a nontornadic storm during VORTEX-95. *Mon. Wea. Rev.*, **128**, 565-592.

Weisman, M., and J. Klemp, 1982; The dependence of numerically simulated convective storms on vertical wind shear and buoyancy. *Mon. Wea. Rev.*, **110**, 504-520.

Walko, R.O., W.R. Cotton, J.L. Harrington, and M.P. Meyers, 1995: New RAMS cloud microphysics parameterization. Part I: The single moment scheme. *Atmos. Res.*, **38**, 29-62.

THREE-DIMENSIONAL STRUCTURE OF DEEPLY DEVELOPED LONG-LIVED CUMULONIMBUS CLOUD IN THE ATMOSPHERIC SITUATION OF WEAK VERTICAL WIND SHEAR

Takao Takeda, Yukari Shusse,*
Haruya Minda, Yasutaka Wakatsuki, Biao Geng
and
Kazuhisa Tsuboki

Institute for Hydrospheric-Atmospheric Sciences, Nagoya University,
Furo-cho, Chikusa-ku, Nagoya, 464-8601, JAPAN

1. INTRODUCTION

The relationship between the structure of an organized cumulonimbus cloud and vertical wind shear has been investigated in detail by many authors. However, even if the atmospheric situation is favorable for the development of an organized cumulonimbus cloud, only a few cumulonimbus clouds can be organized or can develop deeply among many clouds.

It will be very important to study how the organized structure of a cumulonimbus cloud can be realized or why only a few cumulonimbus clouds can develop deeply in the similar environment. In the intensive field observation of the GAME/HUBEX (GEWEX Asian Monsoon Experiment/Huaihe River Basin Experiment) in 1998, a deeply developed and long-lived cumulonimbus cloud was observed by Japanese Doppler radars on July 13. Its structure and evolution are studied in detail in this paper, mainly using the observational data of these radars.

2. DATA

In the intensive observation of the GAME/HUBEX, three Doppler radars were installed at Shouxian, Fengtai and Huainan in Anhui Province in China. Maximum quantitative observation range of each Doppler radar is 64 km.

In the present analysis, rainwater content (M: g m^{-3}) and rainfall intensity (R: mm h^{-1}) were converted from radar reflectivity factor (Z: mm^6 m^{-3}) by using the following relationships (Jones, 1956), respectively:

$$Z = 486R^{1.37},$$

$$M = 0.052R^{0.97}.$$

Upper-air sounding data observed at Fuyang Meteorological Observatories, which is 100 km away north-northwestward from Shouxian Doppler-radar site, are also used in the analysis.

*Corresponding author's address: Yukari Shusse, Institute for Hydrospheric-Atmospheric Sciences, Nagoya University, Furo-cho, Chikusa-ku, Nagoya, 464-8601, JAPAN E-mail: shusse@ihas.nagoya-u.ac.jp

3. BRIEF DESCRIPTION OF ATMOSPHERIC SITUATION AND CONVECTIVE RADAR-ECHOES ON JULY 13 IN 1998

Though not shown here, Baiu front was located about 600 km southeastward from Doppler radar observation sites and observation areas were not covered by synoptic-scale low T_{BB} cloud system on July 13 in 1998.

Convective available potential energy (CAPE) at Fuyang was 2300 J kg^{-1} and atmospheric condition was favorable for cumulonimbus clouds to develop. As seen in wind hodograph of Fig. 1, southwesterly winds were predominant up to 14 km level and winds veered clockwise with height at Fuyang. Their vertical shear was directed from southwest to northeast at low levels and it was 1.8 m $s^{-1}km^{-1}$ below 5 km.

More than forty convective radar-echoes were observed in the Doppler radar observation area on July 13. Most of convective radar-echoes disappeared within one hour after their initiation. However, only one radar-echo (hereafter named C) existed for longer than 3 hours and its echo-top height exceeded the level of 15 km. It is to be noted that total rainwater amount in radar-echo C and the volume of its intensive radar-echo were especially larger than other convective radar-echoes.

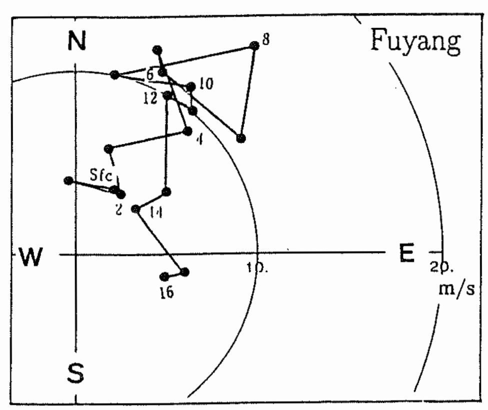

Figure 1 Wind hodograph at Fuyang at 1400 LST on July 13.

4. THREE-DIMENSIONAL STRUCTURE OF CONVECTIVE RADAR-ECHO C

4.1 Evolution of convective radar-echo C

In the present analysis X-axis is defined in the direction normal to the movement of convective radar-echo C, which moved north-northeastward with average speed of 9.7 m s^{-1}.

As shown in Fig. 2, echo-top height of radar-echo C continued to be higher than 14 km for one hour and a half with maximum height of 18.5 km at 1505 LST. The echo-top of radar-echo B, which was the second most-developed convective radar-echo on July 13, ascended gradually up to the highest level of 14.5 km at 1519 LST and then descended. In Fig. 2 total rainwater amount of radar-echo C is also shown. In contrast with echo-top height, it increased rapidly up to maximum value of 3.4×10^{11} g at 1519 LST and thereafter it decreased gradually.

On the basis of Fig. 2 and the time variations of other parameters (not shown here), the evolution of convective radar-echo C from 1437 to 1615 LST is divided into four stages: stage 1 (1437 to 1512 LST), stage 2 (1512 to 1526 LST), stage 3 (1526 to 1554 LST) and stage 4 (1554 to 1615 LST). In stage 1 the height of echo-top increased up to the highest altitude of 18.5 km and in stage 2 the volume of its intensive radar echo was very large and its three-dimensional development was the most vigorous. The evolution of radar-echo C in both stages will be mentioned here.

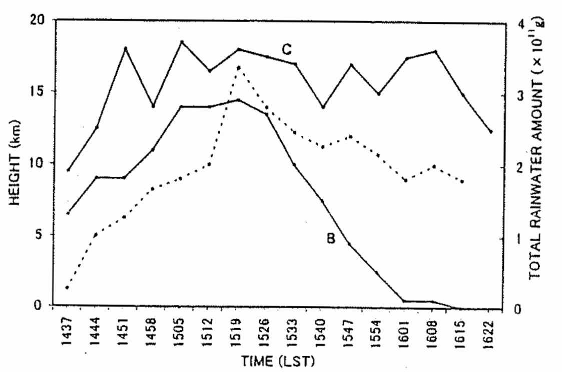

Figure 2 Time variations of echo-top height of radar-echoes B and C (solid lines) and total rainwater amount of radar-echo C (dashed line).

4.2 Three-dimensional structure of radar echo

1) Stage 1 (1437 to 1512 LST)

As shown in Fig. 3, radar-echo C was composed of three cellular echoes X2, X3 and X4 at 1458 and 1505 LST. Horizontal distances between these cellular echoes were 5 km approximately and they were lined along the movement of radar-echo C.

Figure 4 shows the vertical cross sections of radar-echo intensity in the direction normal to the movement of radar-echo C. Both sections cross through the most intensive part of cellular echo X2 which was the most developed one in this stage. As seen in Fig.5, vertical wind shear in this direction was 0.5 m s^{-1} km^{-1} up to 5 km level. At 1458 LST, however, intensive echo region was inclined slightly to WNW (left side) below 5 km and to ESE (right side) above 5 km in this section. It is also to be noted that the contours of echo intensity cut into radar-echo C from right side between 3 km and 7 km levels.

At 1505 LST echo-top height reached 18.5 km. Intensive echo region occupied predominantly the west-northwestern part of radar echo, especially below 10 km. The contours of echo intensity cut into radar-echo C from the east-southeastern side down to 1 km level. Cellular echo X2 was inclined to the right side in this vertical section except below 2 km level.

It is an interesting feature in stage 1 that only cellular echo X2 repeated intermittently the marked development of echo-top height. It was inclined to the ESE side in the direction normal to the movement of convective radar-echo C after 1451 LST despite of weak ambient vertical wind shear in this direction.

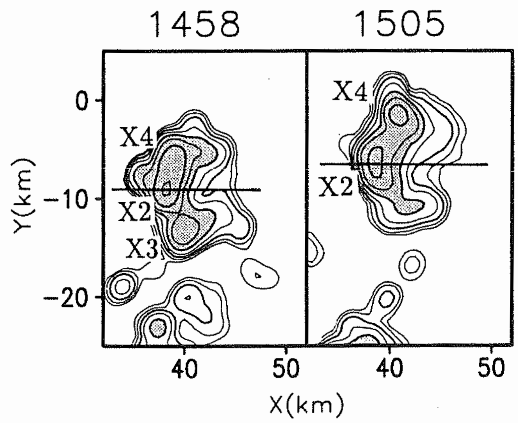

Figure 3 Horizontal distribution of radar-echoes at 5 km levels in stage 1. Contours of radar-echo intensity are drawn every 5 dBZ above 10 dBZ.

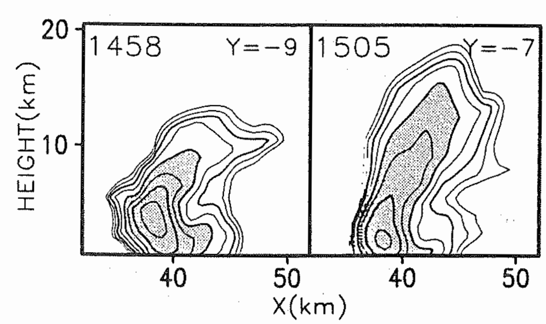

Figure 4 Vertical cross sections of radar-echo C in stage 1. Locations of vertical cross sections are indicated in Fig. 3.

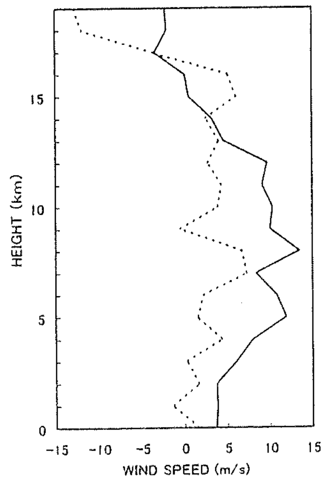

Figure 5 Vertical profile of winds observed at Fuyang at 1400 LST on July 13. Solid line indicates wind component along the motion of convective radar-echo C. Dotted line indicates component normal to its motion.

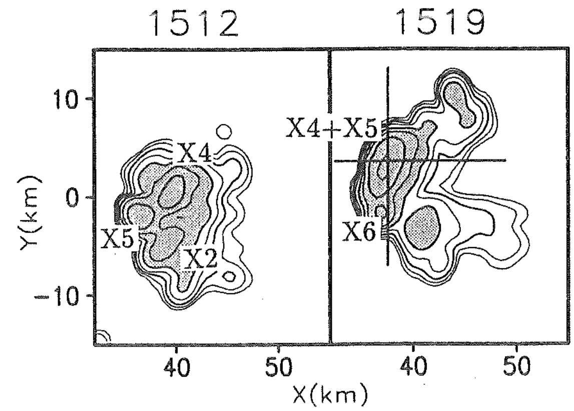

Figure 6 Same as Fig. 3, except in stage 2.

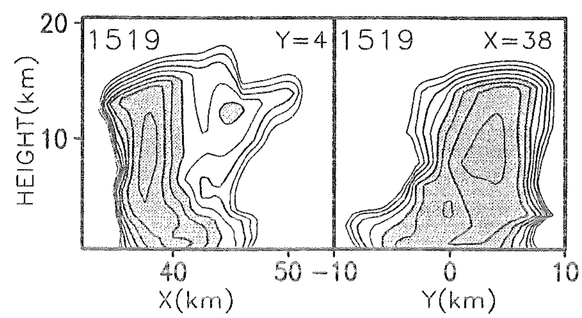

Figure 7 Same as Fig. 4, except in stage 2. Locations of vertical cross sections are indicated in Fig. 6.

2) Stage 2 (1512 to 1526 LST)

As seen in Fig. 6, at 1512 LST new cellular echo X5 formed in the west-northwestern part of convective radar-echo C. Cellular echoes X4 and X5 coexisted very closely to each other.

At 1519 LST cellular echoes X4 and X5 merged and one intensive large radar-echo region was observed in the horizontal sections at 5 km levels. As shown in Fig. 7, radar echo stronger than 30 dBZ extended up to 15 km without change in its horizontal area. This structure brought about the three-dimensional vigorous development of convective radar-echo C in stage 2. Intensive echo region occupied the west-northwestern part, not showing its inclination in the direction of WNW to ESE. The contours of echo intensity less than 30 dBZ cut into radar-echo C sharply from the east-southeastern side around 5 km level.

Though convective radar-echo C was composed of several cellular echoes in stage 2, it did not show the organized multicellular structure and one large cellular echo developed deeply after cellular echoes X4 and X5 merged. It is very interesting that in stage 2 radar-echo C attained three-dimensional vigorous development and its very high echo-top was maintained for a long time without any organized structure.

4.3 Airflows in convective radar-echo C

The horizontal distributions of wind vectors at 0.5, 1.5 and 4.5 km levels in radar-echo C are shown in Fig. 8. Easterly or southeasterly winds were predominant inside and around convective radar-echo C at 0.5 km level at 1458 and 1505 LST. Divergence field was found around intensive radar-echo at 0.5 and 1.5 km level. Convergence field was found in the western to northern part of radar-echo C every time at 0.5 and 1.5 km levels. Southwesterly winds came into radar-echo C in its western part at 1.5 km level. It is to be noted that easterly or southeasterly winds, which had component normal to the movement of radar-echo C, were predominant at least inside and around radar-echo C especially at low levels, though ambient winds of easterly component were not observed at low and mid levels at 1400 LST at Fuyang.

Figure 9 shows the distribution of airflow speed in the vertical section through the centers of cellular echoes in radar-echo C. At 1458 LST airflows of east-southeastward component (to right in this vertical section) were found at 1 to 3 km levels in the west-northwestern part. They extended up to 7 km level in the east-southeast side with width of 5 km in the direction along the movement of radar-echo C. These airflows corresponded to winds from the southwest side in Fig. 8. Airflows of west-northwestward component in the left side existed below the region of east-southeastward airflows. They corresponded to predominant easterly winds in Fig. 8.

It is to be noted that large vertical shear of left to right existed in the direction normal to the movement of radar-echo C inside radar-echo, especially at low levels, though ambient winds observed at Fuyang showed very small vertical shear. This feature of airflow distribution continued at least until 1519 LST when radar-echo C was in the most intensive stage.

Figure 10 reveals the streamlines at 1458 LST. Updraft and downdraft are inferred to have been distributed in the upshear side and in the downshear side of winds, which were observed in this vertical section by Doppler radars, respectively. Usually, in this kind of airflow distribution, strong horizontal convergence can be caused at low levels to the downshear side of downdraft and a new updraft can be initiated there because downdraft transports downward horizontal momentum at higher levels downward. Consequently updraft in the upshear side will be short-lived. However, this cumulonimbus cloud was long-lived for at least 3 hours.

It would be reasonable to say that main strong downdraft in this cumulonimbus cloud was shifted to the frontal side of updraft in the direction of cumulonimbus-cloud movement, that is, the direction of ambient vertical wind shear observed at Fuyang.

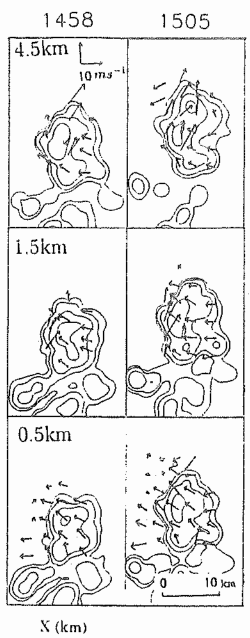

Figure 8 Horizontal distributions of wind vectors at 0.5, 1.5 and 4.5 km levels.

5. SUMMARY

On July 13 in 1998 a deeply developed cumulonimbus cloud lasted for at least 3 hours and its maximum echo-top exceeded 18.5 km. One cellular echo in it developed very deeply, though it was composed of several convective cells. Downdraft in the vertical section in the direction normal to the movement of radar-echo C would not have been strong and it would not have obstructed low-level inflows from the east side toward updraft. Updraft continued to be intensive as a result of low-level persistent supply of wet and warm air from the west side, which was lifted forcedly by low-level cold airflows from the east side. The merging of two convective cells might be one of reasons why the marked three-dimensional development of cumulonimbus cloud C was observed among many other convective clouds.

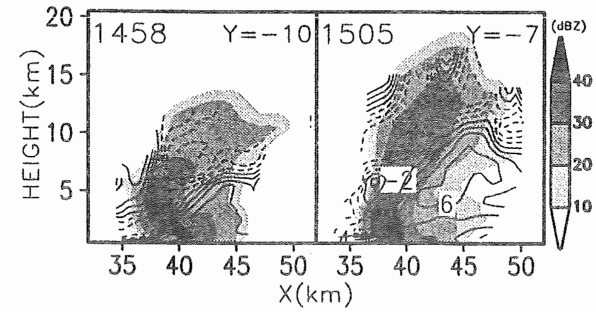

Figure 9 Vertical cross sections through the centers of cellular echoes in radar-echo C. Distribution of airflow speed are shown together with distribution of radar-echo intensity. Contours of airflow speeds are drawn every 2 m s^{-1}.

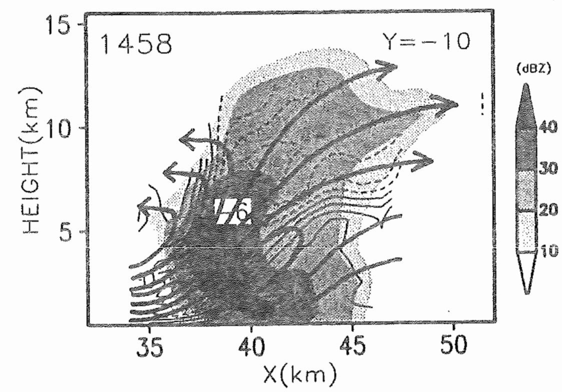

Figure 10 Streamlines at 1458 LST in the vertical section normal to the motion of radar-echo C. Distribution of radar-echo intensity is also shown by shaded areas in the figure. Contours indicate airflow speeds in the direction of radar beam.

ACKNOWLEDGMENT

The authors are grateful to Prof. H. Uyeda and other staff members of Graduate School of Science, Hokkaido University, who kindly provided Doppler radar data in the intensive observation of the GAME/HUBEX.

CANALIZATION AND MESO-γ SCALE RAINSTORM

Biyuan Lin

Meteorological institute of Hunan Province,Changsha,P.R.China 410007

1.INTRODUCTION

There is a meteorological station named Dongkou in Hunan province of south china, where always drop rainstorm, but all the around area have no precipitation, so the weather forecaster in provincial station generally regarded it as a wrong record. As the same thing always appear, meteorological office of Hunan province send me to have an investigation. This paper analyzed the local violent flood in Dongkou, Hunan province on May 26,1986, studied the meso-γ scale canalization effect on violent flood.

2. BASIC FACTS

2.1. RAINFALL

From 2:00 am to 8:00 am on May 26,1986, there is a super rainstorm in Dongkou, Hunan province, result in mountain flood. The precipitation is 207.8mm between 2:25 to 6:30 and the largest precipitation within 1 hour is 111.6mm. The 3h,1h,10min precipitation exceeded provincial record in history, and closed to domestic maximum value .

The rainstorm spread like a band along eastern limb of Xuefeng Mountain, it is about 5-10Km wide, 40Km long. The core of the storm is located in Dongkou town. The horizontal gradient is very large. It's basically belongs to γ mesod-Scale violent flood, and this kind of violent flood only happen in Dongkou sometimes.

To analysis the process of this violent flood, we must make it clear that: How the rainstorm happens? Why the scale is so small and the intensity is so strong? Why the core is located in Dongkou?

2.2. TOPOGRAPHY

Dongkou lies in the south-east of Xuefen mountain,west of Shaoyangbasin.Shaoyang asinlocated between Xuefen mountainand Yuecheng mountain. There is a NW-SE canyon in the middle of Xuefen mountain. The depth of the canyon is over 1000m, the width is about 200-400m and the length is about 40Km, which forms a deep and long pipeline, and the exit is in the NE sides of SE end of the pipeline. (see Fig. 1).

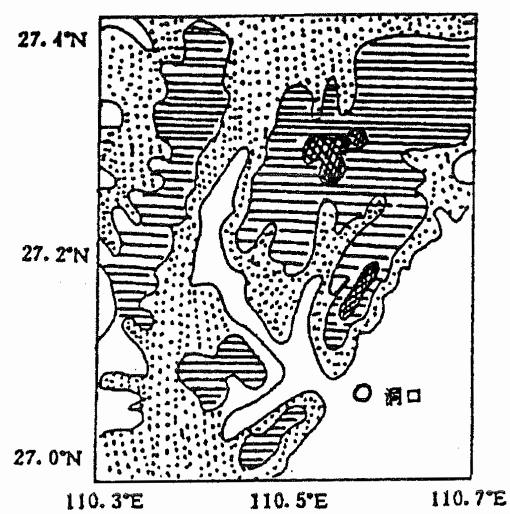

Fig.1 the canyon of Xuefen mountain .

2.3. BACKGROUND FIELD

Biyuan Lin . Meteorological institute of Hunan Province, 163 YuHua Rouad Changsha,P.R.China 410007

On 20:00 May 25, there is no any trough system at the line of 500hPa, which could make rainstorm, no matter before the rainstorm or after the rainstorm, this area is controlled by 500Pha anticyclone, and the wind field is weak. At the same time, there is no any trough system at 700hPa either, all the area of south China is in the homogeneous field of pressure and temperature, the wind field is weak. Though there is a trough between Xi'an city and Chengdu city,but it didn't work at all within 12 hours, so it isn't the trough which directly produced the Dongkou rainstorm. But the 850hPa Sichuan trough moved obviously within 12 hours, it is the meso α -scale system which made the Dongkou rainstorm.

2.4. MESO-SCALE WEATHER SYSTEM

Before the rainstorm, there is a obvious landform pressure of low-mid at the south-west of the storm source. As the inrush of the cold front, the pressure of low-mid became half warm and half cold, so it grew and moved near to Dongkou, where it formed one dual pressure with small high pressure after front, it is the direct maker of the rainstorm process.

2.5. GROUND HEAT FIELD

Diurnal evolution of ground heat field: The bottom glade of Yuan river and Mayang basin are area of low value of heat field, but mountains are area of high value at 09 hour on 25. However the condition is just antithesis.

Section of heat field and degree of stability of stratification : Afternoon on 25 Mayang basin and Xuefeng mountains are warm area at all times. Ground heat field changes atmosphere stratification rapidly. It animates water vapour go to high level from low level and deep degree of humidity layer increate . Because wind field of weather system is weak, above evolution course can persist at a long times .

Anomaly increasion of temperature : Generally temperature is declining in 02 hour in summer by evolution of temperature field in day. There is an anomaly area of increasing temperature near by Tongkou at 02 hour on 26 , which is an indication before rainstorm. Increasing temperature is not inconsistent, the anomaly area of increasing temperature is small and the area is just about location of rainstorm.

2.6 HUMIDITY FIELD ANALYSIS

The features of the rainstorm arefollowing, weather map shows there is an area of high humidity nearby Zijiang and Tongdao , also is so from east of Sichuan to south-west of Hubei, the late is relevance with rainstorm location of front . Above two high humidity area was cut by cold-dry air from Yuanjiang canyon , so about Zijiang comes into being a lone high humidity area of mesos cale. Mesoanalysisshows : There is a dry centre of the east side of Xuefeng mountains, but a wet centre of the west of the mountains . The parts of dry and humidity are long shape of north-south direction. The weak cold air come into east side of Xuefeng mountains. The humidity area north department moves to east before rainstorm. When the thunderstorm close with , Xuefeng mountains are just general humidity area. The wet section is located in west of the rainstorm and wind go to east from west in the canyon , so water vapour pass by the canyon to rainstorm location .

Vertical distribution of difference of Temperature-dew point: The figure 2 shows that before the rainstorm 450-250hPa is greatest level of increasing humidity, 950-750hPa is second, change of humidity degree is not obvious in the 700-600hPa level, by comparison 600-500hPa is a dry level. However, when the rainstorm stars 600-500hPa level is more and more dry, and humidity difference of the dry level with another wet levels is more and more large. This dynamic dry level changes degree of stability in atmosphere and a ccumulates energy and supports downdraft of cumulus. Aside from a deeper saturation level from the ground to 600hPa, nearby 400hPa is too a saturation level.

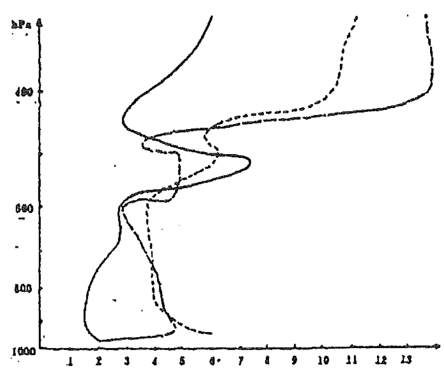

Fig..2 T-Td line,on May 25,1986.(08h is dot-dashed, 20h is dashed) and in the next day 08 hour (it'ssolid).

2.7. THE TEMPERATURE INVERSION

In temperature altitude chart at 08 hour on 25 before rainstorm there are some levels of temperature inversion, where by 600hPa level is the best obvious. In temperature altitude chart at 08 hour on 26 during rainstorm there is no any level of temperature inversion in the midst level, by 900hPa is only lavel of temperature inversion.

2.8. CANALIZATION EFECT

The air stream of pass by canyon causes west wind at Dongkou,but it is east wind in the east aside of the mountains, so a convergence point appears by Dongkou. The air stream of exit of the canyon leads two circulation system of meso-small scale, one is low pressure loop in north of Dongkou air exit and another is high pressure loop in the south, The two loops are in relation to the rainstorm. The analysis of pressure field of 1 hour indicates too two pressure loops. When wind pass by Dongkou, difference value of this one dual pressure increasing obviously.

2.9. MCC AND MULTI-CELL

The top of "Ω" anamorphic cold front on the ground produces a MCC(Meso-scale Convective Complex) at 20 hour on 25. This MCC is just coincidence with a convergence point on inversion trough of 850hPa. This convergence point had changed a meso β -scale whorl which horizontal scale is correspond with MCC at 08 hour on 26. The MCC development is vigorous and a renascent multi-cell become tie shape at 02 hour on 26. This multi-cell develops rapidly and strong precipitation fall down frantically.

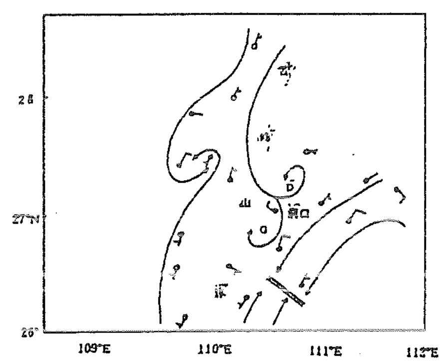

Fig.3 Streamline field small scale at 19hour on 25 may ,1986.

3. CONCEPT MODEL

On the grounds of above-mentioned a concept model was expounded : In a weak weather scale wind field there is a weak cold front on the ground and ground heat is obvious ahead . There is a meso α -scale convergence area which produces a MCC on low level . There is a meso α -scale high pressure which is divergence on middle level. There is a shallow dry level on 500hPa. In vertical distribution of humidity dry and wet is interlace .When weak cold fron come into convergence area and meet with mountains of north-south direction, it take place metamorphosis and changes to "Ω" shape cold front. The top of "Ω" anamorphic cold front is a high value area of temperature and humidity and a mes α -scale mid-low pressure occurrences. Anamorphic cold front go forward and lead a inversion temperature level above . Than canalization efect leads one dual mesoγ-scale pressure. Updraft break through inversion temperature of middle level and multi-cell develops rapidly and downpour falls down frantically.

4. FORECAST

Following conditions is importable :

Wind fields is weaker and there is no any trough and ridge on 700hPa and 500hPa. There is a meso α -scale high pressure on 500hPa an inversion trough on 850hPa in the forecast area. Weak cold front moves to local station and ground heat is obvious ahead the front . The forecast area is located convergence section of east slope of mountains and meso-scale low pressure appears and develops. From ground to 400hPa there are some inversion temperature layers and a deeper saturation level in which there is dry layer from 600hPa to 450hPa. Multi-cell and super-cell are vigorous on south-east side of MCC.

5. CONCLUSION

Above analysis shows that complex topography leads anamorphic cold front which is importable reason. Dry layer in deeper wet layer have specific dynamic efect. Canalization efect can products convergence point and causes mesoγ-scale low pressure and updraft break through inversion temperature of middle level and multi-cell develops rapidly and downpour falls down frantically.

Acknowledgements

Author thanks to Mr. Zengshengjiang for his encouragement and also thanks to Mis. Xiongyuzheng and Mr.Lijianxin of Shaoyang and Huaihua for them data .

REFERENCES

Linbiyuan, Limenxian,1988:Lake-land wind and precipitation on Dongtinghu lake. Academic journal of Nanjing meteorological stitute.1.Linbiyuan ,1988: Analysis and forecast of rainstorm process with lee wave. Miscellany of rainstorm forecast.Public of meteorology.
Zhangyian,Linbiyuan,1988: Analysis and forecast of meso-scale rainstorm. Public of meteorology.

THE NUMERICAL SIMULATION OF A MICROBURST-PRODUCING THUNDERSTORM, SENSITIVITY EXPERIMENTS

M. Torres Brizuela[1*], and M. Nicolini[1]

[1] Dpto Cs. Atmósfera y los Oceános FCEYN, Universidad de Buenos Aires, Argentina/Centro de Investigaciones del Mar y la Atmófera (C.I.M.A./CONICET-UBA)

1. INTRODUCTION

On 20 July 1986 a severe thunderstorm formed over the northern area of Alabama (United States), during the development of the M.I.S.T (Microburst and Severe Thunderstorm) project operated near Huntsville, Alabama (Dodge et al. 1986). This storm was characterized by a weak environmental shear and it produced a strong and damaging moist microburst. During its life cycle a complete data set was collected with the use of Doppler radars and cloud photography in order to understand its three dimensional structure. Previous observational studies such as those conducted by Wakimoto and Kingsmill (1988) and Wakimoto and Bringi (1991) have been done in order to have a detailed analysis of this severe microburst case. Nicolini (1993) have used a 2-D model developed at the University of Buenos Aires, in order to test it with the Alabama storm.

The main goal of this study is to test the sensitivity to different initial conditions, parameterizations of a 3-D model and evaluate its capability to reproduce the intensity of convection and characteristics of a microburst. These experiments are also conducted in order to explore how important are the environmental winds to organize the convection and to influence the microburst. These are necessary steps in to validate and use this numerical model for diverse applications and in particular simulate and understand microburst observed phenomena in convective storms in Argentina.

2. DATA AND METHODOLOGY

As a modeling tool, the numerical code used is the Advanced Regional Prediction System (ARPS), provided by the University of Oklahoma (Xue et al., 1995). ARPS is non-hydrostatic mesoscale model based on the primitive equations. In the present version it includes parameterizations for turbulence and microphysics. The following is a brief description of the configuration used in this study.

- The cloud microphysics follows Linn et al. (1983) which includes five categories of water substance (water vapor, cloud water, cloud ice, rain water, snow and graupel/hail).
- Vertical and horizontal turbulent mixing was parameterized using the turbulent kinetic energy prognostic equation.
- The top boundary condition was a wall on top with a Rayleigh friction absorption layer. The lateral boundary condition is Klemp-Wilhemson (1987a)
- The integration horizontal grid domain is 47.1 km. in the E-W direction and in the N-S direction and covers 17 km. in the vertical.
- Spatial horizontal resolution was set to 0.6 km and vertical resolution was set to 0.45 km.
- The big time step was 3s and 1 s for the small one.

The model was initialized with the Redstone 18Z radiosounding, shown in Figure 1.

In order to initialize the convection a warmer bubble-like perturbation was imposed at the lower boundary and in the middle of the domain. The bubble used has different shapes. At present three series of simulations were carried out:

- A simulation with an ellipsoidal bubble perturbation in potential temperature with a maximum of 0.5°K. was used. The environmental winds were also included. This run is used as control run A1. The turbulence

* *Corresponding author address:* M. Torres Brizuela, Departamento de Ciencias de la Atmósfera, Facultad de Ciencias Exactas y Naturales, Ciudad Universitaria, Pabellón II-2P, 1428 Buenos Aires, Argentina;
email: brizuela@at1.fcen.uba.ar

parameterization used solves the turbulence kinetic equation

- A similar perturbation was used, but the environmental winds were turned off. This run was called A2.
- Similar initial conditions as in A1 except bubble perturbation not only in potential temperature but also in water vapor with a maximum of 0.02 g/g was included. This run was called A3.

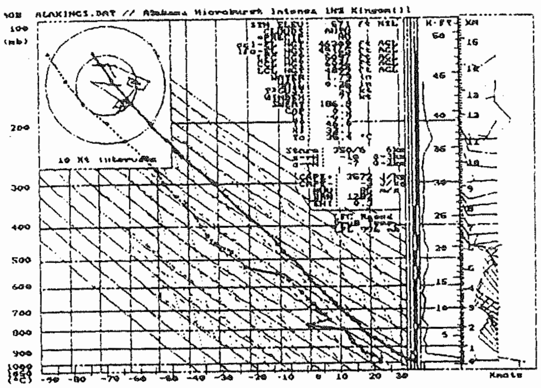

Figure 1. Radiosounding taken at Alabama 18 UTC.

In table I are summarized the main characteristics of the Alabama Storm.

Parameter	Observed Value
Cloud base	1.8 km.
Maximum Cloud Top	14 km.
Outflow divergent winds $\Delta v/\Delta r$	$0.01\ s^{-1}$.
Maximum Radar Reflectivity	>65 dBZ at 6.0 km.
Maximum vertical velocity W (m/s)	30 m/s

Table I. Alabama (20 July 1986) storm characteristics

3. NUMERICAL RESULTS

Previous runs done in order to find the best possible horizontal and vertical resolution show that domain size and resolution chosen for the experiments are optimum for this event simulation.

The three experiments A1, A2 and A3 show a good general representation of the main feature of the cell development, convective intensity and divergent outflow winds. Results are summarized in Table II

Char \ Exp.	Max W (m/s)	Max $\Delta v/\Delta r$ (m/s)	Max Z (dBZ)
A1	45 ms^{-1}	$2x10^{-3}s^{-1}$	< 70 dBZ
A2	50 ms^{-1}	$5x10^{-4}s^{-1}$	< 70 dBZ
A3	30 ms^{-1}	$1x10^{-3}s^{-1}$	60 dBZ

Table II. Results of the numerical experiments.

The divergent outflows simulated by ARPS are better representated in A1 experiment, but it overestimates the maximum updraft.

Figures 2, 3 and 4 show the wind speed pattern relative to the environmental winds near the surface, at the time of the simulated microburst in the different experiments .

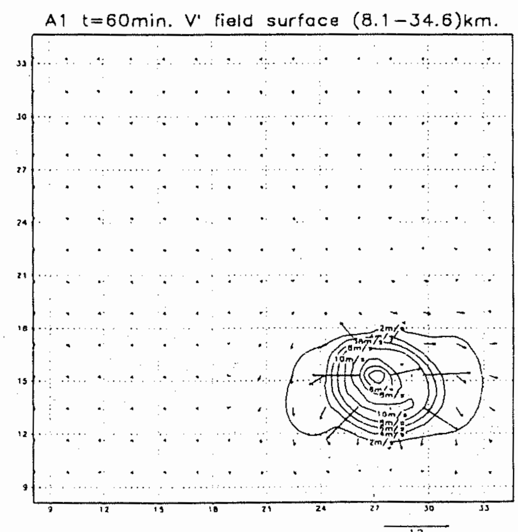

Figure 2: Run A1 (60 min.)at surface. .Isolines denote wind speed relative to the environmental wind and the arrows indicate the wind field

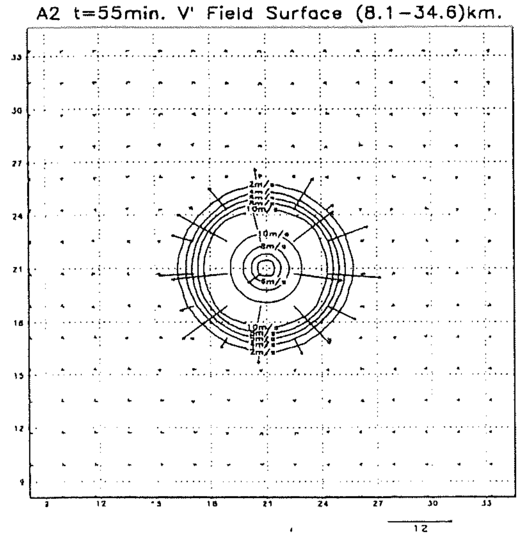

Figure3. Idem Fig.2, except for A2 run and t=55 min.

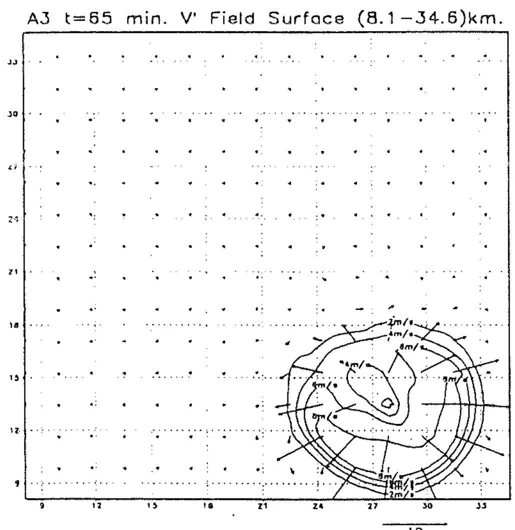

Figure 4. Idem Fig.2, except for A3 and t=65min.

Figures 5, 6 and 7 are vertical slices (y,z plane) for the three experiments. For the two first experiments the rain water and the graupel/hail fields are more intense than A3 run .

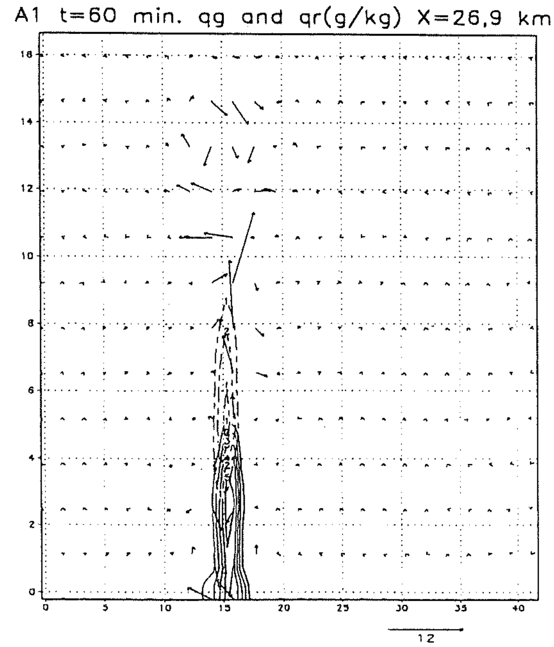

Figure 5: Run A1 (60 min.), slice (y,z) at X.=29.9 km. Isolines denote rain water category and dashed isolines denote graupel/hail category (contours are:1g/kg) and the arrows indicate the wind field

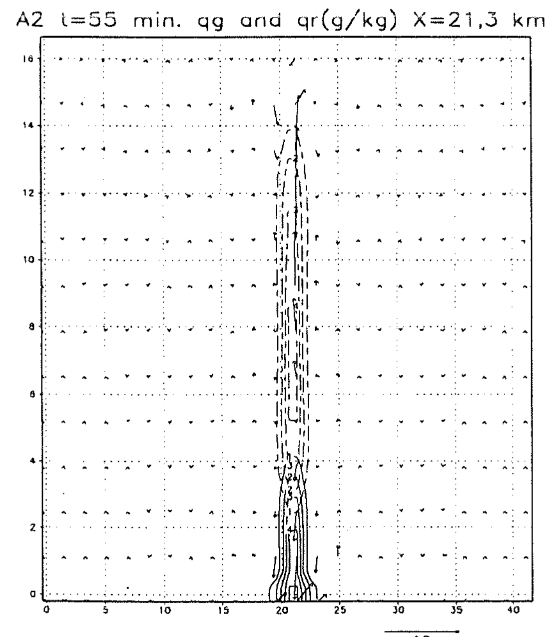

Figure 6: Idem Fig 5.except Run A2 (55 min.),and slice (y,z) at X.=21.3 km.

A3 t=65 min. qg and qr(g/kg) X=27.9 km.

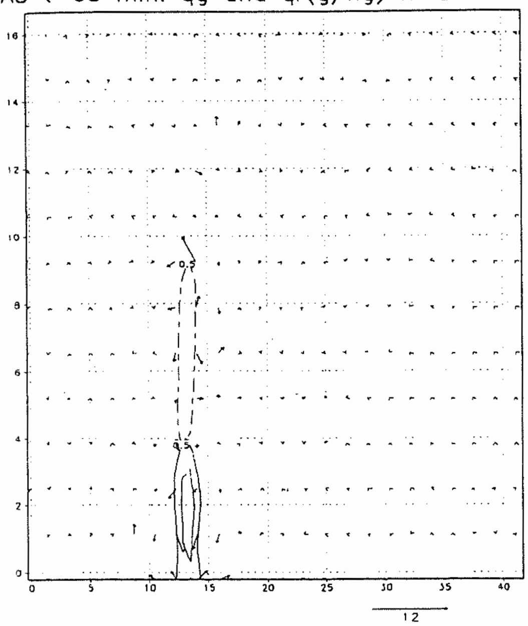

Figure 7. Run A3 (t=65 min.) Slice (y,z) at X=27.9 km. Isoline denotes 0.5 g/kg of rain water categry and the arrows denote the wind field.

4.DISCUSSION AND FUTURE WORK

The analyses of the three runs suggest a strong sensitivity of the maximum updraft to the initial perturbation.

The presence of environmental winds organizes the microburst intensity and thunderstorm evolution

Presently work is in progress to explore impact of different turbulence parameterizations in the microburst intensity and thunderstorm evolution.

6. ACKNOWLEDGEMENTS

This work was supported by CONICET grant PIP N°4520/96, ANPCyT grant PICT N°07-00000-01757 and the University of Buenos Aires, grant TX30 and the first author wishes to thank to the F.O.M.E.C. for her graduate fellowship.

7. REFERENCES

Dodge, J., J. Arnold, G. Wilson, J. Evans and T. T. Fujita, 1986: The Cooperative Huntsville Meteorological Experiment (COHMEX). *Bull. Amer. Soc.*, 67, 417-419.

Kingsmill, D.E. and R.M Wakimoto, 1991: Kinematic, dynamic, and thermodynamic analysis of a weakly sheared severe thunderstorm over northern Alabama. *Mon. Wea. Rev.*, 119, 262-297.

Klemp, J.B., and-R.B. Wilhemson, 1987[a]: The simulation of three-dimensional convective storm dynamics. *J. Atmos. Sci.*, 35, 1070-1096.

Lin, Y.L., R.D. Farley and H.D. Orville, 1983. Bulk parameterization of the snow field in a cloud model. *J. Climate Appl. Meteor.*, 22, 2192-2210.

Nicolini, M., 1993: Simulación numérica de una tormenta generadora de un "microburst", su verificación. *Meteorologica.*, Vol. 18 , Nos. 1-2, 23-32.

Wakimoto, R.M. and V.N. Bringi,1988: Dual-polarization observations of microbursts associated with intense convection: The 20 July storm during the MIST Project. *Mon. Wea. Rev.*, 116, 1521-1538.

Xue, M., K. Droegermeir and V. Wong, 1995: The advanced regional prediction system and real-time storm weather prediction. *Proceedings of the Internat. Workshop on limited-area and variable resolution models,* Beijing, China, World Meteorological Org.

Multi-Dimensional Numerical Model of Convective Cloud and Precipitation.

M.V.Gurovich

Reserch Center for Atmospheric Remoute Sounding,
A.I.Voeikov Main Geophysical Observatory,
7 Karbysheva St., 194018, St.Petersburg, Russia
Phone: +007 812 707-51-51, Fax: +007 812-707-52-38

1. INTRODUCTION

The model proposed Bekriaev, Gurovitch (1991), Gurovitch, Bekriaev (1994), Mazin, Gurovitch (1998) is dedicated to the study of convective cloud's dynamics from the very beginning to the dissipation stage. A set of equations include a motion equation for 3 component of air stream velocity, a conservation of energy equation for a perturbation of temperature, a dissipation of turbulent energy equation, a conservation of fraction in a vapor mass equation (all 3D, non-stationary), a Poison equation for a pressure deviation (3D, stationary), a coagulation kinetic equation for a distribution of sizes of droplets and ice crystals (both 4D, non-stationary).

The joint solution of the listed above systems of non-steady equations practically without simplifying parameterizations within the framework of modeled 4D (5D - for electrification) space allows to investigate thin effects of cloud evolving.

The volume simulated is a parallelepiped of 44*32*14,8 km^3 consists from 651 200 in a rectangular space (a grid of 110*80*74 points with dimensions 0,4*0,4*0,2 km^3). The space of precipitant is divided into 50 irregular gradations, dissimilar for droplets and ice crystals. The values at the heights of horizontal uniform initial fields of pressure, temperature, humidity and wind shear stand duty as boundary conditions. The initialization of convection is performed by the given overheating (0,5 °C) in surface grid-points at the different place of the parallelepiped.

Single convective clouds, initiated by heating of air in were analyzed by Gurovitch, Bekriaev (1994), Mazin, Gurovitch (1998). Now we present an attempt to link the character, of a cloud that develope because of the updruft of overheating termics with number and mutual location of overheated areas. They are simulated as barrels with d=2 km and h=0,4 km. We study the clouds that developed in calm atmosphere and in the conditions of changed value and direction of wind with altitude.

2. NUMERICAL EXPERIMENTS

The temperature stratification presented in the fig.1 was used in every case of our simulation. Two cases of the wind shear are presented in the fig.2. To characterize the intensity of the cloud development we used the fields of radar reflectivity (dBZ) and the fields of kinetic energy heavy precipitation (J*m^{-2}). The mass of liquid (M_r) and heavy (M_h) precipitation for every cell are presented in thousand tons.

The results of calculations for the maximum stage of development of a single cloud (a) and of two cloud (b), the centers of which are on the distance of 8 km, are presented in the fig.3. It's shows that these three cells are practically equal. The mass and character of the fall precipitation are also the same. These results illustrate

1) The weak influence of the boundary conditions on the large distance from the boundaries of the modeling volume;

2) Sufficient quantity of a moisture in the modeling volume.

One can see that in the opposite case the further experiments would be unreasonable.

The same dynamics of the cloud evolution were studied in Mazin, Gurovitch (1998). Now it shoud be

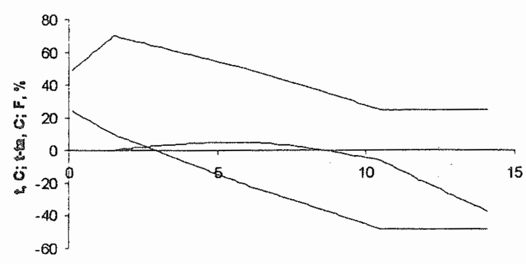

Fig. 1. Atmosphear's paramrteres: temperature t, C; adiabatic overheating t-ta, C; humidity F, %

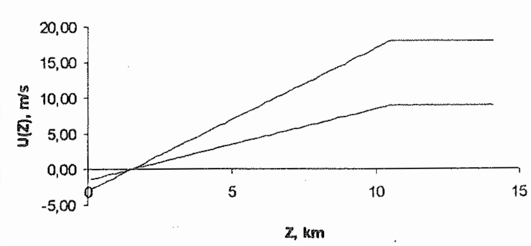

Fig. 2. Wind shear U1(Z): U(0)=-1,5 m/s, dU/dZ=1,5 (m/s)/km and U2(Z): U(0) =-3m/s, dU/dZ=3,0 (m/s)/km.

Mark V. Gurovich, E-mail: mark@mail.rcom.ru

mentioned that some assymetry of cells appears because of the Koriolis force influence, witch value becomes significant because of high values (15...20 $m*s^{-1}$) of updrafts.

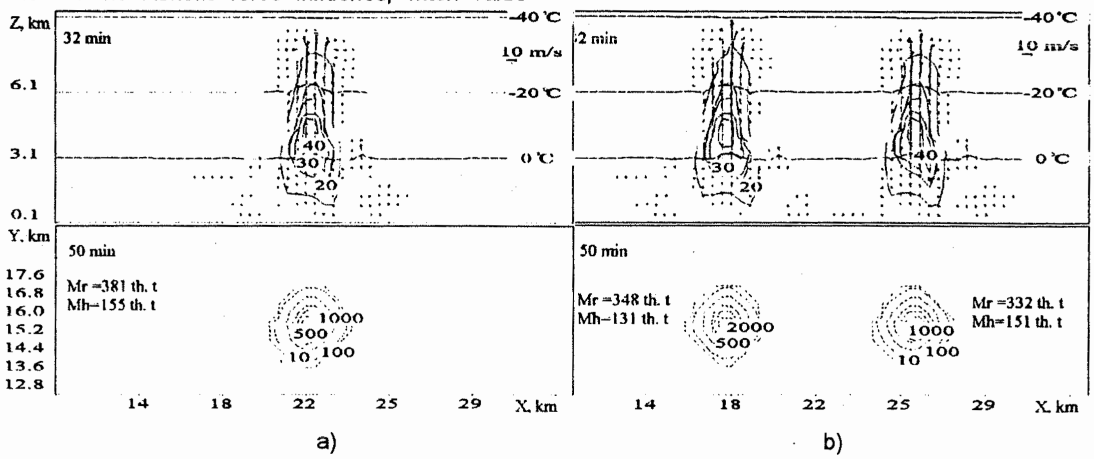

Fig.3. Sequental stages of cloud evolving. Cross-sections of radar reflectivity (dBZ) field through the cloud's center in the plain ZOX (up) and field of total hail kinetic energy ($J*m^{-2}$) jn the ground (down). Value of overheating 0,5 °C in surface barrel with d=2 km, h=0,4 km. a) Single cloud; b) Two cloud with distance between there center is 8 km.

The other experiments for pair of clouds illustrate that the intensity of every cell decays with decreasing of the distance between them. For example, the amount of precipitation (both liquid and heavy) that fall from each cloud (distance between centers is 4 km) in 2 times less from each cloud shown in fig.3b. As the sufficient quantity of a moisture in the modeling volume is lager (the mentioned it earlier), this decreasing can be explained by the beginning of competition between the cells for the humid air from the lower layers of the atmosphere. It should be mentioned that confluence of two overheated surface area into a single one with lager diameter leads to the some effect – the weakening of cells intensity and precipitation amount from them.

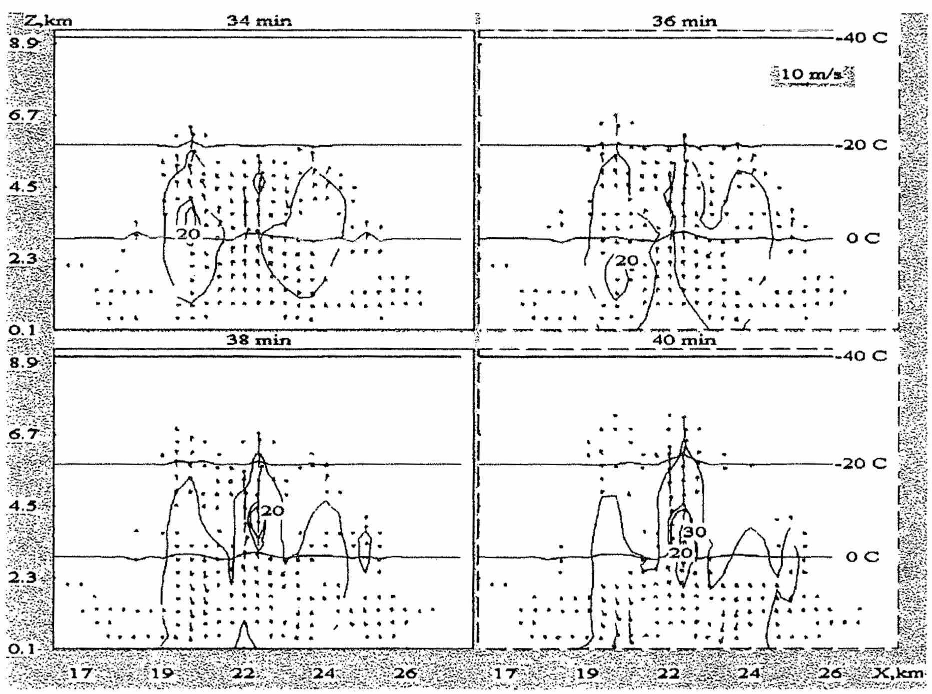

Fig.4. Sequental stages of cloud evolving. Cross-sections of radar reflectivity (dBZ) field through the cloud's center in the plain ZOX (up) and field of total hail kinetic energy ($J*m^{-2}$) jn the ground (down). Value of overheating 0,5 °C in two surface barrel with d=2 km, h=0,4 km. Distance between there center is 2,4 km.

Everything discussed above is true to the single and pair clouds, that develop in the wind field witch increases linearly with height as shown in fig.2. But the further decays of the distance between the centers of overheating areas that initiate the convection lead to the situation when the character and intensity of processes change cardinally.

Fig.4 shows the dissipate stages of two cloud the center of which are parted from each other for 2,4 km. One can see that two primary cells were weak and practically have not produce precipitation that reached the earth. But the precipitation occurred to be (in the other case the cloud would not dissipate) and these precipitation formed the downdrafts. They in it's term initiated updraft (the appeared secondary cell in the center prove it). This secondary cloud have not been very strong - ~ 70 th. t of liquid precipitation have fallen from it. Theoretically the same script is not eliminated for the pair of cells in fig.3b, but because of the large distance between the primary cells the larger time is needed for the appearance of the secondary one. We can only propose that there is some critical distance between such primary clouds, whose dissipation leads to the appearance of a secondary cell during reasonable time.

The situation develops differently in the same initial conditions for clouds evolving exposed to the wind field that increases linearly with a height (Fig.2). The stage of appearance of two clouds with the centers are parted for 2,4 km (the same as in the fig.4) is presented in fig.5. It can be seen that from two primary mentioned for appearance clouds really appear only a single located to the left. The reason is the detection of the wind in the layer < 1,5 km. For account of it the left cell receives more humid air then the right one. In the situation when one of two so nearly located cell have some advantage, the second one practically couldn't develop. Therefore, if in the calm atmosphere in the given initial condition three relatively weak clouds appear – two primary and one secondary, then in the situation with wind shear one strong cloud appear.

Some words for the simulated cases for which the figures do not presented. The situation similar the case in the fig.5, results the calculation for the second profile of the wind in fig.2. The left cell successfully develops into a strong cloud with features of supercell, and the right develops as a weak cloud without precipitation, that can reach the ground. The increase of diameter of overheating surface barrel leads at first to the weakening of convection (d ~ 2,2...2,8 km), and then to formation of ring of weak clouds and at last to formation of relatively strong secondary cloud in the center of this ring. Decreasing of diameter of overheating surface barrel leads to monotonic weakening if convection up to cloud disappearance. Really it's the result of turbulent mixing of the air in updraft and environment – the less the updraft's size – the quicker the air in it do not distinct from environment. Naturally in such case can't reach the condensation layer and a cloud can't appear.

3. CONCLUSIONS

The carried numerical experiments showed that the favourable for the cloud development atmospheric conditions (humid unsuitability, dry unsuitability near the earth) appear to be the necessary but not sufficient condition for the development of strong convection. The character of surface, the non-uniformity of it's overheating are some of the impotent parameter that defined the convective intensity the type of formed clouds and the precipitation amount from them.

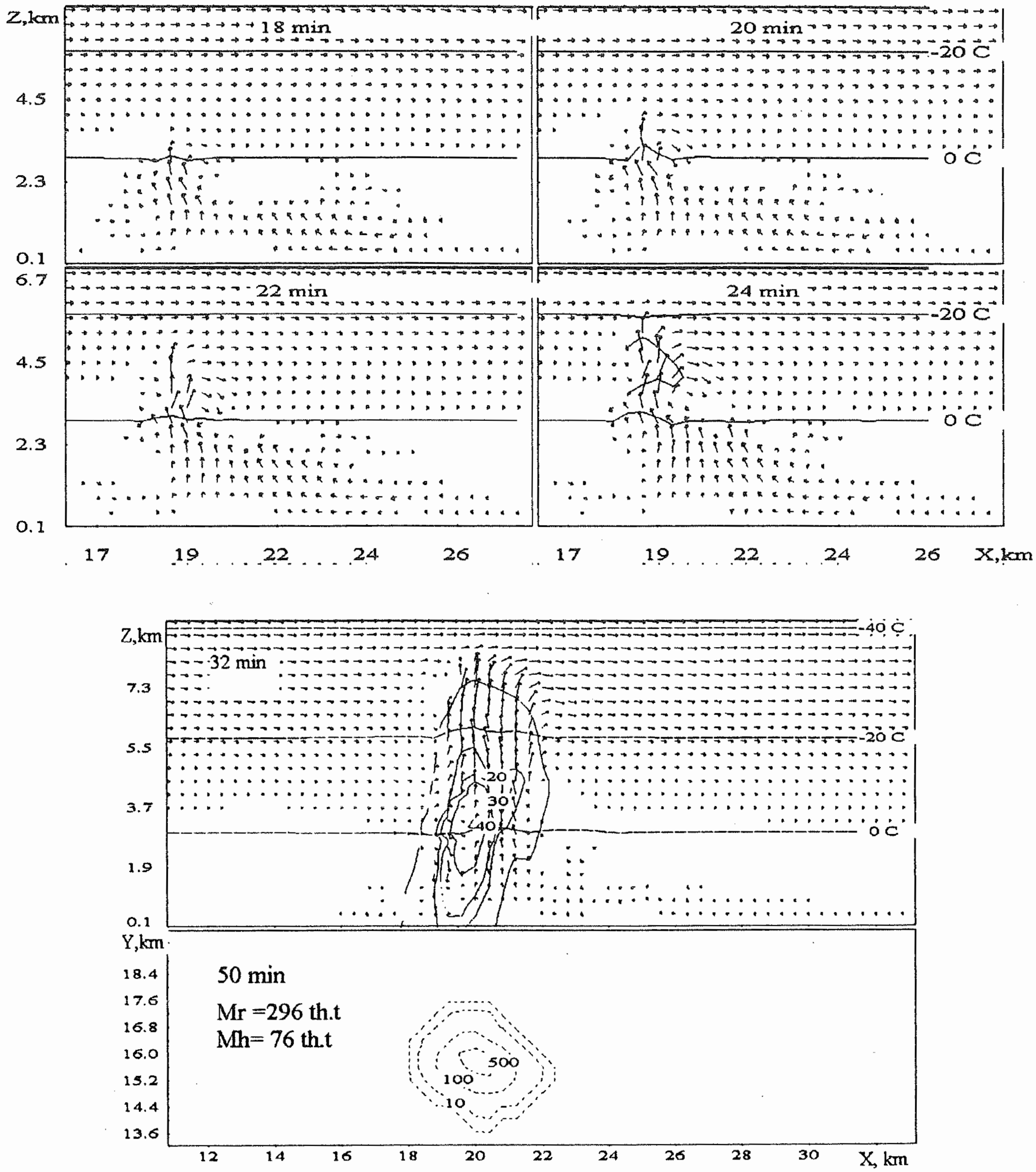

Fig.5. Sequental stages of cloud evolving. Cross-sections of radar reflectivity (dBZ) field through the cloud's center in the plain ZOX (up) and field of total hail kinetic energy ($J{*}m^{-2}$) jn the ground (down). Value of overheating 0,5 °C in two surface barrel with d=2 km, h=0,4 km. Distance between there center is 2,4 km.

References

1. Bekriaev, V. I., Gurovitch, M. V., 1991: Non-stationary numerical model Cb. Trans. of MGO, 538, 109-121 (in Russian).

2. Gurovitch, M. V., Bekriaev, V. I. 1994: Numerical model of convective cloud: some results and conclusions for naturally evolving and suppressed cases. Sixth WMO Sci. conf. On Weather Modific., II, 471-476.

3. Mazin, I. P., Gurovitch, M. V., 1998: Ice nucleation parametrization in numerical cloud models. Izv. AN. Phyzics of Atmosphea and Ocean, 34, 1, 33-44 (in Russian).

MICROPHYSICAL CHARACTERIZATION OF TEXAS CONVECTIVE CLOUDS USING AVHRR IMAGERY

George Bomar[1], William L. Woodley[2], Daniel Rosenfeld[3], Ronen Lahav[3] and Ron Drori[3]

[1]Texas Natural Resource Conservation Commission, Austin, Texas
[2]Woodley Weather Consultants, Littleton, Colorado
[3] Inst. Of Earth Sciences, the Hebrew University of Jerusalem, Jerusalem, Israel

1. INTRODUCTION

The method of Rosenfeld and Lensky (1998), which makes use of data from the Advanced Very High Resolution Radiometer (AVHRR) onboard the NOAA operational weather satellites, was used to infer the microstructure and precipitation-forming processes within Texas convective clouds. These satellites provide sub-satellite 1.1 km data in 5 channels centered at 0.65, 0.9, 3.7. 10.8, and 12.0 microns. The visible wave band (0.65 microns) is used to select points with visibly bright clouds for the analyses. The thermal infrared (10.8 and 12.0 microns) is used to obtain cloud-top temperatures. Cloud-top particle size is inferred from the solar radiation component of the 3.7-micron wave band. The method works also with the VIRS sensors on the TRMM (Tropical Rainfall Measuring Mission) satellite.

In making the inferences of cloud microphysical structure, the effective radius (r_{eff}) of fully cloudy pixels is retrieved in the manner described by Rosenfeld and Lensky (1998). This is done by inverting a radiative transfer model developed by Nakajima and King (1990), using the solar reflectance component of the 3.7 micron channel and the viewing geometry as inputs. Retrieval of particle size at cloud top is based on the fact that water absorbs part of the solar radiation at the 3.7micron wave band. While the back-scattered solar radiation is determined mainly by the surface area of the particles, the amount of absorption is determined by the volume of the particles. Therefore, larger particles absorb more and reflect less, so clouds that are made of larger droplets are seen darker in the reflected 3.7micron radiation.

Knowing the energy radiated from the sun and the portion of that energy reflected back to the satellite sensor, the fraction of the solar energy absorbed can be retrieved. This provides the basis for calculating the ratio between the integral volume and integral surface area of cloud particles in the satellite measurement volume. Conventionally, this ratio has been defined as the particle effective radius, r_{eff}.

The initial research suggests that a r_{eff} of 14 microns is a threshold value above which clouds contain precipitation-size particles that can be detected by weather radar (Rosenfeld and Gutman, 1994; Lensky and Rosenfeld, 1997). The maximum value of r_{eff} that can be retrieved by this method is 34 microns.

The evolution of r_{eff} as a function of cloud-top height or temperature (T) of growing convective elements can reveal the microphysical evolution of the clouds as they grow vertically and undergo the various microphysical process that lead to the formation of precipitation. However, the satellites carrying high-resolution AVHRR sensors typically provide only a twice-daily snapshot image of a specific portion of the earth. Thus, a single cloud cannot be viewed continuously in the imagery. This difficulty is overcome by observing an area containing a convective cloud cluster composed of cloud elements at various stages of vertical growth. This allows the compositing of the r_{eff} calculations for many clouds as if they represented a singe cloud at different times in its lifetime.

The actual composite is done in the following steps:

a) Define a window, typically of several thousand pixels, encompassing convective cloud clusters with growing elements at various stages of development.
b) Calculate the median and other percentiles of the r_{eff} for pixels within each 1°C interval of cloud top temperature (T).
c) Display graphically the T vs. r_{eff} curves of various percentiles, so that both the dependence and spread of r_{eff} as a function of T can be shown.
d) Analyze the shape of a specific T-r_{eff} curve (e.g., the median, which is the 50th percentile) to find the microphysical zones as discussed below.

The shape of the T vs. r_{eff} diagrams contains much information on the microphysical processes in the clouds. It is known that droplets grow by diffusion a small distance above the base of convective clouds while higher up in the clouds the hydrometeor growth rate is often accelerated by coalescence and ice processes. Because nearly all cloud droplets are nucleated at cloud base and cloud water mass increases less than linearly with depth, it is found that the r_{eff} in clouds with mostly diffusional growth increases by a power law of less than $D^{1/3}$, where D is depth above cloud base.

D can be approximated using T_b-T, where T and T_b are cloud top and base temperatures, respectively. It can then be seen that r_{eff} is proportional to $(T_b-T)^{1/3}$ and a plot of r_{eff} versus temperature will look like an upward convexed curve.

Corresponding author's address: William L Woodley, Woodley Weather Consultants, 11 White Fir Court, Littleton, CO 80127; E-Mail: Woodley@compuserve.com.

Therefore, a deviation from such a curve (i.e., an upward concave curve) indicates the existence of amplification mechanisms for the cloud-particle growth rate, such as coalescence and ice formation processes, which lead ultimately to precipitation.

The evolution of convective cloud-top particles as a function of depth above cloud base and cloud-top temperature can be characterized into five distinct vertical zones, not all necessarily appearing in a given cloud system:

Diffusional droplet growth zone (1): Very slow growth of cloud droplets with depth above cloud base, indicated by shallow slope of dr_{eff}/dT.

Droplet coalescence growth zone (2): Large increase of the droplet growth rate dr_{eff}/dT at T > 0°C, indicating rapid growth of the cloud droplets with depth above cloud base. This can only occur by drop coalescence.

Rainout zone (3): A zone where r_{eff} remains stable at about 20-25 microns, probably determined by the maximum drop size that can be sustained by rising air near the cloud top, where the larger drops are precipitated to lower elevations and may eventually fall as rain from the cloud base. This zone is so named, because the clouds seem to be raining out much of their water while growing. The radius of the drops that actually rain out from cloud tops is much larger than the indicated r_{eff} of 25 microns, being at the upper end of the drop size distribution.

Mixed phase zone (4): A zone in which ice first appears along with the existing liquid water. The onset of the mixed-phase zone is a function of the regimes in which the cloud hydrometeors are growing as they rise to temperatures < 0°C. If the droplets are growing by diffusion, the onset of ice is set to the temperature at which the particle size begins to increase rapidly, indicating the growth of ice particles. This is normally about –10°C. If, however, the droplets are already growing by coalescence as they enter the supercooled zone, the onset of the mixed-phase zone is set to –6°C. This is based on observations from cloud physics aircraft. In the extreme, if the drops are already raining out at temperatures ≥ 0°C, the onset of the mixed-phase zone begins at the top of the rainout zone. Such behavior is characteristic of highly maritime clouds with early rainout and glaciation, often at temperatures ≥ -5°C.

Glaciated zone (5): A nearly stable r_{eff} zone at below freezing temperatures at a value greater than that of the rainout zone. The value is probably determined by the maximum ice particle size that can be sustained near cloud top, where the larger particles are precipitated to lower elevations while aggregating and forming snowflakes. The onset of the glaciation zone occurs when the 30^{th} percentile plot of the r_{eff} first reaches a stable value with decreasing T, or a value equal or greater than that occurring at T< -40°C.

Examples of the above cloud-microphysical zones as inferred from AVHRR imagery are provided in Rosenfeld and Lensky (1998). Each zone was determined objectively using algorithms that codify the definitions above. Plotted in the examples are the 5^{th} through the 100^{th} percentiles (inclusive), every 5%, of the r_{eff} for each 1°C interval. By this process different microphysical processes are identified at different heights within the clouds, including zones of diffusional and coalescence droplet growth, rainout, mixed-phase precipitation and glaciation.

2. PROCEDURES

AVHRR imagery was used with the Rosenfeld method to classify the microphysical structure of Texas clouds with emphasis on clouds growing in seven operational seeding targets stretching from the Panhandle southeastward to nearly the south Texas coast (Figure 1). The convective regime was determined for each target on each day there was useable imagery in the period 15 April through 30 September 1999.

The classification matrix shown in Table 1 was used for this purpose. Clouds with very warm glaciation temperatures (i.e., T > -10C) and early precipitation formation (i.e., r_{eff} = 15 microns when T > 15°C) are assigned a rating of 5. These are highly maritime clouds. Conversely, clouds with very cold glaciation temperatures (i.e., T ≤ -25°C) and delayed precipitation formation to cold temperatures (i.e., r_{eff} = 15 microns when T ≤ -15°C) receive a rating of 1. These are highly continental clouds. Most targets were assigned a numerical rating on each day somewhere between these two extremes based on the viewed imagery.

On some days none of the seven targets had deep convection. On others, deep convection in the seven targets was at the edge of the satellite overpass, making analysis impossible. The number of days available for microphysical characterization ranged between 68 in the Panhandle to 41 in the extreme southeast, where there was less convective activity than "normal".

3. RESULTS

The mean convective ratings for each target by month and overall are presented in Table 2. The first value in each box is the number of days contributing to the average. Days without clouds were not included. The second number is the convective rating. This makes it possible to compare convective regimes among targets for the entire period of study and on a month-by-month basis. The study revealed systematic temporal and spatial changes in cloud structure. The clouds in the northwestern targets typically had a more continental structure with greater depths of diffusional droplet growth and lesser coalescence than clouds growing in the southeastern targets. The clouds in all areas were more continental in character early in the convective season (i.e., April) as compared to its end (i.e., September).

On 17 days complete glaciation was not detected in some of the clouds until about -38°C, the laboratory value for homogeneous nucleation. Most of the intense supercooling took place in clouds in the three most northwestern targets. On two of these 17 days the second and third authors found nearly 2 g m^{-3} of supercooled liquid water until –37.5°C using a jet cloud physics aircraft, thereby validating the satellite inferences. Considering that satellite analysis of deep convection was possible on 68 days in 1999, this suggests that such supercooling in Texas clouds takes place on at least 25% of the days. If the study had focused on clouds even farther west in Texas and into New Mexico, the percentage of days with intense supercooling likely would have been greater.

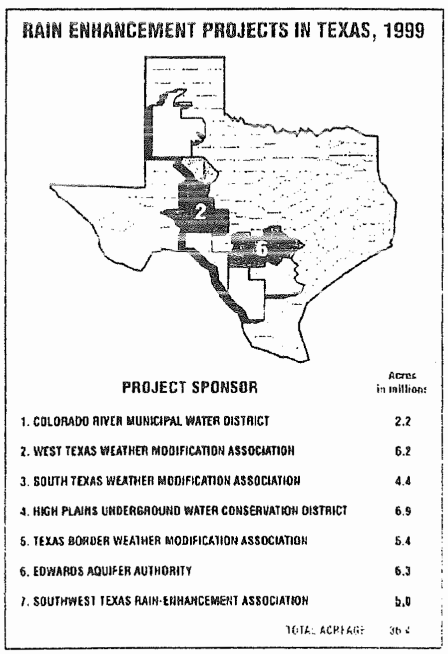

Fig. 1. Map showing the 1999 seeding targets.

Table 1 Cloud Classification Matrix
T(°C) when r_{eff} Equals 15 microns

Glaciation Temperature (°C)	> 15	15 to 5.1	5.0 to –4.9	-5 to –14.9	≤ -15
T > -10	5	4.5	4.0	3.5	3.0
-10 ≥ T > -15	4.5	4	3.5	3	2.5
-15 ≥ T > -20	4	3.5	3	2.5	2.0
-20 ≥ T > -25	3.5	3.0	2.5	2	1.5
T ≤ -25	3	2.5	2.0	1.5	1

4. DISCUSSION

This study represents the first time the microphysical structure of convective clouds has been specified over the scale of an entire state at the same moment in time. It is also the first time such characterization has been done over an entire convective season. Normally such specification is done painstakingly with a cloud physics aircraft by making monitoring passes through a few convective clouds growing over a limited area over the course of a few days.

Before getting too enthused about the satellite methodology, however, it is crucial to validate the satellite inferences of cloud microstructure. This process began with Rosenfeld and Lensky (1998), who obtained cloud physics data from research projects in Israel, Thailand and Indonesia for in situ validation of the satellite inferences of cloud microstructure. They compared satellite inferences of droplet sizes, coalescence and glaciation to the observations from the aircraft with highly encouraging results. In addition, satellite inferences of rain forming processes in Indonesian (Rosenfeld, 1999) and Australian (Rosenfeld, 2000) clouds were validated with observations by the radar on the orbiting TRMM satellite.

Recently, the second and third authors were involved in flights aboard a Lear jet cloud physics aircraft on which measurements of cloud microstructure at temperatures to –45°C were made in vigorous Texas and Argentine clouds. One of the motivations for the flights was to validate the satellite inferences of liquid water to near the point of homogeneous nucleation in these clouds. In the absence of such validation no one would have believed the satellite inferences. Having obtained such validation in virtually every instance, the satellite inferences are now far more credible.

Our inferences of cloud microstructure in Texas during the 1999 season and comparable inferences in Argentine clouds in late November 1999 through early February 2000 suggest that the presence of cloud water to the point of homogeneous nucleation (about –39°C) is far more common than believed previously. In West Texas it likely occurs on at least 25% of the days. In Argentina the frequency is likely greater than 50%. The water values can range as high as 4 g m^{-3} just before homogeneous freezing.

None of this would have been known without the satellite inferences of cloud microstructure. Further, there would have been little motivation to make the high-level cloud-water measurements with instrumentation on the jet had it not been for the satellite inferences. Now that the frequent existence of extremely supercooled water is known, meteorologists worldwide will have to revise their view of cloud physics to accept this new reality.

The satellite inferences of cloud microstructure in Texas also open a new era in the evaluation of both randomized and operational cloud seeding experiments. The effects of seeding are a function

Table 2

Mean Convective Rankings for the Texas Operational Seeding Targets By Month and Overall for the Period 15 April – 30 September 1999

Target	April	May	June	July	August	Sept.	Overall
HPUWCD	5, 1.4	9, 1.9	16, 1.6	7, 2.3	16, 1.9	12, 2.1	65, 1.9
CRMWD	6, 1.2	12, 1.8	15, 1.8	11, 2.9	12, 1.8	12, 2.4	68, 2.0
WTWMA	4, 1.6	10, 2.1	15, 2.2	9, 2.4	14, 1.9	13, 2.5	61, 2.3
TBWMA	4, 1.3	7, 1.9	10, 2.8	5, 2.8	7, 2.0	9, 3.0	42, 2.4
EAA	1, 2.5	4, 2.5	8, 2.7	10, 2.8	7, 2.1	12, 2.8	42, 2.6
SWTWMA	2, 2.5	4, 2.8	8, 3.2	12, 3.6	6, 2.6	9, 3.4	41, 3.2
STWMA	1, 2.5	5, 2.9	8, 3.2	13, 3.3	5, 2.4	10, 3.4	42, 3.1

of cloud structure. Until the satellite inferences, however, there was no way to know the structure of the clouds within the seeding targets unless a cloud physics aircraft was available. Now, with the new satellite methodology even operational seeding programs have the possibility of knowing the structure of the field of seeded clouds. This will be especially important for the partitioning of the days as a function of cloud structure. Then, one can look first for effects of seeding within the microphysical partition that should show the largest effect of seeding according to the conceptual model guiding the seeding effort.

5. CONCLUSIONS

AVHRR imagery was used with the Rosenfeld method to classify the microphysical structure of Texas clouds with emphasis on clouds growing in seven operational seeding targets stretching from the Panhandle southeastward to nearly the south Texas coast. The convective regime was determined for each target on each day there was useable imagery and suitable clouds in the period 15 April through 30 September 1999.

The study revealed systematic temporal and spatial changes in cloud structure. The clouds in the northwestern targets typically had a more continental structure with greater depths of diffusional droplet growth and lesser coalescence than clouds growing in the southeastern targets. The clouds in all areas were more continental in character early in the convective season (i.e., April) as compared to its end (September).

On 17 days complete glaciation was not detected in some of the clouds until about -38°C, the laboratory value for homogeneous nucleation. Most of the intense supercooling took place in clouds in the three most northwestern targets. On two of these 17 days two of the authors (i.e., Rosenfeld and Woodley) found large quantities of supercooled liquid water near –38°C using a jet cloud physics aircraft, thereby validating the satellite inferences. These observational facts would appear to defy conventional meteorological wisdom regarding the supercooling of clouds.

The ability to infer cloud microstructure from space over large areas also will prove to be important to the evaluation of research and operational cloud seeding experiments. These inferences can be used to partition the overall data into microphysical categories. At the two extremes are clouds exhibiting deep diffusional growth, no coalescence and delayed glaciation and clouds with shallow to no diffusional growth zone, rampant coalescence and early glaciation. The evaluation for seeding effects in each of the seeding targets can then be done within each microphysical category, since the effects of seeding likely will be a function of cloud microphysical structure. For example, clouds with intense coalescence that are totally glaciated by –10°C should not be responsive to either a glaciogenic or hygroscopic seeding agent. Thus, evaluation within each microphysical category will decrease the overall natural variability and increase the chances of detecting a seeding effect. If no seeding effect is evident for the clouds identified most suitable by the conceptual model, there will be reason to question either the conceptual model or the execution of the seeding.

6. ACKNOWLEDGEMENTS

This research effort was funded by the Texas Natural Resource Conservation Commission (TNRCC) through a contract with Woodley Weather Consultants. We are most grateful for this support.

7. REFERENCES

Rosenfeld D. and I. M. Lensky, 1998: Spaceborne sensed insights into precipitation formation processes in continental and maritime clouds. Bull. Amer. Meteor. Soc., **79**, 2457-2476.

Rosenfeld, D., 1999: TRMM first observed direct evidence for smoke from forest fires inhibiting rainfall. Geophys. Res. Let., **26**, 3105-3108.

Rosenfeld D., 2000: Suppression of Rain and Snow by Urban and Industrial Air Pollution. Science, **287**, 1793-1796.

Thunder Storm and Noise of Infra sound

Y.J.Han[1], S.W.Li[1], H.Chen[1],T.Chen
[1]Department of Intelligent Sounding ,Guilin Institute of The Electronic Technology,Guilin,541004,China

The Cloud Sc and Cb develop with the storm current ,by the time, the current emitting wide frequency band noise spectrum, if we recognize the acoustic or gravity wave are background noise Vs synopitical wave such as Rossby wave[□]. In the background noise IF-sound, there are wide band of frequency from 2 to 0.01 Hz(0.5'-100'period),the interesting fact is that the strong convection such as thunder storm, tornado, hailstone, not only develop with IF-sound wave emission [2] ,but also exist another shorter period (1-2') IF-sound[5] emission about 2-6 hours in advance. The storm source in the pregnancy time near the center of thunder storm occurring later. During four years (1995 , 1996 , 1997,1999), we defined the IF-sound(1-2') as a precursor IFP of thunder storm . It seems different appearing different from the storm emission IF-sound(2-20') i,e. IFC.

A warning system to be composed of IF-sound sounding star net (six stations, maximum distant about 6Km, minimum distant about 360m) and a single station of VLF coupled IF-sound of lightning emission developed and established a site over the Northern Bay of the South China Sea, near the city ZhanJang. With this observation and warning net of IF sound and VLF electric-magnetic wave, there are 21 times correct predictions of strong convection (even wind speed $\geq$12m/s.gale speed $\geq$ 17m/s ,□ $R_6\geq$10mm,with lightning. thunder sound),but three times not be correct (the even speed $\approx$10-11m/s, gale speed $\leq$15m/s, with weak lightning and thunder sound). The IF-sound sensor response of frequency is 0.5s-500s, direct capacity digital out, not with compensation of DC amplifier. The VLF sensor is three axis passive electric field strength detection. the band of wide frequency about 40KHz. The 1999 result haven't knew because we left from December of 1997 to now. There are two data processors of computer with real data fusion soft wares.

Author' address: Y.J.Han
Guilin Institute of Electronic Technology
GuiLin 541004 China
E-mail: hmyjhan@gliet.edu.cn; decisd@gliet.edu.cn

Time integral filter, two triangle nets used for position technology with arrival time difference of storm IFC and storm precursor IFP, and couple technology from two signal of VLF and IF-sound by lightning emission used for position of IFC. Six lines dynamical display from serious IF signal with real FFT, correlation and adaptive analysis. By means of the precursor IFP characteristics and its track of dynamical motion there are some relations between storm precursor IFP and storm IFC, the acoustics and synoptics, acoustic and electric wave relation is given by fig 1.

The electric field strength measurement of cloud haven't operated to now .From the pregnancy stage to the calm stage, the precursor IFP appears repeat again and again. It suggests that the turbulence (emission high frequency 1-2' of precursor IFP) develop to the strong turbulence and evolute to the prosconvection stage . The pros-convection (emission lower frequency(5—100')IF-sound) develop until the top stage, and forms the strong convection (emission the shortest lightning sound or IFC 0.2-01'). In the calm stage sometimes the acoustic wave disappear but the gravity wave appear and the acoustic-gravity wave present alternatively . From calm stage to outburst stage of the turbulence develops with entrainment of the cool air or wet warm air .The vapor phase change ,the collision of water drops by the gravity or electric charge attraction induce the positive feedback process. The big drops grow up fast than small drops and absorb almost latent heat and the eddy kinetic energy and the turbulent motion evolute to the single direction motion as a prosconvection. The prosconvection induces the tropopause oscillation, so that it stimulate the long period IFC or gravity wave emission.

Above all the conditions of turbulent motion depend on the thermal-dynamical unstability in the cloud but the prosconvection or strong couvection depend on the entrainmen place or time. So the strong convection weather forecast have some occasional factors. At all ,the turbulence to the convection is the catastrophic change. The entropy of system appears negative entropy flow. The process will emission precursor IFP or outburst lightning

Pregnancy stage	Outburst stage
A: Synoptic characteristics Sc cug or Sc cast □3/10 wind speed□1m/s near situation RH>80%	Wind direction change Cb□8/10□R$_6$□10mm Even wind speed□12m/s max speed□17m/s
B: acoustic characteristics Storm precursor IFP 1- 2' period serious pulse not dispersion, half amplitude	Storm IFC 5—20' serious wave +lightning thunder sound (0.5—0.2s)
C: Electric field characteristics 15m high ,field strength($\overline{D}$) $\overline{D}$ -(10^0—10^{-1})mv/cm □D—(10^1—10^3)mv/cm	$\overline{D}$ -(10^0-10^2V/cm) □ D—(10^1—10^2)v/cm □Dmax—10^3 v/cm

The scheme dynamical evolution process seem to be these as follows:

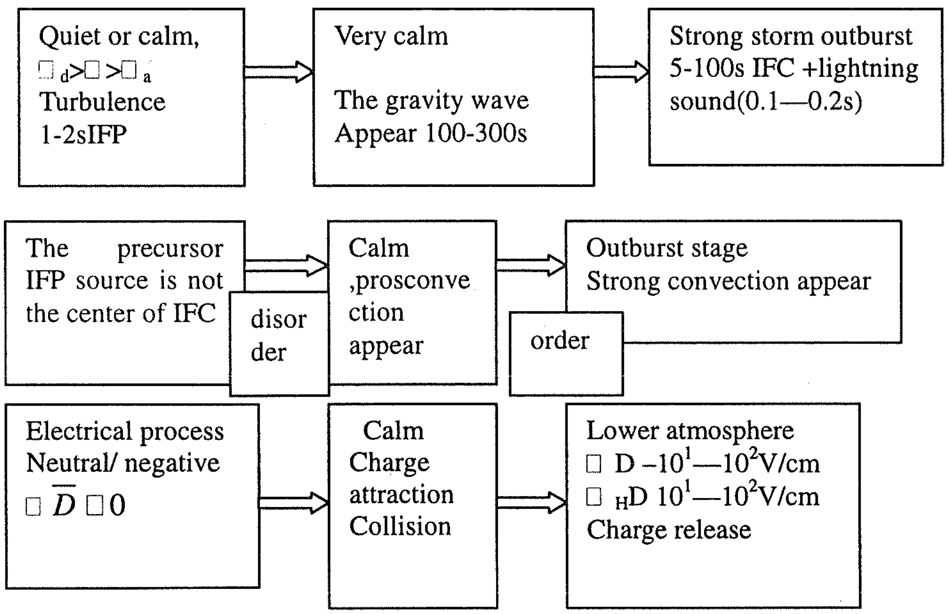

Figure 1

emission sound and VLF wave so that the nowcast of storm might be made by many methods.

The prediction problem of strong storm, such as tornado ,hailstone and cyclone, by means of synoptical or numerical methods, there are some difficult (especially nowcast) as follow: the resound is 2-4 times a day, the time grad(ΔT) is too long that the micro or mesacale weather system is miss out by the time grad, as same as entropy flow forecast methods. One hand, observation station net is too sparse, the strong convection system scale is about < 100Km and it's life is about 2-4 hours. The other hand , in the mathematical model the presume about filter keeps out the gravity and acoustic wave, used the static equilibrium formulae, so the strong convection nowcast constantly by means of extension methods of real weathers condition.

By means of radar, specially by the Doppler synoptical radar(1-3cm), these have some advantages than above synoptical methods, such as real time observation ,real time forecast. But in the pregnancy stage the weak convection cells haven't radar echo or have quite weak backward scattering echo if the vapor quantity is very low at the early time of cumulus developing stage and the turbulent wind speed is small (0-1m/s), so the frequency shift of echo wave is small and water drops scattering echo is small too. But the Sc cug or the Cb cloud in the weak convection system develop so fast as the radars operate hurry up, and constantly miss out the prediction effect time specially in the some countries. The economical value Vs the radar cost is too low. The methods seems well but more difficult on the mountain region or on the sea.

By means of the IF and VLF coupling methods ,these are more interesting in the developing country. Because the precursor(IFP) prediction and the IFC coupling VLF technology cost lower than Dopplor radar system but the economical value as same as the radar monitor. Otherwise the Internet established on more country. The IF and VLF sounding data by ATM cable or CDMA net may transfer to the every family early than radar data by one or two hours. Because the IFP data is the precursor information of storm but the Radar data is the real storm outburst information. In the U.S. the radar sounding net is quite close. But the tornados appear constantly and destroy many lives and houses ,and the correct rate of prediction for it is about 60-70%. the fact tell us that the single method to forecast the mesoscale strong convection weather is not enough to the protection. The information fusion of radar, IFP IFC ,VLF and weather observation have to be made and contrast to each other.

The radar sounding more precise than IFC(IFP)+VIF sounding in the definition of storm position at two orders , but the latter is early than the radar in the discovering of storm take place about 1-2hours. So the joint prediction is important.

Acknowledgement:

The IF-sounding and IF/VLF system study is sponsored by the NHOC here thanks to NHOC and colleagues very much.

Reference:

1. E.E.Gossard&W.H.Hooke Waves in the Atmosphere Elsevier Sci.Co. 1975

2.R.K.Cook. Strange Sounds in the Atmosphere Physical Acoustics Dowden Hutchinson&Ross.Inc 1963

3.Han yuan-jie Some relations between microbaromic Waves and Earthquakes Acta Seismologica Sinica vol2.No2.May 1980

4.R.O.Doaglao,O.W. Whitaker, R.W. Rodney Acoustic efficiency analysis using infrasound from NEOS [C] Proc.Int. conf. Eng. Construct. Oper. Space Vol. 1996. Part1.(of2)

5.Han Yuan-jie, Li shao-wen,Chen Hong The use of VLF and IF-sound sounding system for Developing and Discussion of Mesoscale catastrophic strong convection weather(thunder storms)Nowcasting and warning system over Northern Bay of South China Sea Plateau Meteorology Vol19.No 2 May. 2000

Cloud edges and evolving wave; see Volume 1, paper 9.6, p. 633.